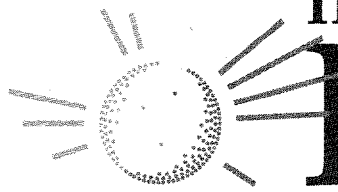

INERTIAL CONFINEMENT FUSION

1995

ICF

Annual

Report

UCRL-LR-105820-95
Distribution Category UC-712
October 1994–September 1995

Printed in the United States of America
Available from
National Technical Information Service
U.S. Department of Commerce
5285 Port Royal Road
Springfield, Virginia 22161
Price codes: printed copy A03, microfiche A01.

MS Date
June 1996

MASTER

Lawrence Livermore
National Laboratory

ACKNOWLEDGMENTS

We thank the 32 authors and their co-authors who contributed to this *Annual Report*. Your work, published in our four *Quarterly Reports*, is compiled here to highlight our accomplishments for the year. We are grateful for your willingness to take time from busy schedules to write the articles that describe your work. To the four *Quarterly Report* Scientific Editors' Jack Campbell, James E. Murray, S. Gail Glendinning, and John D. Lindl, their efforts and diligent review to ensure the quality of each *Quarterly Report* are appreciated. We also thank the secretaries for typing manuscripts, arranging meetings, and offering other invaluable assistance.

We thank Technical Information Department (TID) editors Jason Carpenter, Al Miguel, Peter W. Murphy, and Dabbie P. Schleich for editing and managing the production cycle; and designers Ken M. Ball, Daniel S. Moore, and Linda L. Wiseman for providing expertise in graphic design and layout. Additional thanks to TID's Output Center for working with Dan Moore to convert electronic images to the format needed to provide such high-resolution photographs, separations, and negatives for printing.

We appreciate the support of Ron Natali, the Government Printing Office Coordinator, who worked with the Government Printing Office to obtain high-quality printing; and Mary Nijhuis of TID's Publications Services and TID's Print Plant for making sure that each publication was distributed with dispatch.

To all of you, thank you for your talents and dedication.

TABLE OF CONTENTS

ICF Program Overview

Introduction

Lawrence Livermore National Laboratory's (LLNL's) Inertial Confinement Fusion (ICF) Program is a Department of Energy (DOE) Defense Program research and advanced technology development program focused on the goal of demonstrating thermonuclear fusion ignition and energy gain in the laboratory. During FY 1995, the ICF Program continued to conduct ignition target physics optimization studies and weapons physics experiments in support of the Defense Program's stockpile stewardship goals. It also continued to develop technologies in support of the performance, cost, and schedule goals of the National Ignition Facility (NIF) Project. The NIF is a key element of the DOE's Stockpile Stewardship and Management Program.

In addition to its primary Defense Program goals, the ICF Program provides research and development opportunities in fundamental high-energy-density physics and supports the necessary research base for the possible long-term application to inertial fusion energy (IFE). Also, ICF technologies have had spin-off applications for industrial and governmental use.

Highlights of ICF's FY 1995 Program accomplishments included the following:

- Completed experimentation on Nova to fulfill the National Academy of Science (NAS) Nova Technical Contract[1] ignition target physics goals for indirect drive, and continued weapons physics experiments in support of stockpile stewardship.
- Received approval of Key Decision 1 (KD1) for the NIF Project. On October 21, 1994, Energy Secretary Hazel O'Leary announced her endorsement of KD1, which affirms the Project's mission need and authorizes its transition from conceptual design to preliminary engineering design. Secretary O'Leary also stated that LLNL is the preferred site for the Project because of its resident technical expertise and the existing technical infrastructure.
- Completed the initial Beamlet laser experiments to verify the NIF design performance, and initiated aggressive developments in laser optics and target area technologies to support NIF performance, cost, and schedule goals.

Target Physics

In FY 1995, the Target Physics Program completed a milestone in ignition physics and started a major change in mission and organization. For the past several years, the Program has been oriented toward completing the Nova Technical Contract (NTC) defined by the 1990 NAS report.[1] In particular, the report defined specific experimental goals that address fundamental issues of indirect-drive ICF. Together with Los Alamos National Laboratory (LANL), we have made successful completion of the NTC our highest priority. During the past year, the Inertial Confinement Federal Advisory Committee (ICFAC) concluded that the Target Physics Program achieved a major mission because: (1) the NTC is essentially complete, (2) there has been significant progress in establishing a robust target design for the NIF, and (3) major progress has been made in achieving adequate target surface finish of cryogenic ignition targets. Because of this success, we plan to increase our efforts on direct-drive ignition physics, ignitionless Science-Based Stockpile Stewardship (SBSS) with lasers, and advanced ICF technologies, especially with short-pulse lasers.

X-Ray Drive Ignition Physics

This section discusses progress in three major areas of x-ray drive ignition research that we explored during FY 1995:

- Target experiments using Nova to improve our understanding of ignition target physics,
- NIF ignition design optimization, and
- Demonstrating that cryogenic targets with adequate surface finish can be built.

Target Experiments Using Nova. During the year, successful experiments were conducted by LLNL in collaboration with scientists from LANL and the Centre d'Études Limeil–Valenton, France. Results from these experiments include: (1) demonstrating ways of reducing stimulated Brillouin scatter (SBS) and stimulated Raman scatter (SRS) from NIF-scale plasmas, (2) understanding and controlling symmetry shifts from those predicted by calculations in Nova implosions, and (3) understanding the difference

between predicted and measured yields on Nova implosions with hydrodynamic growth factors ~150. In addition, we have demonstrated reduced hohlraum wall loss using material mixtures.

In hohlraum and laser–plasma physics, investigations have concentrated on reducing the levels of SBS and SRS from "gas-bag" plasmas and gas-filled hohlraums. For the gas bags over the range of NIF intensities (5×10^{14} to 2.5×10^{15} W/cm^2), the measured levels of SRS and SBS meet the NIF specifications of <15% for energetics. For more details, see the articles entitled "Laser–Plasma Interactions in Large Gas-Filled Hohlraums" on p. 97 and "Laser–Plasma Interactions in NIF-Scale Plasmas (HLP5 and HLP6)" on p. 305 of this report.

We have also measured that laser-beam smoothing and enhanced Landau damping in the Au-wall plasma reduce SBS and SRS to 1 to 2% levels in Nova scale-1, gas-filled hohlraums compared with higher levels originally seen without beam conditioning. These measurements were made with only one beam of Nova—only one beam is fully diagnosed for accurate backscatter measurements—but we expect that the conclusion will not change for all 10 beams.

Implosion symmetry studies on Nova have been extended in an effort to understand and control symmetry shifts in gas-filled hohlraums similar to present NIF baseline designs. These experiments were performed by varying the hohlraum length and the beam together, similar to previous symmetry experiments. See the article entitled "Nova Symmetry: Experiments, Modeling, and Interpretation (HLP3 and HLP4)" on p. 293 of this report. The experiments demonstrate that the symmetry is reproducible, and for unsmoothed laser beams, the hohlraum length for a given capsule distortion is offset from the calculation and the empty hohlraums by ~150 ± 25 μm. This offset is largely explained by a shift of the emission pattern at the hohlraum wall towards the laser entrance holes, as measured by directly observing the position of the soft x-rays produced by the laser with a gated soft x-ray framing camera.

Experiments in gas-filled hohlraums to measure soft x-ray hot spot motion simply using a beam smoothed with a binary random phase plate (RPP) were in agreement with LASNEX modeling predictions. With a RPP, the x-ray wall emission patterns for gas-filled hohlraums were very similar to those for empty hohlraums. Three-dimensional (3-D) wave fluid calculations show that at ~2×10^{15} W/cm^2, an unsmoothed laser beam in a transversely flowing plasma would be expected to filament and be deflected, whereas a smoothed laser beam would not filament nor be deflected. The experimental results are consistent with these calculations. We plan to implement beam smoothing on all 10 beams of Nova for an integral test of these results on implosions.

Nova implosion experiments have concentrated on implosions with hydrodynamic growth factors of ~150 [defined as the growth of a small pertubation on the outside surface after Rayleigh–Taylor (RT) instability growth during acceleration, feed through the shell and inner-surface perturbation RT growth during deceleration]. These high growth factors are achieved by doping the plastic capsules with materials (Br or Ge) with high x-ray absorption coefficients that act as a preheat shield thereby increasing capsule performance. For high-growth-factor implosions (HEP4), calculations including the 3-D effects of low-order capsule wall thickness variations (P_1) reproduce the smooth capsule HEP4 experimental neutron yields. Without these effects, the calculated yields are a factor of 2 to 4 too high. These calculations also offer a possible explanation for the experimental yield variation since the effect of the P_1 variation depends on its orientation relative to the intrinsic hohlraum asymmetry. See the article entitled "High-Growth-Factor Implosions (HEP4)" on p. 271 of this report for more details.

Modifications to Nova will make it possible to achieve NIF-like time-dependent symmetry control for HEP4 experiments. Current experiments on Nova with a single ring of five discrete spots on each end of the hohlraum have an $m = 5$ azimuthal variation in flux and cannot control the polar time-dependent flux variation in asymmetry. Kinoform phase plates, similar to those being developed for NIF,[2] provide an approach that will allow us to obtain two rings on each side of a Nova hohlraum. Each ring will be much more uniform in the azimuthal direction than with current Nova illumination. The rings can have independent pulse shapes by using two oscillators that produce different pulse shapes for different halves of each Nova beam.

In addition, Nova experiments similar to those that verified wall loss of x rays in Au[3] have shown that a mixture of Au and Gd results in a lower hohlraum wall loss of x rays than with Au alone. This reduction occurs because of the overlaps of peaks and windows in opacity for the two materials. Projecting these results to NIF hohlraums made using these materials, the reduced wall loss is equivalent to 100- to 200-kJ reduction in laser energy required for ignition.

NIF Ignition Design Work. For NIF, a broad set of target designs has been established. The point design for NIF is a plastic ablator capsule, requiring 1.3 MJ of laser energy absorbed in the hohlraum. Designs have been developed that use a variety of other ablator materials and that ignite using significantly lower laser energy. In addition, many parameter variation studies have been done on the point design to study the effects of outer surface finish and inner cryogenic ice surface finish of the capsule and time-dependent drive asymmetry and their coupling.

Integrated calculations, in which the entire target is modeled from laser deposition through thermonuclear burn, have now been done with good ignition performance at laser energies as low as 900 kJ. For details, see the article entitled "Ignition Target Design for the National Ignition Facility" on p. 215 of this report. These smaller targets are simple geometric scales of the point design at 1.3 MJ, with details of the design adjusted to recover symmetry and pulse shaping.

The point design performs well in modeling that includes all of the following:

- Surface roughness perturbations of 20 nm rms on the CH ablator surface and 0.5 μm rms on the deuterium–tritium (DT) ice inner surface.
- Irradiation asymmetry as determined from integrated calculations.
- Additional irradiation asymmetry that is greater than would result from laser pointing and power balance specifications and is compatible with reasonable experimental precision in a campaign to measure the time-dependent asymmetry.
- Variations in the time-dependence of the total x-ray flux that, once again, are larger than would result from laser power balance specifications and are consistent with an experimental campaign to measure the time-dependent flux.

A sensitivity study was done in which laser powers and pointing were varied in integrated calculations, including both the capsule and hohlraum (see p. 215 of this report). Generally, the tolerance is a factor of several larger than the expected deviations (which are dominated by expected experimental uncertainties—the deviations from laser power imbalance and pointing uncertainty are significantly smaller).

For NIF targets, variation in beam pointing and cone-to-cone pulse shapes can be used to control P_6 flux variations. Using this control, the level of P_6 identified in earlier designs has been reduced. With this reduction, the tolerable pointing variations are increased a factor of 2 to 3 to about 200 μm for the NIF inner beams and 350 μm for the outer beams. This is well within the individual NIF beam pointing specifications of 50 μm. Average ring locations can be specified with even better accuracy because of the significant number of beams in each ring.

NIF Target Fabrication. A smooth surface finish is required for the inner surface cryogenic ice to minimize growth of perturbations, which could degrade the implosion. For the NIF point design, an ice surface finish of ~3 μm rms is required if this is the only source of perturbation growth. When the effects of outer-surface roughness and time-dependent asymmetry are included, an ice surface finish of ~ 1–2 μm rms is required. In FY 1995, an aggressive, collaborative program was conducted with LANL to demonstrate the NIF goal of ~1 μm rms for surface finish of the inner ice layer in a curved geometry. During the past year, improved experimental design and diagnostics have demonstrated surface roughnesses <1 μm produced by native beta layering. To increase the margin for ignition, we are developing several techniques to reduce the DT roughness even further. Three techniques to control DT roughness are (1) applying a heat flux across the gas–solid interface by resistively heating with microwaves the DT gas in the center of the target, (2) increasing the bulk heating rate of DT by pumping the collision-induced infrared (IR) absorption band of the solid, and (3) controlling the DT crystal size with a foam substrate.

Native beta layering produces smooth, thick DT layers (with 1 μm rms surface roughness) because the tritium decay volumetricly heats the solid DT. This volumetric heating causes thicker parts of the layer to have a higher temperature than the mean, producing an increased sublimation, thereby reducing surface roughness. DT roughness is controlled by the increase in surface temperature with increasing layer thickness. The increase in surface temperatures with thickness competes with the anisotropic surface energy of the crystalline layer to determine the final surface finish. We can reduce DT surface roughness by increasing surface temperature gradient. This is done either by applying a heat flux across the gas solid interface or by increasing the volumetric heating rate.

We have demonstrated that increasing surface heat flux can improve surface roughness in D_2 experiments. Interferometric measurements of the surface roughness of D_2 layers on flat substrates show that the surface roughness decreases rapidly with increasing surface heat flux, achieving smoothnesses of ~5× less than obtained using native beta layering. We have also measured the surface roughness of D_2 and DT layers in a curved toroidal geometry with the NIF-scale radius of curvature, using shadowgraphy. Again we find that the surface roughness decreases with increasing heat flux, precisely the same as in the surface roughness measurements on flats. These experiments show that D_2 has the same surface roughness as DT when the heat flux is the same as the native DT value. We will apply this technique to NIF capsules by resistively heating the DT gas in the center of the target. An experiment to measure the DT roughness vs resistive heating is under way at LLNL.

We have also shown by measurements and calculations that IR heating reduces the surface roughness of solid hydrogen layers. By pumping the collision-induced IR absorption band in solid hydrogen, we convert IR light into bulk heating, which allows us to control surface temperature and layer thickness. This technique can also be used to smooth solid D_2 layers as well as DT for the NIF. We have measured bulk heating up to

30× the DT value by native beta layering, limited only by IR laser power. Vibrational relaxation rates suggest we can generate up to 600× the volumetric heating rate in DT by IR heating.

The final technique we are developing to improve surface finish is to control the nucleation and crystal size by using only a thin, DT layer above 100 μm of DT-filled CH foam. Interferometric measurements show that thin D_2 layers over foam are significantly smoother than without foam. A thin layer of DT over a fine cell foam will likely have a surface roughness less than 0.5 μm rms without any external heating. Calculations have shown that a CH foam-lined plastic target will perform as well as one without foam, as long as there is at least 10 μm of DT above the DT-filled foam for the ignition hot spot.

A common feature of all NIF capsule fabrication technologies, except machined Be, is a 2-mm-diam, thin-walled polymer mandrel upon which ablator material is deposited. From our study of Nova capsules, we have demonstrated that (1) the capsule surface finish rms is dominated by the lower (longer-wavelength) modes and (2) that the origin of these modes is the underlying polymer mandrel and not the ablator material. Thus, a key technical challenge for the production of high-quality NIF-scale capsules is the development of techniques that can produce high-quality, 2-mm-diam polymer mandrels.

Current solution-drop-tower techniques that are used for Nova-scale polymer mandrels are limited to mandrel production in diameter sizes less than 1 mm. Thus, several different capsule fabrication technologies are being developed to meet the needs of NIF ignition targets. The most straightforward method is to extend the size range of microencapsulation techniques used currently for Omega targets at the Laboratory for Laser Energetics at the University of Rochester from 0.9 mm to 2 mm. These techniques have been shown to produce shells with very smooth outer surfaces, but, especially on larger, thicker-walled shells, there are often interior wall defects (voids). To solve this problem, we have developed a decomposable mandrel technique in which the flawed microencapsulated shell is overcoated with a thermally stable polymer and then heated. This heating decomposes the mandrel to gaseous products that diffuse through the thermally stable overcoat, leaving a hollow shell whose quality depends only on the outer surface of the initial mandrel. We are also working with scientists at the Lebedev Institute in Moscow to adapt their drop-tower technique, which uses a solid polymer feedstock as opposed to LLNL's solution droplets, to the production of NIF-scale shells. The current size range using this technique is about 1 to 1.5 mm. We are also examining interfacial techniques in which a 2-mm droplet of an oil phase is suspended in an aqueous phase, and mutually reactive components in each phase polymerize at the surface to form a solid shell. Comparison of the surfaces of shells produced by these techniques to the requirements for NIF capsules leads us to expect that one or more of these techniques will provide the needed 2-mm mandrels for NIF targets.

For the CH point design, we are confident that the existing plasma polymerization techniques used for Nova capsules will meet the needs of NIF targets. As an alternative to hemishell machining and bonding for the Be point design, we are exploring the use of metal sputtering techniques. We have demonstrated that NIF-scale ablator thicknesses of Be can be sputter deposited on plastic mandrels. The surface finish of these coatings must be improved. To accomplish this, the sputtering techniques offer several options, such as substrate biasing or chamber pressure modification. One key advantage of the sputtering technique is that the overcoated shells are permeable to hydrogen. In addition, the technique is easily modified to allow graded inclusion of higher-Z metallic dopants such as Cu.

Advanced Code Development

For more than 20 years, LASNEX has been the workhorse for ICF 2-D design done at LLNL, LANL, and Sandia National Laboratories (SNL). To meet the more advanced needs for problems that are inherently 3-D in nature, new hydrodynamics codes (ICF3D and HYDRA) are currently under development. Recently, about half of this effort has been aided and accelerated by the DOE's Accelerated Strategic Computing Initiative. In addition, we continue to improve our plasma–physics codes (e.g., bZOHAR and F3D) and others (WARP3D and BASIS).

3-D Hydrodynamics Codes. ICF3D is radically different than LASNEX in that it is written in C++ and has entirely new treatments of hydrodynamics that are considered to be more flexible and accurate. We envision that eventually it will include full physics, namely the usual high-energy-density physics of hydrodynamics, radiation flow, and burn product transport. This would also include laser transport, non-local thermodynamic equilibrium (LTE) atomic physics, material strength, electromagnetic fields, electron transport, and eventually even approximate plasma–physics simulation capability.

Increased accuracy will be achieved in three ways: replacing finite difference with finite element numerical methods, using the most optimal coordinate system for a given problem, and adaptively refining the mesh to better resolve important features.[4] Robustness and ability to handle complicated geometries will be achieved by an unstructured grid with mesh reconnection and arbitrary Lagrange Eulerian methods. We have made considerable progress on this code in FY 1995, including running its hydrodynamics package in massively parallel mode on up to 128 processors of the T3D machine. The tests performed to date on this parallelization have shown very efficient scaling and speed of the problem

by going to the many processors in parallel. The challenge will be to parallelize the other components of the code, such as radiation and electron transport.

We developed HYDRA, a simplified 3-D radiation–hydrodynamics code to analyze Nova experiments, since 3-D issues are a challenge in interpreting capsule implosions. This code has had a tremendous amount of success explaining 3-D planar RT experiments and in discovering the 3-D effects on implosion capsule yield of the coupling of capsule low-mode asymmetries with Nova hohlraum low-mode drive asymmetries. See the article "Three-Dimensional Simulations of Ablative Hydrodynamic Instabilities in Indirectly Driven Targets" on p. 168 of this report for one application of the HYDRA code.

Plasma Physics Codes. We are actively developing a variety of plasma physics codes to help explain important phenomena at scales too small to be treated properly or efficiently by the hydrodynamics codes. Currently, ZOHAR is our 2-D 3-velocity particle (electron and ion) in cell (PIC) code—used both for the fundamental understanding of laser–plasma interactions in conventional ICF targets and for the fundamental understanding of high-intensity relativistic interactions for the fast ignitor concept.[5] Also, understanding the fundamentals of plasma physics is an important constraint on achieving high radiation temperature (T_r) on NIF. Although a 3-D version of this code has not been developed, we have produced a hybrid plasma code, bZOHAR, for studying SBS and filamentation. In bZOHAR, the ions are treated as particles but the electrons as fluids, allowing the study to calculate for much longer times in the problem. We can therefore investigate the nonlinear development of SBS, crucial in understanding the actual levels to expect of SBS in the NIF hohlraum targets.

At yet another level of description, closer to the hydrodynamics scale, is F3D, a 3-D laser propagation fluid code that treats filamentation, beam steering and smoothing, and models for SBS and SRS. It has played a central role in understanding present Nova plasma–physics experiments and extrapolations to the NIF. Enhancements under way include a better nonlinear hydrodynamics package that will help us better model the startup phase (window and gas burn-through) of Nova and NIF gas-filled hohlraums, beam deflection in gas-filled hohlraums, and a variety of challenging tasks involving channeling for the fast ignitor.

Other Codes. WARP3D is a 3-D PIC code used in the design of accelerators such as heavy-ion accelerators that could one day be the driver in a facility superseding the NIF. For applications of this code, see the article entitled "Progress Toward a Prototype Recirculating Ion Induction Accelerator" on p. 179 of this report. WARP has other stockpile stewardship applications as well. It is used to design accelerators for x-ray radiography for the Advanced Hydrodynamics Testing Facility. Furthermore, it has been identified as an important code in evaluating designs for the accelerator production of tritium.

BASIS is a sophisticated computer science shell in which most of the above-mentioned hydrodynamics and plasma–physics codes reside. It makes each of these applications programmable by its user and supplies common facilities such as a portability layer, input/output, graphics, dump files, and time history collection. Nevertheless, it is becoming obsolete for current technologies, due to its limitations of running the large, monolithic Fortran 77 program on a single computer. In the future, programs are going to be written in a variety of languages, both standard and with experimental parallel extensions, and are going to run on a variety of different hardware, both distributed and massively parallel. Using object-oriented technology, we can respond to the need to make programs programmable by the users in a heterogeneous hardware and software environment. We are currently in the technology evaluation phase, which we expect to complete in FY 1996, having at least some form of the prototype working by the end of FY 1996, and moving to a production system in subsequent years.

Direct-Drive Ignition Physics

In November 1995, the DOE Office of Research and Inertial Fusion requested that the Office of the NIF include direct drive in the NIF preliminary (Title I) design. This coincided with the completion at the University of Rochester of the upgraded Omega facility. As a result, the Target Physics Program at LLNL will play an increasing role in exploring the technical issues of direct-drive ignition targets. LLNL has maintained a collaborative program with the University of Rochester on direct drive for several years.

In FY 1995, we demonstrated and documented[6] a way of simply modifying the NIF beam layout to achieve a low-mode asymmetry of illumination of direct-drive targets (~1%). This modifies the target area illumination symmetry, which involves moving 24 of the 48 quadruplets of beams (16 from the outer rings and 8 from the inner rings) to rings close (~15°) to the equator. This modification could be made in a relatively short time.

We continued efforts to understand the growth of RT instabilities with directly driven targets. Experiments demonstrated that the longer wavelength and increased brightness of an x-ray laser over x-rays from a laser–plasma can be exploited to measure small areal density modulations in the initial phases of laser imprinting. This is the second use of an x-ray laser as a tool to be used for diagnosis of a high-density plasma using either the coherence or high-brightness properties of the x-ray laser.

Ignitionless Science-Based Stockpile Stewardship (SBSS)

For many years, the ICF Program has supplied Nova shots for LLNL's Defense and Nuclear Technology (D&NT) and Physics and Space Technology (P&ST) Directorates for experiments to benchmark weapons design codes. In FY 1995, this work continued with approximately 220 Nova shots supplied to scientists in D&NT and P&ST for experiments in hydrodynamics, equations-of-state (EOS), opacity, radiation flow, atomic microphysics, and x-ray laser diagnostic development.

In FY 1995, the ICF Program identified experiments of direct relevance to weapons, where there is a natural overlap with ICF in which scientists from the ICF Program will participate with D&NT and P&ST scientists. The areas identified so far as the so-called ignitionless SBSS projects are the high-temperature hohlraums, the EOS of cryogenic hydrogen isotopes, and the growth of hydrodynamic instabilities in regimes of high pressure and relatively low temperature where the strength of material modifies growth rate.

Advanced Technologies and Enhancements

In addition to the conventional hot-spot ignition schemes, there are schemes that rely on a high-energy laser to form a core without a hot spot, and then a high-intensity laser to ignite the compressed plasma, i.e., the fast ignitor concept.

Since 1992, we have pursued a laser technology development program to develop a petawatt capability for Nova. In FY 1995, the technology for large gratings developed sufficiently to install a 100-TW short-pulse laser, an engineering prototype of the Petawatt laser, on the Nova 2-beam target chamber (see discussion and Fig. 4 on p. xviii). Target experiments and diagnostic developments are ongoing to study the fast-ignitor concept.

The Target Physics Program has a history of technology transfer (the Micropower Impulse Radar was a direct result of diagnostic development for Nova[7]). In FY 1995, a program element was created within the Target Physics Program to pursue the dual goals of developing technology for ICF Target Physics as well as technology diversification. Also, a new program element (Target Area Technology) was established to coalesce technology development required for the NIF Target Chamber. This program element works on NIF cryogenic targets, first-wall survival issues, and NIF diagnostic development. The NIF diagnostic effort is in conjunction with SNL, LANL, and University of Rochester scientists and is coordinated through a joint central diagnostic team.

National Ignition Facility

On October 21, 1994, the Secretary of Energy issued KD1 for the NIF, thus reaffirming the Justification of Mission Need issued on January 15, 1993, formally approving the NIF Project and establishing LLNL as the preferred site. With this decision, the DOE and the Administration requested FY 1996 congressional line-item funding for the Project. The Justification of Mission Need emphasizes the importance of the NIF to the mission of the National ICF Program—achieving controlled thermonuclear fusion in the laboratory. This important goal, endorsed in a recent government-sponsored report by JASON,[8] supports the DOE mandate of maintaining nuclear weapons science expertise in required areas for stockpile stewardship and for understanding nuclear weapons effects.

During the past year, the role of the NIF in supporting vital U.S. goals for national security was further strengthened. On August 11, 1995, the President announced the continuation of the nation's moratorium on underground testing of nuclear weapons and the U.S. intention of signing a zero-threshold comprehensive test ban treaty in 1996.[9] (The current moratorium on underground testing of nuclear weapons, beginning in 1991, remains in effect.) The confidence expressed by the Secretaries of Energy and Defense in the ensemble of science-based stockpile stewardship facilities was referenced by the President as strengthening the confidence in his decision to seek a zero-threshold treaty.

Consistent with KD1, DOE Defense Programs and the Laboratory Project staff began several activities in FY 1995 to support a Project start in FY 1996, including the following:

- Establishing a DOE Office of the NIF and a Project organization;
- Supporting the DOE study public process (with public participation) to determine nonproliferation impacts of the NIF and initiating the National Environmental Policy Act (NEPA) process for its siting, construction, and operation;
- Preparing the key industrial contracts to support preliminary and final design;
- Establishing interfaces with potential user groups outside the ICF community;
- Initiating specific advanced conceptual design work to optimize the NIF; and
- Drafting key Project documents required for a Strategic System Acquisition.

During FY 1995, the NIF Project organization met all the milestones required to maintain the Project baselines, described in "The National Ignition Facility Project" on p. 110 of this report.

LLNL's Role in Project Organization and Management

In January 1995, DOE Defense Programs chose a Director of the Office of the NIF, reporting to the Assistant Secretary for Research and Development. A Memorandum of Understanding was signed in May 1995 delineating the responsibilities of this Office and that of the Office of Research and Inertial Fusion—the Defense Program's scientific, technical, and administrative organization responsible for the ICF Program. In particular, the ICF Program has the responsibility of developing the laser, optics, and target area technologies required for the NIF.

The DOE national laboratories team is responsible to all stakeholders in executing the NIF Project. This team includes the Director of the Office of the NIF at DOE Headquarters in Washington, DC; the DOE Field Project Manager at DOE Operations in Oakland, CA; and the National Laboratories' Project Manager and Project Deputies. The current Project organization is consistent with both the Project Charter originally issued in March 1993 and the Memorandum of Agreement signed in August 1993 between the participating ICF laboratories: LLNL, the lead laboratory; LANL; SNL, Albuquerque; and the Laboratory for Laser Energetics at the University of Rochester. As during the conceptual design phase, the National Laboratory Project Manager, chosen by the LLNL Director, has other laboratory Project Deputies originally appointed by their respective ICF Programs.

NIF's Role in Nonproliferation and the NEPA Process

To be responsive to the public, the Secretary of Energy initiated two public processes at KD1:

- To have the DOE Office of Arms Control and Nonproliferation review the impact of the NIF on the nation's policy towards the nonproliferation of nuclear weapons.
- To incorporate the NIF site selection, construction, and operation according to NEPA as a part of the Programmatic Environmental Impact Statement (PEIS) for Stockpile Stewardship and Management.

Nonproliferation and Key Decision One Prime (KD1′). This review has been referred to as the Dellums process because it was designed in response to inquiries made by the Congressman who initiated the Key Decision One Prime (KD1′) process. The Secretary made it a requirement for proceeding to the final design phase of the Project. During 1995, open meetings were held by DOE in Washington, DC and Livermore, CA to first seek public input on the scope of the study and then to receive public comment on the draft study. The schedule of these meetings was broadly announced in the *Federal Register*, and their formats were similar to those used in NEPA reviews. The DOE *Draft Report* was also reviewed by other government organizations, such as the Defense Department, State Department, Arms Control and Disarmament Agency, and by a group of independent experts. The DOE *Draft Report* was issued for public comment in October, and public meetings were held in Washington, DC on September 21, 1995 and in Livermore, CA on September 28, 1995. The two major conclusions reached by the DOE *Draft Report* were as follows: the impact of the NIF on proliferation is manageable, and the NIF can be made acceptable and can contribute positively to the U.S. policy on nonproliferation. The Secretary of Energy accepted these conclusions, issued the final document,[10] and made a positive KD1′ decision on December 20, 1995.[11]

Programmatic Environmental Impact Statement (PEIS). The PEIS Notice of Intent was published in June 1995,[12] and Argonne National Laboratories was chosen by DOE as the NEPA document preparer for the NIF section of the PEIS. PEIS public scoping meetings were held at eight Defense Program sites across the country between June and August 1995 (Kansas City, Savannah River, Oak Ridge, Pantex, Los Alamos, Albuquerque, Livermore, and the Nevada Test Site). The *Implementation Plan* will be published in January 1996. NIF will be handled as a Project Specific Analysis (PSA) in the PEIS, reflecting the status of the Project. The NIF PSA contains the necessary information on all the proposed Defense Program sites—Livermore, Los Alamos, Sandia (Albuquerque), and the Nevada Test Site (in North Las Vegas as well as in Mercury)—for site-specific design, construction, and operation of the facility. Public meetings on the draft PEIS are scheduled to begin in April 1996. It is anticipated that the NEPA process will be completed in the fall of 1996, and a Record of Decision for the siting of NIF to be announced at the end of 1996.

Industrial Outreach

In February 1995, LLNL's Laser Programs Directorate held an Industrial Stakeholders' Briefing Meeting in collaboration with the NIF Laboratory Project Office,

representing the participating ICF Laboratories. The meeting, paid for by the industrial participants themselves, attracted 350 individuals from 240 companies representing 35 states. It offered a first-time opportunity for manufacturers and vendors to review NIF requirements with Project technical staff. Follow-on actions included source solicitation and preparatory procurement actions for the following:

- Architect/Engineering (A/E) firms—for the Laser and Target Area Building (LTAB) and the Optics Assembly Building (OAB),
- Construction Management Services,
- Master Task Agreements for Engineering Services—for preliminary and final design phases of the Project, and
- Optics facilitization.

After a rigorous source evaluation process, Ralph M. Parsons of Pasadena, CA and A. C. Martin of Los Angeles, CA were selected as the A/Es for the LTAB and OAB, respectively. Similar processes are under way for the other procurement actions. Final contracts will be signed when the Project is formally funded in FY 1996.

User Groups

In concert with the NIF mission statement, a Project Scientist's Advisory Panel was established to solicit input on the facility from a broad user community. White papers were generated by the ICF direct-drive community, weapons physicists, the Defense Nuclear Agency and Defense Programs' radiation scientists, IFE groups, and the university-dominated high-energy-density community. The Project is considering how to handle features desired by these communities beyond those required to achieve ignition and gain using indirect or x-ray drive as specified in the NIF *Primary Criteria and Functional Requirements*. In particular, DOE has formally requested the NIF Laboratory Project Office recommend a direct-drive option for the NIF (see Fig. 1).

Advanced Conceptual Design

In preparation for completing the advanced conceptual design by February 1996 and starting the preliminary design early in FY 1996, the Project reviewed key technical areas, including structural–vibrational issues, amplifier configurations, beam isolation, and final optics design. A review was held in July 1995 and attended by key Core Science and Technology staff from the participating ICF Laboratories and members of the French Program from Centre d'Études de Limeil–Valenton, France.

Project Documentation

Many key Project documents were generated during FY 1995: a Fire Hazards Analysis, a *Draft Environmental Safety and Health (ES&H) Management Plan*, a *Draft Quality Assurance (QA) Project Plan*, a *Draft Project Execution Plan*, and a *Title I Design Plan*. The *QA Project Plan* and *ES&H Management Plan* were approved by DOE in November 1995. In addition, work has proceeded smoothly on the non–site-specific sections of the *Preliminary Safety Analysis Report*, which is required before construction begins.

Laser Science and Technology

The mission of the Laser Science and Technology (LS&T) Program is to provide technical innovation and leadership for the Laser Programs Directorate and Laboratory in the core competencies of laser science and technology.

Our primary activity in FY 1995 was in support of ICF by providing for laser development for the NIF Project. This year we began a four-year effort to develop critical components for the NIF laser, including the pulse generation system, large multi-aperture amplifiers, and multi-aperture plasma electrode Pockels cells. We continued to use the Beamlet laser, a full-aperture scientific prototype of one NIF beamline, which serves as an invaluable tool for learning more about large multipass lasers. We developed many software design tools to optimize the NIF laser design. We also completed a study reviewing the status and projecting the laser requirement for direct-drive ignition on NIF and worked on associated laser technology development. For ICF experiments on Nova, in collaboration with Nova engineering staff, we completed the 100-TW laser and designed, ordered, and installed much of the hardware for the Petawatt (10^{15}W) laser beam. These ultrashort (<1 ps) pulse, high-energy lasers are used to study the fast ignitor approach to ICF, which could greatly reduce the laser energy required for fusion gain. In another advanced ICF project, we developed critical technology for a laser driver for high average power applications such as for an IFE plant. The LS&T Program continued to advance diode-laser and diode-pumped laser technology for NIF, advanced ICF systems, and other applications. Our proven expertise in building laser systems enabled us to become an important contributor for U.S. Air Force, Army, and Navy projects. We were also involved in several cooperative research and development agreements (CRADAs) with U.S. companies.

NIF Laser Components

The LS&T Program is responsible for developing the key components for the NIF laser on a schedule and at a cost that permits incorporation into the NIF design. Over a four-year period (1995–98), the following areas will be developed: optical pulse generation system (see Fig. 2), multisegment amplifiers, multipass laser components, frequency conversion, diffractive optics, pulsed power systems, laser diagnostics, lasers alignment and wavefront control, and wavefront control systems. A

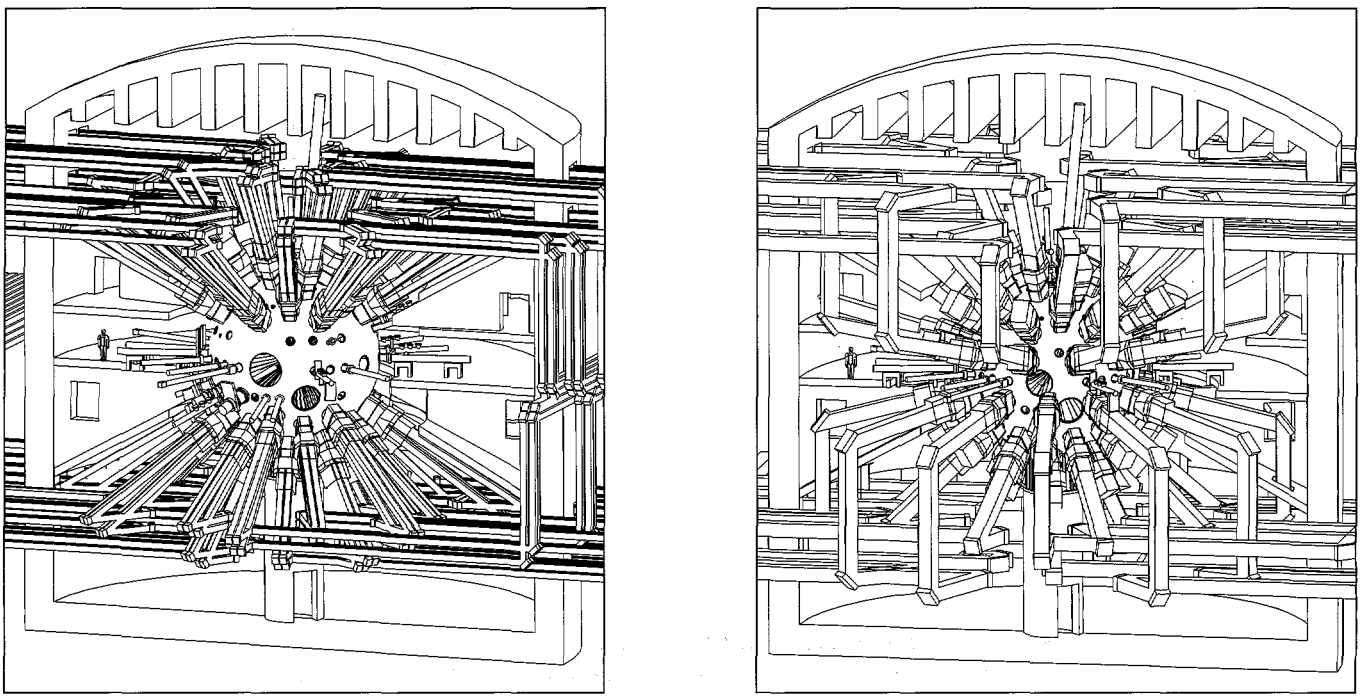

Reposition 24 of the 48 4-beam clusters

Laser target
indirect drive

Laser target
direct drive

FIGURE 1. The current NIF indirect-drive design can be simply reconfigured for direct drive without the costly addition of a second target area and chamber by repositioning 24 of the 48 4-beam clusters. (40-00-0495-0976Apb02)

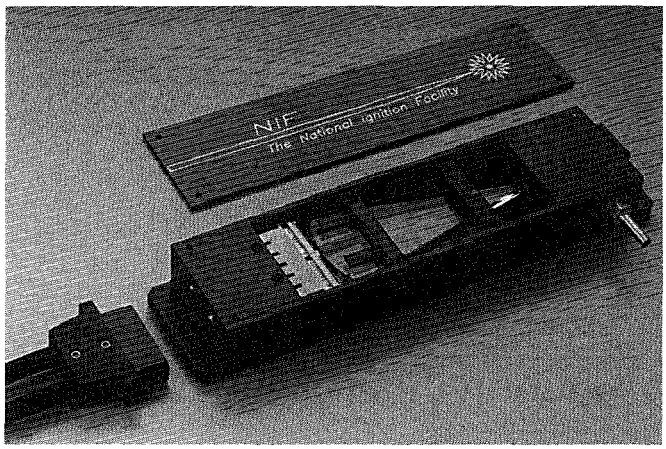

FIGURE 2. Prototype of the diode-pumped regenerative amplifier, which is part of the NIF optical pulse generation system. The prototype has shown ≤ 2% gain stability, operating at an overall gain of 10^6. (99-00-0595-1337pb01)

detailed plan, *Core Science and Technology (CS&T) Development Plan for Indirect-Drive Ignition*,[13] written in 1994 and updated in 1995, describes the activities necessary to develop these components and shows schedules for their completion. The plan includes input from LLNL; LANL; and SNL, Albuquerque; and covers the laser, optics, target chamber, and target science development. In most cases, laser technology prototypes are being built to test the design concept. For example, an effort is under way to build a 4×2 multisegment amplifier and a new laboratory to test it. This laboratory, located in the former Shiva target bay in the Nova building, will be used to prove the optical performance of the amplifier as well as to evaluate the new bottom-loading assembly procedures using a robotic transport cart. The 4×2 amplifier could be coupled to a Pockels cell array, deformable mirror, or large beam diagnostics to evaluate their combined performance.

Many NIF concepts have been tested on the Beamlet using components that are predecessors of those anticipated for NIF. The *ICF Quarterly Report* (95-1 issue, pp. 1–85) was devoted entirely to the Beamlet system and its components, which were developed over several years. The initial Beamlet performance demonstrations are discussed in this issue (see "System Description and Initial Performance Results for Beamlet," on p. 1 of this report). Beamlet has been remarkably successful in reaching its performance goals and has greatly increased our confidence in the NIF design. Also during the year, an alternative laser architecture (beam reverse architecture) was jointly tested with our French colleagues at Centre d'Etudes de Limeil–Valenton, discussed in the article "Testing a New Multipass Laser Architecture on Beamlet," on p. 142. This year we added a large vacuum chamber to Beamlet to evaluate focusing characteristics of the high-power output beam after conversion to the third harmonic and after passing through a phase plate, diagnostics, and debris shield similar to those planned in NIF. The vessel shown in Fig. 3 is 8 ft in diameter and 33 ft long and contains many large-aperture optics, including a front-surface reflecting mirror (1 m diam) to refocus a sample of the high power beam. Beamlet has provided invaluable information on operating a multipass laser; for example, the NIF spatial filter lenses were redesigned and a lens monitoring diagnostic developed, after an optically damaged lens imploded on Beamlet in May. We also performed smaller-scale experiments on the Optical Sciences Laser to resolve basic nonlinear optics issues and to evaluate NIF components.

Many of the computer modeling codes needed to optimize the NIF laser design were written in 1995, as discussed in the article "The National Ignition Facility Project" on p. 110. A network of 28 computer workstations was purchased and linked together to provide rapid laser design and optimization. Design modifications to correct one issue in particular are being investigated—nonlinear growth of beam modulation which, in an extreme case, can lead to beam filamentation and optical damage. Final design optimization of the NIF laser is scheduled for completion by February 1996 to provide many critical design parameters such as the most cost-effective number and thickness of amplifier slabs, beam dimensions, spatial filter lengths, etc.

A white paper study[6] on direct-drive capability for NIF was completed, detailing the additional hardware required for direct drive and predicted laser and target performance. Direct-drive requires a spherical layout of beams entering the chamber to symmetrically radiate the targets and also requires more uniform (smoother) beams in a time-averaged sense than indirect drive. To meet beam smoothness specifications for direct-drive on NIF, we analyzed the technique of two-dimensional smoothing by spectral dispersion (SSD), which was invented by the Laboratory for Laser Energetics at the University of Rochester. A demonstration of SSD on Beamlet is planned for 1996.

Figure 4 shows the 100-TW laser installed and operated on the 2-beam chamber of Nova. This laser is a predecessor to the Petawatt laser and is capable of producing 40 J pulses at 400 fs (400×10^{-15} s) in duration. The 100 TW of peak power is comparable to the peak power normally available for the entire 10-beam Nova system. The 100-TW beam can be operated simultaneously with the primary Nova beams in the 2-beam chamber, thus allowing flexible target studies. The Petawatt laser, expected to generate ten times the power of the 100-TW laser, is scheduled for completion in late 1996. However, because of the long-order times, most of the design work and planning had to be completed in 1995. The Petawatt pulse compression chamber is a vacuum vessel several times larger than the Nova

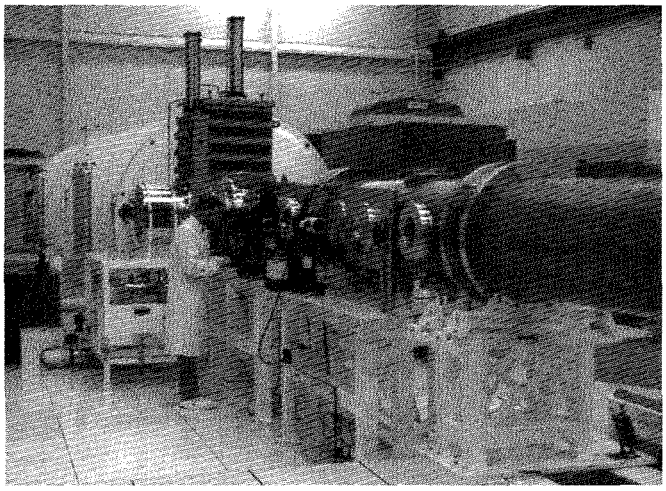

FIGURE 3. A vacuum test station added to Beamlet to evaluate the focusing properties of the beam after conversion to the third harmonic. (70-50-0496-0721pb01)

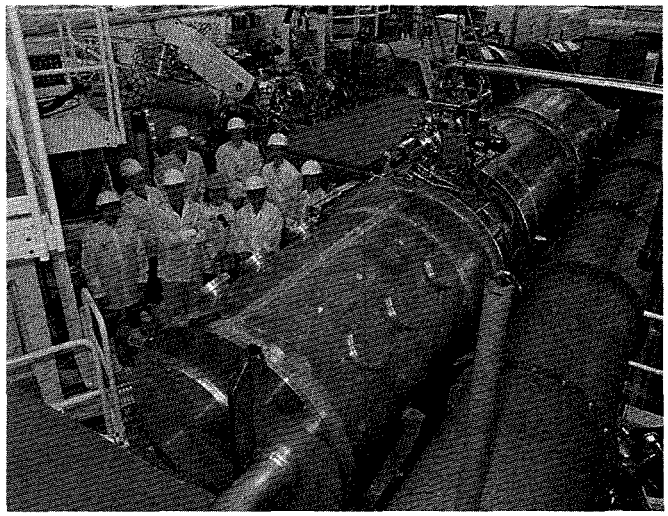

FIGURE 4. The 100-TW laser installed on the Nova 2-beam chamber. (70-60-0895-1969Apb01)

chamber and uses a pair of 1-m aperture, unsegmented gratings, the largest ever made. See the article entitled "High-Efficiency Multilayer-Dielectric Diffraction Gratings" on p. 187 for a discussion of advanced grating development. The power and energy available from the Petawatt laser allow us to test the fast-ignitor approach to ICF.

NIF Optics Development

The specifications for the large NIF optics are similar to those for the Beamlet laser (a scientific prototype of NIF) recently completed at LLNL. For all optics in transmission (except the crystals), the transmitted wavefront error specification (peak-valley) is $\lambda/6$ at 633 nm; for the crystals, the transmitted wavefront specification is $\lambda/4$. The reflected wavefront specifications (peak-valley) for the mirrors and polarizer are 0.4 λ and 0.8 λ, respectively, confined to low-power aberrations. The reflectivities of the mirrors and polarizer (*s*-polarization) must exceed 99%; the transmission of the polarizer must also be greater than 98% for *p*-polarized light. The damage threshold requirement for these optics is extremely demanding. For intracavity and transport optics (1 μm wavelength), the damage threshold requirement ranges from 15 J/cm^2 to 20 J/cm^2 for a 3 ns pulse, depending on location. The damage threshold of the harmonic conversion crystals, focus lens, and debris shield must exceed 12 J/cm^2 at 351 nm. For the NIF, we plan to use the ISO 10110 standard for optics drawings; we are in the process of converting the NIF optics drawings into this format.

Production of most of these optics will begin in late 1998 to early 1999, and continue into early 2002. Crystal production is expected to begin in early 1998. While the U.S. optics industry can manufacture optics meeting the technical specifications (and did so for Beamlet), it lacks the capacity to meet the production schedule. Furthermore, in some areas, such as laser glass, the present manufacturing technology is not cost effective for the quantity of optics needed for the NIF. LLNL has started a comprehensive multi-year development program with leading optics manufacturers to improve the U.S. optics industry's ability to meet the cost and schedule requirements for the NIF. This development program started in mid-1994, and will continue through late-1997. Toward the end of development, equipment will be purchased and installed at the optics manufacturing sites, production teams will be formed, and a pilot production campaign initiated to address any remaining issues prior to the start of production.

In laser glass manufacturing, both Schott Glass Technologies[14] and Hoya[15] had significant accomplishments in FY 1995. Hoya built and tested a sub-scale continuous melter for phosphate laser glass—the first time this glass has been melted continuously. Schott, taking a different development approach, demonstrated casting of continuously melted glass at the NIF-scale using BK-7 as an analog to phosphate glass. The BK-7 also met the NIF specification for homogeneity. In addition, Schott produced five slabs of LG-770 laser glass for testing on Beamlet; this glass composition has been engineered to improve the melting characteristics in Schott's melter design.

Progress was substantial in the KDP crystal growth and finishing activities. We demonstrated high supersaturation levels (greater than 50%) and long-term stability in NIF-size growth tanks as needed for fast growth. We also demonstrated NIF optical specifications on 15-cm boules grown in our small tanks. A continuous filtration system to raise the damage threshold of these crystals was also designed and built. To help understand damage in KDP crystals, we built a dedicated test system with an in-situ scatter diagnostic for characterizing internal features in these crystals.

In fused silica, the new Corning[16] material 7980, made from a non-polluting source material, was qualified for use on NIF. A requirement for low neutron/gamma induced damage from the NIF targets was also included in the qualification criteria.

Finishing and optics specification activities focused on initiation of the development work on deterministic figuring processes for flats and lenses, high-speed polishing, and the use of power spectral densities (PSDs) for specifying mid-spatial length-scale errors. We completed a draft specification package for NIF optics based on PSDs and made provisions for describing these specifications using the ISO 10110 international optics standard. In crystal finishing, we completed an extensive characterization of the existing diamond turning machine at Cleveland Crystals[17] to establish a baseline for planned improvements. The initial upgrades were completed, including building and installing an improved flexure coupling to better isolate the crystal surface from machine irregularies, and a NIF-size flywheel for mounting the diamond tool.

In coatings development, we started upgrading the coating chambers to improve diagnostic capabilities for the damage threshold improvement campaigns in FY 1996. We also found that ion-beam sputtered coatings which have superior spectral properties, have defects that lower damage threshold to levels unacceptable for NIF. Although the density of these defects is quite small, full-area testing readily locates their position. As a result of this problem, this technology probably will not be pursued further in FY 1996. Transport mirrors coated using traditional electron-beam technology were successfully laser conditioned to the NIF baseline level.

The NIF requires a full-aperture phase measuring interferometer. To accommodate this requirement, Zygo[18] and WYKO[19] began working on conceptual designs that will be completed in early FY 1996.

Diode-Pumped Solid-State Laser (DPSSL)

We are developing the technology for upgrading solid-state lasers to provide for an efficient (~10%), repetitively pulsed (~10 Hz) system, suitable for future dual-use ICF laser-fusion facilities for defense and energy research. The technology of this system has a strong connectivity with Nova and NIF laser technologies. Furthermore, the natural modularity and scaling

laws of laser architectures reduce the physics risks and research costs associated with this effort.

Our leading candidate for a laser driver is based on a diode-pumped solid-state laser (DPSSL), for which the gain medium [Ytterbium-doped strontium fluorapatite (Yb:S-FAP)] is cooled by He gas, using the GCS or gas-cooled slab concept. We completed a conceptual study of a DPSSL in the power plant context in FY 1994 and wrote an extensive article on this topic.[20] The detailed laser physics is explicitly included in the model, while costs, target performance, and power plant phenomenology are handled using community-accepted paradigms.

In FY 1995, we pursued an experimental campaign to construct and test a small subscale DPSSL. Early experiments on this laser provide enhanced credibility for this type of novel cooling technology, which is scalable to high-repetition rates and average powers in the megawatt range. The GCS cooling technology is unique, as compared with more conventional transverse water-cooled rod or zig-zag slab designs (the cooling and optical extraction simultaneously occur across the two large faces of the slab). See the summary below for details of this technology and the graphic illustration shown in Fig. 5.

These experiments were also conducted at a thermal flux (out of each face of the slab) up to 3.5 W/cm^2. This is several times greater than that required for a large IFE driver operating at moderate rep-rates. The overall objective of this project was to convincingly show that the DPSSL driver offers adequate performance to serve in a fusion energy power plant.

Advanced Technologies and Enhancements

The LS&T Program also contributed to a DOE project supporting nuclear nonproliferation and delivered a 20 J/pulse laser to the U.S. Navy. For the Air Force, a 4-beam laser for integration into a land-based, space-imaging system is being built, which has an output of 60 J of green light at a pulse length of 600 μs—a unique regime for solid-state lasers. The laser is a flashlamp pumped Nd:glass zig-zag slab laser that uses a special technique of low-threshold phase conjugation.

The CRADAs with several U.S. companies included developing laser driven x-ray light sources for making sub-micron resolution computer chips with x-ray lithography, lasers to remove port-wine stain birthmarks, efficient high-power lasers for cutting and welding, and a very compact three-color laser for incorporation into a prototype of a laser video projector.

Heavy Ion Fusion (HIF) for IFE

LLNL made significant progress in FY 1995 to advance the development of IFE and to initiate new applications of ICF Program technology for U.S. industry and for government-sponsored programs in addition to the ICF Program. The funding for much of this work

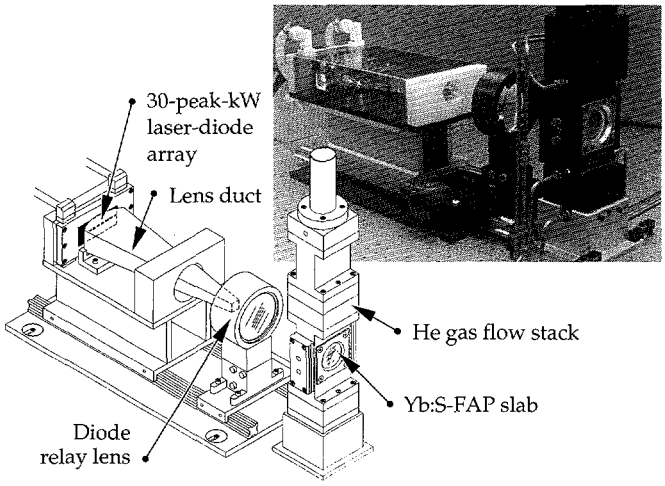

FIGURE 5. A diode-pumped Yb:S-FAP gas-cooled slab laser. (70-00-0795-1744Epb01)

Gas-Cooled Slab Laser

A gas-cooled slab (GCS) laser consists of the gain medium slab, over which gas flows across both faces through narrow (~1-mm-thick) channels, and the laser-diode array. The laser-diode array longitudinally pumps the slab through access windows on either side of the slab. (Figure 5 shows an earlier configuration of only one side of the slab.) The laser-diode array has 192 bars producing 20 kW (with an aperture of 3.5 × 10 cm, a 43% electrical efficiency at 900 nm, and a 5.5-nm full-width half maximum), including the thermal-induced spectral chirp within the millisecond pulse length. The output is ~20 J in 1 ms at a peak current of 140 A. A lensing duct concentrates the diode light down to a 2 × 2 cm aperture with an 85% efficiency. An f_2 relay lens transfers the diode energy from the lensing duct to the Yb:S-FAP laser slab in the gas flow channel.

The coolant gas is He, due to its uniquely low scatter properties (low index) and good thermal conductivity (for a gas). The He gas flow stack separates the gas flow into two broad channels at the bottom of the stack in a diffuser to homogenize the flow. The flow is then accelerated at 4 atm pressure to Mach 0.1 in a nozzle section specifically designed to prevent flow instabilities and is directed to flow across both slab faces in rectangular channels (1-mm-thick × 22-mm-wide). For our operating conditions of 80 std L of He/min, the flow is characterized as well into the turbulent rather than laminar or intermittent flow regime. Turbulent flow is critical because it minimizes the thermal impedance between the gas and the slab by minimizing the effects of the thermal boundary layer. Finally, the flow is gently decelerated in a tapered channel and exhausted through an additional diffuser.

The laser output efficiency is 51% with respect to the absorbed pump power. Using this configuration, we achieved up to 50 W of optical power at 25 Hz. The Yb:S-FAP slab fractures above 25 Hz, which is expected since the laser operates at a significant fraction of the thermal fracture limit. Note that the maximum repetition rate before fracture is two to five times higher than the requirements proposed for megawatt-scale ICF laser facilities.[21]

is independent of ICF Program funds. The work is included here because it demonstrates some of the possible applications and spinoffs of capabilities developed by the ICF Program. During FY 1995, a sequence of experiments in heavy-ion beam physics began with magnetically focused heavy-ion beam transport. This sequence will lead to later experiments in ion-beam bending, recirculation, and drift compression to be conducted during FY 1996.

The U.S. Heavy Ion Fusion (HIF) Program is developing the concept of using ion-induction accelerators as drivers for IFE and post-NIF ICF research. LLNL's HIF project made significant progress in FY 1995 on the accelerator physics and technology, target physics, and chamber propagation physics necessary to make HIF a reality. Our approach combines experiment, analytic theory, and computer simulation to gain the required level of understanding in all of those research areas. A major new thrust was the initiation of an experimental research program in high-current ion beam dynamics. During the year, the first in a sequence of experiments was conducted in magnetically focused beam transport, beam bending, and ultimately recirculation. If successful, this series of experiments will lead to a small prototype recirculating induction accelerator.

The recirculating induction accelerator is a promising approach to a reduced-cost heavy-ion driver. A small, scaled ring was designed to explore this approach and to facilitate studies in beam bending, beam transport over long path lengths, and precise beam sensing and handling. The design uses permanent-magnet quadrupoles for beam confining and electric dipoles for bending. To understand beam-bending effects, we first characterized magnetic beam transport in a linear channel. To achieve this, we installed an electrostatic-focusing "matching section," followed by a transport line, consisting of seven permanent-magnet quadrupole lenses at the output of the injector. Experiments in this beam line are ongoing; initial tests show a high-quality beam that has yet to be optimally "matched" to the line. Associated with this work has been the development of novel beam-sensing diagnostics. The prototype recirculator design, the linear transport experiments, and the associated theory and modeling effort are described in "Progress Toward a Prototype Recirculating Ion Induction Accelerator" on p. 179 of this report.

An important element of a recirculating induction accelerator, or of a multipulse linear accelerator, is an accelerating module capable of generating a series of pulses in rapid sequence, with a repetition frequency up to 100 kHz. We are developing an accelerator power source that is switched entirely by field-effect transistors (FETs). This approach is motivated by the need for an agile device that can afford pulse-to-pulse variability and excellent waveform control. The devices developed are made possible by recent advances in high-power FETs. This research is described in "Evolution of Solid-State Induction Modulators for a Heavy-Ion Recirculator" on p. 103 of this report. In another technology area, we made major strides in understanding how to synthesize a variety of multipole fields using iron-free assemblies of permanent magnets.[22]

LLNL played an important role in the support of the larger HIF experimental program at Lawrence Berkeley National Laboratory (LBNL), including the design of the first phase of the Induction Linac Systems Experiments Program, called Elise. The optimized design point for Elise was derived from a zero-dimensional Mathematica-based program. While the Elise project has not received approval for a construction start, the experience gained will enable the U.S. HIF Program to propose a far more capable machine for construction, beginning in the next few years.

LLNL 3-D, PIC modeling, using the WARP code, precipitated the successful fielding of LBNL's new driver-scale injector. This model uses a novel electrostatic-quadrupole approach to beam acceleration and confinement and also played a critical role in the recirculator physics effort (see Ref. 20 for more details). Other tools, including the Circe moment-equation code, played an important role in both the driver-scale injector and the recirculator physics effort as well. LLNL also provided support in control systems and diagnostic development to the LBNL program.

The HIF group has continued to make progress in the study of IFE heavy-ion beam chamber propagation, target design, and power plant studies. Electromagnetic PIC simulations are being used to better understand transport in the target chamber. Recent results examining near-ballistic focusing through a low-density preformed plasma channel are encouraging—they show that with only half-percent ionization of the background gas, lower-mass or higher-charge-state ions can be focused onto a small spot. In the area of target physics, detailed converter designs have been conducted and preliminary "integrated" simulations using LASNEX are well under way. We recently initiated a LASNEX study of ion beam heating of Au foils, whereby high-energy densities in matter are achieved using highly focused heavy-ion beams.

New Initiatives and Spin-Off Technologies

Spin-off laser program technology initiatives were pursued in medical technology and modeling, night-vision systems, plasma probing, laser pinhole closure, x-ray imaging for semiconductor defects, oil and gas exploration, enhanced surveillance, and Advance Design and Production Technology (ADaPT). A preliminary design was completed for an advanced radiography machine based on megahertz induction pulse rate technology, and work began on building a

test facility for Relativistic Klystron Two-Beam Accelerator (RK–TBA) tests at LBNL as a joint effort with LLNL.

In FY 1995, we identified and initiated efforts to exploit ICF Program expertise and technology to capture a share of industrial and governmental markets in areas such as:

- **Health care technology**—Applications of our expertise/technology that are being applied to medicine include: (a) Modeled laser–tissue interactions, using a 3-D laser–tissue simulation code called LATIS to optimize benign prostate hyperplasia treatment, laser thrombolysis of cerebral and cardiovascular clots, and laser–tissue welding for laparoscopic and endovascular applications. (b) Set up a medical photonics laboratory for developing a host of new medical technologies (e.g., optical sensors for tissue identification and blood and tissue analyte monitoring, Optical Coherence Tomographic imaging, and ultrashort pulse-laser drilling of hard tissue). (c) Developed a user-defined diode and DPSSLs for medical procedures (e.g., port wine stain removal, tattoo removal, and laser surgery).
- **X-ray imaging and lithography**—Developed laser-based debriless x-ray sources for x-ray lithography under contract to the Advanced Research Project Agency and in collaboration with AT&T, Motorola, Silicon Valley Group, and IBM. We are engaged in the development of collimating x-ray optics for minimizing feature sizes printed while maximizing system throughput. Another important technology is the development of x-ray imaging technologies for defect inspection, which is a program we are currently initiating.
- **Military visualization systems**—Pulsed microchannel x-ray imaging technologies are now being applied to developing advanced night- and underwater-vision technologies for the Department of Defense. This work is being done in collaboration with key industrial partners such as Intevac and Litton.
- **Oil and gas exploration**—We have teamed with Shell Oil Co. to develop advanced imaging and image reconstruction algorithms for geostrata mapping.
- **Plasma probing**—X-ray laser technology has been applied to the probing of ICF plasmas, in particular large-scale plasmas necessary for producing ignition with the NIF. The first x-ray laser-based Mach–Zehnder interferometer was developed as part of this effort.
- **Enhanced surveillance**—Advanced x-ray imaging technologies are now being applied to the DOE's enhanced surveillance initiative. This technology, similar to that developed for measuring ICF capsule performance, will be used to nondestructively inspect nuclear weapons in our nation's stockpile to verify nuclear readiness. Modified medical technologies of endoscopic imaging and noninvasive sensors are also being developed to verify the status of nuclear weapons components in the national stockpile.
- **AdaPT**—We are developing advanced sensor technologies for monitoring laser materials processing associated with the ADaPT initiative (providing a means to manufacture nuclear weapons components when or if required in the future).
- **Advanced high-energy particle accelerators**—Three areas are being developed to support advanced accelerator technology. (1) A high-gradient dielectric-wall accelerator is being developed to demonstrate transport of electrons at 1 kA with a record gradient of 20 MeV/m using novel insulating materials. We demonstrated operation of novel pulse forming lines (Asymmetric Blumleins), which provides the accelerating voltage to the dielectric wall. Additionally, we invented and successfully tested a high-gradient laser-induced surface-flashover switch, providing a subnanosecond rise time to initiate the pulse from the Asymmetric Blumlein. Proposed future work will involve tests of a stack of pulse forming lines with laser switches, operating at high gradient. (2) We are supporting the development of a high-current electron-induction accelerator for B-Division's Advanced Hydro-Test Facility proposal (a National Radiographic Facility). We built and tested a 15-kV, 3-kA induction modulator cell that runs at an extremely high repetition rate (300 kHz), necessary for multiple images of a single high-explosive shot. We are completing a second generation modulator that will run at 15 kV, 4.8 kA, and at least 800 kHz. We are developing the beam switching and transport technology that will be required to produce multiple lines of sight to the radiographic object. (3) We began construction during FY 1995 of the RK–TBA Test Facility at LBNL as a joint effort with LLNL. The facility will study physics, engineering, and costing issues of using RK–TBA's as rf power sources for high-energy linear colliders. Important issues to be addressed by the test facility are efficiency, longitudinal beam dynamics, beam stability, emittance preservation, and rf amplitude and phase control. Testing will be performed on a 25-m-long RK–TBA accelerator prototype that includes eight high-power rf output structures. Each structure will produce a 180-MW, 250-ns rf pulse at 11.4 GHz.

Program Resources and Facilities

Resources

In FY 1995, financial resources for the LLNL ICF Program totaled $75.8M in DOE operating funds and $4.6M in DOE capital equipment allocations. Work-for-others funding increased slightly in FY 1995, with $30.8M coming from various sources within the DOE community, other federal sponsors, and international sources. At LLNL, the NIF Project received $4.1M in DOE operating funds for FY 1995. The average LLNL full-time employee equivalent count over the year was 353.1. Supplemental contract labor personnel were used in clerical, design, and engineering positions and as Nova operators. The ICF Program employed approximately 77.3 supplemental labor and other labor personnel in FY 1995.

Figure 6 shows the resources available to the ICF Program over the past 12 years and compares the operating funds provided by DOE in then-year-dollars vs the same funding discounted to reflect 1982 dollars. The figure illustrates that the real purchasing power for the DOE funding, as related to FY 1982, has remained fairly constant and is expected to remain so in FY 1996.

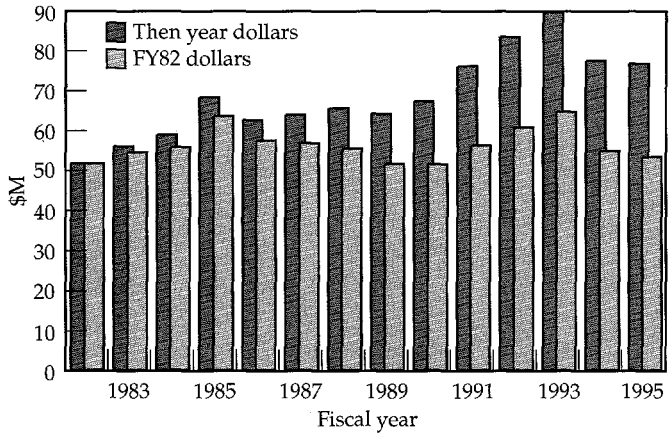

FIGURE 6. ICF program operating funds. (02-20-0396-0582pb01)

Figure 7 illustrates Work-for-Others funding, which is becoming a significant part of the total resources available to the ICF Program, but is expected to decrease slightly in FY 1996.

These resources enabled the ICF Program to continue its support of research and development of high-energy-density physics, laser component development, optics technology, and IFE. A few examples of major projects accomplished during FY 1995 are the completion of the 100-TW modification to the Nova laser system, the addition of the focusing vessel to Beamlet, and the facilitization of the Optics Processing facility in Bldg. 392. The ICF Program also purchased equipment for video teleconferencing, which will provide opportunities to maintain close collaboration with both national and international Program participants.

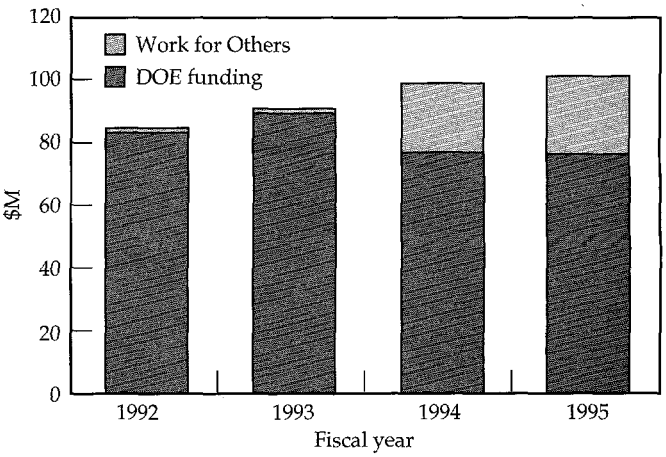

FIGURE 7. LLNL ICF program funding. (02-20-0396-0583pb01)

Facilities

In FY 1995, the ICF Program comprised 36 facilities—laboratories, offices, and specialized facilities in excess of 500,000 ft^2. Figure 8 shows the locations of ICF facilities within the Laser Programs.

The emphasis in facility upgrades during the year was in support of the core science and technology developments in lasers and optics. This included major modification upgrades, renovation, and special projects as summarized below. In addition, several facility maintenance projects were completed.

- Completed the $1.5M clean room installation and modifications to the Bldg. 392 Optics Processing facility to support the development of Nova, Beamlet, and the NIF.
- Completed the $200K Bldg. 165 facility upgrade to grow rapid-growth KDP crystals in support of the NIF.
- Completed a $150K *Conceptual Design Report* for a proposed Advanced Optical Technical Center.
- Completed the detail design for a $1.3M Bldg. 391 basement upgrade for the new NIF amplifier development, flash-lamp development laboratories, capacitor bank, and control room.
- Finished planning and designing the major Bldg. 298 $430K upgrade to house phase-plate development in support of the NIF.

FIGURE 8. A map of the Laser Programs' area with facilities used by ICF shaded.
(40-00-0794-2902Apb01)

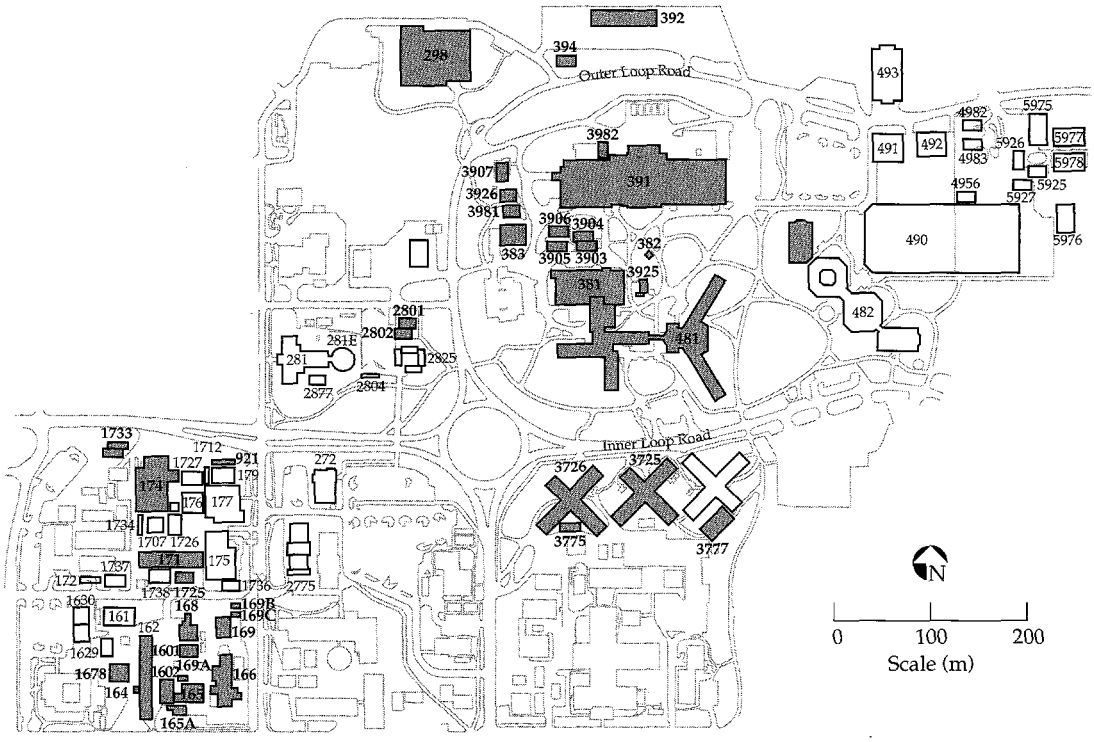

- Completed the Laser Programs' first teleconferencing facility in Trailer 3725.
- Installed two new 350-ton chillers in Bldg. 381 to support a major $700K AC upgrade to one of our key facilities. This installation accommodates 136 offices, several experimental laboratories, and the Beamlet system.
- Allocated $140K to refurbish and paint the Iron Cross triplex—Trailers 3724, 3725, and 3726.
- Finished the design for the Bldg. 481 transformer upgrade.

For FY 1995, the ICF Program continued a proactive management approach to environment, safety, and health (ES&H) issues. To support FY 1994's ICF management reorganization, the Assurances and ES&H managerial position (formerly the Building Superintendent) is now part of the ICF Program Operations office. Examples of the ES&H accomplishments are as follows:

- Completed the required documentation, according to the NEPA, for the Amplifier Development Laboratory to be built in Bldg. 391 in FY 1996.
- Replaced the Personal Protective Equipment (PPE) with reusable nylon suits, resulting in a considerable savings to the Program. PPE was worn during the Nova Target Chamber clean out and was disposed of as low-level hazardous waste.
- Began two NIF-related experiments in Bldg. 298 based on authorization under safety procedures coordinated by the ICF ES&H office.
- Received approval from the Environmental Protection Department (EPD) to allow discharge of Nova sol-gel rinse water to the sanitary sewer. Prior to this petition, all rinse water was sampled before discharge, requiring the sol-gel technical staff to collect rinse water instead of cleaning the Nova optics.
- Secured funding from EPD's Waste Minimization group to purchase and evaluate an ethanol distillation unit to reduce the ethanol waste from Nova's sol gel.
- Coordinated the Preliminary Hazards Analysis performed for Bldgs. 381 and 391 in accordance with DOE Order 5480.23 to reduce their classification from low hazard to radiological/excluded.
- Set up the ICF Emergency Preparedness Plan, participated in the Laboratory-wide earthquake evacuation drill, and located and treated pre-arranged "victims."
- Completed the Self Assessment inspections, covering 230 laboratories with 318 noted deficiencies, and their subsequent repair.
- Secured Air Permits from the Bay Area Air Quality Management District for wipe-cleaning operations in Bldgs. 174 and 381.
- Corrected 177 items from the ICF Def Track—the Laboratory-wide Deficiency Tracking System.

Notes and References

1. National Academy of Sciences Review of the Department of Energy's Inertial Confinement Fusion Program, Final Report (National Academy Press, Washington, DC, 1990).
2. S. N. Dixit, I. M. Thomas, M. R. Rushford, R. Merrill, et al., "Kinoform Phase Plates for Tailoring Focal Plane Intensity Profiles," *1994 ICF Annual Report*, 152–159, Lawrence Livermore National Laboratory, Livermore, CA, UCRL-LR-105820-94 (June 1995).
3. J. L. Porter, T. J. Orzechowski, M. D. Rosen, A. R. Thiessen et al., "The Albedo of Gold at High Temperatures," *1994 ICF Annual Report*, 125–131, Lawrence Livermore National Laboratory, Livermore, CA, UCRL-LR-105820-94 (June 1995).
4. D. S. Kershaw, M. K. Prasad, and M. J. Shaw, "Three-Dimensional, Unstructured-Mesh Eulerian Hydrodynamics with the Upwind, Discontinuous, Finite-Element Method," *1994 ICF Annual Report*, 160–168, Lawrence Livermore National Laboratory, Livermore, CA, UCRL-LR-105820-94 (June 1995).
5. M. Tabak, J. M. Hammer, M. E. Glinsky, W. L. Kruer, et al., "Ignition and High Gain with Ultrapowerful Lasers," *1994 ICF Annual Report*, 90–100, Lawrence Livermore National Laboratory, Livermore, CA, UCRL-LR-105820-94 (June 1995).
6. D. Eimerl, "Configuring the National Ignition Facility for Direct-Drive Experiments," *White Paper*, Lawrence Livermore National Laboratory, Livermore, CA, UCRL-ID-120758 (1995).
7. T. E. McEwan and J. D. Kilkenny, *ICF Quarterly Report* **4**(3), 108–116, Lawrence Livermore National Laboratory, Livermore, CA, UCRL-LR-105821-94-3 (1994).
8. S. Drell, C. Callan, M. Cornwall, D. Eardley, et al., *Science Based Stockpile Stewardship*, JASON, The MITRE Corporation, McLean VA, JSR-94-345 (November 1994).
9. President Clinton's News Release, August 11, 1995.
10. *The National Ignition Facility (NIF) and the Issue of Nonproliferation*, Final Study, Prepared by the DOE Office of Arms Control and Nonproliferation (NN-40), December 1995.
11. H. R. O'Leary, Secretary of Energy, Washington, DC, memorandum to The Honorable Floyd Spence, Chairman, Committee on National Security, U.S. House of Representatives, dated December 20, 1995.
12. Notice of Intent to Prepare a Stockpile Stewardship and Management Programmatic Environmental Impact Statement (6450-01-P), June 9, 1996 (signed by Peter N. Bush, Principal Deputy Assistant Secretary, Environment, Safety, and Health).
13. "Core Science and Technology Development Plan for Indirect-Drive Ignition," a joint effort by Lawrence Livermore National Laboratory, Livermore, CA; Los Alamos National Laboratory, Los Alamos, NM; and Sandia National Laboratory, Albuquerque, NM, UCRL-ID-117076 Rev 1 (December, 1995).
14. Schott Glass Technologies Inc., 400 York Ave., Duryea, PA 18642.
15. Hoya Corporation USA–Optics Division, 3400 Edison Way, Fremont, CA 94538-6190.
16. Corning Glass Works, MP-21-04-2, Corning, NY 14831.
17. Cleveland Crystals, Inc., 676 Alpha Dr., Highland Heights, OH 44143.
18. Zygo Corporation, Laurel Brook Rd., Middlefield, CT, 06455-0448.
19. WYKO Corporation, 2650 East Elvira Road, Tucson, AZ 85706.
20. D. P. Grote and A. Friedman, "3D Simulation of Heavy-Ion Beams for Inertial Confinement Fusion," *National Energy Research Supercomputer Center Buffer* **19**(11), 5 (November 1995).
21. C. Orth, S. Payne, and W. Krupke, *Nuclear Fusion* **36**(1), 75, 1996.
22. The International Symposium in Heavy-Ion Inertial Fusion was held in FY 1995 under the sponsorship of Princeton Plasma Physics Laboratory. The Proceedings of that meeting will be published in *Fusion Engineering and Design* (late 1996), and interested persons are referred to that source for detailed information on many aspects of the HIF program, both at LLNL and worldwide.

System Description and Initial Performance Results for Beamlet

B. M. Van Wonterghem *C. E. Barker*

J. R. Murray *I. C. Smith*

J. H. Campbell *D. F. Browning*

D. R. Speck *W. C. Behrendt*

Introduction

The Department of Energy has proposed to design and construct a National Ignition Facility (NIF) for Inertial Confinement Fusion (ICF) research. This facility will contain a frequency-tripled, Nd:Glass laser system capable of irradiating fusion targets at an energy and power of 1.8 MJ and 500 TW. The laser output pulse contains most of the energy, where the low-intensity leading foot is 15–20 ns long and the final high-intensity pulse is 3–4 ns long. The laser will have 192 independent "beamlets," each having a final square clear aperture of 40×40 cm^2 and an output beam area slightly smaller than the clear aperture. A Conceptual Design Report (CDR),[1] prepared in May 1994, discusses the laser and facility design in detail.

We have constructed and are now testing a scientific prototype of a single beamlet of the proposed NIF laser (Fig. 1). The purpose of these tests is to show that the novel features proposed for the NIF laser design will perform as projected and that the laser is ready for final engineering design. The final dimensions and component arrangements for NIF will differ somewhat from our scientific prototype, but the differences are sufficiently small that tests on the prototype can be used to demonstrate performance essentially equivalent to a NIF beamlet.

The project to build a scientific prototype beamlet (hereafter referred to as "Beamlet") was begun in 1991 and consisted of three main efforts: (1) development of laser components, (2) design and construction of the main laser system, and (3) activation. Previous *Quarterlies* present the results of the component development activities[2–5] and the laser design.[6] This article presents an overview of the constructed Beamlet laser system, and the results from the first integrated tests performed near the end of laser activation. These integrated tests culminated in a third-harmonic milestone shot on

(a) Beamlet laser

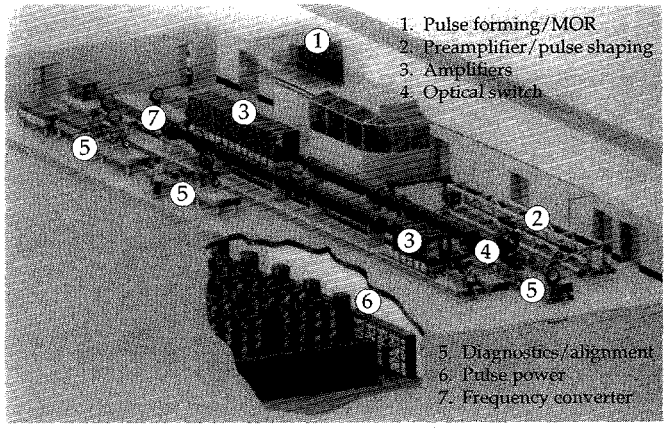

(b) Fully assembled system

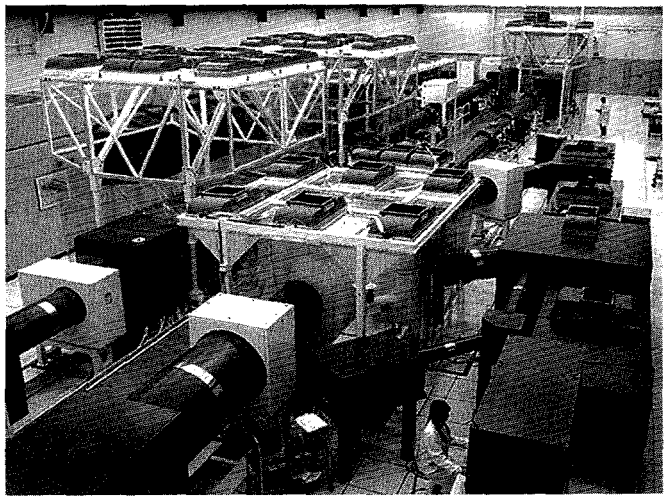

FIGURE 1. (a) Artist's rendering of the Beamlet laser showing the main subsystems. (b) A photograph of the fully assembled system. (70-50-0195-0181pb01)

September 8, 1994 that produced an average output 3ω fluence of 8.7 J/cm^2 in a 29.6 × 29.6 cm^2 beam and a 3-ns square pulse. Table 1 summarizes the key energy and fluence performance results recently achieved on Beamlet at 1ω and 3ω. The fluence levels listed in Table 1 (and discussed later in this article) are higher than the fluences projected for the NIF design.[1]

Subsequent articles in this *Quarterly* present detailed design and test results for many of the major components on Beamlet. The final article compares the results of the performance of Beamlet with recent model calculations.

The NIF Laser Design Compared with Current ICF Lasers

Figure 2 shows the singlepass master oscillator/power amplifier (MOPA) architecture; Fig. 3 shows the multipass architecture proposed for the NIF laser and contrasts that with the prototype Beamlet design.[1]

Current ICF Laser Design—A Singlepass Architecture

Most large glass lasers designed for inertial fusion experiments have the singlepass MOPA architecture: the Nova laser[7] at Lawrence Livermore National Laboratory (LLNL), USA; the Omega laser[8] at the Laboratory for Laser Energetics, University of Rochester, USA; the Gekko XII laser[9] at the Institute of Laser Engineering, University of Osaka, Japan; the Phébus laser[10] at the Commissariat a l'Énergie Atomique, Centre d'Études de Limeil–Valenton, France; and the Helen laser at the Atomic Weapons Research Establishment, England.

A master oscillator generates a few-nanosecond pulse of several millijoules that is then spatially and temporally shaped at about a 1-cm aperture and split into parallel chains of singlepass rod and Brewster's-angle slab amplifiers of increasing size. Gain isolation is provided at small aperture (<~10 cm) by ring-electrode Pockels cells and thin-film polarizers. Faraday rotators, driven by pulsed electromagnets, are used at large apertures to isolate pulses from propagating backward down the laser chain. Single-beam amplifiers with round apertures up to about 32 cm are used in all of these facilities. In addition, Nova and Phébus lasers have amplifiers with apertures of 46 cm using glass slabs that are split into two independent pieces.

The singlepass MOPA is a familiar and well-proven design that can be assembled and tested in stages, so performance risk is low. Cost and complexity are high, however, because of the very large number and variety of components required for a MOPA design. The Nova laser, for example, contains one rod amplifier

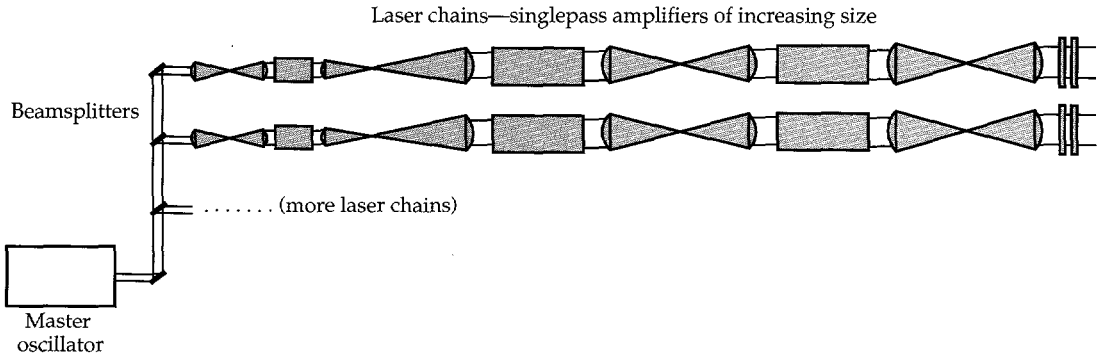

FIGURE 2. Singlepass master-oscillator, power-amplifier (MOPA) laser architecture commonly used by existing ICF lasers. (40-00-0294-0375pb01)

TABLE 1. Initial performance results for the NIF prototype beamlet at 1054 and 351 nm.

Wavelength (nm)	Zero-intensity beam dimensions (cm^2)	Output[a] pulse length (ns)	Fluence (J/cm^2)	Total energy (kJ)	Spatial intensity modulation (pk-avg)[b]
1054	34 × 34	3	12.5	12.1	1.45:1
		5	14.3	13.9	1.25:1
		8	16	15.5	1.25:1
351	29.6 × 29.6	3	8.7	6.4	1.35:1

[a]Temporally square output pulse.
[b]Peak-to-average ratio.

and five sizes of elliptically shaped slab amplifiers (a total of 41 slabs) in each of ten laser chains. There are also eight additional rod amplifiers of several sizes between the oscillator and the chains. In addition, there are relay telescopes and isolators between all of these amplifier stages.

The existing ICF MOPA lasers were all designed for maximum effective operation at pulse lengths near 1 ns. Fusion targets for the NIF, however, require effective pulse lengths typically in the range of 3–5 ns. If the laser design pulse length increases above 1 ns then the corresponding increase in component damage thresholds allows the laser to operate at higher fluences. This significantly increases the efficiency of energy extraction from the laser glass. In the case of the MOPA design, however, these high extraction fluences produce significant gain saturation in the large amplifiers. This, in turn, requires that the successive MOPA amplifiers have increasingly larger apertures so they do not gain-saturate, since gain-saturation effects produce

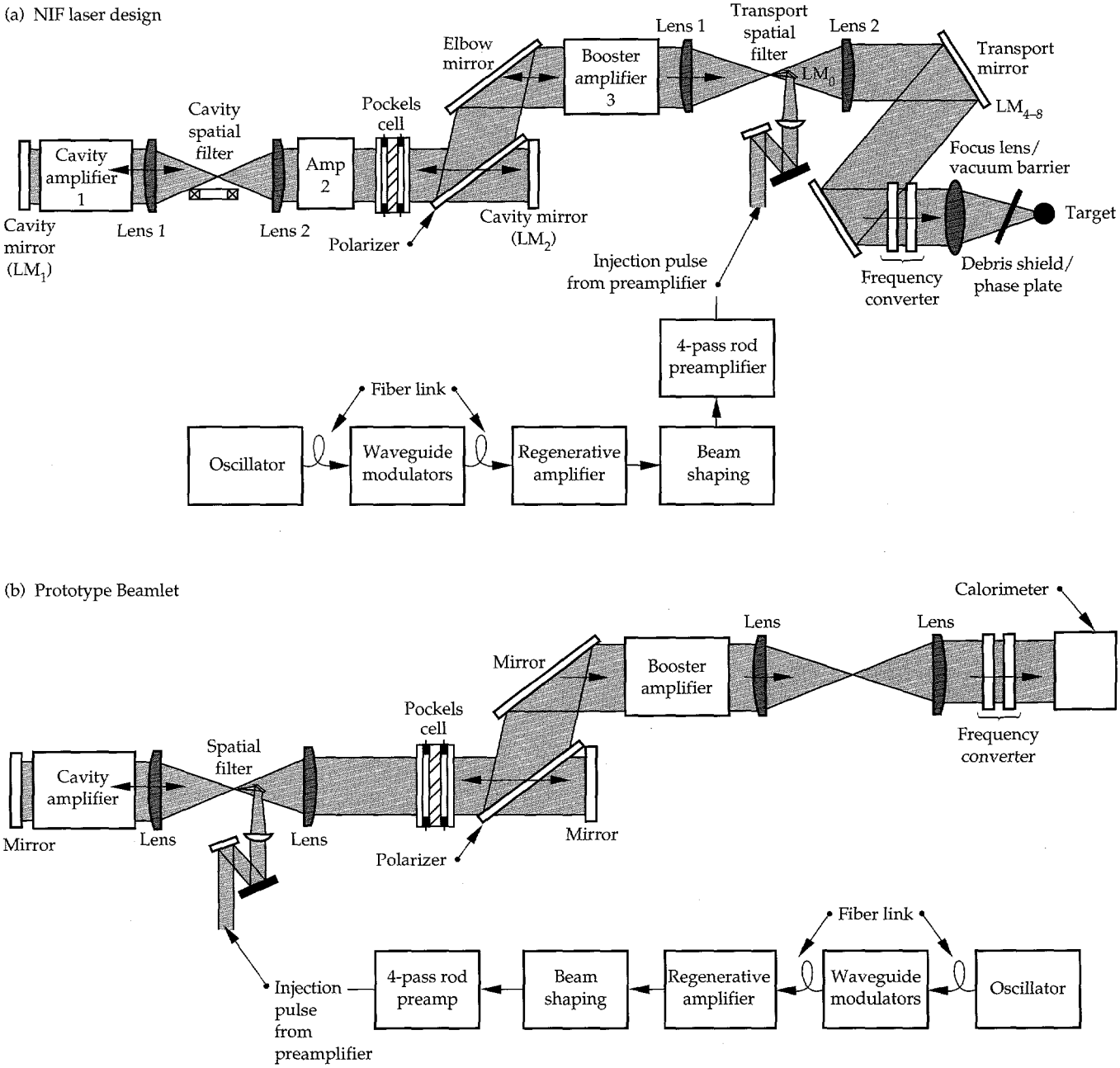

FIGURE 3. (a) Schematic drawing of the multipass NIF laser design. (b) Prototype Beamlet design. (40-00-0394-0789pb02)

severe temporal pulse distortion. (See "Beamlet Pulsed-Power System," p. 62). In contrast, a multipass amplifier uses the full aperture of the main amplifier as a preamplifier on early passes, such that the fluence increases monotonically during propagation, reaching a maximum of several times the saturation fluence in the last slab of the booster amplifier. Temporal pulse distortion is minimized in this configuration.

NIF/Beamlet—A Large-Aperture, Multipass Laser Design

In the NIF design [Fig. 3(a)], the pulse-forming system uses a low-power oscillator to drive an array of single-mode optical fibers, one for each beamlet of the system (the prototype Beamlet oscillator drives only a single fiber). The output from each fiber is input to waveguide-amplitude modulators to temporally shape the pulse and then fed to phase modulators to add the required bandwidth (bandwidth is required to suppress stimulated Brillouin scattering, or SBS, in the output optics when driven at high intensities). These integrated optical modulators are derived from the low-voltage designs used in high-speed fiber communications networks, and ultimately could be operated under direct computer control, although Beamlet has not yet implemented this option. The pulse output from the modulator is then fed to a single-mode, regenerative amplifier that amplifies the pulse to ~10 mJ.[3] A beam-shaping section forms the appropriate spatial intensity profile that is injected into the preamplifier section of the laser amplifier chain. A four-pass, single-rod preamplifier amplifies the pulse to about 1 J and injects it into the main four-pass slab amplifier, where it reaches approximately 10 kJ. The four-pass configuration permits us to make the preamplifier section small enough that the cost savings from any further reduction would be negligible. The prototype Beamlet uses 16 rectangular slabs in the final amplifier stage that have a pumped aperture of 39 cm. The pulse that exits the laser amplifier section proceeds to a frequency converter and, in the case of the NIF, to the target chamber.

A multipass amplifier requires a method for separating input and output beams in the amplifier, which is not necessary in a singlepass system. There are three generic techniques for accomplishing this: (1) a polarization rotator can be used to separate beams at a polarizer [Fig. 4(a)]; (2) the beams can be separated in angle in the near field [Fig. 4(b)]; or (3) they can be separated in angle in the far field near a focal plane [Fig. 4(c)]. Near-field angle separation has been used with large laser systems.[11] It requires either a very long propagation distance, leading to difficulties with diffraction, or a beam size much smaller than the amplifier aperture to accommodate the beam motion, leading to poor utilization of the amplifier volume. Therefore, near-field separation has not been considered for the NIF design.

Far-field angle separation has several desirable features for this application. There is no closed path in the laser cavity, so parasitic oscillations are less of an issue than for a configuration in which there are closed resonant feedback paths. Each pass through the focal plane goes through a separate aperture in that plane, so the propagation of later passes is not affected by plasma generated in the aperture by earlier passes. Any leakage out of the cavity on early passes is at an angle to the final output beam, so it is easily occluded in a transport spatial filter and cannot disturb the laser target. Finally, far-field angular separation gives a convenient location for injecting a low-energy input pulse near the focal plane without requiring additional full-aperture optical components.

The Beamlet test series presented here uses a combination of far-field angle plus polarization separation. Polarization separation is achieved using a full-aperture Pockels cell plus a polarizer in the large final amplifier stage. The far-field angle separation gives the advantages

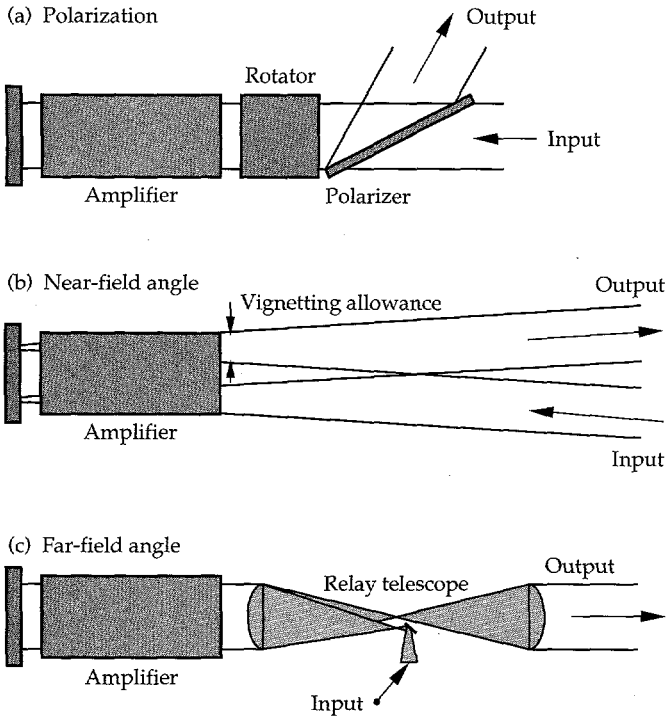

FIGURE 4. Three generic schemes for separating the input and output beams for a multipass laser architecture: (a) polarization rotator and polarizer, (b) near-field angle separation, and (c) far-field angle separation. NIF and the prototype Beamlet use a combination of far-field angle separation and polarization rotator. (70-50-0195-0020pb01)

just mentioned, while the Pockels cell gives gain isolation and isolation from back reflections. The full-aperture Pockels cell also allows the off-axis angle in the far-field to be very small since, at that point, the energy handled on the injection optics is only about 1 J. The small angle allows efficient use of the amplifier aperture with a relatively short laser cavity. It is possible to configure the system to do separation using a far-field angle only, using a smaller Pockels cell for isolation purposes only. This alternate configuration requires handling the beam near the far field and at energies up to 100 J, but avoids the cost of the full-aperture Pockels cell and polarizer. Both configurations will be tested on Beamlet.

The NIF laser design groups beamlet amplifiers into large arrays stacked four high and twelve wide to minimize the number of components and flash lamps (see Fig. 1 in "Design and Performance of the Beamlet Amplifiers," p. 18). The individual beamlets are optically independent, though supported by common mechanical hardware and pumped by common flash lamps. This full array of 48 apertures is too large and expensive to test in a small scientific prototyping effort. Therefore, on Beamlet we constructed the amplifier as an array of four apertures stacked two high and two wide to study many of the major issues of this type of amplifier assembly. (See "Design and Performance of the Beamlet Amplifiers," p. 18.) Only one of the four beamlet apertures contains high-quality laser glass and is used for the tests discussed here. The amplifiers are constrained to have an odd number of slabs, since this cancels asymetric gain gradients in the two end slabs.

A state-of-the-art adaptive wavefront control system is used on Beamlet to correct for static and dynamic optical aberrations. The Beamlet adaptive optic system consists of a deformable mirror (DFM), two Hartmann wavefront sensors, and a closed-loop controller. This adaptive optic technology was developed and demonstrated on the large dye laser systems that are part of the LLNL Uranium-Isotope Separation project.[12] The Beamlet adaptive optics system is discussed further in "Beamlet Pulse-Generation and Wavefront-Control System," p. 42.

The amplifier stages are separated by relay telescopes or spatial filters that reimage a beam-forming aperture at several places through the amplifier chain. This reimaging reduces the diffractive growth of spatial intensity noise and provides Fourier transform planes at the focal planes in the telescopes where high-spatial-frequency intensity noise can be reset to zero. The noise level needs to be kept low because nonlinear propagation effects cause it to grow exponentially at high intensity.[1]

Beamlet Test Configuration

Figure 5 is a plan view of Beamlet as configured for the test series presented here. We use a prototype[3] of the pulse generation and preamplifier system proposed for NIF to produce an approximately 1-J pulse that is injected into the main four-pass laser cavity. The injected pulse is temporally shaped to compensate for gain saturation effects and is designed to produce a 3-ns square pulse output. To compensate for gain roll-off near the edges of the amplifier slabs, the intensity profile is shaped using a transmission filter with a parabolic transmission profile (see "Beamlet Pulse-Generation and Wavefront-Control System," p. 42). Also, all laser experiments reported here use input pulses that are phase-modulated

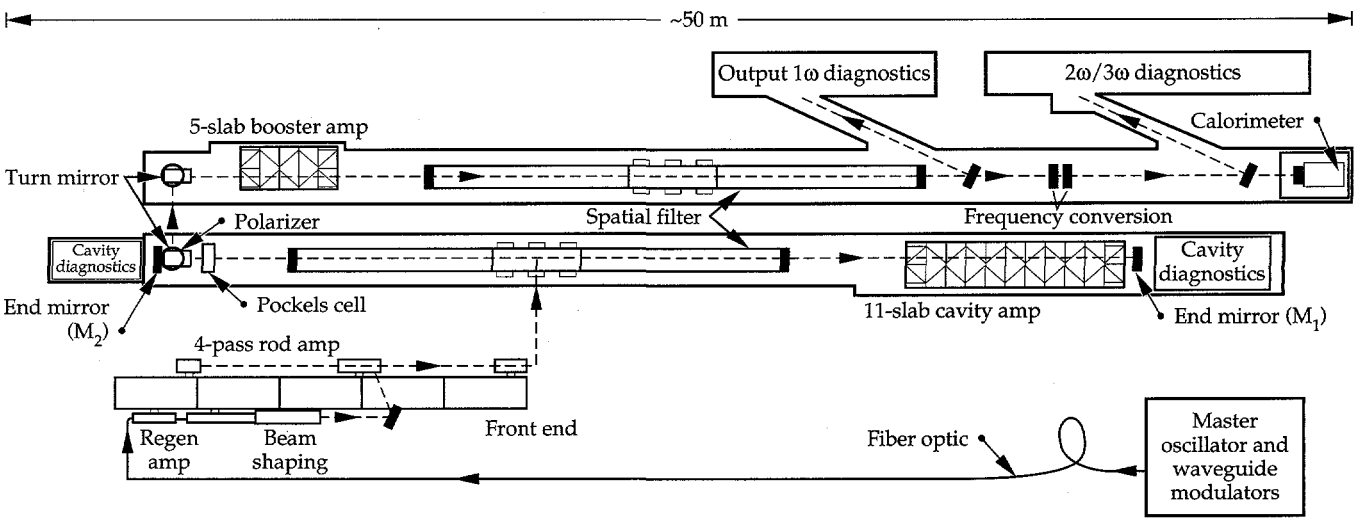

FIGURE 5. Plan view of Beamlet as configured for the tests described in this article. (02-30-1091-3760Epb01)

by the front end at a single modulation frequency of 5 GHz to provide a total bandwidth of about 30 GHz. This additional bandwidth reduces the net SBS gain, thus eliminating the damage threat posed by transverse SBS. The output pulse from the front end is injected using a small 2×2 cm^2 45° mirror, and the pulse comes to a focus at an aperture in the focal plane of a vacuum spatial filter. The pulse expands past focus to fill a recollimating lens and a multisegment amplifier[2] containing eleven Brewster's-angle slabs. (See the article "Design and Performance of Beamlet Amplifiers," p. 18.) It then reflects from a cavity end mirror M_1, and makes a second pass through the multipass amplifier, emerging with an energy of about 100 J.

At the other end of the laser cavity is an optical switch, consisting of a plasma-electrode Pockels cell (PEPC) and a polarizer. (See Ref. 4 and "Design and Performance of the Beamlet Optical Switch," p. 29 for a discussion of optical switches; see "Large-Aperture, High-Damage Threshold Optics for Beamlet," p. 52 for a discussion of polarizers.) As the pulse is injected for its first two passes through the multipass amplifier, the Pockels cell is switched on to rotate the polarization so that the pulse passes through the polarizer and strikes a second mirror, M_2. It then returns to the multipass amplifier for a third and fourth pass, emerging with an energy near 6 kJ. By the time it returns to the Pockels cell, the cell has switched off, so the pulse then reflects from the polarizer and makes a single pass through a second so-called "booster" amplifier containing five Brewster's-angle slabs. A transport spatial filter relays the pulse to the frequency converter. At this point, the 1ω energy is 12–15 kJ, as shown in Table 1.

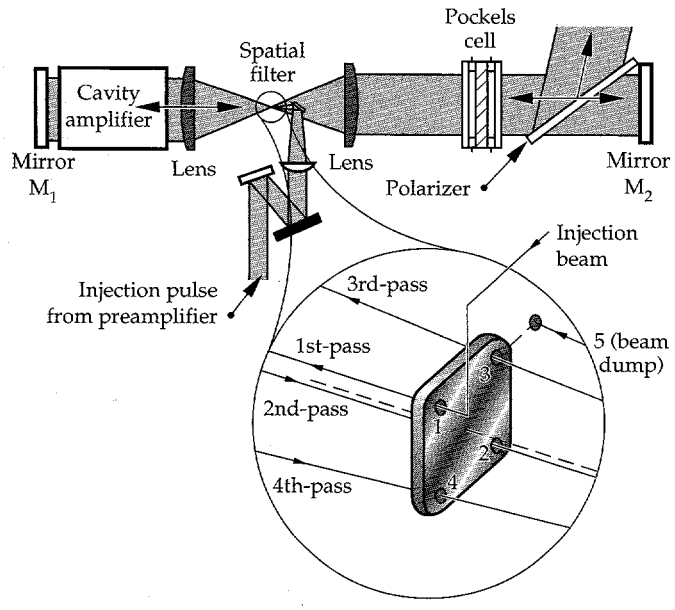

FIGURE 6. Pinhole array layout at the focal plane of the Beamlet multipass cavity. (70-50-0393-0724Bpb01)

Figure 6 is a schematic of the array of pinhole apertures at the focal plane of the cavity spatial filter. Mirror M_1 is positioned such that the pulse injected at pinhole 1 returns to a position at pinhole 2. Similarly, mirror M_2 is aligned so that the return pulse from M_2 is at pinhole position 3. The return from the second pass then automatically lies at pinhole 4. Any energy not switched out of the cavity strikes mirror M_2 and returns to the focal plane at position 5 where it is intercepted by an absorbing glass beam dump. For this series of experiments, we used 3.6-mm-diam pinhole apertures, giving a spatial frequency cutoff wavelength of 7.2 mm in the near field, or an angular acceptance of ±200 μrad in the far field. The separation between pinhole apertures is 3 cm.

The clear aperture of the potassium dihydrogen phosphate (KDP) crystal installed in the Pockels cell for the 1ω tests is 37 cm, which sets a beam hard aperture of about 35 cm. The beam must be smaller than the smallest clear aperture because of the vignetting allowance for beam motion due to off-axis propagation plus an allowance for full-beam alignment. The edge of the beam is apodized to suppress edge diffraction, as discussed later. The 39-cm amplifier aperture is not completely filled under these conditions, and could support slightly larger beam dimensions.

The cavity spatial filter lenses have a focal length of 9 m. The separation between M_1 and M_2 is 36 m and these mirrors lie at relay image planes of the system.

The beam is reflected out of the multipass cavity by the switch polarizer and then routed to the booster amplifier using three turning mirrors. After passing through a second spatial filter identical to the one in the multipass cavity, the beam then passes through an uncoated fused silica beamsplitter. The beamsplitter reflects a small portion of the 1-μm output beam to a diagnostics package. This package captures near- and far-field images on charge-coupled device (CCD) cameras, determines the energy using a calorimeter, and measures the temporal pulse shape using a vacuum photodiode with a transient digitizer or a streak camera. It also includes a 77-element CCD-based Hartmann sensor to measure wavefront distortion and to control the figure of the 39-actuator DFM.

The 1ω output beam enters a dual crystal frequency converter. The frequency converter uses a Type I/II third-harmonic generation scheme (Fig. 7), consisting of a 1.05-cm-thick KDP doubler crystal and a 0.95-cm-thick KD*P tripler crystal. In the experiments described here, 32×32 cm^2 crystals were used and the KD*P was 80% deuterated. The 32×32 cm^2 crystals will support about a 30-cm beam size. Crystals 37×37 cm^2 are currently being manufactured and will be used in future experiments. (Due to the long time required to grow the 37×37 cm^2 crystal boules, these larger crystals

were not available during our initial frequency conversion tests.) Finally, the output beam is absorbed by a 74×74 cm^2 calorimeter/beam dump after first passing through a biconcave expansion lens to reduce the fluence onto the calorimeter below the damage threshold of the absorbing glass in the calorimeter.

Measurement of Laser Performance at 1.05 μm

Optical Transmission with Unpumped Amplifiers

Optical losses reduce the laser output, particularly with long pulses where the laser amplifier gain is highly saturated. It is important to quantify these losses to match the measured laser output to theoretical models. We measured transmission through the system with unpumped amplifiers from pinhole to pinhole of the spatial filters, and also measured individual components to determine what these optical losses are for the Beamlet.

The transmission for a double pass through the eleven-slab-long cavity amplifier section is 84%, which consists of 22 laser slabs having an average transmission of 99.3%, one mirror with 99.6% reflection, and two lens transmissions at 99% each. The 0.5% loss per lens surface is typical of sol-gel antireflection coatings applied to fused silica, although coatings as good as 99.8% transmission have been prepared. The loss in laser slab transmission is dominated by absorption from the Boltzman population in the lower Nd:Glass laser level, and illustrates that bulk and surface losses due to contamination or defects in the laser glass are extremely small.

The double-pass transmission through the Pockels cell (in its "on" position) plus the polarizer is 71%. The crystal in the Pockels cell is 1-cm-thick undeuterated KDP (KH_2PO_4), so it has an absorption of 6%/cm at 1.053 μm, giving a double-pass transmission of 88%. The polarizer singlepass transmission for *p*-polarized light is 97.3%. This includes 1.1% loss due to the 9-cm-thick BK-7 substrate and 1.5% loss in the coating. If we assume 1% loss per surface for 16 antireflection coated surfaces (a lens, two windows, and a KDP crystal) and a mirror reflection of 0.995, the net transmission would be 71%, which is consistent with the measured value. (See "Design and Performance of the Beamlet Optical Switch," p. 29 for a more detailed discussion of the optical performance of the Pockels cell.)

The transmission of amplifier slabs in the booster and lenses in the output spatial filter are consistent with the measurements for the cavity amplifier and spatial filter discussed earlier. The polarizer reflects 99.6% of the *s*-polarized light that strikes it when the Pockels cell is switched to its "off" configuration. At an output energy of ~12 kJ after the booster amplifier, the polarizer reflects 6 kJ out of the multipass cavity and the energy transmitted through the polarizer is less than 30 J (polarizer *s*-polarized leakage plus any light rotated to *p*-polarization by birefringence in the system).

Gain Compensation

Figure 8 shows the singlepass, small-signal gain profile of a five-slab-long Beamlet amplifier pumped to

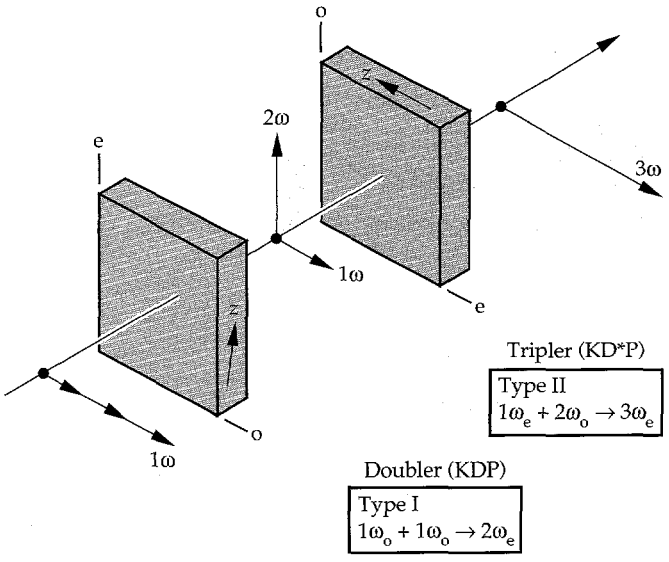

FIGURE 7. Type I/II frequency conversion scheme used on Beamlet. (70-10-0494-1827pb01)

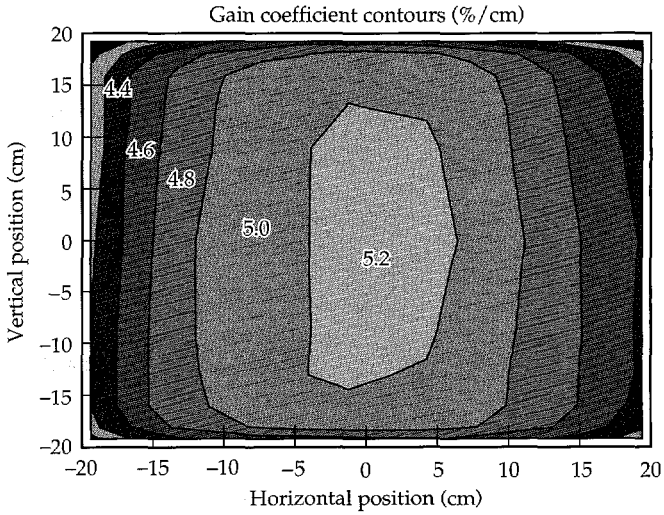

FIGURE 8. Gain profile for a five-slab-long amplifier. Amplified spontaneous emission causes the gain to roll off near the edges in the horizontal direction of the slabs. (02-30-1093-3495pb01)

its nominal operating point, 20% of the flash-lamp explosion energy. The gain peaks in the center of the aperture and is about 15% lower in the extreme corners of the aperture. Most of the gain roll-off is in the horizontal direction, which is the long dimension of the Brewster's-angle slab. Amplified spontaneous emission trapped by total internal reflection within the slab depletes the stored energy in the glass and causes this gain roll-off. (See "Design and Performance of the Beamlet Amplifiers," p. 18.)

To produce a flat intensity profile at the output of the laser requires that the input intensity profile to the multipass amplifier stage be shaped to compensate for the nonuniform gain profile in the horizontal direction (the effect of the vertical gain profile is insignificant). The input intensity profile used for the results presented here is parabolic in the horizontal direction with the edges of the aperture twice as intense as the center. Figure 9 shows the output intensity profile in the horizontal direction from the multipass stage only (without the booster amplifier) showing the effect of the gain compensation on the horizontal intensity profile. Note that without compensation for the gain distribution, the intensity near the edges of the beam rolls off dramatically. However, with gain compensation, a nearly flat, top-hat-shaped intensity profile is obtained. This is very important because the performance is limited by the peak laser fluence on the optical components. Therefore a flat beam profile allows a higher output energy at equal peak fluence: the gain-compensated profile has nearly 30% greater energy extraction for the same peak fluence.

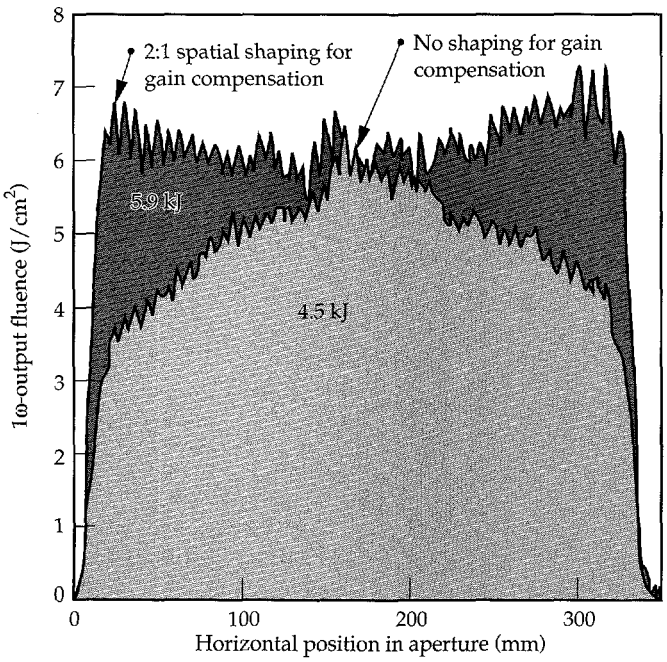

FIGURE 9. Effect of gain compensation on the horizontal intensity profile after four passes through the main multipass cavity. By compensating for the horizontal gain roll-off in the amplifier, the extracted energy increases 30%, and the output has the desired flat-top shape. (70-50-0494-2115pb02)

Edge Apodization and Fill Factor

It is important to fill the beam aperture as fully as possible to maximize the flat-top portion of the beam area and hence the laser output energy. A 1-cm margin around the edge of a nominal 34×34 cm^2 beam contains 11% of the beam area, so changes of only a few millimeters in beam dimensions can have a noticeable impact on the output energy of the system. Edge diffraction from sharp beam edges causes intensity peaks on the beam, however, so the beam intensity at the edge must be apodized. (That is, the intensity must decrease smoothly to zero over a region occupying at least a few Fresnel zones over the propagation distances for which these intensity peaks are not acceptable.)

The edge apodization used in the 1ω tests is an inverted Gaussian profile with the 10^{-2} intensity point at a square aperture of 34×34 cm^2.[13] (For the 3ω tests, we used a smaller square beam size of 29.6×29.6 cm^2.) The 10^{-2} intensity point is considered the "zero intensity" level and is the maximum intensity allowed to strike the edges of the clear aperture of optical components. The corners of the beam are rounded with a radius of 5 cm to suppress diffraction from these regions; this subtracts 20 cm^2 from the beam area.

The 1ω output beam with a zero intensity width of 34 cm has a half-power width of 31.5 cm when the laser is operated under heavily saturated conditions. The flat-top, high-intensity region in the center is 30.6 cm wide. The experimental data show no growth of diffractive intensity peaks around the edge of the beam, though simulations suggest that there is some growth under high-fluence and high-B conditions near the end of the pulse. We project, from simulations, that it should be possible to steepen the edge profile and reduce the edge apodization region by approximately half a centimeter with acceptable diffractive intensity growth. (This will be tested during future experiments on Beamlet.) The effective beam area at half power is 971 cm^2 after allowing for the 20 cm^2 loss in the corners, and we use that value to calculate fluence and intensity in the flat-top portion of the beam. The "fill factor" is 84% (defined as the ratio of the beam energy to the energy if the entire 34×34 cm^2 hard aperture were filled at the fluence of the flat central area of the beam).

Energy Performance

Figure 10 shows the Beamlet 1ω output energy that goes to the frequency converter as a function of energy injected into the main four-pass amplifier cavity. The solid line is the calculated performance from a model that includes measured gains and optical transmissions of the system. The maximum 1ω energy and fluence demonstrated at 3, 5, and 8 ns are listed in Table 1.

The gain-performance curve shown in Fig. 10 does not depend on the temporal pulse shape. However, for this shot series, the input pulses were temporally shaped to give nearly square output pulses. Figure 11 shows an example of input and output temporal pulse shapes under highly saturated conditions with an output of 15.5 kJ in an 8-ns pulse. Under these conditions, the intensity of the leading edge of the input pulse is shaped to be 12.5 times the intensity of the trailing edge to maintain a square output pulse shape.

Near-Field Beam Features

All large glass lasers have intensity noise in the near field as a result of diffraction from small obscurations and flaws in the many optical components through which the beam passes. The operating limit of ICF glass lasers is often set by the peak of the near-field intensity noise because of the threat for optical damage. However, the output power of the laser is determined by the average intensity. Therefore it is desirable to have a peak-to-average intensity ratio as near to unity as possible.

Figure 12 shows the 1ω near-field image of the Beamlet output at 8 kJ and 3 ns. This represents the quality of the beam that is sent toward the frequency converter. The peak-to-average fluence modulation, due to diffractive noise sources, is about 1.3 to 1. For comparison, the Nova laser, when operated at high fluence, typically has a peak-to-average fluence modulation of about 1.5 to 1.

Some of the prominent patterns shown in the near-field image (Fig. 12) originate from identified sources. For example, the small obscurations near the center of the image are originally from optical breakdown in air paths caused by ghost reflections. Ghost reflections refer to the small reflections from antireflection (AR) coated optics. Because AR coatings are not perfect, some very small portion of the incident light is reflected. If these reflections originate from curved surfaces such as lenses, they will either diverge or come to a focus. The focused ghosts can be intense enough to cause optical breakdown in the air path of the beam or even optical damage if the focus occurs at or near an optical component. Ghost reflections from the Beamlet cavity spatial filter lenses come to a focus in air between the lens and the amplifier or Pockels cell where they cause small air breakdown plasmas to form. When the laser pulse returns through that region on a later pass, these ghost foci appear as small obscurations on the beam. The obscurations are much less apparent after the booster amplifier since they fill in due to unsaturated gain in that amplifier stage. Other features faintly visible in the

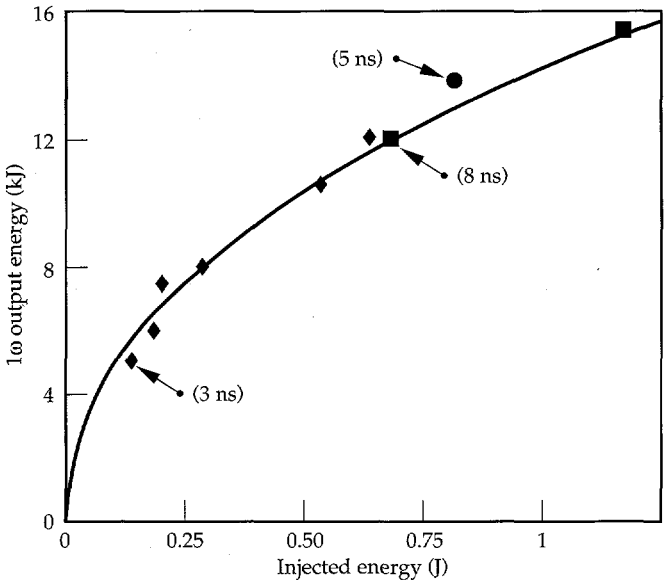

FIGURE 10. Measured 1ω output energy vs energy injected into the large multipass cavity. These tests were carried out with eleven amplifier slabs in the four-pass cavity and five in the singlepass booster amplifier (with a flash-lamp pump explosion fraction of 0.2). (70-50-1094-3626pb01)

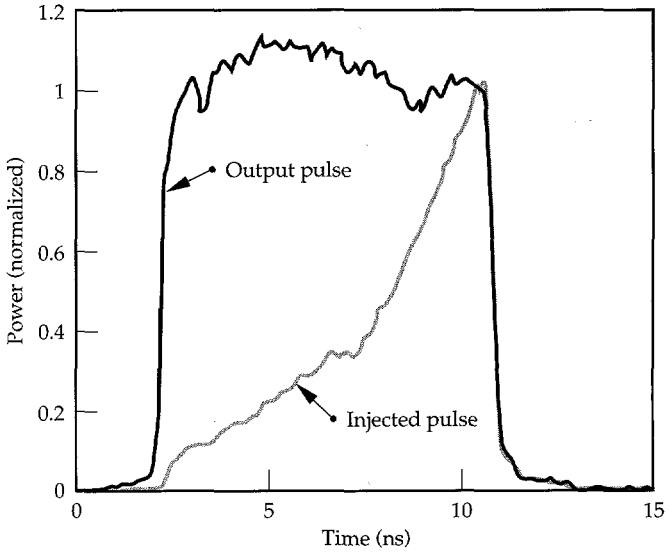

FIGURE 11. Comparison of 1ω input and output temporal profiles for a full-system shot (eleven- and five-amplifier slab configuration). The input energy is 1.2 J and the contrast ratio (ratio of the leading to trailing edge intensities) is about 12.5 to 1. The output energy is 15.5 kJ at 8 ns. (70-50-0195-0024pb01)

near-field image (Fig. 12) include multiple Airy patterns caused by small opaque defects. Nearly all of these originate from tiny particulates on some of the small optics of the diagnostic camera system.

Figure 13 shows the cumulative intensity distributions for image pixels within the flat-top area of the Beamlet output beam under several different conditions, illustrating the effects of saturation and modulation growth due to the nonlinear index of refraction in the optical components. Each pixel corresponds to a beam area of 1.4×1.4 mm^2. The 8-ns pulse at 15.5 J/cm^2 or 1.94 GW/cm^2 has a steeper distribution function than the other shots plotted, particularly in the high-intensity regions. This shows the effect of gain saturation for high-intensity peaks, coupled with the absence of any significant nonlinear effects at this long pulse length and low intensity. The 3-ns pulse at 12 J/cm^2 or 4.0 GW/cm^2 shows some growth of intensity peaks due to nonlinear index; at high intensities, this nonlinear effect tends to amplify light scattered at small angles by defects in the optics.

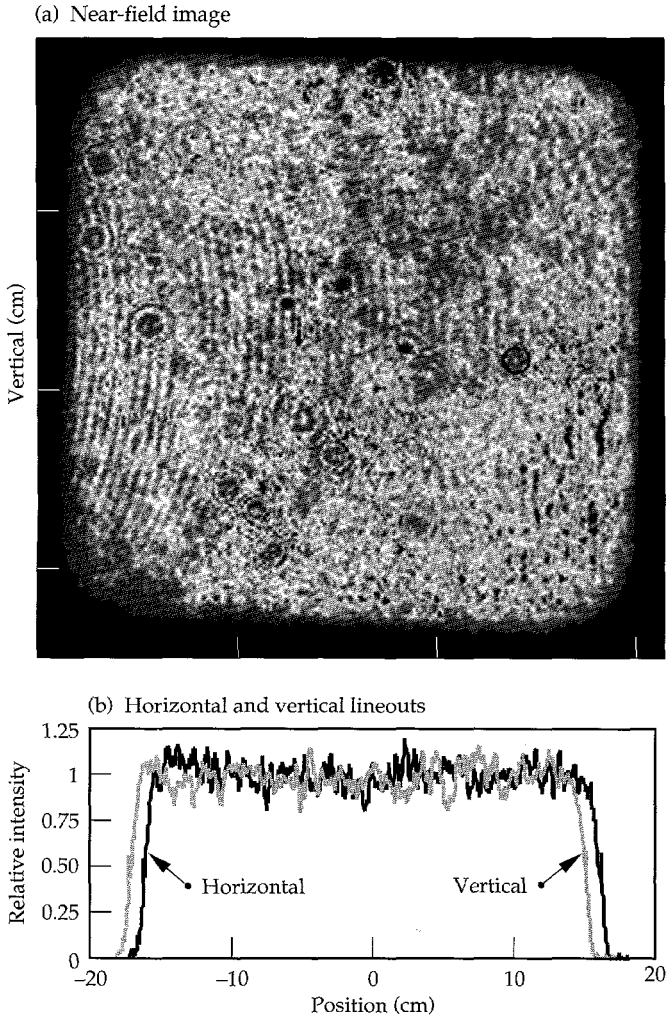

FIGURE 12. (a) Near-field image of the 1ω output from Beamlet for a 5.9-kJ shot at 3 ns; (b) Horizontal and vertical lineouts through the image. (70-50-0494-2124pb01)

Nonlinear Effects at High Intensity

At very high intensities, the intensity-dependent part of the refractive index becomes important. This nonlinear effect causes growth of noise (small angle scattering) by energy transfer from the main beam through a second-order wave mixing process.[14] The gain of noise growth depends on its spacial frequency. This process limits the laser performance, because excessive growth of noise components can lead to damage of laser components. In Beamlet, beam breakup (due to small-scale self-focusing of noise spikes) limits the performance at and below 3 ns. Quantifying this effect on Beamlet is very important to confirm the theory and modeling, which also have been applied to establish the NIF performance.

These studies are hazardous for the laser components, however, because the intensity modulation can grow very quickly to damaging levels. To minimize the risk to the laser, we chose to study the growth of intensity modulation with short pulses (200 ps) and with the booster amplifier unpumped. Note that by using short pulses, we can propagate high-intensity beams at fluences far below the damage thresholds of the optical components. For these shots, the unpumped booster amplifier served as merely an array of nonlinear components in which we could study the growth of beam modulation.

The onset of significant small-scale self-focusing usually occurs when the intensity-driven, nonlinear

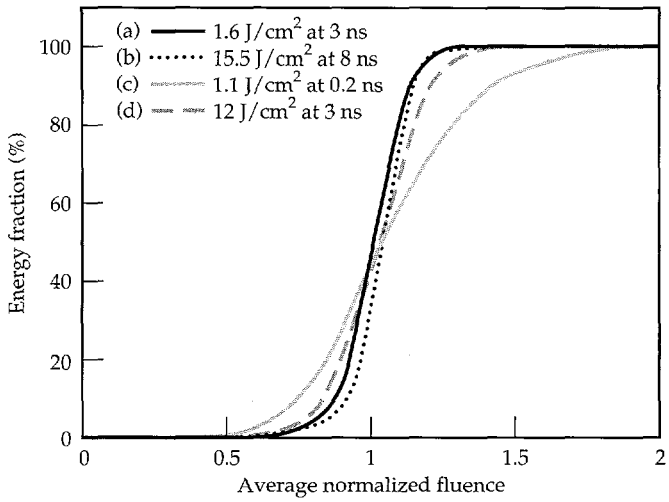

FIGURE 13. Cumulative 1ω intensity distributions determined from near-field image profiles for Beamlet shots at various pulse lengths and mean fluences. (a) 0.53 GW/cm^2, (b) 1.94 GW/cm^2, (c) 5.5 GW/cm^2, and (d) 4.0 GW/cm^2. (70-50-0195-0017pb01)

phase shift reaches about 2 rad. There is a noticeable growth of the intensity modulation in the 4.0-GW/cm^2 image, and serious beam breakup has begun at 5.5 GW/cm^2. Figure 14 shows the near-field appearance of the output beam at this intensity. The nonlinear phase shift through the Pockels cell and booster amplifier amounts to 3 rad for this shot. These shots were taken using the original KDP Pockels cell crystal that had a poor-diamond-turned surface and imposed a 6.4-mm period modulation on the beam. (See "Large-Aperture, High-Damage Threshold Optics for Beamlet," p. 52 for a detailed discussion.) It is clear that this modulation serves as the noise source that seeds the nonlinear intensity growth and beam breakup.

1ω Far-Field Beam Quality

The nominal NIF ignition target design requires a 0.5-mm-diam spot at the focus of a 7-m focal length lens.[1] Energy lying much outside this ±35-μrad angle is not useful and can be harmful if it strikes the wrong area of certain targets. Some experiments planned for NIF require smaller spots, so a smaller beam divergence is desired. The diffraction limit of a normal 35-cm beam is ±5 μrad, so a NIF beamlet should be roughly 3 to 7 times the diffraction limit, as usually defined, at the fundamental 1.053-μm wavelength (this divergence is preserved when the beam is converted to the third harmonic). Efficient frequency conversion also sets a beam divergence specification,[5] but it is less stringent than this spot size requirement for NIF (±35 μrad).

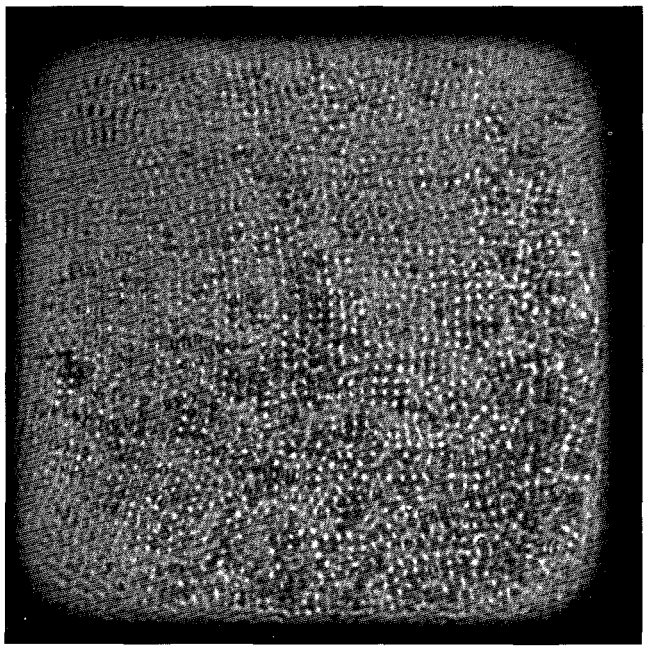

FIGURE 14. Near-field image of the 1ω output beam for a 5.5-GW/cm^2 shot at a 200-ps pulse width. The white dots are hot spots with an intensity nearly twice the average intensity. Figure 13(c) shows the cumulative intensity distribution for this shot. (70-50-0195-0023pb01)

As mentioned earlier, a DFM is used on Beamlet to correct for low-order static and dynamic wavefront aberrations. (See "Beamlet Pulse-Generation and Wavefront-Control System," p. 42.) Figure 15 shows a recent Beamlet 1ω far-field profile obtained using precorrection for static and pump-induced aberrations on a 4.5-kJ 3-ns shot. The rms wavefront aberration is reduced to 0.17 waves, which leads to a calculated Strehl ratio of 0.4. The central spot is diffraction limited and approximately 10-μrad wide. Most of the energy is contained well within the NIF requirement of ±25-μrad divergence angle. The booster amplifiers were not yet installed at the time this shot was taken. For comparison, the beam without wavefront correction by the DFM would almost fill the entire image plane shown in Fig. 15.

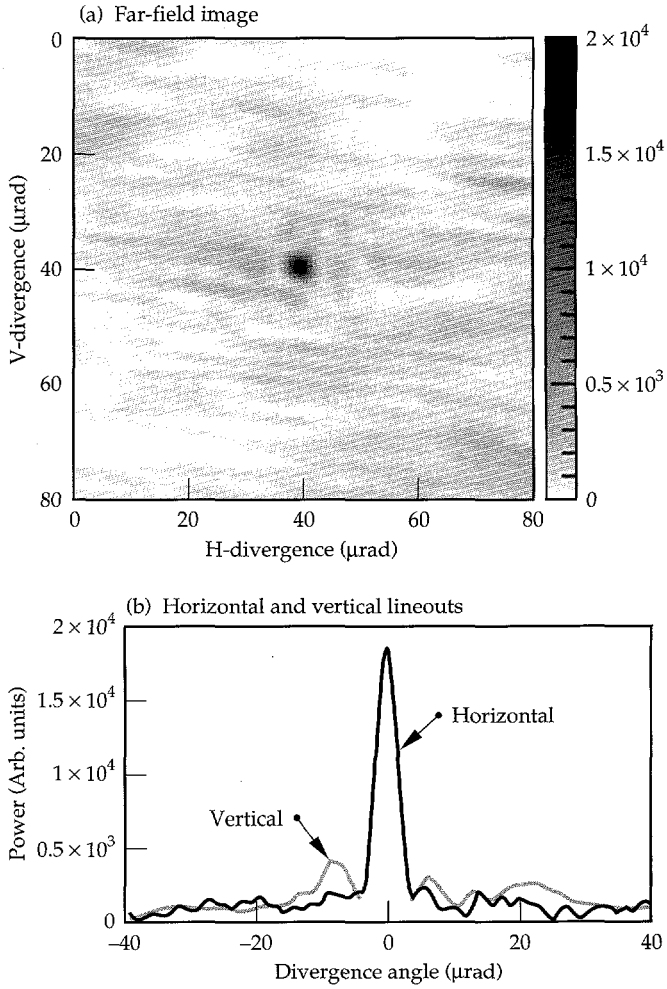

FIGURE 15. (a) 1ω far-field image and (b) horizontal and vertical lineouts of a 4.5-kJ 3-ns Beamlet shot. The wavefront of the 35 × 35 cm^2 beam was fully precorrected for static and pump-induced aberrations using a 39-element DFM. (70-50-0195-0022pb01)

Table 2 summarizes preliminary results obtained using the Beamlet Hartmann wavefront sensor and adaptive optics control system. The DFM corrects for the static aberration in the beamline, such that the output wavefront is nearly flat before a shot. The pump-induced wavefront aberration during a shot is largest near the edges of the beam and amounts to 1.65 waves peak-to-valley (p-V) for a 34-cm beam size.

Preliminary attempts to precorrect the injected wavefront for this dynamic distortion showed a reduction of the output aberration by a factor of two. The large and slowly decaying thermally induced aberration in the amplifier slabs after a shot can again be corrected in real time. These results clearly demonstrate the value of the adaptive optics system to increase the brightness of ICF lasers.

Harmonic Generation Experiments

Beamlet Frequency Conversion System

Third-harmonic generation on Beamlet was achieved by the sequential application of collinear sum-frequency mixing in two nonlinear crystals. A beam at the fundamental laser frequency is incident upon the first nonlinear crystal in which second-harmonic generation takes place via degenerate sum-frequency mixing ($\omega_2 = 2\omega_1$). Two copropagating beams, one at the fundamental and the other at the second harmonic, emerge from this "doubling" crystal. They are incident upon the second nonlinear crystal in which the fundamental and the second harmonic again interact through sum-frequency mixing to create a wave at the third harmonic. To efficiently transfer power from the incident waves to the higher harmonic requires that both waves traverse the crystal in phase. Two methods of phase matching are possible—Type I phase matching, where the two input waves have the same polarization; and Type II phase matching, where the two input waves are orthogonally polarized. Details of the harmonic generation process are described elsewhere.[15,16]

The Type I KDP second-harmonic generation crystal converts a large fraction of the 1054-nm light to the second harmonic at 532 nm. The Type II KD*P "tripling" crystal then converts this residual fundamental and the second-harmonic beam to the third harmonic at 351 nm. The efficiency with which the third harmonic is generated is very sensitive to the ratio of the intensities of the fundamental and the second-harmonic beams incident on the tripler. This mix ratio is controlled by the length of the doubling crystal and a slight mismatch between the propagation direction of the beam inside the doubling crystal and the perfect phase matching direction.

The Beamlet frequency conversion system is designed to hold two different sizes of square crystal plates (32 and 37 cm). These crystals can accommodate maximum beam sizes up to about 30 and 34.5 cm, respectively. We activated the frequency converter with 32-cm crystals, although 37-cm crystals will be installed and tested in early 1995. The smaller crystals were used in our initial tests because they became available about 6 months before the larger ones. This is simply due to the longer time needed to grow the 500-kg single-crystal boules from which the 37-cm plates were cut. (See "Large-Aperture, High-Damage Threshold Optics for Beamlet," p. 52 for more details on the crystals.) The crystals are installed in two 61-cm-diam optical mounts that allow x and y translation, rotation about the axis of beam propagation, and tilt about two orthogonal axes in the plane of the crystal (Fig. 16). The crystals and their mounts are contained within an insulated housing that maintains the temperature to within ±0.1 K and ±10% relative humidity.

TABLE 2. Measured 1ω static and dynamic beam aberration on Beamlet.

Measurement Condition[a]	30-cm beam p-V[b]	30-cm beam rms	34-cm beam p-V	34-cm beam rms
Static aberration (cold cavity)	1.4	0.2	2.6	0.4
Dynamic aberrations starting with a corrected wavefront in a cold cavity				
• Preshot (~10 min)	0.11	0.03	0.13	0.04
• Shot without correction	0.69	0.22	1.65	0.39
• Shot with partial correction	0.50	0.17	0.72	0.20
• Post shot (~+10 min)	2.4	0.85	3.6	1.3

[a]Measured distortion (in waves at 1.05 μm).
[b]Peak-to-valley.

The input and output surfaces of the conversion crystals were coated with a single-layer, quarter-wave-thick, SiO_2 sol-gel AR coating. To simplify the crystal AR-coating process, both the input and output faces of the doubler have an AR coating with optimum transmission at 700 nm. This provides a very good compromise for optimal transmission at both 1054 and 527 nm when using a single-layer AR coating. The output face of the tripler has an AR coating optimized at 351 nm, whereas the input face has an extra coating layer applied to produce the $1\omega/2\omega$ compromise coating thickness.

The tripling crystal was deuterated to reduce the potential for damage from stimulated Raman scattering (SRS). The intense spontaneous Raman band that occurs in KDP near 915 cm^{-1} (and seeds the SRS growth) is split into two weaker bands in KD*P.[17] In addition to using KD*P, we also beveled and AR-coated the edges of the crystal to prevent parasitic oscillations from SRS within the plane of the crystal and orthogonal to the beam propagation vector.

Second-Harmonic Generation

The frequency conversion system was activated in two stages. The 32×32-$cm^2 \times 1.05$-cm-thick Type I doubling crystal was installed and the second-harmonic conversion efficiency was measured as a function of input intensity at the phase matching angle ($\Delta k = 0$). Experiments were carried out with increasing 1ω input intensities up to about 5.3 GW/cm^2 using 1-ns square pulses. The second-harmonic conversion efficiency increased monotonically with drive intensity, reaching a maximum value of 83%. These results

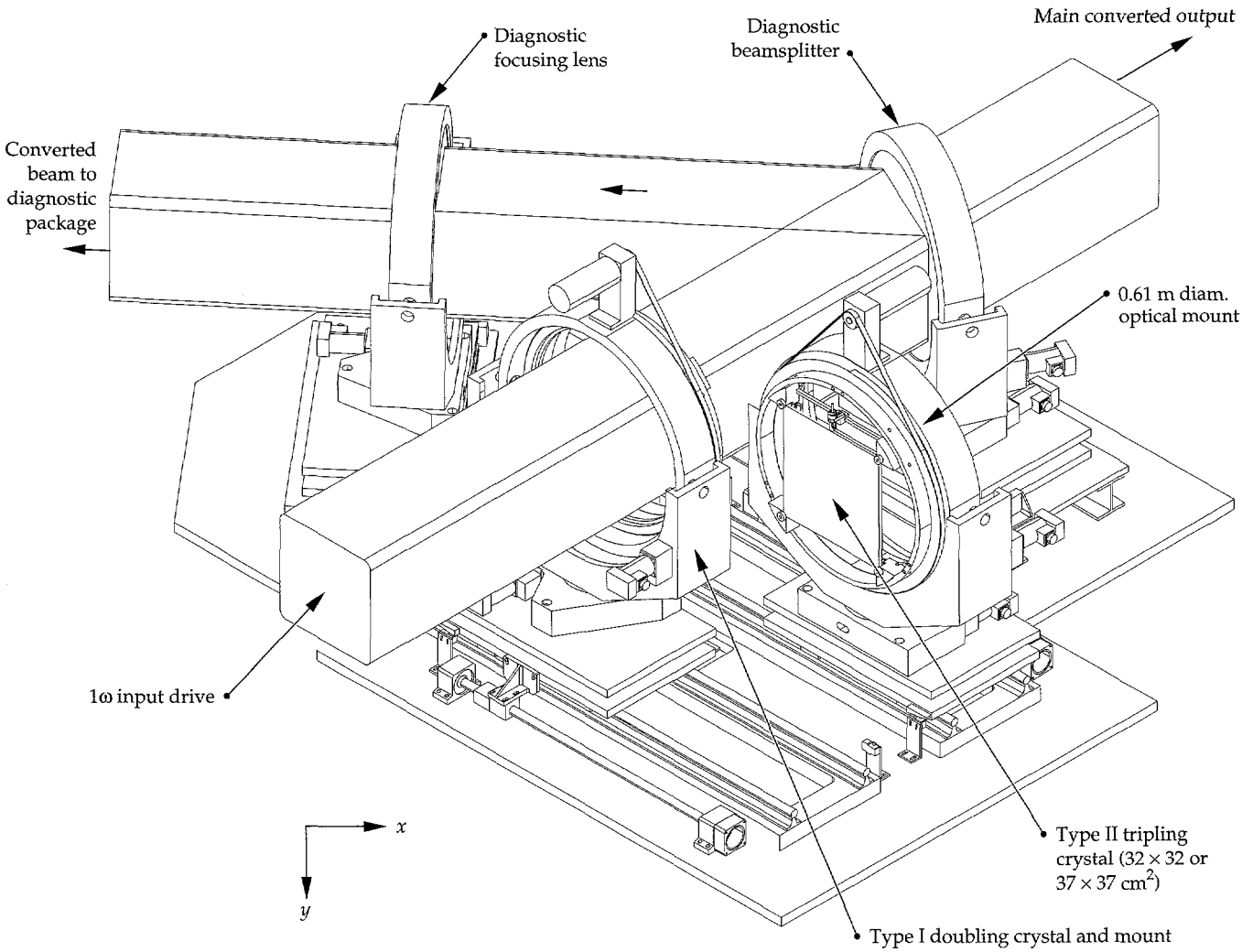

FIGURE 16. Layout of the third-harmonic frequency-conversion system showing the location of the crystals in the optical mounts. The crystals can be independently moved in and out of the beamline. (70-50-0494-1913pb01)

(Fig. 17) were compared with plane-wave model calculations and were found to be in excellent agreement. This attests to the nearly flat wavefront quality (i.e., low distortion) of the Beamlet 1ω drive beam.

The plane-wave model assumes a 1% loss at each AR-coated surface of the crystals and 6%/cm absorption at 1054 nm by the bulk KDP. As noted earlier in this section, the second-harmonic generation crystal is slightly "detuned" from the phase-matching angle to achieve the proper mix ratio of the fundamental and second-harmonic beam that drives the tripler. Theory predicts that a detuning angle of ±250 μrad from the phase matching direction in the crystal will give the correct mix ratio to achieve maximum 3ω conversion at incident fundamental intensities between 3 and 3.5 GW/cm^2.

During the course of the doubling experiments, we also measured the conversion efficiency at detuning angles of ±250 and 350 μrad and compared the results with the plane-wave model (Fig. 17). Again, the agreement between the model and experiment was very good. To do these conversion tests, the doubling crystal was first tilted (detuned) to one side and the conversion efficiency measured. This experiment was then repeated with the crystal tilted an equivalent amount in the opposite direction. Thus, the two points shown in Fig. 17 at each of the detuning angles represent two separate experiments where the crystal was detuned by either "plus" or "minus" the respective angle.

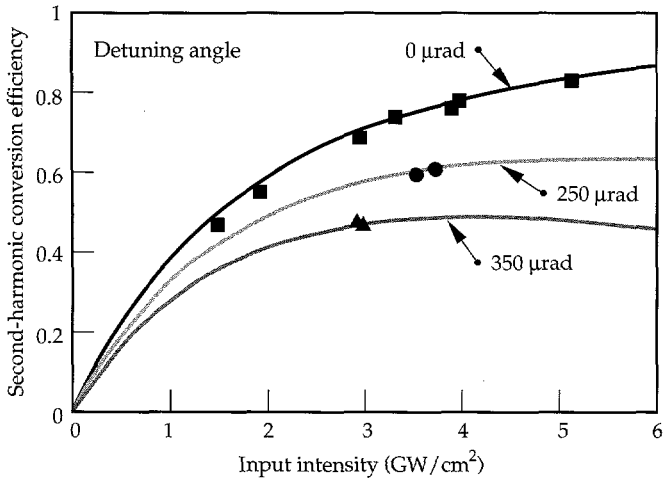

FIGURE 17. Second-harmonic conversion efficiency vs 1ω drive intensity using a 32 × 32 × 1.1 cm^3 KDP Type I doubling crystal. The conversion efficiency agrees well with the plane-wave model at 0, ±250, and ±350 μrad detuning angles. (70-50-1094-3625pb01)

Third-Harmonic Generation

Table 3 summarizes the results from third-harmonic generation experiments carried out with a 3-ns square pulse shape. These results are compared with both the NIF requirements and the Beamlet performance goal established at the beginning of the project at the recommendation by the National Academy of Sciences (NAS).

Beamlet is judged against three key third-harmonic performance criteria: (1) fluence, (2) beam quality, and (3) conversion efficiency. For all three criteria, Beamlet either exceeds or meets the goals of the NIF (see Table 3). The difference in total output energy proposed for a NIF beamlet vs that achieved on the prototype Beamlet is due to the difference in aperture size. The prototype Beamlet aperture was set at the beginning of the project in 1991 and supports a maximum beam size of 35 cm. On the other hand, the somewhat larger NIF aperture reflects the more recent thinking that apertures near 40 cm, rather than 30 cm, are a better compromise between performance and cost.

Perhaps the most critical performance criteria is the 3ω fluence, because of the lower optical-damage limits at shorter wavelengths. Specifically, the optical material most at risk is the tripling crystal, because the laser output is set to be near the damage threshold of this material. Beamlet has operated at a 3ω fluence that exceeds the NIF performance requirement by about 10%. During these initial tests, we carried out 17 shots

TABLE 3. Comparison of Beamlet 3ω performance with NIF and the NAS technical contract specifications.

Parameters	Beamlet Phase I[a]	NIF	NAS technical contract
Mean 3ω fluence J/cm^2	8.7	8.0[b]	6.4–7.6
Quality:			
•Beam size (cm^2)	29.6 × 29.6	38 × 36	30 × 30
•Effective beam area (cm^2)	736	1280	784
•3ω energy (kJ)	6.4	10.2	5–6
•Beam divergence (μrad)	≤ ±25	≤ ±35	≤ ±50
•Bandwidth (GHz)	90	90	90
Conversion efficiency:			
3ω peak conversion efficiency	80%	80%	70%

[a]See Ref. 18.
[b]at 3.6 ns.

in excess of 7.5 J/cm^2 at 3 ns without sustaining any damage to the K*DP tripling crystal.

The third-harmonic converter was activated by first "laser conditioning" the KD*P tripling crystal at 3ω. Laser conditioning refers to the process of increasing the damage threshold of an optical material by exposing it to a series of laser shots with monotonically increasing fluence. (See "Large-Aperture, High-Damage Threshold Optics for Beamlet," p. 52 for a detailed discussion of laser conditioning of Beamlet optics.) Following conditioning, a series of experiments was conducted to characterize the 3ω conversion performance. One of our major goals was to demonstrate >70% conversion efficiency at high peak power (2.5–3.5 GW/cm^2). These experiments were carried out using temporally square, 3-ns pulses. Figure 18 shows the results where the third-harmonic conversion efficiency is plotted vs the 1ω input intensity delivered to the harmonic converter system. At the highest drive intensities (>3.25 GW/cm^2) conversion efficiencies of 80% were achieved. The results were in good agreement with plane-wave model predictions. The model calculations include the effects of the 30-GHz bandwidth (90-GHz at the 3ω output) that we add to the drive pulse to suppress SBS in the output optics. The added bandwidth reduces the conversion efficiency about 3% at the highest drive intensities. The model calculation shown in Fig. 18 does not include the effects of the spatial and temporal edges of the real beam, but instead assumes a perfect top-hat-shaped profile. Including these effects would tend to slightly reduce the conversion efficiency, giving even closer agreement with the experiments.

The maximum average 3ω output fluence achieved during this series of shots was 8.7 J/cm^2, about 10% greater than the NIF performance goal of 8.0 J/cm^2. At the Beamlet beam aperture area of 736 cm^2, this gave 6.4 kJ 3ω output and corresponds to over 11 kJ at the NIF beam area of 1280 cm^2 (Table 3).

The input beam quality and fill factor were maintained during the 3ω conversion process as shown by the 3ω near-field image and lineout in Fig. 19. These data were taken during a 3-ns shot at 2.56 GW/cm^2 producing 7.7 J/cm^2 (5.6 kJ) output at 3ω. The peak-to-mean intensity modulation is about 1.4 to 1 at 3ω compared to about 1.3 to 1 at 1ω.

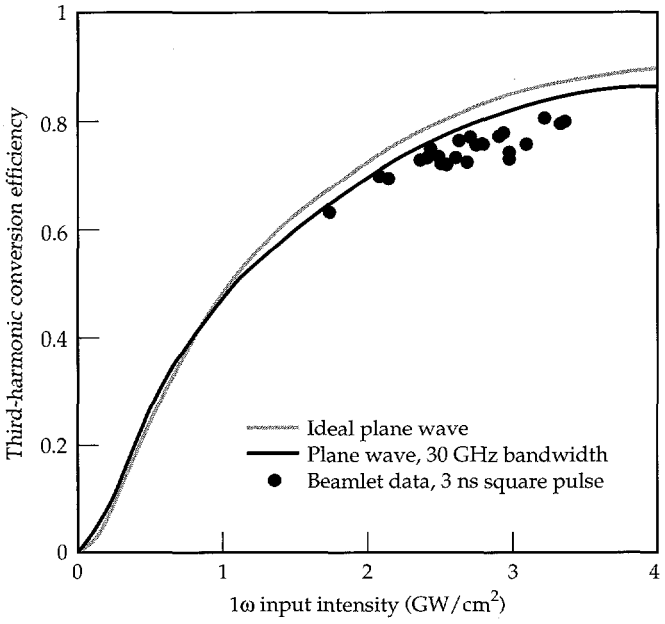

FIGURE 18. Third-harmonic conversion efficiency vs 1ω drive intensity achieved with 3-ns square pulses with 30-GHz 1ω (90-GHz at 3ω) bandwidth. The Type II tripling crystal was 80% deuterated KD*P 32 × 32 × 0.95 cm^3 with 0 μrad detuning. The doubling crystal was detuned at ~250 μrad to achieve optimum 3ω conversion. (70-50-1094-3624pb01)

(a) Near-field image

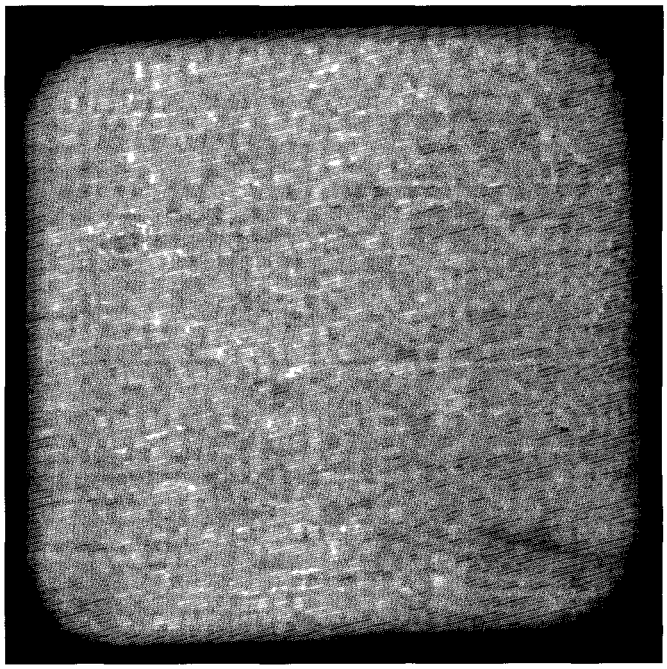

(b) Horizontal and vertical lineouts

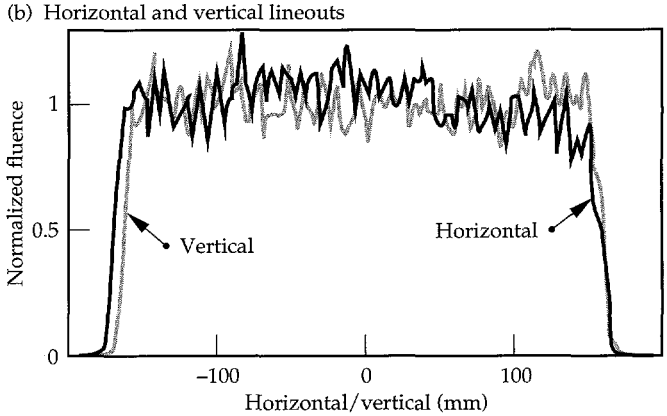

FIGURE 19. (a) Near-field image and (b) horizontal and vertical intensity lineouts of that image for a 3ω output pulse from the Beamlet harmonic generator. The peak-to-mean intensity modulation is about 1.35 to 1. (70-50-0195-0021pb01)

Figure 20 further illustrates the similarity in the fluence modulation observed for the 1 and 3ω near-field images at high drive intensities. Plotted is the normalized probability distribution of fluences observed at 1 and 3ω for a 3-ns shot. The average pulse intensities are 3.3 GW/cm^2 and 2.65 GW/cm^2 at 1 and 3ω, respectively. The wings of the two curves compare the p-V intensity distribution for the 1 and 3ω pulses. The data clearly show that there is no significant growth in near-field fluence modulation during the conversion process.

During the course of our 3ω tests, we also demonstrated frequency conversion for shaped pulses roughly similar to NIF ignition target drive pulses. The proposed NIF ignition target pulse shape consists of a low-intensity "foot" about 15 ns long followed by a higher intensity, 3–3.5-ns, main drive pulse. The harmonic conversion process depends strongly on the product of the beam intensity and crystal thickness and therefore has a limited intensity range over which it is fully optimized. This is illustrated by the data in Fig. 18, where the conversion efficiency is shown to drop-off dramatically at low-drive intensity; in this case, the crystals are optimized for intensities in the range of 2–5 GW/cm^2. In both the NIF and prototype-Beamlet design, the conversion efficiency of the foot will be lower than the main pulse. The NIF requirement is 60% conversion efficiency for the nominal ignition pulse shape. Because the Beamlet preamplifier section was designed to handle a maximum pulse length of 10 ns, we simulated a complex pulse shape (similar to what might be used on NIF) using a 7-ns foot and a 3-ns main pulse. The 1ω input to the harmonic converter had a foot-to-main pulse contrast ratio of 9:1, giving the desired 30:1 contrast ratio for the 3ω output pulse (Fig. 21). The 1ω beam had an equivalent pulse length of 3.9 ns and a mean fluence of 12.4 J/cm^2 compared with 3.2 ns and 8.2 J/cm^2 for the output 3ω pulse. The measured foot and peak pulse conversion efficiencies were 23 and 77%, respectively. The average 3ω conversion efficiency was 64%, which compares quite favorably with our model predictions.

The above 3ω experiments also gave us the added opportunity to more fully test the capability of the integrated optical-pulse forming and preamplifier section of our front end. To create the desired 9:1 1ω NIF-like pulse shape that was used to drive the harmonic converter requires nearly a 75:1 intensity contrast for the shaped pulse at the injection to the main laser cavity [Fig. 21(b)]. The injected pulse was shaped to compensate

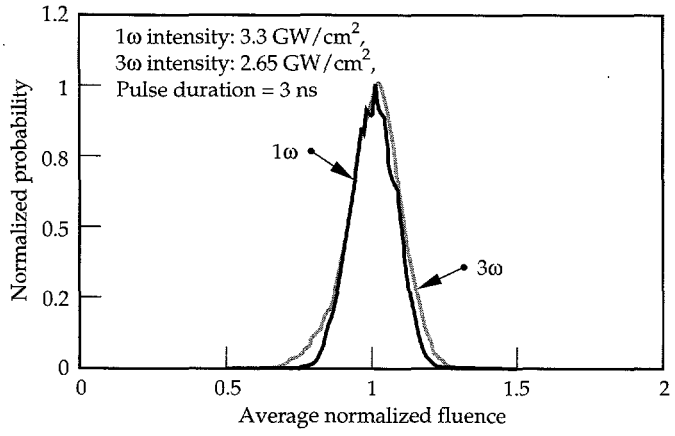

FIGURE 20. Comparison of normalized probability distribution of intensities for the 1ω drive pulse and corresponding 3ω output observed during a 3-ns shot at a 1ω input drive intensity of 3.3 GW/cm^2. (70-50-0195-0019pb01)

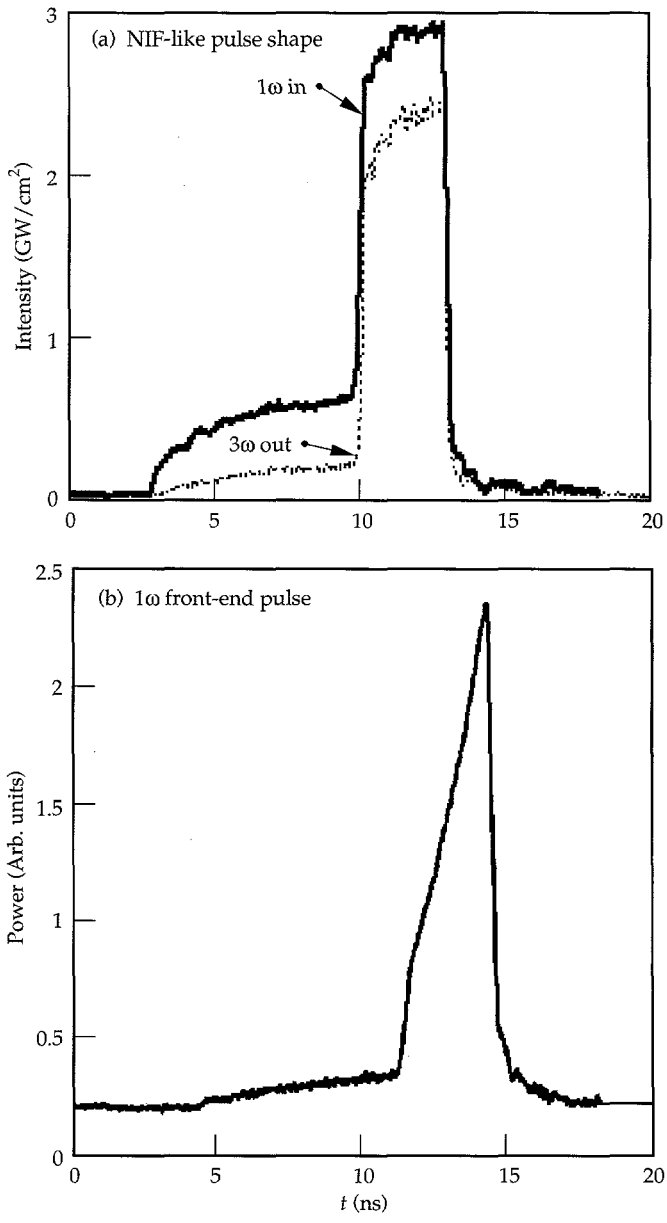

FIGURE 21. (a) Shows a "NIF-like" 3ω pulse shape with a 30:1 contrast ratio generated using a 9:1 1ω drive pulse to the harmonic converter. (b) An injected pulse with a 75:1 contrast and a complex temporal shape was generated using the new front-end architecture to achieve the desired 1ω drive-pulse shape. (70-50-1094-3622pb01)

for effects of gain saturation in the main laser cavity and booster amplifiers. This pulse shape was easily synthesized using the low-voltage waveguide modulators in the pulse generation system.

Summary

We recently completed construction and preliminary testing of the NIF prototype Beamlet laser, a large-aperture flash-lamp-pumped Nd:Glass laser. The laser uses a multipass architecture that represents the first attempt to employ such a design at this scale. The main laser cavity is unique in that it uses a full-aperture plasma-electrode Pockels cell and an angular multiplexing scheme to execute four passes through a group of eleven large phosphate glass amplifiers contained in the cavity. The output from the main laser cavity then makes a single pass through a booster amplifier section comprised of five more amplifiers. The 1054-nm output from the laser is converted to the third harmonic (351 nm) using a Type I/II KDP/KD*P frequency conversion scheme.

We have successfully demonstrated Beamlet's 1ω and 3ω performance at its 3-ns design point. Good beam quality is maintained as defined by the low peak-to-average fluence modulation and small wavefront aberration. We demonstrated several new pre-compensation techniques in the preamplifier that allow control over fill factor, wavefront, and temporal shape of the output beam. Key 1ω performance parameters have been investigated at high 1ω fluence (15.5 J/cm^2), and high intensity (5.5 GW/cm^2). Similarly, at 3ω we demonstrated damage-free operation at fluences in excess of those required for NIF and third-harmonic conversion efficiencies >80% for 3-ns pulses and 64% for NIF-like pulse shapes. The conversion efficiencies mentioned exceed NIF requirements. The results from current and future Beamlet performance tests will be used to validate the NIF laser design.

Acknowledgments

We gratefully acknowledge the contributions of the many LLNL engineers, technicians, scientists, and support personnel whose long hours and tireless efforts made this project possible. We also appreciate the high-quality, state-of-the-art optical, electrical, and mechanical components delivered by numerous vendors, including Aerotech Inc., Aerovox Inc., Cleveland Crystals, Inc., Corning, Eastman Kodak Company, EG&G Inc., Passat Enterprises, Schott Glass Technologies Inc., Spectra–Physics, Tinsley Laboratories, Inc., United Technologies, and Zygo Corporation.[19–30]

Notes and References

1. *National Ignition Facility Conceptual Design Report*, **2** and **3**, Lawrence Livermore National Laboratory, Livermore, CA, UCRL-PROP-117093 (May 1994).
2. A. C. Erlandson, K. S. Jancaitis, R. W. McCracken, and M. D. Rotter, *ICF Quarterly Report* **2**(3), 105–114, Lawrence Livermore National Laboratory, Livermore, CA, UCRL-LR-105821-92-3 (1992).
3. B. M. VanWonterghem, D. R. Speck, M. Norman, R. B. Wilcox, et al., "A Compact and Versatile Pulse Generation and Shaping Subsystem for High Energy Laser Systems," in *Laser Coherence Control: Technology and Applications*, (SPIE—International Society for Optical Engineering, Bellingham, WA, 1993; *Proc. SPIE* **1870**).
4. M. A. Rhodes, J. J. DeYoreo, B. W. Woods, and L. J. Atherton, *ICF Quarterly Report* **2**(1), 23–36, Lawrence Livermore National Laboratory, Livermore, CA, UCRL-LR-105821-92-1 (1992).
5. C. E. Barker, D. Milam, and R. Boyd, *ICF Quarterly Report* **3**(2), 55–62, Lawrence Livermore National Laboratory, Livermore, CA, UCRL-LR-105821-93-2 (1993).
6. J. R. Murray, J. H. Campbell, D. N. Frank, J. T. Hunt, and J. B. Trenholme, *ICF Quarterly Report* **1**(3), 89–107, Lawrence Livermore National Laboratory, Livermore, CA, UCRL-LR-105821-91-3 (1991).
7. J. T. Hunt and D. R. Speck, *Optical Engineering* **28**(10), 461–468 (1989).
8. J. M. Soures, R. C. McCrory, T. R. Boehly, R. S. Craxton, et al., *Laser and Particle Beams* **11**, 317–321 (1993).
9. C. Yamanaka, *Lasers and Particle Beams* **2**, 425–431 (1984).
10. G. Thiell, A. Adolf, M. Andre, N. Fleurot, et al., *Laser and Particle Beams* **6**, 93–103 (1988).
11. J. R. Murray, J. R. Smith, R. B. Ehrlich, D. T. Kyrazis, et al., *J. Opt. Soc. Am. B* **5**, 2402 (1989).
12. J. T. Salmon, E. S. Bliss, T. W. Lang, et al., (SPIE—International Society for Optical Engineering, Bellingham, WA, 1991; *Proc. SPIE* **1542**) p. 452.
13. J. M. Auerbach and V.P. Karpenko, *Applied Optics* **33**(15), 3179–3183 (1994).
14. E. S. Bliss, D. R. Speck, J. F. Holzrichter, J. H. Eskkila, and A. J. Glass, *Appl. Phys. Lett.* **25**, 448–450 (1979).
15. J. A. Armstrong, N. Bloembergen, J. Ducuing, and P. S. Pershan, *Phys. Rev.* **127**, 1918–1939 (1962).
16. R. S. Craxton, *Opt. Commun.* **34**(3), 474–478 (Sept 1980).
17. R. A. Sachs, C. E. Barker, and R. B. Ehrlich, *ICF Quarterly Report* **2**(4), 179–188, Lawrence Livermore National Laboratory, Livermore, CA, UCRL-LR-105821-92-4 (1992).
18. Beamlet Phase I is the Beamlet integration and activation leading to the 1ω and 3ω performance as described in this article. Beamlet Phase II, which started in November 1994, is the expansion of the present configuration to one which mimics a full NIF beamline, including a 3ω focusing vessel, similar to a section of the NIF target chamber, to diagnose on-target performance.
19. Aerotech Inc., 101 Zeta Drive, Pittsburgh, PA, 15238.
20. Aerovox Inc., 740 Belleville Avenue, New Bedford, MA, 02745–6194.
21. Cleveland Crystals, Inc., 676 Alpha Drive, Highland Heights, OH, 44143.
22. Corning, Corning Glass Works, MP-21-04-2 Corning, NY, 14831.
23. Eastman Kodak Company, Department 177, Building 601, Rochester, NY, 14650–0803.
24. EG&G, Inc., Electro-Optics Division, 35 Congress Street, Salem, MA, 01970.
25. Passat Enterprises, P.O. Box 84, Nizhny Movgorod, Russia, 603000.
26. Schott Glass Technologies Inc., 400 York Avenue, Duryea, PA, 18642.
27. Spectra-Physics, 1330 West Middlefield Road, Mountain View, CA, 94039–0517.
28. Tinsley Laboratories Inc., 3900 Lakeside Drive, Richmond, CA, 94806.
29. United Technologies, Adaptive Optics Associates Inc., 54 Cambridge Park Drive, Cambridge, MA, 02140–2308.
30. Zygo Corporation, Laurel Brook Road, Middlefield, CT, 06455–0448.

Design and Performance of the Beamlet Amplifiers

A. C. Erlandson

M. D. Rotter

D. N. Frank

R. W. McCracken

Introduction

In future laser systems, such as the National Ignition Facility (NIF), multi-segment amplifiers (MSAs) will be used to amplify the laser beam to the required levels. As a prototype of such a laser architecture, we have designed, built, and tested flash-lamp-pumped, Nd:Glass, Brewster-angle slab MSAs for the Beamlet project.

In this article, we review the fundamentals of Nd:Glass amplifiers, describe the MSA geometry, discuss parameters that are important in amplifier design, and present our results on the characterization of the Beamlet MSAs. In particular, gain and beam steering measurements show that the Beamlet amplifiers meet all optical performance specifications and perform close to model predictions.

The Beamlet amplifiers also demonstrate advances in MSA mechanical design: hermetically sealed blast shields to protect the laser slabs from contamination generated by the flash lamps; hermetically sealed flash-lamp cassettes to protect the lamp envelopes from outside sources of contamination; modular slab cassettes to reduce the size of the amplifier parts that need to be handled; and flash-lamp cassettes that can be installed and removed without disturbing the laser slabs. These features will be included in the amplifiers for the NIF.

Background

The Amplifier Pumping Process

Many energy transfer steps occur during the amplifier pumping process,[1] which begins when the switch in the flash-lamp discharge circuit is closed and current begins to flow through the flash lamps. Typically, circuits transfer 70–90% of the bank energy to the flash lamps, with the remainder lost as heat to the circuit elements. Flash-lamp plasmas convert about 80% of the delivered electrical energy to photons, with approximately half the optical output energy falling in the 400–1000-nm region of Nd^{3+} pumping bands. As these photons circulate in the pump cavity, some are reabsorbed by the flash-lamp plasma, which in turn re-emits a fraction of this reabsorbed energy; some are absorbed by the metal reflectors or slab holders; and some are lost through the ends of the amplifiers. The remaining photons (about 10% of those emitted by the plasma) are absorbed by the laser slabs.

The photons absorbed by the laser slabs produce stored energy in the form of excited Nd^{3+} ions. However, due to quantum defects between the absorbed photons and the upper laser level, about half of the absorbed energy is immediately converted to heat, depending on the spectral distribution of the flash-lamp light. Energy transfer from excited ions to ground-state ions (concentration quenching) produces additional heating.

Pump-induced beam steering and wavefront distortion arise from two main sources: (1) The laser slabs are warped when pump light deposits more heat on one side than the other. This warping causes beam steering and wavefront distortion that is distributed over the entire aperture. (2) Amplified spontaneous emission (ASE) heats the absorbing edge claddings that are used to prevent parasitics. The resulting thermal expansion produces significant wavefront distortion within approximately one slab thickness of the edge claddings. This edge distortion can be avoided by setting the beam aperture appropriately.

Parameters Governing Amplifier Performance

In Brewster-angle slab amplifiers, the three most important parameters for describing laser performance are α, the average gain coefficient; g, the small signal gain per slab; and a, the hard aperture area. Both α and g are related to the stored energy density, ρ, by the relations

$$\alpha = \sigma\rho / h\nu \qquad (1)$$

and

$$g = \exp\left[\alpha\left(n^2+1\right)^{1/2}(t/n)\right] , \qquad (2)$$

where σ is the stimulated emission cross section for excited Nd ions, $h\nu$ is the laser photon energy, n is the refractive index of the laser glass, and t is the caliper thickness of the laser glass. The term $(n^2+1)^{1/2}(t/n)$ is the beam path length through the Brewster-angle laser slab.

Generally, high values of α, g, and a are desired: as α increases, the desired beam fluence is achieved with less laser glass and, as a result, with smaller nonlinear phase shifts; as g increases, the desired fluence is achieved with fewer slabs; and as a increases, the desired laser energy can be achieved with fewer beamlets. However, it is difficult to attain the desired values for all three key amplifier performance parameters simultaneously. For example, increased ASE causes both α and g to decrease as a is increased. The gain per slab can be increased by making slabs thicker, but, as a result, α falls because flash-lamp light is preferentially absorbed near the slab surfaces. The sophisticated amplifier model[2] that Lawrence Livermore National Laboratory (LLNL) has developed to predict α and g is essential for characterizing tradeoffs between parameters and for arriving at cost-effective fusion laser designs.

Other important amplifier parameters are gain uniformity across the aperture, pump-induced wavefront distortion, and storage efficiency. A measure of gain uniformity is the parameter U, defined as the peak-to-average ratio of the gain coefficient evaluated over the beam aperture. Good gain uniformity, i.e., U close to unity, is desired because gain variations produce fluence variations in the output beam, thereby reducing the damage-limited output energy. Low pump-induced wavefront distortion is desired for good beam focusability and high harmonic-conversion efficiency. To some degree, both gain variations and pump-induced wavefront distortion can be compensated for, albeit at additional cost and complexity to the system. For example, the Beamlet preamplifier section uses a variable transmission filter to tailor the fluence distribution and a deformable mirror to precorrect the wavefront. To evaluate pump cavity designs, models for predicting gain distributions[3] and pump-induced wavefront distortion[4] are being developed at LLNL and at the CEA Laboratory in Limeil, France.

Storage efficiency, η, is defined as the total extractable energy stored in the laser slabs divided by the total electrical energy delivered to the flash lamps. High storage efficiency is desired to reduce the size and therefore cost of the pulsed power system.

Multisegment Amplifier (MSA) Development

Prior to Beamlet, all flash-lamp-pumped Nd:Glass fusion lasers have used one-beam-per-box amplifiers. MSAs, in which several beams are contained in the same amplifier box, were first proposed in 1978 as a way to reduce the cost of flash-lamp-pumped, Nd:Glass fusion laser systems.[5] MSAs cost less than the one-beam-per-box amplifiers in three ways: (1) by making amplifiers more compact, thereby reducing the size and cost of the building; (2) by increasing pumping efficiency, thereby reducing the size and cost of the pulsed power system; and (3) by reducing the number of internal amplifier parts.

Figure 1 shows the MSA design currently envisioned for the NIF. Optical gain at the 1.05-μm wavelength is provided by Nd-doped, phosphate glass, rectangular laser slabs oriented at Brewster's angle with respect to the beam to eliminate reflection losses. The amplifier hard apertures are 40×40 cm^2. The slabs are stacked four-high in holders that are arranged in 12 columns.

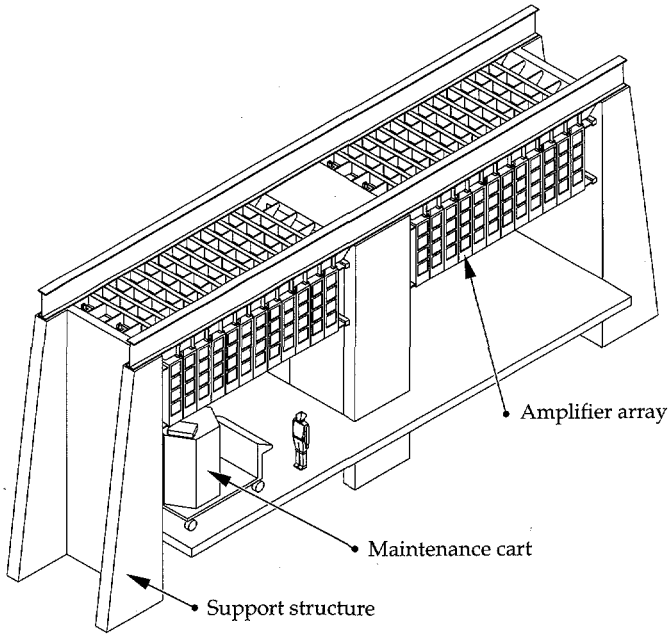

FIGURE 1. The MSA design currently envisioned for the NIF uses 48 apertures arranged in a 4-slab-high × 12-slab-wide matrix. (40-00-0294-0535pb01)

The columns of slabs are separated by arrays of central flash lamps that emit radiation to both sides. The outermost columns are also illuminated by arrays of side flash lamps that have large silver reflectors to redirect the flash-lamp radiation toward the slabs. In this respect, the side flash-lamp arrays are similar to the arrays used in one-beam-per-box amplifiers on Nova and other previous fusion lasers. Glass blast shields, placed between the flash lamps and the laser slabs, serve two purposes: (1) They prevent acoustic waves generated by the flash lamps from propagating into the beam path and causing wavefront distortion; and (2) they provide a contamination barrier between the flash-lamp cavity and the critical slab cavity. The blast shields also form a channel that could potentially be used for flowing cooling gas around the flash lamps. To simplify assembly and maintenance, the NIF MSAs would be assembled from one-slab-long, one-slab-wide, four-slab-high modules. In addition, the flash lamps would be mounted in 6- or 8-lamp removable cassettes.

Since 1989, LLNL has built and tested three MSA designs: MSA-1[2], MSA-2[6], and the Beamlet amplifiers. Although MSA-1 and MSA-2 contained only four apertures, in a one-slab-long, 2×2 array, they were large enough to permit us to study important MSA performance issues. In particular, we discovered that central flash-lamp arrays pump more efficiently than side flash-lamp arrays. In side arrays, the large reflectors return a portion of the flash-lamp radiation to the lamps, where it is absorbed by the plasma. Furthermore, the reflectors themselves absorb a significant fraction of the flash-lamp radiation. In contrast, central flash-lamp arrays allow the lamps to radiate freely in both directions, and the only reflectors are small diamond-shaped reflectors between the lamps that effectively reduce the transfer of radiation from lamp to lamp. Although MSA-1 had high storage efficiency (about 3.5%) and high average gain coefficient (5.5%/cm) at the normal operating point (lamps fired at 20% of the single-shot explosion energy), gain varied significantly across its aperture. MSA-1 was not versatile enough to permit us to explore solutions to the gain uniformity problem or to study how MSA performance is affected by changes in pump cavity design.

MSA-2, also called the Beamlet prototype amplifier, was used to develop pump cavity designs for the Beamlet amplifiers. MSA-2 had a flexible pump cavity that enabled us to study the effect of different designs on gain uniformity and cavity transfer efficiency. Gain gradients in the vertical direction were reduced by installing reflectors at the tops and bottoms of the flash-lamp cassettes to reduce the loss of pump radiation through the gaps between the flash lamps, and by installing dimpled silver reflectors with raised surfaces on the slab holders so that the reflected light illuminated the facing slabs more uniformly. Gain gradients in the horizontal direction were reduced by replacing the cylindrical silver reflectors in the side lamp arrays with flat reflectors. These changes lead to an extremely uniform gain distribution, with a gain uniformity parameter $U = 1.025 \pm 0.004$. Pumping was balanced between the 12-lamp central array and the less efficient side arrays by increasing the number of lamps in the side arrays from six to eight. Balanced pumping is desired to reduce wavefront distortions caused by slab warping due to preferential heating of one side of the laser slab by pump radiation.

Beamlet Amplifiers

Although testing MSA-1 and MSA-2 greatly enhanced our understanding of MSA performance, their 29×29 cm^2 apertures had only about 50% of the area of the 40×40 cm^2 apertures proposed for the NIF, and serious concerns remained regarding the feasibility of manufacturing large laser slabs and the effect of increased ASE on efficiency and gain uniformity. In addition, it remained to be demonstrated that MSAs could be cleanly assembled and operated. These issues were addressed by designing, building, and testing the Beamlet amplifiers.

Amplifier Description

The Beamlet amplifiers use the MSA architecture in which four apertures are arranged in a 2×2 matrix. Figure 2(a) shows an assembled Beamlet amplifier, with one end open. Beamlet contains two large amplifiers: a four-pass, eleven-slab-long cavity amplifier and a singlepass, five-slab-long booster amplifier. The positions of these amplifiers in the laser chain are discussed in "System Description and Initial Performance Results for Beamlet," p 1. The hard apertures of the Beamlet amplifiers are 39.5×39.5 cm^2, larger than the apertures used for any previous Nd:Glass amplifiers and approximately the same size as the amplifiers envisioned for the NIF.

The measurements described below show that at the standard operating point, for which the lamps are driven at 20% of their single-shot explosion energy (in air), the amplifiers have the following characteristics: the average gain coefficient is 5%/cm, the storage efficiency is 3%, and pump-induced wavefront distortion is <1.5 waves at 1.053 μm for the entire system. The ratio of peak gain coefficient to average gain coefficient, evaluated over the central 95% of the amplifier hard aperture, is 1.06:1. The gain distribution is influenced by ASE, which preferentially depumps the edges of the aperture.

The Beamlet amplifiers were designed modular, which facilitates assembly and maintenance. The basic amplifier assembly units (BAUs) are one slab long, one slab wide, and two slabs high. Each BAU consists of an aluminum frame, blast shields mounted on the sides, and a slab

holder mounted internally, as shown in Fig. 2(b). The aluminum frame is nickel-plated, for cleanliness. The BAUs are assembled in a class-100 clean room, bagged, and transported to the laser bay. In the laser bay, a crane lifts the BAUs onto rails, which allows the BAUs to be easily positioned along the direction of the laser beam. The BAUs are installed in pairs and bolted together side by side to form one-slab-long 2×2 units. The flash-lamp cassettes are slid into place from the top, using the crane. All amplifier assembly is performed under portable class-100 clean rooms.

The laser slabs are made of Schott glass (composition LG-750), doped at a Nd ion concentration of 3.5×10^{20} ions/cm^3. The finished slab dimensions are $4 \times 42.4 \times 76.4$ cm^3, excluding the 1.2-cm-thick edge claddings glued onto the perimeter to absorb ASE. The edge claddings are made of Cu-doped LG-750, which has an absorption coefficient of 2.8/cm at the peak gain wavelength of 1.053 μm. The volume of the Beamlet laser slabs is 12 L, nearly twice the volume of the largest laser slabs fabricated previously. Further details about the laser slabs are contained in the article "Large-Aperture, High-Damage-Threshold Optics for Beamlet," p. 52.

To reduce costs, only one of the four Beamlet apertures has real laser slabs. The other three apertures have dummy slabs consisting of two panes of Greylight-14, a relatively inexpensive architectural glass. These dummy slabs are indistinguishable from the real laser slabs in the degree to which they absorb flash-lamp light. The pumped regions of the slabs measure 39.5×75.6 cm^2. The vertical separation between the hard apertures is 5.5 cm. Like MSA-2, the slab masks use dimpled, silver reflectors, to improve gain uniformity.

Figure 3 shows a plan view of the pump cavity, the design of which is based on the MSA-2 results. The bore diameter of the flash lamps is 2.5 cm and the arc length is 91.4 cm. The flash lamps are made of UV-absorbing Ce-doped quartz to protect the pump

(a)

(b)

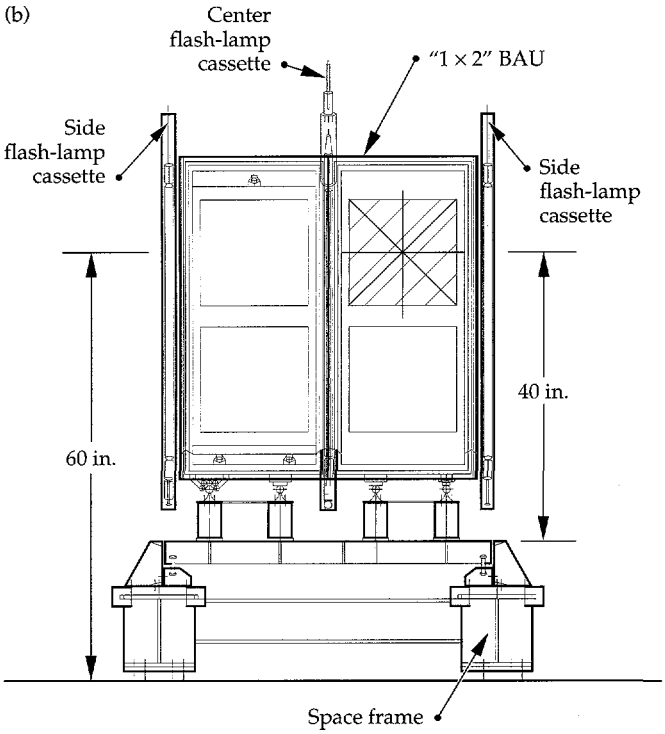

FIGURE 2. (a) Photograph of assembled 2×2 Beamlet amplifiers with 39.5×39.5 cm^2, hard-edged apertures (this supports about a 35×35 cm^2 beam size). (b) Schematic drawing showing key elements of the design: the shaded square represents the active beam aperture. (02-30-1093-3491Apb01)

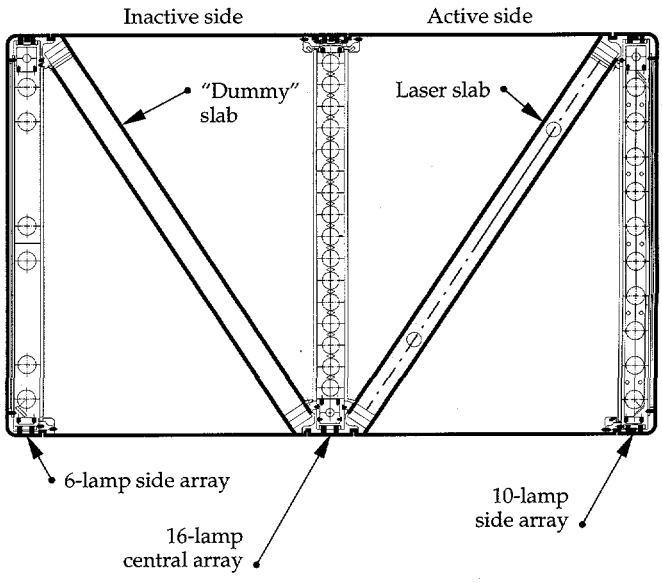

FIGURE 3. Plan view of the Beamlet pump cavity showing flash-lamp and slab locations for two one-slab-long, one-slab-wide modules joined side by side. (02-30-1093-3490Apb01)

cavity from solarization, and are filled with 200 Torr of Xe gas. The flash lamps were manufactured by EG&G, Inc. The 16 flash lamps in each central flash-lamp array are spaced 3.94 cm apart, corresponding to a lamp packing fraction (defined for central arrays as the bore diameter divided by the center-to-center distance) of 0.64. Like MSA-1 and MSA-2, silver diamond-shaped reflectors are placed between the lamps to increase efficiency.

The ten lamps in each side array are spaced 6.29 cm apart, corresponding to a lamp packing fraction (defined for side arrays as half the bore diameter divided by the center-to-center distance) of 0.79. As in MSA-2, a higher lamp packing fraction is used in the side arrays than in the central arrays to better balance pumping on the two sides of the laser slabs.

To further reduce costs, especially for the pulsed power system, only six flash lamps are installed in the side arrays on the inactive side (the side opposite the real Nd:Glass laser slabs) of the amplifiers. Experiments previously performed on MSA-1 showed that very little of the pump light produced by the flash lamps on the far side is transmitted by the central flash-lamp array under normal operating conditions.

Inspections show that after nearly one year of operation the Beamlet flash lamps remain essentially free of the C "brown spots" that commonly appear on Nova lamps. The improved cleanliness is partly attributed to the use of O-ring seals on the lamp bases that protect the lamp envelopes from outside sources of contamination.

During the amplifier activation tests, which were conducted when the Beamlet cavity amplifier was one, two, and five slabs long, the ends of the amplifiers were covered with hard-anodized panels. These panels kept the amplifiers clean and absorbed flash-lamp light. The panels had adjustable slits permitting gain measurements at any location in the amplifier aperture. To reduce the risk of contaminating the laser slabs, either with particles from the laser bay or particles that might have been generated when the panels were moved, each end panel was separated from the amplifier by an empty BAU.

Pulsed Power Description

The Beamlet pulsed-power system is described more fully in "Beamlet Pulsed-Power System" on p. 62 of this *Quarterly*. In brief, we use single-mesh LC circuits (circuits with inductance and capacitance) to drive pairs of flash lamps connected together in series. Each circuit has a 208-μF capacitor and a 140-μH inductor, and the $3(LC)^{1/2}$ pulse length is 500 μs. The measured capacitor-to-lamp transfer efficiency is 71%. To improve pumping efficiency, the flash lamps are preionized with 0.2-J/cm^2 pulses (electrical energy per unit of bore area) delivered 200 μs before the main pulses.[7,8]

The flash-lamp pulse energies, expressed in explosion fraction units, range from 0.075 to 0.30. Flash-lamp explosion fraction, f_x, is defined as the total electrical energy delivered to a flash lamp divided by the electrical energy required to explode the flash lamp on a single shot. Using the standard formula,[9] the single-shot explosion energy for the Beamlet flash lamps is 60.0 kJ per lamp.

Amplifier Gain Characterization Method

An important parameter in amplifier design is the gain of the amplifier. In this section, we describe the experimental layout to characterize gain, and how the gain measured on a one-slab-long amplifier may be used to obtain the gain for a chain of amplifiers.

13-Beam Gain Probe

To measure gain distributions over the entire aperture width on a single shot, we generated thirteen 5-mm-diam probe beams using beam splitters, rattle optics, and an 8-W continuous-wave (cw) Nd:YLF laser. The probe beams, which measure gain distribution by tracking changes in their own intensity, were centered in the aperture horizontally. The beam-to-beam spacing was 3 cm except for the two probe beams nearest the middle, where the spacing was 6 cm. To measure gain distributions over the entire aperture, the probe beams were moved to different vertical locations using a motor-driven stage to translate a turning mirror.

After passing through the amplifier, the probe beams struck an array of 13 PIN-44 photodiodes. To reduce the sensitivity of the gain measurements to lateral translations of the probe beam, we illuminated the photodiodes indirectly, using cavities made of diffusely reflecting material. Background flash-lamp radiation was reduced by the use of narrow-band interference filters and by placing the photodiodes 4–5 m away from the amplifiers. Neutral-density filters protected the photodiodes from saturation. The remaining flash-lamp contributions were eliminated by subtracting the signal produced by a 14th diode, which was physically close to the other diodes but had no incident probe beam. Scale factors for the subtracted signals, which were different for each channel, were obtained by firing the amplifiers with the probe beams turned off.

The photodiode signals were digitized at 0.5 MHz with 10-bit resolution. The shot-to-shot variations in the measured gain coefficients were about ±1%.

Predicting Amplifier Performance

The symmetry of the Beamlet (and NIF) amplifiers leads to a simplified method for predicting their performance. Figure 4 illustrates this method schematically. Here an amplifier N slabs long (in this case $N = 7$) is displayed in plan view [Fig. 4(a)]. Because of the system symmetry it can be shown[6] that the gain for an N-slab-long amplifier is a linear combination of three simple amplifier pump configurations: "X," "V" and "diamond" [Fig. 4(b)]. This observation greatly simplifies the testing needed to predict the performance of a Beamlet or NIF MSA consisting of an arbitrary number of slabs. Rather than having to build the complete N-slab-long amplifier, we can simply test one- and two-slab-long modules and extrapolate the performance of the N-slab-long unit. Note that if a mirror is placed on one end of a V configuration module, a diamond is formed, and if the mirror is placed on the other end of a V configuration module, an X is formed [see Fig. 4(b)]. Thus, by using a flat silver reflector at the end of the one-slab long module, one can also simulate the diamond and X pump configurations without having to build separate two-slab-long test modules [Fig. 4(b)]. This is the approach we have used successfully on Beamlet and will also use for the NIF amplifier development.

The basic assumption in this method is that the main pumping contributions are additive.[6] This assumption leads to an expression for α_i, the gain coefficient for an internal slab that is a function of gain measured in the three test configurations:

$$\alpha_i = \alpha_d + \alpha_x - \alpha_v \quad , \tag{3}$$

where α_d, α_x, and α_v are the gain coefficients measured in the diamond, X and V configurations, respectively. Similarly, α_N, the average gain coefficient for an amplifier N slabs long (where N is odd), is given by

$$\alpha_N = \frac{[\alpha_x + \alpha_d + (N-2)\alpha_i]}{N} \quad . \tag{4}$$

Generally, an odd N is desired to achieve good gain uniformity. This is because of gain gradients in the two end slabs. These gradients can be rather large and are caused by the loss of pump light out the ends of the cavity. By using an odd number of slabs, the gradients can be made to run in opposite directions and therefore tend to cancel each other out.

To test the above extrapolation technique for predicting amplifier performance, we compared measured and predicted gain distributions for a five-slab-long Beamlet amplifier. The gain measurements were made

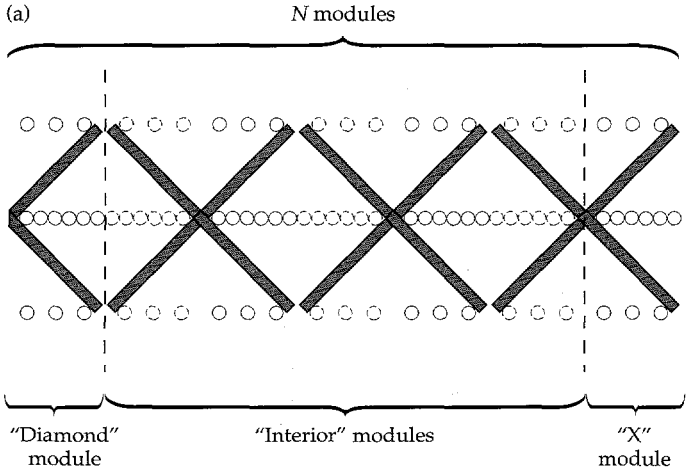

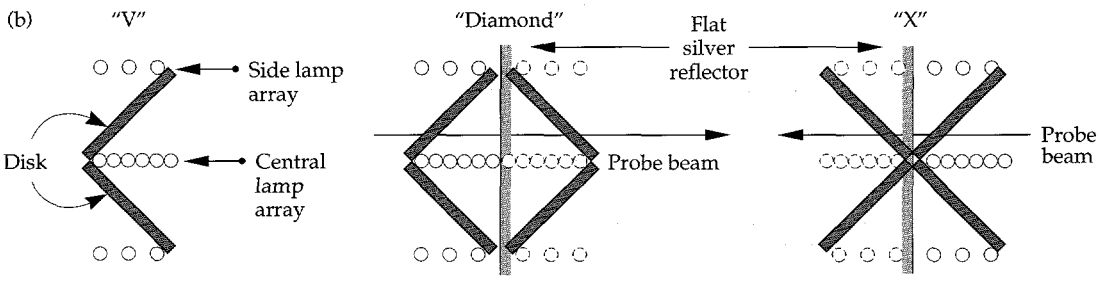

FIGURE 4. (a) Schematic drawing of an N-slab-long amplifier. (b) The three simple amplifier modules (X, V, and diamond) that were tested and used to predict the performance of the N-slab-long amplifier. (70-50-1294-3979pb01)

horizontally across the aperture and at the vertical middle using five different lamp explosion fractions ranging from 0.075–0.25. Figure 5(a) shows the horizontal gain distributions measured at $f_x = 0.2$ for the diamond, X, and V test configurations. From these measurements, we predicted the gain performance of a five-slab-long Beamlet amplifier and then compared it with actual measurements, shown in Fig. 5(b). The predicted and measured gain distributions for the five-slab-long amplifier have about the same shape, but the predicted value is about 5% higher. This discrepancy is because the predicted gain—Eq. (3)—does not take into account the nonlinear effect ASE has on the gain distribution. The slabs interior to the amplifier have higher gain coefficients, and therefore higher ASE decay rates, than the slabs in the X, V, and diamond configurations. For the NIF amplifier development, these and other results taken at different lamp explosion fractions will be used to validate an improved technique for predicting amplifier performance that takes ASE into account.

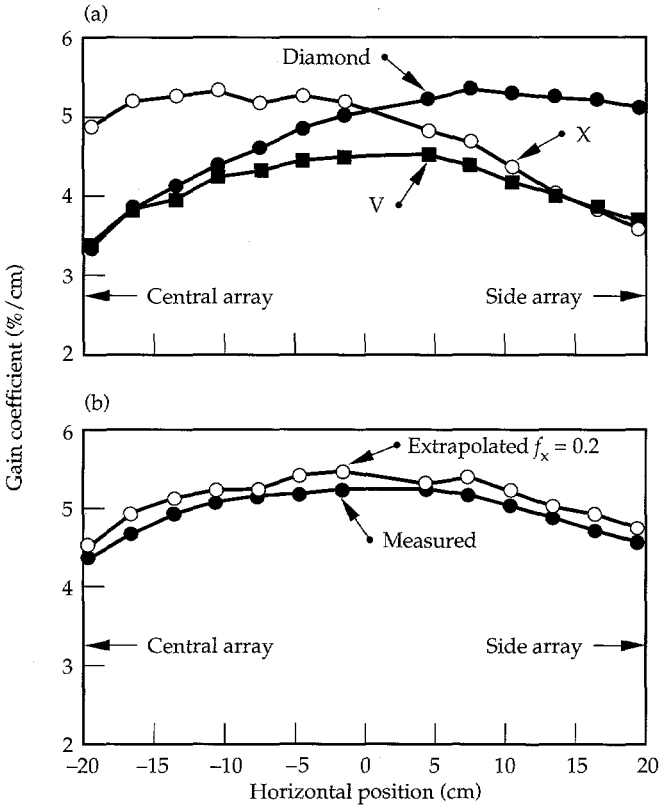

FIGURE 5. Horizontal gain distributions for (a) the V, diamond and X amplifier test configurations, and (b) the five-slab-long Beamlet amplifiers at $f_x = 0.20$. For comparison the predicted "extrapolated" performance for the five-slab-long Beamlet amplifier is also shown. (70-50-1294-3978pb01)

The gain coefficient profiles in Fig. 5(a) illustrate two other points about the amplifiers. First, note that the slopes in the gain distributions of the two slabs in the X and diamond configurations do not cancel out, because they have an even number of slabs (i.e., 2). Second, the one-slab-long amplifier (V) has a gain distribution similar to that of the five-slab-long amplifier (because N is odd), but the gain for the V is much lower due to large end-loss effects. The end losses also cause the two-slab-long amplifiers to have a lower average gain than the five-slab-long case.

Beamlet Amplifier Characterization Measurements

In addition to the gain, the storage efficiency and pump balance are important amplifier parameters. In this section, we discuss the results of our gain measurements and how they may be used to compute storage efficiency and pump balance.

Horizontal Gain Distributions vs f_x

Figure 6 shows horizontal gain distributions for the five-slab-long amplifier, which were measured at six different values of f_x. These gain distributions are relatively flat at low f_x and become more peaked as f_x increases. We attribute the higher gain at the center of the aperture to two effects: (1) ASE, which preferentially depumps the edges of the aperture and becomes more important as the average gain coefficient in the slab is increased; and (2) changes in the pump distribution as

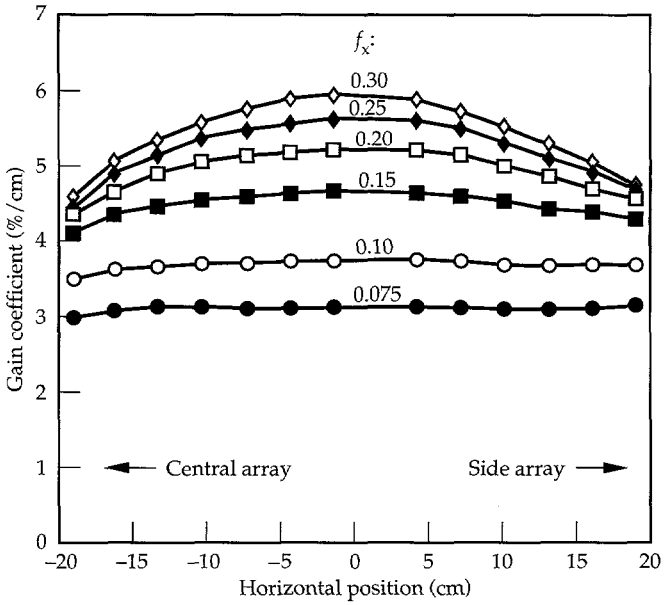

FIGURE 6. Horizontal gain distributions measured on the five-slab-long Beamlet amplifier at six different flash-lamp explosion fractions. (70-50-0494-2129pb01)

energy to the flash lamps is changed. It appears that ASE is the stronger of the two effects, based on MSA-2 experiments that showed that pump distributions produced by similar flash-lamp arrays varied only slightly with changes in how hard the lamps are driven (i.e., f_x).

Temporal Variations in the Horizontal Gain Distributions

Figure 7(a) shows the horizontal gain distributions that were measured on the five-slab-long amplifier at different times after initiation of the main pump pulse. In the figure, time increases from bottom to top for the rising edge of the pulse, and from top to bottom for the falling edge. The times were chosen to facilitate comparisons between gain distributions measured on the rise and fall of the gain, at comparable values of the average gain coefficient, as may be seen in Fig. 7(b). The gain distributions measured at the peak and on the fall of the pump pulse show the gain-peaking near the middle of the aperture that is attributed to ASE. The gain distributions measured on the rise lack this peaking effect, but show other types of variations that are attributed to nonuniform pumping. It appears that the pump distribution is not as uniform early in the pulse as it is later, after the arcs in the flash lamps have become better developed. These curves are indicative of the complexity that must be included in ray-trace codes to accurately predict gain distributions, as well as the wealth of Beamlet amplifier data now available for rigorous validation of such codes.

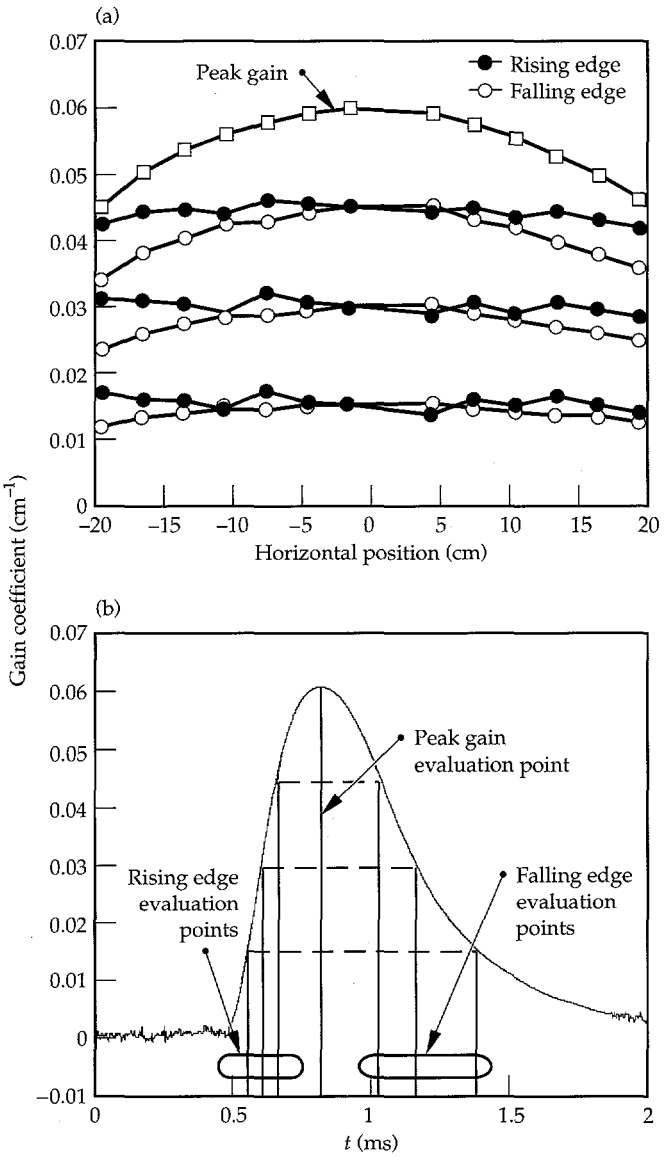

FIGURE 7. (a) Horizontal gain distributions of the five-slab-long Beamlet amplifier at different times during the main flash-lamp pulse, shown vs time in (b). (70-50-1294-3977pb01)

Full-Aperture Gain Distributions

Knowledge of the gain distribution over the full aperture is also required for rigorous validation of amplifier performance models. Full-aperture gain distributions were measured for the diamond, X, and five-slab-long amplifiers, at flash-lamp explosion fractions of 0.15 and 0.20. Figure 8 shows a contour plot of the full-aperture gain distribution measured on the five-slab-long amplifier at $f_x = 0.20$. Except for regions near the top and bottom of the aperture where the slab is partially shadowed by its mask, the gain gradients were larger in the horizontal direction than in the vertical direction because of ASE. For this gain distribution, in the central 95% of the aperture, the

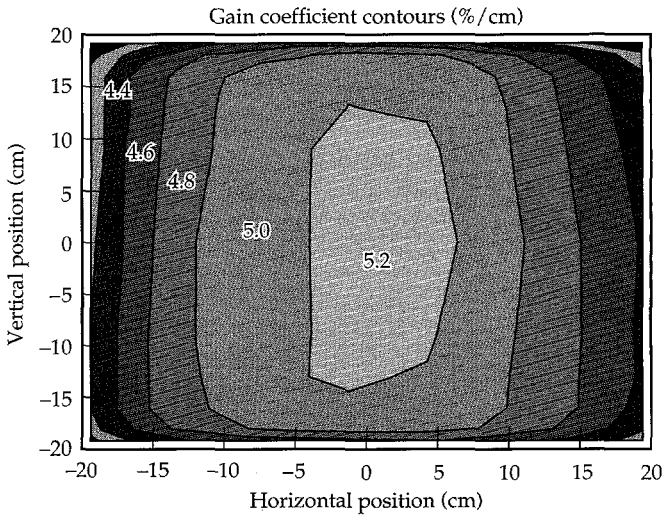

FIGURE 8. Gain distribution across the aperture of the five-slab-long Beamlet amplifier. (02-30-1093-3495pb01)

peak-to-average ratio of the gain coefficient *(U)* was 1.06 ± 0.004. In comparison, the MSA-2 amplifier, which had a similar pump cavity design, attained a *U* value of 1.025 ± 0.004. We attribute most of this difference to the higher ASE rates because of the Beamlet amplifier's larger pumped aperture (39.5 × 39.5 cm^2 compared to 29 × 29 cm^2 for MSA-2).

Storage Efficiency

Figure 9 shows storage efficiency vs gain per slab for the five-slab-long Beamlet amplifier and the Nova 31.5- and 46-cm amplifiers. At $f_x = 0.20$, the normal operating point for all three amplifiers, the Beamlet amplifier has a storage efficiency of 3.0%, compared to 1.8% for the Nova amplifiers. The principal factors causing the Beamlet amplifiers to attain higher storage efficiency are lower lamp packing fraction, shorter flash-lamp pulse length, and the use of more efficient central flash-lamp arrays in the 2 × 2 MSA architecture. Because of the large size of the Beamlet slabs and higher ASE decay rates, the efficiency curve for the Beamlet amplifier decreases faster than for the Nova amplifiers as gain per slab increases.

Pump Balance

Balanced pumping helps to reduce pump-induced beam steering. To determine how well balanced the pumping is between the central and side flash-lamp arrays, we measured horizontal gain distributions in the two-slab-long amplifiers while firing the central and side flash-lamp arrays separately. End losses were minimized by firing the central flash-lamp array in the diamond configuration and by firing the side flash-lamp array in the X configuration. Figure 10 shows the average gain coefficient plotted vs flash-lamp explosion fraction, for both central- and side-array pumping. We calculated average gain coefficients by integrating the measured horizontal gain distribution across the aperture. We found that over the entire explosion fraction range, from $f_x = 0.075$–0.25, pumping by the two flash-lamp arrays was balanced to within 5%, with the central array achieving slightly higher average gain coefficients than the side array.

Pump-Induced Wavefront Distortion

In the MSA geometry, the front and back of the laser slab gets heated unequally by the pump radiation. As a result, thermal stresses build up and cause the slab to deform. This deformation results in wavefront distortion of an initially plane beam. In this section, we describe our work in measuring pump-induced wavefront distortion.

Local Beam-Steering Probe

During the Beamlet amplifier activation, we characterized pump-induced wavefront distortion in the Beamlet amplifiers by measuring local pump-induced beam-steering angles using three 5-mm probe beams, generated with the cw Nd:YLF laser described earlier.

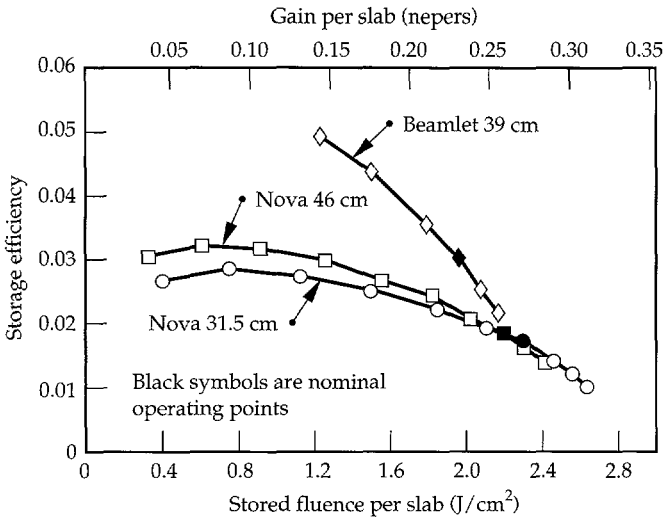

FIGURE 9. Storage efficiency vs the small signal gain per slab (and stored fluence per slab) for the five-slab-long Beamlet amplifier and the Nova 31.5-cm and 46-cm amplifiers. (70-50-0494-19589pb01)

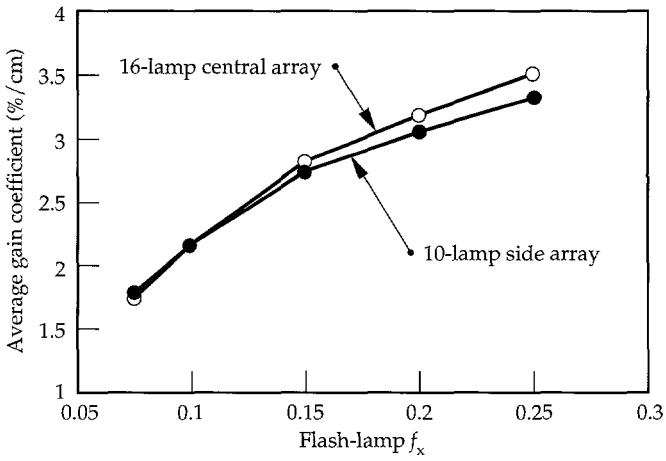

FIGURE 10. Average gain coefficient vs flash-lamp explosion fraction for two cases: (1) only the central array was fired (in the diamond configuration); and (2) only one of the side arrays was fired (in the X configuration). Central and side pumping were balanced over a wide range of explosion fractions. (70-50-1294-4015pb01)

The wavefront distortion in waves, Φ, is related to the local beam-steering angle, $\Delta\Theta$, by

$$\Phi(x) = \frac{1}{\lambda_0}\int_0^x \Delta\Theta(x')\,dx' \quad , \tag{5}$$

where x and x' are positions in the aperture and λ_0 is the wavelength. The three probe beams were arranged in a column, with a 9-cm vertical separation between adjacent probe beams. A motor-driven stage was used to move the three probe beams to different aperture positions.

The method for measuring local beam-steering angles has been described previously.[10] After passing through the amplifier, each probe beam was split, with one part directed to a lateral-effect photodiode and the other part to a conventional photodiode. Lateral-effect photodiodes produce output voltages proportional to the product of the beam power and the displacement of the beam centroid from the center of the detector. Each lateral-effect photodiode was placed at the focus of a 2-m-focal-length lens to ensure that the output voltages were proportional to changes in the propagation direction of the probe beam, and were insensitive to lateral translations of the probe beams. The lateral-effect photodiodes produced two beam-steering signals, one for the horizontal direction and one for the vertical direction. The effects of variations in probe beam power were removed by dividing the output voltages from each lateral-effect photodiode by the output voltage from the corresponding conventional photodiode. Integrating spheres ensured that the conventional photodiode signals were insensitive to lateral beam translations. The apparatus was calibrated absolutely by placing in each probe beam a rotating wedge with 208 μradian of angular deflection. Beam-steering and gain signals were digitized at a 200-kHz rate with 10-bit resolution.

The effects of static and quasi-static distortions were removed by subtracting the beam-steering angle measured during the pump pulse from the beam-steering angle measured 50–100 μs prior to the flash-lamp preionization pulse. The shot-to-shot variations in the beam-steering angles measured at the time of peak gain were approximately ±0.25 μradian. This reproducibility was achieved by placing the laser, amplifiers, and diagnostics under a class-100 HEPA filter hood to shield the beam paths from air turbulence. The blowers in the hood and the N_2 gas flow in the amplifiers were turned off during shots.

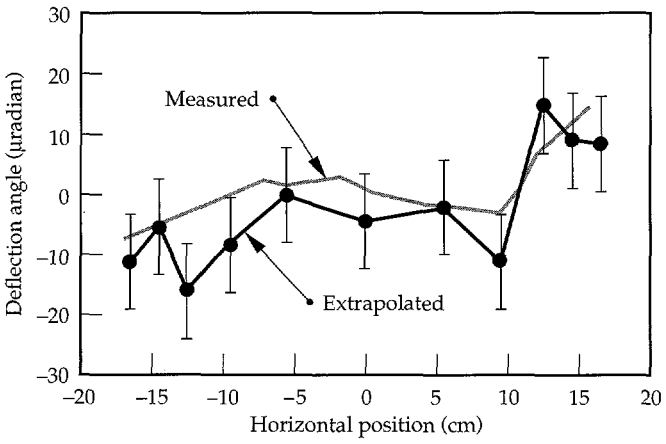

FIGURE 11. Pump-induced horizontal beam-steering angle vs horizontal position in the aperture for the four-pass 11-slab-long amplifier at $f_x = 0.2$. Values extrapolated from the diamond, X, and 5-slab-long amplifier data are in good agreement with values measured directly using a Hartmann sensor. (70-50-1294-3976pb01)

Results from Pump-Induced Distortion Measurements

We measured pump-induced beam-steering angles $\Delta\Theta_d$, $\Delta\Theta_x$, $\Delta\Theta_5$ on the diamond, X, and five-slab-long amplifiers, respectively. Using the formulas

$$\Delta\Theta_i = \frac{\left[\Delta\Theta_5 - \left(\Delta\Theta_d + \Delta\Theta_x\right)/2\right]}{3} \tag{6}$$

and

$$\Delta\Theta_{cav} = 4\left[9\Delta\Theta_i + \left(\Delta\Theta_d + \Delta\Theta_x\right)/2\right] \quad , \tag{7}$$

we obtained the pump-induced beam steering angles $\Delta\Theta_i$ for an interior slab and $\Delta\Theta_{cav}$ for a four-pass eleven-slab-long cavity amplifier, respectively. Figure 11 shows the pump-induced horizontal beam-steering angle vs horizontal position in the aperture for the four-pass eleven-slab-long amplifier, with the flash lamp fired at $f_x = 0.2$. Shown with our data are pump-induced beam-steering angles measured directly on the four-pass eleven-slab-long amplifier with a Hartmann sensor, as described in "Beamlet Pulse-Generation and Wavefront-Control System," p. 42. The beam-steering angles measured with the two techniques are in good agreement, with pump-induced beam-steering angles falling within ±15 μradian over most of the aperture. Negative angles correspond to beam steering toward the central flash-lamp arrays while positive angles correspond to beam steering toward the side flash-lamp arrays.

The pump-induced phase variation across the aperture, calculated using Eq. (5), was <2 waves at 1.053 um. With active wavefront correction using a deformable mirror, the phase variation was reduced to approximately 0.7 waves, well within Beamlet focusing and harmonic conversion requirements.

The major conclusions drawn from our beam-steering measurements are that in the central region of the slab more than one-half slab thickness from the edge claddings, pump-induced wavefront distortion is only weakly dependent on the vertical location in the aperture; pump-induced beam steering is much greater in the horizontal direction than in the vertical direction; and pump-induced beam steering is much greater in the end slabs than in the interior slabs. These results are consistent with previous pump-induced beam-steering measurements conducted at LLNL and with our understanding of pump-induced wavefront distortion. They are important because they confirm our understanding of the process and they establish confidence in our design of the NIF amplifiers.

Summary

We have completed detailed gain and pump-induced beam-steering measurements on the Beamlet amplifiers. The measurement results will be used to rigorously validate new and improved models for predicting amplifier performance, and will be of great value in the development of the NIF amplifiers. For the first time, MSA performance has been demonstrated at approximately the same aperture dimensions that are anticipated for the NIF.

Acknowledgments

The authors wish to thank Schott Glass Technologies[11] for providing lasers slabs, and EG&G, Inc.[12] for providing flash lamps, both critical parts of the work on Beamlet.

Notes and References

1. W. E. Martin, J. B. Trenholme, G. J. Linford, S. M. Yarema, and C. A Hurley, *IEEE J. Quantum Electron.* **QE-9**, 1744–1755 (1981).
2. H. T. Powell, A. C. Erlandson, K. S. Jancaitis, and J. E. Murray, *High-Power Solid State Lasers and Applications* (SPIE—The International Society for Optical Engineering, Bellingham, WA, 1988; *Proc. SPIE* **1277**), pp. 103–120 (1990).
3. K. S. Jancaitis, private communication: ray-trace model.
4. M. D. Rotter, LLNL memorandum AMP 92-006.
5. W. F. Hagen, *Laser Program Annual Report, 1977*, 2-228 to 2-231, Lawrence Livermore National Laboratory, Livermore, CA, UCRL-50021-77 (1978).
6. A. C. Erlandson, K. S. Jancaitis, R. W. McCracken, and M. D. Rotter, *ICF Quarterly Report* **2**(3), 105–114, Lawrence Livermore National Laboratory, Livermore, CA, UCRL-LR-105821-92-3 (1992).
7. J. E. Murray, *Laser Program Annual Report, 1985*, 7-3 to 7-13, Lawrence Livermore National Laboratory, Livermore, CA, UCRL-50021-85 (1986).
8. A. C. Erlandson, *Laser Program Annual Report, 1985*, 7-18 to 7-25, Lawrence Livermore National Laboratory, Livermore, CA, UCRL-50021-85 (1986).
9. J. H. Goncz, *ISA Transactions* **5**, 28 (1966).
10. J. E. Murray, H. T. Powell, G. F. Ross, and J. D. Winemute, Technical Digest, Annual Meeting, *Opt Soc of Am*, Washington, DC, TUU9 (1988).
11. Schott Glass Technologies Inc., 400 York Ave., Duryea, PA, 18642.
12. EG&G, Inc., Electro-Optics Division, 35 Congress St., Salem, MA, 01970.

Design and Performance of the Beamlet Optical Switch

M. A. Rhodes *L. J. Atherton*

B. W. Woods *C. L. Robb*

J. J. DeYoreo *D. H. Roberts*

Introduction

High-energy lasers for Inertial Confinement Fusion (ICF) experiments are typically designed with large apertures (>30 cm) to keep the fluence below the damage threshold of the various optical components. Until recently, no optical switch technology could be scaled to the aperture size, aperture shape (square), and switching speed required for the next generation of ICF drivers. This step is critical: The Beamlet multipass amplifier cavity uses a full-aperture optical switch to trap the laser pulse within the cavity and to divert the pulse out of the cavity when it reaches the required energy.[1] By rotating the polarization of the beam, a Pockels cell in the switch controls whether the beam is transmitted through, or reflected from, the polarizer.

In conventional Pockels cells, a longitudinal electric field is applied to an electro-optic crystal via external ring-electrodes.[2] To achieve a reasonably uniform field distribution in the crystal, the crystal's aspect ratio (diameter:length) must be no greater than 1:1 (1:2 is preferable). Since the required aperture in high-energy ICF drivers is in the range 30 to 40 cm, the crystal would have excessive optical absorption, strain depolarization, and cost. One alternative Pockels cell design approach, which allows for thin crystals, employs transparent, conductive thin films applied to the crystal surfaces as electrodes.[3] Unfortunately, such films exhibit insufficient conductivity to meet our switching speed requirements and do not have a high enough optical damage threshold.

In this article, we describe an optical switch technology that does scale to the required aperture size and shape for Beamlet and the proposed National Ignition Facility (NIF) laser, and can employ a thin crystal. This switch consists of a thin-film polarizer and a plasma-electrode Pockels cell (PEPC), the latter originally invented at Lawrence Livermore National Laboratory (LLNL) in the 1980s[4] and under further development since 1991. After discussing the PEPC concept, we present the design and optical performance of a 32×32 cm^2 prototype PEPC, including discussions of the crystals, the PEPC assembly, the vacuum and gas system, and the high-voltage pulsers. Then we describe the performance of the 37×37 cm^2 PEPC constructed specifically for the Beamlet laser. Finally, we discuss important technology issues that arose during PEPC development: cathode sputtering, cathode heating, nonuniformities in the switching profile, switch-pulse leakage current, and an estimate of the plasma density and temperature produced during PEPC operation.

The Plasma-Electrode Pockels Cell Concept

Figure 1 shows a top view cross-section of a PEPC and a simplified schematic of the required external electronic circuit. Vacuum regions on each side of the crystal are filled with working gas (He + 1% O_2) at an optimized operating pressure (30–40 mTorr). The plasma pulsers ionize this gas with a high-current pulse, forming the plasma-electrodes. Voltage from the switch pulser is applied across the crystal via these plasma-electrodes. As in a conventional Pockels cell, if the potential difference across the crystal is V_π, the half-wave voltage, the polarization of an incoming linearly polarized beam is rotated by 90°. For the crystals considered here, potassium dihydrogen phosphate (KDP) and potassium dideuterium phosphate (KD*P), V_π is 16.4 kV and 6.5 kV (at 1.06 μm optical wavelength) respectively.[5]

Requirements on the plasma and switch pulsers are set by the switching speed requirement placed on the PEPC, which depends on the particular application. In the Beamlet laser, the optical pulse propagates through

the amplifier cavity for two round trips, leading to four passes through the amplifier. The PEPC and the polarizer function together as an optical switch that controls the state of the cavity. If the cavity is closed, the optical pulse and any amplified stimulated emission are trapped within the cavity. If the cavity is open, the optical pulse is switched out of the cavity. The polarizer is arranged so that the cavity is open when no voltage is applied to the PEPC crystal and closed when the cystal is charged to V_π. To switch the optical pulse out of the cavity, the PEPC must change state in less than the cavity round-trip transit time, which is approximately 240 ns for Beamlet. We chose 100 ns as the nominal switching speed to allow extra time for voltage equilibration across the crystal aperture. The time constant by which the voltage on the crystal changes is given by $\tau = Z_{sw}C_{KDP}$, where Z_{sw} is the effective impedance of the switch pulser (parallel combination of the pulser output impedance and the terminating resistance) and C_{KDP} is the capacitance of the crystal. The Beamlet crystal is 37×37 cm^2 and 1 cm thick and consists of ordinary KDP with a relative dielectric constant $\varepsilon_r = 20$. We calculate the crystal capacitance by assuming a simple parallel-plate geometry and obtain $C_{KDP} = 2500$ pF. It takes four time constants to charge the crystal to 98% of V_π, so τ must be one-fourth of our desired switching speed, or 25 ns. This implies that Z_{sw} must be 10 Ω, and this determines the peak current I_{sw} that must be delivered by the switch pulser: $I_{sw} = V_\pi / Z_{sw} = 1.7$ kA. If a KD*P crystal is used, the capacitance is higher because $\varepsilon_r = 50$. An impedance of 4.0 Ω is required to achieve the same 25-ns time constant. The peak current requirement is about the same (2.0 kA) because of the lower V_π for KD*P.

The plasma current I_p at the time the switch pulse is fired must be greater than I_{sw}; otherwise the current from the switch pulser charging the crystal clamps at I_p, which increases the time required to fully charge the crystal.[6] This effect is due to the diode-like nature of the plasma discharge. Figure 1 depicts the discharge current and the KDP charging current. On side 2, the plasma and switch-pulse currents are in the same direction; on side 1 they are in opposite directions, so they cancel. If the peak switch-pulse current is greater than the plasma current, the current at the side 1 anode must go negative, which means that it is emitting electrons. This cannot happen on the time scale of the switch pulse.

A circuit model, shown in Fig. 2, was used to determine the relation between peak switch-pulse current and the plasma current. We model each plasma with a 0.1-Ω resistor in series with a diode, and we model the crystal capacitance with a 2500-pF capacitor. We set the value of the resistors to be on the order of the plasma collisional resistivity (see below), which is much smaller than Z_{sw}. We model the plasma currents with a pair of

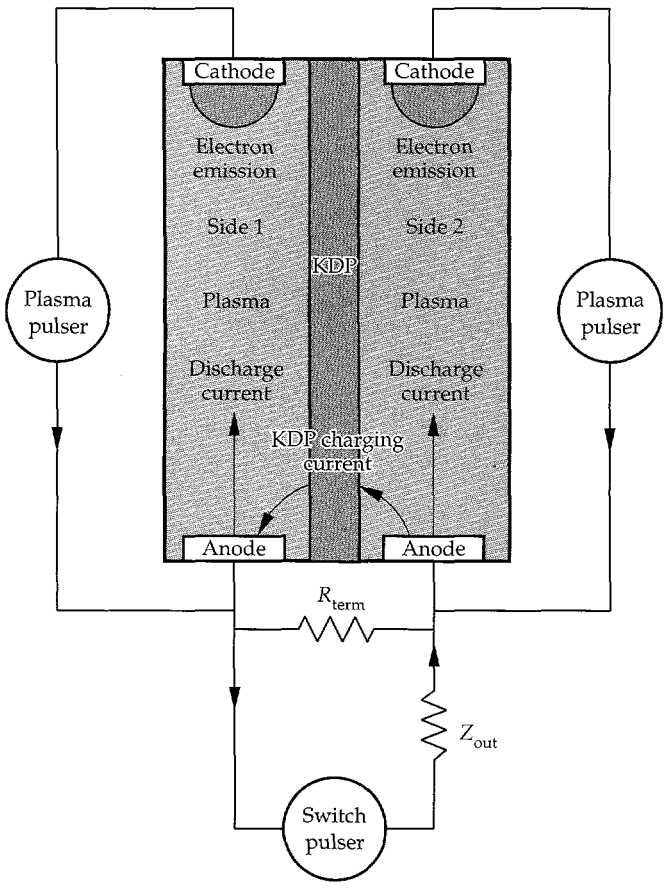

FIGURE 1. A top-view cross-section of the PEPC and its associated electronic circuit. The plasma pulsers produce the plasma electrodes by high-current discharge in He; the switch pulser then applies the switching voltage across the KDP crystal. (70-50-1294-3986pb01)

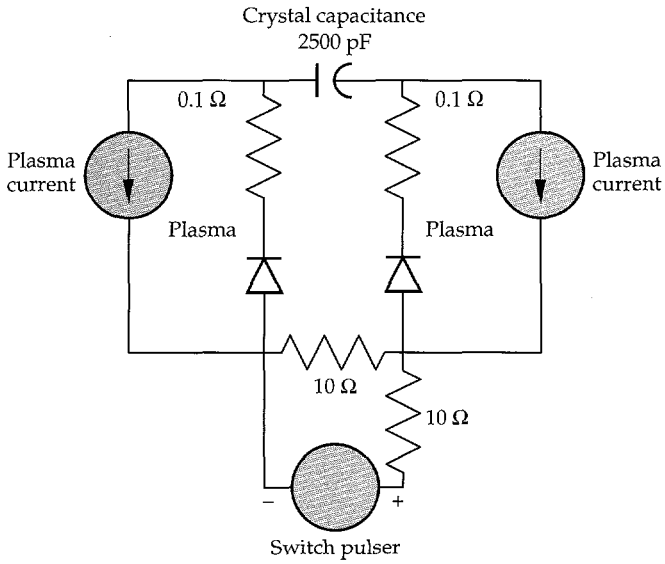

FIGURE 2. Circuit model of the PEPC used to determine the relation between peak switch-pulse current and plasma current (results shown in Fig. 3). (70-50-1294-3980pb01)

current sources; the switch-pulse voltage is applied by a 20-kV rectangular pulse source with a 10-Ω series resistor to model Z_{sw}. Using PSPICE[7] to calculate the circuit response, we find the peak charging current for this case is 2 kA, so the plasma current must be greater than 2 kA if it is not to limit the crystal charging time. Figures 3(a) and 3(b) show the model results for the crystal charging current and voltage, respectively, for cases when the plasma current is 2.0 and 0.5 kA. For the 2-kA case, the current in the crystal peaks at slightly <2 kA (because of the plasma resistance), and the crystal charges with the expected time constant. For the 0.5-kA plasma current case, the charging current clamps at 0.5 kA, extending the charging time. The voltage rise time is longer for the 0.5-kA case.

The preceding analysis puts a lower limit on the required plasma current. In practice, however, we find that optimum performance is achieved at somewhat higher current. This is because the plasma resistance must be small compared to the Z_{sw} assumed in our circuit model, and because the plasma must be sufficiently uniform across the full aperture. Two processes contribute to the plasma resistance: electron scattering by collisions with neutrals and coulomb scattering of electrons by the plasma ions.

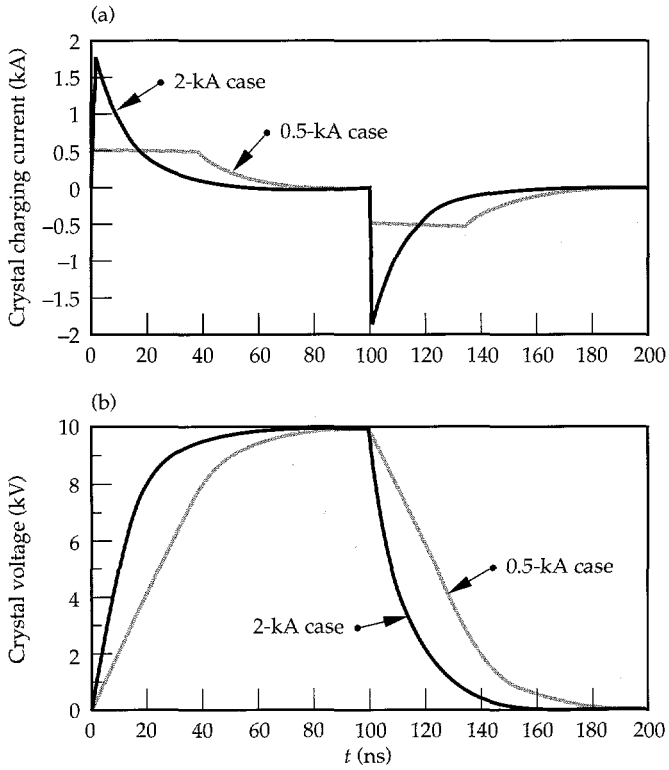

FIGURE 3. (a) Current (based on circuit in Fig. 2) in the crystal capacitance for plasma currents of 2 kA and 0.5 kA. For currents <2 kA, the charging current clamps at the plasma current, extending the charging time. (b) Corresponding voltage waveforms. The voltage rise time is longer for the 0.5-kA plasma current.
(70-50-1294-3981pb01)

The plasma resistivity η_{en} due to electron-neutral collisions is given in Ω-cm by

$$\eta_{en} = 8.93\times10^{11}\,\frac{n_n}{n_e}\left(\frac{m_e\sigma_{en}}{q^2}\sqrt{\frac{kT_e}{m_e}}\right), \qquad (1)$$

where n_n is the neutral density, n_e is the electron density, m_e is the electron mass, σ_{en} is the electron-neutral collision cross-section, which we take to be 5.3×10^{-16} cm^2 for He,[8] kT_e is the electron thermal energy, and q is the electron charge. All quantities are in cgs units.

The resistivity due to coulomb scattering is given by[9]

$$\eta_{ei} = 5.2\times10^{-3}\,\frac{Z\ln\Lambda}{T_{eV}^{\frac{3}{2}}}, \qquad (2)$$

where Z is the average ion charge state, and T_{eV} is the electron temperature in electron-Volts. The Coulomb logarithm ln Λ (≈10) is a correction term for small-angle scattering.

The relative contribution to plasma resistance from these two processes depends on the operating conditions. Using a method described later, we estimate $n_e = 1.6\times10^{12}$ cm^{-3} for $T_{eV} = 5$ eV. With an operating pressure of 35 mTorr, the plasma resistivity is dominated by electron-neutral collisions, and the total plasma resistance is 0.04 Ω, which is much less than the switch-pulser impedance.

Design of the 32-cm Prototype PEPC

In this section, we describe design details for the PEPC and its associated subsystems, including the crystals, the PEPC assembly, the vacuum and gas supply system, the discharge electrodes, the plasma generation system, and the switch pulser.

Crystals

The original design for the Beamlet PEPC called for a KD*P crystal with a high deuterium concentration (>90%). KD*P is desirable because at 90% deuteration, optical absorption for 1.05-μm light traveling parallel to the crystal z-axis is 0.49%/cm compared to 5.8%/cm for KDP.[10] However, when we began this development work it was not known whether KD*P crystals of sufficient size and quality could be grown for use in the Beamlet PEPC. We constructed a prototype PEPC based on the largest KD*P crystal available at that time (32×32 cm^2) and tested it with both KDP and KD*P crystals. Before testing in the PEPC, we measured the strain depolarization of both crystals using an experimental setup described elsewhere.[11] This apparatus

measures the extinction ratio (*ER*) point by point across the surface of the crystal under test. From the array of data points, we construct a strain image of the crystal. For consistency, we convert all *ER*s to effective switching efficiency, S_{eff}, which is given by

$$S_{eff} = 1 - \frac{1}{ER} \quad . \tag{3}$$

An *ER* of 100 corresponds to an efficiency of 99% while an *ER* of 1000 corresponds to an efficiency of 99.9%.

Figure 4 shows the resulting strain images for the KD*P and KDP crystals. The KD*P crystal exhibits more strain structure than the KDP crystal: growth sector boundaries are clearly visible, for example. However, for these particular crystals, the KD*P has slightly higher average efficiency than the KDP (99.987% vs 99.952%) and higher worst-spot efficiency (99.78% vs 99.65%).

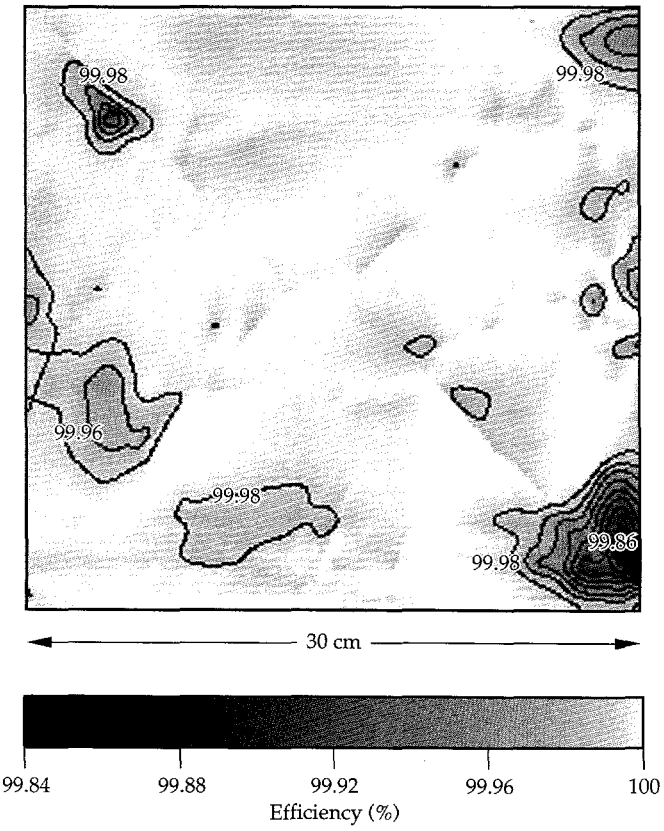

FIGURE 4. Strain map for a 32 × 32 cm² KD*P crystal shown in terms of the switching efficiency (see text for definition). Regions of lower efficiency denote loss due to strain-induced depolarization. (70-50-1294-3982pb01)

PEPC Assembly

Figure 5 shows the PEPC assembly. The crystal is potted into a ceramic frame with silicone elastomer. This frame mounts between two housings, which are in turn sandwiched between two 4-cm-thick fused silica windows. The housings, made from ultrahigh-molecular-weight polyethylene, define the vacuum regions on each side of the crystal. The housings also hold the discharge electrodes in place and interface to the vacuum pumping system. The windows seal the vacuum regions on the outside and allow transmission of the optical pulse. The windows and the KDP crystal are antireflection coated with sol-gel silica particles.[12] The total transmission through the cell was 99.1% with the KD*P crystal and 93.9% with the KDP crystal.

The housing assembly rests on a support structure that provides motorized x and y translation and manual adjustment of tip, tilt, and twist so that we can align the PEPC to our test beam. The support structure also holds the vacuum pumping system.

Vacuum and Gas System

The vacuum and gas system provides the required environment inside the PEPC for optimum formation of the plasma electrodes. A two-stage turbomolecular pump evacuates the PEPC interior to less than 5×10^{-5} Torr. This base pressure ensures that the concentration of impurity species in the plasma is low enough that it does not degrade the discharge uniformity. The gas system injects the working gas (a mixture of He plus 1% O_2) into the cell and maintains the gas pressure at 35 mTorr with active feedback control. The feedback system uses a capacitance manometer to monitor the cell pressure and drives a servo loop actuating a gas metering valve. The operating pressure is maintained by flowing gas while the turbopump continuously evacuates the cell. We discuss the purpose of the oxygen below.

Discharge Electrodes

The plasma electrodes are formed by driving current between pairs of anodes and cathodes. The anodes are simple bars of stainless steel. The cathodes are planar magnetron structures (Fig. 6).[13] Planar magnetrons are commonly used in direct current and radio frequency discharges as sputtering sources, but to our knowledge this is the first application as a cathode for a high-current pulse discharge.

Permanent magnets beneath the cathode surface provide a closed $\mathbf{E} \times \mathbf{B}$ path for electron flow on the cathode surface, leading to increased plasma density near the cathode. The magnetron cathodes result in lower operating pressure and lower discharge voltage

across the anode-cathode gap than with unmagnetized cold cathodes. The lower operating pressure leads to lower plasma resistivity, as explained in "The Plasma-Electrode Pockels Cell Concept" earlier. Lower discharge voltage leads to less cathode sputtering, less cathode heating, and lower potential differences between the side 1 and side 2 plasmas (higher potential differences are more likely to cause partial optical switching before application of the switch pulse).

During the discharge, He ions from the plasma are accelerated by the discharge potential and bombard the cathode, producing electrons by secondary emission. This electron emission sustains the discharge. However, the ion bombardment also leads to sputtering of the cathode material, which can deposit on the crystal and window surfaces, reducing their optical damage threshold. To eliminate this deposition, the cathode surfaces are made from high-purity graphite, so the sputtered material is C. The sputtered C reacts with the 1% O_2 in the plasma to form CO and CO_2, which are pumped away by the vacuum system. We describe experimental tests of this process later in this article.

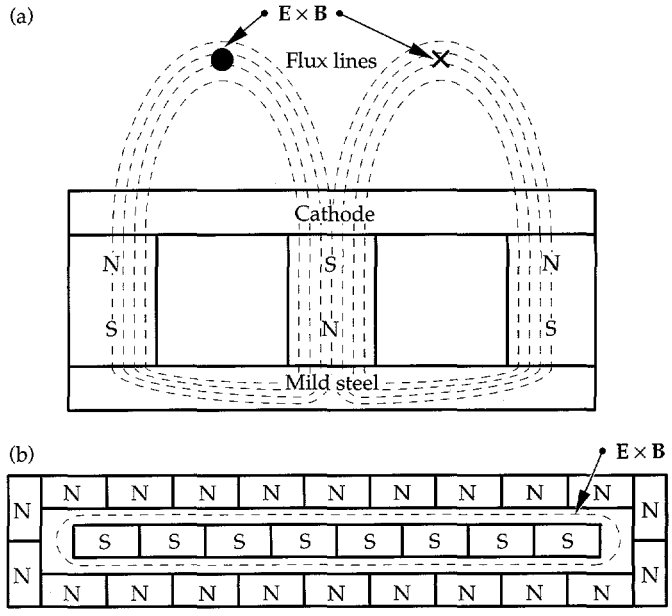

FIGURE 6. (a) Cutaway side view and (b) top view of the magnet layout for the planar magnetron cathodes used in the PEPC. The magnetron cathodes provide a uniform discharge without thermionic emission. (40-00-0494-1608pb01)

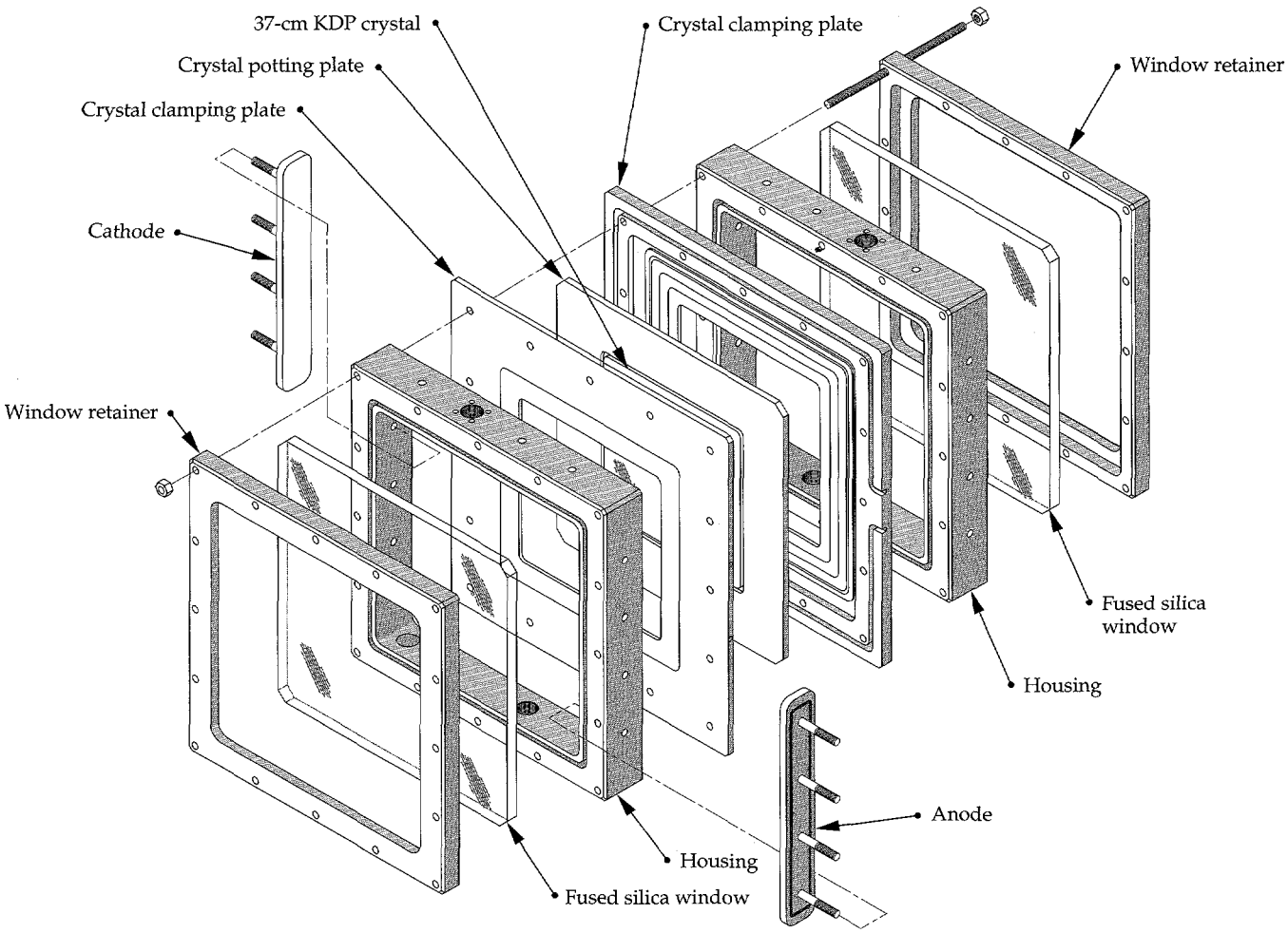

FIGURE 5. Exploded view of the PEPC assembly, showing the sandwich-like structure. (02-30-0391-1444pb01)

Plasma Generation System

The plasma is created in a two-stage process: a low-current preionization (simmer) discharge and a high-current pulsed discharge. The simmer discharge is initiated by a high-voltage, low-current power supply that provides enough voltage to break down the gas (about 1.5 kV) and then provides a constant discharge current of 30 mA. The voltage required to maintain the simmer discharge is about 300 V. The high-current pulse is produced by discharging a 5-μF capacitor charged to 4 to 7 kV depending on the required peak current. We call the capacitor and low-current power supply the *plasma pulser*. Figure 7 shows a typical plasma current waveform and the relative timing of the switch pulse, which we typically time to fire just after the peak in the plasma current.

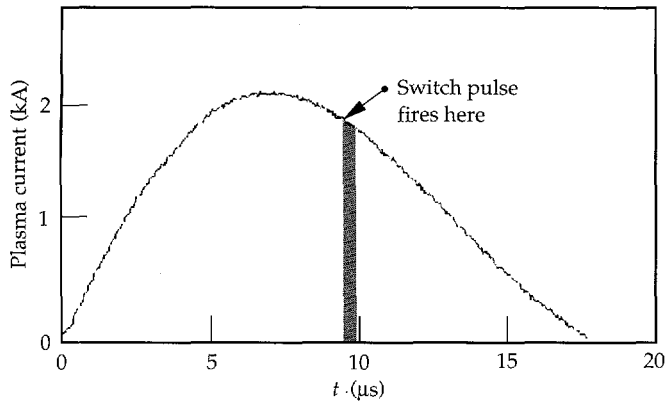

FIGURE 7. Plasma current for a 2-kA pulse, and relative timing of the switch pulse. (70-50-0594-2403pb01)

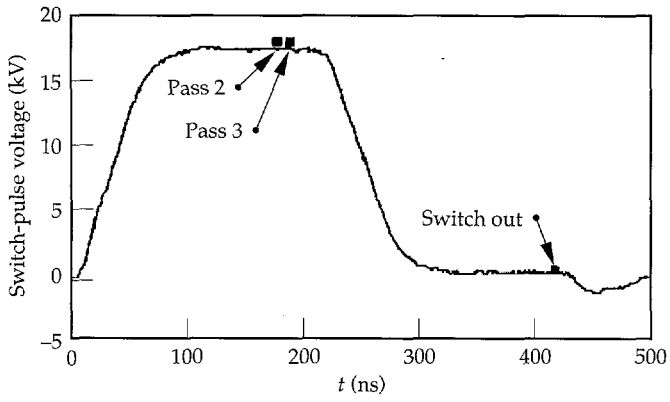

FIGURE 8. Voltage across the PEPC during normal operation, and when the optical pulse traverses the cell—twice when the voltage is on (pass 2 and pass 3) and once after the cell is discharged (switch out). (70-50-0594-2402pb01)

Switch Pulser

The switch-pulse generator[14] produces a nominally rectangular pulse applied across the crystal via the plasma electrodes. The switch pulser satisfies several important requirements: shot-to-shot jitter is <2 ns, a voltage flat-top at least 50 ns long is within ±2% of V_{π}, and the voltage returns to zero (±2% of V_{π}) after the pulse, so that the optical pulse is efficiently switched out of the cavity. The pulse is produced by sections of coaxial cable used as a pulse-forming network (PFN). A high-voltage power supply charges the PFN to twice the required output voltage, and a thyratron switches the charged PFN into the output line, which is also made up of coaxial cable sections. Multiple PFN and output lines are connected in parallel to achieve the switch-pulser impedance required to charge and discharge the crystal in less than the round-trip transit time of an optical pulse in the Beamlet laser-amplifier cavity. The output pulse duration depends on the length of the PFN cables. The output cables are long enough that electrical reflections due to impedance mismatches at the cell do not return to cause voltage ripples until after the required switch-out time.

We can configure the switch pulser for operation with KDP or KD*P. For KDP, we use four 50-Ω PFNs and output lines in parallel to achieve a pulser impedance of 12.5 Ω. For KD*P, we use eight cables in parallel for an impedance of 6.25 Ω. Figure 8 shows a typical voltage waveform produced by the Beamlet switch-pulse generator. Also shown is the relative timing of the optical pulse on the multiple passes through the cell when used in the Beamlet multipass cavity. The laser pulse traverses the cell three times: twice when the voltage is on and once when the voltage is off.

Prototype PEPC Optical Switching Performance

We evaluated the switching performance of the prototype PEPC with both KD*P and KDP crystals. A Q-switched, pulsed laser (10-ns nominal pulse duration at 1.06 μm) was used as the illumination source. A beam splitter diverted a small portion of the beam into a reference detector. After traversing a polarizer, the beam was expanded with a negative lens and collimated through the PEPC with a 30-cm-diam lens. After traversing the PEPC, a second 30-cm-diam lens focused the beam through an analyzing polarizer. A small-aperture positive lens imaged the plane of the PEPC crystal on the detector. We used two types of detectors: a photodiode to look at average performance across the whole aperture and a charge-coupled device (CCD) video camera to produce images of the

performance in two dimensions. With these optics, we could not illuminate the full 32×32 cm^2 aperture at once; we used the x-y translation capability of our support structure to diagnose the cell in four quadrants.

We define several different *ER*s to help describe the switching performance. The system extinction, ER_{sys}, is the ratio of the detected intensity with the polarizers aligned to the intensity with the polarizers crossed without activating the PEPC. ER_{sys} is a measure of depolarization errors in the various optical components. With the beam at small aperture (only the polarizers in the beamline with no expansion optics), we find $ER_{sys} > 1 \times 10^5$. Adding the expansion, collimating, and imaging lenses reduces ER_{sys} to about 3000. Adding the PEPC into the beamline further reduces ER_{sys} to about 1500 because of strain in the windows and crystal.

During PEPC operation, we measure ER_{on}, the *ER* when the voltage is on, and ER_{off}, the *ER* in the switch-pulse tail at the time of switch-out (about 200 ns after the end of the switch pulse). ER_{on} is the ratio of light intensity incident on the PEPC to the light intensity that remains unrotated with the PEPC at V_π. We measure ER_{on} with the polarizers aligned and take the ratio of the detector signal with no voltage on the PEPC to the signal with V_π on the PEPC. Although the switch pulser does a good job of discharging the crystal, some residual charge remains on the crystal at the critical switch-out time, leading to an ER_{off} lower than ER_{sys}. We measure ER_{off} by taking the ratio of the detector signal with the polarizers aligned and no voltage on the switch to the detector signal with the polarizers crossed, 200 ns after the trailing edge of the switch pulse as already defined.

As before, we express the data in terms of efficiency. S_{off} represents the percentage of light that would be switched out of the cavity on pass 4, while S_{on} is the percentage of light that stays in the cavity for gain passes 2 and 3. The goals for S_{on} and S_{off}, set at the beginning of the development program, were >99% (*ER*=100) average across the aperture and no spots worse than 98% (*ER*=50). These efficiencies include only losses due to depolarization of the beam and do not include losses due to surface reflections and absorption.

Figure 9 shows a typical S_{on} image of the prototype PEPC with a KDP crystal. In this example, S_{on} in the worst spot is 99.64%. Table 1 summarizes switching performance with our 30-cm-diam imaging aperture centered on the PEPC for KDP and KD*P. The performance exceeds the required performance for both KD*P and KDP. The shot-to-shot reproducibility is indicated by the standard deviations of the average efficiencies. We obtained the average efficiencies by averaging 10 or more consecutive photodiode signals (with the system operating at a consistent 0.25 Hz). We obtained the worst-spot results by scanning images acquired with our CCD video system for each condition.

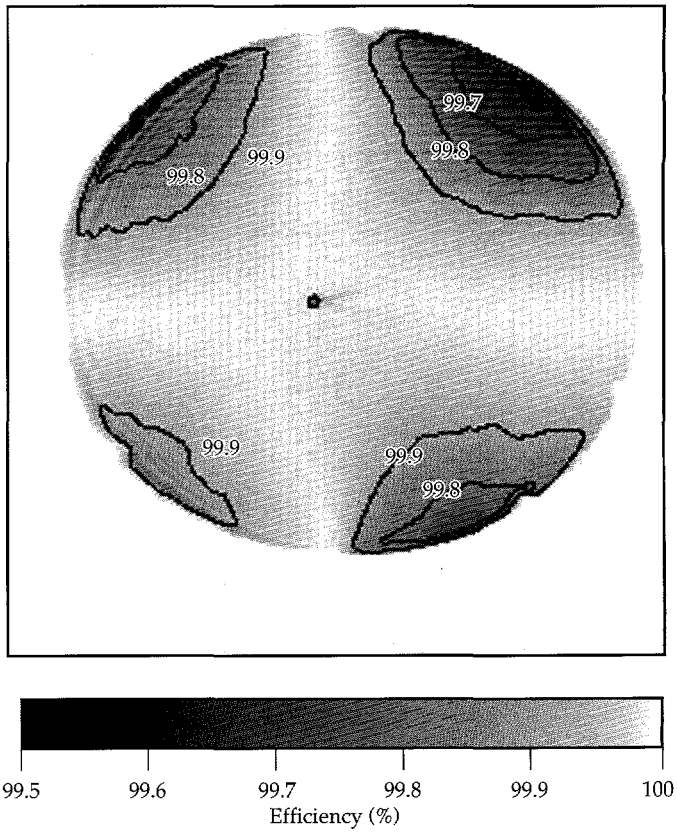

FIGURE 9. Typical S_{on} efficiency image from the prototype PEPC with a 32×32 cm^2 KDP crystal. A 30-cm-diam central view is shown. (70-50-1294-3983pb01)

TABLE 1. Switching performance of prototype PEPC with KD*P and KDP crystals. Goals were average efficiences greater than 99% and no spots worse than 98%.

	During switch pulse, S_{on}		After switch pulse, S_{off}	
Crystal type	**Average (±1 σ)**	**Worst spot**	**Average (±1 σ)**	**Worst spot**
KD*P	99.90 ± 0.02%	99.60	99.85 ± 0.02%	99.39
KDP	99.91 ± 0.01%	99.49	99.91 ± 0.02%	99.64

Design and Optical Performance of the Beamlet PEPC

Based on our experience with the prototype PEPC, we designed and built a PEPC for use in the Beamlet laser. Figure 10(a) shows the Beamlet PEPC fully assembled, and Fig. 10(b) shows it integrated into the Beamlet laser. It is essentially the same as the prototype PEPC, except that it is large enough to accommodate a 37×37 cm^2 crystal, the cathodes are set back from the edge of the crystal by 6 cm in a reentrant cavity, and the outer windows are 3 cm thick (they were 4 cm thick in the prototype).

(a)

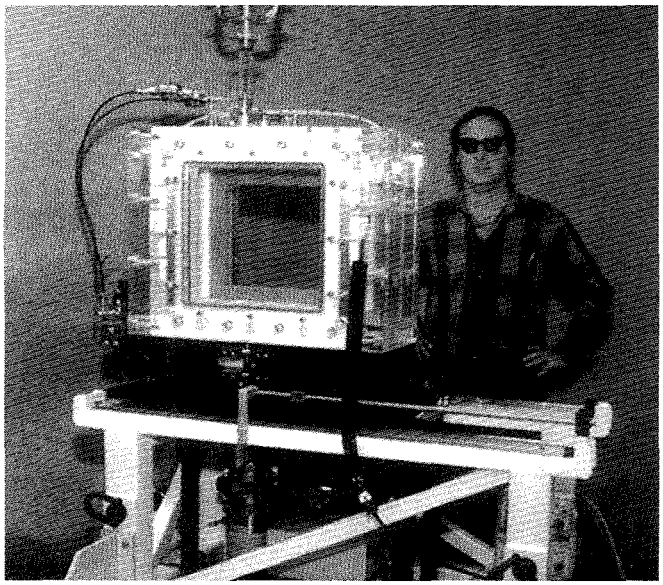

(b)

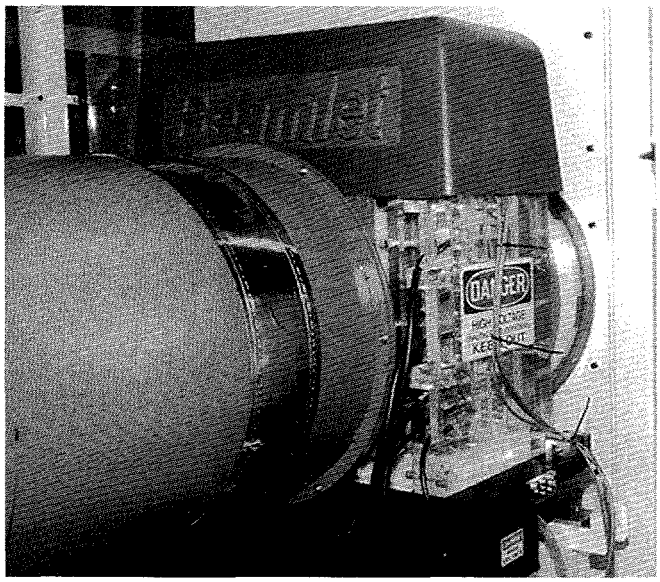

FIGURE 10. (a) Beamlet PEPC before installation into the Beamlet laser. (b) Beamlet PEPC integrated into the Beamlet laser. (70-50-0494-1845pb01)

Operation of the Beamlet PEPC as part of the Beamlet laser began in February 1994. Before operation at high optical fluence, we evaluated the switching performance at low fluence using a 32×32 cm^2 KDP crystal. We performed these tests with the PEPC installed into the Beamlet laser cavity and used the Beamlet diagnostic system. Figure 11 shows the experimental setup we used to test the switching performance at low fluence. At the beginning of a Beamlet shot, an optical pulse from the front-end laser is injected into the spatial filter. A small injection mirror (not shown) reflects the pulse toward cavity mirror M_1 through the cavity amplifier (which was not energized for the low-fluence tests). The pulse reflects from M_1 and passes back through the amplifier and spatial filter before it illuminates the PEPC at full aperture (35 cm). After traversing the PEPC, the beam reflects from the polarizer if the PEPC is off and passes through the polarizer if the PEPC is on (as shown in Fig. 11). A portion of the light transmitted by the polarizer passes through the partially transmitting cavity mirror M_2 into the diagnostic system. The sampled pulse is down-collimated by lens L_3 and other small-aperture optics (not shown) that image the crystal plane of the PEPC onto a high-resolution CCD video camera.

We ratio the switch-on and switch-off images to produce a switching efficiency image as shown in Fig. 12. As before, the switching efficiency data includes only losses due to beam depolarization and not losses from surface reflections or absorption. In this low-fluence test, we observed an average switching efficiency across the aperture of 99.5%; the minimum efficiency was 97.5% in the upper left-hand corner. The regions of lower switching efficiency in the corners are caused by strain-induced depolarization in the fused silica windows arising from vacuum loading.

During a full system shot, the cavity amplifier is energized. The voltage pulse applied to the switch starts at about the same time the optical pulse hits the injection mirror. Voltage across the crystal equilibrates while the optical pulse propagates towards mirror M_1 in Fig. 11 and makes its first two gain passes through the amplifier. While passing through the PEPC, the optical pulse polarization rotates by 90° and thus passes through the polarizer. The optical pulse reflects from mirror M_2 and passes through the polarizer and PEPC (rotating another 90°) before it propagates back toward the amplifier for two more gain passes. During this 240-ns interval, the voltage across the PEPC drops to zero. When the optical pulse returns again, the polarization is not rotated by the PEPC, so the pulse

reflects off the polarizer and out of the cavity. While details of the Beamlet laser performance[15] are not within the scope of this paper, we report that the main Beamlet cavity has produced up to 6 kJ of 1.06-μm light in a 3-ns pulse with switched, four-pass operation. During these tests, the Beamlet PEPC operated reliably and reproducibly, exhibiting high-fluence (average of 5 J/cm^2) switching efficiency >99.5% for both cavity-closed and cavity-open states.

PEPC Technology Issues

In this section, we discuss important technology issues that surfaced during our developmental work, including sputtering of cathode material, indirect crystal heating by the cathode, magnetically induced regions of nonuniform switching (bright spots), and switch-pulse leakage current to the vacuum system.

Although we have no direct measurement of the plasma parameters (density and temperature) except for the low-current simmer plasma, we also present in this section a method for estimating the plasma density based on the observed difference between the known V_π for KDP and the applied voltage required to achieve optimum switching. These plasma parameters are required for estimating the plasma resistance.

Sputtered Cathode Material

As mentioned in "Discharge Electrodes" earlier, the gaseous discharges that form the plasma electrodes sputter the cathode material. In an early cathode design, we used Mo for the cathode surface because of its relatively high secondary-electron emission coefficient under He-ion bombardment. After several thousand shots with this cathode, we illuminated the prototype PEPC with a partially focused beam to test operation at high fluence. Our setup allowed us to vary the fluence to over 25 J/cm^2. During this test, we imaged the crystal with a telescope and watched for optical damage as we increased the fluence. We observed a significant reduction in damage threshold near the cathode, while the threshold for other parts of the crystal remained unchanged. We found that this reduction in damage threshold was due to deposition of Mo on the crystal, which was highest near the cathode and decreased with distance from the cathode.

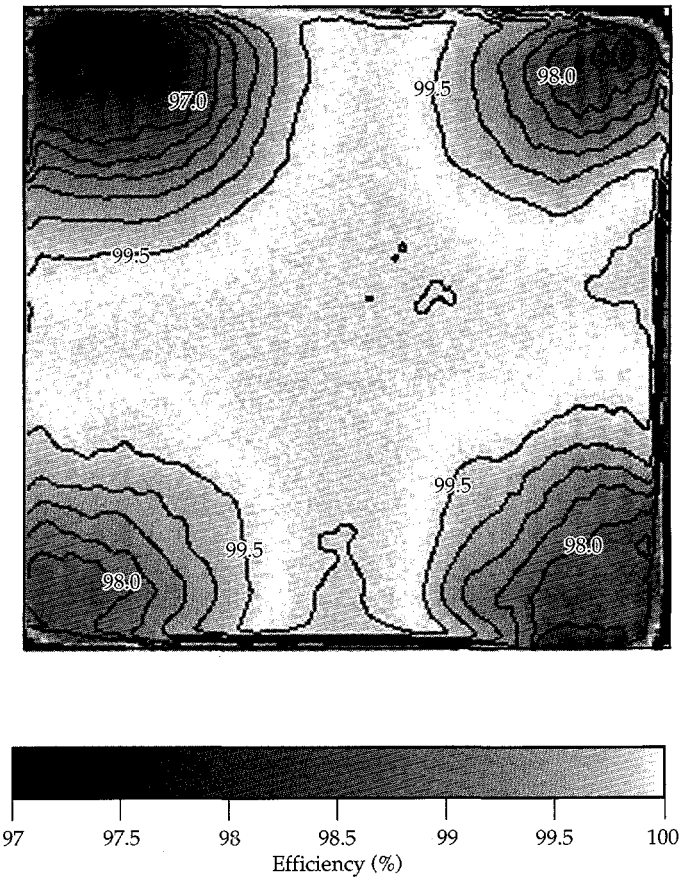

FIGURE 12. Switching efficiency across the 35 × 35 cm^2 aperture of the Beamlet PEPC. Lower switching efficiency in the corners is due to strain-induced birefringence in the silica windows arising from vacuum loading. (70-50-1294-3984pb01)

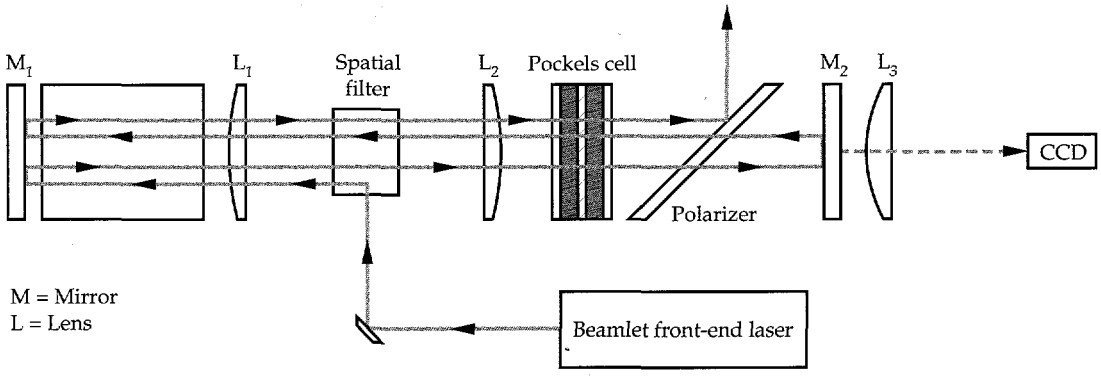

FIGURE 11. Simplified diagram of the experimental setup used to evaluate the switching performance of the PEPC in the Beamlet laser at low fluence. An optical pulse from the Beamlet front-end laser propagates through the PEPC and polarizer. A high-resolution CCD video camera images the light transmitted by the PEPC–polarizer combination. (70-50-1294-3985pb01)

To confirm this sputter coating of the crystal, we exposed witness plates to several thousand shots and detected Mo on the plates with standard analysis techniques, including electron spectroscopy chemical analysis and inductively coupled plasma mass spectroscopy.

We solved this sputtering problem by replacing the Mo cathode covers with high-purity graphite and adding 1% O_2 to the He working gas as described in "Discharge Electrodes." We confirmed the effectiveness of this technique with three experiments: direct measurement of sputter deposition using a quartz crystal microbalance, observation of CO and CO_2 gas production using residual gas analysis, and optical damage tests performed on witness plates exposed to the plasma.

To monitor the deposition of sputtered material directly, we inserted a quartz crystal microbalance into the prototype PEPC, placing the face of the microbalance 4 cm from the cathode surface. The quartz crystal is coated with a thin Au film and is part of a resonant circuit whose frequency depends on the temperature of the crystal and the mass of material on the crystal face. The sensor frequency is also affected by changes in the ambient pressure, which affects the mass of adsorbed gas on the crystal face. As long as temperature and pressure are held constant, changes in the resonant frequency are due to changes in mass arising from deposition.

The results of an experiment in which we initially ran the discharge with a pure He plasma showed C sputtered from the cathode depositing on the nearby sensor head. Without stopping the discharge, we changed the working gas to a mixture of He plus 1% O_2. Initially, the sensor responded with an apparent step increase in film thickness when the gas was changed. However, the sensor response is actually due to a change in the mass of adsorbed gas. After the sensor reached a new equilibrium, the effective film thickness decreased monotonically as the previously deposited C reacted with the O_2 to form CO and CO_2.

For the second test, we directly measured with a residual gas analyzer the formation of CO and CO_2 during the discharge. We estimated the sputtered flux of C to be 1.1×10^{16} atoms/s for a 23-mA discharge current and a sputtering coefficient of 0.1 for He bombarding graphite.[16] We compared this with the throughput of CO and CO_2, which we estimated from the partial pressures of these species and the speed of our pumping system. Within the accuracy of this measurement, we found that 100% of the sputtered C was converted to gaseous species and pumped away.

As a final test of this new cathode design, we placed a high-quality fused-silica substrate (witness plate) as close as possible to the cathode and exposed it to 80,000 consecutive PEPC shots. We compared the optical damage threshold before and after exposure to PEPC discharges and found that it was not significantly changed (we actually observed a slight increase in damage threshold after plasma exposure). During five months of operation in Beamlet, we have subjected the Beamlet PEPC to 50 to 60 high-fluence shots and 10,000 to 15,000 low-fluence alignment shots. We have not observed any reduction in damage threshold from plasma-related effects, proving the effectiveness of the C conversion process in actual use.

Crystal Heating

Most of the electrical energy used to drive the plasma discharges ends up as thermal energy deposited in the cathode surface by ion bombardment. The heated cathode heats the crystal, leading to a thermal gradient in the crystal. This causes strain in the crystal, which increases the depolarization of a beam traversing the PEPC. To quantify this depolarization, we removed the expansion optics from our polarimeter and illuminated a small spot on the crystal near the cathode side.

The results showed how the *ER* in this spot (normalized by the *ER* at the start of the test) decreases as the crystal heats. In one case, the simmer discharge was run continuously and dissipated 9 W at the cathode. The pulsed discharge, running at 0.25 Hz, adds another 3 W of average power. Under these conditions, the *ER* dropped to about 15% of its original value in only 30 minutes of continuous operation. In a second case, we reduced the average power dissipated by gating the simmer discharge on for only 100 ms for each shot. This reduces the average power due to the simmer discharge by a factor of 40. The average power from the pulsed discharge is unchanged, so the total average power for this case is 3 W. With the simmer discharge gated rather than running continuously, the *ER* only decreased to about 50 to 60% of its orginal value in a 30-minute operating period.

We measured heating in the PEPC by installing thermistors at five locations: center of the cathode, center of the $\mathbf{E} \times \mathbf{B}$ path (racetrack region) on the cathode, cathode edge of the crystal, anode edge of the crystal, and surface of the anode. Table 2 summarizes the temperature change at these locations after 100 minutes of operation. As expected, we observe maximum heating in the racetrack region, where the ion flux to the cathode is maximum. Heat conducts through the graphite to the rest of the cathode. The cathode edge of the crystal

exhibits more heating and depolarization than the anode edge. By gating the simmer, we reduced the temperature increase at the cathode edge of the crystal by a factor of 10.

As mentioned above, to further reduce crystal heating in the Beamlet PEPC, we increased the distance from the cathode to the crystal edge by mounting the cathode in a reentrant cavity. This design change, in combination with gating the simmer discharge, permits continuous operation of the Beamlet PEPC without significant thermal degradation of its switching performance.

Magnetic Bright Spots

During experiments with the prototype PEPC, we observed regions of nonuniform polarization rotation at various locations across the crystal. These regions show up as "bright spots" of light in the rejected polarization when imaging the PEPC in our polarimeter. In the PEPC, as originally constructed, we observed these bright spots along the bottom edge of the crystal, particularly in the lower corner near the anode. The bright spots were quite variable from shot to shot, indicating that they were due to a plasma-related effect and not a static optical effect.

We found that these bright spots are caused by the magnetic field surrounding wires carrying the discharge current external to the plasma. The discharge pulse is transmitted to the PEPC from the pulse generator via a pair of coaxial cables. The shields of these cables terminate at the anodes and the center conductors must connect to the cathodes. A magnetic field surrounds the unshielded sections of wire that traverse the PEPC. Figure 13 shows this magnetic field in a cross-sectional side view of the PEPC. The flux density from the current pulse is ≈60 G along the crystal edge near the wires. We verified that this was the cause of the bright spots by moving these wires from the bottom of the cell to the top. When we did this, the bright spots moved from the bottom anode corner to the top anode corner. We found that we could minimize bright spot formation by feeding the discharge current from opposite sides of the PEPC.

Our first explanation of the bright spots was as follows: Electrons carrying the switch-pulse current that charges and discharges the crystal must cross the magnetic field from the discharge wires, which is roughly perpendicular to the crystal surface; since plasma conductivity is lower across a magnetic field, charging and discharging is impeded. If this were a complete explanation, however, we would expect to see a bright spot across the full bottom edge of the image and not just in one corner. This simplistic model also does not explain why feeding current from opposite sides minimizes the bright spots. A better explanation for bright-spot formation will be a focus of future work.

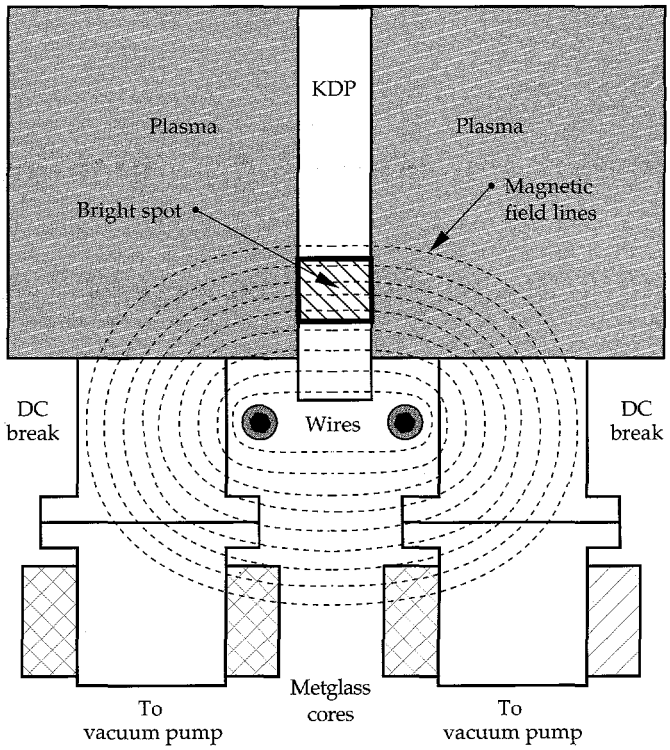

FIGURE 13. Cutaway end-view of the PEPC showing how the magnetic field from wires carrying the discharge current interferes with electron transport, and can therefore cause nonuniform switching. (70-50-0494-1852pb02)

TABLE 2. Heating (increases in °C) due to plasma discharge at five locations inside the prototype PEPC, measured with thermistors.

	Cathode racetrack	Cathode center	Crystal (cathode edge)	Crystal (anode edge)	Anode
Continuous wave simmer	9.0	7.5	4.0	0.3	0.3
Gated simmer	0.7	0.5	0.4	0.25	0.25

Control of Switch-Pulse Leakage Current

The two sides of the PEPC are evacuated by a common vacuum system, most of which consists of metallic pipe sections held at ground potential. During the high-voltage switch pulse, leakage current can flow from the plasmas into the vacuum pipes. This effect is observable as droop in the switch pulse. We implemented two modifications to the original prototype design to control this leakage current (see Fig. 13): DC breaks and Metglass inductive isolators. The DC breaks are simply sections of vacuum line made of insulating material. The Metglass inductive isolators are toroids of tape-wound magnetic material that increase the inductance of the vacuum line for short pulses. During initial prototype experiments, we observed no switch-pulse droop, so we assumed that the leakage current was effectively controlled. However, when we moved the discharge wires to the top of the cell, we observed a significant droop in the switch pulse. When the wires were on the bottom, the magnetic field surrounding them magnetized the DC breaks. The field in the breaks impeded electron flow, so we observed no leakage current. With the wires moved to the top of the cell, there was no field in the breaks. The leakage current was partially limited by the Metglass cores, but the droop was not acceptable.

One way to reduce the droop would have been to increase the inductance by increasing the cross-sectional area of Metglass. We used a more effective and less expensive solution: We mounted a pair of baffles inside the vacuum port and in the region of the DC break. This increases the effective path length through the DC breaks. The baffles also block the line of sight for electron flow and increase the wall area on which plasma can be neutralized. The resulting increase in isolation is enough to eliminate the switch-pulse leakage current.

The baffles also reduce the vacuum conductance through the DC breaks, which increases the base pressure but reduces the required flow of working gas to maintain the operating pressure. The increase in base pressure with one pair of baffles did not reduce switching performance, but the increase with two pairs of baffles on each side was high enough to reduce performance noticeably.

Estimation of Plasma Density

Plasma density and temperature produced during PEPC operation are required to compute the plasma resistance. Our estimation of these parameters is based on the observation that the switch-pulse voltage required to induce 90° of polarization rotation is consistently higher than the known half-wave voltages for KDP and KD*P. We also observe that if we increase the discharge current, lower applied switch-pulse voltage is required, and vice versa. This indicates that the voltage appearing across the crystal depends on plasma density. Since the current in the switch-pulse circuit drops to zero after initial charging, there can be no resistive voltage drops. Voltage not appearing across the crystal must be appearing across other capacitive elements that form a capacitive voltage divider. In this case, the extra capacitance comes from the plasma sheaths that form at the interface between the plasma and the crystal. The voltage divider expression is

$$V_\pi = V_{sw}\frac{C_{sheath}}{C_{KDP}+C_{sheath}} , \quad (4)$$

where V_π = 16.4 kV and is the clamped half-wave voltage for KDP,[6] V_{sw} = 18.1 kV and is the switch-pulse voltage required for 90° rotation, C_{KDP} = 1.81 nF and is the capacitance of the $32 \times 32 \times 1$ cm^3 KDP crystal, and C_{sheath} is the sheath capacitance. Solving for C_{sheath} and inserting numerical values, we find C_{sheath} = 17.5 nF. If we assume that similar sheaths form on each side of the crystal, then the capacitance for each sheath is 35 nF.

To relate the sheath capacitance to the plasma density and temperature, we start with an expression for the potential, $\phi(x)$, in an infinite, planar sheath:

$$\phi(x) = \phi_0 e^{-x/\lambda_D} , \quad (5)$$

where λ_D is the Debye length given by

$$\lambda_D = 740\sqrt{\frac{T_{eV}}{n_e}} . \quad (6)$$

The electric field in the sheath is then given by

$$E = \frac{d\phi}{dx} = -\frac{\phi_0}{\lambda_D}e^{-x/\lambda_D} . \quad (7)$$

The energy W stored in the electric field is then

$$W = \frac{\varepsilon_0}{2}\int E^2 dv = \frac{A\varepsilon_0}{2}\frac{\phi_0^2}{\lambda_D^2}\int_0^\infty e^{-2x/\lambda_D}dx = \frac{A\varepsilon_0\phi_0^2}{4\lambda_D} , \quad (8)$$

where A is the area of the crystal and the sheaths and ε_0 is the dielectric constant of vacuum. The stored electrostatic energy can also be expressed in terms of capacitance C_{sheath} by

$$W = \frac{1}{2}C_{sheath}\phi_0^2 . \quad (9)$$

Equating the expressions for W and solving for C, we obtain

$$C_{\text{sheath}} = \frac{A\varepsilon_0}{2\lambda_D} , \tag{10}$$

which is the expression for the capacitance of a parallel-plate capacitor of area A and separation $2\lambda_D$. Note that we use the dielectric constant for vacuum in the above expressions. Although a region filled with plasma has a modified dielectric constant, most of the sheath electric field is in the region closest to the crystal, where the electron density is very low, so the use of ε_0 is a good approximation. We substitute Eq. (6) for the Debye length in Eq. (10) and solve for the electron density, obtaining

$$n_e = 3.3 \times 10^{11} T_e . \tag{11}$$

For the expected range of electron temperature (1 to 10 eV), the plasma density is then in the range 3.3×10^{11} to 3.3×10^{12}.

Conclusion

In the technology of PEPCs, plasma discharges facilitate uniform application of voltage to large-aperture, thin, electro-optic KDP crystals. PEPC technology makes possible the construction of large-aperture optical switches for use in high-energy ICF laser drivers. After building and testing a 32×32 cm^2 prototype PEPC with KDP and KD*P crystals, we built a 37×37 cm^2 PEPC with a KDP crystal for use in the Beamlet laser. The Beamlet PEPC routinely switches a 5- to 6-kJ, 3-ns optical pulse out of the amplifier cavity after four gain passes. The Beamlet PEPC has demonstrated switching efficiency >99.5% and has operated reliably during Beamlet experiments.

We also discuss PEPC technology issues, including cathode sputtering, cathode heating, and magnetic bright spots. We control deposition of sputtered cathode material by using graphite cathodes and adding oxygen to the plasma; the oxygen reacts with sputtered carbon to form gaseous species. We control cathode heating by reducing the average discharge power with a gated simmer discharge and by moving the cathode further from the crystal. Magnetic fields from the discharge current can cause spatial nonuniformities in the switching profile. We control this effect by feeding the side 1 and side 2 discharge currents from opposite sides to reduce stray magnetic fields. Finally, we show that we can estimate the plasma density from the extra capacitance caused by sheath formation between the plasma and the crystal.

Notes and References

1. J. R. Murray, J. H. Campbell, D. N. Frank, J. T. Hunt, and J. B. Trenholme, *ICF Quarterly Report*, **1** (3), 89–107, Lawrence Livermore National Laboratory, Livermore, CA, UCRL-LR-105821-91-3 (1991).
2. L. L. Steinmetz, T. W. Pouliot, and B. C. Johnson, *Appl. Opt.* **12**, 1469–1471 (1973).
3. M. D. Skeldon, M. S. Jin, D. J. Smith, and S. T. Bui, *Solid State Lasers II*, **SPIE 1410**, 116–124 (1991).
4. J. Goldhar and M. A. Henesian, *IEEE J. Quantum Electron.* **QE-22**, 1137–1147 (1986).
5. D. Eimerl, *Ferroelectrics* **77**, 95–159 (1987).
6. M. A. Rhodes, J. J. DeYoreo, B. W. Woods, and L. J. Atherton, *ICF Quarterly Report* **2** (1), 23–36, Lawrence Livermore National Laboratory, Livermore, CA, UCRL-LR-105821-92-1 (1992).
7. Microsim Corporation, Irvine, CA.
8. D. E. Golden and H. W. Bandel, *Phys. Rev.* **J1 V138**, 14 (1965).
9. F. F. Chen, *Introduction to Plasma Physics*, Plenum Press, New York, p. 162.
10. C. A. Ebbers, J. Happe, N. Nilson, and S. P. Velsko, *Appl. Opt.* **31**, 1960–1964 (1992).
11. J. J. DeYoreo and B. W. Woods, *J. Appl. Phys.* **73**, 7780 (1993).
12. I. M. Thomas, *Optics News*, 18–22, (August 1986).
13. R. K. Waits, *J. Vac. Sci. Technol.* **15**, 179, (1978).
14. M. A. Rhodes and J. Taylor, *Twentieth Power Modulator Symposium*, **IEEE CH3180-7**, 380 (1992).
15. B. M. VanWonterghem, J. R. Murray, D. R. Speck, and J. H. Campbell, *Proc. Eleventh Topical Meeting on the Technology of Fusion Energy*, New Orleans, LA, 1994.
16. D. Rosen and G. K. Wehner, *J. Appl. Phys.* **33**, 1842–1845 (1962).

BEAMLET PULSE-GENERATION AND WAVEFRONT-CONTROL SYSTEM

B. M. Van Wonterghem

J. T. Salmon

R. W. Wilcox

Introduction

The Beamlet pulse-generation system (or "front end") refers to the laser hardware that generates the spatially and temporally shaped pulse that is injected into the main laser cavity. All large ICF lasers have pulse-generation systems that typically consist of a narrow-band oscillator, electro-optic modulators for temporal and bandwidth shaping, and one or more preamplifiers. Temporal shaping is used to provide the desired laser output pulse shape and also to compensate for gain saturation effects in the large-aperture amplifiers. Bandwidth is applied to fulfill specific target irradiation requirements and to avoid stimulated Brillouin scattering (SBS) in large-aperture laser components. Usually the sharp edge of the beam's spatial intensity profile is apodized before injection in the main amplifier beam line. This prevents large-amplitude ripples on the intensity profile.

Beamlet's pulse-generation system provides the same functions as stated, but uses entirely new technology. For example, compact diode-pumped oscillators and integrated optical-waveguide modulators, in combination with a high-gain multipass preamplifier, replace typical room-sized systems, such as used on Nova[1,2] and other ICF lasers. In addition, the Beamlet front end provides a new feature of extensive precompensation for gain nonuniformity in the cavity and booster amplifiers. It also corrects for static and dynamic (pump-induced) phase aberrations in the entire laser chain.

The newly developed Beamlet front end significantly increases the quality of the output beam of a large-amplifier chain and is essential to the National Ignition Facility's (NIF's) conceptual design. (See "System Description and Initial Performance Results for Beamlet," p. 1.) Compensation for optical phase aberrations increases the frequency conversion efficiency and the brightness, and hence the 3ω peak power at the focus of the target chamber. Correction for spatial amplifier gain variations improves the output beam intensity uniformity and thereby increases the aperture fill-factor and the total output energy per beam line. The compact integrated optics approach to temporal shaping allows precise control over individual pulse shapes, which improves control of power balance and irradiation uniformity in a multiple-beam target irradiation scheme such as NIF.

Beamlet's pulse-generation system has proven to be very flexible and reliable in operation with minimal operator intervention; Table 1 summarizes the current performance limits and nominal operating points for this system.

Many aspects of the Beamlet front end are described in other publications.[1,2] In this article, we briefly review the front-end design and discuss improvements to the oscillator and modulator systems. Our main focus, however, is to describe Beamlet's novel beam-shaping and wavefront-control systems that have recently been fully activated and tested.

TABLE 1. Beamlet's front-end performance limits and nominal operating points.

	Maximum	Typical
Energy (3 ns pulse duration)	12 J	1 J
Pulse duration	0.2–10* ns	3 ns
Temporal shaping contrast	100:1	5:1
Bandwidth	100 GHz	32 GHz
Center-to-edge intensity profile ratio	0.2	0.3
Wavefront shaping	±4λ	>3λ peak to valley

*Limited by length of regenerative amplifier cavity.

UCRL-LR-105821-95-1

Beamlet Front-End Description

Figure 1 shows the detailed layout of the Beamlet front-end oscillator and preamplifier. A single-mode oscillator generates high-rep-rate pulses, which are coupled into a single-mode polarization preserving fiber. The fiber couples the light into an integrated high-speed amplitude and phase modulator. Control signals are generated by low-voltage electronic pulse generators. The resulting shaped pulse is transported to the preamplifier section in the laser high-bay using a 60-m-long fiber. A ring regenerative amplifier provides a gain of 10^9 to elevate the energy to the millijoule level. At this point, the Gaussian spatial intensity is flattened and shaped into a one-dimensional (1-D) parabolic intensity profile. A square serrated aperture creates the desired spatial edge shape for injection in the main amplifier. A second four-pass rod amplifier boosts the energy to the joule-level and two 10-cm-aperture Faraday rotators provide isolation against

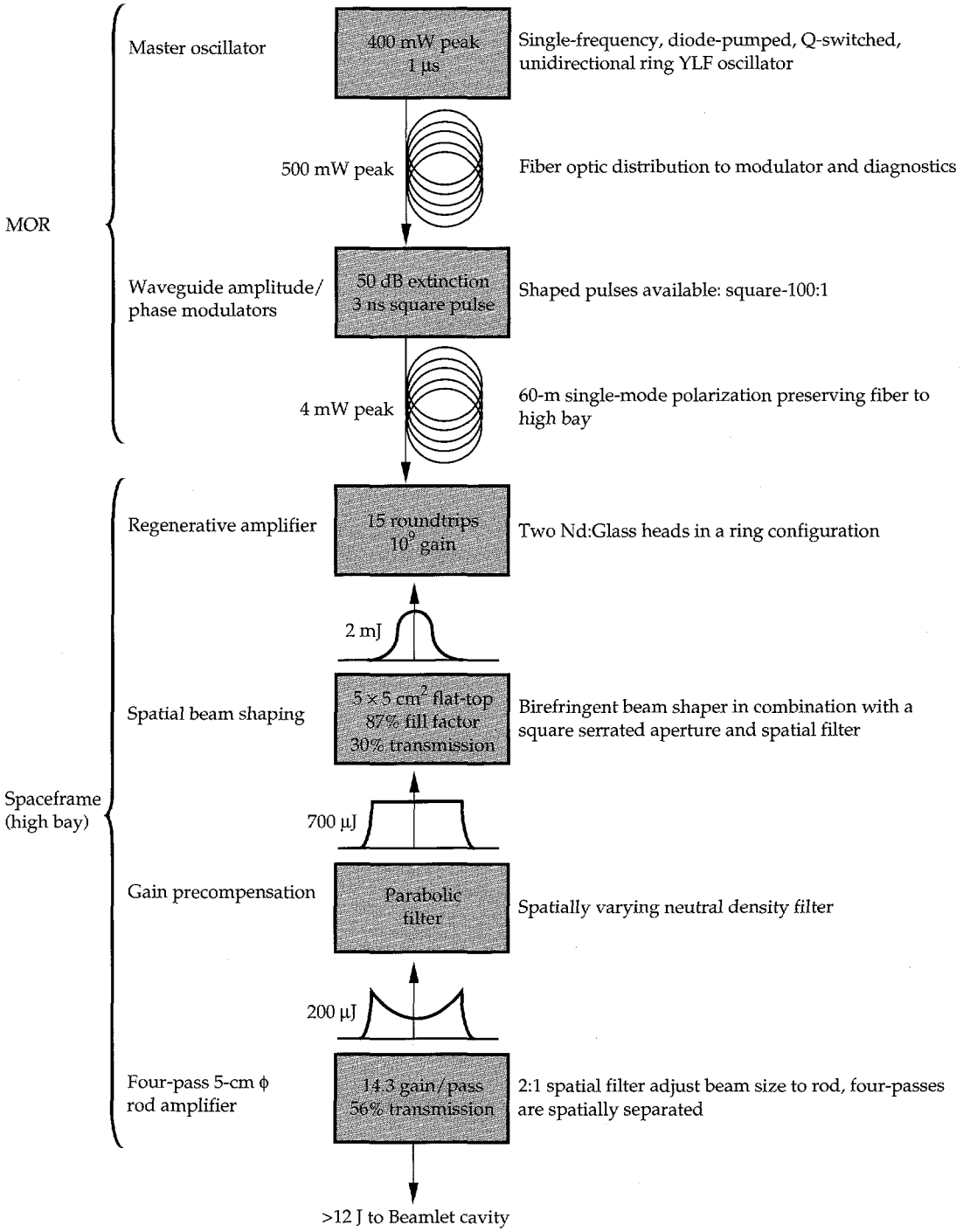

FIGURE 1. Schematic overview of Beamlet's front-end subsystems and how they interface. MOR means that this equipment is housed in the master oscillator room whereas all other front-end components are mounted on a spaceframe in the main laser bay.
(70-50-0194-0033pb01)

back reflections from the main laser amplifier cavity. Then, the beam is incident on a 39-actuator deformable mirror (DFM) and relayed to the injection optics of the Beamlet cavity spatial filter.

Master Oscillator, Temporal Shaping, and Phase Modulation System Upgrades

Several upgrades and improvements have been implemented to the Beamlet master oscillator and modulator system since its initial description by Wilcox et al.[2] The original Nd:YLF microchip oscillator-amplifier system has been replaced by a very stable, compact, and powerful single-mode unidirectional ring oscillator.[3] A diode-pumped Nd:YLF crystal is used as a gain medium, while an acousto-optic Q-switch creates high-peak-power pulses and also serves as a direction-selective element for the three-mirror ring cavity [Fig. 2(a)]. The ring oscillator's higher peak power allows for optimization of the diagnostics and fail-safe systems. Figure 2(b) illustrates the complete oscillator, including the diagnostics and fiber couplers. Specifically, pulse shape and Fizeau bandwidth spectra can be monitored on a continuous basis. Additional fail-safe switches monitor the occurrence of beat modes and the magnitude of the bandwidth modulation created in the waveguide modulators.

The original $LiNbO_3$ amplitude modulator circuit continues to provide Beamlet with pulse widths ranging from 200 ps to 10 ns, and shapes as simple as Gaussian or as complex as the ignition pulse shapes required for NIF. (See "System Description and Initial Performance Results for Beamlet," p. 1.) The performance of the amplitude modulators has been significantly improved by a modification of the modulator bias control system. In the original system,[2] a DC bias voltage was used to optimize extinction of the amplitude modulators, but charge migration effects in the $LiNbO_3$ substrate resulted in a continuous drift of the desired bias point. The present system of short-pulse bias voltages results

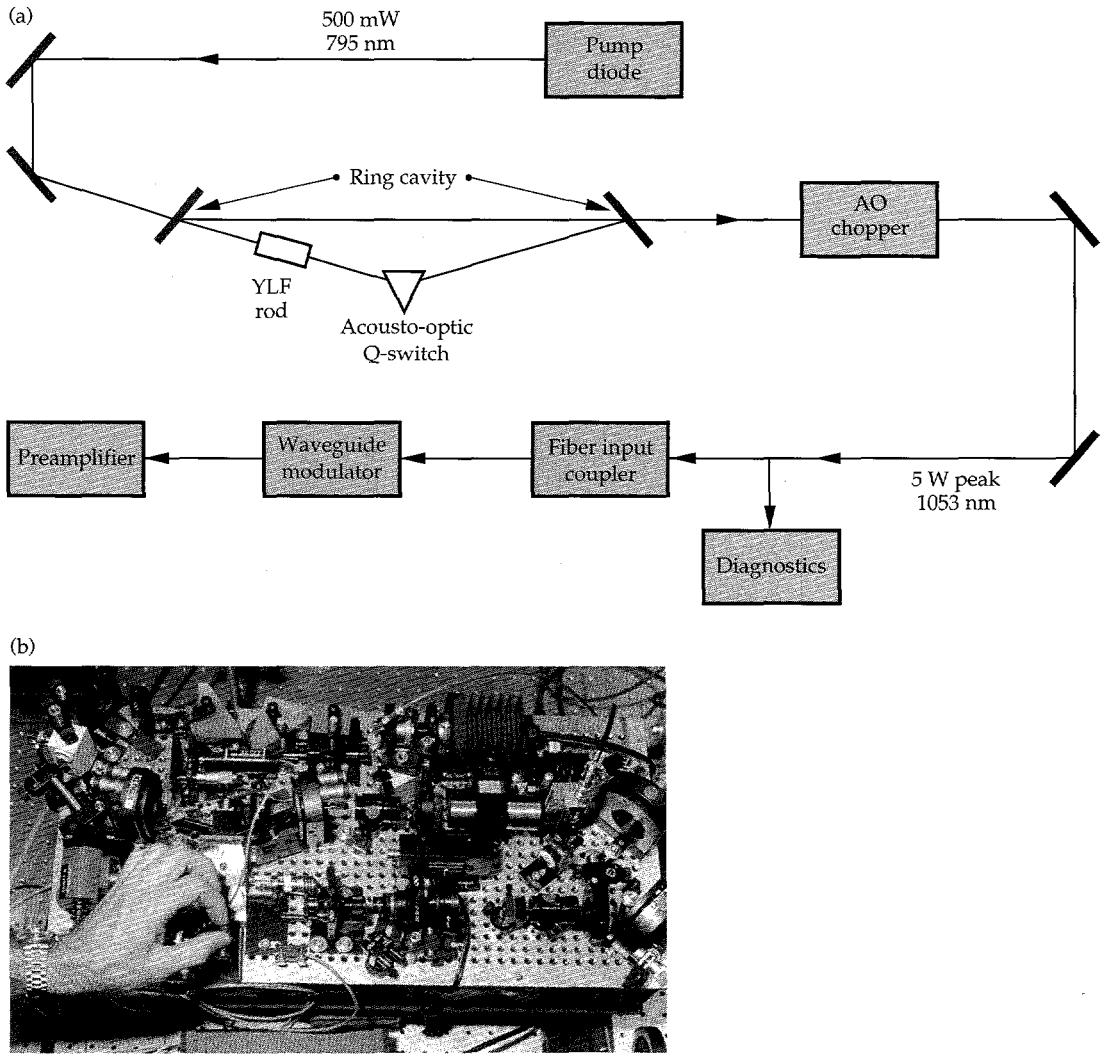

FIGURE 2. (a) Layout and (b) photograph of the new Beamlet unidirectional, single-frequency ring oscillator. The physical dimensions of the complete unit, including the pump-diode laser and diagnostics, are 30 cm × 60 cm; the size is six times smaller than the original oscillator, with a tenfold increase in peak output power. (70-50-0494-1946pb01)

in optimum performance for extended periods of time without adjustments. The $LiNbO_3$ phase modulators easily provide Beamlet bandwidth requirements of 30 GHz at 1ω by using a single radio-frequency (RF) generator (with 3–6 GHz variable frequency output) and a power amplifier. Complex high-density sideband spectra have been demonstrated by driving the phase modulator with the sum of two different RF signals.

Stability requirements for the pulse-generation system are very demanding and several major stability problems have been recently solved. Using an all-fiber-optic polarization compensating device,[4] we reduced long-term fluctuations in the power delivered from the modulators to the regenerative amplifier in the preamplifier section by optimizing the polarization coupling in the long transport fiber. Another major source for shot-to-shot fluctuations is the gain instability of the flash-lamp-pumped amplifier heads in the ring regenerative amplifier. The instability of the output energy E_{out} is given by

$$\frac{\delta E_{out}}{E_{out}} \approx \frac{\delta E_{pump}}{E_{pump}} (\ln G) \quad , \tag{1}$$

where G is the total small signal gain (~10^9) and E_{pump} is the energy delivered by the flash lamps. It is clear from Eq. (1) that an unreasonably high pump stability of ±0.2% is required to maintain the output energy stable to within the required ±5%. To solve this stability problem, we implemented a new and elegant feed-forward stabilization scheme.[5] This scheme uses the existing pulse-slicer Pockels cell as a variable transmission element, controlled by a photoconductive Si switch. Light leaking through one of the regenerative amplifier cavity mirrors is used to control the conductance of the switch (Fig. 3). This scheme increased the shot-to-shot stability of the pulse-generation system to well within the operational requirements for Beamlet.

Spatial Intensity Profile Shaping

Beamlet's front-end spatial intensity shaping optics create the 2-dimensional (2-D) beam profile required for injection in the main cavity amplifier. First, the basic scheme uses a set of birefringent filters to flatten the Gaussian regenerative amplifier beam profile (Fig. 4). Next, the beam passes through a square serrated aperture with rounded corners; this generates a well-defined square edge profile of the beam.[6] The serrated edges of the aperture need to smoothly reduce the beam intensity from its peak to near zero to avoid diffraction ripples on the transmitted beam. However, the width of the serrated edge needs to be sufficiently narrow to guarantee a high fill factor of the beam. Fill factor is defined as the ratio of the power in the actual beam to the power of an equivalent beam that completely fills (100%) the same area. (Note that to completely fill the area the intensity profile at the edge of the beam is discontinuous, i.e., infinitely steep.) Beamlet uses an inverted Gaussian serrated edge profile with a width equal to 10% of the beam size. A new type of serrated aperture, produced by a photolithographic process, resulted in a significant improvement of quality and uniformity of the beam edge profile as shown in Fig. 5. Using this procedure, the shape of the serrations can be controlled to within a precision of 2 μm. The resulting fill factor of the Beamlet output beam exceeds 84% when integrated between the 1% intensity points at the edge of the beam profile.

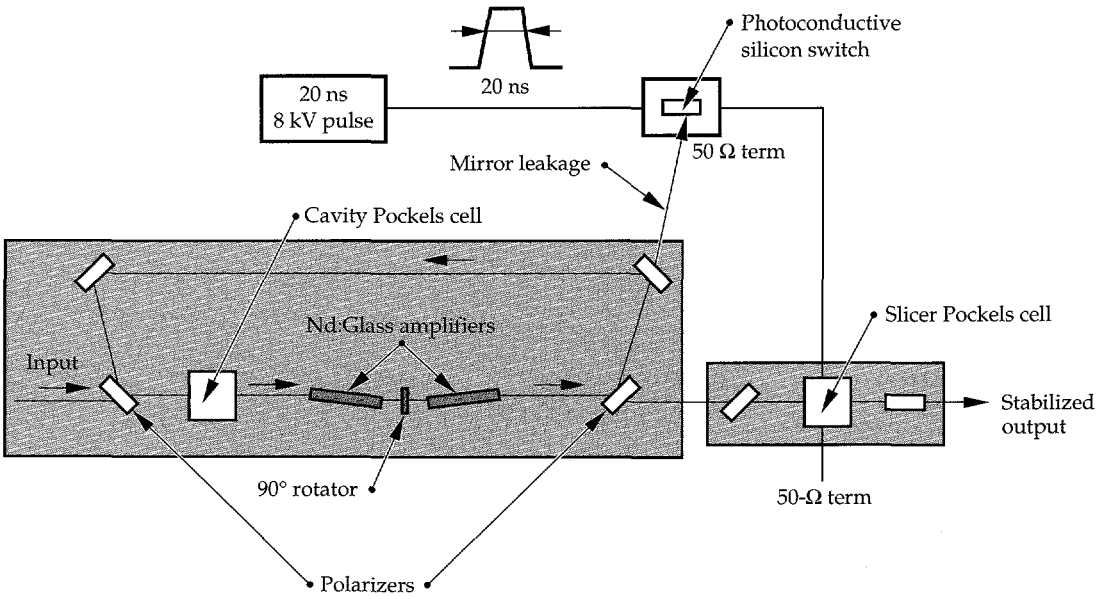

FIGURE 3. The existing pulse slicer behind the regenerative amplifier was modified to a feed-forward energy stabilization system. Light leaking through one of the regenerative amplifier cavity mirrors illuminates a Si photoconductive switch in the Pockels cell driver line, providing negative feed-forward control of the pulse slicer Pockels cell's energy transmission. (70-50-0295-0400pb01)

A major improvement in Beamlet performance is achieved by shaping the spatial intensity profile of the pulse generated by the front end to compensate for spatial gain variations in the main Beamlet multisegment amplifiers. Spatial variations in the gain of the amplifiers result from amplified spontaneous emission within the laser slabs. Briefly, amplified spontaneous emission trapped within the laser slab by total internal reflection depletes the stored energy in the glass, particularly near the edges of the slabs. This depletion in stored energy produces a corresponding roll-off in the gain, largely in the horizontal direction. (See "Design and Performance of the Beamlet Amplifiers," p. 18.) The resulting small signal gain for the combined 44 slabs that the beam traverses during a Beamlet shot resembles a parabola with center-to-edge gain ratio in the horizontal direction exceeding 3.5. Therefore, if a beam with a flat-top intensity profile is injected into the main laser cavity, then the output beam profile will roll off at the edges in the same way as the overall gain profile. This greatly reduces the fill factor. For a system designed to run at beam fluences near the damage threshold of its optical components, a reduction of fill factor reduces the maximum output energy available. Gain saturation at very high output fluences (>>10 J/cm^2) tends to reduce this effect. However, the system fluence limit can be located at nonsaturated points in the amplifier, such as the Beamlet cavity polarizer (its limiting fluence is 11 J/cm^2). Precompensating the lower gain near the edges by increasing the intensity of the injected profile counteracts this effect, as shown in Table 2, where we compare the total modeled output energy at fixed peak fluence with, and without, precompensation for the gain nonuniformity.

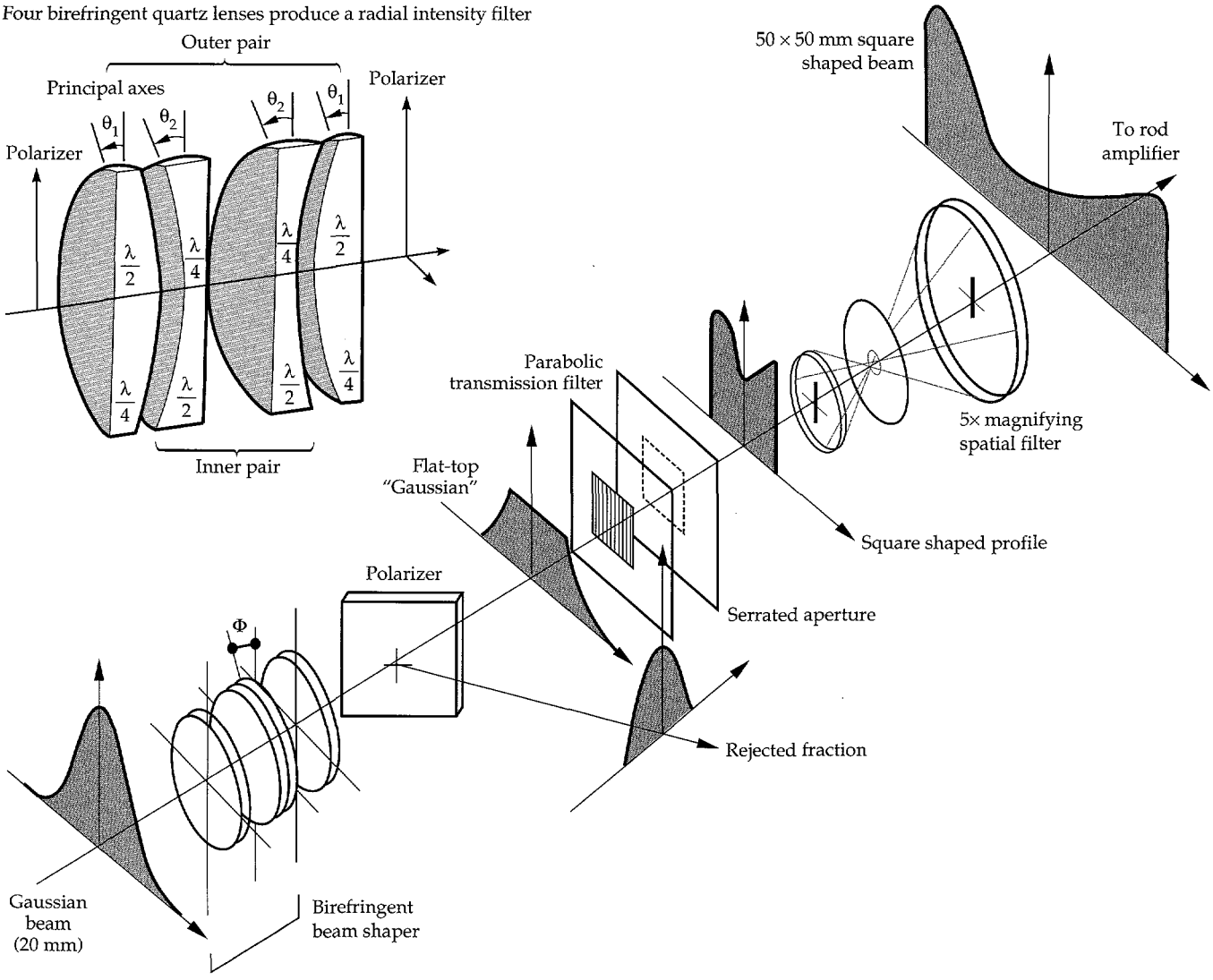

FIGURE 4. The spatial profile of the Beamlet injection pulse is generated in a three-step process in the beam-shaping section: (1) The beam is converted from Gaussian to a flat-topped round beam; (2) the beam is converted to a square footprint using a serrated aperture; and (3) a parabolic profile is created using a special transmission filter. The beam shaping section is located between the regenerative amplifier and the four-pass rod amplifier. (02-07-0892-2883pb01)

(a) Details at the beam's edge

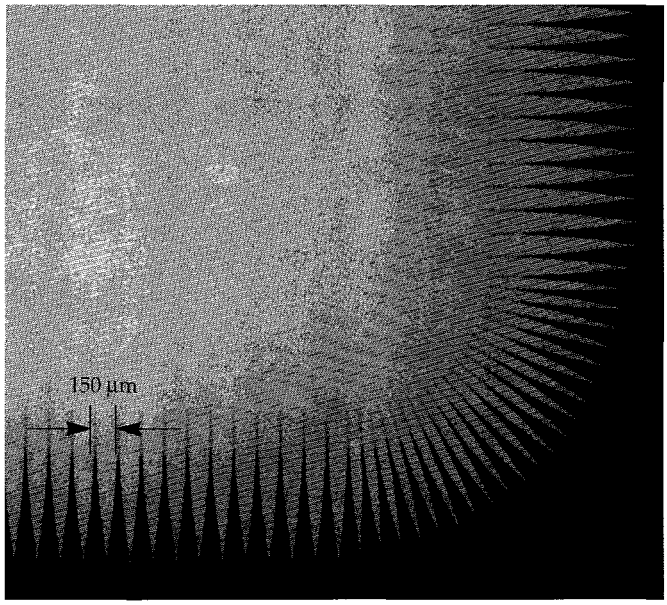

(b) Full-aperture display

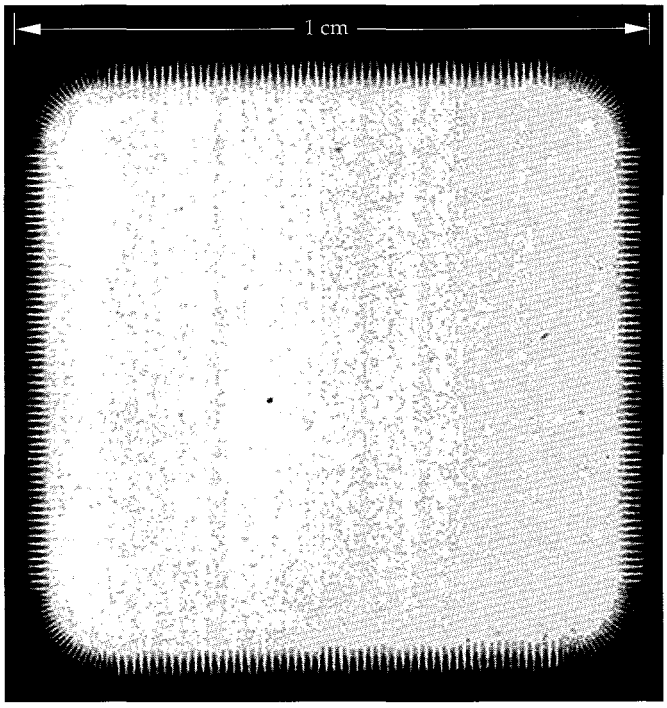

FIGURE 5. A smooth yet rapid roll-off in the intensity profile at the edge of the beam is created using precisely shaped serrations in a photolithographically created pattern. The low-pass spatially filtered image of this aperture is relayed through the main amplifier onto the frequency-conversion crystals. (70-10-1193-3899pb01)

Various methods exist to shape a beam's intensity profile, ranging from simple spatially varying neutral density filters to afocal refractive optical systems and complex high-resolution programmable spatial light modulators. We use the first method on Beamlet. Figure 6(a) compares an actual profile with the specified transmission profile for a shaped neutral density filter.

(a) Transmission scan

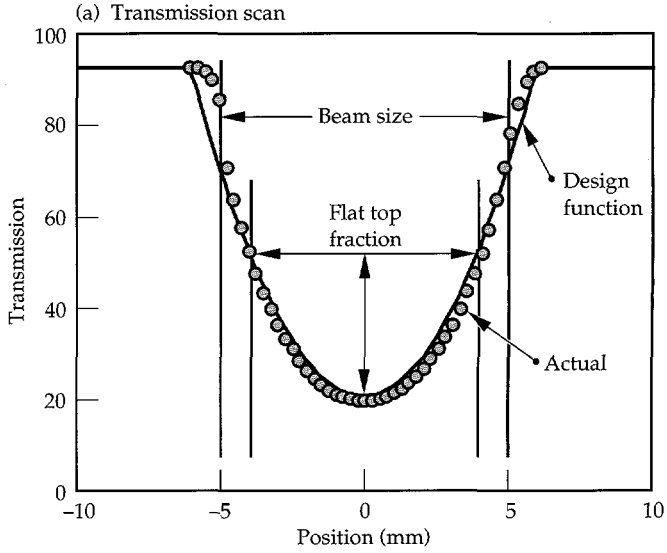

(b) Resulting beam profile

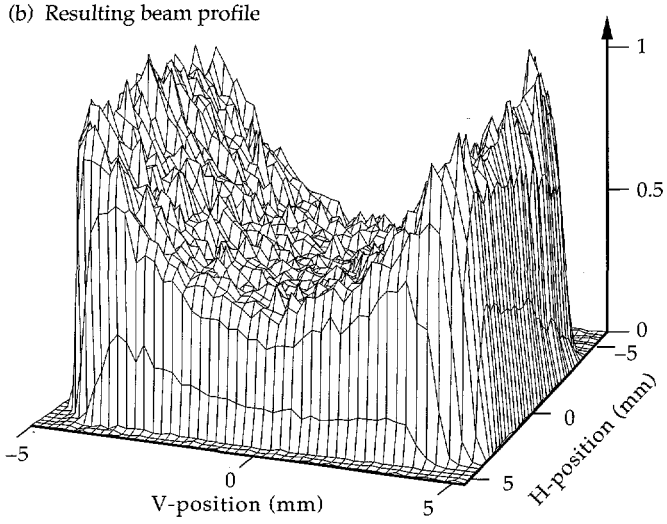

FIGURE 6. (a) Experimental transmission scan of a parabolic 1-D transmission filter compared with the specified transmission curve. The relevant beam size dimensions are overlaid. (b) A 2-D plot of the resulting beam profile measured at the 1ω output diagnostics station for an unpumped amplifier cavity. (70-50-0295-0401pb01)

TABLE 2. Shaping the intensity profile of the injected beam improves the output energy.[a]

Output fluence (Beamlet 11-5)	Output energy flat profile	Output energy shaped profile	Improvement with shaped profile
8 J/cm^2	6.8 kJ	8.2 kJ	21%
10 J/cm^2	8.7 kJ	10.2 kJ	17%
12 J/cm^2	10.8 kJ	12.3 kJ	13.6%

[a]Beamlet baseline, 11-5 configuration, 0.20 explosion fraction, f_x, 34 cm × 34 cm^2 beam.

The filters are created using variable-speed computer-controlled e-beam deposition of Cr on a BK-7 glass substrate. The filter's parabolic transmission profile is slightly wider than the actual beam size, allowing the profile of the transmitted beam to be adjusted to match the slightly skewed Beamlet amplifier gain profile. Figure 6(b) shows the near-field intensity profile of the beam transmitted through this filter and then propagated through the entire *unpumped* amplifier chain and measured at the 1ω output diagnostic station. Figure 7 shows the output near-field profile using the same parabolic transmission filter *pumping* the amplifiers; note the desired flat-top output profile that is achieved. These results are discussed further in the "System Description and Initial Performance Results for Beamlet," p. 1.

Compensation for gain nonuniformity in the amplifiers has a second advantage—it decreases any spatially dependent pulse-shape distortion produced by the main amplifiers. The temporal pulse shape distortion, caused by gain saturation at high fluences during the last pass through the cavity and the booster amplifier, is homogenous because of the fluence uniformity. If the beam is not corrected for spatial gain variations, then it will have lower fluences near the beam edges, and hence will undergo different temporal pulse distortions near the edges than near the center of the beam. The result is that the output temporal profile will be different at the edges of the beam than at the center. Therefore, by correcting for spatial gain variations in the main amplifiers we also produce a uniform-pulse temporal profile across the full aperture.

Wavefront Shaping Using the Adaptive Optics System

The wavefront of a laser beam governs how well the beam propagates. Since rays of light always travel perpendicular to the local wavefront, the wavefront determines whether the laser beam is diverging, converging, collimated, or is generally deforming in shape and size and breaking up. In Beamlet, the wavefront determines the size of the beam's focus and how the energy is distributed at the focus. In addition, the wavefront determines how much of the light is within the acceptance angle for conversion to shorter wavelengths, which impacts the conversion efficiency of the light from the fundamental wavelength at 1054 nm to the third-harmonic wavelength at 351 nm. The Beamlet Type I/Type II frequency converter requires 95% of the 1ω energy be within a divergence angle of ±50 μrad. The beam divergence requirement needed to meet the NIF focusability requirement is much more stringent: 95% of the 3ω energy needs to be within a ±35-μrad divergence angle. Beam divergence is caused by the static aberration of the individual optics surfaces, pump-induced spatially varying beam steering in the amplifiers during a shot, thermal aberrations in hot amplifier slabs, and turbulence in the heated amplifier cavity. Table 3 provides an overview of the various aberrations, the associated time scale on which they occur, and the spatial scale length. The correctability constraints are imposed by the choice of actuator density and control system speed. Both factors can be increased significantly beyond the performance of the system used on Beamlet.

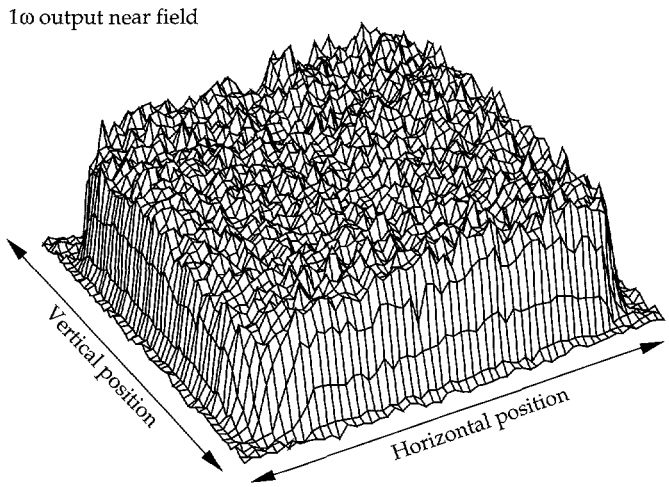

FIGURE 7. Example of the approximately flat-topped near-field intensity profile achieved at the output of the Beamlet amplifier chain using the parabolic gain compensation filter described in the text and shown in Fig. 6(b). (70-50-0295-0594pb01)

TABLE 3. Factors affecting Beamlet's wavefront quality, and the ability to correct for these factors using the 39-element DFM.

Factor	Magnitude of aberration (waves)	Temporal dependence	Aberration spatial scale[a]	Correctability[b]
Optics figure errors	2.5	Static	d/4	Excellent
Pump induced	2.5–3	50 μs	d/4	Good
Thermal effects in slabs	2.5–6	4 hr	d/3	Excellent
Turbulence in amps[c]	0.5–1	Seconds	d/10	Marginal
Small scale errors	0.01–0.2	Static	<d/10	Not possible[d]

[a]d represents the beam size.
[b]Using the present Beamlet DFM hardware.
[c]Turbulence due to thermally driven convection currents.
[d]Limited by the choice of actuator density.

The Beamlet adaptive optics system is designed to correct the wavefront of the laser beam to be nearly "flat," i.e., to as near a plane wave as possible. As mentioned earlier, this maximizes the conversion efficiency of the fundamental IR beam to the UV and minimizes the size of the focus spot, thus maximizing the power density at the target. The adaptive optics system, shown schematically in Fig. 8, consists of a DFM, a wavefront sensor, and a controller. The design is based on an adaptive optics system developed by Salmon et al.[7] for laser isotope separation. The DFM is located in front of the injection spatial filter for the main multipass amplifier. The light is sampled by the wavefront sensor after the DFM, and the controller analyzes the wavefront from the wavefront sensor and drives the DFM until the sensor reads the desired wavefront, which is flat for Beamlet. The DFM is comprised of a single thin-glass substrate with 39 magnetostrictive actuators bonded to its back side. The mirror substrate is 70×70 mm^2 wide and 4 mm thick. Its front surface is coated with a low-stress HfO_2/SiO_2 high-damage-threshold and high-reflectivity multilayer coating (Fig. 9). The arrangement of actuators divides the mirror surface into grids of subapertures, each subaperture being the smallest area

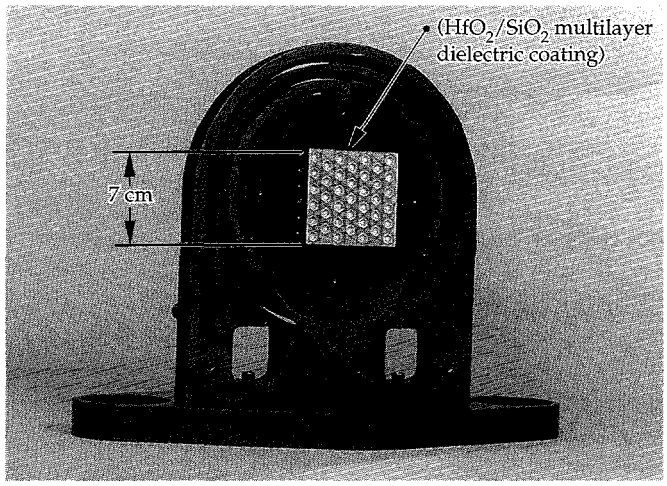

FIGURE 9. The Beamlet DFM has 39 actuators mounted to the back of a $70 \times 70 \times 4$ mm^3 coated substrate. The range of motion of individual actuators is approximately 10 μm. (70-50-0494-2093pb01)

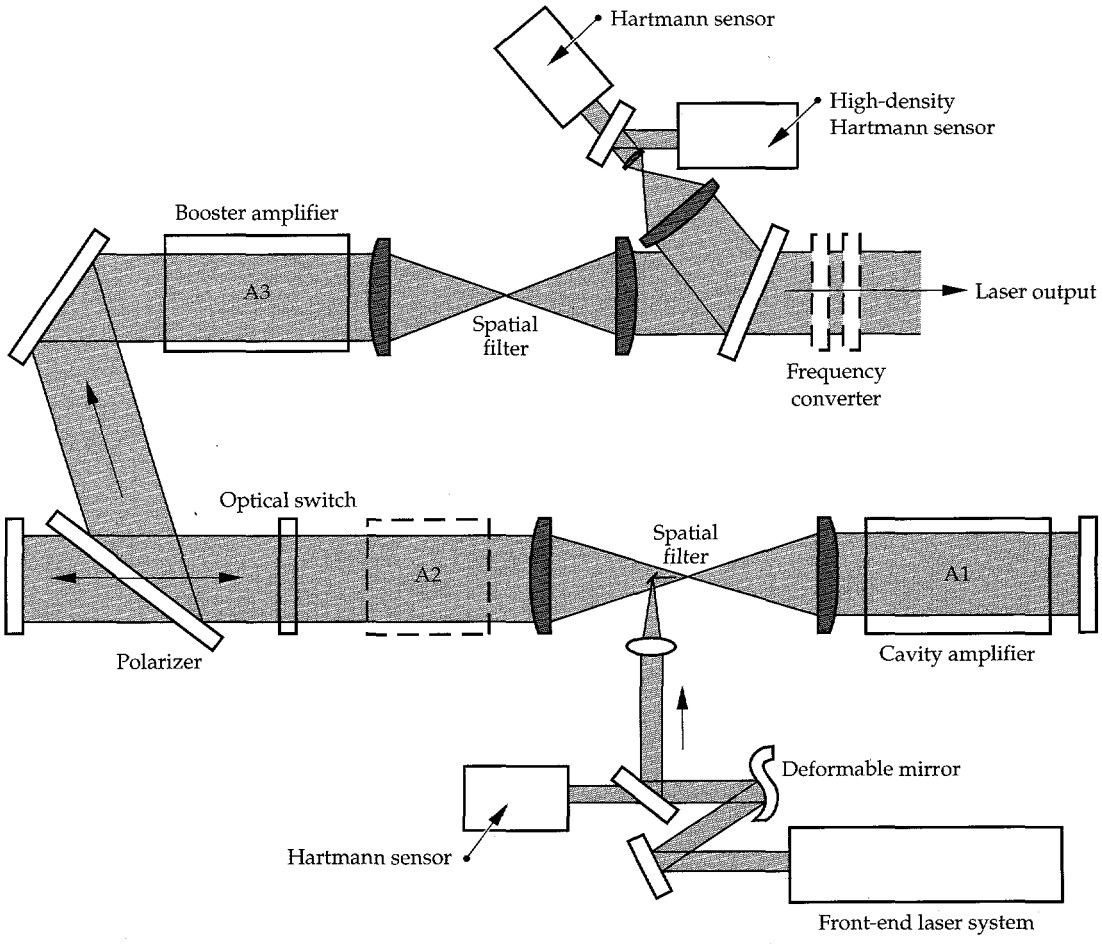

FIGURE 8. Beamlet adaptive optics system layout: a DFM located in the injection beam path is operated by a control system. This system operates in closed loop to a Hartmann wavefront sensor in the injection path (flat injection wavefront), or in the 1ω-output diagnostics of the Beamlet amplifier (flat output wavefront). An additional higher spatial resolution Hartmann sensor is located in the output diagnostics. (70-50-0295-0402pb01)

that is enclosed by a group of adjacent actuators. Each actuator expands when a voltage is applied and produces a local bulge in the front surface opposite the actuator, while the neighboring actuators hold the mirror surface in place. This movement causes the mirror surface to tilt across the subapertures, adjacent to the moving actuator. The wavefront change, induced by the movement of a single actuator, is called the influence function. The influence function is usually Gaussian shaped, with its $1/e$ point located at the neighboring actuator.

The wavefront sensor is a Hartmann sensor, which has a series of lenses that collectively "view" the entire surface of the DFM. Figure 10 shows the relationship between the DFM actuator positions and the Hartmann sensor lenslets. Each lenslet spans a subaperture of the DFM and is configured as a local pointing sensor for that subaperture, i.e., the detector for each lenslet is in the focal plane of that lenslet. As the tilt in the wavefront of light entering the Hartmann lenslet changes, the focus spot on the detector moves laterally from its nominal position on the detector. Moving any actuator will cause the Hartmann spots to move from their nominal positions. Knowing how the spots move when each actuator is moved, the controller can drive the DFM until the displacement of the Hartmann spots is minimized, thus minimizing the wavefront error sensed by the Hartmann sensor.

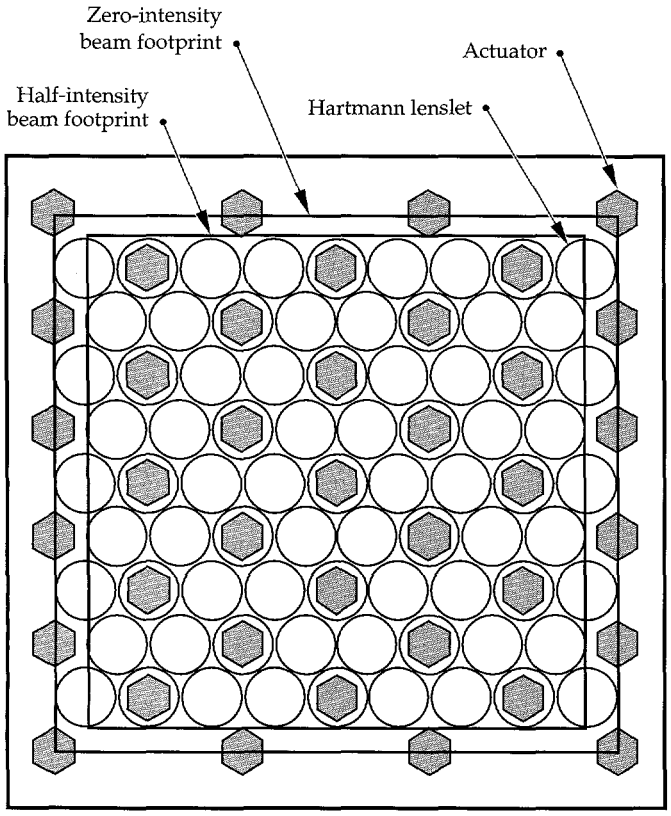

FIGURE 10. Layout of the 39 actuators and the 77 Hartmann sensor lenslets mapped onto the DFM surface. (70-50-0295-0403pb01)

The system uses two Hartmann sensors—one to sample the light immediately after the DFM (input Hartmann sensor) and the other on the 1ω diagnostics table (output Hartmann sensor). Afocal telescopes relay the image of the DFM to each Hartmann sensor, and each Hartmann sensor is calibrated by a wavefront reference source. The wavefront calibration effectively removes any aberration introduced by either the afocal relay telescope or the beam sampler. The wavefront controller is designed to control the wavefront using either of the two Hartmann sensors. The bandwidth for the closed-loop system is about 1/2 Hz for continuous wave (cw) light and about 1/50 Hz for regenerative amplifier pulses. A third Hartmann sensor is installed in the output diagnostic station. It is used for wavefront characterization measurements and provides a higher resolution than the control system sensors. It has a larger density of lenslets over the beam aperture (17×29).

As presently configured, the adaptive optics system can correct the wavefront using either cw light from the alignment laser or a 0.2-Hz pulsed beam from the regenerative amplifier. Precorrection of the injected wavefront to compensate for pump-induced aberration in the amplifier proceeds as follows: (1) The wavefront is flattened before a shot by running the control system closed loop to the output Hartmann sensor using the alignment laser. (2) The Hartmann sensor images are grabbed during the laser shot, and the resulting aberrated wavefront is reconstructed offline. (3) Before the next shot, this wavefront is entered in the control system that subsequently sets the mirror in closed loop such that the output wavefront is the conjugate of the shot wavefront error. The wavefront aberration of the shot should be corrected for pump-induced aberrations. Figure 11 shows recent wavefront data to illustrate this process. Two situations are depicted: the wavefront of a shot with static precorrection only, and a shot where full precorrection is applied. The wavefront shape is typical of the pump-induced wavefront aberration by the Beamlet amplifier slabs added to a focus error in the front-end rod amplifier. Its shape and magnitude agree closely with model predictions and offline beam-steering characterization data. (See "Design and Performance of the Beamlet Amplifiers," p. 18.) The second wavefront is the result of a shot where full precorrection for the errors shown in Fig. 11(a) is applied. The rms value of the resulting aberration is <0.2 waves, leading to a Strehl ratio (ratio of actual peak intensity of the focal spot to the diffraction limited peak intensity) of 0.3. The correction capabilities are presently limited by turbulence-induced wavefront variations between the time of prefiguring the DFM and the actual shot. This effect is small in a cold cavity, but becomes substantial after firing subsequent shots at the nominal 2-hr Beamlet shot rate.

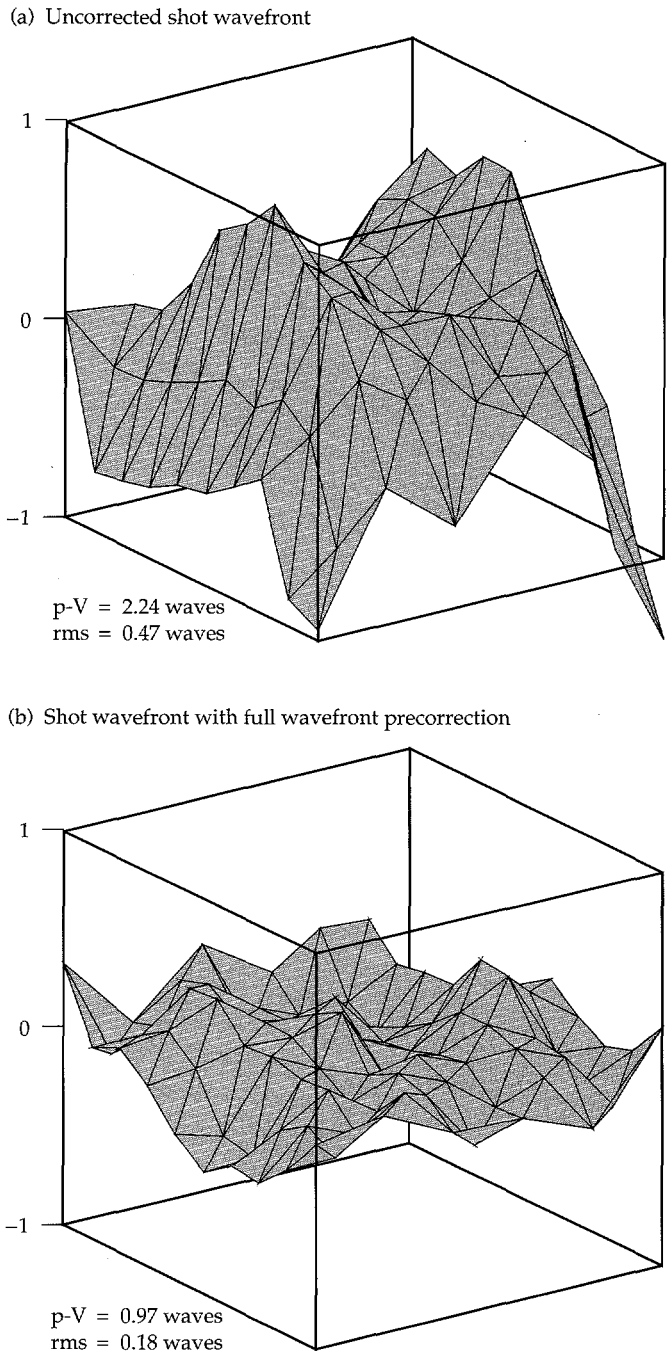

FIGURE 11. Experimental output high-resolution Hartmann sensor wavefronts obtained during 4.5-kJ 3-ns Beamlet shots (34 cm × 34 cm^2 beam). (a) The typical pump-induced wavefront aberration in the Beamlet amplifiers. (b) The output wavefront of a shot with full precorrection of the injected wavefront for static and dynamic aberrations in the Beamlet amplifier. The resulting 0.18 waves rms aberration correspond to a calculated Strehl ratio of 0.3. (70-50-0295-0404pb01)

Summary

We added the capability to control the spatial intensity profile and wavefront of the pulse produced by the Beamlet pulse-generation system (i.e., front end). We also demonstrated how these capabilities can be used to control and increase the beam quality and performance of Beamlet's large-aperture multipass Nd:Glass amplifier—a technology critical to the design of the proposed NIF laser system.

In addition, we have also modified and improved the front-end oscillator and modulator systems to increase the stability and reliability of their performance.

Notes and References

1. B. M. Van Wonterghem, D. R. Speck, M. J. Norman, et al., *ICF Quarterly Report* **3**(1), 1–9, Lawrence Livermore National Laboratory, Livermore, CA, UCRL-LR-105821-93-1 (1993).
2. R. W. Wilcox and D. F. Browning, *ICF Quarterly Report* **2**(3), 115–122, Lawrence Livermore National Laboratory, Livermore, CA, UCRL-LR-105821-92-3 (1992).
3. L. J. Bromley and D. C. Hanna, *Opt. Lett.* **16**(6), 378 (1991).
4. H. C. Lefevre, *Electronics Letters* **16**(20), 778 (1980).
5. R. W. Wilcox, US Patent No. 5,157,676.
6. J. M. Auerbach and V. P. Karpenko, *Appl. Opt.*, 3179–3183 (1993).
7. J. T. Salmon, E. S. Bliss, T. W. Long, et al., *Active and Adaptive Optical Systems* (SPIE—International Society for Optical Engineering, Bellingham, WA, 1991; *Proc. SPIE* **1452**) pp. 459–467.

LARGE-APERTURE, HIGH-DAMAGE-THRESHOLD OPTICS FOR BEAMLET

J. H. Campbell *R. T. Maney*

L. J. Atherton *R. C. Montesanti*

J. J. DeYoreo *L. M. Sheehan*

M. R. Kozlowski *C. E. Barker*

Introduction

Beamlet serves as a test bed for the proposed National Ignition Facility (NIF) laser design and components. Therefore, its optics are similar in size and quality to those proposed for the NIF. In general, the optics in the main laser cavity and transport section of Beamlet are larger and have higher damage thresholds than the optics manufactured for any of our previous laser systems. In addition, the quality of the Beamlet optical materials is higher, leading to better wavefront quality, higher optical transmission, and lower-intensity modulation of the output laser beam than, for example, that typically achieved on Nova. In this article, we discuss the properties and characteristics of the large-aperture optics used on Beamlet.

The damage threshold is perhaps the most critical property of the optical materials, because the cost of the laser system is driven largely by the amount of laser energy that can be delivered in a given aperture size. The higher the transmitted energy density (fluence), the fewer the number of laser beams needed to meet the output energy requirement and, therefore, the lower the overall system cost. Consequently, Beamlet (and NIF) are designed to operate near the damage threshold limit for the optical materials.

Table 1 summarizes the damage threshold requirements at 1.0 and 0.35 μm for the large optics on Beamlet for a nominal operating pulse length of 3 ns and lists the measured damage thresholds for comparison. Note that the measured thresholds represent the absolute maximum operating laser fluence possible for that specific optic. To provide a safety margin for our designed operating limit, we multiply the measured thresholds by a "de-rating" factor that accounts for measurement uncertainties. The product of the measured damage threshold times the de-rating factor is called the "safe operating limit" and represents the fluence limit for that specific optic. Beamlet is designed to never exceed the safe operating limits.

Figure 1 compares the peak designed laser fluence at key optical materials on Beamlet with the safe operating threshold. These peak fluences are reached during the final pass through the laser and are based on model calculations. Note that the peak fluence

TABLE 1. Beamlet's damage threshold requirements and measured values at 3 ns for various optical materials.

	Optics	Measured damage threshold (J/cm^2)	Safe operating limit (J/cm^2)	Beamlet peak fluence (J/cm^2)
1ω	Laser glass	34	28	20
	HfO_2/SiO_2 HR	26	18	8
	HfO_2/SiO_2 polarizer	18	13	8
	SiO_2 sol-gel AR	34	29	21
	KDP doubler	43	30	20
	KDP (Pockels cell)	43	30	8
3ω	KD*P tripler	20	14	11
	SiO_2 sol-gel AR	19	16	11

HR=high reflectivity; AR=antireflection

UCRL-LR-105821-95-1

determines the damage limit of the laser, whereas the average fluence determines the energy output. Therefore on the Beamlet, we have worked hard to keep the peak-to-mean intensity variation within the laser pulse as low as possible to maximize the energy out and to minimize the risk of optical damage. Because laser optical materials do not all have the same damage thresholds, one or two materials generally limit the performance of the system. In the case of Beamlet, the optical material at most risk is the HfO_2/SiO_2 multilayer thin film polarizer (at 1ω) and the deuterated potassium dihydrogen phosphate (KD*P) tripling crystal (at 3ω).

Optical Materials

The optical materials on Beamlet can be divided into four main types: laser glass, potassium dihydrogen phosphate (KDP)/KD*P, dielectric coatings, and lenses and diagnostic beam splitters. This section briefly describes each of these materials and their key properties.

Laser Glass

The energy storage medium for the Beamlet flashlamp-pumped amplifiers is a commercial phosphate laser glass (composition LG-750) manufactured by Schott Glass Technologies Inc. It has an Nd^{3+} doping concentration of $3.4 \times 10^{20}/cm^3$ and consists of a metaphosphate glass composition. Although the details of the composition are proprietary, it contains the major oxides P_2O_5, Al_2O_3, K_2O, BaO, Nd_2O_3, and a number of other miscellaneous components.

For Beamlet (and NIF) the laser glass is in the form of large rectangular plates $78.8 \times 44.8 \times 4$ cm^3 (Fig. 2). The volume of these glass plates or "slabs" is about 14 L. For comparison, the largest pieces of Nova laser glass are elliptically shaped disks and have a volume of about 7 L. Thus, the size and shape of Beamlet's slabs required a significant advancement in the prior laser glass manufacturing process. A total of 20 slabs were manufactured for the Beamlet laser—16 are installed on the system, and 4 are reserved as spares.

The size of the Beamlet laser slabs is driven by four main factors: (1) The maximum beam size, which is 35 cm for Beamlet. In addition, the laser slab is mounted in the amplifier cavity at Brewster's angle, requiring that the slab be lengthened to account for both the angle and the refractive "walk-off" of the beam as it travels through the glass. (2) The vignetting effect, allowing for the beam to propagate back and forth four times through the main laser cavity slightly off-axis to pass through the four different pinholes. (See "System Description and Initial Performance Results for Beamlet," p. 1.) The contribution of the vignette to the slab size is dependent on the length of the cavity amplifier section, the focal length of the spatial filter lens, and the pinhole spacing. (3) The alignment allowance which, within the main laser cavity, is set at 2% of the maximum beam size. (4) The stand-off distance from the edge cladding, required to avoid wavefront distortion of the beam caused by amplified spontaneous emission (ASE) heating the cladding. When the cladding is heated, it expands and distorts the region near the edge of the slab. Based on experiments,[1] the stand-off distance from the edge cladding bond line needs to be at least $t/2$, where t is the slab thickness. Since Beamlet slabs are 4 cm thick, the minimum stand-off distance is 2 cm around the border of the entire slab.

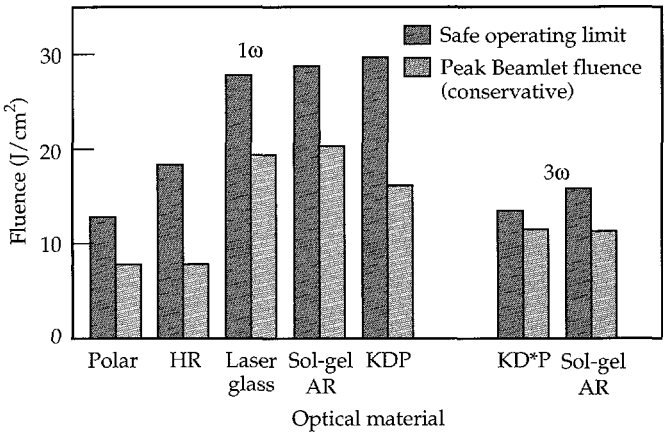

FIGURE 1. Comparison of the peak laser fluence during the final pass through the laser system with the "safe operating limits" of the material. The data are for a nominal square output pulse of 3 ns. (70-50-0693-2242pb01)

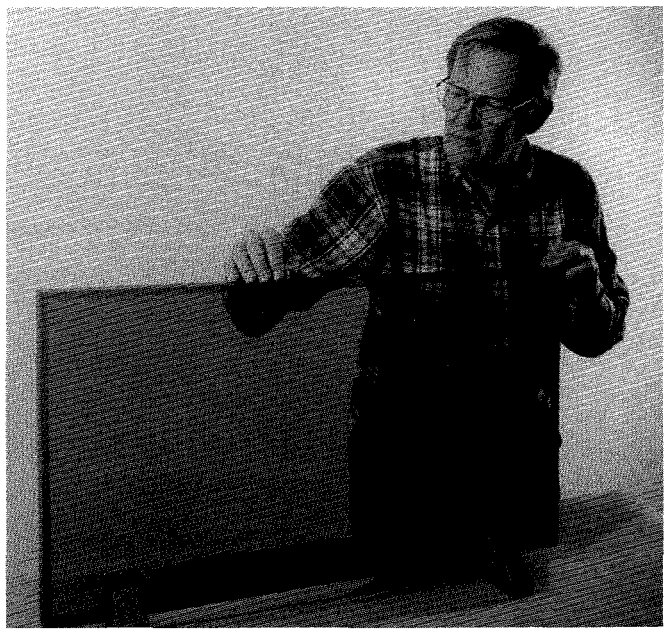

FIGURE 2. Beamlet's $78.8 \times 44.8 \times 4$ cm^3 laser slab containing 3.4×10^{20} Nd^{3+}/cm^3; the edges of the laser slab are clad with a Cu:Doped phosphate glass designed to absorb ASE at 1054 nm. (70-50-0393-0716pb01)

The laser slabs are clad with Cu:Doped phosphate glass having an absorption coefficient at 1.05 μm of 0.28/mm. The base composition of the cladding glass is the same as LG-750 (without the Nd^{3+}) and is bonded to the laser slabs using an epoxy adhesive specially formulated to match the index of the laser glass. Details for the cladding process are described elsewhere.[2] The laser slabs were clad and finished by Zygo Corporation and Eastman Kodak Company.

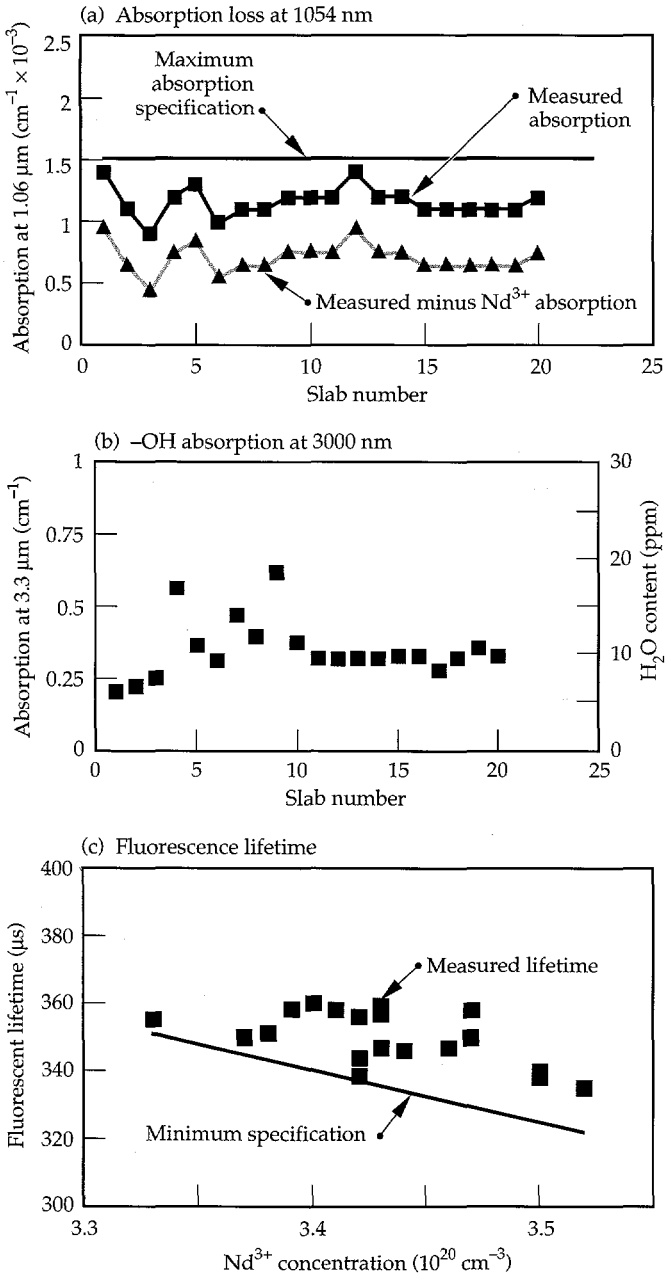

FIGURE 3. Summary of three key properties of the laser slabs produced for Beamlet compared with the design specifications: (a) absorption loss at 1054 nm, (b) –OH absorption at 3000 nm, and (c) fluorescence lifetime. The lifetime measurements were performed on samples 5 × 5 × 0.5 cm^3. (70-50-0295-0397pb01)

Laser glasses are specially formulated to give the desired laser, optical, thermal-mechanical, and physical-chemical properties needed for a specific application. Most of these properties are controlled by the base composition of the glass. However, some critical properties are also impacted by the manufacturing process. These include the optical absorption at 1054 nm, optical homogeneity, Nd^{3+} fluorescence lifetime, and the Pt inclusion content. Because of Beamlet's larger slabs, we were concerned whether these critical properties could be maintained throughout the process. Figure 3(a) shows the variation in optical absorption at 1054 nm for all the slabs produced. Optical absorption arises from either impurities in the raw materials and/or contaminants that enter during the processing (e.g., contaminants added by dissolution of the melter refractory walls).[3] The absorption offsets the laser gain of the material, thereby requiring either more amplifiers or harder pumping. The data in Fig. 3(a) show that the Beamlet slabs have very low absorption loss and meet the necessary absorption specification. In fact, about 30% of the absorption loss (i.e., 4.5×10^{-4} cm^{-1}) is due to absorption by the thermal population of Nd^{3+} in the lower laser level ($^4I_{11/2}$).

The Nd^{3+} fluorescence lifetime is mainly a function of the glass composition. To efficiently store energy in the amplifiers requires long fluorescence lifetimes. Two features of the manufacturing process can affect the lifetime—Nd^{3+} doping concentration and H_2O absorbed in the glass. The Nd^{3+} content affects the lifetime at high concentrations through the well-known concentration quenching mechanism.[4] Therefore, to avoid melt-to-melt variability in fluorescence lifetime, careful control of glass volatility during the melt cycle and precise addition of Nd^{3+} are necessary. Absorbed H_2O of only a few ppm can also affect the lifetime; therefore, very dry conditions must be maintained during melting. The hydroscopic nature of molten-phosphate laser glass makes it particularly vulnerable to H_2O uptake. The H_2O content of the laser glass is quantified by measuring the –OH absorption at 3300 nm; Fig. 3(b) shows the results from the Beamlet melt. Although there is some variability, all slabs are quite dry having H_2O absorptions between ≈ 0.2–0.6 cm^{-1} at 3.3 μm. This absorption corresponds to about 6–18 ppm of H_2O. Because of the good control of the Nd^{3+} doping concentration ($3.4 \pm 0.1 \times 10^{20}$/cm^3) and the H_2O content, all laser glass slabs exceed the Nd^{3+} fluorescence lifetime specification shown in Fig. 3(c). The Nd^{3+} lifetime specification for Beamlet laser glass is

$$\tau_L \geq 340 - 150\left(\left[Nd^{3+}\right] - 3.4\right) \quad , \tag{1}$$

where $[Nd^{3+}]$ is the Nd-ion concentration in units of $10^{20}/cm^3$ and τ_L is the minimum acceptable lifetime (in microseconds). In arriving at this specification, we also included the effects of radiation trapping by the $5.0 \times 5.0 \times 0.5$ cm^3 standard sample size used by vendors for routine fluorescence lifetime measurements. The specification also includes the effects of concentration quenching at high Nd-dopings, derived from work by Jancaitis.[5]

The Beamlet melts have very low residual H_2O content so there is little effect of –OH quenching on the lifetime. At low levels of H_2O contamination, the effect of –OH in reducing the lifetime can be estimated from the expression[6]

$$\Delta\tau = -7.62(\alpha_{3.3\mu m}), \quad (2)$$

where $\alpha_{3.3_{\mu m}}$ is the measured –OH absorption at 3.3 μm and $\Delta\tau$ is the lifetime reduction relative to a sample with zero residual H_2O. For Beamlet's laser glass, the residual H_2O contributed less than a 4-μs reduction in lifetime.

We maintained good optical homogeneity during the manufacturing process with all the laser slabs meeting the homogeneity specifications. Because of the rectangular shape of the glass, there was some concern whether the homogeneity could be maintained in the corners of the slabs. All finished Beamlet laser slabs had <0.1 wave (at 1.054 μm) transmitted wavefront distortion across the clear aperture.

The damage threshold of the laser glass is controlled by the quality of the surface and the presence of absorbing impurities. The typical high-quality "super" polish used to finish laser glass gives a damage threshold in excess of 30 J/cm^2 at 3 ns (1054 nm) and, therefore, exceeds the requirements for Beamlet (Table 1). More important is the presence of absorbing particles within the glass, particularly Pt inclusions. Pt inclusions originate from the Pt containers used to melt the laser glass and can cause optical damage at fluences of 2–3 J/cm^2 at 3 ns, far below the Beamlet operating fluence. In addition, damage from large inclusions can grow with successive shots, eventually rendering the slab useless. Using new glass-melting processes,[7,8] we were able to maintain inclusion levels well below our manufacturing goal of <15 in any given slab and an average for all 20 Beamlet slabs of <3 inclusions per slab. In fact, 50% of the laser slabs had no inclusions at all and 90% had 3 or less.

KDP/KD*P

Large plates of single-crystal KDP are used in the Beamlet Pockels cell and frequency converter. The Pockels cell and second-harmonic generation crystals are undeuterated, whereas the harmonic tripling crystal is deuterated to a level of about 80%. (KD*P is the commonly used representation of the deuterated material.) The KDP and KD*P crystals are arguably the most difficult optics to manufacture and require the greatest production time. In addition, they represent a marked increase in size and quality over the crystals that were manufactured for Nova. For example, the crystal plates used on Beamlet are 37×37 cm^2 compared with 27×27 cm^2 on Nova. In addition, the Beamlet damage threshold requirement exceeds that required for Nova by about a factor of three.

The use of deuterated material for the third-harmonic crystal is driven by the need to suppress stimulated Raman scattering (SRS) at 3ω. At high drive intensities (such as those used on Beamlet) the spontaneous Raman-scattered light is amplified as it traverses the crystal face. The SRS gain coefficient in KDP has been measured to be approximately 0.23 cm/GW[9,10] at 3ω for a Type II tripling crystal. The scattered Raman Stokes intensity I_s grows as it travels a distance l across the crystal, according to the relationship

$$I_s(l) = I_s(0) \exp\left(gI_p l\right) \quad (3)$$

where I_p is the pump intensity (GW/cm^2) and g is the gain coefficient. Because of the large aperture used on Beamlet, there is a significant gain-path length for the SRS light. Therefore, at high operating intensity (>3.0 GW/cm^2), the potential exists for the transversly propagating SRS light to reach intensities high enough to damage the KD*P.

The magnitude of the SRS gain coefficient for a particular Stokes Raman band is proportional to the scattering cross section. Therefore, because the spontaneous Raman band at 915 cm^{-1} is the most intense in KDP, it presents the greatest threat of unacceptable SRS. In KD*P, the mode at 915 cm^{-1} is split into two peaks and the magnitude of each band is dependent on the deuterium concentration (Fig. 4). At high deuteration levels, the Raman scattering cross sections for the two bands are about a factor of two lower than that for the single band of the undeuterated KDP. Therefore, deuterating the KDP greatly reduces the SRS threat to the tripling crystal.

The Beamlet crystal plates were cut from large single-crystal boules of KDP and KD*P, grown from aqueous solution by Cleveland Crystals, Inc. The KDP and KD*P boules produced for Beamlet weigh as much as 500 kg and take up to 2 years to grow (Fig. 5). This is about a factor of three increase in boule volume over those grown for Nova. The crystals required for the Pockels cell and harmonic converter system are

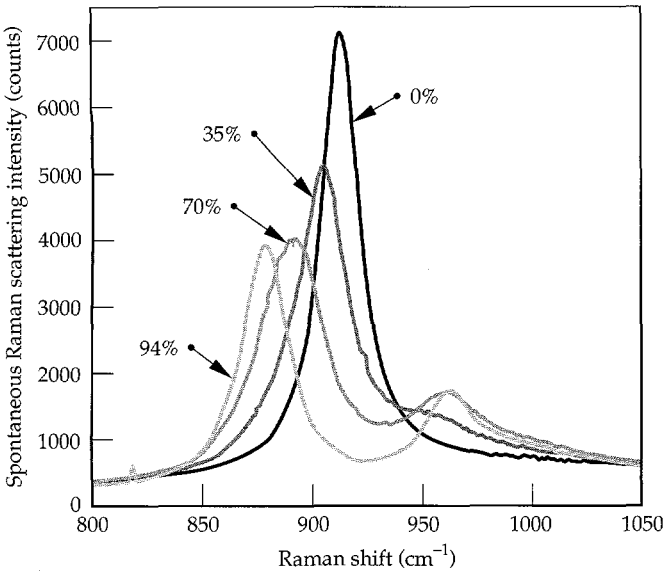

FIGURE 4. Measured spontaneous Raman scattering intensity profile for the 915 cm^{-1} mode at different deuteration levels. (70-35-0195-0316pb01)

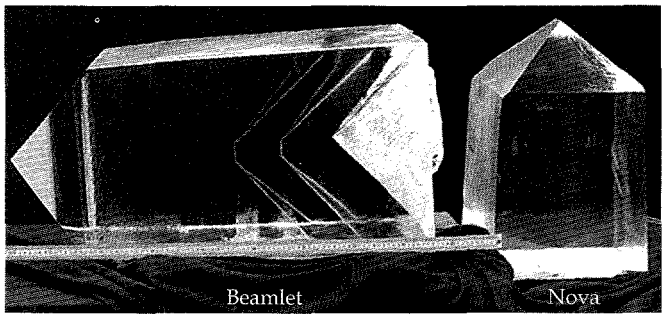

FIGURE 5. Photograph of a large KDP single crystal grown for Beamlet (note the meter stick shown for scale). The Beamlet crystals each weigh about 500 kg and are the largest ever produced. The smaller crystal on the right is the size grown for Nova. (70-39-1093-3487pb01)

then cut from these boules in an orientation shown schematically in Fig. 6. The Pockels cell uses a crystal cut normal to the z-axis of the boule, whereas the frequency-conversion crystals are cut at the phase matching angles required for the specific harmonic generation scheme. Beamlet uses a Type I/II third-harmonic generation method. (The harmonic generation system is described in detail elsewhere.[11])

We chose to grow 80% deuterated material (vs 95%) because the level of stress-induced birefringence was expected to be lower and the time to grow the boules was expected to be shorter. Deuterated water (D_2O), having a deuteration level of 99.7%, was obtained from the Department of Energy's national stockpile. In general, the growth rate for fully deuterated material is as much as 10 times slower than for undeuterated KDP.

Apart from size and deuteration level, the quality of the KDP and KD*P crystals is also of critical importance. Specifically, stresses within the crystal can lead to stress-induced index variations and birefringence that in turn can produce distortions in the optical wavefront and beam depolarization.[12–14] Wavefront distortion and depolarization degrade the performance of the laser. For example, in the case of the Pockels cell, any depolarization in the beam results in a direct transmission loss at the polarizer. Likewise, wavefront distortions can reduce the conversion efficiency of the harmonic generator, produce downstream modulation, and degrade focusability. Our operating goal for the Pockels cell was to produce <1% depolarization loss for any given pass and to keep the transmitted wavefront distortion and wavefront gradients for the finished crystal to $<\lambda/4$ and $\lambda/4$/cm, respectively.

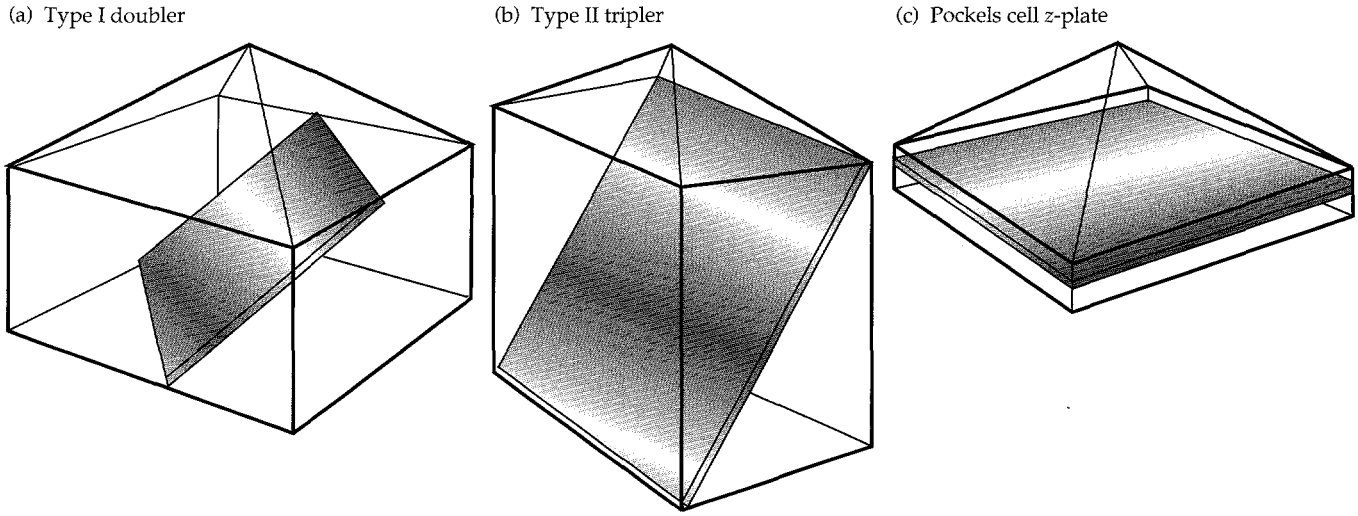

FIGURE 6. Schematic diagram showing the orientation in which the crystal plates used on Beamlet are cut from large KDP and KD*P single-crystal boules. (a) Type I doubler, (b) Type II tripler, and (c) Pockels cell z-plate. In general, several crystals of a given type can be cut from one boule. (70-35-0195-0317pb01)

The birefringence (δn) in a Pockels cell plate, cut normal to the z-axis of the crystal, is dominated by the shear strain and is given by[10]

$$\delta n = n^3 p_{66} \varepsilon_{xy} , \tag{4}$$

where n is the refractive index, ε_{xy} is the shear strain, and p_{66} is the elasto-optic tensor element appropriate for this geometry; p_{66} has the value of 0.028 for KDP and 0.025 for K*DP. The depolarization loss (L), due to this birefringence, is given by[12]

$$L = \sin^2\left[\left(\frac{\pi}{\lambda}\right)\delta n t\right], \tag{5}$$

where t is the crystal thickness and λ is the laser wavelength. Equation (5) is valid for the "on" and "off" states of the Pockels cell (i.e., when the voltage applied across the crystal is either $V\pi$ or 0, respectively). The shear strain can be directly related to the shear stress, τ_{xy}:

$$\tau_{xy} = C_{66} \varepsilon_{xy} , \tag{6}$$

where C_{66} is the elastic constant and has the value of 6.24 and 5.94 GPa for KDP and KD*P, respectively. To achieve a depolarization loss of 1% or less requires a shear stress $<10^6$ Pa.

Distortions in the beam phase front transmitted through the Pockels cell z-plate are controlled by the residual normal strains in the crystal:[12]

$$\Delta n = \left(\frac{n^3}{2}\right)\left[\frac{1}{2}(p_{11} + p_{12})(\varepsilon_x + \varepsilon_y) + p_{13}\varepsilon_z\right] , \tag{7}$$

where Δn is the index shift, the p_{ij}'s are elasto-optic coefficients, and ε_x, ε_y, and ε_z are the normal strains in the crystal. These strains can be related to residual normal stresses using the relationships developed by DeYoreo and Woods.[14] The index shift produces a spatial variation in the transmitted phase given by

$$\phi = \left(\frac{2\pi}{\lambda}\right)\Delta n t . \tag{8}$$

To meet the transmitted wavefront distortion specification of $<\lambda/4$ for the Pockels cell KDP crystal, requires a minimum residual normal stress field of $\approx 10^5$ Pa. Also, to meet the transmitted wavefront gradient specification for the crystal requires that the stress gradient be $<10^5$ Pa/cm.

The birefringence and wavefront distortions of the crystals used on Beamlet are characterized using the method described by DeYoreo and Woods.[13] Figure 7 presents the measured polarization efficiency (i.e., 100%—% depolarization loss) for a 32×32 cm^2

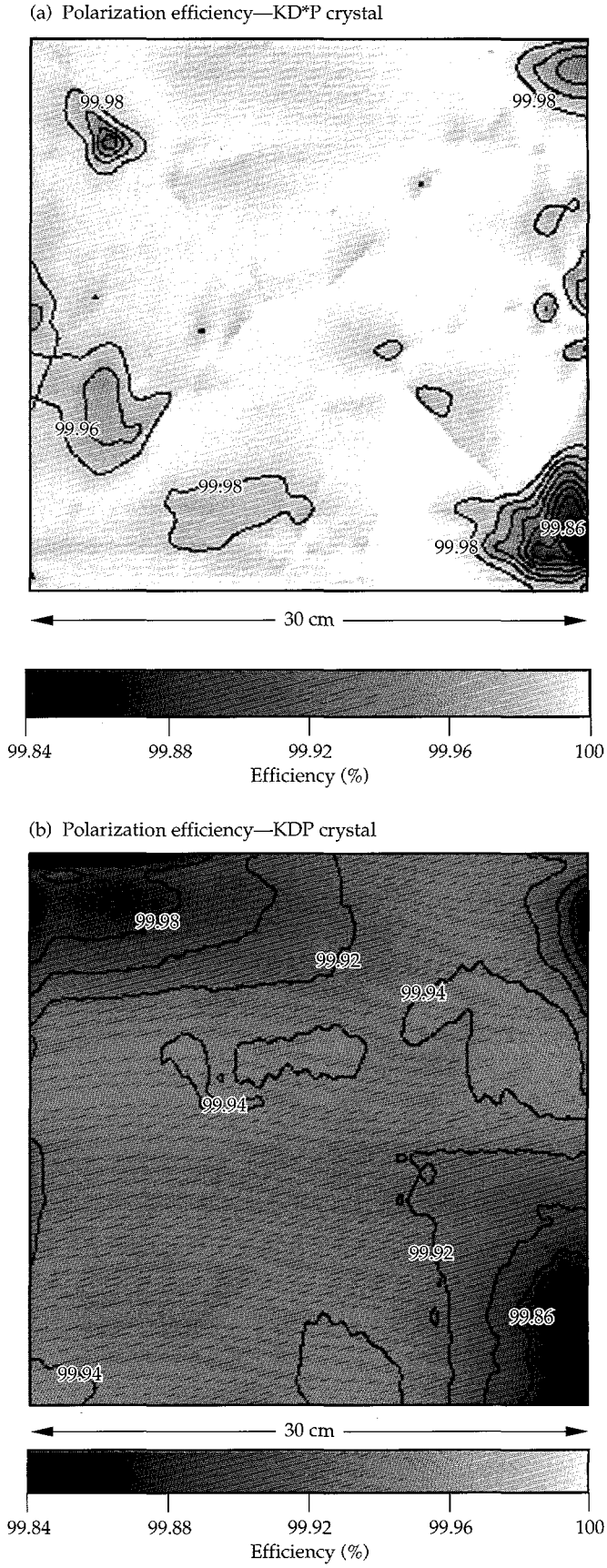

FIGURE 7. Polarization efficiency of z-cut (a) KD*P and (b) KDP plates expressed as the percent of the output energy in the correct polarization state, i.e., 100%—% depolarization loss. The crystal plate dimensions are $32 \times 32 \times 1$ cm^3. (70-50-1294-3982pb02)

KDP crystal. The data show a maximum loss of 0.4% through any point in the crystal with an aperture loss averaging 0.05%. The data show that the maximum residual shear stress in the crystal is $<1.5 \times 10^5$ Pa. Similarly, interferometry measurements show phase-front distortions from the bulk material of less than an eighth of a wave at 1054 nm, again suggesting very low residual normal stresses in the crystal.

The KDP crystal plates are finished by diamond turning instead of polishing. In this process, a crystal blank is mounted on a carriage that translates the crystal blank parallel to the cutting plane. The cutting plane is defined by the single-point diamond tool mounted at a fixed radius in a high-speed spindle. This is commonly referred to as a fly-cutting mode of operation, and the cutting direction can be more closely aligned with a preferred axis on the crystal. By rotating the tool, rather than the crystal, the cutting rate remains the same across the whole face of the crystal. During the final finishing steps, the distance between subsequent tool cuts is usually only a few micrometers. Using this method, surface finishes of about 30 Å (rms) are typical.

One recurring problem we have encountered during finishing of large KDP crystals is a small-scale waviness in the transmitted wavefront. Our initial tests on Beamlet showed this same waviness in the output 1ω near-field image [Fig. 8(a)]. This waviness originated from the diamond-turned surface of the Pockels cell crystal and had a spatial scale length of about 6.3 mm. The measured amplitude of the phase ripple suggests a surface with a 100-Å peak-to-valley (p-V) periodic variation at that scale length. We investigated ways to reduce the surface waviness, because at high laser intensities the phase ripple from the diamond turning process may seed small-scale beam breakup due to self-focusing.[15] The source of the waviness was traced to a problem with the carriage system that translates the crystal. Specifically, we found that the flexure coupling that connects the drive-lead screw to the carriage was not properly aligned. Therefore, the flexure coupling was unable to adequately remove the natural once-per-revolution "wobble" motion of the lead screw. In this condition, the increased transmission of the lead-screw wobble into the carriage caused the crystal blank to move excessively in and out of the cutting plane in a sinusoidal fashion. After adjusting the flexure coupling, we found that the surface waviness was greatly reduced. Transmitted wavefront measurements on crystals finished before and after this repair showed that for scale lengths of ≈6 mm, the p-V surface waviness on the crystals was reduced from ≈60 Å to ≈10 Å above the background roughness near that spatial frequency. Figure 8 compares the near-field image of the Beamlet output beam before and after this corrective measure. Note that the circular arcs due to the spatial ripple are nearly absent in the "after" near-field image [Fig. 8(b)].

The damage threshold of some optical materials can be improved by "laser conditioning." KDP and KD*P are two such materials. During the process of laser conditioning, the optical material is exposed to a series of laser shots with monotonically increasing fluence. The wavelength of the conditioning laser shots is the same as the wavelength at which the optic is intended to be used. At the end of this sequence of exposures, the optical damage threshold is typically increased

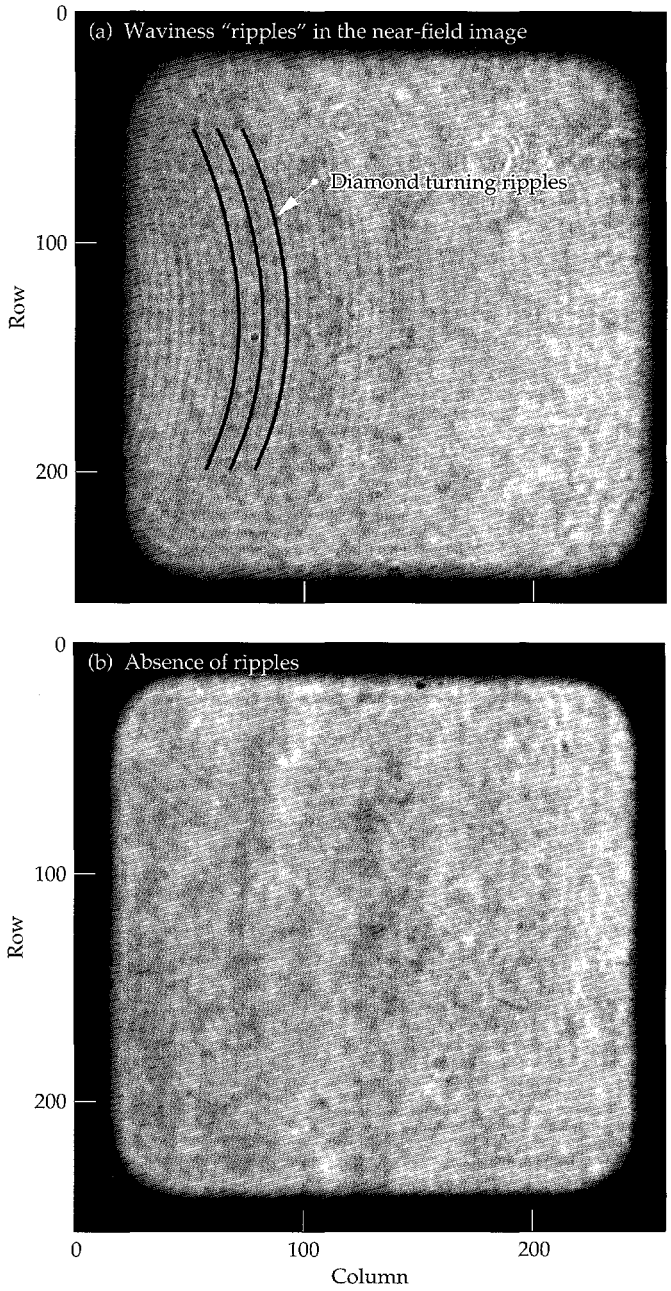

FIGURE 8. Near-field images of the 1ω output on Beamlet showing (a) the intensity modulation caused by diamond turning "ripples" on the Pockels cell KDP crystal, and (b) dramatic reduction of the ripples after the diamond turning machine is properly adjusted. (70-50-0295-0593pb01)

by a factor of two or more over the unconditioned (i.e., single-shot) threshold. As a general rule of thumb, at least five shots are needed to condition the optic to ≈85% of the maximum conditioned threshold. Furthermore, the first shot in the conditioning sequence should be at a fluence of about one-half the unconditioned damage threshold.

Table 2 summarizes the unconditioned and conditioned damage thresholds of KDP and KD*P at 1ω and 3ω, respectively.

Dielectric Coatings

Two main types of optical coatings are used on Beamlet: (1) multilayer HfO_2/SiO_2 high-reflectivity (HR) and polarizer coatings and (2) single-layer SiO_2 sol-gel antireflection (AR) coatings. Figure 9 shows the Beamlet polarizer and two of the mirrors. The sol-gel AR coating design, coating process, optical performance, and damage threshold have been well documented[16–18] and will not be discussed here. We note only that these coatings are routinely applied to all Beamlet and Nova transmissive optics (large and small) and have excellent transmission (>99.5% per surface) and high damage thresholds at 1ω and 3ω (Table 1).

Beamlet uses HfO_2/SiO_2 multilayer coatings because of their demonstrated damage threshold improvement with laser conditioning,[19,20] good optical properties, and relative ease in application over large apertures by electron beam (e-beam) evaporation.[21] All the multilayer coatings on large-aperture Beamlet optics were applied by conventional e-beam processing.

There are three reasons the polarizer is the most difficult optical coating to make: (1) The size of the polarizer is $75 \times 39 \times 9$ cm^3 and is more than twice the size of anything previously manufactured. (2) The damage threshold of the polarizer required for Beamlet represents a three-fold improvement over those used on Nova. (3) The coating layers need to be uniformly and precisely deposited over the entire substrate surface.

The polarizer coating was deposited on a BK-7 silicate glass substrate. BK-7 is significantly lower in cost than SiO_2, although it has the disadvantage of having a low bulk damage threshold due to Pt inclusions in the glass. However, because the polarizers used on Beamlet are used in reflection at high intensity, the BK-7 substrate is never exposed to damaging fluences.

Table 3 summarizes the transmission properties of the four polarizers manufactured for Beamlet by

TABLE 2. Summary of damage threshold for KDP and KD*P crystal plates used on Beamlet. The accuracy of the measurement is ±15% and ±30% for unconditioned and conditioned values.

Optic	Material	Wavelength (nm)	Damage threshold at 3 ns (J/cm^2)	
			Unconditioned	Conditioned
Pockels cell z-plate	KDP	1054	34	43
Type I doubler	KDP	1054	34	43
Type II tripler	KD*P	1054	16	25
		351	10	20

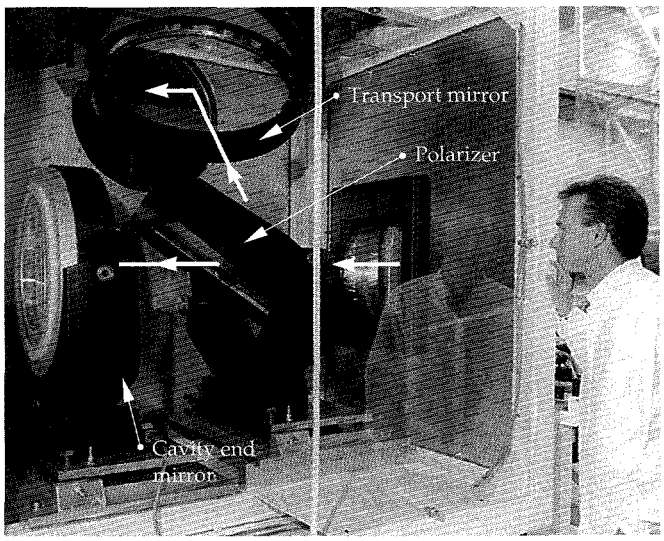

FIGURE 9. Photograph of the large-aperture HfO_2/SiO_2 thin-film polarizer used with the PEPCs on Beamlet to switch the beam out of the multipass cavity. The polarizer is used in a transmissive mode at low fluence (p-polarized incident light) during the first and second pass. On the final pass, the light is s-polarized and reflected off the polarizer coating and out of the cavity. The peak fluence is about 11 J/cm^2 at 3 ns (1054 nm). (70-50-0594-2486pb01)

TABLE 3. Summary of transmission, extinction ratio, reflected wavefront distortion, and conditioned damage threshold for the four $79 \times 39 \times 9$ cm^3 HfO_2/SiO_2 thin film polarizers manufactured for Beamlet (measured in dry N_2). Damage threshold is accurate to ±30%.

Polarizer designation	Optimum use angle	Transmission (%) p-polarized T_p	Transmission (%) s-polarized T_s	Extinction ratio T_p/T_s	Reflected wavefront distortion (in waves at 1.05 μm)	Conditioned damage threshold at 1.054 μm and 3 ns (J/cm^2)[a] p-polarized	s-polarized
1	55.5°	98.2	0.60	163	0.4	18	23
2	54.5°	98.1	0.10	981	0.25	20	26
3	56°	98.0	0.25	392	0.28	13	18
4	54.5°	98.2	0.14	701	0.38	20	35

[a]Damage measurements on witness samples from the production run.

Spectra-Physics. The optimum-use angle is between 54.5 and 56° and the polarizer can be "tuned" to the maximum extinction ratio by rotating the optical mount that holds the polarizer over the specified use range. We manufactured four polarizers: two are used on the system and two are spares. The polarizers were prepared in two separate coating production runs (with two polarizers in each run); the reproducibility between the two runs was quite good. Three of the polarizers had extinction coefficients >390, supporting the excellent control of the deposition process. The reflected wavefront distortion is between ≈0.25 and 0.4 waves and is largely due to spherical aberration that can be easily corrected by other optical elements in the system.

HfO_2/SiO_2 e-beam coatings can be laser conditioned to improve their damage threshold. (The conditioning process is similar to that described previously for KDP.) The conditioned damage thresholds of the polarizers all exceeded the Beamlet safe operating limit of 8 J/cm^2 at 3 ns (Table 3). The polarizers were conditioned off-line using the output from a pulsed Nd:YAG laser, operating at 10 Hz, to scan the full aperture of the optic in incremental fluence steps.[22] The conditioning effect has been associated with the gentle removal of nodular-shaped defects, which are known to limit the damage threshold of these multilayer coatings.[23] Based on measurements, the damage threshold of the polarizers scales with the pulse length as $\tau^{0.35}$.

The HfO_2/SiO_2 thin-film mirrors on Beamlet all had measured damage thresholds exceeding 25 J/cm^2 and reflectivities >99%. Damage thresholds of mirror coatings are typically higher than those of similar polarizer coatings.

Lenses and Diagnostic Beam Splitters

The lenses and diagnostic beam splitters used on Beamlet were all fabricated from fused silica, manufactured by Corning. The fused silica is prepared by flame-hydrolysis of $SiCl_4$ and is inclusion free. As a consequence, the damage threshold is limited by the surface finish and AR coating on the optic, not the bulk material. Extensive front-surface damage measurements at 1.0 and 0.35 μm and over a range of pulse lengths give a simple empirical relationship governing the safe operating limit for bare surface fused silica of

$$D = 22\, t_p^{0.4} \text{ (at 1.0 μm)}$$

and

$$D = 9.2\, t_p^{0.5} \text{ (at 0.35 μm)},$$

where t_p is the pulse length (ns) and D is the damage threshold (J/cm^2). When a sol-gel AR coating is applied to the fused silica surface, the safe operating limit is slightly higher than that measured for the bare surface material, specifically[24]

$$D = 24.6\, t_p^{0.4} \text{ (at 1.0 μm)}$$

and

$$D = 13.7\, t_p^{0.5} \text{ (at 0.35 μm)}.$$

Summary

Nearly all of the large optics used on Beamlet represent a dramatic increase in size and optical quality over those used on previous ICF lasers. Specifically the laser slabs, KDP/KD*P crystals, and polarizers are more than a factor of two larger than those used on Nova. In addition, the damage thresholds and quality of the Beamlet optical materials are also improved by two- to three-fold over those used on Nova. The sizes and quality of optics used in Beamlet closely match those expected to be used in the proposed NIF.

Acknowledgment

The authors gratefully acknowledge Cleveland Crystals, Inc., Corning, Eastman Kodak Company, Schott Glass Technologies Inc., Spectra-Physics, Tinsley Laboratories, Inc., and Zygo Corporation for their outstanding efforts in providing high-quality optical materials or optical finishing for Beamlet.[25–31] We also acknowledge the support of Kevin Kyle for providing the data on deuteration effects on the Raman spectrum of KDP and Frank Rainer and Frank DeMarco for providing damage threshold measurements.

Notes and References

1. J. E. Murray, H. T. Powell, G .F. Ross, and J. D. Wintemute, Technical Digest, Annual Meeting, Opt Soc of Am, Washington, DC, TUU9 (1988).
2. J. H. Campbell, G. Edwards, F. Frick, D. Gemmell, et al., *Laser-Induced Damage in Optical Materials: 1986*, (NIST, Special Publication, Boulder, CO, 1987; *NIST* **752**) p. 19.
3. S. E. Stokowski and D. Krashkevich, *Mat. Res. Soc. Symposium Proc.* **61**, 273 (1986).
4. H. G. Danielmeyer, M. Blatte, and P. Balmer, *Appl. Phys.* **1**, 269–274 (1973).
5. K. Jancaitis, "Updated Model for the Decay of the Inversion in LG-750 ND:Glass," LLNL internal memo, LS&T, 91–35 (Apr 1990).
6. J. A. Caird, N. D. Nielsen, and J. E. Murray, "Water Contamination and Fluorescence Lifetime in Nova Laser Glass," LLNL internal memo, ADG-88-138 (Dec 7, 1988).
7. J. H. Campbell, E. P. Wallerstein, J. S. Hayden, D. L. Sapak, et al., *Glastech. Ber. Glass Sci. Technol.* **68**(1), 11–21 (1995).
8. J. H. Campbell, E. P. Wallerstein, H. Toratani, H. Meissner, et al., *Glastech. Ber. Glass Sci. Technol.* **68**(2), 1–11 (1995).
9. R. A. Sacks, C. E. Barker, and R. B. Ehrlich, *ICF Quarterly Report* **2**(4), 179–188, Lawrence Livermore National Laboratory, Livermore, CA, UCRL-LR-105821-92-4 (1992).
10. W. Lee Smith, F. P. Milanovich, and M. A. Henesian, LLNL memorandum UVM 83–02 (Feb. 25, 1983).
11. C. E. Barker, D. Milam, and R. Boyd, *ICF Quarterly Report* **3**(2), 55–62, Lawrence Livermore National Laboratory, Livermore, CA, UCRL-LR-105821-93-2 (1993).
12. J. J. DeYoreo, J. Britten, R. Vital, K. Montgomery, et al., *ICF Quarterly Report* **3**(3), 103–111, Lawrence Livermore National Laboratory, Livermore, CA, UCRL-LR-105821-93-3 (1993).
13. J. J. DeYoreo and B. W. Woods, *Inorganic Crystals for Optics, Electro-Optics and Frequency Conversion*, (SPIE—International Society for Optical Engineering, Bellingham, WA, 1991; *Proc. SPIE* **1561**) p. 50.
14. J. J. DeYoreo and B. W. Woods, *J. Appl. Phys.* **73**, 1 (1993).
15. J. T. Hunt, J. A. Glaze, W. W. Simmons, and P. Renard, *Appl. Opt.* **17**, 2053–2057 (1978).
16. I. M. Thomas, *Appl. Opt.* **25**, 1481 (1986).
17. I. M. Thomas, J. G. Wilder, W. H. Lowdermilk, and M. C. Staggs, *Laser Induced Damage in Optical Materials: 1984*, (NBS Special Publication, 1986; *NBS* **727**) p. 205–210.
18. M. C. Staggs, D. Milam, I. M. Thomas, and J. G. Wilder, *Laser Induced Damage in Optical Materials: 1985*, (NBS Special Publication, 1988; *NBS* **746**) p. 404–411.
19. M. R. Kozlowski, I. M. Thomas, J. H. Campbell, and F. Rainer, *Thin Films for Optical Systems*, (SPIE, Bellingham, WA, 1992; *Proc. SPIE* **1782**) p. 105–121.
20. M. R. Kozlowski, C. R. Wolfe, M. Staggs, and J. H. Campbell, *Laser Induced Damage in Optical Materials: 1989*, H. Bennett, L. Chase, A. Guenther, B. Newnam, and M. J. Soileau, Eds., (NIST, Special Publication, 1990; *NIST* **801**) p. 375.
21. M. R. Kozlowski, R. Chow, and I. M. Thomas, *Handbook of Laser Science and Technology*, M. Weber, Ed., (CRC Press, 1995) pp. 767–812.
22. L. Sheehan, M. Kozlowski, F. Rainer, and M. C. Staggs, *Laser Induced Damage in Optical Materials: 1993*, (SPIE, Bellingham, WA, 1994; *Proc. SPIE* **2114**) pp. 559–568.
23. M. R. Kozlowski, R. J. Tench, R. Chow, and L. M. Sheehan, *Optical Interference Coatings*, (SPIE, Bellingham, WA, 1994; *Proc. SPIE* **2253**) pp. 743–750.
24. J. H. Campbell and F. Rainer, Lawrence Livermore National Laboratory, Livermore, CA, Report, UCRL-JC-109255, *SPIE '92 Conference Proceedings*, San Diego, CA, July 1992.
25. Cleveland Crystals, Inc., 676 Alpha Dr., Highland Heights, OH 44143.
26. Corning Glass Works, MP-21-04-2, Corning, NY 14831.
27. Eastman Kodak Company, Dept. 177, Bldg. 601, Rochester, NY 14650–0803.
28. Schott Glass Technologies Inc., 400 York Ave., Duryea, PA 18642.
29. Spectra-Physics Components & Accessories, 1330 West Middlefield Rd., Mountain View, CA 94039–0517.
30. Tinsley Laboratories, Inc., 3900 Lakeside Dr., Richmond, CA 94806.
31. Zygo Corporation, Laurel Brook Rd., Middlefield, CT, 06455–0448.

BEAMLET PULSED-POWER SYSTEM

D. Larson

Introduction

The 13-MJ Beamlet pulsed-power system provides power to the 512 flash lamps in the cavity and booster amplifiers. Since the flash lamps pump all of the apertures in the 2 × 2 amplifier array, the capacitor bank provides roughly four times the energy required to pump the single active beam line. Figure 1 is a block diagram illustrating the main pulsed-power subsystems. During the 40 s prior to the shot, the capacitors are charged by constant-current power supplies. Ignitron switches transfer the capacitor energy to the flash lamps via coaxial cables. A preionization system triggers the flash lamps and delivers roughly 1% of the capacitor energy 200 μs prior to the main discharge. This is the first time flash-lamp preionization has been used in a large facility. Preionization improves the amplifier efficiency by roughly 5% and increases the lifetime of the flash lamps. Figure 2 shows a typical Beamlet current pulse. LabVIEW[1] control panels provide an operator interface with the modular controls and diagnostics. Figure 3 shows one of the four aisles of capacitor circuits and the wall of equipment racks containing the controllers, triggers, and charging supplies.

Table 1 shows the primary pulsed-power requirements. The system is assembled from 32 independent modules, each capable of driving 16 flash lamps to 30% of their explosion limit. The circuit architecture (Fig. 4) is similar to Nova's, but the Beamlet system demonstrates several features of the proposed National Ignition Facility (NIF) pulsed-power design. To improve the reliability of the system, high-energy-density, self-healing, metallized dielectric capacitors are used.

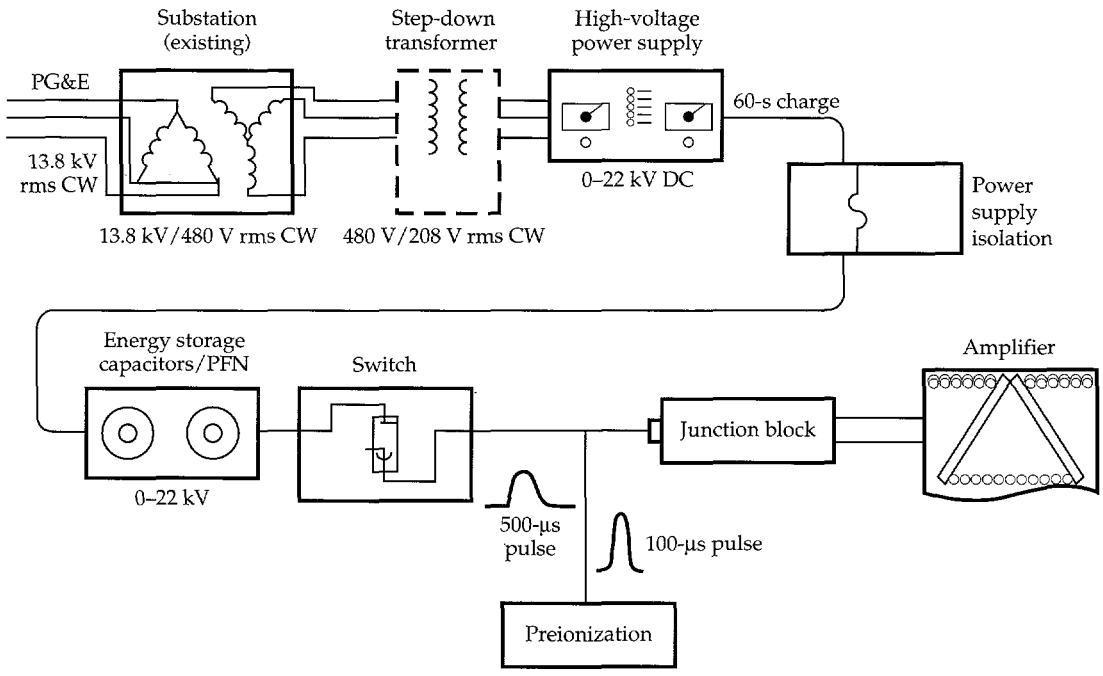

FIGURE 1. Block diagram of the Beamlet pulsed-power system. (40-00-0591-1686pb01)

UCRL-LR-105821-95-1

High-frequency, voltage-regulated switching power supplies are integrated into each module on Beamlet, allowing greater independence among the modules and improved charge voltage accuracy, flexibility, and repeatability. On Nova, by contrast, many modules are charged with a single large unregulated power supply with high-voltage diodes to provide isolation. Failure of these diodes allows very large amounts of energy to be released in a single fault.

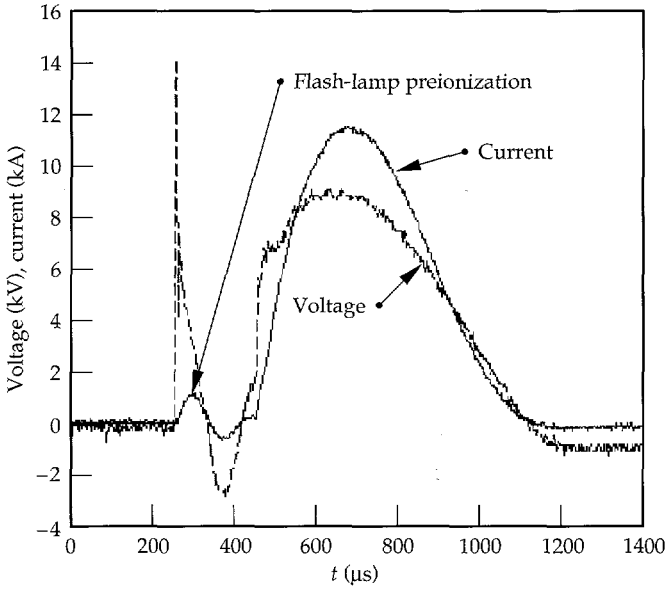

FIGURE 2. Typical flash-lamp current and voltage waveforms during the firing of the Beamlet pulsed-power system. (70-50-1294-4019pb01)

Capacitor Circuits

The Beamlet capacitor bank contains 256 capacitor circuits, each of which stores 52 kJ at 22 kV (Fig. 5). An additional 32 preionization circuits each store 3.6 kJ. The main capacitor circuits include: a single high-energy-density capacitor, a manual disconnect switch, a high-voltage fuse, a pulse-shaping inductor, a charge resistor, and a spark-gap. The capacitor-inductor combination forms the 500-μs current pulse that drives the flash lamps. The manual disconnect switch disconnects the capacitor circuit from the remainder of the module and shorts the capacitor terminals. The high-voltage fuse, rated to carry 45,000 A^2s and open at 180,000 A^2s, is designed to protect the flash lamps from a failure that could exceed their explosion energy rating. This failure mode could occur in the event of a capacitor short circuit prior to triggering the switches. The spark-gap limits the magnitude of the voltage transient generated by the inductor when the fuse clears.

The energy storage capacitors, developed for Beamlet, use the metallized dielectric electrode technology. This technology gives the capacitors improved energy density and reliability in ICF applications and is included in the conceptual design for the proposed NIF pulsed-power system. Figure 5 is a photograph illustrating the evolution of capacitor technology for ICF pulsed-power systems over the past 20 years. The Beamlet capacitor stores 4 times the energy of the Nova capacitor, and 15 times that of Shiva, in roughly the same volume. The Beamlet capacitors have a different construction and failure mechanism compared to conventional

Control panel and charging supplies

Ignitron switches

50-kJ capacitors

FIGURE 3. Photograph of the pulsed-power control panel and one of the four aisles that contain the ignition switches and 50-kJ capacitors. The total bank's stored energy is 12.8 MJ at 20 kV. (70-50-0294-0465pb01)

foil-electrode capacitors. The improvements in the Beamlet metallized electrode result primarily from the self-healing characteristic of the dielectric system. The electrode is a thin (20-nm) layer of Al deposited onto the dielectric. If the dielectric is punctured, the resulting current flow vaporizes the electrode in the vicinity of the fault so that the short is cleared, or "healed," resulting in a small reduction in capacitance. In a conventional capacitor, the punctured dielectric would result in a short circuit and catastrophic capacitor failure. Thousands of healing events may occur before the capacitance is significantly reduced. Failure is typically defined as a 5% reduction in capacitance from the nominal value for metallized dielectric capacitors. Energy density is improved, since the capacitors may be operated near the intrinsic dielectric strength of the material, rather than derated to account for material or manufacturing flaws. System reliability is improved by the "soft" failure mode of the metallized capacitors. The capacitors suffer a gradual capacitance loss, rather than a catastrophic short-circuit. This effect can be monitored directly by periodically measuring the capacitance, or inferred by recording the peak current on each shot and detecting a reduction resulting from reduced capacitance. The second method is implemented on Beamlet. This information allows the operator to monitor the status of the capacitors during normal operation, and to replace aging capacitors during scheduled maintenance times.

Qualification and acceptance tests were performed on the Beamlet capacitors to validate their performance. Qualification testing consisted of a life test at simulated Beamlet operating conditions (22 kV, 13 kA), including 25 fault-mode shots (22 kV, 24 kA, 70% reversal). Acceptance tests were performed on 7 lots of approximately 40 capacitors per lot. Each capacitor received a 25-shot functional test at nominal Beamlet operating conditions, and a DC high-voltage test of the bushing-to-case insulation. Three capacitors from each lot received an additional 1000 shots, and one of those an additional 9000 shots. No failures were observed in any of the tests, although due to a manufacturing defect, one of the capacitors dropped 4% from nominal during the 10,000-shot test. Periodic capacitance measurements were conducted to monitor the capacitor status. Figure 6 shows the results of a typical life test. A Weibull statistical analysis of the qualification and acceptance test data was used to predict the reliability

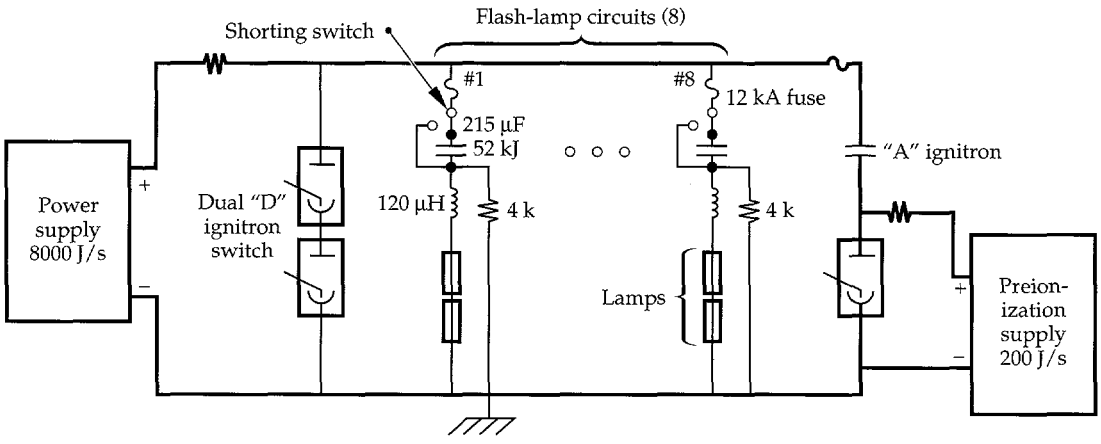

FIGURE 4. Simplified schematic of a Beamlet capacitor-bank module. (40-00-0591-1684pb01)

TABLE 1. Major requirements of the Beamlet pulsed-power system.

Item	Requirement	Purpose
Maximum delivered energy	9.1 MJ	Operates 512 Beamlet flash lamps at $f_x = 0.3$
Explosion fraction range	$0.2 \le f_x \le 0.3$	Operating flexibility
Preionization energy	0.3 J/cm^2 of lamp bore	215 J/lamp, 90 μs pulse
Main pulse length	500 μs	3 $(LC)^{0.5}$
Maximum repetition rate	3 shots/hr	Amplifier characterization shot rate
Bank lifetime	$>10^3$ shots at $f_x = 0.3$, or $>10^4$ shots at $f_x = 0.2$	Capacitors are limiting component. End of life determined by 5% capacitance reduction
Number of capacitor modules	32	Allows separate drive energies of inner and outer flash-lamp arrays
Charge voltage repeatability	±0.5%	Minimize shot-to-shot gain fluctuation

f_x = explosion fraction = lamp energy/theoretical limit.

LC = (L) circuit inductance, (C) circuit capacitance.

of the capacitors.[2] The analysis showed that we can expect a mean-time-between-failures (MTBF) of 2000 shots over the expected 5000-shot life of the Beamlet. If the same capacitors were used in the larger NIF system, a capacitor would require replacement roughly every 100 shots over the same period.

Switches

The Beamlet switch assembly is an evolution of the Nova design. Two size "D" ignitrons, in series, switch the 8 circuits of each module in parallel. The switches operate at 22 kV, 100 kA, and transfer 35 C per shot. A size "A" ignitron is added to the assembly to discharge the preionization circuit. The single tube is operated at up to 22 kV, 11 kA peak current.

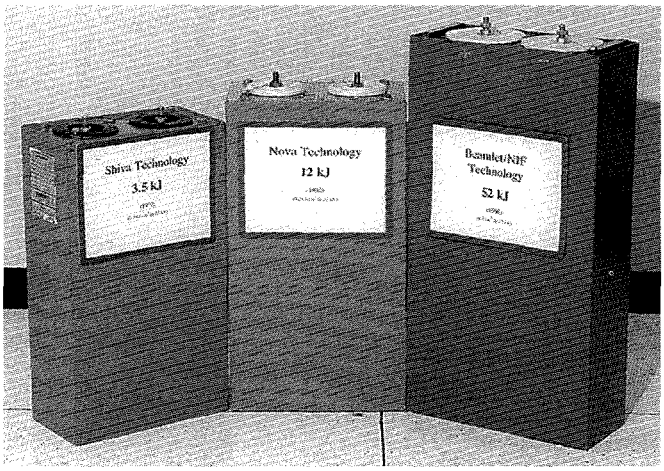

FIGURE 5. Photograph comparing Shiva, Nova, and Beamlet capacitors. The capacitor energy storage density has increased 15-fold in the 20 years since Shiva was built and 4-fold since Nova was built. (70-50-0594-2523pb01)

Charging Supplies

The Beamlet design maximizes system modularity by embedding the charging supplies within each module. In this way, the "copper" connections between modules are limited to common AC power and grounds. This approach is especially important in large systems such as the proposed NIF, in which it is desirable to build a system from 200 independent 1.6-MJ capacitor banks, rather than a single 320-MJ capacitor bank.

This approach has been made practical by the development of efficient, reliable, high-frequency switching power supplies over the past decade. These supplies use advanced insulated-gate bipolar-transistor-power semiconductor devices and reliable architectures such as the series-resonant-inverter. The high operating frequency enables the use of efficient ferrite magnetics, resulting in small size and weight. The Beamlet charging supplies are approximately 30 times smaller than the equivalent supplies used on Nova.

The main capacitors in each module are charged by a supply with an average charge rate of 10 kJ/s, which delivers up to 20 kW at the end of the charge cycle. The output current is a constant 900 mA until the supply reaches its regulation point. It then holds the capacitors at a constant voltage until they are discharged. Additional circuitry is needed to protect the supplies in the event of a bank fault that results in reversal of the capacitor voltage. Voltage reversal tends to drive large values of current through the small diodes in the output rectifier of the charging supply, resulting in failure of the diodes. The circuit shown in Fig. 7 protects the supplies from bank faults. The diode stack diverts the fault current, while the 50-Ω resistor limits the fault current to a safe level for the diodes. The fuse limits the energy deposited in the charging supply in the event of a short circuit in the supply itself.

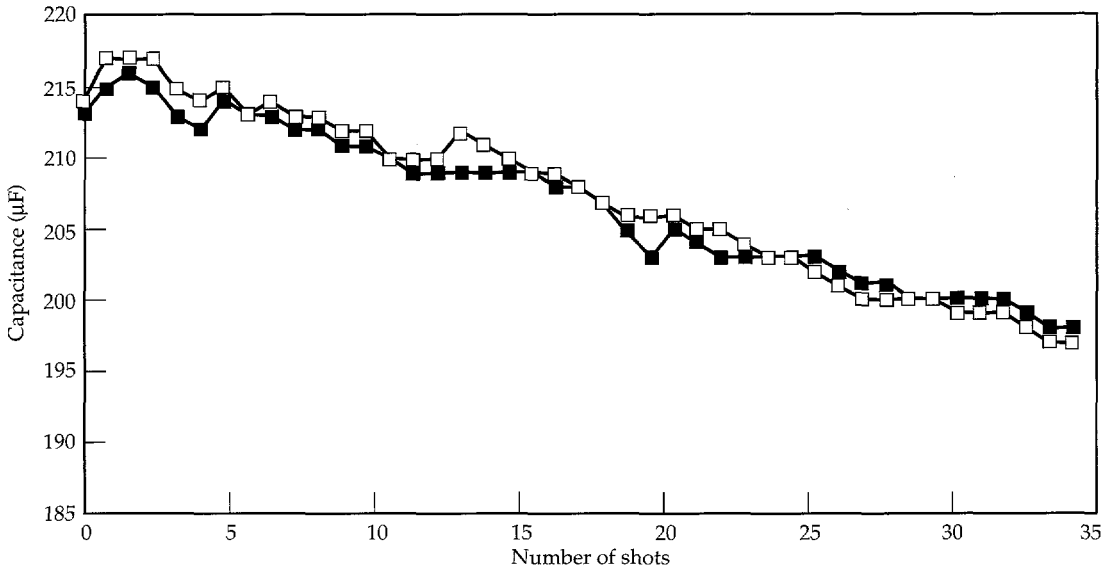

FIGURE 6. Results from lifetime tests on two Beamlet 50-kJ dielectric capacitors. The data show the slow decay in capacitance with the number of shots. (70-50-1294-4018pb01)

The preionization capacitors are charged by a small, 200-J/s power supply similar in design to the large supplies. A 50,000-Ω resistor is placed in series with the output to protect the supply from capacitor voltage reversal. A series of equipment racks contain the charging supplies, triggers, and controls for the system. Each rack bay contains the controls, chargers, and triggers for two capacitor modules.

Power Transmission

Coaxial cables are used to deliver the capacitor energy from the bank to junction blocks near the amplifiers. The length of the cables varies from 25 to 70 m. We chose a 50-Ω, high-voltage coaxial cable (RG-217) since it was used on Nova and Shiva, and many excess fittings and terminators were available for use on Beamlet. This cable, however, resulted in high resistive losses at the elevated Beamlet operating currents. As much as 30% of the capacitor energy is lost in the cables at the highest explosion fractions and longest cable lengths.

The coaxial cables terminate in junction blocks in the Beamlet center tray near the amplifiers. The junction blocks affect the transition from the coaxial cable to the flexible twisted-pair cable, which delivers the energy the last several meters to the flash-lamp cassettes in the amplifier. A custom twisted-pair cable was developed for Beamlet, since the magnetic forces due to increased current caused failures in the Nova-type cables during prototype tests. The cable is made from flexible, silicone-insulated wires that are twisted and covered with a layer of mylar and a strong nylon braid to contain the magnetic forces. A PVC jacket covers the assembly.

Controls and Diagnostics

As shown schematically in Fig. 8, a hierarchical computer system controls the Beamlet pulsed-power system. A central control computer, located in the Beamlet control room, provides a graphical LabVIEW operator interface, data archiving, timing control, and coordination of pulsed-power system operation with other Beamlet subsystems. In the capacitor bank, single-board computers receive high-level commands from the central computer and control bank operation through the control-interface chassis. The single-board computers, their fiber-optic communications system, and the control interface chassis were assembled from industrial process control components to achieve a robust and inexpensive system. Conceptually, this design is very similar to the design of the power conditioning system controls for the proposed NIF.

The principal diagnostic for the Beamlet pulsed-power system is measurement of peak current in each flash-lamp string. The current in each flash-lamp pair is detected by a current transformer. The current-peak-detector chassis in each pulsed-power module provides analog peak-detection measurements that are digitized by the control interface chassis and transferred to the central control computer.

The current-peak-detector chassis also performs a fault protection function. In the event that a capacitor should short while charged, the other capacitors in that module would discharge through it into its lamp string. If the fuse fails to open properly, this fault may result in the explosion of the lamp and serious damage to nearby optics. This failure mode has occurred on Nova and is responsible for nearly all of its flash-lamp explosions to date. To prevent this on Beamlet, the current-peak detector sends an indication of the onset of current flow to the trigger-distribution chassis. If current flow is detected before the system triggers have been generated,

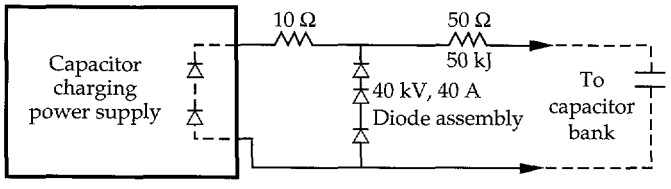

FIGURE 7. A combination of resistors and diodes protects the charging supply in the event of capacitor bank faults. (70-50-1294-4017pb01)

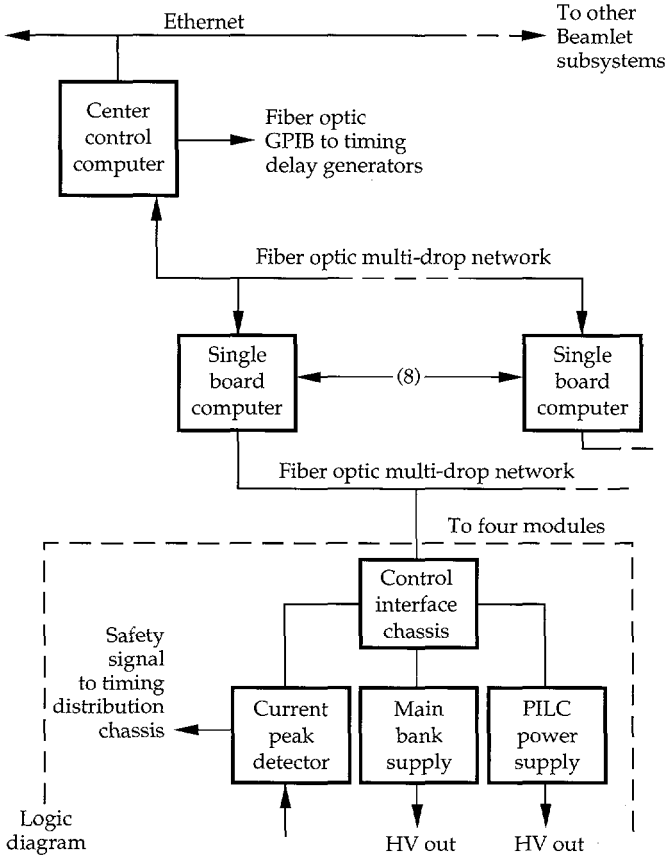

FIGURE 8. Schematic diagram of the pulsed-power control system. (70-50-1294-4016pb01)

the trigger-distribution chassis fires the main bank ignitrons. This diverts the current flow from the failed circuit to the ignitron, thereby preventing the flash-lamp explosion energy from being reached.

The single-board computers also perform a fault protection function by monitoring the value of the voltage on the preionization power supply. If significant charge were left on the preionization capacitors by, for example, an aborted shot, and then the main bank were charged, the output of the preionization supply would be subjected to the sum of the voltages, which could exceed the maximum voltage design rating of the supply. If the single-board computers detect excessive preionization voltage, they automatically shut off the main bank charging supply to protect the system.

The Beamlet timing controls are based on commercial delay generators. A master radio-frequency clock and the 0.2-Hz regenerative amplifier trigger are distributed building-wide on a system of transformer-isolated coaxial cables. A fiber-optic extended GPIB network connects all the delay generators to the Beamlet pulsed-power system's central control computer. The resulting system meets a specification of 250 ps peak-to-peak jitter.

Summary

To date, the reliability of the Beamlet pulsed-power system has been very good. During the first 700 system shots, no failures occurred in the high-current circuitry. The ignitron pre-fire rate was high during the first 100 shots until the weak tubes were culled from the system. A design defect in the preionization supplies resulted in a high initial failure rate. The addition of external components solved that problem. No measurable reduction in capacitance has been detected in any of the metallized dielectric capacitors.

Notes and References

1. LabVIEW, a data acquisition and control programming language, National Instruments Corp., 6504 Bridge Point Parkway, Austin, TX, 78730–9824.
2. D. W. Larson, "The Impact of High Energy Density Capacitors with Metallized Electrode in Large Capacitor Banks for Nuclear Fusion Applications," Digest of Technical Papers, *Ninth IEEE International Pulsed Power Conference*, Albuquerque, NM, June 21–23, 1993.

BEAMLET LASER DIAGNOSTICS

S. C. Burkhart

W. C. Behrendt

I. Smith

Introduction

Beamlet is instrumented extensively to monitor the performance of the overall laser system and many of its subsystems. Beam diagnostics, installed in key locations, are used to fully characterize the beam during its propagation through the multipass cavity and the laser's output section (Fig. 1). This article describes the diagnostics stations located on Beamlet and discusses the design, calibration, and performance of the Beamlet calorimeters. We used Nova's diagnostics packages to develop the Beamlet design to determine beam energy, spatial profile, temporal profile, and other beam parameters.[1,2] Technologic improvements within the last several years in controls, charge-coupled device (CCD) cameras, and fast oscilloscopes have allowed us to obtain more accurate measurements on the Beamlet laser system. We briefly cover some of these techniques, including a description of our LabVIEW[3] based data acquisition system.

Diagnostics Systems

The first diagnostics station in the main laser is at the east end of the cavity where the beam is sampled after the first pass through the amplifier (Fig. 1). The cavity mirrors are designed to leak approximately 0.5% of the incident 1.053-μm (1ω) light, which is down-collimated to a near-field camera, an energy diode, a temporal pulse-shape diode, and an absorbing glass calorimeter. The beam is diagnosed in a similar manner at the west end of the cavity following the second pass through the laser. The third and fourth passes are also sampled and diagnosed to a limited extent, since the imaging and energy diagnostics can only view one pass for any particular shot. In addition, only the depolarized portion of the fourth pass is transmitted through the polarizer to the west cavity diagnostics.

At the output of the 1ω section of the laser, the beam is again sampled using the reflection off an uncoated

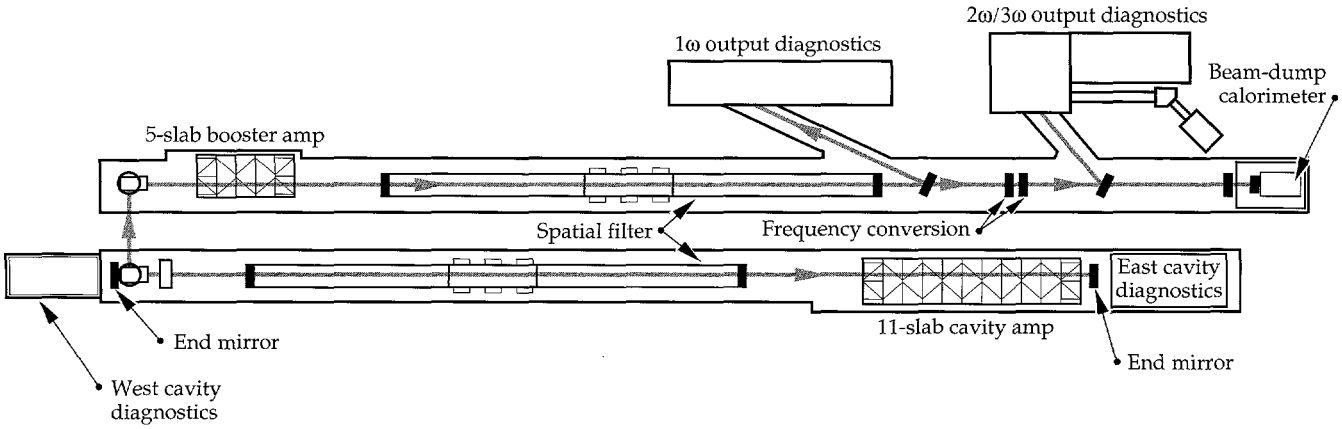

FIGURE 1. View of the Beamlet laser and the diagnostics systems. Dedicated diagnostics are located at both ends of the main cavity and at the output section prior to, and after, the frequency conversion crystals. An instrumented beam-dump calorimeter absorbs all of the remaining beam. (70-50-0395-0662pb01)

fused-silica beamsplitter (Fig. 1). This 1ω output package contains an extensive suite of diagnostics including energy, temporal pulse shape (diode and streak camera), low- and high-resolution near- and far-field imaging, phase front (Hartmann array and a radial-shear interferometer), and beam bandwidth (Fabry–Perot). Another large set of diagnostics are present in the 2ω/3ω diagnostics station that follows the frequency conversion section. This diagnostics package also includes a beam energy balance system that measures the absolute energy in each of the primary (1ω), doubled (2ω), and tripled (3ω) beams. The last diagnostics station consists solely of a single, large-aperture, 74-cm absorbing glass calorimeter that quantifies the combined output beam energy (minus, of course, the small amount of energy that is deflected to the previous diagnostics systems). This calorimeter also serves as a "beam dump."

Cavity Diagnostics

Cavity diagnostics are located at both ends of the main amplifier cavity, with the diagnostic transport shown in Fig. 2 for the east cavity diagnostics. For diagnostic purposes, the cavity mirrors leak a nominal 0.4–1% of the incident beam and the transmitted beam passes through the uncoated backside and the antireflective (AR) coated 7.6-m focusing lens. The converging beam is folded twice by the upper and lower turning mirrors; attenuated by one or two 99.3% mirrors (Fig. 3); and split to the far-field camera, the near-field camera, and to an integrating sphere/photodiode energy diagnostic. The rejected beam from the first attenuator mirror is directed to a calorimeter and a temporal pulse-shape vacuum photodiode diagnostic. The cameras and integrating sphere are discussed here; the calorimeter and temporal diagnostics are discussed in subsequent sections. Figure 2 shows the east cavity diagnostics, including extensive baffling. This baffling prevents the intense off-axis flashlamp light, transmitted through the cavity mirror, from reaching the diagnostics.

The near-field camera (a Cohu 6400 series) images the cavity mirror directly onto the CCD camera through an attenuating protective window mounted on the camera's face. To achieve the right intensity, the beam is transmitted through filter-wheel-mounted neutral-density filters. These filters consist of AR-coated

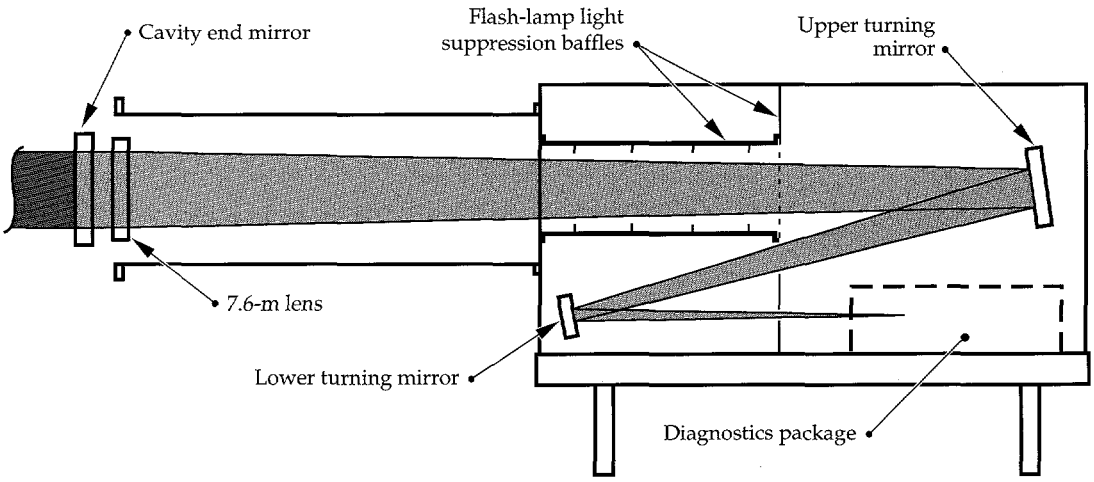

FIGURE 2. Side view of the cavity diagnostic beam transport optics. The 0.5% leakage through the cavity end mirror is focused and folded down to the diagnostic package. The east and west end diagnostic transport optics are identical, but the east diagnostics are substantially baffled to prevent the light of the adjacent cavity amplifier flash lamps from saturating the diagnostics. (70-50-0494-1667pb01)

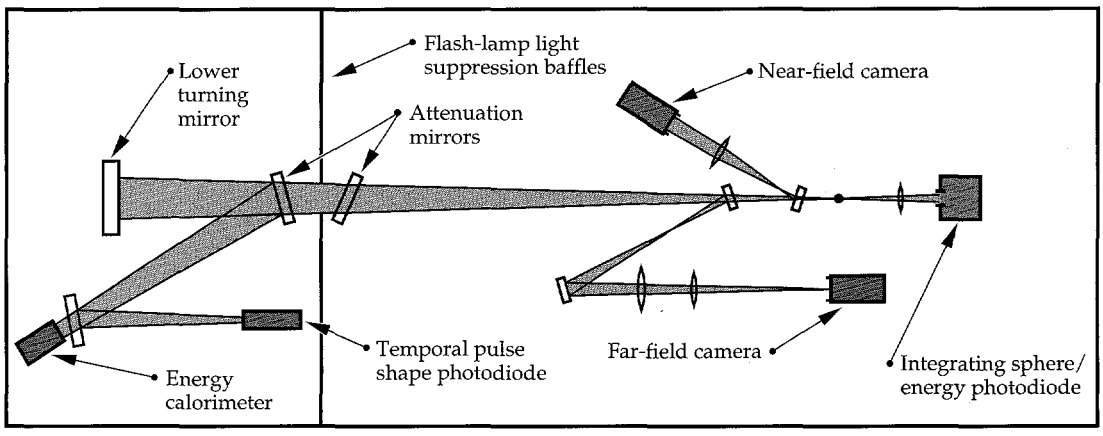

FIGURE 3. Top view showing the east cavity diagnostics. Attenuating filters, beam blocks, and pinholes strip off ghost images, select the desired cavity pass, and set the energy levels to each diagnostic. (70-50-0494-1666pb01)

31-mm-diam glass (NG-1, NG-3, NG-4, NG-5, NG-9, and NG-11). The image is viewed on the alignment display through the Beamlet video switching system for beam centering, with the attenuator mirrors replaced by identical AR-coated blanks. To capture the near-field image during a shot, the attenuator mirrors and filters are set to calculated values, and the 16-channel framegrabbing system is triggered to capture the image field at shot time. The near-field camera is quite useful for centering operations and for shots; however, automation of the attenuator mirror insertion is needed as Beamlet's shot rate increases. The camera images either pass 1 or pass 3 (pass 2 or pass 4 for the west cavity diagnostics) with automated selection between the passes. A stepper-motor-mounted pinhole array at the focus selects pass 1, pass 3, or both passes simultaneously, and strips off the unwanted image from the uncoated back surface of the cavity mirror.

The far-field camera has a complicated design to perform both the diagnostic and pointing functions. The compromised design limited its performance in diagnostic mode, and the pointing function was superceded by a telescope mounted at the cavity pinhole plane. The camera had two fields of view of the cavity spatial filter pinhole plane. The first field (a 4×4 cm image) viewed all four cavity spatial filter pinholes simultaneously for pointing purposes. The other field (a higher resolution 8×8 mm image) required manual replacement of several lenses, and viewed one pinhole at a time. To achieve the wide field of view required a fast lens mounted directly in front of the camera imaging surface. To do this, we glued the lens onto a faceplate ring that replaced the CCD protective cover. In addition, several oversized lenses were required to perform high-quality off-axis far-field imaging. We designed the far-field camera to perform Beamlet pointing in the wide field of view mode, an operation now routinely performed by the Questar telescope. For a time, the camera was used in shot mode, but the angular resolution was too small to be of much use. Thus, the camera was removed as Beamlet activation proceeded to, and beyond, the four-pass experiments.

During the activation stage, the integrating sphere energy diagnostic proved to be exceedingly useful and was instrumental in determining the plasma electrode Pockels cell performance in the west cavity diagnostics. The system consists of a Labsphere 4-in.-spectralon integrating sphere with an EG&G FND-100 Si photodiode reverse biased to 40 V and recorded by a Tektronix TDS-320 digitizing oscilloscope. The bias voltage is coupled in by a Picosecond Pulse Lab bias tee, and the signal is terminated in 50 Ω at the oscilloscope. During initial activation, especially continuous-wave (cw) tests, a slower, more sensitive PIN-8 diode replaced the FND-100 photodiode. The PIN-8 diode was battery biased with the bias tee removed to transmit the 350-μs gain test signal, and the signal was recorded by the TDS-320 in high-impedance mode. In later, more routine, system operations, the integrating sphere signals were recorded but were used largely in a qualitative sense. Software was developed to calculate the charge delivered by the photodiode from the recorded voltage waveform and to infer the energy from the calibrated sensitivity and system transmission. However, with our extensive use of inexpensive and very accurate calorimeters, the integrating sphere energy diagnostic was used only as a relative comparison between the passes and as a post-mortem for shots which did not perform as expected.

1ω Output Diagnostics

A portion of the fully amplified Beamlet beam is sampled by a 61-cm beamsplitter and relay imaged to the 1ω diagnostic station (Fig. 4). The beam sample is approximately 3% of the main beam from the 12° angle of incidence "P" reflection of the uncoated silica splitter. The sampled beam is propagated through an AR-coated, 920-cm, focal-length lens, and folded by three more in-plane reflections off a bare surface BK-7 splitter, and two high-reflectivity mirrors. A minimum of several joules of 1ω light were required for high-resolution near-field imaging onto film in the original 1ω diagnostics design. This design necessitated the incorporation of a vacuum cell at the transport focus. The vacuum cell was designed with a tilted, wedged input window to protect the folding mirrors and to eliminate fringing, and had a collimating lens at its output. It was extremely important to have a well-collimated, representative sample of the beam for the wavefront correction system (Hartmann sensor) and for the 1ω far-field camera. To accomplish this, all flat optics leading to the collimating lens were mounted and interferometrically tested prior to installation. Mounting problems were corrected on several of the large splitters, which allowed us to achieve low-aberration transport to the diagnostic table.

The diagnostics transport enclosure contains the output 1ω calorimeter as shown in Fig. 4, after three uncoated reflections to keep the calorimeter energy below 1 J. Calculating the Fresnel reflection from all three surfaces determines the transmission coefficient from the main beamline to the calorimeter.

Measurements were made to confirm these values. We changed the 12° angle of incidence for the large splitters to 12.2° due to a 14-cm shift of the 61-cm splitter midway through the frequency converter activation. This mitigated a collimated ghost reflection from the frequency converting crystals, which was reflected and focused by the spatial filter lens onto the splitter, causing damage. The increased angle changed the calculated transmission value by 0.4%. All the splitters were wedged to keep unwanted direct backside reflections and double bounce reflections from the three large splitters outside of the calorimeter aperture. The final uncoated splitter had a 2° wedge and a 0.1% AR coating on the backside, with the estimated overlap between the AR surface reflection and the calorimeter aperture of <25%. The additional energy due to the reflection is <0.7%. No unwanted energy from any of the other splitters fell within the calorimeter aperture.

Figure 5 shows the 1ω diagnostics that are located in a separate enclosure from the diagnostics transport optics to prevent scattered light from entering any of the sensitive diagnostics. After the beam enters the table, 10% of the beam is split off and directed to the wavefront control Hartmann sensor (located on the lower part of Fig. 5), and relayed to the Hartmann lenslet array and camera. The rest of the beam passes through a path-compensating splitter, a 50% splitter, and a 1:1 vacuum relay. Several pointing and centering mirrors direct the beam from the 50% splitter to the 1ω far-field camera. Due to pointing problems, it was difficult to implement the far-field camera and it was also difficult to obtain attenuating filters with good optical quality. Most of the optical filters could be placed directly in front of the far-field camera, but enough attenuation had to be placed in the near-field filters to prevent damage to those in the far field. We selected Schott KG glass filters placed in front of the focusing lens, filters which could be checked for wavefront quality at 633 nm, yet are optically dense at 1.053 μm. These are the same filter types as used in the Hartmann sensor.

The far-field camera was used for some time at $f/100$, but was changed to the rattle pair configuration [Fig. 6(a)]. The rattle pair, based on a photographic film design originally prepared for Nova,[2] was adapted for use with the Beamlet high-resolution CCD cameras. The Beamlet design uses two pairs of wedged mirrors to create an array of far-field spots variable in both intensity and focus at the camera image plane [Fig. 6(b)]. The first pair of mirrors on the left side are 3-in.-diam partially (50%) reflecting mirrors, tilted to generate an array of

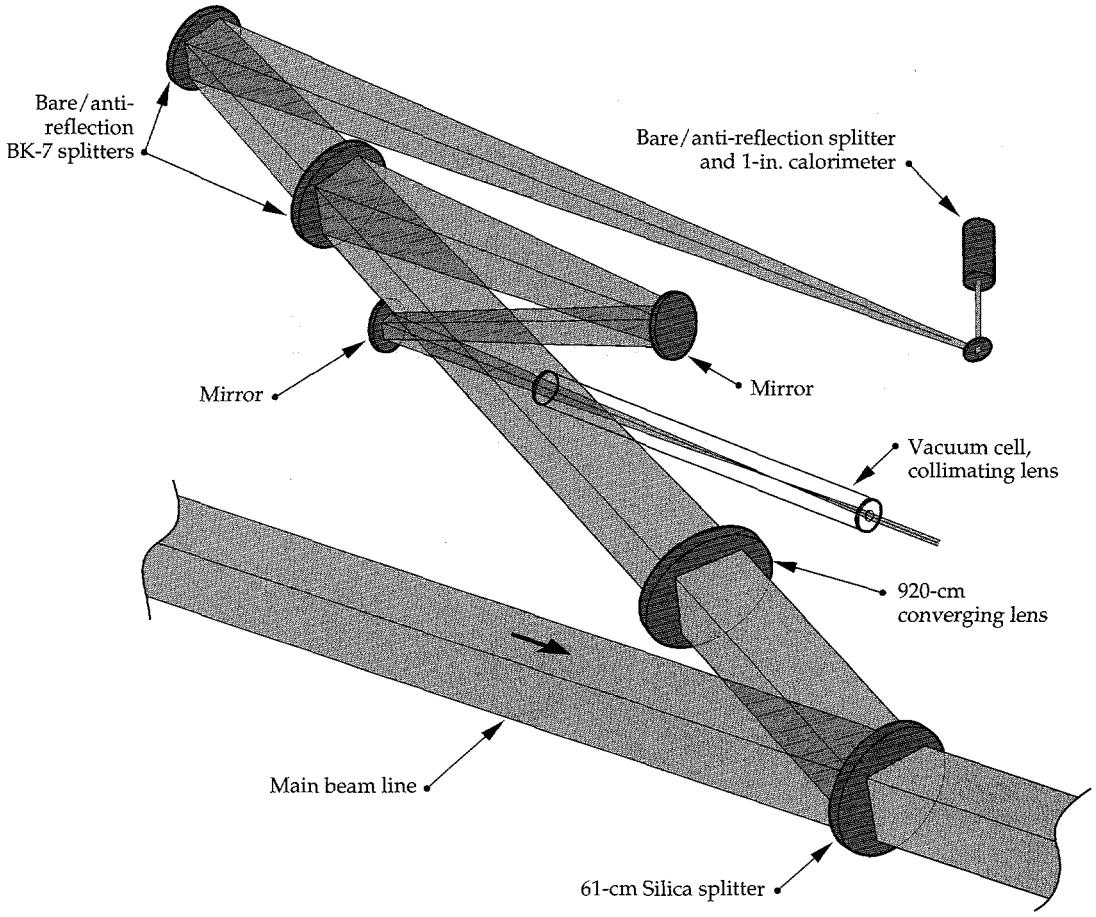

FIGURE 4. The main beam is relayed to the 1ω output diagnostics through a series of uncoated and high-reflector flat optics and is focused by a 9.2-m focal length lens. Up to 10 J is sent through focus in the vacuum cell and collimated. The system 1ω output calorimeter operates directly from three uncoated reflections. (70-50-0494-1682pb01)

spots at the image plane graded in intensity. The focusing lens has a focal length of 1800 mm and is followed by two more wedged mirrors, which have a 90% reflection from their facing surfaces. This second pair of reflectors acts to offset the focus in both angle and longitudinal dimension to take images of the far field through several focal planes. The spacing of the focal planes is adjusted by the spacing between the second pair of mirrors. All rattle pair elements were wedged by 2.4 mr to mitigate the ghost images from the AR-coated transmission surfaces and were mounted in precision mirror mounts to facilitate system setup. The reflected wavefront quality is important since the beam is reflected numerous times from the same surfaces. To help maintain the wavefront quality, the beam size was kept small on the mirrors (18 mm square), and the mirror reflected wavefront was specified to $\lambda/11$ at 1.05 μm, with a gradient $<\lambda/24$/cm. Excellent results were obtained from this system as described in "System Description and Initial Performance Results for Beamlet," p. 11. Using the rattle pair camera, we diagnosed dynamic focal plane shifts during a shot. This was a significant aid in correctly applying wavefront precorrection for dynamic aberrations using the Beamlet Adaptive Optics System.

After the main beam passes through the 1:1 vacuum relay (Fig. 5), the recollimated beam is folded twice and directed back through a holographic beamsplitter (HBS)—designed to transmit most of the beam, while diffracting a small amount to either side for diagnostic purposes. The units transmit 10% of the beam energy into the first order, 1% into the second, etc. This approach was chosen because multiple splitters would have steered the beam and caused unwanted reflections. Initial alignment was difficult, but the HBS performed well for all of the Beamlet activation sequence. Figure 5 shows a first-order beam from the first HBS directed to a vacuum photodiode temporal diagnostic. The photodiode signal is recorded by a Tektronix SCD-5000 transient digitizer for a combined rise time of 110 ps. In addition, the leakage through the second turning mirror, just ahead of the first holographic beamsplitter, is routed out of the diagnostics enclosure to a streak camera for higher-resolution temporal diagnosis. The zero order from the first splitter, which constitutes nearly 78% of the incident beam, is reflected off of a 97% splitter to the radial-shear interferometer and the Fabry–Perot bandwidth diagnostics. Originally, the near-field film camera for high-resolution imaging was to be at this location, but the performance obtained from the high-resolution CCD camera made the film camera unnecessary. The 14-bit dynamic range, 1024×1024 pixel, cooled scientific-grade CCD camera is over 10^6 more sensitive than film and has none of the inherent problems or delays associated with film densitometry. The remainder of the zero-order beam after the 97% splitter is passed through an AR-coated compensating splitter to the second HBS element. The zero order from the second element is relayed into the high-resolution near-field CCD camera, and a first-order beam is relayed to a standard-resolution near-field camera.

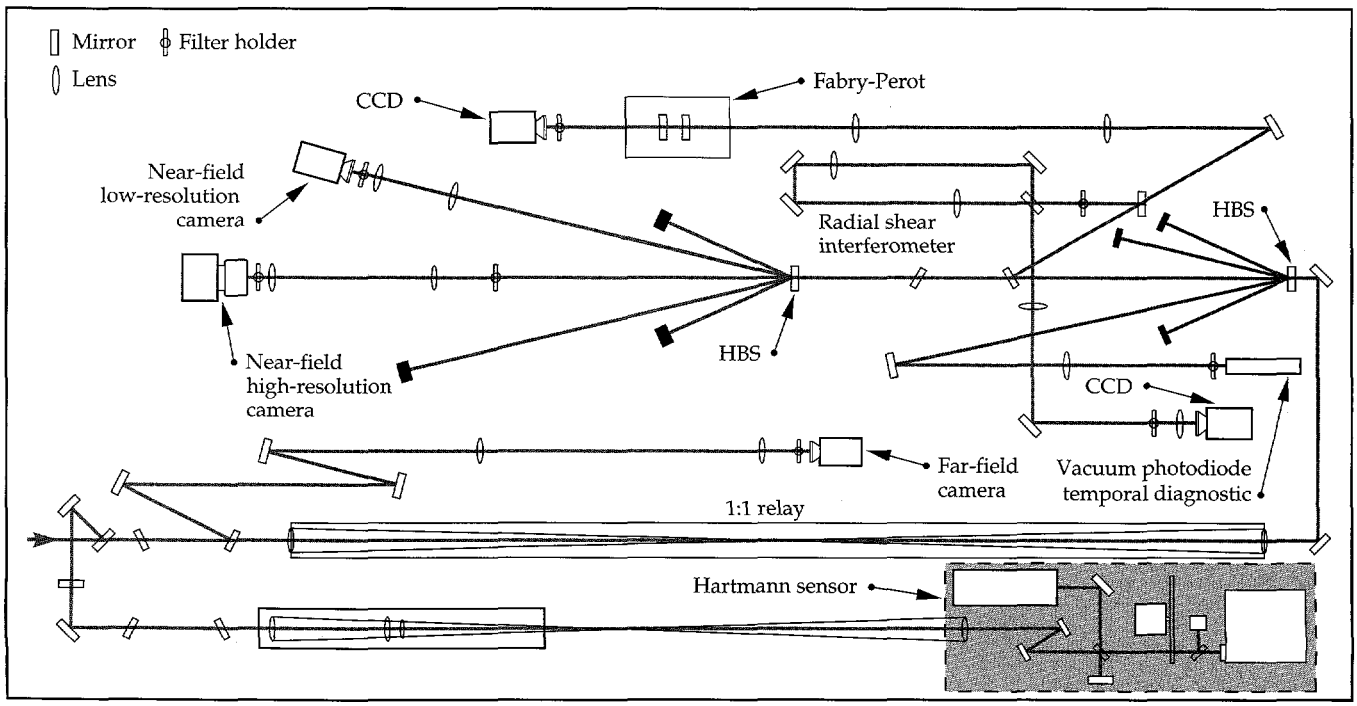

FIGURE 5. Beamlet 1ω output diagnostics include near- and far-field imaging, temporal pulse shape, wavefront, and beam bandwidth. The wavefront control system output sensor (Hartmann sensor) is also located on this table. (See Fig. 4 for the 1ω energy measurement.) (70-50-0395-0666pb01)

2ω/3ω Output Diagnostics

The 2ω/3ω diagnostic transport optics demagnify and relay all three wavelengths to the specific diagnostics as shown in Figs. 7 and 8. The transport optics use a bare-surface silica splitter identical to the 1ω splitter, except the back surface has a 3ω sol-gel AR coating. The splitter is oriented with a 25° angle of incidence, "P" polarized, with the diagnostic beam directed through a 900-cm focal length (at 1ω) Beamlet spatial filter lens. The converging beam is passed through a 40-cm wedged silica splitter (the calorimeter splitter) with the uncoated front surface reflection sent to the energy balance calorimetry station (described below). The beam transmitted through the calorimeter splitter, which is AR coated on the back side with a compromise 2ω/3ω coating, is reflected in plane by a combination bare surface silica splitter and a 1ω/3ω high reflector in the lower vertical fold location. The converging 1ω/2ω/3ω beams are then sent through the 3ω splitter, with a sample of the beams split off by the uncoated front surface, folded by 1ω/3ω high reflectors, and sent to the 3ω diagnostics. The beams are similarly folded to the 2ω diagnostics with that splitter being a high reflector at 2ω, and the folding mirrors being at least 95% reflective at both 1ω and 2ω to relay the 1ω alignment beam to the 2ω diagnostics. The remaining beam, transmitted through the 2ω splitter, is relayed to a Cohu CCD camera and is used for system alignment.

The 3ω beam was thoroughly diagnosed, with two near-field cameras, a far-field camera, a vacuum photodiode temporal diagnostic, and a streak camera temporal diagnostic. The energies were measured in the energy balance diagnostic station. The 2ω beam near-field profile was also diagnosed on a regular basis. Schott filters [UG-5, KG-10, and VG-11 (a nonfluorescing filter glass

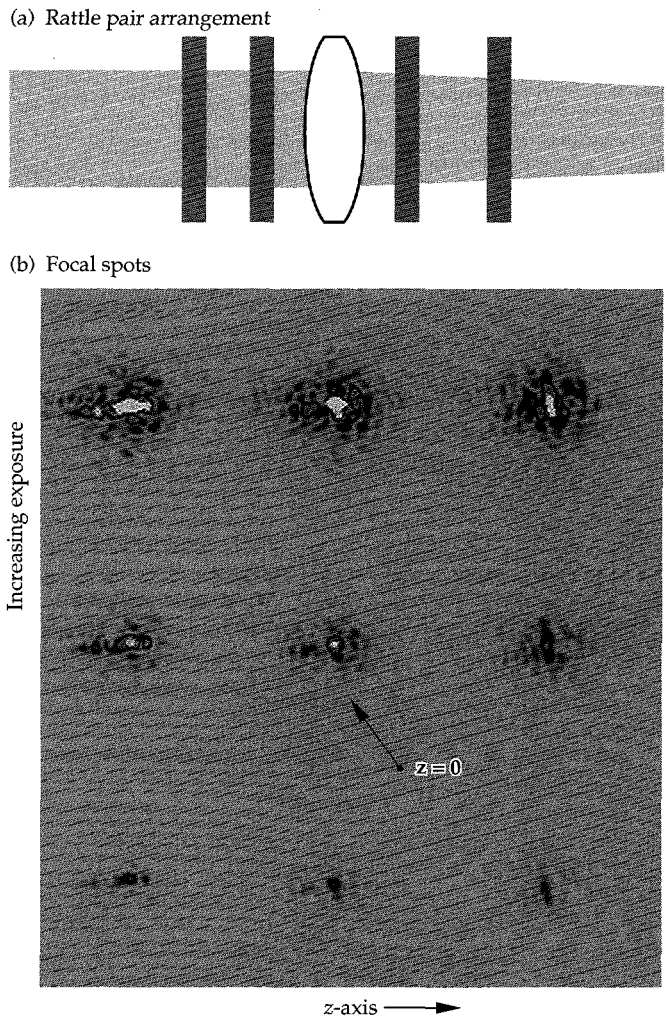

FIGURE 6. Two mirrors arranged as "rattle pairs" and a focusing lens (a) project an array of focal spots onto the high-resolution CCD camera. These focal spots (b) are graded by intensity in one dimension and are different focal planes in the other dimension. (70-50-0395-0667pb01)

FIGURE 7. The doubled and tripled beam is focused and folded using uncoated and dichroic reflectors, and collimated after focus. The 1ω light is transported to all locations for alignment purposes. A vacuum cell is not required, as the beams are attenuated sufficiently before focus. (70-50-0395-0668pb01)

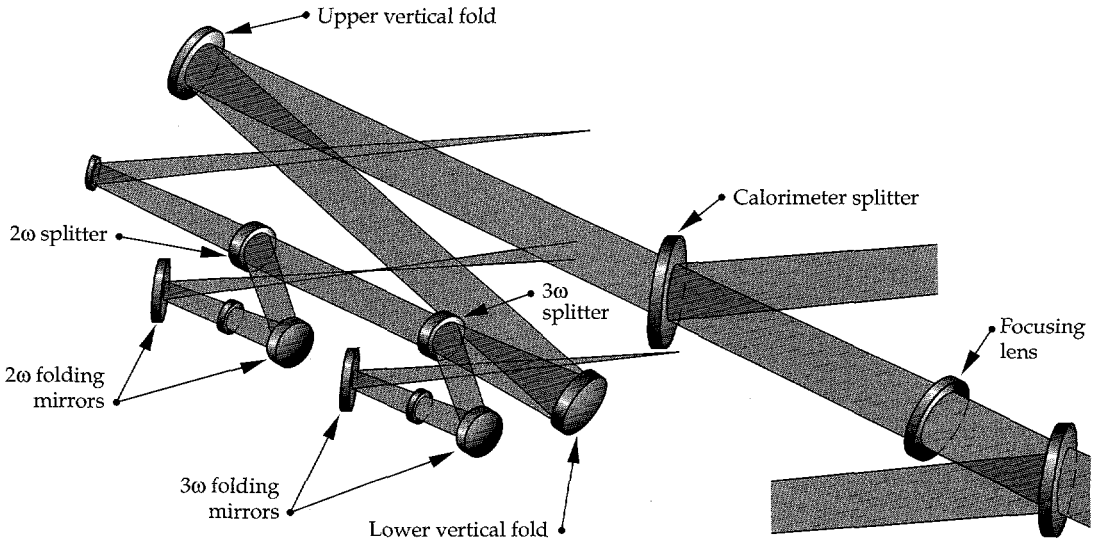

for blocking 3ω)] were used to perform color separation of each diagnostic. We set the energy levels at each diagnostic using attenuating mirrors located just beyond the folding mirrors and by manually inserting neutral density filters.

The 2ω/3ω diagnostics station transport optics use the 1ω alignment beam to perform pointing and centering for 2ω and 3ω diagnostic paths. We employed dichroic transport mirrors to transmit sufficient 1ω light intensity, an achromatic relay system, and a manually insertable collimation lens (Fig. 8). The design worked well for alignment, but did not determine the near-field camera image planes. The depth of focus at the aperture size of the Cohu 6400 series camera is very small, so calculated locations could not be practically used. A temporary alignment beam, a tripled Nd:YAG, injected into the output spatial filter solved this problem. We located the tripler array image plane on each camera at its design wavelength. Another complication was that the pointing for the three wavelengths was slightly different after passing through the wedged optics, including the large calorimeter splitter. For high angular resolution far-field imaging, we offset the alignment focal spot so that the shot focus would fall within the camera's field of view.

Energy Balance Diagnostics

An accurate energy balance is extremely important to understanding Beamlet operation. A good measure of the absolute energy in each of the three wavelengths, following frequency conversion, impacts decisions and conclusions on frequency converting crystal orientation, 1ω beam divergence, conversion efficiency, and a host of other laser and frequency conversion parameters. Figure 9 shows the energy balance calorimetry station. The beam from the main 2ω/3ω uncoated silica splitter is directed to the dispersing prisms after passing through the focusing lens and reflecting from the uncoated silica calorimeter splitter. We used two uncoated silica prisms, each with a 40° apex angle, to achieve a total deviation of 38.9°, 39.9°, and 41.4° for the 1ω/2ω/3ω beams, respectively. We use two prisms instead of one because of the thickness limitations of commercially available silica blanks. The pair of prisms are located at a distance

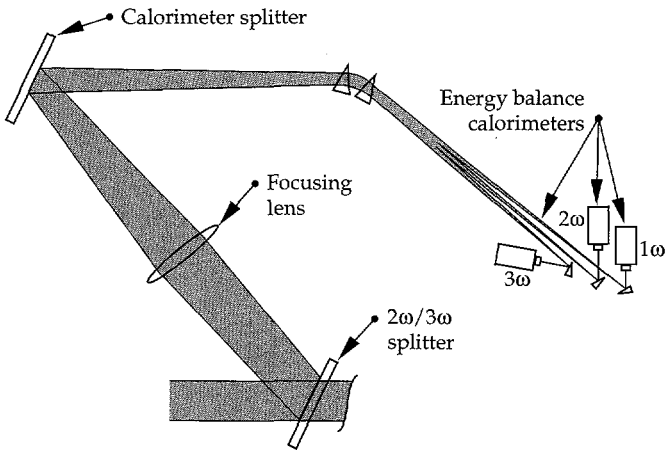

FIGURE 9. The Beamlet energy balance diagnostic relies solely upon uncoated surface reflections to attenuate the beam below 1 J into the calorimeters. Chromatic dispersion is accomplished with two 40° uncoated fused silica prisms, with the total path attenuation calculated from the measured beam incident angles. The sum of the calorimeter energies is routinely within ±2% of the 1ω output calorimeter. (70-50-0395-0670pb01)

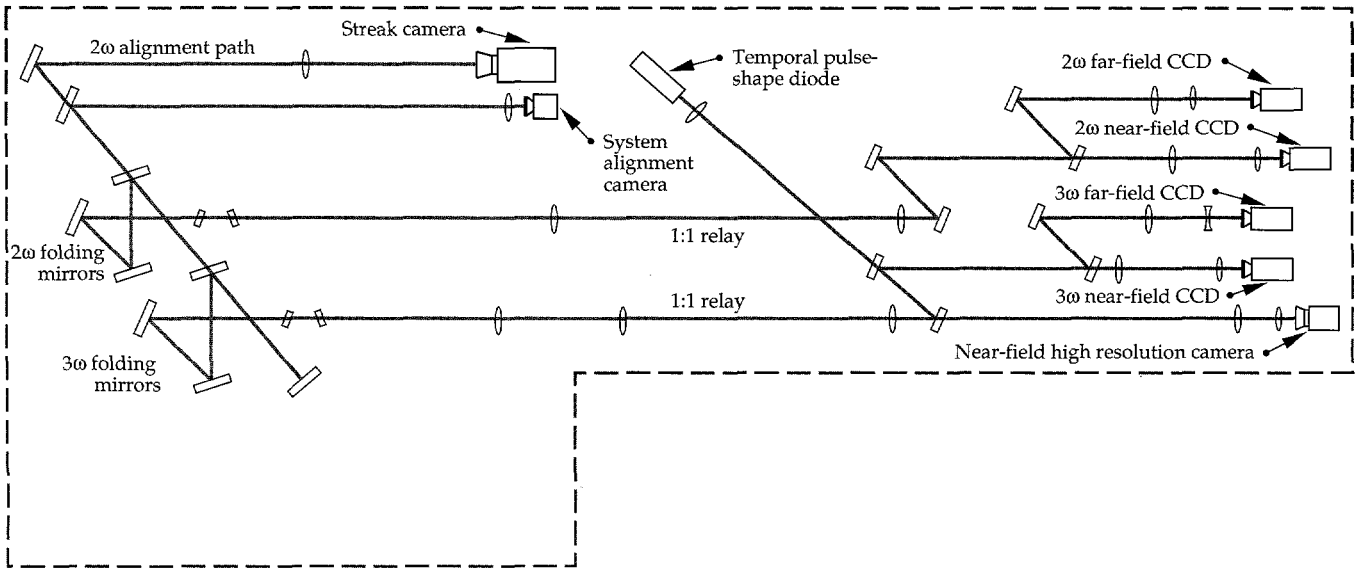

FIGURE 8. Beamlet 3ω diagnostics consist of near- and far-field imaging and temporal pulse-shaping, as well as housing the system alignment camera. (70-50-0395-0669pb01)

from the focusing lens where the beam size allows them to be reasonably small, yet far enough from the calorimeters such that the beams become sufficiently separated. The prisms are mounted on rotation stages with 1 min of resolution, and are aligned to a 30° angle of incidence from the input beam. The dispersed, converging beams are then propagated to a series of uncoated silica 20° wedges that direct the beams into a calorimeter for each of the three wavelengths. We chose the final wedges to ensure that only the first surface reflection would be reflected into the calorimeter.

Altogether, the converging beams undergo three uncoated reflections and are attenuated by about 2×10^{-5} to avoid the possibility of damage to the calorimeter absorbing surface. Using the 1ω alignment beam, all three calorimeters were aligned by rotating the dispersive prisms by a prescribed amount to deviate the 1ω beam along the 2ω path or 3ω path, respectively. The distance used from the main focusing lens is a calculated value. We used exposed polaroid film in a plastic cover taped over the calorimeter input apertures to confirm the beam size and alignment on a shot. The beam size and locations were exactly what we specified. On the system shots, the sum of the energy balance calorimeters and the other two output calorimeters agreed to well within ±5% (described in the calorimetry section).

Beam-Dump Calorimetry

Figure 10 shows the beam-dump calorimeter—the final diagnostic on the Beamlet beam that absorbs all the remaining 1ω, 2ω, and 3ω light. After the main Beamlet beam goes through the 2ω/3ω splitter, it passes through a silica beam expander lens and on to the beam-dump calorimeter. The unit has a 74-cm square aperture, and uses Schott NG-4 glass to absorb all three wavelengths without being damaged by the maximum fluence of any of the wavelengths during the various phases of Beamlet operation.

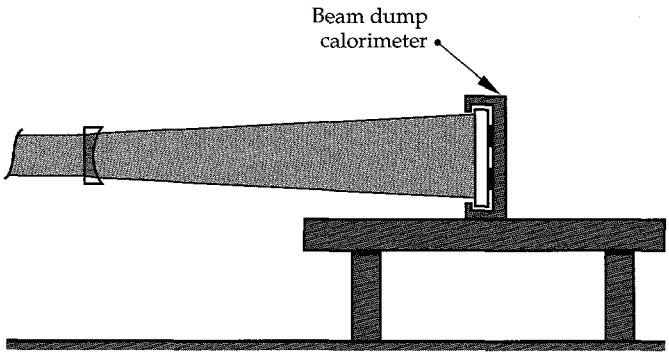

FIGURE 10. Diverging silica lens directs the remaining 1ω/2ω/3ω beam onto the absorbing glass of the beam-dump calorimeter. It is a 74×74 cm^2 design capable of absorbing and diagnosing the full Beamlet output energy at any combination of wavelengths. (70-50-0395-0671pb01)

Calorimetry and Imaging Components

The following sections describe the design, calibration, and performance of the calorimeter components and the imaging components, respectively.

Calorimetry

All of the absolute energy diagnostics on Beamlet consist of absorbing glass calorimeters. A temperature change, due to absorbed laser energy, is measured by thermocouples and is read out by precision nanovoltmeters at a 2-Hz rate. To avoid relying on one model or algorithm, we used three different calorimeter models to measure absolute energy output: (1) The Scientech model 38-0111 (a surplus from Nova) obtained from the Optical Sciences Laboratory; (2) the Scientech model 38-0101 with NG-1 and NG-4 glass to use at all three wavelengths after the frequency converters; and (3) the beam dump calorimeter to absorb the full Beamlet output at all three wavelengths, installed in the main beamline following the fused silica expansion lens.

1ω Output Calorimeter

The calorimeters in the cavity diagnostics and the 1ω output diagnostic stations are 1-in.-aperture Scientech model 38-0111 that have a $1/e$ decay time of 160 s. The voltage from these devices is of the order of a few to several hundred microvolts, with a sample voltage waveform shown in Fig. 11. To determine the incident energy, the step voltage as determined by the difference between two linear fits (see Fig. 11) was multiplied by an experimentally determined calibration factor. The preshot baseline fit was performed over a

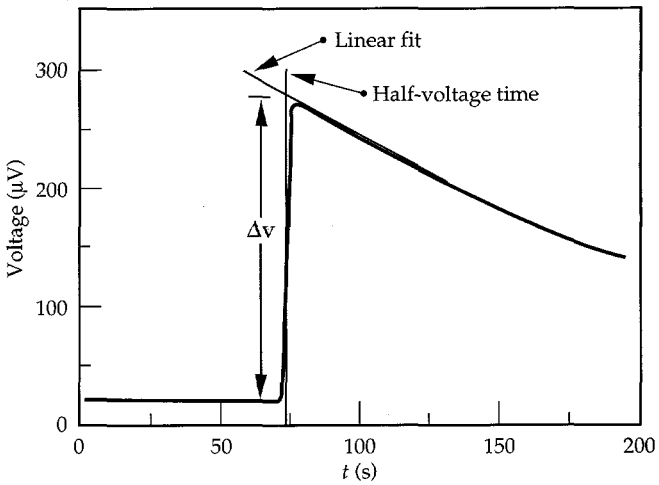

FIGURE 11. Calorimeter waveform for an 8.85-kJ shot. The voltage step is determined between two least-square line fits before and after shot time. The voltage difference is calculated when the rising edge is at the 50% level. Shot energy is then inferred from the calorimeter calibration and optical transport attenuation. (70-50-0395-0672pb01)

60-s interval prior to shot time, and the post-shot fit over a 90-s interval starting 7 s after the shot. This gave the energy on the calorimeter, and the energy in the main beam was inferred from the calculated and measured transmission coefficients of the transport optics.

We used two methods to calibrate the model 38-0111 calorimeter: (1) Using the electronic heater in the calorimeter head for electronic calibration, and (2) by comparison to an optical calorimeter transfer standard from the National Institute of Standards and Technology (NIST). To perform the electronic calibration, we measured the internal heater resistance using the 4-wire technique, then injected a known current over a precise time interval. The amount of injected energy was simply

$$E = I^2 R \Delta t \,, \tag{1}$$

where I is the injected current, R is the heater resistance, and Δt is the current pulse width. The voltage waveform was captured in the voltmeter measurement buffer (512 measurements long) and analyzed using the Macintosh/LabVIEW systems. The analysis program automatically finds the shot time by searching for the step change and calculating the preshot and post-shot linear fits using predetermined intervals prior to, and after, shot time. Voltmeter resolution was 100 nV, which corresponded to approximately 150-μJ energy resolution. After compensation for the Fresnel loss of the calorimeter's uncoated NG-1 absorber, we calculated an equivalent optical calibration factor K in microvolts/joule.

To perform optical calibration we reflected a short pulse from a Nd:YAG laser off an approximately 50% transmission beam-splitter onto the NIST transfer standard calorimeter and transmitted the remaining 50% of the beam to the calorimeter under test. The fraction of energy split to each of the calorimeters is given by

$$E_{\text{ref}} = \beta E \tag{2}$$

and

$$E_{\text{cal}} = \alpha E = KV \tag{3}$$

where α and β are unknown, E_{ref} is the energy incident upon the NIST calorimeter, E_{cal} is the energy incident upon the calorimeter under test, K is the undetermined calibration factor, and V is the voltage step for a particular shot. Manipulating these equations, a constant C_1 can be defined as

$$C_1 = K\frac{\beta}{\alpha} = \frac{E_{\text{ref}}}{V} \,. \tag{4}$$

A series of measurements of E_{ref}/V determined C_1. Then, the NIST calorimeter and the calorimeter under test were exchanged such that the NIST calorimeter was on the αE split and the calorimeter under test was installed in the βE split. Another series of measurements of E_{ref}/V determined constant C_2, which was similarly defined as

$$C_2 = K\frac{\alpha}{\beta} = \frac{E_{\text{ref}}}{V} \,. \tag{5}$$

The calibration constant for the calorimeter under test was then determined from

$$K = \sqrt{C_1 C_2} \,. \tag{6}$$

Note that this calibration technique is entirely independent of the shot-to-shot repeatability of the laser source, does not require knowledge of the splitter ratio, and does not require that the splitter and transport paths be lossless ($\alpha + \beta$ does not have to equal 1). The optical and electrical calibrations are in excellent agreement between the two techniques (±1.5%).

Energy Balance Calorimeters

The Energy Balance Calorimetry station uses the 1-in. Scientech model 38-0101. It has a $1/e$ time constant of 16 s, which is too fast to use the linear extrapolation method previously described. For these calorimeters, the main problem with backward linear extrapolation is the extreme sensitivity to shot time determination. Therefore, we used an alternative method, where we integrate the area under the curve—the volt-seconds of the voltage waveform. As before, we use an edge-detection algorithm to find shot time and then integrate over a 70-s interval starting at shot time (the same used for calibration). An issue with these calorimeters is the baseline drift, due to temperature fluctuations within the laser bay, similar to the slower model 38-0111 calorimeters. The baseline drift is quantified using an algorithm to interpolate between the baseline value

measured before and after the laser shot. The incident energy is then calculated from the total integrated calorimeter signal voltage (minus the correction for baseline), and the integrated signal is related to the laser energy using a calibration constant.

Because of the excellent agreement between electrical and optical calibration demonstrated on the model 38-0111 calorimeters, only electrical calibration was performed on the model 38-0101 calorimeters. While the electrical calibration values were not as repeatable as the slow-decay-time model 38-0111 calorimeters, they still provided results well within the requirements for the Beamlet diagnostics.

Beam-Dump Calorimeter

The beam-dump calorimeter, designed and fabricated using Nova's 74-cm calorimeter as a guide, absorbs the full Beamlet energy at all three wavelengths. The main absorbing element is a 76-cm-square, 0.25-in.-thick Al plate, tiled with 4-mm-thick, 6-in.-square panes of NG-4 absorbing glass. The glass thickness was selected to attenuate incident 1ω energy to <25 mJ/cm^2, which is 10% of the level at which damage to the glue holding the absorbing glass has been known to occur. For this reason, we chose 4-mm-thick NG-4, which is just sufficient for full energy 1ω shots, yet has enough absorption depth at 2ω and 3ω full-energy shots to avoid surface damage. The sensing elements are type K thermocouples glued in a 7×7 array on the back side of the Al plate, wired to reference thermocouples attached to a dummy plate located in the back of the calorimeter body. The thermocouples are standard types from Omega, and are glued to the Al using a high-thermal-conductivity epoxy and are electrically wired in series using similar-metal terminal blocks. The only unwanted thermocouple junctions are where the output connector copper wires connect to the first and last thermocouple leads on one of the terminal blocks. Those connections are adjacent to minimize temperature differences. The entire absorbing plate assembly is mounted using insulating spacers to a support structure, designed to provide protection from air currents.

We use NIST traceable standards and a high-power laser to perform full-scale optical calibration in the Nova calorimeter calibration facility. To achieve reasonable signal levels, approximately 500 J in 1 s was directed onto the calorimeter in a round beam (unlike the square Beamlet beam). This was sufficient to obtain about 70 μV for calibration, and resulted in a calibration factor of 0.1417 μV/J. This calibration factor was about 2% higher than that determined using standard Nova waveform analysis methods, a difference due to how the voltage waveforms are interpreted. In Nova, the voltage step is calculated by the difference between the peak of the voltage waveform and the extrapolated baseline. For Beamlet, the voltage step is calculated by the difference between the linear least-square fit of the baseline before the shot, and the linear fit of a waveform segment after the shot. This difference is calculated at the time when the voltage waveform is half of its peak value. The Beamlet analysis technique has the advantage of averaging many measurements during the voltage waveform decay.

Calorimeter Performance

The performance of the calorimeter system was repeatable to better than ±2% for the model 38-0101 calorimeters and approached ±1% for the model 38-0111 calorimeters during calibration. To test this, we compared their performance during system operation using calculated and measured transmission values to propagate the energy results back to "standard" beamline locations. Comparison between the 1ω output calorimeter and the energy balance calorimeters was done at the first surface of the 2ω/3ω calorimeter splitter. Comparison between the energy balance calorimeters and the beam dump calorimeter was made at the surface of the beam dump calorimeter.

Figure 12 compares the calorimeters for a series of shots taken in August and September, 1994. We met our original specification for the Beamlet calorimetry system, which was to achieve better than ±5% absolute accuracy. The most remarkable observation about the agreement is that three totally independent calorimeter systems, two separate analysis algorithms, and three separate calibration systems were used to achieve this level of accuracy. Because of this agreement, the Beamlet project scientists can report on laser and frequency converter performance with a high degree of confidence.

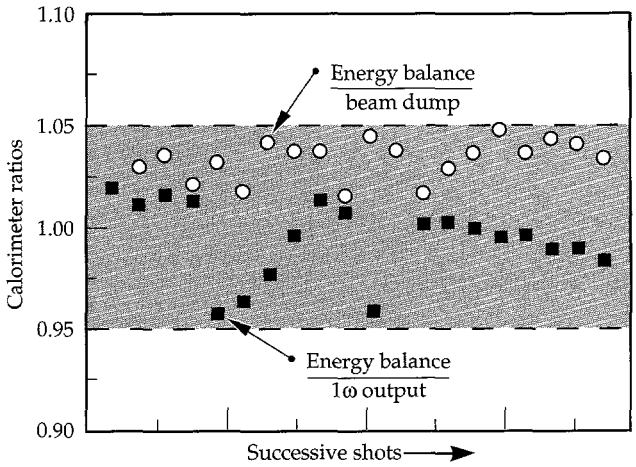

FIGURE 12. Comparison between the three output calorimeter systems for a sequential series of Beamlet shots in August and September 1994. Shown are the ratios of the measured energies between the 1ω output calorimeter, sum of the energy balance calorimeters, and the beam-dump calorimeter. In all cases, the sum of the energy balance calorimeters agrees with the other two systems to better than 5%. (70-50-0395-0673pb01)

Imaging Diagnostics

Imaging of the laser beam is done extensively on Beamlet. This is of great importance for diagnosing the beam during the four passes in the main cavity and out through the booster amplifier. In the cavity diagnostics, near-field imaging of the beam at the cavity mirrors is useful for preshot beam centering, for measuring the spatial beam profile in the various passes, and for measuring the extinction of the plasma-electrode Pockels cell during the fourth pass. In the output 1ω diagnostics, the near-field image at the frequency converter crystals is vital for ensuring that the beam intensity profile converts efficiently and that damaging intensity modulation is not present in the beam. Imaging of the beam at focus is also done in the 1ω output diagnostics to understand the quality of the beam phase-front before conversion. After frequency conversion, both near-field and far-field images of the beam at 2ω and 3ω are taken, and prove to be very useful to understanding the performance of the laser system and the frequency converter crystals. All of the images use CCD cameras/framegrabbers or dedicated high-resolution scientific-grade CCD cameras.

The standard-resolution cameras we use in all the diagnostic packages are Cohu 6400 remote head CCD cameras, which have a 6.4×4.8 mm^2 active area, and have 739 wide × 484 high picture elements. The model 6400 is a frame transfer camera, where the charge storage cell is shared between adjacent horizontal lines. Because of this, only 242 horizontal lines have shot data available for analysis from the framegrabber system. We investigated the use of the interline transfer camera, which is a microlensed CCD chip incorporated into certain models of Cohu and Pulnix cameras. The camera can be configured to integrate over 1/30 s and has the complete image frame in consecutive field transfers that can be merged in software. Another camera type from Cohu, which has a frame transfer CCD chip with dual charge storage cells, also outputs two consecutive fields (a full frame) with image data from a shot. However, it would have required development work by the manufacturer of the framegrabber/analysis system. We therefore stayed with the standard system that produces images with a spatial resolution of 240×240 pixels, digitized 8 bits deep (identical to the Nova framegrabbing system). Higher spatial resolution is somewhat of a liability because of the increased storage space requirements and slower image analysis.

We perform high-resolution imaging using a Macintosh-controlled scientific-grade CCD camera. The camera has 1024×1024 pixels digitized 14 bits deep, and is Peltier cooled to –55°C for low noise integration and readout. It is especially useful in replacing the original film-based camera systems in the 1ω diagnostics, because film has poor sensitivity at 1.054 μm. An additional advantage of the high-resolution camera is that the results are immediately available for analysis. It was also used for high-resolution surveys of Beamlet using the alignment beam, where the high dynamic range proved extremely valuable. Because of our positive experience with these cameras, we purchased an additional camera, 512×512 pixels, which has a full 16-bit dynamic range.

Data Acquisition System

The Beamlet data acquisition system consists of a SUN Sparc Station operating LabVIEW software to control all the laser diagnostics. There are six types of diagnostic devices interfaced to this system: the Tektronix TDS-320 oscilloscope and SCD-5000 transient digitizer, HP 34401A and HP 3478A voltmeters, IO-Tech digital IO box, and Kiethley 220 current source. The streak camera and high-resolution camera are operated in standalone mode, although the streak camera is initiated by the system trigger, and the high-resolution camera uses a software trigger through the IO-Tech box over the GPIB network.

The National Instruments LabVIEW control system is used to provide setup, control, data acquisition, and analysis. Before a shot, each diagnostic has to be specifically activated and in some cases software-triggered. After everything is set up, the diagnostics operator selects a particular menu item to inform shot control that the diagnostics are configured and ready for the shot. Upon initiation of the main capacitor bank charge, the diagnostics control software interprets the shot state and takes background data on all the calorimeter channels; the shot either occurs before the voltmeters run out of buffer space or else is aborted. Following the shot, the acquisition system pauses until the calorimeter voltmeters have completed acquisition and then polls the diagnostics for data. The system acquires all the data from the remote devices, stores it to disk, then retrieves it for analysis. Thus if there is a storage problem, it is discovered immediately and steps can be taken to retrieve the data again from the instruments. Data analysis is limited to basic waveform analysis of the energy diagnostics, calculation of the round-trip cavity system gain, and display of the oscilloscope traces.

Imaging diagnostics, other than the high-resolution camera, is operated by the Coherent Big-Sky system,[4] which performs framegrabbing on 16 channels, simultaneously. All of the cameras in the diagnostics system are routed to the 30×30 video switcher, which supplies the video signals to the Big-Sky system. The Big-Sky system receives a system trigger to select which frame to grab. After the shot, the diagnostic operator manually saves the results on the Big-Sky computer and transfers the video files to the SUN system for storage and archiving.

Summary

We developed a comprehensive set of diagnostics for the Beamlet laser system to provide all of the information necessary for determining the laser performance. Optical transport systems for demagnifying laser beam samples in four separate diagnostics stations demonstrate low-aberration performance, which is key to obtaining far-field images of the 1ω beam at the output section. The primary energy diagnostics, absorbing glass calorimeters, are installed throughout the system and demonstrate outstanding accuracy and reliability. Calibration repeatability is well within ±1%. New acquisition methods, such as using voltmeters to replace the Nova calorimeter amplifiers and analysis techniques adapted from the Optical Sciences Laser, enable us to achieve agreement between multiple calorimeters of much better than ±5%. The imaging diagnostics make wide-scale use of CCD cameras, with nearly half the number of installed cameras as the Nova system. Beamlet is also the pioneer in using high spatial-resolution and high dynamic-range, scientific-grade CCD cameras to replace film for beam profiling and far-field imaging. The diagnostics were activated on time and were key to achieving the Beamlet performance goals.

Acknowledgments

We thank the optical engineers D. Aikens, K. Moore, and W. Whistler, who designed and procured the large number and variety of optical elements required by Beamlet diagnostics. We give special thanks to R. Speck for his excellent analysis, where he compared the different system calorimeters and obtained the outstanding results shown in Fig. 12.

Notes and References

1. C. W. Laumann, J. L. Miller, C. E. Thompson, et al., *ICF Quarterly Report* 4(1), 1–9, Lawrence Livermore National Laboratory, Livermore, CA, UCRL-LR-105821-94-1, (1994).
2. P. J. Wegner and M. A. Henesian, Lawrence Livermore National Laboratory, Livermore, CA, UCRL-JC-106786 (1991).
3. LabVIEW data acquisition and control programming language LabVIEW, National Instruments Corp., 6504 Bridge Point Parkway, Austin, TX, 78730–9824.
4. Coherent Big-Sky System, an imaging diagnostics system, Coherent Inc., Instruments Division, 2301 Lindbergh Street, Auburn, CA 95602, (916) 888-5107.

Modeling Beam Propagation and Frequency Conversion for the Beamlet Laser

J. M. Auerbach

Introduction

The development of the Beamlet laser has involved extensive and detailed modeling of laser performance and beam propagation to: (1) predict the performance limits of the laser, (2) select system configurations with higher performance, (3) analyze experiments and provide guidance for subsequent laser shots, and (4) design optical components and establish component manufacturing specifications.

In contrast to modeling efforts of previous laser systems such as Nova,[1] those for Beamlet include as much measured optical characterization data as possible. This article concentrates on modeling of beam propagation in the Beamlet laser system, including the frequency converter, and compares modeling predictions with experimental results for several Beamlet shots. It briefly describes the workstation-based propagation and frequency conversion codes used to accomplish modeling of the Beamlet.

Propagation Modeling

PROP92 is the new family of single-wavelength propagation codes. It includes PROP1, a code for one-dimensional geometries; PROP2, a code for two-dimensional geometries; and HANK (derived from the HANKEL transforms), a code for circularly symmetric geometries. Multi-wavelength processes, such as frequency conversion, are modeled using other codes. Phase retardation, due to the nonlinear index of refraction, is the only nonlinear process modeled in the PROP92 set of codes. The linear processes that are modeled include bulk and reflective losses and the refractive index effects on propagation length. Amplifier gain is modeled by treating laser slabs as Frantz–Nodvick saturable amplifiers. The codes can thus model spatially varying gain, depletion of gain due to energy extraction, and saturation effects at high extraction.

The "chain editor" is a powerful feature of the PROP92 codes, which allows a complex laser system to be described using a compact, simple input format. By using simple path definitions, the laser beam can be propagated in a multitude of different paths. This is especially useful for Beamlet, which consists of a multipass amplifier cavity that uses a Pockels cell and polarizer to switch the beam out of the cavity.

A useful feature of the PROP1 and PROP2 codes is their capability to assign measured spatial distributions of gain, transmission, or phase to each optical component, which is crucial to accurate modeling of laser systems. Spatial gain distribution measurements of the interior and end slabs of the Beamlet amplifier are discussed in detail in "Design and Performance of the Beamlet Amplifiers," p. 18. (Specifically, Fig. 4 of that article illustrates the diamond, interior, and X slab configuration.) This data is stored in three files—one corresponding to the interior slab and one for each end slab configuration. In a PROP1 or PROP2 input file, each file is assigned to the corresponding amplifier slab defined in the system configuration file.

The phase aberration data consists of two main parts: (1) dynamic or "pump induced" aberrations that are a result of thermally induced distortions produced by flash-lamp pumping of the laser slabs, and (2) static distortions that arise from optical inhomogeneities in the bulk optical material or surface imperfections caused by the finishing process. Beam-steering measurements have been performed to determine the pump-induced aberrations in each amplifier slab configuration as discussed in "Design and Performance of the Beamlet Amplifiers," p. 18. The static aberrations of amplifier slabs, potassium dihydrogen phosphate optical switch and converter crystals, and other optical components have been measured using phase shift interferometry. The phase map data are stored in files and can be

UCRL-LR-105821-95-1

arbitrarily assigned as an aberration to an optical component. These phase maps range in size from 40 cm × 40 cm to 3 cm × 3 cm. The larger maps contain phase data with ripple scale lengths resolved to a few millimeters. The smaller phase maps contain phase data with ripple scale lengths resolved to less than a millimeter.

Transmission masks can also be used by the codes to simulate the effects of various apertures in the propagation path. The most important application for a transmission mask is to model a beam apodizer. For example, the input apodizer for Beamlet is a serrated aperture. The Beamlet input list references a file that holds a transmission mask for a serrated aperture.[2] This mask file was created using a code specifically designed to create serrated aperture transmission patterns.

The PROP1, PROP2, and HANK codes are also capable of including spatial filter/optical relay information. The spatial filter is the optical component used to reduce or eliminate optical component noise. It consists of a set of confocal lenses and a pinhole. The pinhole can be circular or rectangular in shape. The parameters for defining the filter in the model are the focal length of the input lens, the magnification, and the size and shape of the pinhole.

In Beamlet's front end, there is an additional beam-shaping component, called a gain compensator mask, that compensates for the amplifier slab gain roll-off due to amplified spontaneous emission. In the following examples, the gain compensator produces a spatially flat intensity distribution in the output beam. Figure 1(a) shows a calculated beam profile after it has passed through a compensator mask transmission profile, which is parabolic in the x-direction and uniform in the y-direction. The minimum transmission of the mask is 0.3 and the spatial separation between the 0.3 transmission point and the near unity peak transmission is 1.5 mm. Figure 1(b) shows the measured profile of a continuous-wave laser beam after it has passed through one of the actual masks used in Beamlet.

To illustrate the capability of the PROP92 codes, we modeled the 1.053-μm propagation through Beamlet using PROP2. The simulation corresponds to an actual experiment in which Beamlet produced 6.6 kJ of energy at 1.053 μm in a temporally flat pulse of 3 ns duration. Figure 2 shows a schematic of the laser system. The simulation starts at the serrated apodizer and ends at the input to the frequency converter. An output fluence of ~9 J/cm^2 is specified for a temporally flat pulse shape. PROP2 automatically calculates the input fluence and the temporal shape of the input pulse required for these output conditions.

In the PROP2 simulation of Beamlet, the following "real" optical component characteristics were used:

- Small signal gain profiles for the amplifier slabs,
- Pump-induced aberrations for the amplifier slabs,
- Static, large-scale (L >1 cm) aberrations for the amplifier slabs, and
- Static aberrations (L >2 mm) for the optical switch.

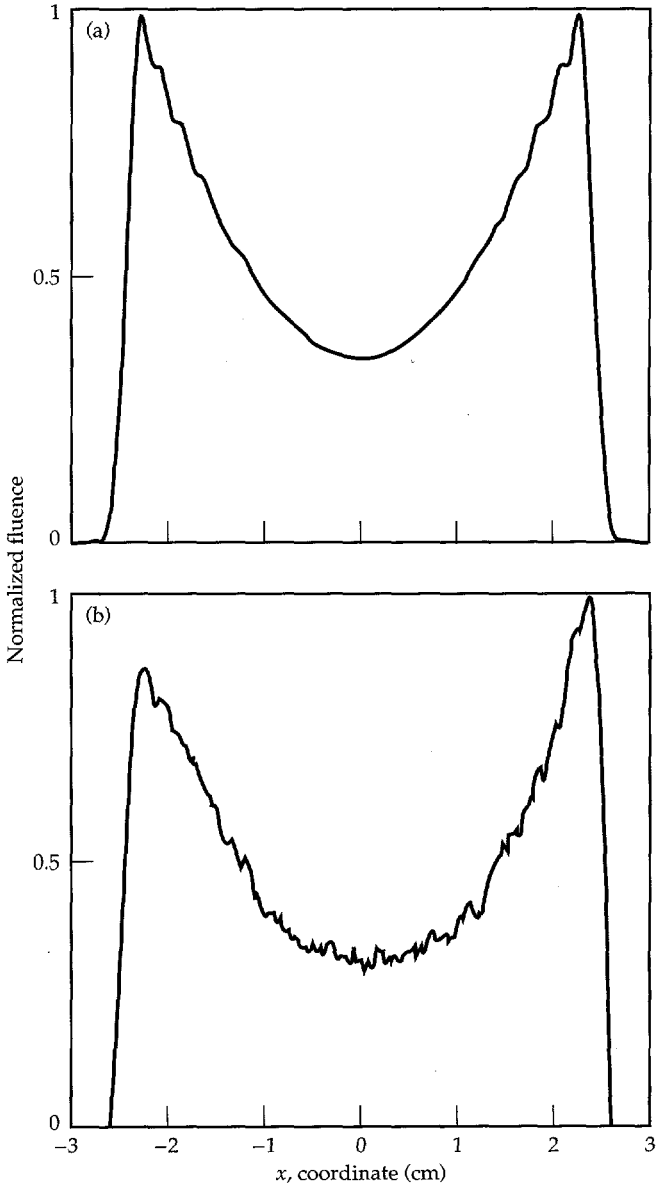

FIGURE 1. Comparison of (a) the modeled and (b) the measured transmission profiles of a continuous-wave laser beam through the gain compensation mask in the front end of Beamlet. (70-35-0195-0319pb01)

In the actual Beamlet, the amplifier slabs also have minor small-scale phase aberrations (~λ/100 peak-to-valley) that cannot be included in the modeling because of grid size limitations. Hence, we expect to see *less* small-scale modulation on calculated beam distributions as compared with actual beam distributions. In addition, PROP2 does not account for small obscurations that result from dust, scratches, or other minor imperfections in, or on, the optical components. These imperfections can lead to spikes in the fluence distribution.

Figure 3(a) shows the PROP2 calculated 1ω fluence central spatial x-profile at the laser system output, which is at the input plane of the frequency converter. The modulation at the top of the profile consists of both small- and large-scale phase aberrations. The small-scale modulation is due to the small-scale aberrations associated with the optical switch. The large-scale modulation is associated with pump-induced aberrations and large-scale static aberrations assigned to the amplifier slabs. Figure 3(b) shows the corresponding measured near-field fluence profile. Note that the measured small-scale modulation is larger than predicted with the model (not all the small-scale noise sources are included in the model). Large-scale modulation for both the measured and calculated profiles are comparable.

To further illustrate Beamlet's modeling performance, we present the calculated and measured output fluence distributions of a Beamlet high-energy shot. In this case, the output pulse has an energy of approximately 12 kJ and a 3.0-ns flat temporal shape. Figure 4 shows the calculated and measured central vertical profiles of fluence. The measured profile has more small-scale modulation than the model results since all small-scale phase noise sources could not be included in the calculation. Figure 5 shows the histogram based on calculated fluence data and the histogram based on measured fluence data at the input to the frequency converter. Note that the measured histogram has a higher peak abscissa value than the calculated histogram. We attribute the difference in the histograms to the fact that the phase noise source for the model does not contain all the noise sources that exist in Beamlet.

Frequency Conversion Modeling

To complement the PROP92 propagation codes, we have developed a family of codes to model frequency tripling in a dual-crystal scheme. The results have been

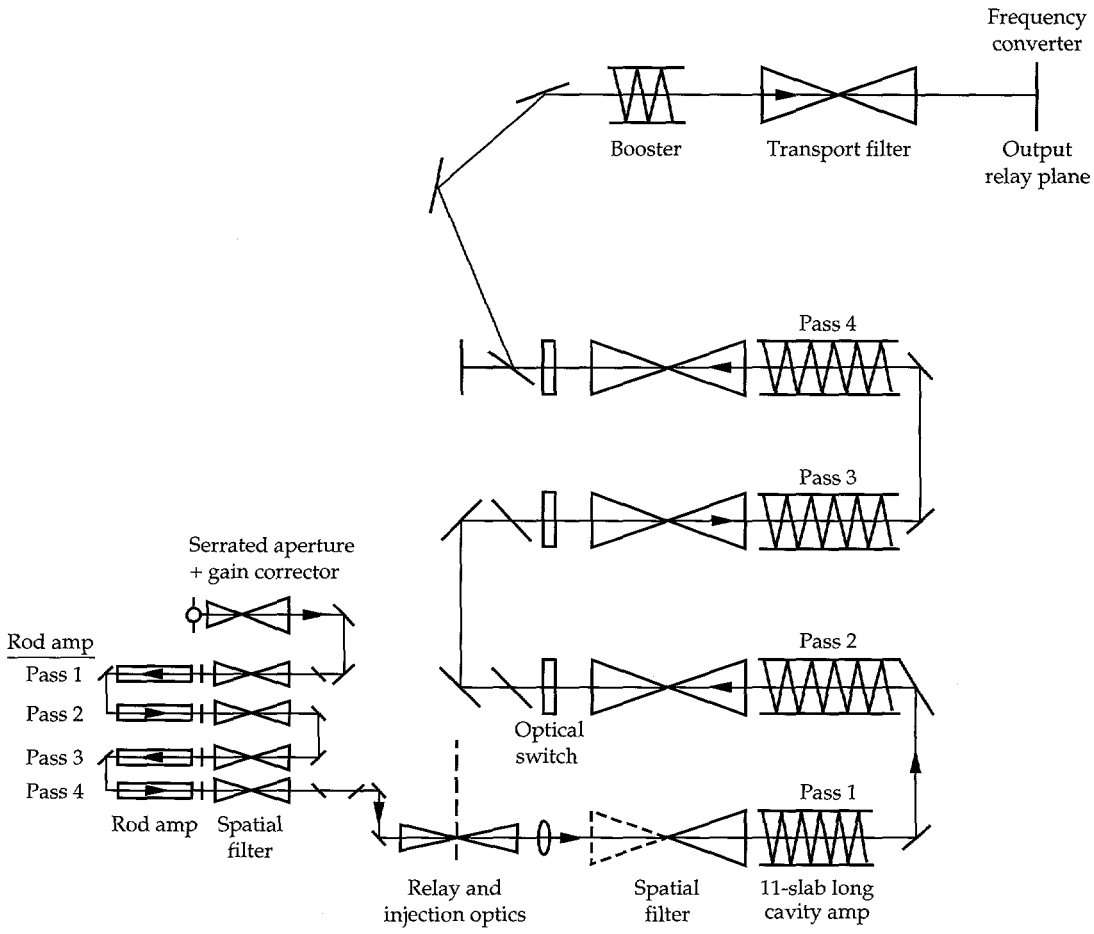

FIGURE 2. Schematic of the propagation path through the Beamlet laser system showing all the components from the serrated aperture in the front end to the frequency tripling system. This diagram shows optical components traversed by the beam during each pass. (70-35-0494-1900pb01)

in excellent agreement with the experiment. These codes have the following modeling capabilities for two-crystal conversion schemes:

- Frequency tripling of plane-wave, steady-state electric fields;
- Frequency tripling of plane-wave, time-varying electric fields—to model beams with applied bandwidth; and
- Frequency tripling of spatially varying (two transverse dimensions) steady-state electric fields—to model tripling of 1ω field distributions calculated by the PROP2 propagation code.

The codes account for the following physical processes and parameters: (1) Three-wave mixing (frequency doubling and frequency tripling), (2) nonlinear index phase retardation (B-integral), (3) paraxial diffraction and walkoff (spatially varying fields), (4) dispersion (temporally varying fields), (5) crystal bulk losses and surface reflections, and (6) crystal surface roughness (spatially varying fields). Item 6 is extremely important in modeling of 3ω beam transport after the converters. Small-scale phase ripples on the 3ω beam convert into intensity ripples by diffraction and nonlinear processes in 3ω transport optics. These intensity ripples and the associated nonlinear growth can lead to optical damage or poor focusability of the beam, or both.

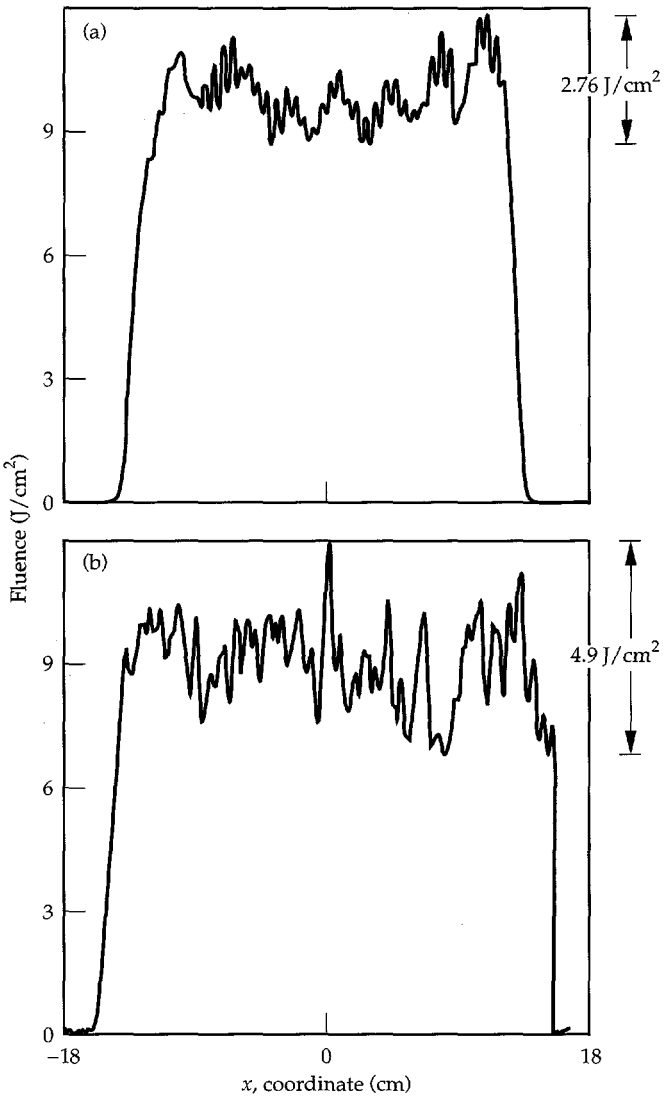

FIGURE 3. Comparison of (a) the modeled prediction and (b) the measured horizontal intensity profile at the input to the frequency converter. The predicted mean output fluence is approximately 9 J/cm² at a pulse width of 3.0 ns and energy of 6.8 kJ. This compares with the measured energy of 6.6 kJ at a pulse width of 3.0 ns. (70-35-0195-0320pb01)

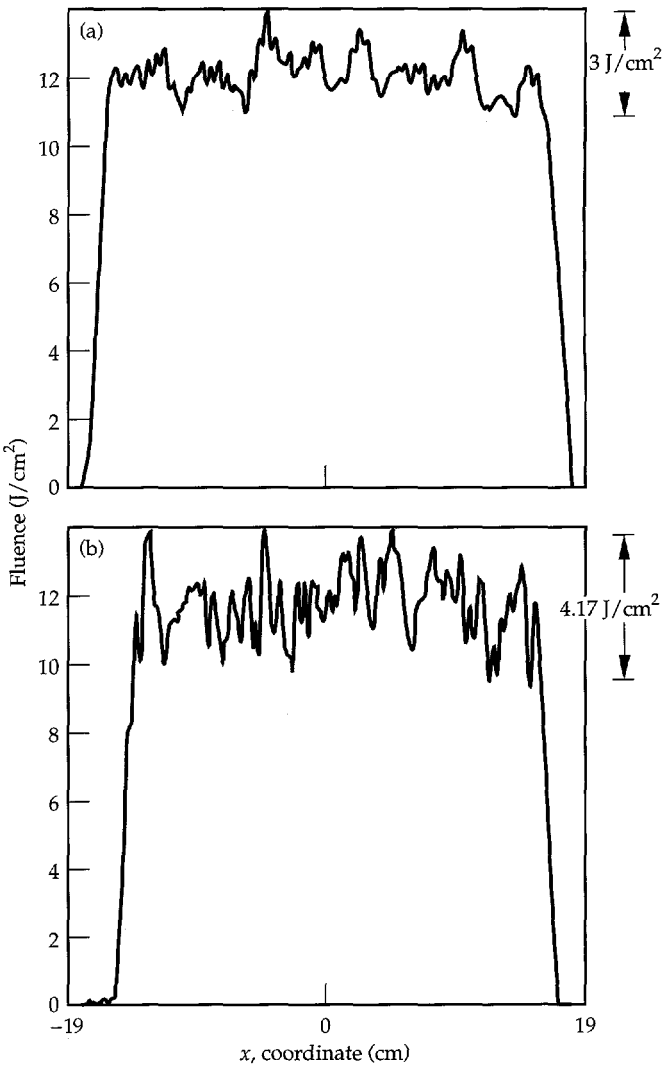

FIGURE 4. Comparison of (a) the modeled and (b) the measured horizontal intensity profile at the input to the frequency converter. The predicted mean output fluence is approximately 12 J/cm². The output pulse is temporally flat with a width of 3.0 ns and an energy of 12.6 kJ. This compares with the measured pulse of 12.0 kJ at a pulse width of 3.0 ns. (70-35-0195-0318pb01)

The time-dependent plane-wave code was used to model Beamlet's 3ω output for a 1ω temporally flat input beam that is phase modulated at 30 GHz bandwidth and has a 1ω intensity range of 2–4 GW/cm^2. Figure 6 shows the calculated 3ω conversion efficiency as a function of 1ω intensity for the case of no-added bandwidth and 30-GHz bandwidth phase modulation. It also shows the measured 3ω conversion efficiency values. The departure at high intensities between calculated and measured values is attributed to spatial intensity and phase variations in the actual beam compared with the ideal plane wave assumed in the model. Also, at high intensities, conversion efficiencies are more sensitive to crystal detuning errors. In the model, we assume a fixed set of detuning angles designed to give the maximum conversion efficiency. However, experimentally the crystal detuning angle is varied to try to achieve an optimum mix-ratio and conversion efficiency. The precision with which the crystal detuning angles can be set experimentally is limited by the accuracy of the crystal mounts and the accuracy with which the exact phase matching angle of the crystal can be determined.

We have also used the frequency conversion code that allows transverse spatial variation in the electric field to model the near-field 3ω intensity profile at the output of the Beamlet tripler. Figure 7 shows these results compared with the actual measured output. In this case, the mean input drive intensity is approximately 3 GW/cm^2 in a 3-ns square pulse and the measured conversion efficiency is about 80%. On average, the two profiles have the same amount of modulation, but their shapes are different since the calculation of the model input 1ω beam does not include all the optical component phase and noise sources that exist in the actual Beamlet laser system.

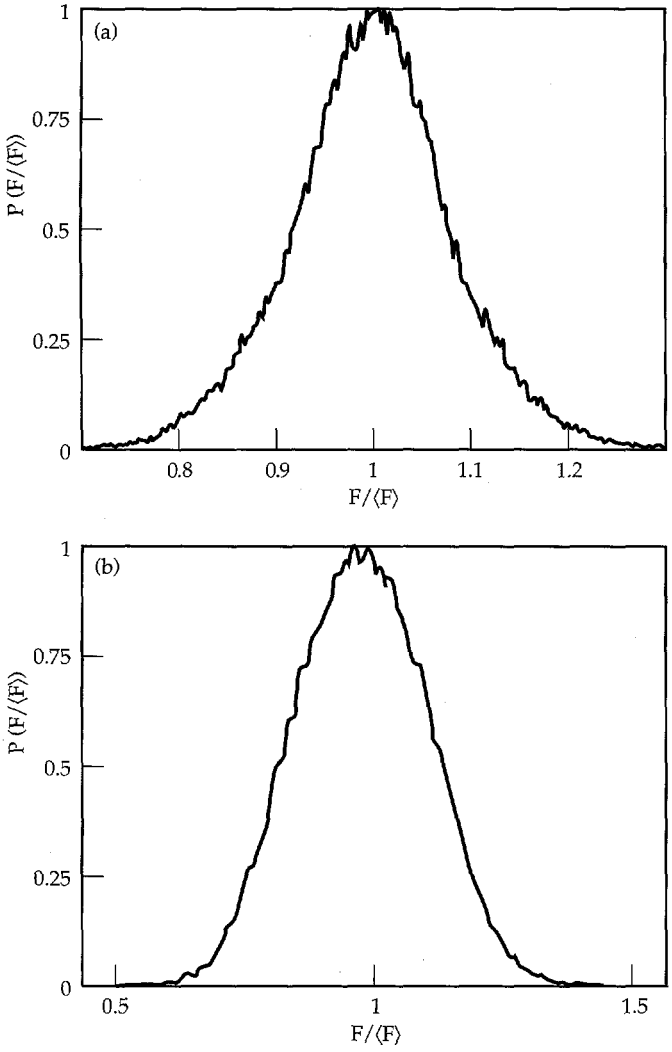

FIGURE 5. Comparison of (a) the modeled and (b) the measured fluence histograms for the Beamlet performance with a 3.0-ns temporally flat pulse with an energy of approximately 12 kJ. The histogram for the measured data has a higher peak abscissa value since the model does not include all noise sources. (70-35-0195-0321pb01)

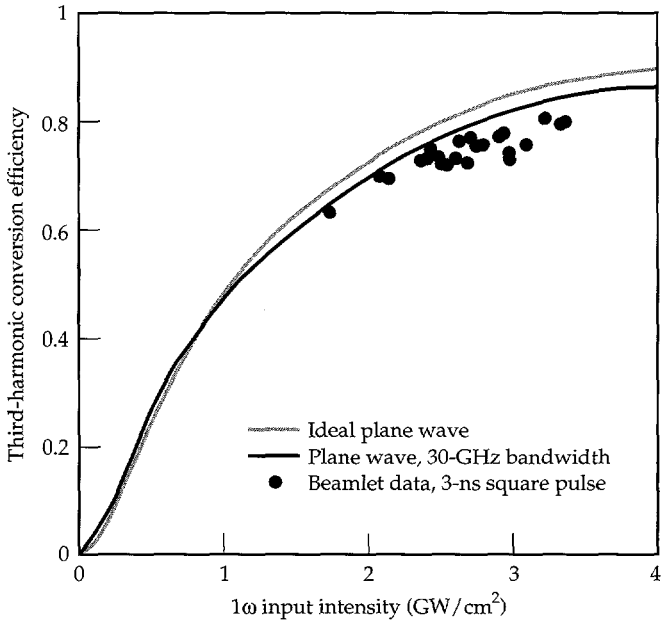

FIGURE 6. Calculated and measured values of 3ω conversion efficiency as a function of input 1ω intensity with 30 GHz of bandwidth applied to the 1ω input beam. (70-50-1094-3624pb02)

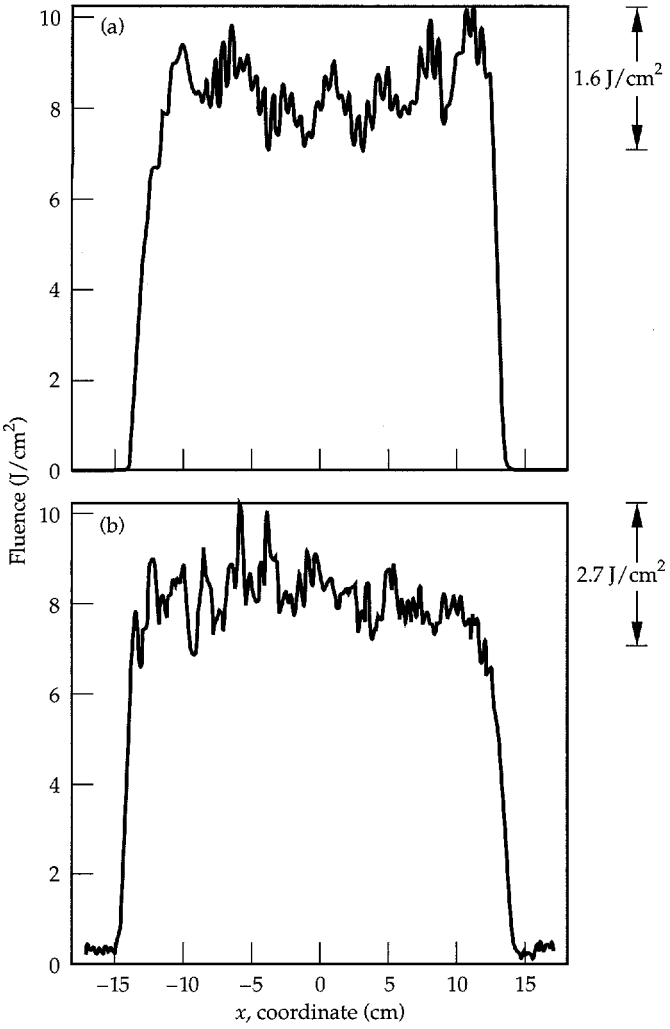

FIGURE 7. Comparison of (a) the modeled prediction and (b) the measured conversion efficiency for the 3ω fluence profiles at the output of the tripler crystal. (70-35-0195-0323pb01)

Summary

A new family of propagation and frequency conversion codes has been used to model Beamlet's performance. These codes incorporate many of the actual measured characteristics of the optical components. In general, the results of the model calculations are in good agreement with the measured Beamlet performance. The models have also proven to be a reliable tool for planning and guiding the experimental program.

Acknowledgments

The author acknowledges C. R. Wolfe, E. English, and M. Kellam for providing phase interferometry data on many of the Beamlet optics; R. Speck, B. Van Wonterghem, and other members of the Beamlet experimental team for their helpful technical discussions and for providing the experimental data that appear here; and J. Trenholme and J. Hunt for comments and input on certain aspects of this work.

Notes and References

1. W. W. Simmons, J. T. Hunt, and W. E. Warren, *IEEE Jour. Quant. Elect.*, QE-17 **1727** (1981).
2. J. M. Auerbach and V. P. Karpenko, *Appl. Opt.* **33**, 3179–3183 (1994).

The Role of the National Ignition Facility in the Development of Inertial Fusion Energy

B. G. Logan

Introduction

We have completed a conceptual design[1] for a 1.8-MJ, 500-TW, 0.35-μm solid-state laser system for the National Ignition Facility (NIF), which will demonstrate inertial fusion ignition and gain for national security, energy, and science applications. Figure 1 shows the size and scale of the facility, which is the minimum size required to achieve inertial fusion ignition. The technical goal of the U.S. Inertial Confinement Fusion (ICF) Program as stated in the current ICF Five-Year Program Plan[2] is "to produce pure fusion ignition and burn in the laboratory, with fusion yields of 200 to 1000 MJ, in support

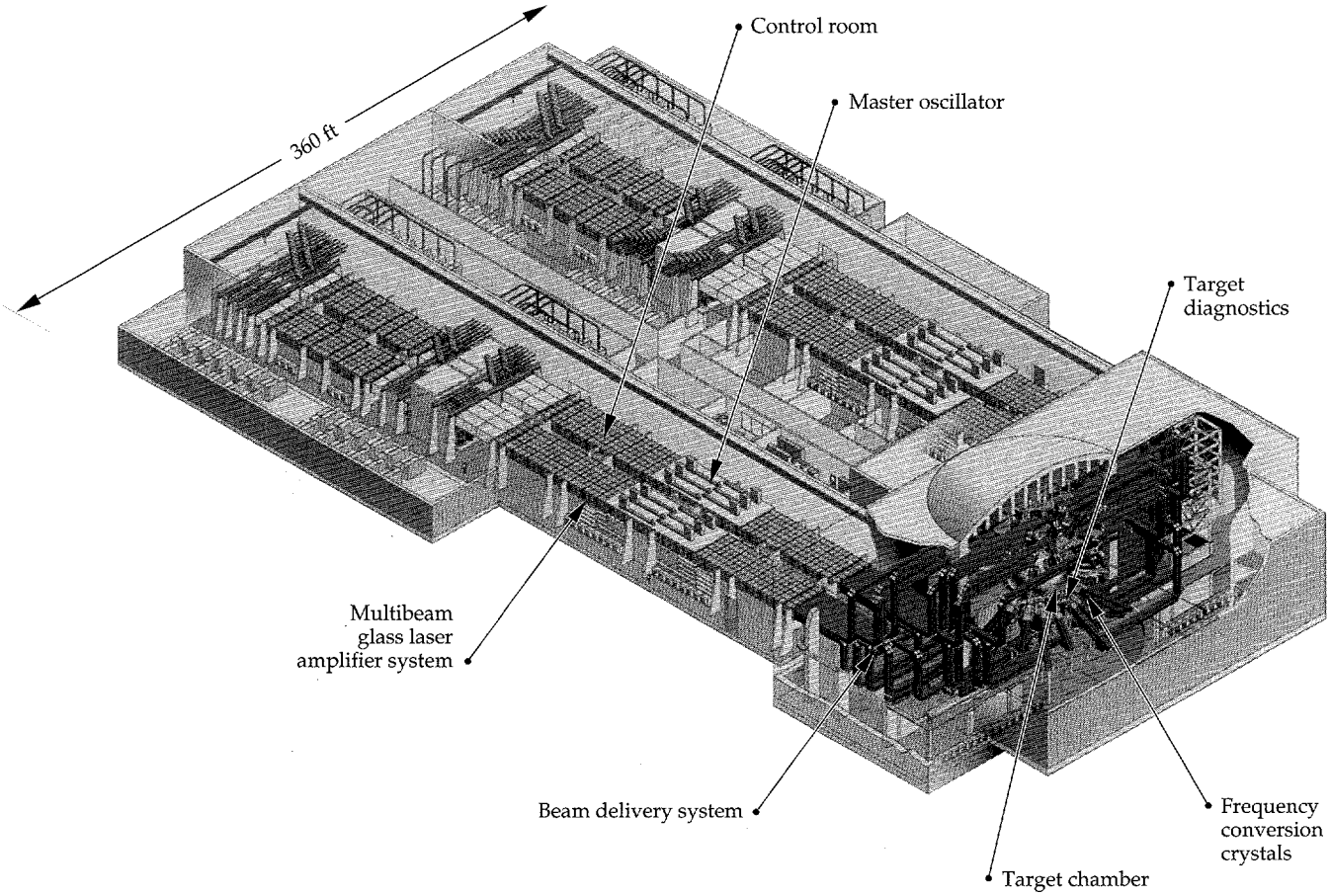

FIGURE 1. The 192-beam National Ignition Facility will demonstrate inertial fusion ignition for defense, energy, and science missions.
(40-00-0294-0498Zpb02)

of three missions: (1) to play an essential role in accessing physics regimes of interest in nuclear weapon design...; (2) to provide an above-ground simulation capability for nuclear weapon effects...; and (3) to develop inertial fusion energy for civilian power production." This article addresses the third goal—the development of inertial fusion energy (IFE).

The NIF plays an important role in IFE development. In October 1994, U.S. Department of Energy (DOE) Secretary O'Leary made the official decision (Key Decision 1, or KD1) to proceed with the NIF. The achievement of inertial fusion ignition, NIF's primary near-term goal, is a key to developing IFE. In addition, the NIF will provide the means of optimizing the conditions for minimum driver energy, power, pulse shape, and symmetry required to get ignition and gain in a cryogenic deuterium–tritium (DT) capsule. This is the most difficult and important test of the feasibility of IFE with any driver. In fact, the 1990 National Academy of Sciences (NAS) review[3] of the ICF Program recommended glass lasers, as used in the NIF, as the only driver sufficiently mature to proceed with an ignition demonstration facility (i.e., the NIF). The review also noted that ignition in the NIF would be a prerequisite to any future inertial fusion facility, even with other, future drivers.

The development of IFE requires both the NIF and a parallel development program in efficient, high-pulse-rate drivers. The NIF, due to its defense mission, is not required to provide laser pulses more frequently than several hours apart; to produce IFE in future power plants, about 5 pulses per second will be required. In addition to a higher pulse rate, an IFE power plant driver must be more efficient than the glass laser driver selected for the NIF. Thus, the NAS has also recommended continued development of other driver technology for defense and energy applications beyond the NIF. As an example, the DOE recently approved KD1 for the first half of the Induction Linac Systems Experiments (ILSE)[4] to demonstrate the feasibility of heavy-ion accelerators as a candidate IFE driver.

This article reports a variety of potential contributions the NIF could make to the development of IFE, drawn from a nationally attended workshop[5] held at the University of California (UC) at Berkeley in February 1994. In addition to demonstrating fusion ignition as a fundamental basis for IFE, the findings of the workshop, summarized later in this article, are that the NIF could also provide important data for target physics and fabrication technology, for IFE target chamber phenomena such as materials responses to target emissions, and for fusion power technology-relevant tests. The NIF's contributions to IFE in all these areas will help define the corresponding design requirements for an integrated IFE technology test facility to follow the NIF, referred to by the Fusion Policy Advisory Committee as the Engineering Test Facility (ETF).[6] In particular, tests of both direct- and indirect-drive targets on the NIF will be critical to the selection of the ETF driver and of the targets that would be compatible for the chosen ETF driver. Figure 2 shows that the NIF plays a central role in decisions for any follow-on ICF facility, including the ETF, the Laboratory Microfusion Facility (LMF),[2,7] and a possible combined ETF/LMF sharing a common driver.[8] This is true even for other driver technology options for the ETF shown in Fig. 2, since the NAS review[3] noted that the most critical target physics issues (capsule symmetry, hydrodynamic stability, and fuel mix) that would be addressed in the NIF are common to all ICF and IFE target options.

Summary of the 1994 NIF–IFE Workshop

Scope of the Workshop

Sixty-one participants from 17 U.S. organizations attended the NIF-IFE workshop convened at UC Berkeley on February 22–24, 1994. The participants were briefed on the NIF laser and target area experimental capabilities, and then were asked to identify possible experimental approaches for the NIF to address critical IFE issues apart from driver development (since drivers other than the glass laser type used by the NIF will be developed for IFE). Nondriver-specific IFE issues in the areas of target physics, fusion chambers, fusion power technology, and target technology were drawn from recent power plant studies.[9–11] Rather than test specific IFE power plant designs, the NIF experiments will be used to provide data to improve understanding of generic target and fusion chamber physics and technologies relevant to IFE. Then, by experimentally benchmarking various design codes using the NIF data, those codes could be applied to many specific designs for future IFE power plants and for defining corresponding tests in the ETF following the NIF.

The workshop participants considered possible NIF contributions in four IFE areas: target physics, target chamber dynamics, fusion power technology, and target systems. Examples in each of these areas will be discussed in the following sections. The participants considered experiments that were generally consistent with the flexibility of the NIF conceptual design.[1] However, recognizing the preliminary nature of the proposed IFE experiments, the participants recommended more

detailed designs of these experiments to adapt them to the NIF target chamber design, and to define IFE development needs prior to the possible fielding of such experiments in the NIF.

IFE Target Physics Experiments

Many of the most important target physics issues for IFE will be addressed by the planned experiments on the NIF for ICF ignition and defense sciences, using the flexibility of the NIF laser system. Each of the 192 beamlets amplify independent light input pulses, allowing significant flexibility to produce variable pulse shapes up to 20 ns and in different illumination geometries, including both direct- and indirect-drive capabilities. Figures 3 and 4 show two possible configurations of the NIF target area for indirect- and direct-drive experiments, along with some schematic examples of targets that might be tested in each beam configuration. For example, in Fig. 3, the indirect-drive target is relevant to heavy-ion IFE concepts,[11] and in Fig. 4, the direct-drive target shown is relevant to Fast Ignitor[12] and Diode-Pumped Solid State Laser[13] IFE options. Figure 4 also shows another target using the direct-drive NIF laser beam configuration that could simulate indirect-drive light-ion-type targets. The NIF ignition target physics program will explore a range of target yields and gain, studying capsule implosion characteristics and symmetry requirements, and capsule ignition and burn physics. In parallel with this effort, there will be development and benchmarking of ICF theoretical models and simulation codes also needed for the understanding of target physics requirements for IFE with laser as well as other drivers, and for direct-drive as well as indirect-drive targets.

Beyond the target physics experiments planned for the initial ignition campaign for ICF and defense applications, NIF can also perform experiments to explore target physics issues specific to IFE. Table 1 lists IFE target physics issues for generic ion and laser drivers, and for direct- and indirect-drive illumination geometries. The spaces marked with an "X" in Table 1 list those target physics issues that could be largely resolved using the NIF capabilities; the NIF can resolve most IFE target physics issues. The Omega Upgrade, PBFA II, and other ICF facilities around the world will be able to address the remaining issues. The completion of these experiments will provide the target physics basis to proceed with an ETF.

Figure 5(a) shows a typical indirect-drive target for IFE using heavy-ion drivers, compared with a typical target planned for the NIF ignition tests shown in Fig. 5(b). The heavy-ion IFE target in Fig. 5(a) is based on the work of Ho and Tabak.[14] The driver energies, target

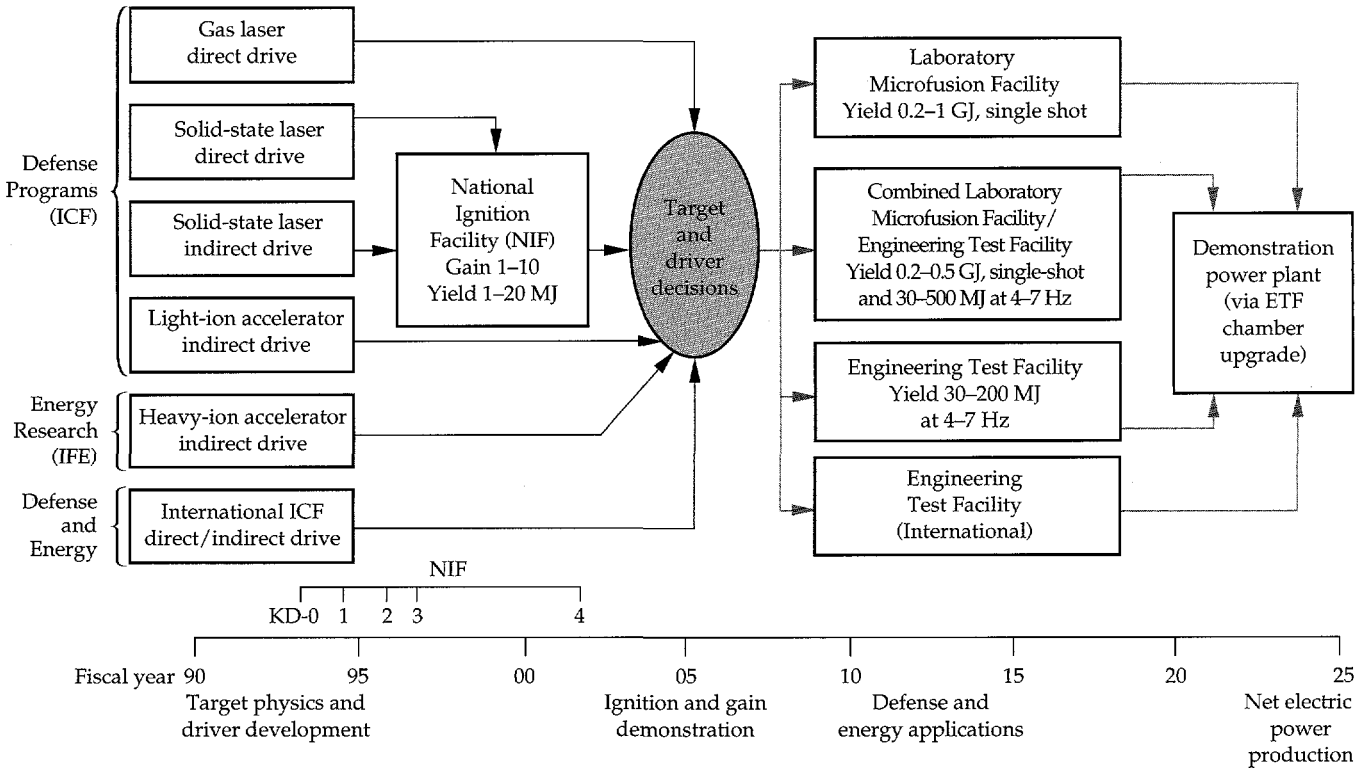

FIGURE 2. The national ICF/IFE program strategy. The NIF provides data critical to driver and target decisions for the ETF facility options, providing integrated IFE technology development. Development of a suitable chamber technology in the ETF, by upgrading one of the ETF chambers to a accommodate a higher average fusion power, can lead to a demonstration power plant by 2025. Gray lines indicate an optional path. (05-00-0295-0387pb01)

fusion yields, capsule convergence ratios, in-flight aspect ratios, capsule implosion speed, maximum compressed fuel density, and maximum hohlraum temperatures for each case are compared in the table immediately below the target cross sections [Fig. 5(a)]. The comparison shows that the NIF targets will achieve target parameters either comparable to, or more challenging than, those required for the IFE target.

Target Chamber Dynamics Experiments

Three of the basic target chamber dynamics issues of IFE identified from past IFE power plant conceptual design studies[9–11] that can be addressed on the NIF are (1) characterization of IFE target soft x-ray and debris emissions, (2) the response of first-wall materials and protective wall fluids to those target emissions, and (3) the subsequent gas dynamics of the vapor blow-off in chamber clearing, vapor condensation, and vacuum recovery. The NIF has a larger laser energy than the existing Nova laser at LLNL, so that tests of the above three issues are possible on material samples large enough to exhibit temporal and spatial scales more relevant to IFE, and at energy fluxes representative of a power plant. A typical NIF target output at a full target yield of 20 MJ will put ~48 J/cm^2 of soft x rays and target debris plasma on surfaces ~1 m away from the target, similar to the deposition from 350-MJ yields on walls ~4 m away in an IFE power plant target chamber. Thus, the NIF can provide a reduced-scale test chamber environment representative of an IFE power plant for a limited number of shots. There are also a number of one- and two-dimensional (1- and 2-D) hydrodynamics and radiation-hydrodynamics codes that could be calibrated and improved with NIF chamber dynamics data, including CONRAD,[15] HYADES,[16] SRIPUFF,[17] L2D,[18] PHD-4,[19] and TSUNAMI.[19] To acquire the data needed for these codes, NIF chamber dynamics experiments will need new diagnostics to measure the ion velocities (energies), species, and flux originating from targets, and modest improvements of existing instruments to measure gas dynamics and condensation phenomena (such as fast-response pressure transducer arrays).

Figure 6 shows an example of a possible NIF experiment designed to test the predictions of a chamber dynamics code such as TSUNAMI. The test assembly consists of a conical chamber in which a test material at the back surface is ablated by x rays that are admitted through a hole in the larger front plate. The conical shape will provide a better test of the 2-D modeling capability of the codes than would a cylindrical chamber. The high fluences attainable on the NIF will permit the use of a relatively long chamber (for longer time-scale gas dynamics) while still providing a large amount of ablated vapor from the rear surface.

The table in Fig. 6 immediately below the drawing shows how this NIF experiment is a relevant test to IFE first-wall designs (OSIRIS, HYLIFE-II and CASCADE),

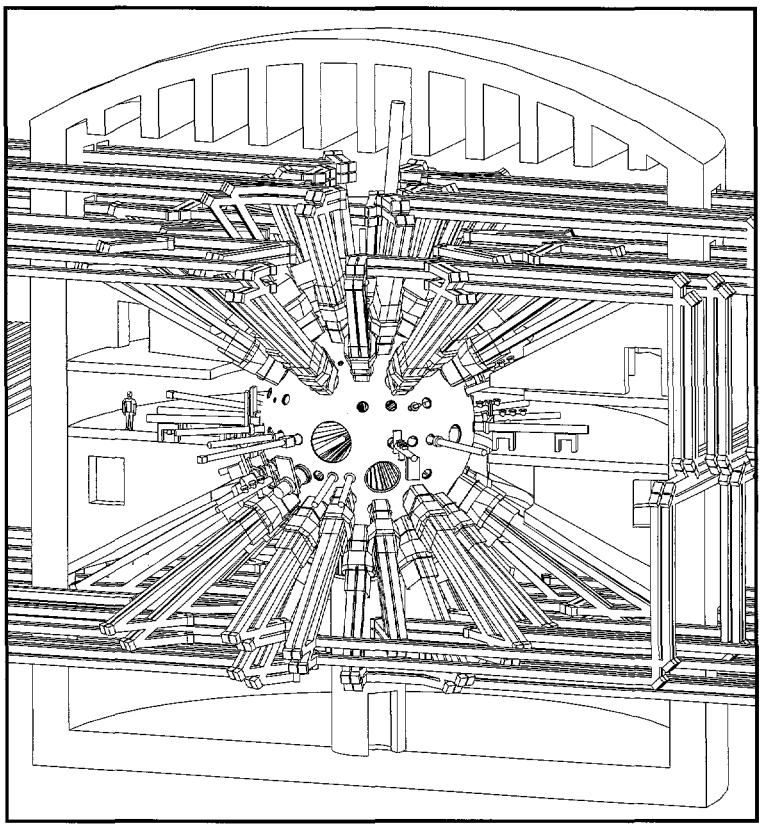

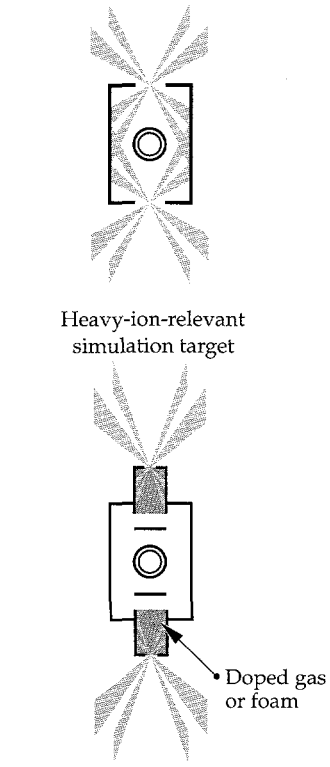

FIGURE 3. The 192 beams of the NIF configured for indirect-drive are distributed around two pairs of cones with a vertical axis of symmetry. Examples of indirect-drive targets are shown on the right. (40-00-0894-3299pb01)

in the areas of x-ray fluence, ablation depth, and time scale for the ablation of material. Passage of the expanding vapor is recorded by pressure transducers placed along the length of the cone. This information will enable the confirmation of model predictions of velocities and shock reflection strengths (from the plate at the large end of the cone). The experiment will also allow estimates of condensation rates to be obtained from the reduction in pressures at later times. Distribution of condensed material will be determined from post-shot analysis of the cone's inner surface. Examination of the ablated disk after the shot will determine the amount of material ablated, an important input parameter for the gas dynamics calculations.

Fusion Power Technology Experiments

Fusion power technology (FPT) in an IFE power plant includes components whose primary functions are energy conversion, tritium production and processing, and radiation shielding. The dominant issues for FPT in IFE power plants involve the nuclear and material

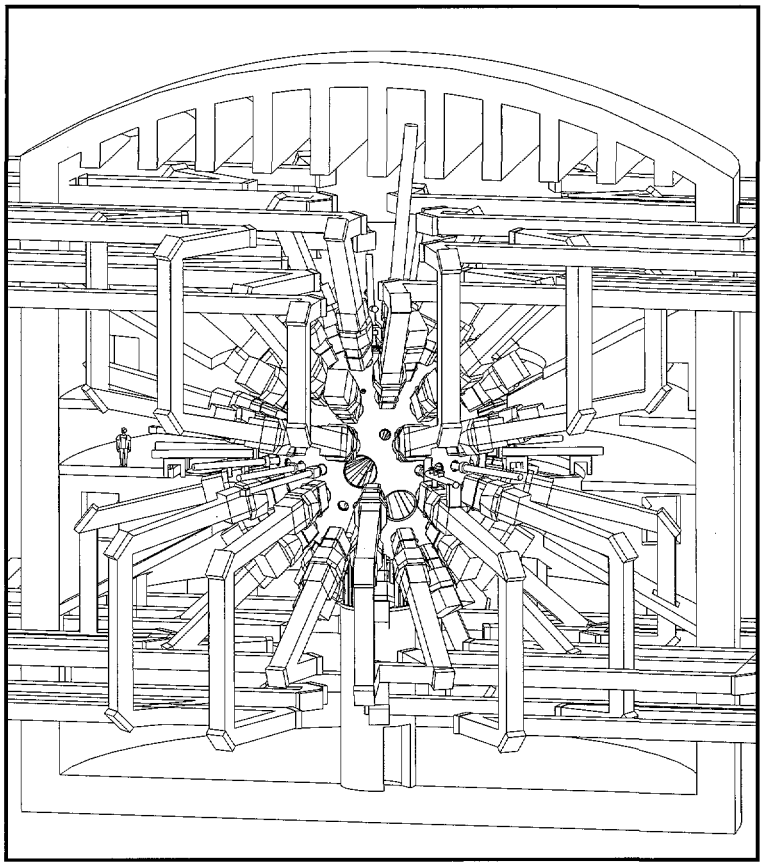

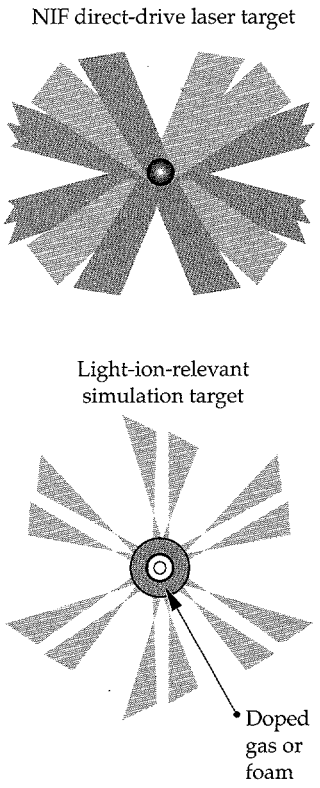

FIGURE 4. By moving 24 final beam optics assemblies to the equatorial plane and repointing each beam, direct-drive experiments with beam clusters illuminating the capsule on 48 spherically symmetric points can be performed. The light-ion simulation target is a potential indirect-drive target using a doped-foam soft-x-ray converter, but uses the NIF direct-drive-illumination configuration for symmetry reasons. (40-00-0894-3299pb02)

TABLE 1. IFE target physics issues for ion and laser drivers, direct and indirect drive. An "X" indicates issues that can be largely resolved with the NIF capabilities.

	Ion drivers		Laser drivers	
	Indirect	Direct	Indirect	Direct
Usability of a variety of pulse shapes	X	X	X	X
Radiation flow, illumination geometry, and internal pulse shaping	X		X	X
Sensitivity of capsules to radiation asymmetry	X		X	X
Materials issues (capsule, hohlraum, ablator)	X	X	X	X
Fabrication surface finish and precision	X	X	X	X
Capsule mounting and injection	X		X	X
Power vs energy trade-offs	X		X	X
Output spectra and shielding	X	X	X	X
Reduced tritium	X	X	X	X
Advanced targets	X	X	X	X

performance of components so as to achieve economic competitiveness and to realize safety and environmental advantages. The NIF will provide valuable information to IFE FPT, both with the demonstrated performance and operation of the basic facility itself and with data obtained from experiments designed specifically to test FPT issues. The NIF's relevance to FPT is in its prototypical size and configuration and its prototypical radiation field (neutrons, x rays, debris) spectra and intensity per shot. The most important limitation of the NIF for FPT experiments is the low repetition rate (low neutron fluence). The most important contributions of NIF to FPT development for IFE are the following:

1. Fusion ignition.
2. Design, construction, and operation of the NIF (integration of many prototypical IFE subsystems.
3. Viability of first-wall protection schemes.
4. Dose rate effects on radiation damage in materials.
5. Data on tritium burnup fractions in the target, some important tritium inventory and flow rate parameters, and data on achievable tritium breeding rate in samples.
6. Neutronics data on radioactivity, nuclear heating and radiation shielding.

Figure 7 depicts an example of a possible NIF experiment addressing item 3: a NIF experiment to study the recovery of a protective liquid metal film flow following the effects of pulsed heating by the target output of soft x rays, target plasma debris, and neutrons, analogous to the first-wall protective film invoked in the Prometheus study.[10] In addition to soft x rays and target debris, the NIF target would generate 10^{19} 14-MeV neutrons/shot, sufficient to test liquid jet breakup at 25 to 50 cm distance due to isochoric neutron heating representative of the liquid-wall HYLIFE-II IFE concept.[12]

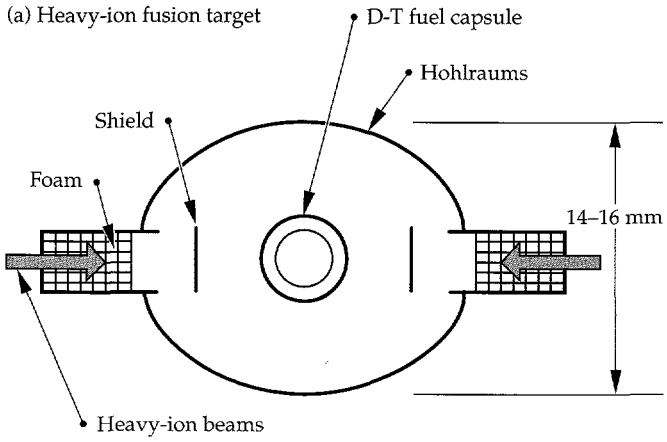

	Heavy-ion fusion target	NIF target
Driver energy (MJ)	4 to 6	1.8
Yield (MJ)	300 to 450	15
Convergence ratio	27	36
In-flight aspect ratio	40	45
Imploded speed (cm/μs)	32	41
Max density ρ (kg/m^3)	6.5×10^5	1.2×10^6
Max hohlraum temp (eV)	260	300

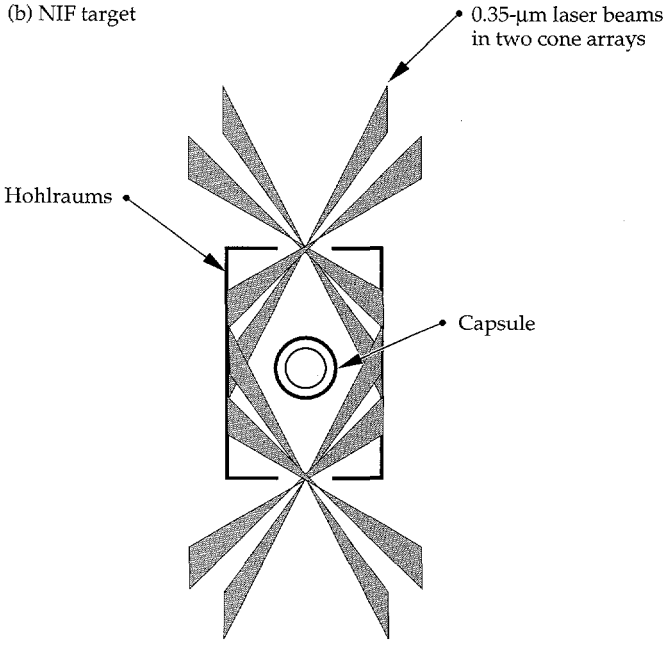

FIGURE 5. Key target parameters compared between (a) a heavy-ion target design for an IFE power plant, shown in schematic views, and (b) a typical NIF ignition target. (70-37-0894-3150pb04)

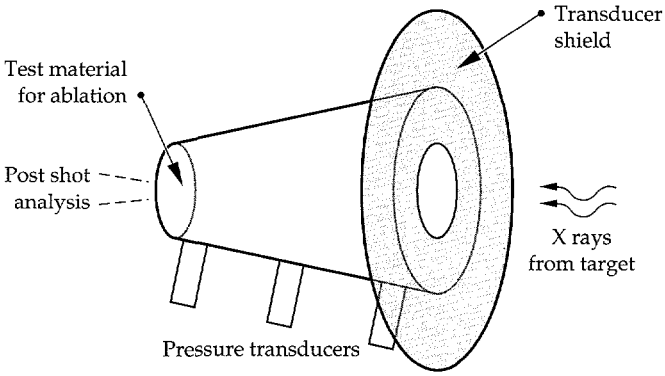

	NIF experiment	IFE first wall		
		OSIRIS	HYLIFE-II	CASCADE
X-ray fluence at radius	200 J/cm^2 0.4 m	60 J/cm^2 3.5 m	2000 J/cm^2 0.5 m	60 J/cm^2 3.1 m
Ablation	20 μm	20 μm	200 μm	3 μm
Time scale	40 μs	100 μs	50 μs	90 μs

FIGURE 6. An experiment on the NIF to calibrate gas dynamic codes. The x-ray fluence, ablation depths, and time scales for the NIF experiment shown are comparable to many cases of interest in IFE first-wall concepts. Where the parameters differ, the NIF experiments can still be useful to calibrate the computational model. (05-00-0894-3048pb02)

One of the more unique features the NIF can provide is a very high dose rate in each shot that can be equivalent to 10–1000 displacements per atom per second. Even with single shot operation, the NIF will be useful for basic physics of radiation effects in materials. Examples include cascades (morphology, size, fraction of free and clustered defects, impurities), microstructural evaluation, electrical properties, optical properties (fiber optics, coatings), and molecular cross linking. In some low-activation materials like SiC, we predict that such a large number of damage sites can be produced in each pulse that the collection of interstitial atoms produced from one damage site can combine with the vacancies created not only at that site, but also from nearby sites. This would lead to higher recombination rates of interstitial atoms with vacancies than the steady-state situation. The very high neutron dose rates provided by the NIF allow these dose rate effects to be tested.

One predictive technique that can calculate and interpret material responses to NIF neutron damage is called Molecular Dynamic Simulation (MDS).[20] MDS calculates responses at an atomic level by quantifying the response of a 3-D matrix of atoms to so-called "knock-on" atoms that impinge on the matrix from a range of angles and with a range of energies, as would result from an incident neutron flux. Potentially, MDS capabilities include predicting for a material the number of vacancies and interstitials that will result from a neutron irradiation pulse, the cluster fraction of defects, atomic mixing and solute precipitation, and phase transformations.

IFE Target Systems

The workshop separated IFE target systems topics into three broad areas: IFE target fabrication, IFE target transport, and IFE target systems. The following subsections discuss each of these areas, including some of the issues that must be resolved to successfully develop an IFE power plant, and examples of experiments that could be done in the NIF to help resolve these issues.

IFE Target Fabrication

IFE target fabrication includes target materials and configuration selection, capsule production, hohlraum production, target assembly, characterization, fill, and layering. The targets that fuel an inertial fusion power plant based upon the indirect-drive approach will be similar to the ignition and high-gain targets developed for the NIF. There are differences, however. The IFE fuel capsules will be two to three times larger in diameter. For a laser driver, hohlraums will scale similarly, but ion targets will require substantially different hohlraums and x-ray converters. As with NIF high-gain targets, IFE targets will be cryogenic. The major issues associated with developing these targets, broadly stated, are (1) assuring the target component quality specifications as sizes increase and fabrication techniques change; (2) assuring a fast enough fuel fill rate to be able to maintain the plant's tritium inventory at acceptable levels; and (3) developing fabrication and inspection techniques that produce high-quality, economically viable targets. A fourth issue, dealt with in the section below on target transport, is providing targets that can

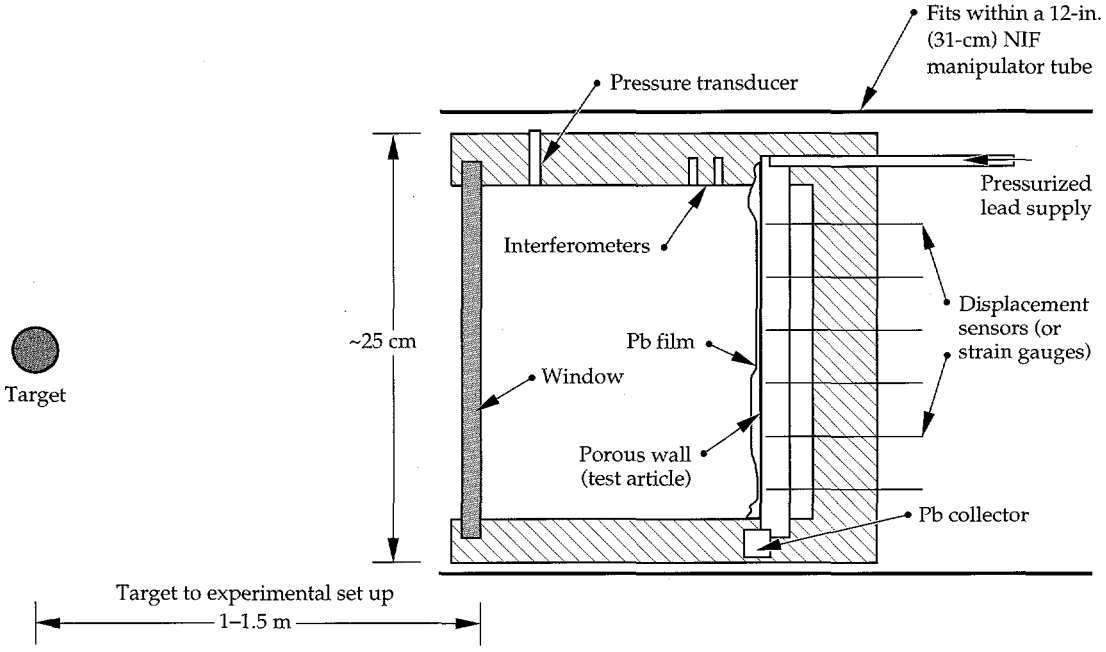

FIGURE 7. Example of a protective liquid metal film flow experiment on the NIF (not drawn to scale). The debris window might be removed to study effects of soft x rays and debris separately. (05-00-0295-0386pb01)

withstand the accelerations attending chamber injection and that can withstand the chamber environment once injected.

Table 2 lists more fine-grained issues that must ultimately be addressed to produce and use IFE targets, and an assessment of the importance of the NIF in developing solutions. Those that require full scaling to IFE sizes, such as the effect of cryogenic layer quality on gain, cannot be completely tested to ignition on the NIF. Those that do not require such scaling, such as materials choices and automated cryogenic assembly techniques, should be tested on the NIF. The NIF would be a unique test bed, since the relevant test of success is ignition.

IFE Target Transport

Under the category of target transport, we include both transport from the target fabrication facility to the target injector and the injection of the target to the point of ignition. Completed targets will be stored in a cryogenic storage system prior to transport to the injector and must be kept at constant temperature throughout the entire transport and injection process. Even after the target leaves the injector and enters the chamber environment, the allowed temperature rise of the cryogenic fuel is very low, estimated to be less than 0.2 K. Targets must also survive the acceleration process. The target transport issues for IFE are listed in Table 2. As indicated, the NIF will be useful for addressing many of these issues.

IFE Target Systems

Target fabrication and injection systems for IFE will require developments listed in Table 3. For each target development activity, Table 3 indicates whether the development is needed for the ICF ignition campaign as well as for IFE ("Needed for NIF"), needed specifically for IFE and able to be tested in the NIF ("Needed for NIF–IFE experiments"), or needed specifically for IFE beyond that which is to be tested in the NIF ("Needed for IFE"). The last column on the right in Table 3 indicates, where applicable, in which ongoing ICF program each target development activity would be included. The label "B—target fabrication development activity" indicates that the activity would be included as part of the present ICF base program for development on noncryogenic targets, and the label "D—National Cryogenic Target (R&D) Research and Development Program" indicates the activity would be part of the ICF Program to develop smooth DT cryolayer targets, initially for the Omega Upgrade direct-drive tests and later for the NIF. Some of the target fabrication issues must be faced early to field ignition targets on the NIF and will require continuation and expansion of current

TABLE 2. IFE target fabrication and target transport issues.

	NIF usefulness*	NIF uniqueness**
Target Fabrication		
Low-cost mass-production techniques for capsules and their effect on quality, materials choice and gain	2	3
Low-cost mass production techniques for laser driver hohlraums	2	3
The effect of cryogenic layer quality on gain	2	3
Automated cryogenic assembly techniques	3	3
Fast fill techniques for low tritium inventory	2	3
High-throughput quality inspection techniques	2	3
Target Transport		
Injection techniques for high-rep-rate cryogenic operation	0	1
Time and space accuracy and sensing	0	1
Integration	2	1–2
Target survival under acceleration	2	3
Thermal protection and temperature control	2	2
Chamber environment effects on trajectory	1–2	3
Demonstration of high-rep-rate operation	2	3

* Usefulness: 3 = complete resolution; 2 = partial resolution; 1 = useful information; 0 = no use.
**Uniqueness: 3 = NIF unique and required; 2 = NIF not unique but could be used; 1 = issues addressed better or cheaper in new facility; 0 = issues addressed better or cheaper in existing facility.

target development activities. The proposed testing in the NIF of IFE-relevant targets will require that those targets first be developed. Relatively little has been done in that area to date, and the workshop recommended a program of target design and fabrication R&D to have prototypical IFE targets ready for testing on the NIF. This testing will come after the NIF primary mission of ignition has been achieved, which is about 5 yr after the startup of the NIF.

Cryogenic ignition experiments on the NIF will require cryogenic target transport systems. Development of these systems will benefit greatly from work on similar systems being developed for OMEGA Upgrade. IFE will require sophisticated target injection and tracking systems that have yet to be seriously studied. IFE target experiments on the NIF will require that a portion of the development needed on these systems be done. The workshop recommended that IFE tracking and pointing studies be done now to define the systems that could be tested on the NIF, followed by development of the required hardware for these experiments. These experiments would logically follow the static tests of IFE prototype targets described above.

The NIF can provide integrated performance tests of candidate IFE targets as a function of reduced precision and manufacture cost. A series of non-ignited model targets could be injected in a 5-Hz burst, by stagger-firing 2–4 groups of laser chains ~100 ms apart, to test the repeatability of beam-target engagement accuracy in a multishot chamber environment. Since each of the 192 beamlets of the NIF can be fired separately, this type of experiment should be possible. It would also be useful to conduct experiments where uniform illumination of a target could be obtained using only a fraction (e.g., 1/4 or 3/4) of the beams.

Conclusions

The role of the NIF can uniquely cover a large and essential portion of needed IFE development in four areas.

1. IFE target physics and design/performance optimization. NIF target physics experiments with both direct and indirect drive will give us the data needed to predict the minimum driver energy, power, pulse shape and symmetry requirements for a variety of potential IFE drivers and targets.

TABLE 3. IFE target systems R&D needs.

Development Item	Needed for: NIF	NIF–IFE experiments	IFE	Current R&D activity*
Target Fabrication				
Targets for Ignition				
Ignition target design	X			A
1–3-mm capsules	X	X	X	B
High-pressure DT fill and condensation	X	X	X	C
Cryogenic layering	X	X	X	D
Cryogenic characterization	X	X	X	D
Cryogenic assembly	X	X	X	—
Targets for IFE				
IFE target design	X	X	—	
IFE target fabrication		X	X	—
Cost-effective fabrication			X	—
Target Transport				
Transport Systems				
Transport to reaction chamber	X	X	X	C
High through-put transport			X	—
Injection and Tracking				
Stationary mounting system	X	X		C
Free-fall injection	X		—	
High-speed injection		X	X	—
High-rep-rate, rad-hardened injection			X	—
Target tracking	X	X	—	
Hardened target tracking			X	—

*A = NIF design activity; B = target fabrication development activity; C = OMEGA Upgrade design; D = National Cryogenic Target Research and Development Program.

2. IFE fusion chamber dynamics and first-wall response. Using the output of ignited targets, NIF experiments will be able to characterize radiation, shock, and debris effects on various first-wall candidates and on driver/reactor interface systems, providing the data necessary to design multiple pulse and high-rep-rate experiments for the ETF.
3. IFE fusion power technology, materials science and safety. NIF experiments will be essential for calibrating and improving the predictive capabilities of x-ray, debris, and neutron emissions and their effects on tritium handling, nuclear heating, materials, and safety and the environment. The NIF facility will be prototypical of future IFE power plants in these areas.
4. IFE target systems tests of precision and performance of mass-fabricated IFE targets and high-rep-rate target-injection systems. NIF experiments can study the target manufacturing tolerances required for mass production and the positioning requirements of the injection, tracking, and beam pointing systems.

In conclusion, the NIF will be a centrally important experimental facility to support a broad range of research on the IFE development path.

Acknowledgments

The author would like to acknowledge the contributions of the 61 participants who attended the workshop at UC Berkeley on February 22–24, 1994, who provided many of the ideas forming the basis of this article. In particular, thanks go to Mike Tobin, who was a key and tireless organizer of the NIF–IFE workshop and who provided much of the written output of this workshop from which much of the article was drawn.

Notes and References

1. J. A. Paisner, *National Ignition Facility Conceptual Design Report—Executive Summary*, Lawrence Livermore National Laboratory, Livermore, CA, UCRL-PROP-117093 ES (1994).
2. *Inertial Confinement Fusion Five-Year Program Plan FY 1992–FY 1996*, DOE Office of Research and Inertial Confinement Fusion, Washington D.C., 20585, Dec. 31, 1991 (revised March 1993).
3. National Research Council, *Second Review of the Department of Energy's Inertial Confinement Fusion Program, Final Report*, (National Academy Press, Washington, D.C., 1990).
4. "Findings and Recommendations for the Heavy-Ion Fusion Program," *Report of the Fusion Energy Advisory Committee (FEAC) to DOE Energy Research Director William Happer*, DOE Office of Fusion Energy, ER-50, Germantown, Washington D.C., 20545 (April 1993).
5. B. G. Logan et al., "Utility of the U.S. National Ignition Facility for Development of Inertial Fusion Energy," *Proc. of 15th IAEA Int. Conf. on Plasma Physics and Controlled Fusion Research*, paper IAEA-CN-60 /B-P-15, Seville, Spain, Sep 26–Oct. 1 (1994).
6. Fusion Policy Advisory Committee, *Review of the U.S. Fusion Program, Final Report*, DOE Office of Energy Research, Washington, D.C., 20585 (1990).
7. *The Laboratory Microfusion Capability Study Phase II Report*, DOE Office of Inertial Confinement Fusion, DOE Office of Research and Inertial Confinement Fusion, Washington D. C, 20585, DOE/DP-0017, May 1993.
8. C. L. Olson, R. O. Bangerter, B. G. Logan, and J. D. Lindl, "ICF Driver Strategies for IFE," *Proc. of the IAEA Technical Committee Meeting on Drivers for ICF*, Paris, France, Nov. 14–18 (1994).
9. W. R. Meier (Ed.), "OSIRIS and SOMBRERO Inertial Fusion Power Plant Designs—Final Report, " W. J. Schafer Associates, DOE Office of Fusion Energy, ER-50, Germantown, Washington D.C., 20545, W. J. Schafer Associates Report WJSA-92-01, DOE Report DOE/ER/54100-1 (1992).
10. L. M. Waganer (Ed.), "Inertial Fusion Energy Reactor Design Studies—Prometheus-L and Prometheus-H," McDonnell Douglas, DOE Office of Fusion Energy, ER-50, Germantown, Washington D.C., 20545, McDonnell Douglas Report MDC 92E0008, DOE Report DOE/ER-54101 (1992).
11. R. W. Moir et al., *Fusion Technology* **25**, 5–25 (1994).
12. M. Tabak et al., "Ignition and High Gain with Ultra-Powerful Lasers," prepared for *Nov. 1993 APS Division of Plasma Physics; Physics of Plasmas* **1** (5) (1994).
13. C. D. Orth, S. A. Payne, and W. F. Krupke, "A Diode-Pumped Solid-State Laser Driver for Inertial Fusion Energy," Lawrence Livermore National Laboratory preprint UCRL-JC-116173 (1994) (to be published).
14. D. D.-M. Ho and M. Tabak, *Proc. of 15th IAEA Int. Conf. on Plasma Physics and Controlled Fusion Research*, paper IAEA-CN-60 /B-P-13, Seville, Spain, Sep. 26–Oct. 1. (Lawrence Livermore National Laboratory private communication: Tabak suggested the concept of using dense gas radiators for NIF–HIF model targets, 1994.)
15. R. R Peterson, J. J. Macfarlane, and G. A. Moses, "CONRAD—a combined hydrodynamic-condensation/vaporization computer code," University of Wisconsin Fusion Technology Institute, 1500 Johnson Dr., University of Wisconsin, Madison, WI, 53706, UWFDM-670 (1980).
16. J. Larsen, Cascade Applied Sciences Inc. code (licensed), version 01.05.04 (1992).
17. L. Seaman and D. Curran, *SRIPUFF—Final Report*, SRI Int., Poulter Laboratory, Stanford Research Institute, Menlo Park, CA, **2** (1980).
18. T. Cooper, *A Computer Code for Numerical Simulation of Shock Waves in Fluids and Solids*, Swedish Detonic Research Foundation, Report No. DS 1980:16 (1980).
19. J. C. Liu et. al., *Fusion Technology* **21**, 1514–1519 (1992).
20. J. Wong et al., "The Threshold Energy for Defect Production in SIC: A Molecular Dynamics Study," Lawrence Livermore National Laboratory, Livermore, CA, UCRL-JC-114789 (1993). Also see *Proc. of the 6th Int. Conf. on Fusion Reactor Mat.*, Stresa, Italy (1993).

LASER–PLASMA INTERACTIONS IN LARGE GAS-FILLED HOHLRAUMS

R. E. Turner *R. L. Kauffman* *T. D. Shepard*

L. V. Powers *B. F. Lasinski* *G. F. Stone*

R. L. Berger *B. J. MacGowan* *L. J. Suter*

C. A. Back *D. S. Montgomery* *E. A. Williams*

D. H. Kalantar *D. H. Munro*

Introduction

Indirect-drive targets planned for the National Ignition Facility (NIF) laser consist of spherical fuel capsules enclosed in cylindrical Au hohlraums. Laser beams, arranged in cylindrical rings, heat the inside of the Au wall to produce x rays that in turn heat and implode the capsule to produce fusion conditions in the fuel. Detailed calculations show that adequate implosion symmetry can be maintained by filling the hohlraum interior with low-density, low-Z gases.[1] The plasma produced from the heated gas provides sufficient pressure to keep the radiating Au surface from expanding excessively.

As the laser heats this gas, the gas becomes a relatively uniform plasma with small gradients in velocity and density. Such long-scale-length plasmas can be ideal mediums for stimulated Brillouin Scattering (SBS). SBS can reflect a large fraction of the incident laser light before it is absorbed by the hohlraum; therefore, it is undesirable in an inertial confinement fusion (ICF) target. To examine the importance of SBS in NIF targets, we used Nova to measure SBS from hohlraums with plasma conditions similar to those predicted for high-gain NIF targets. The plasmas differ from the more familiar exploding foil or solid targets as follows: they are hot (3 keV); they have high electron densities ($n_e = 10^{21}\text{cm}^{-3}$); and they are nearly stationary, confined within an Au cylinder, and uniform over large distances (>2 mm). These hohlraums have <3% peak SBS backscatter for an interaction beam with intensities of $1\text{–}4 \times 10^{15}\,\text{W/cm}^2$, a laser wavelength of 0.351 μm, $f/4$ or $f/8$ focusing optics, and a variety of beam smoothing implementations. Based on these conditions, we conclude that SBS does not appear to be a problem for NIF targets.

Theory

In the NIF targets, the laser beams will propagate through several millimeters of plasma ($n_e \sim 10^{21}\text{cm}^{-3}$) before depositing energy in the hohlraum wall. In this case, $n_e/n_c \sim 0.1$ for 0.351-μm light, where n_c is the critical density or the maximum density through which light of a given wavelength can propagate. The fraction of the laser energy that is collisionally absorbed in the low-Z (low atomic number) gas fill is modest (~10% at the peak of the laser pulse). However, estimates based on simple linear gain theory generate concern that SBS reflectivities could exceed acceptable levels for the large-scale-length plasmas in these targets.

SBS is one of several parametric instabilities that can occur in a plasma. In the case of SBS, the laser light reflects off of an ion-acoustic wave in the plasma. A chain of events occur if certain resonance conditions are met: the size of the ion-acoustic wave increases, which causes the scattered light to increase, which causes the ion-acoustic wave to increase, etc., until nonlinear effects limit the process. SBS reflectivity >10% may unacceptably degrade target performance by reducing the energy available for radiation heating and/or by disrupting symmetry.

In the NIF plasmas, density and velocity gradients are weak (although they limited the growth region for SBS in previous experiments); however, damping of the SBS-produced ion waves by light ions in the gas fill is efficient[2] and limits the SBS gain coefficient. Predicted gain coefficients for NIF plasmas, using linear theory, are >20, whereas gains of <15 are required to insure reflectivities of 10% or less. For such large gains, theoretical estimates[3] indicate that nonlinear mechanisms will limit the scattering to lower levels. Because nonlinear damping is difficult to calculate, we must do experiments to verify these estimates. Previous SBS

experiments are insufficient, since the plasma conditions in past studies[4] differ significantly from expected NIF conditions. For those exploding foil or solid targets, where scale lengths <1 mm and electron temperatures T_e ~ 0.5–2 keV were typical, SBS is limited by detuning (loss of phase matching conditions), due to gradients in the flow velocity. The lack of quantitative theoretical understanding of those experiments discourages extrapolation to NIF conditions. There is little data on the effect of various beam-smoothing techniques, or increased laser bandwidth, interacting with NIF-type plasmas.

Random phase plates (RPP)[5] and temporal smoothing methods such as smoothing by spectral dispersion (SSD)[6] are commonly used in laser–plasma interaction experiments to increase the time-averaged beam uniformity at the target plane. The idea is to avoid having higher-than-average intensities in the interaction region, since high intensities more easily drive SBS. Localized regions of higher intensity can occur because of imperfections in the laser beam. They can also occur when there is filamentation of the beam in the plasma. The filamentation instability has thresholds very similar to those for SBS, and can be initially seeded by imperfections in the laser beam. The smoothing techniques reduce the intensity variations in the beam but on a time scale that is often comparable to the SBS growth time. The interactions among SBS, filamentation, and the short-time-scale smoothed beam are complicated and not completely understood. One goal of these experiments is to test the *f*-number and temporal smoothing scale of SBS.

Instability growth in an RPP intensity distribution[7] can vary with the size of the speckles. The role of speckles in determining instability levels is important for NIF because the underdense plasma size is large compared with the speckle length of the proposed *f*/8 beam focusing. In simulations,[8,9] *f*/8 beams filament more than *f*/4 beams. Three-dimensional simulations[10] show that SBS reflectivity, unlike filamentation, is not directly limited by the speckle length. In these simulations, SBS grows over the entire resonant region, which is several speckles long, with a total gain greater than that calculated for the average intensity. However, even if the bandwidth is less than the SBS growth rate, temporal smoothing reduces SBS by partially destroying the cooperative scattering among hot spots. Modification of the RPP intensity distribution by filamentation could also affect SBS. For the plasma parameters of these experiments and laser intensity $I \sim 2 \times 10^{15}$ W/cm^2, simulations indicate that *f*/4 speckles are stable to filament but *f*/8 speckles are unstable.[9] Temporal smoothing makes filamentation more difficult because the filament must form rapidly, before the hot spot moves to a different location.

Experiment

We use the Nova laser to produce plasmas with conditions similar to those predicted for NIF hohlraum targets and to measure SBS from these plasmas. In these experiments, the targets are cylindrical Au hohlraums with a length and diameter of 2.5 mm.[11] The hohlraums do not contain capsules, but are filled with neopentane (C_5H_{12}) gas at a pressure of 1 atm ($n_e = 10^{21}$cm^{-3} when fully ionized). For some targets, a trace of Ar is also added for diagnostic purposes. As shown in Fig. 1, the gas is contained by two polyimide ($C_{22}H_{10}N_2O_5$) windows ~6500 Å thick. Nine of Nova's beams are used to heat the gas with ~30 kJ of 0.351-μm light in a 1.4-ns shaped pulse. The tenth beam is a probe, or interaction, beam whose intensity, pulse shape, *f*-number, and "smoothness" are varied. The SBS backscatter intensity and spectrum from the interaction beam are measured with temporal resolution of 100 ps and spectral resolution of 1 Å. The interaction beam has a trapezoidal pulse with a ~600-ps flat top and a ~300-ps rise and fall time. The interaction beam is typically delayed ~600 ps relative to starting the heating beams and is smoothed spatially with an RPP, providing peak average intensities in the range of 1–4 × 10^{15} W/cm^2. Temporal smoothing is done either by SSD with FM bandwidth[6] or by four colors. (See "Four-Color Irradiation System for Laser–Plasma Interaction Experiments," p. 130 of this *Quarterly* for a discussion of four-color systems.) The four-color scheme propagates four different frequencies through four quadrants of the laser. The focusing lens overlaps the frequencies at the focal plane. The line separation is $\delta\lambda = 4.4$ Å at 1.053 μm for a total line width of 13.2 Å for these experiments (four-color bandwidth with $\delta\lambda \cong 10$ Å is proposed for the NIF).

To produce a uniformly hot plasma inside the Nova hohlraum, a substantial fraction of Nova's energy (~12 kJ) must be coupled to the gas. Because the

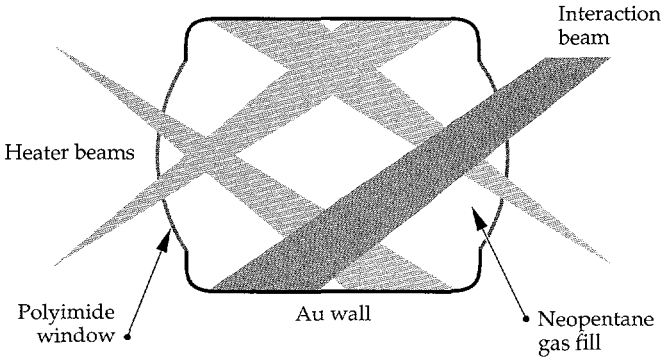

FIGURE 1. Schematic diagram of the target geometry. Shaded regions show the focusing and pointing of the heater beams (light shading) and interaction beam (dark shading). (10-01-0395-0652pb01)

absorption length exceeds the target size for the temperatures of interest (>5 mm for 0.351-μm light at $T_e = 3$ keV), the energy absorbed in the gas is determined by the laser-path length. The heater beam geometry (shown in Fig. 1) has the long path length necessary to maximize the absorption in the gas and to produce the desired plasma temperature. We also use a ramped pulse for the heater beams, which keeps the initial intensities low, to minimize scattering from the solid window material or the initially cold fill gas.

The detailed plasma conditions for the Nova gas-filled hohlraums and NIF targets are obtained from two-dimensional LASNEX[12] simulations. The simulations are cylindrically symmetric about the hohlraum axis and include the Au hohlraum wall, the gas fill (including dopants in the Nova targets), the membrane over the laser entrance hole (LEH) which confines the gas, and (in the case of the NIF target) the capsule. Standard LASNEX models are used for Lagrangian hydrodynamics, laser absorption, electron and radiation transport, and nonequilibrium atomic physics. The simulations predict that a uniform plasma (~2 mm long) with $n_e \sim 10^{21}\text{cm}^{-3}$, $T_e \sim 3$ keV, and flow velocity $<10^7$cm/s is maintained for longer than 0.5 ns during the peak of the interaction pulse. Under these conditions, the small signal intensity gain coefficient for SBS is

$$G_{SBS} = \pi \times 10^{-16} \left(\frac{I\lambda^2}{T_e}\right)\left(\frac{n_e}{n_c}\right)\left(\frac{\omega_a}{\nu_i}\right)\left(\frac{L}{\lambda}\right), \quad (1)$$

where λ is the laser wavelength and L is the plasma length, both in micrometers; T_e is in keV; ω_a and ν_i are the ion-acoustic-wave frequency and amplitude damping rate, respectively; and I is in W/cm^2.

To illustrate the similarity between plasma conditions in NIF target designs and these Nova gas-filled hohlraums, Table 1 summarizes the SBS gain and the calculated values of the plasma parameters in the underdense plasma that determine the gain.

The Nova plasma parameters are within ~50% of the NIF values except for the T_i/T_e ratio (where T_i is the ion temperature), which is lower in the Nova targets due to the shorter time available for electron-ion equilibration to occur. This difference leads to larger ion acoustic wave damping ν_i in NIF than in Nova targets.[2] However, the difference in path length compensates to give similar gain coefficients for NIF and Nova targets at the same intensity ($I \cong 2 \times 10^{15}$ W/cm^2). Hence, these Nova targets access conditions that are very similar to NIF designs both in SBS linear gain and in the individual plasma parameters that determine the scattering characteristics. Calculated gain coefficients for the highest-intensity Nova experiments ($I \cong 5 \times 10^{15}$ W/cm^2) exceed the NIF value by more than a factor of two.

We performed extensive characterization to assure that predicted plasma conditions were achieved in the underdense plasma. The T_e is inferred from both single-element and isoelectronic line ratios[13] using Ti/Cr or K/Cl spectra from thin foils placed in the path of the interaction beam. In the isoelectronic technique, one looks at x rays emitted from different ions, which contain the same number of electrons (e.g., x rays from Ti and Cr ions that each contain one electron "H-like"). The ratio of the x-ray intensity from these differing ions is temperature dependent, but is nearly independent of other parameters, such as density.[13] This makes the analysis and interpretation of the data more straightforward. Detailed analysis of the isoelectronic spectra confirms that $T_e > 3$ keV during the interaction pulse.[14] Time-resolved measurements without the interaction beam verify that electron conduction provides good temperature uniformity. Several diagnostics characterize the propagation of the heating beams through the (initially) cold gas. A streaked x-ray spectrometer records the temporal history of Au M-band x rays emitted through the LEH. This measures the time at which the laser beam begins to heat the Au wall of the hohlraum; from this data, we can deduce the average beam propagation speed through the gas. Time-gated (≅100 ps) x-ray images, dominated by emission from 1% Ar dopant in the gas, provide evidence that the beams propagate without significant breakup or refraction. These experimental observations, which are in good agreement with LASNEX predictions, support important aspects of our modeling of NIF targets.

TABLE 1. Comparison of selected plasma parameters for Nova gas-filled hohlraums and NIF targets.

	Nova	NIF
Interaction length	~2 mm	~3 mm
Line density $\int (n_e/n_c)\, dl$	~0.2 mm	~0.3 mm
T_e	3 keV	5 keV
T_i/T_e ratio	0.1–0.2	0.4
Gain coefficient G_{SBS} (2×10^{15} W/cm^2)	22	21

SBS Data and Discussion

Backscattered light near the laser frequency is collected by the interaction beam focusing lens and is measured with a grating spectrometer-streak camera combination to provide spectrally and temporally resolved data. The resolutions are 0.1 nm (spectral) and 100 ps (temporal). We also use time-integrating

calorimeters to provide an absolute calibration. Figure 2 shows a typical spectrum. Just after time zero, before the interaction (or "probe") beam is turned on, weak sidescattered light is observed from the "heater" beams as they interact with the polyimide window. At 0.6 ns, the "probe" beam is turned on; its reflection from the expanding polyimide window at the LEH produces the unshifted feature observed to start at 0.6 ns. A stimulated Raman scattering diagnostic (not shown) observes $\omega/2$ scattered light (700 nm) at this time; since half-harmonic light is generated at the $n_c/4$, this confirms the LASNEX prediction that the expanding window plasma density is still over $n_c/4$ when the probe beam is first turned on. However, it quickly drops below the gas density of 0.1 n_c, and red-shifted SBS is then observed. This SBS backscatter (shown in Fig. 2) peaks soon after the interaction beam reaches peak intensity and decreases before the intensity drops. We calculate that the decrease is due to an increase in the ion acoustic wave damping rate, as the ratio of T_i/T_e increases. The time dependence of this ratio is due to the relatively slow heating of the ions; the ion heating depends on electron-ion collisions, which are relatively weak for low-Z plasmas. At the time of peak scattering, the wavelength of the peak emission is red-shifted ~3–7 Å. In the fluid limit, the frequency shift of SBS-scattered light $\Delta\omega = 2\,k_0\,(V_{||} - C_s)$, where k_0 is the laser wavenumber, C_s is the ion sound speed, and $V_{||}$ is the flow velocity parallel to the scattering vector; hence the observed red-shift is evidence that the SBS spectrum is dominated by scattering from regions of plasma where $V_{||} < C_s$, as predicted by linear gain analysis. In contrast, SBS spectra from lower-temperature, expanding targets[4] are routinely blue-shifted.

Figure 3 shows the peak SBS backscatter into the lens as a function of intensity for $f/4$ and $f/8$ interaction beams (using an RPP smoothed interaction beam). Peak SBS reflectivities with $f/8$ interaction beams, which closely match the NIF beam configuration, are <3% for C_5H_{12}-filled targets. Time-integrated reflectivities are <1%. The scattering levels for all intensities are well below the >30% reflectivities predicted by linear theory. Reflectivity levels are not changed when four-color bandwidth is added. This insensitivity to bandwidth agrees with simulations[10] only if ad hoc nonlinear damping rates are imposed to match the measured SBS reflectivity. At higher interaction intensities ($>2 \times 10^{15}$ W/cm^2), the simulations indicate that filaments form and scatter significant light outside the lens cone. Experiments are planned to investigate the angular distribution of the reflected light.

Peak scattering levels from $f/4$ interaction beams are comparable to the $f/8$ beams (1–2%). With SSD bandwidth of 3.5 Å, scattering from the interaction beam is below the detection threshold of ~0.1%. The apparent efficiency of SSD in suppressing SBS may be related to the details of the speckle motion: with SSD, the hot spots move in an effectively random way, whereas with four-color smoothing the hot spot pattern exactly recurs in a time $2\pi/\delta\omega$, where $\delta\omega$ is the line separation.

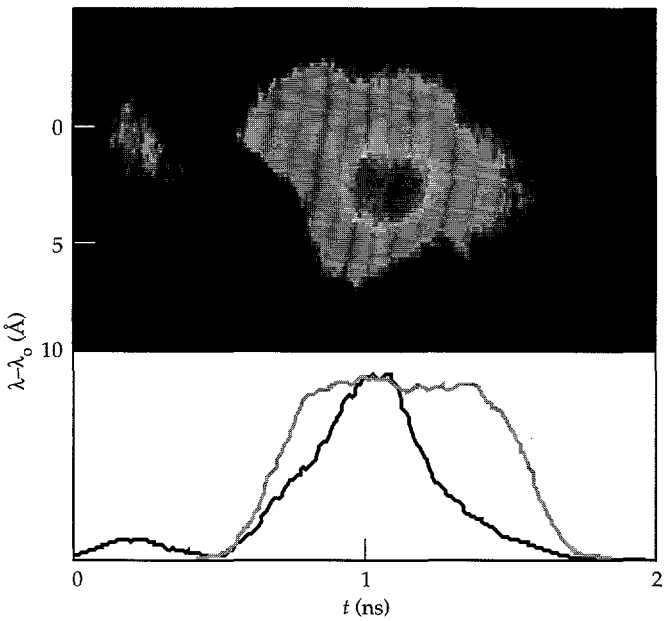

FIGURE 2. Streaked spectrum of backscattered light from the $f/8$ interaction beam. The plot shows temporal lineouts of the frequency-integrated reflectivity (black line) and the interaction beam intensity (gray line). The peak reflectivity is 0.015 and the peak intensity is $I = 1.7 \times 10^{15}$ W/cm^2. (10-01-0395-0653pb01)

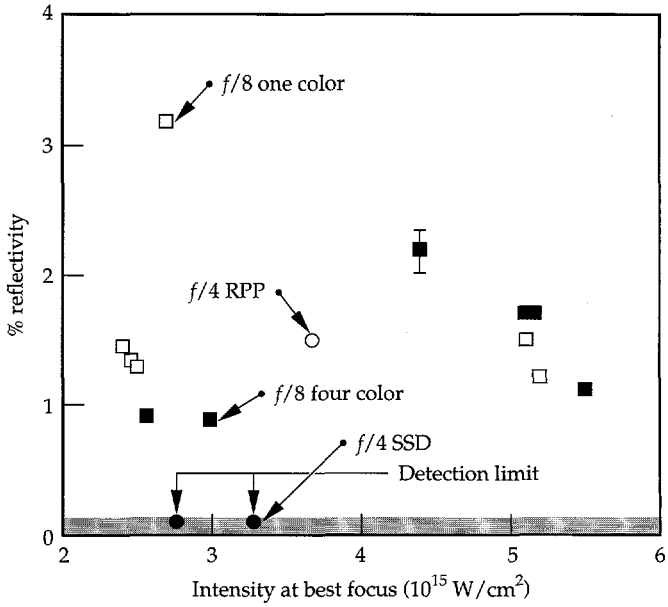

FIGURE 3. Peak SBS reflectivity into the focusing lens for $f/4$ and $f/8$ interaction beams, for an RPP-smoothed interaction beam. Filled squares show $f/8$ shots, adding four-color bandwidth with 4.4-Å line separation. Reflectivities from $f/4$ shots with 3.5-Å SSD bandwidth (filled circles) were below the detection threshold.
(10-01-0395-0654pb01)

The observation of similar reflectivities from single-color $f/4$ and $f/8$ interaction beams at comparable intensities is somewhat at odds with gain scaling calculations. For these large plasmas, beam divergence produces a significant drop in intensity (a factor of ~2 for $f/8$ and ~4 for $f/4$) across the scattering region. This difference leads to larger calculated gain for $f/8$ ($G_{SBS} = 22$) than for $f/4$ ($G_{SBS} = 15$) for the same intensity at best focus. Several possible explanations for these findings are under investigation, theoretically and experimentally. For example, for the large gains calculated for these targets, nonlinear saturation mechanisms may limit the amplitude of the ion waves driven by SBS.[3]

High Levels of SBS

We observed only low levels of SBS when approximately duplicating the expected NIF conditions. We used several Nova shots with $f/4$ focusing to see if truly significant levels of energy could be scattered at more extreme conditions. We found that, with the maximum Nova power, we could generate a high level of SBS by removing all beam smoothing, and simultaneously removing H ions from the target. With no beam-smoothing techniques employed, the interaction intensity is difficult to define, making comparison with theory difficult. The spot size continually increases as the beam propagates from best focus, through the LEH, through the gas, to the Au wall. Furthermore, the unsmoothed Nova beams contain a substantial fraction of their energy in localized regions of high intensity.

Ions of H are particularly adept at damping the ion-acoustic waves. Their low mass means that, at a given temperature, their thermal velocities are higher than those of more massive ions, and thus they are more closely matched to the ion-acoustic wave's phase velocity. This enables them to draw energy away from the wave, effectively damping it. To remove H from the target, we used deuterated C_5D_{12} gas.

Figure 4 shows the resulting time-resolved SBS spectrum from this shot. Its features illustrate brief, nearly unshifted scatter from the window-plasma when the probe beam turns on followed by red-shifted SBS. Unlike the data shown in Fig. 2, taken with smoothed beams, the SBS persists throughout the probe pulse. This shows that the (non-H) ions, in this case, are ineffective at damping the acoustic wave. Also unlike the smoothed beam data, the scattering level is high. In this case, 18% of the probe energy was scattered back into the $f/4$ lens.

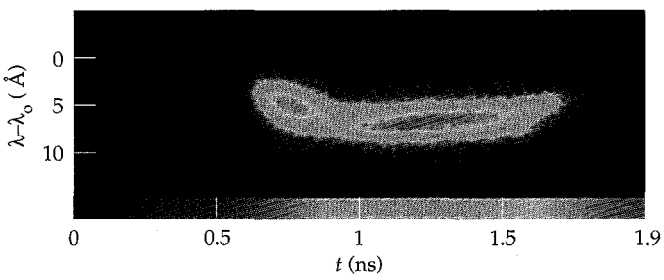

FIGURE 4. Streaked spectrum of backscattered light from the $f/4$ interaction beam with no smoothing and from the fully deuterated C_5D_{12} gas target. In contrast to Fig. 2, the reflectivity is nearly 20% and persists throughout the interaction pulse. (10-01-0395-0655pb01)

Partially as a result of these experiments, the NIF target design now includes a small amount of H gas in the hohlraum to add an increased safety margin to the suppression of SBS.

Summary

We demonstrated low SBS reflectivity in NIF-relevant gas-filled hohlraum experiments on Nova. These targets approximately produced the calculated plasma conditions and SBS gain coefficients for NIF targets. The interaction beam mimics the NIF laser beam intensity, focusing, and beam smoothing. The maximum time-dependent SBS reflectivity is less than 3% for NIF-relevant conditions.

Acknowledgments

The authors thank J. Kilkenny, J. Lindl, and M. Rosen of Lawrence Livermore National Laboratory; and J. Fernandez, W. Hsing, and B. Wilde of Los Alamos National Laboratory. The contributions of the Nova laser operations and target fabrication groups were indispensable in conducting these experiments. Polyimide membranes were fabricated by Luxell, Inc. We acknowledge the LASNEX group for the simulations required to design and analyze these experiments.

Notes and References

1. S. W. Haan, S. M. Pollaine, J. D. Lindl, L. J. Suter, et al., "Design and Modeling of Ignition Targets for the National Ignition Facility," Lawrence Livermore National Laboratory, Livermore, CA, UCRL-JC-117034; submitted to *Phys. of Plasmas*.
2. E. A. Williams, R. L. Berger, A. M. Rubenchik, R. P. Drake, et al., *Phys of Plasmas* **2**, 129 (1995).
3. W. L. Kruer, *Phys. Fluids* **23**, 1273 (1980).
4. H. A. Baldis, D. S. Montgomery, J. D. Moody, C. Labaune, et al., *Plasma Phys. Controlled Fusion* **34**, 2077 (1992) and refs. therein.
5. Y. Kato and K. Mima, *Appl. Phys. B* **29**, 186 (1982).
6. S. Skupsky, R. W. Short, T. Kessler, R. S. Craxton, et al., *Appl. Phys.* **66**, 3456 (1989).
7. S. N. Dixit, I. M. Thomas, B. W. Woods, A. J. Morgan, et al., *Applied Optics* **32**, 2543 (1993).
8. A. J. Schmitt, *Phys. Fluids* **31**, 3079 (1988).
9. R. L. Berger, B. F. Lasinski, T. B. Kaiser, E. A. Williams, et al., *Phys. Fluids B* **5**, 2243 (1993).
10. R. L. Berger, *Bull. Am. Phys. Soc.* **38**, 2012 (1993).

11. This target geometry is one of three simultaneous and complementary experiments performed on Nova, using gas-filled targets to create large-scale-length plasmas. Experiments using targets in which the gas is contained in a low-Z membrane are reported by B. J. MacGowan et al., *Proceedings of the IAEA 15th Int'l Conference on Plasma Physics and Controlled Nuclear Fusion Research*, IAEA-CN-60, 1994. An alternate hohlraum geometry was fielded by a team from Los Alamos National Laboratory led by J. Fernandez.
12. G. Zimmerman and W. Kruer, *Comments Plasma Phys. Controlled Fusion* **2** 85 (1975).
13. R. S. Majoribanks, M. C. Richardson, P. A. Jaanimagi, R. Epstein, *Phys. Rev. A* **46**, 1747 (1992); T. D. Shepard, C. A. Back, B. H. Gailor, W. W. Hsing, et al., *ICF Quarterly Report* **4**(4) 137, Lawrence Livermore National Laboratory, Livermore, CA, UCRL-LR-105821-94-4 (1994).
14. C. A. Back, Lawrence Livermore National Laboratory, Livermore, CA, private communication regarding electron temperature measurements in laser heated hohlraums (1995); to be published later in a journal article.

Evolution of Solid-State Induction Modulators for a Heavy-Ion Recirculator

H. Kirbie *B. Lee*

R. Hanks *M. Newton*

S. Hawkins *C. Ollis*

B. Hickman

Background

The Laser Program at Lawrence Livermore National Laboratory (LLNL) pioneered the use of large-scale glass lasers to heat inertial-fusion targets. Today, that same exploratory spirit applies to our latest laser-fusion effort—the National Ignition Facility (NIF). The NIF has the potential to pave the way to commercial power extraction from inertial fusion, as long as the generating system is affordable and it operates repetitively. These fundamental issues of cost and repetition rate have stimulated a search for alternative fusion-target drivers to replace large, single-shot lasers. We are developing an ion approach whereby converging beams of heavy ions act as the driver. Like lasers, the ions impart their energy to the target and produce fusion temperatures. The difference lies in the ability of particle accelerators to generate repetitive bursts of ions with a higher efficiency at a lower cost.

Several accelerator concepts are being investigated for Inertial Fusion Energy (IFE).[1] The challenge is to identify an accelerator configuration that meets the technical requirements for heavy-ion fusion (HIF) and competes economically with existing and alternate energy sources. To meet the challenge, the LLNL HIF project is investigating a circular induction accelerator called a recirculator,[2] as shown in Fig. 1. The recirculator is economically attractive because the beam acceleration sequence uses the most expensive accelerator components multiple times. However, the recirculator concept presents some unique technical challenges, because the sub-relativistic ion completes a circulation in a short time and is constantly gaining speed with each lap. Consequently, the pulsed modulators that accelerate and shape the beam must produce uniquely tailored pulses at repetition rates that are continuously variable and that can exceed 100 kHz. Therefore, our role in the HIF project is to investigate and to develop agile induction modulators that use the latest in solid-state power technologies.

Development Overview

Our efforts to develop agile induction modulators are guided by the future experimental needs of the HIF project. In close collaboration with Lawrence Berkeley Laboratory (LBL), we are developing a short-term and a longer-range experimental capability that will be shared between the two laboratories. The short-term experiment is a small-scale recirculator (4.5-m-diam ring), presently being built at LLNL, that will be the first demonstration of the recirculator concept. The longer-range experiment is a much larger scale recirculator (30-m-diam ring) that will be built using the proposed Induction Linac Systems Experiments (ILSE) accelerator at LBL as the heavy-ion source. Both of these experimental activities require significant advancements in the technology for induction-accelerator modulators.

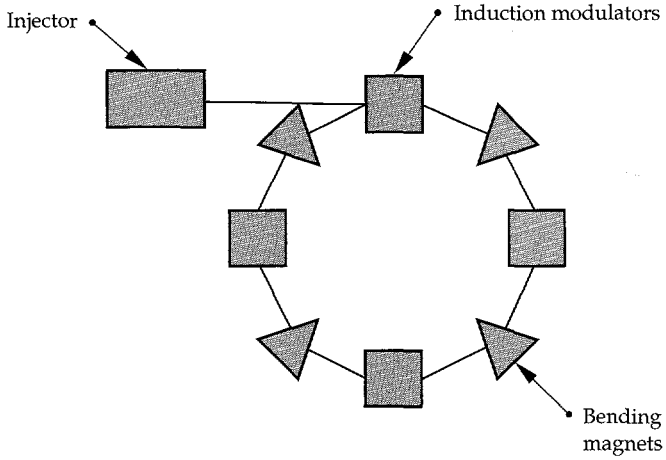

FIGURE 1. The recirculator uses a multipass acceleration concept to reduce system costs. (30-00-0295-0486pb01)

For our initial experiments, we selected a full-scale demonstration of solid-state power management based on the long-range requirements of the proposed LBL recirculator. A prototype modulator was built and tested that achieved the nominal parameters of 5-kV, 200-A pulses that vary in format from 1 μs to 400 ns and repeat at a 50- to 150-kHz repetition rate.

In addition to pulse-width and repetition-rate agility, the induction cell modulators for a recirculator will ultimately incorporate a much more sophisticated power-management scheme. The amplitude and shape of each individual acceleration pulse must be tailored to accurately match the continually changing velocity and shape of the ion beam. This will require the implementation of feedback control capabilities to the basic modulator technology. At LLNL, we are presently developing an induction modulator for our short-term experimental needs on the small-scale recirculator. This new modulator will generate precisely programmed waveshapes in addition to pulse-width and repetition-rate agility. While the total peak power requirements are much smaller in this second developmental modulator (600-V, 100-A pulses), it must still operate in excess of 100 kHz while delivering a sequence of pulses that have a precisely controlled shape and amplitude.

This article describes the requirements, designs, and results from our initial work, which focused on the larger modulator technology for the LBL recirculator experiment, followed by our present efforts to develop a "smarter" modulator technology. We also summarize spin-off applications of the HIF induction technology currently being developed.

Solid-State Induction Technology

Induction machines accelerate the beam through electrical cavities that apply the accelerating voltage to the beam. These cavities contain toroids of ferromagnetic material that encircle the beam axis and enable the applied accelerating voltage to be impressed along the beam while the outer cavity surfaces remain at ground potential.[3] Figure 2 illustrates the differences between a linear induction accelerator and a recirculating induction accelerator. Figure 2(a) shows a linear arrangement of induction cells, where each cell receives fixed duration pulses of a relatively low pulse repetition frequency (prf).[4] Figure 2(b) is a circular arrangement of the induction cells, but the pulse parameters for these cells differ greatly from their linear accelerator counterpart:

- Recirculators operate in a rapid burst of multiple pulses, corresponding to the number of beam circulations in the ring.
- The pulse separation changes during the burst because the ion beam gains speed from each preceding pulse.
- The pulse width changes during the burst because the beam is spatially compressed as it gains speed.
- The prf within the burst is very high (10–150 kHz) because the beam accelerates on each lap around the ring.

The need for complex pulse agility led us to examine solid-state switching components that have an on/off capability. The intrinsic speed of solid-state switching satisfies our high prf requirements, while the on/off switching action of some semiconductor devices enables us to select an arbitrary pulse width. Eventually, we selected field effect transistors (FETs) as the preferred switching elements because they have fast rise and fall times, low gate-drive power, low on-state impedance, and a capacity for high-prf operation.

The basic concept of our solid-state modulator is simple—close the FET switches to connect a large capacitor bank to the accelerator induction cell and open the switches when the pulse is long enough. However,

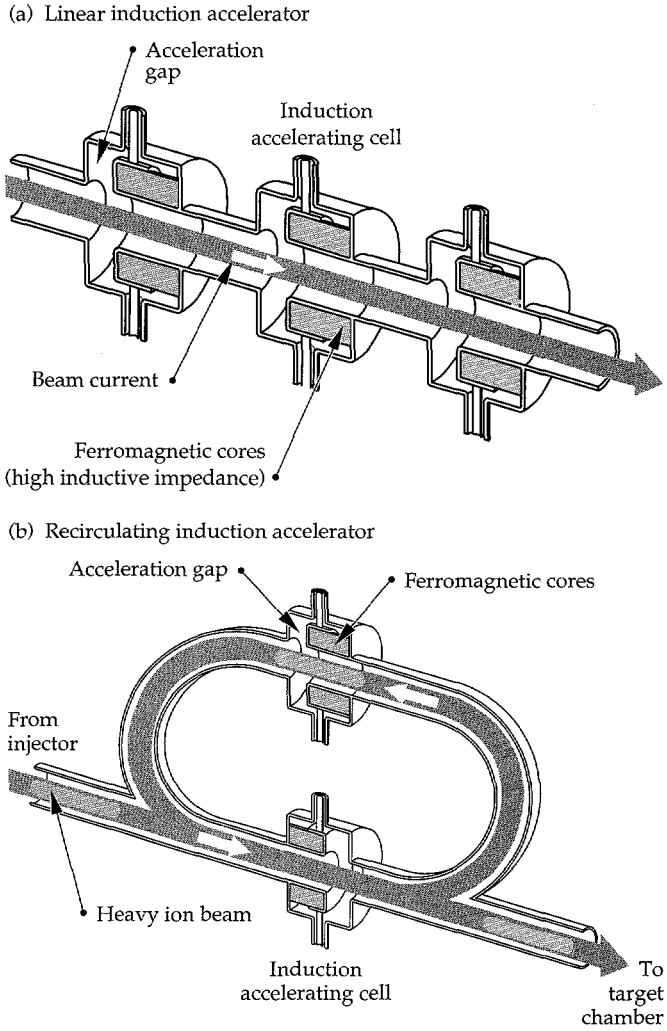

FIGURE 2. Ferromagnetic cores are used in induction cells to accelerate the beams. (99-74-0491-0659pb01)

this action becomes considerably more complicated due to the inductive nature and magnetic properties of the accelerator core: (1) The inductance of the accelerator cell is energized by the applied pulse. When the FET switches are commanded to open, the cell inductance generates a very large voltage in an attempt to maintain a constant current. (2) The applied pulse also magnetizes the core material and leaves it in a different state of polarization following the pulse. The difficulty lies in resetting the core to its former magnetic state in the short time between pulses. We resolved these difficulties by applying the circuit architecture shown in Fig. 3.

When the switch S1 is closed, the energy storage capacitor C1 is connected directly across the induction cell L1. The voltage VC1 accelerates the ion beam, but it also drives a steadily increasing magnetization current in the cell [Fig. 3(b)]. Once the acceleration pulse has ended, S1 opens and the cell current begins to decrease. The sudden change in cell current results in a rapid voltage reversal on L1, which continues in the positive direction until the diode D1 is forward biased. At that time, the cell current is fully diverted from the switch branch to the reset capacitor C2. The reset capacitor is precharged to the voltage VC2, which dictates the rate of cell current decay and helps to restore the magnetic flux density back to its original value. When the cell current reaches zero, D1 turns off and the pulse is ended; however, the core reset action is still incomplete. Additional reset is provided by reversing the flow of cell current. Energy for the current reversal is stored in the FET snubber capacitors (not shown) and reinforced by current from the external charging system. The diversion of cell current to C2 causes VC2 to increase with each pulse and results in a net accumulation of voltage during an acceleration sequence. However, the capacitance value of C2 is equal to or greater than C1, so the net voltage increase is very small. The regulator element in Fig. 3(a) maintains VC2 at a steady-state value by returning the recovered energy back to C1 at the end of each acceleration sequence. Note that C1 contains far more energy than the ion beam and core material need per pulse, so C1 does not require recharging during a burst.

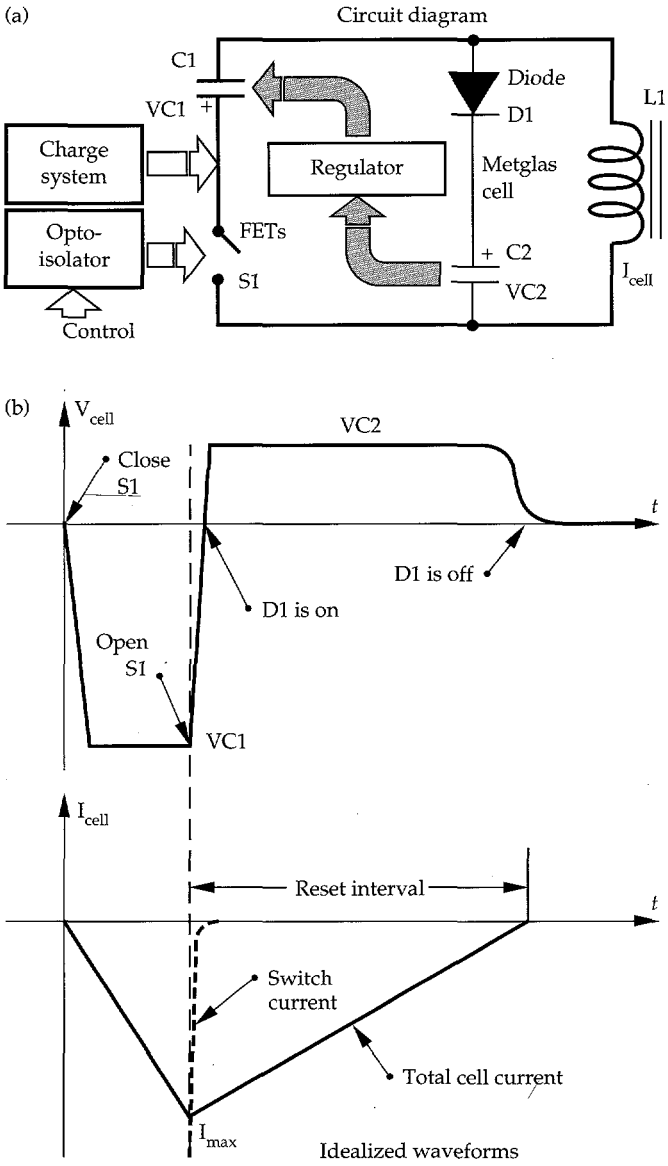

FIGURE 3. (a) Circuit that provides core drive and reset functions for a single induction cell. (b) Waveforms that illustrate the operation of the circuit shown in (a). In (b), t = time. (30-00-0295-0487pb01)

ILSE-Scale Induction Modulator

Our first attempt to implement the circuit architecture of Fig. 3 resulted in a 4-kV modulator and cell switched by a total of 24 FETs.[5] Our latest HIF machine features a larger switching system, containing a total of 128 FETs. Figure 4 shows the physical layout of four parallel 1-kV

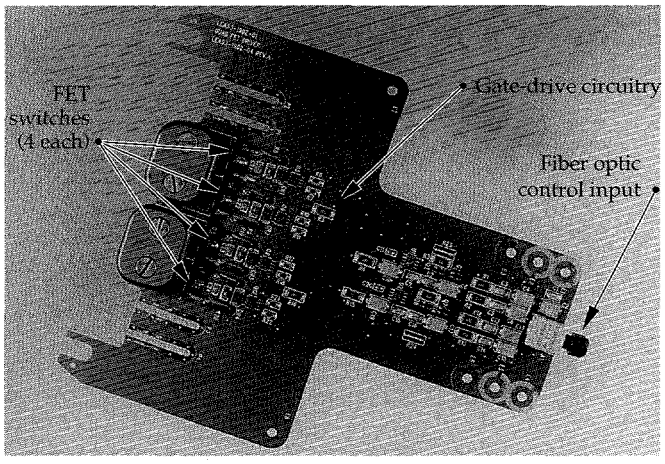

FIGURE 4. Photograph of a circuit board containing FET switches and optically controlled drive circuitry. (30-00-0295-0489pb01)

power FETs on each of 32 circuit boards along with the two isolated gate-drive circuits that control them. The on/off commands to each gate drive are delivered through a single optical fiber. Isolated control power is supplied from a dc/dc converter for each circuit board. The 32 circuit boards are divided into four modules each containing a stack of eight series-connected boards. The four modules and their capacitor banks surround a single induction cell, as shown in Fig. 5.

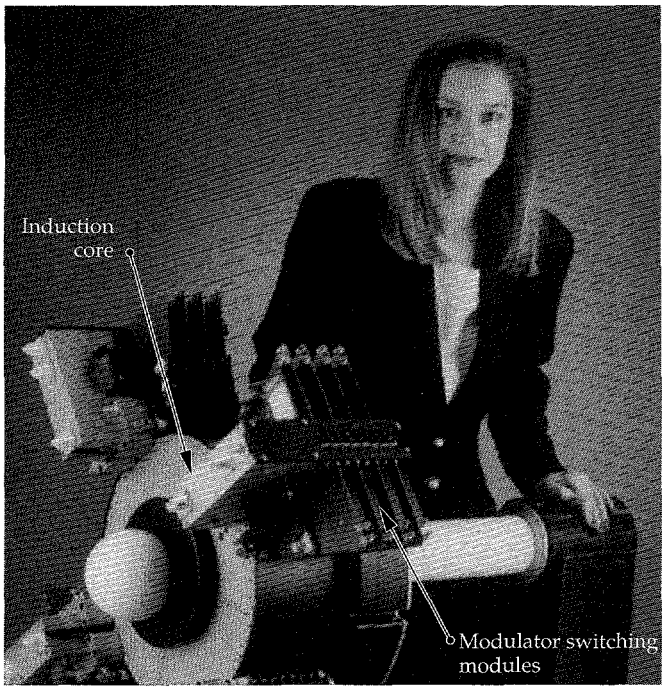

FIGURE 5. Photograph illustrating the close integration between the FET switching modules and the induction core. (30-00-0295-0490pb01)

Space is available to expand this modulator to a total of 8 modules, doubling its peak power capability from 4 MW to 8 MW.

Figures 6 and 7 contain preliminary performance data for 3-kV operation. Figure 6(a) shows cell voltage and the switch voltage on module 4 for a 1-μs pulse. Figure 6(b) shows currents from modules 3 and 4, indicating a good current balance between them. Each module has two current probes so that eight probe signals are needed to show the total machine current. The general ramp-like shape of the current waveform is characteristic of an inductive load with a constant applied voltage. The narrow pulse at the start of the

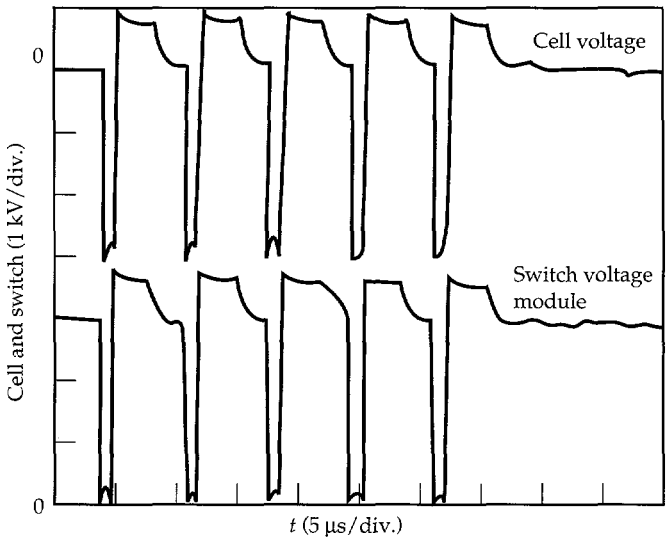

FIGURE 7. Five-pulse burst at 3 kV showing a 150-kHz pulse rate. (30-00-0295-0492pb01)

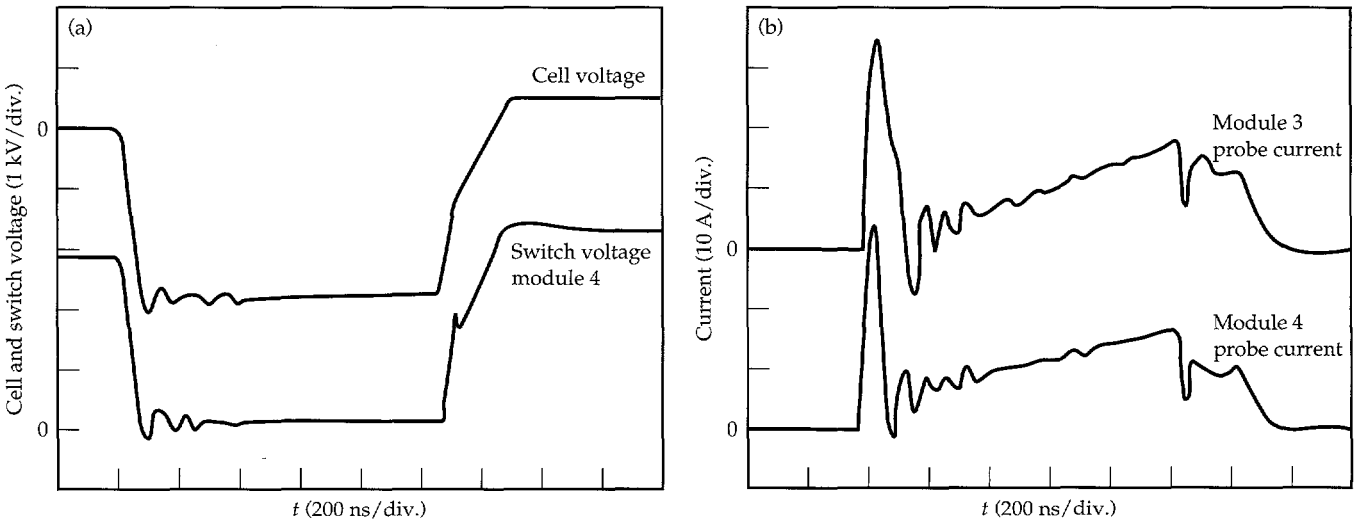

FIGURE 6. (a) Cell and switch voltages for a 3-kV charge voltage and a 400-V reset voltage. Waveforms are the acceleration portion of the whole voltage waveform. (b) Switch currents from modules three and four showing a 15-A peak current at the end of a 1-μs ramp. Peak cell current is the sum of all module currents (= 120 A in this case). (30-00-0295-0491pb02)

current signal is due to the discharge of external cable capacitance. Figure 7 shows the cell and switch voltage of module 4 during a 5-pulse burst at a 150-kHz rate. The machine has achieved full voltage operation at 5 kV, but much work still remains in modeling the system and understanding the behavior of the magnetic core during the burst.

Small-Scale Induction Modulator

The small LLNL recirculator, currently under construction, consists of 32 accelerator stations spaced around a 4.5-m-diam ring. Each accelerator station houses a 600-V induction modulator and cell. When a stream of low-energy ions are injected into the ring, they are steered into a circular path by an arrangement of electrostatic dipoles. As the singly charged ion stream passes by each induction cell, the particles undergo a nominal 500-eV gain in energy. The ions complete 15 revolutions in the recirculator before being extracted.

The transport scenario described is further complicated by the large space charge of the ion bunch. To inhibit ion scattering, the recirculator must provide confinement forces that bind the beam in the radial and axial directions. The electrostatic quadrupoles provide the radial restoration, but the axial spread is controlled by shaping the acceleration pulse so that the space charge forces are balanced by the accelerating voltages. Basically, the ions in the lead receive less acceleration (lower mean voltage) than the trailing ions that receive additional acceleration (higher mean voltage). In practice, the pulse shape is generated by adding a 500-V rectangular pulse with two triangle-shaped "ear" pulses at the leading and trailing edges. The leading-edge ears have a negative polarity to decelerate the head of the beam, while the trailing-edge ears have a positive polarity to speed up the tail. There are several possible combinations of pulses that form an "acceleration schedule" that may be used to accelerate the ion beam. Figure 8(a) shows one example, which details the schedule of acceleration pulses, and Fig. 8(b) shows the ear-pulse schedule. As the ion beam is bunched together, the acceleration pulses grow narrow and the ears become taller to restrain a spatially compressed beam. Figure 9 shows the ensemble of net accelerating voltages from start to finish.

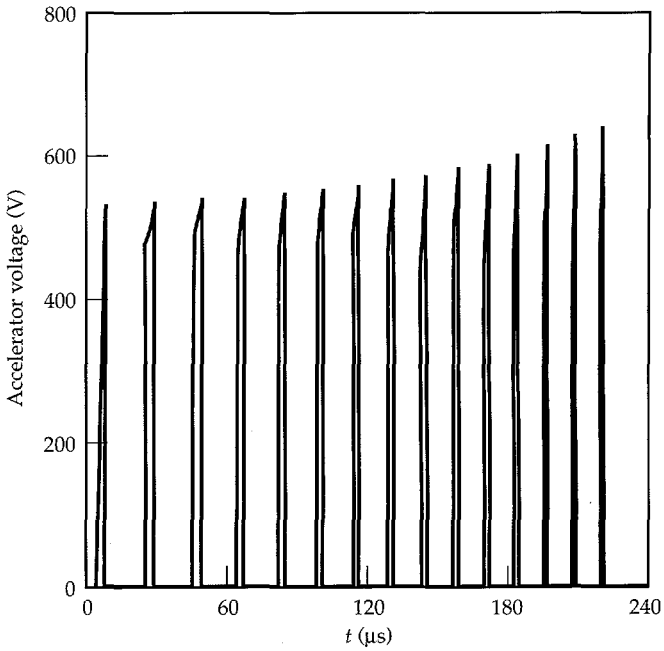

FIGURE 9. This voltage waveform, which appears in the accelerating gap, is the summation of the accelerator and ear pulses shown in Fig. 8. (30-00-0295-0494pb01)

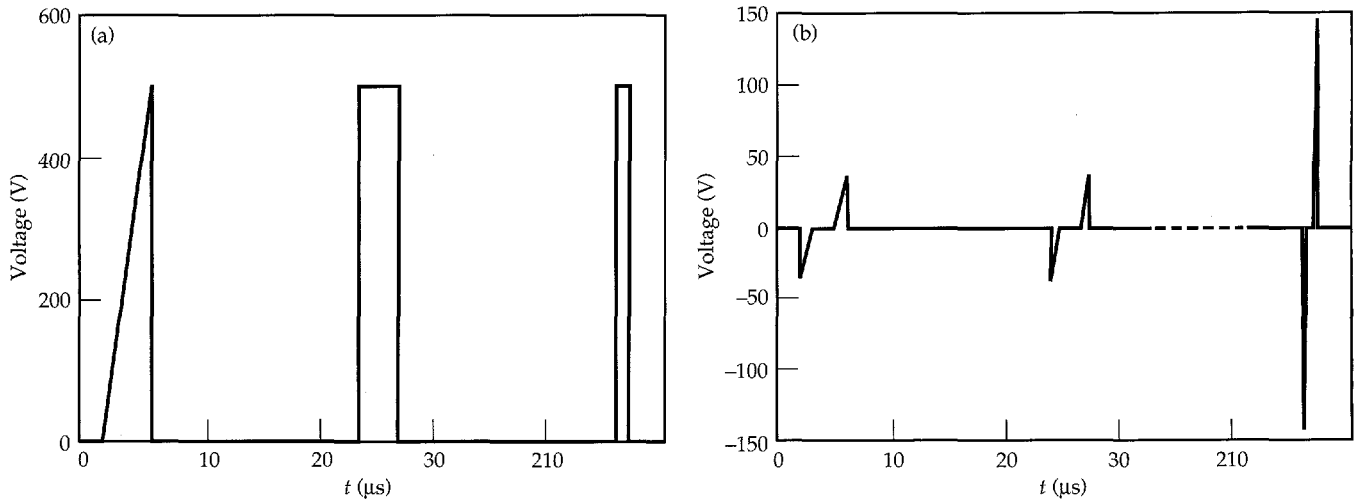

FIGURE 8. (a) Accelerator pulses vary from a 4-μs rise-time ramp to a 1-μs rectangular pulse. Interpulse spacing starts at 17 μs and reduces to 10 μs. (b) These ear pulses are added to the acceleration pulses to provide longitudinal confinement of the ion beam. (30-00-0295-0493pb02)

Generating the pulse format shown in Fig. 9 is the responsibility of our "smart" induction modulator. In this case, FETs are still used to connect a precharged capacitor bank to an induction cell, but the smart feature of this new modulator lies in the use of the FETs as amplifier elements instead of on/off switches. In addition, our new modulator and cell use two separate induction cores, one for the main accelerator pulse and one for the ear pulses, to generate the net voltages of Fig. 9. Figure 10 is a block diagram that illustrates the nesting of two cores and two modulator circuits. Fast feedback amplifiers are used to control two power FET arrays so that each core voltage is a scaled version of an applied input waveform. A computer system is used to command two programmable waveform generators to produce a properly shaped pulse train. The ear core in Fig. 10 is made from PE-11B ferrite while the main accelerator cores are an assembly of three 2605S-3A Metglas[6] cores.

The modulator and core assembly are still in the design phase, but comprehensive modeling of the electronic portion of the design is presently underway. We are using the Micro-Cap IV[7] circuit analysis program to model the cell and power amplification circuits. Figure 11 is a typical simulation showing an input waveform compared with the output voltage at the accelerator cell.

Spin-Off Technologies

The various power-control technologies being developed for HIF are also applicable in other programs. For example, the Advanced Radiographic Machine (ARM), a multipulse electron-beam accelerator for dense-target tomography, derives its power system from the HIF work, but requires a peak power and repetition rate far beyond those needed for heavy-ion recirculators. The ARM induction modulator is designed to generate 15-kV pulses that vary in width from 200 ns to 1 μs at repetition rates up to 1 MHz.[8]

We also applied our HIF knowledge to two other projects. During FY 1992, we built and tested a miniature induction modulator as a power source for pulsed plasma processing.[9] This work was based on the proposition that plasma processing is a dynamic electrochemical reaction that also requires an agile power source to help maintain an optimal process efficiency. During FY 1994, we applied our FET switching experience to the design and construction of a compact power source for a solid state laser array.[10,11] In this case, the work focused on enhancing the industrial and medical uses of the laser array by reducing the size and cost of the power system.

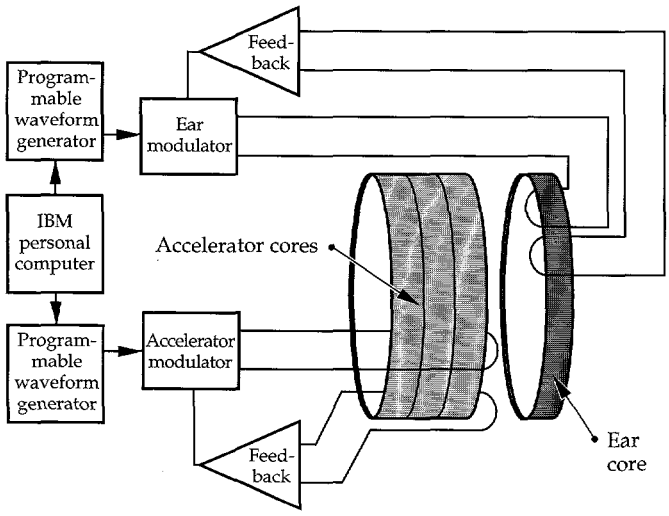

FIGURE 10. The gap voltage is generated by two separate core and modulator circuits. (30-00-0295-0495pb02)

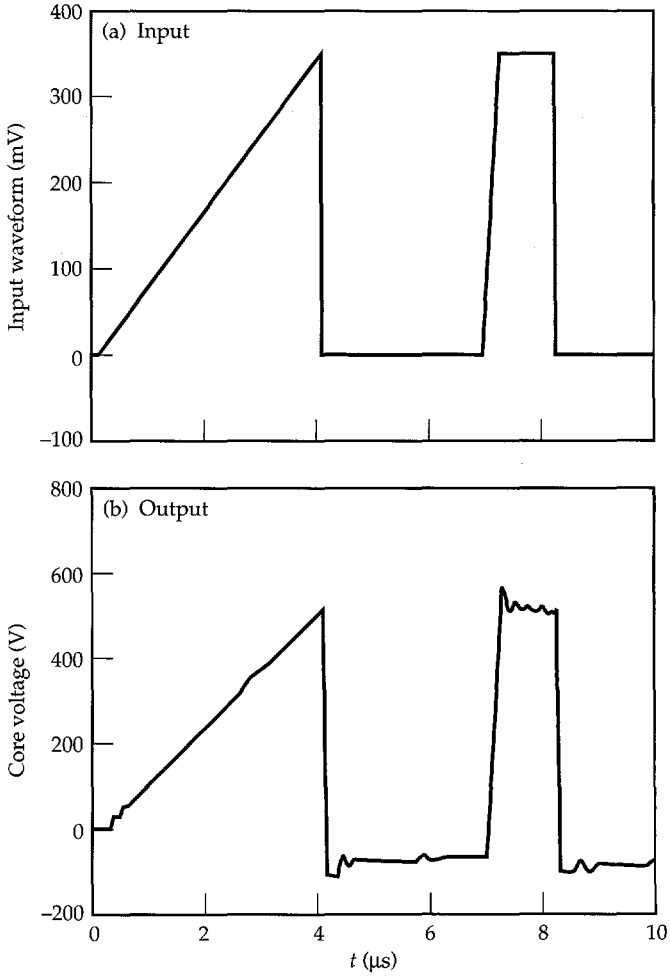

FIGURE 11. Circuit simulation showing two examples of (a) input voltage waveforms and (b) amplified voltages at the cell. The negative bias on the amplified voltage signal is the result of the applied reset voltage. These simulations contain detailed amplifier models that are used to guide our design. (30-00-0295-0496pb01)

Summary

Induction accelerators are typically powered by energy stored in a pulse-forming network that delivers an accelerating pulse of a fixed duration and amplitude. This type of accelerator system is limited in prf to a few kilohertz and treats the dynamic beam as a simple time-invariant load. Our research has merged the growing capability of solid-state power control with induction accelerator technology to produce a new accelerator system that is fast, flexible, and interactive with the beam. As a result, the beam may receive variations in pulse shape, amplitude, width, and prf to suit a specific objective in beam quality or accelerator performance. The solid-state powered accelerator delivers intelligent beam power that is actively directed in the right proportions at the right time. The recirculator is only one example of how smart power management can improve the capability of well-established technologies.

Notes and References

1. D. J. Dudziak, W. W. Saylor, and W. B. Herrmannsfeldt, *Fusion Technology* **13**(2), 207 (February, 1988).
2. J. J. Barnard, *Study of Recirculating Induction Accelerators as Drivers for Heavy Ion Fusion,* Lawrence Livermore National Laboratory, Livermore, CA, UCRL-LR-108095 (September 1991).
3. S. Humphries, Jr., *Principles of Charged Particle Acceleration,* Institute for Accelerator and Plasma Beam Technology, University of New Mexico, Albuquerque, NM (John Wiley & Sons, Inc., New York, 1986) p. 283.
4. H. C. Kirbie, et al., "Evolution of High-Repetition-Rate Induction Accelerators Through Advancements in Switching," *Proceedings of the 1992 Linear Accelerator Conference,* Ottawa, Ontario, Canada, August 24–28, 1992, p. 595.
5. H. C. Kirbie, et al., "A FET-Switched Induction Accelerator Cell," *Proceedings of the 9th IEEE Pulsed-Power Conference,* Albuquerque, NM, 1993, p. 415.
6. Metglas—a family of amorphous alloy ribbons manufactured by Allied–Signal Corporation, Metglas Products Division, 6 Eastmans Road, Parsippany, NJ, 07054.
7. Micro-Cap IV is an electronic circuit analysis program published by Spectrum, 1021 South Wolfe Road, Sunnyvale, CA, 94086.
8. H. C. Kirbie, et al., "Development of Solid-State Induction Modulators for High PRF Accelerators," Lawrence Livermore National Laboratory, Livermore, CA, UCRL-JC-119582 ABS. Prepared for *10th IEEE Pulsed-Power Conference,* Albuquerque, NM, July 10–13, 1995.
9. W. R. Cravey, "Compact Pulsed-Power Supplies," *Engineering Research Development and Technology FY93—Thrust Area Report,* Lawrence Livermore National Laboratory, Livermore, CA, UCRL-53868-93 (1993).
10. H. C. Kirbie, et al., "Smart Power Management for Laser Diode Arrays," *Engineering Research Development and Technology FY94—Thrust Area Report,* Lawrence Livermore National Laboratory, Livermore, CA, UCRL-53868-94 (1994).
11. R. L. Hanks, et al., "Integrated Power Conditioning for Laser Diode Arrays," Lawrence Livermore National Laboratory, Livermore, CA, UCRL-JC-119362 ABS, Rev. 1. Prepared for *10th IEEE Pulsed-Power Conference,* Albuquerque, NM, July 10–13, 1995.

THE NATIONAL IGNITION FACILITY PROJECT

J. A. Paisner

*J. D. Boyes**

S. A. Kumpan

M. Sorem†

Introduction

The Secretary of the U.S. Department of Energy (DOE) commissioned a Conceptual Design Report (CDR) for the National Ignition Facility (NIF) in January 1993 as part of a Key Decision Zero (KD0), Justification of Mission Need. Motivated by the progress to date by the Inertial Confinement Fusion (ICF) program in meeting the Nova Technical Contract[1] goals established by the National Academy of Sciences in 1989, the Secretary requested a design using a solid-state laser driver operating at the third harmonic (0.35 μm) of neodymium (Nd) glass. The participating ICF laboratories signed a Memorandum of Agreement in August 1993, and established a Project organization, including a technical team from the Lawrence Livermore National Laboratory (LLNL), Los Alamos National Laboratory (LANL), Sandia National Laboratories (SNL), and the Laboratory for Laser Energetics at the University of Rochester. Since then, we completed the NIF conceptual design, based on standard construction at a generic DOE Defense Program's site, and issued a 7,000-page, 27-volume CDR in May 1994.[2] Over the course of the conceptual design study, several other key documents were generated, including a Facilities Requirements Document, a Conceptual Design Scope and Plan, a Target Physics Design Document, a Laser Design Cost Basis Document, a Functional Requirements Document, an Experimental Plan for Indirect Drive Ignition, and a Preliminary Hazards Analysis (PHA) Document. DOE used the PHA to categorize the NIF as a low-hazard, non-nuclear facility.

Figure 1 shows the NIF conceptual design, which was exhaustively reviewed during the past year. A subcommittee of the Inertial Confinement Fusion Advisory Committee (ICFAC) reviewed and endorsed the laser performance of the 40-cm aperture, 192-beam multipass architecture in April 1994. The full ICFAC reviewed target design and ignition scaling in May 1994 and recommended DOE approval of the preliminary design phase of the Project. Subcontractors to DOE Defense Programs scrutinized the engineering design during the design period, while an Independent Cost Estimator team commissioned by DOE Field Management intensively reviewed and validated the cost and schedule in March and April 1994. The performance, cost, and schedule represented in the CDR were formally submitted in June 1994 in a Project Data Sheet for inclusion in the FY 1996 DOE funding cycle.

On October 21, 1994 the Secretary of Energy issued a Key Decision One (KD1) for the NIF, which approved the Project and authorized DOE to request Office of Management and Budget–approval for congressional line-item FY 1996 NIF funding for preliminary engineering design and for National Environmental Policy Act activities. In addition, the Secretary declared Livermore as the preferred site for constructing the NIF. In February 1995, the NIF Project was formally submitted to Congress as part of the President's FY 1996 budget. If funded as planned, the Project will cost approximately $1.1 billion and will be completed at the end of FY 2002.

This article presents an overview of the NIF Project.

NIF Design Criteria

The identified laser power and energy operating regimes for indirect-drive fusion ignition targets are displayed in Fig. 2 and are the basis for the primary

* Sandia National Laboratories, Albuquerque, NM
† Los Alamos National Laboratory, Los Alamos, NM

UCRL-LR-105821-95-2

design criteria for the facility (Table 1). Each point on the operating map corresponds to a different temporal pulse shape, typically one with a relatively long foot-pulse (10–20 ns), followed by a short peak-pulse (2–8 ns) having a high contrast ratio (25–100:1). In the high-power, short-temporal-pulse region, performance is limited by laser–plasma instabilities, while in the low-power, long-temporal-pulse region, performance is limited by hydrodynamic instabilities.

The baseline target, shown in Fig. 3, requires a laser system that routinely delivers 500 TW/1.8 MJ at 0.35 μm in a 50:1 contrast ratio pulse through a 500-μm spot at the laser entrance hole of the target hohlraum with a positioning accuracy of 50 μm. Each beam must achieve a power balance of approximately 8% rms (over any 2-ns interval) with respect to a reference value. As summarized by the design rules in Table 2, symmetrical implosion of the capsule requires two-sided target irradiation with two cones per side, each having an outer cone:inner cone laser power ratio of 2:1, and at least eight-fold azimuthal irradiation symmetry. The cone angles, nominally at 53° (outer) and 27° (inner), and laser power ratio are chosen to maintain time-dependent symmetry of the x-ray drive seen by the imploding capsule.

To avoid laser–plasma instabilities, such as filamentation and stimulated scattering, the baseline indirect-drive target hohlraum requires laser spatial beam smoothing using phase plates and laser temporal smoothing with a combination of four beams at different center wavelengths, each separated by 3.3 Å (3.3×10^{-4} μm). This separation is set by a beam-smoothing requirement on the motion of the kinoform-induced speckle pattern at the target focus.

As a consequence of these symmetry design rules, the laser system must deliver at least 192 beams to the target chamber. A laser system designed to meet these criteria has a power and energy safety margin of approximately two for achieving ignition, as indicated in Fig. 2. These laser system requirements, optimized

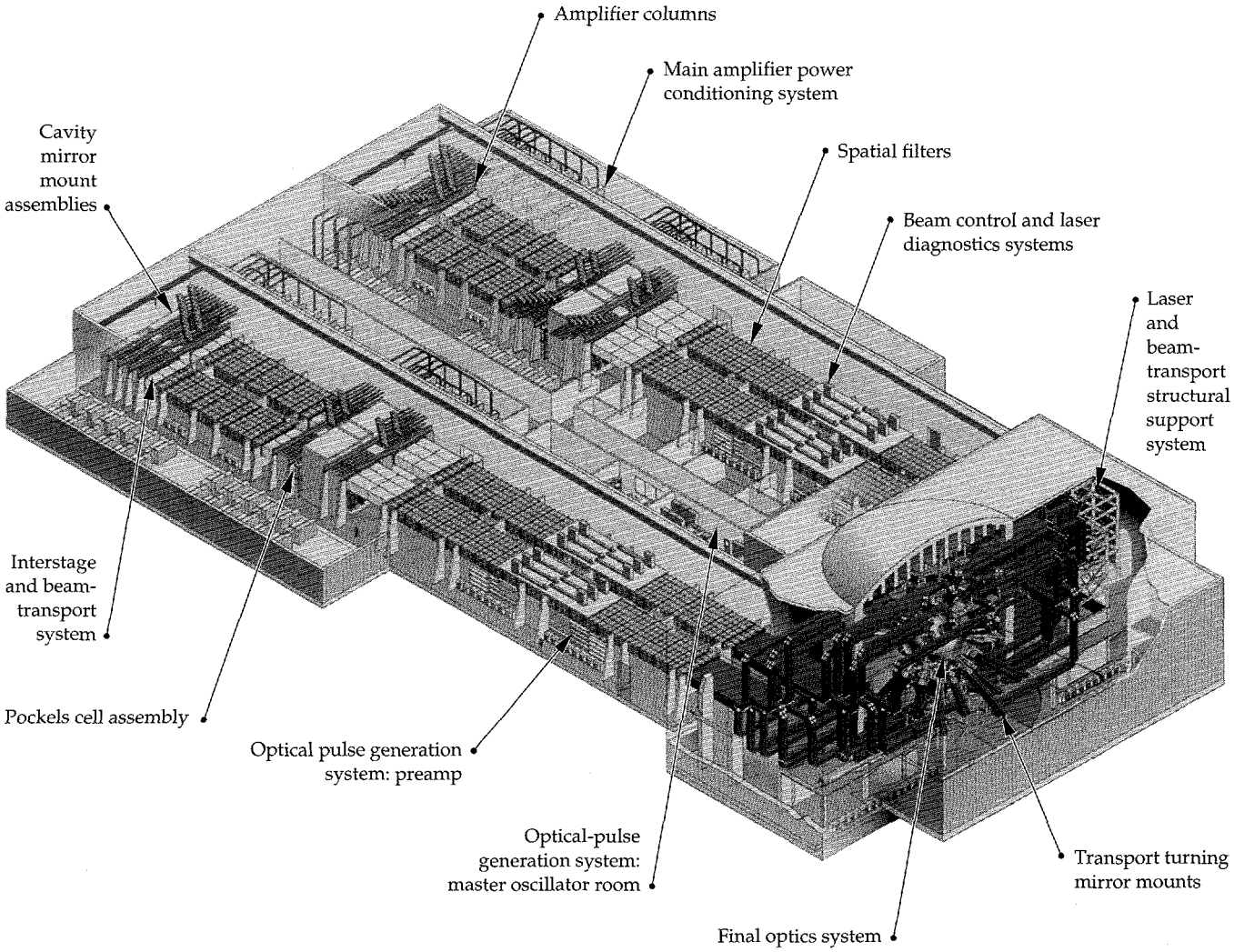

FIGURE 1. The NIF overview. The NIF will be a low-hazard, non-nuclear facility. (40-00-0294-0498Zpb03)

for indirect-drive ignition targets, are consistent with those proposed for direct-drive ignition targets.

The primary criteria for the NIF systems given in Table 1 represent a small subset of the functional requirements for the facility, which include other mission-related and lifecycle requirements for the laser, experimental area, radiation-confinement systems, building and structural systems, safety systems, environmental protection systems, and safeguard and security systems. The NIF was designed for a generic site and is consistent with all relevant orders, codes, and standards. The U-shaped building configuration satisfies a key functional requirement: providing for the future addition of a second large target chamber to accommodate special requirements of other communities, such as for weapons effect tests, with minimal interruptions to system operations. Preliminary analysis

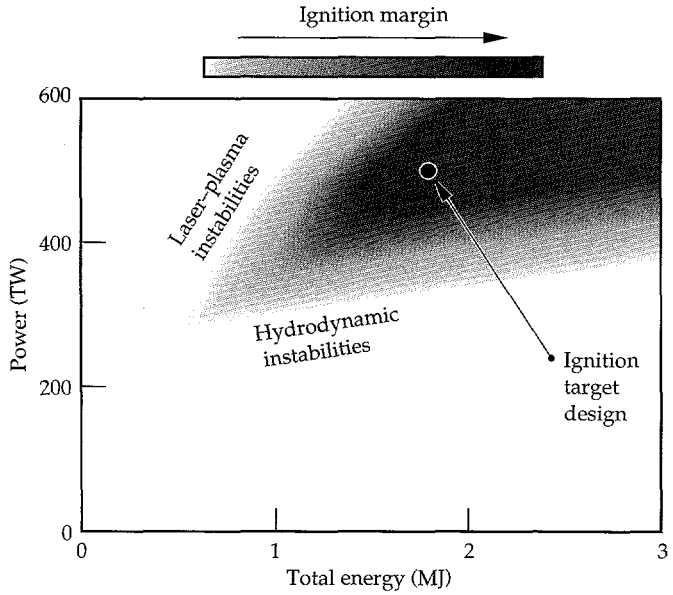

FIGURE 2. The indirect-drive target operating regime in laser power-energy space at 0.35 μm. The operating regime is constrained by laser–plasma instabilities and hydrodynamic instabilities. Each point on the plane corresponds to a unique two-step temporal pulse. The baseline design at 500 TW/1.8 MJ has approximately a factor of two safety margin for ignition. This energy and power safety margin above threshold provides room to trade off asymmetry, laser–plasma instabilities, and other uncertainties. (50-05-0494-1803pb02)

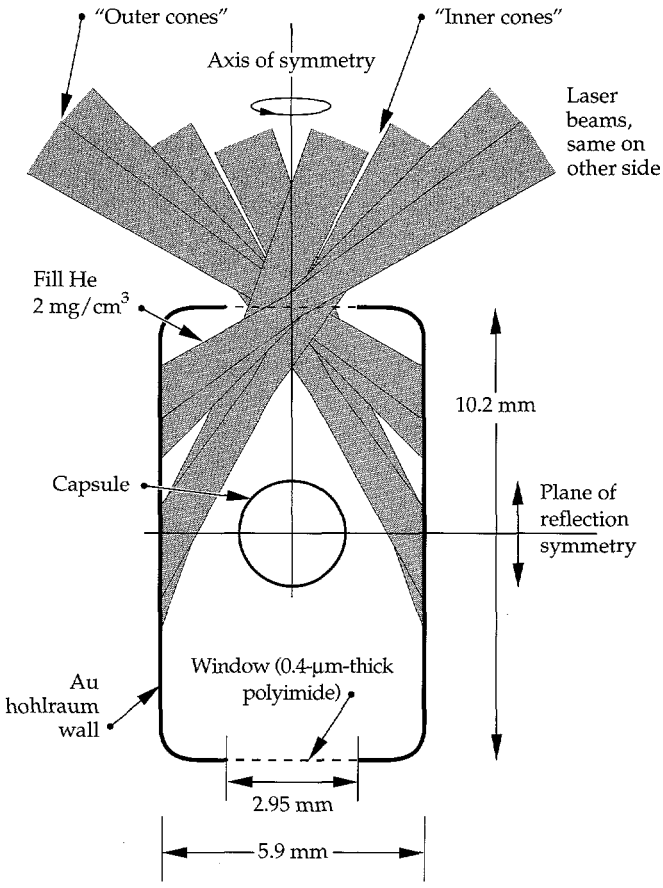

FIGURE 3. A baseline NIF target was used to establish design criteria for the facility. The outer cones enter at 57° and 48°, with a 500-μm best focus at the entrance hole (*f*/8). The inner cones enter at 23° and 32°, with a 500-μm best focus ~3 mm inside the hohlraum (*f*/8). (40-00-0294-0596Apb01)

TABLE 1. Primary criteria for the National Ignition Facility.

Laser pulse energy	1.8 MJ
Laser pulse peak power	500 TW
Laser pulse wavelength	0.35 μm
Beamlet power balance	<8% rms over 2 ns
Beamlet pointing accuracy	<50 μm
ICF target compatibility	Cryogenic and non-cryogenic
Annual number of shots with fusion yield	100 with yield 1 kJ–100 kJ
	35 with yield 100 kJ–5 MJ
	10 with yield 5 MJ–20 MJ
Maximum credible DT fusion yield	45 MJ
Classification level of experiments	Classified and unclassified

TABLE 2. Minimum number of 192 beams delivered to ignition target is determined by implosion symmetry requirements.

Symmetry	Beam multiplier	Notes
Time dependent hydrodynamic	3	Outer cone at ~53° at 2× energy/power
		Inner cone at ~27° at 1× energy/power
Azimuthal	≥8 (or 8, 9, 10...)	Number of inner-cone laser spots on hohlraum wall
Reflection	2	
Beam smoothing	4	Smoothing by multiple apertures/colors
Required number of beams	≥192 (or 192, 216, 240...)	

has shown that a modest upgrade of the currently designed NIF target area and target chamber system would accommodate direct-drive ignition target experiments without impacting the indirect-drive mission.

Laser System Design

The Nd:glass laser system must provide at least 632 TW/3.3 MJ in a 5.1-ns pulse at 1.053 μm to account for modest beam transport losses, and energy and power conversion efficiencies of 60% and 85%, respectively. Figure 4 shows a schematic of one NIF beamline. It uses a four-pass architecture with a large-aperture optical switch consisting of a plasma-electrode Pockels cell and polarizer combination.

The laser chain in this beamline was designed using the CHAINOP family of numerical codes that model the performance and cost of high-power solid-state ICF laser systems. These codes vary a number of design parameters to maximize laser output per unit cost, while remaining within a set of constraints. The constraints include fluence maxima, nonlinear effects, and pulse distortion. CHAINOP contains several analytical models that simulate the optical pumping process, the propagation of the laser beam through the system (including gain, loss, diffraction, and nonlinear optical effects), frequency conversion, and cost. This design procedure is excellent for cost scaling and system trade-off studies, but does not suffice for predicting detailed performance, which requires analysis with a suite of nonlinear physical optics codes, or determining project costs, which are estimated using a detailed engineering design and a rigorous item by item or "bottom-up" costing described later in this article.

The laser chain used in the CDR as the baseline for estimating NIF system cost and performance has a hard aperture of 40 × 40 cm^2. The amplifiers contain 19 Nd-doped glass laser slabs arranged in a 9-5-5 configuration as shown in Fig. 4. Each Brewster-angled slab is 3.4 cm thick. Figure 5 shows the 1.053-μm performance of this laser chain. At the 5.1-ns design point each laser chain should generate 3.9 TW/20.5 kJ. Because only 162 beams are required to achieve the performance criteria, a 192-beam system has a design margin of greater than 15%. A prototype beamline, called Beamlet, is undergoing tests at LLNL to demonstrate NIF performance projections using the large-aperture optical switch. Variations of a NIF design with reduced-aperture switches have comparable performance projections when optimized.

The NIF design incorporates 4-high × 12-wide arrays of laser beams as shown in Figure 1. The design is more compact than previous laser fusion systems, increasing

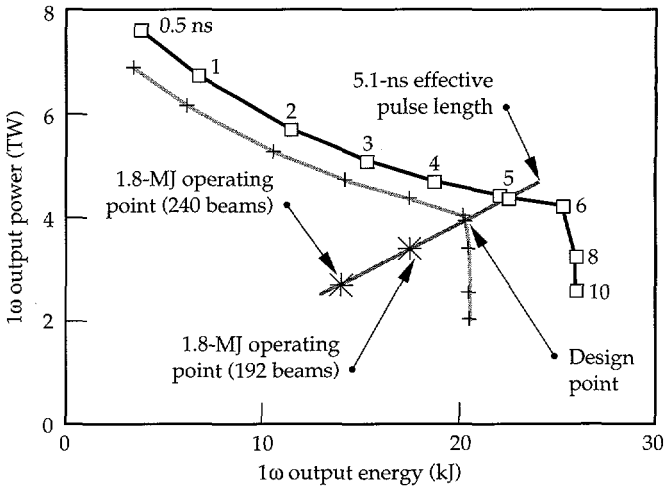

FIGURE 5. The 1.05-μm power/energy performance as a function of pulse length for the 9-5-5 configuration (shown in Fig. 4). The gray line shows the baseline performance (nominal-gain and -loss case). The black line illustrates the performance with line-center gain and with improved optical transmission of the laser glass and optical switch. For a 5.1-ns effective pulse length, determined by the NIF temporal pulse shape, the maximum gray-line performance of 20 kJ sets the number of required beams at 162. This would produce 3.3 MJ of 1.05 μm light and would deliver 1.8 MJ of 0.35-μm light to the laser entrance hole of the target hohlraum. Changing the system total from 162 to 192 (240) beams would provide an 18% (48%) laser design margin to meet the target hohlraum requirements. (40-00-0394-1378pb01)

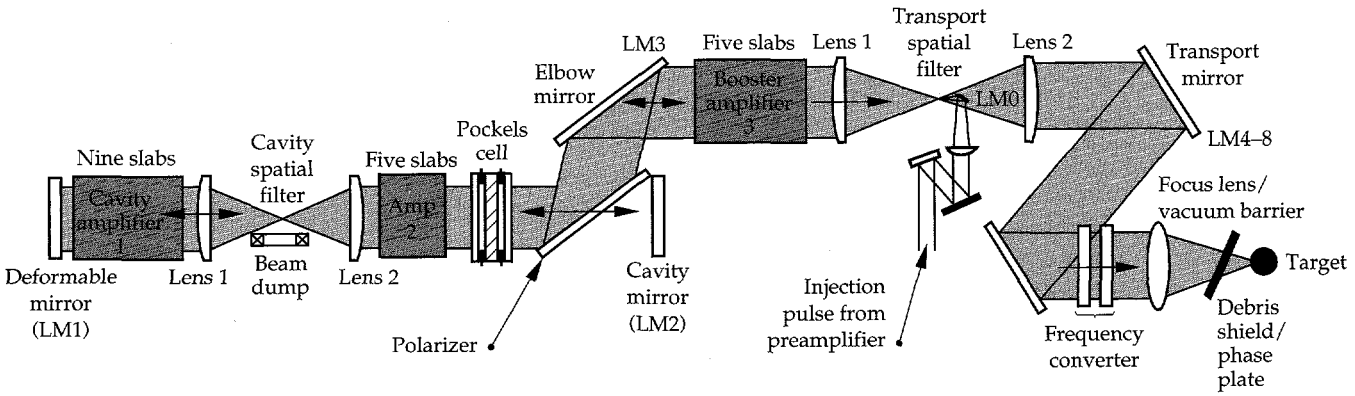

FIGURE 4. A schematic of one beamline of the NIF laser from pulse injection to final focus on target. (40-00-0394-0789Apb02)

overall electrical and optical efficiency while simultaneously reducing system size and cost. The optical-pulse generation system provides individually controlled input pulses from one of four tunable fiber oscillators and an integrated optics network located in the master oscillator room (MOR). The outputs from the MOR are delivered on single-mode polarization preserving fibers to each of 192 preamplifiers. These stand-alone packages, located beneath the transport spatial filters, provide individual power balance capability for each of the 192 beams. The output beams from the preamplifiers are injected into the far-field pinholes of the transport spatial filters, passed through the boost-amplifier stages, the optical switch assemblies, and then captured inside the multipass cavities. The flash lamps located in the amplifier enclosures that uniformly pump the glass laser slabs are energized with approximately 260 MJ of electrical energy from a modular bank of thin film, metallized dielectric capacitors. After four passes through the cavity amplifiers, the pulses are switched out of the multipass cavity, further amplified by the boost stage, and then transported to the target chamber. The laser arrangement allows for top and bottom access to the amplifiers and the optical switch arrays. The pulsed power is transmitted to the amplifiers overhead with large, 30-cm-diam, coaxial conductors. The space below the amplifiers allows access for assembly and maintenance of any four-high amplifier column.

Wavefront aberrations resulting from the long-term thermal cooling of the glass laser slabs ultimately limit the shot rate of the laser system. The NIF is currently designed to achieve about 700 full-system performance shots/year. A novel feature of the current design is the use of deformable mirrors in place of the end cavity mirrors (see Fig. 4) to correct for static and pump-induced short-term wavefront aberrations, which will allow for higher shot rates. It is expected that through continued engineering design of the wavefront-correction and cooling systems, the laser shot rate will increase substantially. This is consistent with engineering improvements on all previous ICF glass laser systems, including Nova, which has had its shot rate increase by a factor of six since operations began in 1985.

Target Area Design

Figure 6 shows a cutaway view of the switchyard and target area. The 192 laser beams are optically relayed via the transport spatial filters in 48 2×2 groupings to the final optics assemblies. The beams are constrained to only *s*- and *p* -polarized reflections in the optical switchyard and target areas so that they maintain linear

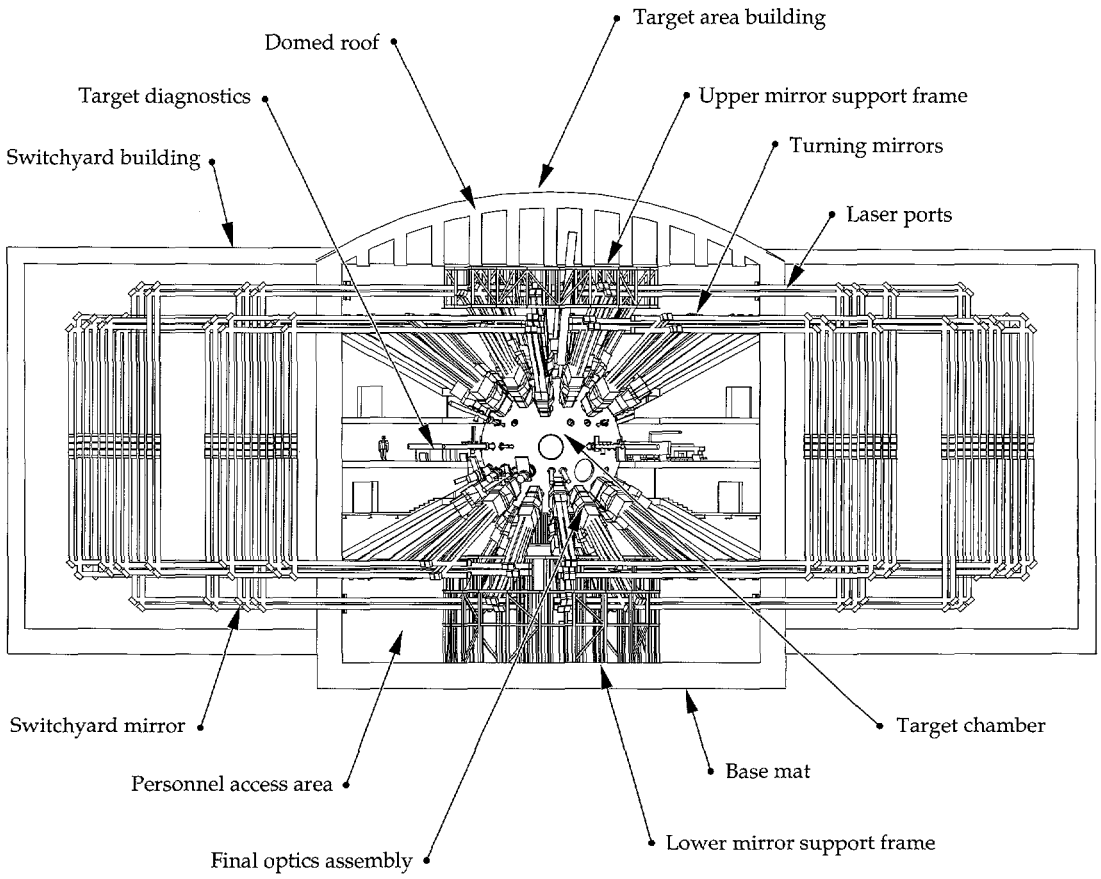

FIGURE 6. A cutaway view of the NIF target area showing major subsystems. (40-00-0394-1030pb01)

polarization and radial symmetry with respect to the cylindrical axis on the hohlraum. Consequently, there is complete azimuthal symmetry. The 48 final optics assemblies (Fig. 7) are positioned on the 53° outer cones (16 assemblies) and 27° inner cones (8 assemblies) at the top and on the bottom of the target chamber. At the chamber each 2×2 grouping is converted to 0.35 μm by a Type I (potassium dihydrogen phosphate, or KDP)/Type II (deuterated KDP, or KD*P) crystal array in the final optics assembly. The final optics assemblies mount to the exterior of the chamber, and also provide 2×2 lens arrays for focusing the light onto the target and 2×2 debris shield arrays for protecting the lenses from target shrapnel. (The debris shields also contain the kinoform phase plates.) Each beam in every 2×2 grouping can be operated at a different center wavelength to provide the requisite laser temporal beam smoothing. The final optics assemblies are offset from the nominal cone angles by ±4° to provide isolation between opposing beamlines.

The target chamber is housed in a reinforced-concrete building with three separate operational areas (see Fig. 6). The upper and lower pole regions of the target chamber house the final optics and turning mirrors in a class 1000 clean room. Personnel access to these areas will be limited to preserve cleanliness levels. The cantilevered floor sections of the building provide a separation of the clean-room enclosures at the polar regions from the equatorial target diagnostics area. This horizontal, planar architecture simplifies the design of the access structures required to service the optical components and target diagnostics.

The NIF baseline target chamber is a 10-cm-thick by 10-m internal-diam spherical Al shell designed to

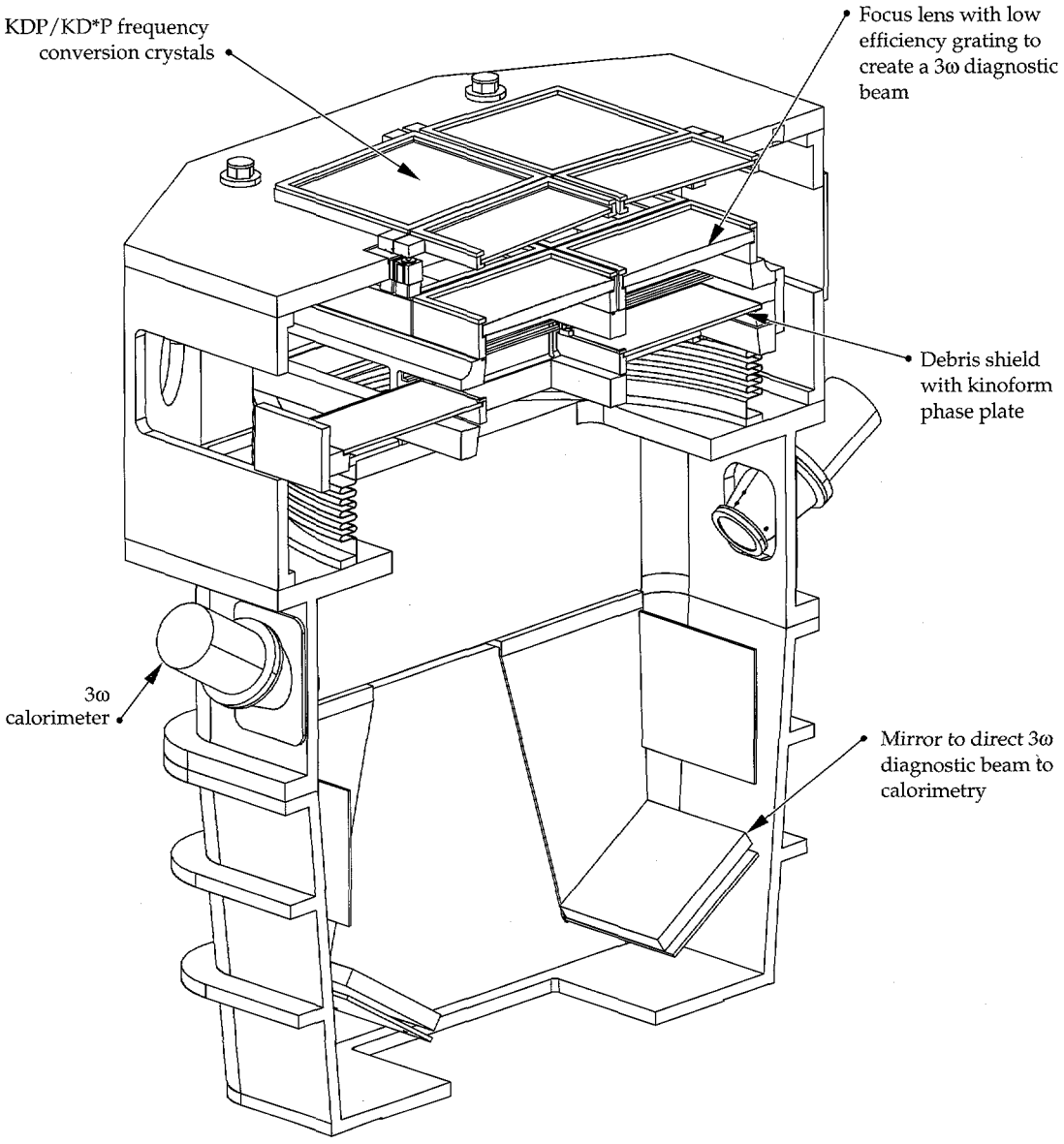

FIGURE 7. The final optics assembly has multiple functions: Frequency conversion, focusing, spatial smoothing, optics protection, 1ω/2ω dispersion, 3ω calorimetry, and vacuum interface. (40-00-0294-0600Bpb01)

accommodate the suite of x-ray and neutron diagnostics required to measure the performance of targets that can achieve ignition. The Al wall provides the vacuum barrier and mounting surfaces for the first-wall panels, which protect the Al from soft x rays and shrapnel. The unconverted laser light hitting the opposite wall is absorbed by other panels offset from the opposing beam port. The exterior of the chamber is encased in 40 cm of concrete to provide neutron shielding. The chamber is supported vertically by a hollow concrete pedestal and horizontally by radial joints connected to the cantilevered floor. The target area building, chamber, and auxiliary systems are designed to handle 145 shots/year of yields up to 20 MJ as shown in Table 1.

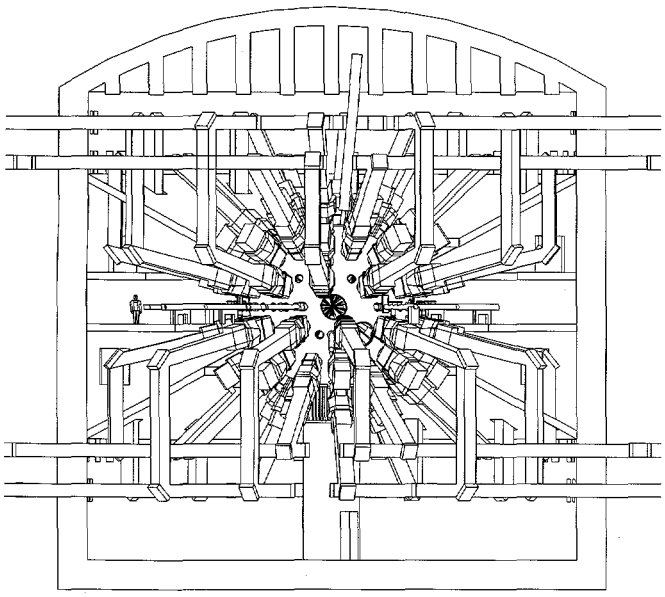

FIGURE 8. Implementation of direct drive requires that 24 of the 48 beams be repositioned. This can be accomplished easily using the NIF optical system design. Compare to Fig. 6. (40-00-0694-2750pb01)

Recent engineering analyses and target physics calculations show that the baseline design can be easily modified, as illustrated in Fig. 8, to incorporate a direct-drive ignition capability, further broadening the utility of the facility.

NIF Project Schedule

The summary schedule shown in Fig. 9 illustrates the sequence of events leading to NIF operations in October 2002. This overall schedule assumes the NIF Project is initiated by line-item funding in FY 1996 consistent with a KD1. A more detailed integrated Project schedule (not shown) reveals the critical path that affects the Project duration. The major NIF critical path consists of design, site selection, design and construction of the laser and target areas building, laser and other special equipment installation, completion of the acceptance test procedures, and start-up. Construction completion, equipment installation, and start-up are overlapped to shorten the critical path within limits of a practical funding profile. The release of design, construction, procurement, and operating funds is constrained by the DOE Key Decision (KD1 through KD4) process.

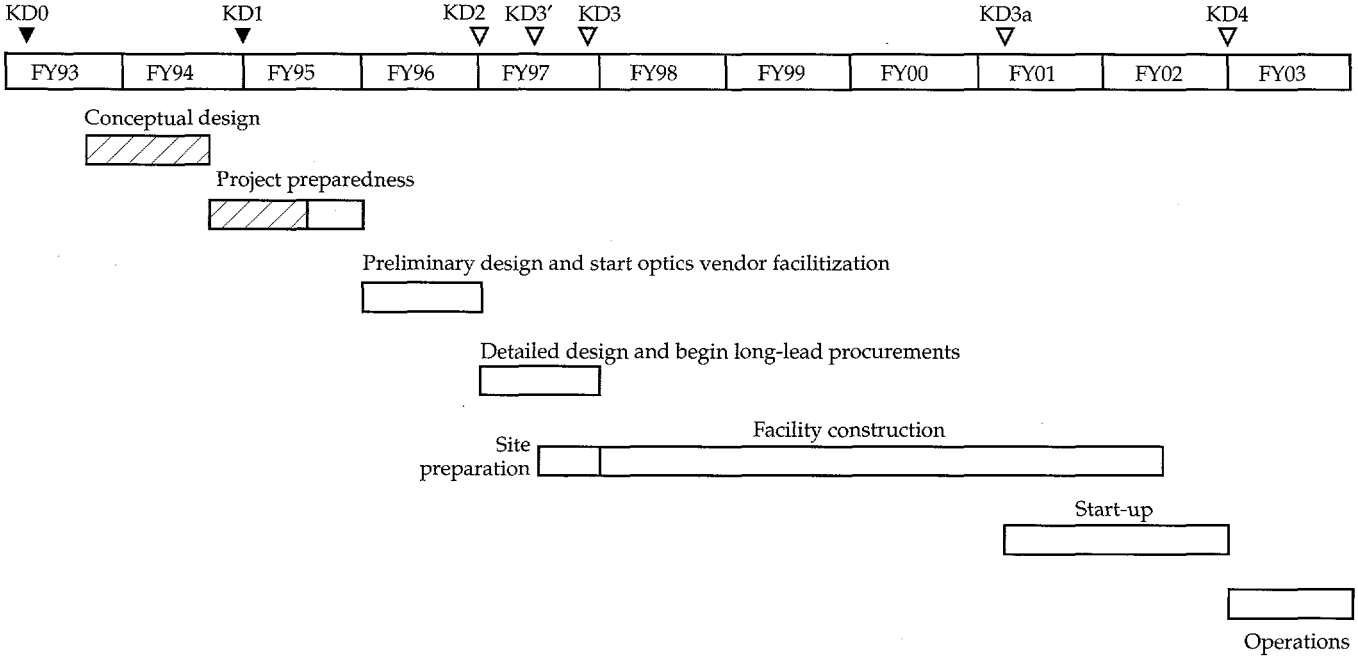

FIGURE 9. NIF Project schedule (hash marks and solid triangles indicate completion). (40-00-0195-0269Hpb01)

NIF Project Cost

The NIF Total Project Cost (TPC) is the sum of the Total Estimated Cost (TEC) and the Other Project Cost (OPC). The TEC is funded by Plant and Capital Equipment (PACE) funds and the OPC is funded by Operating Expense (OPEX) funds. Division of costs between TEC and OPC is provided in DOE guidelines. TEC activities include, for example, Title I and II design, and Title III engineering; building construction; procurement; assembly and installation of all special equipment; and sufficient spares to pass the acceptance test procedures. OPC activities include, for example, conceptual design; advanced conceptual design; NEPA documentation; vendor facilitization and pilot production; vendor component qualification/reliability/lifetime testing; operational readiness reviews; startup costs; and operational spares.

TABLE 3. Summary of NIF costs for 192-beam system, in millions of dollars.

	Base costs ($M FY94)	Contingency ($M FY94)	Total ($M FY94)	Total ($M escalated)
TEC	586	121	707	842
OPC	199	N/A	199	231
TPC	785	121	906	1073
Annual operating costs	57	N/A	57	N/A

The costs shown in Table 3 were derived from a bottom-up estimate based on a detailed work breakdown structure (WBS) that is summarized at WBS Level 3 in Fig. 10. The Project adopted the Martin Marietta Energy Systems, Inc. Automated Estimating System (AES) as its cost management tool. The AES is consistent with DOE Order 5700.2d, "Cost Estimating Analysis and Standardization," and has been used in many other DOE projects in the past. The labor rates,

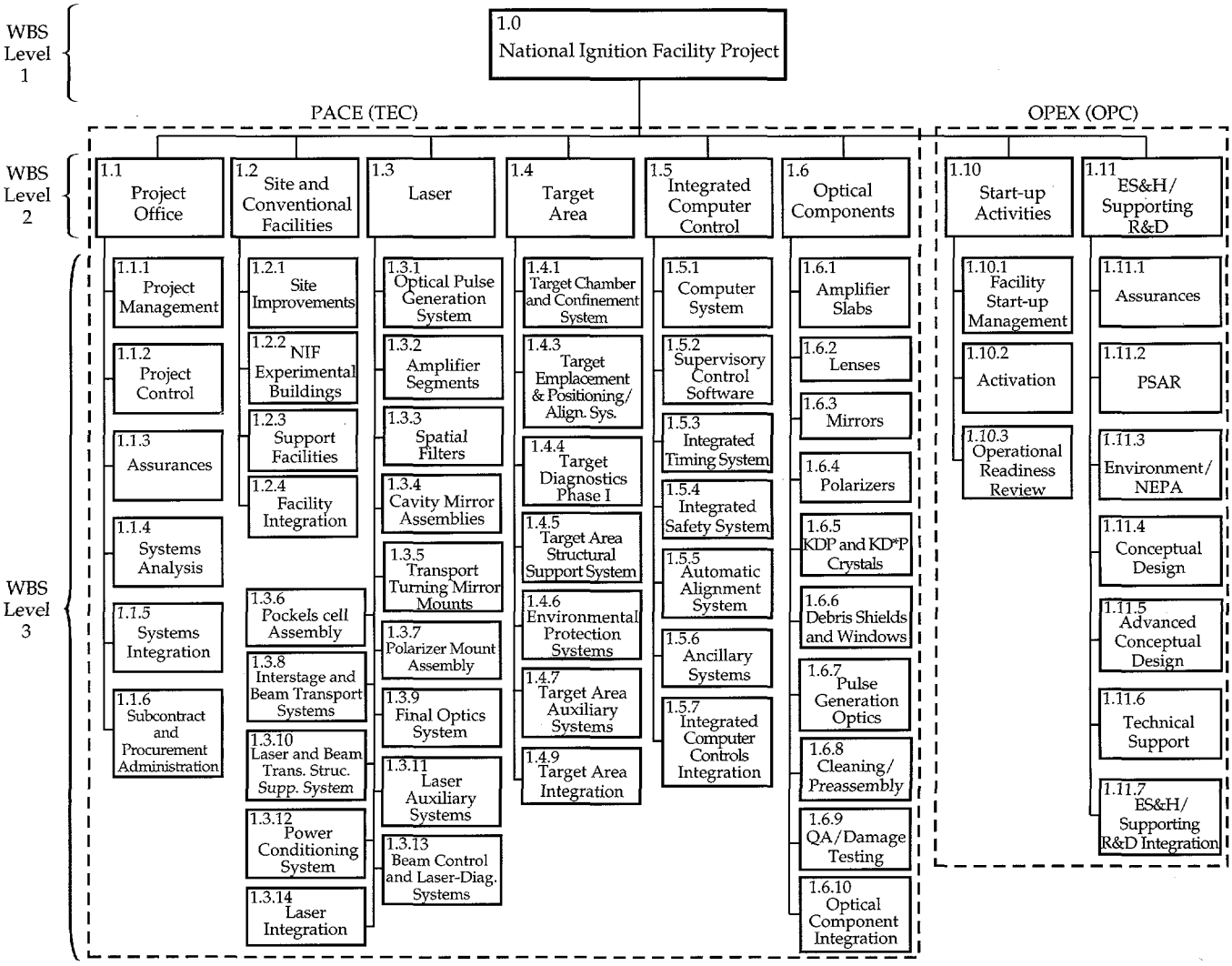

FIGURE 10. NIF Project WBS elements to Level 3. (1.4.0893.2859Mpb01)

overhead costs, allowances for incidental costs not directly estimated, and other indirect costs were applied to the database using the AES. Contingency information provided by each estimator for every Level 3 item was used in a separate probabilistic contingency analysis performed by Bechtel Corporation using their MICRORAC code. The results of that analysis were entered into the AES. Integrated project schedule data were combined with the cost information in the AES to estimate escalation and calculate the Budget Authority and Budget Outlay profiles required in the Project submission to DOE. The annual operating costs for the facility, shown in Table 3, were estimated by identifying all the NIF unit operations based on Nova experience. It does not include, per DOE guidance, the annual ICF Program costs (currently at approximately $175 million/yr).

Figure 11 gives a second-level breakout of TEC and a third-level breakout of OPC (without contingency or escalation). The engineering design was sufficiently detailed to generate costs, typically, at Level 5, and, in some cases, at Level 6 or 7. Approximately 70% of the costs (in dollars) were derived from catalog prices, vendor estimates, or engineering drawings. The costs in Table 2 have been validated by the DOE and by an Independent Cost Estimator team commissioned by DOE.

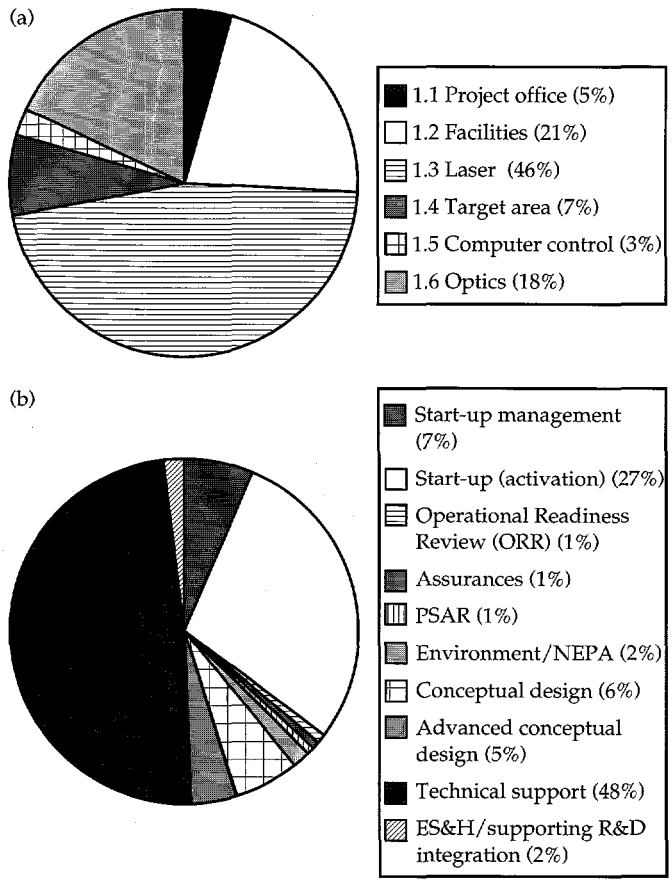

FIGURE 11. Cost breakouts for (a) TEC without contingency in unescalated dollars, broken down to Level 2 and for (b) OPC in unescalated dollars, broken down to Level 3. (40-00-0494-1720Apb01)

Summary

The NIF design is the product of the efforts of a multilaboratory team, representing more than 20 years of experience at the LLNL, LANL, SNL, and the Laboratory for Laser Energetics at the University of Rochester. Using the world's most powerful laser to ignite and burn ICF targets, the NIF will produce conditions in matter similar to those found at the center of the Sun and other stars. New, well characterized, high-energy-density regimes will be routinely accessible in the laboratory for the first time. The NIF will impact and extend scientific and technical fields such as controlled thermonuclear fusion, astrophysics and space science, plasma physics, hydrodynamics, atomic and radiation physics, material science, nonlinear optics, advanced coherent and incoherent x-ray sources, and computational physics. The importance and uniqueness of the NIF to these wide-ranging fields of science and technology have been recently reviewed in a series of workshops.[3] If authorized in FY 1996, the NIF could begin operations in FY 2003.

Notes and References

1. Committee for a Second Review of DOE's ICF Program, *Final Report—Second Review of the Department of Energy's Inertial Confinement Fusion Program*, National Academy of Sciences, Commission on Physical Sciences, Mathematics, and Applications, National Research Council, National Academy Press, Washington, D.C. (September 1990).
2. J. A. Paisner, *National Ignition Facility Conceptual Design Report*, Lawrence Livermore National Laboratory, Livermore, CA, UCRL-PROP-117093 (1994).
3. J. A. Paisner, *Utility of the National Ignition Facility*, Lawrence Livermore National Laboratory, Livermore, CA, NIF-LLNL-94-240, UCRL-117384 (1994).

TERMINAL-LEVEL RELAXATION IN ND-DOPED LASER MATERIALS

C. Bibeau

S. A. Payne

Introduction

During the energy extraction of a 1-μm pulse in a Nd-doped laser material, the Nd-ion population is transferred from the metastable $^4F_{3/2}$ level into the terminal $^4I_{11/2}$ level, as shown in Fig. 1. The *terminal-level lifetime*, $\tau_{11/2}$, is defined in this case as the time it takes the Nd-ion population to decay from the $^4I_{11/2}$ level into the $^4I_{9/2}$ ground state. Several experimental and theoretical approaches over the last three decades have been made to measure the terminal-level lifetime. However, an agreement in the results among the different approaches for a large sampling of laser materials has never been demonstrated.

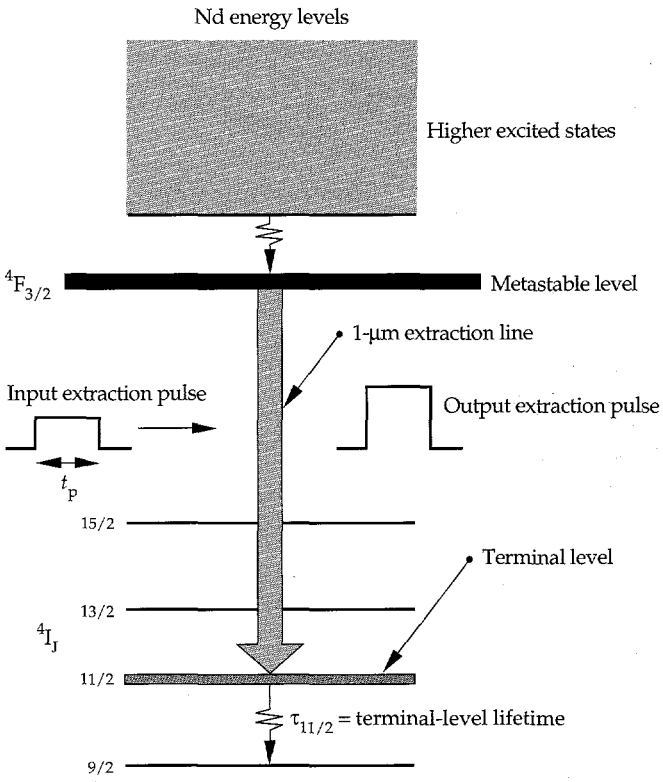

FIGURE 1. A Nd^{3+} energy level diagram that shows the 1-μm laser transition from the $^4F_{3/2}$ metastable level into the $^4I_{11/2}$ terminal level. During this transition, the input extraction pulse is amplified to produce a more energetic output pulse. The nonradiative relaxation from the $^4I_{11/2}$ level into the $^4I_{9/2}$ ground state is known as the terminal-level lifetime ($\tau_{11/2}$). (70-15-0993-3196pb01)

This article presents three independent methods (pump-probe, emission, and energy extraction) for measuring the terminal-level lifetime in Nd:phosphate glass LG-750. We find remarkable agreement among the data and determine the $\tau_{11/2}$ lifetime to be 253 ± 50 ps. We extend our studies to show that the results of the pump-probe and emission methods agree to within a factor of two for additional Nd-doped glasses and crystals investigated, thus offering validation for the emission method, which is a simpler, indirect approach.

Background

As explained, $\tau_{11/2}$ is the time it takes the Nd-ion population to decay from the $^4I_{11/2}$ level into the $^4I_{9/2}$ ground state during the energy extraction of a 1-μm pulse. If the decay time is infinitely fast compared with the length of the extraction pulse ($\tau_{11/2} << t_p$) then the $^4I_{11/2}$ level will appear to be virtually unpopulated for the duration of the extraction pulse. Since the small signal gain coefficient (g_0) is directly proportional to the population inversion (ΔN) between the upper $^4F_{3/2}$ level and the lower $^4I_{11/2}$ level, the incoming laser pulse will extract more of the stored energy if the $^4I_{11/2}$ level remains unpopulated. Conversely, if the length of the extracting pulse is much less than the terminal-level lifetime ($t_p << \tau_{11/2}$) then the population in the $^4I_{11/2}$ level will remain populated or bottlenecked. As a consequence, the extraction process will be less efficient

since stimulated emission and absorption processes can become competitive and thus cause the re-excitation of the Nd-ion population in the $^4I_{11/2}$ level back into the $^4F_{3/2}$ level during extraction.

Figure 2 is a plot of the ideal extraction efficiency for Nd:phosphate glass as a function of the ratio $R = t_p/\tau_{11/2}$. For comparison, a few additional data are shown, including the oxide crystals Nd:YAG and Nd:YALO and the fluoride crystal Nd:YLF. The data points for these materials do not lie exactly on the phosphate curve due to differences in the spacing of the energy levels that affect the degeneracies of the upper and lower laser levels and thus the values for the extraction efficiency. The pulse lengths are assumed to be square in shape with a length of 3 ns, with the exception of the National Ignition Facility (NIF) data point, where t_p is 8 ns. The proposed design of the NIF will use a Nd-doped phosphate glass similar to LG-750 and will require longer pulse lengths. We discuss a derivation of this curve in a later section, but for now it illustrates that the extraction efficiencies for a Nd:phosphate glass laser are only moderately impacted by the short terminal lifetime (< 1 ns), whereas for Nd:YLF the long terminal lifetime (~10 ns) can become a limiting factor.

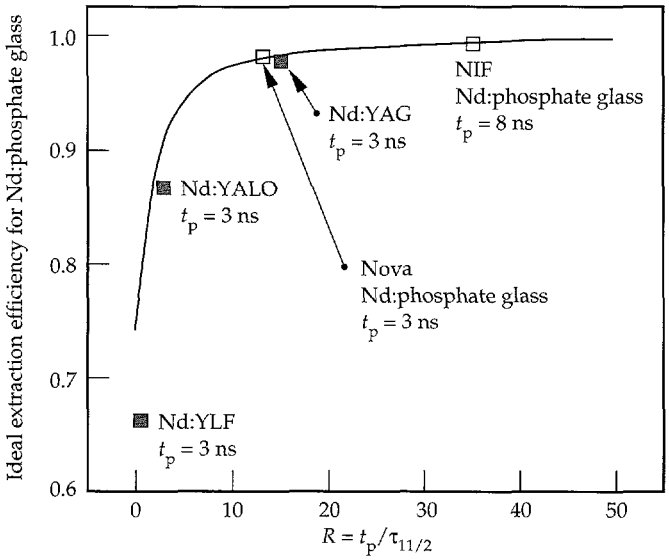

FIGURE 2. The ideal extraction efficiency plotted as a function of the ratio of the pulse length t_p to the terminal-level lifetime $\tau_{11/2}$ for Nd:phosphate glass. For comparison, additional data are shown (solid squares). The plots illustrate that the relatively short terminal lifetimes (<1 ns) of the phosphate glass used in the Nova laser and of the glass used in the design of the NIF are not a limiting factor in obtaining the highest possible extraction efficiency. In comparison, the long lifetime (~10 ns) of the fluoride crystal, Nd:YLF, can be a limiting factor. (70-00-0295-0392pb01)

Given the importance of the terminal-level lifetime for phosphate glass, we employ three different methods for measuring its value. We first describe a novel and more accurate direct approach that employs a pump-probe technique.[1] We also explore an indirect emission method, which is based on the "energy-gap law,"[2,3] since this method continues to be the preferred method due to its simple and straightforward approach. However, it is a method that presupposes that the lifetime of a different nonradiative transition ($^4G_{7/2} \rightarrow {}^4G_{5/2}, {}^2G_{7/2}$), whose energy gap coincidentally matches that of the relevant transition ($^4I_{11/2} \rightarrow {}^4I_{9/2}$), provides a reasonable assessment of the actual terminal-level lifetime. Based on the validity of the energy gap law, the two lifetimes are expected to be equal. Finally, we model data taken from a previous set of experiments and show that the terminal lifetime for phosphate glass derived from the best fit to the data is in agreement with the values derived from the pump-probe and indirect emission experiments.

In addition, we found in the process of modeling the extraction data that it would be useful if an approximate solution of the energy transport and kinetic differential equations existed that explicitly include the terminal lifetime and the pulse length. The motivation for finding an empirical solution was to be able to use a simple expression within the existing models that would include the effects of the terminal-level lifetime without having to tediously integrate the energy transport and kinetic differential equations. To date, the only analytic solutions that exist are for the two extreme cases of $t_p/\tau_{11/2} << 1$ and $t_p/\tau_{11/2} >> 1$, that is, very short or long pulse lengths relative to the terminal lifetime.[4] We formulated an empirical solution of the saturation fluence that explicitly includes the ratio $t_p/\tau_{11/2}$ and is therefore valid in the intermediate region of $t_p/\tau_{11/2} \approx 1$ as well. Our empirical solution of the saturation fluence can be substituted within the well known Frantz–Nodvik[4] analytic solution to model the energy extracted from an amplifier. We present a modified expression for the saturation fluence and describe how we used it to model the energy extraction data for Nd:phosphate glass.

We first describe the direct (pump-probe) method followed by the indirect (fluorescence) method and discuss the lifetime results for LG-750. Next, we model the extraction data previously taken by Yarema and Milam[5] and discuss our model. We show concurrence among the three methods with an averaged lifetime of $\tau_{11/2}$ = 253 ps with an rms error of ±50 ps. In the final section we compare the results from the direct and indirect methods for 13 materials and show that the simpler, indirect method can be used to determine the terminal lifetimes with an uncertainty of less than a factor of two in most circumstances.

Direct Method: Experiment and Results

To directly measure the population decay time between two electronic levels of interest, we must first find a way to selectively populate the upper level and then be able to detect and accurately measure the population decay. The total decay rate of the emission signal is a sum of the radiative and nonradiative decay rates. In most Nd-doped hosts, the small energy gap (<1500 cm^{-1}) of the $^4I_{11/2} \rightarrow {}^4I_{9/2}$ transition and high phonon frequencies (up to 1300 cm^{-1}) enable the nonradiative rate to be much faster than the radiative rate. This causes the photon emission signal from the $^4I_{11/2}$ level to be very weak, thus making an accurate measurement of the nonradiative lifetime inherently difficult. Until recently, many of the direct measurements employed either an energy-extraction or gain-recovery method coupled with a numerical model.[6,7]

We designed a unique pump-probe experimental technique to directly measure the nonradiative lifetime for the $^4I_{11/2} \rightarrow {}^4I_{9/2}$ transition in various Nd-doped glasses and crystals. Figure 3 shows a series of energy level diagrams describing the sequence of events for the experiment: (1) A 2.41-μm pump beam excites a fraction of the ground state Nd ions into the $^4I_{13/2}$ level, after which the Nd ions will nonradiatively decay into the $^4I_{11/2}$ level. (2) After an incremental time delay, a 1.06-μm probe beam excites a fraction of the $^4I_{11/2}$ population into the $^4F_{3/2}$ level. (3) The $^4F_{3/2}$ population can decay into several of the lower ^4I_J levels, but we chose to record the 0.88-μm emission signal corresponding to the $^4F_{3/2} \rightarrow {}^4I_{9/2}$ transition. The time-integrated 0.88-μm signal is proportional to the $^4I_{11/2}$ population. This sequence of events is repeated for each increased time delay between the pump and probe pulses. Therefore, as the time delay between the pump and probe pulses increases, the value of the integrated 0.88-μm emission signal diminishes since most of the $^4I_{11/2}$ population will eventually return into the ground state. A plot of the *time-integrated* 0.88-μm emission values vs time delay (τ_d) will construct the temporal evolution of the $^4I_{11/2}$ population. In passing we note that directly populating the $^4I_{11/2}$ level can be difficult due to the increased intrinsic absorption of the host medium at 5 μm.

Figure 4 shows a simplified experimental diagram. The 1.06-μm output of a mode-locked laser operating at a repetition rate of 76 MHz is injected into a regenerative amplifier. The output pulses emerge from the amplifier at a 10-Hz repetition rate with an energy of 55 mJ per pulse. Two nonlinear frequency conversion processes are required to generate the 2.41-μm pump beam: a Raman process to generate 1.91-μm output and a difference frequency generator to produce the 2.41-μm output. The 1.06-μm pulse is split with a beam splitter that allows 80% of the 1.06-μm energy to pass through a high-pressure (55-atm) Raman cell filled with H_2. The 1.06-μm beam excites several vibrational modes of the H_2 molecules, allowing the output beam to emerge with several different Stokes- and anti-Stokes-shifted frequencies. We chose a difference frequency mixing scheme with a lithium niobate ($LiNbO_3$) crystal that requires the collinear mixing of a 1.91-μm and a 1.06-μm beam. Therefore, the first Stokes-shifted 1.91-μm output from the Raman cell is mixed with the other 1.06-μm beam in the $LiNbO_3$ crystal to produce the 2.41-μm pump beam. The residual 1.06-μm beam from the conversion process is used as the probe beam and is sent into a variable time delay that consists of a reflective corner cube mounted onto a computer-controlled translation stage. The delay stage allows for precise incremental time delays between the pump and probe beams. The pump and probe beams are independently focused into the sample, and the 0.88-μm emission signal is recorded with a photomultiplier tube placed at the side of the sample. Two independent reference detectors are used to account for fluctuations in the laser output. All three signals from the detectors are

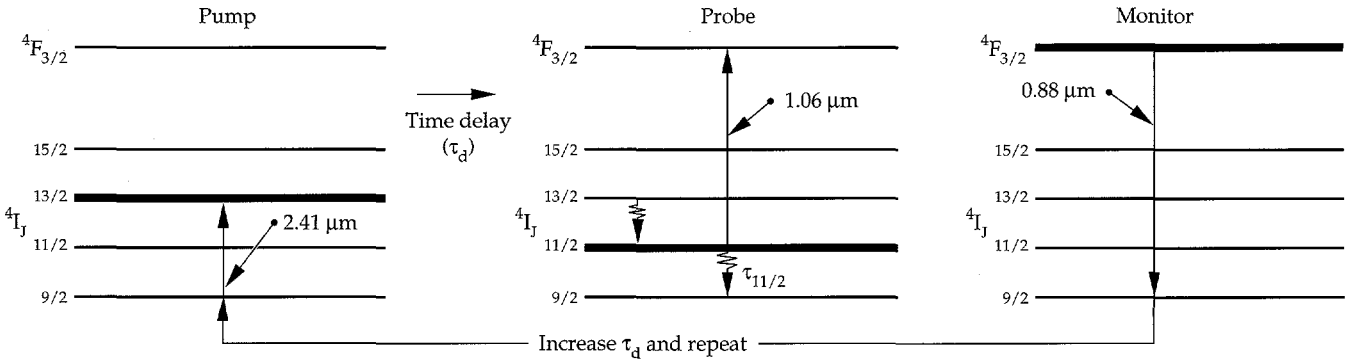

FIGURE 3. The pump-probe experiment. A 2.41-μm pump pulse excites a fraction of the ground state population into the $^4I_{13/2}$ level. After a time delay (τ_d), the 1.06-μm probe pulse excites the Nd ions from the $^4I_{11/2}$ level into the upper $^4F_{3/2}$ level. The 0.88-μm emission corresponding to the $^4F_{3/2} \rightarrow {}^4I_{9/2}$ transition is time integrated and recorded. This sequence of events is repeated for longer time delays. (70-15-0194-0202pb02)

sent into electronic boxcars that integrate the waveforms. A hardware interface allows a computer to store the integrated signals. After the data are stored, the computer translates the delay stage and records a new set of data.

Figure 5 shows an example of the data taken with this setup. The data are illustrated with circles; the line is the numerical model. Details of the numerical model have been described elsewhere.[1] In brief, the model of the data includes information about the $^4I_{13/2} \rightarrow {}^4I_{11/2}$ and $^4I_{11/2} \rightarrow {}^4I_{9/2}$ nonradiative transitions. Three adjustable physical parameters fit the data to the model. We calculated a lower bound of the terminal lifetime by correcting the effective lifetime for the ~200 cm^{-1} smaller gap in the $^4I_{11/2} \rightarrow {}^4I_{9/2}$ transition compared with the $^4I_{13/2} \rightarrow {}^4I_{11/2}$ transition. The terminal lifetime (lower-bound) was found to be 250 ps with an error of ±100 ps.

Indirect Method: Experiment and Results

Before discussing the indirect method, we first briefly explain the energy gap law. The nonradiative rate for the transition of a rare-earth ion such as Nd within a glass or crystalline host medium can be written as

$$W_{nr} = A \exp(-\alpha p) \quad , \tag{1}$$

where A and α are host-dependent parameters and p is the normalized energy gap of the transition, $\Delta E_{gap}/h\nu_{eff}$.

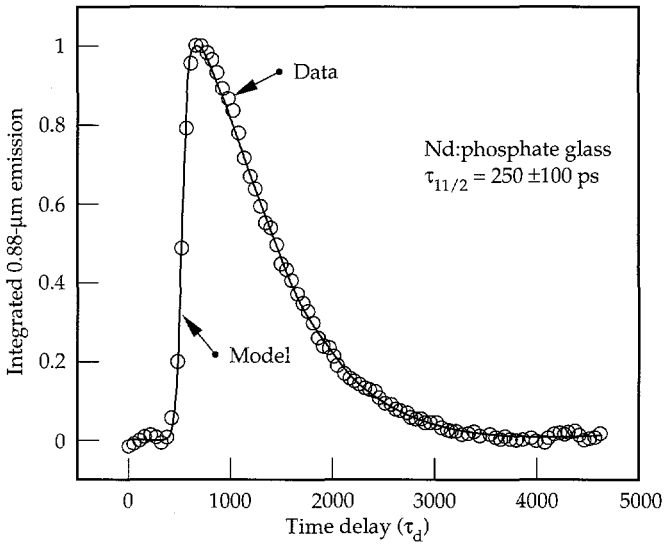

FIGURE 5. The analysis of the data yielded a terminal lifetime of $\tau_{11/2}$ = 250 ps with an error of ±100 ps. (70-15-0194-0202pb04)

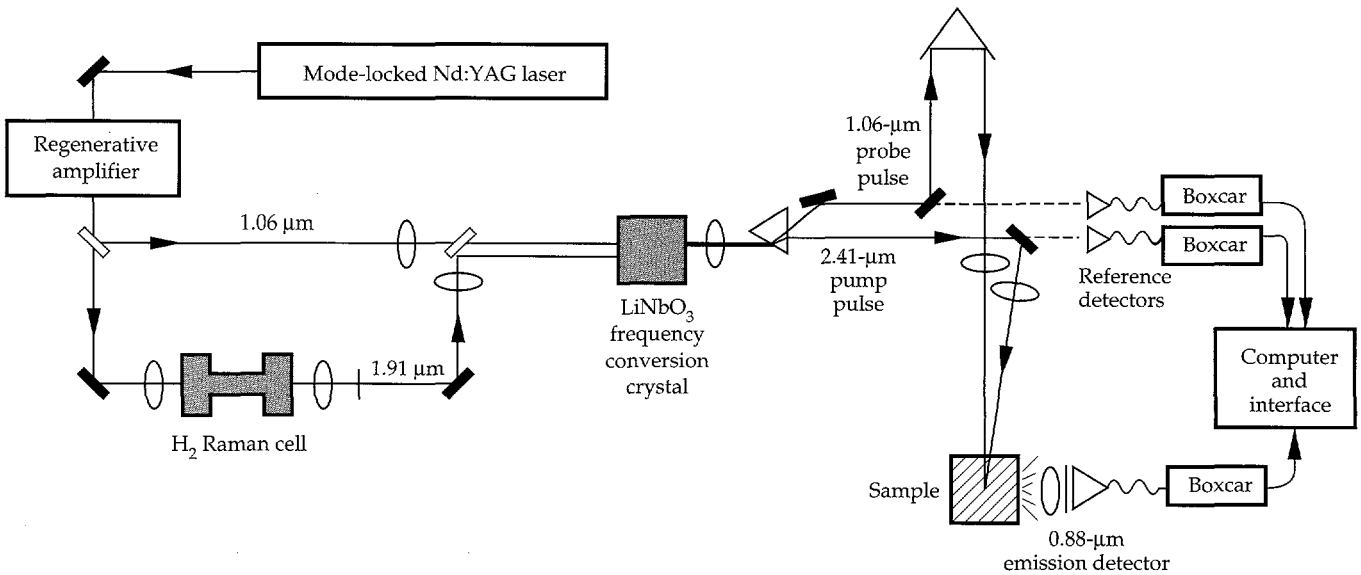

FIGURE 4. A simplified experimental diagram for the pump-probe experiment. The 1.06-μm output of the laser is mixed with the 1.91-μm Stokes-shifted output from an H_2 Raman cell to produce a 2.41-μm pump beam. The residual 1.06-μm beam is delayed and used as the probe beam. Three individual detectors and boxcars record and integrate the signals, which are stored on the computer for subsequent data analysis. (70-15-0194-0202pb03)

This expression assumes that for transitions involving approximately two or more phonons, only the highest frequency of vibration (ν_{eff}) in the host plays a significant role in enabling the nonradiative transition. Therefore the smallest number of high-frequency phonons needed to bridge the energy gap (ΔE_{gap}) tends to dominate the nonradiative decay. In addition, the theory assumes that only the size of the gap is important and not the specific details of the initial and final electronic states over which the transition takes place—hence the reason for the name "energy gap law."

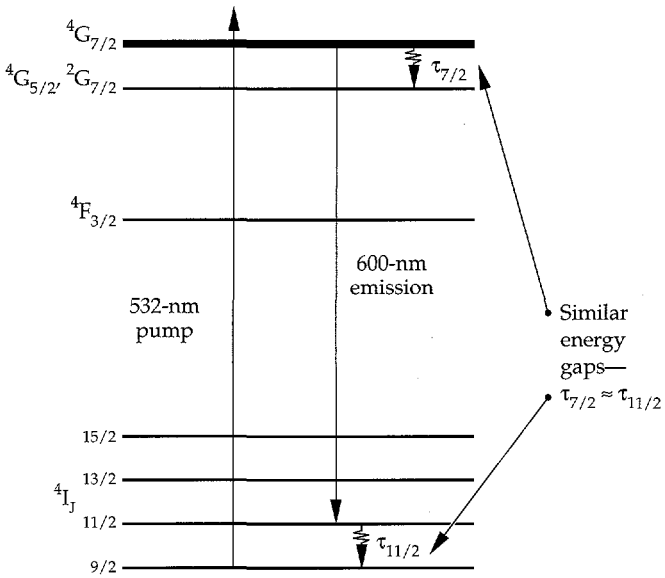

FIGURE 6. An energy level diagram for the emission experiment. A 532-nm pump beam transfers a fraction of the ground state population into the $^4G_{7/2}$ level. The resulting emission at 600 nm from the $^4G_{7/2}$ level is recorded. Since the nonradiative decay for the $^4G_{7/2} \rightarrow {}^4G_{5/2}$, $^2G_{7/2}$ transition will be much faster than the radiative decay rate, the 600-nm emission signal will be a direct measure of the $\tau_{7/2}$ lifetime. (70-00-0295-0391pb01)

For most Nd-doped materials, the upper $^4G_{7/2} \rightarrow {}^4G_{5/2}$, $^2G_{7/2}$ transition and the lower $^4I_{11/2} \rightarrow {}^4I_{9/2}$ transition have a similar-size energy gap. Figure 6 shows the energy level diagram for the pumping and emission processes. If the energy gap theory is assumed valid, then the values of the $\tau_{7/2}$ and $\tau_{11/2}$ lifetimes should also be quite similar. Since the Nd ions are easily excited from the ground state to the $^4G_{7/2}$ level with the frequency-doubled output of a 1.06-μm laser, one must only monitor emission signals from the $^4G_{7/2}$ level for a direct measure of the $\tau_{7/2}$ lifetime. This is because the rate of decay of the emission signal will be largely dominated by the $^4G_{7/2} \rightarrow {}^4G_{5/2}$, $^2G_{7/2}$ nonradiative rate. After exciting the ground-state Nd ions with the 532-nm pump, the 600-nm emission signal corresponding to the $^4G_{7/2}$ population decay is recorded. A technique suitable for measuring time-resolved fluorescence emission spectra characterized by weak signal levels and/or picosecond lifetimes is called "time-correlated single photon counting."

Figure 7 illustrates an experimental scheme for measuring the $\tau_{7/2}$ lifetime that employs a photon counting system. The frequency-doubled output of a mode-locked Nd:YAG laser produces 1 W of 532-nm light with a 90-ps pulse length at a rate of 76 MHz. The 532-nm light is split into two paths. In path 1, the sample is illuminated and the fluorescence is collected and focused into the monochromator. A multichannel plate photomultiplier tube (MCP-PMT) is placed at the output of the monochromator and detects the 600-nm

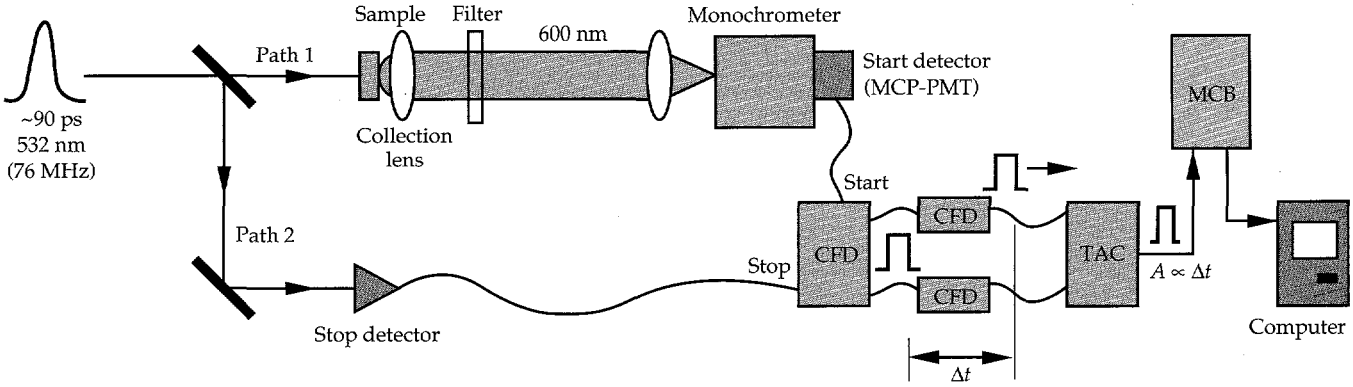

FIGURE 7. An experimental scheme for the emission experiment using a time-correlated single-photon counting technique. The 532-nm pulse is split into two beams. In path 1, a beam illuminates the sample, and the resulting 600-nm emission is detected with a multichannel plate detector. The beam from path 2 is time delayed and focused onto a silicon detector. The photon counting electronics (constant fraction discriminator, time-to-amplitude converter, multichannel buffer) condition the electronic pulses from the two detectors. After multiple excitation pulses, the 600-nm emission waveform is reconstructed. (70-00-0295-0391pb02)

emission signal. The photon counting method assumes that the probability distribution for the emission of the first photon after excitation is also the intensity vs time distribution of the photons emitted as a result of the excitation. Therefore, by measuring the time at which the first photon is emitted for a large number of excitation events, the experiment eventually constructs the full probability distribution.[8] This method uses the high repetition rate of the laser system to build up the emission signal after many excitation pulses.

The sequence of electronic events, as shown in Fig. 7, is as follows: The MCP-PMT monitors the arrival of the first 600-nm photon emitted after the sample has been excited. From the single photon event, the MCP-PMT is able to generate an electronic signal known as the start pulse. The constant fraction discriminator (CFD) conditions the electronic signal from the detectors so that the signals going into the time-to-amplitude converter (TAC) have a precisely timed leading edge independent of the amplitude fluctuations. The pulses entering the TAC initiate the charging of a capacitor. In path 2, the 532-nm pulse is time delayed and sent into a silicon photodetector, which outputs an electronic pulse to stop the charging of the capacitor. The amount of charge stored on the capacitor is proportional to the time interval (Δt) between the start and stop pulses. The TAC outputs an electronic pulse with an amplitude (A) that is directly proportional to the stored charge on the capacitor. A multichannel buffer (MCB) stores the value of the pulse amplitude.

The sequence is repeated until enough single-photon events have been sampled to accurately reconstruct the emission signal. Figure 8 shows the data and model for LG-750. The $\tau_{11/2}$ lifetime inferred from the kinetic analysis is found to be $\tau_{11/2} \cong \tau_{7/2} = 228 \pm 50$ ps on the basis of the $^4G_{7/2} \rightarrow {}^4G_{5/2}, {}^2G_{7/2}$ relaxation time.

Energy Extraction Experiments and Modeling

In 1982, Yarema and Milam[7] performed a series of energy extraction experiments for several Nd-doped glasses, including LG-750. Figure 9 shows a plot of the fluence out vs fluence into an LG-750 amplifier for 1-ns and 20-ns pulse durations. The data show that at higher input fluences, the 20-ns pulses begin to extract the stored energy more efficiently. Based on the experimental values of the terminal lifetime derived from the two experiments previously discussed, we would expect the 20-ns data to extract the energy more efficiently since there is virtually no bottlenecking of the terminal level. This is because the 20-ns pulses are 80 times longer than the terminal lifetime, as opposed to the 1-ns pulses, which are only 4 times longer. The difference in the two data curves can be accounted for by including the terminal-level lifetime in the solution to the coupled population rate and transport differential equations. However, as mentioned earlier, no analytic solution exists, and therefore the equations must be integrated for each new value of the pulse length t_p or the terminal

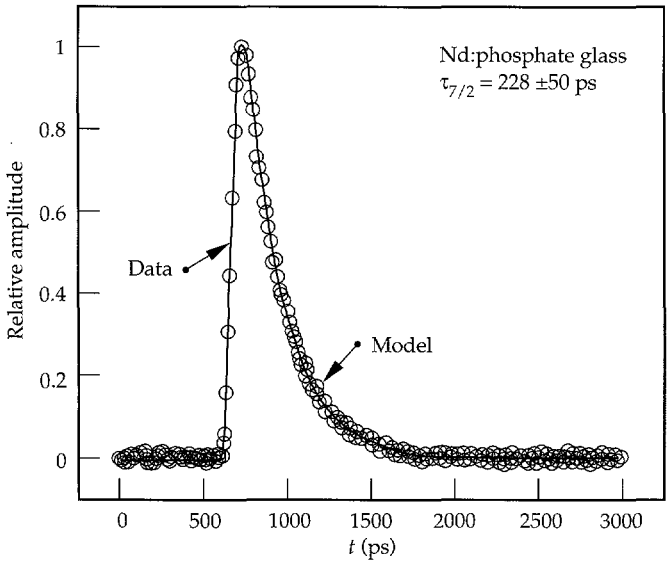

FIGURE 8. A plot of the 600-nm emission as a function of time. The $\tau_{7/2}$ lifetime derived from the data analysis is 228 ± 50 ps. (70-00-0295-0391pb03)

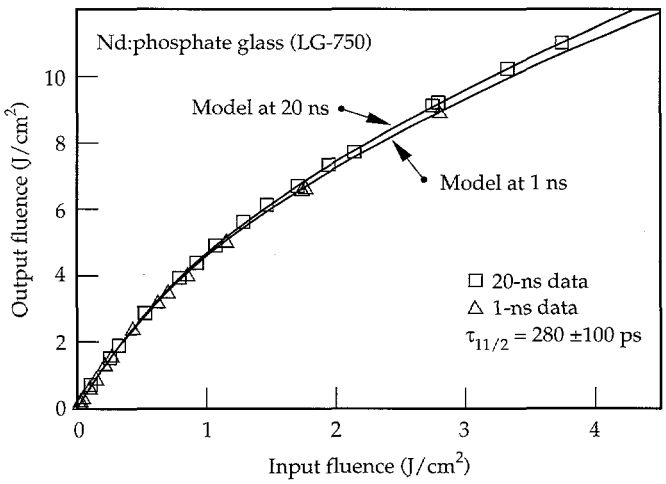

FIGURE 9. A plot of the extraction data taken by Yarema and Milam for 1- and 20-ns square pulses in the phosphate glass composition LG-750. A model that includes the ratio of the pulse width to the terminal-level lifetime is shown as the two solid lines. The terminal-level lifetime was left as a variable fitting parameter within the model. A best fit to the data yielded $\tau_{11/2} = 280 \pm 100$ ps. (70-00-1194-3749pb02)

lifetime $\tau_{11/2}$. We have found an empirical formula for the saturation fluence F'_{sat} that explicitly includes t_p and $\tau_{11/2}$:

$$F'_{sat} = \left[\frac{h\nu/\sigma_{em}}{1+\frac{g_2}{g_1}B(R)} \right] , \quad (2)$$

where $B(R)$ is a function of $R = t_p/\tau_{11/2}$, σ_{em} is the emission cross section, and g_2/g_1 is the ratio of upper to lower level degeneracies of the laser transition. The derivation of the function $B(R)$ will be discussed in the next section. The empirical formula for the saturation fluence can be substituted within the Frantz–Nodvik[6] solution for energy extraction to model both the 1-ns and 20-ns data. The Frantz–Nodvik solution is written as

$$F_{out} = F'_{sat} \ln\left\{1 + G_0\left[\exp\left(F_{in}/F'_{sat}\right) - 1\right]\right\} , \quad (3)$$

where G_0 is the small signal gain and F_{in} is the input fluence. The model is shown as the curves in Fig. 9. The terminal-level lifetime was left as a fitting parameter within Eq. (3). The best fit to the data yielded a terminal lifetime of $\tau_{11/2} = 280$ ps ± 100 ps. This result is within the experimental error of the lifetimes derived from the previous sections. The average terminal lifetime and estimated error from all three experiments is 253 ps with an rms error of ±50 ps.

Derivation of the Modified Saturation Fluence

There are six steps involved in finding the functional form of $B(R)$ in Eq. (2).

1. Transform the coupled rate and transport equations that include the terminal-level lifetime ($\tau_{11/2}$) to a coordinate system that moves within the frame of the pulse.
2. Simplify the equations by integrating over the spatial dimension so that only a set of coupled ordinary differential equations in time remain.
3. Integrate the coupled equations for a range of R values.
4. Substitute the modified saturation fluence defined in Eq. (2) into the Frantz–Nodvik solution, Eq. (3), fit each of the empirical output-vs-input fluence solutions to the exact numerical solutions found in step 3, and determine $B(R)$.
5. Find an analytic form for $B(R)$.
6. Determine the range of input parameters over which the modified saturation fluence F'_{sat} can be used.

We begin by assuming that the upper laser level has a population $N_2(0)$ created by a previous pumping process when the input pulse arrives. The coupled rate and energy transport equations for a lossless system can be written as

$$\frac{\partial N_2(t)}{\partial t} = -\frac{I(z,t)}{h\nu}\left[\sigma_{em}N_2(t) - \sigma_{abs}N_1(t)\right] , \quad (4a)$$

$$\frac{\partial N_1(t)}{\partial t} = \frac{I(z,t)}{h\nu}\left[\sigma_{em}N_2(t) - \sigma_{abs}N_1(t)\right] - \frac{N_1(t)}{\tau_{11/2}} , \quad (4b)$$

and

$$\frac{\partial I(z,t)}{\partial z} + \frac{n}{c}\frac{\partial I(z,t)}{\partial t} = I(z,t)\left[\sigma_{em}N_2(t) - \sigma_{abs}N_1(t)\right] , \quad (4c)$$

where $N_2(t)$ and $N_1(t)$ represent the upper ($^4F_{3/2}$) and lower ($^4I_{11/2}$) level populations, σ_{em} is the single-ion stimulated emission cross section for the $^4F_{3/2} \rightarrow {}^4I_{11/2}$ transition, and σ_{abs} is the single-ion absorption cross section for the $^4I_{11/2} \rightarrow {}^4F_{3/2}$ transition. The intensity of the laser pulse is denoted by $I(z,t)$. In a glass, σ_{em}, σ_{abs}, and $\tau_{11/2}$ are supposed to be site-averaged or ensemble values.

Eqs. (4a)–(4c) can be simplified by transforming them to a moving coordinate system that travels at the velocity of the pulse by making the following transformation of variables: $T = t-(zn/c)$ and $Z = z$. Using the prescription of Trenholme et al.[9] we also define $\beta = N_2\sigma_{em}$ to be the gain coefficient of the upper level ions and $\alpha = N_1\sigma_{abs}$ to be the absorption coefficient of the lower level ions. The ratio of degeneracies is defined to be the constant $K = \sigma_{abs}/\sigma_{em}$. The result is

$$\frac{\partial \beta}{\partial T} = -\frac{I}{h\nu/\sigma_{em}}\left[\beta - \alpha\right] , \quad (5a)$$

$$\frac{\partial \alpha}{\partial T} = \frac{IK}{h\nu/\sigma_{em}}\left[\beta - \alpha\right] - \frac{\alpha}{\tau_{11/2}} , \quad (5b)$$

and

$$\frac{\partial I}{\partial Z} = I\left[\beta - \alpha\right] . \quad (5c)$$

Eqs. (5a)–(5c) can be further simplified by observing that integration over their spatial dimension is possible, leaving a set of ordinary differential equations in time to be solved. Continuing to follow Trenholme, the quantities $U(t)$ and $L(t)$ are defined as

$$U(t) = \int_0^{\ell} \beta(z,t)\,dz \quad (6a)$$

and

$$L(t) = \int_0^{\ell} \alpha(z,t)\,dz \quad . \tag{6b}$$

Integrating Eqs. (5a)–(5c) along the length of the amplifier, we find that the problem now reduces to solving the following set of coupled differential equations of Trenholme[9]:

$$\frac{dU}{dt} = -\frac{I_{in}\left(e^{U-L}-1\right)}{h\nu/\sigma_{em}} \quad , \tag{7}$$

$$\frac{dL}{dt} = \frac{I_{in}K\left(e^{U-L}-1\right)}{h\nu/\sigma_{em}} - \frac{L}{\tau_{11/2}} \quad , \tag{8}$$

and

$$\frac{dF_{out}}{dt} = I_{out} = I_{in}e^{U-L} \quad , \tag{9}$$

where the known initial conditions $U(0)$, $L(0)$, and $I_{in}(t)$ are used to integrate Eqs. (7)–(9) forward in time. The integrated output intensity yields the output fluence

$$F_{out}(\text{numerical}) = \int_0^{\infty} I_{out}(t)\,dt = \int_0^{\infty} I_{in}(t)e^{U-L}\,dt \quad , \tag{10}$$

where F_{out} (numerical) is the exact solution to the lossless coupled rate and energy transport equations that includes effects of the terminal-level lifetime ($\tau_{11/2}$). The numerical solutions of Eq. (10) for square pulses with $R = t_p/\tau_{11/2} = 0.01$, 2, and 100 are plotted in Fig. 10(a). For each numerical solution shown, a best fit of the empirical solution, Eq. (3), was found by adjusting the value of $B(R)$ to minimize the χ^2 fitting error. The empirical solutions are also shown in Fig. 10(a) along with the corresponding $B(R)$ and χ^2 values where we define

$$\chi^2 = \sqrt{\sum_{i=1}^{N=100}\left[F_{out}^{num}(i) - F_{out}^{emp}(i)\right]^2 \frac{1}{N-1}} \quad . \tag{11}$$

In Fig. 10(a), only three different values of $B(R)$ were determined. To find a functional form for $B(R)$, additional values were needed. In Fig. 10(b), over 1000 fits are shown to produce a nearly continuous curve for $B(R)$ (solid line). As required, $B(R)$ converges to the asymptotes of 1 and 0 for $t_p/\tau_{11/2} << 1$ and $t_p/\tau_{11/2} >> 1$, respectively. The $B(R)$ curve shown in Fig. 10(b) was fit to three exponentials (open circles). This allowed for an improved fit to the $B(R)$ curve compared with the single exponential form originally proposed by Trenholme.[10] The exponential sum is written as

$$B(R) = a_1 \exp\left(-R/b_1\right) + a_2 \exp\left(-R/b_2\right) + a_3 \exp\left(-R/b_3\right) \quad , \tag{12}$$

where the coefficients are

$$a_1 = 0.59735, a_2 = 0.34025, a_3 = 0.0605 \tag{13a}$$

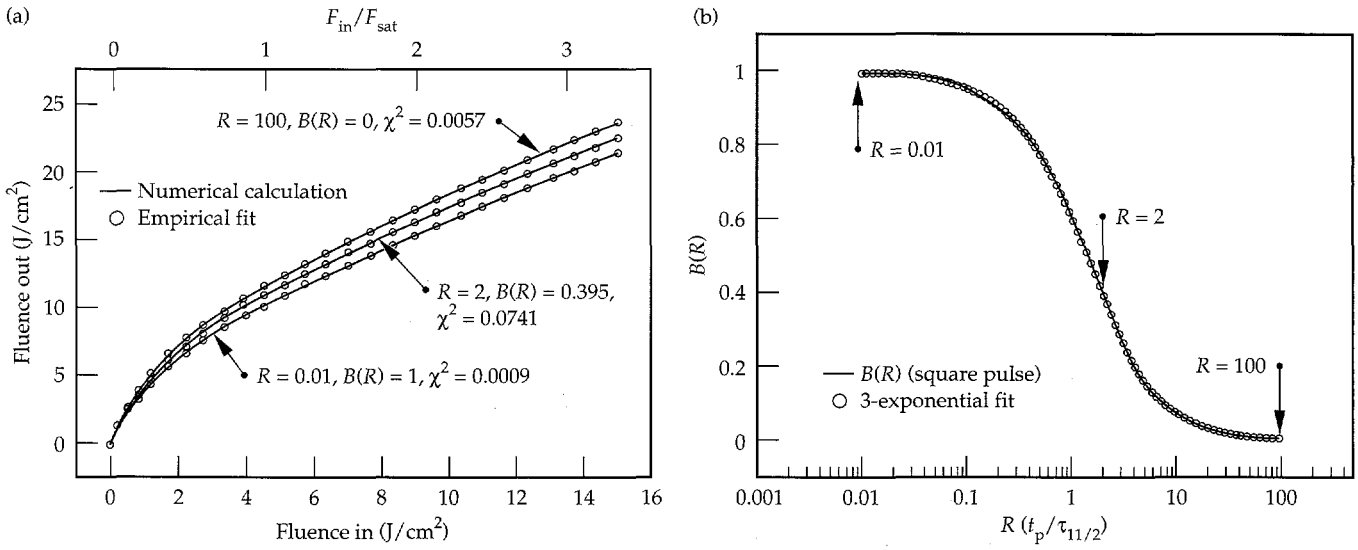

FIGURE 10. (a) A plot of the numerical solution of the coupled differential equations, Eq. (10), is shown as the solid line. The open circles represent the empirical solution, Eq. (3). The value for $B(R)$ and the χ^2 fitting error are also shown. (b) Over a thousand fits, such as those shown in (a), were made to form a nearly continuous curve for $B(R)$. A best fit to the curve for a sum of three exponentials is shown by the open circles. (70-00-0295-0393pb01)

and

$$b_1 = 1.29348, b_2 = 4.14937, b_3 = 30.38384 \quad . \tag{13b}$$

To match the experimental data, Eq. (12) was evaluated for the following input parameter values:

$$g_2 / g_1 = 0.35 \quad , \tag{14a}$$

$$G_0 = 6.9 \quad , \tag{14b}$$

and

$$I_{in}(t) = I_0 \exp\left[-(t/w)^{30}\right] \quad , \tag{14c}$$

$I_{in}(t)$ being a square pulse approximated by a super-Gaussian of power 30. In addition, the relevant range of input fluences are defined with

$$\frac{F_{in}}{h\nu/\sigma_{em}} < 3.5 \quad . \tag{14d}$$

The empirical expression for the saturation fluence, Eq. (3), with $B(R)$ defined in Eq. (12), can be used to calculate the output energy with an error of less than 1.5%. Our choices for the value of the parameters—g_2/g_1, G_o, and $I_{in}(t)$—and therefore $B(R)$ are specific to Yarema and Milam's extraction experiment. Equation (12) has some applicability for alternative ranges of input parameters.[11]

In a recent publication by Beach et al.,[12] an approximate form for $B(R)'$ was derived and shown to be

$$B(R)' = \frac{1-\exp(-R)}{R} \quad . \tag{15}$$

However, Eq. (15) proved to be useful only for input fluences less than the saturation fluence of the medium ($F_{in} < h\nu/\sigma_{em}$). We have nonetheless found that an adequate fit to $B(R)$ can be achieved over a larger F_{in} range if an additional phenomenological parameter is introduced by taking the entire expression to the 1.13 power (i.e., $[B(R)']^{1.13}$). By substituting this alternative form of $B(R)$ into Eq. (2), we can determine the output energy with an error of less than 1.5% for the input parameters in Eqs. (14a)–(14c).

Comparison of the Direct and Indirect Methods for Several Nd-Doped Materials

We have discussed three possible experiments for measuring the terminal lifetime for Nd:phosphate glass. It would be convenient if the simplest method were shown to be sufficiently accurate for measuring the terminal lifetime of any Nd-doped laser material. Table 1 lists lifetime data for 13 different Nd-doped laser materials taken from the pump-probe and emission experiments previously discussed. In Fig. 11, the lifetime from the direct data ($\tau_{11/2}$) is plotted against the lifetime from the indirect method ($\tau_{7/2}$). The figure shows a line representing the best fit to the data of the form $y = mx$. Ideally, if both methods yielded the same results, then the slope m would be equal to one. However, the best fit produced a slope of 1.15, which suggests that the simpler, indirect method can be used to determine the terminal-level lifetime for most Nd-doped materials within a factor of two provided that the excitation pulses are short enough and the detectors and electronics have the required sensitivity and resolution.

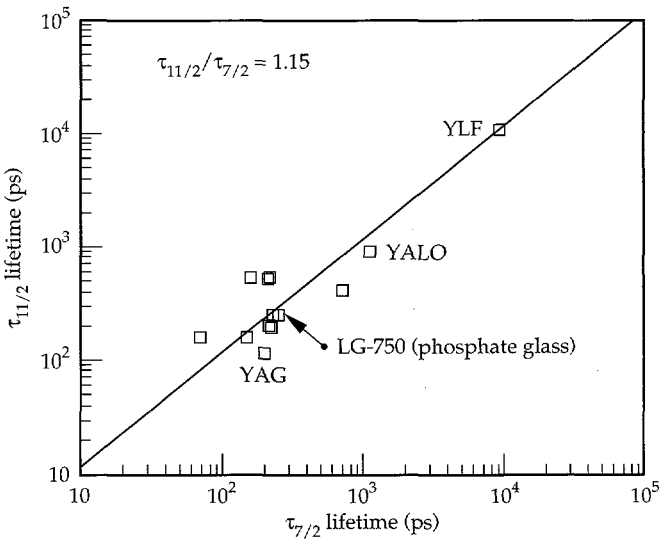

FIGURE 11. The terminal lifetimes from the direct and indirect measurements are plotted. A best fit to the data is shown as the solid line of the form $y = mx$. The slope is 1.15. We find that the indirect method can be used to measure the terminal lifetime to within a factor of 2 for most Nd-doped laser materials. (70-00-0295-0394pb01)

The rightmost column of Table 1 lists our best assessment of the terminal lifetime from the two approaches. In comparing the lifetimes of the various groups of materials, we find that the phosphate glasses have a factor-of-two shorter lifetime than the silicate glasses. This is primarily due to the high phonon frequencies of the network forming PO_4 complexes in the phosphate host as opposed to the relatively low-frequency SiO_4 complexes in the silicate glasses. The shortest lifetime measured was from the phosphate crystal Nd:C-FAP. This material has both high phonon frequencies and a small energy gap. Within the oxide crystals, we find that Nd:YAG has the shortest lifetime and correspondingly the smallest energy gap. And finally, as expected, we find that for the fluoride materials, including Nd:YLF, the relatively low 300–600 cm^{-1} phonon frequencies give rise to slower (nanosecond) lifetimes.

Conclusions

We measured the terminal-level lifetime of the Nd-doped phosphate glass LG-750 from three independent measurements and found the average value to be $\tau_{11/2}$ = 253 ps with an rms error of ±50 ps. In the process of modeling data from the energy extraction experiments, we developed an empirical formula for the saturation fluence that can be used to account for the bottlenecking effects of the $^4I_{11/2}$ level in the Frantz–Nodvik analytic solution for energy extraction. We determined that the indirect emission measurements yield lifetimes that are within a factor of two of the direct pump-probe measurements. This result gives us confidence in using the simpler indirect approach for estimating the terminal lifetime for new prospective Nd-doped laser materials.

TABLE 1. Results from the direct, pump-probe measurements and the indirect, emission measurements. The right column lists our best assessment of the terminal lifetimes.

Material	Lifetime $\tau_{11/2}$ (ps)	Lifetime $\tau_{7/2}$ (ps)	Best assessment of lower-level lifetime (ps)
Phosphate glasses			
LG-750	250	228	250[a]
APG-1	192	215	192[a]
APG-x	200	210	200[a]
APG-y	158	150	158[a]
Phosphate crystal			
C-FAP, $Ca_5(PO_4)_3F$	156	70	70[b]
Silicate glasses			
LG-660	535	215	535[c]
LG-650	510	210	510[c]
SOL-GEL	247	245	247[a]
Oxides			
YAG, $Y_3Al_5O_{12}$	115	200	200[b]
YALO, $YAlO_3$	896	1090	1090[b]
GSGG, $Gd_3Sc_2Ga_3O_{12}$	401	715	715[b]
Vanadate			
YVO_4	531	190	531[d]
Fluorides			
YLF, $LiYF_4$	10,500	9100	9100[b]
SrF_2	>5000	7000	7000[b]
Fluoride glass			
ZBLAN, ZrF_4-BaF_2-AlF_3-LaF_3-NaF	>5000	18,000	18,000[b]

[a] Lower limit of the lifetime from the direct method agrees with the lifetime measured from the indirect method.

[b] Indirect method is preferred since data is more accurate.

[c] Energy gap relevant to $^4I_{11/2}$ and $^4G_{7/2}$ states are anomolously different so the $\tau_{11/2}$ and $\tau_{7/2}$ lifetimes do not agree.

[d] Basis for difference between the $\tau_{11/2}$ and $\tau_{7/2}$ lifetimes is uncertain.

Acknowledgments

We thank John Trenholme for sharing his insights into modeling this process with his laser extraction code and for his helpful editorial suggestions. We also thank Howard Powell for emphasizing the need for a direct experimental measurement of the terminal-level lifetime. We thank Ray Beach for his helpful discussions and notes on the derivation of the extraction efficiency of Nd:YLF. We also recognize Steve Velsko, Chris Ebbers, Mark Hermann, and Laura DeLoach for their help with the frequency conversion scheme, Chris Marshall for helping with the photon counting system, Joel Speth for supporting the laser systems, Gary Wilke for assistance with the spectroscopy, and Ron Vallene and Peter Thelin for preparing the samples. In addition, we thank Bill Krupke for his helpful discussions on the material physics issues and Ann Orel for periodically reviewing the progress on this project. We also extend our appreciation to Wolfe Seka and Jonathan Zuegal of the University of Rochester[13] for initially sharing an alternative approach for measuring the Nd terminal-level lifetime, and to Schott Glass, Inc.[14] for the LG-750 phosphate glass.

Notes and References

1. C. Bibeau, S. A. Payne, and H. T. Powell, "Evaluation of the Terminal-Level Lifetime in Sixteen Neodymium-Doped Crystals and Glasses," Lawrence Livermore National Laboratory, Livermore, CA, UCRL-JC-117099 (1994).
2. L. A. Riseberg and H. W. Moos, *Phys. Rev.* **174**, 429–438 (1968).
3. C. B. Layne, W. H. Lowdermilk, and M. J. Weber, *Phys. Rev. B* **16**, 10–20 (1977).
4. L. M. Frantz and J. S. Nodvik, *J. Appl. Phys.* **34**, 2346–2349 (1963).
5. S. M. Yarema and D. Milam, *IEEE J. Quantum Electron.* **QE-18**, 1941–1946 (1982).
6. W. E. Martin and D. Milam, *Appl. Phys. Lett.* **32**, 816–818 (1978).
7. K. Palombo, S. Matthews, S. Sheldrake, and C. Capps. *OSA Proc. on Advanced Solid-State Lasers* **15**, 78–80 (1993).
8. D. V. O'Connor and D. Phillips, *Time-Correlated Single Photon Counting* (Academic Press, 24–28 Oval Rd., London, NW1 7DX, 1984).
9. J. B. Trenholme and E. J. Goodwin, "Numerical modeling of gain recovery," *Laser Program Annual Report* **1**, 2.236–2.238, Lawrence Livermore National Laboratory, Livermore, CA, UCRL-50021-77 (1977).
10. J. Trenholme, J. Hunt, and J. Murray, Lawrence Livermore National Laboratory, "Assumptions which produced the upgrade design," Internal memorandum, LS&T 91-65 (1991).
11. C. Bibeau, J. B. Trenholme, and S. A. Payne, "Pulse length and terminal level lifetime dependence of energy extraction for neodymium-doped phosphate amplifier glass," Lawrence Livermore National Laboratory, Livermore, CA, UCRL-JC-120909, to be published in *IEEE J. Quantum Electron.*
12. R. Beach et al., *Opt. Lett.* **18**, 1326–1328 (1993).
13. University of Rochester, Rochester, New York, 14623–1299.
14. Schott Glass Technologies Inc., 400 York Ave., Duryea, PA, 18642.

Four-Color Laser Irradiation System for Laser–Plasma Interaction Experiments

D. M. Pennington
T. L. Weiland
M. A. Henesian
D. Eimerl
R. B. Wilcox

Introduction

Since 1986, optical smoothing of the laser irradiance on targets for Inertial Confinement Fusion (ICF) has gained increasing attention.[1–5] Optical smoothing can significantly reduce wavefront aberrations that produce nonuniformities in the energy distribution of the focal spot. Hot spots in the laser irradiance can induce local self focusing of the light, producing filamentation of the plasma. Filamentation can have detrimental consequences on the hydrodynamics of an ICF plasma, and can affect the growth of parametric instabilities, as well as add to the complexity of the study of such instabilities as stimulated Brillouin scattering (SBS) and stimulated Raman scattering (SRS).[6–10] As experiments approach and exceed breakeven (i.e., where driver energy = fusion yield), the likelihood of significant excitation of these processes increases. As a result, we are including a scheme for implementing optical-beam smoothing for target experiments in the baseline design for the proposed next-generation ICF facility—the National Ignition Facility (NIF).[11]

To verify the efficacy of this design for the suppression of parametric instabilities in NIF-like indirect-drive targets, we successfully modified a Nova beamline to simulate the proposed NIF conditions. In this article, we discuss the laser science[12] associated with a four-color target campaign on Nova to test the effect of *f*-number (ratio of focal length to beam diameter) and temporal smoothing on the scaling of SBS with a four-segment interaction beam using NIF-like parameters. The results of the target series associated with the four-color configuration are discussed in "Laser–Plasma Interactions in Large Gas-Filled Hohlraums," p. 97 of this *Quarterly* and elsewhere.[13–15]

The NIF[11] design has four beamlets per beamline, which overlap to form an effective $f/8$ beam focus. Each beamlet is smoothed by a random phase plate (RPP). RPPs consist of many randomly distributed on/off phase elements deposited on a fused-silica substrate.[16,17] The focal-plane intensity distribution resulting from focusing light through a bilevel RPP consists of an overall envelope, modulated by fine-scale spatial structure within that envelope. The envelope is produced by diffraction from a single-phase element, and the fine-scale structure, or speckle, is due to the superposition of the diffraction patterns from each of the phase elements. The speckle size corresponds to the diffraction limit of the full-aperture beam incident on the RPP. Because speckle size increases with *f*-number, an $f/8$ beam should filament more than the $f/4.3$ beams on Nova.[18,19] Simulations indicate that SBS reflectivity increases due to filamentation, with a total gain greater than calculated for a uniform laser intensity. SBS reflectivities >10% may unacceptably degrade target performance by disrupting symmetry or reducing the energy available for radiation heating. The introduction of temporal and spatial incoherence over the face of the beam using techniques such as smoothing by spectral dispersion (SSD)[1] or induced spatial incoherence (ISI)[5] reduce the rms-intensity variations in the laser irradiance when averaged over a finite time interval, providing temporal smoothing. Temporal smoothing makes filamentation less likely because the filament must form before the hot spot moves to a different location.

Figure 1 is a schematic of the SSD technique. Broadband light, produced in this case by electro-optic phase modulation (FM), is spectrally dispersed by a grating, and then amplified, frequency converted, and focused through an RPP on to a target. Each distinct frequency component produces a speckle pattern, resulting in a superposition of many speckle patterns. Since each frequency propagates at a different angle through the phase plate, the speckle patterns spatially shift as a function of frequency. As the frequencies change throughout the length of the pulse, the rapidly

UCRL-LR-105821-95-2

fluctuating interference of the displaced speckle fields for the different spectral components causes the irradiance to appear smooth on a time-averaged basis. The most effective beam smoothing is obtained when the speckle field for each spectral component is spatially shifted at the target plane by at least one-half speckle diameter, $d_{1/2} = 1.22\lambda f/D$, where D is the beam diameter on the phase plate, λ is the third harmonic (3ω, 351 nm) wavelength, and f is the focal length of the lens.[4] This level is achieved when the 3ω dispersion at the output aperture is fixed at $d\theta/d\nu = d_{1/2}/f \cdot \delta\nu$ in rad/Hz, for a specified spacing between spectral components, $\delta\nu$, and speckle size, $d_{1/2}$.

The time-integrated smoothness, σ/I, is defined as the spatial rms-intensity variance normalized to the average at the target plane. The smoothness is equal to $1/\sqrt{N}$, where N is the number of decorrelated speckle fields superimposed at each point on the target. The effective time-integrated smoothing level for spectrally dispersed beams can be approximated by

$$\sigma/I = \sqrt{\tau\,\delta\nu} = \left[\frac{1.22\lambda\tau}{D}\left(\frac{d\theta}{d\nu}\right)^{-1}\right]^{\frac{1}{2}} \qquad (1)$$

where $\delta\nu$ is the effective separation between independent spectral components in Hz, τ is the coherence time in seconds (inverse of the frequency-converted bandwidth), and $d\theta/d\nu$ is the spectral dispersion at 3ω in rad/Hz. For optimal dispersion, N is the total number of spectral components in the beam and $\delta\nu$ is the modulation frequency of the electro-optic phase modulator. Instantaneously, $\sigma/I \cong 1$ due to basic Rayleigh speckle statistics, but this value decreases rapidly as the irradiance variations are averaged over time. The initial smoothing occurs on a time scale proportional to $1/\tau$, reaching the asymptotic level given by Eq. (1) in a time determined by $1/\delta\nu$. The initial onset of smoothing is delayed due to the spatially varying time delay across the beam imposed by the grating (i.e., a delay of λ/c per illuminated grating line). This time delay δt is proportional to $1/\delta\nu$, and therefore N is proportional to $\delta t/\tau$.

In the case of m beamlines, each with a different central frequency and n decorrelated FM components per beamline, $\sigma/I = 1/\sqrt{N}$, where $N = nm = \Delta\nu/\delta\nu$. The value of D in Eq. (1) becomes the individual beamlet diameter, and the coherence time τ is proportional to $1/\Delta\nu$, where $\Delta\nu$ is the total bandwidth of the four FM-modulated central frequencies. With a four-color segmented beam, as used in the current Nova experiments, the superposition of the four narrowband speckle fields should produce a smoothing level of 50% ($\sigma/I = 0.5$) at the target plane. Since all four colors are present simultaneously throughout the pulse, the asymptotic level is achieved within a few picoseconds. The smoothing rate is proportional to the number of beamlines and is unaffected by the grating time delay, δt. The resulting pattern fluctuates with a periodicity determined by the narrowest frequency separation. The addition of FM bandwidth to the four-color beam allows additional temporal smoothing by creating many additional decorrelated speckle fields. This smoothes very rapidly due to the wide overall bandwidth. The rate of four-color beam smoothing with FM bandwidth and spectral dispersion is four times faster than one-color FM smoothing, assuming the same bandwidth per beamline, reaching a 50% lower σ/I at the same f-number per beamlet.

One of the primary limitations on previously used beam-smoothing techniques is the reduced frequency conversion efficiency to the third harmonic due to bandwidth.[20] High-efficiency frequency tripling can be achieved only over a narrow spread in wavelength for a given crystal phase matching condition; thus to remain within 10% of the maximum conversion efficiency, the input bandwidth should be limited to ~0.2 nm, or ~60 GHz. However, while beam smoothness is strongly dependent on both the amount of dispersion and spectral bandwidth used, the larger the bandwidth (i.e., the shorter the coherence time), the more rapidly the structure changes, and the more rapidly the time-averaged intensity smoothes.

The NIF design can simultaneously achieve high third-harmonic conversion efficiency with broad

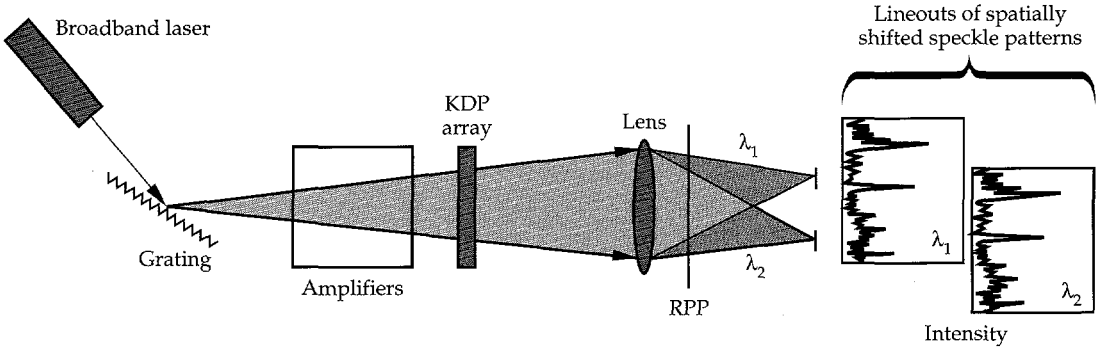

FIGURE 1. Schematic illustration of the smoothing by spectral dispersion (SSD) technique. (70-00-0395-0824pb01)

bandwidth for rapid smoothing. The NIF is proposed to have four beamlets focused to a single spot per beamline, each with a different frequency and separated by 1 nm.[11] Each individual beamlet will have a bandwidth of only 0.25 nm, allowing high-efficiency frequency tripling. The superposition of four beamlets with different frequencies will produce the wide overall-spectral width required for good temporal smoothing.

To simulate this configuration, a Nova beam was modified to have an $f/8$ geometry, with a segmented four-quadrant beam. We developed a multifrequency bandwidth source that is spatially separated into four quadrants, each containing a different central frequency separated by up to 0.88 nm. Each quadrant is independently converted to the third harmonic in a four-segment Type I/Type II potassium dihydrogen phosphate (KDP) crystal array with independent phase matching in each quadrant for efficient frequency conversion of the four frequencies. In addition, a limited amount of bandwidth (~0.2 nm) can be added to each frequency component to more closely approach a continuous broadband spectrum. We compared the results obtained with this method with those previously obtained on Nova with a continuous bandwidth source and a single-frequency conversion array.[20] Using this method, we obtained a factor of four increase in 3ω output energy with comparable overall bandwidth.

Four-Color Implementation on Nova

Significant modifications to the oscillators, mid-chain optics, SSD table, frequency-conversion arrays, laser diagnostics, target diagnostics, and final focus lens allowed implementation of four-color capability on Nova, as shown in Fig. 2. To perform target experiments, the four-color input spectrum must be stable to ±10% in energy, with frequency jitter <0.0019% and be reproducible from shot to shot. Energy balance between the four quadrants must be better than ±10% at 1ω and ±20% at 3ω. The composite beam is required to have $>2 \times 10^{15}$ W/cm^2 at the third harmonic in a 500-μm-diam focal spot. This section describes the modifications

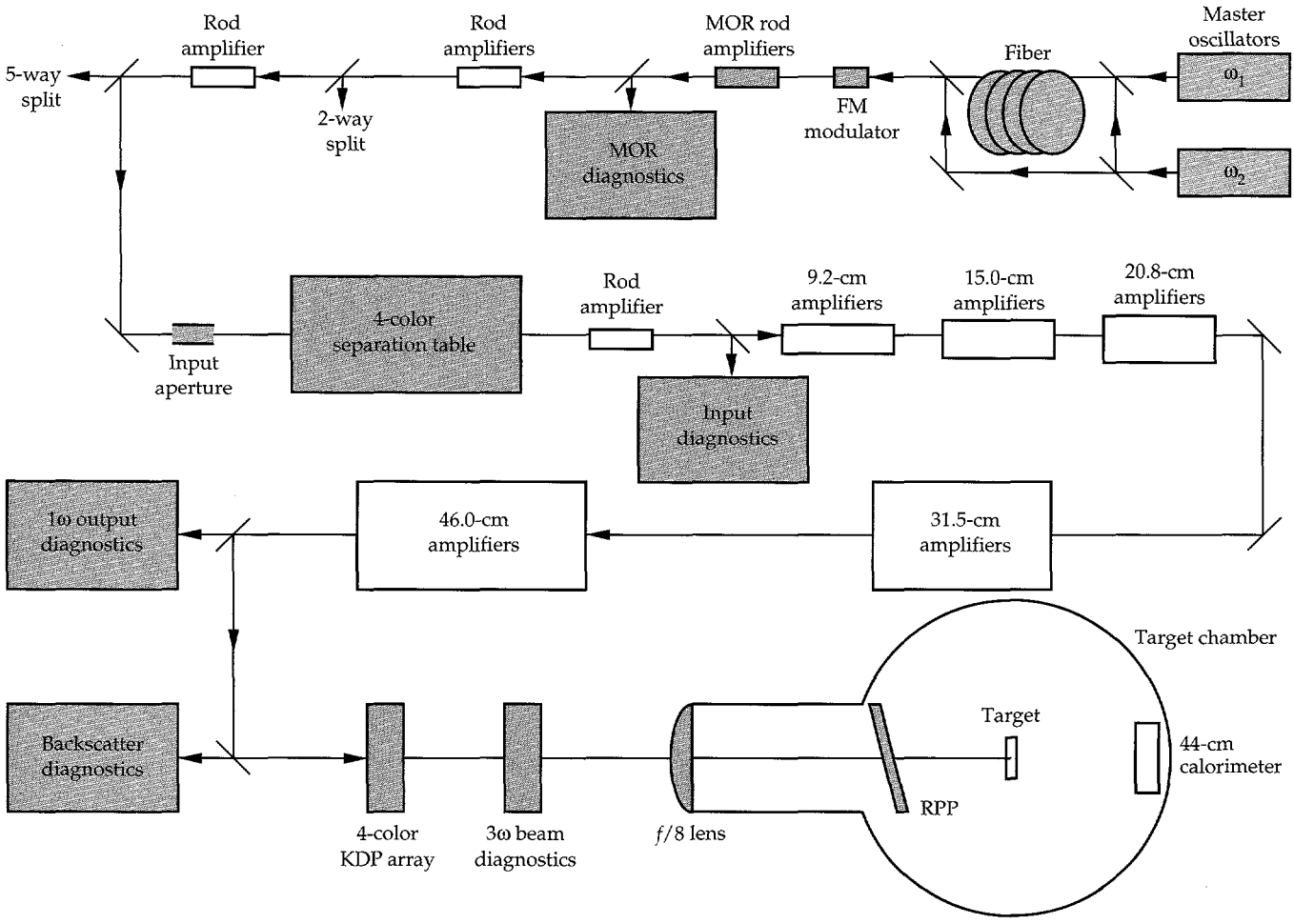

FIGURE 2. Layout of Nova's four-color system. Areas modified to accommodate the four-color system are shaded. (70-00-0395-0792pb01)

required to meet these conditions and the overall laser performance of the four-color system.

Four-Color Bandwidth Source

Four-color target experiments required the development of a four-color laser source with a bandwidth capability similar to that planned for the NIF. The technique chosen to provide the four discrete frequencies is based on the nonlinear mixing of two frequencies in an optical fiber. Two photons at the pump frequencies are annihilated to create two photons at frequencies shifted toward the blue and red sides.[21,22] These newly created spectral components result in self-phase modulation (SPM)-induced broadening of the pulse. The phase shift incurred by propagation through the fiber is proportional to the fiber length L and the pulse intensity I, and the number of sidebands generated is linearly proportional to this phase shift. The number of lines generated is controlled by changing the pump intensity into the fiber, while the separation between frequencies is varied by tuning the frequencies of the oscillators. This technique produces a broad comb of discrete single-mode frequencies (up to ~40 lines), which can be spectrally separated to provide a tunable single-frequency source.

We produce the two-frequency input to the fiber by etalon-tuning two single longitudinal mode, Q-switched Nd-doped yttrium lithium fluoride (Nd:YLF) oscillators[23] to 1053.23 nm and 1052.79 nm, respectively. The measured frequency variation of each oscillator is <0.0016%. The output beams are temporally and spatially overlapped, and shortened to a 15-ns nominally square pulse and coupled into a single-mode polarization preserving fiber. The spectrally integrated beam energy is recorded at the input and output of the fiber. The time-integrated and time-resolved output spectra and spectrally integrated pulse shape are also recorded.

Time-integrated spectral measurements, like the example shown in Fig. 3(a), indicate that the energy content of the central spectral lines remains constant to within ±10% as the input energy increases and the spec-

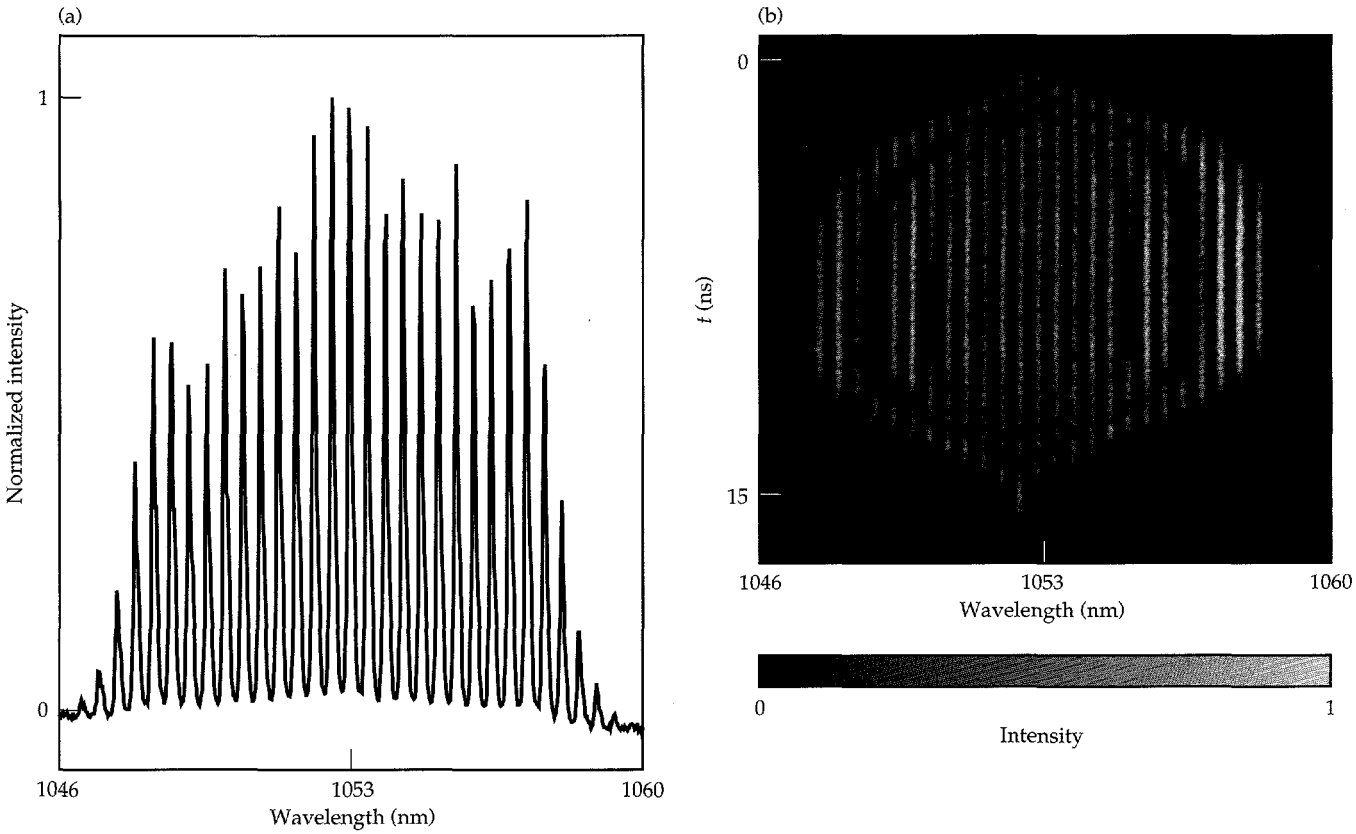

FIGURE 3. Multifrequency spectrum generated by self-phase modulation of two frequencies separated by 0.44 nm in an optical fiber. (a) Shows a representative time-integrated spectrum for an intensity-length product, IL = 1.2 TW/cm. (b) Shows the temporal evolution of the same spectrum. The number of spectral lines increases and decreases linearly with the 4-ns rise and fall of the pulse. (70-00-0395-0793pb02)

trum broadens. The amplitude between lines varies <±10%, while the output energy of the integrated spectrum varies <±3% from shot to shot. A maximum spectral width of 14-nm full-width at half maximum (FWHM) is obtained by this technique. The temporal buildup of the SPM spectrum, shown in Fig. 3(b), reflects the change in pulse intensity caused by the 4-ns rise and fall time of the input pulse. The central 3–5-ns section of the 15-ns pulse is nominally flat in time across the generated spectrum. A temporally uniform 1-ns slice is selected from the center of that section by the main pulse shaping system in the Master Oscillator Room (MOR), then shaped to precompensate for square-pulse distortion later in the laser chain.[24,25] The time-resolved spectra shown in Fig. 4 demonstrate that each spectral component is stable on the time scale required for four-color experiments for low- and high-energy input to the fiber.

To produce the main pulse for the other nine Nova beams, we split off a percentage of the energy in one of the frequencies before it enters the fiber, as shown in Fig. 2. The split-off pulse is then re-injected into the main beam path before it enters the temporal pulse shaping system. Following spectral and temporal shaping, the beam propagates through a double-pass electro-optic phase modulator, which allows the addition of 0.2 nm of FM bandwidth to each frequency component to provide SSD. The time-resolved spectrum of the FM-modulated pulse is shown in Fig. 4(c). Since both the multifrequency and single-frequency beams share this beam path, FM bandwidth is present on all 10 Nova beamlines when the modulator is active.

Grating Separator

The multifrequency beam from the MOR is amplified in the preamplifier section of Nova, where its energy increases to several Joules before being routed to the appropriate beamline. The time-multiplexed multifrequency and single-frequency beams are separated into different beamlines by a Pockels cell/polarizer combination in the preamplifier section. The multifrequency pulse is directed to beamline 7 (BL7), which contains the wavelength separation optics, while the single-frequency pulse is sent to the other nine beamlines via beam splitting and delay optics. The four-color separation optics in BL7 introduce sufficient delay, relative to the other arms, to allow all pulses to arrive simultaneously at the target.

We modified the existing SSD table[2] in BL7 to accommodate the four-color separation optics. These optics, shown schematically in Fig. 5, convert the single multifrequency beam into a four-quadrant beam with one frequency per quadrant. The system is equivalent to four monochrometers sharing a common output slit; as a result, the four output beams are coincident and parallel. This "multichrometer" consists of a four-segment grating array followed by a 1:1 relay with the slit at the focal plane. The image of the grating array is relayed to the output plane where the wavelength of

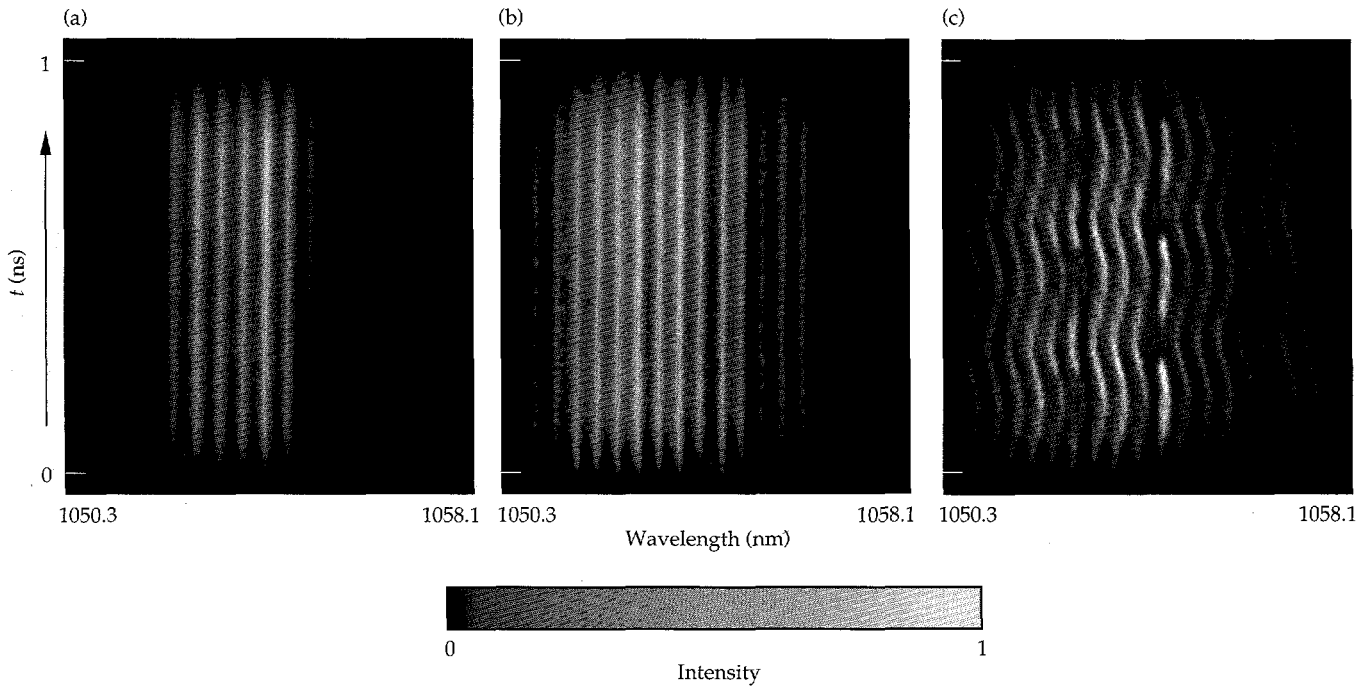

FIGURE 4. The time-resolved spectra of the amplified 1-ns sliced pulse demonstrate that each component of the multifrequency spectrum is stable on the time scale required for four-color experiments. The separation between each color is 0.44 nm. (a) Low-energy input to the fiber, IL = 0.2 TW/cm. (b) High-energy input to the fiber, IL = 1.3 TW/cm. (c) High-energy input into the fiber with 0.2 nm of FM bandwidth per component, IL = 1.3 TW/cm. (70-00-0594-2299pb01)

each segment is selected by independently angle tuning each grating. The unwanted frequencies in each segment are blocked by the slit. A charge-coupled device (CCD) camera imaging the slit monitors the unselected frequency components, allowing alignment of the grating components before each shot. A spectrometer after the slit provides a record of the four-color output spectrum.

The gratings separate each of the four main frequency components with up to 0.3 nm of FM bandwidth per frequency, by more than the focal spot size, allowing passage through the slit without interference from adjacent frequency-modulated bandwidth components. In addition, sufficient dispersion is used to separate each frequency-modulated bandwidth component at the target by at least one-half speckle diameter to achieve optimal beam smoothing. We chose 1800 grooves/mm gratings with a dispersion of 5.64×10^{-3} rad/nm at 1053 nm to meet these constraints. The gratings used in the array were fabricated in-house to obtain the highest possible diffraction efficiency and damage threshold.[26] To reduce the temporal delay of the pulse front across the beam, the gratings are arranged in a "V" configuration. This reduces the temporal skew from 600 to 300 ps, producing a chevron–shaped temporal distortion across the face of the beam, symmetric about the horizontal midline. The non-Littrow grating configuration produces a geometric distortion that is corrected with a four-quadrant heart-shaped apodizer, as shown schematically in Fig. 5. This preforms the beam into a heart-shaped design before the grating array, which then diffracts into a circular beam.

To compensate for unequal SPM sideband amplitudes, the line shape of the amplifier gain, and other spectral inhomogeneities, we independently adjust the energy in each segment to achieve an equal distribution of energy at the target. To balance the quadrant energies, a four-quadrant array of absorbing filters, adjustable in 5% increments, is placed before the grating. Rod shots, in which only the preamplifier section fires, are used to balance the energies between the quadrants. Using this method, better than ±6% energy balance at 1ω and ±17% at 3ω is routinely achieved.

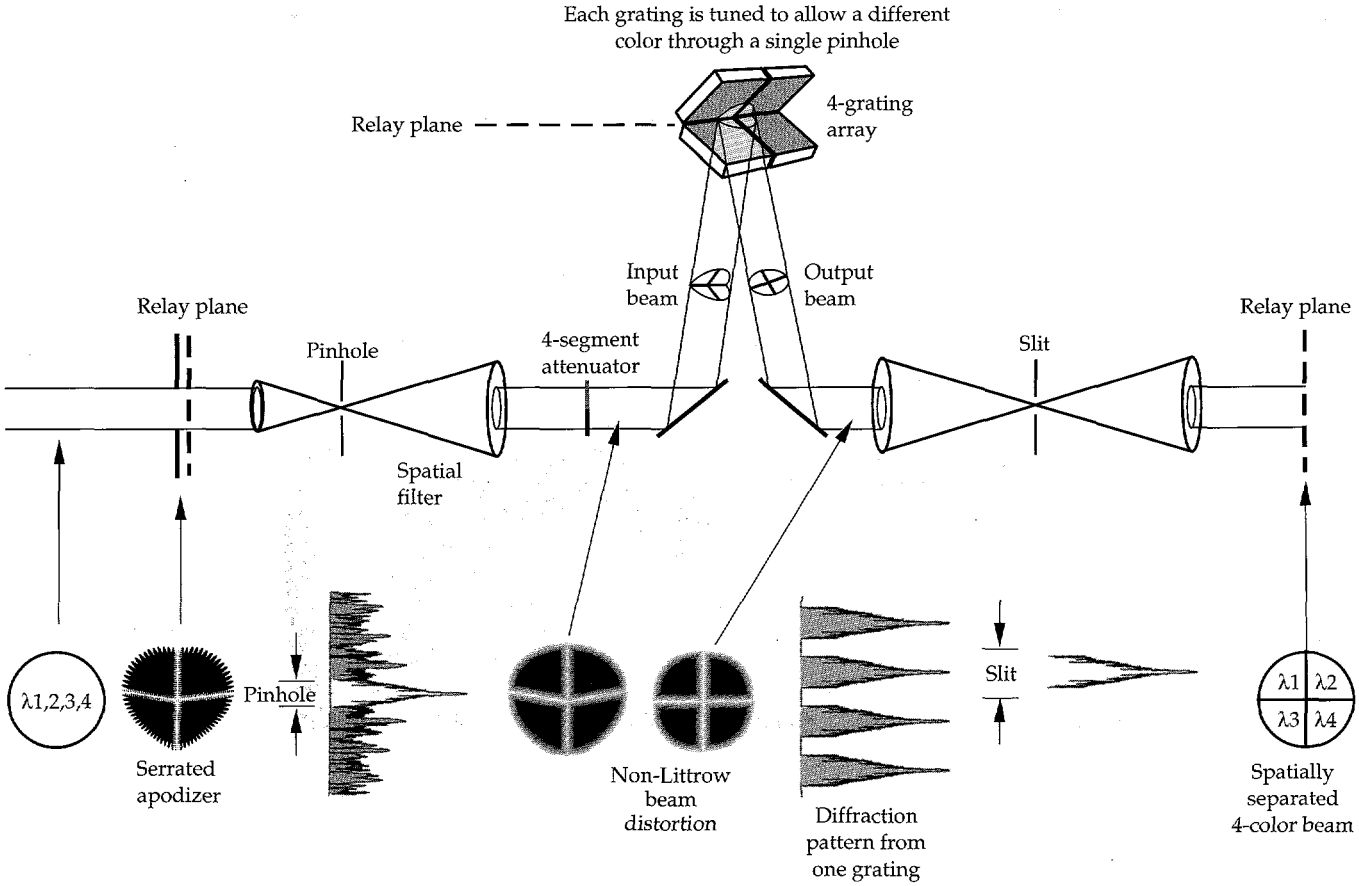

FIGURE 5. Schematic of the special optics installed in the four-color beamline to convert the single multifrequency beam into a four-quadrant beam with one frequency per quadrant. In the output plane, the wavelength of each segment is selected by independently angle-tuning each grating. The unwanted frequencies are blocked by a slit at the focal plane. The beam shape is preformed into a heart-shaped design before the grating array, which diffracts into a circular beam due to the grating configuration. (70-50-0993-3246pb01)

Frequency Converter

The full-aperture 2 × 2 frequency conversion array, shown in Fig. 6, converts the four-color beam to the third harmonic. Each quadrant contains a 12-mm-thick Type I doubler and a 10-mm-thick Type II tripler, using 27-cm Nova KDP crystals. We use the Type I/Type II frequency tripling scheme because of increased performance previously demonstrated on Nova,[20,27] and its adaptability to angle tuning. The four crystal segments are mechanically offset in angle and independently tunable, to allow placement of any of the four wavelengths in each quadrant. The array allows independent tuning of all eight crystals, although the bandwidth of the doublers is sufficient to accommodate the frequency span of the four colors with a single angular orientation. Although the area provided by the four 27-cm crystals is smaller than the full Nova aperture (~80%), the expected energy on target is sufficient for four-color target experiments. We chose the crystal separation to maximize the beam area (~2600 cm^2), compatible with the beam apodization on the grating separation table. Once installed and aligned, a rocking curve was performed to tune the array for maximum performance. This four-color array design achieves up to 65% 3ω conversion efficiency, providing up to 2.3 kJ on target.

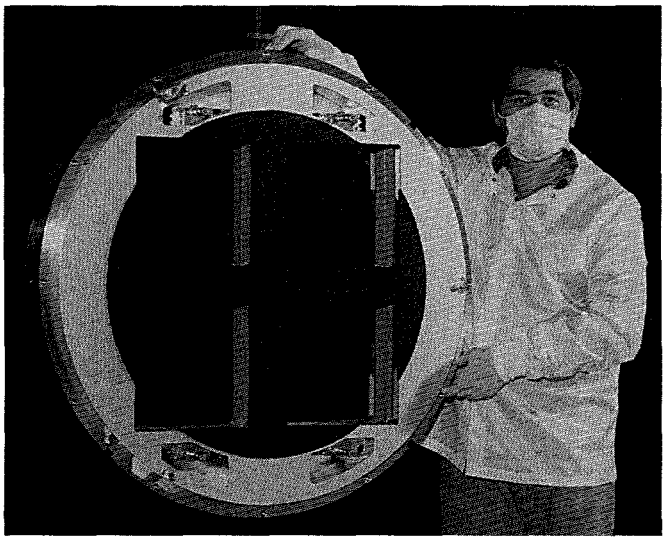

FIGURE 6. Photograph of the Type I/Type II four-color frequency conversion array. (70-10-0494-2032pb01)

Four-Color System Performance

1ω Propagation Experiments

We performed a series of 1ω propagation tests to assess various issues associated with the propagation of a multifrequency beam through the Nova preamplifier section. The energy and near-field image of the unsegmented multifrequency beam are recorded midway through the Nova preamplifier section. The characteristics of the 1ω segmented four-color beam are recorded in the input sensor immediately following separation, and again in the output sensor package before conversion to the third harmonic. The output sensor diagnostics include near-field photography of the spatially separated four-color beam, measurement of the integrated beam energy via calorimetry and diode measurements, and measurement of the integrated pulse shape of the full beam. The energy in each frequency is determined by integrating the fluence in each quadrant of the output sensor near-field camera. A 1-m spectrometer provides a time-integrated spectrum of the full beam. In addition, an array of four photodiodes records the pulse shape of the individual frequencies.

We observe substantial spectral gain narrowing of the SPM spectrum in the Nova chain. Amplification (gain ~ 10^{21}) reduces the unamplified SPM spectrum shown in Fig. 3(a) from ~9.8 nm FWHM to the ~2.1 nm FWHM spectrum shown in Fig. 7(a). This results from spectral gain narrowing produced by the 2.15-nm

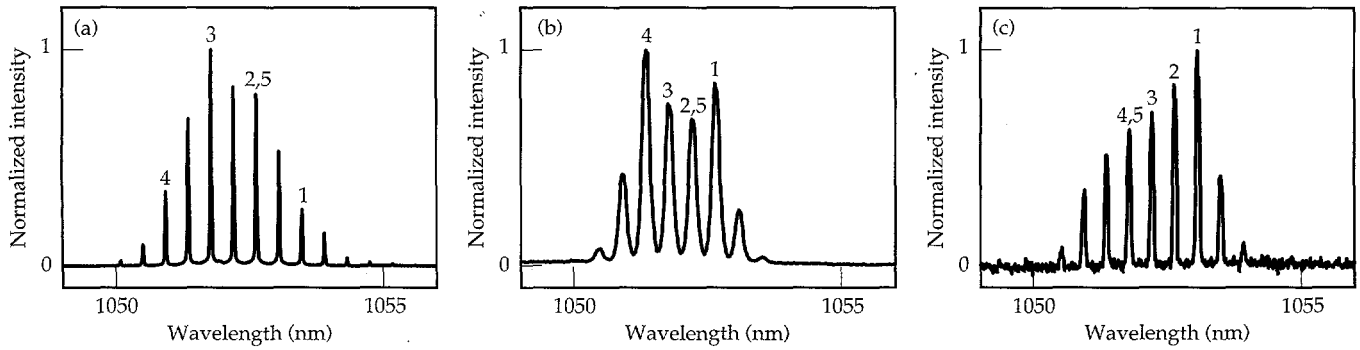

FIGURE 7. (a) Significant gain narrowing of the input spectrum occurs after full amplification in the Nova chain (gain ~ 10^{21}). A frequency spacing of 0.88 nm can be obtained with this spectrum by selecting alternate lines. (b) The central four lines of a low-power SPM spectrum produce a 0.44-nm separation for the first set of four-color target experiments. (c) A series of lines offset from the center of the spectrum are selected for the second four-color target series. The four colors selected by the grating array are indicated by 1, 2, 3, and 4, while 5 is the heater beam frequency. (70-00-0395-0794pb02)

FWHM fluorescence line width of Nd:glass[28] and bandwidth limiting components in the laser chain. As the extraction frequency moves off the peak of the laser glass fluorescence spectrum, the gain coefficient decreases. Thus, to maintain a constant output fluence from the amplifier chain, the input energy must increase to compensate for the reduction in gain off the peak. Experimental measurements show that although the gain and saturation fluence differ for each wavelength as expected, the differences in square pulse distortion are minimal. We performed small-signal gain measurements for the multifrequency spectrum by propagating low-power shots through the laser chain without firing the disk amplifier section. These measurements indicate that the maximum bandwidth that can be supported by the Nova chain is ~3 nm. At maximum bandwidth, it is necessary to keep the energy in the preamplifier section below the fluence threshold for self-focusing and other nonlinear interactions.

For the first four-color target series, we chose a 0.44-nm separation between the four selected frequencies. The intensity propagated through the optical fiber was reduced to allow the generation of only six lines, as shown in Fig. 7(b). The four lines selected on the grating table are centered on the peak of the Nd:glass gain curve to maximize the gain in the amplifier chain, producing 6 kJ at 1ω in 1 ns. Figure 7(c) shows the 8-line spectrum propagated to the grating array for subsequent target experiments. For these experiments, the four-color gratings were tuned to select four colors shifted off the peak of the gain curve. Four colors with a maximum separation of 0.88 nm can be obtained by selecting alternate lines in the SPM spectrum shown in Fig. 7(a), with sufficient 3ω energy to perform target experiments simulating the NIF frequency separation.

Figure 8 compares the pulse shape of each frequency at the source and the output of the laser chain for a 0.44-nm separation between the four colors. The pulse shapes of each frequency at the source, shown in Fig. 8(a), are comparable to within the diagnostic background noise. In Fig. 8(b), the four-quadrant output-diode traces show that three of the pulses lie on top of each other, while the fourth shows a slight difference in contrast ratio, consistent with the higher output fluence in this quadrant. At this fluence and line separation, it is possible to balance the 1ω energy between the four quadrants to better than ±6%, with temporally smooth pulses to within the diagnostic resolution. Figure 9 shows a representative near-field image of the 1ω beam taken with the output sensor diagnostic CCD camera.

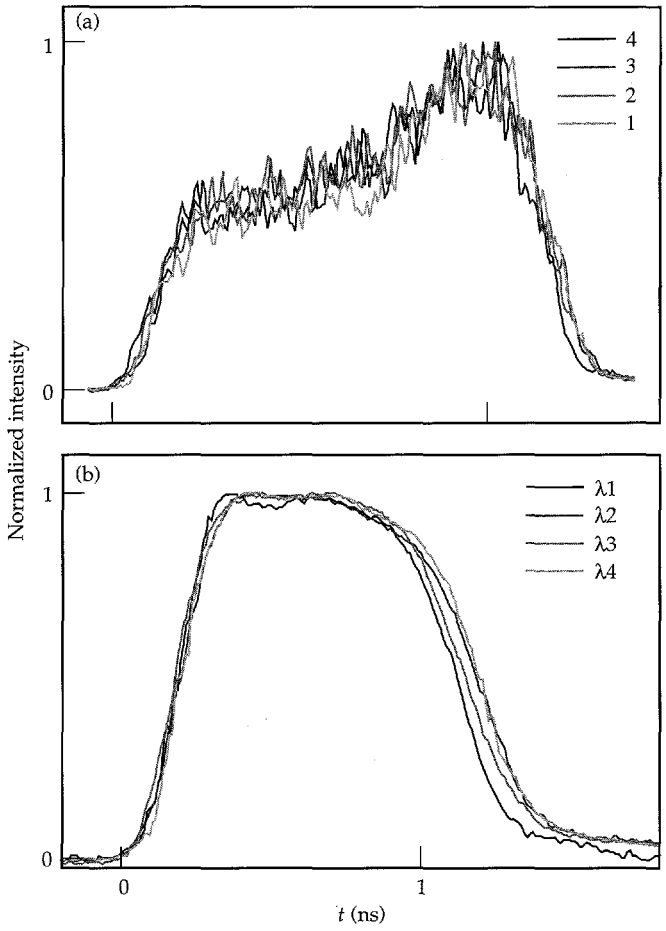

FIGURE 8. Comparison of the temporal pulse shape for each of the four colors (a) at the source and (b) at the output of the laser chain for a 0.44-nm separation. (70-00-0395-0795pb01)

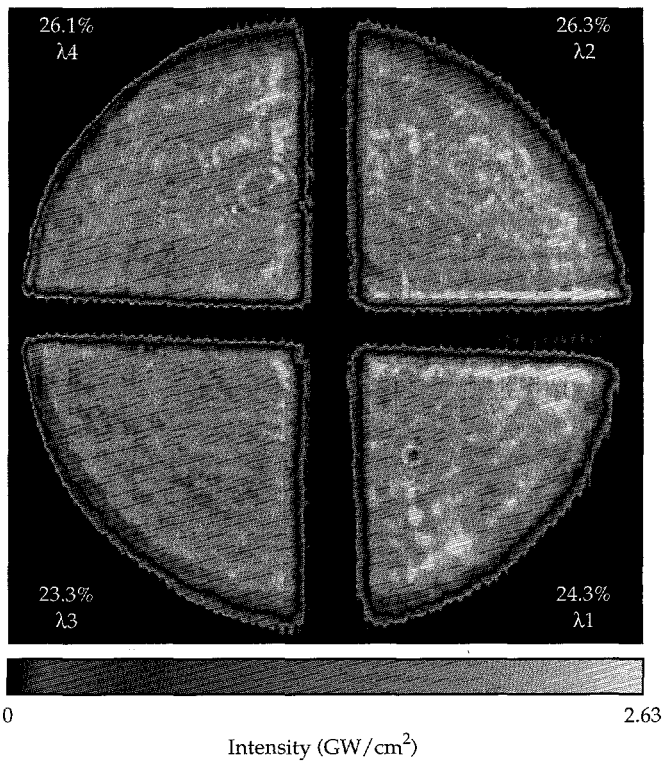

FIGURE 9. Representative near-field image of the 1ω beam taken with the output sensor diagnostic CCD camera. The 1ω energy in each of the four quadrants is balanced to better than ± 6%. (70-00-0495-0924pb01)

Four-Color Beam Smoothing

The two-beam laser diagnostic station (TBLDS)[29] was used to characterize the beam smoothing properties of the four-color irradiance. We used a 3.3-mm-diam, square element phase plate with the standard Nova $f/4.3$ focal geometry to produce approximately the same size focal spot (550 μm) as the $f/8$ geometry in the 10-beam chamber. The near-field, far-field, and expanded far-field images; temporal profile, energy, and spectra were recorded in the TBLDS following frequency conversion to the third harmonic. Figure 10 shows the effect of beam smoothing at 3ω in the equivalent target plane images for (a) an unsmoothed Nova beam; (b) a single-frequency beam with an RPP; (c) a four-color beam with 0.44 nm, or 122 GHz, separation between colors at 1ω and an RPP; and (d) a four-color beam with 0.2 nm or 5.4 GHz of FM bandwidth per component at 1ω and an RPP. All four images have equivalent magnification. The nonuniformities in the unsmoothed irradiance shown in Fig. 10(a) demonstrate the need for beam smoothing. The far-field image of a single-frequency beam with the RPP in Fig. 10(b) shows that the intensity structure is broken up into a homogeneous well-controlled speckle pattern. This pattern remains static throughout the pulse length. The normalized rms variance of the focal irradiance, σ/I, is ~0.79 for this image. This is less than the theoretical predicted value of one for a single speckle pattern, but consistent with previous measurements on Nova and elsewhere.[20,30] This may be an indication that some polarization smoothing is occurring due to birefringence in the focus lenses. In Fig. 10(c), the pattern produced by the four-color beam shows the smoothing obtained by superposition of four independent speckle patterns, with the significant residual speckle structure expected from the limited number of static patterns. The four-color beam produces a time-integrated smoothing level of $\sigma/I \sim 0.25$, in contrast to the theoretically predicted value of $\sigma/I = 0.50$. The reduced σ/I may be associated with the effects seen in Fig. 10(b). Also note that the intensity-length product for these experiments exceeds the threshold for stimulated rotational Raman scattering in air by ~25%,[31,32] as observed experimentally. The chromatic dispersion of this additional bandwidth by the additional optics used to direct the beam to the TBLDS may also contribute slightly to the lower σ/I measured on this shot. Figure 10(d) clearly shows that SSD with four colors and FM bandwidth produces a much smoother focal spot than the previous three images. Discrete speckles are no longer observable and the irradiance is smooth and uniform. The vertical streaks in the image are formed by the one-dimensional nature of the dispersion. This image has a $\sigma/I \sim 0.16$. This is less smooth than theoretically predicted, but is consistent with previous measurements of smoothing with FM bandwidth on Nova.[20]

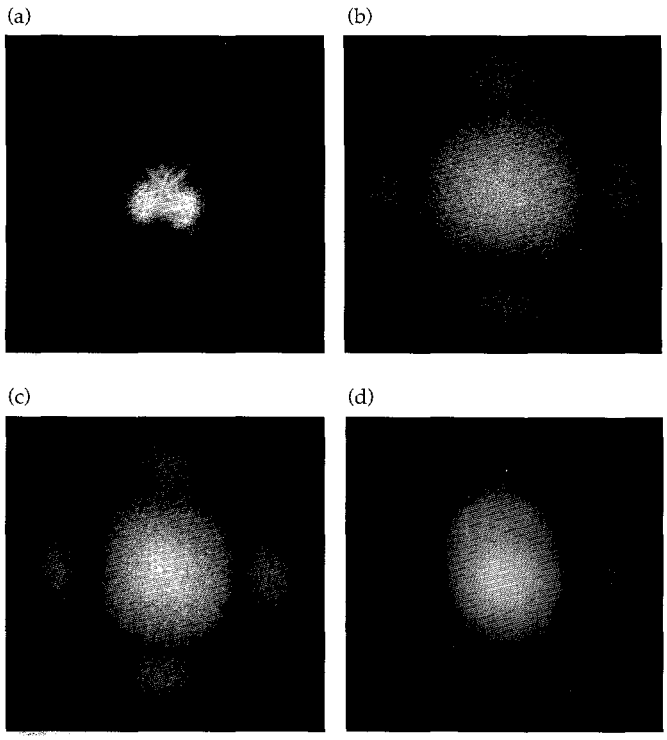

FIGURE 10. (a) Nonuniformities in the equivalent target plane image of the 3ω beam at best focus demonstrate the need for beam smoothing. The effect of beam smoothing at 3ω can be seen in the equivalent target plane images for (b) a single-frequency beam with an RPP, (c) a four-color beam with a 0.44-nm separation and RPP, and (d) a four-color beam with a 0.44-nm separation, 0.2 nm of FM bandwidth per color, and RPP. The normalized rms intensity variance, σ/I, for these images is (b) ~0.79, (c) ~0.25, and (d) ~0.16. (70-00-0395-0796pb01)

Theoretical modeling of the temporal dynamics of beam smoothing demonstrates that the multiple-aperture SSD technique described here can give very rapid and effective beam smoothing at the target plane. Simulations of the power spectra and the smoothing capability for (a) one-color SSD with 108 GHz of bandwidth at 1ω, (b) four colors with 136 GHz separation at 1ω and no FM bandwidth, and (c) four colors with 136 GHz separation and 54 GHz of bandwidth at 1ω are shown in Figs. 11 and 12. Figure 11(a) shows the spectrum for a one-color beam with 108 GHz of FM bandwidth at 1ω, 324 GHz at 3ω. There is sufficient dispersion to decorrelate each FM component of this spectrum at the target plane (0.21 μrad/GHz at 3ω). These values represent the maximum bandwidth/dispersion that can be propagated through the Nova chain with decorrelated spectral components without clipping in the spatial filter pinholes. The smoothing rate, $(d\sigma/dt)/\sigma$, reaches a peak rate of 0.11 ps^{-1} in 2–3 ps, comparable to the inverse of the total bandwidth. The intensity cross-correlation between the speckle field at

a given time and the initial speckle field drops from 1.0 to a value near zero in the same 2–3 ps. The normalized smoothing level, σ, drops from near unity to 0.707 in the first 2–3 ps, and to 0.5 in 8–10 ps, as shown in Fig. 12(a). It reaches an asymptotic level of ~0.15 after 1 ns, consistent with time-integrated smoothing levels previously measured on Nova under these conditions.[20]

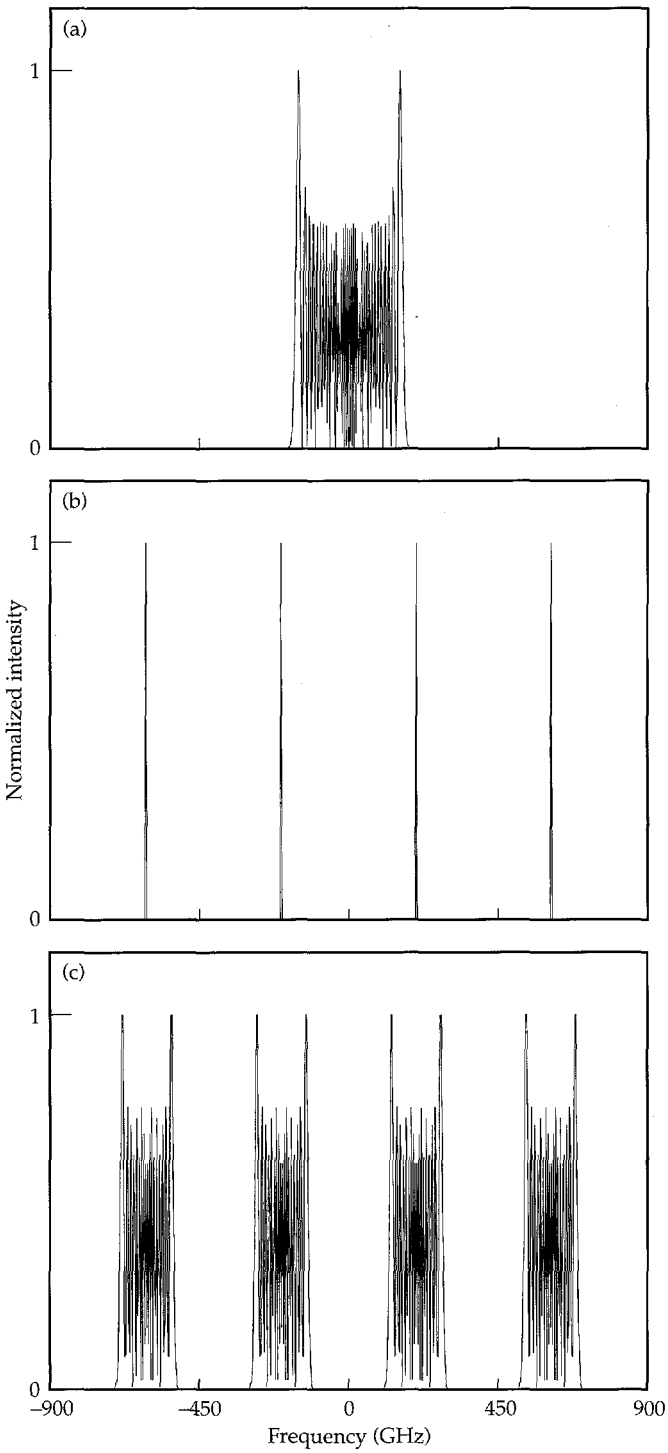

FIGURE 11. Power spectrum of a beam with (a) 324 GHz of FM bandwidth at 3ω, (b) four colors with 405 GHz separation at 3ω, and (c) four colors with 405 GHz separation and 162 GHz of FM bandwidth on each color. (70-00-0395-0797pb01)

Figure 11(b) shows the 3ω output spectrum for a four-color beam with frequencies separated by 136 GHz at 1ω or 405 GHz at 3ω. Figure 11(c) shows the same four-color spectrum, but with 54 GHz of 1ω FM bandwidth (162 GHz at 3ω) added to each of the four colors. We use a spectral dispersion of 0.29 μrad/GHz at 3ω in the simulations, corresponding to the value used in the four-color experiments on Nova. The initial smoothing rate for four-colors alone is five times faster than for the single-color FM bandwidth case. A peak rate of 5 ps^{-1} is achieved in less than 1 ps, corresponding to the inverse of the total frequency spread of 1.2 THz, reaching $\sigma = 0.5$ within 2.5 ps. The speckle field initially decorrelates in <1 ps, but the cross-correlation returns to unity at every beat period of the closest frequency spacing (405 GHz), and the field repeats every 2.47 ps. Thus even though the initial smoothing rate is very high, once σ reaches 0.5, as expected for the sum of four independent speckle fields, no further smoothing is obtained, as shown in Fig. 12(b). With the addition of FM bandwidth to each of the four colors, the initial high smoothing rate is still achieved, but the integrated smoothing level continues to decrease rapidly, reaching an asymptotic value of 0.08 in a few tens of picoseconds [Fig. 12(c)]. Since the overall spectrum is not continuous, the intensity cross-correlation shows secondary and tertiary peaks at times related to the beat frequencies of the principal four colors; however, these peaks are significantly damped within 8–10 ps, reducing in magnitude over one FM period when all frequency components are available for smoothing. The combination of four colors with FM bandwidth provides both a rapid initial smoothing level and effective time-averaged beam smoothing at the target plane.

3ω Four-Color Performance

To simulate the $f/8$ geometry proposed for the NIF, we retrofitted the four-color beamline to accommodate an $f/8$ target chamber lens on the 10-beam chamber. The incident beam diagnostic (IBD) is used to diagnose the 3ω performance of the four-color system.[33] The IBD records the spatially integrated 3ω energy, the near-field image, and the temporal pulse shape integrated over all four quadrants. Figure 13 shows a representative near-field image of the 3ω beam taken with the IBD CCD camera. The energy in the four quadrants is balanced to better than ±17%.

After installation on the 10-beam chamber, the four-color KDP array was rocked ±500 μrad to establish the best tuning coordinates, achieving a 3ω array efficiency

of up to 65%. This delivers up to 2.3 kJ at 3ω in 1 ns to the target. In addition, since the standard master oscillator is tuned 0.22 nm off Nd:YLF line center to produce the four-color beam, the pulse to the other nine arms is also shifted in frequency. Thus, the KDP arrays on the other nine arms of Nova are appropriately tuned to compensate for this shift. Conversion efficiencies on the other nine arms with the Nova Type II/Type II arrays at the shifted wavelength are within 10% of their nominal conversion efficiencies on YLF line center. The addition of 0.2 nm of FM bandwidth to the four-color beam and the other nine arms reduces the 3ω conversion efficiency by <5%.

Pointing experiments performed with the $f/8$ lens after the four-color array activation show the expected beam symmetry and size at best focus, with all four quadrants within 50 μm of their expected positions. The arrival of the four-color beam at target chamber center relative to the other nine arms is synchronized to within 20 ps using techniques developed for the Precision Nova project.[34] A 5.8-mm-diam, square element phase plate inserted in the four-color beamline after the $f/8$ lens, produces a 570-μm focal spot diameter with a peak intensity of 2×10^{15} W/cm^2 for target experiments. To determine the effectiveness of the four-color system in controlling instabilities in NIF-like plasmas, the Full-Aperture Backscatter Station was used to measure the spatial distribution of the backwards propagating SBS from a target in each of the four beam quadrants, as well as the wavelength-resolved temporal evolution of the SBS in each quadrant. Measurements show that the four-color system produces <1% SBS backscatter at $>2 \times 10^{15}$ W/cm^2 when used to

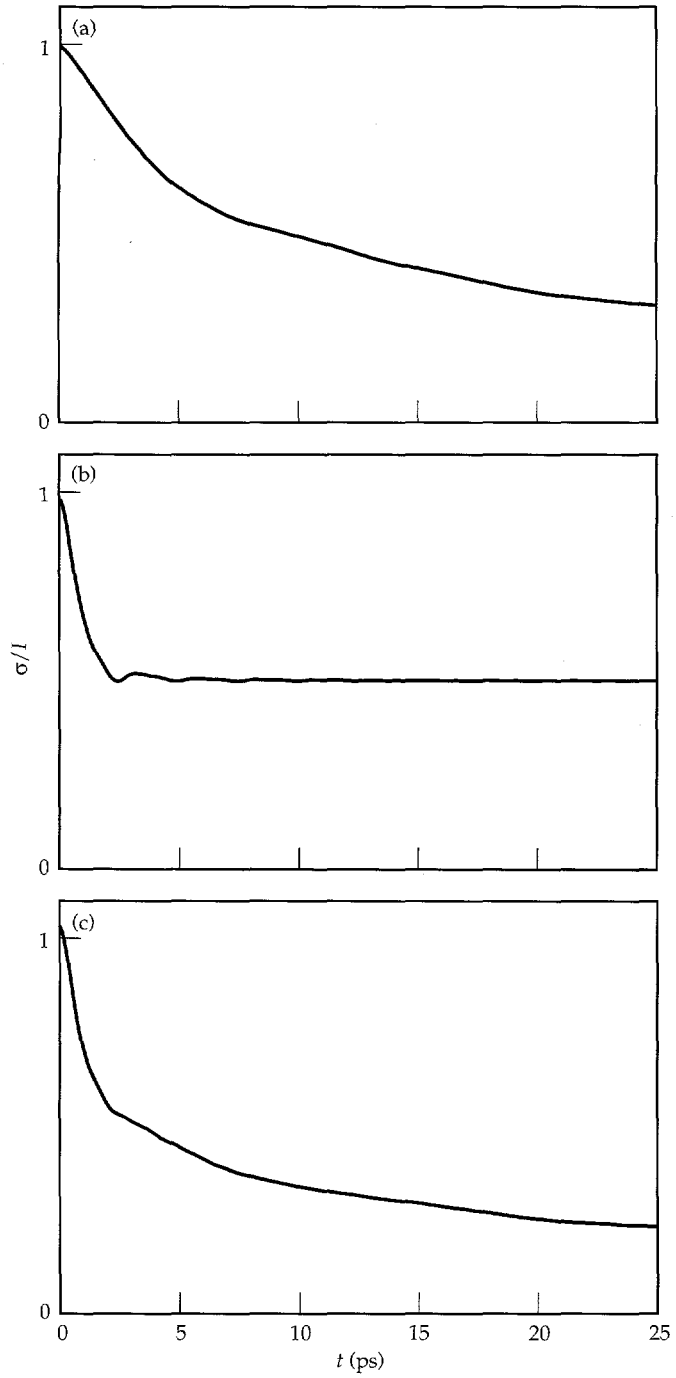

FIGURE 12. Calculated rms intensity variance, σ/I, of the focal irradiance plotted as a function of integration time for (a) 324 GHz of FM bandwidth at 3ω, (b) four colors with 405 GHz separation at 3ω, and (c) four colors with 405 GHz separation and 162 GHz of FM bandwidth on each color. (70-00-0395-0798pb01)

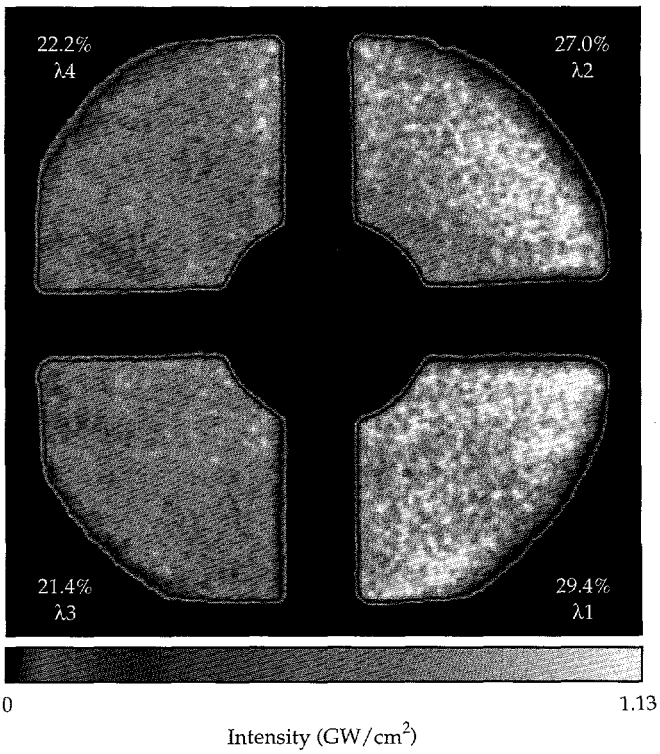

FIGURE 13. Representative near-field image of the 3ω beam taken with the incident beam diagnostic CCD camera in the 10-beam chamber area. The 3ω energy in each of the four quadrants balances to better than ± 17%. (70-00-0495-0924pb02)

probe NIF-like plasmas. Further details of the plasma physics experiments performed using the four-color system are described in "Laser–Plasma Interactions in Large Gas-Filled Hohlraums," p. 97 of this *Quarterly* and elsewhere. [13–15]

Summary

We successfully deployed a four-color bandwidth system with optical characteristics similar to that of the proposed NIF on Nova for laser experiments. A multi-frequency bandwidth source is spatially separated into four quadrants, each containing a different central frequency, providing a total bandwidth of 1.32 nm at 1ω. The four colors are spatially separated into four quadrants using a novel grating multichrometer design. Each quadrant is independently converted to the third harmonic in a four-quadrant frequency conversion array with independent phase-matching, providing up to 2.3 TW at the third harmonic. The measured far-field irradiance shows ~25% rms intensity variation with four colors alone, reaching this level within 3 ps. The addition of 0.2 nm of FM bandwidth to each frequency component reduces the rms intensity variation level to ~16% without significant impact on the conversion efficiency.

Acknowledgments

The authors thank the Nova laser operators staff for their contributions and dedication, particularly E. Padilla, C. Brown, J. Vickers, and H. Orrell of the MOR, whose efforts throughout these experiments allowed us to achieve our goals. We also thank C. Brown and P. Danforth for their assistance with the development of the four-color bandwidth source. We gratefully acknowledge R. Ellis, R. Kent, and K. Stanion for mechanical design and activation of the four-color grating and frequency conversion arrays, and the $f/8$ lens assembly. We also thank our colleagues C. Laumann, J. Miller, R. Ehrlich, and C. Thompson for their contributions to the four-color diagnostics developed for these experiments, and S. Dixit for developing the phase plates.

Notes and References

1. S. Skupsky, et al., *J. Appl. Phys.* **66**(8) 3456–3462 (1989).
2. H. T. Powell, S. N. Dixit, M. A. Henesian, *ICF Quarterly Report* **1**(1), 28–38, Lawrence Livermore, National Laboratory, Livermore, CA, UCRL-LR-105821-91-1 (1991).
3. P. H. Chaffee, F. G. Patterson, M. A. Henesian, *Technical Digest, Conference on Lasers and Electro-Optics* **10** (Optical Society of America, Anaheim, CA, 1989) p. 106.
4. M. A. Henesian, et al., *Technical Digest, International Quantum Electronics Conference* **9**, Paper TuE3 (1992).
5. S. P. Obenschain, et al., *Phys. Rev. Lett.* **56**, 2807 (1986).
6. W. L. Kruer, *The Physics of Laser Plasma Interactions* (Addison–Wesley,NY, 1988).
7. J. F. Drake, et al., *Phys. Fluids* **17**(9), 778 (1974).
8. R. L. Berger, *Phys. Rev. Lett.* **65**, 1207–1210 (1990).
9. W. Seka, et al., *Phys. Fluids B* **4**, 2232–2240 (1992).
10. R. L. McCrory, et al., *Laser Part. Beams* **8**, 27–32 (1990).
11. J. A. Paisner, *National Ignition Facility Conceptual Design Report*, Lawrence Livermore National Laboratory, Livermore, CA, UCRL-PROP-117093 (1994).
12. D. M. Pennington, et al., *Technical Digest, Conference on Lasers and Electro-Optics* **8** (Optical Society of America, Anaheim, CA, 1994) p. 161.
13. L. V. Powers, et al., *Phys. Rev. Lett.* **74**, 2957–2960 (1995).
14. B. J. MacGowan, et al., "The Study of Parametric Instabilities in Large-Scale-Length Plasmas Produced by Laser Irradiation of Thin-Walled Gas-Balloons," Lawrence Livermore National Laboratory, Livermore, CA, UCRL-JC-117044 ABS; prepared for *Anomalous Absorption Conference*, Pacific Grove, CA, June 5–10, 1994, p. AO–1.
15. D. S. Montgomery, et al., "Experimental Study of SBS and SRS in the Nova Gas-Target Large Plasmas," Lawrence Livermore National Laboratory, Livermore, CA, UCRL-JC-117072 ABS; prepared for *Anomalous Absorption Conference*, Pacific Grove, CA, June 5–10, 1994, p. BP–22.
16. Y. Kato, et al., *Phys. Rev. Lett.* **53**(11), 1057–1060 (1984).
17. S. N. Dixit, et al., *Appl. Opt.* **32**, 2543–2554 (1991).
18. L. V. Powers, et al., "Gas-Filled Targets for Large Scalelength Plasma Interaction Experiments on Nova," Lawrence Livermore National Laboratory, Livermore, CA, UCRL-JC-118104(1995); to be published in *Physics of Plasmas*.
19. B. F. Lasinski, et al., "SBS and Filamentation in Current and Future Experiments," Lawrence Livermore National Laboratory, Livermore, CA, UCRL-JC-116795 ABS, Rev 1; prepared for *Anomalous Absorption Conference*, Pacific Grove, CA, June 5–10, 1994, p. AP–14.
20. D. M. Pennington, et al., *Proc. Soc. Photo–Instrum. Eng.* **1870**, 175–185 (1993).
21. R. H. Stolen, C. Lin, *Phys. Rev. A* **17**, 1448–1453 (1978).
22. J. R. Thompson and R. Roy, *Phys. Rev. A* **43**, 4987–4996 (1991).
23. D. J. Kuizenga, *Laser Program Annual Report–79*, Lawrence Livermore National Laboratory, Livermore, CA, UCRL-50021-79 (1980).
24. R. B. Wilcox, *Lasers Part. Beams* **4**, 141–143 (1986).
25. J. K. Lawson, et al., *Appl. Opt.* **31**, 5061–5068 (1992).
26. R. D. Boyd, et al., *Appl. Opt.* **34**, 1697–1706 (1995).
27. P. J. Wegner, et al., *Appl. Opt.* **31**, 6414–6426 (1992).
28. S. E. Stokowski, R. A. Saroyan, M. J. Weber, *Laser Glass Handbook*, Lawrence Livermore National Laboratory, Livermore, CA, M-095, Rev. 2 (1981).
29. P. J. Wegner, M. A. Henesian, *Proc. Soc. Photo–Opt. Instrum. Eng.* **1414**, 162 (1991).
30. T. Jitsuno and N. Nishi, Osaka University, ILE, Osaka, Japan, private communication (May 16, 1994).
31. M. A. Henesian, C. D. Swift, J. R. Murray, *Opt. Lett.* **10**, 472 (1985).
32. M. D. Skeldon, et al., IEEE J. *Quantum Electron.* **28**, 1389–1399 (1992).
33. C. W. Laumann, et al., *ICF Quarterly Report* **4**(1), 1–9, Lawrence Livermore National Laboratory, Livermore, CA, UCRL-LR-105821-94-1 (1993).
34. J. A. Caird, et al., *ICF Quarterly Report* **4**(1), 10–17, Lawrence Livermore National Laboratory, Livermore, CA, UCRL-LR-105821-94-1 (1993).

Testing a New Multipass Laser Architecture on Beamlet

C. S. Vann *S. Seznec*

F. Laniesse *J. E. Murray*

H. G. Patton *B. M. Van Wonterghem*

Introduction

We completed proof-of-principle tests on Beamlet for a new multipass laser architecture that is the baseline design for the French Megajoule laser and a backup concept for the U.S. National Ignition Facility (NIF) laser. These proposed laser facilities for Inertial Confinement Fusion (ICF) research are described in their respective *Conceptual Design Reports*.[1,2] The lasers are designed to deliver 1.8 MJ and 500 TW of 0.35-μm light onto a fusion target using 240 independent beams for the Megajoule laser and 192 beams for the NIF laser. Both lasers use flash-lamp pumped glass amplifiers and have approximately 38-cm square output beams. However, there are significant differences in their architecture.

Figure 1 shows the NIF baseline architecture. A single beam consists of three amplifier modules with a total of 19 laser slabs, cavity and transport spatial filters, two cavity mirrors to form a multipass cavity, and a full-aperture Pockels cell and polarizer to switch the beam out of the cavity after four passes. During a shot, a beam from the optical pulse generator is injected into the transport spatial filter. The beam passes through the booster amplifier, makes four passes through the cavity amplifier, exits the cavity, and again passes through the booster amplifier and out of the laser towards the target. The Pockels cell and polarizer are required to switch the beam out of the cavity. After pass 1, the Pockels cell is turned "on" to rotate the beam polarization 90°, making passes 2 and 3 the correct polarization to pass through the polarizer and stay in the cavity. The Pockels cell is turned "off" at the end of pass 3, so pass 4 reflects off the polarizer to leave the cavity. Because the beam is reflected out of the cavity, the booster amplifier is at a different level than the cavity amplifier.

In contrast, the Megajoule laser and the NIF backup designs do not use a full-aperture Pockels cell and polarizer to switch the beam out of the cavity. Instead, they use a relatively small set of optics, called a Reverser, located in the center section of the transport spatial filter to steer the beam from pass 2 to pass 3 (Fig. 2). This steering is possible because the beam is intentionally pointed off-axis through the amplifiers for both architectures so that each pass focuses at a separate location at the center of the spatial filter. (Beams are focused through a small hole at the center

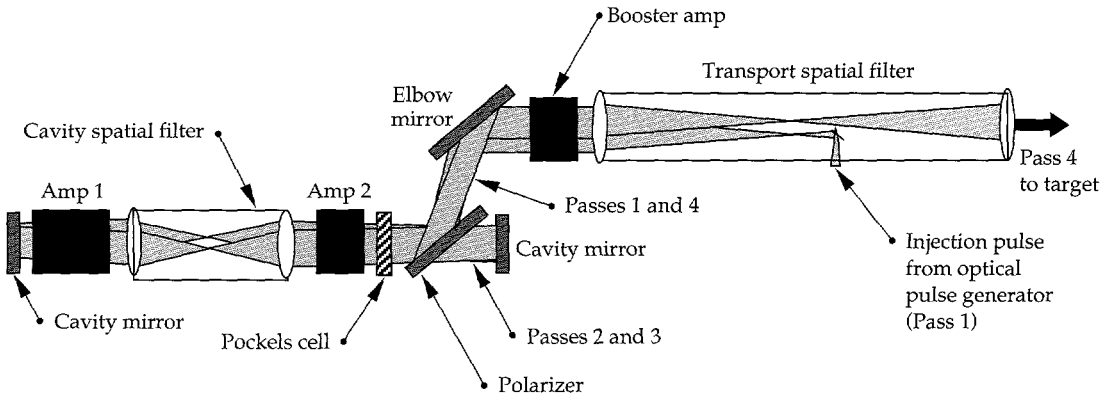

FIGURE 1. A single beam of the proposed National Ignition Facility (NIF) laser. (70-50-0495-1005pb01)

UCRL-LR-105821-95-2

of the spatial filter to remove high spatial-frequency noise from the beam.) Separation of the passes permits the Reverser to extract the beam on pass 2, manipulate it, and re-inject it on pass 3. This same feature permits beam injection into the laser using a small mirror near the pinholes as shown in Figs. 1 and 2. The energy of the beam after pass 2 is low enough that a mirror only a few centimeters square can survive without being damaged. Consequently, the beam can be turned around with small optics rather than a large Pockels cell and polarizer.

The Reverser

In its simplest form, the Reverser consists of a small pick-off mirror that directs the pass 2 beam to a collimating lens and a retro-mirror. The retro-mirror points the beam back through the same collimating lens and along the beamline of pass 3. Practical considerations lead to at least one additional turning mirror between the pick-off mirror and lens, as shown in Fig. 2, and an isolation unit to protect against back reflections. The size of the beam in the collimated section is determined by the desired fluence on the Reverser component with the lowest damage threshold. The pick-off mirrors are sized to withstand the amount of energy expected at the end of pass 2. The size of the pick-off mirrors determines the pinhole spacing, and the pinhole spacing determines the off-axis angle of the beam through the laser. This angle causes the beam position to shift slightly in the amplifier aperture from pass to pass and reduces the maximum beam size that can pass through a given amplifier aperture. Since a smaller beam size means less energy on target, this loss, called vignetting loss, should be minimized. For NIF, a pick-off mirror about 5×5 cm^2 is large enough to avoid damage, but small enough to cause about the same vignetting loss as the NIF baseline.

The French and U.S. Reverser designs are the same in principle, but are implemented differently—the French version is the L-turn and the U.S. version is the U-turn. The L-turn is simpler, with only seven components required (see Fig. 3). After the pick-off mirror, a second mirror directs the beam through a collimating lens to the cavity mirror, which is oriented to reflect pass 2 back along pass 3. The isolation system, a Pockels cell between crossed polarizers, blocks forward and backward transmission, except during a 50-ns window to allow passage of the shot pulse. The insertable half-wave plate is used for alignment, but not for a shot. Both passes 2 and 3 go through each of the L-turn components. This requires component apertures slightly larger than for the beam by itself, due to vignetting. Also, if the pulse length is long enough to overlap in time on an L-turn optic, interference increases the fluence on that optic substantially.

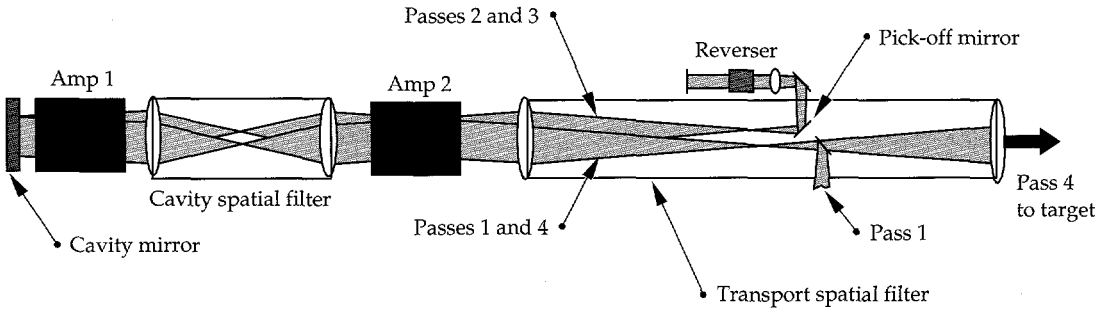

FIGURE 2. The generic Reverser in a four-pass laser architecture. (70-50-0495-1006pb01)

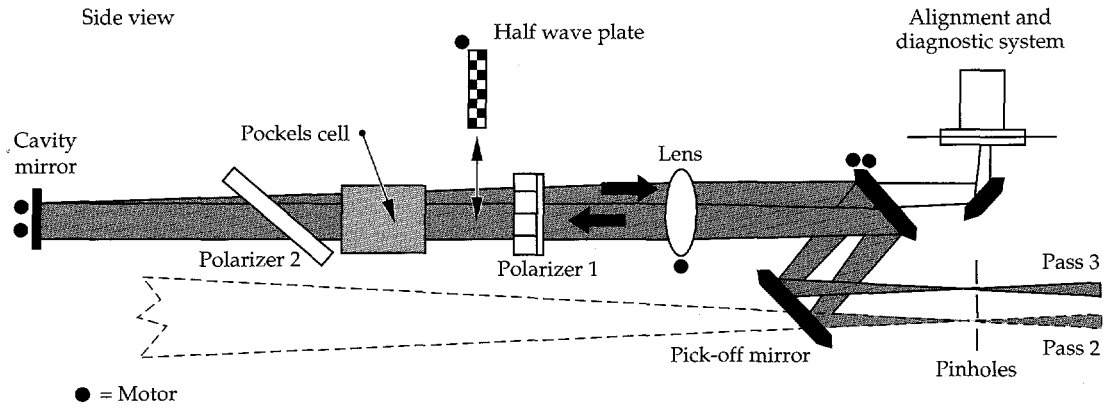

FIGURE 3. The French version of the Reverser, called L-turn. (70-50-0495-1003pb01)

In the U-turn, the pulse passes through each component only once, as shown in Fig. 4. Consequently, it has about twice as many components (13 vs 7), which are slightly smaller because there is no vignetting. The isolation system uses a half-wave plate to properly orient the polarization of the output pulse. With these exceptions, the corresponding components function the same as in the L-turn. The added complexity required to separate passes 2 and 3 in the U-turn provides design flexibility. For example, the cavity mirror of the L-turn can be replaced by a corner cube as shown in Fig. 4, which potentially improves the output pointing stability of the laser. The corner cube inverts the beam profile horizontally and vertically, so that any odd-order aberration that accumulates on passes 1 and 2, such as a drift in pointing, is canceled on passes 3 and 4.

Separation of passes 2 and 3 also makes it possible to change the beam size between passes 2 and 3. If passes 1 and 2 have a beam area about half that of passes 3 and 4, vignetting loss is determined by passes 3 and 4 only, not all four passes, which reduces vignetting loss by about 50%. This scheme also reduces aberrations, because the first two passes are through the center of the amplifiers, avoiding the more aberrated edges of the amplifier slabs. However, this scheme requires a change to the pinhole configuration that we did not attempt in these tests.

The L- and U-turn Reverser architectures have potential advantages over the NIF baseline architecture. They replace the large Pockels cell and polarizer with much smaller ones (10×10 vs 40×40 cm^2 apertures). Smaller components are lower in cost, easier to fabricate, and generally have better quality. They allow a straight, more compact layout with all the amplifier slabs in two modules to improve amplifier efficiency by reducing end losses. They eliminate the elbow mirror and one of the full-aperture cavity mirrors and allow the beam to pass through all the amplifier slabs four times. The beam passes through the booster amplifier only twice in the NIF baseline. This increases the total system amplification and allows a smaller output energy from the front end. Nevertheless, a full-size, proof-of-concept device had never been built before and was needed to establish the viability of the Reverser concept.

Joint French/U. S. Testing of the L- and U-Turn Designs

In March 1994, a team from Lawrence Livermore National Laboratory (LLNL) visited the French Centre d'Études de Limeil–Valenton (CEL-V) to discuss a joint venture to build and test a Reverser on LLNL's Beamlet laser. CEL-V had previously expressed its desire to test the L-turn on Beamlet, and U-turn tests were scheduled for early FY 1995. It was impractical to test each design independently, because of the limited time available on Beamlet (October–December 1994). Therefore, both teams hoped to jointly decide on one design.

The goal was to prove the feasibility of the basic concept. In both cases the device would be installed into the transport spatial filter of Beamlet. The requirements for isolation components and alignment and diagnostic sensors were the same. However, it was important to test the unique features of each design. Therefore, rather than decide on either the L- or U-turn, the teams jointly agreed to share responsibility for building a Reverser that could be reconfigured to test both designs by changing only a few components. The objectives were to (1) compare performance of L-turn, U-turn, and baseline concepts; (2) evaluate L- and U-turn alignment; (3) learn about control of parasitic beams caused by back reflections and amplified spontaneous emission; and (4) determine vulnerability of Reverser optics to pinhole debris.

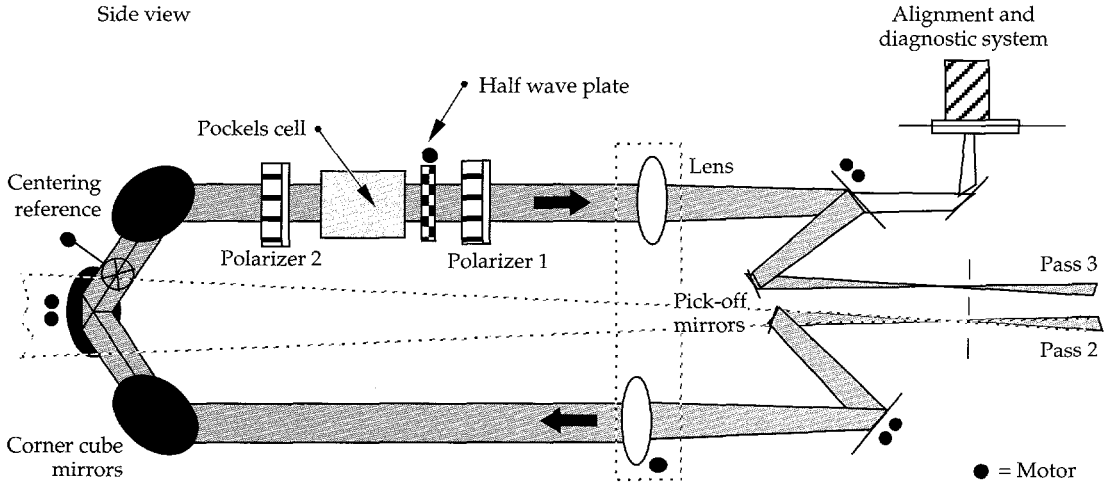

FIGURE 4. The U.S. version of the Reverser, called U-turn. (70-50-0495-1002pb01)

Since our primary goal was to prove viability of the Reverser concept, we did not modify the Beamlet layout for optimum Reverser performance. We added the Reverser hardware and removed the large Pockels cell and the harmonic generators, which were not needed. Figure 5 shows the baseline Beamlet layout, indicating the location of the Reverser hardware in the center of the transport spatial filter. All the Reverser components fit within the existing transport spacial filter's 24-in.-diam vacuum tube, and existing ports on the tube were used for access. Figure 6 shows the U-turn corner cube mounted in the mid-section of the Beamlet transport spatial filter.

Figure 3 illustrates the configuration of the L-turn that was tested on Beamlet. The beam enters through the pass 2 pinhole on the lower right, makes two passes through all the L-turn optics, and exits through the pass 3 pinhole. The alignment and diagnostic system includes a calorimeter for determining the energy of the pulsed beam, and a near-field camera that can image any of the components during alignment or at shot time. A motorized cavity mirror provides pointing adjustments during routine alignment. The half-wave plate was inserted during alignment to allow transmission of the system alignment laser. As shown, other components were also motorized to allow adjustment under vacuum, but they were only needed for the initial setup.

Figure 4 illustrates the U-turn layout, which we tested. It has similar optics to simplify conversion between the two layouts. Only the corner cube mirrors and the two pick-off mirrors replace corresponding components of the L-turn. The pass-2 lens was present for the L-turn, but not used. When reconfiguring from the L-turn, polarizer 2 had to be rotated 90° and the half-wave plate was inserted during shot time and removed for alignment.

For both L- and U-turn tests, the temporal and spatial profiles of the injected beam from the front end were the same as they had been for previous tests with the baseline configuration.[3] The injected beam had a parabolic spatial profile, higher at the edges than the center by about a factor of two, to compensate for gain roll-off toward the edges of the amplifiers. The input pulse was shaped temporally to compensate for gain saturation and to give an approximately square pulse

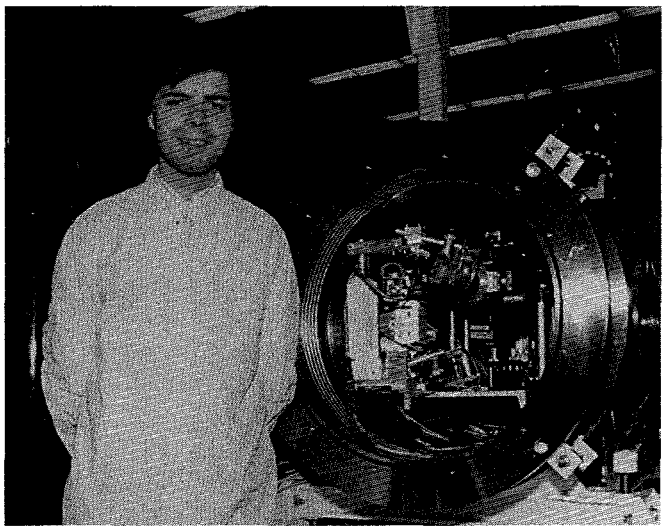

FIGURE 6. The middle section of the Beamlet transport spatial filter (end section removed). The corner-cube assembly of the U-turn is shown inside the 2-ft-diam tube. (70-50-0595-1191pb01)

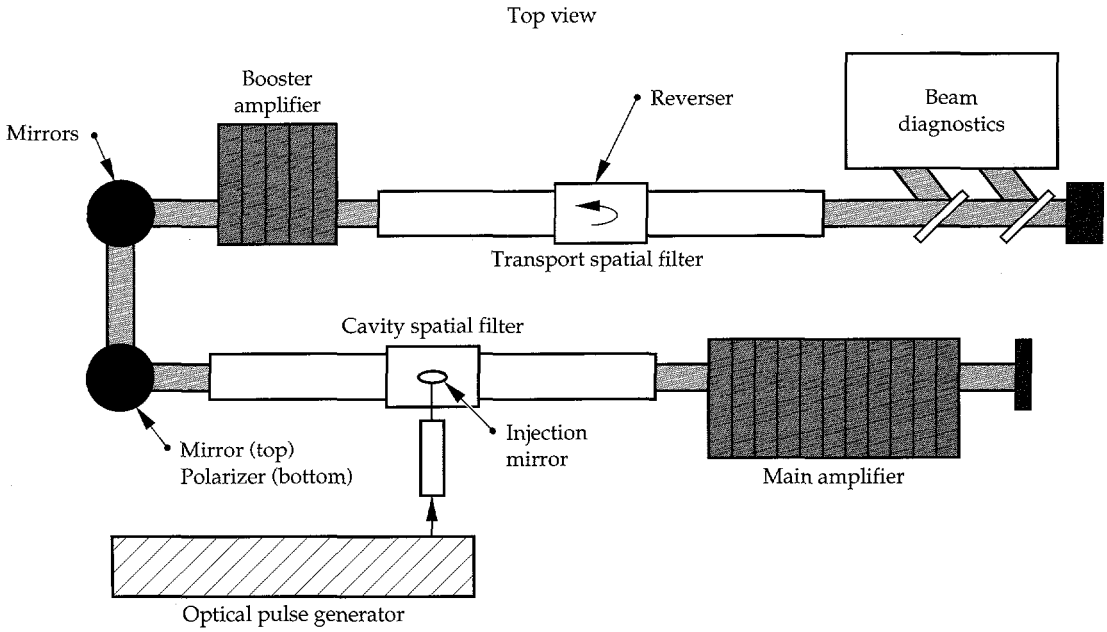

FIGURE 5. The Reverser's position in the transport spatial filter of the Beamlet laser. (70-50-0495-1001pb01)

at the output. The main beam was 32.5 cm square at its 10^{-2} intensity boundary with corners rounded at a radius of 5 cm and a fill factor of 84% (defined as the ratio of the beam energy to the energy if the entire 32.5×32.5 cm^2 beam were filled at the fluence of the central area of the beam).

The focal length of the lenses in the L- and U-turn optics was 110 cm to give a 4.0-cm square beam at the 10^{-2} intensity point in the collimated sections. The corresponding beam size on the first pick-off mirror was 2.2 cm square. For the L-turn, the angle between passes 2 and 3 was 27.3 mrad. The Pockels cell was a cylindrical-ring-electrode type with a 95% deuterated potassium dihydrogen phosphate (KD*P) crystal, an aperture of 7.3 cm in diam, and a length of 9.2 cm. The polarizers transmitted ≥97% of the *p*-polarized light and rejected up to 99.8% of the *s*-polarized light. The measured damage threshold of the polarizers was ≥10 J/cm^2 at 1.5 ns. In the L-turn configuration, the pulse length was limited to 2.3 ns to avoid beam overlap on polarizer 2.

L-Turn Tests

We arbitrarily chose to test the L-turn configuration first. In its original configuration, we used only polarizer 1 in the isolation unit. The Pockels cell was oriented such that it gave a quarter-wave retardation for a single pass with no applied voltage. The resulting isolation was 8×10^{-4}, good for a Pockels cell and polarizer of that aperture, but not enough to protect the front end against back reflections from lenses in the transport spatial filter. To increase the isolation, we added polarizer 2, as shown in Fig. 3, and oriented the Pockels cell for zero retardation with no applied voltage. Then, back-reflected energy made two complete passes through the isolation unit to reach the front end, and the isolation improved to 1.5×10^{-5}. This reduced the back-reflected energy at the front end to that of the injected energy, a level for which the front end was adequately isolated. The transmission through the L-turn was 53%.

Figure 7 shows the output fluences (energy per unit area) for the L-turn and baseline architectures as functions of input energy. Output fluence was used for the comparison rather than output energy, because the beam size for the L-turn was slightly smaller, 32.5 vs 34 cm square, to avoid clipping on the turning mirrors. (The turning mirror mounts were designed to clear only one pass, as required for the baseline. In the Reverser configuration, the beam reflects three times off the turning mirrors at offset positions. Since the mounts were not big enough to clear the three offset positions, we reduced the beam size slightly.) The maximum output energies for the L-turn at 2.3 ns and the baseline at 3 ns were 11.0 and 12.5 kJ, respectively. Note that the L-turn input energy required for a given output was 10 times less than for the baseline, because of the two extra passes through the booster amplifier. Clearly, the L-turn architecture gives comparable energy performance to the Beamlet baseline.

Figure 8 shows output irradiance (power per area) relative to output fluence (energy per area) for Beamlet. The Beamlet baseline architecture was originally optimized to provide maximum performance at 3 ns, but tests were also conducted at other pulse lengths, as shown. Outputs were limited by potential optical damage due to self-focusing at pulse lengths below 3 ns, and by the damage threshold of the polarizer above 3 ns. The shaded area in Fig. 8 indicates the maximum expected output at varying pulse lengths. The 11-kJ L-turn shot is the maximum irradiance attempted on Beamlet to date.

Because the large Pockels cell was removed for the Reverser tests, the amount of glass in the beamline was less, lowering the potential for nonlinear growth of output modulations. However, the two additional beam passes through the booster amplifier and the two

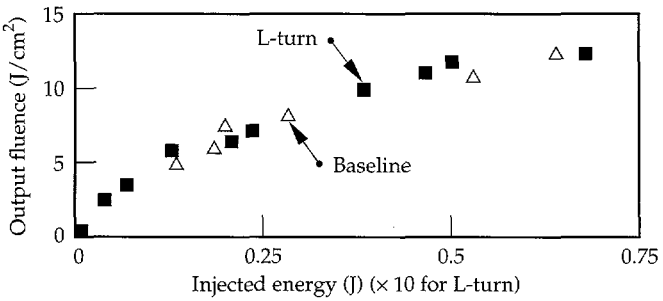

FIGURE 7. Injected energy vs output fluence for the Beamlet baseline and with the L-turn. The L-turn input energy required for a given output was 10 times less than for the baseline due to the two extra passes through the booster amplifier. (70-50-0495-1096pb01)

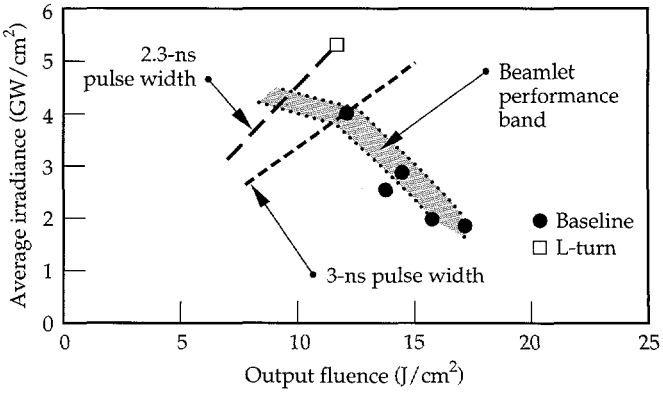

FIGURE 8. Irradiance vs fluence for Beamlet baseline and L-turn shots. (05-00-0494-2167pb01)

passes through the L-turn optics added aberrations. Consequently, the output modulation for the L-turn was slightly worse than for the baseline. For example, Fig. 9(a) shows the near-field image of the L-turn output at 4.3 GW/cm^2, which is equivalent to the highest irradiance baseline shot at 4.2 GW/cm^2. This image is a cumulative intensity distribution for the flat-top area of the output beam. There are 400 × 400 pixels, with each pixel corresponding to a beam area of 0.7 × 0.7 mm. Figure 9(b) shows horizontal and vertical lineouts. The peak-to-average fluence modulation in the image was 1.4:1. The comparable baseline modulation at this irradiance was 1.3:1.

Figure 10 shows near-field image data from L-turn shots at three values of peak irradiance. The number of pixels at each fluence (normalized to the maximum) is plotted vs that fluence (normalized to average fluence). There is virtually no difference between the modulation at 1.53 and 4.25 GW/cm^2. However, at 5.4 GW/cm^2, the modulation jumps from 1.4 to 1.5, implying the onset of nonlinear growth. To avoid risking optical damage, this regime of nonlinear growth is generally avoided, limiting the performance of the laser. This type of increase in modulation has also been observed in the baseline configuration.[3]

U-Turn Tests

In the U-turn configuration tests, the isolation provided by one pass through the polarizers and Pockels cell was 1 × 10^{-4} (see Fig. 4), which was barely acceptable for protection against back reflections. Note that the L-turn isolation was higher because the beam made two passes through the polarizer and Pockels cell. Conversely, the 70% U-turn transmission was better, because one pass through the isolation unit had less loss than the two passes with the L-turn.

Before the first U-turn tests, it was necessary to turn the L3 lens around so that the surface previously in vacuum was in air. Two damage spots on the vacuum side of L3 were created during tests before the L-turn experiments, and they increased to 6 and 8 mm at the lens surface during the L-turn shots. Since the vacuum side of the lens was in tension, these damage spots could have lead to crack propagation and lens failure, so the lens was turned around before the U-turn experiments began. This put the damage spots on the air

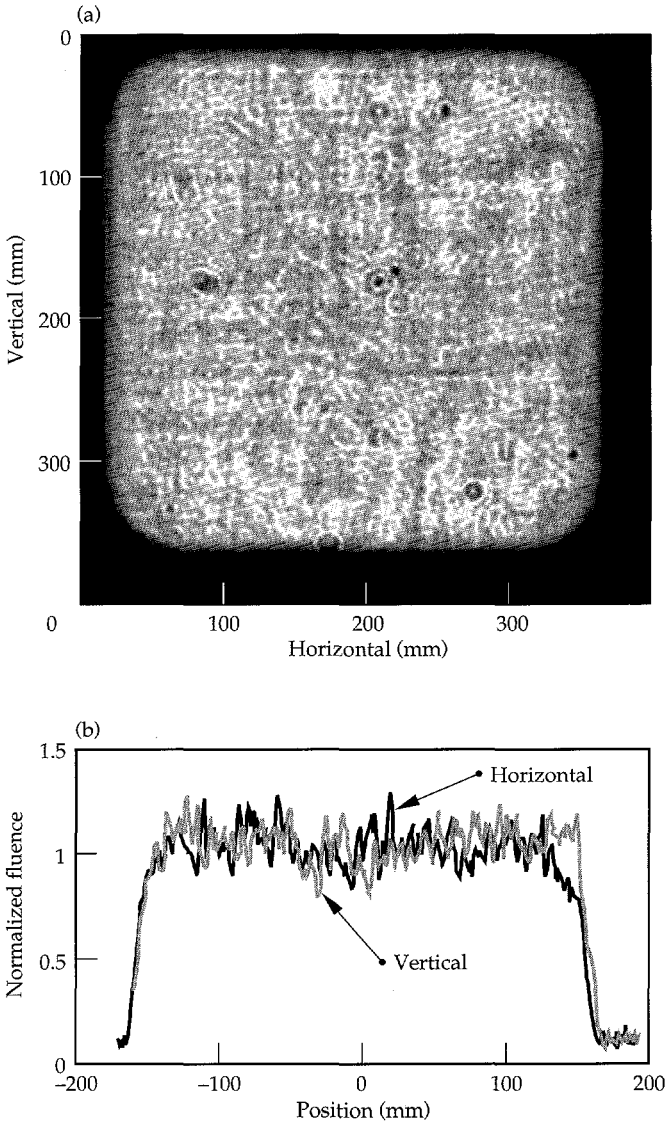

FIGURE 9. Near-field (a) image of the output beam with the L-turn at 4.3 GW/cm^2 and (b) horizontal and vertical lineouts through the image. (70-50-0595-1265pb01)

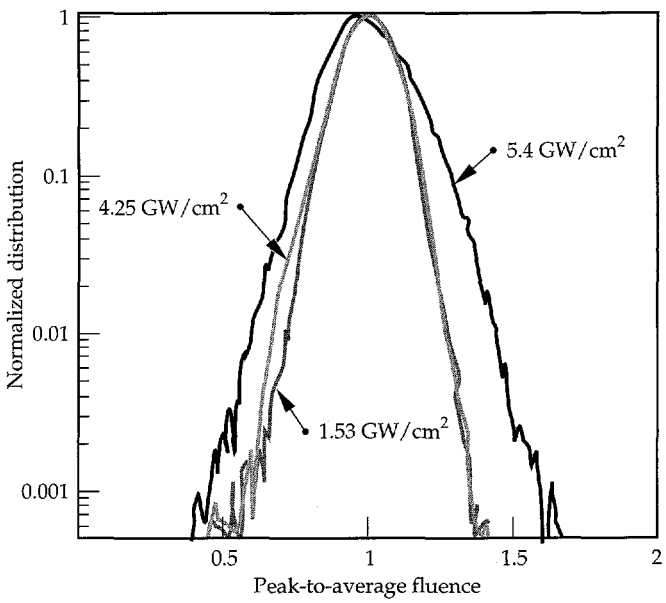

FIGURE 10. Near-field image data for output with the L-turn at three irradiances, showing nonlinear modulation growth at 5.3 GW/cm^2. (70-50-0595-1266pb01)

surface where they were in compression and not a threat to the lens integrity.

Attempting to duplicate the L-turn shots, the first U-turn shot delivered 780 J, but caused damage to several of the U-turn and front-end optics. In the front end, the injection mirror had a 1-mm portion of the coating removed, and small pits formed on the injection window and injection lens. In the U-turn, the pass 3 lens, both polarizers, and the Pockels cell had 1-mm damage, although none of the mirrors was damaged. In the Pockels cell, there were two damage tracks through the KD*P crystal.

The damaged components were replaced or repositioned, and low-energy shots allowed a detailed investigation of what caused the damage. Near-field images of the beam showed numerous pencil beams and ghost foci, but the most prominent was the one generated by L3's air surface. Reflectivity tests on the spatial filter lenses indicated that the antireflection coating (sol-gel) on that surface had deteriorated, from the typical value of about 0.1% to 3.2%. The measured reflectivities of the L3 vacuum surface and both L4 surfaces were normal. The cause of the coating deterioration is not known.

It became clear that turning the L3 lens around caused the U-turn to damage, whereas in L3's earlier orientation the L-turn was protected. This was because the deteriorated coating was on the vacuum-side during the L-turn tests. The vacuum side of the lens is concave with respect to pass 4, causing the reflection from that surface to focus in the air between the lens and booster amplifier. This focus causes the air to break down and absorb or deflect most of the energy in the reflection. Consequently, the unusually high energy of this reflection was greatly decreased by air breakdown, and the L-turn components were protected. However, when the lens was turned around at the start of U-turn tests, the defective coating went to the air surface of the lens, which is convex with respect to pass 4. The reflection from the convex surface did not focus, and consequently, there was no air breakdown to protect the U-turn optics.

We believe the optical damage was caused by parasitic pencil beams originating from the reflection off the air surface of L3. Figure 11 shows how the pass-4 output beam generates pencil beams from L3. (All beam passes through the lenses create reflections, but the final pass reflection is the most dangerous because it has the most energy.) Both reflections (one from each surface) pass through the booster amplifier and focus near the pinhole plane in the cavity spatial filter. Most of the light is blocked by the cavity pinhole plate, but some light passes through the pinholes forming three beams. (There are four pinholes, but the injection mirror blocks light from going through pinhole 1.) These beams are diffraction limited, and they remain small throughout the laser, from a couple of millimeters to about 1 cm, thus, the name "pencil beams." Because these pencil beams propagate parallel to the shot beam, they pass through the amplifiers and increase in fluence.

The pencil beam that caused damage in the U-turn was formed by cavity pinhole 4. That pencil beam continued backwards through the system to pass through the main amplifier twice, through cavity pinhole 3, through the booster amplifier, through pinhole 3 in the transport spatial filter, and into the U-turn. With a calculated fluence of around 270 J/cm^2, this pencil beam was more than sufficient to damage optics. Five factors contributed to this pencil beam's high fluence. (1) It had 15 to 30 times more energy than typical, because the coating reflected 3.2% rather than the typical 0.1 to 0.2%. (2) It propagated through both amplifiers twice, experiencing a gain of about 1200× before entering the Reverser. (3) It was down collimated into the Reverser (in this case 32.5- to 4-cm^2), which magnified the fluence of the pencil beam by a factor of 66. (4) It focused near the U-turn Pockels cell, which further increased its fluence by about 2×. (5) It was generated during a low-output-energy shot, 780 J, that was close to the most dangerous output with respect to back reflections. (As laser output energy is increased, gain saturation reduces the amount of energy left to amplify back reflections. Therefore, the highest-energy back reflections do not occur at maximum output but at about 2-kJ output.) Note that factors 1, 2, and 5 are system factors, and only factors 3 and 4 relate to the Reverser.

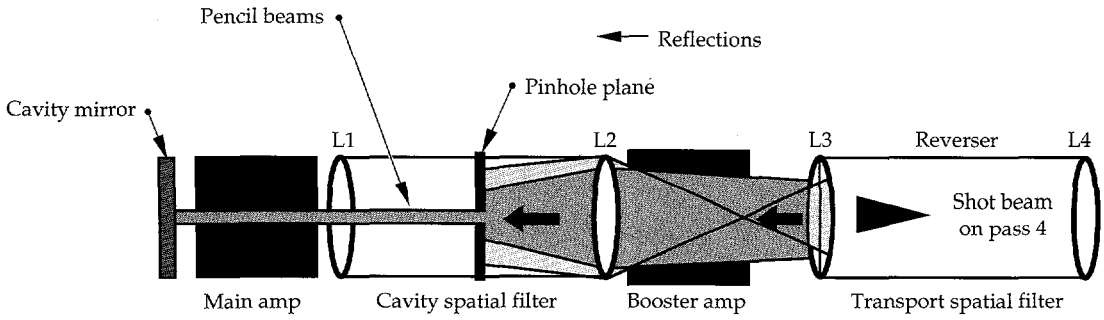

FIGURE 11. Reflections from the input lens to the transport spatial filter lens, L3, are formed into pencil beams by the pinholes in the cavity spatial filter. (70-50-0495-1004pb01)

Some energy from this same pencil beam passed through the U-turn as it damaged the Pockels cell and continued in reverse direction along passes 2 and 1. This energy was amplified by another pass through the booster amplifier and two more passes through the main amplifier, resulting in enough fluence to damage the injection mirror. The source of the damage to the injection lens and window was traced to a different pencil beam from the same L3 air surface. This pencil beam was formed by pinhole 2 in the cavity spatial filter, passed twice through the main amplifier (backwards along passes 2 and 1), and focused enough to damage the injection window and injection lens. It is important to emphasize that this damage had nothing to do with the U-turn and would have occurred in the baseline configuration if L3's air surface reflectivity had been 3%.

Two attempts were made to eliminate the L3 pencil beams—tilting L3 and inserting a beam block on the cavity mirror. Tilting L3 far enough eliminates the pencil beams by preventing its reflections from illuminating the pinholes in the cavity spatial filter. However, this required a tilt of more than 2°, which caused unacceptable output aberrations. The goal of the second scheme was to absorb the pencil beams with a 1-cm disk of absorbing glass fixed on the cavity mirror. The beams were blocked, but diffraction around the edges of the glass caused an unacceptable 20% increase in output beam modulation.

A more ambitious solution would have been to reduce the energy of the pencil beams at the Reverser by taking the Pockels cell and polarizer out of the Reverser and locating them at full-aperture near the cavity mirror, as shown in Fig. 12. In this configuration, the Pockels cell would cause half-wave retardation with applied voltage and zero retardation with no applied voltage. Unlike the NIF baseline, this Reverser architecture uses the Pockels cell and polarizer only for isolation and not to switch the beam from the cavity. Consequently, this isolation unit can be located anywhere in the beamline. By being located at the start of pass 4 (near the cavity mirror), the Pockels cell and polarizer reject the back reflections at full aperture and after only one pass through the amplifiers. This lowers the fluence of the pencil beams entering the Reverser by a factor of more than 10,000. This change would also be effective in eliminating other types of back reflections such as from pinholes or targets. It does, however, require a full-aperture Pockels cell and polarizer, which would eliminate some of the initial appeal for the Reverser concept, but the other benefits remain. This change is of interest for future Beamlet tests, but moving the large Pockels cell and polarizer would have taken longer than the remaining time available for these Reverser experiments. As a result, we did not risk damage by taking any more high energy shots.

Summary

These experiments demonstrated the basic viability of the Reverser concept. They showed that the concept of turning pass 2 into pass 3 with small mirrors and lenses in the transport spatial filter is valid. The Reverser output compares well with the results for the baseline architecture, and it achieved the highest irradiance output to date on Beamlet of 5.3 GW/cm^2. We encountered no problems with ASE or degradation to optics due to pinhole blowoff or vacuum conditions. Also, routine alignment of both L- and U-turn architectures was straightforward.

These experiments also exposed a serious weakness. They identified the inadequacy of a small-aperture isolation unit to protect the laser against back reflections. Although the damage to the front end from the L3 pencil beams would have occurred even with the baseline architecture, the severity of the damage to the Reverser optics resulted from two features of this Reverser design. (1) Back reflections make two complete passes through the amplifiers before entering the Reverser. (2) Back reflections are down collimated into the Reverser, magnifying their fluence by a large factor.

A change to the Reverser design would provide much greater tolerance to back reflections. Moving the isolation unit so that it attenuates the back reflections sooner along their backwards path through the laser substantially reduces their maximum fluence. With the Reverser, the Pockels cell and polarizer are not used to

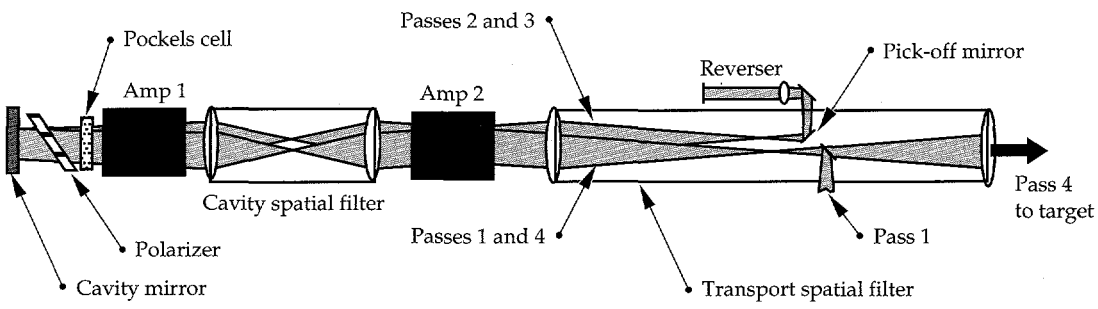

FIGURE 12. Locating a full-aperture Pockels cell near the cavity mirror would provide better isolation. (70-50-0595-1187pb01)

switch the beam from the cavity, so they can be located anywhere. One attractive location is near the start of pass 4, where the fluence of the out-going pulse is lower than in its baseline position, and where it attenuates reflections from final optics after only one backwards pass. This location for the isolation unit provides significantly better tolerance to back reflections. Therefore, we are considering a large Pockels cell and polarizer at this location for future Reverser tests on Beamlet.

Acknowledgments

The authors are grateful for the insight and direction provided by Howard Powell* and Michel Andre,† and for significant contributions from the technicians—Mireille Guenet,† Alain Pierre,† Cal Robb,* Dave Roberts,* Raymond Rossage,† and Ron Wing.* We also thank Mark Rhodes for managing the offline Pockels cell test.

Notes and References

1. *Avant Projet Sommaire*, Laser Megajoules, Direction Des Applications Militaires (CEA), 14 March, 1995.
2. J. Paisner, *National Ignition Facility Conceptual Design Report*, Lawrence Livermore National Laboratory, Livermore, CA, UCRL-PROP-117093 (May 1994).
3. B. M. Van Wonterghem, et al, *ICF Quarterly Report* 5(1), 1–17, Lawrence Livermore National Laboratory, Livermore, CA, UCRL-LR-105821-95-1 (1994).

*Lawrence Livermore National Laboratory, National Ignition Facility Project, Livermore, California
†Centre d'Études de Limeil–Valenton, Laser Megajoules, Valenton, France

Fabrication and Testing of Gas-Filled Targets for Large-Scale Plasma Experiments on Nova

G. F. Stone *M. R. Spragge*

*C. J. Rivers** *R. J. Wallace*

Introduction

The proposed next-generation ICF facility, the National Ignition Facility (NIF), is designed to produce energy gain from x-ray heated "indirect-drive" fuel capsules. For indirect-drive targets, laser light heats the inside of the Au hohlraum wall and produces x rays which in turn heat and implode the capsule to produce fusion conditions in the fuel.[1] Unlike Nova targets, in NIF-scale targets laser light will propagate through several millimeters of gas, producing a plasma, before impinging upon the Au hohlraum wall. The purpose of the gas-produced plasma is to provide sufficient pressure to keep the radiating Au surface from expanding excessively into the hohlraum cavity. Excessive expansion of the Au wall interacts with the laser pulse and degrades the drive symmetry of the capsule implosion.

We have begun an experimental campaign on the Nova laser to study the effect of hohlraum gas on both laser–plasma interaction and implosion symmetry.[1,2] In our current NIF target design, the calculated plasma electron temperature is $T_e \approx 3$ keV and the electron density is $n_e \approx 10^{21}$ cm^{-3}. To simulate NIF conditions in a Nova target requires a target with a gas confined in an ~0.01 cm^3 vol. at ≈1 atm.[2] These gas-filled targets are calculated to produce the required plasma conditions based on an initial gas fill of 1 atm neopentane C_5H_{12}. To measure the T_e of the plasma by spectroscopic line ratios, Ar and Cl bearing gases are added to the mixtures. Metal coated carbon fibers and plastic foils are added as an additional spectroscopic temperature diagnostic. Changes in n_e are made by varying the density of the main and spectroscopic seed gases. To aid in diagnosing the plasma, additional features such as diagnostic shields, x-ray backlighting patches, and imaging slits are added to the target design as experimental requirements dictated.

To study these plasma conditions, targets are being fabricated and shot on the Nova laser using open- and closed-geometric designs. *Open geometry* refers to the gas-bag style targets that have a fairly unlimited or open diagnostic view of the plasma and are nearly spherical, plastic gas cells built on a metal or plastic support ring.[3,4] *Closed geometry* refers to indirect-drive style targets with a radiation enclosure that confines the plasma within a cylindrical Au hohlraum.[1,2] Views of the plasma in a closed-geometry target are through diagnostic holes or slots cut into the wall of the Au hohlraum and covered with gas-tight patches. This article describes the major steps and processes necessary to fabricate, test, and deliver these gas targets for shots on the Nova laser at LLNL.

Target Design

To fabricate these gas-filled Nova targets to simulate the NIF-like conditions, we integrate a gas manifold with a pressure transducer, the target and gas fill lines, gas mixing, testing and filling systems, and the Nova target positioner. To ensure a proper fit and interference with existing target handling hardware, we analyze scaled computer-aided design (CAD) drawings of the target and associated components.

Figure 1 is a CAD drawing of a closed-geometry target. CAD drawings are essential for the closed-geometry targets to allow the precise placement of shields, fibers, foils, and other target components relative to diagnostics on the Nova target chamber. In three dimensions, alignment tolerances for the closed-geometry targets are ±25 μm and ≤ 2°.

*W. J. Schafer, Livermore, California

Target Material Selection and Fabrication

To aid in target and feature alignment at the Nova target chamber, both types of targets need an optically transparent, thin, low-Z ductile material for the gas/vacuum barrier. The density of the gas is chosen so that when completely ionized and heated to 3 keV, the electron pressure will be sufficient to significantly slow the hohlraum wall motion in a NIF target. The density cannot be too large, however, or the plasma n_e will exceed the critical value for 0.25 μm light propagation, resulting in complete reflection of the incident light. The density of 3 mg/cm^3 of neopentane results in a 0.1 critical density (10^{21} electrons/cm^3), which is calculated to hold off wall motion and to allow light propagation to the wall for x-ray conversion. Ideally, actual NIF hohlraums, or experiments to simulate NIF hohlraum conditions for testing the laser–plasma interaction physics, would have no solid-material gas barriers. Early in a laser shot, these barriers, or windows, are heated to a plasma state and rapidly expand, severely perturbing the interior gas. The windows must be as thin as possible to reduce this perturbation. However, they must be thick enough to withstand the 1-atm pressure difference. In Table 1, we compare several window materials. The thickness required is calculated from the simple hoop-stress formula, $\sigma = Pr/2t$, using appropriate yield stress σ for each material. P is the pressure, r the radius of curvature of the window, which is assumed to be 1 mm, and t is its thickness. The equivalent gas thickness is calculated as the distance the initial window will expand to reach 10^{21} electrons/cm^3, based on the initial n_e shown in the second column of Table 1. This equivalent distance must be minimized. Based on these considerations, we chose polyimides as the window material, of which Kapton is a well-known commercial example. Polyimide is a family of plastic CH polymers used in integrated circuit fabrication. Although the chemical formula for the specific material used is proprietary, it is nominally $C_{22}H_{10}N_2O_4$ with a density of 1.4–1.5 g/cm^3.

The open-geometry targets need a nearly spherical volume of gas and must hold the pressure for 1–3 hr.

TABLE 1. Comparison of window materials.

Material	Electron density (moles/cm^3)	Thickness required	Equivalent gas thickness (μm)
Si_3N_4	1.72	0.2 μm	206
Lexan	0.74	0.8 μm	355
Kapton	0.72	0.3 μm	130
Parylene	0.56	0.8 μm	268

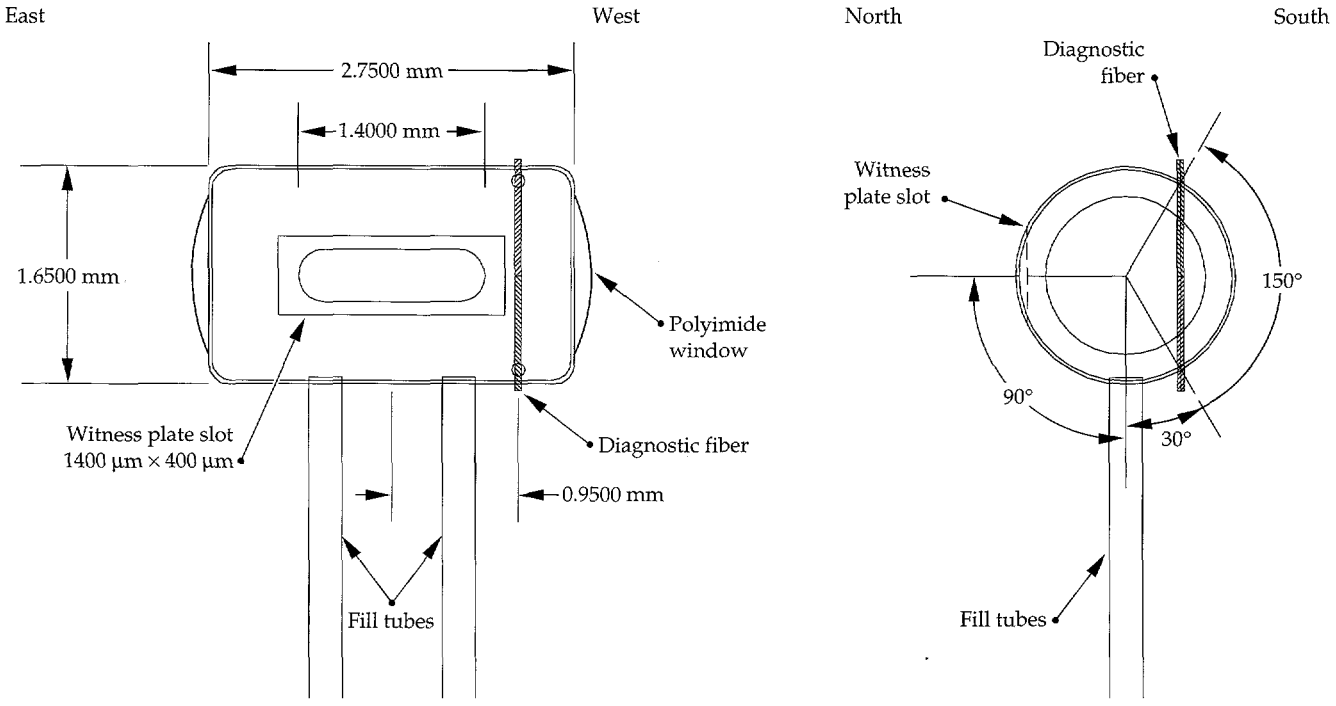

FIGURE 1. A CAD drawing of a closed-geometry target. (10-00-0795-1777pb02)

The target skin must endure >1 atm pressure over an area of ~20 mm^2, surrounded by a vacuum of $<10^{-5}$ Torr and be ductile enough to form a nearly spherical bubble from two flat sheets. The gas-bag targets are fabricated using brass, Lucite, and Al support washers (~400 μm wide). Fill tube holes (270 μm diam) are drilled through the side walls of the washers, which are microbead blasted to increase the surface area and to improve the polyimide/epoxy adhesion. A thin sheet of polyimide (~0.4 μm) is glued across both sides of a thin washer and two small-diameter stainless-steel fill tubes (~250 μm) are passed through the side wall into the inner diameter of the washer and glued in place. Pressurizing the fill lines (>20 psia) causes the films to distend, forming a nearly spherical bubble. Figure 2 is a photograph of a gas-bag target (with a 2.75-mm washer and a 2.4–2.5-mm-wide bag).

Nova's Au-hohlraum design serves as the model for the closed-geometry targets. Holes or slots are milled in the side of the target mandrel to view the target's interior (Fig. 3). Fill tube holes are also drilled into the side of the hohlraum mandrel to allow gas filling. After the Au-plated Cu mandrels are machined and inspected for accuracy, the outer surface is microbead blasted to produce a roughened finish. The mandrels are then leached in a nitric-acid solution ($HNO_3 \approx 0.5$ N solution) at 60°C and etched (1–3 hr). The laser entrance holes (LEHs) and any diagnostic windows in the hohlraum are then covered with a thin (0.2–0.7-μm) sheet of polyimide.

The requirement to hold gas behind thin CH windows complicates target fabrication. The same basic assembly procedures used for non-gas targets are employed on the gas-cell target series. Target fabrication is generally performed using an optical microscope, with micromanipulators holding target parts in place with vacuum chucks and fast curing or UV/visible cured cements to affix target components.

For the open-geometry targets, the final assembly consists of mounting the target on a Nova magnetic target base at the desired orientation. Shields and imaging slits are attached to some of the open-geometry targets. The closed-geometry targets have additional alignment restrictions placed on them by alignment fibers and flags, backlighter patches, diagnostic holes, and slots. The target components are required to be placed within ±25 μm and ≤2°, relative to the Nova target base.

Gas Specification

The gas mixture and pressure are specified to mock up the experimental conditions for the point design of the NIF targets, using neopentane C_5H_{12} as the main gas in this series. To aid in measuring the ion temperature T_{ion} spectroscopic seed gases Ar and Freon–13 $CClF_3$ are added in concentrations from 0.25–10 at.%. The nominal standard target gas for the early experiments was 98% C_5H_{12} + 1% Ar + 1% $CClF_3$ at ~1-atm pressure. To achieve lower target densities, CO_2, C_3H_8, and CH_4 are used as the base gases. J. Colvin of Los Alamos National Laboratory (LANL) suggested obtaining a deuterated gas C_5D_{12} to potentially use the fusion neutron yield from the D as a diagnostic for the experiment.

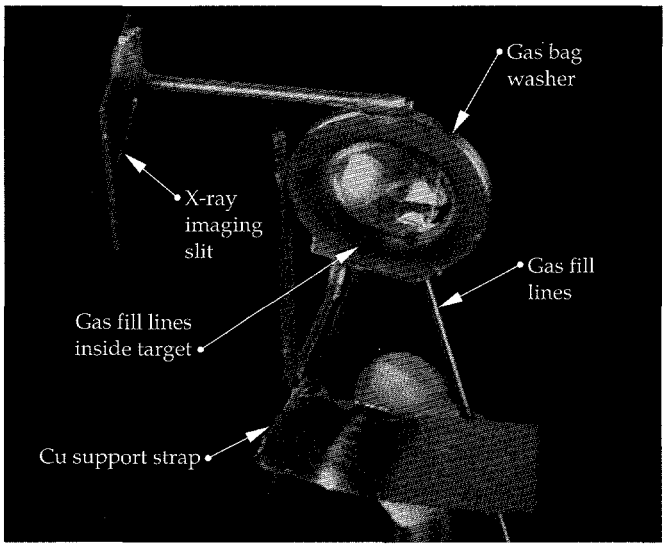

FIGURE 2. Photograph of a gas-bag target with an x-ray imaging slit. (10-00-0795-1778pb01)

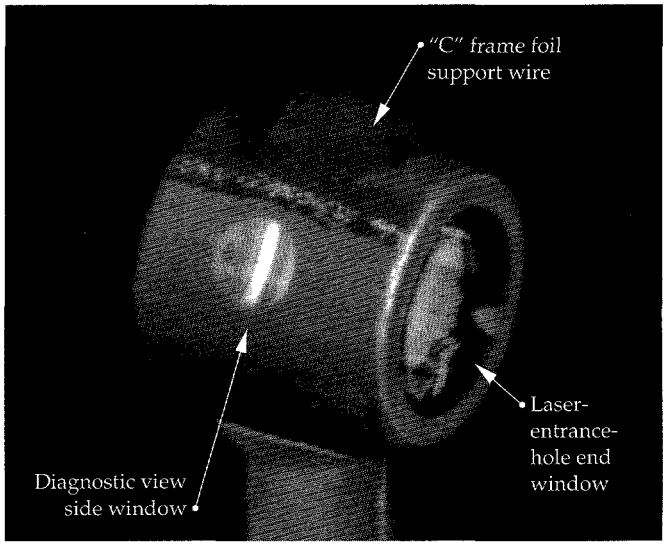

FIGURE 3. Photograph of a closed-geometry target showing the diagnostic view window. (10-00-0795-1780pb01)

A gas mixing manifold permits mixing of various gases into a sample bottle for later use in filling the targets (Fig. 4). As the main base gas C_5H_{12} condenses to a liquid at ~1300 Torr, an upper limit on the system is set at 1000 Torr. The gas mixture is specified in atomic percentage for the individual components. A diaphragm-style pressure manometer, insensitive to gas densities, monitors pressure in the gas mixing manifold and sample bottle. The sample bottle is connected to the manifold and the system is evacuated. The sample bottle valve is closed and the individual gases are purged three to four times to limit contamination of the final gas mixture. Exceptions to this purging process are C_5H_{12} and deuterated neopentane C_5D_{12}, due to their limited availability. The C_5H_{12} and C_5D_{12} bottles are directly connected to the main manifold with a small prechamber and a valve, which permits a small positive gas pressure to be maintained in the gas regulators and fill lines.

The gas with the lowest percentage in the mixture is first introduced into the manifold, and the pressure is allowed to increase until it reaches the desired partial pressure. The other gases are then added by partial pressure until the total pressure in the sample bottle reaches 1000 Torr.

To interpret the target results, it is necessary to know the ratios of the gases to <0.1 at.%. The gas mixtures are analyzed using a mass spectrometer with a resolution down to Z = 1 (H) and a discrimination down to 0.01 at.%. To improve the accuracy of the analysis, pure samples of each gas are drawn off into small (<75 cm^3) sample cylinders to be used as "reference" standards for all the starting gases and when primary gas source bottles are changed.

Target Manifold Design

A major restriction for the gas target fabrication is the limited space within the Nova target inserter (a cylindrical space 5 in. diam 16 in. long with the center 2 in. occupied by the target pylon); this space limitation drove our hardware choices. Figure 5 is a CAD drawing of a manifold fabricated out of brass to support the transducer, gas flow valves, and target fill lines. The valves were not designed for vacuum sealing but rather for liquid/gas flow metering, and after 6–10 shots, it is necessary to change the valves because they become one of the main sources of leaks on assembled targets.

A strain-gage-style, absolute-pressure transducer monitors manifold gas pressure. Prior to using this type of transducer, we field tested the unit to ensure its ability to operate not only at atmosphere on the bench but also in vacuum in the Nova target chamber. When the target is shot on Nova, a plasma is produced that has a designed T_e of 3 keV; to electrically protect the transducers, we added a Zener diode to each connector line on the transducer cable to strip off voltage spikes >50 V. The initial test transducer was calibrated before and after the first laser shot to check for any anomalies. The post-shot transducer voltage values were within ±0.001 V of the preshot values, verifying their robustness.

The early gas-cell targets used a flow-through method to fill the targets with gas, and two valves and gas lines were used on the manifold. One port on the target manifold was connected to the gas sample bottle. The gas flowed until it was estimated that all of the air in the target assembly had been displaced with the sample gas. The current system of evacuated backfill of targets retains the two valves to safeguard against one of the

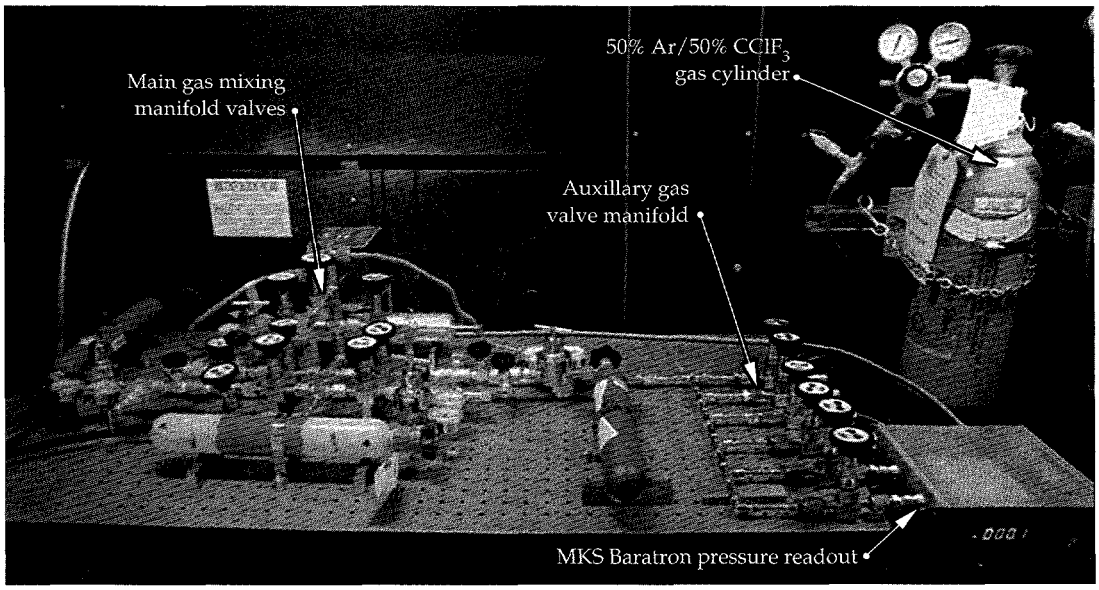

FIGURE 4. Photograph of a gas mixing system on an optical bread board table. (10-00-0795-1779pb01)

fill lines being blocked.[5] A pair of 1-mm-o.d. stainless-steel fill lines is attached to the top of the manifold. Plastic tubing is used to connect the manifold to the target. The target has stainless-steel fill lines (~250 μm o.d.) with smaller i.d. plastic tubing used to inter-connect the target to the plastic tubing on the manifold.

A separate pressure testing system, fabricated by LANL,[5] is used to test the target manifold. The test procedure is divided into three steps: (1) The target manifold is tested as a standalone unit. (2) The target body is tested and certified gas tight. (3) The assembled target attached to the manifold is tested as an integrated system before filling.

Target Filling Hardware and Procedures

The first targets were filled by flowing gas through the target, a method that used a large quantity of gas to ensure that only the sample gas remained inside the target. The new method, using an evacuation/backfill chamber, significantly reduces the total gas used per target.[5]

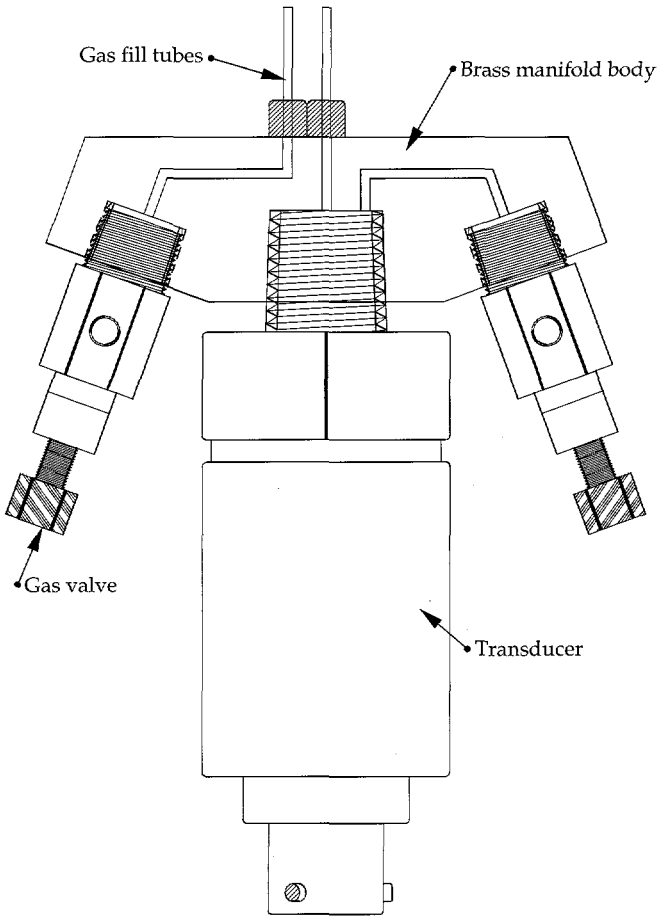

FIGURE 5. A CAD drawing of a target manifold with a transducer, valves, and gas fill lines. (10-00-0795-1781pb01)

The target filling manifold, with its calibrated pressure transducer attached, allows monitoring of internal target pressure at shot time. From this calibrated transducer, a pair of points for pressure vs voltage for vacuum and atmosphere are measured and the resulting values allow the final target pressure at shot time to be calculated. A mechanical manometer is also placed in-line with the fill chamber to monitor the external target pressure in the 1–200-Torr range. A small valving manifold is attached to the evacuation/backfill chamber to control the independent pumping of the target's interior and exterior and filling the target. Figure 6 is a photograph of this gas filling system.

The target and the gas fill line are connected to the target manifold. A purge line (~0.25–0.5 psig) is attached to the target manifold to verify that the fill lines are not blocked. The assembly is then placed in the evacuation/backfill chamber and the air around the target is slowly pumped out until the chamber pressure reaches ~5 mm Hg, then the interior of the target is slowly pumped out. Due to the low conductance of the fill tubes (100–250 μm), the pumping continues for ~15 min to fully remove the air from the target interior.

Once the base pressure inside the target is reached, the valves to the gas sample bottle are opened and the pressure inside the target is monitored. After the pressure inside the target has increased to the desired value, the chamber is slowly vented to atmosphere. The target manifold valves are closed and the transducer reading is observed for drift—if the target pressure is stable, the fill line is disconnected and the target is ready for delivery to Nova.

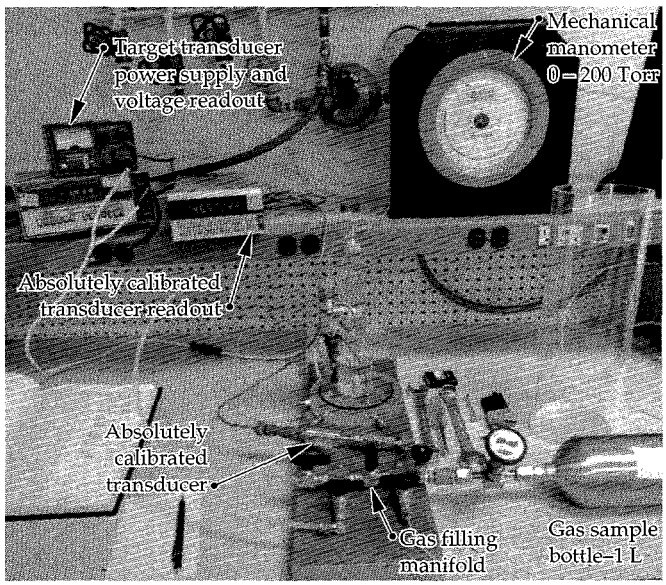

FIGURE 6. Photograph of the evacuation/backfill chamber and gas filling system. (10-00-0795-1816pb02)

Summary

Targets to test the point design for the proposed NIF were developed and fabricated for use on the Nova laser at LLNL. Sub-micrometer-thick polyimide windows capable of holding >1 atm were attached to closed-geometry (Nova-hohlraum-style) and open-geometry (nearly spherical gas-bag) targets. Together with the Target Fabrication group at LANL, we fabricated a system to pressure-test targets and to verify gas integrity, prior to delivery to Nova. We also developed a gas-mixing system that permits mixture ratios as low as 0.25 at.% for individual gases and a system to measure gas pressure inside the target to integrate into the Nova target positioner. In support of the ICF programs at LANL and LLNL, more than 450 gas-cell targets have been successfully fielded on Nova.

Notes and References

1. L. Powers, et al., *Phys. Rev. Lett.* **74**, 2957 (1995).
2. J. Lindl, "Development of the Indirect-Drive Approach to Inertial Confinement Fusion and the Target Physics Basis for Ignition and Gain," Lawrence Livermore National Laboratory, Livermore, CA, UCRL-JC-119015 (1995).
3. D. H. Kalantar, et al, *ICF Quarterly Report* **4**(4), 145–151, Lawrence Livermore National Laboratory, Livermore, CA, UCRL-LR-105821-94-4 (1994).
4. B. J. MacGowan, C. A. Back, R. L. Berger, et al, "The Study of Parametric Instabilities in NIF-Scale Plasmas on Nova," Lawrence Livermore National Laboratory, Livermore, CA, UCRL-JC-118524 (1995); prepared for the Proceedings of the International Atomic Energy Agency *15th International Conference on Plasma Physics and Controlled Nuclear Fusion Research*, Seville, Spain, Sept. 26–Oct. 1, 1995.
5. M. Salazar and the LANL Target Fabrication group are responsible for the original design and fabrication of the evacuation test chamber system and the evacuation backfill method. Their staff is also responsible for fabricating the additional gas handling hardware used for target testing.

Optimization of X-Ray Sources from a High-Average-Power Nd:Glass Laser-Produced Plasma for Proximity Lithography

P. Celliers *S. Mrowka* *D. Matthews*

L. B. Da Silva *M. Norton* *J. A. Abate**

C. B. Dane *L. Hackel* *J. Maldonado*†

Introduction

The concept of a laser-based proximity lithography system for electronic microcircuit production has advanced to the point where a detailed design of a prototype system capable of exposing wafers at 40 wafer levels per hr is technically feasible with high-average-power laser technology. In proximity x-ray lithography, a photoresist composed of polymethylmethacrylate (PMMA) or similar material is exposed to x rays transmitted through a mask placed near the photoresist, a procedure which is similar to making a photographic contact print. The mask contains a pattern of opaque metal features, with line widths as small as 0.12 μm, placed on a thin (1-μm thick) Si membrane. During the exposure, the shadow of the mask projected onto the resist produces in the physical and chemical properties of the resist a pattern of variation with the same size and shape as the features contained in the metal mask. This pattern can be further processed to produce microscopic structures in the Si substrate.

The main application envisioned for this technology is the production of electronic microcircuits with spatial features significantly smaller than currently achievable with conventional optical lithographic techniques (0.12 μm vs 0.25 μm). This article describes work on optimizing a laser-produced plasma x-ray source intended for microcircuit production by proximity lithography.

Background

To obtain the best transmission through the Si substrate, followed by absorption in the PMMA, the illumination source should occupy a band of x-ray wavelengths somewhere above the Si K-edge (6.74 Å) but long enough that the x rays are efficiently absorbed in the PMMA resist layer (possibly up to 15 Å). The x-ray wavelength is short enough that blurring due to x-ray diffraction from edges in the pattern will not be significant. Current system designs for proximity lithography require a source with a median emission wavelength in the range of 10–14 Å and a 20% bandwidth. The mask can be illuminated with a collimated source of x rays, such as from a synchrotron tuned to operate at the desired wavelengths. In fact, the basic principles of proximity lithography have already been demonstrated using synchrotron sources.[1,2] However, synchrotron facilities are inherently expensive and therefore not amenable for most circuit manufacturers to acquire and operate.

Laser-produced plasmas have been recognized as a promising alternative to synchrotrons for a number of years. The physical specifications that the plasma source must meet can be summarized as follows: the source must deliver approximately 15 mJ/cm^2 of x-ray fluence to the resist with a uniformity of 1% over a 3×3 cm^2 area within an exposure interval of approximately 1.3 s; the x-ray spectrum must occupy a 20% bandwidth centered on a wavelength ~12 Å. These requirements can be met using a 1-kW laser assuming about $10\%/(2\pi$ sr) conversion of laser energy into the desired x-ray band; the mask and resist are assumed to be about 50 cm from the source point to satisfy the uniformity requirements. Variations on these figures may occur depending on a number of design options, but it is clear that in any system a substantial portion of the costs are directly

* AT&T Bell Laboratories, Murray Hill, New Jersey

† IBM Microelectronics, Hopewell Junction, New York

driven by the average power level needed from the laser, which in turn hinges on achieving high x-ray yields.

X-ray yields from laser-produced plasmas have been investigated in great detail for nearly two decades and have been examined over a wide variety of laser parameters (wavelength, pulse duration, focused intensity) as well as target material and x-ray emission wavelengths.[3–12] Several studies have focused specifically on lithography applications to match target materials with realistic laser parameters to produce the required x-ray spectrum (keV x rays) at an acceptable yield.[13–19] X rays from laser-produced plasmas in the 1-keV energy range required for proximity lithography are produced most efficiently with focused laser intensities around 10^{13} W/cm^2 and from targets with atomic numbers in the range Z = 26–30 (Ne-like ions, L-shell emission) or Z = 53–56 (Ni-like ions, M-shell emission). As a general finding, x-ray yields are known to improve substantially with decreasing laser wavelength.[4,5,7]

X-ray yields from laser-produced plasmas also depend on the pulse duration, which determines the characteristic plasma volume achieved during the pulse. High conversion efficiency has been usually observed with moderate-duration pulses (0.5–10 ns).[11,16] However, it can also be achieved with shorter pulses (<100 ps) in combination with a weak prepulse to generate a long-scale-length plasma.[12,20] It is not clear from the findings of previous studies whether high conversion efficiency can be achieved from pulses longer than 10 ns. Experiments with 8-ns Nd:glass laser pulses indicate that efficiencies around 8%/(2π sr) could be achieved.[3] However, experiments with 30-ns KrF pulses focused to more than 10^{14} W/cm^2 failed to achieve yields comparable to measurements with shorter pulses at the same wavelength.[17] Chaker et al.[19] suggest a practical limit on the pulse duration of less than about 5 ns, but this conclusion is tentative in the absence of experimental data. The requirements of high average power with high focused intensities and moderate pulse duration are potentially in conflict with the pulse parameters of current high-average-power laser technology, which operate more reliably with rather long pulse durations in the range of 10–15 ns for Nd:glass technology and 25–30 ns for excimer lasers.

One potential laser driver for proximity lithography is a high-average-power Nd:glass slab design operating with high pulse energy and moderate repetition rate. Currently, the most advanced realization of this technology is available at Lawrence Livermore National Laboratory (LLNL)[21] and consists of a flash-lamp-pumped system capable of producing near-diffraction-limited pulses with approximately 13-ns full-width at half maximum (FWHM) duration at energies of ~20 J at a rate of 6 Hz to produce an average power of 120 W. The design is scalable to higher average power by increasing the pulse energy and/or repetition rate; we envision average powers approaching 2 kW. An important characteristic of this high-average-power capability is the use of phase conjugate wavefront correction[22] to ensure a uniform intensity and a near ideal phase front in the final pass of the slab amplifier, which is necessary to ensure reliable operation. This technology operates most effectively with a rather long pulse duration (12–14 ns), which raises the issue of whether the x-ray yields produced with this laser can approach the maximum yields observed with shorter pulses. We examined this issue experimentally in the work described in this article.

Experiment

We measured and optimized the x-ray conversion efficiency from several L-shell emitters (Fe, Cu, Zn, brass, stainless steel) and one M-shell emitter (Xe). The studies with Xe examined the solid form using a cryogenic target. In addition to producing high x-ray yields at the desired wavelengths, Xe targets offer the potential to design a source with considerably reduced debris generation. We investigated all targets at two operating wavelengths of the laser: the fundamental wavelength, 1.053 μm, and the second harmonic, 0.527 μm.

Figure 1 shows the layout for the experiments with solid planar targets. This section describes the five main parts identified by Fig. 1: the laser beam, the solid targets, the charge-coupled device (CCD) camera and spectrometer system, the filtered photoconductive diamond (PCD) detectors, and the pinhole camera.

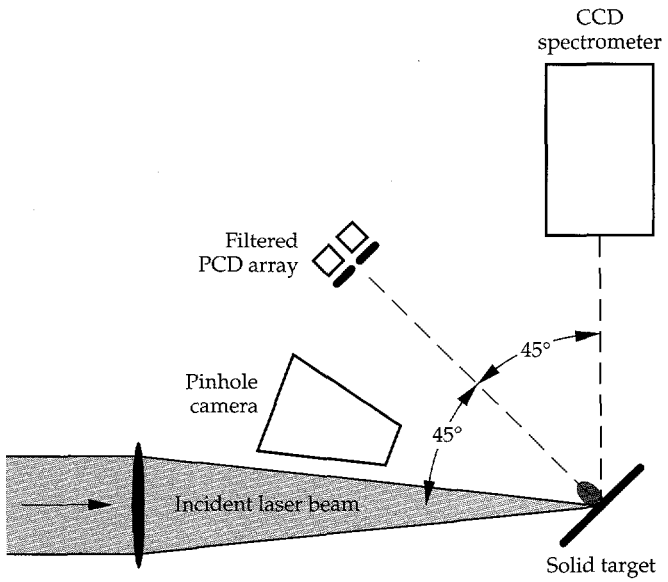

FIGURE 1. Experimental arrangement employed for solid target x-ray yield measurements. (10-06-0595-1100pb01)

Laser Parameters

A 330-mm lens focused the laser into the center of the experimental chamber onto a planar target oriented at 45° to the laser axis. We monitored the laser energy with a fast pyroelectric detector and cross-calibrated it with a calorimetric energy meter. Pulse energy varied from ~1–20 J at 1.053 μm and ~0.5–12 J at 0.527 μm. The beam delivered to the target chamber was square in cross-section, measuring 25 mm per side. We used a 330-mm focal-length lens to produce an $f/13$ focus. We adjusted the beam focus by translating the lens on a translation stage. In a separate test of the beam quality, we projected a series of far-field beam images with 0.527-μm light onto a CCD camera using a well corrected microscope objective. We found that, at best focus, 80% of the beam energy was contained within a diameter of 27 μm, equivalent to about 1.5× diffraction limit. The maximum focused intensities achieved with this beam quality are 7×10^{13} W/cm^2 for 1.053-μm light and 2×10^{14} W/cm^2 for 0.527-μm light. These peak intensities meet or exceed the intensities needed to obtain good x-ray yields in the kilovolt range.

Solid Targets

The target mount consisted of an x–y–z translation stage with an aluminum mounting frame for attaching the target. Motion in a plane parallel to the target surface (x–y) allowed us to position a fresh surface of the target in the beam for each shot while maintaining the same axial position relative to the laser focus. All of the solid targets could be mounted (as tapes or thin plates) directly onto the mounting frame. For most of these materials, the target thickness was much larger than typical ablation depths. In the particular case of Fe, however, the target consisted of a thin layer of Fe powder (3–5 μm) bonded to a mylar tape substrate. This "mass-limited" target is designed to provide enough material to produce x rays while limiting debris production.

In the particular case of solid Xe, the target apparatus consisted of a 1-mm-thick Cu plate thermally connected with a 2-in-long Cu braid to a cold finger and cooled to approximately 20 K. By condensing Xe gas onto the cryogenic surface, we produced a thin (~100 μm), solid Xe layer on the Cu substrate. Although the melting point of Xe (at atmospheric pressure) is around 160 K, a temperature of 20 K was required in vacuum to maintain a low enough Xe vapor pressure to produce a stable condensed layer on the Cu substrate and to minimize reabsorption of the Xe emission by residual cold Xe gas in the chamber.

Curved Crystal Spectrograph

To determine x-ray yields, we needed accurate measurements of the x-ray spectrum produced by each source. The spectra varied not only with target material, but also with the laser parameters (wavelength, pulse energy, and focus). A curved potassium acid pthalate (KAP) crystal spectrograph recorded x-ray spectra 90° relative to the laser axis and 45° to the target normal, using a high-resolution CCD camera system operating with 16-bit readout resolution.[23] The spectrometer—three separate KAP crystals bent to the same radius of 79 mm—rested ~350 mm from the plasma. The detector was a back-illuminated Tektronix TK1024 CCD chip. The system was sensitive enough that all spectra recorded in these experiments were produced by a single laser pulse. To obtain the complete spectrum, we placed the KAP crystals at slightly different standoff distances from the plasma to sample the 9–19-Å spectral region in three overlapping segments. To block out visible and UV portions of the spectrum, we placed one or two layers of a light-tight aluminized mylar film (5000 Å Al/1.5 μm mylar) at the entrance to the spectrograph. This film was subject to occasional damage from target debris; therefore, we checked and replaced it at appropriate intervals.

We calibrated the spectrometer dispersion by identifying known features of the Fe and Cu L-shell spectrum and applying a low-order polynomial mapping from detector position to a wavelength scale. Within the 9–19-Å band, the CCD array detector responds linearly to the x-ray fluence independent of wavelength. Corrections had to be applied to the raw data to account for the filter transmission and the KAP crystal reflectivity. The filter transmission was independently calibrated at an in-house facility to determine its transmission over the 9–19-Å wavelength band. Henke, et al. previously calibrated the KAP reflectivity.[24]

Absolutely Calibrated PCD and Yield Measurements

We recorded x-ray yields with a set of four filtered type IIA PCD detectors.[25] These were mounted in a compact 2 × 2 square array 15.9 cm from the target at an angle approximately normal to the target surface. For all measurements, the PCDs were biased with 600 V, and the signal was coupled through a capacitor into a 50-Ω cable connected to a high-speed digital oscilloscope for recording. These detectors have been used in previous x-ray yield experiments at LLNL,[26] and have been absolutely calibrated.[27] Within the 9–19-Å wavelength band observed in these measurements, the detectors have a flat wavelength response. For the bias conditions and spectral range used in the measurements, the sensitivity of these devices was nominally 7.5×10^{-4} A/W. We assumed an uncertainty of approximately 20% on this value, as reported in the original absolute calibration.

Figure 2 shows examples of a PCD signal trace and a trace of the laser pulse recorded on high-speed oscilloscopes. The x-ray pulses displayed the same temporal structure, if any, produced in the laser pulses. The FWHM pulse duration of the x-ray signals observed from solid targets was similar to, but somewhat shorter than, the laser pulse by an amount ~20–30%. Hence the x-ray pulses from solids were typically 10 ns FWHM, while the laser pulse was 12–14 ns FWHM.

We monitored contributions from various parts of the x-ray spectrum using a set of four different filters on the PCD detector array. The filter set was designed to sample the 8–20-Å band in three intervals: a 10.6-μm Al filter (8–12 Å), a 2-μm Zn filter (12–16 Å), and a 2-μm Co filter (16–20 Å). The fourth channel used an aluminized mylar filter to sample most (8–20 Å) of the spectrum. Prior to all measurements, we performed a cross-calibration of the individual PCD sensitivities. We did this by recording the signals from each detector using 2-μm Zn filters on each and with all detectors simultaneously illuminated by x rays from an Fe or type 302 stainless steel (SS302) laser-produced plasma. We took several data points for each of three rearrangements of the individual Zn filters so that we could eliminate effects due to variability in the filter transmission. We found variation in detector response among the four devices consistent with a ±20% spread in sensitivity. The extracted filter transmissions were consistent with a 10–15% variability from one piece to the next. Based on these uncertainties alone, the absolute uncertainty in yield for these measurements is around ±25%. Relative uncertainties in comparing different target materials or laser parameters are much better, around 10%, determined primarily by shot-to-shot variations.

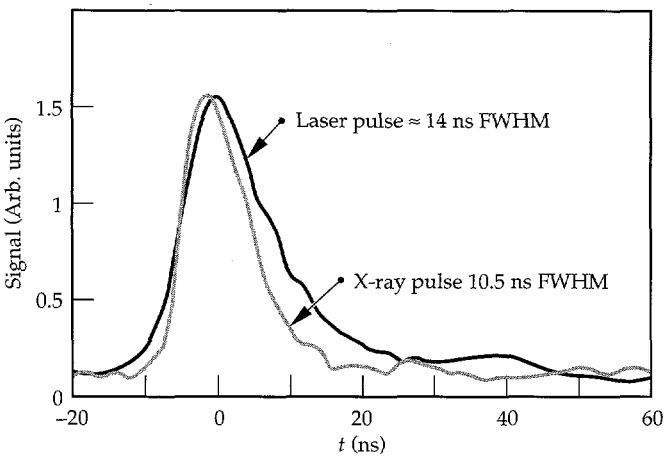

FIGURE 2. Sample oscilloscope traces of the laser pulse measured with a photodiode and an x-ray pulse measured with a photoconductive diamond (PCD) detector. Vertical scales and temporal offsets for both pulses are arbitrary, and were adjusted for comparison. (10-06-0595-1101pb01)

To determine the absolute x-ray yield, we integrated the recorded oscilloscope signals to produce a value proportional to the total x-ray fluence striking the detector. We then converted this raw data value to an absolute measure of the x-ray fluence by factoring in corrections for detector sensitivity, solid angle, filter transmission, and the emission spectrum. Simultaneous measurement of the spectrum is crucial for an accurate determination of the fractional weight of the spectrum viewed by each channel. We determined x-ray yields by multiplying each detector signal by a factor inversely proportional to the known filter response multiplied by the measured spectrum at each incident energy. We then obtained the resulting conversion efficiency from an average of the contributions measured from each channel and the known input laser energy.

The CCD detector on the spectrometer also provided an accurate method of assessing relative x-ray yields (from one target to the next, or for changes in other parameters, such as laser energy). This provided us with a cross-check against the yields inferred on the basis of the PCD measurements. We found good agreement between the relative yields determined from integrating the spectrum recorded on the CCD and the signals measured with the PCD array.

Pinhole Camera

We monitored plasma source size with an x-ray pinhole camera coupled to a video CCD and a computer-controlled readout. We placed the pinhole about 3 cm from the target and operated at a magnification of 2–3. Because it was filtered with 18-μm Al foil, the x-ray spectrum was sensitive mostly to the 8–12-Å portion of the emitted spectrum.

Methods and Results

This section provides specific details about methods and results for the experiment. We divide the section into four subsections: focus optimization, yield variation with pulse energy, x-ray spectra, and angular distribution.

Focus Optimization

For each target type and laser wavelength investigated, we optimized and measured the x-ray yield with a standard procedure consisting of two parts. First, we did a focal scan consisting of a series of shots examining yield as a function of axial lens position at maximum laser energy (20 J at 1.053 μm and 12 J at 0.527 μm). From this procedure, we identified the lens position corresponding to maximum yield as determined by the PCD measurements. Second, with the lens fixed at the maximum yield position, we systematically reduced the laser energy (described in the next section).

Figure 3 shows an example of the variation of x-ray yield with lens position for Cu and type SS302 irradiated with 1.053-μm laser light. We found in general that the x-ray yield reached a broad maximum within ±1 mm of the lens focus. The position of optimum conversion was largely independent of the target material, varying by an amount of approximately ±0.5 mm for different targets.

Figure 4(a) shows pinhole photographs of the x-ray source region throughout the focal scans for 1.053-μm irradiation. The double-lobed structure apparent at lens positions of 14 and 15 mm originates from the intensity distribution in the square beam as it approaches the focus. Similar lobed structures were also evident in the 0.527-μm laser-produced plasmas. Analyzing these images, we assume that the size of the x-ray emitting region correlates with the spatial extent of the laser intensity distribution illuminating the plasma. Figure 4(b) shows the variation of x-ray source size measured in these focal scans. The emitting region of the plasma was considerably larger than the beam diameter close to best focus since under no conditions did we observe an x-ray source region smaller than about 150 μm in diameter, a size 3–5 times larger than the beam diameter expected at best focus for the 1.5× diffraction limited beam. We took the lens position corresponding to best focus to be the point where the observed source diameter reached a minimum. The geometrical extent of the focal cone for the $f/13$ focus is also displayed in these figures for comparison with the data.

The most important information from these sequences is an assessment of the size of the x-ray emitting region in the source and an approximate idea of the laser intensity illuminating the plasma at these optimum positions. At the lens position corresponding to optimum x-ray yield, the diameter of the source region evident from the pinhole images was around 280 μm for 1.053-μm laser light and 240 μm for 0.527-μm light. It is also evident that the focal cone of the $f/13$ focus is smaller than the plasmas at most positions where significant x-ray emission was observed, and that the lens position corresponding to best yield does not correspond to the position of best focus, although it was much closer to best focus for 0.527-μm light than for 1.053-μm light. (X-ray yield on the converging side of the 1.053-μm focused beam should be similar to the diverging side; for all measurements reported here the beam was focused on target with a diverging focus.) Average

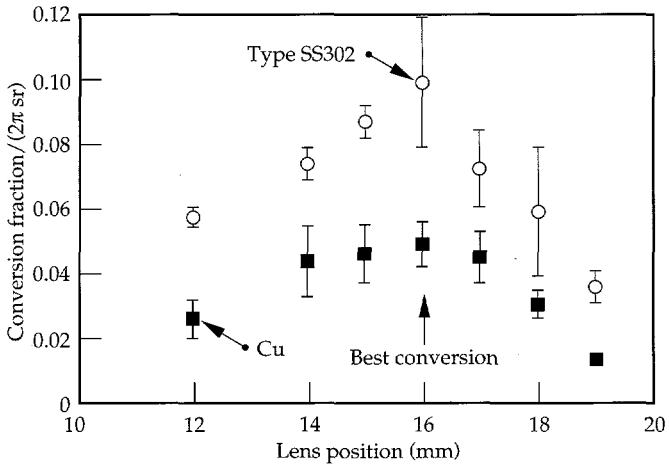

FIGURE 3. Variation of x-ray yield with focusing lens position for 1.053-μm laser light; we used this procedure to optimize the yield for a given target type. (10-06-0595-1102pb01)

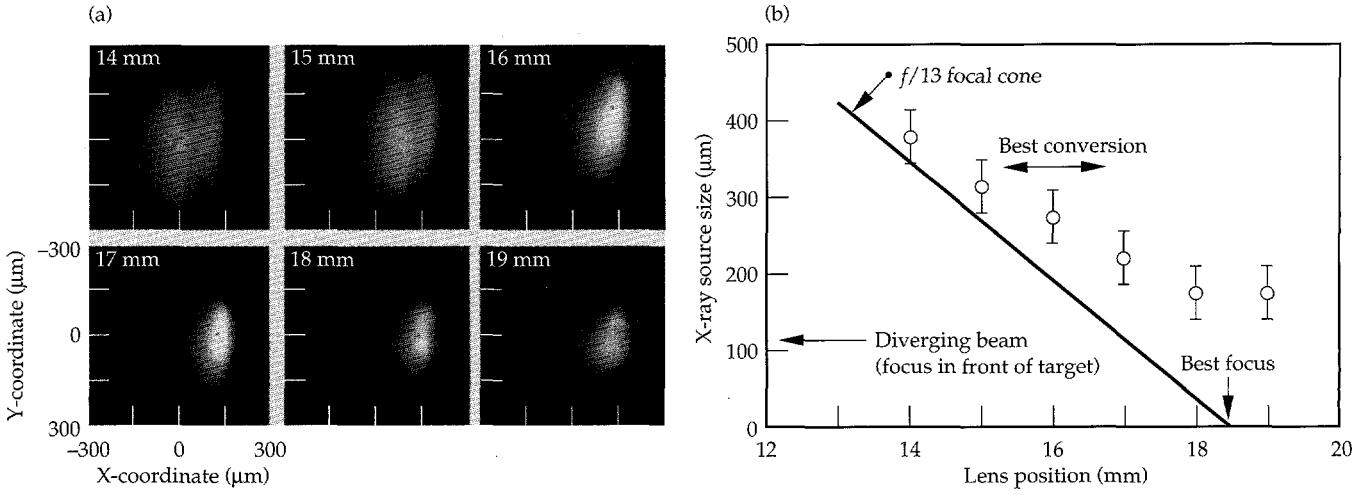

FIGURE 4. Variation of x-ray emitting plasma volume with focusing lens position for 1.053-μm laser light irradiating a solid Fe target. The origin of the lens position scale is arbitrary. (a) A sequence of pinhole photographs of the plasma x-ray emission taken at various lens positions (indicated on the individual frames). (b) Variation of plasma size with lens position measured from the pinhole photographs. Also shown for comparison is the beam size assuming a geometric $f/13$ focal cone with best focus assumed to occur at the lens position producing the smallest plasma volume. (10-06-0595-1103pb01)

beam intensities illuminating the plasma at these lens positions can be estimated from the geometrical extent of the focal cone and the distance of the optimum lens position from best focus. For 1.053-μm light, the beam diameter at optimum focus was ~190 μm, to produce a beam intensity ~5×10^{12} W/cm^2. For 0.527-μm light, the beam diameter was approximately 100 μm, a factor of two smaller than for the optimum 1.053-μm situation, producing intensities ~1.2×10^{13} W/cm^2.

Yield Variation with Pulse Energy

After we determined the optimum focus position, we fixed the lens at its optimum position and measured x-ray yields while the laser energy was varied throughout the available range below the maximum setting. We easily adjusted laser energy by varying a waveplate within the preamplifier chain to control the pulse energy prior to the final amplifier passes. Both the temporal pulse shape and spatial beam parameters (focus position) were unaffected by this adjustment.

An important characteristic of all of the measurements from planar targets measured in this research was an increasing x-ray yield with pulse energy. For all materials, the conversion increased monotonically from near zero at low pulse energies and increased to a saturation value before leveling off. Figure 5 shows an example of this dependence for (a) type SS302 and (b) Cu. Within the energy range available there was no evidence of a regime where conversion fraction decreased with increasing pulse energy. The saturation value varied with the target material and the laser wavelength. With type SS302 (median emission wavelength at 15 Å), the laser energy at saturation is clearly lower than for Cu (median emission wavelength at 11.5 Å). In the case of Cu, it is not clear that the dependence of x-ray yield with energy has reached a final saturation level at the maximum laser pulse energies available in these experiments, although saturation appears to be ~5–10 J for type SS302. Correlated with the pulse energy dependence of yield was a clear shift in the x-ray spectrum for any given target to shorter wavelengths (harder photons) with increasing pulse energy. We expected this due to the fact that increasing pulse energies produce higher intensities and drive hotter plasmas.

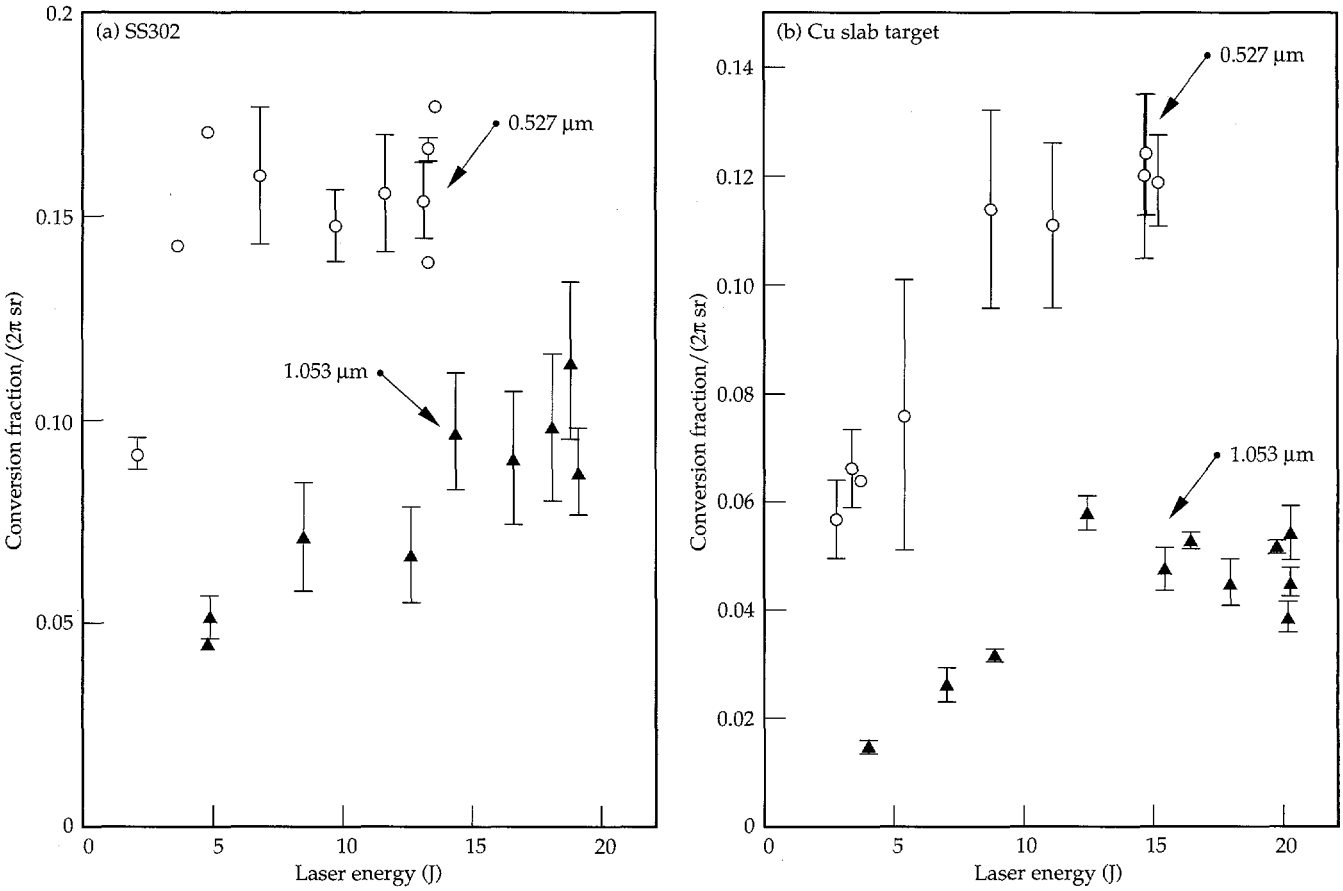

FIGURE 5. Pulse energy dependence of x-ray yield for two target materials and both drive wavelengths. Target materials are (a) type SS302 and (b) Cu. (10-06-0595-1104pb01)

X-Ray Spectra

Figure 6 shows a catalogue of spectra for all of the materials tested using 0.527-μm laser light. Also identified on the spectra are integral curves depicting the integrated conversion fraction through the short to long range of emission wavelengths. We observed a similar set of spectra using 1.053-μm light, with the main difference being a shift in the distribution of emission to longer wavelengths within the characteristic spectrum of each material. For the materials selected, Fig. 7 summarizes the x-ray wavelength range (10–15 Å).

All of the Xe spectra exhibit a bilobed distribution of emission with a main component emitting at wavelengths from 10–15 Å, and a second component from 17–20 Å. We also included this latter component, accounting for about 20–30% of the emitted energy, in our yield determination, although the component is of little use for lithography applications. Excluding this component (i.e., excluding wavelengths >16 Å), the Xe conversion measured with 1.053-light is less than 10%, but still comparable to the type SS302 conversion. With 0.527-μm light the Xe spectrum becomes harder, shifting to shorter wavelengths, and the total conversion improves to around 12%.

The conversion efficiency measured with type SS302 is significantly higher than with pure Fe. We can attribute this largely to the addition of significantly more spectral lines with contributions from Cr, Mn, Ni, etc., present in the stainless steel alloy. Figure 6(b) demonstrates this, showing the dense spectrum of stainless steel as compared with the pure Fe spectrum in Figure 6(c). We discuss this improved conversion efficiency later in the article.

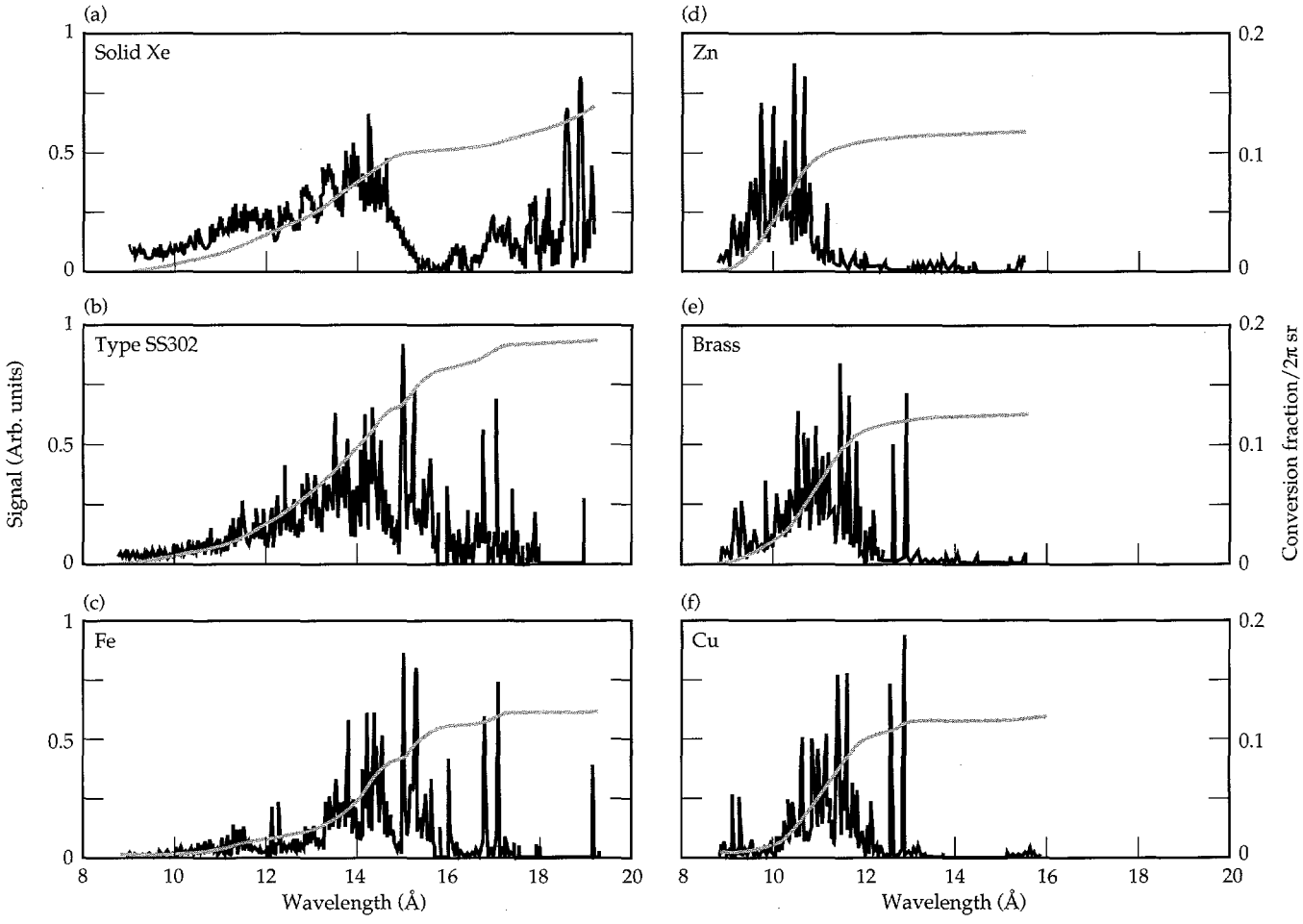

FIGURE 6. X-ray spectra measured for all solid targets using 0.527-μm laser light. Spectral intensity is displayed on the arbitrary left hand scale; the wavelength-integrated x-ray yield for each material can be measured against the right hand scale. Conversion fraction indicates the ratio of x-ray energy to incident laser energy. Target materials are (a) solid Xe, (b) type SS302, (c) Fe, (d) Zn, (e) brass, and (f) Cu. (10-06-0595-1105pb01)

Angular Distribution

For planar targets, we also measured the angular distribution of x-ray yield. We recorded all yield measurements with the PCD array at target normal, where the yield is expected to reach a maximum. For historical reasons, and to ease comparison with other work, we report the x-ray yield as the conversion fraction into 2π sr as if the angular distribution were isotropic and equal to the angular fluence measured at target normal. In general, the angular fluence varies relative to target normal and depends on target material, laser wavelength, laser pulse duration, and possibly other factors. The yield is generally reduced away from target normal and can be fitted with a $\cos^{\alpha}\theta$ distribution, where $\alpha \leq 1$, and the total conversion into 2π sr is less than the fraction reported in this work. There may be reasons to place the lithography exposure system at a location other than target normal; for example, to mitigate against debris, which is also maximized at target normal. Thus an assessment of the angular distribution is important to ascertain any reduction in x-ray yield at other angles.

We did the angular distribution measurements for Fe and type SS302 targets at the optimized conditions for both wavelengths. We fitted all PCD detectors with 2-μm Zn filters, which transmit the main component of the Fe spectrum. We arranged the detectors in four angular positions in the plane of the laser beam spanning angles from 18–75° from the target normal. We took several sets of shots for each measurement, for which the Zn filters were rotated through the detectors, to eliminate effects due to variations in the filter transmissivities. We discuss results from these measurements in the next section.

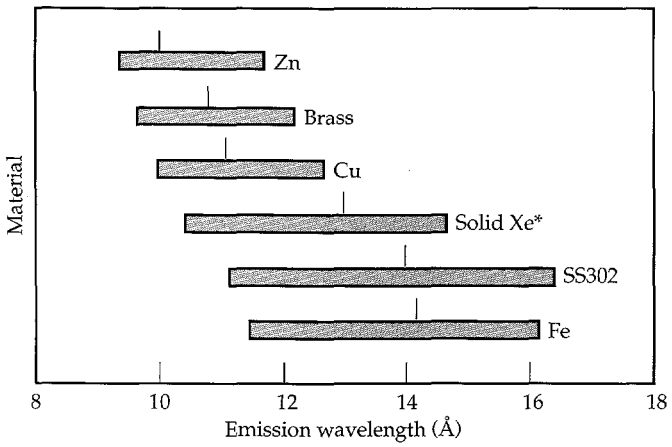

FIGURE 7. Emission wavelengths determined from the spectra measured for all the solid elements using 0.527 μm laser irradiation. The bar end points indicate wavelengths spanning 10 to 90% of the wavelength-integrated emission (i.e., containing 80% of the emission). The points within the bars indicate the median emission wavelengths (50% point on the integral curve) for each material. *In the special case of Xe, this evaluation was restricted to wavelengths less than 16 Å, which eliminates the long-wavelength emission component (~18 Å) from the weighting process. (10-06-0595-1108pb01)

Discussion

There are four main areas of discussion for this experiment: x-ray yields and spectra, pulse energy dependence, laser-drive wavelength dependence, and angular distribution.

X-Ray Yields and Spectra

Figure 8 summarizes x-ray yields from all of the solid targets, and compares the optimized yield for each material at both wavelengths. We obtained high x-ray yields using the longer wavelength emitters (~14 Å) with 1.053-μm laser-drive wavelength, the best examples of these being type SS302 and cryogenic Xe. Conversion efficiency of these targets was approximately 10%/(2π sr) at the target normal. Conversion for shorter wavelength emitters using 1.053-μm was significantly less, dropping to <4%/(2π sr) for Zn targets emitting at around 10.5 Å. We observed a significant improvement in x-ray conversion with 0.527-μm light, where conversion efficiencies for all targets was ~12%/(2π sr) or better. For the range of shorter-wavelength emitters, including Cu, brass, and Zn, this represents a factor of 3–4 improvement in the yield measured at target normal. Since the energy conversion efficiency for doubling the laser-light frequency is expected to be around 80%,[21] this result indicates that operation at 0.527 μm will provide a substantial improvement in conversion of energy from the fundamental laser wavelength to x rays in the 10–12-Å band using a frequency-doubled laser.

Solid Xe offers the attractive possibility of building a reduced-debris source. The Xe spectrum contains two main components, with a longer-wavelength portion occupying the 17–20 Å. For lithography, the 75–80% energy portion of the spectrum emitted in the 10–14 Å band is the most useful part. With 0.527-μm laser irradiation, this portion of the spectrum is significantly

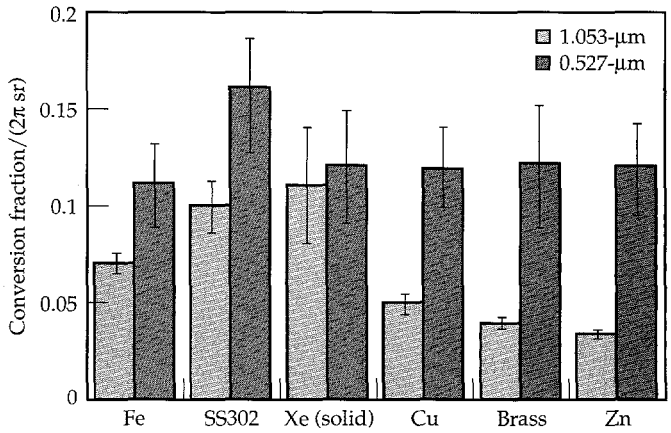

FIGURE 8. Optimized x-ray yields measured for all solid targets and both drive wavelengths. (10-06-0595-1107pb01)

harder than with 1.053-μm irradiation. Solid Xe provides x-ray yields comparable to, or better than, other solid targets at both drive wavelengths investigated. In the form of cryogenic pellets, frozen Xe offers the potential for producing a reduced-debris source with yields comparable to other solid target yields.

We attained the best yields with type SS302 targets. The improvement in conversion efficiency compared with pure Fe targets is apparent with 1.053-μm laser light, and becomes quite dramatic with 0.527-μm light, where the optimum conversion efficiency exceeds 16% for type SS302. Stainless steel is an alloy comprised mainly of several transition metals with atomic numbers from Z = 24 through Z = 28 (the chemical composition of type 302 is approximately 70% Fe, 18% Cr, 9% Ni, and 2% Mn). These elements emit kilovolt radiation efficiently in the plasmas produced by the laser. The increased yield from the alloy occurs because the strongly emitting lines characteristic of each element are optically thick, or nearly so in these high-density plasmas produced with solid targets; thus, the reduced concentration of Fe found in stainless steel as compared with pure Fe targets does not lead to a noticeable reduction in the intensity of the characteristic Fe spectral components, while the other alloyed elements in stainless steel provide emission features that fill the gaps in the spectrum. This result indicates the possibility for improving x-ray yields by designing mixtures of elements that emit in the desired wavelength band. These will produce high yields by filling in the spectrum with more lines. The high yields of Xe are produced for a similar reason, namely that the much more complicated electronic structure of the Xe M-shell provides many more emission lines to fill in the spectral band than the simpler L-shell emitters.

Pulse Energy Dependence

The pulse energy dependence of the observed x-ray yield is most easily understood in light of previous 0.5-ns pulse duration work by Chaker et al.[16], in which the conversion efficiency into kilovolt x rays from Cu targets was observed to drop abruptly below intensities of ~5×10^{12} W/cm^2 for 1.06-μm light. Optimum conversion efficiencies for Cu measured in this work are comparable to the values reported by Chaker et al. As noted, our procedure for optimizing the conversion by scanning the focus automatically places the irradiance near this saturation intensity and not necessarily at the best focus. Consequently, the measurements at decreasing pulse energy will produce lower than optimum intensities, and therefore produce lower x-ray yields. An implication of this interpretation is that it may be possible to attain high yields at lower pulse energies using a faster focusing lens (e.g., $f/4$ instead of $f/13$) that achieves ~10^{13} W/cm^2 within the beam focus. However, we stress that achieving 10^{13} W/cm^2 is necessary but may not be sufficient to achieve high yields (with long pulses)—this possibility needs to be explored experimentally. In our research, we made no attempts to exploit this method of obtaining high conversion efficiency at lower pulse energies.

Laser-Drive Wavelength Dependence

As a general rule, the conversion fraction (laser energy to x-ray energy) into 2π sr is higher at 0.527 μm than at 1.053 μm. The phenomenon is most accentuated for the short wavelength (10–12-Å) emitters (Cu, Zn, and brass), where the conversion fraction improves by a factor of 3–4 times over the 1.053-μm result. This dramatic improvement in conversion for the shorter-wavelength emitters using frequency-doubled laser light more than compensates for losses introduced by converting the fundamental to the second harmonic, and provides a means to obtain high x-ray yields at a range of desired wavelengths from 10.5 Å (Zn) to 15 Å (SS302) with a single laser driver.

As increasing pulse energy causes spectral shifts, changing the drive wavelength from 1.053 to 0.527 μm clearly caused the spectra of the various target types to shift to shorter wavelengths. This spectral dependence is consistent with (1) the improved coupling of the laser light into plasma heating at higher densities and (2) the improved conversion. Figure 9 shows an example of this spectral shift for solid Xe targets. We observed similar laser-drive-wavelength-dependent spectral shifts for the other materials investigated.

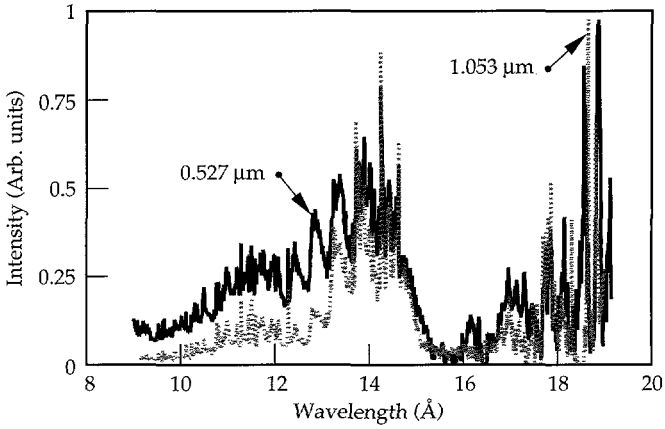

FIGURE 9. Comparison of x-ray spectra from solid Xe measured from plasmas produced with 1.053-μm (dashed line) and 0.527-μm (solid line) laser light. (20-07-0695-1659pb01)

Angular Distribution

Figure 10 shows the angular distributions measured for both drive wavelengths irradiating Fe or type SS302 targets. Fits to a $\cos^{\alpha}\theta$ distribution yielded $\alpha \approx 0.2$ for 1.053-μm irradiation and $\alpha \approx 0.6$ for 0.53-μm irradiation. Neither of these angular distributions is Lambertian ($\alpha = 1$). At 1.053 μm, the emission is very close to being isotropic, such that at angles of 60–70° from the target normal, the observed yield remains at 80% or more of the peak yield at target normal. At 0.53 μm the emission is closer to Lambertian, with the yield reduced to half of the peak at angles of >65° off target normal. The difference in angular distribution reflects the difference in laser light coupling between the two wavelengths. The shorter wavelength couples much more efficiently into higher density plasma layers, which are optically thick and closer to the target plane, thus producing a physical situation that is close to that of a planar, optically thick Lambertian surface emitter.

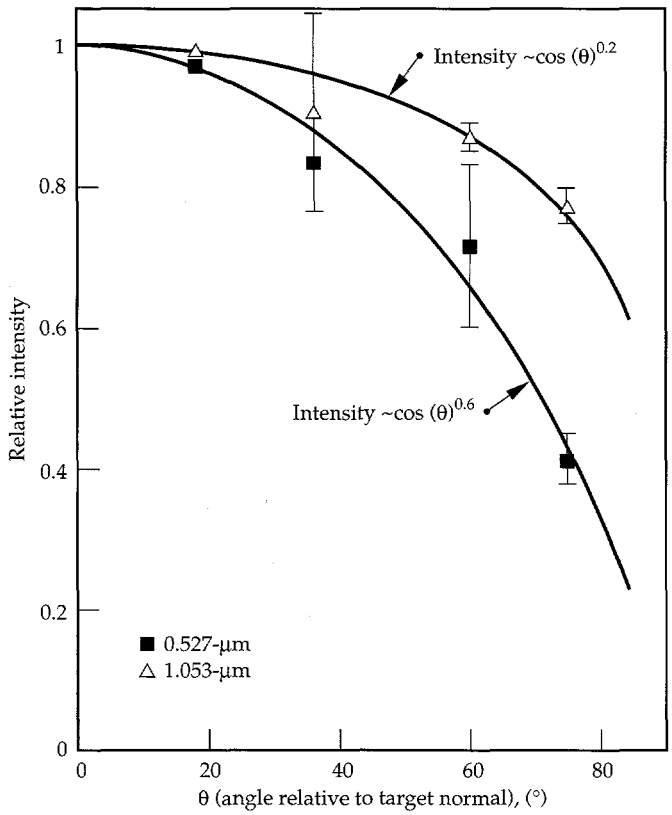

FIGURE 10. Angular distribution of x-ray emission relative to target normal measured for 14-Å emitters Fe or type SS302 at both drive wavelengths. (10-06-0595-1106pb01)

Conclusions

The intended operating x-ray wavelength of a proximity lithography system will be determined by a number of considerations beyond the scope of the present study. For most situations, x-ray wavelengths spanning the range from 10–15 Å may be used. The materials selected in this study embrace this wavelength region. These results demonstrate a significant degree of flexibility in delivering x-ray energy within a desired wavelength band using a laser-produced plasma.

X-ray conversion efficiency from all targets increased with increasing laser pulse energy from small values at low pulse energies (<5 J). A minimum pulse energy of ~5–10 J was necessary to approach the yields close to the optimum. Above ~10 J, the yield vs pulse energy curve begins to saturate. This behavior is consistent with the observed saturation of conversion with laser intensity observed by Chaker et al.[16] using 0.5-ns pulses, thus indicating that the 10-ns plasma behaves similarly in this pulse energy range. At optimum conditions, the average intensity illuminating the plasma was approximately 5×10^{12} W/cm^2 for 1.053-μm light, and 1×10^{13} W/cm^2 for 0.527-μm light. For both wavelengths the source diameter at optimum conversion was ~250–300 μm.

The x-ray conversion efficiencies produced with the long-pulse laser driver used in these experiments matched efficiencies measured previously with shorter (nanosecond-duration) pulses. The duration of the x-ray pulse matched the duration of the laser pulse, indicating that, at least in the 12–14-ns range, the long pulse duration does not degrade the conversion efficiency. A frequency-doubled Nd:glass laser driver can be used to produce a source with median emission wavelength anywhere from 10.5 to 15 Å at x-ray yields that meet the needs of a proximity lithography production system.

Acknowledgments

We acknowledge technical support from Jim Wintemute for operating the laser, as well as Jim Cox and Ken Haney for fabrication and assembly of the target facility, and Joe Smith for filter calibrations. This work was supported by a contract from the U.S. Department of Defense Advanced Research Projects Agency.

Notes and References

1. J. Warlaumont, *J. Vac. Sci. Technol. B7*, 1634 (1989).
2. G. Zwicker, W. Windbracke, H. Bernt, D. Friedrich, H.-L. Huber, et al., *J. Vac. Sci. Technol. B7*, 1642–1647 (1989).
3. K. M. Gilbert, J. P. Anthes, M. A. Gusinow, M. A. Palmer, et al., *J. Appl. Phys.* **51**, 1449–1451 (1980).
4. B. Yaakobi, P. Bourke, Y. Conturie, J. Delettrez, J. M. Forsyth, et al., *Opt. Commun.* **38**, 196–200 (1981).
5. H. Nishimura, F. Matsuoka, M. Yagi, K. Yamada, et al., *Phys. Fluids* **26**, 1688–1692 (1983).
6. D. L. Matthews, E. M. Campbell, N. M. Ceglio, G. Hermes, R. Kauffman, et al., *J. Appl. Phys.* **54**, 4260–4268 (1983).
7. W. C. Mead, E. M. Campbell, K. G. Estabrook, R. E. Turner, W. L. Kruer, et al., *Phys. Fluids* **26**, 2316–2331 (1983).
8. P. Alaterre, H. Pépin, R. Fabbro, and B. Faral, *Phys. Rev. A* **34**, 4184–4194 (1986).
9. T. Mochizuki, T. Yabe, K. Okada, M. Hamada, N. Ikeda, S. Kiyokawa, and C. Yamanaka, *Phys. Rev. A* **33**, 525–539 (1986).
10. R. Popil, P. D. Gupta, R. Fedosejevs, and A. A. Offenberger, *Phys. Rev. A* **35**, 3874–3882 (1987).
11. K. Eidmann and W. Schwanda, *Laser and Particle Beams* **9**, 551–562 (1991).
12. J. N. Broughton and R. Fedosejevs, *Appl. Phys. Lett.* **60**, 1818–1821 (1992).
13. D. J. Nagel, M. C. Peckerar, R. R. Whitlock, J. R. Greig, and R. E. Pechacek, *Electron. Lett.* **14**, 781–782 (1978).
14. B. Yaakobi, H. Kim, J. M. Soures, H. W. Deckman, and J. Dunsmuir, *Appl. Phys. Lett.* **43**, 686–688 (1983).
15. H. Pépin, P. Alaterre, M. Chaker, R. Fabbro, B. Faral, et al., *J. Vac. Sci. Technol. B* **5**, 27–32 (1987).
16. M. Chaker, H. Pépin, V. Bareau, B. Lafontaine, I. Toubhans, et al., *J. Appl. Phys.* **63**, 892–899 (1988).
17. G. M. Davis, M. C. Gower, F. O'Neill, and I. C. E. Turcu, *Appl. Phys. Lett.* **53**, 1583–1585 (1988).
18. M. Chaker, B. L. Fontaine, C. Y. Côté, J. C. Kieffer, H. Pêpin, et al., *J. Vac. Sci. Technol. B* **10**, 3239–3242 (1992).
19. M. Chaker, J. F. Pelletier, and J. C. Kieffer, in *Materials Aspects of X-Ray Lithography*, G. K. Celler and J. R. Maldonado, Eds. (Materials Research Society, San Francisco, CA, USA, 1993) pp. 151–167.
20. R. Kodama, T. Mochizuki, K. A. Tanaka, and C. Yamanaka, *Appl. Phys. Lett.* **50**, 720–722 (1987).
21. C. B. Dane, L. E. Zapata, W. A. Neuman, M. A. Norton, and L. A. Hackel, *IEEE J. Quantum Electron.* **31**, 148–163 (1995).
22. C. B. Dane, W. A. Neuman, and L. A. Hackel, *Opt. Lett.* **17**, 1271–1273 (1992).
23. Princeton Instruments, Inc., 3660 Quakerbridge Rd., Trenton, NJ, 08619 USA.
24. B. L. Henke, P. Lee, T. J. Tanaka, R. L. Shimabukuro, and B. K. Fujikawa, *At. Data Nucl. Data Tables* **27**, 1–144 (1982).
25. D. R. Kania, L. Pan, H. Korblum, P. Bell, et al., *Rev. Sci. Instrum.* **61**, 2765–2767 (1990).
26. D. R. Kania, H. Kornblum, B. A. Hammel, J. Seely, C. Brown, et al., *Phys. Rev. A* **46**, 7853–7868 (1992).
27. D. R. Kania, L. S. Pan, P. Bell, O. L. Landen, H. Kornblum, et al., *J. Appl. Phys.* **68**, 124–130 (1990).

Three-Dimensional Simulations of Ablative Hydrodynamic Instabilities in Indirectly Driven Targets

M. M. Marinak *S. W. Haan*

R. E. Tipton *S. V. Weber*

B. A. Remington

Introduction

To model ignition in a National Ignition Facility (NIF) capsule implosion, we must understand the behavior of instabilities that can cause breakup of the pellet shell. During a capsule implosion, shocks that transit the shell cause growth of perturbations at the surface or at an interface because of a Richtmyer–Meshkov type of instability.[1] Following shock breakout, or earlier for a shaped pulse, the low-density ablated plasma accelerates the pusher, and the ablation front is Rayleigh–Taylor (RT) unstable.[2] Ablation and finite density gradients have the effect of stabilizing the short wavelength modes. Unstable modes present on the outer surface grow and feed through to the inner surface. Once the shell encounters the rebounding shock from the capsule center, it decelerates and the inner surface becomes RT unstable. If perturbations grow large enough, pusher material mixes into the core, degrading implosion performance.

Capsule designs for the NIF depend on ablative stabilization and saturation to prevent perturbations initially present on the capsule surface from growing large enough to quench ignition. The shape of the perturbation is a key factor in determining the amplitude at which its RT growth saturates. Classical RT experiments of an air-water interface and third-order theory carried out by Jacobs and Catton[3] demonstrated that for a particular rectilinear wave number $k = (k_x^2 + k_y^2)^{1/2}$, the symmetric square mode ($k_x = k_y$) will start to saturate at the largest amplitude of any mode. Two- and three-dimensional (2- and 3-D) simulations by Dahlburg et al.[4] revealed the same dependencies in thin foils. Since the 3-D shape affects the perturbation saturation and ultimately capsule performance, a quantitative understanding of 3-D shape effects on perturbation growth is of considerable interest to inertial confinement fusion (ICF) research.

In this article, we examine the first simulations and experiments to study the effect of 3-D perturbation shape on instability growth and saturation in indirectly driven targets. The first section discusses HYDRA, the radiation hydrodynamics code we developed for these simulations. The subsequent section examines 3-D shape effects in single-mode perturbations in planar foil simulations and experiments. A discussion of the evolution of multimode perturbations on planar foils is followed by a discussion of 3-D simulations of instability growth in Nova capsule implosions.

HYDRA

We developed a new 3-D radiation hydrodynamics code, called HYDRA, to perform these simulations. HYDRA uses a structured mesh and has arbitrary Lagrange Eulerian (ALE) capability. Several forms of equations of state (EOS) are available, including the EOS4 tabular database and the inline quotidian EOS (QEOS). Multigroup radiation diffusion is implemented using tabular opacities. The thermal conduction routine applies conductivities calculated with the model of Lee and More.[5] HYDRA has an Eulerian interface tracker that allows users to resolve material interfaces while making full use of its ALE capability. "Mixed" zones, which contain one or more material interfaces, are subdivided into separate components. Radiation transport, thermal conduction, and other physical processes are treated separately for all of the components of the mixed zones. The interface tracker allows one to avoid distorted meshes, and the accuracy problems they can cause, even while resolving shear flows.

UCRL-LR-105821-95-3

The capability of coupling several adjacent zones together has been incorporated in HYDRA. This allows greater freedom in zoning without the full additional computational overhead and increased memory requirements associated with an unstructured mesh. This coupling is essential to avoid the small Courant time step limits that would occur, for example, in narrow zones near the center or near the pole of a 3-D capsule implosion simulation. This capability can also be applied in the presence of mixed zones, allowing one to adjust the local resolution in different directions relative to a material interface.

We developed a technique for treating radiation transport that enables us to run 3-D simulations of a variety of targets with viable computational requirements. The method involves two separate calculations. In the first, we obtain a detailed treatment of the spectrum by using a large number of photon groups while the geometry is approximated. All the detailed spectrum and opacity information is then collapsed into group constants for a small number of photon groups. In the second calculation, these few group opacities are applied in a simulation that treats the detailed spatial variation with use of the diffusion operator. The method yields estimates of the group opacities that are vastly superior to those obtained with the standard Rosseland mean. Compared with the standard method, this new development has enabled us to perform highly accurate numerical solutions at a small fraction of the computational expense. The implementation of this method, combined with the high run speeds and reduced memory requirements attainable with algorithms written on a structured mesh, make HYDRA well suited for a variety of problems that contain some degree of symmetry.

Shape Effects

Single-Mode Perturbations on Planar Foils

We first examine foils having single-mode rectilinear perturbations $\psi = a \cos(k_x x) \cos(k_y y)$, with $k_x = k_y$, $k_x = 3k_y$, and $k_y = 0$ (2-D). Each perturbation has the same wave number $k = (k_x^2 + k_y^2)^{1/2} = 2\pi/80\ \mu m^{-1}$. To study growth extending from the linear regime through the late nonlinear stage, we use a hypothetical drive that gives a long period of acceleration and thus large growth factors. We take the drive spectrum from a LASNEX hohlraum simulation. The drive temperature history imposed starts with a foot at ~100 eV, then ramps up to 162 eV over the first 1 ns and is then held constant through 4 ns. This drive is used for all the planar simulations discussed here except for simulations of Nova experiments. Supertransition array (STA) opacities for CH(Br) are used. The foil is initially 50 μm thick. We use an ideal-gas EOS in this simulation for generality.

Figure 1 shows the evolution of the fundamental mode amplitude of areal density for the three perturbation aspect ratios listed above. Since each perturbation has the same wave number and is initialized with the same amplitude, each should grow at the same rate during the shock transit and early acceleration phases when the perturbation is linear; Fig. 1 shows that this is the case. The two shocks generated during the foot and subsequent rise to the peak of the drive coalesce as they break out of the foil at 1 ns. After a period of linear RT growth, the point at which each mode begins to saturate shows a clear progression with the mode shape. As the mode shape is varied from the least symmetric 2-D mode to the most symmetric 3-D square mode, the

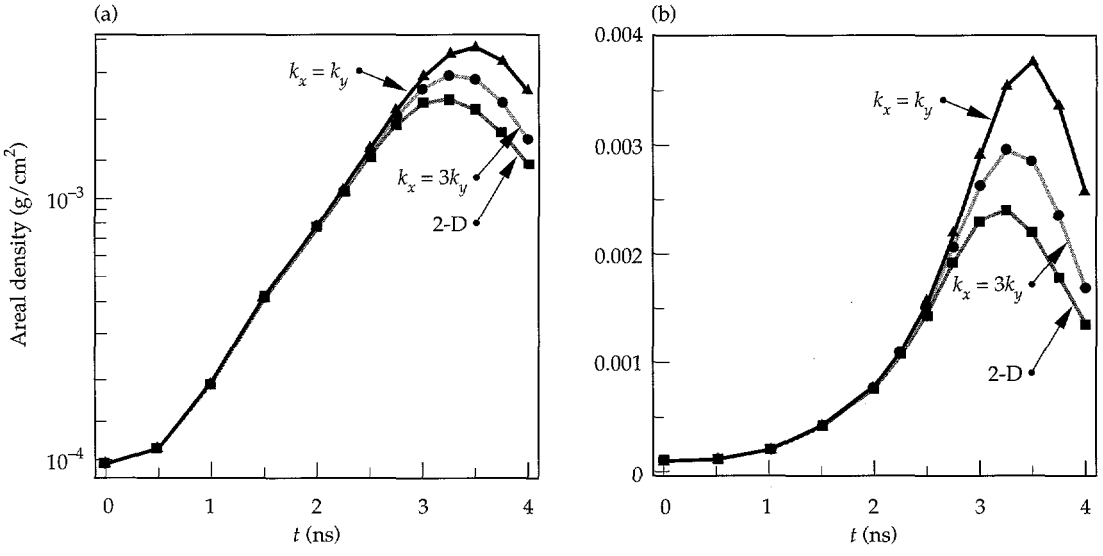

FIGURE 1. Evolution of the fundamental Fourier mode of areal density for three Cartesian mode simulations. Mode amplitudes are plotted (a) on a logarithmic scale and (b) on a linear scale; symbols indicate calculated points.
(50-05-0595-1109pb01)

perturbation begins to saturate later and achieves a larger amplitude. The 3-D square mode reaches a peak amplitude 56% larger than the 2-D mode.

Figure 2 shows the $\rho = 0.3$ g/cm^3 isodensity surface at 3.25 ns for the 3-D square and 2-D modes. In the nonlinear phase, the 3-D square mode has evolved into a broad bubble surrounded by narrow spikes and adjoining spike sheets. The peak-to-valley (p–V) displacements of the isodensity contours are very similar between the 2- and 3-D modes. The larger amplitude of the square mode is manifest primarily because of its greater density in the spike.

The hexagonal mode perturbation,

$$\psi = a\left[\cos\left(\frac{k_0 x}{2}\right)\cos\left(\frac{\sqrt{3}k_0 y}{2}\right) + \cos(k_0 x)\right], \quad (1)$$

consists of a hexagonally packed array of either bumps or pits, depending on the sign of the perturbation. Reversing the sign of this mode results in a different shape, not just a shift in the phase. Simulations of foils with the two orientations of hexagonal-mode perturbations show rather different evolution in the nonlinear regime. The bubble-centered orientation, consisting of an array of pits, develops into hexagonal bubbles surrounded by spike sheets in the nonlinear stage as shown in Fig. 3(a). The spike-centered orientation, shown in Fig. 3(b), develops isolated individual spikes. The maximum p–V areal density modulations obtained are 45.3 g μm/cm^3 for the bubble-centered perturbation and 83.8 g μm/cm^3 for the spike-centered perturbation. Growth of the spike-centered mode is favored on the ablating foil because it has a smaller surface area subject to ablation and because more material surrounds the base of the axisymmetric spike. The bubble-centered

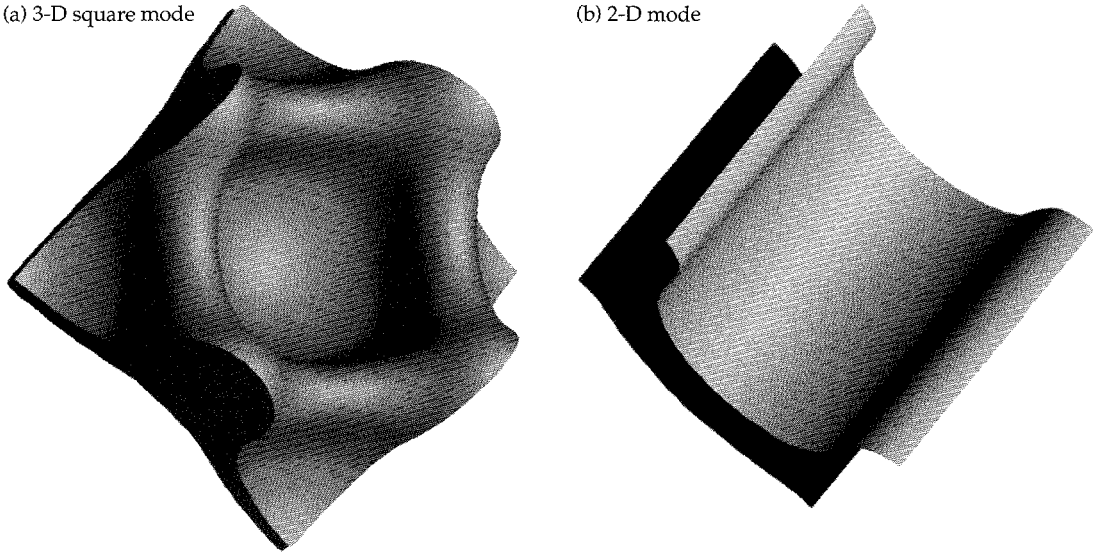

FIGURE 2. Isodensity plots for $\rho = 0.3$ g/cm^3 at 3.25 ns: (a) for the simulations of the $k_x = k_y$ square mode and (b) for the $k_y = 0$ (2-D) mode. One period of the perturbations is shown ($k = 2\pi/80$ μm^{-1}). For each plot, the perspective is from the side of the target ablated by x rays. (50-05-0595-1110pb01)

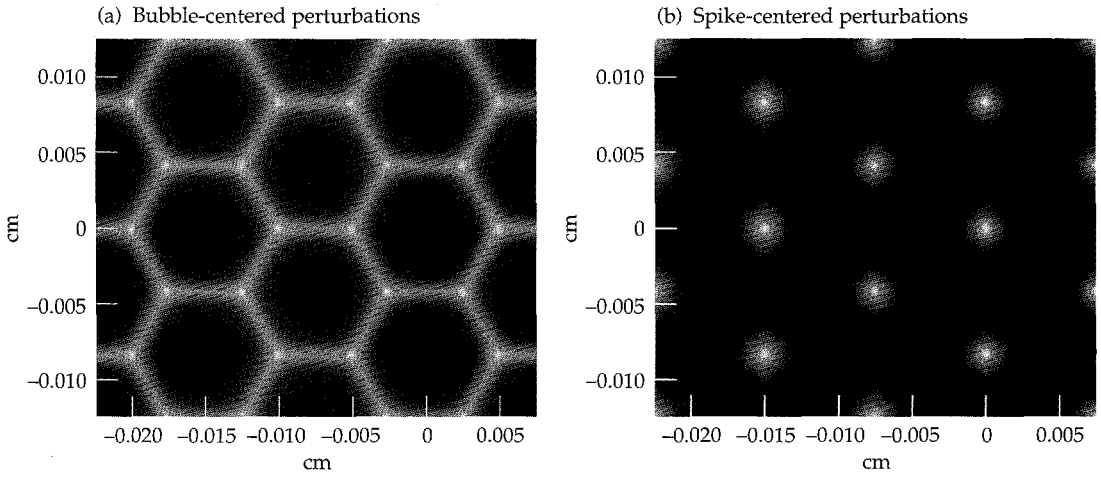

FIGURE 3. Plots of areal density for the two hexagonal-mode orientations in the saturated regime. (a) Bubble-centered perturbations; (b) spike-centered perturbations. Brightest regions correspond to spikes. (50-05-0595-1167pb02)

perturbation attains smaller minimum areal density, and it burns through the foil faster. The axisymmetric bubble is the perturbation shape most dangerous to the survival of thin capsule shells.

3-D Shape Effects in Experiments

We performed an experimental study of single-mode shape effects with planar foils on Nova. In this article, we consider some of these results and compare them with simulations. For these experiments, surface perturbations are molded onto one side of a CH(Br) foil ($C_{50}H_{47}Br_{2.7}$) 750 μm in diameter, 53–57 μm thick, density 1.26 g/cm^3. The foil is mounted across a hole in the wall of a 3000-μm-long, 1600-μm-diam Au cylindrical hohlraum with the perturbations facing inward. It is illuminated from the back by a 500–700-μm-diam source of "backlighter" x rays created by irradiating a disk of either Rh or Sc with one or two Nova beams. We use measurements of the transmitted intensity of backlighter x rays to determine the growth in the areal density of the perturbations. For targets with 2-D perturbations, a time-resolved image $I(x,t)$ is recorded onto film using a 22× magnification streaked Wölter x-ray microscope[6] with a Rh backlighter. For foils with 3-D perturbations, we collect gated images $I(x,y,t)$ at several times during the shot using the flexible x-ray pinhole imager (FXI)[7] in conjunction with a Sc backlighter. We characterized the spatial resolution of these instruments and included it wherever simulations are compared with data.

Eight 0.351-μm, 2.2-kJ shaped Nova beams irradiate the hohlraum. The shaped drive, termed laser pulse shape 23, has a low-intensity ~1.5-ns foot, which is followed by a rapid increase to peak power at 2.5–3.0 ns with a peak-to-foot intensity ratio of 10. Our most recent model of this x-ray drive is based on a 2-D LASNEX Au hohlraum simulation. During the foot of the pulse ($t < 2$ ns), we increase the preheat portion of the spectrum ($h\nu > 1.4$ keV) by a factor of 10 over that predicted by LASNEX while maintaining the same total power in the drive. The result is that during the foot an average of 8% of the total energy in the drive spectrum is above 2 keV. This adjustment stems from uncertainty in the total preheat energy deposited in the foil early in time. It has the effect of reducing growth somewhat, systematically improving the fit throughout the database. This drive model reproduces well the foil trajectories and thus the zero-order hydrodynamics.[8]

We examine the effect of perturbation shape on saturation amplitude by comparing a foil having a square-mode perturbation ($k_x = k_y$) with one having a 2-D perturbation ($k_y = 0$), each having the same effective wave number $k = 2\pi/50$ μm^{-1} and similar amplitudes. We used a laser ablation technique to create the periodic 3-D perturbation on the mold.[9] With the relatively short acceleration period of pulse shape 23, large initial amplitudes are required to allow the foils to evolve well into the nonlinear regime. Fourier analysis of an x-ray radiograph of the square-mode foil yields the initial amplitude of the fundamental perturbation as 2.7 μm. Small-amplitude higher harmonics are also present, but their amplitudes are typically less than 10% of the fundamental mode amplitude. The foil with the 2-D perturbation had an amplitude of 2.5 μm. In the HYDRA simulation of the square-mode foil, the surface perturbation initialized includes the predominant $\cos(k_x x)$ $\cos(k_y y)$ modes as well as $\cos(mk_x x)$ $\cos(nk_y y)$ modes having $(m,n) = (0\text{–}3,0\text{–}3)$ taken from the radiograph.

Figure 4(a,b) compares images of ln(exposure) calculated from the simulation and measured with the FXI at 4.3 ns, including the effect of instrumental resolution. At this time, the mode has progressed well into the nonlinear phase. The HYDRA simulation reproduces well the structure of the dark narrow spikes, adjoining spike sheets, and wide bubbles. A slight elongation of the central spike is due to the small asymmetry present in the initial perturbation, contained in higher harmonic modes. Figure 4(c,d) makes the same comparison as surface plots of ln(exposure) vs (x,y), where the bubble is centered instead of the spike.

Figure 5(a) compares the measured time evolution of the fundamental modes for the 2- and 3-D foils with results from simulations. The data represented by the solid squares and open circles correspond to the $\cos(k_x x)$ $\cos(k_y y)$ components of the Fourier transform of ln(exposure) for the $k_x = k_y$ perturbation. The open diamond symbols represent the amplitude of the $\cos(k_x x)$ 2-D perturbation. Curves from the HYDRA simulations match well the time evolution of the data. The 3-D mode saturates later at a larger amplitude, consistent with our expectations. Figure 5(b) compares higher harmonics of measured growth factors in Fourier amplitude of ln(exposure) with values from the simulation of the square mode. Observe that mode (0,2) reverses sign at 3.8 ns as a consequence of mode coupling. Despite initially having different signs, the amplitudes of modes (0,2) and (2,0) tend to converge later in the nonlinear regime as the perturbation evolves toward a more symmetric shape. This dynamic evolution shows that the growth of the most symmetric 3-D shape is favored in the saturated regime.

Our results are consistent with the notion that the saturation amplitudes are a consequence of the mode shape. The calculated flow carries material away from the more spherical 3-D bubble on all sides, allowing it to transit more easily into the spike regions. The resulting faster growth for the 3-D bubble-spike pattern increases the rate of mass flow into the spikes relative to the rate at which it is consumed by ablation, allowing the 3-D square mode to achieve a larger peak amplitude.

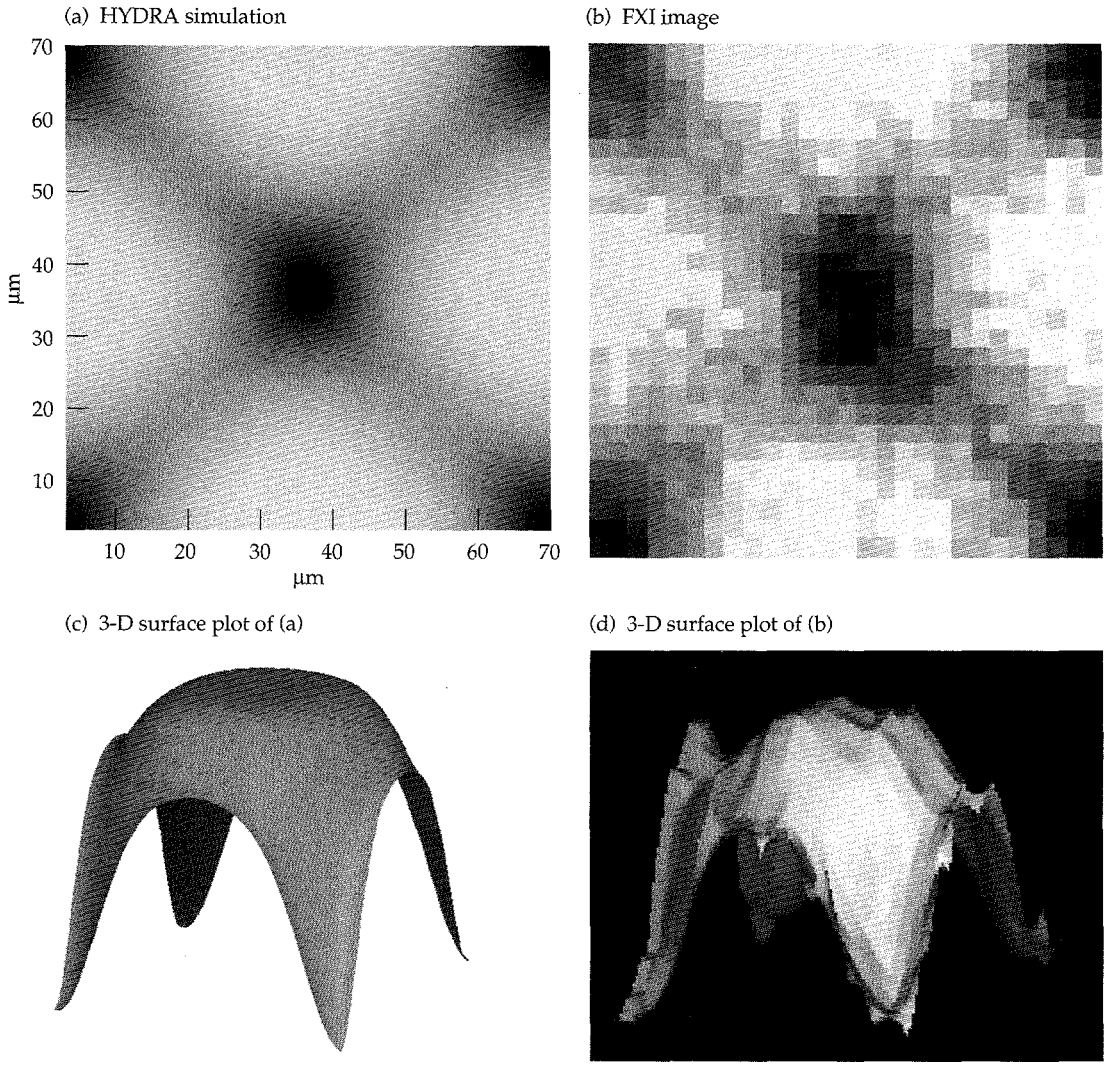

FIGURE 4. (a) Contour plot of ln(exposure) from the simulation at 4.3 ns for one period on the $k_x = k_y$ foil. Dark regions have low exposures, corresponding to high areal density. The effect of the instrument resolution function has been included. The FXI image (b) has been averaged over an area encompassing 4×4 periods on the foil. (c), (d) The same numerical and experimental results are displayed in the form of 3-D surface plots in which the height is proportional to intensity. (50-05-0595-1116pb01)

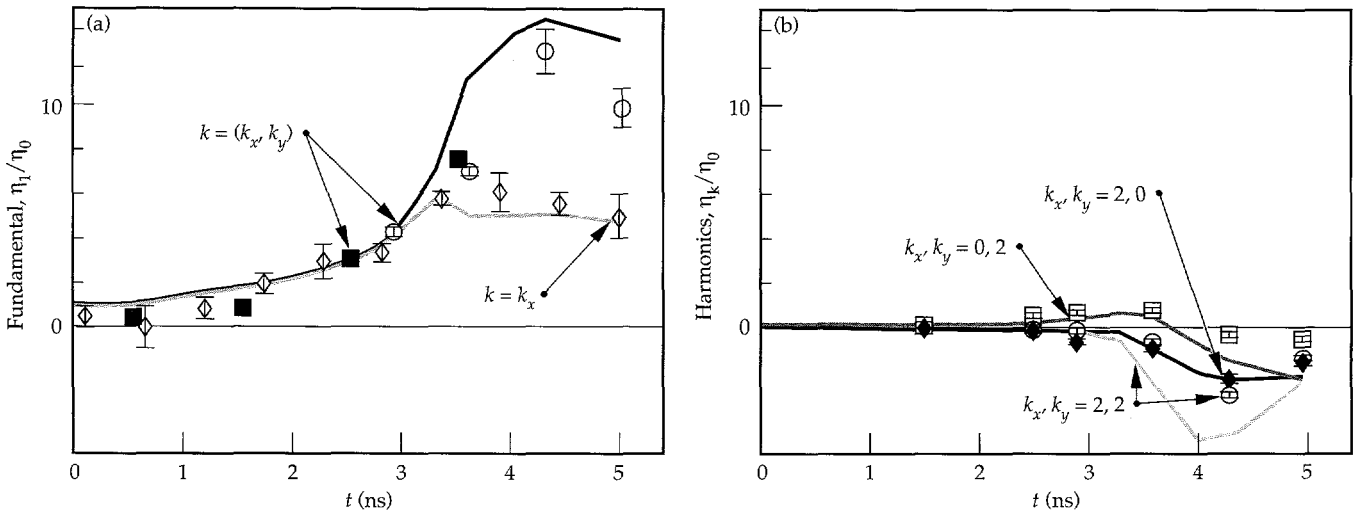

FIGURE 5. Measured and simulated perturbation Fourier amplitudes vs time, normalized to the fundamental mode amplitude at $t = 0$. (a) The solid squares and open circles represent the measured growth factor of ln(exposure) of the fundamental $k_x = k_y$ mode. The open diamonds are the same quantity for the 2-D mode. The curved lines are the corresponding results from HYDRA simulations. (b) The open circles, solid diamonds, and open squares correspond to the square-mode higher harmonics (2,2), (2,0), and (0,2), respectively. The curved lines give the corresponding simulation results. Experimental error bars represent the corresponding magnitude of the background level in Fourier space. (20-03-0395-0791pb02)

Multimode Perturbations on Planar Foils

Capsule implosion experiments currently being performed on Nova examine the growth of surface perturbations created by ablation with an excimer laser.[9] Each individual perturbation formed by the laser is in the shape of a pit. Many of these pits may be placed randomly on the capsule to create a spectrum that is random for the low-l mode numbers, but the higher modes that form the shapes of the individual pits are not randomly phased. There is some difference between the nonlinear evolution of this perturbation and that for a truly random spectrum of modes.

A planar surface that contains a number of Gaussian perturbations centered at (x_i,y_i) with amplitudes a_i each having identical widths σ is represented as

$$Z(x,y) = \sum_i a_i \exp\left\{\frac{-\left[(x-x_i)^2+(y-y_i)^2\right]}{\sigma^2}\right\}. \quad (2)$$

We consider a system with reflection symmetry across each boundary. By using the convolution theorem, we obtain the Fourier spectrum:

$$Z(k_x,k_y) = 16\pi\frac{\sigma^2}{L^2}\sum_i a_i \exp\left[\frac{-(k_x^2+k_y^2)\sigma^2}{4}\right] \times\cos(k_x x_i)\cos(k_y y_i), \quad (3)$$

where L is the foil width. For k_x or $k_y = 0$, the amplitude of the mode coefficient a_i is multiplied by 0.5 when we express the spectrum in terms of cosine modes instead of complex exponentials.

Consider two similar foils. In the first, the initial perturbation consists of a set of Gaussian bumps (all a_i positive). Figure 6(a) shows a contour plot of the initial areal density. In the second, the signs of all of the a_i are reversed, which is the corresponding pattern formed with Gaussian pits. [A contour plot for this case would be just the reverse of that shown in Fig. 6(a).] Figure 6(b) is a contour plot of the areal density at 5.0 ns, in the saturated regime, for the first case (Gaussian bump perturbations). The individual bumps have evolved into spike sheets surrounding bubbles. Figure 6(c) shows the nonlinear stage for the second case (Gaussian pit perturbations) at 4.5 ns, which also develops broad bubbles surrounded by narrow spike sheets in the nonlinear regime. This bubble-spike structure is characteristic of the nonlinear development of a random multimode foil.[10] In the saturated regime, both foils have very similar values for p–V and rms areal density. The ratio of the spike amplitude to bubble amplitude is usually taken as $1 + A$, where A is the Atwood number, which is ~1 here. We define the bubble side areal density as the rms average over all locations at which the areal density is less than the average value. For the foil with the bump perturbations, the ratio of spike side to bubble side areal density is 2 in the saturated regime, a value that is typical for random multimode perturbations as well. But the bubble-centered random Gaussian foil has an rms areal density on the bubble side essentially equal to that on the spike side in the saturated regime. This bubble amplitude is unusually large. Because of its larger bubble growth, the foil with bubble perturbations burns through first, prior to 5.0 ns for this case.

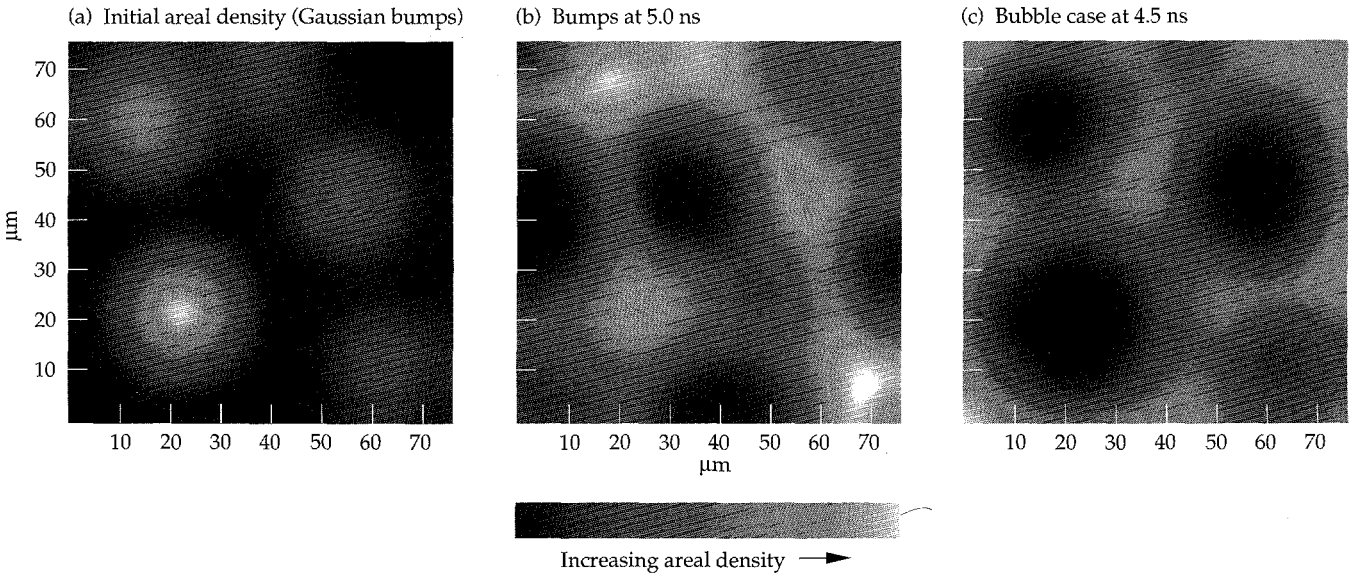

FIGURE 6. Contour plots of areal density for foils with randomly placed Gaussian perturbations. (a) Initial areal density for bumps with various amplitudes. Bumps appear as bright spots. (b) Foil with bump perturbations at 5.0 ns in the saturated regime. (c) Corresponding foil with bubble perturbations at 4.5 ns. (50-05-0595-1111pb01)

The accelerated pace at which the random bubble perturbation burns through the foil is the most significant characteristic distinguishing it from a truly random perturbation.

Next we consider a random multimode foil on which the imposed perturbation

$$\psi = \sum_{m=0}^{8} \sum_{n=0}^{8} a_{mn} \cos(mk_0 x) \cos(nk_0 y) \qquad (4)$$

consists of 80 modes with random amplitudes, yielding an initial rms perturbation amplitude of 0.61 μm rms. With a fundamental wavelength of 250 μm, the spectrum of perturbations spans the range of wavelengths most relevant to indirectly driven targets. The foil thickness is initially 50 μm.

Figure 7(a) shows a contour plot of the initial multimode-foil areal density. The simulation shows that by 2.5 ns [Fig. 7(b)], in the early nonlinear stages of the foil evolution, mode coupling has caused broadening of the bubbles and the formation of narrow spike sheets. Areal density contours calculated with the Haan second-order mode-coupling theory[11] are in good agreement with those from the simulation in the early nonlinear stage. At this time the perturbations still bear some resemblance to those initially on the foil. By 4.0 ns [Fig. 7(c)], strongly nonlinear interactions lead to increased average width of the features. This process is termed *bubble merger* in physical space or *inverse cascade* in Fourier space.

Layzer[12] derived the terminal-rise velocity of a bubble in a semi-infinite incompressible fluid: $u_b = a(g\lambda)^{1/2}$. The Froude number a is 0.23 for a 2-D bubble and 0.36 for a round 3-D bubble. Larger bubbles have less kinematic drag per unit volume, so bubble expansion in the nonlinear regime leads to increasing bubble rise velocities. When driven far enough into the nonlinear regime, substantial displacements develop between bubbles in the longitudinal direction due to the spread in their rise velocities. Some displacement is already apparent in Fig. 8(a), which shows the isodensity

(a) Initial areal density (b) 2.5 ns areal density (c) 4.0 ns areal density

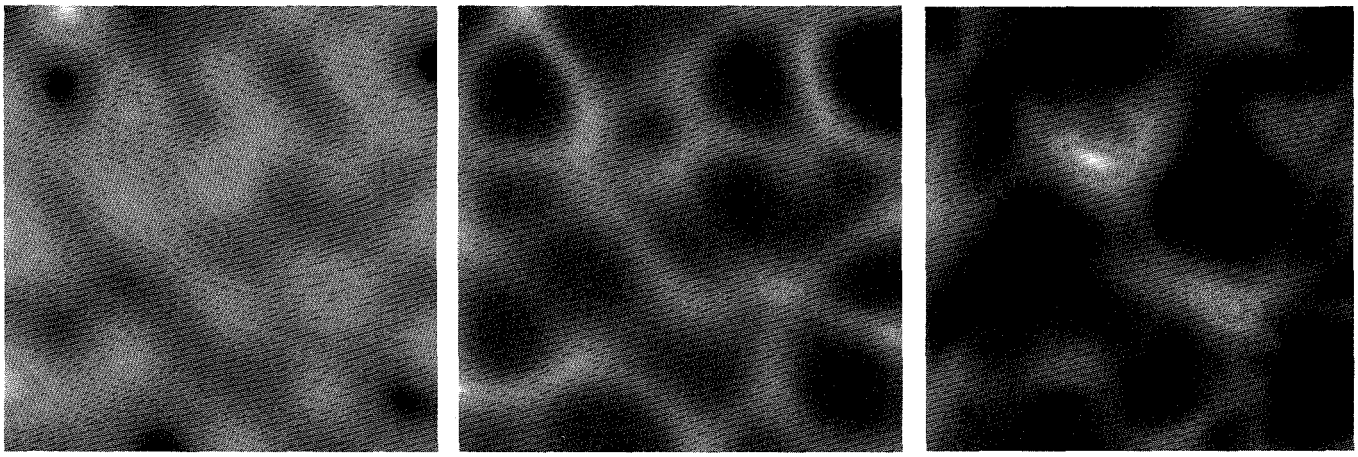

FIGURE 7. Areal density for random multimode foil (a) initially, (b) at 2.5 ns, and (c) at 4.0 ns. Bumps appear as bright spots. (50-05-0595-1112pb01)

FIGURE 8. (a) Three-dimensional plot of 0.75 g/cm^3 density surface at 2.5 ns. View is of the side of the foil ablated by x rays. (b) The 0.3 g/cm^3 density surface at 3.0 ns. View is of bubbles on the side of the foil away from the x-ray source. (50-05-0595-1113pb01)

(a) 2.5 ns isodensity surfaces (b) 3.0 ns isodensity surfaces

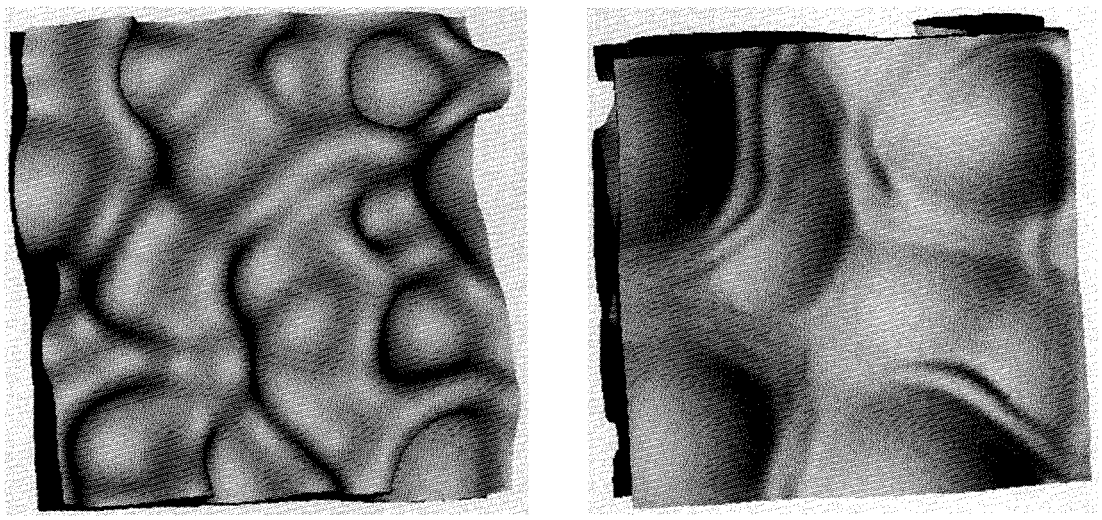

surface $\rho = 0.75$ g/cm^3 at 2.5 ns, early in the nonlinear stage. As this longitudinal displacement increases, the bubbles tend to expand laterally to fill the available space. As they move ahead of the others, the tips of the largest bubbles become round, minimizing drag and yielding the highest rise velocity. The isodensity surface shown in Fig. 8(b) shows that the largest bubbles have advanced farthest toward the back side of the foil at 3.0 ns. These bubbles are already much broader than the features of the initial foil perturbation.

Figure 9 plots the Fourier spectrum at 0, 2.5, and 4.0 ns. By 2.5 ns, the spectrum peaks at the wave number having the highest linear growth rate. Mode coupling has driven up higher harmonics. By 4.0 ns, the inverse cascade is apparent as the peak of the spectrum shifts to lower wave numbers. The spectrum has the appearance of a turbulent form, with mode coupling transferring spectral power that originates from the growth of moderate wavelengths to shorter, ablatively stabilized wavelengths and to very long wavelengths. There is little change in the ablatively stabilized portion of the spectrum (above 5000 cm^{-1}) during the saturated phase of evolution, after 3.0 ns.

We used the Haan saturation model to predict rms amplitudes of bubbles and spikes in the weakly nonlinear regime arising from isotropic random multimode perturbations.[13] In the model, individual modes grow exponentially in the linear regime until the modal saturation amplitude v/Lk^2 is attained. Then the mode growth changes to secular. Rms bubble and spike amplitudes are obtained by summing modal amplitudes in quadrature. A value of $v = 2$ is generally used for the saturation parameter. As shown in Fig. 10, the departure of the rms bubble growth from linear theory in the simulation initially resembles the model predictions for $v = 1$. The simulated bubble areal density soon rolls over because of burn-through of the foil, which is not accounted for in the saturation model. Since the foil is initially only 50 μm thick, thin-foil effects appear to have an influence on the saturation amplitude. Perturbation growth continues in low-density regions, and thus contributes little to perturbed areal density. Despite thin-foil effects, the onset of saturation is still roughly consistent with the prediction of the Haan saturation model. This increases our confidence that the model can be used to predict rms perturbation amplitudes in the weakly nonlinear regime.

Capsule Implosion Simulations

The experimental program on Nova is beginning to examine instability growth on capsules that have pits ablated at the 92 positions corresponding to the vertices and face centers of the pattern on a soccer ball.[9] The shape of an individual pit has been characterized experimentally as a superGaussian function

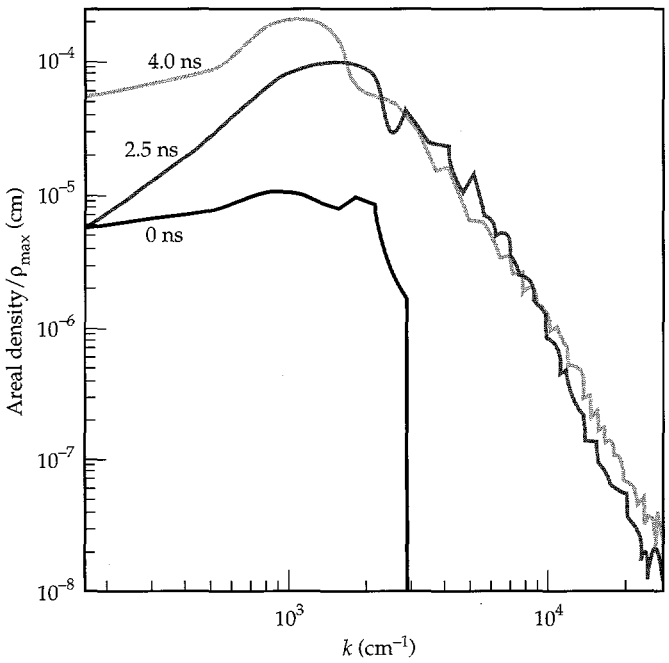

FIGURE 9. Fourier spectra of mode amplitudes vs mode number for multimode foil at 0, 2.5, and 4.0 ns. (50-05-0595-1114pb01)

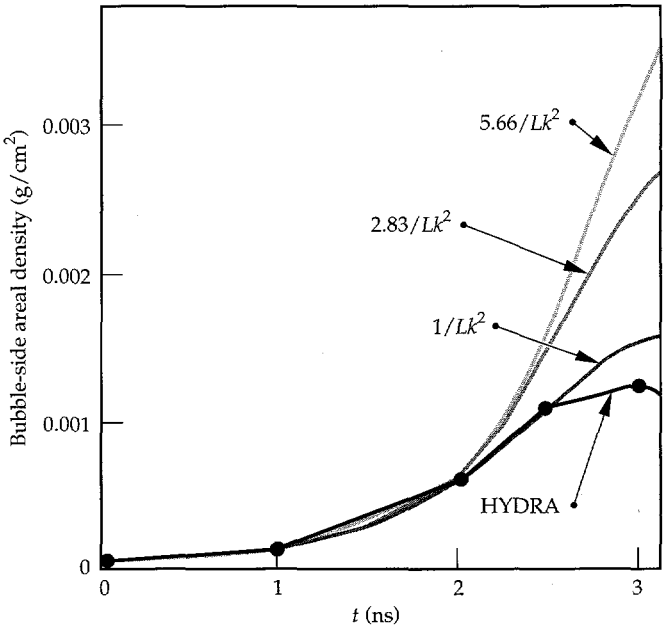

FIGURE 10. The symbols on the solid black line represent the bubble-side rms areal density for the multimode foil calculated with HYDRA. The gray-tone curves represent the bubble-side areal density predicted by the Haan saturation model for three values of the saturation parameter. After 2.5 ns, the values from the simulation begin to roll over because of the effect of finite foil thickness, which is not accounted for in the saturation model. (50-05-0595-1115pb01)

$\psi(r) = -a_0 e^{-(r/\sigma)3}$ in the radius r, with a_0 the pit depth, and $\sigma = 28$ μm. The overall surface perturbation resulting from these 92 pits can be expressed in terms of the spherical harmonics Y_{lm}:

$$G(\theta,\phi) = \sum_{i=1}^{92} \sum_{l>1}^{\infty} a_l \frac{4\pi}{2l+1} \sum_{m=-l}^{l} Y_{lm}(\theta_i', \phi_i') Y_{lm}(\theta,\phi) , \qquad (5)$$

where a_l is the coefficient of the Legendre polynomial P_l in an expansion for an individual pit:

$$a_l = \frac{2l+1}{2} \int_0^{\pi} P_l(\cos\theta) g(\theta) \sin\theta \, d\theta \quad . \qquad (6)$$

Here $g(\theta)$ is the shape function for an individual pit expressed in polar coordinates. For the soccer ball pattern, most of the perturbation is contained in spherical harmonics with $l = 16, 18$. Capsules can also be created with one hemisphere of the pattern rotated by 36° so that the perturbation is reflection-symmetric about the equator. This modification has a minor impact on the mode structure and the spacing between pits. This geometry is treated exactly by simulating 1/20 of a sphere over a region extending from the pole to the equator and 36° in the azimuthal angle. Symmetry boundary conditions are applied at the transverse boundaries.

The Nova capsules simulated have a fuel region 220 μm in radius containing equimolar amounts of H and D. The fuel is bounded by a 3-μm-thick polystyrene mandrel, which is surrounded by a 3-μm layer of polyvinyl alcohol (PVA) and 39 μm of Ge-doped polystyrene ablator. We first consider a capsule having pits 0.25 μm deep on the outer surface. As the capsule shell accelerates inward, the solid angle occupied by each pit remains essentially constant while it grows into the shell. At the onset of deceleration, isolated bubbles of fuel begin to rise into the shell at the locations of the initial pits, where the fuel column density is lowest, while interconnected sheets of pusher material surrounding these bubbles fall inward. Concurrently, the amplitude of the bubbles on the outer surface begins to decrease. Since the Atwood number at the fuel–pusher interface is ~0.4 at this time, shear leads to a Kelvin–Helmholtz instability, causing the material interface to roll up at the tips of the fuel bubbles. The characteristic "hammerhead" shapes are visible in Fig. 11, a plot of the $\rho = 18$ g/cm^3 isodensity surface at 2.1 ns. The asymmetric shape of the roll-up, localized near the bubble tip, is due to the bubble-like shape of the initial perturbations. Fuel entrained into the rising bubbles is relatively cool, having temperatures of ~400–500 eV. Thus significant neutron production arises only from the center of the hot spot in regions that are many micrometers from spike material. For this 0.25-μm initial perturbation amplitude, the neutron yield is 82% of that obtained with no perturbation. Most of the neutron production has occurred before 2.1 ns.

Simulations have been performed for a range of initial perturbation amplitudes spanning 0.25–2.5 μm p–V. For each of these cases, the perturbation of the fuel–pusher interface becomes nonlinear quite soon after it encounters the first rebounding shock. During the first 100 ps of deceleration, the average bubble rise velocity, defined relative to the interface motion in the unperturbed simulation, exceeds the Layzer asymptotic rise velocity for an axisymmetric bubble in a semi-infinite fluid $0.36(g\lambda)^{1/2}$. The differences between the bubble rise velocities obtained from the simulations and from the Layzer formula increase with the initial perturbation amplitude, becoming substantial for capsules with the larger perturbations. These differences are similar in magnitude to the estimates of linear growth rates for the Richtmyer–Meshkov instability induced by the passage of the first rebounding shock. For example, with an initial 1.25-μm-deep perturbation, the average bubble rise velocity during the first 100 ps of deceleration is 89 μm/ns. The calculated

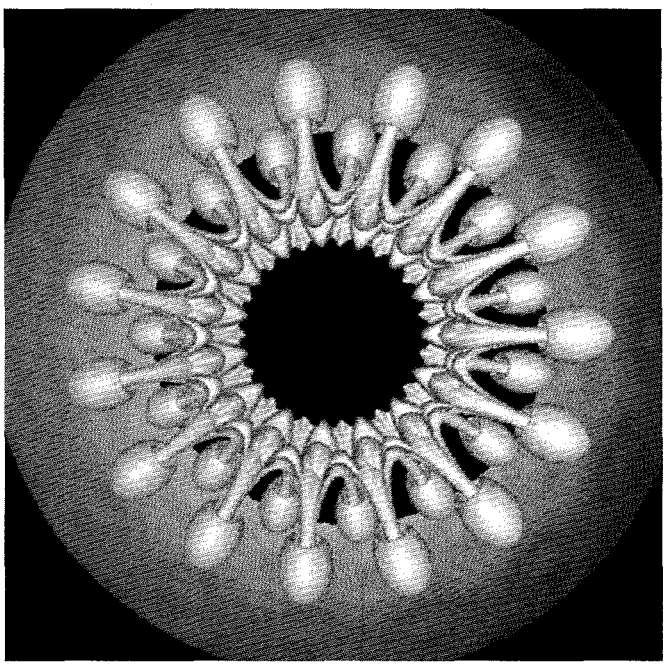

FIGURE 11. Three-dimensional plot of isodensity surface for $\rho = 18$ g/cm^3 at 2.1 ns for a Nova capsule with a "soccer ball" perturbation on its exterior. The initial pit depth is 0.25 μm. Contours are shown over a subset of a hemisphere near the equator. The outer shell is near the ablation region, while the inner surface shown corresponds to the fuel–pusher interface. (50-05-0595-1118pb01)

Layzer rise velocity is 40 μm/ns, and the estimated Richtmeyer–Meshkov growth rate due to the first rebounding shock is 56 μm/ns.

Bubble rise velocities are also affected by spherical convergence, expansion of the rising bubbles, finite shell thickness, and the rise through multiple fluid layers. Further increases are seen later in the bubble rise velocities during a period when they encounter a reflected shock rebounding from the center. The Richtmyer–Meshkov instability clearly has a substantial impact on the perturbation growth during deceleration, particularly on the less massive bubbles. For perturbations in the nonlinear regime, the shocks appear to have a less pronounced effect on growth of the more massive spikes.

As discussed earlier, for a given wavelength a perturbation in the shape of an axisymmetric bubble is able to penetrate the capsule shell fastest. For an initial bubble depth of 2.5 μm, the bubble growth in the ablation layer is sufficient to burn through the capsule by the onset of deceleration. As the capsule material ahead of the bubble thins, the bubble tip accelerates inward, forming a highly elongated shape. Doped polystyrene ablator penetrates the PVA and mandrel layers, which are more dense at that time. The resulting spikes of pusher material encounter the rebounding shock ~50 ps sooner than does the fuel–pusher interface in the corresponding unperturbed simulation. The trajectory that the unperturbed interface would follow in the absence of deceleration is termed the fall line. For this large perturbation amplitude, the spike penetrates farther inward, approaching the center of the capsule sooner than the fall line. The neutron production rate is greatly reduced once the spike approaches within several micrometers of the center of the hot spot. Overall neutron yield is only 7.8% of the value obtained for the unperturbed capsule. Nova capsule simulations show perturbation growth causing a large yield degradation only when a spike of pusher material crashes into the center of the hot spot during the period of peak neutron production.

Summary

We examined 3-D growth of ablative hydrodynamic instabilities for a variety of indirectly driven targets. All cases simulated show linear growth rates that are independent of mode shape. For a single-mode rectilinear perturbation of a given wave number, the 3-D square mode, which is most symmetric, saturates at the largest amplitude. We verified this for indirectly driven foils through simulation and experiment. Differences in the nonlinear evolution of foils due to perturbation shape are in good quantitative agreement with predictions of the simulations. Of all perturbation shapes, an axisymmetric bubble will burn through a foil the fastest. An isolated axisymmetric spike will attain the largest areal density amplitude.

We simulated a random multimode foil containing perturbations spanning the range of wavelengths of interest for indirect drive. Early in the nonlinear regime, the multimode foil forms broad bubbles and narrow spikes consistent with second-order mode-coupling theory. The onset of multimode saturation is found to be roughly consistent with the prediction of the Haan saturation model. Later, strongly nonlinear interactions lead to an increase in the average width of features. The largest bubbles rise the fastest and continue to grow broader than the initial perturbations.

Simulations of the "soccer ball" capsule show that the positions initially occupied by pits are where fuel bubbles rise during the deceleration phase. A secondary instability at the fuel–pusher interface leads to roll-up at the tips of these bubbles. Most of the neutron production originates in regions that are several micrometers away from any spikes of pusher material. In Nova capsules, mix causes a large reduction in yield only when a spike of pusher material crashes into the capsule center during the time of peak neutron production.

Notes and References

1. R. D. Richtmeyer, *Commun. Pure Appl. Math.* **13**, 297 (1960); E. E. Meshkov, *Izv. Akad. Nauk SSSR, Mekh. Ahidk. Gaza* **5**, 151 (1969); and G. Dimonte and B. Remington, *Phys. Rev. Lett.* **70**, 1806 (1993).
2. J. D. Lindl and W. C. Mead, *Phys. Rev. Lett.* **34**, 1273 (1975).
3. J. W. Jacobs and I. Catton, *J. Fluid Mech.* **187**, 353 (1988), and J. W. Jacobs and I. Catton, *J. Fluid Mech.* **187**, 329 (1988).
4. J. P. Dahlburg and J. H. Gardner, *Phys. Rev. A* **41**, 5695 (1990).
5. Y. T. Lee and R. M. More, *Phys. Fluids* **27**, 1273 (1984).
6. R. J. Ellis, J. E. Trebes, D. W. Phillion, J. D. Kilkenny, et al., *Rev. Sci. Instrum.* **61**, 2759 (1990); B. A. Remington, S. G. Glendinning, R. J. Wallace, S. Rothman, and R. Morales, *Rev. Sci. Instrum.* **63**, 5080 (1992); B. A. Remington and R. I. Morales, *Rev. Sci. Instrum.* **66**, 703 (1995).
7. K. S. Budil, T. S. Perry, P. M. Bell, P. L. Miller, et al., "The Flexible X-Ray Imager," Lawrence Livermore National Laboratory, Livermore, CA, UCRL-JC-120837 (1995).
8. B. A. Remington, S. V. Weber, M. M. Marinak, S. W. Haan, et al., *Phys. Plasmas* **2**, 241 (1995).
9. R. J. Wallace, R. L. McEachern, and W. W. Wilcox, *ICF Quarterly Report* **4**(3), 79, Lawrence Livermore National Laboratory, Livermore, CA, UCRL-LR-105821-94-3 (1994).
10. M. J. Dunning and S. W. Haan, *ICF Quarterly Report* **3**(4), 179, Lawrence Livermore National Laboratory, Livermore, CA, UCRL-LR-105821-93-4 (1993).
11. S. W. Haan, *Phys. Fluids B* **3**, 2349 (1991).
12. D. Layzer, *Astrophys. J.* **122**, 1 (1955).
13. S. W. Haan, *Phys. Rev. A* **39**, 5812 (1989).

PROGRESS TOWARD A PROTOTYPE RECIRCULATING ION INDUCTION ACCELERATOR

A. Friedman *H. C. Kirbie* *W. M. Sharp*

J. J. Barnard *B. G. Logan* *T. J. Fessenden*[†]

M. D. Cable *S. M. Lund* *D. L. Judd*[†]

D. A. Callahan *L. A. Nattrass* *S. Eylon*[*]

F. J. Deadrick *M. B. Nelson* *H. A. Hopkins* [‡]

D. P. Grote *M. A. Newton* *D. B. Longinotti*[**]

V. P. Karpenko *T. C. Sangster*

Introduction

The U.S. Inertial Fusion Energy (IFE) Program is developing the physics and technology of ion induction accelerators, with the goal of electric power production by means of heavy ion beam–driven inertial fusion (commonly called heavy ion fusion, or HIF). Such accelerators are the principal candidates for inertial fusion power production applications, because they are expected to enjoy high efficiency, inherently high pulse repetition frequency (power plants are expected to inject and burn several fusion targets per second), and high reliability. In addition (and in contrast with laser beams, which are focused with optical lenses) heavy-ion beams will be focused onto the target by magnetic fields, which cannot be damaged by target explosions. Laser beams are used in present-day and planned near-term facilities (such as LLNL's Nova and the National Ignition Facility, which is being designed) because they can focus beams onto very small, intensely illuminated spots for scaled experiments and because the laser technology is already available.

LLNL has participated in HIF research since its inception and has worked on HIF target physics and fusion-chamber beam-propagation physics, accelerator physics and technology, and advanced power-plant concepts. Here we discuss a newly initiated experimental effort aimed at developing a low-cost approach to high-current heavy-ion acceleration, based on recirculation of the ion beams.

An induction accelerator works by passing the beam through a series of accelerating modules, each of which applies an electromotive force (emf) to the beam as it goes by; effectively, the beam acts as the secondary winding of a series of efficient one-turn transformers. Each of these transformers requires a sizable ferromagnetic toroid, or core. The cores must be large enough to sustain enough volts of emf for long enough to impart the required impulse to the entire beam. In the recirculating induction accelerator, or recirculator, the beam is repeatedly passed through the same set of accelerating cores and focusing elements, thereby reducing the length of the accelerator and the number of cores and magnets required. In a recirculator, it is not necessary to accelerate the beam quickly to minimize length and cost, as is the case in a linear accelerator, or linac; acceleration can be more gradually, over many laps, and this allows the cores to be made smaller and less expensive (the required voltage is lower). This promises a very attractive driver cost if the technical challenges associated with recirculation can be met.

The recirculator concept as it applies to an ICF driver was presented in two previous *ICF Quarterly* articles,[1–2] and elsewhere[3]; another recent article[4] describes LLNL's work on a pulse modulator for use in a recirculator. Figure 1 shows an artist's conception of an IFE power plant driven by an induction recirculator.

We present plans for and progress toward the development of a small (4.5-m-diam) prototype recirculator, which will accelerate singly charged potassium ions

[†]Lawrence Berkeley Laboratory, Berkeley, California
[*]Titan Beta, Dublin, California
[‡]U. C. Berkeley, Berkeley, California
[**]EG&G, Inc., Pleasanton, California

(atomic weight 39 u) through 15 laps, increasing the ion energy from 80 to 320 keV and the beam current from 2 to 8 mA. Beam confinement and bending are effected with permanent-magnet quadrupoles and electric dipoles, respectively. The design is based on scaling laws and on extensive particle and fluid simulations of the behavior of the space charge–dominated beam. The dimensionless beam dynamics parameters were chosen to resemble those of a driver; the experiments should serve to validate major elements of the recirculator concept.

This Small Recirculator is being developed in a build-and-test sequence. An injector and matching section are operational, and we are already investigating intense-beam transport in a linear magnetic channel. Near-term plans include studies of space charge–dominated beam transport around a bend. Later we will study insertion and extraction of the beam into and out of the ring, and acceleration with centroid control. The ultimate goal is demonstration of flexible recirculator operation.

In contrast with conventional rf-driven accelerators, the beam in the Small Recirculator experiments is space-charge dominated. That is, the transverse force balance is a near-cancellation of the applied confining force and the beam's self-induced electrostatic expanding force; thermal pressure plays only a minor role. Effectively, the beam is a non-neutral plasma in nearly laminar flow. The fully operational Small Recirculator will confine and accelerate many more ions than a conventional circular accelerator of this scale and beam energy.

Recirculator Concept

A recirculating induction accelerator is expected to cost considerably less than a conventional ion-induction linac. The overall accelerator length is reduced—by a factor of ~2 to 3, to about 3.6 km (and possibly shorter) in the "C-design" recirculator of Ref. 3. The accelerating cores are smaller, because acceleration can be slower. Research on recirculator drivers has centered on four-beam multi-ring designs, in which each ring increases the beam's energy by an order of magnitude over 50 to 100 laps. In contrast with most HIF induction linac concepts,[5] recirculator designs considered to date do not use beam merging. Hybrid designs (with a recirculator at the low-energy end and a linac at the high-energy end) are also possible and may prove attractive.

The beam-dynamics issues that must be resolved before a recirculating driver can be built include centroid control, longitudinal control, and beam insertion and extraction. Beam compactness must be preserved throughout, so that the beam can eventually be focused onto a small spot. The critical measure in this context is compactness in the 6-D phase space of particle positions and velocities. Accelerator researchers commonly use a measure of compactness called emittance, which is the area occupied by the beam in a two-dimensional projection of that 6-D phase space. For example, the horizontal transverse emittance ε_x is the area occupied by particles in the space (x,x'), where x is the horizontal coordinate normal to z (the mean direction of beam motion) and x' is the velocity along that coordinate normalized to the velocity along z, *i.e.*, the angle between a particle's velocity and the local mean velocity. For many purposes the normalized emittance $\varepsilon_n = \beta\gamma\varepsilon$ is used, where β is the particle speed normalized to the speed of light and $\gamma = (1 - \beta^2)^{-1/2}$. The normalized emittance enjoys the property of being conserved during acceleration if no nonlinear (with respect to the individual coordinates) forces act on the beam. Of course, some nonlinearity is always present in real accelerators, so some emittance growth will in general occur, but the concept of normalized emittance remains useful.

As described below, beam-dynamics issues can be addressed at reduced scale in a small prototype recirculator. The waveform generators in a driver must supply variable accelerating pulses at repetition frequencies of

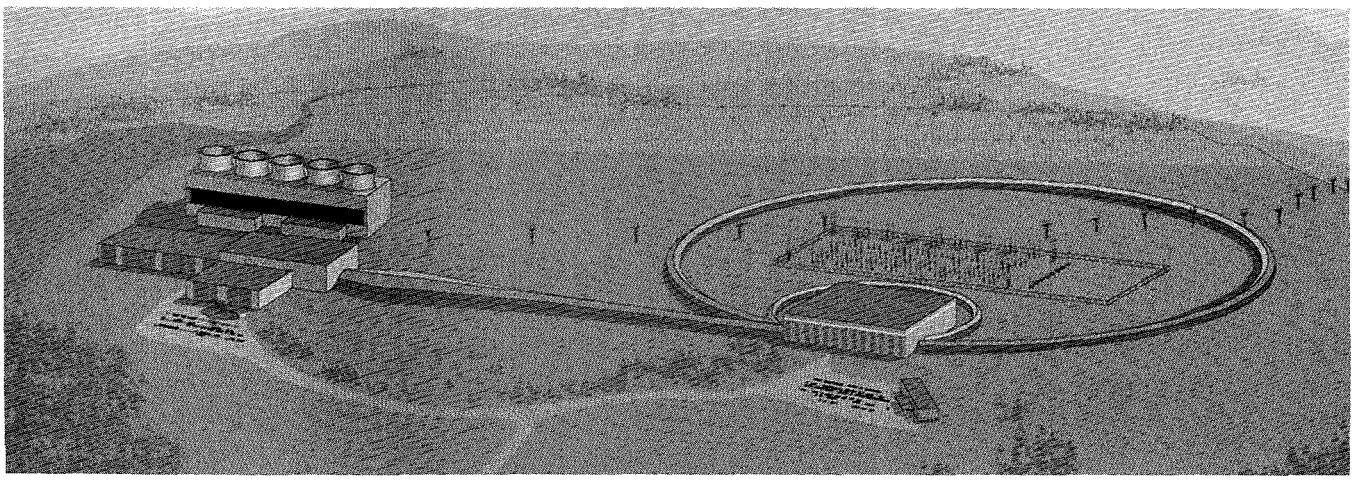

FIGURE 1. Artist's rendering of recirculator-driven power plant. (05-00-1194-3846pb03)

~50 kHz and must supply accurate time-varying dipole fields with good energy recovery. These requirements are challenging, but advances in solid state power electronics should make it possible to meet them through a technology development program. Present technology has achieved 200-kHz bursts at 5 kV and 800 A with pulse durations of 0.5 to 2 ms, but with a nonvariable format.[6] Because of its long (~200 km) beam path length, and because the beam repeatedly visits each section of the beam line, a recirculator driver will require a vacuum of $\sim 10^{-10}$ to 10^{-11} Torr.

Design of the Small Recirculator

LLNL is developing a small prototype ion recirculator in collaboration with LBL, EG&G, and Titan-Beta. This Small Recirculator will be assembled and operated as a series of experiments over several years. Figure 2 illustrates the overall physics design of the Small Recirculator and lists some of the elements that must all work together in the Small Recirculator and in a full-scale fusion driver.

The Small Recirculator will have a circumference of 14.4 m, a 3.5-cm aperture (pipe) radius for the beam-confining (commonly called focusing) and beam-bending elements, and a 72-cm lattice period (segment of the repetitive lattice of focusing and bending elements). The beam will be transversely confined by permanent-magnet quadrupole lenses with a field of ~0.294 T at the pipe wall, and will be bent with electric dipole deflector plates. These quadrupoles and dipoles will each physically occupy about 30% of the axial lattice length, and the full recirculator ring will consist of 40 half-lattice periods, including one or two periods using special large-aperture quadrupole magnets through which the beam will be inserted and/or extracted. The fundamental building block is actually the 36-cm half-lattice period, but the polarity of the quadrupole lenses is reversed in each alternate half-lattice period; this provides so-called alternating-gradient or strong focusing as in most modern particle accelerators.

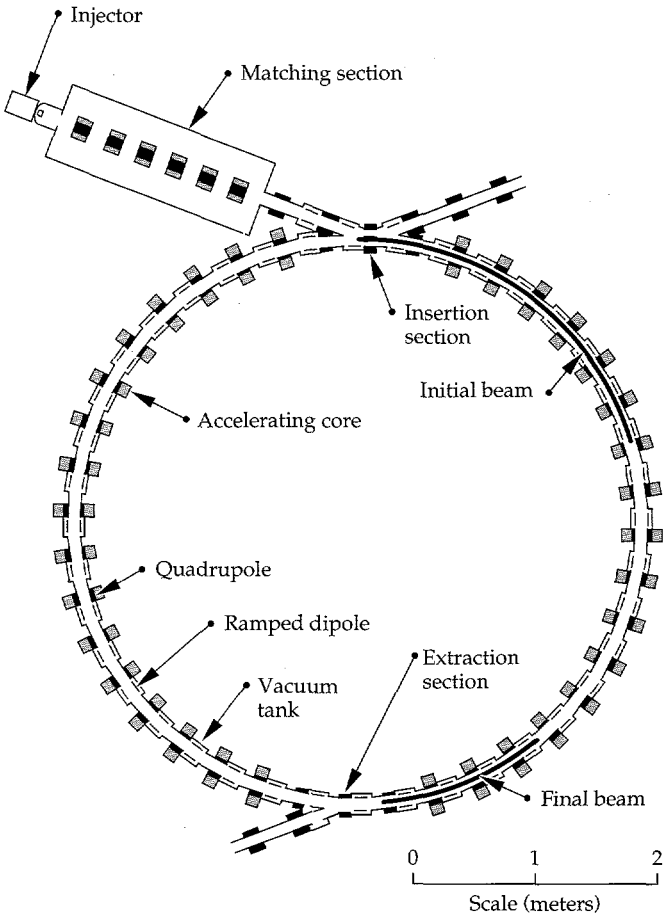

FIGURE 2. Final configuration of the Small Recirculator.
(30-00-0695-1644pb01)

The K^+ beam ions will be accelerated from an initial kinetic energy of 80 keV to 320 keV over 15 laps by 34 induction cores (no induction cores will be present in the lattice periods where the beam is inserted and extracted). The initial beam current will be 2 mA, corresponding to a line-charge density of 3.6 nC/m and a characteristic beam radius of 1.1 cm, and the initial pulse duration will be 4 μs. After 15 laps of acceleration, the beam current will have increased to 8 mA, the line-charge density will be 7.21 nC/m, the average beam radius will be 1.3 cm, and the pulse duration will be 1 μs.

Because the quadrupole magnets provide a transverse restoring force to confine the beam, the beam centroid will, if displaced off-axis, oscillate back and forth across the centerline of the beam pipe. Over a full oscillation, the phase of the displacement will sweep through 360°. The initial phase advance of these "betatron oscillations" per lattice period of beam motion will be $\sigma_0 = 78°$. Thus a beam-centroid oscillation will require $360°/78° \approx 4.6$ lattice periods, or about 4.6/20 = 23% of the circumference of the ring. Individual particles also execute betatron oscillations back and forth within the confines of the beam, but the frequency of these oscillations is lower than the "undepressed" frequency because the net focusing force is reduced by the repulsive effects of space charge, which (if unopposed) would blow up the beam. Initially, the net effect is a phase advance depressed to $\sigma = 16°$ by space charge. After 15 laps of acceleration, the phase advances will decrease to $\sigma_0 = 45°$ and $\sigma = 12°$. These parameters were chosen to resemble those of a driver-scale recirculator, although of course the latter would have many more betatron oscillations per lap.

Because the heavy-ion beam in the Small Recirculator is nonrelativistic and accelerating, obtaining the variable-format accelerating and bending waveforms will be technologically challenging. Those waveforms will require the accurate synthesis of detailed voltage pulses with repetition rates rising from about 40 kHz at the

initial beam energy to 90 kHz at the final beam energy.[4,7] The voltage pulses for the electric dipoles must be correctly ramped in concert with the increasing beam energy. Properly shaped "ear" pulses must be applied at the beginning and end of the main pulses to provide longitudinal confinement, and lap-to-lap variation of the pulse duration and shape must be added to the accelerating waveforms to maintain or decrease the beam length.

To switch the beam into or out of the ring, time-varying dipole (bending) fields must be applied. Transverse confinement of the beam must be carried out during insertion or extraction. Our design uses a permanent-magnet quadrupole with an expanded aperture. Figure 3 shows the physics design of the insertion/extraction section. The main ring runs along the lower part of the figure; the insertion line (which brings the beam from the matching section into the ring) comes in from the upper left, and the extraction line runs toward the upper right. The beam trajectory is shown as it will appear during extraction.

Mechanical design of the Small Recirculator was challenging because of the necessity of fitting bending, focusing, and accelerating elements, as well as provisions for vacuum pumping and beam diagnostics, into each half-lattice period. Figures 4 and 5 show the nearly complete computer-aided design, as rendered by the CAD software.

Recirculator Modeling

Because the space charge–dominated beams in an induction accelerator are effectively non-neutral plasmas, theoretical and computational modeling of these beams is carried out using techniques related to those used in the accelerator and plasma physics communities. Models used range from simple zero-dimensional codes based on analytically derived scaling relations, through fluid- and moment-equation simulations, up to large and elaborate discrete-particle simulations.

The CIRCE code[8] is a multidimensional model that solves an envelope equation (evolving moments such as centroid position and transverse extent) for each of a number (typically a hundred or greater) of transverse beam "slices," each at different longitudinal positions. The longitudinal dynamics of the beam is modeled by evolving the positions and velocities of the slices using fluid equations. CIRCE is used to assess alignment tolerances, accelerating schedules, and steering techniques in linacs and recirculators. It is useful for any application in which the evolution of the detailed internal degrees of freedom of the beam (e.g., emittance growth processes) need not be resolved; at present, beam normalized emittance is assumed constant in CIRCE.

Because the beam resides in the accelerator for relatively few plasma oscillation periods, particle-in-cell

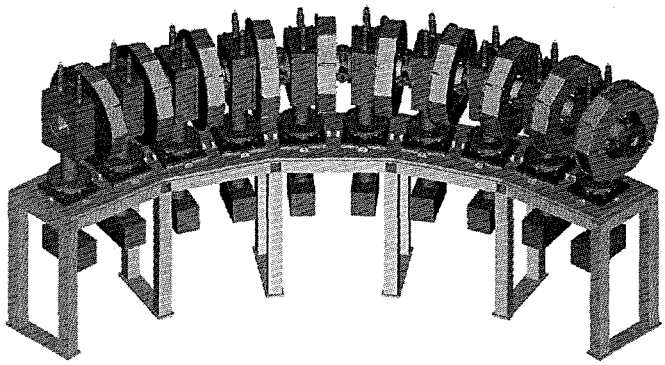

FIGURE 4. One-quarter of the Small Recirculator (CAD rendering). (30-00-0695-1649pb01)

FIGURE 3. Insertion/extraction section. (30-00-0695-1646pb01)

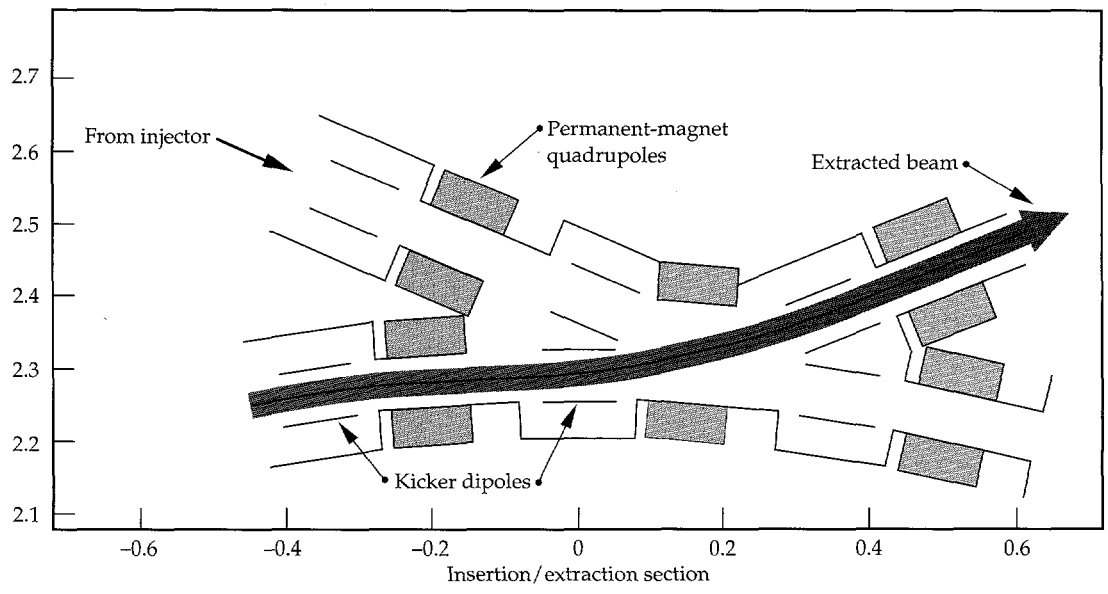

(PIC) simulation techniques are especially effective and have been invaluable in the design and analysis of experiments and in the prediction of the behavior of future machines. The WARP code includes fully three-dimensional (WARP3d)[9] and axisymmetric (WARPrz)[10] PIC simulation models. WARPrz is used for long-term beam dynamics studies, including the effects of accelerating module impedance. WARP3d is heavily used for "near–first principles" studies of accelerator elements and experiments.

Several novel techniques make WARP3d both accurate and efficient. These include capabilities for subgrid-scale placement of internal conductor boundaries and for simulating "bent" accelerator structures, as well as a technique for rapidly following particles through a sequence of sharp-edged accelerator lattice elements, using a relatively small number of time steps while preserving accuracy. On some problems, WARP3d is run in a quasi-steady state mode, which permits the completion of a 3-D run in just a few minutes of computer time; this makes it suitable for iterative design calculations. The ultimate goal of this code development is effective simulation of present-day experiments and of an HIF driver, from the source through the final focus, with a link from WARP into the codes used to model propagation in the fusion chamber and ultimately into the target design codes.

A number of other PIC codes employ a "slice" description of the beam (assuming slow variation of quantities along the beam); much application, as well as detailed studies of the properties of such PIC models of beams and plasmas, has been carried out.[11]

Emittance growth can result from the nonuniform distribution of beam space charge resulting from the action of centrifugal forces. As revealed in particle simulations using WARP3d[9] and interpreted theoretically,[12] growth occurs at changes in the accelerator's curvature where the distribution of beam particles relaxes toward a new equilibrium. A circular recirculator is therefore to be preferred over one with an elongated "racetrack" shape. Since the Small Recirculator is effectively circular (the changes of curvature that occur within a single half-lattice period are too rapid to matter), the only significant changes in curvature occur during insertion and extraction. The electric dipoles also introduce field aberrations. Detailed 3-D simulations show that proper shaping of the dipole plates should render the beam distortion minimal. We have studied the behavior of the beam in the Small Recirculator in some detail using CIRCE and WARP. A measurable amount of emittance growth is expected to take place over the 15 laps, mostly in the first two laps.[13]

Here we show the results of a WARP3d simulation of the beam in the Small Recirculator. For reasons of economy, the simulated beam is often made shorter than the actual beam will be. Figure 6 shows top and side views of the beginning of the simulation; the final

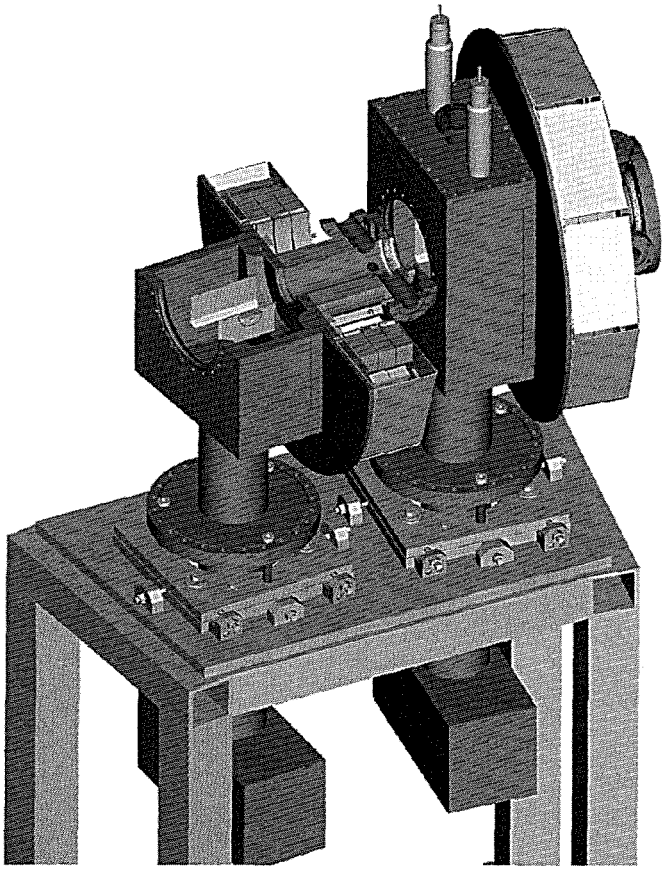

FIGURE 5. Two half-lattice periods of the Small Recirculator (CAD rendering). The top of the left-hand half-lattice period is cut away to reveal the internal structure. (30-00-0695-1650pb01)

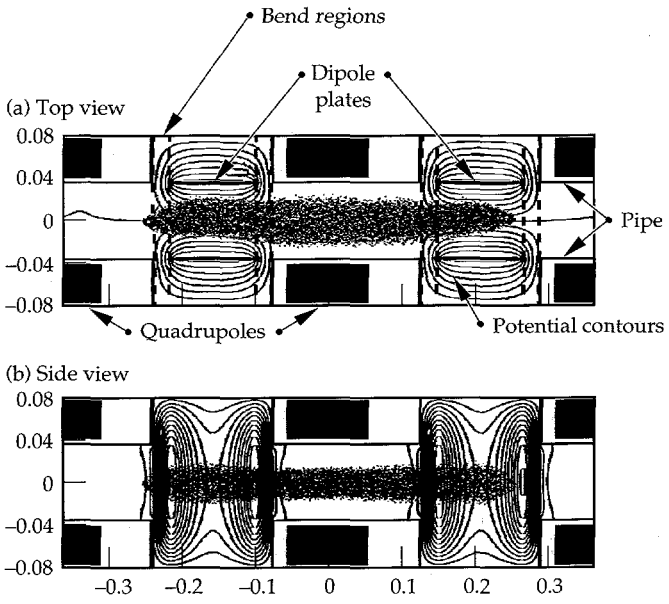

FIGURE 6. Top and side views of Small Recirculator beam simulated using WARP3d. "Bends" are shown straightened. (30-00-0695-1656pb01)

beam is very similar. Figure 7 shows the evolution of the emittance at mid-pulse; in this case, the beam length is kept roughly constant. After the initial jump arising from the transition to the bent lattice, there is little emittance growth over the 15 laps.

Experiment Plans

Linear experiments now getting under way will measure space charge–dominated beam quality after transport through a permanent-magnet quadrupole lattice, characterize the beam before injection, provide a test bed for diagnostic development, and afford a preliminary assessment of the role of electrons in magnetic beam transport (see Fig. 8).

The next experiments will study beam transport around a bend of order 90° (at first without any accelerating modules). The transition of the beam from a straight transport line into the ring will represent a change of curvature, and will allow us to study the resulting emittance growth. Emittance growth can also result from imperfections in the focusing and bending fields; the small imperfections expected in our experiments will be well characterized by theory and measurement. Even over a short bend, detailed intercepting beam diagnostics (using a two-slit apparatus to measure both transverse ion position and velocity) should be able to detect relatively small changes in the distribution of beam particles as a result of the bend. An important goal of these initial experiments will be validation of the computer models and scaling laws used to predict the behavior of linear and recirculating drivers.

Later experiments will study insertion and extraction, acceleration (at first in a partial ring to facilitate measurement of the beam using intercepting diagnostics), beam steering, bunch compression, and fully integrated operation of the recirculator. Preservation of a small emittance will again be the central beam-physics issue to be addressed.

Until the ring is complete it will be possible to use intercepting diagnostics to characterize the beam and to calibrate the nonintercepting diagnostics that will be critical to the successful operation of the full ring. As currently planned, the ring will incorporate two extraction sections 180° apart, so the extracted beam can be diagnosed with detailed intercepting diagnostics twice each lap. As with earlier linac experiments at LBL, excellent shot-to-shot repeatability is anticipated and, so far, observed. The principal nonintercepting diagnostic under development is a segmented capacitive pickup to be located inside the quadrupoles.[14] The long duration of beam residence in the machine (up to, and possibly exceeding, 300 full lattice periods) will provide a unique opportunity to observe and characterize the longitudinal propagation of space-charge waves along the beam. Such waves will be launched (deliberately or otherwise) by mismatching the applied ear fields. The Small Recirculator will afford the longest beam path length of any near-term HIF research facility, and so will be able to explore issues such as slow thermalization that are important to both recirculating and linear drivers.

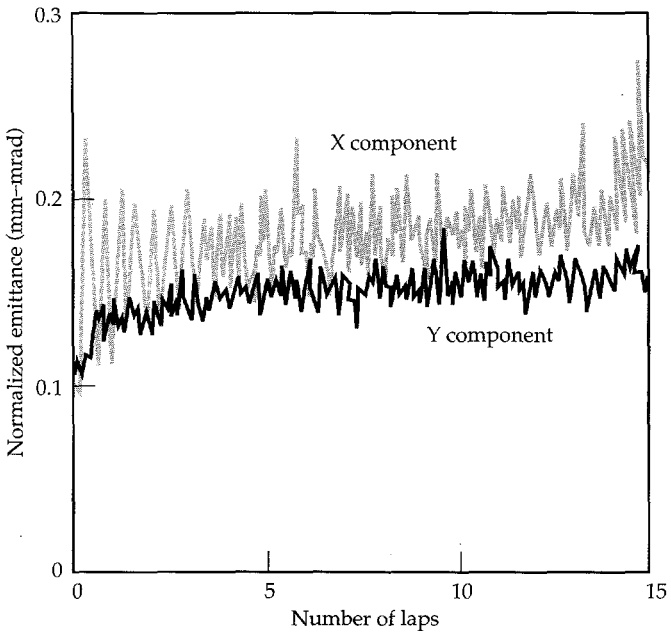

FIGURE 7. Time dependence of normalized beam emittance at mid-pulse for X (in-plane) and Y (out-of-plane) components. (30-00-0695-1658pb02)

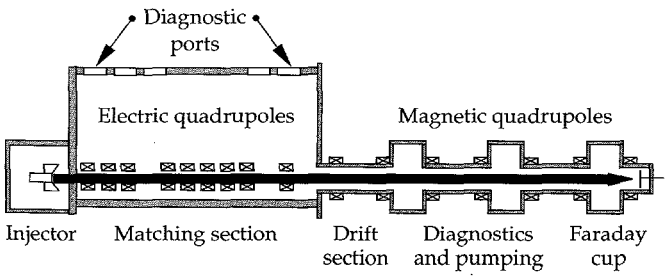

FIGURE 8. Linear configuration (length 4.568 m from source to final Faraday cup). (30-00-0695-1657pb01)

Status and Initial Results

The injector diode,[15] matching section, and straight experiment have been fabricated and are now operating; Fig. 8 shows the layout. Fifteen permanent-magnet quadrupoles have been procured; seven are being used in the straight experiment (see Fig. 10). A shorter line will serve as the link from the matching section to the ring. As shown in Figs. 4 and 5, the mechanical design of the half-lattice period is nearly complete.[16]

The electrostatic-quadrupole matching section (Fig. 8) gives the circular beam that leaves the diode an elliptical cross section suitable for alternating-gradient transport in the transfer line and the recirculator. A section of the Single Beam Transport Experiment (SBTE) apparatus from LBL was adapted by EG&G to serve this function. The potentials applied to the various quadrupole elements to obtain a matched beam were derived using an envelope calculation and range from ±1.8 to ±4.0 kV. The fifth and seventh elements are intended for minor beam steering rather than for focusing. Insertable Faraday cups are located after the third and ninth elements.

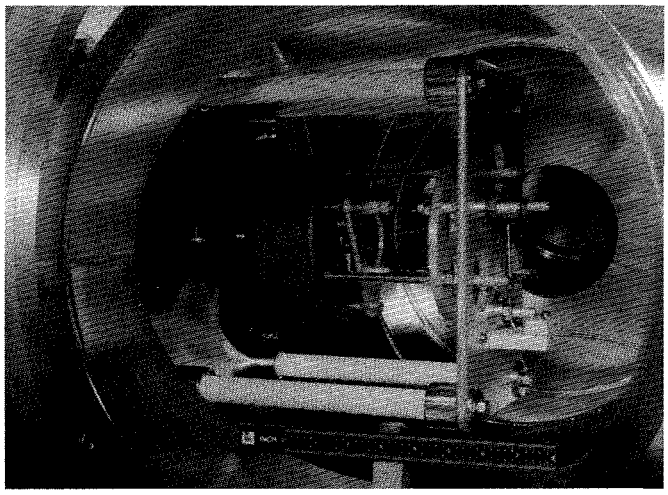

FIGURE 9. Interior of source tank, showing back of source and (at left) hole through which beam passes on its way into matching section. Holes of varying size can be used. (30-00-0695-1653pb01)

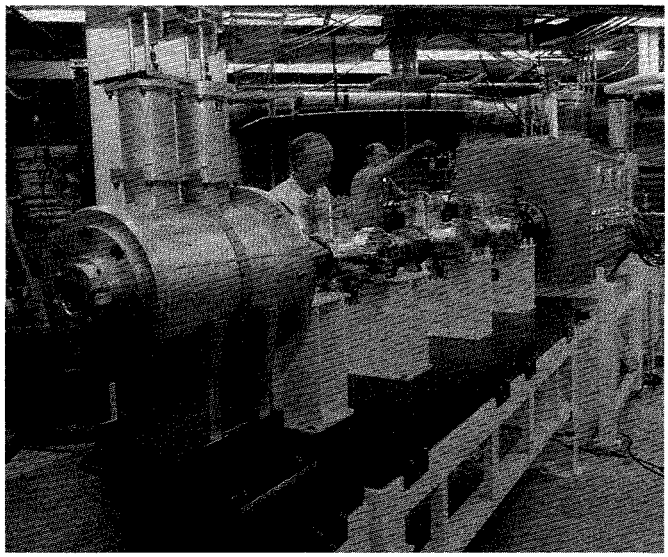

FIGURE 10. Straight transport section. Each spool holds two permanent-magnet quadrupoles; the entire section uses seven quadrupoles. The large enclosure at the left foreground contains diagnostic apparatus. (Orientation is opposite to that of Fig. 8, which does not show diagnostics enclosure.) (30-00-0695-1651pb01)

Figures 9 and 10 show some of the experimental apparatus. Figure 9 shows the source and diode. A potassium-impregnated zeolite element is heated by an internal filament; the beam passes through the hole visible at the left end of the anode–cathode gap. Figure 10 shows the linear transport section.

Time-resolved measurements of beam properties have been obtained at various locations throughout the matching and magnetic transport sections. The current has been measured using Faraday cups 0.67 and 1.9 m downstream from the diode source in the matching section and 3.16 m downstream in the magnetic transport section. An energy analyzer developed at LBL (consisting of curved electrostatic plates across which various potential differences are placed) was located 1.75 m downstream from the source. A two-slit scanner was placed at positions 0.2 and 1.6 m downstream from the source, providing measurements of emittance, beam radius, and beam centroid location.

Figure 11 shows an example of current vs time at the Faraday cup 1.9 m downstream from the diode source and corresponding results from the 1-D code HINJ[17]; there is close agreement between simulation and experiment. The large current spike at the head of the pulse arises because the rise time of the diode voltage (about 1 μs) is longer than the ideal rise time of 0.48 μs.[18] With the longer rise time, particles emitted at the beginning of the pulse have significantly lower energy than particles emitted later, so particle overtaking occurs. A modification of the pulser circuitry to reduce the rise time by a factor of two is planned. The code results are slightly noisier than those from the experiment; this results from a numerical deconvolution of the voltage waveform (to account for time lags in the voltage monitor), which introduces noise into the voltage waveform used by the code. Figure 12 shows a measurement of the horizontal normalized emittance at the end of the matching section. The high initial value appears to be due to the instantaneously high line-charge density.

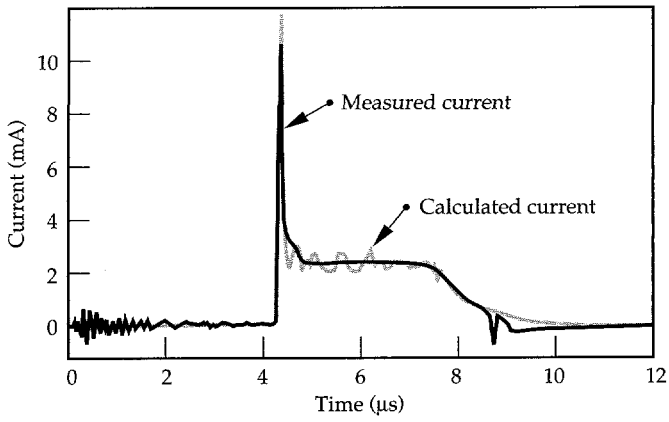

FIGURE 11. Current at the Faraday cup 1.9 m downstream of the diode source, and corresponding results from the 1-D code HINJ. (30-00-0695-1647pb01)

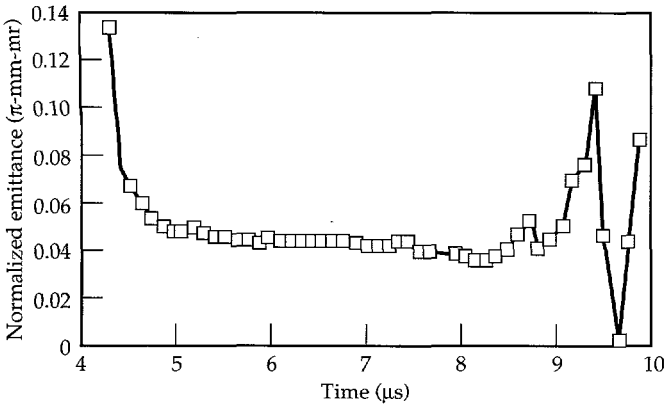

FIGURE 12. Measurement of horizontal normalized emittance at end of matching section. (30-00-0695-1648pb01)

Conclusions

The linear induction accelerator remains a very attractive Inertial Fusion Energy driver; the recirculator offers the promise of significant cost reduction, if the technical challenges of recirculation can be met. The LLNL Small Recirculator experiments are designed to provide a test bed for the necessary technology and to show that the beam dynamics in an induction recirculator are favorable; these experiments will pave the way to a larger-scale follow-on facility. These experiments, in conjunction with the ILSE experimental program at LBL and with detailed computer simulations, will lead to much more precise and credible predictions of heavy-ion driver behavior and cost and will allow the staged construction of the first IFE driver to begin shortly after ICF ignition is demonstrated on the National Ignition Facility.

Notes and References

1. J. J Barnard, F. J. Deadrick, A. Friedman, D. P. Grote, et al., *ICF Quarterly Report* 3(1), 41–49, Lawrence Livermore National Laboratory, Livermore, CA, UCRL-LR-105821-93-1 (1993).
2. W. M. Sharp, *ICF Quarterly Report* 4(2), 70–77, Lawrence Livermore National Laboratory, Livermore, CA, UCRL-LR-105821-94-2 (1994).
3. J. J Barnard, F. J. Deadrick, A. Friedman, D. P. Grote, et al., *Phys. Fluids B: Plasma Physics* 5, 2698 (1993).
4. H. C. Kirbie, R. L. Hanks, S. A. Hawkins, B. C. Hickman, et al., *ICF Quarterly Report* 5(2), 103–109, Lawrence Livermore National Laboratory, Livermore, CA, UCRL-LR-105821-95-2 (1995).
5. R. O. Bangerter, *Il Nuovo Cimento* **106 A** (11), 1445–1457 (1994).
6. H. C. Kirbie, W. R. Cravey, S. A. Hawkins, M. A. Newton and C. W. Ollis, "A FET-Switched Induction Accelerator Cell," *Proceedings of the 9th IEEE International Pulsed Power Conference,* Vol. 1 (Institute of Electrical and Electronic Engineers, New York, IEEE Cat. No. 93CH3350-6, 1993), p. 415.
7. T. J. Fessenden, D. P. Grote, and W. M. Sharp, "Accelerator Waveform Synthesis and Longitudinal Beam Dynamics in a Small Induction Recirculator," *Proceedings of the 1995 Particle Accelerator Conference,* Dallas, TX, May 1–5, 1995 (to be published).
8. W. M. Sharp, J. J. Barnard, D. P. Grote, S. M. Lund, and S. S. Yu, "Envelope Model of Beam Transport in ILSE," *Proceedings of the 1993 Computational Accelerator Physics Conference,* Pleasanton, CA, February 22–26, 1993 (AIP Conf. Proc. Vol. 297), R. D. Ryne, Ed., pp. 540–548.
9. A. Friedman, D. P. Grote, and I. Haber, *Phys. Fluids B: Plasma Physics* 4, 2203 (1992).
10. D. A. Callahan, A. B. Langdon, A. Friedman, and I. Haber, "Longitudinal Beam Dynamics for Heavy Ion Fusion," *Proc. 1993 IEEE/APS Part. Accel. Conf.,* IEEE Cat. No. 93CH3279-7 p. 730 (1993).
11. I. Haber and H. Rudd, "Numerical Limits on P.I.C. Simulation of Low Emittance Transport," *Proc. Conf. on Linear Accelerator and Beam Optics Codes,* La Jolla Inst., (AIP Conf. Proc., Vol. 177, AIP, NY, 1988), C. R. Eminhizer, Ed., p. 161.
12. J. J. Barnard, H. D. Shay, S. S. Yu, A. Friedman, and D. P. Grote, "Emittance Growth in Heavy Ion Recirculators," *Proc. 1992 Linear Accel. Conf.,* Ottawa, Ontario, Canada, AECL-10728, 229 (1992).
13. D. P. Grote A. Friedman, and I. Haber, "Three Dimensional Simulations of a Small Induction Recirculator Accelerator," *Proceedings of the 1995 Particle Accelerator Conference,* Dallas, TX, May 1–5, 1995 (to be published).
14. F. J. Deadrick, J. J. Barnard, T. J. Fessenden, J. Meredith, J. Rintamaki, "Development of Beam Position Monitors for Heavy Ion Recirculators," *Proceedings of the 1995 Particle Accelerator Conference,* Dallas, TX, May 1–5, 1995 (to be published).
15. S. Eylon, E. Henestroza, and F. J. Deadrick, "K+ Diode for the Heavy Ion LLNL Recirculator Accelerator Experiment," *Proceedings of the 1995 Particle Accelerator Conference,* Dallas, TX, May 1–5, 1995 (to be published).
16. V. P. Karpenko, J. J. Barnard, F. J. Deadrick, A. Friedman, et al., "Mechanical Design of Recirculating Induction Accelerator Experiments for Heavy-Ion Fusion," *Proceedings of the 1995 Particle Accelerator Conference,* Dallas, TX, May 1–5, 1995 (to be published).
17. J. J. Barnard, G. C. Caporaso, and S. S. Yu, "1-D Simulations of Heavy-Ion Injectors," *Proceedings of the 1993 Particle Accelerator Conference,* Washington, DC, May 17–20, 1993, Vol. 1, p. 712.
18. M. Lampel and M. Tiefenback, *Appl. Phys. Lett.* 43, 57 (1983).

HIGH-EFFICIENCY MULTILAYER-DIELECTRIC DIFFRACTION GRATINGS

M. D. Perry *D. Decker*

R. D. Boyd *B. W. Shore*

J. A. Britten

Introduction

The ability to produce short laser pulses of extremely high power and high irradiance, as is needed for fast ignitor[1] research in inertial confinement fusion, places increasing demands on optical components such as amplifiers, lenses, and mirrors that must remain undamaged by the radiation. Amplifiers pose particular problems, because as pulses become shorter it becomes increasingly difficult to extract the stored energy without causing detrimental effects originating from the dependence of the refractive index $n = n_0 + n_2E^2I = n_0 + \gamma I$ on irradiance I. The higher refractive index in the center of an intense laser beam acts as a focusing lens. The resulting wavefront distortion, left uncorrected, eventually leads to catastrophic filamentation. Major advances in energy extraction and resulting increases in focused irradiance have been made possible by the use of chirped-pulse amplification (CPA), long used in radar applications and newly applied to optical frequencies.[2]

Optical-frequency CPA systems, typified by the schematic diagram in Fig. 1, begin with a mode-locked oscillator that produces low-energy seed pulses with durations of ten to a few hundred femtoseconds. As a result of the classical uncertainty relation between time and frequency, these short pulses have a very broad frequency distribution. A pair of diffraction gratings (or other dispersive elements) lengthens the laser pulse and induces a time-varying frequency (or chirp). Following amplification, diffraction gratings compress the pulse back to nearly the original duration. Typically a nanojoule, femtosecond pulse is stretched by a factor of several thousand and is amplified by as much as 12 orders of magnitude before recompression. By producing the short pulse only after amplification, this technique makes possible efficient extraction of energy from a variety of broadband solid state materials, such as Ti:sapphire,[3,4] alexandrite,[5] Cr:LiSAF,[6,7] and Nd:glass.[8,9]

Constraints on Gratings for CPA

Achieving high focused irradiance from a pulse ultimately requires both high peak power and excellent beam quality. There is therefore a demand for diffraction gratings that produce a high-quality diffracted wavefront, have high diffraction efficiency, and exhibit a high threshold for laser damage. With careful attention to control of linear and nonlinear aberrations in the lasing medium, and with the addition of a deformable mirror to the beam transport system to correct for other wavefront aberrations, it should be possible to produce nearly diffraction-limited petawatt pulses.

The grating pairs used for pulse compression are typically planar reflection gratings that direct the first-order ($m = -1$) diffraction nearly back along the incident direction, as occurs at the Littrow angle.[10] It is important that the gratings send almost all of the radiation into this order. The need for high efficiency follows from the fact that the beam is diffracted by a grating four times in a typical double-pass pulse compressor. Thus a grating whose diffraction efficiency is η gives a maximum compressor efficiency (for double-pass compression) of η^4. As a result of this quartic dependence, even a small increase in grating efficiency provides a large increase in the energy output from the pulse compressor. With a typical diffraction efficiency into the $m = -1$ order of 86%, the maximum compressor efficiency is approximately 55%. By increasing the grating efficiency to 95%, one can achieve compressor efficiencies of over 80%. We have recently achieved nearly this theoretical limit with a record double-pass compressor throughput of 78%.

Commercial gratings[11] are often replicas, in which a master grating structure is reproduced on a secondary substrate and then given a thin metal coating to achieve high diffraction efficiency. High-quality master gratings for optical frequencies are produced mechanically, by ruling the grating pattern into a metal blank, or

holographically, by exposing a substrate coated with photoresist to a stable interference pattern, developing the latent image, and overcoating with a metal layer. Carefully designed metal-coated master and replica gratings have achieved diffraction efficiencies as high as 95% in the $m = -1$ order.[12,13] High-quality commercial metallic gratings more commonly have diffraction efficiencies of 80 to 92%.

For high-power lasers, the damage threshold of a grating is as important as its diffraction efficiency. In pulse compression, the damage threshold limits the amount of energy that can be tolerated in the pulse for a given grating area. The low damage threshold of diffraction gratings is responsible for their limitation to use in low-power tunable oscillators. Narrow-linewidth, grating-cavity laser systems based on broadband solid state materials such as Ti:sapphire, alexandrite, and Cr:LiSAF require gratings exhibiting damage thresholds above 2 J/cm^2 to access the high energy storage capacity of these materials.

Unfortunately, metallic diffraction gratings, whether produced by mechanical ruling or holographic techniques, have an inherently low threshold for optical damage due to optical absorption. Energy deposited into a thin surface layer (the skin depth) will raise the surface temperature, eventually to the boiling point, unless it is conducted away more rapidly than it arrives. The theoretical damage threshold[12] for metallic (gold) gratings operating in the region 700–1100 nm is less than 1.5 J/cm^2 for nanosecond pulses and less than 0.6 J/cm^2 for picosecond pulses. Our holographically produced gold-coated master gratings[12] exhibit damage thresholds for 1053-nm radiation of approximately 1.2 J/cm^2 for nanosecond pulses and 0.4 J/cm^2 for subpicosecond pulses. These values are near the theoretical maximum and are a factor of two higher than those available with commercial gratings.

Dielectric materials offer the potential for significantly higher optical damage thresholds than those of metals. At a laser wavelength of 1053 nm, fused silica exhibits

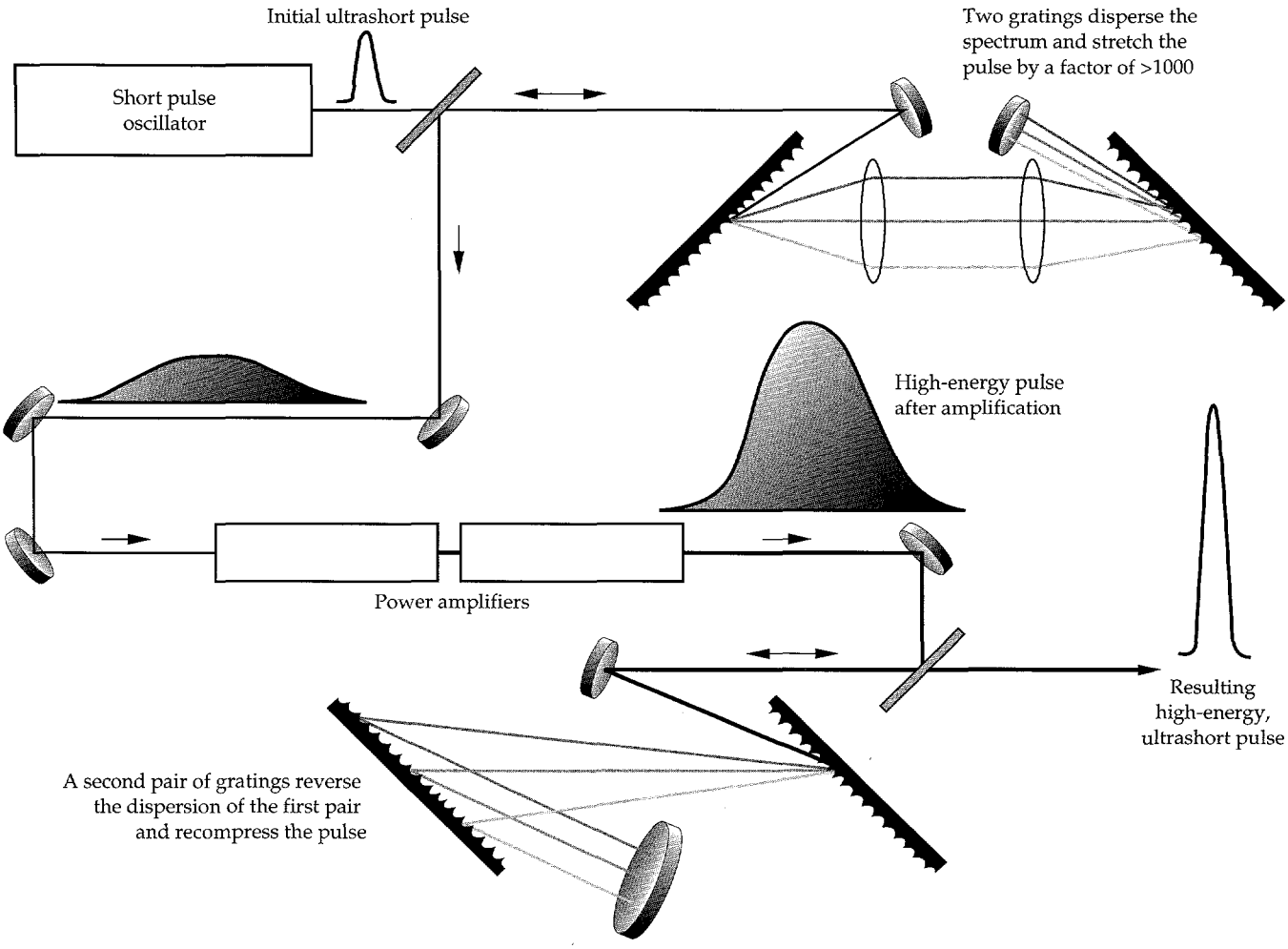

FIGURE 1. Partial schematic of beam stretching, amplifying, and compressing system used in high-power chirped pulse amplification (CPA), showing location of gratings and their function—giving different beams longer or shorter paths to stretch or compress the pulse. (70-60-0695-1670pb01)

a damage threshold above 40 J/cm^2 for 1-ns pulses and above 2 J/cm^2 for 400-fs pulses.[14] Dielectric transmission gratings exhibiting high diffraction efficiency have been produced.[15] Unfortunately, the efficiency of these gratings in reflection is poor. In this article, we describe the design and performance of multilayer dielectric gratings that can achieve up to 98% diffraction efficiency in reflection in the $m = -1$ order, and that exhibit damage thresholds higher than those achievable with metallic gratings.

Basic Grating Considerations

The basic geometric properties of any planar grating follow from the grating equation, which expresses the condition for constructive interference from successive periodic elements on a surface and which relates the incident angle θ_i, the diffracted angle θ_m for order m, and the ratio of wavelength λ to groove spacing d:

$$sin\theta_m = sin\theta_i + m\lambda/d. \quad (1)$$

Although these few parameters control the possible presence and direction of various diffracted orders, the distribution of energy among the orders (quantified by the grating efficiency) is determined by the wavelength and polarization of the incident light, the depth and shape of the grooves, and the optical properties of the diffracting structure. The groove profile depends on the method of manufacture and differs between ruled gratings (triangular profiles), holographic gratings (typically sinusoidal profiles) and etched lamellar gratings (rectangular or fin-shaped profiles).

For a reflection grating used in a first-order Littrow mount, the angle of incidence is fixed by the condition $\sin\theta_i = \lambda/2d$. When $\lambda/d > 2$, only specular reflection ($m = 0$) and evanescent orders occur; for $2 > \lambda/d > 2/3$, two propagating orders occur (specular reflection, $m = 0$, and retrodiffraction, $m = -1$). This latter two-order regime accounts for nearly all high-power laser applications.

Our grating designs are based on a rigorous solution of Maxwell's equations (with appropriate boundary conditions) for diffraction from a multilayer structure with a periodic surface-relief profile as shown in Fig. 2. We idealize the radiation as a monochromatic plane wave, linearly polarized as either transverse electric, TE (electric field along the grooves), or transverse magnetic, TM (magnetic field along the grooves). The grating profile can be of arbitrary shape, and the dielectric layers are specified by the layer thickness and an index of refraction. Our computations use the multilayer modal method.[16–19] This method replaces the corrugated grating surface by a succession of slices (rectangular in cross section), in each of which the complex-valued dielectric constant alternates periodically between two values, corresponding to the materials above and below the grating surface. Exact normal-mode solutions to the vector Helmholtz equation are found within the slices (an eigenvalue problem), and boundary conditions are matched in moment form to produce a complete solution. Solutions are carried between layers using an R-matrix method. The mathematical methods employed are discussed in detail elsewhere.[12,18,19]

Figure 3 presents the predicted $m = -1$ diffraction efficiency of a 1550-groove/mm grating used at the Littrow angle (56°) for TE-polarized 1053-nm light incident on the multilayer structure of Fig. 2. The multilayer is composed of alternating layers of high-index ZnS ($n = 2.35$) and low-index ThF_4 ($n = 1.52$) to form a highly reflecting quarter-wave stack. The top layer, containing the grating, is composed of the high-index (ZnS) layer. High diffraction efficiency is achieved by controlling the thickness t of the top layer and the depth h of the trapezoidal grooves. The maximum diffraction efficiency (predicted to be above 98%) occurs for an infinite periodic series of choices for t. To simplify fabrication, we always choose the thinnest solution.

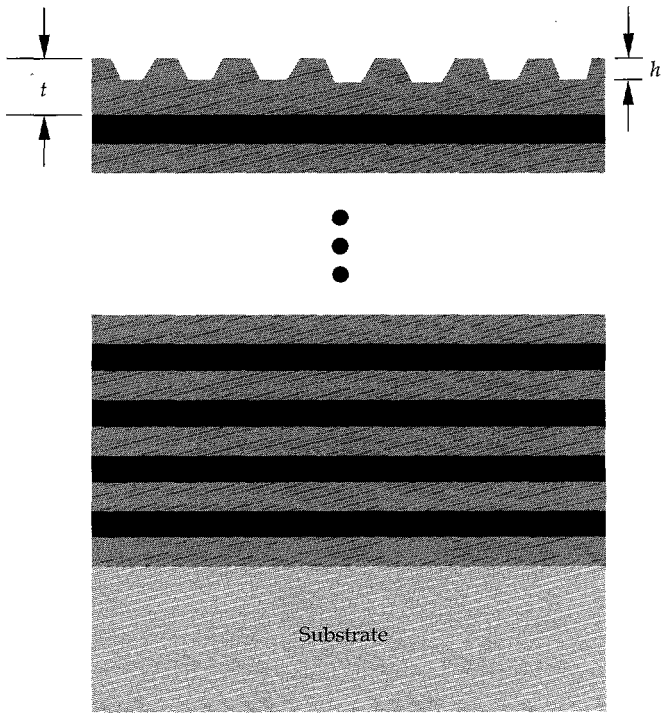

FIGURE 2. Basic multilayer dielectric grating concept (h = groove depth, t = top layer thickness). Dark and light layers represent materials of high ($n \approx 2$) and low ($n \approx 1.5$) refractive index, respectively. (70-60-0695-1667pb01)

Figure 3 gives a detailed view of the diffraction efficiency as a function of h and t. Strong diffraction occurs when the optical depth of the grooves is near one quarter of a wavelength and the optical thickness of the top layer is near three quarters of a wavelength. Our calculations suggest high sensitivity to the incident polarization, as might be expected from the polarization sensitivity of conventional multilayer coatings. The peak diffraction efficiency for TM (p-polarized) light on this structure is predicted to be less than 50%; that for TE (s-polarized) light is predicted to be near 98%.

Manufacturing Procedure

Our gratings are fabricated using lithographic techniques following holographic exposure. The dielectric multilayer structure is vacuum-deposited by e-beam evaporation on an optically flat (better than $\lambda/12$) substrate. The substrate is then coated with a thin (~300 nm) film of photoresist (Shipley 1400) and cured at 80°C for 30 min. The surface relief pattern spacing d is produced in the photoresist by intersecting two laser beams, each of exposure wavelength λ_e and each incident at an angle θ_e according to the formula

$$d = \frac{\lambda_e}{2 \sin \theta_e \cos \phi} , \qquad (2)$$

where ϕ is the angle between the normal to the substrate and the bisector of the incident laser beams (see Fig. 4). The interference pattern was produced by an equal-path, fringe-stabilized interferometer utilizing a 2-W single-longitudinal-mode Kr-ion laser (Coherent) operating at 413 nm. Straight, parallel grooves are produced only by highly collimated radiation; even the slightest wavefront curvature of the interfering beams produces curved grooves with nonuniform spacing. This groove distortion reduces the spectral resolution of the grating and produces undesirable curvature in the wavefront of the diffracted beam.

Once the interference pattern is recorded in the photoresist, development removes those regions exposed to the laser light (positive resist), producing a corrugated surface relief profile that is transferred into the substrate material by reactive-ion etching.[19] Although the interference fringe pattern exhibits a sinusoidal intensity distribution, the groove shape ultimately produced in the grating is affected by a number of process variables. Our most common profile is trapezoidal, so we optimize the designs for trapezoidal grooves.

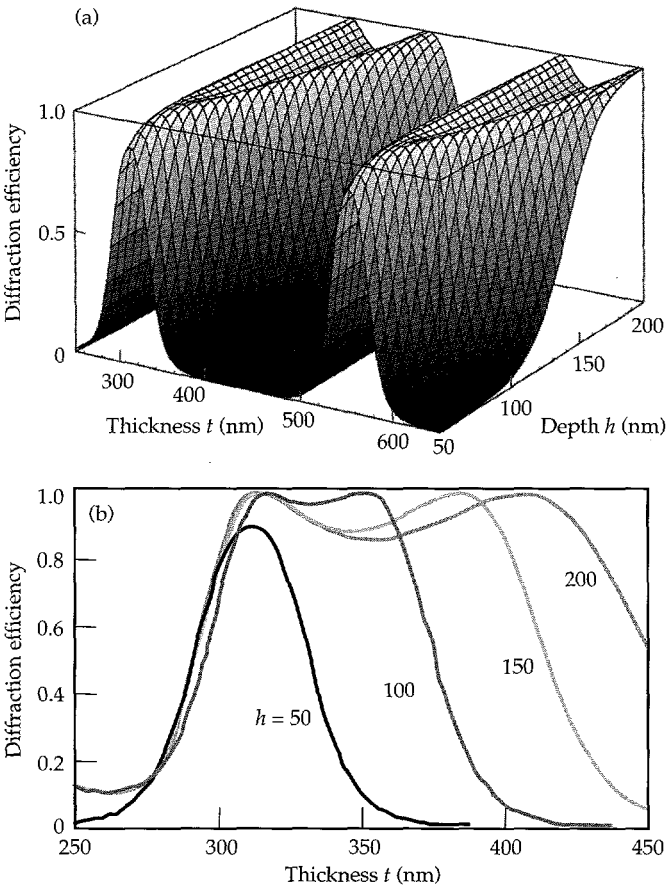

FIGURE 3. (a) Theoretical diffraction efficiency (order $m = -1$) for TE-polarized light at 1053 nm for a multilayer dielectric grating consisting of alternating layers of ZnS and ThF_4. Trapezoidal grooves are etched into the top layer as illustrated in Fig. 2. (b) Expanded view of first maxima of efficiency surface, showing efficiency (order $m = -1$) for depths $h = 50$, 100, 150 and 200 nm. (70-60-0695-1668pb01)

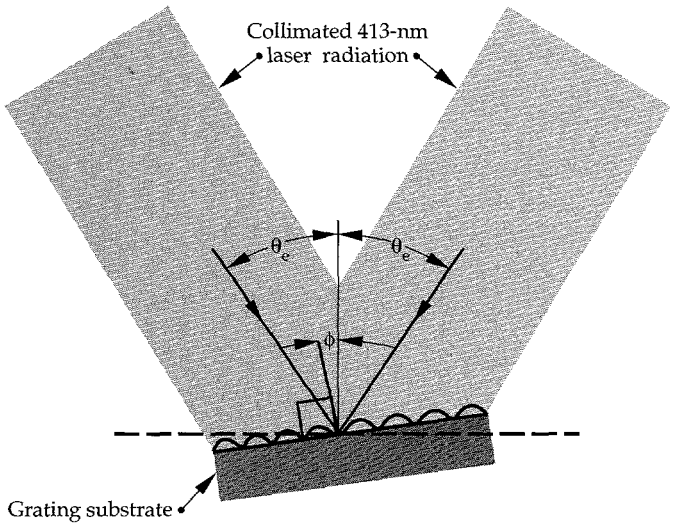

FIGURE 4. Holographic exposure geometry, showing definition of angle of incidence θ and angle ϕ between grating normal and bisector of incident waves. (70-60-0695-1669pb01)

Figure 5 shows a typical scanning electron micrograph of a cross section of a completed grating.

We determined the dependence of the diffraction efficiency of this grating on the angle of incidence by measuring the average power of the diffracted ($m = -1$, near the Littrow angle), reflected ($m = 0$), and incident beams produced by a narrow-linewidth Ti:sapphire cw laser operating at 1053 nm. Figure 6 shows the results of this measurement. The difference between the incident beam and the sum of the diffracted and reflected beams arises from a net scattering of ~1% and a transmission loss of ~0.5%. Low diffraction efficiency is observed until the design angle of 56° is approached; there the reflected ($m = 0$) energy for TE polarization drops to approximately 1% of the incident energy and the $m = -1$ diffracted beam reaches a peak efficiency of 96.1%. For TM polarization, the maximum diffraction efficiency is 50%, in good agreement with the predicted value. We observe a small variation of efficiency (from a high of 96% to a low of 94%) over the surface of our gratings.

The measured damage threshold of our oxide (HfO_2/SiO_2)–based multilayer dielectric gratings for 1-ns laser pulses is over 5 J/cm^2, nearly ten times that of the best metallic gratings. For pulse durations from 0.3 to 5 ps, our gratings exhibit a damage threshold of approximately 0.6 J/cm^2, three times higher than the short-pulse damage threshold of commercial metallic gratings. Further refinement of our multilayer design is expected to increase the short-pulse damage threshold to over 1 J/cm^2.

In addition to the requirement of high diffraction efficiency and high damage threshold, gratings used for pulse compression must maintain high efficiency over a large bandwidth. Figure 7 shows the calculated

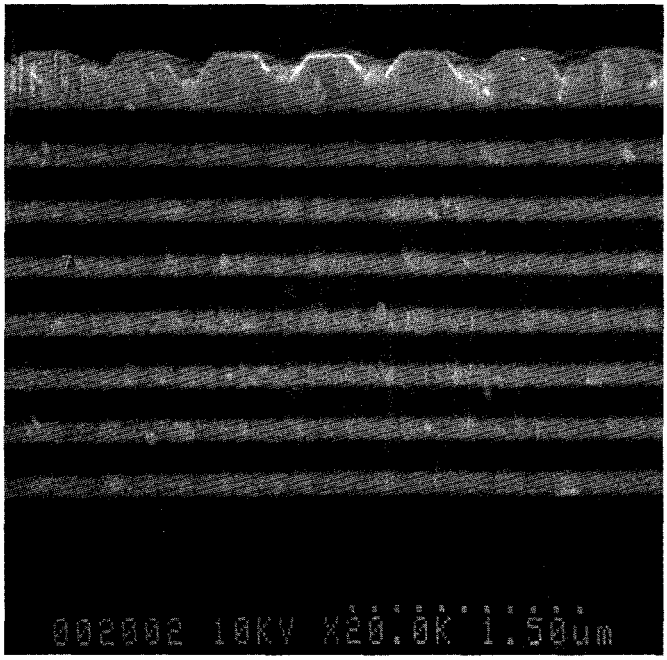

FIGURE 5. Scanning electron micrograph of multilayer dielectric grating structure. (20-03-0795-1855pb01)

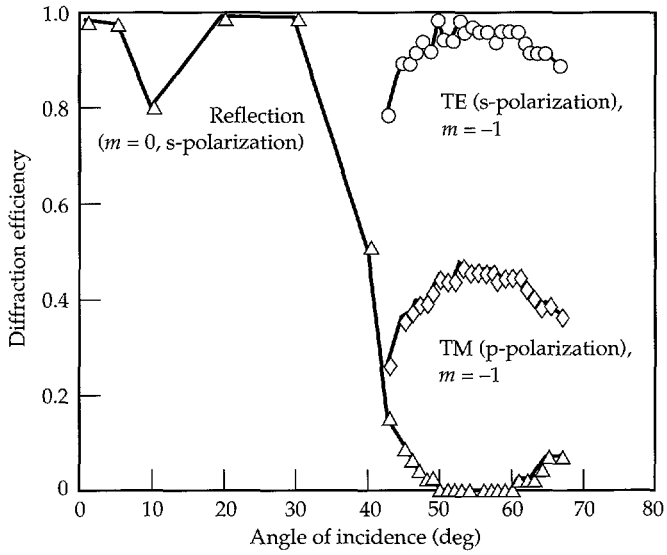

FIGURE 6. Absolute diffraction efficiency (order $m = -1$, Littrow mount) at a wavelength of 1053 nm and for various polarizations for the grating shown in Fig. 5. (70-60-0695-1671pb01)

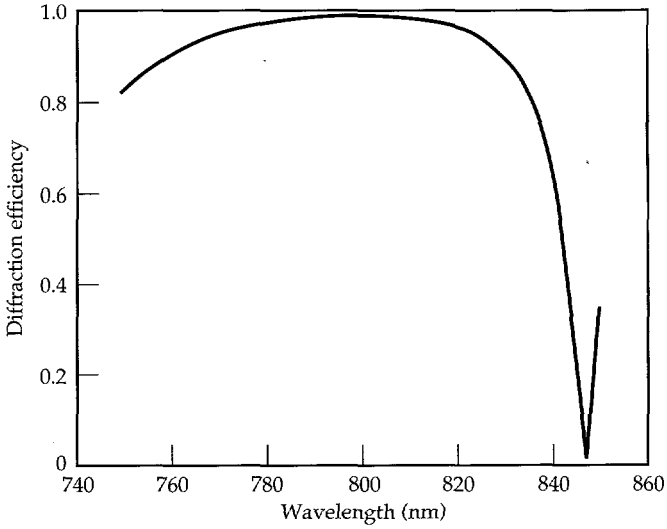

FIGURE 7. Theoretical diffraction efficiency ($m = -1$) vs wavelength of an oxide-based multilayer grating (1800 grooves/mm). Bandwidth is over 85 nm. (70-60-0695-1672pb01)

wavelength dependence of the diffraction efficiency of diffraction efficiency an oxide-based multilayer grating (8 layer pairs) optimized for use with 100-fs pulses at 800 nm. Diffraction efficiency above 90% is maintained from 760 to over 830 nm. Such gratings could easily handle pulses as short as 20 fs. We can increase the bandwidth, at the price of a slightly reduced peak diffraction efficiency, by reducing the number of layers or changing the design slightly. We have produced designs that can support pulses as short as 10 fs with greater than 90% diffraction efficiency. At these extremely short pulse durations, the dispersion of the multilayer coating itself will become important. We have not yet examined this effect on our ability to use these gratings for stretching and compressing 10-fs pulses.

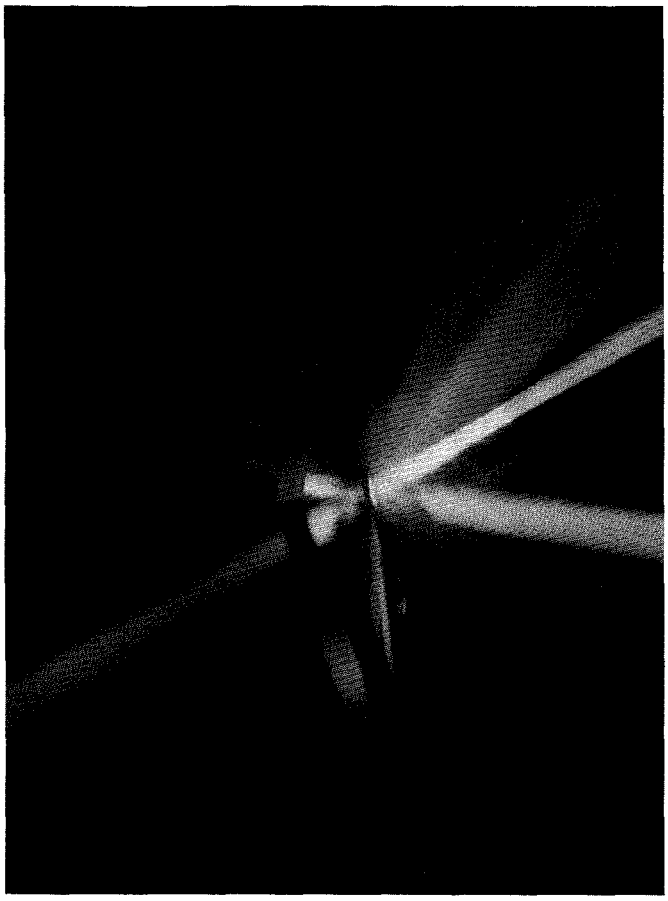

FIGURE 8. Multilayer dielectric diffraction grating designed to reflect yellow light, diffract broadband visible radiation (bottom left), eliminate all green and yellow light in the transmitted diffracted beam (right), and transmit blue–green light. The grating pictured is 15 × 20 cm. (70-15-0294-0178Apb01)

Applications of Multilayer Dielectric Gratings

Another feature of this new type of diffraction grating is the ability to design the grating to perform a multitude of functions simultaneously. Specifically, the gratings can be designed as beamsplitters that transmit, diffract, and reflect light. By controlling the design of the multilayer and the grating, specific wavelengths can be transmitted, others reflected, and still others diffracted, all with specified efficiency. As an example, we fabricated a grating that operated simultaneously as a broadband diffraction grating in reflection (10% efficiency in the $m = -1$ order from 390 to 700 nm), a high reflector in the yellow (90% reflection from ~570 to 590 nm), a high transmitter in the blue-green (~90% from 500 to 570 nm), and a notch filter for the transmitted diffracted ($m = -1$) beam [extremely low efficiency (<1%) for 500 to 600 nm and relatively high efficiency (>50%) for 400 to 500 nm and 600 to 700 nm). Figure 8 displays this performance.

Summary

We have demonstrated techniques for designing and holographically creating diffraction gratings, based on a multilayer dielectric structure, that exhibit diffraction efficiency exceeding 96% into the $m = -1$ order in a near-Littrow configuration. The high diffraction efficiency is obtained by proper coating design and by adjustment of the depth of the grooves and the thickness of the top layer. By adjusting the coating design, gratings of essentially any efficiency and variable bandwidth can be produced.

The damage thresholds of these all-dielectric gratings surpass those of metal gratings. To date, relative to commercial metallic diffraction gratings, our dielectric gratings have achieved an order-of-magnitude increase in damage threshold for nanosecond pulses and a factor-of-three increase for subpicosecond pulses.

Acknowledgments

We thank E. Lindsay and C. Moore for producing the electron and atomic-force micrographs and C. Hoaglan for his technical assistance. We are indebted to Lifeng Li, of the University of Arizona, for ongoing advice and assistance.

Notes and References

1. M. Tabak, J. M. Hammer, M. E. Glinsky, W. L. Kruer, et al., *ICF Quarterly Report* **4**(3), 90–100, Lawrence Livermore National Laboratory, Livermore, CA, UCRL-LR-105821-94-3 (1994).
2. P. Maine, D. Strickland, P. Bado, M. Pessot, and G. Mourou, *IEEE J. Quantum Electron.* **QE-24,** 398–402 (1988).
3. J. Kmetec, J. J. Macklin, and J. F. Young, *Opt. Lett.* **16,** 1001–3 (1991).
4. A. Sullivan, H. Hamster, H. C. Kapteyn, S. Gordon, *Opt. Lett.* **16,** 1406–8 (1991).
5. M. Pessot, J. Squier, G. Mourou, and D. Harter, *Opt. Lett.* **14,** 797–799 (1989); M. Pessot, J. Squier, P. Bado, G. Mourou, and D. Harter, *IEEE J. Quantum Electron.* **QE-25,** 61–66 (1989).
6. T. Ditmire and M. D. Perry, *Opt. Lett.* **18,** 426–428 (1993); T. Ditmire, H. Nguyen, and M. D. Perry, *J. Opt. Soc. Amer. B* **11,** 580 (1993).
7. P. Beaud, M. Richardson, E. J. Miesak, and B. H. T. Chai, *Opt. Lett.* **18,** 1550–52 (1993).
8. M. D. Perry and R. Olson, *Laser Focus World* **27,** 69 (1991).
9. C. Rouyer, E. Mazataud, I. Allais, A. Pierre, et al., *Opt. Lett.* **18,** 214–216 (1993).
10. E. B. Treacy, *IEEE J. Quantum Electron.* **QE-5,** 454–8 (1969).
11. M. C. Hutley, *Diffraction Gratings* (Academic, NY, 1982).
12. R. Boyd, J. Britten, D. Decker, B. W. Shore, et al., *Appl. Opt.* **34,** 1697 (1995).
13. E. Popov, L. Tsonev, and D. Maystre, *J. Mod. Opt.* **37,** 367–377 (1990).
14. B. C. Stuart, M. D. Perry, and B. W. Shore, "Pulsewidth-Dependent Damage Measurements of Dielectric Materials," Lawrence Livermore National Laboratory, Livermore, CA, UCRL-JC-118115. Prepared for proceedings of *Physics with Intense Laser Pulses*, St. Malo, France, August 1994.
15. J. J. Armstrong, *Holographic Generation of Ultra-High-Efficiency Large-Aperture Transmission Diffraction Gratings* (Ph.D. Thesis, University of Rochester, 1993).
16. R. Petit, Ed. *Electromagnetic Theory of Gratings* (Springer, Berlin, 1980).
17. D. Maystre, "Rigorous Vector Theories of Diffraction Gratings," in *Progress in Optics*, E. Wolf, Ed. (Elsevier, NY, 1984), vol. 21, pp. 1–67.
18. L. Li, *J. Opt. Soc. Am. A* **10,** 2581–91 (1993); L. Li, *J. Mod. Opt.* **40,** 553–73 (1993); L. Li, *J. Opt. Soc. Am. A* **11,** 2816–2828 (1994).
19. L. Li and C. W. Haggans, *J. Opt. Soc. Am. A* **10,** 1184–1189 (1993).

Experimental Characterization of Hohlraum Conditions by X-Ray Spectroscopy

C. A. Back *B. F. Lasinski* *L. J. Suter*

E. J. Hsieh *B. J. MacGowan* *G. F. Stone*

R. L. Kauffman *L. V. Powers* *R. E. Turner*

T. D. Shepard

Introduction

Spectroscopy is a powerful technique used to measure the plasma parameters relevant to Inertial Confinement Fusion (ICF) plasmas. For instance, the onset of spectral signals from multilayer targets have been used to determine ablation rate scalings.[1] Temperature and density measurements in coronal plasmas have enabled the study of laser coupling efficiency as a function of the laser wavelength.[2] More recently, dopants have been successfully used to determine capsule conditions of ICF targets.[3] However, few spectroscopic studies have been performed to diagnose plasma conditions of the hohlraum itself. Several laboratories have studied enclosed cavities,[4] previously concentrating on measurements of the radiative heat wave, the x-ray conversion efficiency, and temporal evolution of Au x rays. Measurements of electron temperature T_e and electron densities n_e are difficult because many physical processes occur and each diagnostic's line-of-sight is restricted by the hohlraum wall. However, they are worth pursuing because they can provide critical information on the target energetics and the evolution of plasma parameters important to achieving fusion.

In this article, we discuss spectroscopic tracers to diagnose plasma conditions in the hohlraum, using time- and space-resolved measurements. The tracers are typically mid-Z elements (Z = 13–24), which are placed on the hohlraum wall or suspended in the hohlraum volume. To demonstrate the breadth of measurements that can be performed, three types of experiments are presented. The first set tests ablation inside hohlraums by using tracers under the laser beam focal spot. The second set examines the heating of the wall by the tracers buried at different depths. The third set measures T_e by analysis of line intensity ratios. Spectroscopy has an advantage over imaging studies because it can provide nonperturbative measurements of local plasma parameters, i.e., T_e and n_e. Furthermore, not only can a spectra allow a measurement of plasma conditions, but its temporal behavior can reveal information about the hydrodynamics and heating of the hohlraum.

Experimental Approach

Microdots aid the spectroscopic analysis by limiting optical depth, localizing the tracer, and reducing edge effects of laser irradiation.[5] Target fabrication techniques successfully produce versatile hohlraums having tracer dopants deposited as high-precision microdots or strips. The tracers are deposited on a thin substrate such as an 800-Å CH foil or on a 25-μm-thick Au foil that mimics the hohlraum wall. The advantages of using tracers for probing the plasma include: (1) creating a localized plasma to track the dopant by emission or absorption, (2) controlling the thickness of the dopant, (3) systematically varying the depth of the tracer to probe different layers below the surface, and (4) defining the transverse plasma length probed to produce optically thin transitions. These advantages are important to successfully diagnose the complex hohlraum environment. LASNEX simulations of plasmas created from tracers indicate that the plasma can remain localized inside the hohlraum. For instance, different positions of the density gradient can be probed by suitably choosing the depth at which a tracer is buried.[6] Thus the experiments can be particularly effective in understanding ablation, plasma formation in nonplanar geometries, and overall energy balance.

UCRL-LR-105821-95-3

Since the plasmas may be >1 mm, the accuracy of spectroscopic measurements have benefited from the development of x-ray streak cameras and gated imagers. Streak cameras provide continuous temporal resolution of the spectral signal while gated imagers allow imaging of the spectra produced from a microdot or strip. Recently, we developed and fielded a spectrograph using a Bragg x-ray diffraction crystal coupled to a gated module,[7] which converts one dimension of the spatial resolution to spectral resolution. Its primary advantage over other diagnostics is that it *spectrally* images x-ray emission from laser-produced targets in 250 ps time frames. These technological developments have been essential to achieve sufficient spatial and spectral resolution of these targets.

Experimental Results

Figure 1 is a schematic of the target showing the placement of tracer foils. Tracers are placed on the wall for ablation and wall heating experiments, as indicated in the figure. Tracers are deposited on a free-standing foil that is suspended inside the hohlraum for recent experiments measuring the T_e of gas-filled targets, also shown in the figure. This section discusses three types of experiments that can be performed: ablation measurements, embedded microdot emission measurements, and T_e measurements.

Ablation Measurements

In ablation experiments, we compared a lined and unlined hohlraum by monitoring the emission of KCl that was deposited on a Au foil on the hohlraum's inside surface. The KCl was directly irradiated by a laser beam and observed with x-ray streak cameras. The dot provided spectral signals that served as a temporal marker of the laser incident on the hohlraum's inside surface.

The targets were scale-1 hohlraums that were either lined with 7500 Å of CH or unlined. At the position of beamline 6, a hole was drilled into the hohlraum and covered with a foil patch with the KCl facing the inside of the hohlraum. The patch consisted of a 25-μm Au foil overcoated with 3500 Å of KCl. Eight Nova beams at $3\omega_0$ irradiated the target in the standard pointing and focusing geometry to produce focal spots on the hohlraum wall ~550 μm × 900 μm diam. The total laser energy was 22.3 kJ with <5% variation. In a 1 ns square pulse, this produces an intensity of 6×10^{14} W/cm^2 in each focal spot.

Figure 2 shows an example of the data. Line intensity traces as a function of time were taken for the He-like α line (n = 2–1) of Cl, $1s^2$ ($^1S_0$) –$1s2p$ ($^1P_1$). For comparison, the Au emission was taken as close as possible to the short wavelength side of the line to minimize differences in detector response and to avoid the Cl satellites.

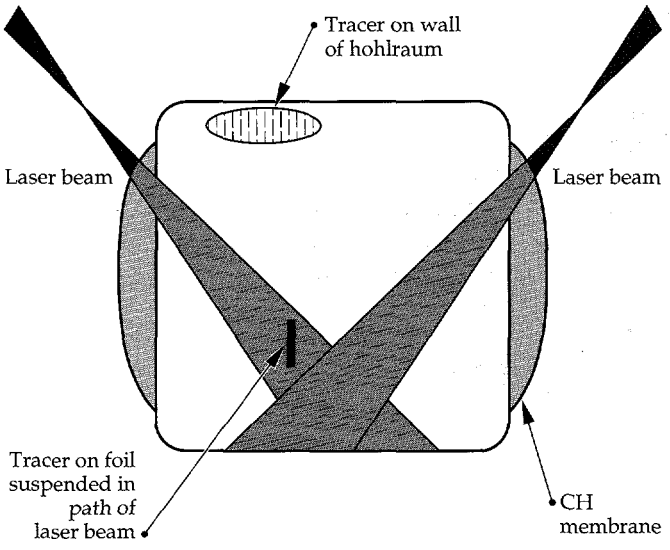

FIGURE 1. Schematic of a hohlraum target showing the position of patches and suspended foils. (08-20-0695-1660pb01)

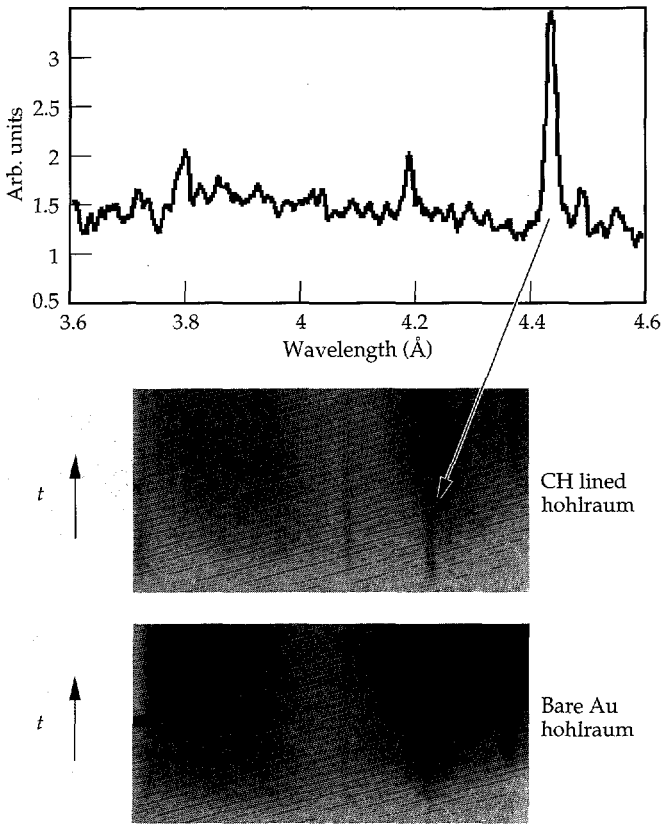

FIGURE 2. Example of data and a lineout from ablation experiments. (08-20-0695-1661pb01)

Figure 3 compares these four traces. There are two salient features of the temporal evolution. Early in time, the slope of the emission can be approximated by a straight line for all the lineouts. Later in time, the slope changes abruptly for all the cases except the Au emission from the lined hohlraum.

We define the burnthrough time as the temporal delay between the Cl emission from the tracer and Au emission from the lined or unlined hohlraum. In the unlined case, the KCl burns through and Au emission is detected 40 ps later when comparing the half maximum intensity. The lined case shows burnthrough to the Au 100 ps later. The onset of the signal taken is $t = 0$, where we assume that the delay in ionizing to He-like Cl is negligible. Here, the relative difference in the Au vs Cl emission is more important than the absolute value of the timing. The reference intensity for each case is the intensity when the KCl signal is no longer distinct from the Au signal. The difference reveals that there is a lag of 60 ps between the lined and unlined case.

A noticeable shoulder in the data exists where the slope of the intensity changes. Initially, the KCl in both the unlined and lined case follow the same curve, then their evolutions differ. If we consider the KCl as only a timing marker, the delay in burnthrough, as determined from the relative time lag of Au emission, is 80 ps. This delay has physical significance since the KCl foil was *not* overcoated with 7500 Å of CH and is therefore exactly the same in the two cases.

Because the intensity of the Cl emission is identical for the first 40 ps of emission, it is consistent to interpret the departure of the Cl slope as the inability of the laser to continue to heat the KCl in the CH lined hohlraum in the same way as the KCl in the unlined hohlraum. In addition, the intensity of the unlined and lined cases are different by a factor of two after 600 ps. Although the unlined and lined data are from two different experiments, the shots were performed on the same day, the target setup and spectrometer were identical, and differences due to film processing are minimal. Ablated CH inside of the hohlraum would produce a negligible attenuation of the signal. Therefore, the difference in intensity would indicate that less emission is detected in the lined hohlraum from both Au and Cl than from the unlined hohlraum.

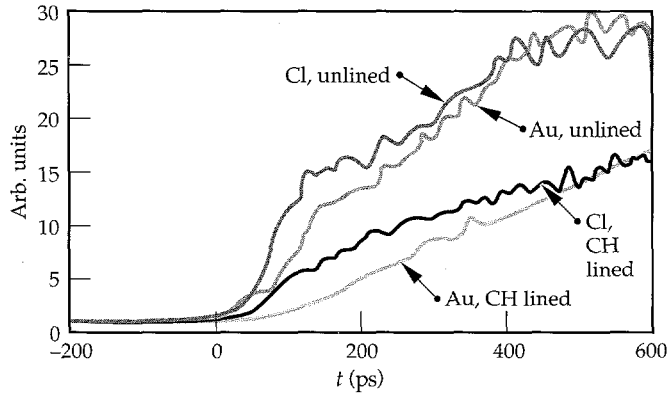

FIGURE 3. Comparison of the emission from Fig. 2.
(08-20-0695-1662pb01)

Another measure of the target ablation is the time at which the KCl emission is no longer distinct from the Au emission. For the lined hohlraums, a detectable KCl signal persists for a longer period of time, 470 ps vs 280 ps. The duration of the KCl signal can be correlated with the amount of time that the KCl is localized enough to produce a signal above the Au background. When the KCl is no longer discernible from the Au, the total signal of the lined hohlraum is 70% of the unlined signal. When the KCl contribution is subtracted from the Au signal, the peak intensity of the lined hohlraum is 85% of the unlined signal. The result implies that the CH lined hohlraum has a slower ablation rate and does not cause Au emission of equal intensity within the first 600 ps of the laser pulse.

The measure of the burnthrough rate shows a measurable delay in time corresponding to ~80 ps. However, intensity of the Au emission is markedly different in both magnitude and evolution. Clearly at 600 ps, the Au has roughly half the integrated intensity, and the projection of the slope of the intensity vs time indicates that even after 1 ns, the Au emission of the lined hohlraum may not reach that of the unlined hohlraum.

Embedded Microdot Hohlraum Experiments

Embedded microdot hohlraum experiments employed tracers buried under CH at a depth of 1 to 3 μm. The tracers were 250-μm-diam microdots of cosputtered Ti and Cr placed under a laser focal spot in a 3.2-mm-long hohlraum. Analysis of the spectra allowed us to examine heating of the inside hohlraum wall under a laser focal spot. Figure 4 shows an example of a TiCr K-shell spectrum where there is no appreciable H-like Cr. The top graph of Fig. 4 shows the laser pulse used to heat the hohlraum. The emission becomes detectable by a gated spectroscopic imager only ~2.2 ns after the beginning of the shaped pulse. Contrary to expectations, the tracer plasma does not become more ionized as the laser intensity increases to its peak. Calculations from foil burnthrough targets predict an T_e of ~2.5 keV. Due to the absence of H-like Cr in the experimental data, we conclude that the plasma remains less ionized than expected during the laser pulse. Based on the intensity of the He-like β resonance lines (n = 3–1) of Ti and Cr, the temperature derived from the isoelectronic sequence ratio is <2 keV. The spectra are 5% wider than the experimental width,

which indicates that line broadening or source motion may also be occurring. The late time spectrum shows the return of the Cr He-like β line, which probably indicates that recombination is occurring. Because the tracer plasma was cooler than expected and the TiCr spectral lines were weak, we can only infer an estimate of the T_e from the data. The most plausible explanation for the discrepancy between calculations and experiments is that the tracer dot remains well localized and moves out of the laser beam path, thereby sampling a cooler plasma.

T_e Measurements

We designed this set of experiments to measure the T_e of gas-filled hohlraum targets. The target was a 2.5-mm-diam and 2.5-mm-long Au hohlraum. To confine the gas, all openings were covered with thin polyimide windows (1 μm thick over the diagnostic holes, 6000 Å thick over the laser entrance holes). The hohlraum was filled with neopentane gas C_5H_{12} and

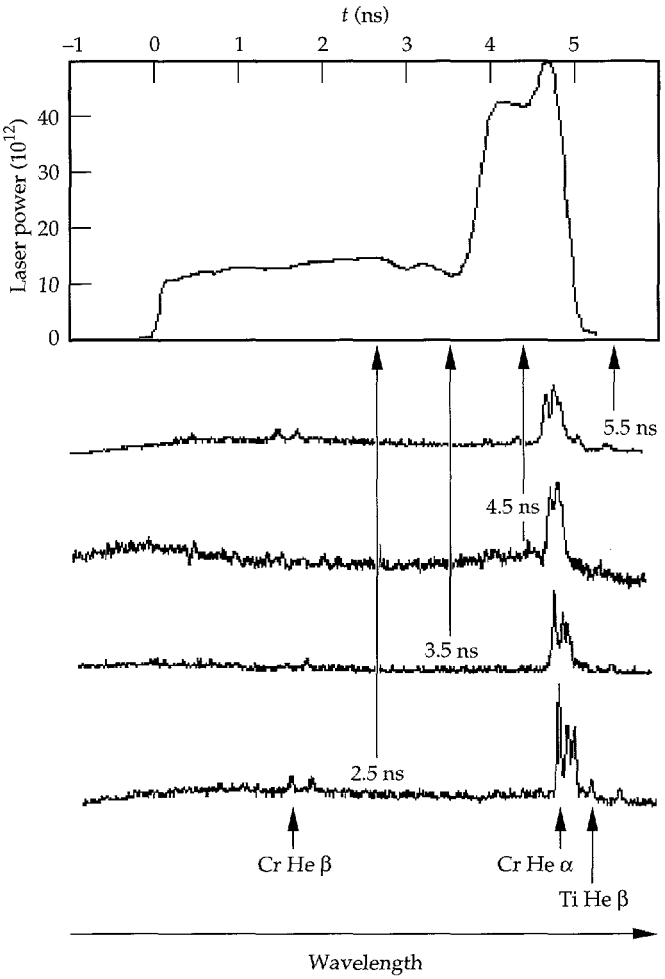

FIGURE 4. Data from a CH lined hohlraum showing a tracer embedded at 1 μm. (08-20-0695-1663pb01)

was designed to create a large millimeter-size plasma for stimulated Brillouin scattering and stimulated Raman scattering studies.[8]

These hohlraums are smaller than those used in the previous experiments and are expected to have a higher radiation temperature T_R. In the presence of an intense external photon flux, the ionic populations become more difficult to calculate because the introduction of the radiative transfer requires a solution of an integrodifferential equation which depends on the population and the field. Previous spectroscopic diagnostics cannot be extrapolated to these cases because they do not include the effects of an intense photon field. In the smaller hohlraums, the T_R can be high enough to actively perturb the level populations of the dopants and thereby will change the standard dependencies of these level populations on the T_e and n_e. This means that the ratios will now have an added dependence on the radiation field, which was previously assumed negligible. This radiation field will tend to deplete lower level populations by photoionization and photoexcitation and will cause mixing between excited levels, as they thermalize with the radiation field. Since these effects depend on the population and depopulation of energy levels, which are intricately coupled to the radiation field, and the plasma response to that photon field, the ratios will depend not only on the T_R, but on the *detailed spectral structure* of the radiation field.

To analyze the spectra from gas-filled hohlraums, the radiation field generated inside the 2.5-mm-diam hohlraums was measured by an x-ray diode diagnostic called Dante.[9] These experiments provided data that were used as input to the spectroscopic plasma models. Figure 5 shows the spectra of the radiation drive obtained at the peak of the pulse. Overall, the peak T_R was ~190 eV. In the experiments, the diagnostic observed

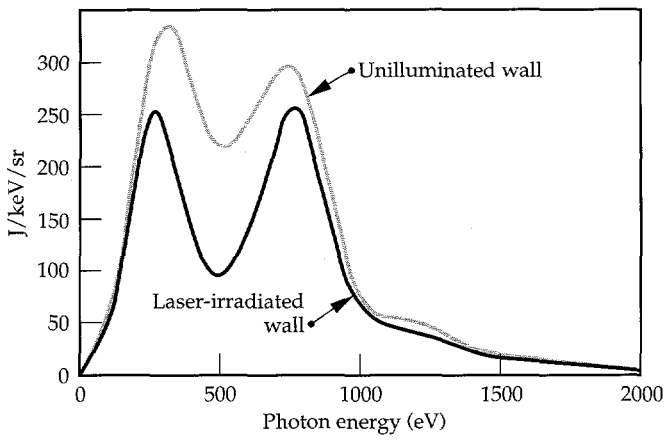

FIGURE 5. Dante spectra of the flux from a 2.5-mm-diam hohlraum at the peak intensities generated during the pulse. M bands are not shown. (08-20-0695-1665pb01)

either a beam focal spot or an area that was not irradiated by the beam. The measurements allow a comparison of the frequency dependence of the radiation field for these two cases. As shown in Fig. 5, both spectra are non-Planckian and there is a marked difference in the relative intensities of the O and N spectral bands. In general, measurements observing a laser focal spot on the wall have more pronounced N and M bands. For the T_R measured in these types of targets, the radiation effects on the spectra are not significant enough to affect the temperature measurements. This effect does become important in targets with higher T_R and research in this area continues.

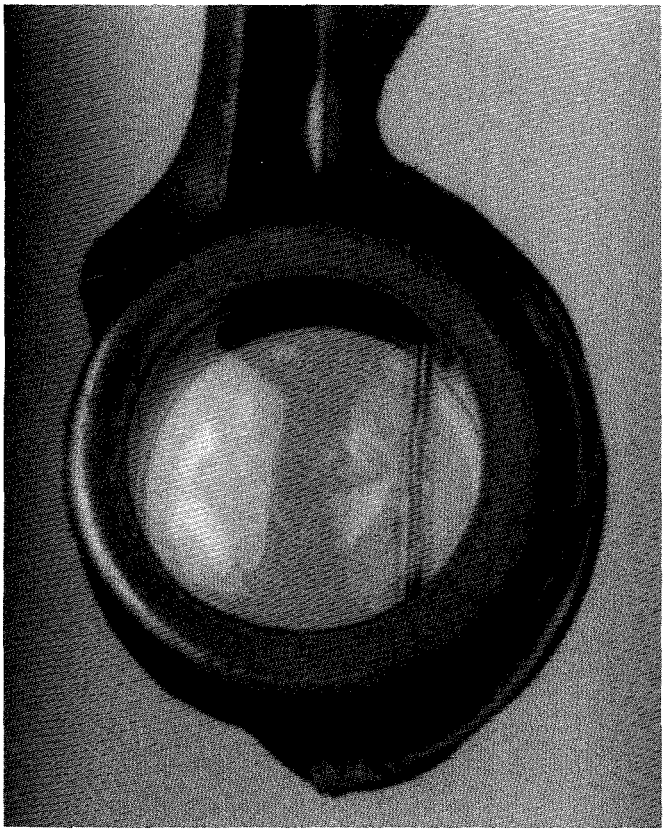

FIGURE 6. Photograph of a foil suspended in a hohlraum target. (10-00-0394-0788Apb01)

To measure the T_e in these hohlraums, a tracer plasma was formed from a 2000 Å deposit of Ti and Cr cosputtered onto a 800 Å thick CH foil substrate. Figure 6 is a photograph of the target, which shows a vertical foil suspended in the hohlraum. The measurement is based on a technique which uses isoelectronic lines from ionized plasmas to diagnose T_e.[10] Briefly described, it is a line intensity ratio of emission from the same transition originating from two different ionic species having the same ionization stage. For instance, in this case we use the Cr He β resonance line, $1s^2\ (^1S_0)$ –$1s3p\ (^1P_1)$, and the Ti He β resonance line.

Because of the potential nonuniformity of the inside of the hohlraum, the tracer is deposited in a 100-μm-wide strip that is suspended in the hohlraum with the deposit facing the beam, as shown in Fig 1. Figure 7 shows an example of the spectra that have been corrected for the instrument response and gain. The experimental data, represented by circles in Fig. 8, show that $T_e \geq 3$ keV for 500 ps. The full results and other experimental details of the measurements will be reported elsewhere.[11]

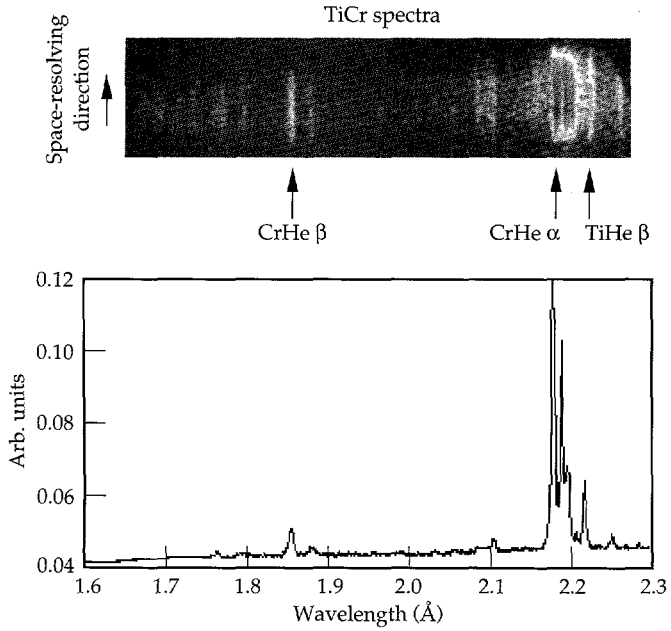

FIGURE 7. Data and lineout of the x-ray emission from a hohlraum target. (08-20-0695-1664pb01)

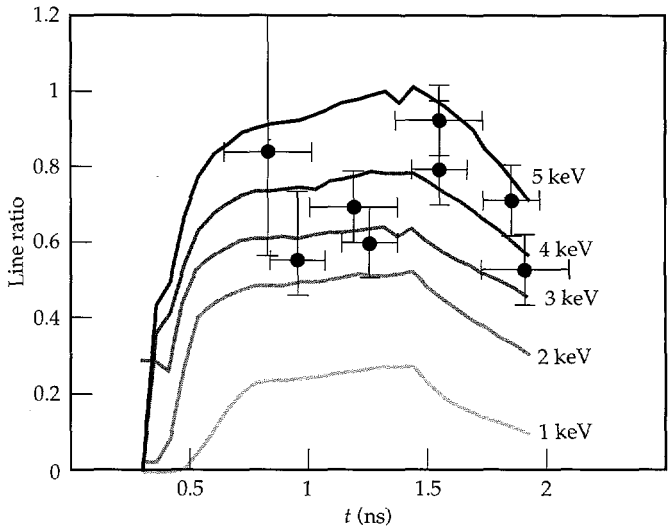

FIGURE 8. Example of data from a hohlraum target. (08-20-0895-1871pb01)

Summary

To achieve fusion by indirect drive, a confined cavity creates an x-ray source to provide proper symmetry for the implosion of a microballoon. The experiments described here are designed to diagnose the hohlraum plasma conditions by spectroscopy. The detailed behavior of hohlraums can be explored by these techniques because tracers can diagnose the *local* plasma conditions.

Experiments have demonstrated that line emission from microdot tracer plasmas can be observed above background emission. Emission from dopants on the hohlraum wall have revealed that spectra obtained from lined hohlraums have a temporal delay and are not as intense as those of unlined hohlraums. Recent results from lined and gas-filled hohlraums have shown that the T_e can be diagnosed by a line intensity ratio technique. Large lined hohlraums achieve temperatures of <2 keV while gas-filled 2.5-mm hohlraums reach $T_e > 3$ keV. Near-term experiments will develop the spectroscopic techniques to test the effect of high radiative fluxes on the plasma kinetics models and will explore the time-dependent effects.

Notes and References

1. W. C. Mead, et al., *Phys. Fluids* **26**, 2316 (1993).
2. H. Pepin, R. Fabbro, B. Farai, F. Amiranoff, et al., *Phys. Fluids* **28**, 3393 (1985); D. Phillion and C. J. Hailey, *Phys. Rev. A* **34**, 4886 (1986).
3. C. L. S. Lewis and J. McGlinchey, *Opt. Commun.* **53**, 179 (1985); A. Hauer, R. D. Cowan, B. Yaakobi, O. Barnouin, and R. Epstein, *Phys. Rev. A* **34**, 411 (1986); B. A Hammel et al., *Phys. Rev. Lett.* **70**, 1263 (1993).
4. B. Thomas, S. J. Davidson, C. C. Smith, and K. A. Warburton, ACO-UK-7839, 1985; R. Sigel, et al., *Phys. Rev. Lett.* **65**, 587 (1990); R. Weber, P. F. Cunningham, and J. E., *Appl. Phys. Lett.* **53**, 2596 (1988); R. L. Kauffman, et al., *Phys. Rev. Lett.* **73**, 2320 (1994); H. Nishimura, H. Takabe, K. Kondo, T. Endo, et al., *Phys. Rev. A* **43**, 3073 (1991).
5. P. G. Burkhalter, M. J. Herbst, D. Duston, J. Gardner, et al., *Phys. Fluids* **26**, 3650 (1983); M. J. Herbst, P. G. Burkhalter, J. Grun, R. R. Whitlock, and M. Fink, *Rev. Sci Instrum.* **53**, 1418 (1982); J. J. Herbst and J. Grun, *Phys. Fluids* **24**, 1917 (1981).
6. T. Shepard, Lawrence Livermore National Laboratory, Livermore, CA, private communication (1994).
7. C. A. Back, R. L. Kauffman, P. M. Bell, J. D. Kilkenny, *Rev. Sci. Instrum.* **66**, 764 (1995).
8. L. V. Powers, et al., *Phys. Rev. Lett.* **74**, 2957 (1995).
9. H. N. Kornblum, R. L. Kauffman, and J. A. Smith, *Rev. Sci. Instrum.* **57**, 2179 (1986).
10. T. D. Shepard, C. A. Back, B. H. Failor, W. W. Hsing, et al., *ICF Quarterly Report* **4**(4), 137–144, Lawrence Livermore National Laboratory, Livermore, CA, UCRL-LR-105821-94-4 (1994).
11. C. A. Back, D. H. Kalantar, B. J. MacGowan, R. L. Kauffman, et al., "Measurements of Electron Temperature by Spectroscopy in Millimeter-Size Hohlraum Targets," Lawrence Livermore National Laboratory, Livermore, CA, UCRL-JC-122046 (in progress, 1995), in preparation for *Phys. Rev. Lett.*

Modeling the Effects of Laser-Beam Smoothing on Filamentation and Stimulated Brillouin Backscattering

R. L. Berger *C. W. Still* *S. N. Dixit*
T. B. Kaiser *A. B. Langdon* *D. I. Eimerl*
B. F. Lasinski *E. A. Williams* *D. Pennington*

Using the three-dimensional code (F3D), we compute the filamentation and backscattering of laser light. The results show that filamentation can be controlled and stimulated Brillouin backscattering (SBBS) can be reduced by using random phase plates (RPP)[1] and small *f*-numbers or smoothing by spectral dispersion (SSD)[2] with large bandwidth. An interesting result is that, for uniform plasmas, the SBBS amplification takes place over several laser axial coherence lengths (coherence length ≈ speckle length ≈ $8f^2\lambda_0$, where λ_0 is laser wavelength).

Introduction

Controlling stimulated Brillouin scattering (SBS) and filamentation are essential to the success of laser fusion because together they affect the amount and location of laser energy delivered to the hohlraum wall for indirect drive and to the absorption region for direct drive. Filamentation and self-focusing occur when a density depression is produced by the nonuniform light intensity through ponderomotive and thermal pressures. Light refracts toward lower densities, and the light intensity increases until diffractive losses limit the lateral dimension of the nonuniformity. The incident laser beam has strong intensity nonuniformities, so that even modest filamentation gain may be unacceptable. Moreover, filamentation is the suspected reason that significant levels of SBS and stimulated Raman scattering (SRS) are observed even when calculated gain exponents are modest ($G < 5$). Because the length of laser beam hotspots is much larger than the width (ratio of length to width is ~8*f*), backscattering is expected to be more important than sidescattering. Without hotspots, the gain rate and the growth rate of backscattering in a uniform plasma are not much different from those of sidescattering. For example, if the acoustic wave is weakly damped, the backscattering Brillouin growth rate is only $2^{1/4}$ times the sidescatter rate. Laser-beam smoothing schemes such as SSD and induced spatial incoherence (ISI)[3] illuminate the target at best focus where the laser spot is comprised of a large number of diffraction-limited hotspots. Therefore, understanding the laser–plasma interaction with hotspots is essential. We illustrate the effects of filamentation in Figure 1 where surfaces that enclose volumes in which laser intensity is higher than five times the average intensity are shown. Figure 1(a) shows the surfaces before any self-focusing has developed. Figure 1(b) shows the surfaces after the filaments have developed. There is an obvious increase in the number of high-intensity regions.

In previous reports[4,5] we presented the equations, the approximations and their justification, the numerical techniques, and some results obtained with the F3D code. This code does three-dimensional (3-D) calculations of the propagation of laser beams in which the laser light self consistently filaments and Brillouin backscatters.

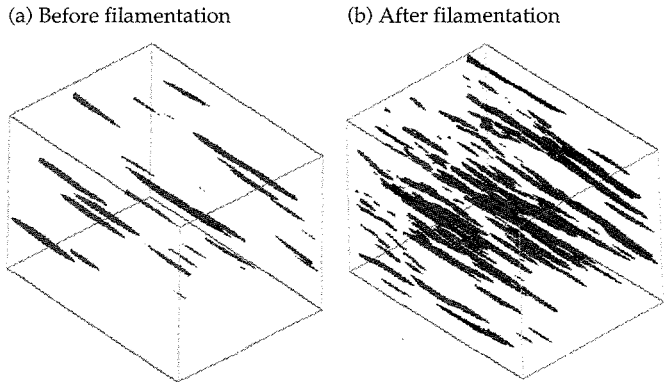

FIGURE 1. Three-dimensional surfaces within which the laser intensity is greater than five times average (a) before filamentation and (b) after filamentation. (50-01-0895-1872pb01)

UCRL-LR-105821-95-3

Here, we review laser-beam smoothing techniques and present the effects of temporal beam incoherence on filamentation and SBBS. Because filamentation and backscattering are the dominant interactions in the problems we consider, we can separate the light wave into a nearly forward- and nearly backward-moving wave, each treated within the paraxial approximation. Similarly, we can separate the acoustic wave response into long-wavelength modes, driven by filamentation or forward scattering, and short-wavelength modes, driven by backscattering. This separation allows us to consider fairly large regions of underdense plasma, containing many hotspots, because the spatial resolution necessary with this scheme is much less than in treatments that solve the full wave equation.[6] This allows us to consider the influence of SSD and other temporal beam-smoothing techniques on filamentation and SBBS.

Effect of Laser-Beam Smoothing on Filamentation

In the focal spot of a laser beam focused with an RPP, the laser intensity is highly modulated with a $\mathrm{sinc}^2(X)$ $\mathrm{sinc}^2(Y)$ envelope; here $X = \pi x d_x/f_1\lambda_0$, $Y = \pi y d_y/f_1\lambda_0$, where d_x and d_y are the RPP element sizes in the transverse x and y directions, f_1 is the lens focal length, and λ_0 is the laser wavelength. On the smaller scale of the diffraction-limited spot for the full lens aperture D, there are hotspots (speckles) with a distribution of intensities up to N times the average, where $N = D/d_x$ for square RPP array. The laser beam can focus on the scale of the laser spot $f_1\lambda_0/d_x$ (whole-beam self-focusing), on the scale of the speckles $f\lambda_0 = f_1\lambda_0/D$ (filamentation), and on scales between these limits (filamentation). Laser-beam smoothing is primarily intended to suppress the filamentation process, which occurs on a much shorter time scale than whole-beam effects. Here, we consider the evolution of filamentation for a representative portion of the beam because simulation of the whole beam, including the small-scale structure, cannot be done for realistic laser beam diameters ($>1000\lambda_0$). In previous reports[4,5,7] we showed that filamentation is stable if the length of the speckle l_s is shorter than the minimum spatial gain length l_g, where

$$l_g^{-1} = K_{\max} = 0.125\frac{v_0^2}{v_e^2}\frac{n_e}{n_c}\frac{\omega_0}{c} \quad . \tag{1}$$

with $\omega_0/c = 2\pi/\lambda_0$. K is the filamentation spatial gain rate, c is the speed of light, n_e is the electron density, n_c is the critical density, $v_0 = eE/m_e\omega_0$ is the jitter velocity of an electron in the laser electric field, and v_e is the electron thermal velocity. An equivalent statement is that stability against filamentation requires that the gain exponent for filamentation in a plasma one speckle length long be less than unity.

When this criterion is not satisfied, temporal smoothing is required to stabilize filamentation. For example, we have $l_g < l_s$ for parameters appropriate to the National Ignition Facility (NIF) design[8,9] (e.g., for $f/8$, $0.1n_c$, electron temperature $T_e = 3$ keV, intensity $I = 2\times10^{15}$ W/cm^2, $\lambda_0 = 0.351$ μm, we have $l_g = 0.8l_s$ and $l_s = 180$ μm). For an ISI or SSD scheme, the speckles dissolve and reform in different locations on the time scale of the laser coherence time $\Delta\omega^{-1}$. Conversely, the intensity in a speckle increases at the rate Kc; thus, we estimate that SSD or ISI will stabilize filamentation if $\Delta\omega > Kc$. The criterion $\Delta\omega > Kc$ corresponds to

$$\frac{\Delta\omega}{\omega_0} = \frac{\Delta\lambda}{\lambda_0} > 4.6\times10^{-4}\frac{n_e}{10^{21}\,\mathrm{cm}^{-3}}\frac{I}{2\times10^{15}\,\mathrm{W/cm}^2} \times\frac{3\,\mathrm{keV}}{T_e}\left(\frac{\lambda_0}{0.351\,\mu\mathrm{m}}\right)^4 \quad . \tag{2}$$

Figures 2 and 3 show two measures of the effect of SSD bandwidth on filamentation. The simulation dimensions were typically 160 wavelengths along x and y and 530 wavelengths along z, the direction of propagation. Figure 2(a) shows the fraction, F, of laser beam energy above five times the average intensity as a function of laser bandwidth for a simulation case that was strongly unstable without SSD (i.e., for the NIF parameters listed previously but with laser intensity 4×10^{15} W/cm^2). This fraction F varies with z from the initial value of ~4% at $z = 0$ to a maximum value followed in general by a decrease at larger z as the beam breaks up. The fraction displayed is the maximum value. For sufficient bandwidth, this fraction is reduced to that for an RPP beam in vacuum. Figure 2(a) also shows the extent to which four-color illumination (described below) combined with SSD inhibits filamentation.

Figure 2(b) compares the distribution of intensities in several cases with that for an RPP beam in vacuum.[10] The distributions plotted are for the simulation region in which the fraction shown in Fig. 2(a) is largest. In the no-SSD case (3120) beam energy is transferred to very high intensity at the expense of energy between 1–5 times the average. Note that this intensity-weighted distribution peaks at 2–3 I_0 in all cases, but the total energy is constant except for the loss to collisional absorption; thus the initial distribution has the most energy. The addition of a small bandwidth, $\Delta\omega/\omega_0 = 0.025\%$ (case 3123), is not very effective, but it does reduce the population of the most intense hotspots. In the large-bandwidth case (3205), $\Delta\omega/\omega_0 = 0.15\%$, very little energy is transferred to intensities $I > 10I_0$. In fact between 4 and 10 I_0, this distribution has less energy than the initial RPP case. The fraction of beam energy at high intensity peaks near the region where the first foci occur and

relaxes to a less energetic distribution at greater distances. However, this relaxation comes at the expense of increased beam divergence as the speckles get narrower and shorter.

Figure 3 shows contour plots of the total laser energy in transverse Fourier modes at a given z vs k_x and k_y for the small and large SSD bandwidths. The incident wave has no energy for values of $|k_x| > k_0/2f = 0.0625k_0$ or $|k_y| > k_0/2f$ for an $f/8$ lens. Filamentation breaks the beam into smaller-scale hotspots, which appear in this type of plot as an increase in the energy at higher $k_\perp$. Thus in Fig. 3(a), the filamented distribution shows a significant amount of energy outside the incident beam cutoff, whereas the SSD-stabilized case in Fig. 3(b) shows a small amount of energy at these $k_\perp$. These plots also represent the amount of energy outside a given angle in the near field (lens image plane) vs the angle. Such measurements are being made in Nova experiments.[11]

For 3ω illumination, the bandwidth required to stabilize filamentation at intensities in excess of 2×10^{15} W/cm^2 cannot be used because the tripling efficiency is too low for bandwidths $\Delta\lambda/\lambda_0 \geq 3 \times 10^{-4}$. A different temporal scheme was proposed[12] wherein four narrow-band laser beams with slightly different wavelengths are focused using different quadrants of the lens to overlap in the target plane. The interference pattern (the speckles) then moves periodically in time,

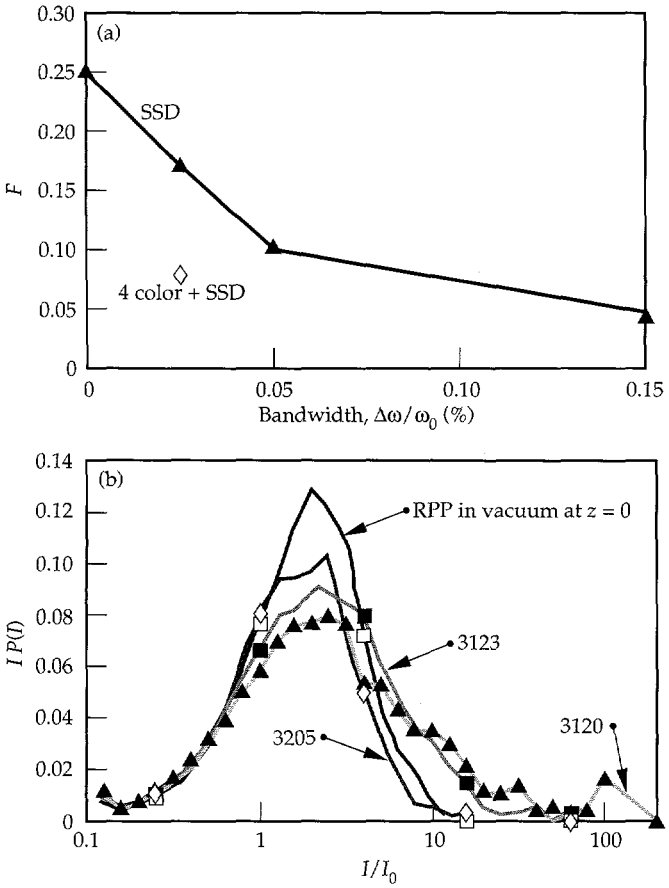

FIGURE 2. (a) Fraction F of the laser beam energy above five times the average intensity as a function of the SSD bandwidth for an $f/8$, $I_0 = 4 \times 10^{15}$ W/cm^2 laser beam. Also shown is one case combining four-color illumination with SSD. (b) The intensity weighted distribution. For the initial distribution at $z = 0$, the integral of the distribution is unity (i.e., the average is I_0), but it is less than unity for $z > 0$ because of collisional absorption. (50-01-0895-1882pb01)

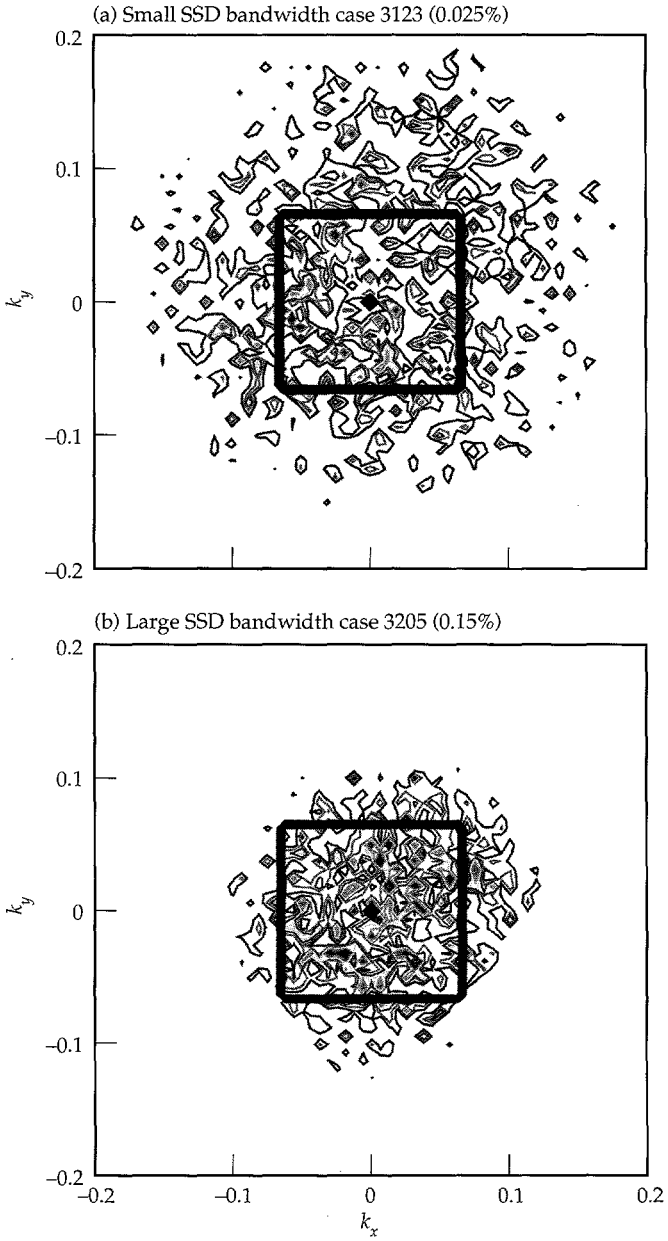

FIGURE 3. Fourier components of the laser beam energy with average $I_0 = 4 \times 10^{15}$ W/cm^2 for the incident beam at $z = 0$, and after propagating $500\lambda_0$ for (a) an SSD bandwidth of 0.025% and (b) an SSD bandwidth of 0.15%. The incident laser beam energy is uniformly distributed over perpendicular wavelengths that fit within an $f/8$ square aperture lens. (50-01-0895-1874pb01)

not randomly as in an SSD or ISI scheme. If the frequency separation between adjacent lines is $\delta\omega$, the time t_r for the speckle pattern to repeat is $t_r = 2\pi/\delta\omega$. The time-averaged speckle pattern is not smoothed because the $f/16$ speckles produced by each quadrant of the lens are unaffected. This four-color scheme[13] stabilizes filaments from the $f/8$ structure but unfortunately does not stop filaments from forming due to the remaining static $f/16$ speckles. Nonetheless, with four-color illumination, it is the intensity per quadrant that counts, and the spatial growth rate is decreased by a factor of four. However, since the speckle length has effectively increased by a factor of four, the net effect in plasmas longer than an $f/16$ speckle is to increase the distance over which the beam propagates before breaking up. Filamentation stability can be recovered with the introduction of SSD with a bandwidth of 0.025% (if used in conjunction with four-color illumination) because the $f/16$ speckles (and even longer wavelength structures) are now temporally smoothed. Equation (2) can be used to estimate the minimum four-color separation needed with $\delta\omega = \Delta\omega_{min}/3$ provided $\Delta\omega_{SSD} > \Delta\omega_{min}/4$. For the nominal parameters of the NIF, $\Delta\lambda_{min} \approx 0.5$ nm before frequency tripling ($\Delta\lambda_{min} = 0.17$ nm at 0.351 μm), so an SSD bandwidth $\Delta\lambda_{SSD} = 0.25$ nm is twice what is estimated as necessary.

This work only addresses the stability of the speckles on the small scale. Focusing can also occur on the larger scale of the whole beam. Four-color illumination and SSD will have little effect on that process. Dixit has pointed out[14] that the grating dispersion need only be large enough to displace the hotspots by a speckle width to temporally smooth the intensity pattern, at least in a model that neglects phase errors and lens aberrations. We surmise that, in the more general case, laser beams may filament on scales intermediate between the speckle size and the whole beam, and larger grating dispersion may help in this case.

Effect of Laser-Beam Smoothing on Stimulated Brillouin Backscattering

The spatial structure of the laser beam on the scale of a speckle and temporal smoothing of the hotspots have an effect on the spatial and temporal growth of SBBS. For SBS, there is an additional effect possible that survives in a 1-D treatment even if the hotspots are stationary, namely that the convective or early-time growth rate of SBS is reduced if $\gamma_0 < \Delta\omega$ and $\Delta\omega > \mathrm{Max}(\upsilon_a, \upsilon)$, where υ_a and υ are the damping rates of the acoustic and light wave, respectively. The weakly coupled SBBS growth rate γ_0, given by

$$\frac{\gamma_0}{\omega_0} = \frac{1}{4}\frac{v_0}{v_e}\frac{\omega_{pe}}{\omega_0}\left(\frac{\omega_a}{\omega_0}\right)^{1/2}$$

$$\cong 8\times10^{-4}\left(\frac{I}{2\times10^{15}\,\mathrm{W/cm^2}}\right)^{1/2}\left(\frac{\lambda_0}{0.351\,\mu\mathrm{m}}\right)^{2}$$

$$\left(\frac{n_e}{10^{21}\,\mathrm{cm^{-3}}}\right)^{1/2}\times\left(\frac{3\,\mathrm{keV}}{T_e}\right)^{1/4}\left(\frac{Z}{A}\right)^{1/4}, \qquad (3)$$

is in general larger than the laser bandwidth, especially in the hotspots. For multispecies plasmas, $Z/A \to \left(Z_j^2/A_j\right)/\left(Z_j\right)$, where the averages of the charge states Z and atomic numbers A are taken over the ion species j. This expression for γ_0 applies if $ZT_e/T_i \geq 3$ for all species in multispecies plasma and $k\lambda_{De} < 1$ where λ_{De} is the electron Debye length. If the fluid approximation for either species does not apply, the frequency and damping characteristics of the acoustic mode are significantly modified.[15] For narrowband four-color illumination, $\Delta\omega$ can be larger than γ_0, and a reduction in SBS without beam smoothing might occur. However, in our simulations, since four-color illumination always causes the hotspots to move, the pure bandwidth effect on SBS has not been studied. In summary, we expect no effect on SBS from bandwidth without smoothing (i.e., there is no dispersion and the speckles are stationary); none is observed in our $\gamma_0 < \Delta\omega$ simulations.

As discussed in the previous section, the laser speckle size in the focal plane region affects the stability of the laser light against filamentation. Our initial expectation was that the SBBS would occur independently in each speckle and thus be very sensitive to the laser f-number,[16] but our simulations in uniform plasmas showed that the spatial amplification occurred over many speckle lengths. The primary determinant of the reflectivity, when the laser intensity is below the absolute growth threshold, is the convective gain exponent

$$G = \frac{1}{8}\frac{v_0^2}{v_e^2}\frac{n_e}{n_c}\frac{\omega_a}{\upsilon_a}\frac{\omega_0 L}{c}, \qquad (4)$$

where L is the axial system length. Note that the spatial gain rate for SBBS is higher than that for filamentation by the ratio ω_a/υ_a. This fact has consequences in the simulations, which we discuss later.

Figure 4 shows the SBBS reflectivities from our simulations without temporal smoothing as a function of G for $f/8$ and $f/4$ laser illumination. The $f/8$ reflectivity is systematically higher than that for $f/4$ for the same plasma conditions and laser intensity. The difference is much less than a single-hotspot model would predict because, then, the gain exponent per speckle would be

the figure of merit. For example, for a single-hotspot model, the $f/4$ reflectivity with a gain exponent of 20 should be four times the $f/8$ value with a gain exponent of 5 if all other factors were constant. The factor of four comes from the fact that the number of hotspots per axial length is larger for $f/4$. That clearly is not the result of the simulations.

Another measure of f-number effects is the gain exponent above which significant reflectivity occurs. Figure 4 indicates that this gain exponent is ~4 for $f/8$ and ~6 for $f/4$; these exponents are in the ratio 1.5, not $(8/4)^2 = 4$, as would be expected from a single-hotspot model.

Some of the difference between the $f/8$ and $f/4$ simulations may be the result of some filamentation in the $f/8$ case since, for intensities higher than $\sim 2 \times 10^{15}$ W/cm^2, the $f/8$ laser light is unstable against filamentation. Simulations for $f/8$ in which the light refraction was neglected (but the hotspots remained) showed about a factor of two decrease in reflectivity at $G = 12$. Another reason may be incomplete phase conjugation, as discussed below.

We have concentrated on modeling laser and plasma processes relevant to the NIF and to current Nova experiments. For these parameters, filamentation in fact has less influence on the SBBS results than we expected. First, with average laser intensities less than 5×10^{15} W/cm^2, $f/4$ speckles are stable against filamentation. With $f/8$ focusing, filamentation is important above 2×10^{15} W/cm^2, but then the SBS gain is so high in our uniform plasma simulations (for the range of damping rates used) that the laser intensity becomes depleted before filaments *fully* develop. That is, as the hotspots start to focus, the laser intensity increases,

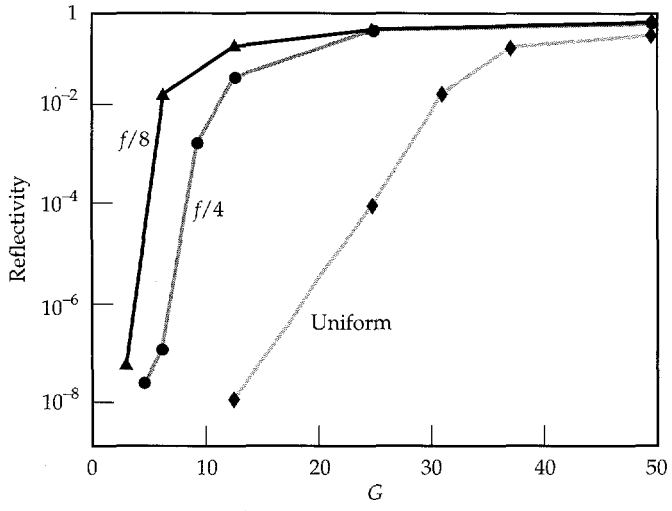

FIGURE 4. SBS reflectivity vs 1-D gain exponent for temporally unsmoothed $f/8$, $f/4$, and uniform laser beams. (50-01-0895-1876pb01)

which increases the growth rate of SBBS. Then the backward-moving light robs power from the forward-moving light, making the rate of focusing less than it would be without SBBS. If the gains were lower, filamentation would cause more of a difference between $f/4$ and $f/8$ reflectivities. In reality, SBBS may saturate before the laser intensity is depleted because of *nonlinear limits* on the SBBS growth;[17] this is the focus of our current research.[18]

A heuristic explanation for the weak dependence of SBBS on the f-number involves the notion of phase conjugation.[19] The pattern of speckles at any $z > 0$ for the incident laser light is determined by the amplitude and phase of the transverse Fourier components at $z = 0$. A light wave of nearly the same frequency propagating in the backward direction, e.g., an SBBS wave, would have the same pattern of speckles between zero and z if its components had the same relative amplitude but the conjugate phase of the incident light at z. (Of course, this is only true if filamentation, sidescattering, or other nonlinear processes do not alter the propagation substantially.) From all the light waves that the plasma produces as a result of collisional emission or Thomson scattering, those whose phase and Fourier components match those of the incident light will be amplified most because, over many speckle lengths, their hotspot patterns overlap that of the incident light. As yet, we do not have a statistical measure of the degree of phase conjugation; however, we have examined sequences of 2-D x–y plots comparing the incident-beam and reflected-light hotspots at several planes in z separated by more than a speckle length. The reflected-light hotspots are always associated with a laser-beam hotspot.

Now, consider a plasma one $f/8$ speckle length long. For $f/8$ illumination, the SBBS will grow in hotspots of about the same length as the plasma and will experience a gain in excess of the uniform-intensity gain. The $f/4$ SBBS will initially grow in the backward direction in a hotspot of 0.25 the plasma length, and, if phase conjugation does not occur, it will grow at a reduced rate once the waves leave their hotspots. However, because of the collective effect of phase conjugation, the backward light wave's hotspots overlap those of the incident laser wave and continue to drive ion acoustic waves efficiently through the ponderomotive force (proportional to the product of the light wave amplitudes). Thus the SBBS grows in $f/4$ hotspots almost as effectively as in the $f/8$ hotspots.

As discussed earlier, the laser bandwidth available at 0.35 μm on Nova is too low to reduce the amplification or growth rate directly . However, given that the SBBS grows in hotspots and takes many growth times to reach saturation, SSD or an equivalent beam-smoothing technique may be effective in reducing the reflectivity because the hotspots are no longer stationary. In addi-

tion, if the gain occurs over an extended region of plasma, the phase coherence of the incident wave with the reflected wave will be reduced with the reduction in reflectivity.

Figure 5 shows the reflectivity as a function of G for $f/4$ illumination with and without temporal beam smoothing. The results for one-color, four-color, SSD (nominal and large-bandwidth), and a combination of four-color with SSD are shown. The adjacent color separation $\delta\lambda$ and the laser bandwidth $\Delta\lambda$ were chosen as appropriate for Nova experiments, namely $\delta\lambda = 0.42$ nm and $\Delta\lambda = 0.25$ nm at 1.06 μm. The ratios $\delta\omega/\omega_0$ and $\Delta\omega/\omega_0$ of frequency separation and bandwidth to laser frequency are assumed to be preserved by frequency tripling or doubling. All the reflectivities shown in Fig. 5 exceed those produced by bremsstrahlung emission or by Thomson scattering from thermal ion acoustic fluctuations. The one-color results are the same as shown in Fig. 4. Below $G = 10$, the effect of beam smoothing is quite dramatic; the reflectivities drop below 10^{-6} for $G \leq 6$.

Other $f/4$ simulations have been done with different damping rates, plasma lengths, and laser intensities. At $G \approx 12$, the SSD reflectivities for different simulations vary by five orders of magnitude. The highest reflectivity (1.8%) occurs at the highest intensity, 4×10^{15} W/cm^2, with $L = 515\lambda_0$ and $v_a/\omega_a = 0.2$; the lowest reflectivity (2×10^{-7}) occurs at the lowest intensity, 1×10^{15} W/cm^2, with $L = 515\lambda_0$ and $v_a/\omega_a = 0.05$. Increasing the intensity by a factor of two and halving the length to keep G constant also results in higher reflectivity. The reflectivity is increased by an order of magnitude, from 2×10^{-6} to 4×10^{-5}, by doubling the damping v_a/ω_a from 0.05 to 0.1 and L from $256\lambda_0$ to $515\lambda_0$; it is increased by another order of magnitude to 2×10^{-4} as v_a/ω_a increases to 0.2 and L to $1030\lambda_0$. Figure 6 shows these results. Both these trends would make sense if the addition of SSD bandwidth increased the effective acoustic wave damping to a value as high as $0.2\omega_a$, so that the effective gain exponent increased with L and/or I. This appears plausible because $\Delta\omega_{SSD}/\omega_0 = 2.5 \times 10^{-4}$, whereas $v_a/\omega_0 \cong 2(v_a/\omega_a) \times 10^{-3} = 10^{-4}$ at the lowest damping rate. The light absorption rate $v = 1/2(n_e/n_c)v_{ei}$ is even smaller: $v/\omega_0 \approx 10^{-5}$ for $n_e = 10^{21}$ cm^{-3}, $T_e = 3$ keV, $\lambda_0 = 0.351$ μm, and $Z_{eff} = 5$ (where v_{ei} is the electron–ion collision frequency).

In Fig. 5, the combination of four-color illumination and 0.025% bandwidth SSD brings the reflectivity below that for any four-color or 0.025% bandwidth SSD simulation at a given gain exponent, as one might expect. Only with gain exponents $G > 20$ is there significant reflectivity; here, the variation of reflectivity with G approaches that calculated for a uniform laser beam. The uniform laser beam reflectivities were calculated with $v_a/\omega_a = 0.05$ and $L = 515\lambda_0$ and for various intensities up to 4×10^{15} W/cm^2. At the highest gain exponents simulated, $G \approx 50$, all simulations with and without beam smoothing have high reflectivity, $R_{SBS} > 20\%$, for which nonlinear saturation effects other than pump depletion are important. That is, these reflectivities are associated with large-amplitude acoustic waves ($|\delta n_b/n| > 0.5$). A mere reduction in the local magnitude of δn_b without a corresponding limit on the length of plasma over which the waves remain in phase may not produce much reduction in reflectivity. That is, the laser will take longer to deplete but the overall reflectivity will stay nearly constant for large systems.

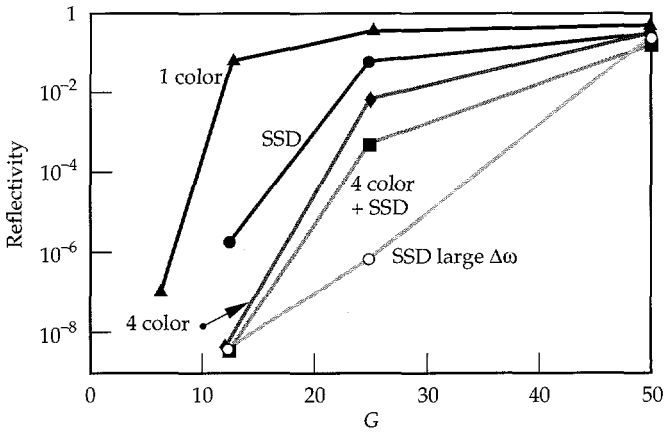

FIGURE 5. $f/4$ SBS reflectivity vs 1-D gain exponent for one-color, SSD, four-color, four-color plus SSD, and SSD with large bandwidth. (50-01-0895-1877pb01)

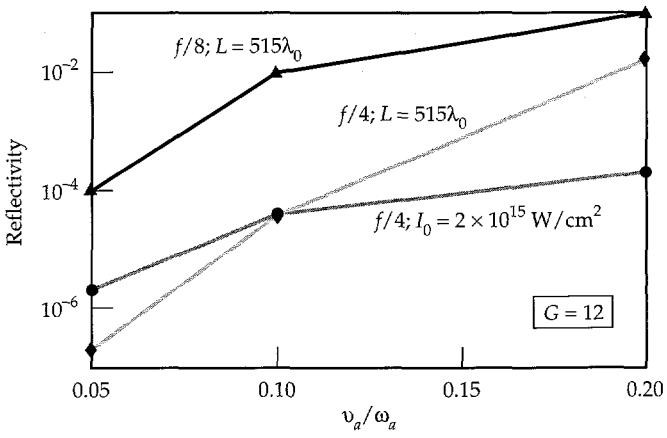

FIGURE 6. SBS reflectivity vs acoustic wave damping rate for a fixed gain exponent $G = 12$ and either a fixed intensity and varying length for $f/4$, a fixed length and varying intensity for $f/4$, or a fixed length and varying intensity for $f/8$. (50-01-0895-1878pb01)

Figure 7 shows the $f/8$ reflectivity calculations for one color, four colors, and four-colors plus SSD. Fewer calculations were carried out for $f/8$ than for $f/4$, but the benefit of the four-color plus SSD combination is also dramatic at $f/8$. Since the speckle length is four times larger than for $f/4$, the smallest length system is $515\lambda_0$, one speckle length. The four-color scheme is not as effective at $f/8$ as at $f/4$ for moderate gain exponents ($G < 20$). The four-color plus SSD reflectivity shows the same trends with intensity and length as the $f/4$ runs for SSD (see Fig. 6).

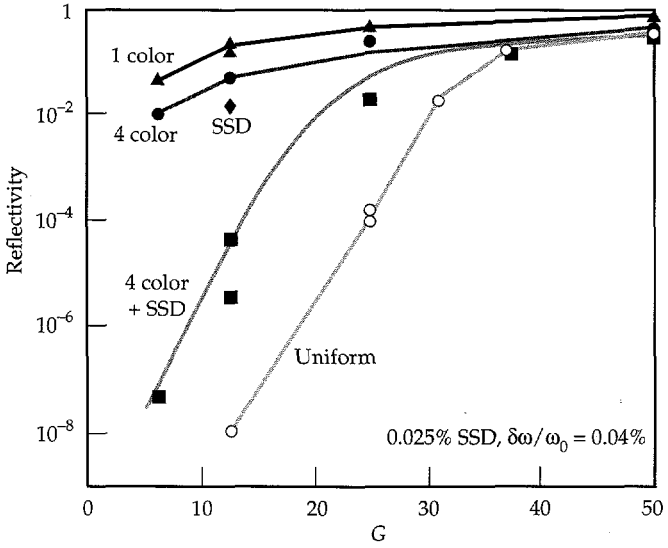

FIGURE 7. $f/8$ SBS reflectivity vs 1-D gain exponent for one-color, four-color, SSD, four-color plus SSD, and uniform laser beams. (50-01-0895-1879pb01)

Conclusions

We have presented three-dimensional calculations of the propagation of laser beams in which the laser light self consistently filaments and Brillouin backscatters. We established that filamentation can be controlled by temporal and spatial beam smoothing for laser and plasma parameters of interest to the proposed NIF. Beam smoothing also reduces the SBBS reflectivity, especially when four-color illumination is combined with SSD. For the gain exponents expected in the NIF,[7] and in experiments designed to reproduce the NIF conditions on Nova,[8] the calculated reflectivities are about 10–20%, whereas the observed reflectivities[20,21] are less than 1–5%. We believe that nonlinear processes, which are not yet modeled in this code, may explain the discrepancy, although other effects that limit the linear gain exponent[22] may also be responsible. A simple nonlinear model[23] (which had some success in modeling disk experiments in which velocity gradients also played a role) did not have much effect on the reflectivity unless the ion wave amplitudes were limited to lower values than typically observed in 1-D particle-in-cell simulations. Recent 2-D simulations have shown much lower ion wave amplitudes than 1-D simulations; we hope to incorporate this amplitude reduction into our code once the effects are understood well enough to reduce to a fluid model.

We also simulated SBBS in plasmas with strong velocity gradients, which limit the reflectivity to small values ($\sim 10^{-4}$). We observed that the reflectivity was produced in one or two spots in which the local reflected light intensity was a significant fraction ($\sim 10^{-2}$) of the local laser intensity. These simulations used the parameters of exploding-foil targets,[24] for which images of the SBBS light were taken at the target plane. These images also showed that only a few spots were responsible for most of the light emission. The reflectivities in the simulations and the experiments were of similar magnitude.

Acknowledgments

We are pleased to acknowledge the benefit of discussions with the Lawrence Livermore National Laboratory plasma experiments group and D. Dubois, J. Kilkenny, W. L. Kruer, J. D. Lindl, L. V. Powers, H. Rose, M. D. Rosen, and S. C. Wilks.

Notes and References

1. Y. Kato, et al., *Phys. Rev. Lett.* **53**, 1057 (1984).
2. S. Skupsky, et al., *J. Appl. Phys.* **66**, 3456 (1989).
3. R. H. Lehmberg and S. P. Obenschain, *Opt. Commun.* **46**, 27 (1983).
4. R. L. Berger, et al., *Phys. Fluids B* **5**, 2243 (1993).
5. R. L. Berger, et al., *Phys. Rev. Lett.* **75**, 1078 (1995).
6. M. R. Amin, et al., *Phys. Rev. Lett.* **71**, 81 (1993); ibid, *Phys. Fluids B* **5**, 3748 (1993).
7. C. Labaune, et al., *Phys. Fluids B* **4**, 2224 (1992).
8. S. W. Haan, S. M. Pollaine, J. D. Lindl, L. J. Suter, et al., *Phys. Plasmas* **2**, 2473 (1995).
9. L. V. Powers, R. L. Berger, D. H. Munro, and B. F. Lasinski, *Phys. Plasmas* **2**, 2480 (1995).
10. H. A. Rose and D. F. Dubois, *Phys. Fluids B*, 590 (1993).
11. J. Moody developed a Transmitted Beam Diagnostic (TBD) at Lawrence Livermore National Laboratory to measure the angular distribution of the transmitted laser energy.
12. J. Murray, Lawrence Livermore National Laboratory, Livermore, CA, private communication (1995).
13. D. Pennington, et al., *Tech. Dig.* **8**, 161 (1994).
14. S. Dixit, Lawrence Livermore National Laboratory, Livermore, CA, private communication (1995).
15. E. A. Williams, et al., *Phys. Plasmas* **2**, 129 (1995).
16. H. A. Rose and D. F. Dubois, *Phys. Rev. Lett.* **72**, 2883 (1994).
17. S. L. Wilks, et al., *Phys. Rev. Lett.* **74**, 5048 (1995).
18. B. I. Cohen, et al., "Two-Dimensional Hybrid Simulations of Ponderomotively Driven Nonlinear Ion Waves," Lawrence Livermore National Laboratory, Livermore, CA, UCRL-JC-121297 ABS; prepared for the *37th Annual Mtg. of APS Div. of Plasma Phys.*, Louisville, KY, Nov 6–10, 1995.
19. B. Ya Zel'dovich, N. F. Pipiletsky, and V. V. Shkunov, *Principles of Phase Conjugation*, Springer Series in Optical Sciences, T. Tamir, Ed. (Springer, Berlin, 1985), Vol. 42.
20. B. MacGowan, Lawrence Livermore National Laboratory, Livermore, CA, private communication (1995).
21. J. Fernandez, J. A. Cobble, B. H. Failor, W. W. Hsing, et al., *"Dependence of SBS on Laser Intensity, Laser F Number and Ion Species in Hohlraum Plasmas,"* Los Alamos National Laboratory, Los Alamos, NM, LAUR-95-186; submitted to *Phys. Rev. Lett.*
22. B. B. Afeyan, Lawrence Livermore National Laboratory, Livermore, CA, private communication (1995).
23. C. Randall, *1978 Laser Program Annual Report* **1**, 3–53, Lawrence Livermore National Laboratory, Livermore, CA, UCRL-50021-78 (1978).
24. C. Labaune, H. A. Baldis, N. Renard, E. Schifano, et al., *Phys. Rev. Lett.* **75**(2), 248 (1995).

INTRODUCTION TO THE NOVA TECHNICAL CONTRACT

J. D. Lindl

J. D. Kilkenny

The 1990 National Academy of Sciences (NAS) final report[1] recommended proceeding with the construction of a 1- to 2-MJ Nd-doped glass laser designed to achieve ignition in the laboratory (a laser originally called the Nova Upgrade, but now called the National Ignition Facility, or NIF, and envisioned as a national user facility). As a prerequisite, the report recommended completion of a series of target physics objectives on the Nova laser in use at the Lawrence Livermore National Laboratory (LLNL). Meeting these objectives, which were called the Nova Technical Contract (NTC), would demonstrate (the Academy committee believed) that the physics of ignition targets was understood well enough that the laser requirements could be accurately specified. Completion of the NTC objectives was given the highest priority (it was Recommendation 1.1) in the NAS report. The NAS committee also recommended a concentrated effort on advanced target design for ignition. As recommended in the report, completion of these objectives has been the joint responsibility of LLNL and the Los Alamos National Laboratory. Most of the articles in this issue of the *ICF Quarterly* were written jointly by scientists from both institutions.

Several of the NTC objectives required the completion of improvements to Nova's power balance and pointing accuracy and of new diagnostics and new target fabrication capabilities. These improvements were called "Precision Nova" and are documented in Ref. 2.

The original NTC objectives have been largely met. This Introduction summarizes those objectives and their motivation in the context of the requirements for ignition. The articles that follow describe the NIF ignition target designs and summarize the principal accomplishments in the various elements of the NTC. Reference 3 gives a much more extensive discussion of ignition requirements.

Ignition Requirements

The strong connection between the compression achievable in a spherical implosion and the ignition threshold was pointed out by Nuckolls et al.[4] in 1972. Because the compression that can be achieved in an implosion is related to the implosion velocity v_{imp}, the ignition threshold depends strongly on v_{imp}. If a laser pulse shape can be achieved that maintains compressibility independent of v_{imp}, the ignition threshold varies[3,5] as v_{imp}^{-n}, where $n \approx 5$ for the target type shown in Fig. 1.

The implosion of a shell such as that shown in Fig. 1 is driven by the ablation of material from the surface of the shell and can be described by a spherical rocket equation. The work W done on the imploding shell is given by $W = \int P\,dV$, where P is the pressure generated by ablation and V is the volume enclosed by the shell. For a given shell mass, the implosion velocity is maximized by generating the highest possible ablation pressure on a shell that encloses the greatest possible volume.

The ablation pressure is related to the energy flux incident on the surface of the shell. In laser-driven inertial confinement fusion (ICF), laser–plasma interaction effects limit the incident flux to ~10^{15} W/cm^2. In ion beam–driven ICF, the pressure is limited by the focused intensity achievable. In general, ablation pressures are limited to about 100 Mbar.

As the volume enclosed by a shell with fixed mass and density (and thus with a fixed volume of shell material) is increased, the shell must become thinner. Hydrodynamic instabilities during the acceleration and deceleration phases of the implosion limit the so-called in-flight aspect ratio to $R/\Delta R < 25$–35, where R = shell radius and ΔR = shell thickness as it implodes. For thin shells, the shell aspect ratio increases linearly with the

volume enclosed. This limitation on shell aspect ratio, and the pressure limitation described above, together limit implosion velocities. If driver technology can be developed so that other details of an implosion, such as pulse shaping and pulse symmetry, can be controlled, these two limitations ultimately set the ignition threshold for laboratory fusion to a driver of about 1 to 2 MJ for capsules with implosion velocities of 3 to 4×10^7 cm/s.

As shown in Fig. 2, two principal approaches are used with lasers to generate the energy flux required to drive the implosion. In the direct-drive approach, the laser beams are aimed directly at the target. The beam energy is absorbed by electrons in the target's outer, low-density corona, and they transport that energy to the denser shell material to drive the ablation and the resulting implosion. In the indirect-drive approach, the laser energy is absorbed and converted to x rays by high-Z material inside the hohlraum that surrounds the target. The NTC has concentrated on indirect drive.

Because of the x-ray conversion and transport step, indirect drive is less efficient than direct drive. However, ablation driven by electron conduction is in general more hydrodynamically unstable than ablation driven by x rays.[3] (Indirect drive is less sensitive to hydrodynamic instability because x rays generate a higher ablation rate than electrons.) Measures taken to mitigate hydrodynamic instability in direct-drive targets[3,6] largely offset the efficiency advantage. Also, direct-drive targets are very sensitive to intensity variations within individual beams. These variations imprint perturbations on the target that are then amplified by hydrodynamic instability. If adequate beam uniformity can be achieved, calculations for current target designs[6] indicate that direct-drive targets have about the same ignition threshold as indirect-drive targets, but that they can have about a factor of 2 higher gain. The NIF will be configured with a beam geometry capable of being used for either direct or indirect drive.[3] Beam smoothing and hydrodynamic instability requirements for direct drive will be determined in an implosion physics program on the Omega Upgrade laser at the University of Rochester and in planar experiments on Nova and on the Nike laser at the Naval Research Laboratory.

Although indirect drive is less sensitive to individual beam nonuniformities than direct drive, beam placement inside the hohlraum must be accurately controlled to achieve adequate symmetry. As indicated in Fig. 1, typical capsule convergence ratios are $C_r = R_A/r_{hs} \approx 25$–$35$, where R_A is the initial outer capsule radius and r_{hs} is the final compressed hot fuel radius (the "hot spot" radius). Achieving a convergence ratio this high requires x-ray fluxes uniform to 1 to 2%. Use of a relatively large hohlraum (with a ratio of hohlraum radius to capsule radius of 3–4) greatly reduces imbalances in irradiation between points close together on the capsule surface;[3,7] imbalances between points farther apart can be controlled by hohlraum geometry and laser beam placement. In the NIF laser, two rings of beams, each with an independent pulse shape, will enter each end of the hohlraum. (In Nova, a single ring

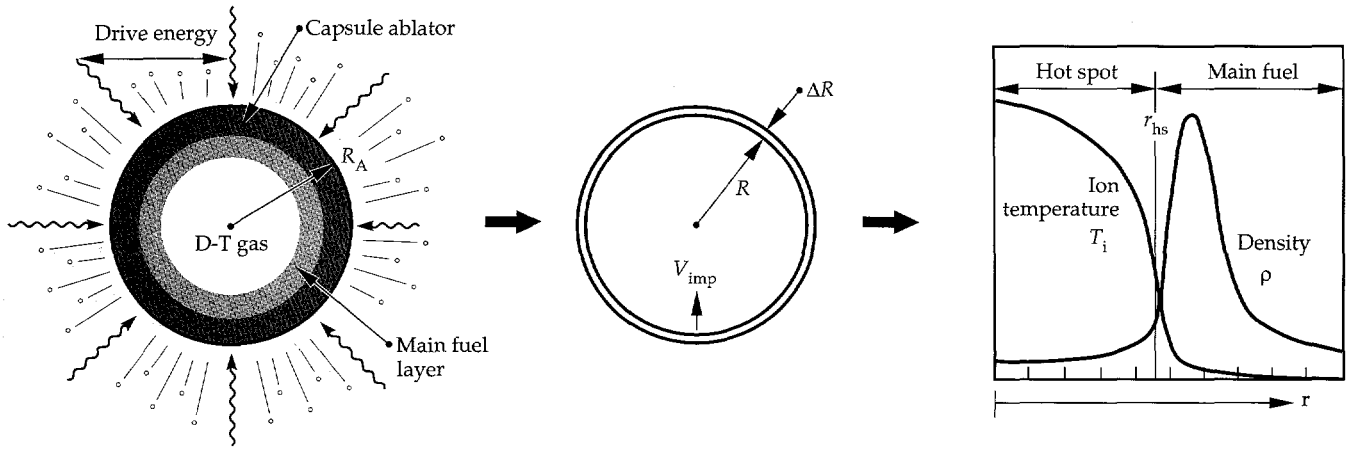

Driver–target coupling
$\Rightarrow I_r \lesssim 10^{15}$ W/cm^2 or $\lesssim$300 eV

To control:
- Absorption/preheat
- X-ray conversion
- Transport/drive

Symmetry:	$\frac{R_A}{r_{hs}}$ = Convergence ratio	≈ 20–$35 \Rightarrow$	Coupling $\eta \approx 10$–15%
Stability:	$\frac{R}{\Delta R}$ = In-flight aspect ratio	≈ 25–$35 \Rightarrow$	$I_R \gtrsim 4 \times 10^{14}$ W/cm^2 or 250 eV Surface <1000 Å
Ignition:	• $T_{i,hs} = 10$ keV • $\rho r_{hs} \approx 0.3$ g/cm	$\Rightarrow$	V_{imp} 3–4 $\times 10^7$ cm/s for $E_{driver} = 1$–2 MJ

FIGURE 1. Physics specifications on current ICF ignition targets include constraints on drive intensity, symmetry, stability, and ignition.
(02-08-0692-1865Cpb02)

of five beams enters each end.) The two rings will allow "beam phasing," in which the power in the individual rings is varied independently to control time-dependent asymmetry. For a short-wavelength laser such as Nova (or NIF) (laser wavelength $\lambda = 0.35$ μm in most experiments), about 70% of the incident laser energy is converted to x rays by the high-Z hohlraum material, but symmetry requirements limit overall coupling efficiency to 10 to 15% of the laser energy into the capsule for typical ignition designs.

Since the hohlraum wall physics and the capsule physics are essentially the same for any x-ray source, much of what is learned on Nova is also applicable to ion-beam drivers. Because of this, Sandia National Laboratories has been able to carry out experiments on Nova to test pulse-shaping schemes important in light-ion-driven targets. Indirect-drive laser experiments also provide much of the target physics basis for the Heavy Ion Driver Program, supported by the DOE Office of Fusion Energy.

The laser requirements for ignition by indirect drive can be shown in a plot of laser power P_L vs laser energy (Fig. 3). As laser power increases for a given laser energy, the achievable hohlraum temperature T_R increases. The ablation pressure increases approximately[3] as $T_R^{3.5}$, so v_{imp} is a strong function of T_R. Generation of plasma in the hohlraum increases as T_R increases; this results in laser–plasma collective effects that limit T_R and the usable power that can be put into the hohlraum. This power depends on laser wavelength, laser beam spatial and temporal uniformity, pulse duration, hohlraum size, and other variables. At $T_R = 400$ eV, for the long pulses required for ignition capsules, the hohlraum plasma density n will approach $n/n_c \approx 1/4$ (the critical density $n_c = 10^{21}\ \lambda^{-2}\ \text{cm}^{-3}$, where λ is the

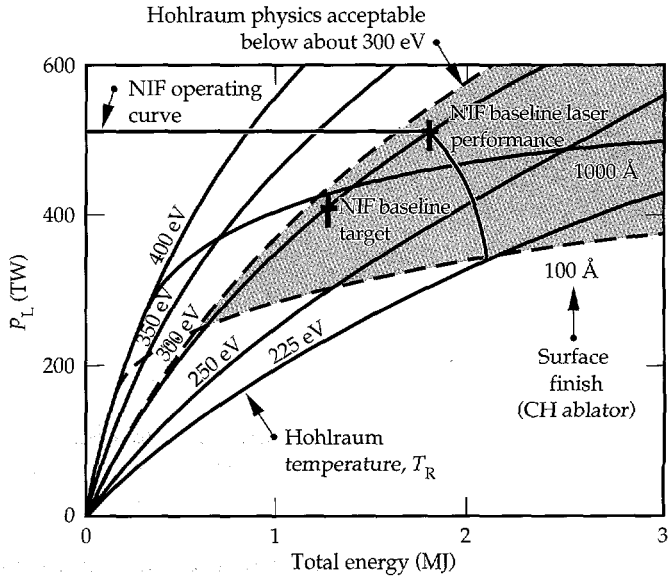

FIGURE 3. For laser-driven indirect-drive ignition targets, plasma physics issues constrain the achievable hohlraum temperature, and hydrodynamic instabilities (represented here by surface finish) establish the minimum required temperature at a given driver energy. The shaded region constitutes the accessible region in power–energy space where ignition with indirect-drive capsules is predicted. The NIF power–energy operating curve shown here has ample margin. (08-00-0693-2196Dpb01)

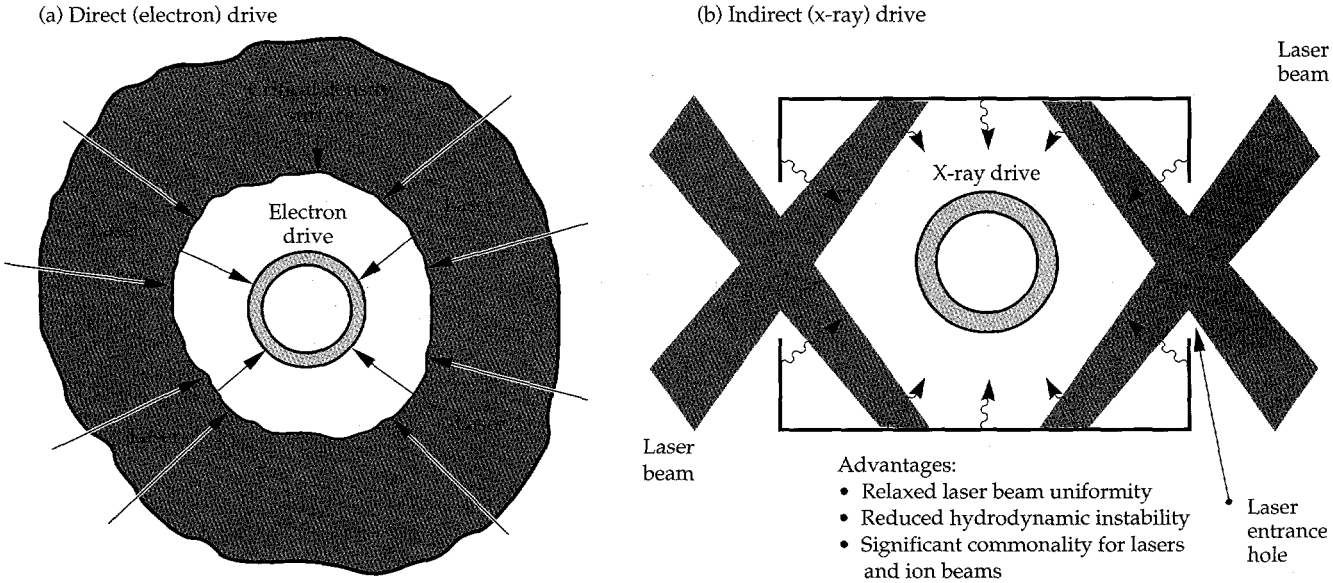

FIGURE 2. ICF uses either (a) electron conduction (direct drive) or (b) x rays (indirect drive) to produce a high shell ablation pressure to drive an implosion. (08-00-0894-3312Apb01)

laser wavelength in micrometers). Experiments[3] at $\lambda = 1$ μm suggest that this is an upper-limit temperature for ignition hohlraums. (It should be possible to achieve higher temperatures for short pulses with reduced plasma filling.) We limit peak hohlraum temperatures in current ignition target designs to $T_R \approx 300$ eV, which limits plasma densities to $n/n_c \approx 0.1$. Above this temperature, it is likely that a significant fraction of laser light would be scattered out of the hohlraum or be absorbed in a way that results in the production of high-energy electrons that heat the fusion fuel and thereby reduce the achievable compression.

At a given driver energy, hydrodynamic instabilities place a lower limit on the temperature required to drive a capsule to ignition conditions. A larger capsule requires a lower implosion velocity, which can be achieved with a lower radiation temperature consistent with the shell aspect ratio constraints. The value of the required minimum temperature at a given energy will depend on the allowed shell aspect ratio, which depends on the smoothness of the capsule surface, currently limited to 200 to 300 Å rms for Nova capsules. Below a certain size, the required implosion velocity will exceed the velocity achievable within the temperature and capsule uniformity constraints, and ignition is not possible. Above this threshold energy, there is a region in power–energy space where ignition is feasible. This is the shaded area in Fig. 3, which encloses the region limited by 300-eV hohlraum temperatures and 100-Å capsule surface finishes.

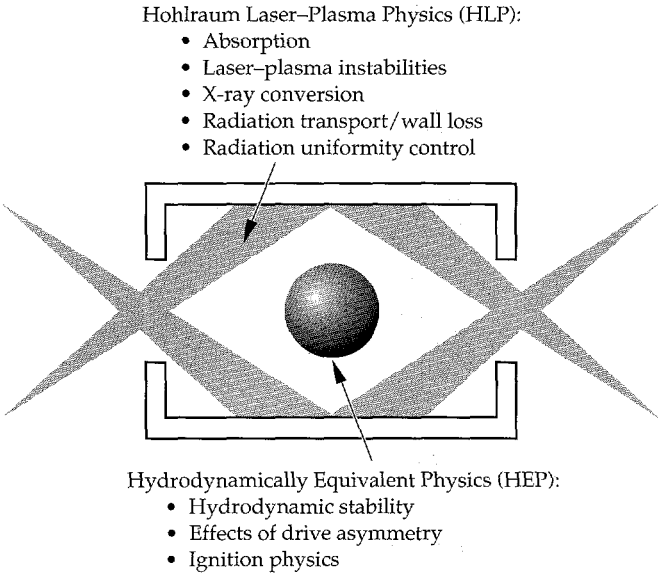

FIGURE 4. The Nova program comprises two elements that address the hohlraum and capsule physics of ignition and high gain: hydrodynamically equivalent physics (HEP) and hohlraum laser–plasma physics (HLP). (05-00-0995-2136pb01)

The NIF laser is being designed to operate at an energy of 1.8 MJ and a power of 500 TW; both values are about a factor of 2 above the threshold ignition values shown in Fig. 3, allowing for remaining uncertainty in the implosion process. Within the ignition region shown in Fig. 3, a wide variety of targets have been evaluated, as discussed in the article "Ignition Target Design for the National Ignition Facility," p. 215. The predicted yields of these targets range from about 1 to greater than 25 MJ.

Elements of the Nova Technical Contract

The objectives of the NTC have been to experimentally demonstrate and predictively model laser–plasma interaction, hohlraum characteristics, and capsule performance in targets that have been scaled in key physics variables from NIF targets. Since the Nova geometry consists of a single ring of five beams in each end of the hohlraum, Nova experiments have been limited to controlling only the time-averaged symmetry. To address the hohlraum and hydrodynamic constraints on indirect-drive ignition, the NTC comprises so-called Hydrodynamically Equivalent Physics (HEP) goals and Hohlraum Laser–Plasma Physics (HLP) goals, as shown in Fig. 4.

The HEP program addresses capsule physics issues associated with ignition. These include hydrodynamic instability in planar and spherical geometries, the effects of drive nonuniformity on capsule performance, and the physics associated with ignition (energy gain and energy loss to the fuel) in the absence of α-particle deposition. The HEP program was subdivided into five subgoals:

- **HEP1:** Demonstrate fuel densities of 20 to 40 g/cm^3 using high-contrast pulse shaping with noncryogenic targets. The fuel density will be inferred from measurements of fuel areal density ρR using advanced neutron-based diagnostics.
- **HEP2:** Measure the reduced linear growth and early nonlinear behavior of the Rayleigh–Taylor (RT) instability at the ablation surface for x-ray-driven targets. Using planar targets, observe single-mode growth at the ablation surface by factors of >30, from which reductions by factors of 2 to 3 from the classical RT growth rate are inferred. Targets of various compositions will be used to confirm the modeling of plasma opacity as it affects x-ray-driven hydrodynamics.
- **HEP3:** Using x-ray spectroscopy, demonstrate pusher/fuel mixing that is dependent on initial target surface quality. The targets will be low-growth (perturbations grow by a factor of ~10), low-convergence ($C_r < 10$) plastic capsules with a multimode spectrum of initial surface perturbations.

- **HEP4:** Demonstrate quantitative understanding of implosion experiments to convergence ratios $C_r \approx 10$ with overall hydrodynamic instability growth factors of 100 to 500 for an *l*-mode spectrum similar to those characteristic of ignition target designs (for which maximum growth occurs for mode numbers $l \approx 30$).
- **HEP5:** Extend HEP4 experiments to convergence ratios $C_r = 20$–40 with capsule performance consistent with Nova's symmetry limitations.

The HLP program addresses laser–plasma coupling, x-ray generation and transport, and the development of energy-efficient hohlraums that provide the appropriate spectral, temporal, and spatial x-ray drive. The HLP program was divided into seven subgoals:

- **HLP1:** Demonstrate acceptable coupling of laser light to x rays in low-Z-lined hohlraums using shaped laser pulses and peak radiation temperatures up to $T_R \approx 210$ eV.
- **HLP2:** Demonstrate acceptable coupling of laser light to x rays in lined hohlraums with peak radiation temperature $T_R \geq 270$ eV with 1-ns square pulses. Acceptable coupling for HLP1 and 2 was defined as follows:
  - Absorption fraction $f_{abs} > 90\%$.
  - Stimulated Brillouin scattering fraction $f_{SBS} < 5$–10%.
  - Suprathermal-electron fraction $f_{hot} < 5\%$ at $T_{hot} \geq 50$ keV.
  - Stimulated Raman scattering fraction $f_{SRS} < 5\%$.
- **HLP3:** Demonstrate an ability to measure and calculate energy balance in a hohlraum with emphasis on wall loss and albedo and an ability to diagnose and predict the (time-dependent) position of the laser-produced x-ray source within the hohlraum. Demonstrate an ability to characterize and model plasma evolution in a hohlraum.
- **HLP4:** Demonstrate symmetry control with low- and intermediate-Z-lined hohlraums. Achieve low-order *l*-mode (P_2, P_4) time-integrated symmetry ≤2–4%.
- **HLP5:** Demonstrate acceptable levels of scattering in large-scale plasmas that match the plasma conditions, beam geometry, and beam smoothing of ignition hohlraums as closely as possible. The plasmas should have density and velocity scalelengths ~2 mm, electron temperature >1.5 keV, and $n/n_c < 0.15$. Acceptable levels of scattering were defined as follows:
  - Stimulated Brillouin scattering fraction f_{SBS} (back, side) < 5–10%.
  - Stimulated Raman scattering fractions f_{SRS} (back, side) < 5–10% and f_{SRS} (forward) < 5%.
- **HLP6:** Evaluate the impact of laser beam filamentation on SBS and SRS and develop control techniques to the extent necessary to ensure acceptable levels of scattering.
- **HLP7:** Develop an improved understanding of x-ray conversion efficiency in hohlraums under conditions appropriate for NIF ignition targets.

Table 1 shows where each NTC element is discussed in detail in this *Quarterly*. The degree to which convergence ratio can be increased on Nova for HEP5 is yet to be determined. The appendix gives a more detailed statement of the objectives of the NTC as presented at the 1990 NAS Review. Because of the declassification of many aspects of ICF in 1993, the appendix includes many details, such as specific hohlraum temperature goals, left out of the unclassified summary contained in the NAS report. These goals have served as a very valuable guide to the Nova Target Physics Program for the past five years, and have largely been carried out as specified.

Changes to the NTC Objectives and Plans for Further Work on Nova

One notable change to the Nova targets has been made as we have learned from the results of more detailed NIF target designs. Ignition-scale hohlraums require some sort of a low-Z fill to control the position of laser beam absorption and x-ray emission. At the time of the NAS report, ignition targets used low-Z liners on the inside of the hohlraum wall to create this plasma. These "lined hohlraum" targets, spelled out in the NTC, worked well in the Nova experiments

TABLE 1. List of NTC elements in this *Quarterly*.

Subgoal discussion	Article title	Page no.
HEP:		
• HEP1	Indirectly Driven, High-Convergence Implosions	226
• HEP2	Planar and Cylindrical Rayleigh–Taylor Experiments on Nova	232
• HEP3	Diagnosis of Pusher–Fuel Mix in Indirectly Driven Nova Implosions	265
• HEP4	High-Growth-Factor Implosions	271
HLP:		
• HLP1, HLP2, and HLP7	Energy Coupling in Lined Hohlraums	281
• HLP3 and HLP4	Nova Symmetry: Experiments, Modeling, and Interpretation	293
• HLP5 and HLP6	Laser–Plasma Interactions in NIF-Scale Plasmas	305
Appendix	Nova Technical Contract as presented to the 1990 NAS Review of ICF	A-1

described below. But detailed NIF target calculations predicted a significant asymmetric pressure pulse on the capsule when the liner plasma collapsed onto the hohlraum axis. Although this pulse may have been an artifact of calculations that are currently constrained to be axisymmetric, the baseline NIF target design has been switched from a liner to a low-Z gas fill. Symmetry control with gas-filled targets has been demonstrated on Nova, but the experiments are still in progress and will not be described here.

Continuing work aimed at gaining further understanding of ignition targets is covered under a set of goals called the Target Physics Contract, which are extensions of goals in the NTC. Most of these goals should be reached within about a year.

HEP2 has been extended to include direct measurement of perturbation growth in spherical and/or cylindrical geometry and demonstration of a quantitative understanding of the three-dimensional (3-D) evolution of the RT instability. This objective has included the development of 3-D radiation hydrodynamics codes, which are now used in the planning and evaluation of experiments.

HEP4 and HEP5 are continuing, with emphasis on 3-D calculations of the effects of capsule surface and hohlraum flux perturbations on capsule performance. Target designs that minimize the flux asymmetry are being evaluated to determine the limits to the achievable convergence ratio on Nova.

The goals of the HLP program, including energetics, x-ray emission pattern and hohlraum-wall blowoff, and symmetry have been extended to include gas-filled hohlraums. HLP5 and HLP6 will continue to explore the limits to hohlraums imposed by laser–plasma interaction with various forms of laser-beam coherence control.

Notes and References

1. National Academy of Sciences Review of the Department of Energy's Inertial Confinement Fusion Program, Final Report (National Academy Press, Washington, DC, 1990).
2. H. T. Powell and D. L. Correll, *ICF Quarterly Report* **4**(1), Lawrence Livermore National Laboratory, Livermore, CA, UCRL-LR-105821-94-1 (1994).
3. J. D. Lindl, *Phys. Plasmas* **2** (11), 3933–4024 (1995).
4. J. H. Nuckolls, L. Wood, A. Thiessen, and G. B. Zimmerman, *Nature* **239**, 139 (1972).
5. W. K. Levedahl and J. D. Lindl, *Energy Scaling of ICF Targets for Ignition and High Gain*, Lawrence Livermore National Laboratory, Livermore, CA, X-Division Memorandum CLY-95-004 (1990).
6. C. Verdon, *Bull. Am. Phys. Soc. II* **38** (10), 2010 (1993).
7. S. W. Haan, *Radiation Transport Between Concentric Spheres*, Lawrence Livermore National Laboratory, Livermore, CA, X-Division Memorandum COPD 83-64 (1983).

IGNITION TARGET DESIGN FOR THE NATIONAL IGNITION FACILITY

S. W. Haan	*P. A. Amendt*	*G. L. Strobel*	*D. B. Harris**
S. M. Pollaine	*J. A. Futterman*	*M. Tabak*	*N. M. Hoffman**
J. D. Lindl	*W. K. Levedahl*	*S. V. Weber*	*B. H. Wilde**
L. J. Suter	*M. D. Rosen*	*G. B. Zimmerman*	*W. S. Varnum**
R. L. Berger	*D. P. Rowley*	*W. J. Krauser**	*F. J. Swenson**
L. V. Powers	*R. A. Sacks*	*D. C. Wilson**	*P. A. Bradley**
W. E. Alley	*A. I. Shestakov*	*S. Coggeshall**	

Introduction

The goal[1,2] of inertial confinement fusion (ICF) is to produce significant thermonuclear burn from a target driven with a laser or ion beam. To achieve that goal, the national ICF Program has proposed a laser capable of producing ignition and intermediate gain.[3] The facility is called the National Ignition Facility (NIF). This article describes ignition targets designed for the NIF[4] and their modeling. Although the baseline NIF target design, described herein, is indirect drive, the facility will also be capable of doing direct-drive ignition targets—currently being developed at the University of Rochester.[5]

Figure 1 illustrates the baseline target, which is typical of all our ignition targets. A spherical cryogenic capsule, composed of deuterium–tritium (DT) gas, DT solid fuel, and an ablator, is encased in a cylindrical Au hohlraum with two laser entrance holes (LEHs) at opposite ends. The hohlraum peak radiation temperature (T_R) is 250–300 eV, with a shaped prepulse for a low-entropy implosion. The ablation pressure allows the fuel shell to reach a velocity of $3–4 \times 10^7$ cm/s. The central part of the DT is then compressed and heated, forming a hot spot that reaches ignition conditions of density times radius $\rho r \sim 0.3$ g/cm^2 and ion temperature ~10 keV. Then, α deposition "bootstraps" the central temperature to >30 keV. The hot-spot density at ignition is typically 75–100 g/cm^3. The hot spot is tamped by a colder main fuel layer, with $\rho\Delta r \approx 1$ g/cm^2 and density ≈1000 g/cm^3. The burn propagates into the main fuel layer, and 10–15% of the total DT mass is

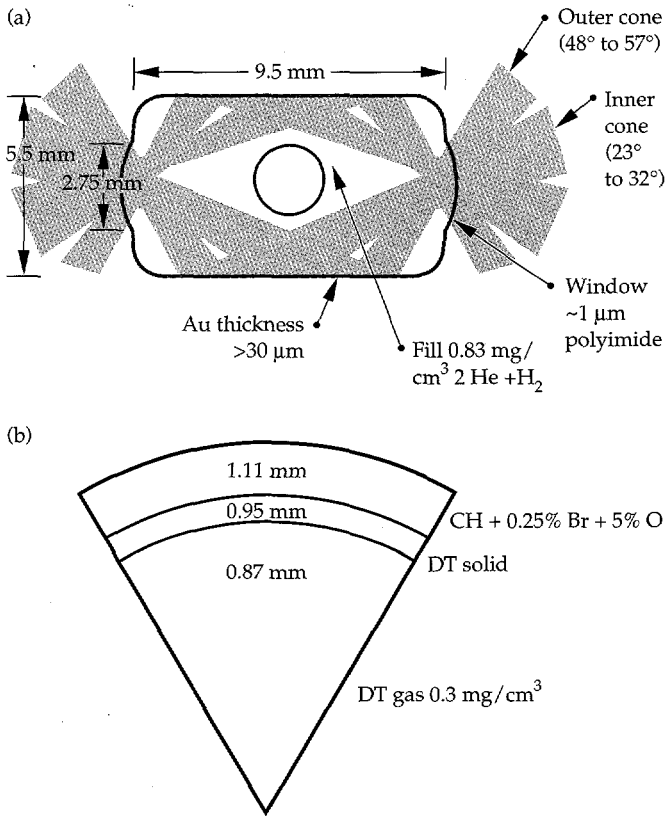

FIGURE 1. This ignition target (referred to as the point-design target or PT) uses 1.35 MJ of laser energy. (a) Shows the entire target, and (b) shows details of the central spherical capsule. The DT fuel is in a cryogenic layer, surrounded by a CH ablator doped with 0.25% Br. The capsule is in the center of a Au hohlraum, which the incoming laser beams heat to 300 eV. The beams are arranged in two cones entering from opposite sides. (50-05-0494-1802pb01)

*Los Alamos National Laboratory, Los Alamos, New Mexico

burned. The target shown in Fig. 1 produces 10–15 MJ of yield in simulations, depending on the modeling used.

Assuming the laser meets other specifications, the two most important laser parameters determining the margin for ignition are the total energy and the peak power.[6] Ignition requires both energy and power, as indicated in Fig. 2. The ignition region is bounded on one side by hydrodynamic instabilities. Ultimately, this boundary of the ignition region is determined by the capsule surface smoothness; Fig. 2 assumes the surface finish currently achieved on Nova capsules in modeling described in this article. On the other side, the ignition region is bounded by laser–plasma instabilities. Laser intensity and other parameters determining the instabilities (especially the electron density n_e) depend primarily on the desired peak hohlraum T_R. Estimates of the laser–plasma instabilities, described here, indicate that laser–plasma instabilities will be acceptable in targets driven to at least 320 eV (shown as the upper boundary of the ignition region in Fig. 2).

The smallest possible ignition target with this assumed surface finish, at 0.8 MJ and 300 TW, would have no remaining margin for uncertainties or errors in the target modeling. We have specified the NIF at 1.8 MJ and 500 TW to provide margin for such uncertainties. This margin is adequate to cover our estimates of energetically significant uncertainties, as described in this article.

Baseline Ignition Targets

Figure 1 shows the baseline design, referred to as the PT: "point-design target." Cryogenic hardware, not shown, is external to the hohlraum. The spherical capsule is a doped CH ablator around a shell of solid cryogenic DT. The solid DT layer is self-smoothing, because of the β-smoothing effect.[7] The cryogenic temperature controls the density of the central DT gas. The hohlraum is filled with a 50–50 (atomic) mixture of He and H. This gas conducts away the β decay energy before the target is shot and maintains the open hohlraum cavity during the implosion. The mixture of gases minimizes stimulated Brillouin scattering (SBS).

The PT uses 1.35 MJ of 3ω light, which is intermediate between the full 1.8 MJ and the "ignition cliff" at 800 kJ. Most of our modeling concentrates on this intermediate-scale target. It is sufficiently robust that we can make a good case for its ignition, while it leaves margin for uncertainty with a 1.8-MJ facility. Also, by using a relatively small target to set specifications for power balance, pointing, target fabrication quality, and so forth, we can be sure that the specifications are adequate for a range of likely targets.

Figure 3 shows an optimal T_R profile for the capsule, used as input to our capsule modeling, and an input laser profile. The target can tolerate moderate deviations from the nominal profile. For example, Fig. 4 shows the yield from integrated calculations (described later in more detail) as the duration of the peak power portion of the pulse is varied. Our robustness study of the PT is described in more detail below.

The light entering each LEH is in two cones, as shown in Fig. 1, and we can minimize time-dependent asymmetry in the x radiation incident on the capsule by dynamically varying the relative power of the cones. About one third of the energy must go into the waist

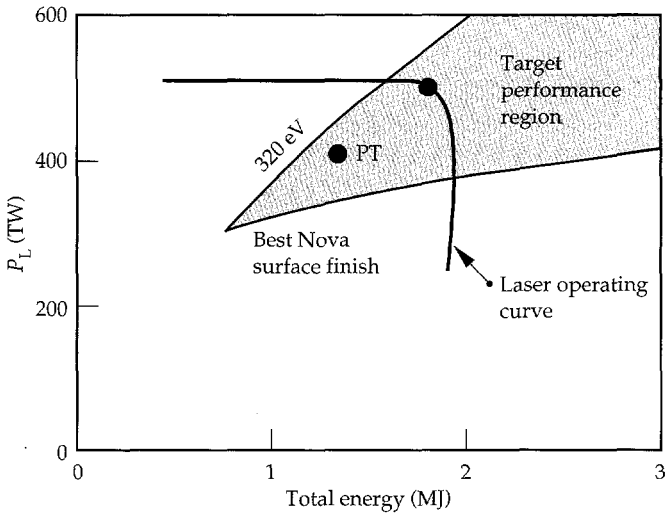

FIGURE 2. Total laser energy and peak power determine the margin for ignition. Powers and energies along the indicated curve will be accessible to the NIF, as currently planned. The upper dot illustrates the laser's nominal operating point (1.8 MJ, 500 TW); the lower dot illustrates the energy and power needed to drive the PT (1.35 MJ, 410 TW). (50-05-0494-1805pb01)

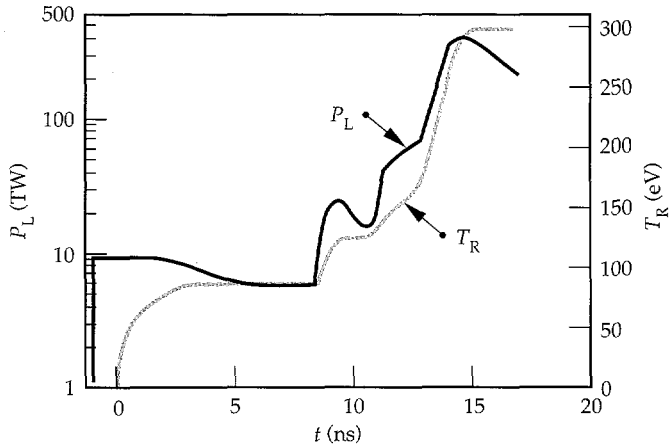

FIGURE 3. Temperature vs time optimal for the PT capsule, and laser power vs time to drive the target. The shaped pulse prior to peak drive is needed to compress the target, increasing the pressure in a controlled way before applying peak power. The gray curve is the radiation temperature vs time that drives capsule simulations, and the black curve is the laser power vs time used as input to hohlraum simulations. (50-05-0295-0395pb01)

cones. The 192 beams are clustered in groups of four, so that there are effectively 48 spots. These are divided as 8 spots in each of the inner cones and 16 in the outer cones. We may use slightly separate wavelengths in the four beams in each spot to limit laser–plasma instabilities. The four beams combine at an angle corresponding to an effective $f/8$ optic.

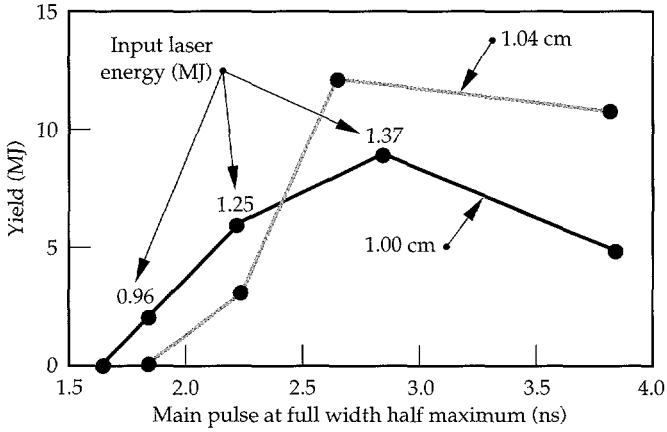

FIGURE 4. Yield vs duration of the peak power pulse, from integrated 2-D simulations. The pulse width changes by varying the cut-off time. The energy in a sample of the pulses is shown. The failure at short pulse appears to be due to asymmetry, not energetic failure to ignite. Two different hohlraum lengths, providing different symmetry "tunes," are shown. (50-05-0295-0388pb01)

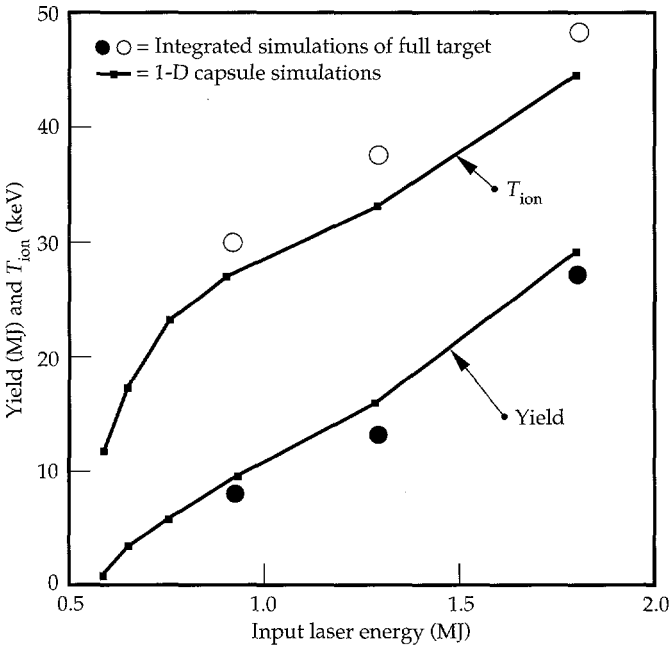

FIGURE 5. Yield and burn-weighted ion temperature for geometric scales of the PT. The lines show 1-D calculations of the capsule alone, in which linear dimensions and times are scaled together (the horizontal scale is effective energy, that is, 1.35 MJ times the scale factor cubed; the dots are integrated calculations, plotted against the laser energy). For these, linear dimensions and times were scaled, and laser powers were scaled as the square of the scale factor. Hohlraum length and cone-to-cone power ratios were adjusted to recover symmetry. (50-05-0295-0389pb01)

Each beam is focused to an elliptical spot, with the minor axis in the plane of the laser ray and the hohlraum axis. This maximizes the LEH clearance while minimizing the laser intensity. The spot has a shape approximating a flat top (probably a sixth-order super-Gaussian), again to minimize the peak intensity while maximizing LEH clearance. The nominal spot is 500 μm × 1000 μm at best focus. Such a spot can be made with recently developed kinoform phase plate techniques.[8]

The pulse shape shown in Fig. 3 creates four shocks, with the final shock bringing the ablator up to peak pressure with sufficiently low DT entropy. The entropy requirement implies a corresponding requirement on the precision of the pulse shaping. For optimal performance, the shocks must be timed within about 200 ps. Adequate shock timing may not be predictable *a priori* given uncertainties in opacity and equation-of-state (EOS), but is achievable with an experimental program using techniques currently in use on Nova.[9]

The CH ablator contains 0.25% Br dopant. (Some Nova targets currently use Br-doped CH.[10]) The dopant is used to control the stability of the ablator/DT interface. It reduces the preheat in the CH and eliminates an unstable density step at the CH/DT interface. The CH is assumed to contain 5% O as an incidental fabrication by-product.

We conclude this section with a brief description of our baseline one-dimensional (1-D) capsule simulations. These simulations are performed with the LASNEX code,[11] using Legendre decomposed radiation transport,[12] EOSs calculated in line with a "Quotidian EOS" package,[13] and average-atom opacities calculated with the XSN code.[14] We have also simulated the capsule implosion with other radiation transport schemes, but find no difference in the calculations. Implosion calculations use as a source nonPlanckian frequency-dependent radiation determined from hohlraum simulations. The spectrum affects the short-wavelength hydrodynamic instability growth; other than this, the spectrum has little effect on target characteristics. We normally calculate the deposition of α particles produced by the burn with the multigroup diffusion package in LASNEX.[15] Hatchett[16] performed a baseline 1-D simulation of the PT using a Monte Carlo charged-particle transport code[17] and found that the ignition and burn are essentially the same as with multigroup charged-particle diffusion.

Other Possible Ignition Targets

Modeling of a wide variety of other targets has been performed at various levels of detail. Several important aspects of the target can be varied, providing

different trade-offs of the remaining uncertainties in our understanding.

We can vary the size of the target, and the energy it uses. Direct geometric scales of the PT produce good burn at any laser energy above about 700 kJ, as shown in Fig. 5. This energy margin allows for loss of energy to stimulated scattering processes and laser coupling. Also, it allows us, if necessary, to change the relative size of the hohlraum and capsule. This allows a trade-off of the capsule ignition physics, and hydrodynamic instability, with symmetry and hohlraum filling.

The knee at 600–800 kJ in Fig. 5 and the two thresholds at 1.6 and 1.8 ns in Fig. 4 are typical signatures of ignition. Without α deposition and thermonuclear bootstrapping, NIF targets would be expected to produce no more than 10–100 kJ of yield at the likely ion temperatures of less than about 10 keV. Experimental demonstration of ignition will be clear when we do a series of targets that scan through the threshold between such a non-bootstrapping mode and burn producing about 1 MJ or more. This could be done by varying the target size, as shown in Fig. 5, or more likely by varying the implosion velocity (implicit in Fig. 4). Varying the D to T ratio will provide another easy-to-interpret lever on the burn rate. Curves of yield vs implosion velocity, for various D to T ratios, should show an inflection and a large increase in yield when the burn threshold is crossed for ratios near 50–50.

Various other target designs, described next, are at various scales in the ignition range.

Uncertainty in ablation characteristics can be addressed by using other ablator materials. In particular, Be generally performs better than CH as an ablator. (The PT uses a CH ablator because of fabrication experience with Nova.[18]) Be must be doped more heavily than CH, and radially varying the doping allows for complete optimization. Designs exist in which the Be is doped with Cu, which appears attractive from a fabrication point of view, and others with a mixture of Na and Br. In the most highly optimized targets, the additional performance margin obtained by using Be instead of CH is equivalent to about 25 eV in peak hohlraum T_R. The advantage is better at 250 eV than at 300 eV.

Another important advantage of Be is more hydrodynamic stability. Using the modeling described below in the section on hydrodynamic instabilities, we have found a clear advantage to Be targets. Because it ablates faster, Be is more stable—the initial mass of the Be ablator is nearly twice that of the CH. The outer surface roughness specification is somewhat looser for Be than for CH, but the most important difference is in the required surface quality for the inner surface of the DT ice. Perturbations initially on the ice grow by coupling to the outer surface, the unstable ablation front, during acceleration; this coupling is much less effective through the more massive Be shell. As a result, a Be target (driven at 300 eV) can tolerate about four times larger perturbations initially on the inner surface of the ice than a CH target.

We can modify the convergence ratio (defined as the initial outer radius of the ablator divided by the ignition-time hot-spot radius) by varying the initial central DT gas density. Since reducing the convergence ratio reduces the final ρr, it also reduces the yield. If the initial gas fill is increased the ignition is marginal, i.e., the yield is reduced from 15 MJ nominal to about 1 MJ. These low-convergence targets require gas densities that would initially be in vapor equilibrium with liquid DT (as opposed to solid for the PT), and fielding them will require some modifications in the fabrication and fielding technology. The triple-point gas density,[19] 0.68 mg/cm^3, corresponds to a PT yield of 10 MJ.

Various peak drive temperatures are possible—high temperatures stress laser–plasma instabilities while minimizing hydrodynamic instabilities, and low temperatures provide the opposite trade-off. The baseline is 300 eV, a compromise between the two constraints. We have designed capsules driven at temperatures as high as 400 eV that appear to be very resistant to hydrodynamic instabilities. Using doped Be as an ablator, we have designed targets driven at 250-eV for which ignition is nearly as robust as with CH at 300 eV. Laser–plasma instabilities are estimated to be very benign in the 250-eV hohlraum.

There is also a wide variety of possible pulse shapes. The pulse shown in Fig. 3 has four pulses or steps, each at a time and power to launch a shock, as needed, for the low-entropy implosion. Many other pulses can result in the same shocks in the fuel. We can use shorter pulses at higher powers (sometimes called "picket fence pulses"); we have used steps with the power held constant for a few nanoseconds in each step; at the other extreme, we have used pulses in which the power increases smoothly from an initial 10 TW up to peak power. Each of these shapes represents a different trade-off of laser, hohlraum, and capsule physics.

We have also designed targets in which the solid DT fuel is supported in a foam layer.[20] This may be an important option if β layering is inadequate. DT-wettable foams of density 0.05 g/cm^3 with micrometer-scale cell structure have been fabricated, and our designs assume this density. The foam targets work nearly as well as the solid DT targets. If β layering, or some other technique, can be used to maintain a pure DT layer about 10 μm thick on the inside of a foam-supported main fuel layer, ignition occurs in clean DT and target performance is barely degraded by the presence of the foam. If all of the solid DT must be supported by foam, it is somewhat more difficult to ignite, although targets at the PT scale still ignite with some remaining margin.

There are numerous possible ignition designs that have attractive features, and may actually perform better

than the point design, but that are not as closely connected to the existing experimental data. Direct-drive targets are an important option, pending experimental results from the Omega Upgrade at the University of Rochester. Other hohlraum designs are being investigated on Nova—for example, Au shields placed between the capsule and the LEHs can reduce the time-dependent asymmetry. Recent results on Nova for such a hohlraum are in excellent agreement with expectations based on simulations.[21] As the NIF is being planned and built, experiments on Nova will continue to refine our understanding of the target physics and will allow us to optimize the NIF design further.

So far we have described the various target options that work according to current modeling; we have also found two target concepts where our modeling predicts difficulties:

- We considered lining the hohlraum with CH, instead of the He/H gas fill described earlier. However, we find that the lining stagnates on axis, creating a pressure spike that perturbs the capsule implosion unacceptably. Unfilled hohlraums have too much Au absorption of the light. We intend to consider alternate liners and unfilled hohlraums with short, low-temperature pulses.
- In principle, it seems possible to achieve ignition with noncryogenic gaseous DT. However, we have found that the implosion velocities required for ignition at the NIF scale result in high core temperatures before ignition ρr is reached, and then conduction from the hot spot is very high. In a cryogenic target, energy conducted from the hot spot into the DT pusher heats more DT—this increases the mass of the hot spot, and the energy is not lost. If the hot spot is surrounded by inert material, the energy is not only lost from the fuel, but it serves to degrade the compressibility of the pusher. Rayleigh–Taylor (RT) instabilities would also be much more problematic if the igniting fuel were surrounded with inert material. Therefore, we have been unable to calculate ignition successfully in noncryogenic capsules at the NIF scale.

Hohlraum Design and Modeling

The size of the hohlraum relative to the capsule is determined by a variety of trade-offs. The required profile of T_R vs time is determined by the capsule, and any hohlraum larger than some minimum size could provide the needed T_R vs time profile. A larger hohlraum takes more laser energy and power, and the optimal size is a trade-off of the energy and power requirements and the need for symmetry and acceptable plasma filling. Our modeling indicates that the symmetry and laser–plasma instabilities are acceptable in the baseline hohlraum. Assuming a 1.8-MJ, 500-TW NIF, there will be margin to increase the hohlraum size with the PT capsule, increasing the margin for laser–plasma instabilities or asymmetry. If necessary, we can further increase this margin by using a smaller capsule, at the cost of either increasing hydrodynamic instabilities or developing Be-ablator fabrication technology.

Even with perfect laser pointing and beam-to-beam power balance, there is some asymmetry that we call the intrinsic asymmetry. This asymmetry arises because of the LEH and the bright laser-irradiated spots (the LEH alone causes a 15% peak-to-valley asymmetry). As described in Ref. 6, the laser spots are placed to cancel the LEH asymmetry. The symmetry can be adjusted by changing the hohlraum length and the pointing of the beams. The quantities determining the intrinsic symmetry change in time: the LEH shrinks, the laser spots move due to plasma evolution, and the spots become less bright relative to the overall hohlraum brightness. With a single cone of beams, we found that the time-dependent asymmetry was too large. Two cones of beams can be arranged to provide adequate symmetry. Also, with two cones the time-dependent asymmetry can be corrected dynamically by varying the relative power in the cones as a function of time. This detailed symmetry tuning will have to be done with a time-dependent symmetry campaign similar to those being done on the Nova laser.[22]

To model the intrinsic asymmetry, we use a detailed two-dimensional (2-D) simulation with a radiation-hydrodynamics code such as LASNEX.[13] We use the best available radiation transport model for the hohlraum/capsule coupling, and simulations are continued all the way through burn. The simulations track the laser beams, calculating inverse Bremsstrahlung energy deposition and any refraction that occurs. We typically use XSN nonLTE multigroup opacities,[16] although we have also performed simulations with an opacity table derived from the super transition array opacity model.[23] Any coupling to the capsule via hydrodynamic pressure or electron conduction is included.

We have achieved adequate symmetry and good burn in such integrated simulations of a variety of designs: the PT at several scales as shown in Fig. 5, two Be designs driven at 250 eV and at 300 eV, and a smooth-pulse 250-eV Be design. All except the PT scales shown in Fig. 5 use 1.1–1.5 MJ, at powers ranging from 365–500 TW. They give yields in the integrated simulations that are between 50–90% of clean 1-D yields and show unambiguous ignition.

Modeling asymmetry from imperfect power balance and pointing of the laser beams requires fully three-dimensional (3-D) asymmetry. This asymmetry has been estimated analytically using laser-spot brightness and positions determined from the 2-D LASNEX simulations. Also, the asymmetry has been calculated in 3-D with a view-factor code.[24] We have used fully integrated

calculations (described earlier) to confirm the modeling and for some sensitivity studies. The actual asymmetry on the capsule is 3-D, and its effect on the implosion must be estimated with 2-D simulations of the implosion driven with an asymmetric radiation source.

We have imposed a wide variety of asymmetries on 2-D capsule implosions to ensure that the specified asymmetry levels are acceptable. Asymmetry can affect ignition in a variety of ways: the obvious kinematic effects of differing velocities; initiation of RT instability growth, especially evident during deceleration; mass flow toward less driven regions, seeding RT instability; irregular hot-spot compression, sometimes forming jets that protrude from the core and disrupt the imploded configuration; and delayed ignition, resulting in more RT growth. The maximum tolerable asymmetry depends on its temporal and spatial specifics. In summary, the capsule can tolerate less than about 1% time-averaged asymmetry, 5–10% time-dependent swings in asymmetry that last for ~2 ns, and larger swings if they last much less than 2 ns.

We do not find much variation in sensitivity to asymmetry among the various targets we have designed. Smaller capsules are slightly more sensitive to asymmetries that couple to deceleration RT growth. The difference is not large, and symmetry sensitivity is not an issue that is important in deciding the overall trade-offs of laser size and power. Varying the hohlraum size, with a given capsule, is the symmetry issue likely to be more important in the trade-offs.

The 3-D view factor calculations indicate that with nominal pointing errors—each beam is to point within 50 μm of its nominal position, rms deviation—the resulting additional asymmetry on the capsule will be significantly <1%. This pointing specification also ensures more than adequate clearance of the LEH. This requirement is similar to that met by the Nova laser (30 μm rms,[25] which is 10 μrad, while 50 μm rms on NIF is 7 μrad because of the longer focal length).

The 3-D view factor calculations also indicate that 10% rms power imbalance results in <1% asymmetry on the capsule, provided the deviations are uncorrelated among the 192 beams. The tolerable power imbalance can be much larger than this, depending on its temporal dependence. If there are correlations between the beams' powers, a much tighter power balance requirement is necessary. Groups of eight beams, with each group entering the same area of the hohlraum, must be balanced within about 3%. Generally the requirements are consistent with purely independent statistical deviations of the 192 beams; any correlations significantly beyond this may increase the asymmetry unacceptably.

These requirements on the laser are well within current Nova performance parameters of 3% rms energy imbalance, and 5–10% power imbalance over time scales that are generally less than half the pulse length.[26] This does not mean that symmetry in Nova hohlraums is as good as in NIF hohlraums; the looser requirements for NIF are a result of the larger number of beams.

Asymmetries might also arise from laser–plasma interaction processes or other phenomena, such as RT instability at the Au/He interface, which are currently predicted not to be significant but for which uncertainty remains. Light can be scattered or it can be absorbed more or less efficiently at different positions in the hohlraum. The effect in all cases is equivalent to a power balance change, a movement of the x-ray emission spots, or perhaps a spreading of the laser deposition spots (for small-angle side-scattering). Difficulties could arise only if these effects are so large that the irreproducible part of them is larger than the limits described here. If any of these processes occurs but is reproducible and not too large, the effect can be compensated for by changing the hohlraum design parameters. Estimates based on Nova experiments and appropriate theory and modeling indicate that these processes can be kept within acceptable limits. If not, our ultimate recourse will be to increase the hohlraum size, reduce the laser intensity, and correspondingly reduce the hohlraum drive temperature.

Laser–Plasma Instabilities

The most important laser–plasma scattering processes are SBS, stimulated Raman scattering (SRS), and filamentation. In SBS and SRS, the incident laser beam scatters from electron waves and ion waves, respectively, in the forward, side, or backscatter direction. Backscatter is calculated and observed to be the most unstable process, although sidescatter must be examined for its possible effect on capsule symmetry. SRS forward scatter is a very weak process; forward SBS is being evaluated for possible symmetry effects because of the exchange of energy between overlapping beams.[27] Filamentation or whole-beam self focusing results from the refraction of the laser light into low-density regions, which are themselves produced by the pressure gradients from nonuniform laser heating or by ponderomotive forces. All of these processes are sensitive to the n_e and temperature, and laser intensity and wavelength.[28] In addition, SBS is sensitive to the electron-ion temperature ratio, velocity gradient, and the fraction of light and heavy ions in multiple species plasma.[29] Also, we have shown with 3-D filamentation simulations[30] that filamentation is sensitive to the speckle length (the axial length of a diffraction-limited hot spot near the focal plane of the laser beam). The speckle length increases with the square of the f-number of the focusing system.

The laser must propagate through 3–5 mm of hot (T_e ~ 3–5 keV at peak power), low-density ($n_e \leq 1 \times 10^{21}$ cm^{-3}), low-Z (mixture of He and H) plasma. The density is about 0.05 critical over most of the beam path. For the inner ring of beams, the density reaches as high as 15% of critical for the last millimeter

of pathlength. However, this far into the hohlraum the individual laser beam intensity has decreased substantially from its peak of 2×10^{15} W/cm^2.

These scattering processes affect the target performance in several ways. Of course, energy scattered back out of the hohlraum is unavailable for x-ray conversion. The total energy lost comes out of the ~50% energy margin shown in Fig. 2. The irreproducible part of this becomes a pulse-shape uncertainty, and any resultant geometrical nonuniformity can affect the symmetry of the irradiation on the capsule. These effects will be tolerable if the scattering is less than about 10%. We do not expect hot electrons produced by SRS to have any effect on target performance.

We estimate that the scattering processes will be acceptable under these predicted plasma conditions. Experimentally verifying these estimates is an action part of the Nova program, described in "Laser–Plasma Interactions in NIF-Scale Plasmas (HLP5 and HLP6)" on pg. 305 of this *Quarterly*.

Modeling of Hydrodynamic Instabilities

The shell is subject to RT instability on the outside during its acceleration and on the inside during deceleration. There is also Richtmyer–Meshkov (RM) instability at all interfaces. (These instabilities are reviewed in Ref. 31.) Short-wavelength RT growth in these capsules is stabilized by ablation of material through the unstable interface and by the finite scale length on the ablation front. Experimental[32] and calculational[33] aspects of this stabilization are well documented. During deceleration, the growth of short wavelengths is also reduced from classical RT since the unstable interface is between two DT regions, the hot spot and the main fuel, and again there is ablation (driven by electron conduction in this case) and a finite gradient scale length. Also, perturbations that grow on the outside must couple through the shell to affect the ignition, and short wavelength modes couple less effectively. These effects all reduce the impact of the short wavelengths, so the system is only weakly nonlinear. The targets have been designed so that this is the case.

We have based our modeling on linear analysis that is as accurate as possible, with an extension into the weakly nonlinear regime, as necessary. The linear analysis is based on a decomposition of the surface perturbations into spherical harmonics, which are eigenmodes of the linear evolution. We determine the single-mode growth spectrum by running multiple 2-D simulations, each of one single mode in the linear regime throughout the simulation. This provides the most accurate calculation of all known effects, including stabilization, RM growth, and convergence effects. This set of calculations provides a spectrum of growth factors, which we combine with an assumed initial surface spectrum to determine the ignition-time perturbation. Using a nonlinear saturation model from Ref. 34, we determine whether the perturbations are nonlinear and estimate the nonlinear saturation. This results in a curve of ignition-time perturbation amplitude as a function of initial perturbation amplitude.

To test the weakly nonlinear analysis, we also run full simulations of multimode perturbations with realistic initial amplitudes. Currently simulations must be 2-D, and the number of modes that can be included is limited. We have run a variety of multimode simulations on several capsules, at solid angles ranging from relatively small conic sections to half-spheres. Results are consistent with the modeling described earlier, although further substantiation is an area of current work. Recent development of 3-D codes will allow testing of possible differences between 2- and 3-D evolution.[35]

We must also estimate how the perturbations around the hot spot at ignition time will affect the ignition. The unstable interface is between relatively cold, dense DT and the hot, lower-density DT. Material mixing of different elements is not occurring, and there is only thermal mixing. The actual perturbations are 3-D, and multimode, and the weakly nonlinear perturbation growth analysis indicates that the spectrum is strongly dominated by mode numbers around $l = 10$–$15°$. The 3-D character cannot be fully represented in any existing code; available 3-D codes do not include all of the relevant physical processes. There is experimental[32] and calculational[35] evidence that the multimode 3-D perturbation is probably an array of spikes penetrating in toward the hot-spot center, surrounding approximately hexagonal bubbles. In 2-D, we modeled this array of spikes and bubbles five ways: (1) We simulated a single bubble of appropriate solid angle surrounded by a curtain of material falling along a reflecting boundary condition. The circular cone represents approximately a multifaceted 3-D cone of similar size and gross shape. (2) We ran perturbations with the opposite sign: a spike on axis surrounded by a circular bubble. (3) We simulated perturbations on the waist that represent long circular ridges and curtains. (4) We continued through burn time the multimode 2-D simulations mentioned earlier. (5) We did 1-D modeling in which the thermal mixing caused by the perturbation growth is represented as an enhanced thermal conductivity in the perturbed region.

All of these approaches give similar results, regarding how large a spike can be tolerated before ignition is quenched. Combined with the modeling described earlier, this corresponds to a maximum tolerable initial ablator surface roughness of about 50 nm rms. This compares with 30 nm rms on current Nova capsules.

We have also considered the bubble penetration from the outside of the shell at peak velocity. We find that the surface finish requirements for shell integrity during acceleration and for ignition are similar. This

equivalence depends weakly on the shape assumed for the spectrum of initial perturbations.

Because we have modeled the perturbation growth and its effects with a variety of different approaches, and get generally consistent results, we are fairly confident that our modeling is accurate. The modeling relies on 2-D code simulations of linear-regime perturbation growth, so it is very important that these be tested thoroughly. The dominant uncertainties are the dependence on the spectrum of the drive x rays, and on zoning, resulting in a net uncertainty in the outer surface finish specification that we believe to be about a factor of two. Finally, of course, it is very important to test the modeling experimentally. A major fraction of the Nova program is oriented toward verifying this modeling, with a variety of experiments measuring perturbation growth and its effects in planar[32] and spherical[5,10,36] geometry. Results from these experiments have been consistent with the modeling.

The modeling described so far pertains to surface perturbations that are initially on the outside of the ablator. Of course, there will be perturbations on the other interfaces, as well as material inhomogeneity and other fabrication defects. Any of these can be modeled in a conceptually identical way, using LASNEX simulations that assume the existence of the perturbation of interest. We have determined that the capsule tolerates perturbations initially on the other interfaces, which are much larger than tolerable perturbations initially on the outside. Perturbations on the DT/CH interface are unlikely to be large enough to matter. Ignition does not occur if perturbations on the DT gas/solid interface are greater than about 3.0 μm for the PT, and more than about 8 μm for Be capsules, which are the same size as the PT and are driven at 300 eV. Current estimates[37] of the smoothness of β layer surfaces are ~1 μm. Solid DT in a low-density foam is somewhat smoother.

In summary, the PT has a factor of about two margin in surface finish beyond surface finishes on the best current Nova capsules. The requirement on the DT gas/solid interface also gives about a factor of 2 margin compared with roughness measured on recent DT ice surfaces.

Robustness Studies

We performed extensive studies of the robustness of the PT target following the initial design work, which we categorize into two studies discussed below.

Robustness of Yield in Integrated Simulations

Choosing a particular configuration as nominal, we varied the laser powers and pointing in detailed integrated calculations (described earlier). Figure 4 is an example of such a variation (although the calculations shown there used a laser pulse slightly different from what we chose as nominal for the full set of variations). Table 1 shows the sensitivities we found, and compares them with estimates of the reliability with which we can determine and maintain these parameters. This study produced three valuable results. (1) We verified that the target can tolerate plausible variations in the input parameters (shown in Table 1). This allays concern that the performance of the target is a finely tuned optimum that would be impossible to achieve experimentally. (2) We identified ways in which the configuration we chose as nominal was not in fact optimal (most importantly, we found significant room for improvement in the pointing we were using for the inner cone). We are currently doing a second iteration, with improved pointing and better optimization of the other parameters, which should show a margin of performance even larger than that shown in Table 1. Some results of the study with the new optimization are shown in Table 1. (3) This study provides a context for designing the experimental campaign to achieve ignition. Table 1 (and subsequent revisions) shows which parameters must be measured and maintained and to what accuracy.

We are also doing integrated simulations varying several parameters at once. We have varied both the inner and outer cone laser powers separately (in addition to the variations shown in Table 1), and see sensitivity similar

TABLE 1. Sensitivity analysis of the PT using integrated calculations of the entire hohlraum/capsule target.

Laser parameter*	Determined sensitivities	Preliminary estimate
Power during foot	30%	<5%
Peak power	35%	<5%
Second-rise timing	500 ps	<100 ps
Third-rise timing	500 ps	<100 ps
Duration of peak power	800 ps	<100 ps
Inner beam power during foot (total power fixed)	25%	<5%
Inner beam power during peak (total power fixed)	35%	<5%
Inner beam power during peak (outer cone power fixed)	25%	<5%
Pointing of inner beams	85 μm (200 μm)†	<20 μm
Pointing of outer beams	100 μm (350 μm)†	<20 μm

*For each indicated parameter describing the laser input power, we tabulated the full-width at half maximum of the yield as that parameter was varied. We also tabluated estimates of the precision with which the parameters can be determined and maintained in an experimental campaign working toward ignition. In all cases, the indicated precision is dominated by estimates of experimental precision, and the corresponding specification on the laser itself is significantly smaller.

†These values are for a new optimization with the P_6 asymmetry reduced.

to that shown in Table 1. Ultimately we will explore the entire parameter space of possible variations, although we will use the new nominal design mentioned above instead of continuing to center the variations on our first preliminary optimization.

Sensitivity to Combinations of Asymmetry, Pulse-Shaping Errors, and Hydrodynamic Instabilities

To create a complete model for what could affect the implosion adversely, we utilized a series of capsule-only simulations. We started by simulating the capsule with the asymmetry determined from the nominal integrated calculation, then added perturbed surfaces, and finally added asymmetric drive sources. The asymmetry can be made to match that in the integrated calculations by extracting from the integrated simulation the asymmetry in ablation pressure in the imploding capsule. (The asymmetry can be characterized with Legendre polynomial moments, with P_2 through P_6 contributing.) Then a matching radiation drive asymmetry, in a simulation of the capsule alone, produces an identically out-of-round implosion. This technique matches the asymmetry both for a nominal design and for the off-nominal integrated calculations represented in Table 1. (We chose as nominal the same integrated calculation used as the central point for the variations presented in Table 1). We performed three variations given the "baseline" nominal asymmetric implosion.

1. **Asymmetry alone**. We found that the "nominal" asymmetry has about 50% margin in the P_6 moment and >100% margin in the P_2 and P_4 moments. This suggests that the overall robustness can be improved by reoptimizing to minimize P_6. This is part of the reoptimization mentioned above, increasing further the margin of the PT.
2. **Nominal asymmetry plus short-wavelength surface roughness**. We performed implosions with the nominal asymmetry and perturbations on both the inner and outer capsule surfaces. The spectral features of the perturbations were based on characterization of β layered DT for the ice roughness and of Nova CH capsule surface roughness for the outside. The capsule ignites and burns well with nominal asymmetry and nominal surface roughnesses of 30 nm on the CH and 1.0 μm on the DT.
3. **Off-nominal asymmetry and drive, plus short-wavelength surface roughness**. In addition to the nominal asymmetry, we included further random asymmetry—up to 4.5% rms P_2 and 1.5% rms P_4. The additional asymmetry was a random function of time, with zero mean and about 2 ns typical period of variation. We also included variations in the drive profile (the net flux onto the capsule, P_0) of ±5%. The combination of asymmetry, drive profile errors, and surface roughness represents the most complete possible model of the implosion. We found that the additional asymmetry and profile variations had little effect on the yield; for example, with 30 nm outer roughness and 1.0 μm inner roughness, we obtain 11.5 MJ of yield with the nominal asymmetry plus the variations of 4.5% rms P_2, 1.5% rms P_4, and ±5% P_0.

These robustness results are extremely encouraging assurance of the nominal design's performance.

Summary

Given the experimental substantiation from the Nova program, we have good reason to expect ignition with a 1.8-MJ, 500-TW laser. Such a laser will provide an adequate safety margin, above the ignition threshold indicated by modeling supported by Nova experiments. This margin is sufficient to cover estimated uncertainties.

We can compensate for the remaining uncertainties by adjusting the target design if necessary after additional Nova experiments, or after the NIF experiments begin. Some possible changes in the target design or performance will be energetically significant. These include:

- A factor of two in hydrodynamic instability growth (equivalent to a factor of two in surface finish, or a factor of two in the acceptable size of the bang-time perturbations) shifts the ignition cliff from 0.8 MJ to about 1.0 MJ. Improvements in surface finish could probably recover the original margin.
- The combined uncertainties in x-ray conversion and hohlraum wall loss are less than about 20% in energy.
- SBS and SRS should be less than about 10%, based on the experiments described in "Laser–Plasma Interactions in NIF-Scale Plasmas (HLP5 and HLP6)" on pg. 305 of this *Quarterly*.
- Achieving the correct power balance between the inner and outer cones of beams may require reducing the power in one or the other, so that it cannot run at its full power. This may result in a net energy loss of 10–15%.
- An error in hohlraum optimization that requires increasing the LEH radius 50% would require an increase in laser energy of 15% to regain the same hohlraum temperature.
- Similarly, increasing the hohlraum area by 35% increases the required laser energy by 15%.

Several other uncertainties are energetically insignificant. For example, the EOS and opacity of the CH ablator are sufficiently uncertain that we expect to adjust the details of the pulse shape phenomenologically, but this will not significantly affect the performance

requirements from the laser or the target performance. These errors, in combined effect, are consistent with the factor of two margin provided by a 1.8-MJ, 500-TW laser.

There are some issues that we are addressing to substantiate this conclusion further and to progress with plans for the facility. We need to make a final decision regarding the optimal cone-to-cone energy ratio, and beam angles, which will be built into the target chamber and will be difficult to change once detailed facility design is in progress. To maximize our understanding of the options available to us, we are continuing to pursue other designs—e.g., hohlraums with shields between the capsule and the LEH. Finally, we also continue to pursue more detailed modeling of the PT. These results, along with the ongoing experimental program on Nova, will either lead to increasing confidence in the performance of the PT or will indicate what changes need to be made in the design.

Notes and References

1. J. H. Nuckolls, L. Wood, A. Thiessen, and G. B. Zimmerman, *Nature* **239**, 129 (1972).
2. J. D. Lindl, R. L. McCrory, E. M. Campbell, *Physics Today* (Sept. 1992).
3. J. T. Hunt, K. R. Manes, J. R. Murray, P. A. Renard, et al., "Laser Design Basis for the National Ignition Facility," Lawrence Livermore National Laboratory, Livermore, CA, UCRL-JC-117399 (1994).
4. S. W. Haan et al., *Phys. Plasmas* **2**(6) (1995).
5. C. Verdon, Laboratory for Laser Energetics, Rochester, NY, private communication (1994).
6. J. D. Lindl, "Development of the Indirect-Drive Approach to Inertial Confinement Fusion and the Target Physics Basis for Ignition and Gain," UCRL-JC-119015218 (1995); submitted to *Phys. Plasmas* (1995).
7. A. J. Martin, R. J. Simms, and R. B. Jacobs, *J. Vac. Sci. Technol.* A **6**(3), 1885 (1988).
8. S. N. Dixit, J. K. Lawson, K. R. Manes, H. T. Powell, and K. A. Nugent, *Opt. Lett.* **9**, 417–419 (1994).
9. R. L. Kauffman, L. J. Suter, C. B. Darrow, J. D. Kilkenny, et al., *Phys. Rev. Lett.* **73**, 2320–2323 (1994).
10. C. J. Keane, R. C. Cook, T. R. Dittrich, B. A. Hammel, et al., "Diagnosis of Pusher–Fuel Mix in Spherical Implosions Using X-Ray Spectroscopy," Lawrence Livermore National Laboratory, Livermore, CA, UCRL-JC-116787 (1994); submitted to *Rev. Sci. Inst.* (1995).
11. G. B. Zimmerman and W. L. Kruer, *Comm. Plasmas Phys. Cont. Thermonuclear Fusion* **2**, 51 (1975).
12. D. S. Kershaw, "Flux Limiting in Nature's Own Way," Lawrence Livermore National Laboratory, Livermore, CA, UCRL-78378 (1976).
13. R. M. More, K. H. Warren, D. A. Young, and G. B. Zimmerman, *Phys. Fluids* **31**(10), 3059 (1988).
14. W. A. Lokke and W. H. Grasberger, "XSNQ-U: A NonLTE Emission and Absorption Coefficient Subroutine," Lawrence Livermore National Laboratory, Livermore, CA, UCRL-52276 (1977).
15. E. G. Corman, W. B. Loewe, G. E. Cooper, and A. M. Winslow, *Nucl. Fusion* **15**, 377 (1975).
16. S. P. Hatchett, Lawrence Livermore National Laboratory, Livermore, CA, private communication (1993).
17. G. B. Zimmerman, "Recent Developments in Monte-Carlo Techniques," Lawrence Livermore National Laboratory, Livermore, CA, UCRL-105616 (1990).
18. A. K. Burnham, J. Z. Grens, E. M. Lilley, *J. Vac. Sci. Technol.* A **5**(6), 3417 (1987).
19. P. C. Souers, *Hydrogen Properties for Fusion Energy* (University of California Press, Berkeley, CA, 1986).
20. R. A. Sacks and D. H. Darling, *Nuc. Fus.* **27**, 447 (1987).
21. P. A. Amendt, Lawrence Livermore National Laboratory, Livermore, CA, private communication regarding symmetry tuning and increased x-ray drive in modified Nova hohlraums, to be published in *Phys. Rev. Lett.* (1995).
22. A. Hauer, et al., *Phys. Plasmas* **2**(6) (1995).
23. A. Bar Shalom, J. Oreg, W. H. Goldstein, D. Shvarts, and A. Zigler, *Phys. Rev.* **A** 40, 3183 (1989).
24. R. C. Kirkpatrick and C. A. Wingate, Los Alamos National Laboratory, Los Alamos, NM, private communication (1980); R. C. Kirkpatrick, J. E. Tabor, E. L. Lindman, A. J. Cooper, "Indirect Solar Loading of Waste Heat Radiators," *Proc. Space 88*, S. W. Johnson and J. P. Wetzel, Eds. (the American Society of Civil Engineers, 1988) p. 964; D. S. Bailey (1981), D. H. Munro and G. B. Zimmerman (1993), Lawrence Livermore National Laboratory, Livermore, CA, private communication.
25. J. E. Murray, M. C. Rushford, C. S. Vann, R. L. Saunders, and J. A. Caird, *ICF Quarterly Report* **4**(1), 18, Lawrence Livermore National Laboratory, Livermore, CA, UCRL-LR-105821-94-1 (1993).
26. J. A. Caird, R. B. Ehrlich, O. L. Landen, C. W. Laumann, et al., *ICF Quarterly Report* **4**(1), 10, Lawrence Livermore National Laboratory, Livermore, CA, UCRL-LR-105821-94-1 (1993).
27. K. Marsh, C. Joshi, and C. J. McKinstrie, *BAPS* **39**, 1585, Minneapolis, MN, November 7–11, 1994.
28. W. L. Kruer, *The Physics of Laser Plasma Interactions* (Addison–Wesley, NY, 1998).
29. E. A. Williams, R. L. Berger, R. P. Drake, A. M. Rubenchik, et al., *Physics of Plasmas* **2**, 129 (1995); S. C. Wilks, W. L. Kruer, J. Denavit, K. Estabrook, et al., "Nonlinear Theory and Simulations of Stimulated Brillouin Backscatter in Two and Three Species Plasmas," Lawrence Livermore National Laboratory, Livermore, CA, UCRL-JC-117313 (1995); accepted for publication in *Phys. Rev. Lett.*
30. R. L. Berger et al., *Phys Fluids B* **5**, 2243 (1993).
31. S. W. Haan, "Hydrodynamic Instabilities on ICF Capsules," Lawrence Livermore National Laboratory, Livermore, CA, UCRL-JC-107592 (1991); to be published in *Lecture Series on Inertial Fusion*, Dept. of Astrophysical Sciences, Princeton University.

32. B. A. Remington, S. V. Weber, S. W. Haan, J. D. Kilkenny, et al., *Phys. Fluids B* **5**, 2589 (1993).
33. S. V. Weber, B. A. Remington, S. W. Haan, B. G. Wilson, and J. K. Nash, *Phys. Plasmas* **1**, 3652 (1994); H. Takabe, K. Mima, L. Montierth, and R. L. Morse, *Phys. Fluids* **28**, 3676 (1985); M. Tabak, D. H. Munro, and J. D. Lindl, *Phys. Fluids B* **2**, 5 (1990); J. H. Gardner, S. E. Bodner, and J. P. Dahlburg, *Phys. Fluids B* **3**, 1070 (1991).
34. S. Haan, *Phys. Rev. A* **39**, 5812 (1989).
35. J. P. Dahlburg et al., *Phys. Plasmas* **2**(6), (1995); M. Marinak, Lawrence Livermore National Laboratory, Livermore, CA, private communication (1994).
36. T. R. Dittrich, B. A. Hammel, C. J. Keane, R. McEachern, et al., *Phys. Rev. Lett.* **73**, 2324–2327 (1994).
37. G. W. Collins, E. R. Mapoles, J. Hoffer, J. Simpson, et al., *ICF Quarterly Report* **3**(2), 81, Lawrence Livermore National Laboratory, Livermore, CA, UCRL-LR-105821-93-2 (1993).

INDIRECTLY DRIVEN, HIGH-CONVERGENCE IMPLOSIONS (HEP1)

S. P. Hatchett *S. M. Lane* *M. B. Nelson*

M. D. Cable *C. Laumann* *D. W. Phillion*

J. A. Caird *R. A. Lerche* *H. Powell*

J. D. Kilkenny *T. J. Murphy* *D. B. Ress*

H. N. Kornblum *J. Murray*

Introduction

High-gain inertial confinement fusion will most readily be achieved with hot-spot ignition,[1,2] in which a relatively small mass of gaseous fuel at the center of the target is heated to 5–10 keV, igniting a larger surrounding mass of approximately isobaric fuel at higher density but lower temperature. Existing lasers are too low in energy to achieve thermonuclear gain, but hydrodynamically equivalent implosions using these lasers can demonstrate that the important, scalable parameters of ignition capsules are scientifically and technologically achievable. The experiments described in this article used gas-filled glass shells driven by x rays produced in a surrounding cavity, or hohlraum. These implosions achieved convergence ratios (initial capsule radius/final fuel radius) high enough to fall in the range required for ignition-scale capsules, and they produced an imploded configuration (high-density glass with hot gas fill) that is equivalent to the hot-spot configuration of an ignition-scale capsule. Other recent laser-driven implosions[3,4] have achieved high shell density but at lower convergences and without a well defined hot spot. Still other experiments[5,6] have used very-low-density gas fill to reach high convergence with unshaped drive (see below), but that approach results in a relatively low shell density. Moreover, even at the highest convergence ratios the implosions described here had neutron yields averaging 8% of that calculated for an idealized, clean, spherically symmetric implosion—much higher than previous high-convergence experiments.

As we discuss below, the implosions described here were characterized by a number of diagnostics. In particular, convergence ratios were directly determined by measurements of the areal density of the imploded fuel using a technique based on secondary-neutron spectroscopy. The implosions were modeled, with the inclusion of non-ideal effects, with detailed computer codes such as LASNEX,[7] a coupled radiation transport, hydrodynamics, and burn-particle transport code. All observable quantities were in close agreement with these simulations, demonstrating good understanding of the implosions.

Experimental Design

The capsules, shown in Fig. 1, were indirectly driven gas-filled microballoons. We chose a relatively small capsule (capsule diameter 16% of hohlraum diameter) to limit the areal density of the imploded fuel, allowing the use of secondary neutrons for the determination of this quantity (see below). We used glass capsules filled with deuterium (D) or equimolar deuterium/tritium (DT). Capsule fill pressures varied from 25 to 200 atm, which changed the capsule convergence for constant drive (see "Measuring Convergence"). Ten Nova beams (2.1 kJ each at 0.35 μm) were incident on the interior of a uranium (U) hohlraum at 2×10^{15} W/cm^2 and produced an x-ray drive flux on the surface of the capsule; the hohlraum geometry is shown in Fig. 1(b). Figure 2 shows the measured laser power P_L, corresponding brightness temperature of the x-ray drive T_{rad}, and the neutron production rate R_n.

We measured x-ray drive using a multichannel, K- and L-edge–filtered x-ray spectrometer looking into the hohlraum at both directly illuminated laser spots and the indirectly illuminated wall;[8] observed spectra were nearly Planckian. Subject to hydrodynamic instability limitations,[9] we chose the x-ray drive vs time dependence, or pulse shape, to optimize the pressure–density trajectory of the capsule compression. Use of a glass shell and a U hohlraum minimizes the x-ray preheating of the capsule. The capsule implosion is driven by pressure generated by ablation of the outer surface material. Under the conditions of these experiments—x-ray brightness temperature low enough that the ablation front is subsonic, time-scale short enough that the ablated material is optically thin to the driving x rays—it can be shown[10] that the ablation pressure is

UCRL-LR-105821-95-4

approximately given by $P_{abl} = 0.5\sigma T_{rad}^4/(RT_{rad}/\mu)^{1/2}$ where σ is the Stefan–Boltzmann constant, R is the gas constant and μ is the molecular weight. This gives ablation pressures of 8 Mbar at the foot of the pulse (t = 0.2 ns) and 110 Mbar at the peak of the pulse (t = 1.4 ns).

Achieving High Convergence

In implosions such as these, several factors limit the convergence ratio achievable. The most important are pusher entropy, drive asymmetry, and Rayleigh–Taylor (RT) instability. These factors must be minimized in the experiments and properly accounted for in models.

The first factor is pusher entropy. The less dense the pusher is near stagnation, the less efficiently it can couple its kinetic energy into compressing the fuel. X-ray preheat of the pusher raises its specific entropy; ablation pressure cannot then hold it at as high a density during inward acceleration, and at stagnation more of its kinetic energy will be spent compressing itself rather than compressing the fuel. X-ray preheat is minimized by the use of a U hohlraum, with the resulting near-Planckian x-ray spectrum, and a glass pusher, which self shields from hard x rays. Similarly, pulse-shaping is required to limit pusher entropy generation by shocks and to keep the pusher dense during inward acceleration. In the ideal, lowest entropy state, the pusher pressure results entirely from the Fermi degeneracy of the free electrons. In Figure 3, we plot the ratio of the pressure to the electron degeneracy pressure as a function

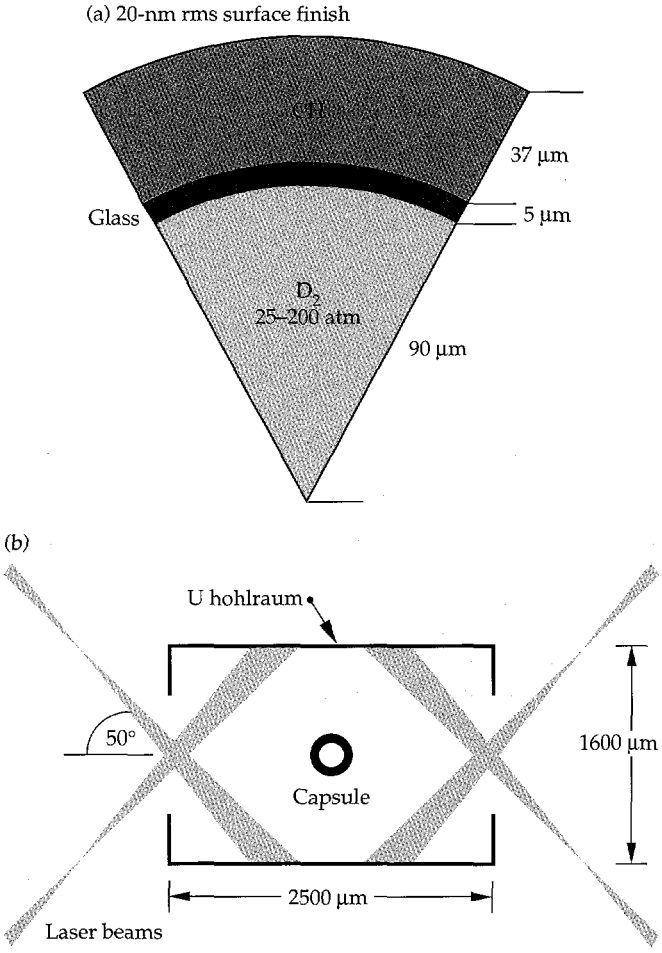

FIGURE 1. Capsule and indirect-drive hohlraum geometry. (50-05-0695-1562pb01)

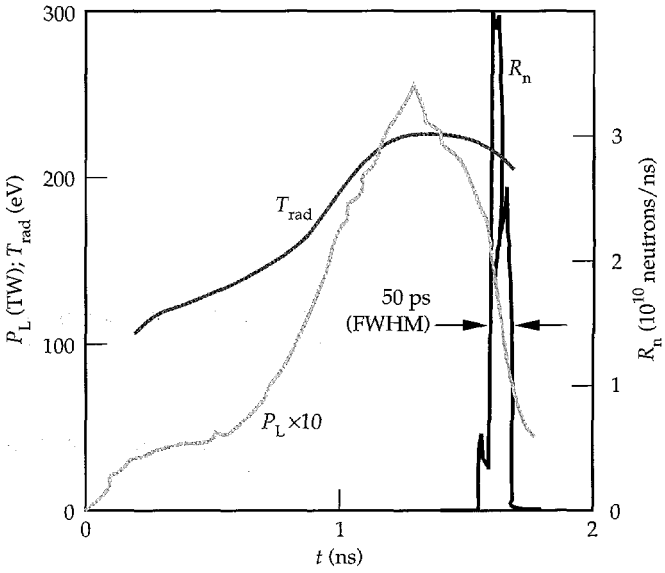

FIGURE 2. Observed laser power P_L, hohlraum temperature T_{rad}, and neutron production rate R_n for 100-atm DT-filled capsules. (50-05-0695-1563pb01)

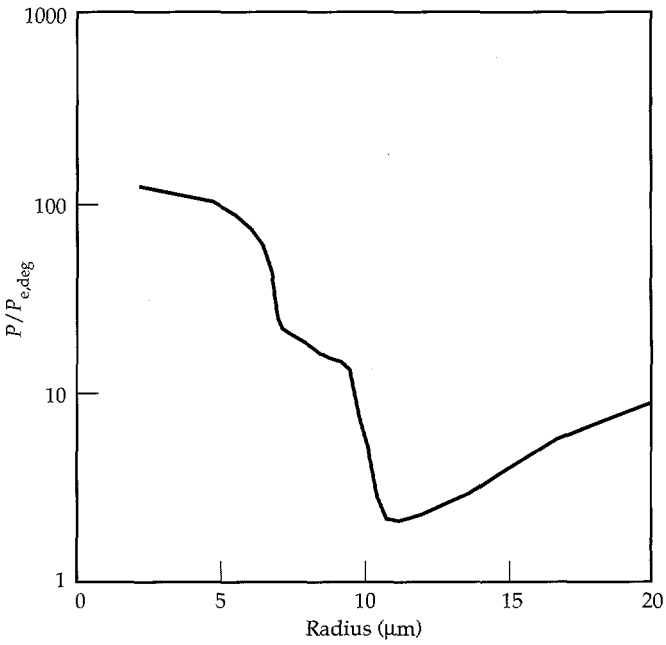

FIGURE 3. Ratio of pressure to electron degeneracy pressure in fuel and pusher of 100-atm fill capsules at bang time as calculated with the Haan mix model. The dense glass pusher, from 10 to 15 μm, is in a good, low-entropy state. (50-05-0695-1564pb01)

of radius through the fuel and pusher at the time of peak neutron production (*bang time*) in a model calculation of the implosion of a 100-atm DT-filled capsule. Figure 3 shows three more or less distinct regions: clean fuel (0–7 μm), mixed fuel and glass (7–10 μm), and dense glass pusher (10–15 μm). The pusher has been compressed along a good low-entropy $P(\rho)$ trajectory, or adiabat, so that its pressure is only a factor of about two above the Fermi degeneracy pressure. This capsule has the sort of compressed configuration—isobaric with a hot spot surrounded by colder and denser matter—described in the introduction for a high-gain capsule implosion.

X-ray drive asymmetry is the second factor limiting convergence. The hohlraum does not produce a perfectly uniform drive distribution, but any position on the capsule "sees" radiation from all the various elements of the hohlraum (directly illuminated wall regions, indirectly illuminated regions, and entrance holes), so higher moments of the drive distribution are strongly smoothed. (Typically the drive symmetry is analyzed in terms of spherical harmonics, which reduce to Legendre polynomials P_l with cylindrical symmetry.) The remaining systematic asymmetry is controlled by choosing the relative values of capsule radius, hohlraum dimensions, and the first bounce position of the laser beams along the hohlraum wall to minimize the P_2 and P_4 effects. P_1 and P_3 effects are eliminated by the left-right symmetry of the hohlraum. The remaining lower-moment asymmetry is time-dependent: both the albedo of the wall and the effective positions of the laser spots change as hot wall material moves into the hohlraum. By design with simulations, the configuration used in this work produces a P_2 asymmetry that changes sign, is at most 8%, and averages to a very low value. Details of hohlraum design are being reported in "Nova Symmetry: Experiments, Modeling, and Interpretation (HLP3 and HLP4)" on p. 293 of this *Quarterly*.

A second source of time-dependent drive asymmetry is random variations due to imprecise laser beam-to-beam power balance and pointing. This is minimized by precise control of the laser.[11,12] We maintain tolerances of 8% rms beam-to-beam power balance during the foot of the laser pulse and 4% power balance during the peak. Pointing tolerance is ±30 μm rms. This control gives a power balance on the capsule that from simulations is uniform to within 2% rms at peak power and 4% in the foot. Early experiments demonstrated that this level of power balance is necessary for high convergence. A version of Figure 6 with the early data showed convergence *declining* as fill was reduced.

Finally, since the fuel is compressed at stagnation by a denser pusher, convergence may be limited by RT instability at the fuel–pusher interface, which leads to what is commonly called *mix*. Calculations show that perturbations on the interface are primarily seeded by the feed-through of growing perturbations at the ablation front, which in turn are seeded by initial ablator surface finish perturbations. We have applied Haan's multimode, moderately nonlinear mix model[9] to calculations of the implosions of the 25- and 100-atm fill capsules. In this model, growth factors (final amplitude at fuel–pusher interface/initial amplitude at ablator surface) are calculated at a number of l-modes, initial amplitude $\propto P_l(\cos\theta)$, for perturbations small enough that the growth factors remain linear in the initial amplitudes. We then obtain an estimate of the rms depth of mix penetration by multiplying the initial surface-finish mode spectrum by the growth factors, applying a saturation model in which nearby modes contribute to the saturation of a particular mode, and then adding the saturated mode amplitudes in quadrature. There is an empirical parameter in the saturation model, which Haan calls ν, that must be estimated from mix experiments. (In the presence of a dense spectrum of modes, mode l has a saturation amplitude at radius R_0 of $\nu R_0/l^2$.) Haan's current best estimate of this parameter is $\nu = 2$, which is the value we have used in our analysis.

Figure 4 shows the linear growth factors we calculated. At low l values (long wavelengths), the growth factors are comparable for the 25- and 100-atm capsules, whereas at higher l values the 100-atm capsules have much larger growth factors. This is a reflection of much more feed-through in the 100-atm case. When the first shock breaks out of the back of the glass pusher into the fuel, there is less decompression in the 100-atm case, leading to a thinner, denser pusher during inward acceleration. Were our pulse shape more highly

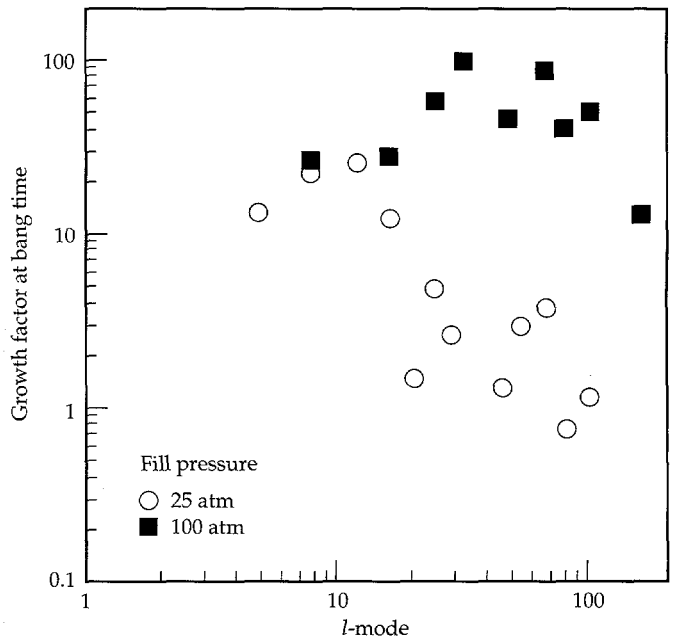

FIGURE 4. Calculated growth factors for surface perturbations on 25- and 100-atm fill capsules. (50-05-0695-1565pb01)

tuned, the 25-atm shells would have been thinner, but then mix and shell breakup might have destroyed their convergence altogether. As it is, with saturation applied, most of the quadrature sum of amplitudes at bang time comes from $l \leq 20$ for either fill pressure.

One way of expressing the depth of mix penetration is in terms of the distance from the fuel–pusher interface to the *fall line*, which is the trajectory the interface would have if it never decelerated at stagnation. For our capsules, the Haan model gives a bang-time mix depth—defined as the height of bubble tops above the interface—of about 35% of the distance to the fall line. Mix depth is not a constant with time, but rather it peaks at about that fraction near bang-time. Were it a constant, we would have another, simpler mix model, known as a *fracmix* model. In either model, the spike penetration—the distance from interface to spike tips—is estimated at $(1 + \alpha)$ times the bubble height, where α is the interface Atwood number.

Measuring Convergence

We determined burn-averaged fuel density and capsule convergence by measuring burn-averaged fuel areal density $\rho R \equiv \int_{\text{fuel}} \rho(r) dr$. If ρ is uniform, as we assume, then $\rho = \rho_0(\rho R/\rho_0 R_0)^{3/2}$, so a determination of ρR gives both ρ and R. When we make comparisons later with calculations of ρ and R, we shall calculate those quantities in exactly the same way, with ρR determined from the calculated secondary neutron spectrum as described below for the experimental analysis. In fact, the uniform-ρ assumption gives a slight underestimate of the actual convergence and density because the actual density must increase with radius as the temperature decreases. From simulations, this is about a 15% effect in the density for the 25-atm capsules and about a 25% effect in the 100-atm capsules.

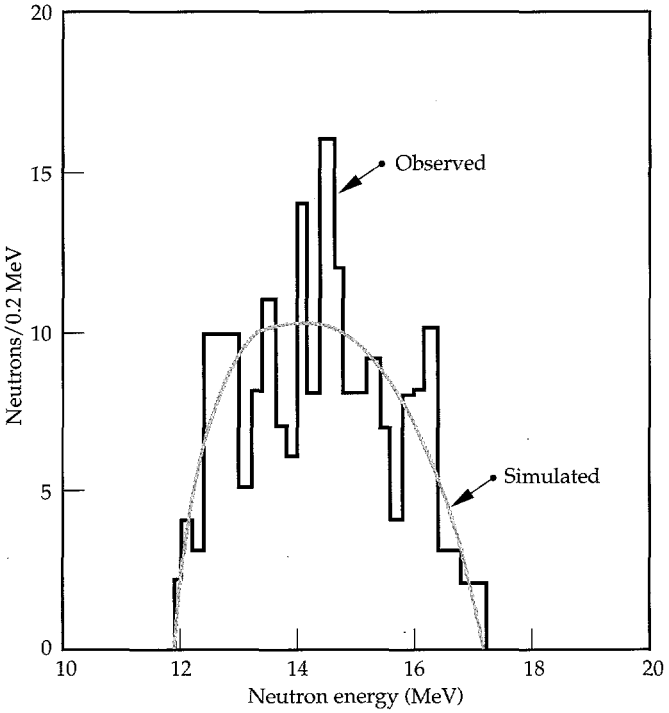

FIGURE 5. Secondary-neutron energy spectrum measured with array of neutron time-of-flight detectors (LaNSA). Observed is sum of spectra from all 25-atm capsules. (50-05-0695-1566pb01)

We measured fuel ρR by the secondary-neutron technique.[13–17] This technique relies on the observation of 12–17-MeV secondary neutrons produced via the D(T,n)^{4}He reaction in an initially pure D fuel. The 1.01-MeV tritium nuclei, or *tritons*, are produced in the primary fusion reaction D(D,p)T. If the tritons do not slow significantly as they traverse the fuel, then the fraction of tritons producing secondary neutrons is proportional to fuel ρR. For the fuel conditions in this work, (low temperature with mixed pusher material), ρR values above a few mg/cm^2 cause significant triton slowing, and corrections must be made for the energy dependence of the D(T,n)^{4}He cross section. Cable and Hatchett[13] have outlined how this can be done based on a measurement of the secondary-neutron energy spectrum. Since the cross section rises with decreasing triton energy, this correction typically results in a ρR value lower than that calculated for the case of little slowing. We measured the secondary-neutron energy spectrum with an array of neutron time-of-flight detectors (LaNSA).[18] Figure 5 shows a spectrum obtained by summing all the 25-atm capsule data; the figure also shows the spectrum obtained from calculations of these implosions with the Haan mix model, as discussed further below.

Observed fuel areal densities, which ranged up to 16 mg/cm^2, allowed us to determine the densities and convergences plotted in Fig. 6. For this figure, observed values were averaged over several implosions (two at 200 atm, six at 100 atm, and ten at 25 atm), and the errors were dominated by statistics related to the number of the observed secondary neutrons. Figure 6 shows that the observed values are consistent with or better than those expected from simulations if the effects of fuel–pusher mixing are included at the level that current models[9] predict given the capsules' surface finish. (The calculations labeled "clean 1-D" include no mix effects and assume perfect spherical symmetry; this is physically unrealistic but is commonly quoted as an "ideal" limit). Fuel–pusher mixing introduces two important effects: mixing of high-Z matter into the fuel enhances the triton slowing, and mixing of fuel outward into the pusher decreases the fuel convergence. Secondary-neutron spectroscopy allows us to quantify these effects since the secondary-neutron energy spectrum is dependent on the rate of the triton slowing. Figure 5 shows that the calculated and observed secondary spectra are in good agreement, which further supports the validity of the mix modeling.

proportional to T^5 for this temperature range) and because the fuel temperature is affected by small variations in capsule surface finish, capsule dimensions and laser energy. (The yield would be much less sensitive to mix if the glass pusher were replaced by a layer of cryogenic liquid DT, as it is in most current ignition-scale capsule designs.)

Fuel ion temperatures were 0.9 ± 0.4 keV for all cases; at this temperature, the observed fuel density corresponds to a final fuel pressure of 16 Gbar.

The glass shell ρR was 73 ± 16 mg/cm^2 (100 atm) and 60 ± 19 mg/cm^2 (25 atm) in a pair of shots at each fill. These values are about 1σ from the simulated values of 54 and 81 mg/cm, respectively. In the 25-atm simulations, the peak burn-time glass density is 160 g/cm^3.

Burn duration for the 100-atm capsules was 50 ± 15 ps; burn occurred at 1600 ± 100 ps after the start of the laser pulse (see Fig. 2); simulations gave 33-ps burn duration occurring at 1603 ps. We see in both simulations and measurements from a separate, brief experimental series that shock breakout, which corresponds to initial fuel movement, does not occur until 1 ns after the start of the laser pulse. This gives an average implosion velocity of 1.4×10^7 cm/s; simulations show that peak velocity is 1.8×10^7 cm/s. Using the observed fuel density and burn duration, we obtain a confinement parameter of $n\tau = 1.9 \pm 0.6 \times 10^{14}$ s/cm^3.

Summary and Conclusion

We have done a series of indirectly driven high-convergence implosions with the Nova laser fusion facility. These implosions were well characterized by a variety of measurements, and computer models are in good agreement with the measurements. We measured the imploded fuel areal density using a technique based on secondary-neutron spectroscopy. At capsule convergence ratios of 24, comparable to what is required for the hot spot of ignition-scale capsules, these capsules achieved fuel densities of 19 g/cm^3. Independent measurements of density, burn duration, and ion temperature gave $n\tau\theta = 1.7 \pm 0.9 \times 10^{14}$ keV-s/cm^3.

These experiments, which used better diagnostic techniques than previous work, have allowed detailed comparisons with simulations and have permitted a deeper understanding of the sensitivity of the implosion process to factors such as laser power balance. These implosions have provided an integrated test of our ability to control and model the implosion dynamics enough to achieve convergence ratios comparable to those required for the hot spot of an ignition-scale capsule.

Notes and References

1. J. Nuckolls, et al., *Nature* **239**, 139 (1972).
2. J. D. Lindl, R. L. McCrory, and E. M. Campbell, *Physics Today* **45**, 32 (1992).
3. F. J. Marshall, et al., *Phys. Rev. A* **40**, 2547 (1989).
4. H. Azechi, et al., *Laser Part. Beams* **9**, 193 (1991).
5. J. D. Kilkenny, et al., *Plasma Physics and Controlled Nuclear Fusion Research* (International Atomic Energy Agency, Vienna, 1989), vol. 3, p. 29.
6. H. Nishimura, et al., *Plasma Physics and Controlled Nuclear Fusion Research 1992* (IAEA, Vienna, 1993), vol. 3, p. 97.
7. G. B. Zimmerman and W. L. Kruer, *Comments Plasma Phys. Controlled Fusion* **11**, 51 (1975).
8. H. N. Kornblum, R. L. Kauffman, and J. A. Smith, *Rev. Sci. Instrum.* **57**, 2179 (1986).
9. S. Haan, *Phys. Rev. A* **39**, 5812 (1989).
10. S. P. Hatchett, *Ablation Gas Dynamics of Low-Z Materials Illuminated by Soft X Rays*, Lawrence Livermore National Laboratory, Livermore, CA, UCRL-JC-108348 (1991).
11. J.A. Caird, R.B. Ehrlich, O.L. Landen, et al., *ICF Quarterly Report* **4**(1), 10–17, Lawrence Livermore National Laboratory, Livermore, CA, UCRL-LR-105821-94-1 (1994).
12. J.E. Murray, M.C. Rushford, C.S. Vann, et al., *ICF Quarterly Report* **4**(1), 18–24, Lawrence Livermore National Laboratory, Livermore, CA, UCRL-LR-105821-94-1 (1994).
13. M. D. Cable and S. P. Hatchett, *J. Appl. Phys.* **62**, 2223 (1987).
14. E. G. Gamalii, et al., *JETP Lett.* **21**, 70 (1975).
15. T. E. Blue and D. B. Harris, *Nucl. Sci. Eng.* **77**, 463 (1981).
16. H. Azechi, et al., *Appl .Phys. Lett.* **49**, 555 (1986).
17. M. D. Cable, et al., *Bull. Am. Phys. Soc.* **31**, 1461 (1986).
18. M. B. Nelson and M. D. Cable, *Rev. Sci. Instrum.* **63**, 4874 (1992).
19. S. M. Lane, et al., Lawrence Livermore National Laboratory, Livermore, CA, UCRL 50021-86 (1986).
20. S. M. Lane and M. B. Nelson, *Rev. Sci. Instrum.* **61**, 3298 (1990).
21. R. A. Lerche, D. W. Phillion, and G. L. Tietbohl, in *Proceedings of SPIE 2002*, P. W. Roehrenbech, Ed. (San Diego, 1993), p. 153.
22. T. J. Murphy and R. A. Lerche, *Rev. Sci. Instrum.* **63**, 4883 (1992).

PLANAR AND CYLINDRICAL RAYLEIGH–TAYLOR EXPERIMENTS ON NOVA (HEP2)

B. A. Remington

S. V. Weber

M. M. Marinak

W. W. Hsing

N. M. Hoffman

Introduction

A high-density fluid on top of a low-density fluid is Rayleigh–Taylor[1] (RT) unstable. Driven by gravity, random perturbations at the interface between the two fluids will grow: fingers ("spikes") of the heavier fluid will poke through the lighter fluid, and bubbles of the lighter fluid will rise into the heavier fluid. The RT instability and its shock-driven analog, the Richtmyer–Meshkov[2] (RM) instability, have been a focus of research in inertial confinement fusion (ICF) for some time.[3–19] In ICF, the driver—laser light, x rays, or ions—heats the outer layer of the capsule wall, causing it to ionize and expand rapidly. The result is a low-density ablated plasma accelerating the high-density capsule wall ("pusher"). The ablation front is RT unstable, and outer-surface imperfections grow. This growth can seed perturbations at the pusher inner wall, which in turn become RT unstable during deceleration and stagnation. Ultimately, pusher material can mix into the fuel, degrading performance.

The role of the RT instability in ICF can be understood heuristically as follows. The goal of ICF is to maximize the fuel core pressure P_{core} for a minimum applied (ablation) pressure P_a. To see how we might do this, we write[20]

$$\frac{P_{core}}{P_a} = 10\left(\frac{R_0}{\Delta R}+1\right)\left(\frac{R_0}{R_s}\right)^{0.9}, \tag{1}$$

where $R_0/\Delta R$ is the capsule aspect ratio (the ratio of initial shell radius to shell thickness) and R_0/R_s the convergence ratio [the ratio of outer capsule radius to final compressed hot fuel radius (the "hot spot" radius)]. The $[(R_0/\Delta R) + 1]$ factor results from converting the kinetic energy of the pusher into pressure at stagnation, by using Bernouilli's theorem, i.e., $P_{stag} = P_a + (1/2)\,\rho v^2$. The $(R_0/R_s)^{0.9}$ factor results from the pressure multiplication due to the spherically imploding shock wave and is based on the self-similar solutions of Guderley.[20]

From Eq. (1), we immediately see that maximum pressure amplification occurs for high-aspect-ratio capsules with a high convergence ratio.

The RT instability limits the aspect ratio, however, as we see from the following. In the linear regime, perturbation growth is exponential in time,

$$\eta = \eta_0 e^{\int \gamma dt}, \tag{2}$$

where the exponent $\int \gamma dt$ represents growth in terms of perturbation *e*-foldings. A dispersion curve for the RT growth rate γ can be written as [8]

$$\gamma \approx \left(\frac{kg}{1+kL}\right)^{1/2} - \beta k v_a, \tag{3}$$

where $k = 2\pi/\lambda$ is the perturbation wave number, g is the pusher acceleration, $L = \rho/\Delta\rho$ is the density gradient scalelength at the ablation front, β is a multiplier usually set in the range of 1 to 3, $v_a = \dot{m}/\rho$ is the ablation velocity, $\dot{m}$ is the mass ablation rate per unit area, and ρ is a characteristic density at the ablation front. If we assume (1) a constant acceleration over a distance $S \approx R_0/2$, (2) that 80% of the pusher is ablated over this distance ($\int v_a dt \approx 0.8\Delta R$), and (3) a density gradient scale length that is 10 to 20% of the shell thickness ($L = \alpha\Delta R$, with $\alpha = 0.1$–0.2), then we can approximate the perturbation *e*-foldings as

$$\int \gamma dt \approx \left(\frac{\ell}{1+\alpha\ell\frac{\Delta R}{R}}\right)^{1/2} - 0.8\ell\frac{\Delta R}{R}. \tag{4}$$

Here we have substituted $k = \ell/R$, where ℓ is the mode number of a spherical harmonic. We have chosen $\beta \sim 1$ which is typical of indirect drive. When $\Delta R/R$ is small, Eq. (4) shows that the perturbation *e*-folding is large. One can maximize $R_0/\Delta R$, and hence the pressure

UCRL-LR-105821-95-4

amplification, only to the extent that the RT growth will allow.

The situation for a capsule implosion, illustrated in Fig. 1, can be approximated as $G_T = G_1 f G_2$, where the total growth factor G_T has been decomposed into growth at the ablation front or outer surface G_1, fractional feedthrough f to the inner surface or pusher–fuel interface, and growth at the inner surface G_2. Experiments to measure mix (and hence G_T) directly in implosions are difficult, typically relying on spectroscopic tracer layers or yield degradation to signal the onset of mix.[18,19] The dominant source for the total perturbation growth and subsequent mixing, however, is the growth G_1 of outer-surface perturbations during the acceleration phase. This can be measured directly with high precision with face-on experiments in planar geometry. The integral effect, namely, outer-surface growth, feedthrough, and inner-surface growth, can be measured with side-on imaging of cylindrical implosions. The HEP2 campaign comprises these two areas—planar and cylindrical RT experiments.

The evolution of a single-mode perturbation at the ablation front of an accelerated planar foil is expected to have three distinct phases. (1) When the drive first turns on, a strong shock is launched through the foil during compression. The shock front will typically be deformed, bearing the imprint of any initial surface imperfections. The behavior of this perturbed (or "rippled") shock front is dynamically similar to that produced by the RM instability.[2] Material behind the shock develops a lateral velocity component, moving from regions in which the foil was thinner (initial perturbation valley) towards regions in which the foil was thicker (initial perturbation peak), increasing the areal density modulation. The shape of the shock front is not constant, but evolves with time.[21,22] The areal density modulation may decrease or even reverse phase, if the foil is thick enough with respect to the perturbation wavelength. (2) After the shock breaks out of the back of the foil (the side away from the drive), and a rarefaction wave returns to the ablation front, the compressed foil accelerates as a unit. Perturbation growth continues, now as a result of the RT instability. The linear regime is defined by $k\eta << 1$, where $k = 2\pi/\lambda$ represents the perturbation wave number and λ and η are the perturbation wavelength and spatial amplitude. In the linear regime, the perturbation grows exponentially as given in Eq. (2), namely, $\eta(t) = \eta_0 e^{\gamma t}$, where the growth rate γ can be written approximately as in Eq. (3) in the form of a dispersion curve,[8]

$$\gamma \approx \left(\frac{kg}{1+kL}\right)^{1/2} - \frac{\beta k \dot{m}}{\rho}.$$

(3) After sufficient growth, $k\eta$ is no longer small and the perturbation enters the nonlinear regime. The shape of the perturbation changes from sinusoidal to "bubble and spike," which corresponds in Fourier space to the generation of higher harmonics.[7] Within the framework of third-order perturbation theory,[23] the amplitudes of the perturbation fundamental mode (first harmonic) η_1, second harmonic η_2, and third harmonic η_3 can be written as

$$\eta_1 \approx \eta_L\left(1 - \frac{1}{4}k^2\eta_L^2\right), \tag{5a}$$

$$\eta_2 \approx \frac{1}{2}k\eta_L^2, \tag{5b}$$

$$\eta_3 \approx \frac{3}{8}k^2\eta_L^3, \tag{5c}$$

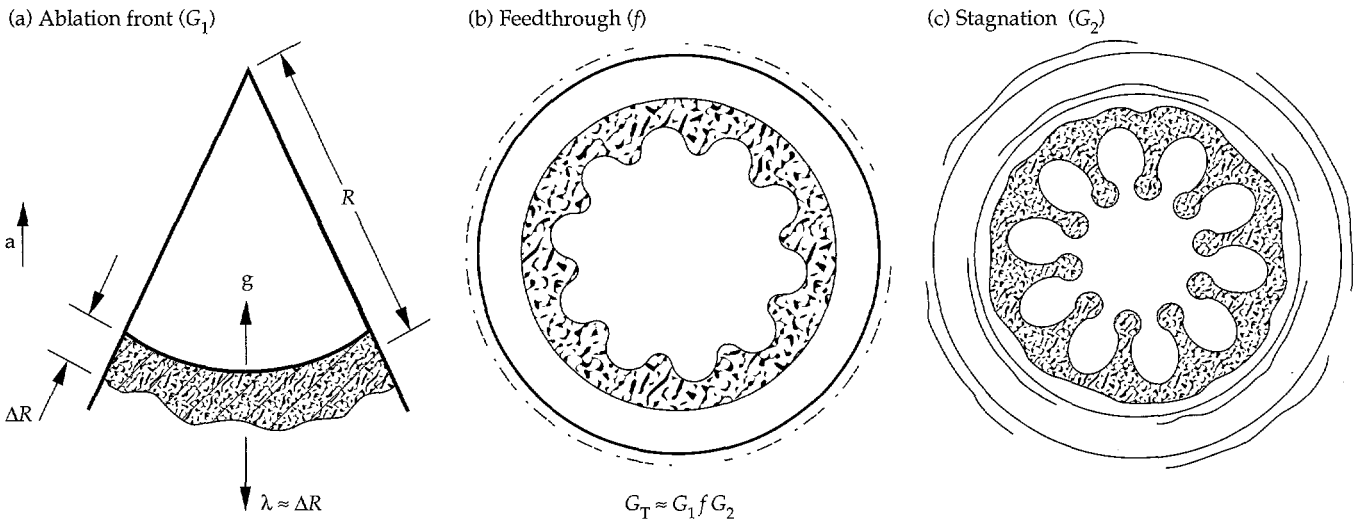

FIGURE 1. Schematic showing how RT perturbation growth affects an implosion. The quantities G_T, G_1, f, and G_2 correspond to the total growth factor, growth factor at the outer surface during acceleration, feedthrough to the inner surface, and growth factor at the inner surface during deceleration. (20-03-1293-4392pb02)

where η_L is the linear-regime spatial amplitude given by Eq. (2). The wave numbers of the first three harmonics correspond to $k_n = 2\pi n/\lambda$, $n = 1, 2, 3$. At third order, we see in Eq. (5a) the occurrence of negative feedback to the first harmonic; that is, the growth of the fundamental is decreased. The perturbation growth is said to "saturate." In the asymptotic limit of the nonlinear regime, the bubble amplitude can be written as

$$\eta(t) = \int (Fg\lambda)^{1/2} dt, \tag{6}$$

which corresponds to a perturbation growing at its terminal bubble velocity,[24]

$$v_B = (Fg\lambda)^{1/2}, \tag{7}$$

where $F = u^2/gl$ is the dimensionless Froude number, which depends only on the shape of the perturbation (here u, g, and l are characteristic flow velocity, acceleration, and spatial scale, respectively). As derived by Layzer,[25] $F^{1/2} = 1/(6\pi)^{1/2} = 0.23$ in two dimensions (2-D) and 0.36 in three dimensions (3-D) for an axisymmetric bubble. If we define the transition into the nonlinear regime as taking place when the growth in the fundamental mode is reduced by 10%, then from Eq. (5a) we have $k^2\eta_L^2 = 0.1$, or $\eta_L/\lambda \approx 0.1$, which is a typical and widely used threshold for nonlinearity. This same transition criterion results if one assumes that the onset of nonlinearity occurs when the linear-regime perturbation velocity is equal to the asymptotic nonlinear bubble velocity, namely, $\dot{\eta} \approx v_B$, or $\gamma\eta = (kg)^{1/2}\eta = (g\lambda/6\pi)^{1/2}$. Rearranging again leads to $\eta/\lambda \approx 0.1$ at saturation.

In the nonlinear regime,[26–31] mode coupling leads to the appearance of "beat" modes $k_i \pm k_j$. To second order, this can be written as

$$\eta_{k_i \pm k_j} \approx \mp \frac{1}{2}(k_i \pm k_j)\eta^L_{k_i}\eta^L_{k_j}; \tag{8}$$

Eq. (8) is derived in the Appendix. Mode coupling redistributes a multimode perturbation to longer and shorter wavelengths and affects the saturation of individual modes. If a perturbed interface has a sufficiently dense Fourier composition, it becomes convenient to think of the perturbation in terms of a characteristic wave number $k_{char} = 2\pi/\lambda_{char}$ and a characteristic spatial amplitude η_{char}. In these terms, the criterion for the onset of saturation becomes $k_{char}\eta_{char}$ no longer being small. Within a continuum model,[32] this leads to *individual* constituent modes saturating when their amplitudes reach a threshold S_k given by

$$S_k = \frac{v_{2D}}{L^{1/2}k^{3/2}}, \text{ in 2-D} \tag{9a}$$

$$S_k = \frac{v_{3D}}{Lk^2}, \text{ in 3-D} \tag{9b}$$

where L represents the system size and v is a parameter determined by comparison with simulations or data.

We present here the results of an extensive, multiyear experimental and computational study of perturbation growth on planar foils and on imploding cylinders

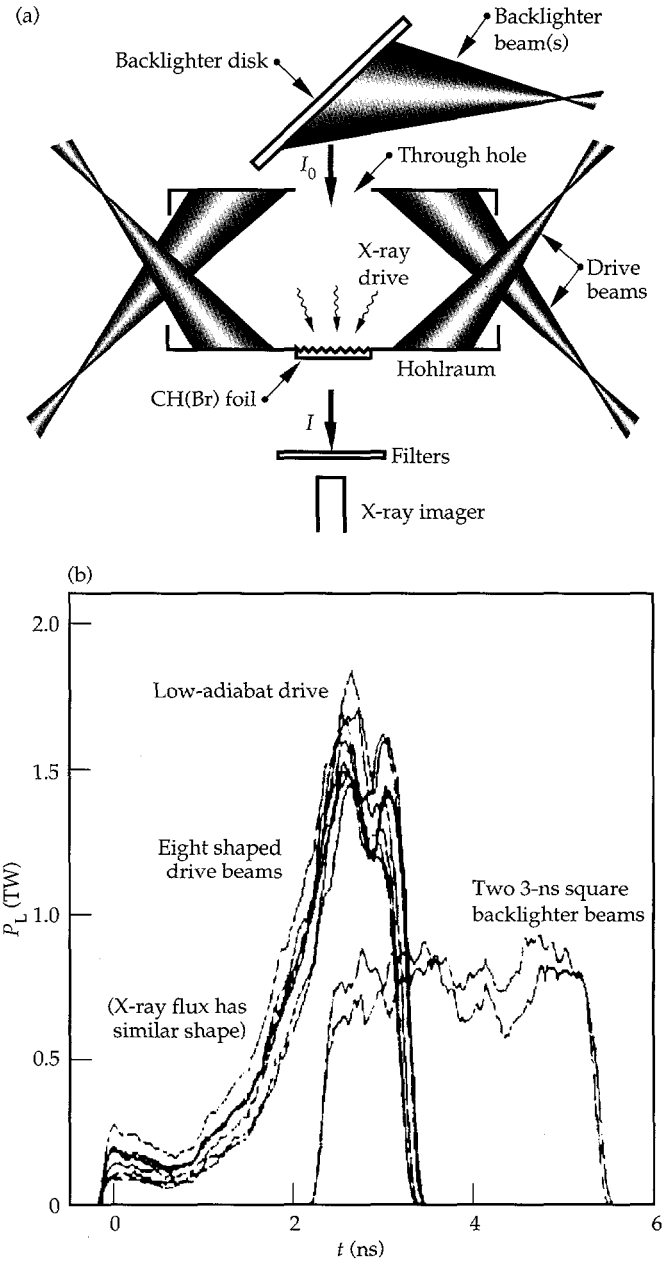

FIGURE 2. (a) The experimental configuration consists of a cylindrical Au hohlraum (3000 μm long, 1600 μm diam) with the modulated CH(Br) foil mounted on the wall. (b) In the hohlraum, eight $\lambda = 351$-nm laser beams are converted to x rays, which ablatively accelerate the foil. Two additional laser beams at $\lambda = 528$ nm generate backlighter x rays used for in-flight diagnosis of the foil. (20-03-1293-4392pb03)

driven with an x-ray drive. We investigated initial perturbations of the form

$$\eta(x) = \sum_{n=1}^{m} \eta_n \cos(k_n x),$$

where $k_n = 2\pi n/\lambda$, for $m = 1$, 2, and 8. The modes are enumerated as harmonics of the longest repeating pattern. In the next section, we discuss the "Experimental Details," and in "Drive Characterization" we present our drive characterization work. The following sections discuss "Single-Mode Experiments," "Two-Mode Experiments," and "Eight-Mode Experiments." Our 3-D single-mode experiments and simulations are discussed in "3-D Single-Mode Experiments." The cylindrical experiments are discussed in "The RT Instability in Cylindrical Implosions," and conclusions are given in "Summary." The final section, "Appendix: Amplitude of Coupled Modes," discusses a second-order perturbation model.

Experimental Details

Figure 2 shows the experimental setup for the planar experiments using a shaped, low-adiabat drive. Sinusoidal surface perturbations are molded onto one side of a planar 750-μm-diam bromine-doped CH foil [$C_{50}H_{47}Br_{2.7}$, or "CH(Br)"] of density $\rho = 1.26$ g/cm^3. A subset of the experiments were with fluorosilicone ($SiOC_4H_7F_3$ or "FS", at $\rho = 1.28$ g/cm^3). As shown in Fig. 2(a), the foil is mounted across a hole in the wall of a 3000-μm-long, 1600-μm-diam cylindrical Au hohlraum with the perturbations facing inwards. The foil is diagnosed by back-illumination with an 800-μm-diam spot of x rays created by irradiating a backlighter disk with one or two $\lambda = 528$-nm Nova[33] beams, typically delayed relative to the drive beams, as shown in Fig. 2(b). The modulations in foil areal density cause modulations in the transmitted backlighter x-ray flux, which are recorded as a function of time with gated or streaked x-ray imaging diagnostics. This is illustrated in Fig. 3 (taken from Refs. 14 and 15).

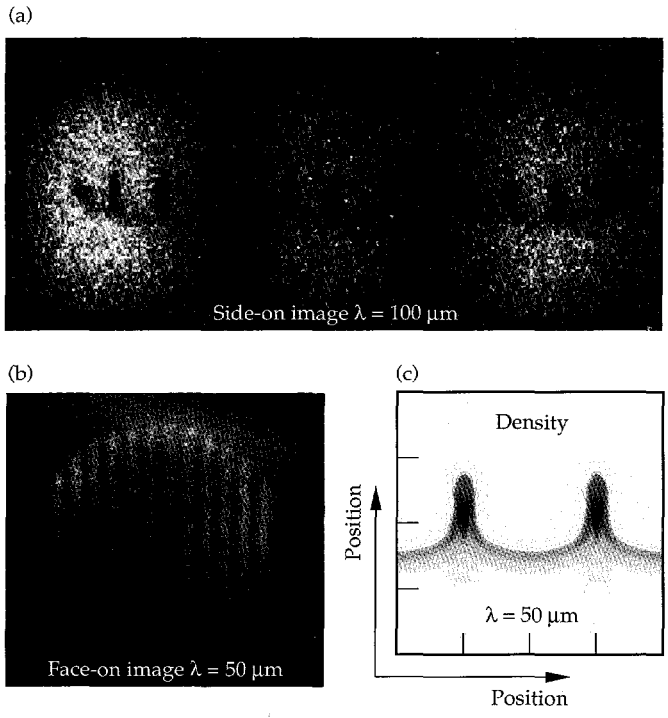

FIGURE 3. Sample images taken (a) in side-on geometry, (b) in face-on geometry, and (c) from 2-D simulations for planar experiments with FS foils. (20-03-1293-4393pb01)

Instrumental spatial resolution is most conveniently expressed as the modulation transfer function (MTF), namely, the ratio of observed to actual contrast [$\Delta \ln E$, where E = film exposure]. The MTF for the 22×-magnification grazing-incidence Wölter x-ray microscope[34] used for most of these experiments is given by[35–37]

$$M(k) = \frac{1}{1 + (k\sigma)^2}, \tag{10}$$

with $\sigma = 6.65$ μm; Fig. 4(a) shows M vs perturbation wavelength. The inverse Fourier transform of $M(k)$ corresponds to an exponential resolution function,

$$R(x) = e^{-x/\sigma}. \tag{11}$$

Figure 4(a) also shows a curve corresponding to Eq. (10) with $\sigma = 8.1$ μm; this is the lowest MTF that is consistent with the data.

Equations (10) and (11) correspond to the "top" sector of the Wölter microscope, which was used for most of the shots in this work. The "west" sector was used in one experiment; its resolution (which is slightly worse than that of the top sector) is given by

$$R(x) = \frac{1}{1+\alpha}\left[\exp(-x/\sigma_1) + \alpha \exp(-x/\sigma_2)\right], \tag{12}$$

with $\alpha = 0.22$, $\sigma_1 = 3.5$ μm, and, $\sigma_2 = 18$ μm. Table 1 gives the correspondence between experiment and Wölter sector used. Figure 4(b) shows the MTF for one of the gated x-ray pinhole cameras used for some of these experiments, the FXI.[38] This camera was run at 8× magnification with 10-μm pinholes.

The Wölter microscope is a grazing-incidence x-ray optic, so it has a high-energy cutoff in its reflectance. We measured this cutoff on an identical second Wölter optic,[36] as illustrated in Fig. 5. The solid curve in Fig. 5(a) gives the x-ray emission spectrum resulting from electron-beam excitation of a cold Nb target at 5 kV. The dotted curve represents the same spectrum after double reflection off the x-ray optic. The ratio of these two curves (dotted/solid) gives the reflectance, shown in Fig. 5(b). The high-energy cutoff is at ~3 keV; the peak reflectance is only about 10%. The smooth dashed curve in Fig. 5(b) is the theoretical double-bounce

reflectance of an ideal Ni surface at grazing angles of 1.1° and 1.2°, multiplied by an overall degradation factor of 0.3, and represents the reflectance assumed in the post-processing of the simulations for these experiments. The degradation factor is presumably caused by surface roughness and absorption by contaminants that have settled onto the Wölter optic surface.

Figure 6 shows the measured (time-integrated) spectra for Mo, Rh, and Sc, the backlighter materials used in the face-on experiments. On separate shots, the backlighter disks were irradiated with 528-nm light at $I \approx 1 \times 10^{14}$ W/cm^2. The Mo spectrum [Fig. 6(a)] is dominated by $n = 3 \rightarrow 2$ L-band emission at 2.4–2.8 keV; the Rh spectrum [Fig. 6(b)] is also dominated by $n = 3 \rightarrow 2$ L-band emission, here at 2.8–3.3 keV. The Sc spectrum [Fig. 6(c)] is dominated by the $n = 2 \rightarrow 1$ He_α K lines. These backlighter materials were chosen by considering the total optical depth (OD) of the experimental foils and the response of the recording instruments.

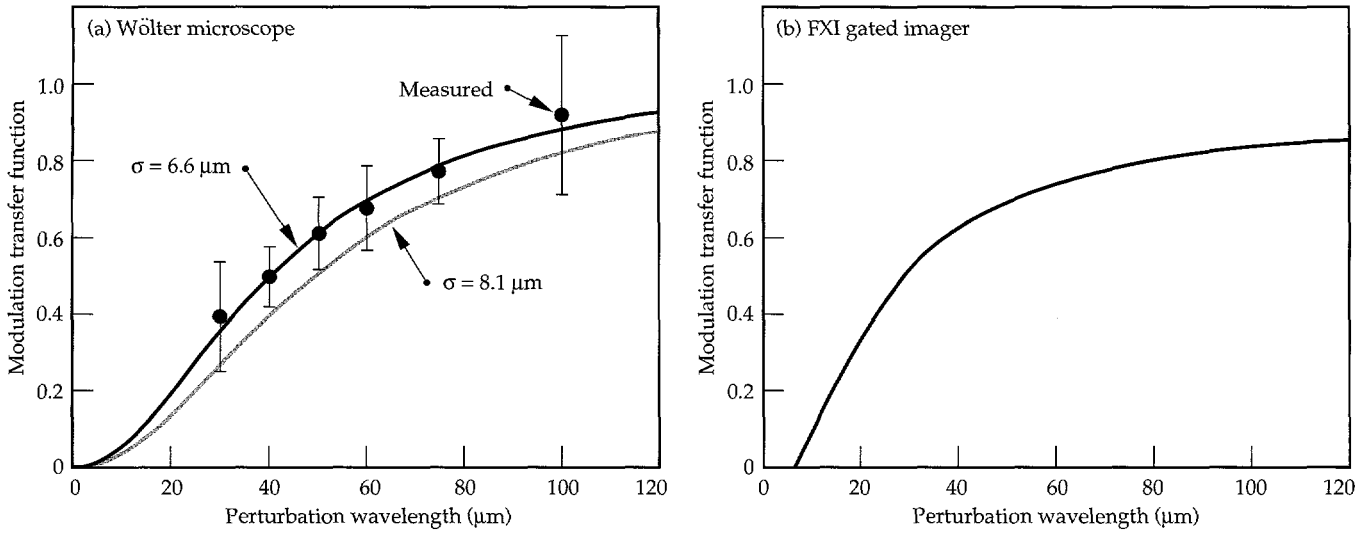

FIGURE 4. (a) Instrument modulation transfer function (MTF) vs perturbation wavelength for the 22×-magnification grazing-incidence Wölter x-ray microscope. The data points represent the measured MTF from the observed $t = 0$ contrast from accelerated rippled-foil targets. The data points and error bars for the $\lambda = 50$ μm and $\lambda = 75$ μm perturbations correspond to the means and standard deviations of the deduced MTF from seven and nine separate rippled-foil shots, respectively. The other data points correspond to single shots at each wavelength, and the error bars correspond to the standard deviation assuming that each individual period is independent data. The black curve represents a best fit of the data with the function $M(k) = 1/[1 + (k\sigma)^2]$, with $\sigma = 6.65$ μm; the gray curved is $M(k)$ for $\sigma = 8.1$ μm. (b) MTF for the FXI gated imager at 8× magnification with 10-μm pinholes and a Sc backlighter. (20-03-0394-0738pb03)

TABLE 1. Compilation of the data for each face-on single-mode shot, using the Wölter x-ray microscope. The ten columns in order give (1) foil material, (2) drive pulse shape, (3) perturbation wavelength, (4) the perturbation initial amplitude, (5) the foil thickness, (6) the total laser energy, (7) the sector (top or west) of the Wölter microscope used, (8) the backlighter material used, (9) the observed growth factor, and (10) the predicted growth factor from the LASNEX simulations.

Single-mode

Foil	Drive	λ (μm)	η_0 (μm)	Thk (μm)	E_{Laser} (kJ)	Sector	Back-lighter	G_{obs}	G_{LASNEX}
CH(Br)	Shaped	100	2.4	48	16.1	Top	Rh	3.8	5.8
CH(Br)	Shaped	70	2.4	50	18.5	Top	Rh	6.5	7.3
CH(Br)	Shaped	50	0.42	57	17.4	West	Mo	19.9	24.0
CH(Br)	Shaped	30	1.5	53	15.1	Top	Rh	7.2	9.7
FS	Shaped	50	4.5	57.5	19.3	Top	Rh	6	4
FS	Shaped	50	0.8	56.0	16.6	Top	Rh	22	20
FS	Shaped	50	0.16	65.5	16.7	Top	Rh	75	75
FS	1 ns sq.	50	2.2	34.2	13.4	Top	Dy	2.9	2.8
CH	1 ns sq.	50	2.5	59.4	13.9	Top	U	1.7	1.9

Drive Characterization

Figure 7 shows the low-adiabat x-ray drive used in most of these experiments.[14,15,37] This drive was generated by focusing eight 351-nm, 2.0–2.4-kJ, 3.3-ns temporally shaped Nova beams into the hohlraum, where they are converted to approximately thermal x rays. The black curve shows the total power of the eight laser beams on a typical shot. The intensity during the first 1.6–1.8 ns of the drive, called the "foot," is about a factor of 10 lower than in the 16-TW peak, which occurs at 2.6 ns. This shaped pulse leads to a lower adiabat and higher compression than if the same total laser energy were delivered in a square pulse. The x-ray drive used in our analysis results from a two-dimensional (2-D) hohlraum simulation[39] using the experimental laser power P_L, and is shown as radiation temperature $T_R(t)$ by the gray curve in Fig. 7. This x-ray drive has been checked by two independent experimental techniques: (1) shock breakout trajectory through an Al wedge mounted on the hohlraum and viewed with a streaked UV imager,[40] and (2) accelerated-foil trajectory using streaked side-on radiography.[14,37] The resulting T_R profile has a ~95-eV foot increasing to 200 eV in the peak at about 3 ns. This shape mimics, on a short time scale, the early stages of an ignition pulse shape, which typically has a ~90-eV foot followed by a stepped ramp to a 300-eV peak.[41]

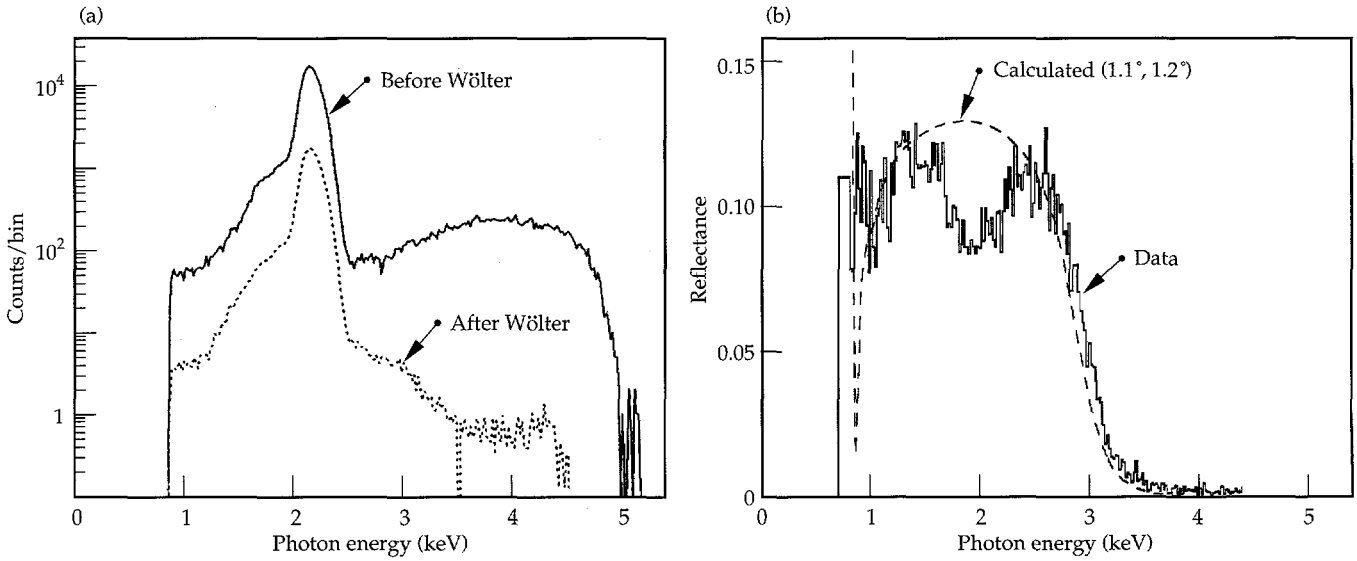

FIGURE 5. Measured Wölter reflectivity vs x-ray energy. In (a) the solid curve corresponds to the x-ray emission spectrum from a Nb transmission target bombarded by a focused electron beam accelerated across a potential difference of 5 kV. The dotted curve is the same except the x rays have undergone two ~1° grazing-incidence reflections off the Ni surface of the Wölter x-ray optic. (b) The solid histogram gives the ratio (dotted/solid) of the two curves in (a) and corresponds to the Wölter reflectance. The smooth dashed curve represents the calculated reflectance for two ideal Ni surfaces at grazing angles of 1.1° and 1.2°, with an overall degradation factor of 0.3. (20-03-0394-0740pb02)

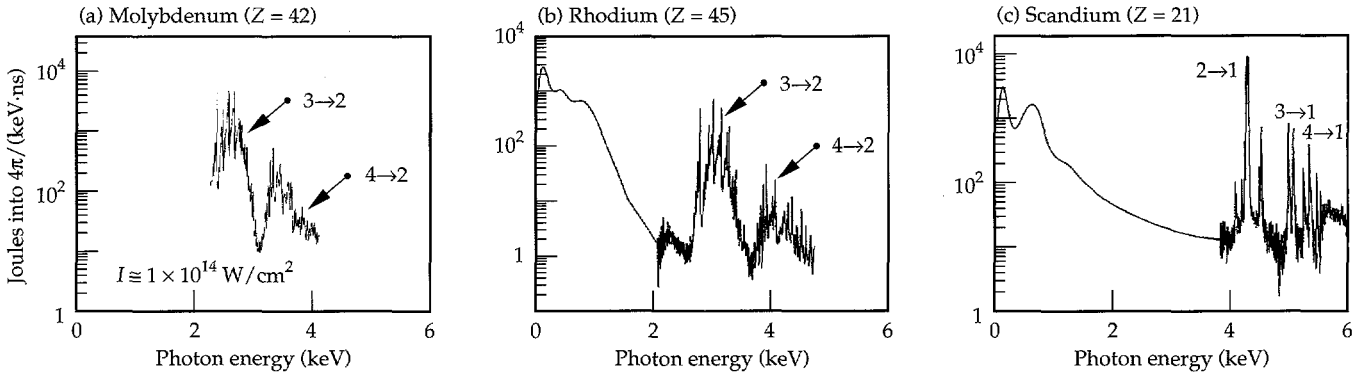

FIGURE 6. Time-integrated spectra for the backlighters used in the face-on experiments. In each case, a single 5-ns laser beam (λ = 528 nm, $I \approx 1 \times 10^{14}$ W/cm^2) was used. The backlighter disks were (a) Mo, (b) Rh, and (c) Sc. The dominant transitions are marked. The high-energy portion of each spectrum was measured with a static crystal (RAP) spectrometer, and the low-energy portions with a filtered photodiode array. (20-03-0394-0739pb02)

Figure 8 shows the drive spectrum during the foot and at peak power for the nominal conditions of this investigation. For comparison we also show Planckian spectra corresponding to radiation temperatures T_R = 95 eV during the foot and T_R = 200 eV during the peak. The actual drive spectrum used derives from a full hohlraum simulation,[39] but is not too different from the time-dependent combination of a Planckian with the spectrum from a planar Au disk illuminated by a shaped λ = 351-nm laser pulse. The weighting of the two spectra for this case (shown in Fig. 8) corresponds to the relative solid angles subtended by the foil mounted on the hohlraum wall for the eight laser spots in the hohlraum versus that for the wall area not directly illuminated with laser light. The contribution of the Au M-band emission from the laser spots causes the drive spectrum to be "harder" than a Planckian spectrum.

From the strong-shock relations for ideal fluids,[42] the shock-front velocity v_s and pressure P behind the shock front are related by $P \approx \rho_{us} v_s^2$, where ρ_{us} is the density of the unshocked material. From Ref. 43 we can write $P \propto T_R^{7/2}$, so we have $T_R \propto P^{2/7} \propto v_s^{4/7}$. When applied to Al, for example, and after correcting for albedo effects, this becomes[40]

$$T_R = \frac{v_s^{0.63}}{80}, \tag{13}$$

with T_R in eV and v_s in cm/s; the numerical factor arises from the equation of state (EOS) of Al. A

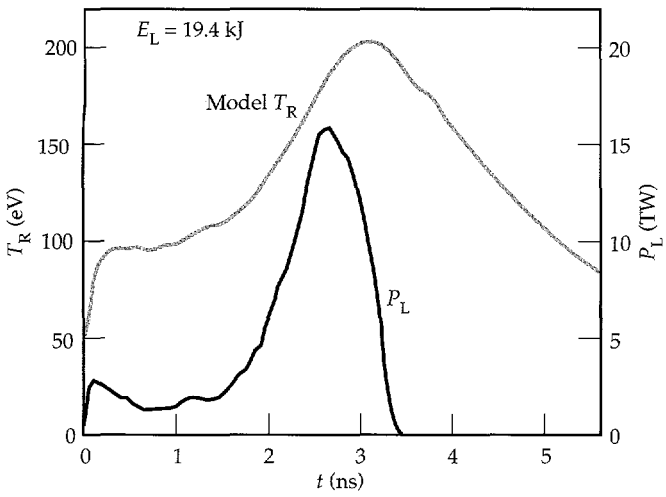

FIGURE 7. Drive expressed in terms of laser power and x-ray radiation temperature. Black curve (scale on right) gives total power vs time of the eight λ = 351-nm drive laser beams. The adopted drive temperature $T_R(t)$, shown by the gray curve (scale on left), was obtained from a 2-D hohlraum simulation. The first 2 ns represents the "foot"; peak laser power P_L occurs at 2.6 ns; peak T_R occurs at 3 ns. (20-03-1293-4397pb02)

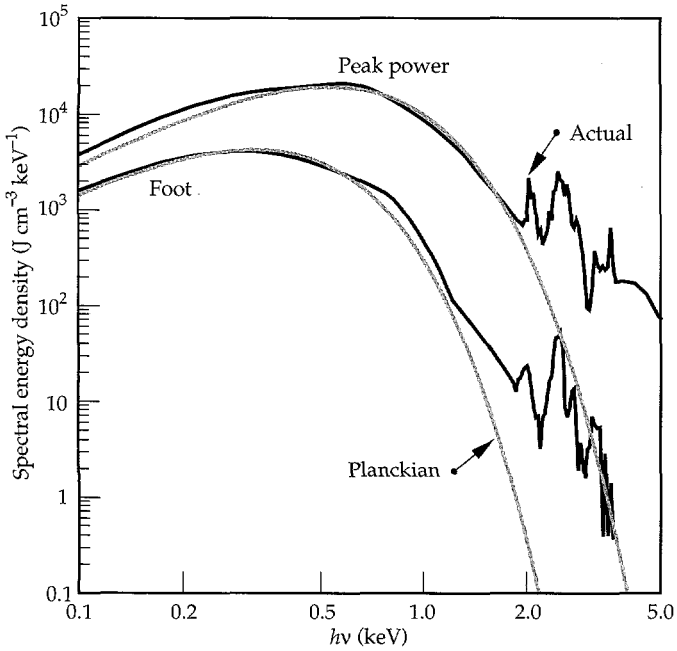

FIGURE 8. Black curves represent nominal drive spectra during the foot and the peak of the drive shown in Fig. 7. Gray curves correspond to Planckian spectra at T_R = 100 and 200 eV. (20-03-0394-0743pb02)

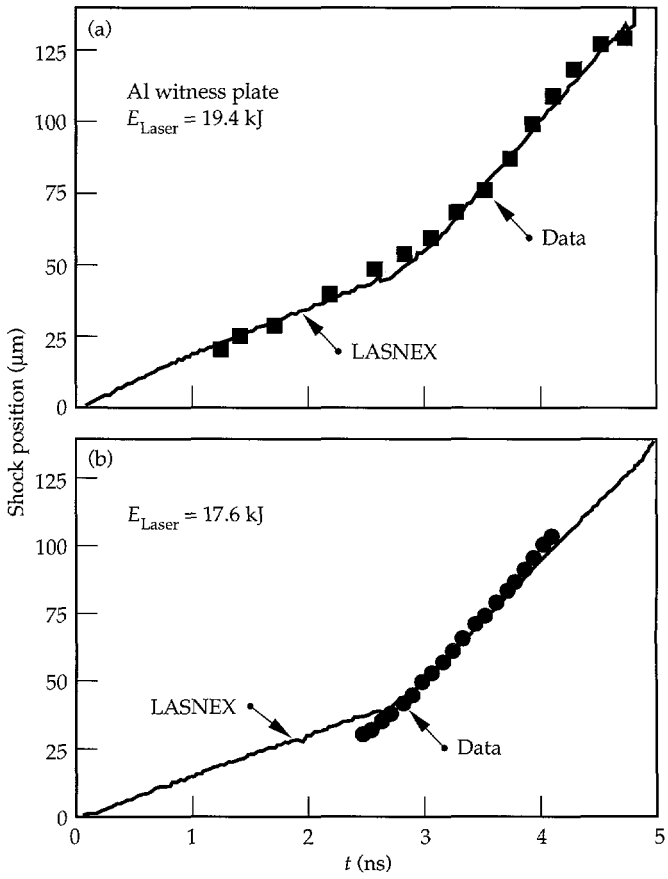

FIGURE 9. The drive is characterized with measurements of shock trajectory, deduced from measuring in face-on geometry the shock breakout time across a variable-thickness Al wedge mounted on the wall of the hohlraum. Corresponding 1-D LASNEX simulations are shown. (a) Results for 19.4-kJ shot discussed in Figs. 7 and 8. (b) Results for E_{Laser} = 17.6 kJ. (20-07-0394-0744pb03)

measurement of shock velocity therefore allows us to deduce the ablation pressure and drive temperature.

Figure 9 shows measured shock trajectories for two shots. The measurements were made by viewing a wedged Al witness plate face-on with a streaked UV imager.[40] The shock breakout time is recorded as a function of position across the increasing thickness of the witness plate, allowing the shock trajectory to be reconstructed. Figure 9 shows the experimental trajectories at two laser energies and the corresponding simulations from 1-D LASNEX[44] using the drive described above (scaled in proportion to the laser power history for the lower-energy shot). The absolute timing of the shock trajectory data relative to drive turn-on ($t = 0$) was experimentally determined in the data shown in Fig. 9(b) but not in Fig. 9(a), where only the relative time was measured. The agreement between the data and simulation is very good. The data for the higher-energy shot [Fig. 9(a)] and the simulations for both shots show a two-component trajectory corresponding to an initial shock launched by the foot, and a delayed second shock coming from the peak of the drive. For the measured two-shock system in Fig. 9(a), the first shock has a velocity $v_1 \approx 20$ μm/ns, and the second shock has a peak velocity of $v_2 \approx 53$ μm/ns. The simulations give velocities of 16 and 46 μm/ns, respectively. Applying Eq. (13) directly to the data gives $T_R \approx 120$ and 215 eV for the foot and peak of the drive, as compared to 100 and 200 eV from the simulations.

The foil trajectory, which is a measure of the gross hydrodynamics, was obtained by viewing across the rear edge of the foil in side-on geometry,[14,15] as shown in Fig. 10. This trajectory is reproduced very well with the 1-D simulation using the drive model described above, as illustrated in Fig. 11 for a CH(Br) foil. The back edge of the foil does not begin to move until shock breakout at ~2.6 ns. The foil then accelerates during the interval $2.6 \le t \le 3.6$ ns, after which the drive is turning off and the foil begins to coast. The black curve represents the foil trajectory from the 1-D LASNEX simulation; the gray curve represents the acceleration of the ablation front, defined as the zone of half peak density. The fluctuations in the acceleration at 0.2 and 2.2 ns are due to the passage of the first and second shocks. The inset in Fig. 11 gives the ablation velocity $v_a = \dot{m}/\rho_{max}$ and density gradient scalelength $L = \rho/\nabla\rho$, where $\dot{m}$ is the mass ablation rate per unit area, ρ_{max} is the peak density, and ρ and $\nabla\rho$ are the density and its gradient. (Computationally, the scalelength L is taken as the minimum value of $\left[\partial(\ln\rho)/\partial z\right]^{-1}$.) Calculations based on this drive give better agreement with experiment than was obtained in preliminary results.[45]

It is instructive to look in more detail at the effect of this shaped drive on the foil. Figures 12(a)–12(c) show results from the 1-D LASNEX simulations for radiation drive temperature, ablation pressure (defined as peak pressure in the simulation), and foil peak density as functions of time. Figures 12(d)–12(f) give the corresponding spatial profiles of electron temperature $T_e(z)$, pressure $P(z)$, and density $\rho(z)$ at five times spanning

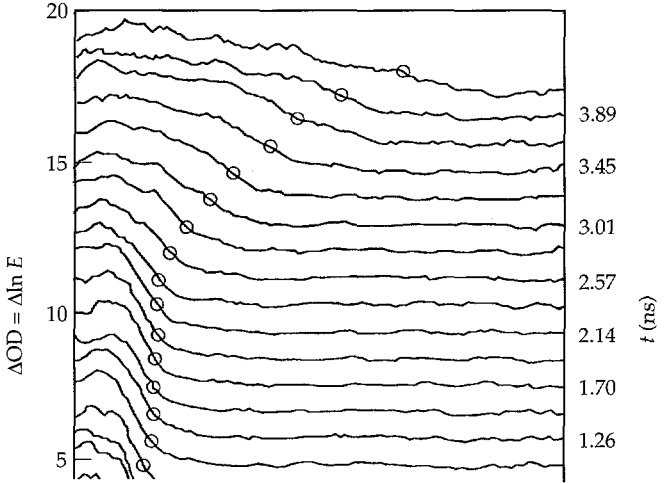

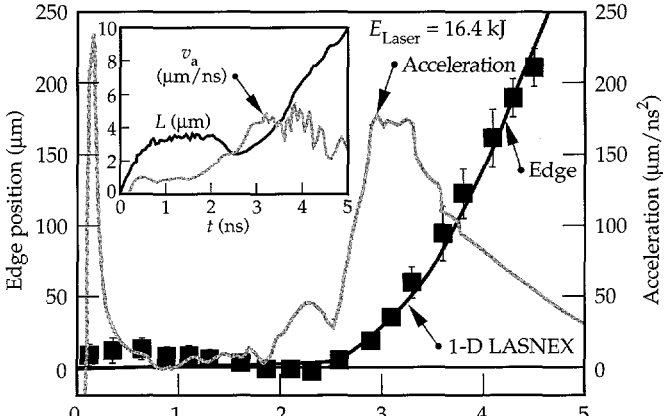

1.3–2.9 ns. In Fig. 12(a), the drive $T_R(t)$ shows a ~90-eV foot for the first 1.5 ns, an increase to a peak of 190 eV at 3 ns, and a decay to ~100 eV at 5 ns. The resulting ablation pressure in the CH(Br) foil (Fig. 12b) shows a 3–5 Mbar foot and a peak of 28 Mbar at 3 ns, i.e., at the same time as the peak in T_R. [This is also the time of peak acceleration and peak ablation velocity (Fig. 11).] The peak density of the foil [Fig. 12(c)] is generated just behind the strongest shock, reaching 6.5 g/cm^3 or a compression of 5.2 at 2.6 ns, when the second shock breaks out of the back of the foil and is at maximum strength. (This is also the time of minimum L, shown in the inset in Fig. 11.) The $T_e(z)$ profile at 1.3 ns [Fig. 12(d)] shows a sharp increase at $z = -20$ μm because of the passage of the first shock. Notice, however, that a low level of heating precedes the first shock ($z > -20$ μm). This "preheat" results from the deep penetration of the hard component ($h\nu \gtrsim 1.4$ keV) of the drive spectrum. By 2.5 ns, the second shock has overtaken the first, and the sharp features in $T_e(z)$ are washed out. The pressure profiles [Fig. 12(e)] convey a similar picture. During the interval 1.3–2.1 ns, the sharp rise in pressure to 4 Mbar due to the first shock is readily apparent. At 2.5 ns, the second shock has overtaken the first, increasing the pressure to 20 Mbar, and at 2.9 ns the pressure reaches its maximum of 28 Mbar. Figure 12(f) shows the effect on the foil compression of this staged two-shock drive. The compression at 1.3 ns just behind the first shock increases the foil density from 1.26 to 3.3 g/cm^3. By the time the second shock has overtaken the first at 2.5 ns, the peak density has reached 6.4 g/cm^3, corresponding to a compression of 5. This is greater than the maximum possible compression of 4 for a single strong shock (in the ideal-gas limit). The staging of multiple shocks allows a higher compression by maintaining the foil on a lower adiabat.

We illustrate the lower adiabat achievable with this shaped drive by characterizing an adiabat with the ratio $\alpha = P/P_{FD}$ of pressure at peak density to that of a Fermi-degenerate gas at the same density (which represents the lowest possible internal energy). For P_{FD}, we use the pressure at zero temperature for the EOS of the foil. For the low-adiabat drive shown in Fig. 12, we have $\alpha \approx 2$; for a 1-ns square drive at the same laser energy[13] we have $\alpha \approx 9$, a factor of 4.5 higher. Note that the EOS for a real material differs significantly from that of an ideal Fermi fluid for densities only a few times solid density. The value of the parameter α defined above does not uniquely characterize an isentrope but changes with density along one. The value of α goes to infinity at solid density because $P_{FD} \to 0$. The value of α does, however, approach a constant along an isentrope in the limit $\rho \to \infty$. This asymptotic limit of α is about 1.25 for our low-adiabat drive, but it is 2.3 for a 1-ns square drive. Thus, if the foil driven with the shaped pulse were to be compressed to high density without introducing additional entropy, as in a capsule implosion, its compression would be close to that expected in the degenerate limit.

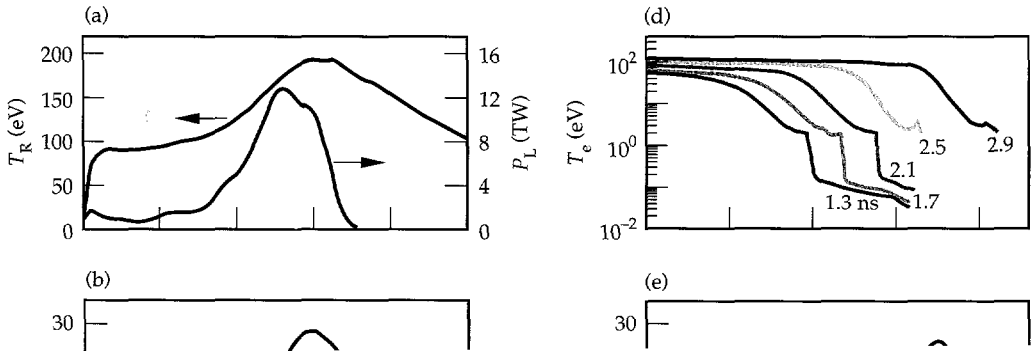

FIGURE 12. Various representations of the 16.4-kJ drive corresponding to results shown in Fig. 11 from 1-D simulations to illustrate the effect of pulse shaping. (a) Laser power P_L and radiation temperature T_R vs time. (b) Ablation pressure (defined as the peak pressure in the simulation) vs time. (c) Peak density vs time.

measurement of shock velocity therefore allows us to deduce the ablation pressure and drive temperature.

Figure 9 shows measured shock trajectories for two shots. The measurements were made by viewing a wedged Al witness plate face-on with a streaked UV imager.[40] The shock breakout time is recorded as a function of position across the increasing thickness of the witness plate, allowing the shock trajectory to be reconstructed. Figure 9 shows the experimental trajectories at two laser energies and the corresponding simulations from 1-D LASNEX[44] using the drive described above (scaled in proportion to the laser power history for the lower-energy shot). The absolute timing of the shock trajectory data relative to drive turn-on ($t = 0$) was experimentally determined in the data shown in Fig. 9(b) but not in Fig. 9(a), where only the relative time was measured. The agreement between the data and simulation is very good. The data for the higher-energy shot [Fig. 9(a)] and the simulations for both shots show a two-component trajectory corresponding to an initial shock launched by the foot, and a delayed second shock coming from the peak of the drive. For the measured two-shock system in Fig. 9(a), the first shock has a velocity $v_1 \approx 20$ μm/ns, and the second shock has a peak velocity of $v_2 \approx 53$ μm/ns. The simulations give velocities of 16 and 46 μm/ns, respectively. Applying Eq. (13) directly to the data gives $T_R \approx 120$ and 215 eV for the foot and peak of the drive, as compared to 100 and 200 eV from the simulations.

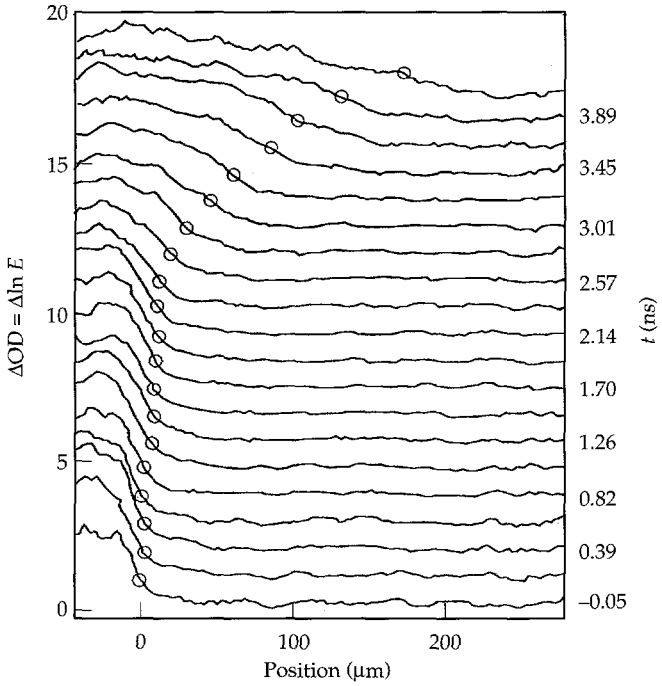

FIGURE 10. Foil trajectory (for a FS foil) in side-on geometry measured with the Wölter x-ray microscope. The profiles are of optical depth OD, and are artificially offset vertically by time, as indicated on the right-hand vertical axis. The circles represent the position that was taken as the foil rear edge (side away from x-ray drive). (20-03-0895-2047pb01)

The foil trajectory, which is a measure of the gross hydrodynamics, was obtained by viewing across the rear edge of the foil in side-on geometry,[14,15] as shown in Fig. 10. This trajectory is reproduced very well with the 1-D simulation using the drive model described above, as illustrated in Fig. 11 for a CH(Br) foil. The back edge of the foil does not begin to move until shock breakout at ~2.6 ns. The foil then accelerates during the interval $2.6 \le t \le 3.6$ ns, after which the drive is turning off and the foil begins to coast. The black curve represents the foil trajectory from the 1-D LASNEX simulation; the gray curve represents the acceleration of the ablation front, defined as the zone of half peak density. The fluctuations in the acceleration at 0.2 and 2.2 ns are due to the passage of the first and second shocks. The inset in Fig. 11 gives the ablation velocity $v_a = \dot{m}/\rho_{max}$ and density gradient scalelength $L = \rho/\nabla\rho$, where $\dot{m}$ is the mass ablation rate per unit area, ρ_{max} is the peak density, and ρ and $\nabla\rho$ are the density and its gradient. (Computationally, the scalelength L is taken as the minimum value of $[\partial(\ln\rho)/\partial z]^{-1}$.) Calculations based on this drive give better agreement with experiment than was obtained in preliminary results.[45]

It is instructive to look in more detail at the effect of this shaped drive on the foil. Figures 12(a)–12(c) show results from the 1-D LASNEX simulations for radiation drive temperature, ablation pressure (defined as peak pressure in the simulation), and foil peak density as functions of time. Figures 12(d)–12(f) give the corresponding spatial profiles of electron temperature $T_e(z)$, pressure $P(z)$, and density $\rho(z)$ at five times spanning

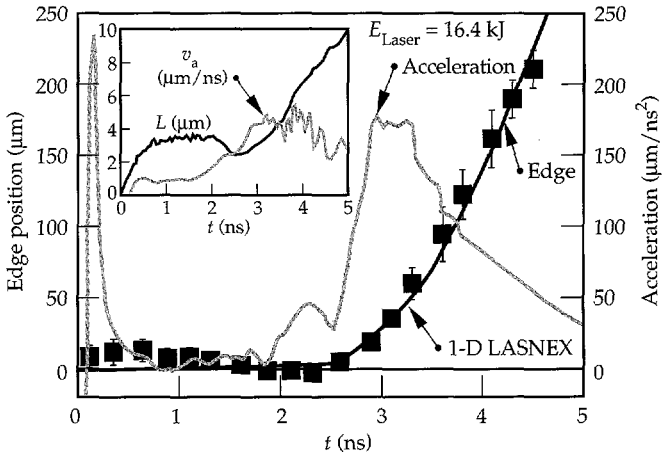

Figure 11. The square plotting symbols represent the measured position of the rear edge (side away from the x-ray drive) of the foil as a function of time. These data represent the average of two shots, one using a 50-μm-thick and the other a 48-μm-thick CH(Br) foil. Error bars represent uncertainties in defining the edge of the foil. The black curve represents the result of the 1-D LASNEX simulation. The rear edge of the foil does not start to move until after shock breakout at 2.6 ns. The gray curve represents the acceleration of the ablation front (defined as the zone of half peak density). Inset: ablation velocity and density gradient scalelength from the simulation. (20-07-0592-1702Bpb02)

1.3–2.9 ns. In Fig. 12(a), the drive $T_R(t)$ shows a ~90-eV foot for the first 1.5 ns, an increase to a peak of 190 eV at 3 ns, and a decay to ~100 eV at 5 ns. The resulting ablation pressure in the CH(Br) foil (Fig. 12b) shows a 3–5 Mbar foot and a peak of 28 Mbar at 3 ns, i.e., at the same time as the peak in T_R. [This is also the time of peak acceleration and peak ablation velocity (Fig. 11).] The peak density of the foil [Fig. 12(c)] is generated just behind the strongest shock, reaching 6.5 g/cm^3 or a compression of 5.2 at 2.6 ns, when the second shock breaks out of the back of the foil and is at maximum strength. (This is also the time of minimum L, shown in the inset in Fig. 11.) The $T_e(z)$ profile at 1.3 ns [Fig. 12(d)] shows a sharp increase at $z = -20$ μm because of the passage of the first shock. Notice, however, that a low level of heating precedes the first shock ($z > -20$ μm). This "preheat" results from the deep penetration of the hard component ($h\nu \gtrsim 1.4$ keV) of the drive spectrum. By 2.5 ns, the second shock has overtaken the first, and the sharp features in $T_e(z)$ are washed out. The pressure profiles [Fig. 12(e)] convey a similar picture. During the interval 1.3–2.1 ns, the sharp rise in pressure to 4 Mbar due to the first shock is readily apparent. At 2.5 ns, the second shock has overtaken the first, increasing the pressure to 20 Mbar, and at 2.9 ns the pressure reaches its maximum of 28 Mbar. Figure 12(f) shows the effect on the foil compression of this staged two-shock drive. The compression at 1.3 ns just behind the first shock increases the foil density from 1.26 to 3.3 g/cm^3. By the time the second shock has overtaken the first at 2.5 ns, the peak density has reached 6.4 g/cm^3, corresponding to a compression of 5. This is greater than the maximum possible compression of 4 for a single strong shock (in the ideal-gas limit). The staging of multiple shocks allows a higher compression by maintaining the foil on a lower adiabat.

We illustrate the lower adiabat achievable with this shaped drive by characterizing an adiabat with the ratio $\alpha = P/P_{FD}$ of pressure at peak density to that of a Fermi-degenerate gas at the same density (which represents the lowest possible internal energy). For P_{FD}, we use the pressure at zero temperature for the EOS of the foil. For the low-adiabat drive shown in Fig. 12, we have $\alpha \approx 2$; for a 1-ns square drive at the same laser energy[13] we have $\alpha \approx 9$, a factor of 4.5 higher. Note that the EOS for a real material differs significantly from that of an ideal Fermi fluid for densities only a few times solid density. The value of the parameter α defined above does not uniquely characterize an isentrope but changes with density along one. The value of α goes to infinity at solid density because $P_{FD} \to 0$. The value of α does, however, approach a constant along an isentrope in the limit $\rho \to \infty$. This asymptotic limit of α is about 1.25 for our low-adiabat drive, but it is 2.3 for a 1-ns square drive. Thus, if the foil driven with the shaped pulse were to be compressed to high density without introducing additional entropy, as in a capsule implosion, its compression would be close to that expected in the degenerate limit.

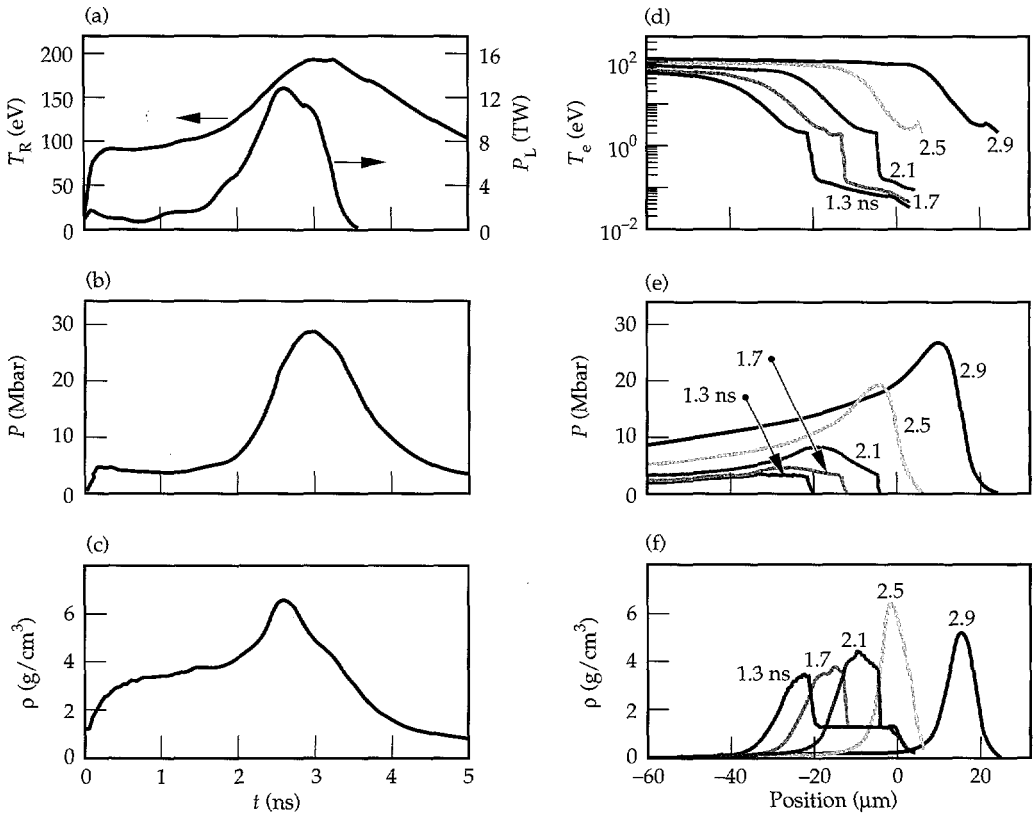

FIGURE 12. Various representations of the 16.4-kJ drive corresponding to results shown in Fig. 11 from 1-D simulations to illustrate the effect of pulse shaping. (a) Laser power P_L and radiation temperature T_R vs time. (b) Ablation pressure (defined as the peak pressure in the simulation) vs time. (c) Peak density vs time. (d)–(f) Spatial profiles of (d) electron temperature T_e, (e) pressure in the foil, and (f) foil density at 1.3, 1.7, 2.1, 2.5, and 2.9 ns, spanning the foot through the peak of the drive. The 0-μm position corresponds to the initial position of the back edge of the foil (the side away from the drive). The drive is incident from the left (negative) side. (20-03-0794-2831pb04)

Single-Mode Experiments

Figure 13 shows the data from a single-mode face-on experiment with a $\lambda = 100$ μm, $\eta_0 = 2.4$ μm initial perturbation on a 48 μm thick CH(Br) foil.[37] Figure 13(a) shows the "raw" image; Fig. 13(b) shows profiles of modulations in optical depth $\Delta OD \approx -\ln E$ at early, intermediate, and late times. The initial perturbation amplitude was large, and we observe clear sinusoidal contrast (ΔOD) even at the earliest time, 0.2 ns. At 2.2 ns, the contrast is slightly greater and still sinusoidal, indicating that the growth is still in the linear regime. At 4.2 ns, the shape of the perturbation has deviated substantially from sinusoidal, forming sharp spikes and bubbles of high and low OD, respectively; the perturbation has entered the nonlinear regime. The transition from the linear to nonlinear regime is particularly clear in Fourier space; Fig. 13(c) shows the real components of the Fourier transform for the three ΔOD profiles. At 0.2 ns, only the η_1 fundamental mode (first harmonic) exists, indicating a purely sinusoidal perturbation. At 2.2 ns, η_1 has grown slightly but is still the only component, indicating a purely sinusoidal shape and linear regime. At 4.2 ns, a whole spectrum of higher Fourier harmonics—up to the fifth—is observed, corresponding to the bubble-and-spike shape of the top lineout in Fig. 13b. The perturbation is fully into the nonlinear regime.

Figure 14 shows the results of our λ-scaling experiments with single-mode CH(Br) foils. The data points represent the observations for the fundamental and the second harmonic. The error bars represent the standard deviation of the ensemble formed by treating each individual period of the perturbations as independent data. The solid curves are the corresponding 2-D LASNEX[44] simulations. The $\lambda = 100$ μm data shown in Fig. 14(a) is the full time evolution of the results shown at three particular times in Fig. 13. The perturbation growth evolves through three stages. Before shock breakout ($t < 2.5$ ns), the perturbation is growing only slowly because of the rippled shock dynamics.[21,22] For a brief period after shock breakout ($2.5 \text{ ns} \le t \le 3.2$ ns) the perturbation is growing strongly because of the RT instability in the linear regime. Late in time ($t > 3.2$ ns), the perturbation "saturates." The evolution has entered the nonlinear regime, the second harmonic appears, and the observed contrast rolls over. The growth factor G, defined as the ratio of peak to initial contrast, was small here—$G = 4$. A similar situation occurs for $\lambda = 70$ μm, $\eta_0 = 2.4$ μm [Fig. 14(b)]. Here, the overall growth was slightly greater, $G = 6$, reflecting the higher growth rate. For $\lambda = 50$ μm, $\eta_0 = 0.4$ μm [Fig. 14(c)], the situation is qualitatively different. Because the initial amplitude is small, the perturbation evolution remains primarily in the linear regime, achieving the higher growth $G = 20$. Figure 14(d) shows the results for $\lambda = 30$ μm, $\eta_0 = 1.5$ μm. Because of the low instrumental MTF at $\lambda = 30$ μm (see Fig. 4), the contrast remains low and no higher harmonics are observed. The observed growth factor for the fundamental mode was $G = 7$. Table 1 lists the key parameters for these experiments, including observed and simulated growth factors.

The solid curves in Fig. 14 represent the corresponding results from 2-D LASNEX simulations, after convolution

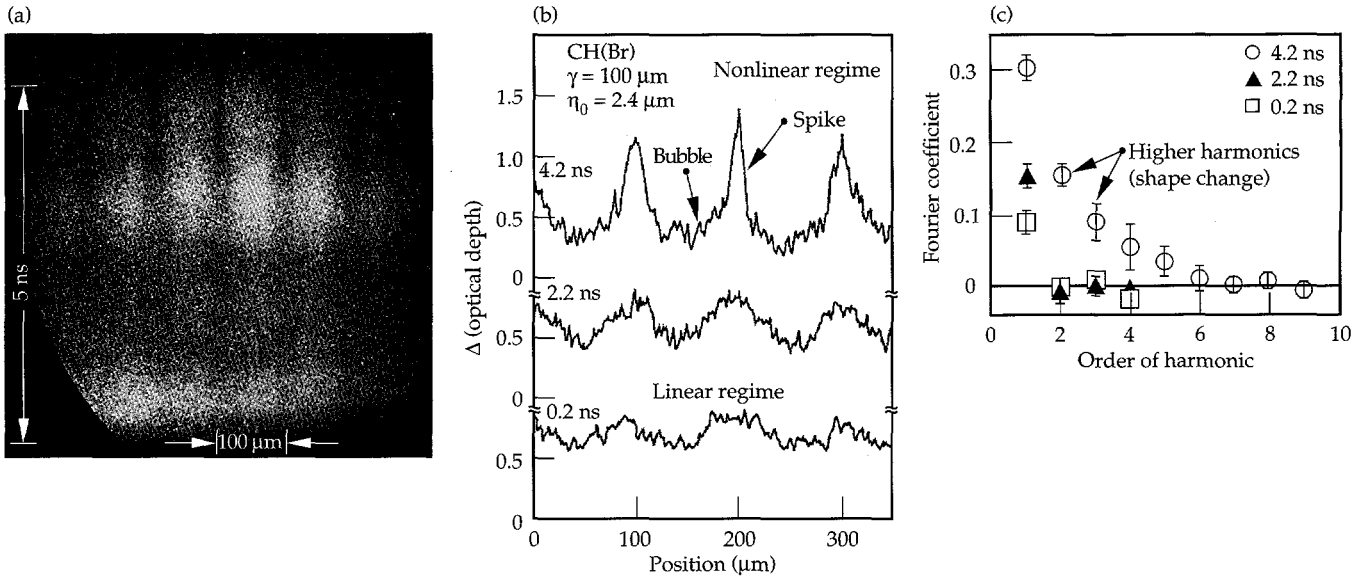

FIGURE 13. Various representations for single-mode face-on data for a $\lambda = 100$ μm, $\eta_0 = 2.4$ μm perturbation imposed on a 48-μm-thick CH(Br) foil. (a) The "raw" streaked image is shown as film density. The film response is removed using a calibrated exposure across a precision P20 optical density wedge. (b) Profiles of Δ(optical depth) ≈ $-\Delta \ln E$ at 0.2, 2.2, and 4.2 ns. (c) Real components of the Fourier transforms for the profiles in (b). At late time, the perturbation enters the nonlinear regime, and up to the fifth harmonic of the perturbation Fourier composition is observed. (20-03-0394-0748pb02)

of the simulated image exposure with the instrumental resolution function [Eq. (11)]. (Our modeling is discussed in detail in Ref. 45.) Qualitatively, the simulations agree quite well with the data. There is modest growth during the shock transit phase, strong growth after shock breakout, and then saturation with the appearance of the second harmonic, indicating entry into the nonlinear regime.

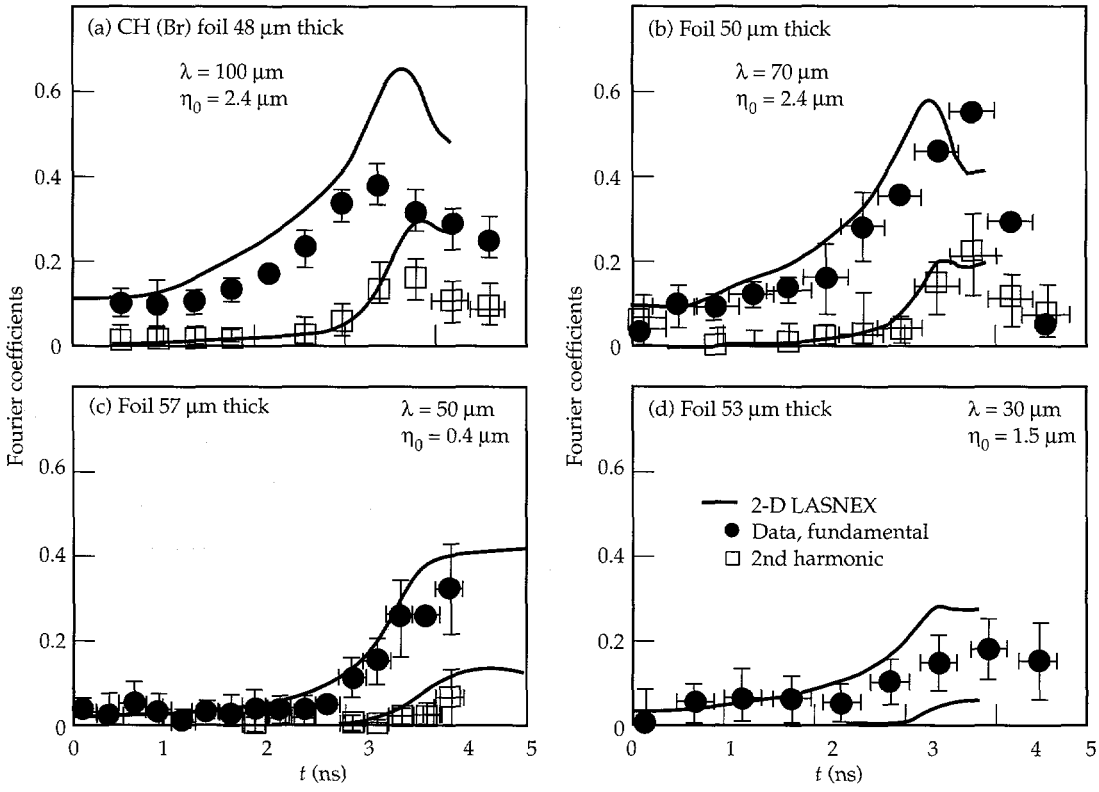

FIGURE 14. Results from single-mode, λ-scaling series for various values of λ and η_0. Data points represent first harmonic (fundamental mode) and second harmonic Fourier coefficients of lnE. Solid curves are corresponding results from 2-D LASNEX simulations. (a) Shows full time dependence for data of Fig. 13. All shots except that in (c) used the "top" sector of the 22× and a Rh backlighter; in (c), the west sector was used, and a Mo backlighter was used for slightly improved contrast. (20-03-0394-1063pb02)

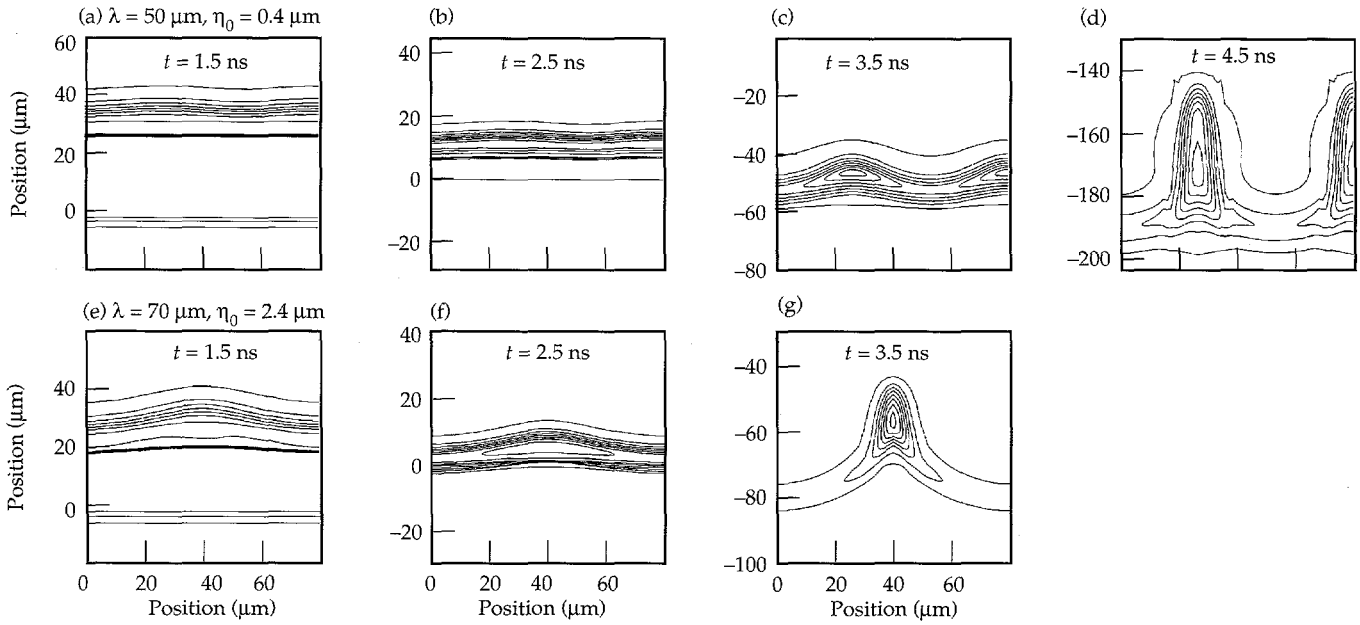

FIGURE 15. Isodensity contour plots from 2-D simulations, in 1-ns steps, for perturbation growth from (a–d) λ = 50 μm, η_0 = 0.4 μm and (e–g) λ = 70 μm, η_0 = 2.4 μm, corresponding to the results shown in Figs. 14(c) and 14(b), respectively. The contours correspond to equal density steps and span densities of (a) 0.2177–3.265, (b) 0.4837–7.256, (c) 0.3389–5.084, (d) 0.1548–2.322, (e) 0.2287–3.431, (f) 0.4976–7.464, and (g) 0.5786–8.679 g/cm^3. (20-03-0894-3227pb02)

This basic behavior can be understood in terms of the simple linear and perturbation theories outlined in Eqs. (2, 3, 5). In the linear regime, RT growth is exponential. For $\eta/\lambda \gtrsim 0.1$, the evolution enters the nonlinear regime, higher harmonics appear, and at third order, the growth in the fundamental mode is reduced. The late-time rollover in the simulations (and presumably in the data), is partially an instrumental artifact, however. Mass is being concentrated in long, narrow spikes in the nonlinear phase, as illustrated in Fig. 15 with isodensity contour plots from the simulations for $\lambda = 50$ and 70 μm. For example, at $t = 3.5$ ns for $\lambda = 70$ μm [Fig. 15(g)], 50% of the highest density contours lie within a 10-μm region at the center of the spike, which is difficult to resolve with the 10–15-μm resolution of the imaging instrument used (see Fig. 4). The observed contrast is therefore decreasing after $t = 3.5$ ns. Notice that there is much less concentration of material in the spike at 3.5 ns for $\lambda = 50$ μm [Fig. 15(c)]. For this case, spatial resolution does not become an issue until very late ($t \approx 4.5$ ns). For completeness, Fig. 16 shows the simulations before and after convolution with the instrument resolution function. The contrast is greater before inclusion of the MTF, the difference being greatest for the shortest wavelengths.

The simulations systematically predict slightly more growth than is observed (Fig. 14). The seeds of this discrepancy occur early—by 1.5 ns for the $\lambda = 100$ and 70-μm foils, well before the shock has broken out—so the disagreement occurs during the shock transit phase. We consider possible causes for this discrepancy in Fig. 17, using the $\lambda = 70$ μm experiment as a test case.

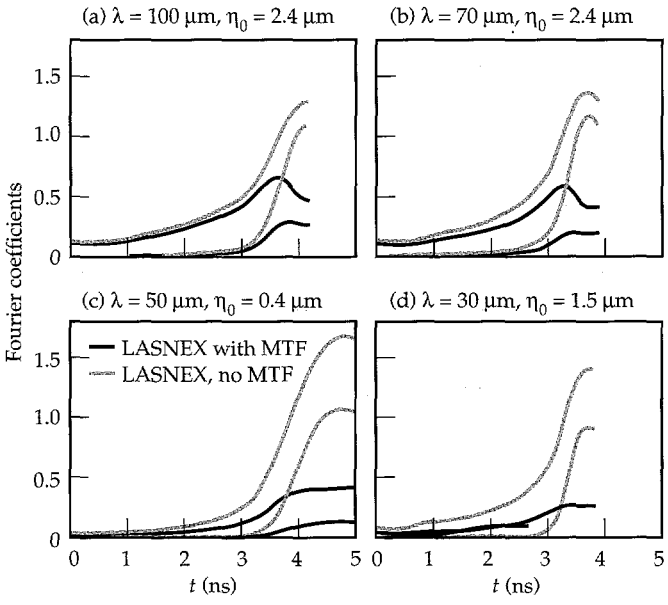

FIGURE 16. Effect of instrument resolution on the results from the simulations. Black curves in (a)–(d), which include the effects of instrumental MTF, are reproduced from Fig. 14. Gray curves represent the simulation results before inclusion of MTF. (20-03-0394-0745pb03)

Possible uncertainties in the drive $T_R(t)$ could arise from uncertainties in the albedo of the Au hohlraum wall early in time and from stagnation of Au plasma on the hohlraum axis late in time. To assess the sensitivity of perturbation growth to uncertainties in the drive, we compare in Fig. 17(a) the results of simulations in which the foot of the drive was 10 eV higher and the peak 10 eV lower than the nominal drive. This variation in the drive produces very little variation in the predicted overall growth for $\lambda = 70$ μm.

Different EOS models can lead to different predicted foil compression, which affects the RM-like growth during shock transit. In Fig. 17(b) we compare the effect of using a tabular EOS library with that of using an in-line QEOS model.[46] The QEOS model generates a slightly stiffer EOS, which leads to less foil compression and hence to ~15% less perturbation growth.

There is also uncertainty in the exact magnitude of preheat in the drive spectrum early in time. In Fig. 17(c) we assess the sensitivity of perturbation growth to preheat by comparing simulations with a nominal drive spectrum and with a "high preheat" drive, in which the drive spectrum above $h\nu = 1.4$ keV is increased by a factor of 10 for the first 2 ns, while keeping the total

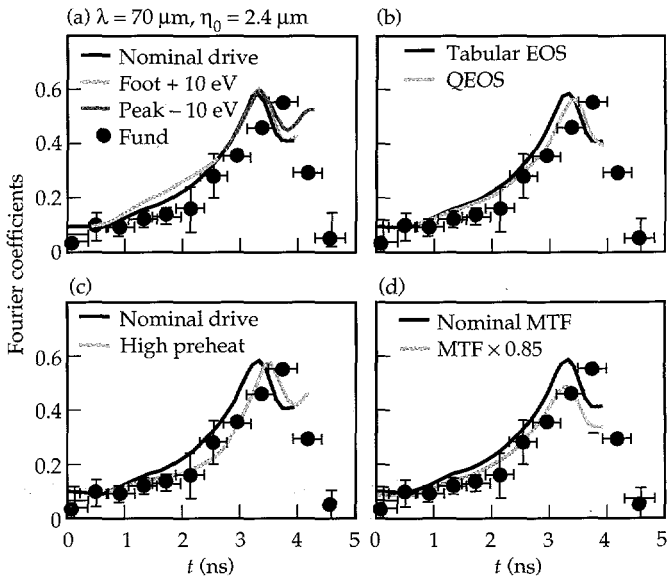

FIGURE 17. Sensitivity of perturbation growth for $\lambda = 70$ μm, $\eta_0 = 2.4$ μm to (a) drive, (b) EOS, (c) preheat, and (d) MTF. Data and black curves are reproduced from Fig. 14(b). (a) The light gray curve corresponds to a simulation in which the radiation temperature in the foot of the drive was increased by 10 eV; the dark gray curve represents a simulation in which the peak of the drive was reduced by 10 eV. (b) The nominal simulation (black) uses a tabular EOS library. The gray curve uses an in-line model called QEOS, which results in a slightly "stiffer" EOS. (c) The gray curve corresponds to a simulation in which the preheat in the drive was artificially increased: during the first 2 ns (the foot), the drive for $h\nu \geq 1.4$ keV was increased by a factor of 10, and the drive for $h\nu < 1.4$ keV was decreased to maintain the same total energy. (d) The gray curve corresponds to post-processing the simulation with a resolution function artificially degraded to give a 15% lower MTF. (20-03-0894-2839pb03)

drive power constant. Enhancement of the preheat significantly reduces perturbation growth.

We also illustrate the sensitivity of observed growth to uncertainties in the MTF. Decreasing the MTF by 15%, the maximum reduction consistent with the data shown in Fig. 4(a), decreases the predicted growth by 15%, as shown in Fig. 17(d).

To summarize, the simulations slightly but systematically overpredict perturbation growth during the shock transit phase. A possible cause is higher preheat in the foot of the drive, but a combination of stiffer EOS and degraded MTF may also be involved.

We have also done single-mode 2-D experiments aimed at measuring large RT growth factors.[14] These experiments differed from those described above only in the use of fluorosilicone ($SiOC_4H_7F_3$, or "FS") as the foil material. We used FS because its admixture of opacities shields the foil from x-ray preheat, keeping the foil on a lower adiabat. The density gradient at the ablation front is therefore steeper, and the ablation velocity is lower, leading to higher RT growth factors.

We did these experiments in an amplitude-scaling series, starting with large amplitude to see the initial contrast easily. In this case, however, the RT evolution quickly enters the nonlinear regime, higher harmonics are formed, the perturbation takes on the classic bubble-and-spike shape, and the growth slows sharply, ultimately changing from exponential to linear. We then shot an intermediate-amplitude target, which entered the nonlinear regime only towards the end of the acceleration. Finally, to maximize the observed growth, we used a very-small-amplitude perturbation, so that the foil remained in the linear regime throughout the acceleration. Figure 18 shows the results. For the smallest amplitude perturbation, a growth factor of 75 was observed in the fundamental mode. The peak-to-valley amplitude grew by a factor of 80 (that is, 4.4 *e*-foldings of growth), in agreement with the simulations.

To better illustrate the differences between the evolution of these three targets, we use the simulations to show in Fig. 19 the actual shape of the perturbations at peak growth. The large-η_0 foil [Fig. 19(a)] shows the classic bubble-and-spike shape of the nonlinear RT

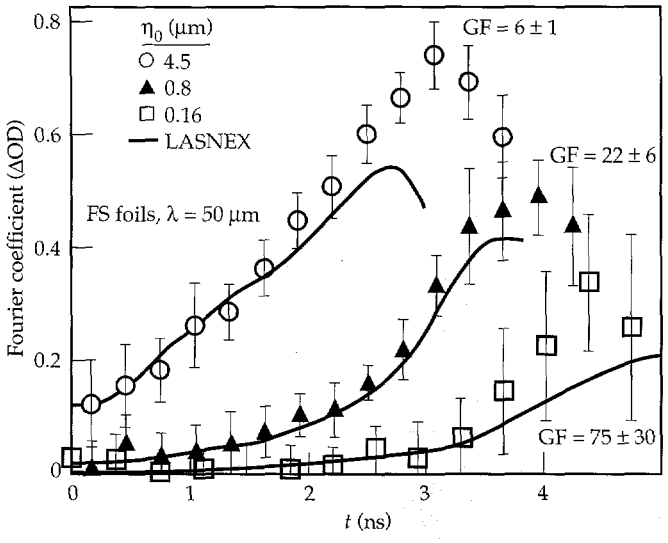

FIGURE 18. Amplitude (η_0) scaling results for three fluorosilicone (FS) foils. Perturbations were λ = 50 μm, η_0 = 0.16, 0.8, and 4.5 μm; the smallest-η_0 perturbation yielded the highest growth factor (G = 75). (20-03-1293-4395pb01)

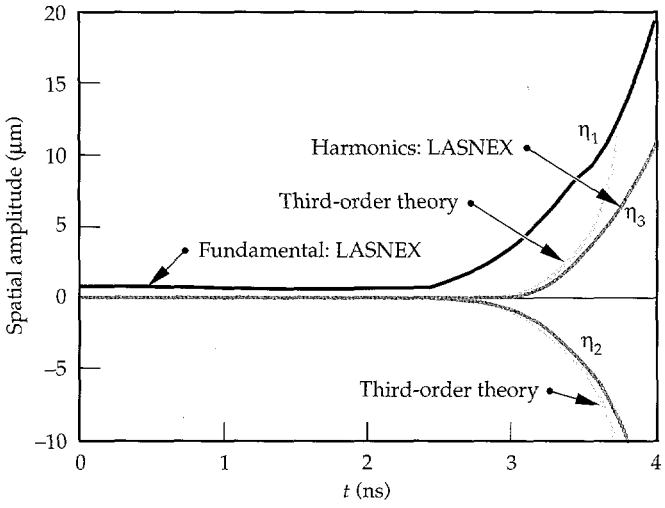

FIGURE 20. LASNEX simulations of the RT evolution for the intermediate-η_0 foil (from Fig. 18), and corresponding results from third-order perturbation theory. (20-03-0895-2046pb01)

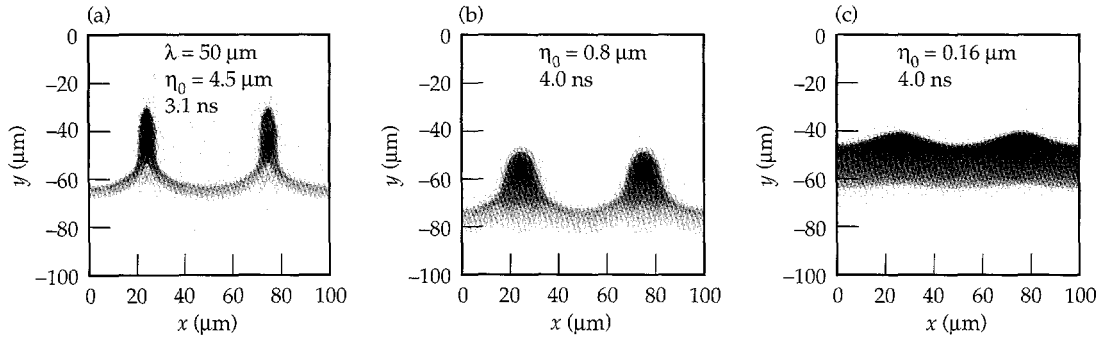

FIGURE 19. Shapes of perturbations (from Fig. 18) at peak growth, from 2-D LASNEX simulations. Increased darkness corresponds to higher density. (20-03-1293-4542pb01)

regime; the small-η_0 foil [Fig. 19(c)] still looks largely sinusoidal, indicating linear RT evolution; the intermediate-η_0 foil [Fig. 19(b)] is midway in between.

The transition to the nonlinear regime can be illustrated qualitatively with third-order perturbation theory.[14,23] We compare the results from the LASNEX simulation for the intermediate-η_0 foil (η_0 = 0.8 μm) with those obtained from perturbation theory [Eq. (5)]. Amplitudes in areal density ρR are converted to spatial amplitude by dividing by a characteristic density. Figure 20 shows the results. Third-order perturbation theory predicts the entry into the nonlinear regime very well.

The quantity of most interest in RT instability studies is the growth rate γ in Eq. (2), which is often parametrized as in Eq. (3) in terms of foil acceleration g, density ρ, and density gradient scalelength L. Unfortunately, because of the nature of our low-adiabat drive, the foil g, ρ, and L are not constant, as shown in Figs. 11 and 12. Hence, our RT growth cannot be characterized in terms of a single value of γ over the full duration of the foil acceleration. Nevertheless, from linear-regime simulations for λ = 50 μm [Figs. 21(b), 21(c)], we show the dispersion curves in Fig. 21(d) for CH(Br) and FS, using parameters characteristic of the foils at t = 3.0 ns. Even though the exact quantitative form of Eq. (3) for indirect drive is not settled, the equation appears qualitatively to describe the effect of stabilization at the ablation front. This has recently been demonstrated conclusively by comparing RT growth at the ablation front with that at an embedded interface, away from the ablation front, for this same drive and ablator material. At the ablation front, no growth was observed for wavelengths shorter than 30 μm, whereas at the embedded interface, strong growth down to wavelengths as short as 10 μm was observed.[47]

Earlier experiments were done with a 1-ns drive pulse shape, using FS and CH foils.[13] Figure 22 shows the results. This drive puts the foils on a much higher adiabat; the duration of the acceleration was short, and the growth was predominantly due to the rippled shock dynamics. Growth factors were $G \approx 2.5$ and $G = 1.5$ for the FS and CH foils, respectively.

All of our single-mode 2-D experiments can be qualitatively understood by the density profiles in Fig. 23, where we have carried out 1-D LASNEX simulations with the shaped drive, changing only the foil material. The FS foil remains on the lowest adiabat, has the steepest density gradient at the ablation front, and (as we saw above) exhibits the largest RT growth factors. The CH foil is at the opposite extreme. With no opacity shield against the hard x rays in the drive, the CH foil jumps to a very high adiabat, the density gradient at

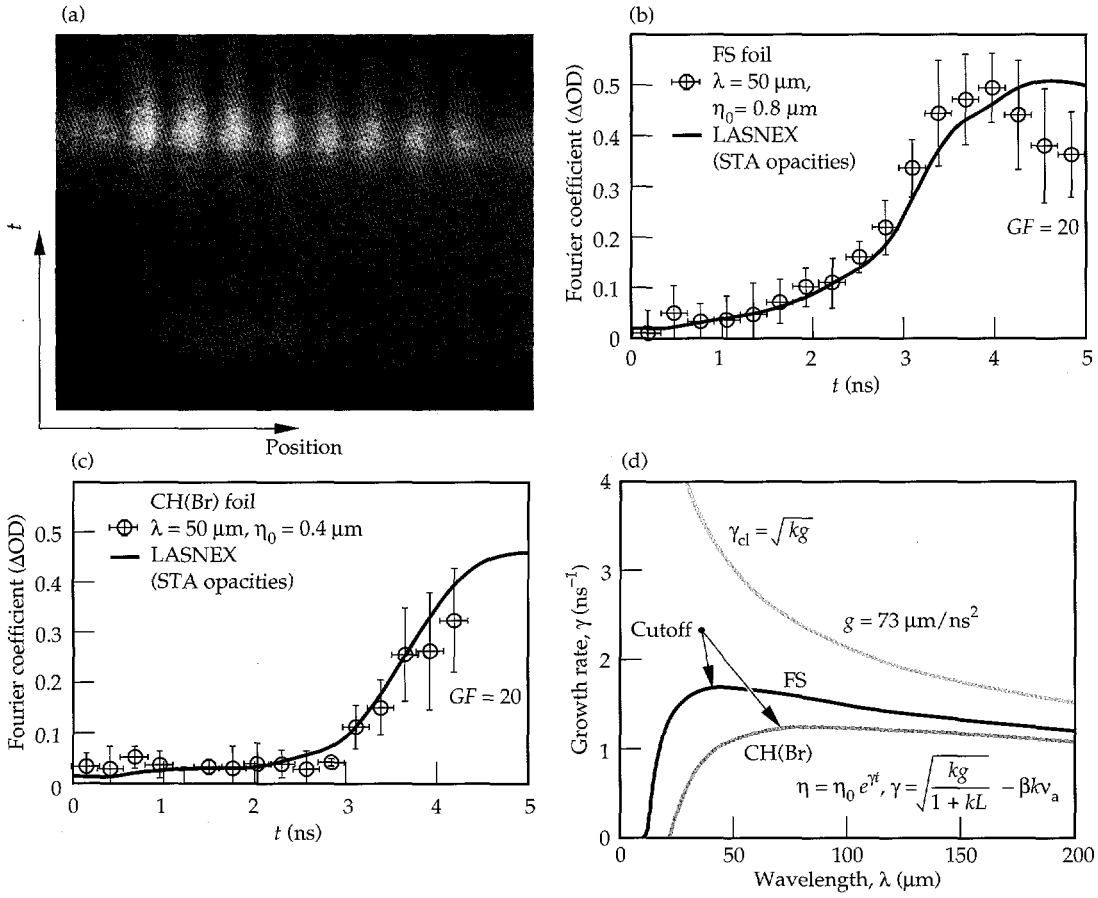

FIGURE 21. Results for intermediate-η_0 foil (from Fig. 18): (a) raw data, (b) Fourier coefficient of fundamental mode vs time. (c) As in (b), but for a CH(Br) foil (from Fig. 14c). (d) Dispersion curve for FS and CH(Br) with β = 2.5: for FS, L = 1.6 μm, v_a = 3.2 μm/ns; for CH(Br), L = 4.0 μm, v_a = 3.9 μm/ns. (20-03-1293-4398pb01)

the ablation front has only a very gentle slope, the ablation velocity is very high, the RT growth is practically zero, and the foil burns through quickly. The CH(Br) foil falls between these two extremes.

Two-Mode Experiments

We next turn to the two-mode experiments.[37,48] Figure 24(a) shows the two-mode perturbations we investigated; the upper side of each curve corresponds to the foil. Figure 24(a) shows a large-amplitude two-mode perturbation given by $\lambda_2 = 75$ μm and $\lambda_3 = 50$ μm, with $\eta_2 = \eta_3 = 2$ μm.

Characterization of the initial perturbations is critical for proper interpretation of the RT growth. The initial perturbations are characterized by three independent techniques—interferometry, contact profilometry, and x-ray radiography—and are accurate to 10% or better. Figure 25 shows examples of characterization by profilometry and radiography for the two-mode foils (and for the eight-mode foils of the next section, "Eight-Mode Experiments"). The agreement between the two techniques is very good except at the shortest wavelengths ($\lambda \leq 25$ μm) because of the finite resolution of our radiography setup. We use the η_n from contact profilometry as the most accurate initial amplitudes.

Figure 26 shows the results for the large-amplitude two-mode foil shown in Fig. 24(a). Figure 26(a) shows the raw image, and Fig. 26(b) shows a profile of ln$E$ at 2.7 ns aligned relative to the mold, showing how the phase of the data is established. Figure 26(c) illustrates the analysis technique with a profile of ln$E$ at 3.3 ns. To remove the long-range structure arising from the backlighter, we fit a low-order polynomial to the profile of ln$E$, shown by the gray curve. The lower solid curve in Fig. 26(c) shows the ln$E$ profile after having subtracted the fit to the backlighter structure. The vertical dotted lines represent the boundaries for the Fourier analysis. The histogram in Fig. 26(d) shows the real component of the Fourier transform of ln$E$ at 3.3 ns. Because of the cosine symmetry of the perturbation, the imaginary component (not shown) is identically zero except for random noise.

The Fourier modes are enumerated as harmonics of the longest repeating pattern (150 μm). Hence, the two pre-existing modes are k_2 ($\lambda = 75$ μm) and k_3 ($\lambda = 50$ μm). Because the initial amplitudes are large, the perturbation

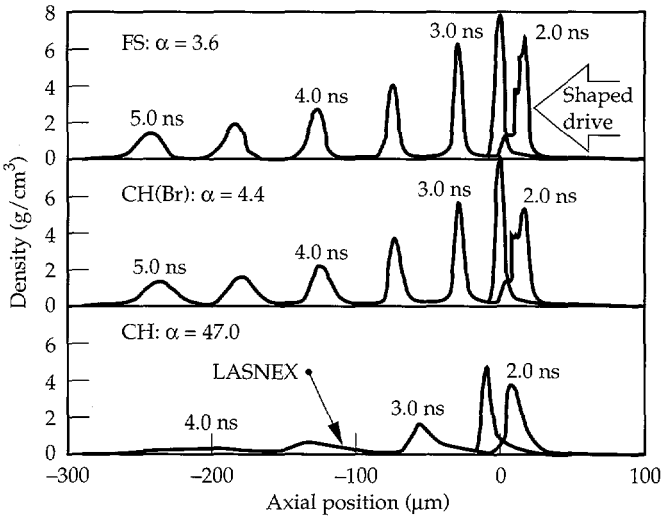

FIGURE 23. Density profiles from 1-D LASNEX simulations for FS, CH(Br), and CH, assuming the same low-adiabat drive for each. (20-03-1293-4401pb01)

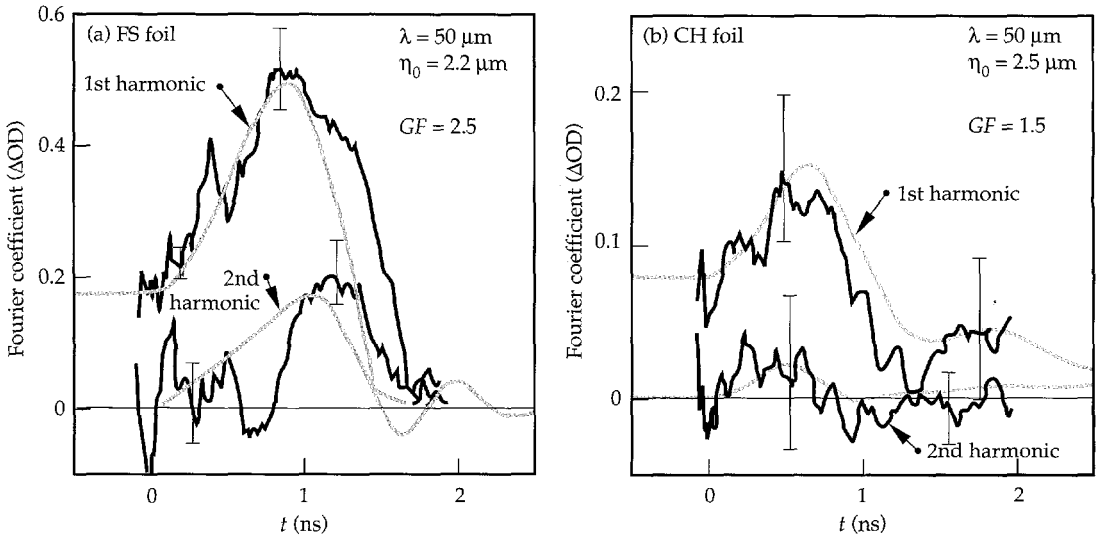

FIGURE 22. Results from the 1-ns square drive pulse shape for (a) FS and (b) CH foils. For this high-adiabat drive, the growth factors were $G < 3$. (20-03-1293-4400pb02)

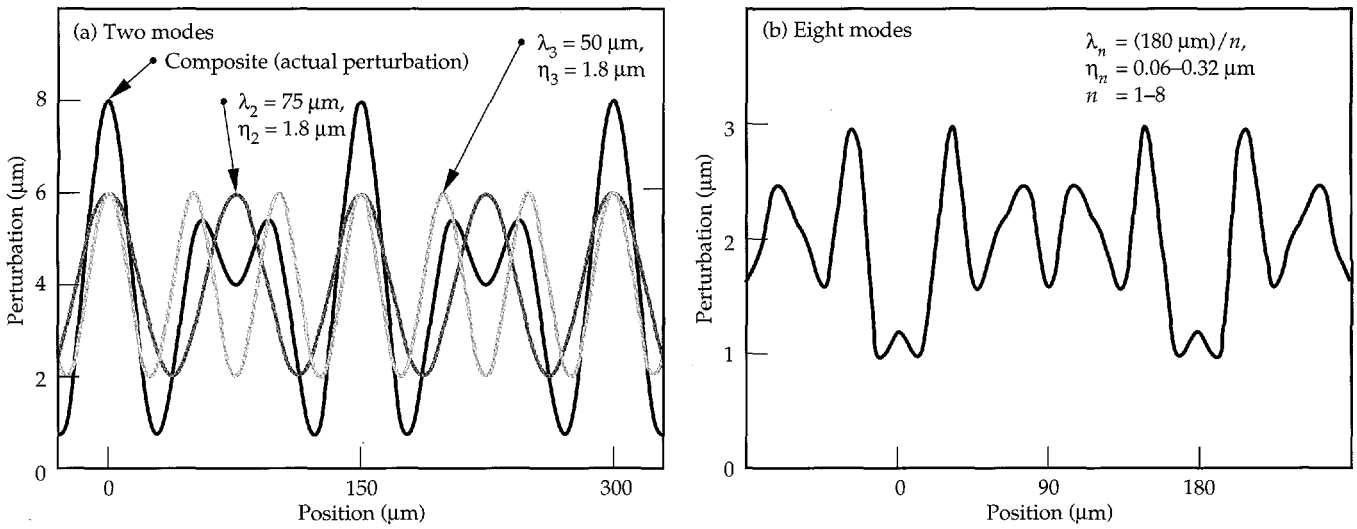

FIGURE 24. Multimode perturbation patterns investigated. (a) Two-mode perturbation: curves correspond to λ_2 = 75 μm, η_2 = 1.8 μm and λ_3 = 50 μm, η_3 = 1.8 μm. Their superposition represents the actual perturbation. The foil corresponds to the upper side of the curve. (b) Eight-mode perturbation corresponds to the sum of wavelengths λ_n = (180 μm)/n, n = 1–8; Table 1 gives corresponding amplitudes.
(20-03-0394-0741pb03)

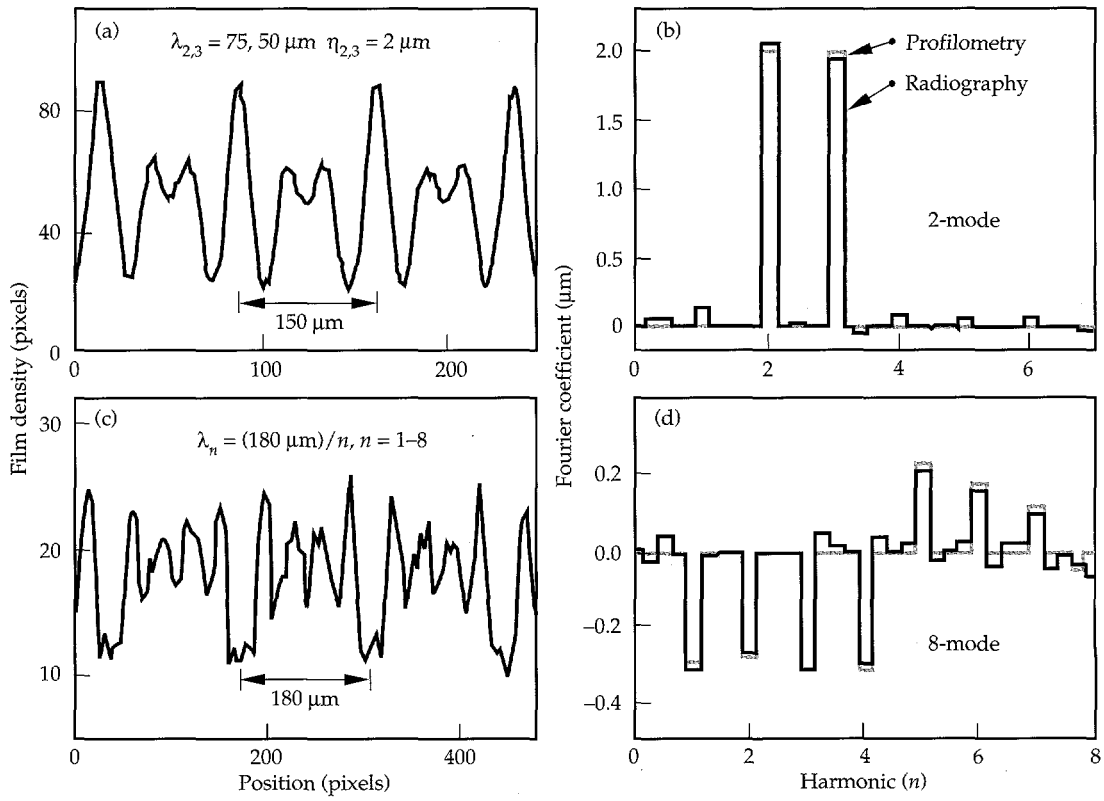

FIGURE 25. Multimode perturbations characterized by contact profilometry and radiography. (a) Lineout from the 2-D radiograph of the large-amplitude two-mode perturbation shown in Fig. 24(a). The contact radiograph corresponds to a 2-hr exposure on Kodak high-resolution glass plate film using a Mo anode at an electron accelerating voltage of 5 kV and a 1-μm Ag filter. (A film density of 1024 pixels corresponds to an optical depth of 5.115.) The film response is removed using a simultaneous exposure across a Be step wedge covering the same range in optical depth. (b) The black histogram is the real component of the Fourier transform of the curve shown in (a). The gray histogram represents the Fourier transform of the contact profilometer trace (not shown), and is essentially identical with the radiography result. (c) Same as (a) except for the eight-mode perturbation shown in Fig. 24(b). (d) Same as (b) except for the eight-mode perturbation. (20-03-0394-0742pb03)

quickly evolves into the nonlinear regime with the appearance at 3.3 ns of the second harmonic of k_2, namely, $2k_2$. We also observe very distinct $k_1 = k_3 - k_2$ and $k_5 = k_3 + k_2$ coupled modes corresponding to $\lambda = 150$ and 30 μm, respectively. Notably absent is the second harmonic of k_3, namely, $2k_3$. This is because $3k_2$, the third harmonic of k_2, has the same magnitude as $2k_3$ but the opposite sign, leading to a cancellation.

The results shown in Fig. 26(d) are rather insensitive to the exact functional form used in fitting the background. The smooth gray curve shown in Fig. 26(c) corresponds to a fifth-order polynomial fit. If we had chosen a second-order polynomial to fit the background, the k_1 term would have been 5% larger, and the other modes would have changed by ~1%. With no background subtraction at all, the k_1 mode would have been only 20% different, and the other modes would have varied by ~5% or less. This is illustrated by showing the Fourier composition of the background itself. The gray curve in Fig. 26(d) corresponds to the Fourier transform of the gray curve in Fig. 26(c). Thus there is little sensitivity to the exact details of how we treat the backlighter background subtraction.

It is instructive to view these nonlinear mode coupling effects within the context of perturbation theory.[26] We consider here only a qualitative application for the coupling from two pre-existing modes k_2 and k_3 using Eq. (8) from the Introduction, namely,

$$\eta_{k_i \pm k_j} \approx \mp \frac{1}{2}\left(k_i \pm k_j\right)\eta^{\mathrm{L}}_{k_i}\eta^{\mathrm{L}}_{k_j}; \tag{8}$$

where $\eta^{\mathrm{L}}_{k_n}$ represents the spatial amplitude of mode k_n had the growth been entirely in the linear regime. Notice that $\eta_{k_3-k_2}$ has the same sign as the product $\eta^{\mathrm{L}}_{k_2}\eta^{\mathrm{L}}_{k_3}$, whereas $\eta_{k_3+k_2}$ has the opposite sign, in agreement with the experimental observation shown in Fig. 26(d). If the boundaries of the Fourier transform are shifted by 75 μm (that is, by half of the fundamental $n = 1$ period), the k_2 and k_3 modes have opposite signs (not shown). The $k_3 - k_2$ mode is then negative, and the $k_3 + k_2$ mode is positive, again in agreement with Eq. (8). Qualitatively at least, the observation of the $k_3 \pm k_2$ coupled terms can be understood from second-order perturbation theory. The modes are too large already by shock breakout to apply second-order theory quantitatively, however.

Figure 27 shows the full time dependence of the two-mode data shown in Fig. 26. The plotting symbols represent the data, which again correspond to the real

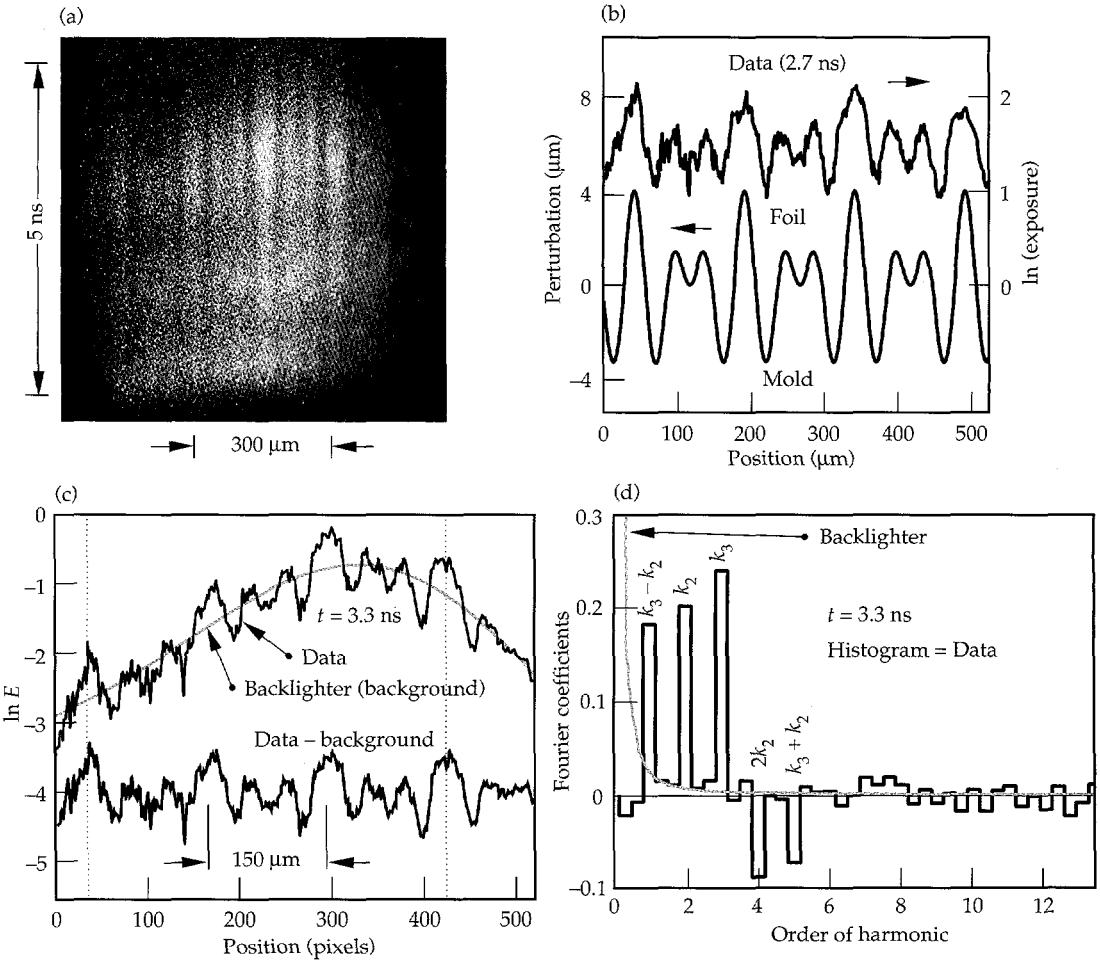

FIGURE 26. Various representations for the large-amplitude two-mode data. (a) Raw streaked image. (b) Late-time (2.7 ns) profile of ln$E$ and initial perturbation on the mold, corresponding to the superposition of a $\lambda = 75$ μm and $\lambda = 50$ μm, $\eta_0 = 1.8$ μm perturbation. Data are aligned relative to the mold, showing how the perturbation phase is established. (c) Background-subtraction technique, illustrated on a late-time (3.3 ns) profile of ln$E$: "raw" profile, polynomial fit, and result after subtracting background. Vertical dotted lines represent boundaries for Fourier analysis. (d) Real component of Fourier transform of background-subtracted profile in (c), and Fourier transform of background itself.
(20-03-0394-0746pb02)

component of the Fourier transform of ln$E$. Because of symmetry, the imaginary component of the Fourier transform should be zero, and we take its value as a measure of the error for each point. The $k_3 \pm k_2$ coupled terms are not observed until after about t = 2.5 ns, after the perturbation has entered the nonlinear regime. The black curves in Fig. 27 are the corresponding results from 2-D LASNEX simulations, after convolution of the simulated image exposure with the instrumental spatial resolution function [Eq. (11)]. The gray curves in Fig. 27(a) correspond to simulations of the evolution of each mode had it been the only mode initially present. The departure of the black curves from the gray curves for $t \geq 3$ ns coincides with the growth of the coupled terms, as shown in Fig. 27(b). The Fourier composition of the perturbation is redistributed into a broader spectrum because of the $k_3 \pm k_2$ mode coupling. This corresponds in physical space to a change of shape: mode coupling makes the bubbles broader and flatter and the spikes narrower. This is illustrated explicitly in the next section.

Eight-Mode Experiments

Figure 24(b) shows a small-amplitude eight-mode perturbation given by $\lambda_n = (180\ \mu\text{m})/n$. The individual amplitudes η_n (given in Table 1) are about a factor of 10 smaller than those for the two-mode foil. Figure 28(a) shows the raw image of the experimental shot, and Fig. 28(b) gives a late-time profile of ln$E$ aligned relative to the mold, showing how the phase of the data is established.[37,48] The vertical dashed lines indicate the boundaries for the Fourier analysis. The black histograms in Figs. 28(c) and 28(d) show the real component of the Fourier transform at an early time (3.2 ns) and at late time (4.4 ns). Because of the cosine symmetry, the imaginary component (shown by the gray histograms) oscillates around the baseline as random background and serves as an estimate of the error. Early in time in the linear regime [Fig. 28(c)], only the pre-existing modes grow, in accordance with their initial amplitudes and growth rates. The k_3 mode (λ = 60 μm) dominates. Late in time [Fig. 28(d)], the perturbation has entered the nonlinear regime and the modes no longer grow independently. The k_3 mode no longer dominates, its magnitude having been reduced by $k_3 - k_2$ mode coupling to drive up the k_1 mode. This causes the k_1 term to reverse phase; the initial sign of the k_1 mode was negative, as given in Table 1.

Figure 29 shows the full time evolution of the eight-mode data. The plotting symbols correspond to the real component of the Fourier transform of the data, and the error bars correspond to the imaginary component. The black curves represent the eight-mode LASNEX simulation after convolving ln$E$ with the spatial resolution function [Eq. (11)]; the qualitative agreement with the data is good. The light gray curves represent the single-mode simulations, in which it is assumed that each mode existed alone. As a result of mode coupling, modes k_2 through k_5 grow less than they would have alone. Growth reduction is least for mode k_4, which has the largest amplitude at the time of saturation. The presence of multiple modes causes nonlinearity to occur earlier than if the modes had existed alone.

Modes k_1, k_6, and k_7 reverse phase and grow with the opposite sign. These modes show most prominently the effects of coupling from the dominant modes, k_2, k_3, and k_4. The dark gray curves show the amplitudes predicted for these modes from second-order theory, described in more detail below. The phase reversal for mode k_1, for example, can be understood from Eq. (8) and considering only the dominant modes k_2, k_3, and k_4. Both the $k_3 - k_2$ and $k_4 - k_3$ coupled terms are positive, tending to cause a phase reversal in the growth of

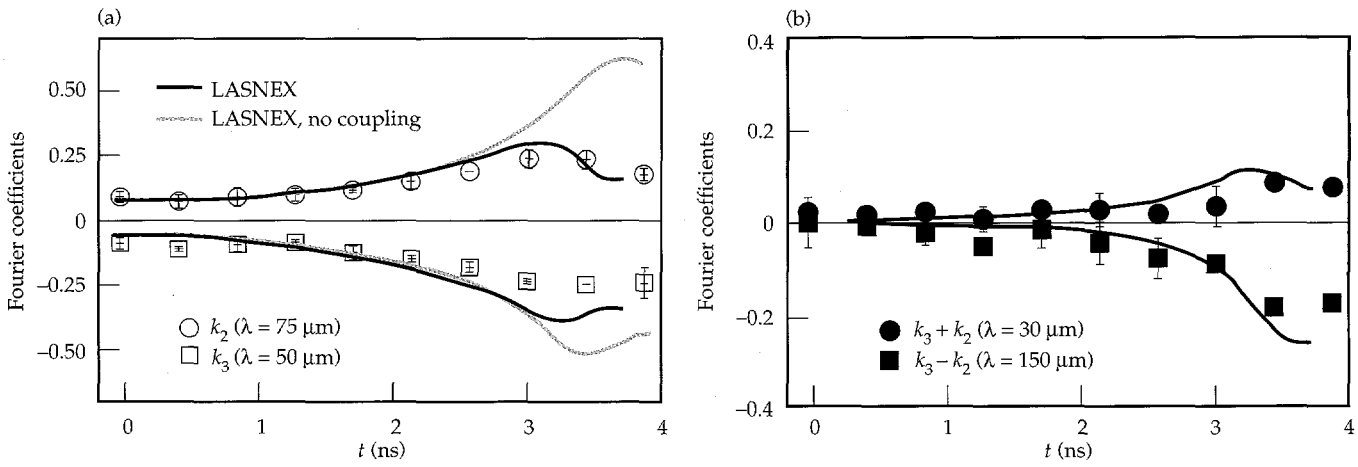

FIGURE 27. Full time dependence for two-mode data of Fig. 26. (a) Results for the λ = 75 μm component of the pre-existing perturbation and for k_3 (the λ = 50 μm component). (b) The $k_3 + k_2$, λ = 30 μm and $k_3 - k_2$, λ = 150 μm coupled terms and corresponding 2-D LASNEX two-mode and single-mode results. (20-03-0394-0747pb03)

the k_1 mode (which was initially negative), as observed. Similarly, the phase reversals of modes k_6 and k_7 can also be understood from Eq. (8), considering $k_i + k_j$ coupling from the dominant modes k_2, k_3, and k_4. Figure 29(d) also shows (dashed curve) the result for mode k_4 of an eight-mode simulation with enhanced preheat in the drive (factor of 10 increase in drive spectrum for $h\nu > 1.4$ keV and $t < 2$ ns, as discussed in the earlier section "Single-Mode Experiments"). As in Fig. 17(c), the enhanced preheat reduces the perturbation growth considerably, bringing the simulation into good agreement with the data. This is true for all eight modes, although we show only the enhanced-preheat result for mode k_4.

The second-order perturbation model can be quantitatively applied to the eight-mode experiment[26,37,48,49] using Eq. (A3) from the final section "Amplitude of Coupled Modes,"

$$\eta_k \approx \eta_k^L + \frac{1}{2}k\left(\sum_{k'}\eta_{k'}^L\eta_{k+k'}^L - \frac{1}{2}\sum_{k'<k}\eta_{k'}^L\eta_{k-k'}^L\right), \qquad \text{(A3)}$$

by summing over the products of all pairs of modes whose sum or difference equals the k of interest. The η_{k_n} represent spatial amplitudes, which we define from the LASNEX simulations by dividing the modulations in areal density by the foil peak density, that is,

$$\eta\ (\mu\text{m}) \approx \frac{\delta\int \rho\, dz}{\rho_{max}}. \qquad (14)$$

We apply this model to our experiment as follows. For each λ_n in the eight-mode foil, 2-D LASNEX simulations are run for perturbations of very small initial amplitude, ensuring that the RT evolution remains in the linear regime. The $\eta_{k_n}^L(t)$ are then obtained by scaling by the ratio of actual to the assumed initial amplitude. This technique of generating the $\eta_{k_n}^L(t)$ automatically includes the effects of the time-dependent acceleration, compression, density gradient, and ablative stabilization. The dark gray curves in Figs. 29(a), 29(f), and 29(g) show the results from this perturbation analysis for $t \leq 3.7$ ns. After this time, the central assumption of

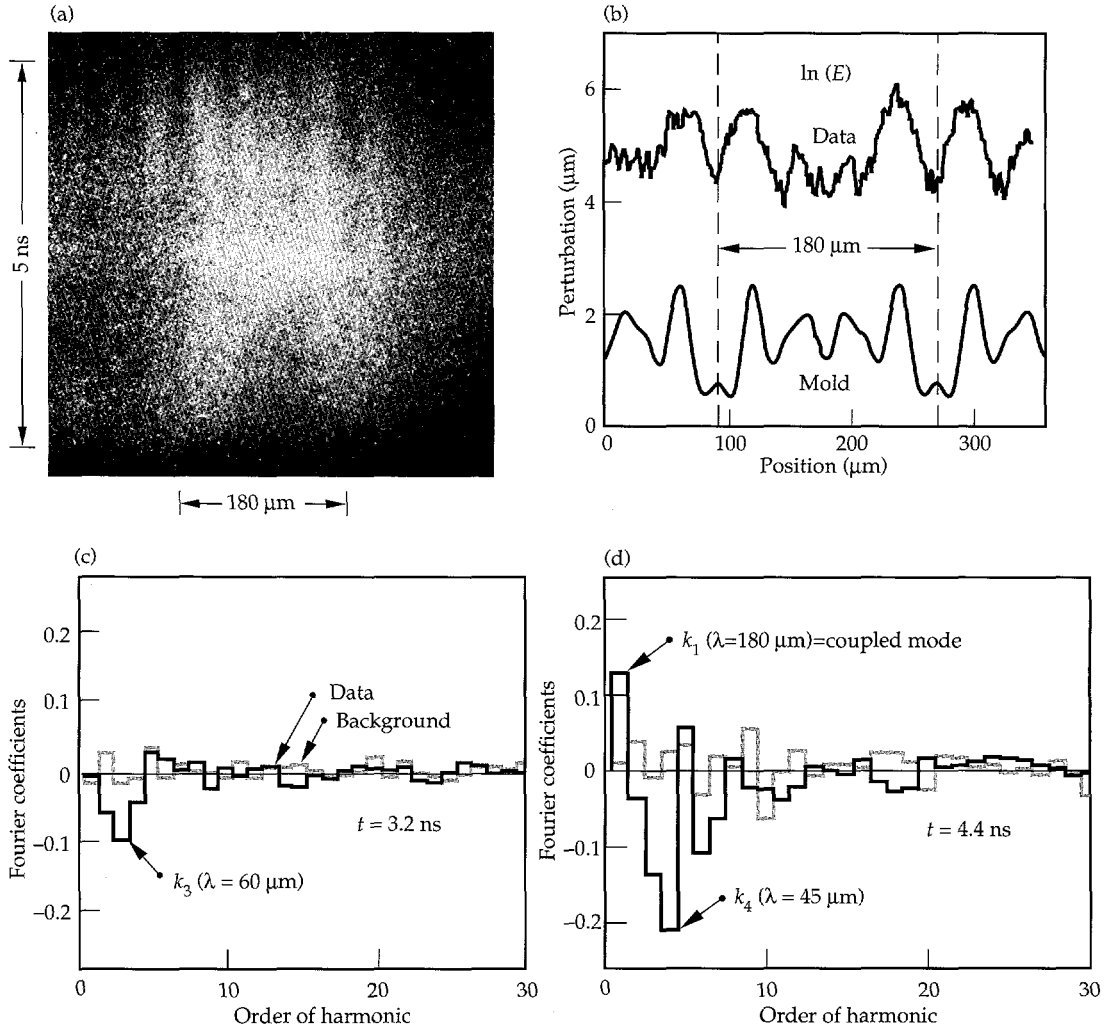

FIGURE 28. Eight-mode data in various representations. (a) Raw streaked image. (b) Late-time profile of ln$E$, aligned with the mold as in Fig. 26. Vertical dashed curves give boundaries used in Fourier analysis. (c) Real and imaginary components of Fourier transform of "early-time" (3.2 ns) profile of ln$E \approx -$OD. The imaginary component (which should be zero because of the cosine symmetry) illustrates the level of background noise and can be used for an estimate of the error. The dominant k_3 ($\lambda = 60$ μm) mode is indicated. (d) Same as (c) except at late time (4.4 ns). The dominant term is now k_4 ($\lambda = 45$ μm), and the strength from the k_2 and k_3 terms has been redistributed into the $k_1 = k_3 - k_2$ coupled mode, as indicated. (20-03-1293-4406pb02)

the model (dominant modes not affected by the coupling terms) is violated and the model is no longer applicable. In each case, the phase reversals are well described by second-order perturbation theory.

At late times ($t \geq 4$ ns), the saturation of modes k_2 and k_3 results from the redistribution of the Fourier components because of mode coupling. In physical space, this corresponds to a change in shape, as illustrated in Fig. 30 for the two-mode and eight-mode perturbations. The black curves correspond to profiles of ln$E$ taken from the LASNEX simulations before inclusion of the instrument spatial resolution function. The gray curves represent the sum of the results from the single-mode simulations. Comparing the gray and black curves, we see that the shapes of the perturbations with and without mode coupling differ. With mode coupling, the bubbles are broader and flatter and the spikes are narrower. This shape effect has been observed in other simulations,[29] but to our knowledge this is the first experimental observation of the effect in ablatively accelerated foils.

The results from our eight-mode experiment can also be compared with results from a saturation model developed for a full continuum of initial modes.[32] The basic premise of this model is that a perturbation corresponding to a full continuum of modes saturates when the product $k_{char}\eta_{char}$ is no longer small, that is, when

$$\eta_{char} = \varepsilon_1 \lambda_{char} = \frac{2\pi\varepsilon_1}{k_{char}}, \qquad (15)$$

where η_{char} and λ_{char} are a characteristic spatial amplitude and wavelength and ε_1 is some number less than unity. But η_{char} can be approximated as the quadrature sum of individual modes within a band Δk centered around $k_{char} = 2\pi/\lambda_{char}$, namely,

$$\eta_{char} = \left(\sum_{\Delta k} \eta_k^2\right)^{1/2} \approx \left(\Delta k \frac{L}{2\pi} S_k^2\right)^{1/2} \approx \left(\varepsilon_2 k \frac{L}{2\pi} S_k^2\right)^{1/2}, \qquad (16)$$

where $\Delta k = \varepsilon_2 k$ for some $\varepsilon_2 < 1$, L is the system size, $L/2\pi$ is the 2-D density of Fourier states, and S_k is a

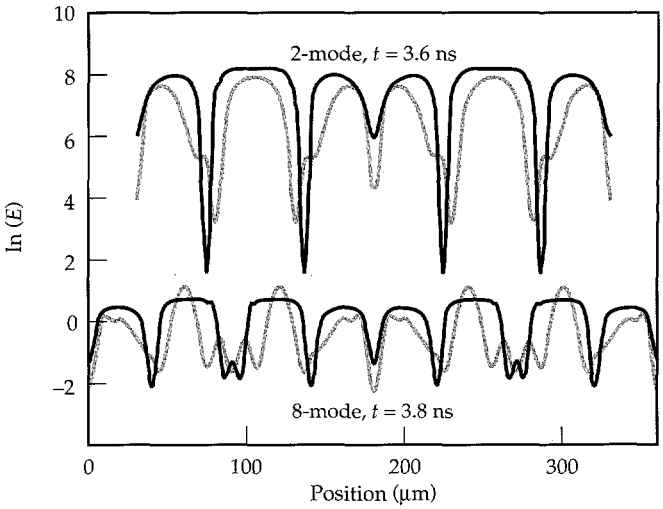

FIGURE 30. Effect of mode coupling on perturbation shape. The upper black curve represents the two-mode simulation at 3.6 ns, and the upper gray curve corresponds to the sum of the simulations for the two individual modes run alone. The lower curves are the same only for the eight-mode perturbation at 3.8 ns. (20-03-0194-0106pb02)

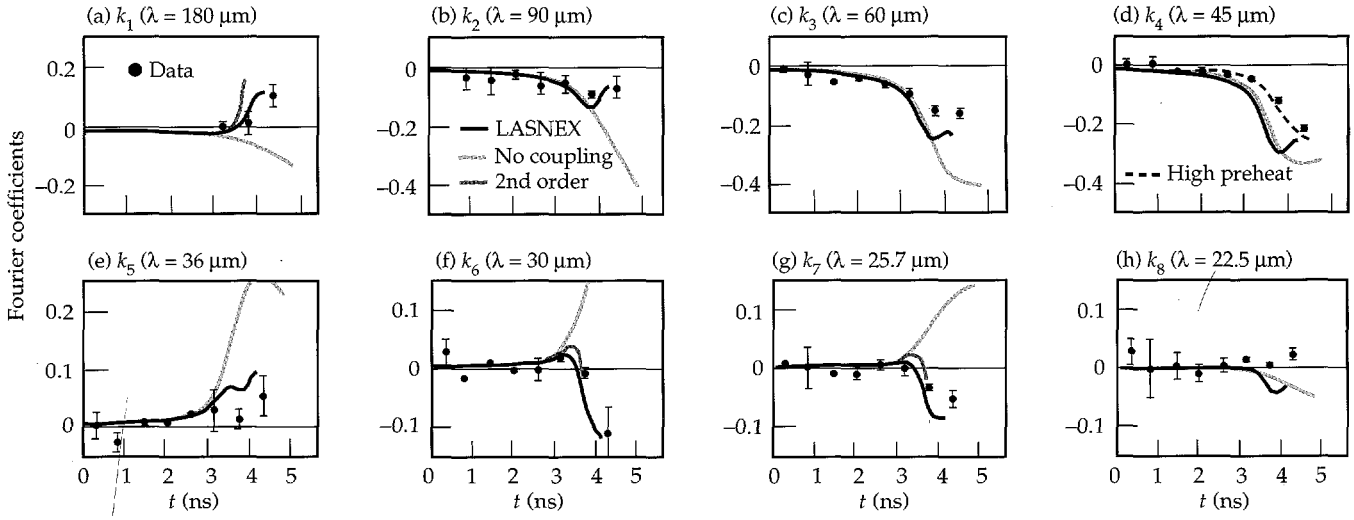

FIGURE 29. Full time dependence for data shown in Fig. 28. (a)–(h) Growth of modes $\lambda_n = (180\ \mu m)/n$, $n = 1$–8, vs time. Solid circles represent data; black curves represent corresponding 2-D LASNEX simulations. Light gray curves represent simulations under the assumption that each individual mode existed alone, and the dark gray curves for modes k_1, k_6, and k_7 correspond to the results of a calculation using weakly nonlinear, second-order perturbation theory. The dashed curve for mode k_4 corresponds to a simulation with assumed enhanced preheat in the foot of the drive. (20-03-0394-0749pb03)

typical spatial amplitude of an *individual* mode within Δk. Combining Eqs. (15) and (16) gives

$$S_k = \frac{\nu_{2D}}{L^{1/2}k^{3/2}}, \quad \text{(in 2-D)}, \tag{17a}$$

$$S_k = \frac{\nu_{3D}}{Lk^2} \quad \text{(in 3-D)}, \tag{17b}$$

where ε_1 and ε_2 have been combined into a single parameter ν (set in Ref. 32 for the 2-D case to $\nu_{2D} = 1.14$), and L represents here the longest wavelength in the periodic perturbation, $L = 180$ μm. The result for 3-D given in Eq. (17b) is derived the same way, but with $\varepsilon_2 k$ replaced by $(\varepsilon_2 k)^2$, and the density of states factor becomes $(L/2\pi)^2$. The normalization $\nu_{2D} = 1.14$ was arrived at by comparison with the classical (incompressible) fluid RT experiments of Read and Youngs.[50] The above saturation results, namely Eq. (17a) and (17b), can be derived more elegantly as follows. A multimode perturbation in a localized region of space can be thought of as a wavepacket. Over a small but finite spectral range, this wavepacket cannot be distinguished over short distances from a single-mode at wave vector **k**. We expect RT saturation to occur at roughly the same amplitude in both cases (wavepacket vs single-mode), which means that amplitudes at saturation of the individual components of the wavepacket will be less than the amplitude of the single mode. Based on the criterion of Layzer for a single mode,[25] saturation is expected to occur when the spacial amplitude η reaches $\sim(0.6/k)$. In the multimode case, an additional factor of λ/L enters to account for the number of similar modes about k that can contribute to the saturation of mode k. Hence $S_k \approx \lambda/kL = 2\pi/k^2L$, as given by Eq. 17(b). We apply this saturation model, namely Eq. 17(a), to our eight-mode experiment by calculating with LASNEX the growth of each mode k_n in the linear regime until its spatial amplitude defined by Eq. (14) exceeds the S_{k_n} given by Eq. (17). At this time we make a smooth transition to bubble growth that is linear in time, corresponding to a terminal bubble velocity equal to the velocity at saturation. This transition to saturated growth is accomplished with the logarithmic construction

$$\eta_k(t) = S_k\left\{1 + \ln\left[\eta_k^L(t)/S_k\right]\right\}, \tag{18}$$

where $\eta_k^L(t)$ represents the spatial amplitude had the growth remained in the linear regime. The modes are added in quadrature to produce the predicted root-mean-square (rms) bubble amplitude. We compare this with the rms bubble amplitude from the LASNEX eight-mode simulation. Bubbles are defined in terms of foil areal density $\int \rho\, dz$ (that is, the foil ρr) by considering only those perturbations leading to $\rho r < (\rho r)_{av}$. Figure 31 shows the result for the nominal $\nu_{2D} = 1.14$ and for values of ν_{2D} a factor of 2 higher and lower than 1.14. The result corresponding to $\nu_{2D} = 0.57$ agrees best with the LASNEX eight-mode simulation. This is only a crude test of the model for ablatively accelerated foils, because the density of Fourier modes is low. Future work will involve 3-D experiments with a near continuum of modes and larger growth factors as a better test of this saturation model.

3-D Single-Mode Experiments

The nonlinear RT growth of a perturbation depends upon its shape. Perturbations of the same magnitude wavenumber $k = (k_x^2 + k_y^2)^{1/2}$ can have different shape and can therefore evolve differently in the nonlinear regime while having the same linear-regime RT growth rate. In this section we examine how the 3-D shape affects the growth of single-mode perturbations on planar foils.[51] The CH(Br) foils were made using a new laser ablation technique to make molds in Kapton or Mylar substrates.[52] We prepared perturbed foils all with the same magnitude wave vector $k = (k_x^2 + k_y^2)^{1/2}$ and nominally the same amplitude. The "2-D" foil (1-D wave vector $\mathbf{k} = k_x$) was a simple $\lambda = 50$ μm sinusoid with initial amplitude $\eta_0 = 2.5$ μm. One of the "3-D" foils [2-D wave vector $k = (k_x, k_y)$] corresponded to a "stretched" $k_x = 3k_y$ perturbation, and the other was a square $k_x = k_y$ mode. The three foils were characterized using contact radiography [Fig. 32(a)–32(c)] and contact profilometry. The radiographs were converted to spatial amplitudes using a CH(Br) step wedge. Figure 32(d)–32(f)] show corresponding images from Nova shots at 4.3 ns, which is near peak growth. The gated x-ray pinhole camera for these images was run at 8× magnification

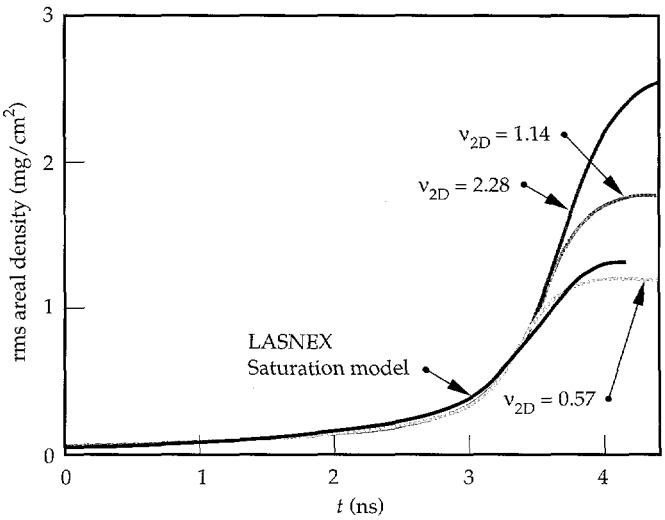

FIGURE 31. Results of eight-mode LASNEX simulation and corresponding results from multimode saturation theory. Black curve corresponds to the rms perturbation in areal density $\Delta\int \rho\, dz$ from the eight-mode simulation, where we consider only the bubble amplitude. Other curves correspond to results of the saturation model for normalizations [Eq. (17a)] of $\nu_{2D} = 2.28$, 1.14, and 0.57. (20-03-0194-0131pb02)

with 10-μm pinholes and 150-μm Be filtering. The backlighter was Sc at 4.3 keV.

Each image from the Nova shots [Fig. 32(d)–32(f)] is converted to $\ln E \propto -\mathrm{OD} = -\int \rho\kappa\, dz$. Hence, modulations in ln$E$ correspond to modulations in foil areal density. To visualize the 3-D RT evolution better, we focus momentarily on the $k_x = k_y$ mode. Figure 33(a) gives a 3-D surface perspective of the data shown in Fig. 32(f). Figure 33(b) shows the corresponding simulation with the new 3-D radiation–hydrodynamics code HYDRA.[53] The height of these surfaces is proportional to –(areal density), and crudely speaking, represents the boundary between the hot, low-density ablated plasma and the dense pusher material ahead of it.

In the reference frame of the accelerating ablation front, one would see a broad, hot bubble of ablated plasma rising up through the pusher and spikes of dense pusher fluid falling essentially freely through the ablated plasma. This canonical shape of the 3-D RT instability can be understood from a simple buoyancy-vs-drag equation,[54,55]

$$\rho_1 V \frac{\partial u}{\partial t} = (\rho_1 - \rho_2) V g - c_D \rho_1 u^2 S, \qquad (19)$$

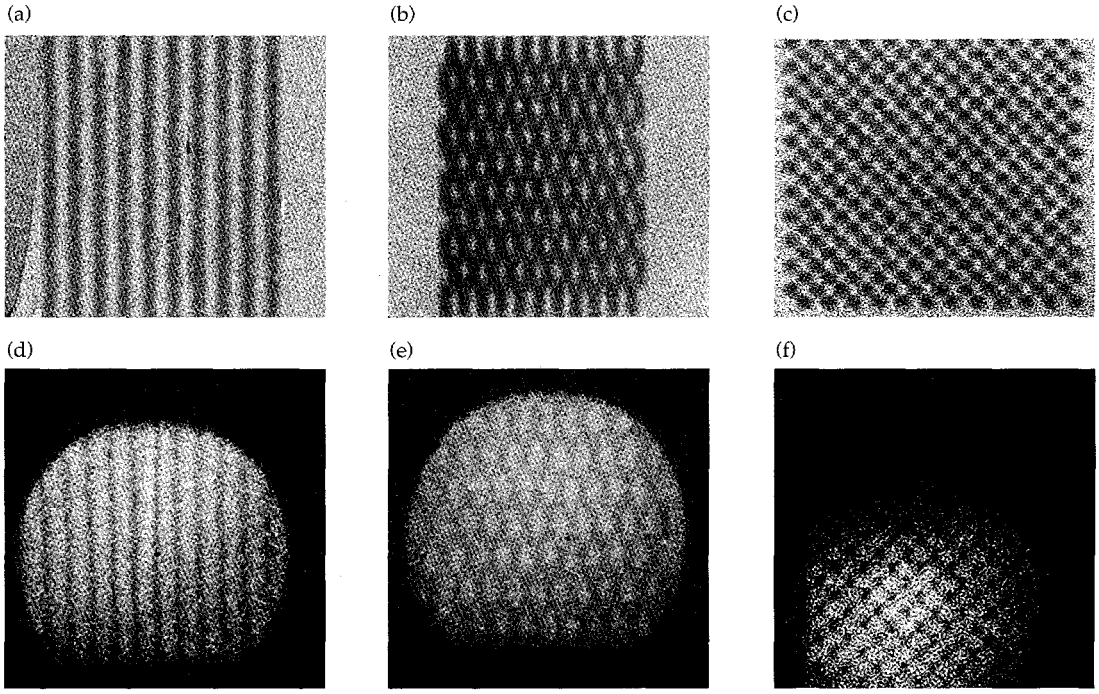

FIGURE 32. (a)–(c) Contact radiographs of foils identical to those used in the 3-D single-mode Nova experiments. Perturbations correspond to (a) 2-D $\lambda = 50$ μm, $\eta_0 = 2.5$ μm; (b) 3-D $k_x = 3k_y$, $\lambda_x = 53$ μm, $\lambda_y = 158$ μm, $\eta_0 = 2.4$ μm; and (c) 3-D $k_x = k_y$, $\lambda_x = \lambda_y = 71$ μm, $\eta_0 = 2.7$ μm. (d)–(f) Corresponding images from Nova shots at 4.3 ns. (20-03-0595-1390pb01)

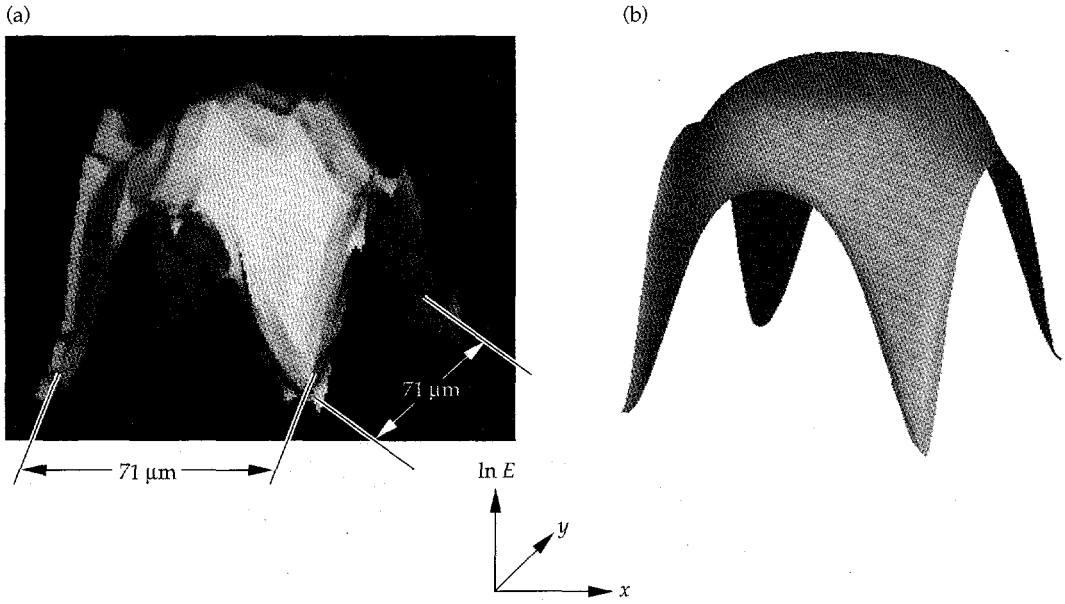

FIGURE 33. 3-D surface perspective of the $k_x = k_y$ case from Fig. 32 as (a) measured on the Nova shot at 4.3 ns and (b) simulated with the 3-D radiation–hydrodynamics code HYDRA.[53] The height is proportional to ln E. (50-05-0595-1116pb01)

where subscripts 1 and 2 refer to the dense pusher fluid and low-density ablation plasma, respectively, V is the volume of fluid pushed aside by the bubble passage, S is the cross-sectional area of the bubble, and c_D is the drag coefficient. Equation (19) states that the net force on the mass $\rho_1 V$ of the heavy fluid equals the buoyancy force minus drag. The bubble tip naturally acquires the shape that minimizes the drag per unit mass, i.e., the bubble evolves towards a shape that minimizes S/V, which implies a spherical bubble tip shape, as observed. This is entirely equivalent to the common interpretation that for a spherical 3-D bubble the flow can carry material away from the bubble tip on all sides, allowing it to transit more easily into the spike regions.[51,56] One can also obtain from Eq. (19) the form of the terminal bubble velocity of Eq. (7). When buoyancy is exactly balanced by drag, one has $(\rho_1 - \rho_2)\, Vg = c_D \rho_1 u^2 S$. If we let $V \propto \lambda^3$, $S \propto \lambda^2$, and $\rho_2 \approx 0$, we then have $\rho_1 \lambda^3 g \propto c_D \rho_1 u^2 \lambda^2$; this yields $u^2 \propto g\lambda$, as in Eq. (7). Also note that if $g = 0$, as in the Richtmyer–Meshkov instability (long after shock passage), we obtain $u_{RM} \sim \lambda/t$, as pointed out by Alon et al.[55] and as was recently observed.[57]

The images are Fourier analyzed, and the amplitudes corresponding to the fundamental mode are extracted. For an experimental demonstration of the effects of dimensionality on perturbation growth, we conducted shots for three targets (2-D $\lambda = 50$ μm, 3-D $k_x = k_y$ and $k_x = 3k_y$). The total laser energy for these shots was similar, and the timing and filtering of the diagnostic were identical. Figure 34(a) shows the results for the evolution of the fundamental mode. The $k_x = k_y$ square 3-D mode grows the most, the $\lambda = 50$ μm 2-D mode

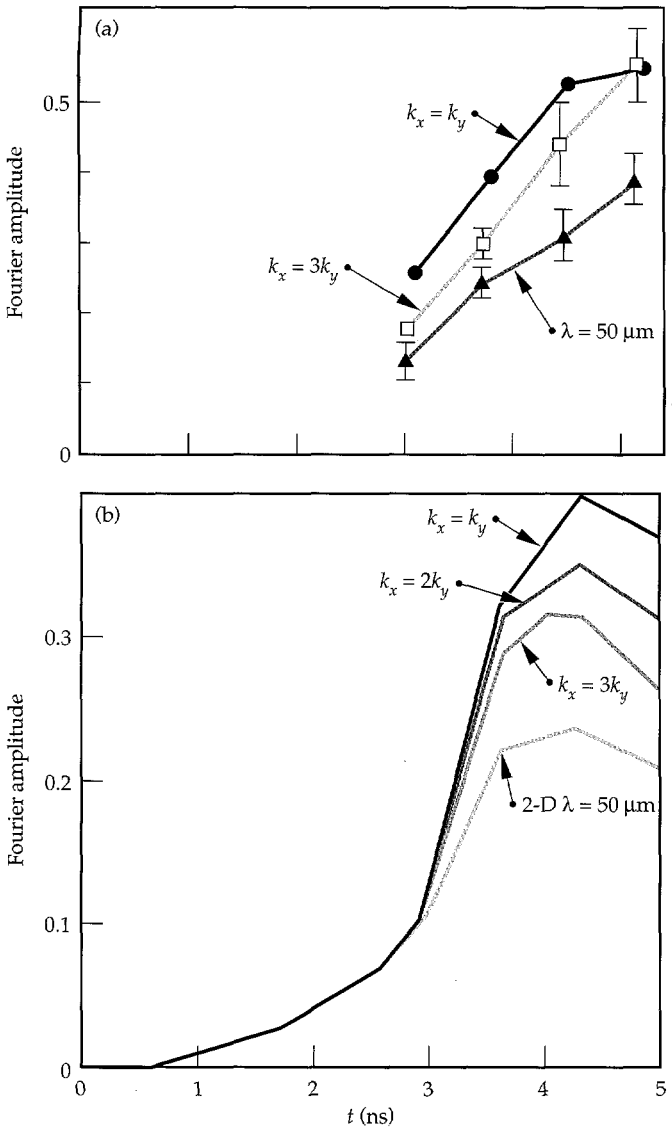

FIGURE 34. (a) Results of the evolution of the fundamental mode Fourier amplitude of ln$E$ for the 3-D $k_x = k_y$, $k_x = 3k_y$, and 2-D $\lambda = 50$ μm perturbations. Connecting lines are meant only to guide the eye. (b) Predicted Fourier amplitude of ln$E$ from 3-D HYDRA simulations for the evolution of four perturbation shapes, all with the same wave vector magnitude $k = (k_x^2 + k_y^2)^{1/2}$, for somewhat different drive histories and foil thicknesses from those of (a). The most symmetric ($k_x = k_y$) mode is predicted to grow the most, the 2-D $\lambda = 50$ μm mode to grow the least, and the 3-D stretched cases fall in between, in agreement with the experiments. (20-03-0595-1389pb01)

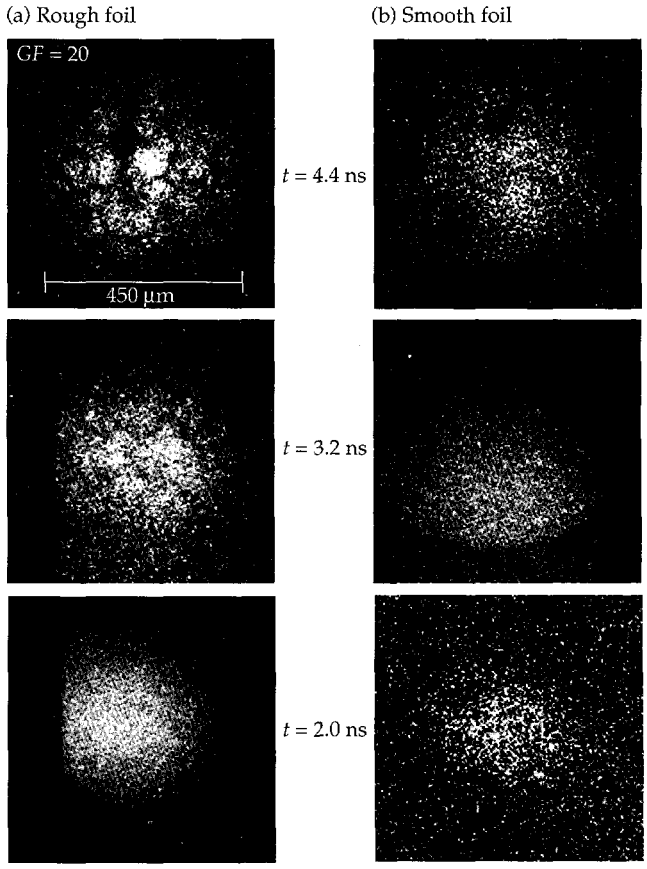

FIGURE 35. Typical 2-D images from surface-finish experiments using CH(Br) foils with two surface finishes, (a) rough ($\sigma_{rms} = 1.7$ μm) and (b) smooth ($\sigma_{rms} = 10$ nm). The diagnostic was a gated x-ray framing camera filtered with 381 μm Be; foil was back-illuminated with x rays generated by a ~500-μm-diam random phase plate (RPP)-smoothed laser beam incident on a Sc backlighter disk. (20-03-1293-4408pb01)

grows the least, and the $k_x = 3k_y$ stretched 3-D mode falls in between.

Figure 34(b) shows results from HYDRA simulations which were performed to help select parameters for the experiments. The foil thicknesses and drive histories in the experiments were somewhat different than those used in these simulations. The perturbations, in order of decreasing peak growth, correspond to $k_x = k_y$, $k_x = 2k_y$, $k_x = 3k_y$, and 2-D $\lambda = 50$ μm. Our simulations clearly show that the most symmetric perturbations grow the most, as reported by others.[23,56,58,59] This agrees qualitatively with our experimental observations; quantitative comparisons are under way.

Ultimately we are interested in the fully 3-D evolution at the ablation front of a perturbation consisting of a full continuum of modes. Recent progress has been made in developing 3-D modeling capability.[5,51,53,56,58–61] We have therefore begun a series of surface-finish experiments to compare the perturbation growth from a randomly roughened surface with that from a smooth surface. We generated the rough surface by sand blasting a glass mold with 50-μm Al_2O_3 pellets. The typical deviation from the average for the smooth foil is $\sigma_{rms} = 10$ nm, whereas $\sigma_{rms} = 1.7$ μm for the rough foil.

Figure 35 shows gated images taken at 2.0, 3.2, and 4.4 ns when such foils were accelerated. Late in time, the surface of the rough foil has evolved into large, roughly hexagonal bubbles of transverse size ~100 μm. Figure 36(a) shows this more quantitatively in $\Delta \ln E \approx -\Delta OD$ profiles. These horizontal lineouts represent the central region of each image shown in Fig. 35; the late-time lineout contains the prominent central bubble at 4.4 ns. Figure 36(b) shows similar profiles for a standard smooth foil; there is no obvious perturbation growth into bubbles and spikes. Figure 37 shows the

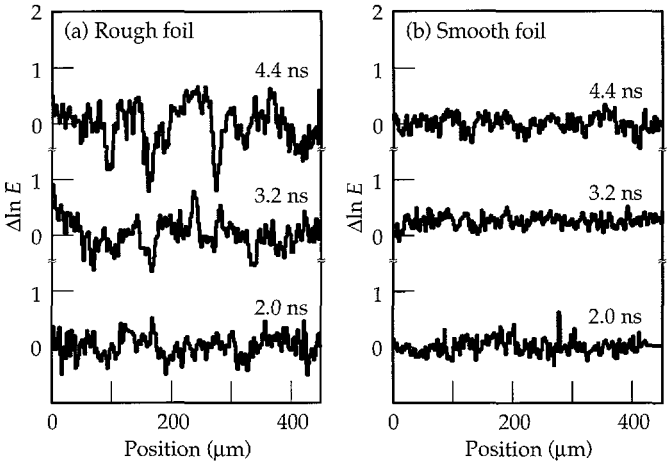

FIGURE 36. Corresponding $\Delta \ln E$ lineouts from Fig. 35 for (a) rough foil, (b) smooth foil. (20-03-0293-0379pb01)

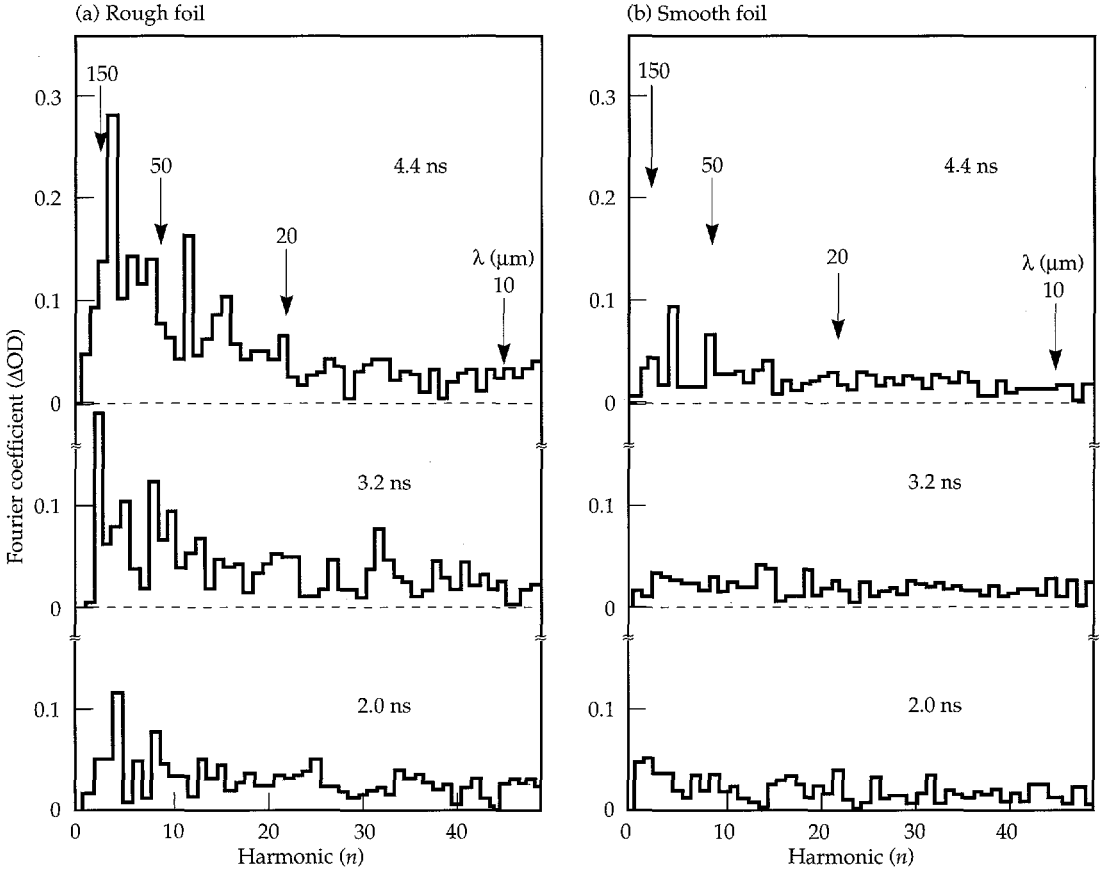

FIGURE 37. Absolute value of the real component of the Fourier transform of the $\Delta \ln E$ profiles shown in Fig. 36. Harmonic n and wavelength λ_n are related by $\lambda_n = (450\ \mu m)/n$, as indicated for a few cases by arrows. (20-03-1293-4409pb01)

corresponding Fourier transforms. The smooth foil again shows no significant growth. For the rough foil, the growth late in time is dominated by harmonics n = 3–8, corresponding to λ = 150–56 μm. This is reasonable, because perturbations with $\lambda > 150$ μm grow too slowly, and perturbations with $\lambda < 56$ μm are more strongly ablatively stabilized [see Fig. 21(d)].

Late in time, the Fourier spectrum for the rough surface is dominated by the fourth harmonic, with peak amplitude $\eta = 0.28$. This fourth harmonic results from the prominent 112-μm-diam bubble shown in the center of the image at 4.4 ns in Figs. 35(a) and 36(a). We use this amplitude to make a crude estimate of growth factor in optical depth, G_{OD}, for the dominant mode. From the surface profile of a similar rough foil, we estimate $\eta_0(\lambda = 100\ \mu m) \approx 0.3\ \mu m$. The initial contrast for a CH(Br) foil with a $\lambda = 100$ μm, $\eta_0 = 5$ μm pure sinusoidal initial perturbation was measured on a separate shot (using the same diagnostic, backlighter, and filtering) to be $\Delta OD_0 = 0.14$. We therefore estimate the growth factor for the dominant mode in Fig. 37(a) to be $G_{OD} = \eta/\eta_0 \approx 0.28/[(0.14)(0.3\ \mu m)/(5.0\ \mu m)] = 33$. This is considerably less than expected in a typical implosion, but it represents a first step towards experimentally addressing the question of 3-D growth from a random initial surface finish. An analysis based on 2-D LASNEX simulations and Haan's 3-D saturation theory [32] has been done for this rough surface experiment. The results, shown in Fig. 38, suggest that the multimode RT evolution was just entering the saturation regime, according to Haan's criterion. We are therefore designing a drive to produce a higher growth factor and having a longer acceleration interval, to allow a more discriminating test of multimode saturation physics.

The RT Instability in Cylindrical Implosions

The RT growth during ablative acceleration has been measured in many direct- and indirect-drive experiments. These measurements have verified the predicted stabilizing effect of mass ablation and density gradients. But few of these experiments have examined the role of feedthrough or of the deceleration phase, during which the growing perturbations may enhance thermal losses from the "hot spot" or reduce the efficiency of compressional work done by the shell on the fuel. Qualitatively, RT growth on the inner surface during deceleration differs from growth on the outer surface during acceleration by the lack of ablative stabilization. The RT growth at the inner surface is moderated, however, by the density gradient. In addition, convergent effects are important during these three phases. During ablative acceleration, convergence introduces a different threshold for nonlinear effects because of a decrease of perturbation wavelength in time,[32] thin-shell effects,[7,29,62] and a change in perturbation amplitude arising from the combination of convergence and compressibility.[63] Feedthrough is decreased because the pusher shell thickens during convergence. Convergence effects are magnified during deceleration.[5,32,61,63]

Current designs for indirectly driven ignition capsules[41] operate near the edge of present capabilities to fabricate smooth surfaces. It is important to assess the magnitude of feedthrough in ICF implosions if we are to correctly model the relative roles of perturbations on the outer and inner surfaces of capsules for these capsule designs. The effect of convergence on feedthrough is an integral part of the problem, so experiments in

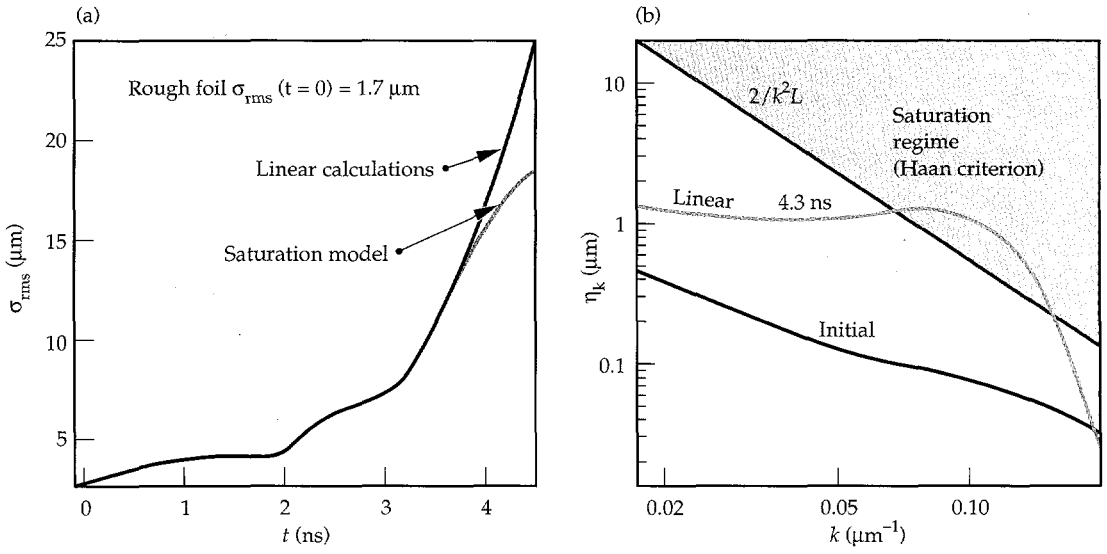

FIGURE 38. Saturation analysis based on 2-D LASNEX simulations and the Haan 3-D saturation theory[32] for the rough surface foils, shown in terms of (a) σ_{rms} vs time and (b) Fourier spectrum at peak growth.
(20-03-1293-4501pb02)

convergent geometry are desirable. Few experiments to study convergent RT instability have been performed[64] because of the difficulty of diagnosis. Perturbations and mixing-layer widths are difficult to measure in spherical geometry because of the lack of a direct line of sight and because of errors associated with Abel inversions in spherical geometry near peak convergence. Although perturbation growth can be indirectly inferred from time-dependent x-ray spectral line ratios in spherical implosions,[18,19,65] the results depend on the details of difficult atomic physics and radiative transport calculations. We have used an indirectly driven cylindrical configuration to allow diagnostic access and superior control of the shell's inner surface during target fabrication, although questions arise concerning edge effects and implosion symmetry. We chose a feedthrough experiment to demonstrate that quantitative RT experiments can be performed in cylindrical geometry and to measure feedthrough in a radiation-driven target for the first time.

Figure 39 shows the experiment geometry. The cylindrical polystyrene shell was mounted orthogonal to the hohlraum axis, to allow a direct line of sight to the diagnostics, to avoid interference with laser beams, and to avoid radiation flow into the ends of the cylinder (as may occur in a coaxial configuration). Eight 351-nm, 2.5-kJ, 2.2-ns Nova drive beams are pointed symmetrically about the cylinder. A low-adiabat drive was used, consisting of a low-power foot followed by a ramp to higher power, with a peak-to-foot ratio of about 3. A separate 528-nm, 2-ns beam was used to irradiate a 2-mm-diam Ag disk to create an x-ray backlighter of photon energy ~3–3.6 keV. An RPP[66] was used to smooth the beam intensity onto the Ag disk, and the resultant laser spot was ~750 μm in diameter. The disk was located ~3.5 mm away from the center of the cylinder and was oriented so that the disk normal bisected the angle between the cylinder axis and the backlighter laser direction. A 1-mil Be foil was placed between the backlighter and cylinder to filter out soft x rays and to keep reflected 2ω light from the backlighter from striking the inside of the cylinder. There should be no 2ω unconverted light from the eight Nova drive beams with a line of sight to the cylinder, so a Be shield on the other side of the cylinder is unnecessary.

Figure 40 shows the polystyrene cylinder in detail. The cylinder has an outer diameter of 630 μm, an inner diameter of 430 μm, and length of 1800 μm. The outer diameter is tapered toward the center of the cylinder, allowing the central region of the cylinder to implode before the ends and minimizing edge effects. Perturbations were machined onto the outer surface of the central 400-μm-long region of the cylinder in a dodecagon shape (fundamental mode number $m = 12$). (A sine wave perturbation would be preferable, because it contains no harmonics, but a sine wave is much more difficult to fabricate than a dodecagon.) A 4-μm-thick, 160-μm-long dichlorostyrene ($C_8H_6Cl_2$) belt was placed around the center of the cylindrical shell, flush with the shell's inner surface. The belt served as a marker layer, because it is opaque to the x-ray backlighter, whereas the polystyrene cylinder is relatively transparent. The time-resolved pinhole camera diagnostic images the marker layer; late in time, it also images some of the surrounding compressed material. The marker layer is on the inner surface of the cylinder and has no initial perturbations, so any perturbations observed indicate feedthrough of the initial outer-surface perturbations to the inner surface. The marker

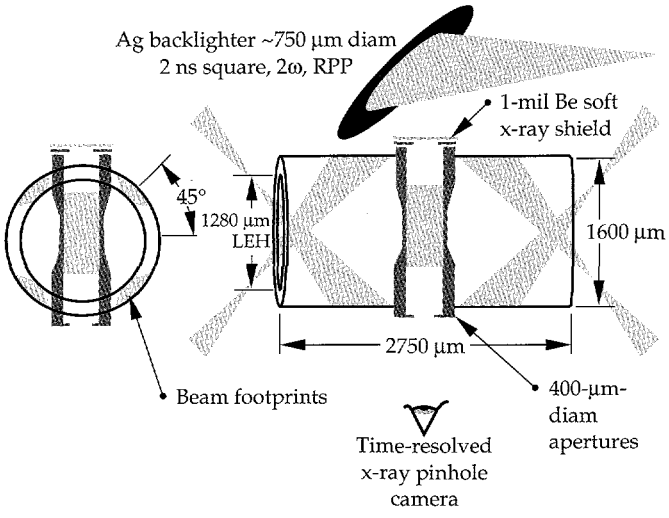

FIGURE 39. Side and transverse views of experimental geometry for the cylindrical implosion Rayleigh–Taylor experiment.
(20-03-0895-2048pb01)

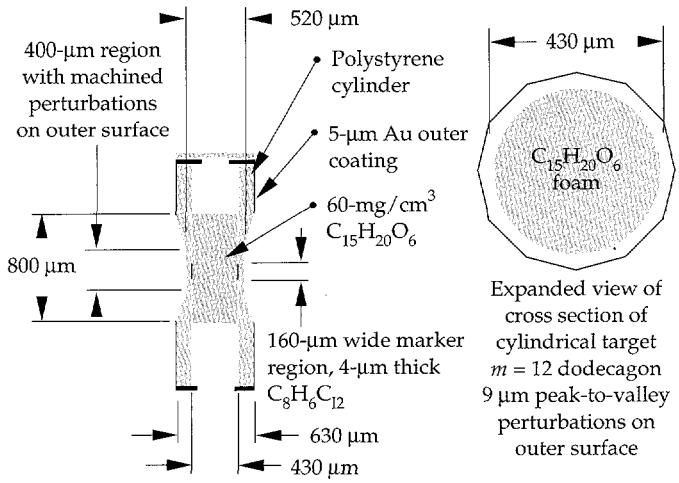

FIGURE 40. Side and end views of target of Fig. 39.
(20-03-0895-2049pb01)

layer has a density close to that of the unchlorinated polystyrene (1.4 g/cm^3 vs 1.0 g/cm^3); calculations show that this slight density mismatch does not cause significant RT growth. A 60-mg/cm^3 microcellular triacrylate foam ($C_{15}H_{20}O_6$) is placed inside the shell to provide a back-pressure as the cylinder implodes. The foam has a cell size ~1–3 μm. The foam is shorter than the cylinder to minimize opacity to the backlighter. The cylinder is fabricated by coating the marker layer on a mandrel, machining the marker layer to size, coating the other polymer layers onto the mandrel and marker layer, machining the coatings, leaching the mandrel out, inserting the cylinder inside the hohlraum, and inserting the foam inside the cylinder. On each end of the cylinder, a 400-μm-diam circular aperture made of 25-μm-thick gold was placed concentric with the cylinder axis. These apertures prevented any x rays emitted by the walls of the cylinder from entering the pinhole camera diagnostic, provided an alignment and parallax diagnostic on the shot, and provided a centering fiducial for each frame on the pinhole camera. The fiducial is crucial for quantitative Fourier analysis of the data.

The cylinder was viewed along its axis with a time-resolved, gated x-ray pinhole camera (GXI).[67] A 4 × 4 pinhole array with pinhole diameters of ~7 μm allowed 16 images spaced ~55 ps apart to be projected onto four microchannel-plate strip lines with a magnification of 12. The filters used were 12.7-μm Ti and 150-μm Be. The Ti was chosen to block x rays with energies above 4.75 keV and to allow the silver L-shell backlighter radiation through.

To determine the contrast ratio expected between the tracer layer and the central foam region, a backlit nonimplosion shot was taken with a 40-μm-thick piece of chlorinated polystyrene on top of part of the foam. The contrast in exposure was measured to be 16:1 after a density-to-exposure correction of the film. A streaked x-ray crystal (KAP) spectrometer viewed the Ag backlighter disk and provided the backlighter spectrum as a function of time. Figure 41 shows a measured backlighter spectrum on an implosion shot. The opacity of cold chlorinated polystyrene and the gold photocathode GXI response are overlaid. The chlorinated polystyrene absorbs virtually all the Ag L-shell radiation, and the GXI detects most of the backlighter where there is no chlorinated polystyrene. The transmission of 3.5-keV x rays through 100 μm of cold polystyrene is ~0.6. Figure 42 shows the total 3ω laser power into the hohlraum and the spectrally integrated x-ray backlighter flux as a function of time. The GXI is timed to measure during the peak x-ray backlighter fluence. The hohlraum was viewed along its axis with the west axial x-ray imager (WAX)[68], another time-resolved pinhole camera with a serpentine microchannel plate strip. This was used to verify that there was no beam clipping on the laser entrance holes.

One purpose of a narrow 160-μm tracer region is to minimize the effect of misalignment on the pinhole camera measurement of the interface location. For example, a 1° tilt in the cylinder with respect to a point on the GXI would result in a lateral spread of 2.8 μm in an interface. Since the pinhole array also has a lateral spread in location, there is parallax between images. For a perfectly aligned cylinder, the four center pinholes have a parallax of 0.9°, the next eight surrounding pinholes have a parallax of 2°, and the four corner pinholes have a parallax of 2.7°. The alignment of the cylinder relative to the GXI, measured on a shot with fiducial wires across the front and back faces of the cylinder, was 0.4° ± 0.6°. Thus the lateral spread in an image is primarily due to parallax.

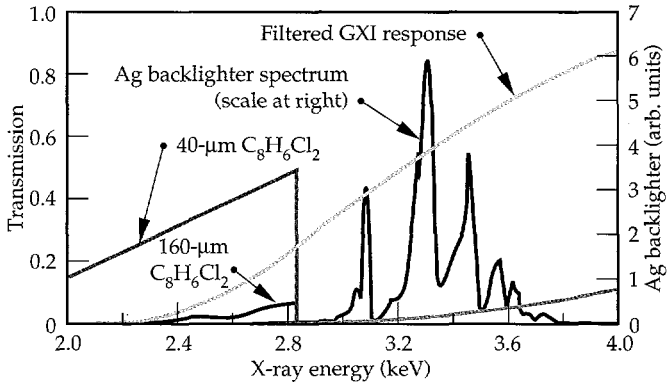

FIGURE 41. The measured x-ray spectrum of the Ag backlighter compared with the gated x-ray imager spectral response and the transmission assuming cold opacities of the tracer layer. 160 μm is the initial length of the marker layer, and 40 μm represents an expansion of the marker layer by a factor of 4. (20-03-1095-2284pb01)

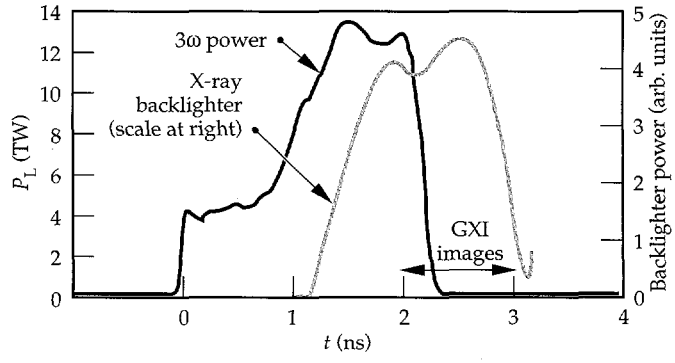

FIGURE 42. The 3ω (λ = 351 nm) power of eight Nova laser beams (left scale) and x-ray backlighter power (right scale). The x-ray images are taken between 2 and 3 ns, near the peak of the backlighter emission. (20-03-1095-2285pb01)

Figure 43 shows 12 frames from an implosion with the initially perturbed surface described above. The $m = 12$ perturbation is clearly visible. The perturbation amplitude grows in time, and the wavelength decreases as the radius decreases. At $t = 2.11$ ns (first image), calculations indicate that the ablation front has not burned through to the marker layer, so the observed $m = 12$ feature is the result of feedthrough of the initial perturbation to the marker layer. The tips of the dodecagon have grown into spikes at the ablation front. Figure 44(a), an image of an unperturbed cylindrical implosion under identical conditions to a perturbed implosion [Fig. 44(b)], shows no $m = 12$ perturbations. The absence of any $m = 12$ feature in this case verifies that the initial perturbations caused the observed feedthrough. (We attribute the small bump at the upper left of the unperturbed shell to a target defect).

In the perturbed image [Fig. 44(b)], we identify a contour $r(\theta)$ at the outer edge at about the 50% exposure level and draw it in [Fig. 45(a)]. The contour can then be fitted with a Fourier series according to the usual prescription

$$r(\theta) = \frac{a_0}{2} + \sum_{m=1}^{\infty} (a_m \cos m\theta + b_m \sin m\theta),$$

where

$$a_m = \frac{1}{\pi} \int_{-\pi}^{\pi} r(\theta) \cos m\theta \, d\theta$$

and

$$b_m = \frac{1}{\pi} \int_{-\pi}^{\pi} r(\theta) \sin m\theta \, d\theta.$$

The results of the fit are shown in Fig. 45(b) and the Fourier composition is shown in Fig. 46, where the modal amplitude $\left(a_m^2 + b_m^2\right)^{1/2}$ is plotted vs mode number m. The term a_0 represents the average diameter of the contour, and a_1 and b_1 represent the offsets of the center of the contour from the axes of symmetry. The coefficients depend on the choice of the center of the contour. We examined several methods to choose the center of the contour: a least-squares fit to a circle, a minimization of a_1 and b_1, and a center based on the measurement of the center of the defining aperture. Of these methods,

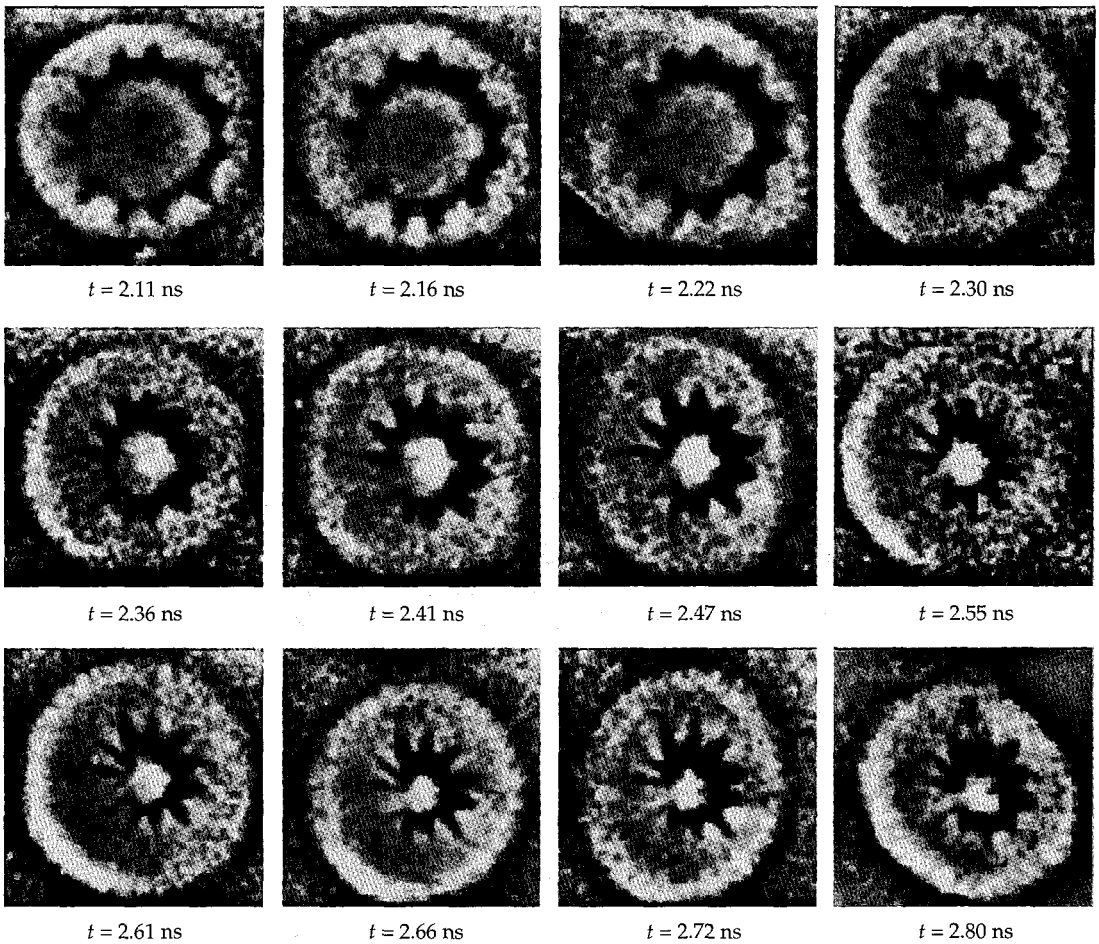

FIGURE 43. A sequence of gated x-ray images of the cylindrical backlit implosion from one experiment ($t = 0$ corresponds to the start of the laser pulse). Shock emission appears on center at 2.30 ns. The backlighter spatial extent is limited by the circular apertures at each end of the cylinder, and the deviation from circularity is a measure of the effect of parallax. (20-03-0895-2050pb01)

only the latter proved reliable and resulted in mode number conservation during the implosion. Figure 47 shows images of the perturbed implosion later in time. One side of the target has imploded closer to the center than the other side. This is probably due to a slight manufacturing imperfection in the target, as if the marker layer were thinner on one side than on the other. The apertures also indicate, on each image, the parallax due to the offset of each pinhole from the axis of the cylindrical shell; the images can be corrected for this effect.

At 2.11 ns, there are significant components at $m = 1$, 4, 8, and 12. Mode 1 exists because one side of the cylinder implodes faster than the other. Mode 4 is expected because of the discrete number of beams illuminating the hohlraum. Mode 2 was minimized by the proper choice of beam pointing. Mode 12 has an amplitude of $\eta = 10$ μm. Since the instrumental resolution is insufficient to distinguish between mode 12 and modes 11 and 13, it is reasonable to expect that the effective amplitude of the perturbation at mode 12 is the quadrature sum of modes 11, 12 and 13, resulting in an amplitude of 12 μm. Other methods of analysis, including curve fits to the functional form

$$r(\theta) = \frac{a_0}{2} + \sum_{n=1}^{4} (a_n \cos 12nx + b_n \sin 12nx)$$

and variations in the choice of a center, result in a mode-12 amplitude of 9–11 μm; we assign the value 10 ± 2 μm as the amplitude of mode 12. A Fourier analysis of a dodecagon inscribed in a 260-μm-radius circle gives amplitudes of 3.5, 0.85, and 0.34 μm for modes 12, 24, and 36 respectively. Thus at $t = 2.11$ ns, the fundamental has grown by a factor of 2.9 ± 0.6 with respect to its initial value.

To test the sensitivity of the analysis to the choice of 50% isodensity contour, we analyzed several images with isodensity contours ranging from 40% to 60%.

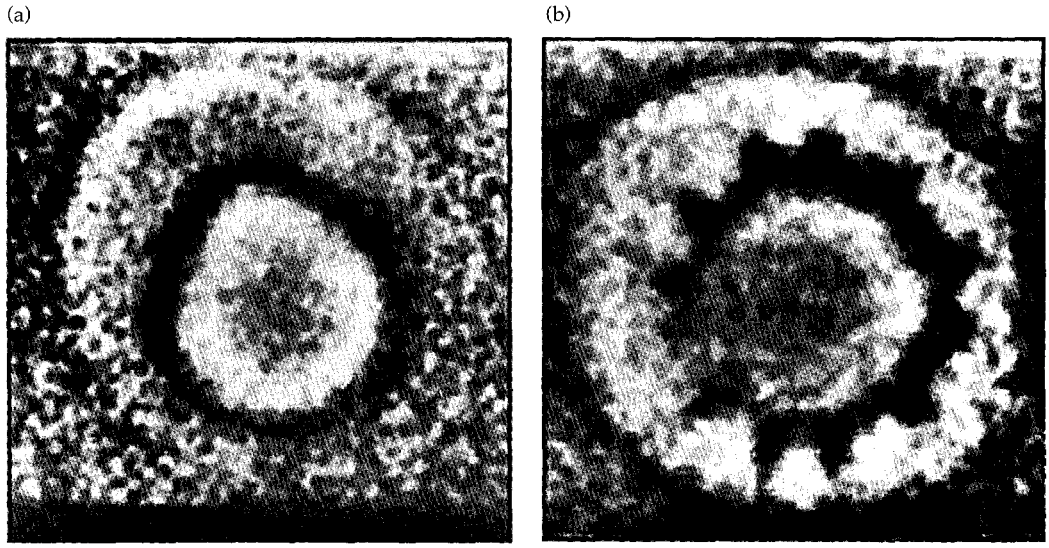

FIGURE 44. (a) Gated x-ray image of an implosion taken with a target with no initial perturbations and (b) an otherwise identical implosion taken with a dodecagon initial perturbation. Images taken $t = 2.16$ ns. (20-03-0895-2053pb01)

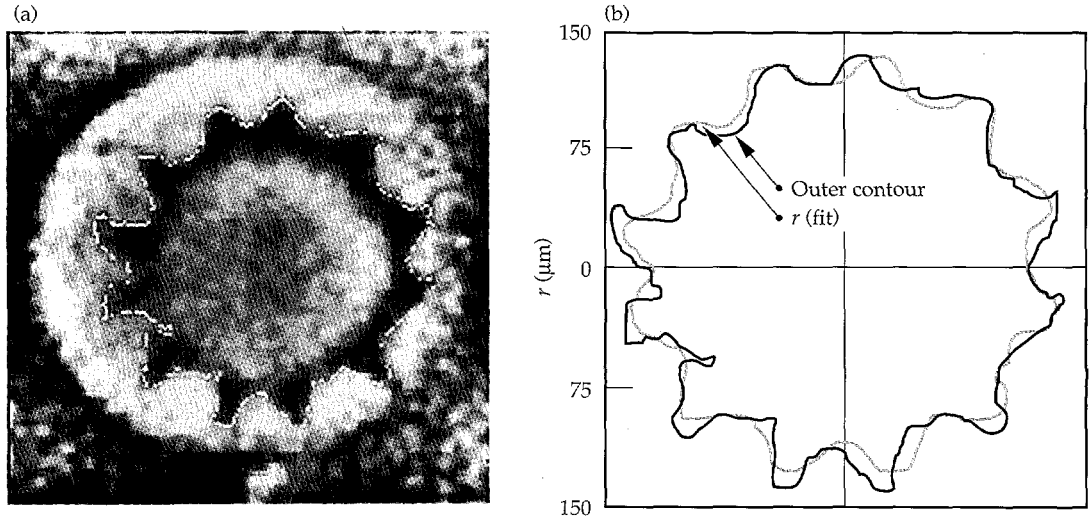

FIGURE 45. (a) An outer contour taken at 50% peak exposure, superposed over the initial x-ray image taken at 2.11 ns. (b) Results of a Fourier series fitted to the contour shown in (a). The horizontal and vertical axes are equal, each covering a range of 300 μm. (20-03-0895-2053pb02)

The results were insensitive to choice of isodensity contour. For isodensity values outside this range, the background noise from the microchannel plate occasionally affected the contour, with unphysical contours appearing because of noise spikes.

For each image, we Fourier analyzed the contours for the inner edge of the marker layer (the interface between the marker layer and the TPX foam) and the outer edge (the interface between the marker layer and surrounding polystyrene cylinder). Figure 48 shows the time dependence of $a_0/2$, which represents the average radius. The implosion trajectory is consistent with a 195-eV peak drive temperature in a calculation with the 1-D radiation–hydrodynamic code HYADES.[69]

The perturbation was initialized in its linear regime. At $t = 0$, the wavelength of mode $m = 12$ is $\lambda = 2\pi R/m = 136$ μm, where $R = 260$ μm. The amplitude of mode $m = 12$ is $\eta_0 = 3.50$ μm initially, so that $\eta/\lambda = 0.026$. At 2.11 ns, the radius of the shell is $R = 122$ μm, so that $\lambda = 2\pi R/m = 64$ μm. The amplitude of mode $m = 12$ is $\eta = 10$ μm, so $\eta/\lambda = 0.16$. The perturbation at the marker layer has exceeded the nominal threshold for nonlinearity $\eta/\lambda \approx 0.1$ at 2.11 ns.

Growth of perturbations on the marker layer result both from shock imprinting and from feedthrough from RT growth at the ablation front. Simple estimates suggest that the latter dominates. To illustrate this, we estimate the marker layer amplitude that would result from shock imprinting alone. The shock is launched from a rippled surface at the ablation front, and hence is itself rippled. A rough estimate of the amplitude of the ripple imparted to the marker layer upon passage of the rippled shock is given by

$$\eta_m = \eta_0(1 - \Delta R_o/\lambda_o)u_p / v_s \quad .$$

Here η_m is the amplitude of the imprinted ripple on the marker layer, η_0 is the ablation front surface

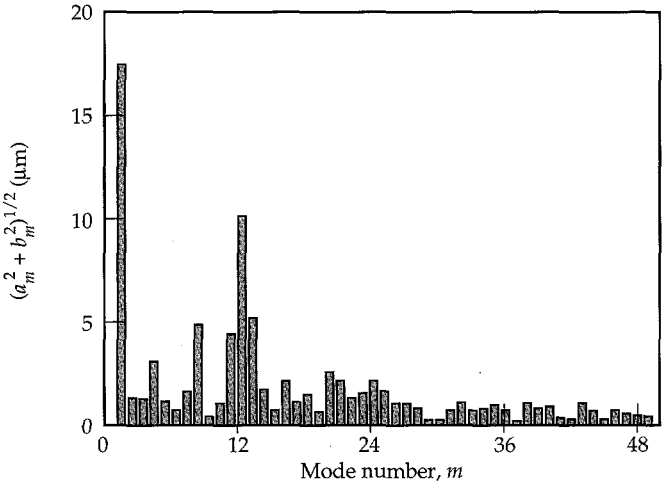

FIGURE 46. Fourier amplitudes vs mode number m for a 50% outer contour of the gated x-ray image at $t = 2.11$ ns. The largest physically significant amplitude corresponds to $m = 12$. (20-03-1095-2286pb01)

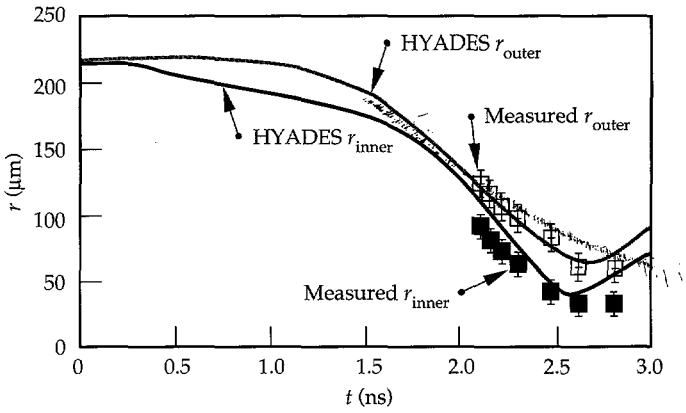

FIGURE 48. Measured outer and inner diameters of the tracer layer vs time, and corresponding trajectories from a HYADES calculation (20-03-0895-2052pb01)

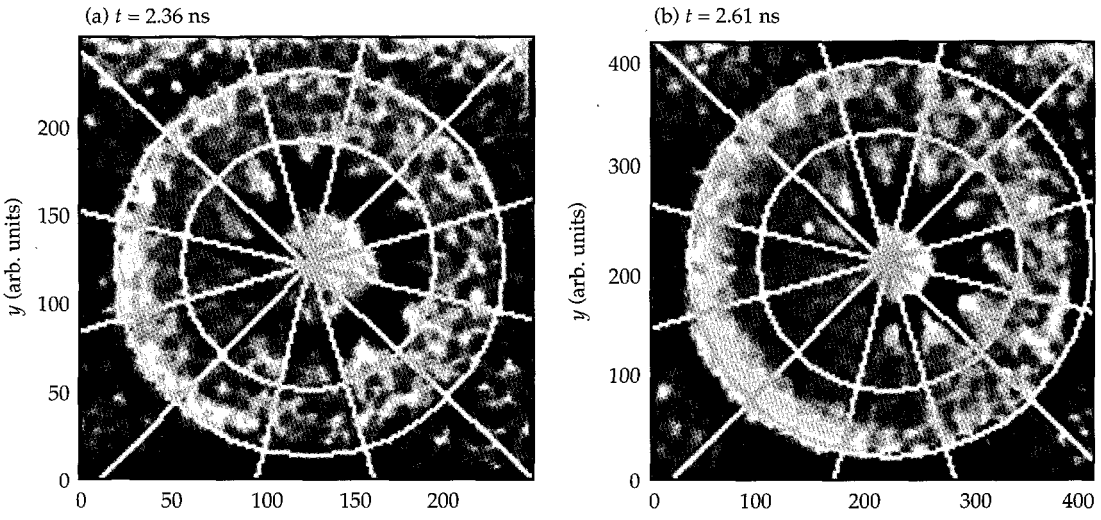

FIGURE 47. Gated x-ray images at (a) 2.36 and (b) 2.61 ns, with a mode 12 uniform in angle grid superposed. Outermost circular contour is a fit to the 400-μm-diam Au defining aperture in both images. One side of the target has imploded faster than the other, yet the mode number is preserved using a center corresponding to the original cylinder axis. (20-03-1095-2295pb01)

perturbation initial amplitude, ΔR_o is the initial distance from the ablation front to the marker layer, λ_o is the initial perturbation wavelength, u_p the particle velocity behind the shock front, and v_s the shock velocity. The factor $\eta_0(1-\Delta R_o/\lambda_o)$ is an estimate, based on the shock oscillation data of Endo et al.,[22] of the amplitude of the shock-front ripple, assuming that it reverses phase after having traveled a distance of λ_o. Since $\Delta R_o \approx 40$ μm and $\lambda_o \approx 100$ μm, the rippled shock has not reversed phase by the time it reaches the marker layer, but its amplitude is ~40% lower than η_0. Assuming that this marker layer perturbation then grows linearly in time via the Richtmyer–Meshkov instability, we write

$$\eta_{12}(t) = \eta_m + \eta_m A^* k u_p \Delta t,$$

where $\eta_{12}(t)$ is the amplitude of the fundamental mode at time t, A^* is the post-shock Atwood number, and $\Delta t = t - t_s$, where $t_s = 0.4$ ns is the time when the first shock reaches the marker layer. Using reasonable estimates for the various parameters in this equation, we estimate that η_{12} (2.11 ns) ≈ 2.5 μm. Allowing for some additional growth due to the higher u_p after the second shock reaches the marker layer at 1.6 ns, we get η_{12} (2.11 ns) ≈ 3 μm. The measured amplitude of 10 μm at 2.11 ns is considerably larger, suggesting that feedthrough from RT growth at the ablation front is the dominant source of the observed growth.

During deceleration, the inner surface becomes RT unstable and perturbations fed through to the inside surface grow without ablative stabilization. At 2.72 and 2.80 ns (Fig. 43), visible spikes protrude into the core. The spikes on the inner edge of the marker layer correspond radially to bubbles on the outer surface, such as can be seen in Fig. 43 at 2.30 ns and 2.47 ns. This suggests that ablation-front bubble growth is the dominant feed-through mechanism.

Summary

We have conducted an extensive series of experiments and simulations to examine the growth of single modes over a range of wavelengths and to examine the effect of multiple modes on perturbation growth. For single modes, the perturbation evolves before shock breakout because of the rippled shock dynamics. After shock breakout, the perturbations grow rapidly in the linear regime and saturate in the nonlinear regime, with the appearance of higher harmonics. In multimode foils, the individual modes grow independently in the linear regime. In the nonlinear regime, the modes become coupled and $k_i \pm k_j$ terms are clearly observed, in agreement with simulations and second-order perturbation theory. Mode coupling redistributes the perturbation in Fourier space, which in physical space corresponds to a change in perturbation shape. The bubbles become broader and flatter and the spikes narrower. In terms of a continuum model, the individual modes of the 2-D perturbation saturate when they exceed $S_k = v_{2D}/k^{3/2}L^{1/2}$ in amplitude. The simulations systematically predict slightly more growth than is observed. This could be caused by greater than expected preheat in the foot of the drive, a stiffer EOS for CH(Br), or a degraded instrumental MTF.

Single-mode experiments very clearly indicate the differences between 2-D and 3-D perturbation shape. Axisymmetric 3-D bubbles grow the largest in the nonlinear regime, consistent with a simple buoyancy-vs-drag argument, third-order perturbation theory, and with full 3-D radiation–hydrodynamics simulations. The obvious next step is to measure the full multimode 3-D perturbation evolution and to compare the results with 3-D simulations and with the predictions of Haan's saturation theory.

In radiation-driven cylindrical implosions, we have observed the RT instability seeded by feedthrough from the outer surface to the inner surface. The mode number was conserved during the implosion. This proof-of-principle cylindrical experiment shows the potential for new studies of RT instability in convergent geometry. Ablation-front growth and feedthrough were measured. With higher resolution, studies of the stagnation phase and inner surface breakup may be possible.

Appendix: Amplitude of Coupled Modes

Following Ref. 26, a solution to a second-order perturbation expansion of the 3-D hydrodynamic equations for inviscid, incompressible fluids can be written as

$$\eta_{\mathbf{k}}(t) = \eta^{\mathrm{L}}_{\mathbf{k}}(t) + 2Ak\sum_{k_2}\eta^{\mathrm{L}}_{k_2}(t)\eta^{\mathrm{L}}_{k_2'}(t)G(\mathbf{k},\mathbf{k}_2)H(\mathbf{k},\mathbf{k}_2,t), \quad \text{(A1)}$$

where $\mathbf{k}_2' = \mathbf{k} - \mathbf{k}_2$ and where superscript L designates results in the linear regime. The time-independent part of the kernel $G(\mathbf{k}, \mathbf{k}_2)$ is given by

$$G(\mathbf{k},\mathbf{k}_2) = \frac{1}{2}\frac{\gamma_2^2(1-\hat{\mathbf{k}}_2\cdot\hat{\mathbf{k}}) + \frac{1}{2}\gamma_2\gamma_2'(1-\hat{\mathbf{k}}_2\cdot\hat{\mathbf{k}}_2' - 2\hat{\mathbf{k}}_2\cdot\hat{\mathbf{k}})}{(\gamma_2+\gamma_2')^2 - \gamma^2(k)}, \quad \text{(A2)}$$

where $\mathbf{k} = (k_x, k_y)$ is the perturbation wave vector, $\hat{\mathbf{k}} = \mathbf{k}/k$ is the unit vector, and $\gamma(\mathbf{k})$, γ_2, and γ_2' are the linear growth rates for perturbations with wave vectors $\mathbf{k}$, $\mathbf{k}_2$, and $\mathbf{k}_2'$, respectively. This weakly nonlinear theory is valid only so long as the dominant modes are not being changed significantly by the nonlinear terms. The full expression for $H(\mathbf{k},\mathbf{k}_2,t)$ is complicated, but for the regime considered here we have $H \approx 1$.

Considerable simplification occurs for 2-D cosine perturbations with Atwood number $A = (\rho_1 - \rho_2)/(\rho_1 + \rho_2) \approx 1$. If we assume that $\gamma_k \propto k^{1/2}$, then Eq. (A1) reduces to

$$\eta_k \approx \eta_k^L + \frac{1}{2}k\left(\sum_{k'}\eta_{k'}^L\eta_{k+k'}^L - \frac{1}{2}\sum_{k'<k}\eta_{k'}^L\eta_{k-k'}^L\right), \qquad \text{(A3)}$$

where $k, k' > 0$, and the time dependence has been dropped from the notation for simplicity. For example, Eq. (5b) for the second harmonic of a single-mode perturbation, $\eta_2 \approx \frac{1}{2}k_1\eta_L^2$, comes from the second term in the summation in Eq. (A3), where $k = 2k_1$ and $k' = k_1$.

Another simple case of general interest arises for $k = k_3 \pm k_2$. Here, Eq. (A3) reduces to

$$\eta_{k_3\pm k_2} \approx \mp\left(k_3 \pm k_2\right)\eta_{k_2}^L\,\eta_{k_3}^L, \qquad \text{(A4)}$$

where $\eta_{k_n}^L$ represents the spatial amplitude attained by mode k_n had the growth been entirely in the linear regime.

Notes and References

1. S. Chandrasekhar, *Hydrodynamic and Hydromagnetic Stability* (Oxford U. P., London, 1968), Ch. 10; Lord Rayleigh, *Scientific Papers*, Vol. II (Cambridge U. P., Cambridge, 1900), p. 200; G. I. Taylor, *Proc. Roy. Soc.* **A201**, 192 (1950).
2. R. D. Richtmyer, *Commun. Pure Appl. Math.* **13**, 297 (1960); E. E. Meshkov, *Izv. Akad. Nauk. SSSR, Mekh. Zhidk. Gaz.* **5**, 151 (1969) (translation, NASA TTF-13-074, 1970).
3. J. D. Lindl and W. C. Mead, *Phys. Rev. Lett.* **34**, 1273 (1975).
4. E. Gamaly, "Hydrodynamic Instability of Target Implosions in ICF," in *Nuclear Fusion by Inertial Confinement: A Comprehensive Treatise*, G. Velarde, Y. Ronen, and J. M. Martinez–Val, Eds. (CRC Press, Boca Raton, 1993), p. 321.
5. H. Sakagami and K. Nishihara, *Phys. Rev. Lett.* **65**, 432 (1990); *Phys. Fluids B* **2**, 2715 (1990).
6. S. E. Bodner, *Phys. Rev. Lett.* **33**, 761 (1974).
7. R. L. McCrory, L. Montierth, R. L. Morse, and C. P. Verdon, *Phys. Rev. Lett.* **46**, 336 (1981).
8. J. D. Lindl, *LLNL Laser Program Annual Report*, 2-40 to 2-46, UCRL-56055-83, Lawrence Livermore National Laboratory, Livermore, California (SRD, 1983); H. Takabe, K. Mima, L. Montierth, and R. L. Morse, *Phys. Fluids* **28**, 3676 (1985); D. H. Munro, *Phys. Rev. A* **38**, 1433 (1988); M. Tabak, D. H. Munro, and J. D. Lindl, *Phys. Fluids B* **2**, 1007 (1990).
9. A. Caruso, V. A. Pais, and A. Parodi, *Laser Part. Beams* **10**, 447 (1992).
10. J. Grun et al., *Phys. Rev. Lett.* **58**, 2672 (1987).
11. M. Desselberger, O. Willi, M. Savage, and M. Lamb, *Phys. Rev. Lett.* **65**, 2997 (1990); M. Desselberger, O. Willi, M. Savage, and M. Lamb, *Phys. Fluids B* **5**, 896 (1993).
12. S. G. Glendinning et al., *Phys. Rev. Lett.* **69**, 1201 (1992).
13. J. D. Kilkenny, *Phys. Fluids B* **2**, 1400 (1990).
14. B. A. Remington et al., *Phys. Rev. Lett.* **67**, 3259 (1991); B. A. Remington, S. W. Haan, S. G. Glendinning, J. D. Kilkenny, D. H. Munro, and R. J. Wallace, *Phys. Fluids B* **4**, 967 (1992).
15. B. A. Remington et al., *Phys. Fluids B* **5**, 2589 (1993).
16. Guy Dimonte and Bruce Remington, *Phys. Rev. Lett.* **70**, 1806 (1993).
17. B. A. Hammel et al., *Phys. Fluids B* **5**, 2259 (1993); B.A. Hammel, J.D. Kilkenny, D. Munro, B. A. Remington, H. N. Kornblum, T. S. Perry, D. W. Phillion, and R. J. Wallace, *Phys. Plasmas* **1**, 1662 (1994).
18. B. A. Hammel et al., *J. Quant. Spectrosc. Radiat. Transfer* **51**, 113 (1994).
19. J. Delettrez, D. K. Bradley, P. A. Jaanimagi, and C. P. Verdon, *Phys. Rev. A* **41**, 5583 (1990); D. K. Bradley, J. A. Delettrez, and C. P. Verdon, *Phys. Rev. Lett.* **68**, 2774 (1992).
20. R. G. Evans, *Can. J. Phys.* **64**, 893 (1986); J. Meyer–Ter–Vehn, *Nucl. Fusion* **22**, 561 (1982); G. I. Guderley, *Luftfahrtforschung* **19**, 3032 (1942).
21. D. H. Munro, *Phys. Fluids B* **1**, 134 (1989).
22. T. Endo et al., *Phys. Rev. Lett.* **74**, 3608 (1995).
23. J. W. Jacobs and I. Catton, *J. Fluid Mech.* **187**, 329 (1988); J. W. Jacobs and I. Catton, *J. Fluid Mech.* **187**, 353 (1988).
24. R. M. Davies and G. I. Taylor, *Proc. Roy. Soc. A* **200**, 375 (1950); G. R. Baker, D. I. Meiron, and S. A. Orszag, *Phys. Fluids* **23**, 1485 (1980).
25. D. Layzer, *Astrophys. J.* 122, 1 (1955).
26. S. W. Haan, *Phys. Fluids B* **3**, 2349 (1991).
27. D. Ofer, D. Shvartz, Z. Zinamon, and S. A. Orszag, *Phys. Fluids B* **4**, 3549 (1992).
28. E. G. Gamaly et al., *Laser Part. Beams* **8**, 173 (1990).
29. C. P. Verdon et al., *Phys. Fluids* **25**, 1653 (1982).
30. G. R. Baker, D. I. Meiron, and S. A. Orszag, *Phys. Fluids* **23**, 1485 (1980).
31. J. P. Dahlburg, J. H. Gardner, and M. H. Emery, *Bull. Am. Phys. Soc.* **35**, 1969 (1990).
32. S. W. Haan, *Phys. Rev. A* **39**, 5812 (1989).
33. E. M. Campbell, *Laser Part. Beams* **9**, 209 (1991).
34. R. J. Ellis et al., *Rev. Sci. Instrum.* **61**, 2759 (1990).
35. B. A. Remington, S. G. Glendinning, R. J. Wallace, S. Rothman, and R. Morales, *Rev. Sci. Instrum.* **63**, 5080 (1992).
36. R. Morales, B. A. Remington, T. Schwinn, *Rev. Sci. Instrum.* **66**, 700 (1995); B. A. Remington and R. I. Morales, *Rev. Sci. Instrum.* **66**, 703 (1995).
37. B. A. Remington et al., *Phys. Plasmas* **2**, 241 (1995).
38. K. S. Budil et al., "The Flexible X-Ray Imager," Lawrence Livermore National Laboratory, Livermore, CA, UCRL-JC-120837; in press, *Rev. Sci. Instrum.* (1996).
39. L. J. Suter et al., *Phys. Rev. Lett.* **73**, 2328 (1994).
40. R. L. Kauffman et al., *Phys. Rev. Lett.* **73**, 2320 (1994).
41. S. W. Haan et al., *Phys. Plasmas* **2**, 2480 (1995).
42. Ya. B. Zel'dovich and Yu. P. Raizer, *Physics of Shock Waves and High-Temperature Phenomena* (Academic, New York, 1966), Vol. I, p. 52.
43. S. P. Hatchett, Lawrence Livermore National Laboratory, Livermore, CA, UCRL-JC-108348 (1991).
44. G. B. Zimmerman and W. L. Kruer, *Comm. Plasma Phys. Controlled Fusion* **2**, 51 (1975).
45. S. V. Weber, B. A. Remington, S. W. Haan, B. G. Wilson, and J. K. Nash, *Phys. Plasmas* **1**, 3652 (1994).
46. R. M. More, K. H. Warren, D. A. Young, and G. B. Zimmerman, *Phys. Fluids* **31**, 3059 (1988).
47. K. S. Budil et al., Lawrence Livermore National Laboratory, Livermore, CA, UCRL-JC-121565 (1995); to be submitted to *Phys. Rev. Lett.*
48. B. A. Remington et al., *Phys. Rev. Lett.* **73**, 545 (1994).
49. M. J. Dunning and S. W. Haan, *Phys. Plasmas* **2**, 1669 (1995).
50. D. L. Youngs, *Physica* **12D**, 32 (1984); K. I. Read, *Physica* **12D**, 45 (1984).
51. M. M. Marinak et al., *Phys. Rev. Lett.* **75**, 3677 (1995).
52. R. J. Wallace, R. L. McEachern, and W. W. Wilcox, *ICF Quarterly Report* **4**(3), 79, Lawrence Livermore National Laboratory, Livermore, CA, UCRL-LR-105821-94-3 (1994).
53. M. M. Marinak, R. E. Tipton, B. A. Remington, et al., *ICF Quarterly Report* **5**(3), 168, Lawrence Livermore National Laboratory, Livermore, CA, UCRL-LR-105821-95-3 (1995); M. M. Marinak et al., *Phys. Plasmas*, in press (1996).
54. L. D. Landau and E. M. Lifshitz, *Fluid Mechanics*, 2nd ed. (Pergamon Press, New York, 1987), p. 180.
55. U. Alon, J. Hecht, D. Ofer, and D. Shvarts, *Phys. Rev. Lett.* **74**, 534 (1995).

56. J. P. Dahlburg et al., *Phys. Fluids B* **5**, 571 (1993).
57. T. A. Peyser et al., *Phys. Rev. Lett.* **75**, 2332 (1995); G. Dimonte et al., *Phys. Rev. Lett.* **74**, 4855 (1995).
58. J. Hecht, U. Alon, and D. Shvarts, *Phys. Fluids* **6**, 4019 (1994).
59. D. Shvarts, U. Alon, D. Ofer, R. L. McCrory, and C. P. Verdon, *Phys. Plasmas* **2**, 2465 (1995).
60. D. L. Youngs, *Phys. Fluids* A **3**, 1312 (1991); *Laser Part. Beams* **12**, 725 (1994).
61. R. P. J. Town, A. R. Bell, *Phys. Rev. Lett.* **67**, 1863 (1991).
62. G. R. Baker, R. L. McCrory, C. P. Verdon et al., *J. Fluid Mech.* **178**, 161 (1987).
63. F. Hattori, H. Takabe, and K. Mima, *Phys. Fluids* **29** (5), 1719 (1986).
64. M. A. Sweeney, F. C. Perry, *J. Appl. Phys.* **52**, 4487 (1981); J. S. Wark, J. D. Kilkenny, A. J. Cole, M. H. Key, P. T. Rumsby, *Appl. Phys. Lett.* **48**, 969 (1986); H. Nishimura, et al., *Phys. Fluids* **31**, 2875 (1988).
65. T. R. Dittrich et al., *Phys. Rev. Lett.*, **73**, 2324 (1994).
66. Y. Kato and K. Mima, *Phys. Rev. Lett.* **53**, 1057 (1984).
67. J. D. Kilkenny et al., *Rev. Sci. Instrum.* **59**, 1793 (1988); O. L. Landen et al., "Gain Uniformity, Linearity, Saturation and Depletion in Gated Microchannel-Plate X-Ray Framing Cameras," *Ultrahigh- and High-Speed Photography, Videography, and Photonics '93*, P. W. Roehrenbecks, Ed. (SPIE, San Diego, California, 1993), Vol. 2002, pp. 2–12.
68. P. M. Bell, J. D. Kilkenny, G. Power, R. Bonner, and D. K. Bradley, in *Ultrahigh Speed and High Speed Photography, Photonics, and Videography '89*, SPIE Vol. 1155 (SPIE, Bellingham, WA, 1989), pp. 430–444.
69. J. T. Larsen, "HYADES—A Radiation Hydrodynamics Code for Dense Plasma Studies," *4th International Workshop on Radiative Properties of Hot Dense Matter*, W. Goldstein, C. Hooper, J. Gauthier, J. Seely, R. Lee, Eds. (World Scientific, Sarasota, Florida, 1990), p. 321.

Diagnosis of Pusher–Fuel Mix in Indirectly Driven Nova Implosions (HEP3)

T. R. Dittrich
B. A. Hammel
C. J. Keane
R. McEachern
R. E. Turner
S. W. Haan
L. J. Suter

Introduction

A key issue for inertial confinement fusion (ICF) is the hydrodynamic stability of the imploding capsule. Imperfections on the capsule surface can grow into large perturbations that degrade capsule performance. Understanding this process is crucial if we are to successfully predict requirements for future high-gain ICF capsules. Experiments on the Nova laser at Lawrence Livermore National Laboratory have directly measured perturbation growth on planar foils,[1] and three experimental groups have investigated backlit perturbation growth using imploding spheres.[2–4] In addition to these efforts, which concentrate on indirectly driven implosions, is work investigating the hydrodynamic stability of directly driven ICF capsules.[5,6] In these direct-drive experiments the laser light shines directly on the capsules, causing the implosion and providing the seed for perturbation growth.

This article reports measurement, via emission from spectroscopic tracers,[7] of the full process of perturbation growth leading to pusher–fuel mix in spherical implosions, and shows perturbation growth dependence on initial perturbation amplitude and wavelength. In contrast to the cited direct-drive work, we have in this experiment separated the drive from the perturbation seed. (For a review of x-ray spectroscopy of ICF plasmas see Refs. 8 and 9.)

The purpose of the experiments described here was to study, in a controlled manner, the effects of the Rayleigh–Taylor (RT) instability on capsule implosion performance. The mechanism by which RT growth degrades capsule performance can be summarized as follows: As the ablation phase of the implosion proceeds, surface imperfections grow via the RT instability as low-density ablated material pushes on the high-density shell. This growth causes the imploding shock to deviate from spherical, carrying the perturbation information through the shell and rippling the interface between pusher and fuel. When the fuel is compressed later in time, the pusher–fuel interface becomes RT unstable, which causes this rippling to grow and produce a region of mixed pusher and fuel material. Increasing the initial outer surface perturbation increases the degree of pusher–fuel mixing.

Experiment

These Nova experiments use plastic-shelled capsules filled with deuterium (D_2). A typical capsule shell in the experiment had a 420-μm inside diameter and a 55-μm-thick wall, and consisted of three layers. The inner layer, the pusher, was ~3 μm of polystyrene doped with 1.0% (atomic) Cl. The middle layer was a 3-μm-thick permeation barrier made of polyvinylalcohol (PVA), which sealed in the fuel gas. An outer layer of plasma polymer ($CH_{1.3}$) was deposited over the inner layers,[10] forming the ablator. The capsules were filled with 50 atm D_2 gas and 0.1 atm Ar.

The Nova laser indirectly drove the implosion of these capsules. A square pulse of laser light with a duration of 1 ns heated a cylindrical gold case, or *hohlraum*, with (typically) 17 kJ of laser energy. The hohlraum, reaching a peak radiation temperature of 230 eV, then emitted x rays that ablated the plastic and caused the implosion.

The capsules had relatively low convergence (~8) and had considerably less sensitivity to growth of surface perturbations compared to that predicted for current high-gain ICF capsule designs. We chose capsule implosions with low convergence so that asymmetries in the x-ray drive would have little effect on the implosions and would, therefore, not complicate the perturbation growth effects.

To make capsules with various degrees of surface roughness, many polystyrene beads, ranging in diameter from 0.6 to 7 μm, were embedded in the PVA layer. When the ablator layer was deposited onto this rough PVA surface, the perturbations were imprinted on the

outer surface. This method of using a capsule with a controllably rough outer surface as seed for RT growth during implosion contrasts with the method used in Refs. 5 and 6, where direct-drive laser illumination nonuniformity was assumed to be the dominant source of initial amplitude seeds to the RT instability and to be representable by a semi-empirical analytic expression.

After shooting these capsules, we developed the capability of characterizing shell surfaces using an equatorially tracing atomic force microscope (AFM). Using this AFM, we took equatorial traces of capsules from the same production runs as capsules that were shot. (To verify surface similarity, we compared scanning electron microscope images of these traced capsules with images of the shot capsules.) We converted the equatorial traces to power spectra and combined them to form ensemble averages. By assuming that the surface bumpiness is isotropic, we transformed these one-dimensional (1-D) average power spectra into 2-D (spherical surface) power spectra:[11]

$$P_{2D}(l)=\left(l+\frac{1}{2}\right)\sum_{n=l,l+2}^{\infty}\left[P_{1D}(n)-P_{1D}(n+2)\right]\times\frac{(n+l)!!(n-l-1)!!}{(n-l)!!(n+l+1)!!} \quad (1)$$

where l is the perturbation mode number, P_{1D} is the 1-D power spectrum and P_{2D} is the 2-D power spectrum. Figure 1 shows 2-D (spherical surface) power spectra of capsules with rms = 0.03, 0.31, and 1.75 μm.

We diagnosed enhanced pusher–fuel mix due to these surface perturbations in two ways. First, we monitored the variation in capsule DD neutron yield with roughness; this we expected to decrease with increasing surface roughness as cold dense pusher material increasingly poisoned the fuel. Second, we monitored the variation in the x-ray self-emission of included trace elements, or dopants,[7,12] with roughness. We expected the x-ray emission of the pusher dopant, Cl, to increase relative to the x-ray emission of the fuel dopant, Ar, as the surface roughness was increased. In the temperature and density regime accessed in these experiments, the variation of x-ray line radiation from these dopants depends strongly on temperature. During the implosion, PdV work heated the fuel and the Ar, but conduction and convection, due to mix, heated the Cl. At peak x-ray emission the imploded capsule had steep gradients through the mix region in both electron temperature and density as a function of radius. This made a simple one-temperature, 1-D understanding of this process difficult. We therefore observed the x-ray emission by means of a crystal spectrometer coupled to an x-ray streak camera, which had temporal resolution of ~30 ps and a spectral resolving power ($\lambda/\delta\lambda$) ~700.[13]

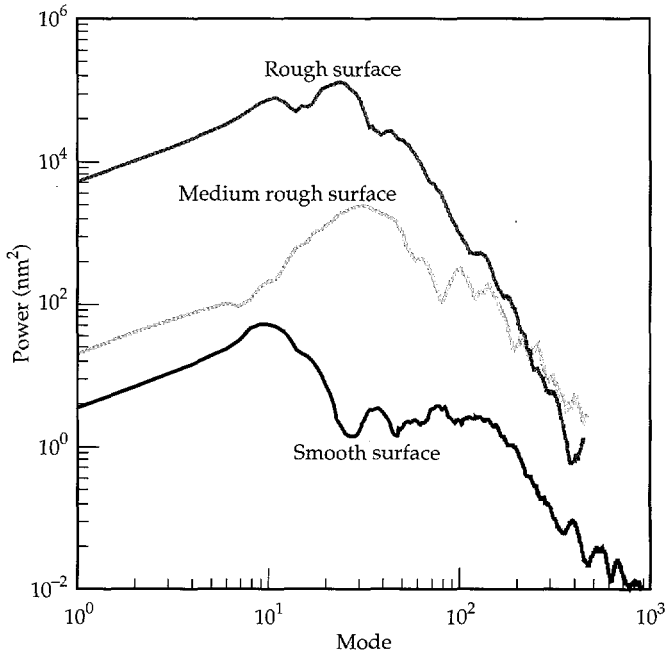

FIGURE 1. The 2-D (spherical surface) power spectra characterizing the outer surface of three representative capsules with rms = 0.03, 0.31, and 1.70 μm. (20-03-0795-1848pb01)

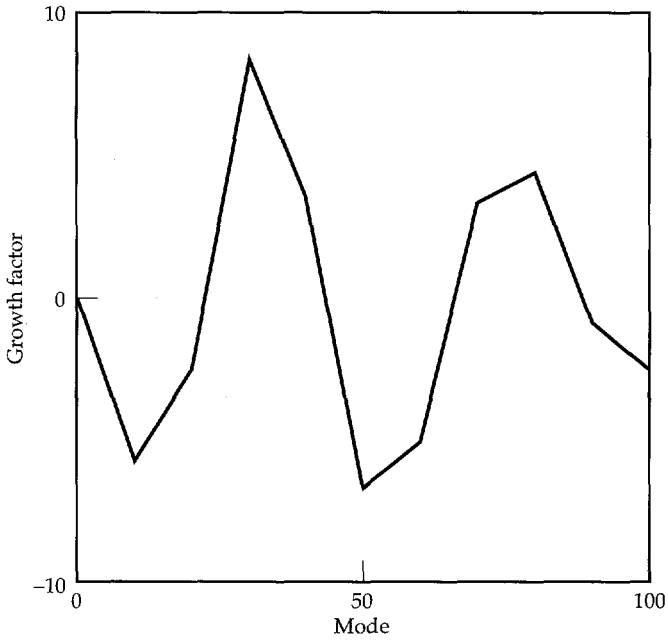

FIGURE 2. Growth factor at pusher–fuel interface vs mode number for perturbations initially on the capsule outer surface. This is a snapshot at time of peak neutron production. Negative values indicate phase change of the perturbation. (20-03-0795-1849pb01)

Analysis Method

Simulating the implosion of these capsules was a multistep process. First, we estimated the capsule's sensitivity to surface perturbations. Second, we combined the surface roughness with the perturbation growth factors. Third, we ran implosion simulations to generate emission spectra. This section describes the three steps.

First, we estimated the capsule's sensitivity to surface perturbations using several 2-D LASNEX[14] simulations, from which we estimated linear growth for several single modes. The initial perturbations in these simulations were small to ensure that only linear growth would occur. This perturbation growth included the effects of stabilization at the ablation surface, feed-through between the interfaces, and RT/Richtmyer–Meshkov instability growth at the pusher–fuel interface. Figure 2 plots these linear growth factors at the pusher–fuel interface vs perturbation mode number. This growth factor is the amplification of a perturbation initially on the outer surface as it imprints on the inner capsule surface. It is typically quoted at peak neutron emission. Negative growth factor values indicate phase change of the perturbation. This linear perturbation growth is small relative to high-gain ICF capsules because of favorable stabilization mechanisms at the ablation surface.

Next, we combined the surface roughness, $P_{2D}(l)$, with the linear perturbation growth factors per standard linear analysis. We estimated nonlinear saturation with Haan's criterion,[15] which states that saturation occurs on a spherical surface of radius R when amplitudes become larger than $4R/l^2$. These saturated amplitudes then grow at a constant rate, rather than exponentially. This procedure predicted the pusher–fuel mixing vs time, estimated from the calculated rms deviation, σ, of the pusher–fuel surface from spherical. The limit of the bubble tips outward was taken to be $\sqrt{2}\sigma$, and the extent of spike tips inward to be $(1+A)\sqrt{2}\sigma$, where A is the Atwood number. This mix-region size estimate also included contributions from both initial pusher–fuel surface imperfections and effects of embedding microspheres in the PVA layer of some of the capsules. Atomic mixing of the pusher and fuel was assumed throughout the mixed region. This modeling distributed the materials within this region so as to maintain a constant concentration while conserving individual material amounts.

Finally, LASNEX implosion simulations used this time-dependent mix region in a self-consistent manner (i.e., the mixing affected the hydrodynamic evolution) and generated emission spectra by means of Detailed Configuration Accounting (DCA).[16,17] These 1-D simulations used detailed atomic models for both Ar and Cl. The DCA simulated spectra were calculated using 69- and 70-level atomic models for Cl and Ar, respectively. We produced the models with the DSP[18] code, which contains atomic physics identical to that used in the RATION code.[19]

TABLE 1. Nova shots in the Ar/Cl implosion series.

Shot	Imbedded bead diameter (μm)	Surface rms (μm)	Observed yield (10^9 neutrons)	Observed yield/ clean (no mix) yield
1	None	0.031	1.21	0.72
2	None	0.031	1.26	0.83
3	None	0.064	0.53	0.33
4	None	0.065	1.01	0.60
5	0.6	0.307	0.60	0.35
6	2.0	0.308	1.22	0.49
7	2.0	0.308	0.65	0.44
8	3.9–7.0	1.70	0.66	0.20
9	3.9–7.0	1.70	0.70	0.20

Data Analysis

Table 1 lists capsule surface conditions and observed and simulated yields for the nine Nova shots that comprise this experimental series. We have chosen three of these shots to illustrate the variation in x-ray spectral output during implosion with initial capsule surface roughness.

Figure 3 shows spectra at peak x-ray emission for the implosion of a smooth (0.03-μm-rms) capsule. Figure 3(a) shows the spectrum observed with the spectrometer and Fig. 3(b) shows the analogous DCA simulated spectrum. Very little Cl Ly-α emission, relative to Ar Ly-α, is evident in either of these spectra. The simulations indicate that 6% of the total Cl mass has reached at least 600 eV. The simulated Ly-α satellite line strengths, on the low-energy side of the Ly-α lines, differ from those observed; the large absorption feature evident in Fig. 3(b) at 2.75–2.80 keV is probably due to errors in calculating the opacity of the Cl He-α line in the colder plastic away from the pusher–fuel interface. Figure 4 shows the spectra from an intermediately rough (0.31-μm-rms) capsule. In this case the Ly-α emissions from both the Cl and Ar are comparable in strength, and 10% of the total Cl mass (according to simulation) has reached at least 600 eV. Figure 5 shows the spectra from a very rough (1.75-μm-rms) capsule. In this case the Cl Ly-α emission is stronger than the Ar Ly-α emission, and 15% of the total Cl mass (according to simulation) has reached at least 600 eV. The simulations show that from smooth to rough capsules the Cl Ly-α emission increased by 350% but the Ar Ly-α emission decreased by 30%.

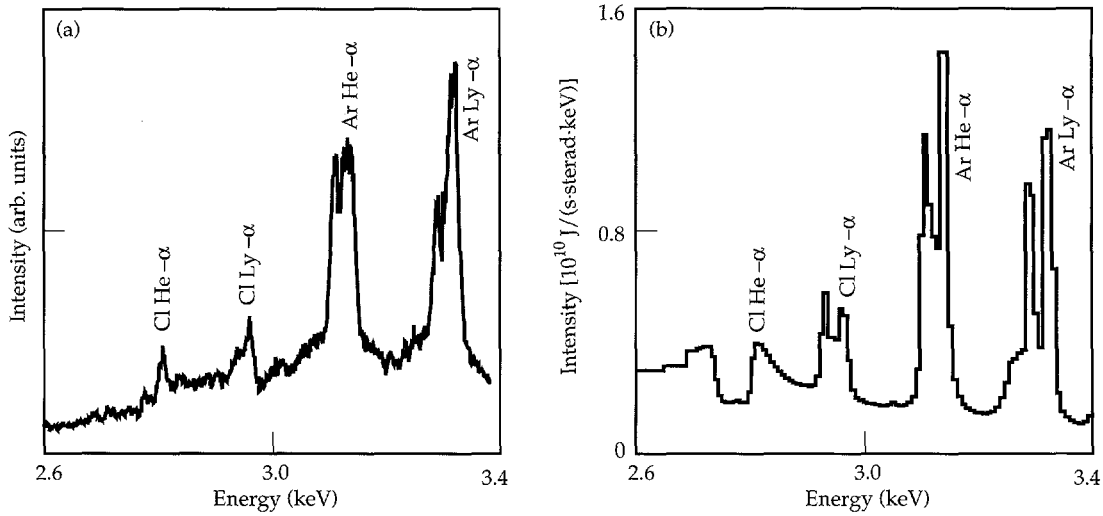

FIGURE 3. Spectra at peak x-ray emission from the implosion of a smooth surface (rms = 0.03 μm) capsule. (a) is as observed by the streaked crystal spectrometer. (b) is the 1-D DCA simulation of this shot. Relevant emission lines of Cl and Ar are labeled.
(20-03-0795-1850pb02)

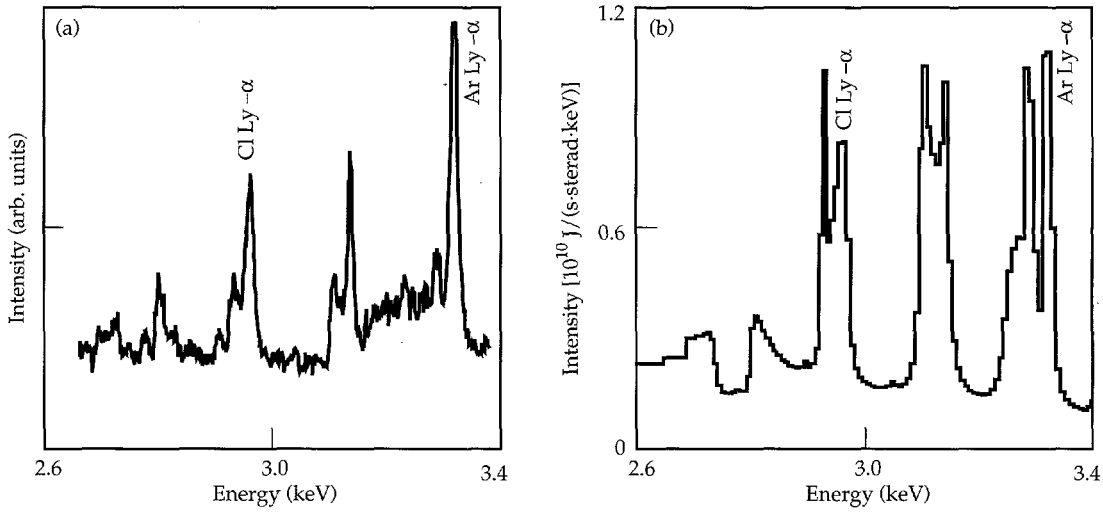

FIGURE 4. Same as Fig. 3, for an intermediate roughness (rms = 0.3 μm) capsule.
(20-03-0795-1851pb02)

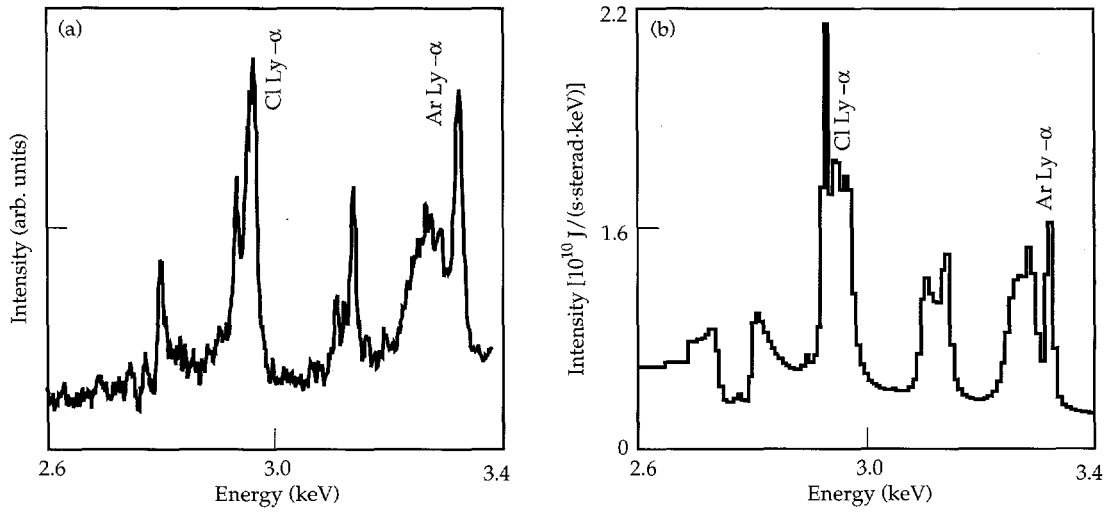

FIGURE 5. Same as Fig. 3, for a very rough (rms = 1.7 μm) capsule.
(20-03-0795-1852pb02)

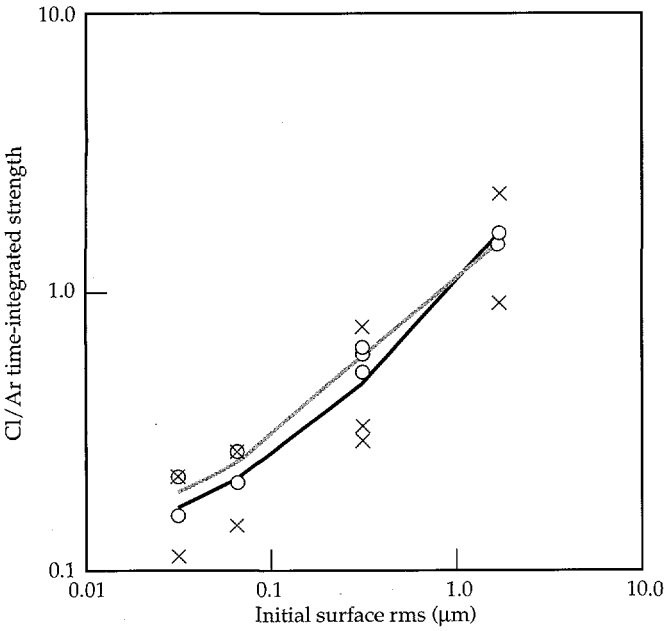

FIGURE 6. Comparison of simulated and observed emission spectra from the nine shots in the series. The ratio of time-integrated Cl and Ar Ly-α emission is plotted vs surface finish. X marks experimental points; O marks simulation points. The black and gray lines are the results of averaging the experimental and simulation values, respectively, at each distinct rms value. (20-03-0795-1853pb01)

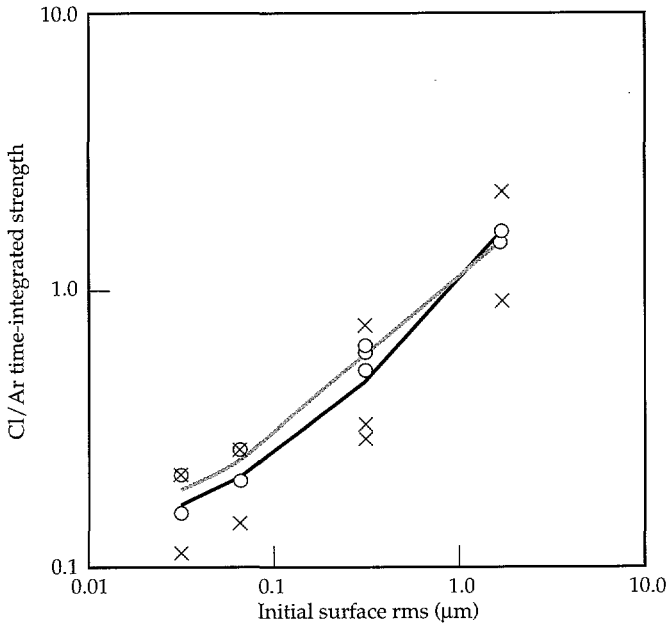

FIGURE 7. Observed and simulated mixed neutron yield over clean yield, vs surface finish for the same nine-shot data set. The black and gray lines are the results of averaging the experimental and simulation values, respectively, at each distinct rms value. (20-03-0795-1854pb01)

To quantitatively compare the observed and simulated spectra, we ratio the time-integrated Ly-α emission from the two dopants. (At each time we estimated this line emission by subtracting the continuum and background and deconvolving the result into distinct Gaussian-shaped peaks. In this manner we eliminated contributions from the strong satellite lines of the Ly-α transitions and the Cl He-β line at 3.27 keV.) The Ar Ly-α strength effectively normalizes the Cl Ly-α strength to the specifics of capsule performance such as capsule size, laser drive, and diagnostic calibration.

Figure 6 shows this comparison of observed and simulated emission spectra by means of the ratio of time-integrated Ly-α lines for all nine shots. The ratio of emission strength smoothly changed a factor of ~9 for a surface rms change of ~50. Figure 7 shows observed and simulated mixed neutron yield over clean yield vs rms surface finish for the same nine-shot data set.

To test the importance of the saturation modeling, we also estimated the perturbation growth with unmodified linear analysis. The modification due to saturation is quite small, and given the large spread in experimental results, no conclusion can be made regarding the correctness of the saturation modeling procedure.

Conclusion

Both the observed x-ray emission and neutron yield from the 1-ns-drive Nova implosions show significant variation as a function of initial capsule surface finish. Furthermore, we can successfully interpret this variation as a dependence of pusher–fuel mix on initial surface roughness. This interpretation derives from modeling based on linear analysis using multiple 2-D LASNEX simulations and 1-D mixed implosion modeling using LASNEX and DCA to simulate neutron output and x-ray emission of included dopants.

Acknowledgments

The authors wish to thank Craig Moore for his efforts in capsule characterization, Ravi Upadhye and Blanca Haendler for their early work in rough-surfaced capsule fabrication, and Steve Langer, Steve Hatchett, and Yim Lee for assistance in simulation details.

Notes and References

1. B. A. Remington, S. V. Weber, S. W. Haan, J. D. Kilkenny, et al., *Phys. Fluids B* **5**, 2589–2595 (1993).
2. J. S. Wark, J. D. Kilkenny, A. J. Cole, M. H. Key, and P. T. Rumsby, *Appl. Phys. Lett.* **48**, 969–971 (1986).
3. H. Nishimura, H. Takabe, K. Mima, F. Hattori, et al., *Phys. Fluids* **31**, 2875–2883 (1988).
4. W. Mead, A. Hauer, Los Alamos National Laboratory, Los Alamos, NM, private communication, 1988.
5. D. K. Bradley, J. A. Delettrez, and C. P. Verdon, *Phys. Rev. Lett.* **68**, 2774–2777 (1992).
6. J. Delettrez, D. K. Bradley, P. A. Jaanimagi, and C. P. Verdon, *Phys. Rev. A* **41**, 5583–5593 (1990).
7. B. A. Hammel, C. J. Keane, T. R. Dittrich, D. R. Kania, et al., *J. Quant. Spectrosc. Radiat. Transfer* **51**, 113–124, (1994).
8. A. A. Hauer, N. D. Delamater, and Z. M. Koenig, *Laser and Particle Beams* **9**, 3–48 (1991).
9. C. J. Keane, B. A. Hammel, D. R. Kania, J. D. Kilkenny, et al., *Phys. Fluids B* **5**, 3328–3336 (1993).
10. S. A. Letts, D. W. Meyers, and L. A. Witt, *J. Vac. Sci. Technol.* **19**, 739–742 (1981).
11. S. Pollaine, S. P. Hatchett, S. H. Langer, *ICF Quarterly Report* **4**(3), 87–89, Lawrence Livermore National Laboratory, Livermore, CA, UCRL-LR-105820-94-3 (1994).
12. B. A. Hammel, C. J. Keane, M. D. Cable, D. R. Kania, et al., *Phys. Rev. Lett.* **70**, 1263–1266 (1993).
13. B. A. Hammel, P. Bell, C. J. Keane, R. W. Lee, *Rev. Sci. Instrum.* **61**, 2774–2776 (1990).
14. G. B. Zimmerman, W. L. Kruer, *Comments on Plasma Physics and Controlled Fusion* **2**, 51–61 (1975).
15. S. W. Haan, *Phys. Rev. A* **39**, 5812 (1989).
16. Y. T. Lee, D. S. Bailey, and G. B. Zimmerman, *Laser Program Annual Report 1985*, UCRL-50021-85, 2.81–2.86 (1985).
17. Y. T. Lee, *J. Quant. Spectrosc. Radiat. Transfer* **38**, 131–145 (1987).
18. C. J. Keane, R. W. Lee, and J. P. Grandy, in *Proceedings of the 4th International Workshop on the Radiative Properties of Hot Dense Matter*, Eds., W. Goldstein, C. Hooper, J. Gauthier, J. Seely, and R. W. Lee (World Scientific, Singapore, 1991), p. 233.
19. R. W. Lee, B. L. Whitten, and J. E. Strout, III, *J. Quant. Spectrosc. Radiat. Transfer* **32**, 91 (1984).

HIGH-GROWTH-FACTOR IMPLOSIONS (HEP4)

O. L. Landen *N. D. Hoffman** *M. D. Cable* *H. N. Kornblum*
C. J. Keane *J. D. Colvin** *R. Cook* *R. A. Lerche*
B. A. Hammel *P. A. Amendt* *T. R. Dittrich* *R. L. McEachern*
W. K. Levedahl *S. P. Hatchett* *S. W. Haan* *T. J. Murphy*
*R. E. Chrien** *M. M. Marinak* *R. G. Hay* *M. B. Nelson*
L. J. Suter *R. J. Wallace*

Introduction

In inertial confinement fusion (ICF),[1,2] the kinetic energy of an ablating, inward-driven, solid spherical shell is used to compressionally heat the low-density fuel inside. For a given drive, the maximum achievable compressed fuel density and temperature—and hence the maximum neutron production rate—depend on the degree of shell isentropy[2,3] and integrity maintained during the compression. Shell integrity will be degraded by hydrodynamic instability growth[2,4–7] of areal density imperfections in the capsule. Surface imperfections on the shell grow as a result of the Richtmyer–Meshkov[8] and Rayleigh–Taylor[9] (RT) instabilities when the shell is accelerated by the ablating lower-density plasma. Perturbations at the outer capsule surface are transferred hydrodynamically to the inner surface, where deceleration of the shell by the lower-density fuel gives rise to further RT growth at the pusher–fuel interface. A widely used dispersion relation[5,10] for the RT growth rate γ in the presence of a density scalelength L and a mass ablation rate dm/dt is

$$\gamma = \left[\frac{kg}{(1+kL)}\right]^{1/2} - \frac{\beta k}{\rho}\frac{dm}{dt}, \qquad (1)$$

where k is the wave number of the seeding perturbation, g is the acceleration or deceleration, β is a constant between 1 and 3 determined empirically, and ρ is the peak shell density. Equation (1) indicates that γ increases as interfaces become sharper (smaller L), as peak shell densities increase, and as mass ablation rates decrease.

Implosion Design

In the HEP3 implosion campaign,[6] the unsaturated to weakly nonlinear low-growth regime was studied. See the previous article, "Diagnosis of Pusher–Fuel Mix in Indirectly Driven Nova Implosions (HEP3)," p. 265 for a discussion. Unshaped drive pulses and low-opacity plastic capsules were used, which allowed strong shock and hard x-ray preheating. This led to shallower ablation-front gradients and lower shell densities during the implosion phase. The goal of the HEP4 campaign was to increase susceptibility to RT growth in a more isentropic implosion. HEP4 designs[11] have used shaped drive, and x-ray preheat shielding,[12] by adding mid-Z dopants in the capsule ablator for reducing preheat.

Role of Doped Ablators

Use of a mid-Z dopant in the ablator has three principal effects. First, these dopants are chosen to preferentially absorb the 1–3-keV x rays (arising from the Au hohlraum laser plasmas) that volumetrically preheat Nova-scale plastic shells most efficiently. A cooler shell will expand less quickly, thereby maintaining a higher shell density ρ and steeper interface density gradients for a longer time.[13] Second, doping reduces the ablation scalelength by reducing the distance over which the soft drive x rays[14] are absorbed. Third, the increase in shell density leads to a thinner shell during compression and thus gives rise to more efficient feedthrough of surface perturbations with skin depths $\approx 1/k$. These effects combine to increase predicted maximum linear growth factors GF (ratios of final pusher–fuel to initial outside surface perturbation amplitudes) from 10 to 110 as the doping is increased from 0 with no pulse shaping (HEP3 conditions)[6] to 2 at.% Ge or Br

* Los Alamos National Laboratory, Los Alamos, New Mexico

with a two-step pulse (HEP4 conditions).[13] Mid-Z dopants, in particular Br, were used extensively to increase growth factors[15] in planar RT experiments[16] conducted in the HEP2 campaign.

A linear GF of 100, for example means that, in the absence of saturation, an initial perturbation amplitude of 0.1 μm with mode number $l = kr(t)$ on the surface of a capsule of radius r would lead to a 10-μm perturbation of the same mode number at the pusher–fuel interface at peak neutron production time. In general, a full spectrum of randomly phased modes will initially be present. Each mode number will have a different predicted GF through the dependence on wave number k in Eq. (1). Growth of high-mode-number perturbations (large k) is reduced by ablation, density gradients, inefficient feedthrough, and (when amplitudes become comparable to the wavelength) by the onset of saturation. Long wavelengths (small k) have low growth rates from the outset. One can therefore expect a bell-shaped growth factor spectrum that peaks near some intermediate mode number.[13]

Instability Growth Modeling

Until recently, three-dimensional (3-D) codes handling multimode growth up to and beyond saturation have not been available or practicable. In their place, a multimode mix model[4,6] has been used extensively, as described more fully in "Diagnosis of Pusher–Fuel Mix in Indirectly Driven Nova Implosions (HEP3)" on p. 265 of this *Quarterly*. Briefly, a series of linear single-mode growth-rate simulations is used to calculate the amplitude evolution of each mode initially present on the capsule surface, starting with amplitudes small enough to ensure that the growth remains linear throughout the implosion. The time dependence of the linear mode amplitudes are then obtained by multiplying these growth factors by the initial amplitude spectrum. If the individual amplitudes grow large enough ($\geq 2r/l^2$), they are corrected for saturation in the presence of a full spectrum of modes.[4] The quadrature sum of the perturbation amplitudes fed through to the pusher–fuel interface is then used to set the annular width for a one-dimensional (1-D) model of atomically mixed shell and fuel located at the shell–fuel interface. A 1-D implosion simulation incorporating this evolving mix layer is then used to predict observables such as neutron yield. The yield drops as the calculated mix width becomes a larger fraction of the converged fuel radius, principally because of enhanced conduction cooling by shell material penetrating closer to the central, hottest fuel region, which provides most of the fusion reactions.

Figure 1 shows the calculated mix amplitudes (normalized to converged fuel radius at peak neutron emission time and defined as approximately one-third the mix width) vs initial outside surface roughness for the low-growth HEP3 implosions, the present HEP4 implosions, and the proposed National Ignition Facility (NIF) conditions.[17] The gray lines with unit slope correspond to assuming no growth saturation. The departure from unit slope for each black curve signifies the predicted onset of growth saturation. A typical intrinsic surface roughness power spectrum was assumed for these calculations. The large fractional mix widths calculated for the NIF implosions are a consequence of the more elaborate pulse shaping used to keep NIF implosions nearly isentropic. Ignition for NIF will require that the final mix amplitude not exceed about one-fifth of the converged capsule radius.[17] This criterion is equivalent to a factor of ~2 yield reduction for nonigniting target designs such as those used in HEP3 and HEP4. The present HEP4 experiments were designed to span both sides of this threshold by varying initial surface roughnesses from 0.01 μm rms upward, while approaching the growth factors expected of the NIF targets.

Figure 1 shows that a necessary condition for ignition sets the upper limit on initial capsule outside surface finish at a currently achievable roughness of 0.03 μm rms. If there were no growth saturation, NIF capsules would need to be considerably smoother (by a factor of 2), which is at the limit of current technology. A specific goal of the HEP4 campaign was therefore to test the validity of the growth saturation model.

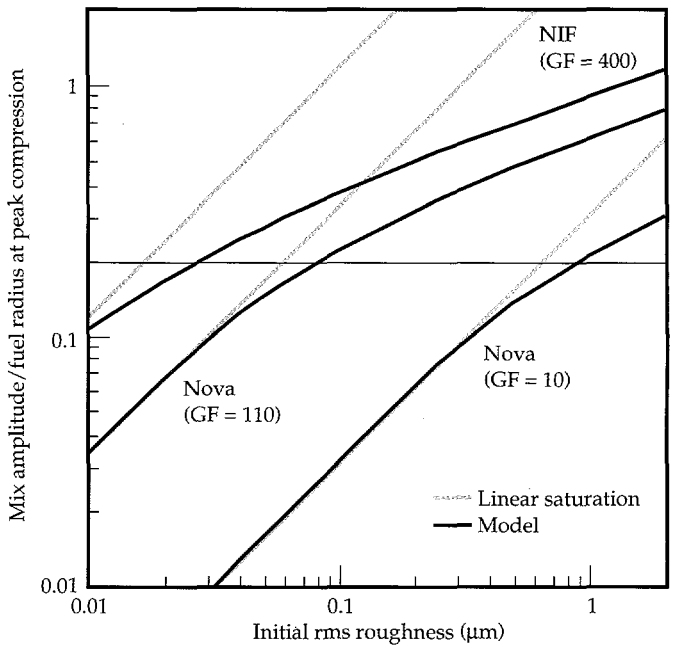

FIGURE 1. Calculated mix amplitude (normalized to fuel radius at peak neutron emission time) vs initial surface roughness. Starting from the right, the three curves correspond to the low-growth HEP3 design, the present higher-growth HEP4 design, and the NIF design. Black and gray curves correspond to calculations with and without growth saturation, respectively. The section of the NIF curve above a normalized mix amplitude of 0.2 corresponds to loss of ignition. (20-03-0995-2096pb01)

Capsule Design

Figure 2 shows the cross section of a typical capsule. The ablator, a 1.1–1.3 g/cm^3 plasma-polymerized plastic ($CH_{1.3}$), typically 39 μm thick, is doped[18] with up to 3 at.% Br or Ge. The early experiments used Br doping; the later experiments switched to Ge, which was more robust and easier to fabricate. A 3-μm polyvinyl alcohol (PVA) intermediate layer serves to confine the fuel. In early experiments, the inner polystyrene shell (~440 μm i.d. and 3 μm thick) was doped with 0.07 at.% Ti. The fuel consists of 25 atm each of D_2 and H_2, doped with 0.05 at.% Ar. The dilution of the D with H was necessary to avoid saturation in the secondary-neutron detector. The Ar and Ti serve as noninvasive emission diagnostics of electron temperature and electron density and of the spatial profile of the fuel and shell during the burn phase. Figure 3 shows the initial shell optical depth vs photon energy and shows, for example, that 1.3 at.% Ge doubles the initial capsule optical depth above the Ge (n = 2) bound–free absorption edge at 1.2 keV. Simulations using the measured photon flux above 1.2 keV indicate that such shielding reduces the entropy of the inner shell surface relative to the undoped case by 20% before the first shock arrives at 1 ns.

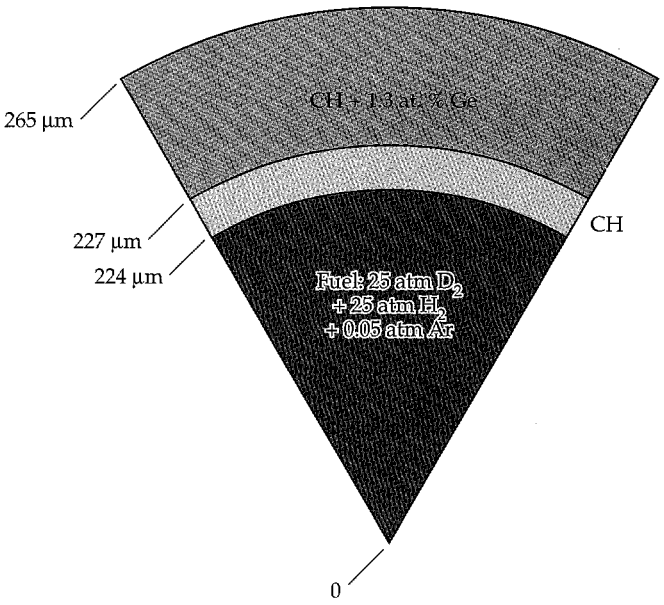

FIGURE 2. Cross section of a typical deuterated-fuel capsule design. (20-03-0995-2107pb03)

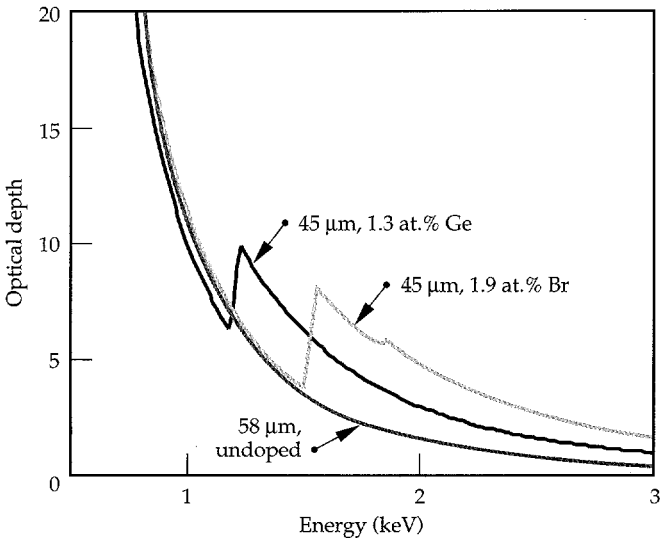

FIGURE 3. Initial capsule ablator opacity vs photon energy for 58-μm-thick undoped plastic ablators and for 45-μm-thick 1.3 at.% Ge and 1.9 at.% Br-doped plastic ablators. (20-03-0995-2099pb01)

The RT seeding is provided by pre-roughening the capsule surface by ultraviolet (UV) laser ablation[19] of 200 randomly distributed 75-μm-diam pits of equal depths, which yields a continuous distribution of perturbation wave numbers. The surface roughness is quantified by averaging a series of circumferential depth profiles obtained by atomic force microscopy.[20] The profiles are Fourier-transformed to yield 1-D power spectra, which are found to be in excellent agreement with spectra predicted by a model assuming randomly located pits of the measured shape. By assuming isotropy, 1-D spectra can be converted[21] to 2-D power spectra, which serve as input to simulations. A simple measure of the surface roughness is taken to be the square root of the summed power spectra, expressed as a rms roughness. For the purposes of defining roughness, the lowest order modes (l < 10), which grow the least according to Eq. (1), are not included. By varying the pit depths, rms roughnesses so defined covered the range between 0.01 and 2 μm.

Hohlraum Drive

The capsules are mounted in the center of a 2400-μm-long, 1600-μm-diam Au hohlraum with 1200-μm-diam laser entrance holes on each end. A hohlraum of pentagonal cross section was used to avoid line focusing of reflected laser light onto the capsule surface, as is observed with cylindrical hohlraums. X-ray and optical measurements indicate that such line foci reach irradiances of 10^{14} W/cm^2 over the first 200 ps, which could seed RT-unstable perturbations of similar magnitude to some of the smaller amplitude ablated pits.

The soft x-ray drive was generated by irradiating the inner hohlraum walls with ten accurately synchronized (10 ps rms fluctuation), precision-pointed (30 μm rms fluctuation), power-balanced (<10% rms fluctuation),[22] 0.35-μm, 2.2-ns-long, 3-kJ Nova pulses. Figure 4(a) shows the absorbed power from a ramped pulse shape, called PS26, chosen to provide reduced shock preheating[23] and to more closely approximate ignition-scale drive. The average x-ray flux at the capsule, plotted in Fig. 4(a) as a blackbody flux temperature, was inferred from filtered, time-resolved, multichannel (Dante)

measurements[24] of x-ray re-emission from the hohlraum walls. Measurements were performed on both laser-irradiated and unirradiated walls.[25] The drive was independently inferred from simultaneous UV shock breakout measurements[26] using Al wedges [Fig. 4(b)]; the results are in good agreement with simulations based on the measured drive shown in Fig. 4(a). The peak drive temperature was 237 ± 7 eV; the uncertainty corresponds to a factor of 2 uncertainty in calculated neutron yield.

Harder x rays emanating from the high-temperature, low-density Au laser plasmas (principally Au $n = 4$ to $n = 3$ and $n = 5$ to $n = 3$ transitions between 2 and 4 keV) are also present. Figure 3 shows that the ablator optical depth is only 1 to 2 for these x rays, making them an important source of preheating of the inner shell. Their fractional contribution to the total drive at the capsule (shown in Fig. 5) was determined from a solid-angle average formed by combining the Dante localized absolute flux measurements with 2-D spatially resolved x-ray images of the hohlraum wall. We attribute the initial spike in the hard x-ray fraction to reflected laser light efficiently illuminating much of the hohlraum walls; 0.1 ns later, plasma expansion has greatly diminished the reflectivity and localized the hard x-ray production at the first-hit locations of the laser. The error bars represent only Dante uncertainties; the assumption of an optically thick Lambertian source for the harder x rays may result in an additional 2× underestimate of their fraction. However, simulations show that admitting a total factor of 3 underestimate in hard x-ray fraction will decrease yields for 1.3 at.% Ge-doped capsules by only 30%.

Deuterated Fuel Capsules

The implosions are diagnosed by primary and secondary neutron yields,[27] neutron production times,[28] time-resolved x-ray imaging,[29] and time-resolved x-ray spectroscopy of tracer dopants in the shell and fuel.[13,23,30,31] The results of an early campaign with Br-doped capsules have been published elsewhere.[30] The newer Ge-doped capsule implosion results described here have been more thoroughly characterized and modeled. Results are compared with predictions made using the 2-D radiation hydrodynamics code LASNEX.[32] A new 3-D radiation hydrodynamics code, HYDRA,[33] is also being used to simulate these high-growth-factor implosions.

Performance vs Preheat Shielding

The first HEP4 implosions served to test our understanding of the behavior of the smoothest available plastic capsules as ablator doping was increased. In the limit of negligible RT growth, one would expect that the increase in in-flight shell density ρ due to preheat shielding provided by the mid-Z dopant would improve capsule performance. Specifically, for a fixed implosion velocity v, the compressional pressure[2,3,10] ρv^2 that determines the final fuel areal density and yield achievable should increase with ρ.

Figure 6 shows that the measured yield does indeed increase with Ge doping, with a slope consistent with that of the corresponding 1-D simulations. Peak neutron production times (2.2 ± 0.1 ns) and hence implosion velocities were kept fixed by varying the initial ablator thicknesses (from 44 μm at 2 at.% Ge to 58 μm for undoped ablators) to compensate for changes in initial shell density and opacity when incorporating Ge in the ablator. Capsules were selected for best surface finish

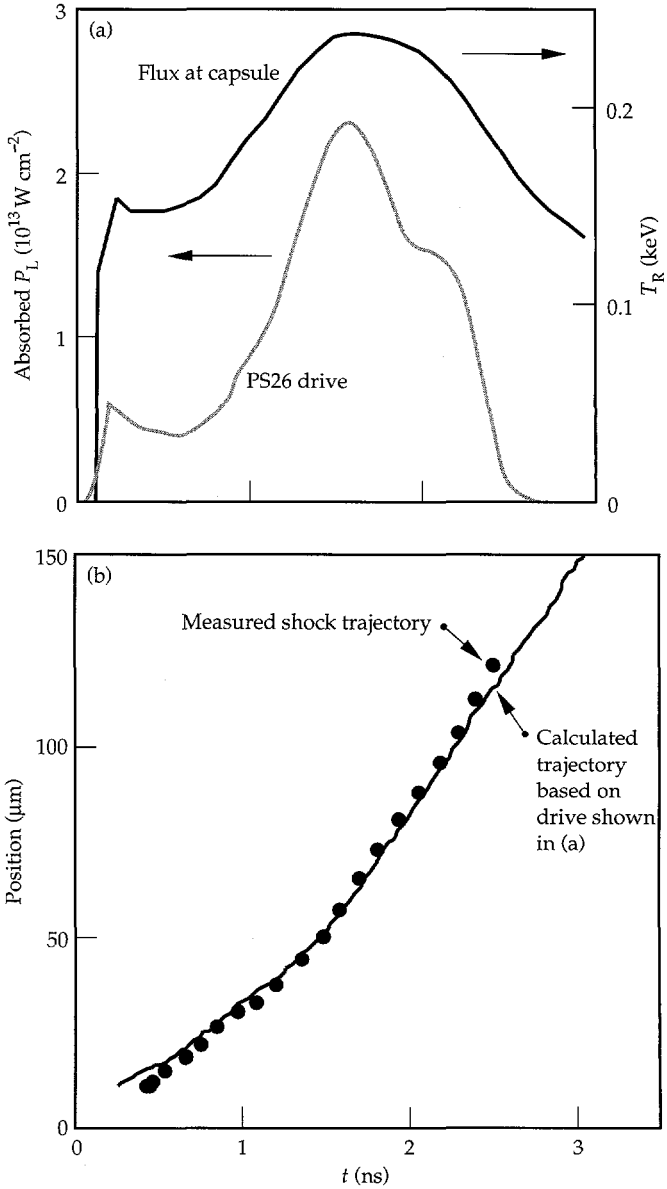

FIGURE 4. (a) Measured absorbed laser power and measured soft x-ray flux (plotted as a blackbody flux temperature) from absolutely calibrated filtered diode array (Dante). (b) Measured shock trajectory in Al wedge and corresponding predicted trajectory based on the x-ray drive in (a). (20-03-0995-2100pb01)

(<0.03 μm rms roughness). The simulations used the measured drive flux and spectrum at each time as baseline input, with slight modifications for (<10%) shot-to-shot variations in laser energy and capsule dimensions. The systematic factor of 3–4 discrepancy between simulated and measured yields for smooth capsules is not completely understood, but 3-D calculations which include long wavelength shell thickness variations significantly reduce this discrepancy. These calculations are described in the section "Recent Modeling Advances." Nevertheless, the increase in yield as preheat shielding is increased for best surface finish capsules is encouraging for NIF, because it demonstrates a hydrodynamically similar implosion for which the beneficial effects of a more isentropic compression outweigh the detrimental effects of increased susceptibility to RT growth.

Figure 7 displays 4-keV x-ray snapshots showing a reduction in imploded core image size as the ablator doping is increased from zero to 1.3 to 2.7 at.% Ge. The core images, captured with 7-μm and 80-ps resolution by gated pinhole cameras, are dominated by Ar bound–free emission from the doped fuel. Figure 7(d) shows the azimuthally averaged 50% contour diameters extracted from such images. The average measured x-ray radii decrease monotonically with increasing Ge doping, with a slope consistent with post-processed 2-D integrated hohlraum and capsule simulations of image size, but with an overall 30% size reduction.

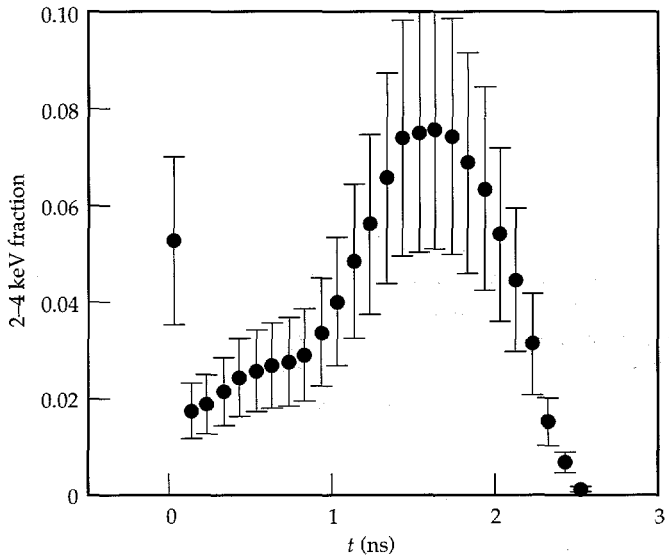

FIGURE 5. Measured 2–4-keV hohlraum power as a fraction of total x-ray power. Error bars represent uncertainty in Dante calibration and unfold only. (20-03-0995-2101pb01)

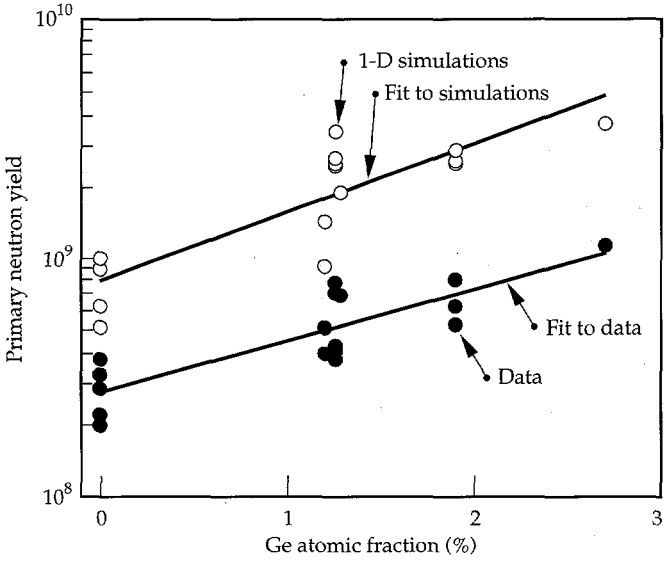

FIGURE 6. Measured and calculated primary (DD) neutron yields vs doping for smooth capsules. Solid lines are linear fits to data and simulations. (20-03-0995-2103pb01)

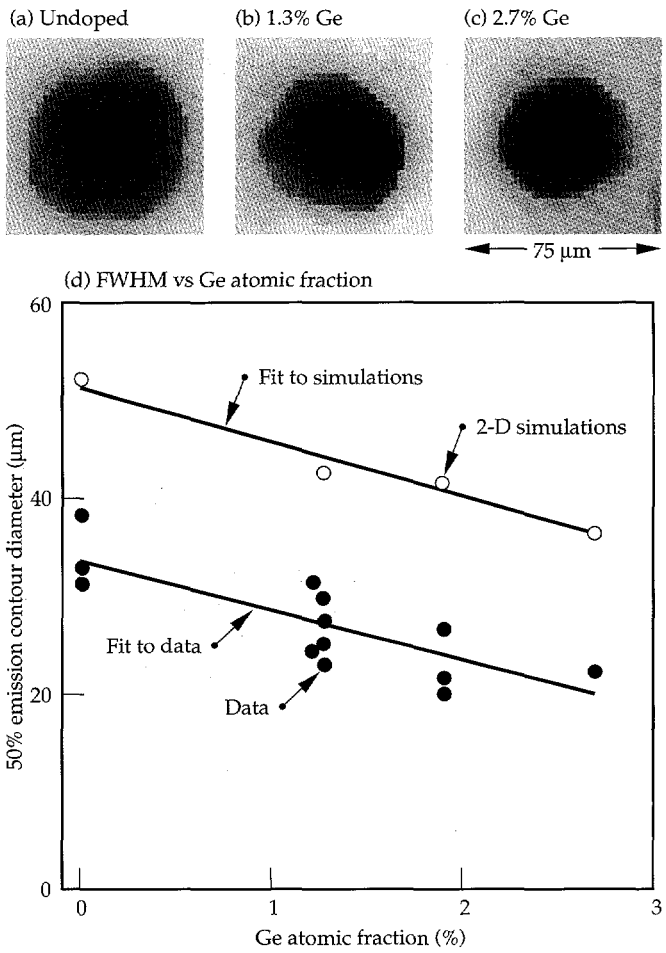

FIGURE 7. X-ray images at 4 keV of imploded cores from smooth capsules at peak emission time for (a) no doping, (b) 1.3 at.% Ge, and (c) 2.7 at.% Ge. (d) Measured (solid circles) and calculated (open circles) azimuthally averaged diameters of 50% x-ray emission contours vs Ge doping. Solid lines are linear fits to data and simulations. (20-03-0995-2102pb01)

Fuel areal densities and (by invoking particle conservation) fuel convergences were also inferred from the fraction of secondary DT reactions and the resultant secondary-neutron energy spectrum[27] measured by a large neutron scintillator array (LaNSA). This diagnostic technique, used extensively in the HEP1 campaign,[25] works on the principle that the triton produced in the primary DD reaction undergoes secondary DT reactions with a probability that depends on the areal density of deuterons seen by the escaping triton. At all Ge dopings, the inferred fuel convergences are within 10% of the values obtained from simulations. To reconcile the x-ray size discrepancy with the agreement in convergence, we note that emissivities for kilovolt x-ray photons are sensitive to sub-kilovolt variations in plasma temperature, while the secondary reaction between MeV tritons and deuterons is not. Hence the 30% overprediction in x-ray core image size shown in Fig. 7(d) may be evidence that the simulations, while correctly predicting the final fuel radius, overpredict the plasma temperature in the outer regions of the compressed fuel. Such increased cooling is seen in 3-D calculations which include long wavelength variations in capsule wall thickness.

Spatially integrated, time-resolved spectra of Ar and Ti line and continuum emission were also recorded during the fusion phase.[30] The emission lines of interest are those of He-like Ti ($1s2p–1s^2$) and of optically thin He-like Ar ($1s3p–1s^2$) and H-like Ar (3p–1s). The measured Ar and Ti line durations for 1.9 at.% Br-doped capsules were 150 and 80 ps FWHM, respectively, half the corresponding durations for undoped capsules and in good agreement with simulations. Predicted H-like emission from the Ti dopant in the inner portion of the shell was not observed, again suggesting that the volume comprising the outer regions of the fuel and the inside of the shell is cooler than expected.

The agreement between measured and predicted trends in capsule performance as preheat shielding is increased indicates that the goal of mimicking more isentropic NIF-like implosion conditions has been attained. Specifically, smaller cores, shorter burn phases, and higher neutron production rates are observed as preheat shielding is increased.

Performance vs Surface Roughness

Figure 8 shows primary neutron yield for undoped and doped capsules vs initial surface roughness. Between best surface finish (<0.03 μm rms) and 1 μm rms roughness, the yields of undoped capsules drop by a factor of only 1.5, while those of 1.3 at.% Ge-doped capsules drop by a factor of 6. This finding is qualitatively consistent with the transition from low- (GF ~10) to high-growth-factor (GF = 110) behavior expected with doping. Moreover, we observe a statistically significant factor-of-2 yield degradation between doped capsules with best surface finish and doped capsules with 0.1-μm rms roughness; from Fig. 1, the latter correspond closely to the 20% mix fraction growth that determines the NIF ignition threshold.

Figure 9 compares the averaged doped capsule yields vs surface finish with various simulation results. The lowest curve, which represents the atomic mix model with no saturation, severely overestimates the yield degradation for large initial surface roughnesses. The other curves represent the same model corrected for the different saturation behavior predicted for 3-D or 2-D multimode growth.[34] The atomic mix models are in fairly good agreement with data at the rough end. As discussed in the section on 3-D modeling advances, the factor of 3–4 yield discrepancy, which remains at the smooth capsule end can be largely accounted for by long wavelength capsule wall thickness variations. The larger yield degradation calculated for the 3-D saturation model is a consequence of the later onset of saturation[4] and of the higher terminal velocity of low-density 3-D fuel bubbles rising into the shell. The atomic mix model with the 2-D saturation prescription, although not strictly comparable with the 3-D nature of perturbation growth in the experiment, is included to show good agreement with 2-D finely zoned multimode simulations (shown as triangles).

These multimode simulations, which follow perturbation growth past saturation and do not need to combine modes into a 1-D mix description, were made possible by using only a few photon groups.[33] This method is

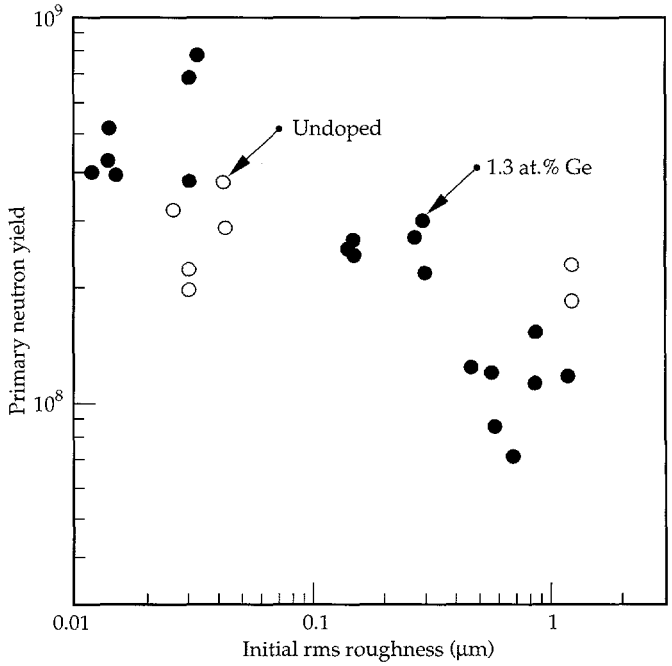

FIGURE 8. Measured primary neutron yields for 1.3 at.% Ge-doped (solid circles) and undoped (open circles) capsules vs initial rms surface roughness. (20-03-0995-2104pb01)

only applicable when diffusive radiation transport is used, speeding up computer simulations. The 3-D nature of the perturbations is accounted for by adjusting the 2-D surface power spectra so that each mode makes the same relative contribution to the total rms roughness as in three dimensions. As 2-D simulations are carried out on a 90° quadrant, power in odd modes is "aliased" into the adjacent even modes. At peak neutron emission time, the 2-D simulations show classic "bubble and spike" saturated RT growth for the dominant modes at the pusher–fuel interface for initial surface roughnesses greater than 0.1 μm. The effects of low-mode drive nonuniformities, which distort the pusher–fuel interface, were included in some 2-D multimode calculations. For example, the predicted extra yield degradation due to flux nonuniformities for a smooth, doped capsule is ~30%, as shown by the square in Fig. 9. More appropriate 3-D multimode simulations treating such flux asymmetries in their exact 3-D orientations are described under Recent Modeling Advances, below. In particular, the effects of synergism between growth of low-order surface perturbations and flux asymmetry–seeded perturbations are quantified there.

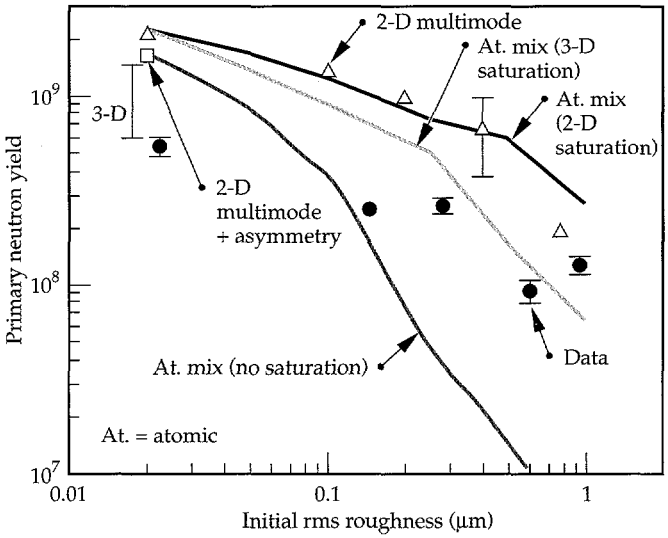

FIGURE 9. Measured and calculated primary neutron yields for 1.3 at.% Ge-doped capsules vs initial surface roughness. Solid circles are averaged data points from Fig. 8. Solid curves are predictions from the atomic mix model with no saturation, with a 2-D saturation, and with a 3-D saturation prescription. The square and the triangles are predictions from 2-D multimode simulations with and without flux nonuniformities. The vertical line at the upper left represents the range of yields calculated by the 3-D HYDRA code for a smooth capsule by varying the relative orientation between low-order capsule and radiation flux nonuniformities. (20-03-0995-2105pb01)

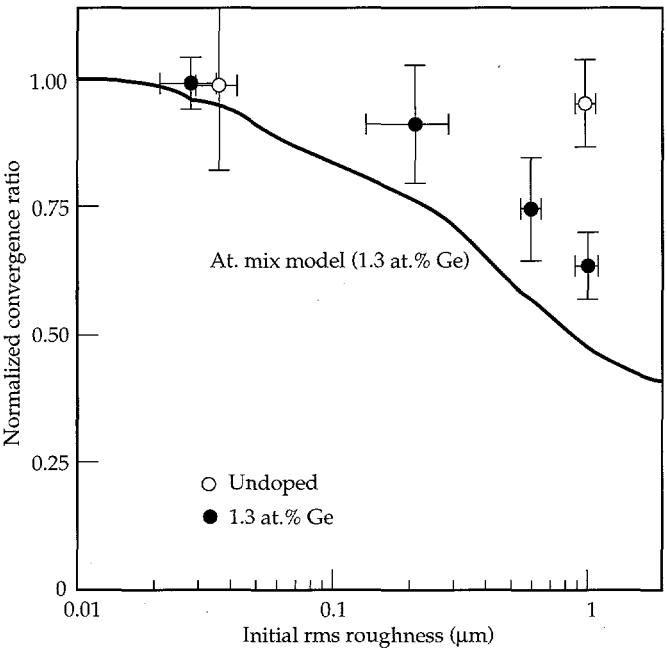

FIGURE 10. Relative capsule convergence (inferred from secondary neutron yields and spectra) vs initial surface roughness for undoped and 1.3 at.% Ge-doped capsules. The curve is a prediction for 1.3 at.% Ge doping, using the atomic mix model with 3-D saturation. Convergences are normalized to calculated convergence for smooth, doped capsules. (20-03-0995-2106pb01)

Figure 10 shows relative capsule convergences inferred from secondary-neutron yields and spectra from doped and undoped capsules vs initial surface roughness. The data points are averaged over capsules of similar roughness, and standard errors are shown. As expected, only the convergence of the high-growth, doped capsule drops significantly as capsule surface roughness is increased to 1 μm rms. The solid line is in fair agreement with the data. It represents post-processed predictions of the inferred convergence for 1.3 at.% Ge doping based on following the triton trajectory through both the pure fuel and the 1-D atomically mixed layer.

Figures 9 and 10 show that the primary and secondary gas yields are best suited to inferring large mix fractions. This is because the gas yield for nonigniting capsules is dominated by the hottest (central) region, which is farthest from the pusher–fuel interface and least affected by conduction cooling. By contrast, shell conditions can be most sensitive to small amounts of mix as penetrating spikes of shell material enter a region of steeply rising temperature.[6,13] For the lower-convergence HEP3 targets, moderate shell–gas mix was inferred from ratios of shell to gas dopant x-ray line emissivities.[6] Analogous measurements[23,30] attempted for HEP4 are sensitive to the significant x-ray reabsorption by the more converged and compressed shells. For example, for the Ar 3–1 lines, the shell optical depth at peak neutron production time is ~5.[13]

Deuterated-Shell Implosions

One technique for circumventing the problem of high shell x-ray opacity in inferring shell mix is to measure the neutron yields from capsules with deuterated shells.[35] Figure 11 shows a cross section of the capsule design. The only differences with respect to the usual capsule (Fig. 2) are a 75-atm H fill (to provide

an inert fill with the same convergence as the 50-atm fill shown in Fig. 2) and a 4-μm-thick deuterated polystyrene inner shell. Peak growth factors are a factor of 2 higher, principally because the shell yield (which depends on thermal conduction) is delayed with respect to the fuel yield, allowing more time for perturbation growth. Small amounts of mix should now act to increase the yield by introducing D into the hotter central gas region. For example, the fusion rate at the ~1-keV temperature of interest and for an ion density n scales as n^2T^7, and hence as T^5 for a profile with constant pressure nT. For larger mix fractions, compression is reduced (see Fig. 10), reducing temperatures throughout the capsule. Therefore, after an initial rise in yield with increasing mix fraction, a drop in shell yield might be expected.

Figure 12 shows the observed dependence of shell primary yield on surface roughness. The implosion conditions were identical to those in the deuterated-fuel implosions except for a 7% lower drive designed to reduce ultra-hard x-ray contamination of the neutron diagnostics measuring the low yields. The yield remains nearly constant with increasing surface roughness up to 0.5 μm and finally falls for rougher surfaces. The standard atomic mix model with 3-D saturation, shown as the middle curve in Fig. 12, predicts only a slight increase in yield with surface roughness, in fair agreement with the data. The explanation for this behavior is that the shell yields are sensitive to an additional ingredient in the model that does not affect gas yields: an enhanced heat diffusivity term scaling as $\alpha L(dL/dt)$ over the 1-D mix layer of width L, where α is a heat diffusivity multiplier.[13] This extra heat flow is used to mimic the heat dilution that occurs as the surface area of a more realistic RT-modulated interface grows. The middle curve in Fig. 12 uses $\alpha = 1$, but the result changes little for α between 0.5 and 2. If α is set to 0, the top curve results, in significant disagreement with the data. The reduction in yield with enhanced heat diffusivity is a consequence of reducing temperature gradients in the mix region, thereby dropping peak temperatures in the innermost shell region, which dominates the yield. For NIF 1-D capsule designs, such a heat flux term is essential in the 1-D atomic mix model to correctly account for heat transfer from the inner hot DT gas to the outer cold DT pusher. The absence of H-like Ti shell emission in earlier experiments is also more consistent with a reduction in shell temperature gradients. By contrast, gas yields are factors of 5 less sensitive than shell yields to the heat diffusivity term; in the atomic mix predictions of gas yields shown in Fig. 9, we used $\alpha = 1$.

Figure 12 also shows predictions of 2-D multimode ($l = 2, 4, 6, \ldots, 48$) and single-mode ($l = 24$) calculations, which are in good agreement with the data and with the atomic mix model, including enhanced heat diffusion. The simpler single-mode simulations assume that all the roughness is concentrated in a dominant mode. The predicted yields fall rapidly at about 0.4 μm rms roughness, for which the increased heat losses to the deuterated layer are insufficient to raise or even maintain the D temperature because of the reduced compressional

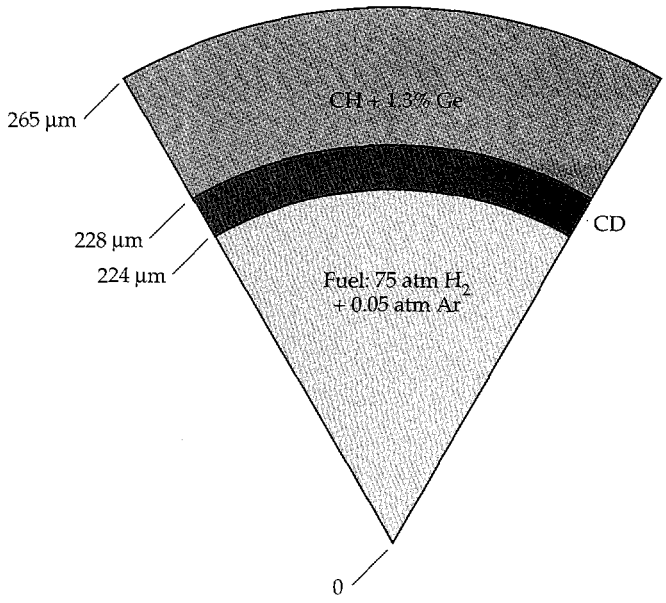

FIGURE 11. Cross section of a typical deuterated-shell capsule design. (20-03-0995-2107pb02)

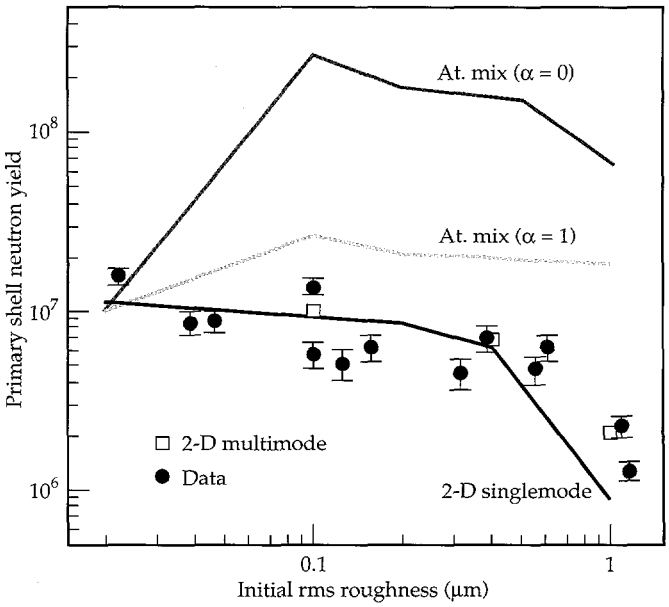

FIGURE 12. Measured and calculated primary yields for 1.3 at.% Ge-doped deuterated-shell capsules vs initial surface roughness. Solid circles are the data with experimental uncertainties. The top and middle curves are predictions from the atomic mix model without ($\alpha = 0$) and with ($\alpha = 1$) enhanced heat diffusion. The lower curve and squares are predictions from 2-D single-mode ($l = 24$) and multimode ($l = 2, 4, 6, \ldots, 48$) simulations. (20-03-0995-2107pb01)

heating of the gas. For example, the peak compressional heating power in the implosion of a capsule with 1 μm rms roughness is only 72% of the unperturbed value. The simulations indicate shell breakup for capsules above 0.4 μm rms roughness.

Recent Modeling Advances

In current HEP4 work, we have advanced to 3-D modeling using the new HYDRA code.[33] Simulations in progress include modeling of both multimode and single-mode perturbation growth; additional distortion from radiation flux asymmetries can be included. The code uses multigroup radiation diffusion.

Figure 13 shows a snapshot of the ablation front and pusher–fuel interface for a typical single-mode growth simulation ($l = 18$) of a 0.25-μm rms perturbation. The interfaces shown represent an isodensity surface at 17.2 g/cm^3, 40 ps before peak neutron production time. The white contour lines show the 90° × 36° repeating sector used in the simulation. The 92 pits on the outside surface (modeled as hyperGaussians) have fed through to form bubbles of fuel rising into the shell and parabolic ridges of shell material penetrating the fuel. A Kelvin–Helmholz instability at the fuel–pusher interface causes significant roll-up in the bubble tips. The calculated yield was 82% of the yield for a perfectly smooth capsule surface.

Recently, the measured lowest-order capsule imperfections have been added to the input of a 3-D multimode simulation, which included radiation flux asymmetries. In particular, the importance of a worst-case 5-μm variation in capsule shell thickness from pole to equator has been studied. By aligning the capsule so that the thinnest part of the shell faces the hohlraum midplane, where a combination of P_2 and $m = 5$ radiation flux asymmetries already act coherently, 3-D HYDRA simulations predict a 60% drop in yield, from 1.44×10^9 to 6×10^8 (see Fig. 9). The yield drops sharply because the thinner sections of the shell converge faster and allow spikes of shell material from RT growth of $m = 5$ seeded perturbations to meet at peak neutron emission time. Hence, the scatter in the smooth capsule yields may be due to the arbitrary capsule-to-hohlraum orientation inherent during target assembly and the variable amplitude of lowest-order fluctuations in capsule shell thickness.

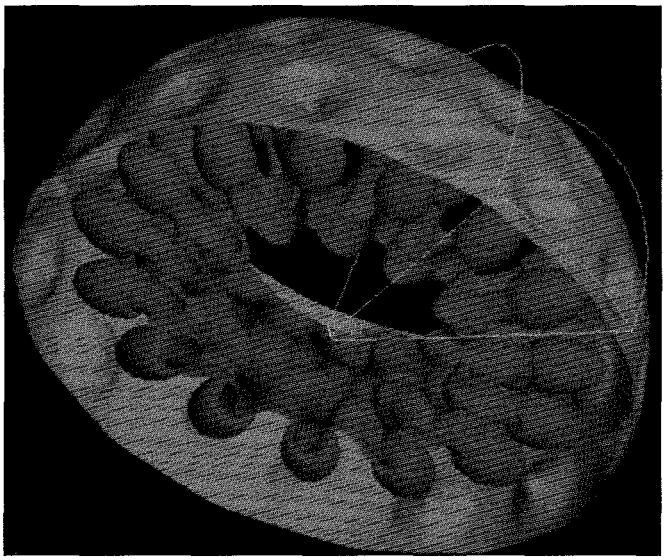

FIGURE 13. Three-dimensional simulation of isodensity (17.2 g/cm^3) surface contour of imploded capsule, 40 ps before peak neutron emission time. Outside surface (70 μm diam) shows ablation front growth. Initial perturbation was a 0.25-μm rms single-mode pattern ($l = 18$) created by 92 pits on 1.3 at.% Ge-doped capsules. White contour lines define the 90° × 36° repeating sector used in the simulation. (08-00-0695-1495pb01)

Conclusion

Low-entropy Nova implosions using x-ray preheat shielded, doped plastic capsules with reproducible, well-characterized pre-roughened surface finishes have demonstrated large hydrodynamic instability growth similar to that expected in ignition-scale targets. The expected transition to lower entropy and higher instability growth, and hence to ignition-scalable behavior, was experimentally demonstrated by comparing the performance of doped and undoped capsules inferred from x-ray and neutron measurements. To avoid difficulties with high shell x-ray opacities, pusher–fuel mix was inferred from neutron yields rather than from the dopant x-ray line ratios described in HEP3. The large scatter in the yields of the smoothest capsules may be related to the arbitrary orientation of low-order capsule-shell-thickness nonuniformities with respect to radiation-seeded asymmetries, which could lead to large differences in imploded capsule shape. Average neutron yields for the smoothest capsules remain lower than expected for both undoped and doped capsules, although 3-D calculations which include the low order capsule, wall thickness variations are expected to significantly reduce this discrepancy. Neutron yields from roughened capsules suggest that there is similar or less growth than predicted by models including growth saturation, thereby validating current capsule surface finish requirements for ignition designs. Yields from complementary deuterated-shell experiments agreed with the models and clearly show that enhanced heat diffusion must be included in the traditional atomic mix model.

Acknowledgments

We thank B. A. Remington, S. V. Weber, J. D. Kilkenny, and J. D. Lindl for their useful input. The authors are also indebted to the LLNL (and LANL) staff for providing high-quality targets, diagnostic maintenance, and laser shots.

Notes and References

1. J. H. Nuckolls, L. Wood, A. Thiessen, and G. B. Zimmerman, *Nature* **239**, 139 (1972).
2. J. D. Lindl, R. L. McCrory, and E. M. Campbell, *Phys. Today* **45**, 32 (1992).
3. J. Meyer-ter-Vehn, *Nucl. Fusion* **22**, 561 (1982).
4. S. W. Haan, *Phys. Fluids B* **3**, 2349 (1991); S. W. Haan, *Phys. Rev. A* **39**, 5812 (1989).
5. J. D. Kilkenny, S. G. Glendinning, S. W. Haan, B. A. Hammel, et al., *Phys. Plasmas* **1**, 1379 (1994).
6. T. R. Dittrich, B. A. Hammel, C. J. Keane, R. McEachern, et al., *Phys. Rev. Lett.* **73**, 2324 (1994).
7. J. D. Lindl and W. C. Mead, *Phys. Rev. Lett.* **34**, 1273 (1975); S. E. Bodner, *Phys. Rev. Lett.* **33**, (1974); H. Sakagami and K. Nishihara, *Phys. Fluids B* **2**, 2715 (1990).
8. R. D. Richtmyer, *Commun. Pure Appl. Math.* **13**, 297 (1960); E. E. Meshkov, *Izv. Akad. Nauk. SSSR, Mekh. Zhidk. Gaz.* **5**, 151 (1969) (NASA TTF-13-074, 1970).
9. Lord Rayleigh, *Scientific Papers* (Cambridge Univ. Press, Cambridge, 1900), Vol. II, p. 200.
10. J. D. Lindl, *LLNL Laser Program Annual Report*, 2–40 to 2–46, Lawrence Livermore National Laboratory, Livermore, CA, UCRL-56055-83 (SRD, 1983); H. Takabe, K. Mima, L. Montierth, and R. L. Morse, Phys. Fluids 28 (1985); D. H. Munro, *Phys. Rev. A* **38**, 1433 91988); M. Tabak, D. H. Munro, and J. D. Lindl, *Phys. Fluids B* **2**, 1007 (1990).
11. W. K. Levedahl and B. A. Hammel, *ICF Program Annual Report 1988/89 (U)*, 86, Lawrence Livermore National Laboratory, Livermore, CA, UCRL-LR-116901-88/89 (report SRD).
12. J. H. Gardner and S. E. Bodner, *Phys. Rev. Lett.* **47**, 1137 (1981); B. Yaakobi, J. Delettrez, L. M. Goldman, R. L. McCrory, et al., *Opt. Commun.* **41**, 355 (1982); H. Nishimura, T. Kiso, H. Shiraga, T. Endo, et al., *Phys. Plasmas* **2**, 1 (1995).
13. C. J. Keane, R. C. Cook, T. R. Dittrich, B. A. Hammel, et al., *Rev. Sci. Instrum.* **66**, 689 (1995); C. J. Keane, G. W. Pollak, R. C. Cook, T. R. Dittrich, et al., *J. Quant. Spectrosc. Radiat. Transfer* **54**, 207 (1995).
14. R. Pakula and R. Sigel, *Phys. Fluids* **28**, 232 (1985); M. Murakami and J. Meyer–ter–Vehn, *Nucl. Fusion* **31**, 1315 (1991); R. L Kauffman, L. J. Suter, C. B. Darrow, J. D. Kilkenny, et al., *Phys. Rev. Lett.* **73**, 2320 (1994).
15. S. V. Weber, B. A. Remington, S. W. Haan, B. G. Wilson, and J. K. Nash, *Phys. Plasmas* **1**, 3652 (1994).
16. B. A. Remington, S. W. Haan, S. G. Glendinning, J. D. Kilkenny, et al., *Phys. Rev. Lett.* **67**, 3259 (1991); B. A. Remington, S. V. Weber, S. W. Haan, J. D. Kilkenny, et al., *Phys. Fluids B* **5**, 2589 (1993).
17. S. W. Haan et al., *Phys. Plasmas* **2**, 2480 (1995).
18. R. Cook, G. E. Overturf, S. R. Buckley, and R. McEachern, *J. Vac. Sci. Technol. A* **12**, 1275 (1994).
19. R. J. Wallace, R. L. McEachern, and W. W. Wilcox, *ICF Quarterly Report* **4**(3), 79, Lawrence Livermore National Laboratory, Livermore, CA, UCRL-LR-105821-94-3 (1994).
20. R. L. McEachern, C. Moore, G. E. Overturf, III, S. R. Buckley, and R. Cook, *ICF Quarterly Report* **4**(1), 25 Lawrence Livermore National Laboratory, Livermore, CA, UCRL-LR-105821-94-1 (1994).
21. S. M. Pollaine, S. P. Hatchett, and S. H. Langer, *ICF Quarterly Report* **4**(3), 87, Lawrence Livermore National Laboratory, Livermore, CA, UCRL-LR-105820-94-3 (1994).
22. C. W. Laumann, J. A. Caird, J. E. Murray, R. E. McEachern, et al., *ICF Quarterly Report* **4**(1), 1–30, Lawrence Livermore National Laboratory, Livermore, CA, UCRL-LR-105820-94-1 (1994).
23. E. M. Campbell, *Laser Part. Beams* **9**, 209 (1991); B. A. Hammel, C. J. Keane, T. R. Dittrich, D. R. Kania, et al., *J. Quant. Spectrosc. Radiat. Transfer* **51**, 113 (1994).
24. H. N. Kornblum, R. L. Kauffman, and J. A. Smith, *Rev. Sci. Instrum.* **57**, 2179 (1986).
25. M. D. Cable, S. P. Hatchett, J. A. Caird, J. D. Kilkenny, et al., *Phys. Rev. Lett.* **73**, 2316 (1994).
26. R. L. Kauffman, H. N. Kornblum, D. W. Phillion, C. B. Darrow, et al., *Rev. Sci. Instrum.* **66**, 678 (1995).
27. M. D. Cable and S. P. Hatchett, *J. Appl. Phys.* **62**, 2223 (1987).
28. R. A. Lerche, D. W. Phillion, and G. L. Tietbohl, *Rev. Sci. Instrum.* **66**, 933 (1995).
29. J. D. Kilkenny, *Laser and Part. Beams* **9**, 49 (1991).
30. O. L. Landen, C. J. Keane, B. A. Hammel, M. D. Cable, et al., *J. Quant. Spectrosc. Radiat. Transfer* **54**, 245 (1995).
31. C. J. Keane, B. A. Hammel, D. R. Kania, J. D. Kilkenny, et al., *Phys. Fluids B* **5**, 3328 (1993); C. J. Keane, B. A. Hammel, A. L. Osterheld, and D. R. Kania, *Phys. Rev. Lett.* **72**, 3029 (1994).
32. G. B. Zimmerman and W. L. Kruer, *Comm. Plasma Phys. Controlled Fusion* **11**, 51 (1975).
33. M. M. Marinak, B. A. Remington, S. V. Weber, R. E. Tipton, et al., "Three-Dimensional Single Mode Rayleigh-Taylor Experiments on Nova," Lawrence Livermore National Laboratory, Livermore, CA, UCRL-JC-120191 (1995); submitted to *Phys. Rev. Lett.*; M. M. Marinak, R. E. Tipton, B. A. Remington, S. W. Haan, and S. V. Weber, *ICF Quarterly Report* **5**(3), p. 168, Lawrence Livermore National Laboratory, Livermore, CA, UCRL-LR-105821-95-3 (1995).
34. C. J. Keane, O. L. Landen, B. A. Hammel, P. Amendt, et al., "Observation of Large-Growth Factor Behavior in Indirectly Driven Spherical Implosions," Lawrence Livermore National Laboratory, Livermore, CA, UCRL-JC-123022 ABS (1995).
35. R. E. Chrien, N. M. Hoffman, and J. D. Colvin, "Fusion Neutrons from the Gas-Pusher Interface in Deuterated-Shell ICF Implosions," Los Alamos National Laboratory, Los Alamos, NM, LA-UR-95-2307 (1995).

ENERGY COUPLING IN LINED HOHLRAUMS (HLP1, HLP2, AND HLP7)

R. L. Kauffman *C. W. Hatcher* *D. W. Phillion* *R. J. Wallace*

L. J. Suter *H. N. Kornblum* *J. L. Porter*[*] *P. E. Young*

R. L. Berger *E. F. Lindsey* *M. D. Rosen* *F. Ze*

C. B. Darrow *D. S. Montgomery* *R. Thiessen* *J. C. Fernandez*[**]

S. N. Dixit *T. E. Orzechowski* *R. E. Turner* *J. A. Cobble*[**]

Introduction

Indirect-drive inertial confinement fusion (ICF) uses high-Z cavities, or hohlraums, to confine x rays for compressing and igniting deuterium–tritium fuel contained in spherical capsules.[1,2] For laser-driven ICF, the intense laser beams enter the hohlraum through small laser entrance holes (LEHs), heating the high-Z hohlraum walls. The laser-produced radiation heats the unirradiated high-Z walls producing a nearly isotropic radiation environment for spherically compressing the ICF capsule.[2] The radiation flux on the capsule is not completely isotropic, however, because the laser-irradiated area is generally brighter than the surrounding x-ray heated walls and the LEHs do not radiate. Furthermore, the angular distribution of flux on the capsule is time dependent because the unilluminated walls become hotter and more emissive as a function of time, and plasma dynamics cause the laser-irradiated area to move. Symmetric implosions are obtained by dynamically balancing the effects of the LEHs, wall heating, and laser-spot motion.[3]

The laser absorption and thus radiation symmetry depend on the dynamics of the hohlraum plasma. For long pulses, such as those required for ignition targets on the proposed National Ignition Facility (NIF), a large volume of the hohlraum can fill to plasma electron densities of $n_e \approx 10^{21}$ cm^{-3} or greater, which can cause significant movement of the absorption region. In NIF hohlraum designs, a low-Z plasma replaces the low-density, high-Z blowoff to better control the laser-spot motion.

Inverse bremsstrahlung is lower in the low-Z plasma compared with a high-Z plasma at the same density, allowing the laser to deposit its energy in higher-density, high-Z plasma nearer the initial wall position.[2,4] Calculations indicate that the low-Z plasma reduces the movement of the laser deposition region, making symmetry more easily obtainable. For initial NIF target designs, the low-Z underdense plasma was produced by initially coating the high-Z wall with low-Z material. The laser and radiation ablate the thin low-Z coating from the wall, filling the hohlraum with low-Z plasma. For more recent designs, the hohlraum is initially filled with low-Z gas which, when ionized, produces the underdense low-Z plasma. Gas-filled hohlraums avoid problems with plasma stagnation and jetting, which computationally degrade capsule symmetry in the lined-hohlraum designs.

NIF designs using low-Z plasma to control spot motion had not previously been tested. Many of the Hohlraum and Laser Physics (HLP) tasks for the Nova Technical Contract (NTC) were developed to experimentally test the physics for low-Z lined hohlraums. Specifically, HLP1 and HLP2 are tasks to test the energetics of lined hohlraums and to understand the scaling to NIF hohlraums within the energy and power constraints of Nova. HLP1 experiments investigate drive using shaped pulses where the underdense plasma evolution better approximates the NIF plasma but at lower powers than attainable on the NIF. The goal of HLP1 is to demonstrate acceptable laser coupling in hohlraums with a shaped drive pulse producing radiation temperatures T_R in the range of ~100 to ~210 eV. HLP2 experiments investigate drive in lined hohlraums at high powers to understand radiation drive scaling to NIF peak drive regimes. HLP2 goals are to demonstrate acceptable coupling in hohlraums with T_R of ≥270 eV. For both tasks, acceptable coupling is defined as absorption fraction $f_{abs} > 90\%$; stimulated Brillouin scattering (SBS) fraction $f_{SBS} < 5$–10%; hot electron fraction $f_{hot} < 5\%$ at a hot electron temperature, $T_{hot} \geq 50$ keV, and stimulated Raman scattering (SRS) fraction $f_{SRS} < 5\%$.

[*] Sandia National Laboratories, Albuquerque, New Mexico

[**] Los Alamos National Laboratory, Los Alamos, New Mexico

Results from both HLP1 and HLP2 experiments successfully attain the drive goals defined in the NTC, although the liner does reduce the peak drive compared with experiments using unlined hohlraums. Calculations partly predict this reduction in drive as being due to enhanced hydrodynamic losses to the underdense plasma. Although the diagnostics were not optimal, measurements of SBS using subaperture sampling and SRS using x-ray bremsstrahlung from fast-electron production suggest that enhanced plasma instability production in the lined hohlraums also contributes to the observed reduced drive. The drive experiments performed for HLP1 and HLP2 use unsmoothed laser beams. Recent experiments demonstrate that stimulated scattering levels are reduced to about the 1% level using beam-smoothing techniques. These experiments are described in "Laser–Plasma Interactions in NIF-Scale Plasmas (HLP5 and HLP6)" on p. 305 of this *Quarterly*. For the same laser intensity and pulse length, x-ray conversion efficiency inferred in hohlraums is significantly higher than that obtained from isolated flat foils. The HLP task is focused on experiments to understand this difference.

Experiments

Experiments on Nova use hohlraums whose shape is a right circular cylinder, shown schematically in Fig. 1(a). Nova scale-1 hohlraums are Au and are 1.6 mm diam × 2.55–2.75 mm long. Typically, the hohlraum wall thickness is 25 μm, and in some experiments is thinned to ~2 μm to image kilo-electron-volt x rays through the wall. Different hohlraum lengths are sometimes used for symmetry or for satisfying other experimental constraints. Different hohlraum sizes are scaled from the scale-1 size by the ratio of their dimensions to those of a scale-1 size. For example, a 0.75-scale hohlraum is 1.2 mm diam × 2 mm long. The LEH is varied, depending on the experiment, from 50 to 100% of the hohlraum diameter. For the energetics scaling, the results are scaled to 50% LEH for the square pulses and 75% for the shaped pulses, unless otherwise noted. For all of the energetics studies, the hohlraums are empty, not containing a fuel capsule.

The lined hohlraums are coated with either Ni or CH in the form of parylene. The parylene coating is done using vacuum deposition and by allowing the parylene to enter through the LEHs and randomly collide with the wall until it sticks. Since parylene has a low probability of sticking when colliding with a solid surface, it statistically has many collisions with the wall before it sticks. This method can produce uniform surfaces even on the inside hohlraum wall. Typically, the coating thickness is 0.75 μm with a density $\rho \approx 1.10$ g/cm^3 unless otherwise stated. When fully ionized, this layer would fill the initial volume to a density of ~10^{21} electrons/cm^3. The coating thickness is characterized by measuring the Au x-ray fluorescence from a scanning electron microscope (SEM). The SEM signal is calibrated using a series of flat Au targets overcoated with various thicknesses of parylene. The coating thicknesses on the flat targets are characterized using optical interferometry and a stylus profilometer. In this way, coating thickness for the hohlraums can be measured to an accuracy of ±20%. Uniformity along the inside hohlraum wall is checked using the SEM by cutting open test hohlraums. Also, coating thicknesses on a target used for an experiment could be checked by measuring the thickness on the outside wall.

Ni-coated hohlraums are made using electrodeless Ni plating. The coating is 88% Ni by weight with the remaining 12% by weight being P. Its average density is 8.2 g/cm^3, with the nominal coating thickness of 0.15 μm. Thicknesses on hohlraums are also characterized

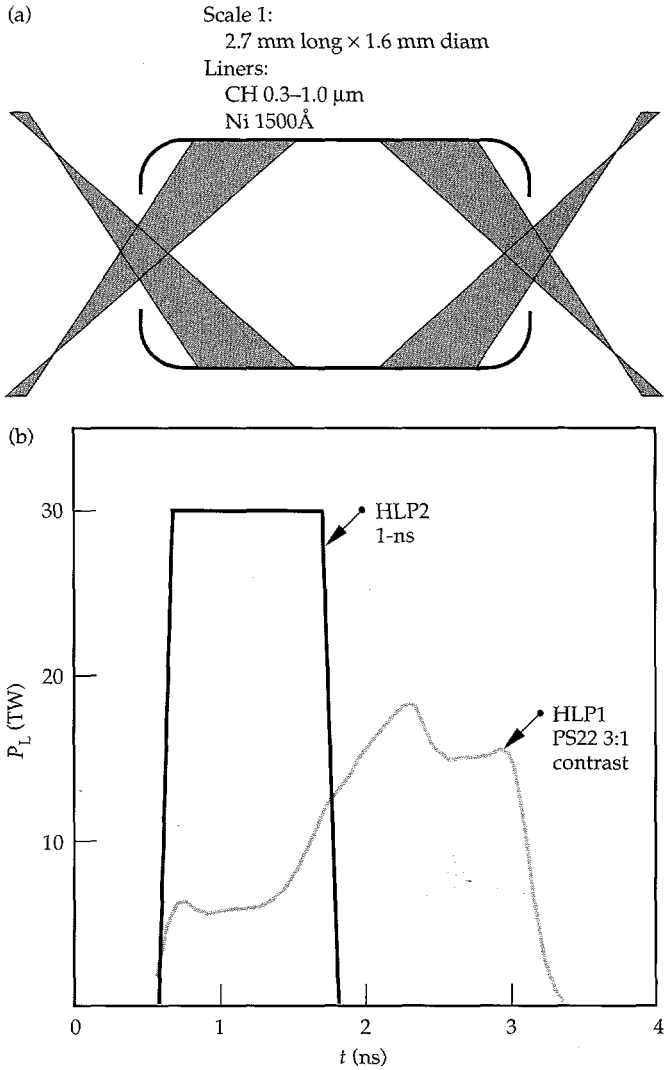

FIGURE 1. Schematic of hohlraum drive experiments. (a) The hohlraum and irradiation geometry. (b) Representative pulse shapes of the incident laser pulses at 0.35 μm wavelength. PS22 is a 3:1 contrast shaped pulse for HLP1 and HLP2, using a 1-ns square pulse with a maximum power of 30 TW. (20-05-0995-2111pb01)

using the SEM, measuring the relative x-ray fluorescence signal of Ni compared with Au. Again, the system is calibrated using coated Au flats. Errors in thickness are estimated to be ±20%.

Hohlraums are irradiated using the 10 Nova laser beams, 5 per side. Figure 1(b) shows the laser pulses. The pulse shape for HLP1, designated PS22, is a 2.2-ns-long pulse with a 3:1 contrast between the peak intensity and the foot intensity. This is the same pulse shape used for the bulk of the pulse-shaped symmetry experiments described in the next article, "Nova Symmetry: Experiments, Modeling, and Interpretation (HLP3 and HLP4)," on p. 293. Pulse shapes for HLP2 are 1-ns-long approximately square pulses with total powers up to 30 TW (maximum power available on Nova). The beams are pointed through the center of the LEH and defocused to reduce the intensity of the laser on the wall, shown schematically in Fig. 1(a). For a scale-1 target, the defocusing is ~1 mm, in the diverging direction from best focus, at the LEH. This allows ~100 μm clearance of the beam for a 50% LEH, assuming geometrical optics for an $f/4$ beam. The beam irradiates the wall of the hohlraum at an angle of 40° with respect to the normal of the wall and has a first bounce intensity of $\sim 8 \times 10^{14}$ W/cm^2 for 2 TW of laser power P_L per beam.

Diagnostics

X-ray drive is measured using two complementary techniques.[5] One technique measures the shock wave generated by the absorbed x-ray flux in an Al witness plate. The Al witness plate is a piece of Al whose thickness continuously varies from one end to the other, or has discrete steps of known thickness, placed over a hole in the hohlraum wall. The shock front is measured by observing the optical emission produced by the emerging shock at the rear of the Al plate. The optical emission is measured using an ultraviolet (UV) Cassegrain telescope coupled to an optical streak camera. X-ray drive is derived by comparing the measured shock velocity with hydrodynamic calculations or semi-empirical models as described in the article "Planar and Cylindrical Rayleigh–Taylor Experiments on Nova (HEP2)," p. 232. The estimated error for measuring drive is ±5 eV, which includes the accuracy of the measurement and the uncertainty in the comparison with the calculations. The other technique measures the x-ray flux irradiated from the hohlraum wall using an array of x-ray diodes (XRD).[6] A number of broadband channels are defined in the range from 0.1 to 1.8 keV using thin absorption filters and, for some channels, grazing incident x-ray mirrors. The XRD array measures the hohlraum drive by measuring the flux from an opposite wall in the hohlraum through a hole in the hohlraum wall. The hole is lined with Be to prevent high-Z plasma from occluding the line of sight into the hohlraum. Time-resolved spectra are unfolded from the signals using calibrated channel response. The time resolution is on the order of 150 ps limited by the bandwidth of the detectors and oscilloscopes and the correlation of the timing among the detectors. The spectrally integrated flux is measured to an accuracy of ~20% including calibration accuracies and unfolding uncertainties resulting in a ±5% uncertainty when converted to an equivalent radiation drive temperature.

The two measurement techniques are complementary since the shock velocity measures the flux incident on the wall while the XRD array measures the reradiated flux. The two are related by the wall albedo,[2] or effective reflectivity. The shock velocity is best suited for measuring peak drive and can provide only coarse time-dependent measurements. The XRD array provides much better time-dependent reradiated flux measurements, but the data must be corrected for albedo, which is time dependent, to obtain incident x-ray flux. For both techniques, the measurement is usually made in the midplane of the hohlraum between the two sets of beam cones where it is not directly irradiated by the laser. The flux on the ICF capsule, or other areas of the hohlraum, must be derived using detailed radiation hydrodynamic calculations or semi-empirical view factor estimates.

Laser coupling is also studied by measuring the scattered light and x-ray bremsstrahlung produced by superthermal electrons. SBS light into the lens is measured using a subaperture sampling on one of Nova's ten beamlines, beamline six (BL6).[7] The light from approximately 5% of the beam area is extracted from the reflected beam using an uncoated piece of fused silica. It is then optically relayed to a diagnostic table equipped with an optical calorimeter, a fast-photodiode coupled to a Tektronix 7912 transient digitizer, and a time-resolved optical spectrometer. The calorimeter and photodiode are absolutely calibrated by placing a partially reflecting retroreflector in front of the calorimeter mounted opposite BL6. The retroreflector reflects 7.6% of the incident energy, and the data is reduced assuming the incident light and backscattered light uniformly fill the lens aperture. More recent experiments with improved diagnostics developed for HLP5 [as discussed in "Laser–Plasma Interactions in NIF-Scale Plasmas (HLP5 and HLP6)" on p. 305] have shown that there can be significant variations in the near-field distribution of the backscattered light in the lens aperture as well as some light being scattered outside of the lens.[8] The scattered light data presented here have large uncertainties due to the subaperture sampling, but the relative trends in the data among different target types should be qualitatively valid.

Fast-electron production from SRS is studied by measuring the x-ray bremsstrahlung from the target in the 20–200-keV spectral range.[9] The x rays are produced when the fast electrons deposit their energy in the high-Z case. For most of the measurements,

hohlraums with thin walls (~2–3 μm) are used to minimize x-ray absorption in the hohlraum walls. This measurement does not include fast electrons that escape the target or that lose their energy in the plasma before reaching the wall. In addition, time-resolved SRS light spectra are measured 28° from an incident beamline. Also, a photodiode array measures the angular distribution of the SRS light. SRS light was not measured inside of the lens cone. Recent experiments have shown that a significant amount of SRS light can be scattered into the lens cone.[8]

Results

Lined hohlraums reduce the amount of high-Z material filling the interior of the hohlraum. The effect of liners on plasma filling can be seen qualitatively in Fig. 2, which shows time-resolved images of kilovolt x rays viewing along the axis of Nova hohlraums.[10] Figure 2(a) is an image of an unlined hohlraum, and Fig. 2(b) shows a hohlraum lined with 0.75 μm of CH. Both images are taken at around 1.5 ns after the beginning of PS22, which is near the peak of the laser intensity. Both images show five bright spots placed nearly equally inside of the hohlraum. These spots are Au blowoff from the laser beams irradiating the hohlraum walls. The hohlraum wall itself is masked by the LEH, which defines the viewing area. For the unlined hohlraum, the figure also shows five spokes and a central bright spot. These are produced by stagnation of the high-Z plasma from the wall blowoff, indicating that by this time the high-Z plasma has filled the laser irradiation part of the hohlraum. For the lined hohlraum, the bright spokes and central region are replaced by an absence of emission. This region is filled by low-Z CH plasma, which is a much poorer radiator than high-Z plasma. These images indicate that qualitatively, at least, low-Z plasma does reduce the filling of the hohlraum by high-Z plasma.

Drive at high power has been investigated using 1-ns square pulses for HLP2. Figure 3 shows peak T_R measured using shock breakout for both CH- and Ni-lined hohlraums. Data are included for both scale-1 and scale-0.75 hohlraums. Most of the data are taken with 2.55-mm-long hohlraums. Some of the data are from longer hohlraums and have been corrected (<5 eV) to account for this. The data is plotted as a function of P_L/wall area where the wall area is the total area of the hohlraum not corrected for LEH or diagnostic holes. Drive from unlined hohlraums, reported previously, is also plotted for comparison.[11] Drive from lined hohlraums is below the measured drive for unlined hohlraums. Table 1 summarizes the average reduction in drive for lined hohlraums compared with unlined hohlraums. The uncertainties listed in Table 1 are the standard deviations of the data set. For scale-1 targets, the reduction is 16–18 eV, representing ~25–30% decrease in available x-ray drive for both CH- and Ni-lined hohlraums.

Figure 4 shows drive from lined hohlraums heated with shaped pulses. Figure 4(a) shows the time-resolved drive derived from the XRD array for both CH- and Ni-lined hohlraums compared with drive measured from

(a) Unlined hohlraum

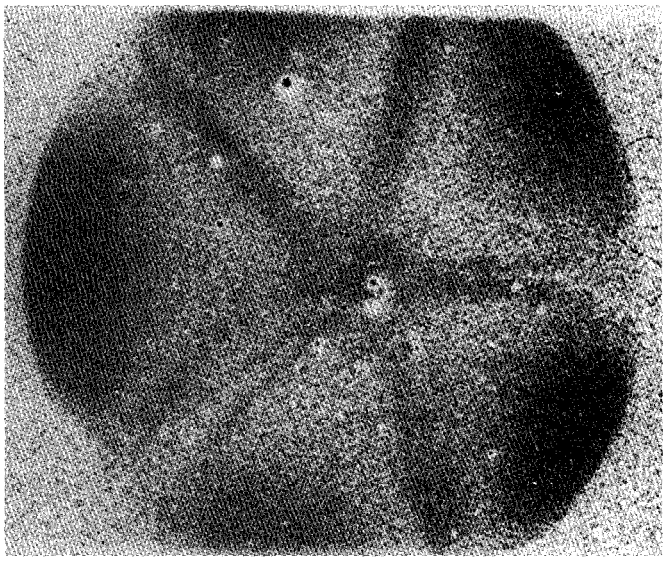

(b) Lined hohlraum

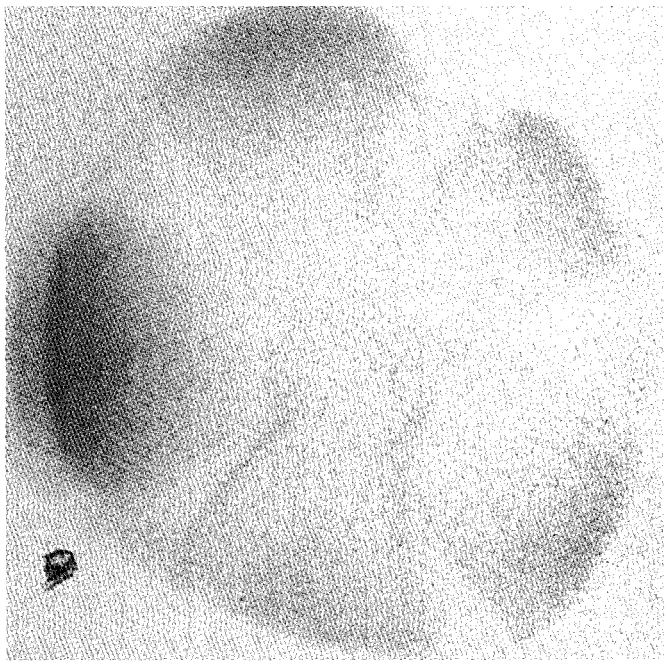

FIGURE 2. X-ray images of the hohlraum heated with PS22 viewing along the axis of the cylinder. The time-resolved images are taken at approximately 1.5 ns, which is about the peak of the laser pulse. The image in (a) is from an unlined hohlraum and (b) is from a hohlraum lined with 0.75 μm CH. (20-05-0995-2112pb01)

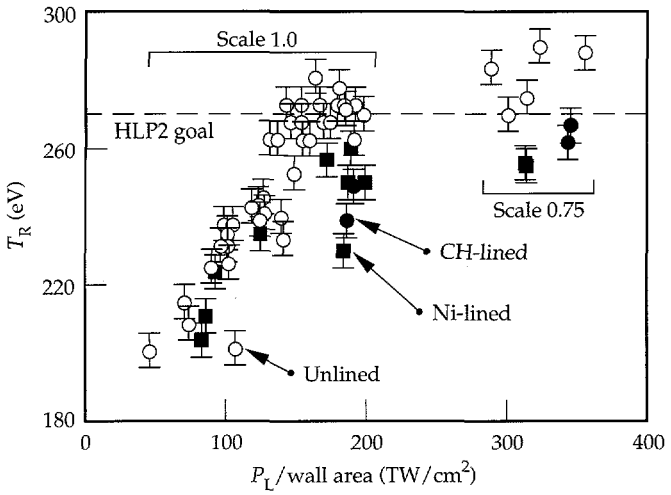

FIGURE 3. Peak radiation temperature T_R measured in scale-1 and scale-0.75 hohlraums heated with 1-ns square pulses of 0.35-μm light. Measurements are made using the shock breakout technique in Al witness plates. Open circles are from unlined Au hohlraums and closed circles and closed squares are from CH- and Ni-lined hohlraums, respectively. The HLP2 goal of 270 eV is shown as a dashed line.
(20-05-1093-3696pb01)

TABLE 1. Reduction in drive of lined hohlraums compared with unlined hohlraums.

Hohlraums	ΔT_R (eV) experiment	ΔT_R (eV) LASNEX
Scale 0.75		
1 ns, 1500Å Ni, 25 TW	26 ± 9	—
1 ns, 7500Å CH, 25 TW	17 ± 9	—
Scale 1.0		
1 ns, 1500Å Ni, 12 TW	16 ± 3	14
1 ns, 1500Å Ni, 25 TW	18 ± 6	14
PS22, 1500Å Ni	18 ± 5	14
PS22, 4000Å CH	6 ± 3	9
PS22, 7500Å CH	11 ± 9	12

unlined hohlraums. The main differences in the drive between the lined and unlined hohlraums are that the beginning of the drive is delayed in the initial foot of the pulse and that the peak drive is less for lined hohlraums. Figure 4(b) plots the peak drive as measured from the shock breakout, which also confirms the reduction in peak drive for lined hohlraums. The difference in peak drives for Figs. 4(a) and (b) is the correction for wall albedo. The delay in the beginning of the drive can be understood qualitatively as the reduction in x-ray flux initially as the laser burns through the liner before heating the Au walls. As summarized in Table 1, the reduction in peak drive for lined hohlraums is ~20–30% of the x-ray flux for unlined hohlraums. Drive data from unlined hohlraums have been empirically fit with a simple power balance model.[11] This simple model balances the heating sources with the heat losses. The heating source is the x-ray energy produced by the incident laser drive heating the hohlraum walls. The heat losses are the energy absorbed by the hohlraum walls and energy radiated through the laser entrance and diagnostic holes.[12,13] The hohlraum wall loss is modeled using a Marshak scaling[14] for wall loss. The power balance equation is

$$\eta_{HOHL} P_L = \sigma T_R^4 A\left[1-\alpha\left(1-f_H\right)\right]. \quad (1)$$

The source term on the left is the incident P_L multiplied by the effective efficiency for converting laser light to drive energy, η_{HOHL}. The loss terms are on the right. σ is the Stefan–Boltzman constant, A is the hohlraum area, f_H is the fraction of the hohlraum area that is holes, and α is the wall albedo. All of the parameters in the equation can be determined independently by the experimental geometry and the measurement except for η_{HOHL} and α. α is both time and temperature dependent. It can be calculated from LASNEX or simple

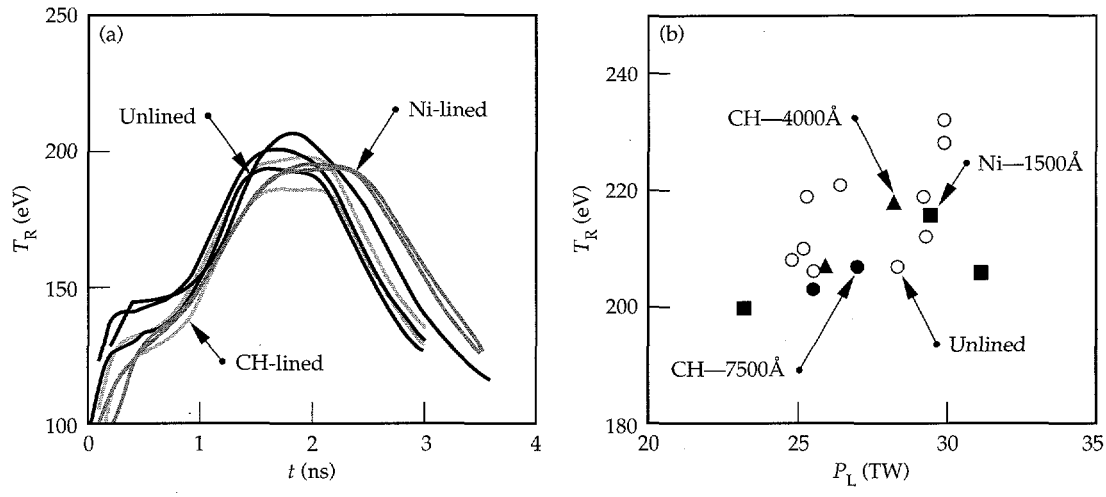

FIGURE 4. Radiation drive measured from scale-1 hohlraums heated with 0.35-μm light using PS22. (a) Compares time-resolved Dante measurements of the drive from unlined and CH- and Ni-lined hohlraums. (b) Shows peak drive measured using the shock breakout technique in Al witness plates from the different targets.
(20-05-1093-3696pb01)

models of radiation wave scaling and depends on the opacity and equation of state for the material.

Figure 5 shows the data fit with Eq. (1) from the scale-1 hohlraums heated with square pulses. The fits use power-law scaling of α derived from self-similar solutions to Marshak's wave heating of materials with power-law dependencies for opacity and equation of state.[12,13] η_{HOHL} is treated as a fitting parameter. Results of the fits are shown Fig. 5. For unlined hohlraums, $\eta_{HOHL} \approx -0.75$ while $\eta_{HOHL} \approx 0.53$ to 0.64 for the lined hohlraum data. This simple model suggests that the effective coupling is reduced by 15–30%. The data set is much sparser for the scale-0.75 data, but it is consistent with similar reduction in effective coupling. The pulse-shaped data cannot be fit easily with an analytic model because of the dependence of α on time and temperature, but the decrease in drive is approximately similar to the 1-ns square results, and therefore the reduction in coupling is expected to be similar.

The reduced coupling for lined hohlraums can be due to several effects. Some reduction is expected, as discussed in the next section, because of the energy expended to heating the liner and to differences in coupling to hydrodynamic motion. Other potential differences are decreased absorption due to higher levels of reflected light, SBS, and SRS.

The absorption is studied by measuring both the scattered SBS and SRS light and fast electrons produced by SRS. Table 2 shows the fraction of SBS light scattered into the lens for the various targets for both CH- and Ni-lined hohlraums. The data are taken using the subaperture sampling, as discussed earlier. The quoted errors are the standard deviations of the data scatter and are not intended to represent the total error in the experiment. The CH- and Ni-lined hohlraum experiments were done at different periods on the laser, and the unlined data acquired during the two periods are listed separately for meaningful comparison. The two sets of unlined data show that the measurements are reproducible.

Within the data scatter, no increase in SBS from CH-lined hohlraums is observed compared with SBS from unlined hohlraums. For Ni-lined hohlraums, higher SBS levels are observed for both scale-0.75 hohlraums heated with 1-ns square pulses and scale-1 hohlraums heated with PS22. The scale-0.75 hohlraum data during the Ni-lined experiments consist of only two data points for the Ni-lined hohlraums and one data point for the unlined hohlraums. This increase is therefore based on a sparse data set, but it is apparently real. For the CH-lined scale-0.75 data set, there are three data points for the unlined hohlraums and five data points for the CH-lined hohlraums. There are many shots for the PS22 data, and the increase in scattering for the Ni-lined hohlraums is apparently real. Some of the large scatter in the data may be due to changes in experimental conditions such as changes in the focusing. Some of the data were taken during symmetry studies where the crossing point of the beams changed with respect to the LEH. Some correlations in the data could be observed with the change in focusing.[3] When scattering data from unlined and Ni-lined hohlraums are compared with similar targeting geometries, scattering levels from Ni-lined hohlraums are consistently higher, although quantitative levels differ.

A significant limitation to these measurements is due to the subaperture sampling and the assumption that it represents the average over the entire beam cone. A full-aperture backscattering station (FABS) as well as a near backscatter imaging (NBI) system have been implemented on Nova since these experiments were done.[8] These diagnostics can make near-field measurements of the SBS up to angles of 14° from direct backscatter around beamline 7 (BL7). They have shown that SBS from hohlraums is well collimated but can be shifted with respect to direct backscatter for some targets.[15] Although no experiments have been done with lined targets since the FABS and NBI have been fielded, results from the FABS and NBI can be

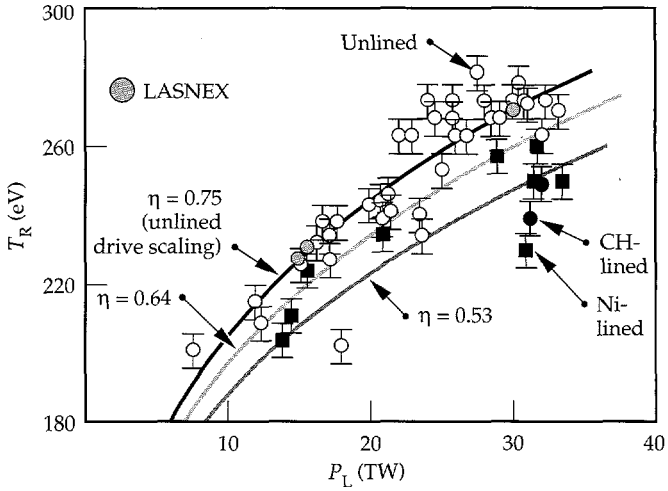

FIGURE 5. Drive scaling for scale-1 hohlraums heated with 1-ns pulses. The data is the same as presented in Fig. 1. The curved lines are fits to the power balance model with different coupling efficiencies. Results of 2-D LASNEX modeling for unlined hohlraums are also shown. (20-05-1093-3697pb01)

TABLE 2. SBS reflectivity from lined hohlraums.

	CH data		Ni data	
	Unlined	CH-lined	Unlined	Ni-lined
1 ns scale 1	1.5 ± 1%	2.8 ± 0.6%	1.6 ± 1%	1.7 ± 1.2%
1 ns scale 0.75	4.6 ± 1.3%	4.5 ± 1.6%	3.5*%	8.7 ± 0.3%
PS22 scale 1	5.8 ± 2.9%	4.5 ± 2.9%	7.3 ± 4.7%	15.1 ± 5.3%

*Value represents only one experiment.

compared with the subaperture results for unlined hohlraums. In all cases, the SBS into the lens measured by FABS alone is about half of the results listed in Table 2 for unlined hohlraums. Generally, SBS levels measured with NBI are comparable to those measured by FABS so that the total SBS from unlined hohlraums is comparable to the levels listed in Table 2. This may be purely coincidental, and there is no guarantee that it applies to the lined hohlraum results.

Time-resolved SBS spectra are measured using a grating spectrometer coupled to an optical streak camera. Figure 6 shows an example of the data, displaying isointensity contours of the two-dimensional (2-D) image. The spectral and time resolution are of 3 Å and 30-ps, respectively. Spectra from Ni-lined hohlraums for both 1-ns square and PS22 pulses are red-shifted by 7–8 Å relative to the incident light wavelength.

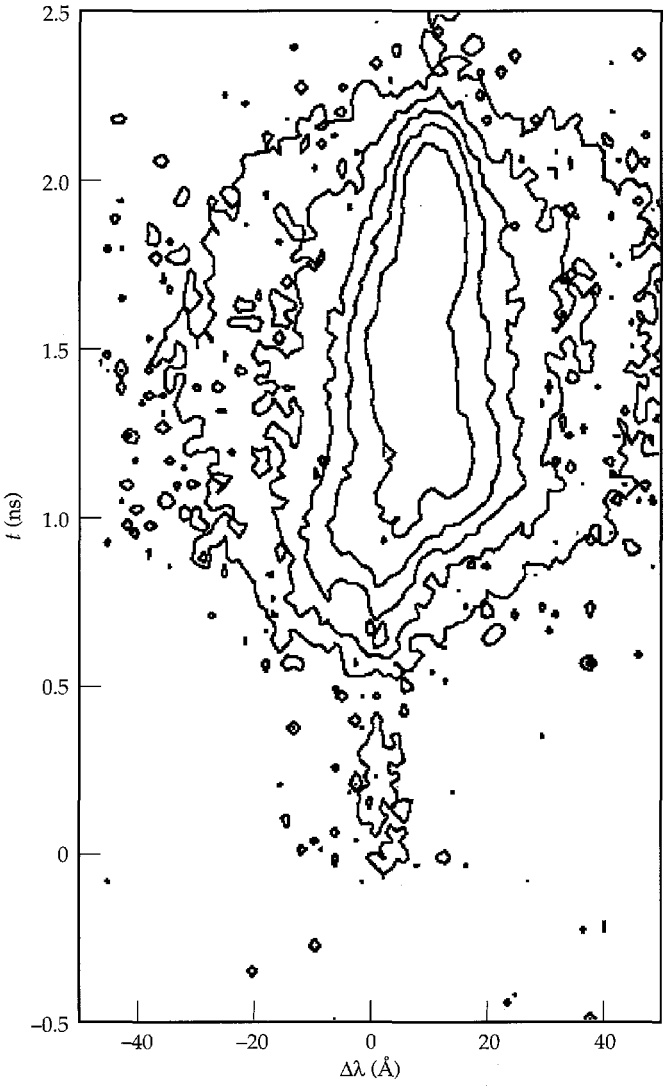

FIGURE 6. Spectrum vs time contour plot of SBS light from a Ni-lined hohlraum. The spectral shift is measured from the incident 0.35-μm wavelength light. (20-05-1095-2364pb01)

Typically, the spectra from unlined hohlraums show little or no shift. This is qualitatively similar to disk targets where the SBS spectrum is shifted more to the blue for high-Z targets compared with low-Z targets. SBS spectra from hohlraums are more red shifted than SBS spectra from disks at similar irradiances. This is presumably due to less Doppler shift, because the plasma flow in the backscatter direction is reduced by the hohlraum, confining the plasma.

As shown in Fig. 7, the spectral data can be integrated over wavelength to obtain the time history of SBS. The time history has been normalized to the calorimeter data for this shot to obtain time-resolved reflectivity. Figure 7 also shows the incident laser pulse. For PS22, the intense part of the SBS signal begins around 1.3 ns, when the incident laser pulse power begins to increase and lasts during the entire high-intensity part of the pulse. A small signal is seen at the beginning of the pulse, but it is a factor of 100 lower. Time history of SBS from 1-ns pulses heating scale-1 hohlraums are qualitatively similar. A signal is seen during the first 300 ps and then it goes away. A second feature turns on at around 700 ps, lasting the rest of the pulse. The intensity of the initial feature is higher because the incident beam intensity is higher for 1-ns pulses compared with PS22.

Fast-electron production is studied by measuring the x-ray bremsstrahlung from electrons depositing their energy in the hohlraum walls. Figure 8 shows spectra from experiments using both PS22 and 1-ns pulses. For PS22, the superthermal electron production is quite low. Using the expression derived from thick target bremsstrahlung for converting x rays to electron flux,[16] the superthermal electron levels for PS22 are less than 0.1% for all of the targets. For comparison, the

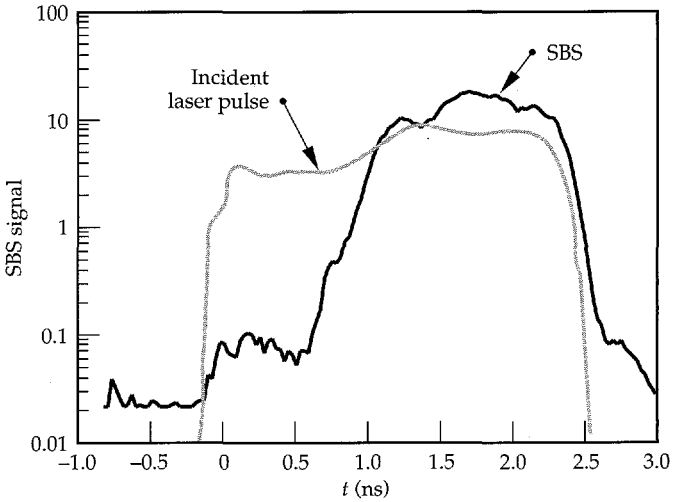

FIGURE 7. Time history of the backscattered light into the BL6 lens. The time history is derived from integrating in wavelength the time-resolved spectrum shown in Fig. 6 and normalizing the time history to the total backscattered light. (20-05-1095-2366pb01)

black line in Fig. 8 is the x-ray spectrum calculated assuming 1% of the incident laser energy is converted to a 50 keV superthermal electron tail. The calculated spectrum does not include self absorption in the target. The data for both lined and unlined hohlraums are an order of magnitude lower. The hot-electron temperatures for the Ni-lined and unlined hohlraums are ~50 keV while the CH-lined hohlraums have slightly lower hot-electron temperatures (~40 keV). A limited amount of data was taken measuring the SRS light levels using diodes positioned around the chamber. The integrated SRS is ~0.2–0.4%, which is slightly higher than levels that would be inferred from fast-electron levels.

The superthermal electron production is higher for both CH-lined and unlined hohlraums heated with 1-ns pulses at high powers. Figure 8(b) shows experiments using 30-TW pulses. For comparison, the black line denotes a fast-electron fraction of 5% with a 50-keV hot-electron temperature. For the scale-1 hohlraums, fast-electron fractions are 0.4 and 1.8% for unlined and CH-lined hohlraums, respectively. For scale-0.75 hohlraums, the fast-electron fractions are 3% and 3.8%, for unlined and CH-lined hohlraums, respectively. The fast-electron production levels in unlined hohlraums qualitatively agree with levels measured in disk experiments for similar laser irradiances on the hohlraum wall.[17] Irradiances on the hohlraum wall are $\sim 1.3 \times 10^{15}$ W/cm^2 and $\sim 2.3 \times 10^{15}$ W/cm^2 for scale-1 and scale-0.75 hohlraums, respectively. Fast-electron production in disk experiments are ~1–2% with irradiances above 10^{15} W/cm^2. The higher levels inferred in hohlraums may be due to less loss of fast-electron energy to hydrodynamic expansion and the hohlraum walls absorbing a greater fraction of the electrons. The underdense profiles in hohlraums may also be altered with increasing scalelengths at, or below, quarter critical density due to plasma confinement, which also could enhance SRS production. Levels for CH-lined hohlraums are slightly above unlined hohlraums but are still only a small part of the overall energy budget. The increase in fast-electron levels may be due to less collisional damping in the low-Z underdense plasma for the CH-lined hohlraums. Simulations, as discussed below, suggest that SRS is produced in the underdense plasma near the transition region between the Au and CH. The observations are consistent with these results. SRS light measurements were not made in these experiments.

Recent experiments using the FABS and NBI indicate that SRS light is highly collimated in the backward direction and that total levels can be much higher than inferred from the scattered light diodes or from hard x-ray bremsstrahlung measurements.[8] SRS levels of 13% have been observed for one shot in a scale-0.75 unlined hohlraum heated with ~25 kJ in a 1-ns square pulse, which is significantly higher than the 3% inferred from x-ray bremsstrahlung. For PS22, SRS levels from FABS and NBI are ~2–3% compared with ~0.1% levels inferred from x-ray bremsstrahlung. Conversely, SRS levels are ~1% for a scale-1 unlined hohlraum heated with a 1-ns square pulse, which is comparable to levels inferred from x-ray bremsstrahlung. No FABS and NBI data have been taken for lined hohlraums, so the SRS levels scattered into the lens are not known.

Despite the uncertainties in scattered light measurements, lined hohlraums do not show significantly larger scattering losses for most targets compared with unlined hohlraums. For scale-1 targets heated with 1-ns pulses, SBS from CH-lined hohlraums is ~2–3% comparable to unlined hohlraums, and f_{hot} from CH-lined

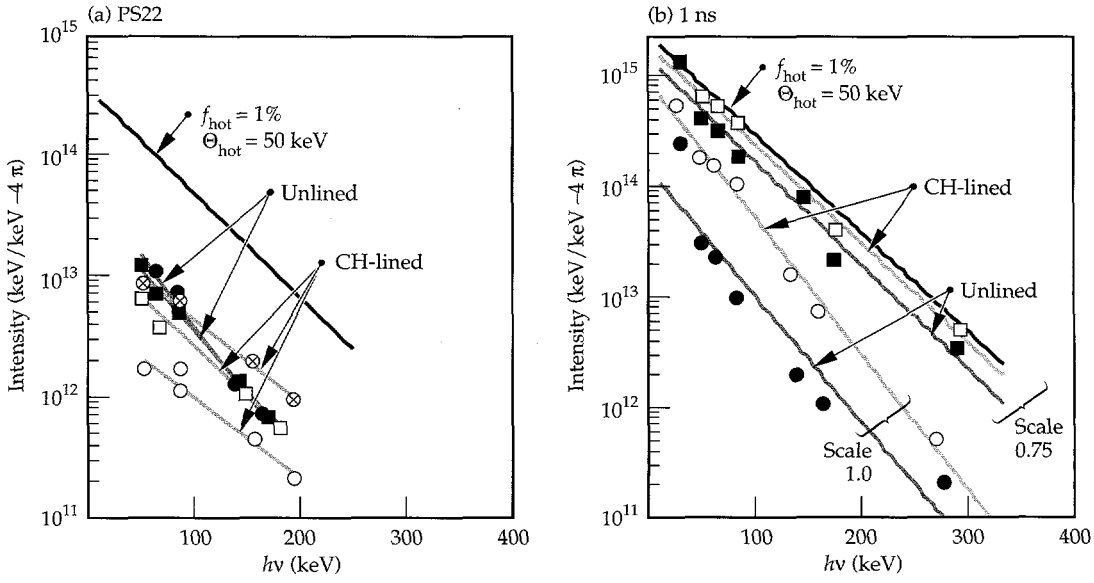

FIGURE 8. The x-ray bremsstrahlung spectra from hohlraums heated with (a) PS22 and (b) 1-ns square pulses. The data and fit from unlined (lined) hohlraums are the open (closed) symbols and dark gray (light gray) lines, respectively. The black lines are calculated spectra for f_{hot} of 1% (5%) for PS22 (1-ns square) laser pulse with a T_{hot} of 50 keV. (20-05-1093-3874pb01)

hohlraums is ~2%, a factor of two higher than unlined hohlraums. Even correcting for more recent scattering data, the targets still have $f_{abs} > 90\%$. For scale-0.75 hohlraums with 1-ns pulses, recent measurements from unlined hohlraums show higher levels of f_{SRS} than set by the HLP goals consistent with the lower η_{HOHL}. Beam smoothing techniques have not been applied to lined hohlraums. The lined hohlraums show slightly increased levels of f_{hot} but not enough to explain the decreased drive. For shaped pulses, f_{SBS} is ~15% for Ni-lined hohlraums compared with 5–7% for unlined or CH-lined hohlraums. A 10% reduction in coupling for PS22 would result in about a 5-eV-lower T_R consistent with the difference in drive between CH- and Ni-lined hohlraums. Although scattering losses can explain some of the differences in observed coupling, much of the reduction in drive for lined hohlraums is probably due to the difference in energy partition, as discussed in the "LASNEX Modeling" section of this article. All these results are for unsmoothed laser beams. Beam smoothing has been effective in reducing stimulated scattering levels in recent gas-filled hohlraum experiments.[8,15]

Semi-Empirical Modeling

The power balance model described in Eq. (1) provides a reasonable fit to the data for unlined hohlraums. Although the data set is not as extensive for lined hohlraums, the model also can explain the data, but with a reduced coupling efficiency. The model depends on two parameters: α and η_{HOHL}. The other parameters depend on hohlraum geometry and are usually assumed to be defined by the target geometry although, in principle, they could vary during the experiment due to plasma motion. Parts of NTC tasks are to study the wall albedo and laser coupling efficiency. The wall albedo experiments use burn-through patches measuring the time for the radiation wave to heat a known thickness of Au. These experiments show that present opacity and radiation wave models correctly predict burn-through times for x-ray drive above 200 eV. Details of these experiments have been reported elsewhere.[18]

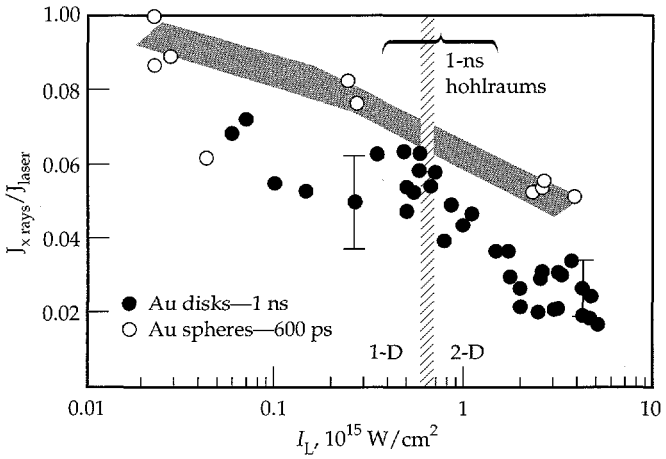

FIGURE 9. Conversion efficiency of converting laser energy into x rays from 0.1–4 keV vs laser intensity I_L. The solid circles are data from single-beam irradiation of Au disks with 1-ns pulses of 0.35-μm light. The open circles are data from Au spheres uniformly irradiated. The bracket denotes the range of intensities on the wall of a scale-1 Nova hohlraum whose data is shown in Fig. 5. The shaded bar shows the division between the regions where the underdense plasma expansion is quasi-1-D vs 2-D. (20-05-1292-3811pb01)

Two sets of experiments have investigated the effective efficiency for converting laser light to drive energy. In one set of experiments defined in HLP7, the conversion efficiency of laser light to x rays using planar disk targets η_{DISK} is studied. The other experiment investigates the difference in x-ray production between disk targets and hohlraums.

Scaling of x-ray conversion efficiency, η_{DISK}, has been studied as a function of laser intensity I_L, using 1-ns square laser pulses of 0.35-μm light. Figure 9 shows the results. The laser energy for most of the shots is ~1.5 kJ using a single beam of Nova. Intensity is varied by changing the spot size on the target. The x-ray intensity includes the spectrum from 0.1 to ~4 keV. The intensity from 0.1 to 1.5 keV is measured using the XRD array and the intensity in the 2–4 keV range is measured using absolutely calibrated x-ray spectrographs. For disk experiments shown in Fig. 9, η_{DISK} varies from 0.6 to 0.4 for intensities in the range of $\sim 4 \times 10^{14}$ W/cm^2 to 1.3×10^{15} W/cm^2. This is the intensity range of the initial wall irradiances for scale-1 hohlraums in Fig. 5 where η_{HOHL} is ~ 0.75. For scale-0.75 hohlraums, the initial wall irradiance is ~ 2.3×10^{15} W/cm^2 and η_{HOHL} is ~0.65 while η_{DISK} is ~0.25 at that intensity. Some of the lower conversion efficiency for a disk may be due to 2-D effects, especially at the higher intensity where the spot size is smaller than the expanding plasma. This transition is noted by the shaded line in Fig. 9 that denotes the estimated transition region between 1-D and 2-D corona expansion. For comparison, conversion efficiency from Au spheres, which are more uniformly irradiated, indicate a higher conversion efficiency (as shown in Fig. 9). Higher efficiencies are also obtained using longer pulses. Instantaneous conversion efficiencies increase from 50% after 1 ns to ~70% at 3 ns for an intensity of $\sim 4 \times 10^{14}$ W/cm^2.[19]

As discussed below, the hydrodynamic losses are reduced in a hohlraum as the hohlraum walls confine the underdense plasma expansion and more energy couples into x-ray heating. To test this modeling, experiments compared the brightness of the laser irradiated spot inside of the hohlraum with the brightness of the spot on a laser-irradiated disk. The results show that the peak brightness for both the hohlraum and the

disk is similar, but the extent of the bright spot in the hohlraum is greater and consistent with the enhanced conversion efficiency in the hohlraum. The increase in size of the hot spot in a hohlraum, as a function of time, is shown in Fig. 10 for a 1-ns square pulse experiment. The increase in width of the emission spot is plotted for three shots as a function of time for emission at 450 eV in Fig. 10(a) and 1200 eV in Fig. 10(b), defined by broadband filters and grazing incident x-ray mirrors.[20] The initial width is consistent with the size of the laser beam on the hohlraum wall. The increase in spot size is consistent with LASNEX predictions of the spot width, which are also shown in Fig. 10 (see the shaded circles).

Limited theoretical and experimental work has been done on extending the power balance model to lined hohlraums. The effect of the liner should be minimal on the dynamics of x-ray heating on the wall. The liner thicknesses used are typically optically thin to the radiation. Assuming cold opacities,[21] the 7500-Å CH and 1500-Å Ni liners are ~1.5 and 1 Planck mean-free paths thick, respectively, to a 200-eV blackbody radiator. These decrease significantly to much less than one optical depth when the plasma is heated to 100 eV.[22] The low-Z plasma therefore should not significantly modify the radiation heating dynamics of the wall (verified by LASNEX calculations).

To test the effects of the thin overcoat on laser hohlraum coupling, x-ray production from Ni-coated Au disks has been measured in a limited number of disk experiments. No experiments have been done on CH-coated disks. Figure 11 compares the conversion efficiency from the overcoated disks with that of pure Au disks as a function of time. Two experiments are done at ~4×10^{14} W/cm^2 with 2-ns square pulses and one experiment is done at ~1×10^{15} W/cm^2 with a 1-ns pulse. The data show a slight delay in x-ray production (~200 ps) for a Ni overcoat compared with a Au disk. The time required to burn through the Ni overcoat is estimated to be ~100–300 ps depending on the model and laser intensity.[23] After the initial burn-through of the Ni, x-ray production is nearly equal to that of Au for 4×10^{14} W/cm^2 but is only 50% of the pure Au conversion efficiency for 1×10^{15} W/cm^2. The effect of the overcoat on x-ray production at high intensity is not presently understood. At high intensity the laser spot is smaller than corona expansion scales and is in the 2-D regime. Possible effects of lateral transport and conduction could be affecting the conversion efficiency.

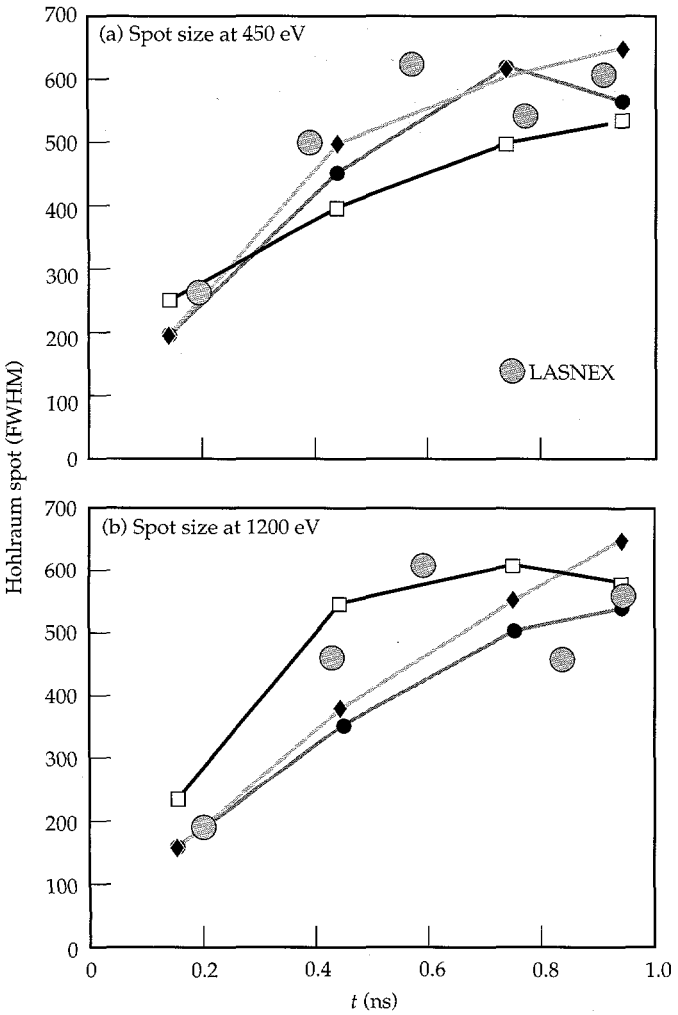

FIGURE 10. The full width at half maximum (FWHM) of the hot spot in a hohlraum produced by the laser spot vs time. The data is taken from three shots for x rays at (a) 450 eV and (b) 1200 eV. (20-05-1292-3806pb01)

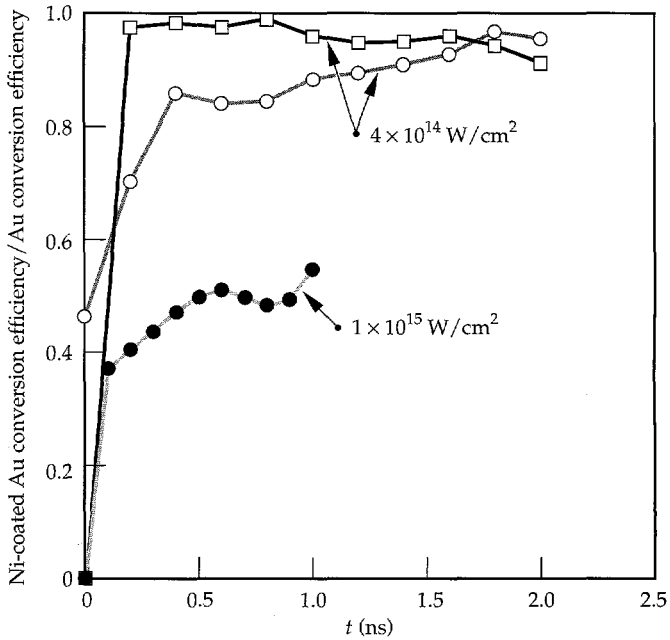

FIGURE 11. The ratio of x-ray conversion efficiency from a 1500-Å Ni coated Au disk to an uncoated Au disk vs time. Data are from a 0.35-μm laser irradiation of 4×10^{14} W/cm^2 in a 2-ns square pulse and 1×10^{15} W/cm^2 in a 1-ns square pulse. (20-05-1095-2365pb01)

LASNEX Modeling

Using LASNEX, extensive work has been done modeling the hohlraums.[24] Calculations are fully "integrated" and 2-D. The laser deposition is modeled by using a 2-D representation of the 3-D Nova laser irradiation geometry in a statistical ray generation method. To extract radiation drive from the simulation, a small "virtual" sphere is placed at the center of the hohlraum simulation, and incident flux on the sphere is calculated. The simulations reproduce the x-ray drive measured in unlined hohlraums quite well. Figure 5, shown earlier, compares the peak drive calculated for 1-ns laser pulses with shock velocity measurements. The simulations assume 100% absorption consistent with experiments for scale-1 unlined hohlraums where absorption is greater than 95%. Simulations also reproduce drive in shaped-pulse experiments. LASNEX calculates a peak drive of 215 eV for PS22 when time-dependent SRS and SBS scattering and diagnostic hole losses are included.

Simulations have also been done for several of the lined hohlraum experiments. Generally, the peak drive is calculated to be lower for lined hohlraums compared with unlined hohlraums. Table 1 lists the decrease in calculated peak drive and compares it with experimental decrements. The lower peak drive agrees with the measurements within the statistical uncertainty of the data. The one data set that has the largest difference is the PS22 Ni-lined data. The calculations assume no change in absorption between lined and unlined targets. When the Ni-lined data is reduced by ~10% for the increased f_{SBS} of ~10%, the calculations and data show even better correlation.

Lined hohlraums are calculated to be cooler because more energy couples into plasma blowoff compared with unlined hohlraums. Figure 12 shows calculations of the energy partitioning in an unlined Au hohlraum and a 2150-Å Ni-lined hohlraum. The energy in wall blowoff, defined as the energy contained in the underdense plasma filling the hohlraum, increases by ~1.5 kJ for the lined hohlraum. This produces a lower T_R because it leaves less energy to heat the walls and, self-consistently, to reradiate out the holes. The cause of the increased blowoff energy is due to the higher specific heat for the low-Z blowoff compared with the high-Z blowoff. The specific heat scales

$$\left[\frac{(Z+1)}{A}\right] + E_{ion}, \qquad (2)$$

where Z is the average ion charge and A is the atomic number. For Au irradiated by the laser, Z is ~55 while CH and Ni are nearly fully ionized. The specific heat for Ni and CH are factors of 2 to 2.5 times as high as Au from similar plasma conditions.

Summary

The drive goals for HLP1 and HLP2 are met with over 200 eV obtained for PS22 and 270 eV obtained for a scale-0.75 hohlraum with 30 TW in a 1-ns pulse. The drive is lower for lined hohlraums compared with unlined hohlraums and is generally explained by higher coupling to plasma blowoff in the hohlraums. Although the diagnostics were not optimal for the experiments, the HLP1 coupling goals for f_{abs}, f_{SBS}, f_{hot}, and f_{SRS} appear to have been met for the PS22 CH-lined experiments, although for Ni-lined hohlraums $f_{SBS} \approx 15\%$. To verify this, more experiments need to be done with the improved Nova diagnostics. The higher levels in Ni-lined hohlraums, compared with CH-lined hohlraums, are consistent with SBS in CH-lined hohlraums being Landau damped by the H and C

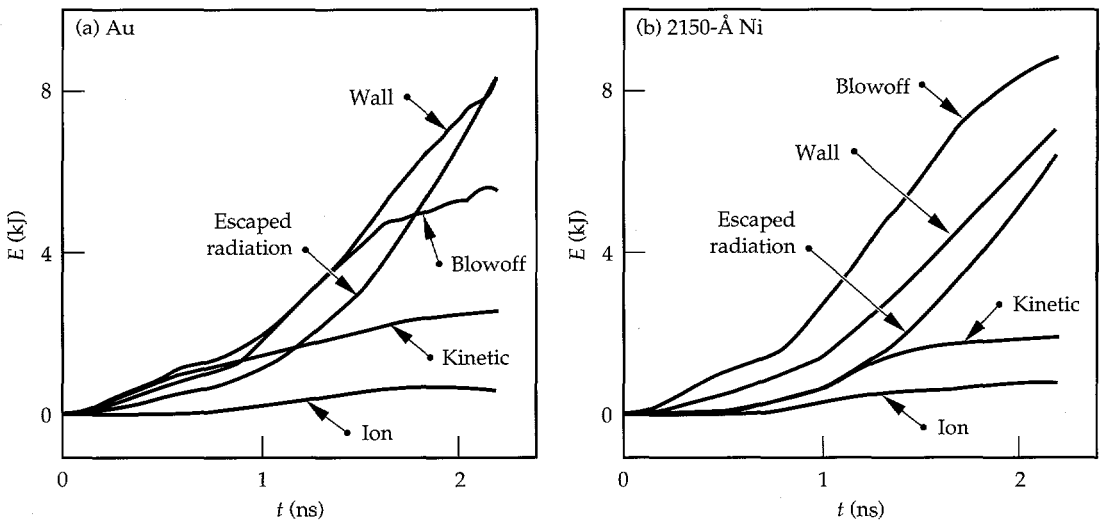

FIGURE 12. Partition of energy E as a function of time from a LASNEX simulation for (a) a pure Au hohlraum and (b) a hohlraum lined with 2150-Å Ni. Both hohlraums are heated with 0.35-μm light using PS22.
(50-04-1093-3913pb01)

mixed species plasma.[25] By producing a Ni and H mixed liner, Landau damping could also be effective for reducing SBS in the Ni-lined plasmas. For HLP2, the scale-1 hohlraums appear to meet the coupling goals, but f_{SRS} for scale-0.75 hohlraums appear to be higher than 5%. The most recent measurements for unlined scale-0.75 hohlraums is ~13%. SRS from lined hohlraums have not been measured, but x-ray bremsstrahlung measurements suggest that f_{SRS} for lined hohlraums may be only slightly higher. The lower η_{HOHL} for scale-0.75 unlined hohlraums is consistent with the measured f_{SRS} and with hohlraum modeling, which includes the scattering models. Future experiments can explore reducing SRS by the use of beam conditioning, as demonstrated in gas-filled hohlraums.[15]

Notes and References

1. J. H. Nuckolls, *Phys. Today* **35**(9) 24 (1982).
2. J. D. Lindl, *Phys. Plasmas* **2**(11), 3933–4024 (1995).
3. L. J. Suter, A. A. Hauer, L. V. Powers, D. B. Ress, et al., *Phys. Rev. Lett.* **73**, 2328 (1994).
4. S. W. Haan, S. M. Pollaine, J. D. Lindl, L. J. Suter, et al., *Phys. Plasmas* **2**, 2480 (1995).
5. R. L. Kauffman, H. N. Kornblum, D. W. Phillion, C. B. Darrow, et al., *Rev. Sci. Instrum.* **66**, 678 (1995).
6. H. N. Kornblum, R. L. Kauffman, and J. A. Smith, *Rev. Sci. Instrum.* **57** 2179–81 (1986).
7. P. E.. Young, K. G. Estabrook, W. L. Kruer, E. A. Williams, et al., *Phys. Fluids B* **2**, 1907–1917 (1990).
8. R. K. Kirkwood C. A. Back, K. S. Bradley, D. H. Kalantar, et al., *Bull. APS* **39**, 1753 (1994); B. J. Macgowan et al., "Laser–Plasma Interactions in NIF-Scale Plasmas (HLP5 and HLP6)," p. 305 of this *Quarterly*.
9. *Laser Program Annual Report–1978*, 6–8, Lawrence Livermore National Laboratory, Livermore, CA, UCRL-50021-78 (1979).
10. P. M. Bell, J. D. Kilkenny, G. Power, R. Bonner, and D. K. Bradley, *Ultrahigh Speed and High Speed Photography, Photonics, and Videography '89* (SPIE, Bellingham, WA, 1989; *Proc. SPIE*, **1155**) pp. 430–444.
11. R. L. Kauffman, L. J. Suter, C. B. Darrow, J. D. Kilkenny, et al., *Phys. Rev. Lett.* **73**, 2320 (1994).
12. R. Sigel, R. Pakula, S. Sakabe, and G. D. Tsakiris, *Phys. Rev. A* **38**, 5779 (1988).
13. M. D. Rosen, Lawrence Livermore National Laboratory, Livermore, CA, private communication (1995).
14. R. E. Marshak, *Phys. Fluids* **1**, 24 (1958).
15. B. J. MacGowan, R. K. Kirkwood, and D. S. Montgomery, Lawrence Livermore National Laboratory, Livermore, CA, private communication (1995).
16. W. C. Mead, E. M. Campbell, K. G. Estabrook, R. E. Turner, et al., *Phys. Fluids* **26**, 2316 (1983).
17. *Laser Program Annual Report–1985*, 4–4, Lawrence Livermore National Laboratory, Livermore, CA, UCRL-50021-85 (1986).
18. J. L. Porter, T. J. Orzechowski, M. D. Rosen, A. R. Thiessen, et al., *1994 ICF Annual Report*, 125, Lawrence Livermore National Laboratory, Livermore, CA, UCRL-LR-105820-94 (1995).
19. F. Ze, D. R. Kania, S. H. Langer, H. Kornblum, et al., *J. Appl. Phys.* **66**, 1935–39 (1989).
20. F. Ze, R. L. Kauffman, J. D. Kilkenny, J. Wiedwald, et al., *Rev. Sci. Instrum.* **63**, 5124–6 (1992).
21. B. L. Henke, E. M. Gullickson, J. C. Davis, *Atomic Data and Nuclear Data Tables* **54**, 181 (1993).
22. *WorkOp–III: 94 Final Report*, Eds., A. Rickert, K. Eidmann, J. Meyer–ter–Vehn, F. J. D. Serduke, and C. A. Iglesias, *Max–Planck–Institut für Quantenoptik* (Report MPQ 204), Hans–Kopferman–Strasse 1, 85748 Garching, Germany (1995).
23. R. Fabbro, C. Max, and E. Fabre, *Phys. Fluids* **28**, 1463 (1985).
24. G. B. Zimmerman and W. L. Kruer, *Comments Plasma Phys. Controlled Fusion* **2**, 51 (1975).
25. E. A. Williams, R. L. Berger, R. P. Drake, A. M. Rubenchik, et al., *Phys. Plasmas* **2**, 129 (1995).

NOVA SYMMETRY: EXPERIMENTS, MODELING, AND INTERPRETATION (HLP3 AND HLP4)

L. J. Suter *N. Delameter** *E. K. Lindman**
*A. A. Hauer** *S. G. Glendinning* *A. R. Thiessen*
L. V. Powers *W. W. Hsing** *R. E. Turner*
D. B. Ress *O. L. Landen*

Introduction

Understanding and controlling capsule implosion symmetry is a key requirement for inertial confinement fusion (ICF). Symmetry was specifically called out in the Nova Technical Contract (NTC) as the HLP4 task. Later, elements of HLP3 were expanded to include symmetry work. For nearly a decade and a half it has been recognized that the fundamental asymmetry in a laser-heated hohlraum is a long-wavelength pole-waist radiation flux variation[1] that varies like the P_2 Legendre polynomial.[2] It has also been recognized that we can control this asymmetry and achieve nearly symmetric implosions by appropriately pointing the laser beams.[3]

Review of Symmetry in Hohlraums

To understand symmetry in hohlraums, consider a cylindrically shaped, Nova-like hohlraum with beams aimed as shown in Fig. 1(a). An observer at the capsule location would see a collimated source flux vs angle approximately as shown in the flux vs polar angle plot. The laser-produced hot spot causes a peak in this source at ~60° polar angle. The cold, nonemitting laser entrance hole (LEH) provides zero flux at low polar angle. If we resolve this source flux vs angle into its Legendre polynomial coefficients, we find a P_0 and P_4 component of order unity and a substantial, negative P_2 component. However, because each point on the capsule's ablation surface integrates radiation flux over its 2π sky, the absorbed flux vs angle will be different from the source. For a small capsule, Green[2] showed that this integration causes the P_2 component to be attenuated by ~4, the P_4 component by 24, and higher modes by even more. Consequently, the major asymmetry in the absorbed flux is the P_2 asymmetry. For the capsule in the hohlraum of Fig. 1(a), that asymmetry has a *negative* P_2 component which, ultimately, produces a prolate implosion.

We can control the P_2 asymmetry by changing the pointing/aiming of the laser beams.[3] Figure 1(b) illustrates a situation where the beams are aimed to form hot spots much farther apart. Then, the collimated source flux has a substantial, *positive* P_2 component as well as P_0 and P_4 components of order unity. The 2π integration at the ablation surface causes the capsule absorbed flux to be dominated by a P_0 and positive P_2 component only, which ultimately produces an oblate implosion. Somewhere in between the situations shown in Figs. 1(a) and 1(b) is a beam pointing where the P_2 component of the source asymmetry vanishes [(Fig. 1(c)]. There, the ablation flux is dominated by the P_0 component and small, higher-order modes to produce an implosion that is substantially spherical.

Green's work on the attenuation of the P_2, P_4, and higher components was done for a small capsule inside a spherical hohlraum. Finite-size capsules and cylindrical hohlraums cause quantitative changes[4–6] but no significant qualitative changes.

Summary of Symmetry Experiments

Between 1987 and 1993, we performed a number of scaling experiments to examine our ability to understand the time-integrated P_2 asymmetry and to control it with beam pointing. In the most mature method of assessing the asymmetry, a pure-plastic capsule[7] filled with D_2 and a trace of Ar gas is placed in the center of a Nova hohlraum and is imploded by x-ray drive. Following the implosion is a bright flash of x rays produced by the hot, compressed fuel. At that time, we take pictures of the images formed by x rays viewed 90° off the polar axis through a hole in the side of the

* Los Alamos National Laboratory, Los Alamos, New Mexico

hohlraum. The resulting images show emission that is round, oblate, or prolate, depending on the beam pointing. (We discuss beam pointing later; also see Fig. 4 for an illustration.) Figure 2 shows some of our earliest images, from pure Au hohlraums irradiated by 1-ns flat-top pulses.

These first experiments demonstrated our ability to produce round, relatively symmetric implosions and confirmed that the long-wavelength mode dominated the hohlraum asymmetry. They also showed that we could control implosion asymmetry with beam pointing.[8] These experiments were done in early versions of our scale 1.0 hohlraums (1600-μm-i.d., ~2700-μm-long, 800-μm LEH diam) and used what has become our standard symmetry capsule—nominal dimensions of 440-μm-i.d., 55-μm-thick CH ablator/pusher, filled with 50 atm D_2 and 0.1% (at.%) Ar.

We have produced x-ray images of implosions using a number of gated and time-integrated diagnostics that have evolved over the years.[8–12] Numerical simulations of our standard symmetry capsule show good sensitivity to asymmetry. For pulse-shaped, convergence-10 implosions, we estimate that a 7%, fixed-in-time, pole-to-waist flux asymmetry will produce a 2:1 distortion of the x-ray image. We can measure distortions much closer to 1:1; therefore, we believe that the accuracy of our diagnostic technique is about 1%. That is, we can resolve equivalent, fixed-in-time asymmetries of ~1% pole-to-waist flux variation. A large body of evidence[13] indicates that these capsules, which operate at a pusher convergence of 7 to 10 depending on the pulse shape, do perform approximately as our model. There is good agreement between simulated and experimental capsule neutron yields, time-of-neutron production, and

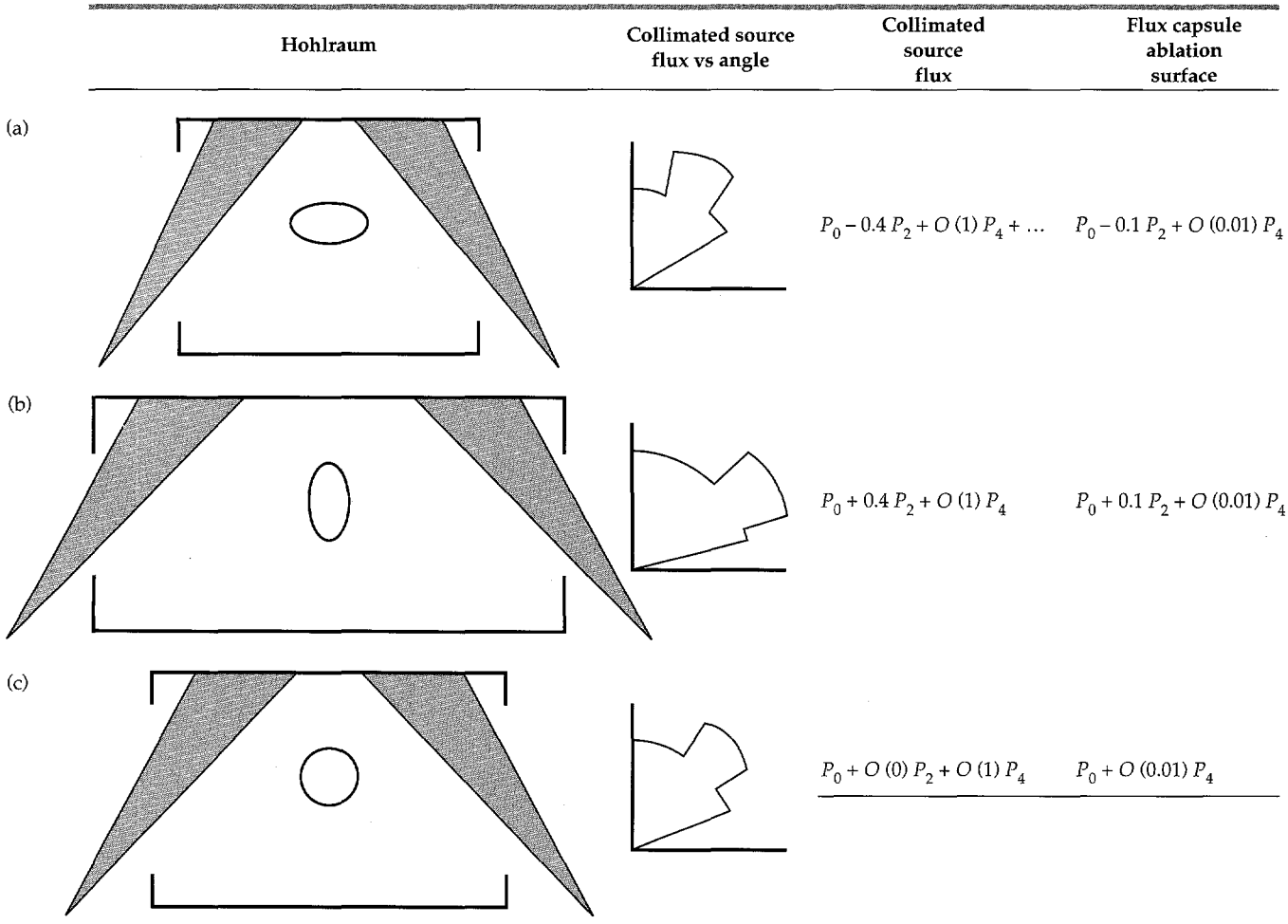

FIGURE 1. The collimated source flux vs angle viewed by a capsule in a laser-heated hohlraum has a substantial P_2, P_4, etc., component in addition to the P_0 component. Since each point on the ablation surface integrates over its 2π sky, the P_4, etc., components of drive asymmetry are heavily damped, leaving only the long-wavelength P_2 component as an asymmetry. This asymmetry can be controlled by beam pointing (see variations in a, b, and c for comparison). (20-03-0995-2123pb01)

image sizes. Spectroscopy confirms theoretical predictions that the x rays are principally produced by the Ar and that we are, in fact, imaging the fuel volume. Analysis of spectroscopy data and neutron data confirms calculated convergences. Reference 14 provides a comprehensive review of current drive asymmetry measurement techniques. Reference 15 provides a review of symmetry analysis.

The earliest experiments confirmed that the long-wavelength mode dominated and that it could be varied from shot to shot by changing the beam pointing in our out, as demonstrated in Fig. 2.[16] These results were largely qualitative. In 1990, we began producing systematic, quantitative symmetry studies.[14] The basic procedure of these experiments has been the same—for a given pulse shape and hohlraum type, we produce a symmetry scaling by varying the beam pointing while observing the resulting shapes of the capsules in self emission. Moving the beam pointing in tends to make a more prolate implosion; moving it out makes a more oblate implosion.

Between 1990 and 1993, we produced nine different symmetry scaling databases with the Nova laser using the three pulse shapes illustrated in Fig. 3. We have done three scalings with 1-ns flat-top pulses, five scalings with our 26-kJ, 2.2-ns, 3:1 contrast ratio pulse shape, called PS22, and one scaling with an 8:1 contrast ratio, 3.2-ns, 27-kJ pulse shape, called PS23. We have used these pulse shapes to irradiate both pure Au hohlraums and lined hohlraums as specified in the NTC. Lined hohlraums are Au hohlraums lined on the inside with a thin layer of either low-Z material (e.g., CH) or mid-Z material (e.g., Ni). We investigated lined hohlraums because we believe something like a liner to be necessary at larger, ignition scales.[17] For ignition hohlraums, we calculate that pure Au designs will fill with high-Z plasma. This causes the laser absorption region to move almost to the LEH, producing an unacceptably large radiation flux asymmetry on the capsule. Liners are one way to mitigate this effect by replacing the high-Z blowoff with low- or mid-Z blowoff.

With 1-ns flat-tops, we shot both pure Au and Ni-lined (1500-Å) Au hohlraums fixed in length at 2700 μm. We have also shot pure Au hohlraums where we varied the length of the hohlraum with the pointing so that the beams always cross in the plane of the LEH. We have done five scalings with PS22: fixed-length Au, Ni-lined Au, variable-length pure Au, Ni-lined Au, and CH-lined (0.75-μm) Au hohlraums. Our PS23 series used pure Au hohlraums that were open cylinders. As mentioned in the Introduction and in "Ignition Target

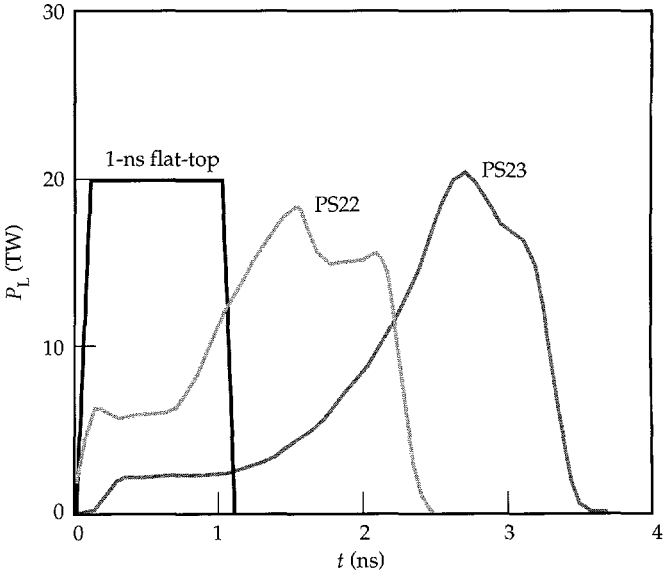

FIGURE 3. Symmetry scaling experiments using three different pulse shapes. (20-03-0995-2124pb01)

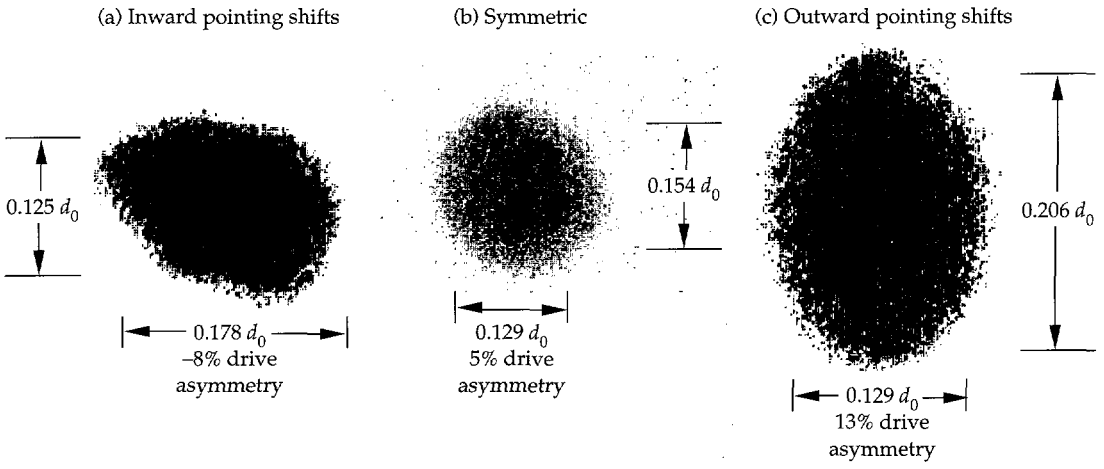

FIGURE 2. Capsule self-emission x-ray images from 1-ns experiments at three different beam pointing angles: (a) inward pointing, (b) symmetric, and (c) outward pointing. This illustration demonstrates that the fundamental hohlraum asymmetry is the long-wavelength P_2 asymmetry and can be controlled with beam pointing. (20-03-0995-2125pb01)

Design for the National Ignition Facility" on p. 215, the NIF baseline target now uses an initial gas fill to displace the Au blowoff. Nova experiments with gas-filled hohlraums have also demonstrated control of symmetry. However, these experiments are still in progress and therefore will be reported at a later time.

Modeling the Experiments

We use our 2-D LASNEX computer code[18] to perform detailed modeling of these experiments. Figure 4 is a cut-away, at $t = 0$, from a simulation of a hohlraum containing a pure-plastic capsule that is irradiated by a "realistic" 2-D representation of a three-dimensional (3-D) Nova laser beam.[19] The wall materials, laser power vs time, etc., of a given simulation are our best estimate of what was used in the experiments we are trying to model. To model a given symmetry scaling, we performed a number of simulations with different beam pointings. At stagnation, our simulated capsules, like real capsules, produce a burst of x rays that can be imaged. A post-processor simulates the actual x-ray diagnostics, producing synthetic images that vary with pointing from oblate or prolate (like the experiment). The ratio of the image's full-width at half maximum (FWHM), perpendicular to the polar axis to the FWHM along the polar axis is the "distortion," the quantity we vary with pointing and compare with experiment.

Our calculations start off fully Lagrangian (matter is fixed in the zones of a moving mesh). Later in time, after a considerable amount of blowoff has filled the hohlraum, we perform a major rezone and change our numerical scheme. The main part of the hohlraum becomes Eulerian (matter flows through a fixed mesh), allowing the calculation to run in spite of the large sheer flows. Most of the capsule, however, remains Lagrangian—the accepted procedure for modeling nearly spherical implosions. We interface the Eulerian and Lagrangian regions with a stretching region that maintains equal-ratio zoning—a hybrid mesh that has matter flowing through it while moving slowly. Using three numerical schemes in the same calculation allows us to simulate both the main hohlraum and the capsule with the most appropriate numerical technique.

To provide an example of how we model a given scaling, consider a series of shots with Au hohlraums (1600-μm-diam with 1200-μm-diam LEHs lined with 1500-Å Ni). In this series, to keep LEH effects approximately the same for all pointings we varied the hohlraum length with pointing so that the beams always crossed in the plane of the LEH. We used the nominal capsules, defined earlier, and irradiated these targets with PS22. The self-emission x-ray images from the imploded capsule were the key observations made on this (and all other) scaling series. Our x-ray diagnostics were time-resolved (~100-ps frame time) and time-integrated cameras filtered to measure emission >3 keV from the Ar fuel dopant.

Figure 5 displays the results of the PS22 series experimental scaling and compares it with our model. The solid circles are distortions from our experiments as a function of beam pointing. The horizontal error bar shows an estimated ±50-μm systematic uncertainty in the absolute pointing of the beams (the relative shot-to-shot pointing jitter is believed to be considerably smaller than this). The open circles are modeling distortions. Both experiment and modeling agree that we can control Nova symmetry by varying the beam pointing. Also, they both produce about the same

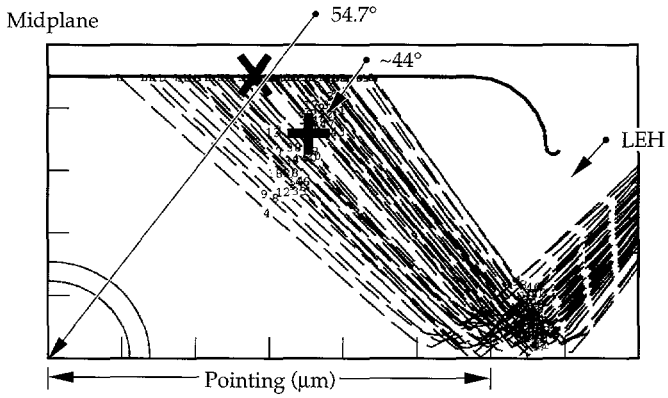

FIGURE 4. Cutaway at $t = 0$ from a 2-D simulation of a hohlraum containing a pure-plastic capsule with a realistic representation of Nova's beams. The calculation is cylindrically symmetric around the horizontal axis and left-right symmetric across the midplane. The beams enter through LEHs at the ends of the hohlraum. Pointing is the distance between the midplane and where the beams cross (i.e., the reflection off the horizontal, rotational axis of symmetry). The "X" and "+" show the center of emissivity early in time at 1.4 ns, respectively. (20-03-0995-2126pb01)

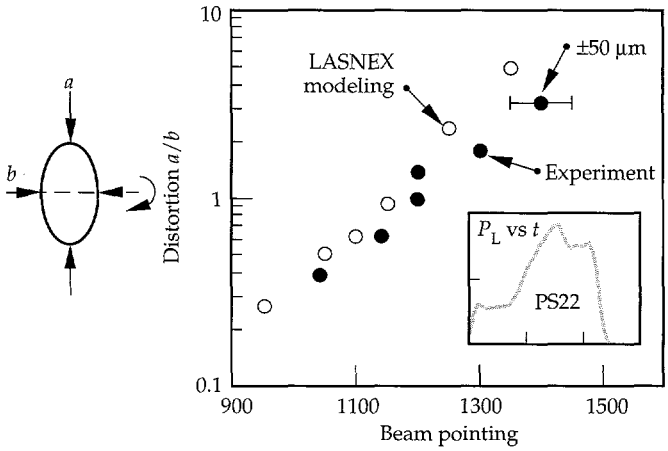

FIGURE 5. Capsule image distortion vs pointing from a series using Ni-lined hohlraums irradiated by PS22. (Inset: Relative laser power vs time for PS22.). Experimental uncertainty is ±50 μm. (20-03-0995-2127pb01)

pointing of best symmetry (~1200 ± 50 μm in experiment and ~1150 μm in modeling).

The pointing of best symmetry changes as we vary the pulse shape. For example, another scaling series used fixed length (2700-μm), Ni-lined Au hohlraums irradiated with 1-ns flat-top pulses. In this series, both modeling and experiment also verified that we can control Nova symmetry by varying the beam pointing. However, for this pulse shape, the pointing of best symmetry is about 100 μm outward from the best pointing found in the PS22 series. For this 1-ns experiment, the pointing of best symmetry is ~1320 ± 50 μm in experiment and ~1250 μm in modeling.

Scaling of the Pointing of Best Symmetry

Figure 6 summarizes our ability to estimate the pointing of best symmetry over our nine symmetry scaling databases. It plots the pointing of best symmetry inferred from experiment against that of our integrated LASNEX simulations. Overall, we find the agreement to be very satisfactory. The vertical error bars in this plot indicate only the uncertainty in the pointing of best symmetry extracted from each experimental dataset, using the nominal pointing. The error bars do not include the systematic uncertainty in Nova's absolute pointing (~50 μm), which would allow all the points to be moved as a group, either up (toward poorer agreement) or down (better agreement). Regardless of systematic differences, the most significant and apparent feature of the plot is this: *the longer the pulse shape, the farther in we must point the beams to get good symmetry.*

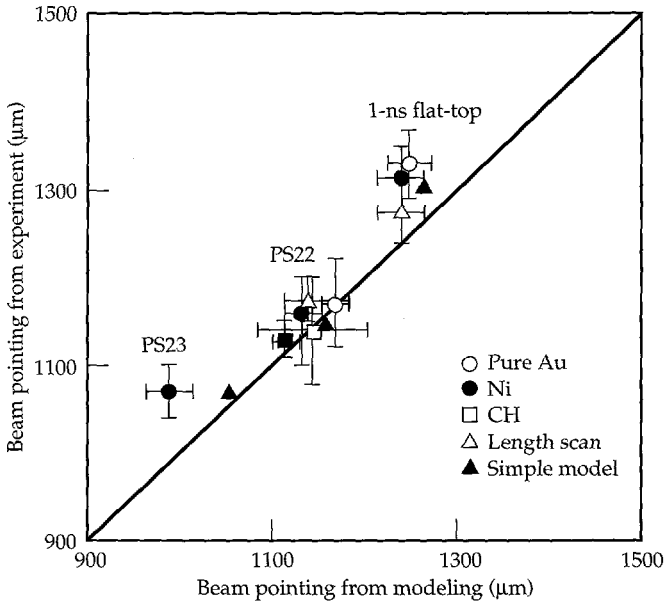

FIGURE 6. Pointing of best symmetry in our experiment vs pointing of best symmetry from our modeling. The longer the pulse shape, the farther in the beams need to be moved to get good symmetry. The solid triangles plot the pointing to compare with Eq. (2).
(20-03-0995-2128pb01)

The reason for this is found in the basic principles of symmetry scaling in Nova-type hohlraums. First, there are hot, laser-produced emission rings that migrate toward a smaller polar angle (when viewed from the capsule position) because of bulk plasma evolution. We refer to this migration as "spot motion." Second, there is also an "optimal" polar angle for the rings where time-integrated pole-flux equals equator flux (~48° for these hohlraums). Third, to get good symmetry we must point the beams so the emission rings pass through 48° when we deliver ~50% of a shape's useful energy. Since spot velocity is weakly dependent on laser intensity, we move the beams farther inward with longer pulses.

In our simulations, there are three components to spot motion. First, dense plasma evolution from the cylindrical walls causes the laser deposition region to move inward and, because of the beam geometry, toward the LEH. Second, there is a refractive component off plasma that accumulates on axis. Third, there can be a low-intensity volume emission when Au blowoff fills the hohlraum, pulling the average center of emissivity farther down from the walls. In our simulations, which use a nonLTE, average-atom atomic physics model,[20] the Au blowoff is optically thin to thermal radiation. Consequently, volume absorption does not play a significant role in determining the capsule flux.

To see how spot motion can cause the scaling shown in Fig. 6, first recall that the fundamental asymmetry in a left-right symmetric, Nova-like hohlraum is a long-wavelength, pole-to-waist flux variation that varies like the P_2 Legendre polynomial.[2] Whether the asymmetry is pole high or equator high depends on the polar angle to the center of the laser-produced, x-ray emission ring. In an idealized hohlraum without LEHs and with otherwise uniform walls, the drive asymmetry will clearly be pole high when the emission ring is at a very small polar angle and equator high when the emission ring is near the midplane of the hohlraum. Somewhere in between, the pole and equator fluxes will be equal. In a spherical hohlraum, the P_2 component of capsule flux vanishes when the P_2 component of the source flux is zero.[2] This occurs when the "center of emissivity" of the emission ring is at the polar angle where P_2 is zero, 54.7°. For larger angles, the flux onto the capsule will be equator high, and for smaller angles, pole high.

An LEH modifies this description quantitatively, but not qualitatively. To compensate for the lack of wall radiation from the LEH, the angle to the center of emissivity in a spherical hohlraum must be smaller

than 54.7° for the net P_2 component to vanish. Exactly how much smaller than 54.7° is a function of both the emission-ring to background-wall intensity ratio and the LEH size. For example, the angle where the P_2 component of the source vanishes is about 44° in an idealized spherical hohlraum with wall and LEH areas the same as ours and a wall albedo (which determines the emission-ring to background-wall intensity ratio) of ~0.7. This albedo is typical of a rising, nanosecond-scale pulse shape. In our more detailed LASNEX simulations, we find the pole:waist fluxes are balanced when the center of emissivity is at ~48°. These simulations include higher *l*-mode components, volume emission, and mode-coupling due to having a sphere inside a cylinder.

With this background, we can simply interpret features found in our LASNEX modeling. Figure 7 plots ratios of capsule ablation pressure at the pole to that at the equator vs time in pure Au hohlraums near the pointing of best symmetry for each pulse shape. Early in time, the ablation pressure is equator high. Later in time, the pressure is pole high. Analysis of our simulations indicates that this time-dependent asymmetry is produced mainly by spot motion. As shown in Fig. 4, the angle to the center of the beam at $t = 0$ for PS22 is >54.7°. Quantitative analysis shows the center of emissivity to be located at the "X" in Fig. 4 at ~57°. The simple symmetry arguments lead us to expect the drive to be equator high, as Fig. 7 shows in the early PS22 curve. By 1.4 ns, spot motion has caused the center of emissivity to move to the "+" in Fig. 4 to ~44°. There, the ablation pressure ratio has become about 10% pole high.

Spot motion, the migration of the radiation production region to smaller polar angles, causes a simulated Nova-type hohlraum to have the characteristic equator-high to pole-high asymmetry swing shown in Fig. 7. For all three pulse shapes, we find that near the pointing of best symmetry the center of emissivity sweeps through the "optimal angle" (where pole pressure = equator pressure, ~48° for these hohlraums) when ~50% of a shape's useful energy has been delivered. This 50% value makes sense. If the pressures were equal when a very different fraction of energy was delivered, the implosion would be dominated by either pole-high or equator-high flux and would be obviously distorted. Therefore, since spot velocity depends weakly on laser power P_L, longer pulses need more inward pointing for best symmetry because $t_{50\%}$, the time to deliver ~50% of the energy, is longer, leading to more spot motion.

LASNEX simulations show spot-angular velocity to be very weakly dependent on P_L. Figure 8 is a plot of the angle to the center of emissivity vs time for our three pulse shapes (refer to Fig. 3). Over the period when the first 50% of the laser energy is delivered, the angular velocity $d\theta/dt$ of the center of emissivity in our simulations increases only as the logarithm of P_L (measured in TW) closely following

$$\frac{d\theta}{dt} = \frac{6^\circ}{\text{ns}} + \frac{3.9^\circ}{\text{ns}}\left(\log_{10} P_L\right). \qquad (1)$$

We can couple this expression for spot motion with the need to have the center of emissivity at ~48° when ~50% of the laser energy has been delivered to produce a simple expression for the pointing of best symmetry

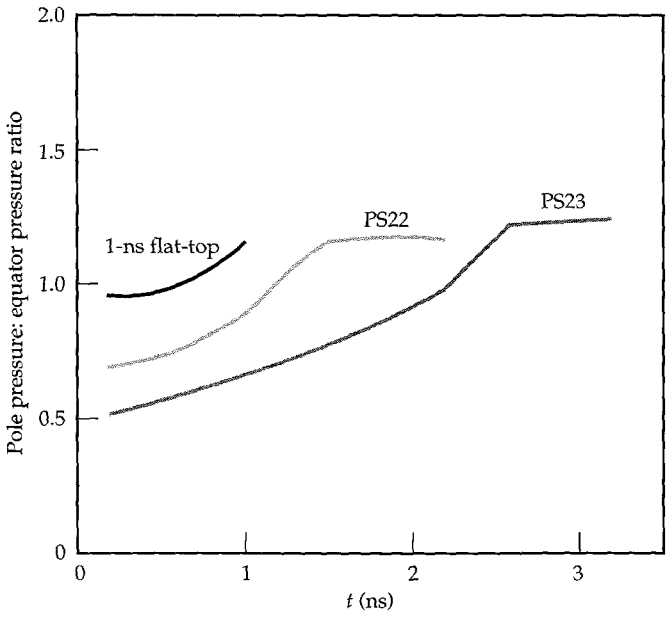

FIGURE 7. Ratio of capsule ablation pressure at the pole to the ablation pressure at the equator vs time for our three pulse shapes. (20-03-0995-2129pb01)

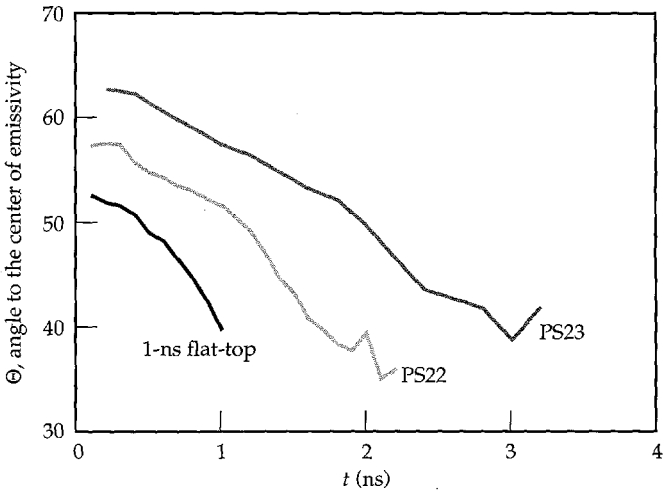

FIGURE 8. Angle to the center of emissivity vs time in our LASNEX simulations of the three pulse shapes. The angular velocity during the period when the first half of a pulse shape's energy is delivered varies slowly with laser intensity. (20-03-0995-2130pb01)

$$\text{best pointing} = 671\ \mu\text{m} + \left[\frac{800\ \mu\text{m}}{\tan\left(48^\circ + \frac{d\theta}{dt} \times t_{50\%}\right)}\right]. \quad (2)$$

This expression is for our standard 800-μm radius hohlraums and Nova's 50° half-cone angle. The results of this very simple model are plotted as the filled triangles in Fig. 6 and also agree well with our database.

Spot Motion

Since 1986, we have performed separate experiments to observe laser-produced x-ray emission spots and their migration.[21] We cut an 800 μm × 1200 μm rectangular observation port into the side of a hohlraum through which we take time-resolved x-ray images of the opposite wall with a three-channel x-ray framing camera that takes snapshots at four different times.[22] Our field of view includes the initial spot of a beam as well as some of the surrounding region. Figure 9 shows the images from the 450-eV channel for a pure Au PS22 experiment. Qualitatively, these images verify that there are spots and that they do migrate toward the LEH. Quantitatively, we analyze these images to find the center of emission, within the port's field of view, at various times. For comparison, we quantitatively analyze LASNEX simulations of the experiment with a postprocessor that mimics the imaging diagnostic and the analysis. Figure 10 shows such a comparison, plotting the position of the center of emission for the 450-eV channel from pure Au PS22 simulations and experiments. The good comparison with LASNEX shows that we can calculate the component of spot motion observed—the component along the hohlraum wall. The data from four different shots show that the motion is reproducible. Reproducible spot motion has also been indirectly corroborated by Precision Nova shots that produced nearly identical capsule shapes and performances for five PS22 shots at one pointing and four shots at another (see Fig. 11).

Time-Dependent Asymmetry

An essential feature of theory and simulation is that the asymmetry in a Nova-like hohlraum will vary over

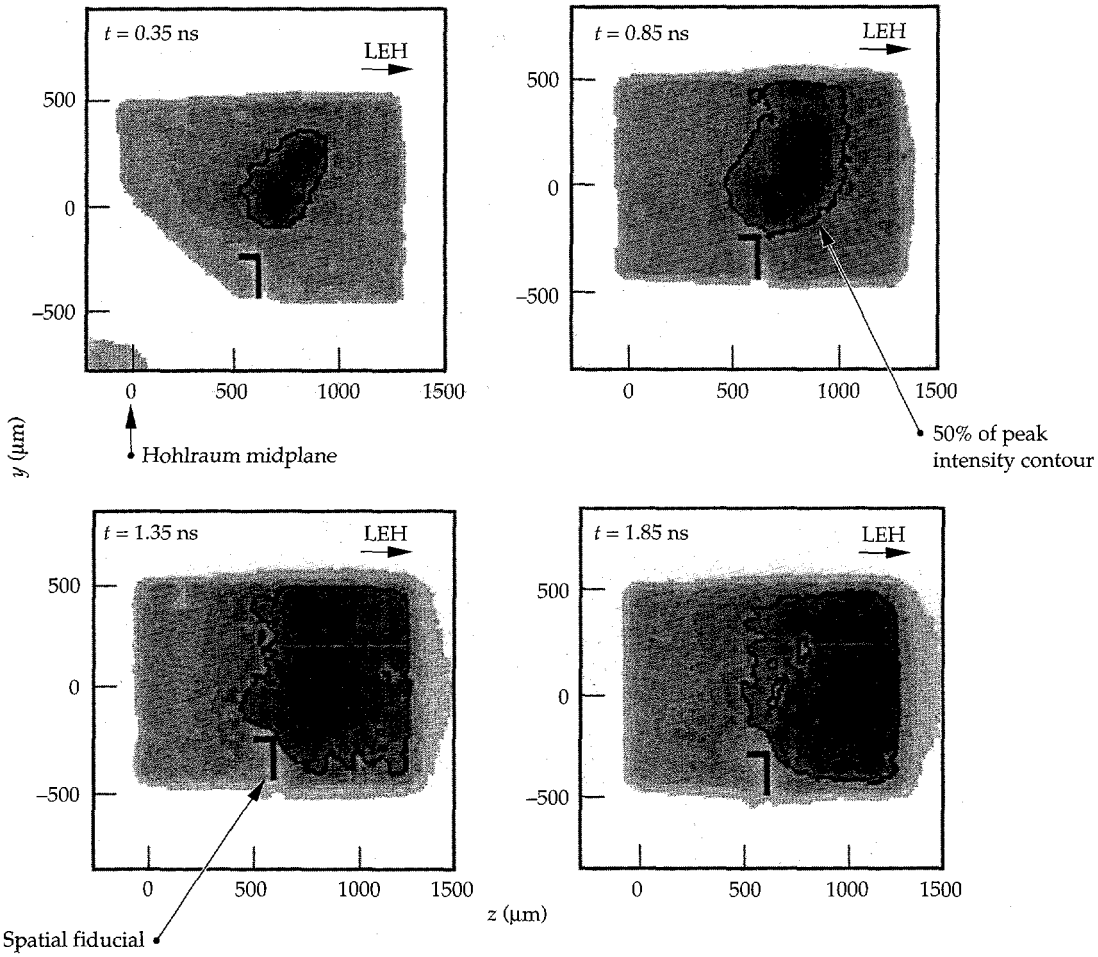

FIGURE 9. 450-eV images of spots inside a pure Au hohlraum during a PS22 experiment. The black "7" is a spatial fiducial. These images show a well defined soft x-ray spot that moves toward the LEH.
(20-03-0995-2131pb01)

time. This causes the variation in the pole-to-equator ablation pressure ratio shown in Fig. 7. Time-dependent asymmetry results both from changing hot spot to background-wall ratio and from spot motion.

Experiments provide persuasive evidence that the time-dependent asymmetry in Nova hohlraums is about as we expect. The hot spot to background-wall ratio is largely determined by the albedo of the Au wall. Separate measurements of Au wall losses[23] indicate that LASNEX accurately estimates Au albedo at standard Nova temperatures (~220 eV). The spot-motion experiments described earlier are qualitatively and quantitatively close to what we expect. Finally, the changes in the pointing of best symmetry (Fig. 6) with pulse shape indicate that the variation in flux at the capsule is qualitatively what we expect—the asymmetry goes from waist high early in time to pole high later in time.

To understand this final point, consider PS22 at its experimental pointing of best symmetry, 1200 μm. According to Fig. 7, the first 1 ns of PS22 should provide a waist-high radiation flux that drives a prolate implosion. However, our 1-ns implosions at 1200 μm are prolate, showing that at ~20 TW the first 1 ns of drive at this pointing is predominantly waist high. Because the first nanosecond of PS22 is actually at much lower power, ~6 TW, we expect it to also be predominantly waist high since there is (slightly) less spot motion at lower power, and spot motion is needed to get into the pole-high regime. Moreover, we argue that the entire first nanosecond should be waist high. If the PS22 flux did change to pole high before 1 ns, so much of the PS22 energy would be generating pole-high flux that 1200 μm would not be PS22's pointing of best symmetry. Continuing the argument, since the early part of PS22 is waist high, some latter part of PS22 must be pole-high to compensate for this early-time asymmetry. Consequently, the scaling of the pointing of best symmetry with pulse length (shown in Fig. 6) is evidence that the time-dependent asymmetry goes from waist-high early in time to pole-high later in time, therefore corroborating the qualitative behavior of Fig. 7.

Other experiments are ongoing to more directly measure the time-dependent asymmetry in Nova hohlraums. One approach, proposed by Wilson,[24] uses the full pulse with a series of capsules designed to implode at different times during the pulse. This is accomplished

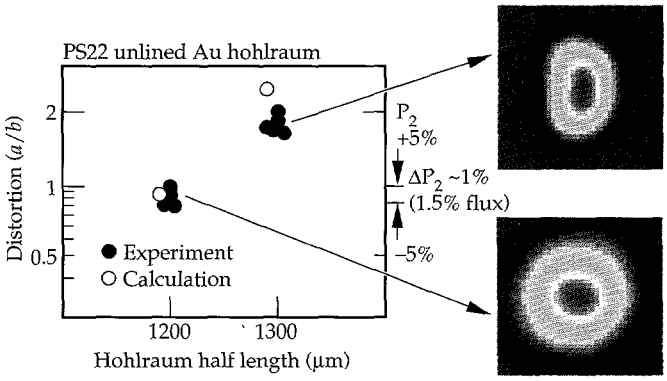

FIGURE 11. Precision Nova implosions have shown excellent reproducibility of symmetry. (08-00-1293-4416pb01)

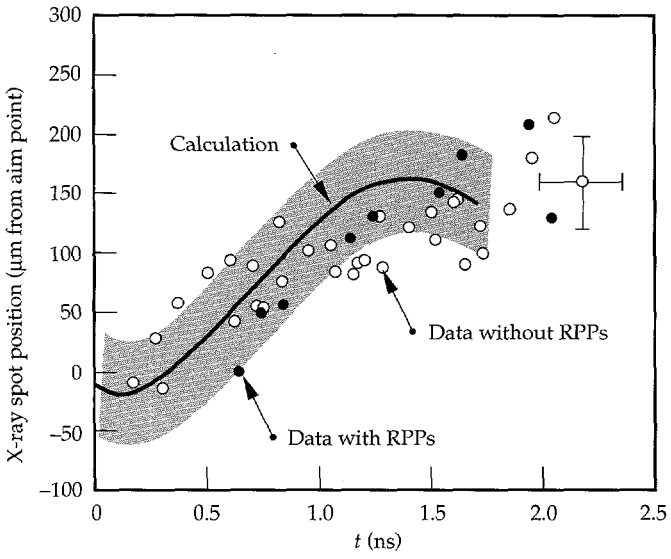

FIGURE 10. Distance from the hohlraum midplane to the center of emission at $h\nu \approx 450$ eV, vs time in a pure Au hohlraum irradiated by PS22. We observe spots that migrate about as expected from simulations. (20-03-0995-2132pb01)

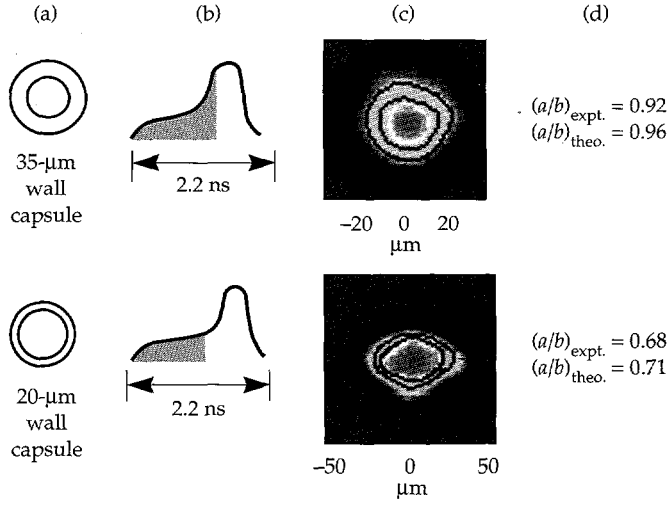

FIGURE 12. Data from PS22 using the variation in implosion time of capsules with different wall thickness: (a) initial capsule configuration; (b) shaded portion of the drive represents the effective sampling interval for the implosion for the two cases; (c) implosion image data taken orthogonal to the hohlraum axis; (d) comparison of the measured capsule eccentricity with the calculated value. (02-08-1094-3596pb03)

by keeping the capsule's i.d. approximately fixed and thinning the ablator to significantly less than its standard 55-μm thickness. The thinnest capsules view only the early-time asymmetry, and a record of the evolution of asymmetry can be obtained. Figure 12 shows results of this technique for PS22 and Au hohlraums.[25] Another technique replaces the capsule with a uniform sphere of material. The x-ray flux in the hohlraum will drive a shock into this material, which can be imaged by x-ray backlighting (see Fig. 13). Distortion of the shock front is approximately related to the drive pressure nonuniformity by

$$\frac{d}{dt}\left(r_{\text{equator}} - r_{\text{pole}}\right) \approx \frac{1}{2}\sqrt{\frac{\bar{P}}{\rho}}\left(\frac{P_{\text{pole}}}{P_{\text{equator}}} - 1\right) . \qquad (3)$$

For PS22, Fig. 13 shows the calculated ratio of $P_{\text{pole}}/P_{\text{equator}}$, which can then be compared with the measurement. The average pressure $\bar{P}$ can be obtained from the shock velocity. Figure 14 shows the results from a Nova experiment.[26] In this figure, A_2 is the second Legendre coefficient of the position of the shock trajectory, and A_0 is the average distance moved by the shock. The numerical calculation and the data are in agreement for this experiment. Calculations[27] show that, with the current resolution of about 2 μm in the shock position, time variations in NIF target fluxes can be obtained to about 2%.

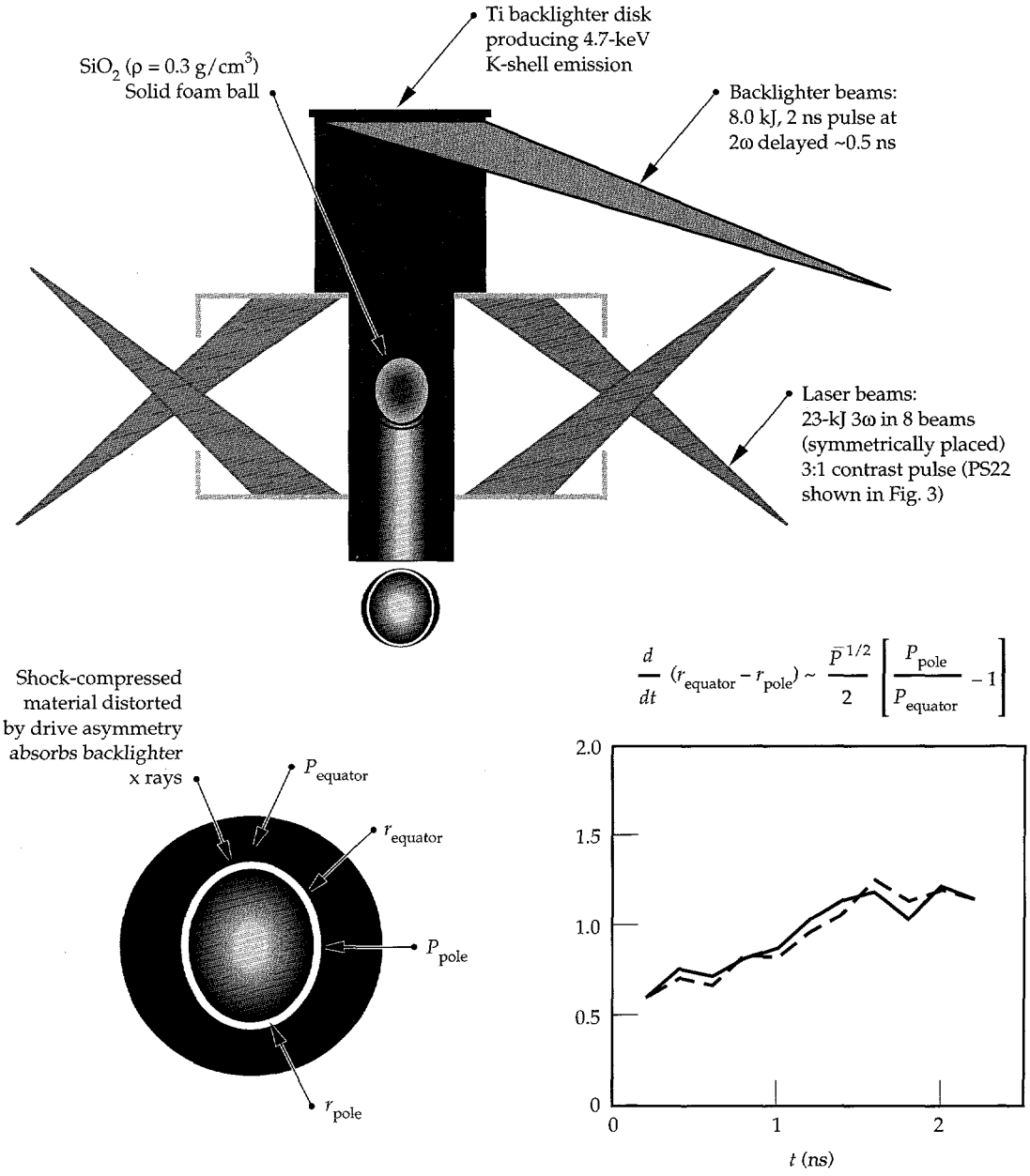

FIGURE 13. X-ray radiography can be used to infer time-dependent asymmetry from imaged shock distortion.
(50-04-1093-3882Apb03)

The Role of the LEH

Figure 15 summarizes the main effect an LEH can have on simulated beam propagation. It shows rays and electron density contours 2 ns into PS22. For nominal pointing shown in Fig. 15(a), when Nova's beams initially cross in the plane of the LEH, all rays are far from the blowoff that expands from the lip. Consequently, they are unaffected by LEH blowoff. However, Fig. 15(b) shows what can happen if we move the beams farther inward, close to the LEH. The part of the beam closest to the LEH intersects blowoff dense enough to refract those rays downward. Since these rays otherwise strike closest to the midplane of the hohlraum, the effect of the refraction is to shift the center of deposition toward the LEH. This shifts the asymmetry back in the pole-high direction. Note, however, that even when there is considerable interaction between the rays and the lip blowoff, the density distributions shown in Fig. 15 are very similar. This implies that there is no significant amount of additional blowoff produced by the interaction. These LEH results basically reproduce earlier findings of Lasinski,[28] who modelled an isolated LEH as a thin bracelet of material subjected to both a radiation source and a laser source. Her modeling agrees quite well with available data on radiation-driven LEH hydrodynamics.[28,29]

Modeling and experiment show that bringing the beam too close to the LEH can cause different symmetry behavior, as shown in Fig. 15(b). Consider a case where the LEH should have no effect—the distortion vs pointing scaling shown earlier in Fig. 5. This is the Ni-lined, PS22 scaling where the hohlraum length changed with pointing. In the experiments of Fig. 5, we expect the laser-LEH interaction to always be the nominal situation shown in Fig. 15(a). The straight-line scaling of Fig. 5 indicates there is no obviously "different" symmetry regime at inner pointing.

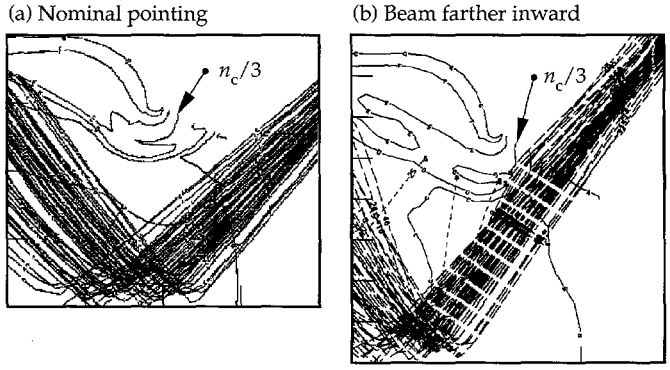

FIGURE 15. Simulated laser rays and density contours 2 ns into PS22 in a Ni-lined hohlraum. (a) With nominal pointing the laser is sufficiently far from the cylindrically expanding blowoff from the LEH lip that there is no significant interaction. (b) If the beam is moved too far inward, it can intercept relatively dense plasma and be partially refracted. (20-03-0995-2133pb01))

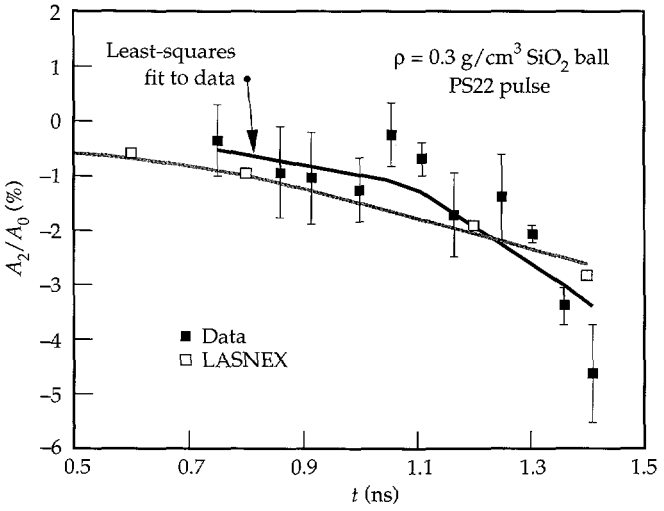

FIGURE 14. The foam witness ball technique can measure pressure asymmetries with nearly 10% accuracy on Nova. A_2 is the second Legendre coefficient of the shock trajectory. A_0 is the average shock position. (50-04-1093-3891Apb02)

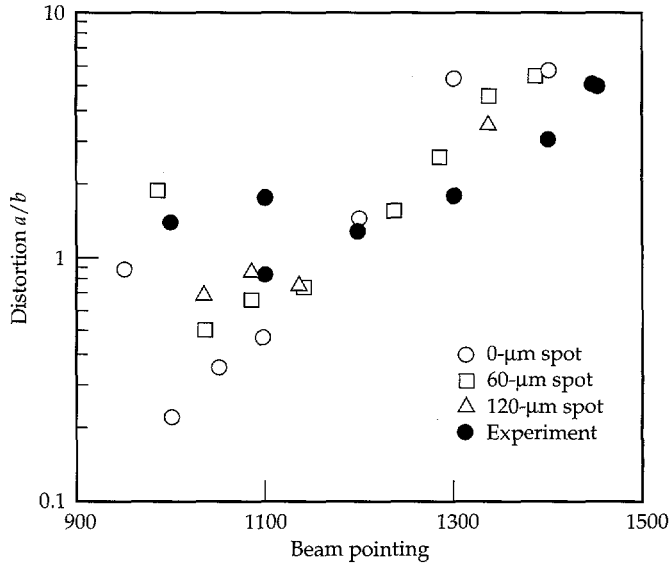

FIGURE 16. Symmetry scaling experiments (solid circles) in fixed length hohlraums show a "different" behavior at inner pointing than experiments where we vary the length with the pointing (see Fig. 5). This trend is reproduced in our simulations where we see it is due to refraction such as shown in Fig. 11(b). (20-03-0995-2134pb01))

Figure 16 plots simulations and experiments where the symmetry at inner pointing is different, showing a Ni-lined, PS22 scaling performed with fixed-length (2700-μm) hohlraums. At inner pointing, the beams approach the LEH and can be refracted. Comparison with Fig. 5 shows a different behavior at inner pointing.

Similar to the experiment, the LASNEX modeling shows a different symmetry regime can be found at inner pointing with fixed-length hohlraums. This is due to refraction by LEH blowoff. The size of the effect depends on the details of the beams. We studied this effect with simulations of three different realizations of Nova's beams, all of them using the 3-D geometric optics raytrace algorithm devised by Friedman.[19] The nominal beam representation has, at best focus, a 60-μm-diam, 1-sigma circle of confusion. This produces the rays shown in Figs. 4 and 15 and is a best-guess lower bound on the wings of Nova's beams. This beam representation produces the open squares of Fig. 16.

In addition to the 60-μm circle of confusion, we simulated beams with 120-μm-diam circles of confusion (upper bound to Nova) and 0-μm-diam circles of confusion (better than diffraction limited). The 0-μm circle of confusion beams (open circles of Fig. 16) cause no break in the distortion vs pointing scaling until the beam is so far in that it strikes the LEH. The 120-μm circle of confusion (open triangles of Fig. 16) representation shows somewhat more of an inner pointing refractive effect than the nominal beam representation.

The scalings of Fig. 16, together with those of Fig. 5, are evidence that the LEH can have an effect on symmetry. They also indicate that LASNEX can estimate when, and roughly how much, an LEH will have a major effect on hohlraum symmetry.

Summary

Our 2-D LASNEX simulations of Nova's nine symmetry scaling databases reproduce the fundamental features seen in the experiments. In particular, we predict how we must change Nova's beam pointing to achieve best symmetry with various pulse shapes. Analysis indicates that the need to change pointing with different pulse shapes is a result of spot motion. Complementing direct-symmetry measurements, we have also observed and modelled hot spots in hohlraums. We find hot-spot motion to be real, reproducible, and very close to what we expect from LASNEX. These measurements also indicate that time-dependent asymmetry in the Nova hohlraums behave close to our modeling. Experiments and modeling also indicate that we estimate when, and roughly how much effect, an LEH will have on hohlraum symmetry.

Notes and References

1. *Laser Program Annual Report–1979*, 2-77 to 2-88, Lawrence Livermore National Laboratory, Livermore, CA, UCRL-50055-79 (1979, report SRD); *Laser Program Annual Report–1980*, 2-10 to 2-22, Lawrence Livermore National Laboratory, Livermore, CA, UCRL-50055-80 (1980, report SRD).
2. J. Green, Research and Development Associates, private communication (1980); M. Murakami and K. Nishihara, *Jpn. J. Appl. Phys.* **25**, 242 (1986); A. Caruso, *Internal Confinement Fusion* (Proc. Course and Workshop, Varenna, 1988), *Casa Editrice Compositori*, Bologna (1988) 139.
3. *Laser Program Annual Report–1984*, 2–13, Lawrence Livermore National Laboratory, Livermore, CA, UCRL-50055-84, M-3679, C-72 (December 1985, report SRD).
4. S. W. Haan, "Radiation Transport Between Concentric Spheres," Lawrence Livermore National Laboratory, Livermore, CA, UCRL-ID-118152 (1994); J. Green, Research and Development Associates, private communication (1983).
5. *Laser Program Annual Report–1983*, 2–21, Lawrence Livermore National Laboratory, Livermore, CA, UCRL-50055-83 M3679, C-72 (September 1984, report SRD).
6. *Laser Program Annual Report–1985*, 30–31, Lawrence Livermore National Laboratory, Livermore, CA, UCRL-50055-85 M3679, C-72 (September 1986, report SRD).
7. A. Burnham, J. Grenz, and E. Lilley, *J. Vac. Sci. Technol. A* **5** (6), 3417 (1987).
8. *Laser Program Annual Report 1986/87*, 2–50 to 2–54 and 4–25 to 4–34, Lawrence Livermore National Laboratory, Livermore, CA, UCRL-50055-86/87 (1988, Title U, report SRD); *Laser Program Annual Report: Target Design 1988*, 51–75, LLNL, XDIV-90-0054 (Title U, report SRD); *ICF Program Annual Report 1988/89 (U)*, 192, LLNL, UCRL-LR-116901-88/89 (report SRD).
9. D. B. Ress, Lawrence Livermore National Laboratory, Livermore, CA, private communication (1995).
10. A. Hauer, Los Alamos National Laboratory, Los Alamos, NM, private communication (1992).
11. J. D. Kilkenny P. Bell, R. Hanks, G. Power, R. E. Turner, and J. Wiedwald, *Rev. Sc. Instrum.* **59** 1793 (1988).
12. A. Hauer, Los Alamos National Laboratory, Los Alamos, NM, private communication (1995).
13. *ICF Program Annual Report 1988/89 (U)*, 9, Lawrence Livermore National Laboratory, Livermore, CA, UCRL-LR-116901-88/89 (report SRD).
14. A. Hauer, et. al., *Rev. Sci. Instrum* **66**(1), 672 (1995).
15. L. J. Suter, A. A. Hauer, L. V. Powers, D. B. Ress, et al., *Phys. Rev. Lett.* **73**(17), 2328 (1994).
16. R. E. Turner and L. J. Suter, *Bull. Am. Phys. Soc.* **1** (1988); Y. Kato, et. al., *Proc. 13th Int'l Conf. Plasma Physics and Controlled Nuclear Fusion Research*, Washington, DC, 1990.
17. *Laser Program Annual Report: Target Design 1988 (U)*, 223, Lawrence Livermore National Laboratory, Livermore, CA, XDIV-90-0054 (May 1990, report SRD).
18. G. Zimmerman and W. Kruer, *Comments Plasma Phys. Controlled Fusion* **2**, 85 (1975).
19. A. Friedman, *Laser Program Annual Report 83*, 3–51, Lawrence Livermore National Laboratory, Livermore, CA, UCRL-50021-83 (1983).
20. D. E. Post, R. V. Jensen, C. B. Tarter, W. H. Grasberger, and W. A. Lokke, *Atomic Data and Nuclear Tables* **20**(5) (Nov 1977); G. B. Zimmerman and R. M. More, *JQSRT* **23**, 517 (1980).
21. D. Ress, L. V. Powers, L. J. Suter, R. J. Wallace, and F. Ze, *Bull.*

Am. Phys. Soc. **38**, 1885 (1993); L. V. Powers, D. B. Ress, L. J. Suter, and F. Ze, *Defense Research Review* **6**(10), (1994, report SRD).
22. G. Glendinning, Lawrence Livermore National Laboratory, Livermore, CA, private communication (1995).
23. J. L. Porter, T. J. Orzechowski, M. D. Rosen, A. R. Thiessen, et al., *ICF Quarterly Report* **4**(4), 125–131, Lawrence Livermore National Laboratory, Livermore, CA UCRL-LR-105821-94-4 (1994).
24. D. Wilson, Los Alamos National Laboratory, Los Alamos, NM, private communication (1992).
25. A. A. Hauer, "X-Ray Driven Implosions in Laser Heated Hohlraums," *Laser Plasma Interactions*, Eds., M. Hooper and A. Cairns (Redwood Burn, Trowbridge, England, 1995), vol, 5, pp. 5–24.
26. P. Amendt, S. G. Glendinning, B. A. Hammel, R. G. Hay, and L. G. Suter, *Rev. Sci. Instrum.* **66**(1), 785 (1995).
27. P. Amendt, Lawrence Livermore National Laboratory, Livermore, CA, private communication (1995).
28. B. F. Lasinski, Lawrence Livermore National Laboratory, Livermore, CA, private communication (1990).
29. C. Gomez, Los Alamos National Laboratory, Los Alamos, NM, private communication (1991).

LASER–PLASMA INTERACTIONS IN NIF-SCALE PLASMAS (HLP5 AND HLP6)

B. MacGowan	*M. Casanova**	*K. Estabrook*	*R. Kirkwood*	*J. Moody*
R. Berger	*B. Cohen*	*S. Glenzer*	*W. Kruer*	*D. Munro*
*J. Fernandez***	*D. Desenne**	*D. Hinkel*	*A. Langdon*	*L. Powers*
B. Afeyan	*D. Dubois***	*D. Kalantar*	*B. Lasinski*	*H. Rose***
C. Back	*A. Dulieu**	*R. Kauffman*	*D. Montgomery*	*C. Rousseaux**
*G. Bonnaud**	*R. Turner*	*B. Wilde***	*S. Wilks*	*E. Williams*

Introduction

The understanding of laser–plasma interactions in ignition-scale inertial confinement fusion (ICF) hohlraum targets is important for the success of the proposed National Ignition Facility (NIF). The success of an indirect-drive ICF ignition experiment depends on the ability to predict and control the history and spatial distribution of the x-radiation produced by the laser beams that are absorbed by the inside of the hohlraum wall. Only by controlling the symmetry of this x-ray drive is it possible to obtain the implosion symmetry in the fusion pellet necessary for ignition.[1] The larger hohlraums and longer time scales required for ignition-scale targets result in the presence of several millimeters of plasma (electron density $n_e \approx 0.1 n_c \approx 10^{21}$ cm^{-3}), through which the 3ω (351-nm) laser beams must propagate before they are absorbed at the hohlraum wall. Hydrodynamic simulations show this plasma to be very uniform [density-gradient scalelength $L_n = n_e(dn_e/dx)^{-1} \approx 2$ mm] and to exhibit low velocity gradients [velocity-gradient scalelength $L_v = c_s(dv/dx)^{-1} > 6$ mm].[2]

The propagation of the beams to the hohlraum wall can be affected by various scattering and laser self-focusing (filamentation) processes within the low-density plasma inside the hohlraum. For example, while traversing such a plasma, the incoming light wave can resonantly decay into a backscattered light wave and either an ion sound wave or an electron plasma wave. The backscattered light wave can beat with the incident light wave at a frequency that pumps the plasma wave; this process can increase the amplitude of the plasma wave, increasing its scattering efficiency. Hence an unstable feedback loop is formed that can cause the amplitudes of the plasma and scattered light waves to grow exponentially on time scales of 0.1 to 10 ps. For scattering from ion sound waves, these parametric scattering instabilities are called stimulated Brillouin scattering (SBS); for scattering from electron plasma waves, they are called stimulated Raman scattering (SRS).[3] Both of these instabilities can lead to undesirable effects, including significant amounts of light reflecting from the plasma or shining directly onto the capsule, spoiling the illumination symmetry.

Another instability that can affect laser beam propagation is beam filamentation,[4] which occurs when individual speckles ("hot spots") within the beam self-focus as a result of refractive index changes caused by changes in the local plasma density produced by the laser field through transverse ponderomotive pressure. This effect can result in a local increase in intensity and eventual beam breakup. Filamentation is of particular concern for NIF hohlraums, because the intensity threshold for filamentation is affected by the length and transverse scale of the hot spot. For a beam smoothed with a random phase plate (RPP), these scales are determined by the beam f/number. The $f/8$ focusing geometry planned for the NIF will have speckles 180 μm long for 351-nm light, contrasting with 50-μm speckles for the $f/4.3$ optics used at the LLNL Nova laser. Calculations indicate that at the expected 2×10^{15} W cm^{-2} irradiance planned for the NIF, a significant fraction of an $f/8$ beam would be above the intensity threshold for filamentation, in the absence of any beam smoothing beyond use of a RPP.[4]

In most laser-produced plasmas, SBS and SRS are limited by plasma inhomogeneity[3]; in the plasmas expected in the NIF hohlraums, however, wave damping,

* Centre D'Etudes de Limeil–Valenton, France

** Los Alamos National Laboratory, Los Alamos, New Mexico

pump depletion, or some other nonlinear saturation mechanism would be the only limitations on instability growth. Some of our interaction experiments in homogeneous low-density plasmas have shown as much as 35% of the incident laser energy backscattered as SBS; in other experiments, SRS reflected fractions as high as 25% have been observed. Although these are extreme cases that represent scattering from plasmas that have less damping of instabilities than we expect in the NIF plasma, they illustrate the potential of parametric instabilities to cause problems. This amount of backscattering would obviously reduce coupling to the hohlraum wall, reducing the x-ray drive and increasing the incident laser energy required to drive a target to ignition. (SRS could cause additional problems, because the process not only transfers energy into backscattered light and electron plasma waves but also produces suprathermal electrons with tens of keV energy. These "hot" electrons can preheat the DT fuel in the capsule, reducing the efficiency of the subsequent implosion.) Significant energy scattering due to instabilities such as SBS and SRS would also make it more difficult to meet the NIF power-balance specification of <8% variation in power between beams, which is needed to meet the symmetry requirements for a high-convergence implosion.[5] SRS and SBS exacerbated by beam filamentation are therefore a concern for indirect-drive ICF, especially in the larger and more uniform plasmas expected in an ignition-scale hohlraum.

The basic design for the NIF hohlraum [Fig. 1(a)] is an Au cylinder about 9 mm long containing a low-Z gas (a mixture of He and H_2). The low-Z gas slows the expansion of the Au hohlraum wall and provides a medium (other than low-density Au ablated from the wall) through which the beams can propagate without significant loss of energy from inverse bremsstrahlung absorption. The current NIF design has two cones of beams (called the inner and outer cones) on each side of the hohlraum. Figure 1(b) shows the history of the NIF laser pulse; Fig. 1(c) shows the density and beam intensity along the beam path for the time of peak calculated SRS and SBS gain (also the time of peak power, 13.5 ns). Figure 1(d) shows the calculated temperature profiles at the same time. The profiles in Figs. 1(c) and (d) represent the beam intensity, electron density, and electron temperature encountered along the inner and outer cone beam paths.

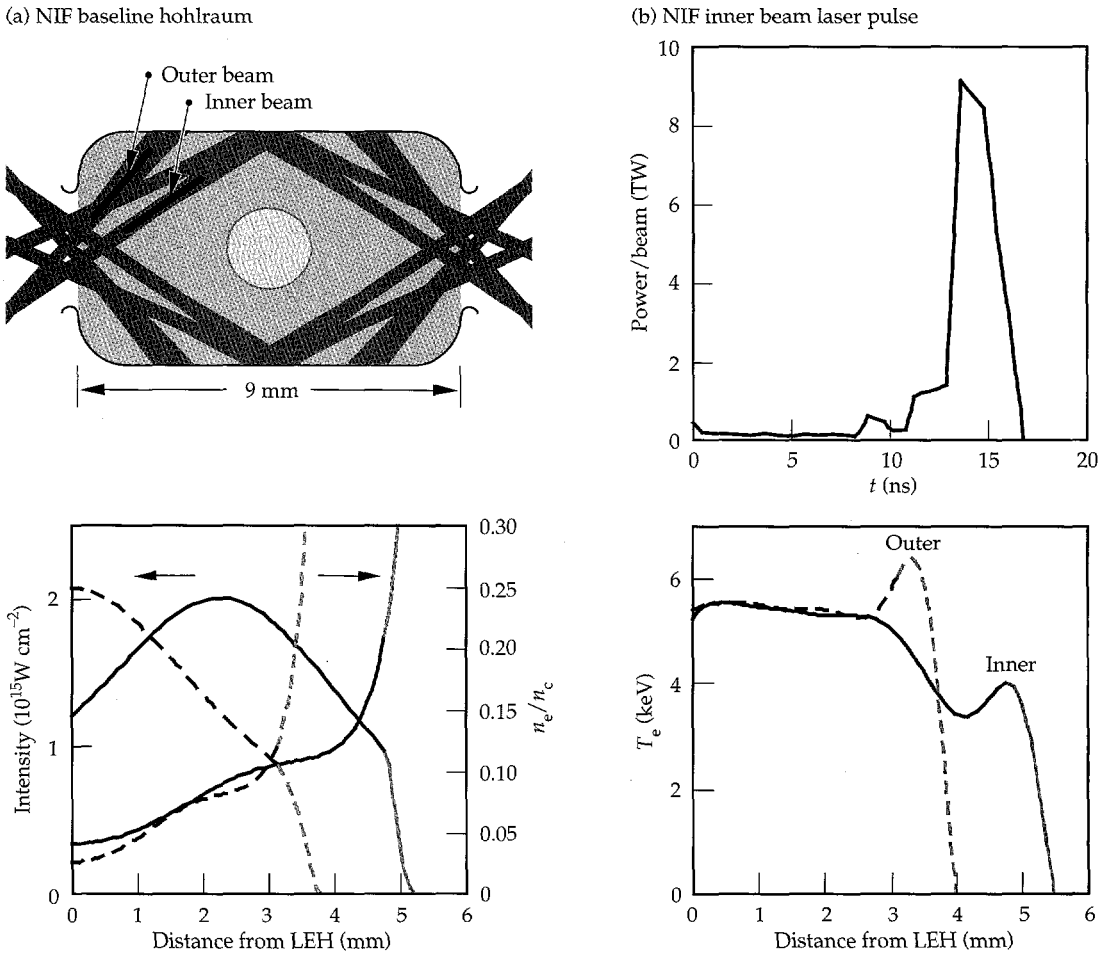

FIGURE 1. (a) NIF baseline hohlraum, showing inner and outer beam cones; (b) power history for one NIF beam; (c) electron density (as a fraction of critical density $n_c = 9 \times 10^{21}$ cm^{-3}) and laser beam intensity vs position in NIF hohlraum at time of peak laser power. Laser beam incident from left. Dashed and solid curves represent parameters for outer and inner beam cones, respectively. Lighter portions of each curve indicate where the laser is interacting with Au plasma; other regions correspond to low-Z (a He/H mix) fill gas plasma. (d) Electron temperature for inner and outer beams. (20-07-1095-2434pb01)

The output from the 2-D hydrodynamics simulations of the NIF target can be post-processed with the Laser Interactions Post-processor (LIP)[6] to obtain the total gain exponent for SBS and SRS as a function of time and scattered-light wavelength. The calculated peak gain exponents along the path of a 2×10^{15} W cm^{-2} NIF beam are 25 for SRS and 30 for SBS. Figure 2 shows the post-processed linear gain exponents for SBS and SRS, as functions of scattered-light wavelength and of time throughout the NIF pulse, for the inner and outer beam cones. The plots show gray-scale contours of equal calculated gain exponent; darker regions correspond to higher gain exponent.

Figures 2(a) and (b) show the history of the SBS for the inner and outer beams, respectively. Some of the spectral features of the SBS gain calculations and differences between the inner-beam and outer-beam cases can be understood in terms of the plasma conditions under which the scattering would occur. For instance, Fig. 1(c) indicates that the inner beams traverse a longer length of low-density fill plasma than the outer beams. The SBS gain peaks at a wavelength of $\Delta\lambda \approx 14$ Å for the inner-beam case; for the outer beam, which has less path length in the low-Z plasma, the main spectral feature is a narrow gain spike at $\Delta\lambda \approx 7$ Å.

To understand these observations, consider that the wave-number-matching condition for SBS requires that

$$\mathbf{k}_0 = \mathbf{k}_s + \mathbf{k}_{ia}, \qquad (1)$$

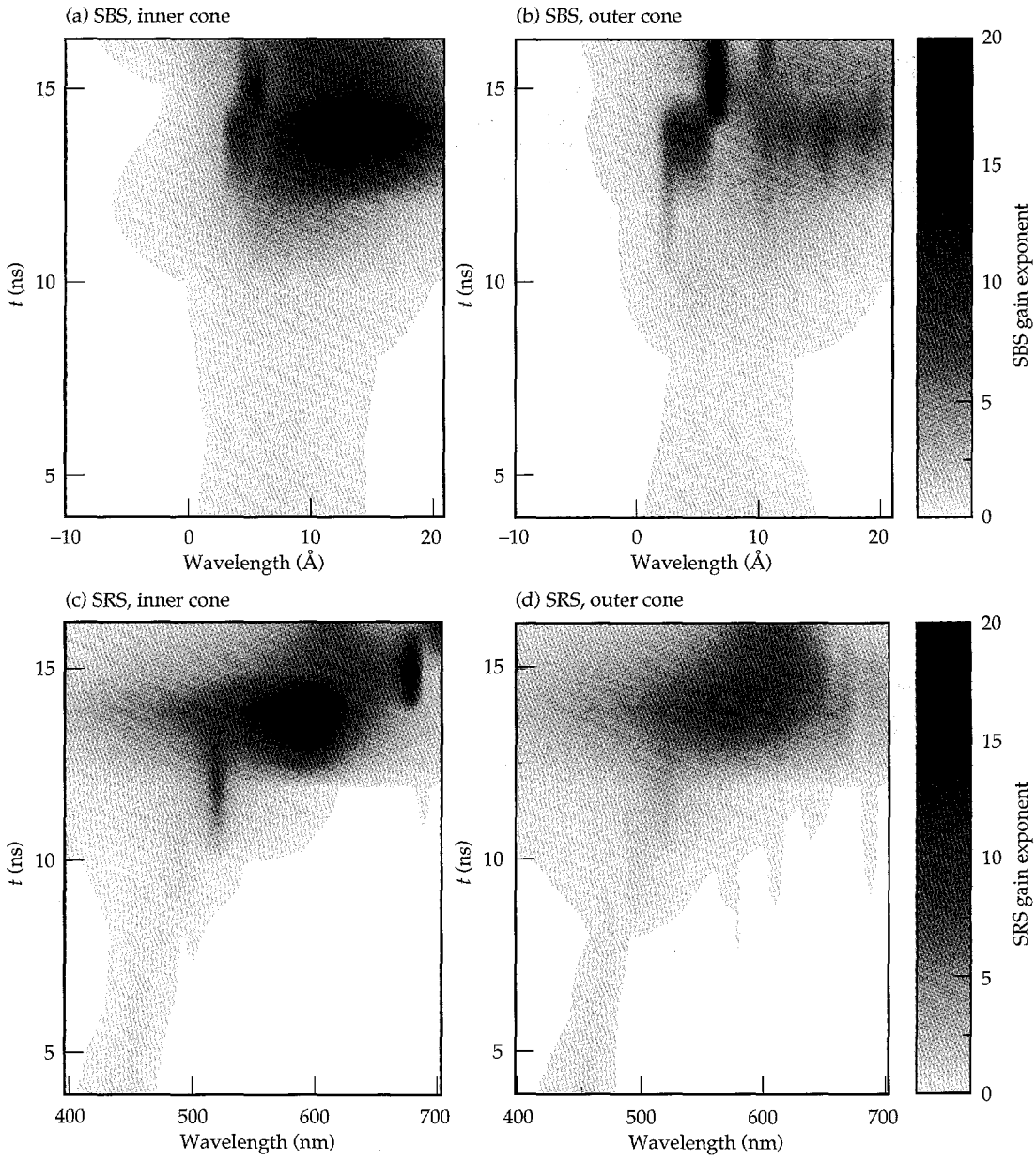

FIGURE 2. Post-processed (LIP) gain exponents along laser beam paths using plasma parameters from 2-D LASNEX hydrodynamics calculations of NIF. (a) SBS for inner cone; (b) SBS for outer cone; (c) SRS for inner cone; (d) SRS for outer cone. (20-07-1095-2435pb01)

where $\mathbf{k}_0$ and $\mathbf{k}_s$ are the incident and scattered light wave vectors in the plasma. The wave number of the ion-acoustic wave $\mathbf{k}_{ia}$ has a magnitude equal to $2k_0$ for direct backscattering (since $\mathbf{k}_s \approx -\mathbf{k}_0$), where k_0 is related to the vacuum wave number k_{vac} of the light by

$$k_0 = k_{vac}(1 - n_e / n_c)^{1/2}; \quad (2)$$

this is a minor correction for densities near $0.1n_c$.

Although most of the incident photon energy goes into the backscattered photon, the ion-acoustic wave takes away some energy according to

$$\omega_0 = \omega_s + \omega_{ia}; \quad (3)$$

the frequency shift $\Delta\omega$ in the scattered light wave is therefore approximately

$$\Delta\omega = \omega_{ia} \approx 2k_0 c_s, \quad (4)$$

resulting in a wavelength shift

$$\Delta\lambda \approx 2\lambda_{vac}(1 - n_e / n_c)^{1/2} c_s / c, \quad (5)$$

where c_s is the sound speed. For a plasma flowing towards the observer with Mach number $M = v/c_s$, we have

$$\Delta\lambda \approx 2\lambda_{vac}(1 - n_e / n_c)^{1/2}(1 - M)c_s / c. \quad (6)$$

The strongest dependence here is on the sound speed and Mach number of the plasma in which the scattering is occurring. The sound speeds in Au and He/H are very different, because the sound speed scales as $[(Z_{eff}T_e + 3T_i)/A]^{1/2}$ and Au is a heavy atom ($Z < A/2$) that is not completely ionized (i.e., $Z_{eff} < Z$) while the low-Z plasma is fully ionized and has $Z \geq A/2$. Typical sound speeds are 3 to 4×10^7 cm s^{-1} for Au and 6 to 7×10^7 cm s^{-1} for He/H for the temperatures expected in the NIF plasma. The shifts in wavelength for SBS backscattering from Au and He/H are then 7 and 14 Å, respectively, for stationary plasmas. Note that flows in the plasma will also shift the scattered light wavelength according to the [1 – M] term.

The feature at 7 Å appearing at 15 ns for the outer-beam SBS calculation [Fig. 2(b)] corresponds to SBS gain in the Au, with a peak gain exponent of 30. The broad gain peak at 14 Å in the inner-beam case [Fig. 2(a)] represents gain in the low-Z plasma with a peak gain exponent of 20. Although there is a small amount of gain at 6 Å in the inner-beam case, the observation can be made that the main SBS threat is from the wall material in the outer-beam case and from the low-Z fill gas in the inner-beam case. Hence we can break down the SBS problem into a high-Z problem, which is best addressed in experiments with Au walls (e.g., hohlraums), and a large, low-Z plasma SBS problem, which can be addressed in gas-filled hohlraums or with open-geometry gas targets.

The SRS gain exponents calculated by LIP are shown in Fig. 2(c) and (d) for the inner and outer beams, respectively. Figure 1(c) indicates that when the beams reach the Au they are absorbed in a short distance (~300 to 500 μm) in a region with steep density gradients. Since SRS gain is higher in large, homogeneous regions with shallow density gradients, most of the calculated SRS gain is in the low-density, low-Z plasma. Beams in the inner cone have higher expected SRS gain [with a maximum of 26, shown in Fig. 2(c)], because the beams have longer paths in the low-Z plasma, and the total exponentiation is a product of the spatial gain rate with the length over which that exponentiation can occur. The outer beams traverse less low-Z fill plasma and so have a lower calculated gain exponent for SRS [with a maximum of 11, shown in Fig. 2(d)].

The SRS plots show the calculated gain exponent for SRS as a function of the wavelength of the scattered photon. The wavelength of the scattered optical light carries information about the density and temperature of the plasma from which it scattered, because the electron plasma wave from which it scatters must satisfy

$$\omega_p^2 = \omega_{pe}^2 + v_T^2 k_p^2, \quad (7)$$

where ω_p and $\mathbf{k}_p$ are the frequency and wave number of the electron plasma wave, ω_{pe} is the plasma frequency (which introduces density dependence), and v_T is the electron thermal velocity (which introduces temperature dependence). The incident and scattered wave numbers are related by energy and momentum conservation:

$$\omega_0 = \omega_s + \omega_p, \quad (8)$$

$$\mathbf{k}_0 = \mathbf{k}_s + \mathbf{k}_p, \quad (9)$$

where $\mathbf{k}_0$ (ω_0) and $\mathbf{k}_s$ (ω_s) are the incident and scattered light wave vectors (frequencies). The wavelength of the scattered light that satisfies these conditions is strongly dependent on density and less strongly dependent on electron temperature. The large gain exponent at 590 nm for the inner beam corresponds to SRS growing at $n_e \approx 0.1n_c$ and a $T_e = 3$ to 4 keV. The long-scalelength targets described below were designed to explore this gain region. The lower-gain parts of the plot correspond to different densities within the NIF plasma; longer wavelengths correspond to higher densities. The small region of gain near 690 nm for the inner beam represents light scattering from plasma at $n_e \approx 0.2n_c$ and $T_e = 4$ keV. This region of plasma is low-Z material that has ablated from the capsule and produces

a slightly higher-density region of low-Z plasma where it collides with the Au wall. This region is difficult to reproduce experimentally and is less significant to the NIF problem because the laser energy in the part of the beam that reaches this plasma is very low because the laser light is being rapidly absorbed by this higher-density plasma.

As can be seen in Fig. 2, calculated gain exponents occasionally reach or exceed 20. Amplification of thermal fluctuations by 20 *e*-foldings is sufficient to produce both significant backscattering and plasma waves of sufficient amplitude that nonlinear saturation mechanisms begin to be important. The LIP calculations include no nonlinear effects, so the LIP results should be interpreted as telling us that there might be a significant scattering due to SBS and SRS in the NIF plasma for the period during which gain exponents exceed 20, but that we cannot predict the saturation level of that scattering. Hence we were motivated to try to reproduce plasma conditions with such gain exponents on Nova (where LIP can be used to compare the gains to the NIF case) in order to include saturation and other plasma effects that are omitted by the simple linear gain analysis.

The NIF beams will interact with the plasma at intensities up to 2×10^{15} W cm^{-2}, with a variation of intensity along the beam path as shown in Fig. 1(c). In the transverse direction, the laser intensity is assumed to be averaged over the beam profile, and the LIP calculations use this spatially averaged intensity. However, each beam is composed of small (~6 μm diam) speckles with a distribution of intensities above and below the average. The speckles can self-focus as they interact with the plasma, increasing the intensity within individual "hot spots," although beam smoothing such as smoothing by spectral dispersion (SSD), which moves the speckle pattern around rapidly, can reduce filamentation. This nonlinearity in the laser–plasma interaction is also omitted from the LIP calculations, so a further requirement of understanding laser–plasma interactions in the NIF by means of Nova-scale experiments was to use a laser beam with the intensity, smoothing, and *f*/number appropriate to a NIF beam. These experiments would address the legitimate concern that some fraction of each NIF beam will drive saturated levels of SBS and SRS and be reflected from the NIF hohlraum with the loss of energy and other consequences described above. The goals of these experiments were expressed in the HLP5/6 part of the 1993 NAS Nova Technical Contract as follows:

- **HLP5:** Demonstrate acceptable levels of scattering in large-scale plasmas that match the plasma conditions, beam geometry, and beam smoothing of ignition hohlraums as closely as possible. The plasmas should have density and velocity scalelengths ≈ 2 mm, electron temperature >1.5 keV, and $n_e/n_c < 0.15$.

Acceptable levels of scattering were defined as follows:

— Stimulated Brillouin scattering fraction f_{SBS} (back, side) < 5 to 10%.

— Stimulated Raman scattering fraction f_{SRS} (back, side) < 5 to 10% and f_{SRS} (forward) < 5%.

- **HLP6:** Evaluate the impact of laser beam filamentation on SBS and SRS and develop control techniques to the extent necessary to ensure acceptable levels of scattering.

Target/Plasma Development

To experimentally evaluate the severity of SRS and SBS scattering and filamentation on the propagation of an *f*/8 beam traversing a long-scalelength plasma, we reproduced the laser beam conditioning (*f*/number and smoothing) to be used on the NIF. At the same time, it was necessary to reproduce the plasma conditions expected within the NIF using plasmas produced by the Nova laser. Late 1993 and early 1994 saw a significant effort to produce plasmas that met the criteria expressed in the first part of the HLP5 statement of work. It was necessary to both reproduce the density (~$0.1n_c$) and temperature (at least 3 keV) of the NIF target but also to do so over a volume large enough that the total gain exponent of the NIF target for SBS and SRS could be approached.

Various targets were explored, including low-density foams and thin exploding foils. The most promising targets were large gas-filled hohlraums (of which two types were developed) and "gasbags." The plasmas were created by irradiating a thin-walled gas balloon or a sealed hohlraum[7] containing of order 1 atm of a low-Z gas (e.g., C_5H_{12}, C_5D_{12}, or CO_2). All three of these targets relied on heating a large volume of a heavy gas that, when ionized, produced the appropriate plasma conditions and was large enough to last for a reasonable time and to provide the right amount of SRS and SBS amplification.

Figure 3 shows the three targets developed to investigate laser–plasma interactions in NIF-scale plasmas. Figure 3(a) shows the GASBIG hohlraum, which is larger than the typical Nova hohlraum. Normal (scale-1) Nova hohlraums are the same length (~2.5 mm) but have a smaller diameter (1.6 mm), with the laser beams pointed so that they hit the wall before they reach the midplane of the hohlraum. The GASBIG hohlraums maximized the length over which the beams interacted with the plasma by pointing them at the opposite end of the hohlraum so that they crossed in the hohlraum mid plane. The hohlraum was filled with C_5H_{12} gas retained with a thin (6500 Å) polyimide window.

Figure 3(b) shows the toroidal hohlraum developed by LANL. This target produced a large length of plasma with which to interact by moving the wall of the standard Nova hohlraum radially outward to produce a more doughnut-shaped hohlraum. Figure 3(c) shows the open-geometry gasbag target, which was essentially two thin windows on either side of a thin washer. The target is inflated to make an almost spherical volume of gas. Figures 3(d) and (e) show density and temperature plots for the GASBIG and gasbag plasmas after they have been heated by the Nova laser beams, at the time at which the interaction with the NIF-like probe beam was studied (1 ns for the GASBIG, 750 ps for the gasbag). Both Figs. 3(d) and (e) show a relatively flat region of plasma near $0.1n_c$ at a temperature of 3 keV; this is the portion of the plasma that is approximating the region of high gain for SBS and SRS in the NIF inner beam.

The concept of producing a large, hot plasma by irradiating a gas-filled target has been discussed by Denavit and Phillion.[8] A cold gas volume of a few millimeters dimension can be heated by pulsed laser beams (typical duration 1 ns, intensity of order 10^{14} W cm^{-2}). When the laser beams strike the cold gas, a plasma is formed by multiphoton ionization. The initial low temperature of the plasma leads to energy deposition through inverse bremsstrahlung at the edge of the plasma. As that plasma is heated and becomes more transmissive, the laser beams propagate further into the gas. Our targets contained a high-molecular-weight gas (typically C_5H_{12}) that on ionization produced a plasma (electron) density $n_e = 10^{21}$ cm^{-3}. The velocity of propagation of the laser light into such a gas was measured for various laser conditions and is typically a few millimeters per nanosecond for 3ω light. For a 2.75-mm-diam gasbag plasma, the laser beams propagate to the center of the plasma by about 400 ps. Thereafter the laser beams steadily heat the plasma that they traverse; thermal conduction heats parts of the gas not directly irradiated by the laser beams. For the gasbag targets, the edge of the plasma is free to expand into the surrounding vacuum, so an isothermal rarefaction wave propagates towards the middle of the plasma at the ion sound speed (~0.5 mm/ns). The density plateau in the center of the plasma is therefore eroded by the converging rarefaction wave at a rate of about 1 mm/ns. After the plasma is formed and heated, we have a few hundred picoseconds to perform laser–plasma interaction experiments on our 2-mm size plasma before the rarefaction wave shrinks the

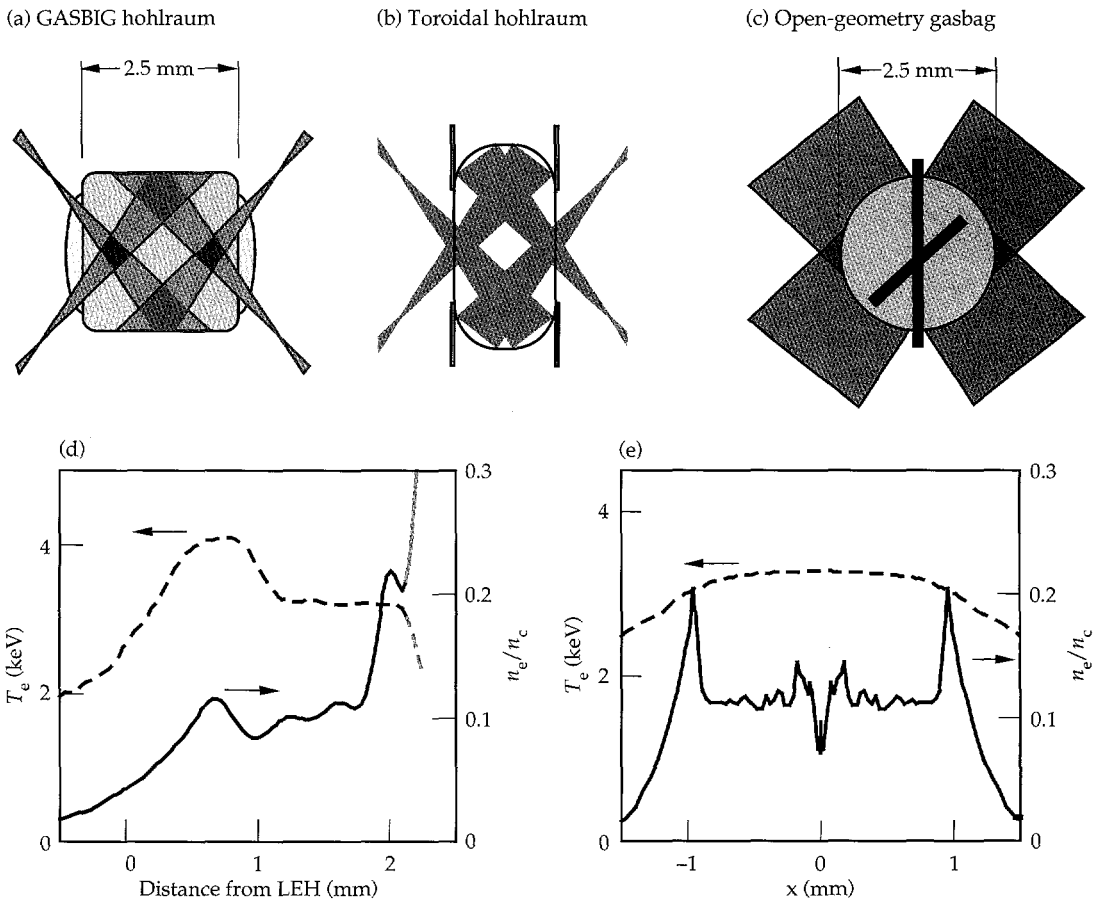

FIGURE 3. Targets developed to study laser–plasma interactions in long-scalelength plasmas similar to those of NIF. (a) GASBIG hohlraum; (b) toroidal hohlraum; (c) open-geometry gasbag target; (d) density and temperature for GASBIG hohlraum targets at a time (1 ns) at which interaction with NIF-like probe beam was studied. Lighter part of each curve indicates Au plasma. (e) Density and temperature for gasbag target at a time (750 ps) at which interaction with NIF-like probe beam was studied.
(20-07-1095-2436pb01)

density plateau and so reduces the length available for amplification of SBS and SRS.

For each of the three targets, there was a period during which the plasma was ionized and heated using nine of the Nova beams. For the gasbags these "heater" beams were on for 1 ns; the interaction beam was turned on at t = 500 ps and also lasted for 1 ns. There is therefore a 500-ps period during which the heaters and interaction beams overlap in time. During this period the plasma temperature is still rising. When the heater beams turn off there is a 500-ps period during which the plasma is cooling but the interaction beam remains on.

The balloon targets were constructed by placing a thin membrane of polyimide ($C_{14}H_6O_4N_2$) on each side of a thin (400 μm) washer. The membranes were then inflated to an almost hemispherical shape through hypodermic fill tubes that penetrated the washer. Figure 3(c) shows the target and the laser-beam focusing geometry used to heat the plasma. Nine heater beams with a total energy of 18 to 22 kJ in a 1-ns pulse were used to create the plasma.

Unlike the more traditional targets for high-density laser–plasma interactions (solid or exploding-foil targets) the gas balloon targets convert most of the incident heater laser energy into thermal energy of the electrons and less into kinetic energy of bulk plasma motion. The energy budget for a typical gas balloon simulation is 22 kJ incident, 12.5 kJ absorbed, 8.8 kJ in electron thermal energy (T_e = 3.2 keV) and only 2.6 kJ (21% of absorbed energy) in kinetic energy. These numbers should be compared with those for typical exploding-foil plasmas, for which similar calculations (to produce a $0.1n_c$ plasma) show 22 kJ incident, 8 kJ absorbed, 3.1 kJ in electron thermal energy (T_e = 2.4 keV) and 4.5 kJ in kinetic energy (56% of absorbed energy). The heating of a stationary low-density target is therefore a much more efficient way of producing a high-temperature plasma, and it has the added benefit that density and velocity gradients are much less severe and therefore more suitable for interaction experiments that mimic laser–plasma interactions within indirect-drive ICF hohlraums. Exploding-foil targets are excellent for producing the kind of flowing plasmas found in the corona around direct-drive ICF pellets.

Figure 4(a) shows a gated x-ray pinhole image of the plasma. The image is one of a series of gated images,

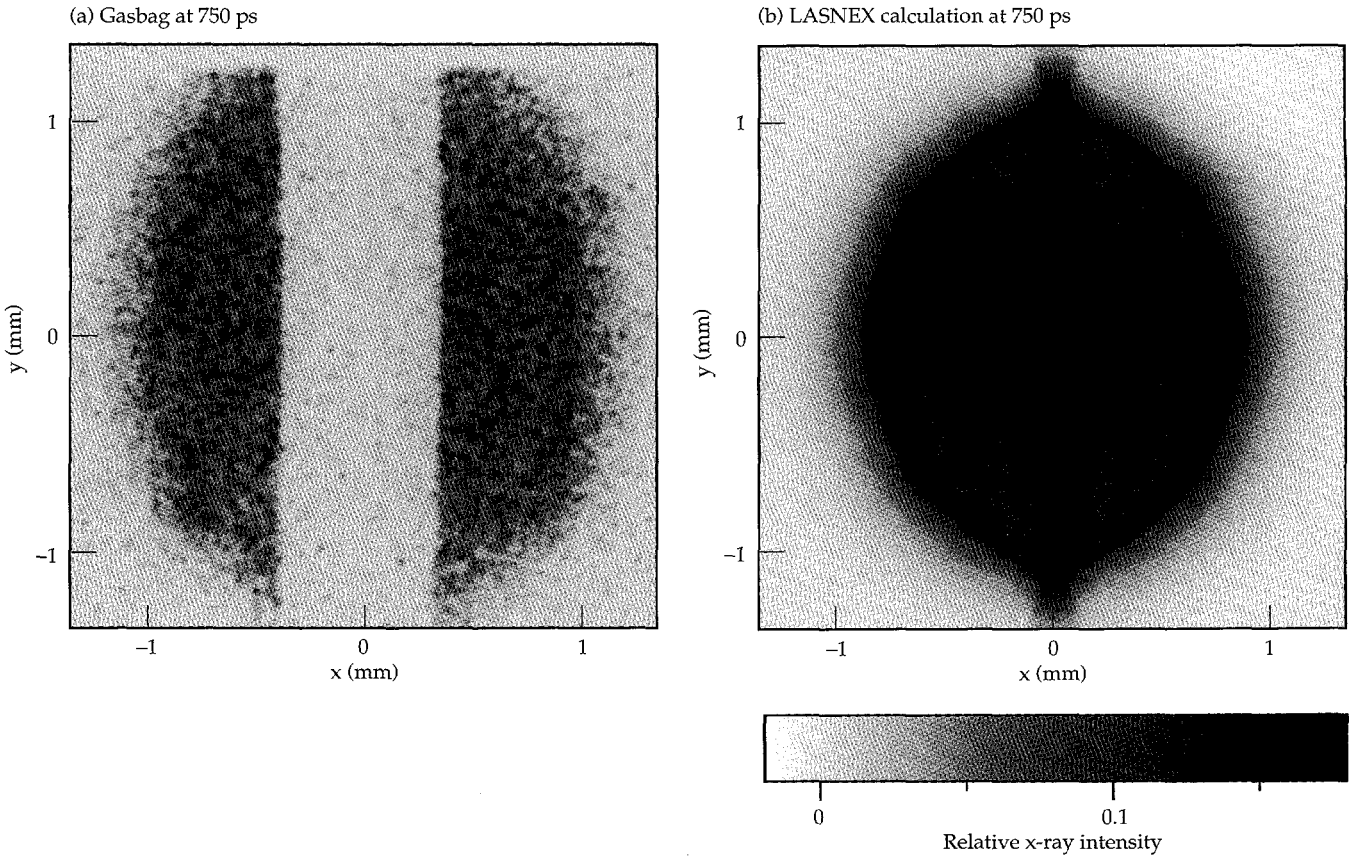

FIGURE 4. (a) Gated x-ray pinhole image of gasbag at 750 ps; large stripe across image is the shadow of a shield that is well away from the plane of the plasma. Support washer (shown in Fig 3c) is only 400 μm wide. (b) Simulated x-ray image from a LASNEX calculation at 750 ps. In both images, the gray scale indicates x-ray intensity integrated along the pinhole camera line of sight. Note the bright edge in this simulated image that is not seen in the data (a). The bright vertical stripe in the middle of the simulated image corresponds to a density peak that is propagating radially inwards in the plane of the washer. (20-07-1095-2437pb02)

with 100 ps time resolution, and was recorded 750 ps after the start of the heater pulses. The large vertical stripe across the image is not the support washer (shown in Fig. 3c) which is only 400 μm wide, but is the shadow of a shield that is well away from the plane of the plasma. The x-ray emission looks uniform within the limits of the microchannel plate noise; the camera was filtered to view x rays at photon energies above 1.5 keV, where the target was optically thin. The image represents the integration of x-ray emissivity along a chord through the plasma and could average changes in the emissivity caused by density fluctuations. Abel inversion of images such as this can show us if the plasma has a cold (less emissive) center, as is the case before the heater beams propagate to the center of the target. Some kind of 3-D tomographic imaging would be preferable, and we might eventually develop such a capability. Another alternative for better quantifying the uniformity of our plasmas is to do space-resolved thermal Thomson scattering using a 4ω (264 nm) probe beam. Again, this capability may be developed for future experiments.

The membrane that represents the initial bag wall perturbs the situation somewhat. The membrane is ~2000 to 3000 Å thick after the bag has been inflated and the material has stretched. The lasers heat the membrane, causing it to expand and rarefy, much like an exploding foil.[9] That process launches a weak shock into the bag, which propagates into the center of the target at about the sound speed. The peak density in this shock is calculated to be 2×10^{21} cm^{-3} for a C_5H_{12} gas fill [Fig. 3(e)]; the density scales with the fill density of the gas. Figure 4(b) shows a simulated image taken from a post-processed LASNEX calculation. A brightening due to this density peak is visible at the edge of the plasma. Although such a feature is seen at early times in our experiments, we do not see such a feature after the plasma has achieved its full size (at ~500 ps). The area in front of the shock wave is the region that has a flat density profile with no significant velocity gradients. The structure visible near the middle of the profile in Fig. 3(e) is produced by the symmetry of the calculation and has not been observed in experiments (with framing cameras viewing down the washer axis). The bright vertical stripe in the middle of the simulated image corresponds to a density peak that is propagating radially inwards in the plane of the washer. This peak has been seen in axial images, but it is never in the path of the interaction beam, which enters the plasma shown in Fig. 4(b) from 50° below the horizontal, crossing the image almost diagonally.

Electron temperatures were measured[10,11] by x-ray spectroscopy using K-shell line spectra from mid-Z elements (such as 2000 Å of cosputtered Ti and Cr or 2500 Å of KCl) placed in different locations inside the gas-filled targets. Analysis of the line intensity ratios uses a time-dependent collisional-radiative model of the plasma.[12] Isoelectronic ratios of the He-like emission were used because they are less affected by time-dependent ionization effects. Density variations are not expected to introduce large effects in the analysis and are included in the error estimates of the results.

The electron temperature in the C_5H_{12}-filled gasbag was measured with TiCr dopants and with Ar/Cl gas dopants. These spectroscopic measurements, using three different line ratios, consistently indicate that peak temperatures of 2.8 to 3.2 keV are achieved in the gasbags. Recent measurements of Ar and Cl satellite and resonance lines over several shots have enabled us to obtain a history of the temperature rise; these measurements show a peak temperature of 2.8 ± 0.5 keV, slightly below the LASNEX predictions. The measured temperature lags behind the temperature rise indicated by the simulation. Gasbags attain their peak electron temperature at 1 ns, when the heater beams turn off, but they are homogeneous after 400 ps when they are heated with 3ω heater beams.

The quoted electron temperature was measured in the gasbag plasmas with 3ω heater beams. Early experiments using 2ω (527 nm) heater beams (which would give higher temperatures because of increased collisional absorption) showed poor coupling of the laser energy into the initially cold plasma, which then stayed cold. Since $n_e = 10^{21}$ cm^{-3} is $0.25n_c$ for 2ω light, it was suspected that $2\omega_{pe}$ decay and/or SRS at the quarter-critical density was converting much of the incident energy to fast electrons,[13,14] which then deposited their energy in the target superstructure without heating the plasma effectively. Hence most of the experiments described here used 3ω heater beams and a 3ω interaction beam.

The electron temperature of the large gas-filled hohlraums ("GASBIGS") was determined using dopants deposited on 150-μm-wide, 800-Å-thick CH substrates. The gas volume of the hohlraums is not uniformly heated by the laser beams as in the gasbags, so the measurements were performed in and out of the beam path. Peak electron temperatures in the beam path of 3.6 keV were measured by the isoelectronic line intensity ratios of the He-like emission. Figure 5 shows the temperature history calculated by LASNEX and the corresponding measured temperatures. Measurements earlier than 1 ns are not included because accounting for the transient effects of the ablation and equilibration of the foil with the surrounding plasma introduces large uncertainties in the measurements. The temperature in the GASBIG is also observed to lag at early times. This discrepancy may be related to the heat capacity of the gas, because volumes not heated by the laser light must be heated by lateral heat flow; alternatively, it may imply that beam propagation is not as fast as the LASNEX calculation predicts. The out-of-beam measurements (not shown) show a temporal lag, but still achieve peak temperatures of 3 keV. Similar measurements using Ti/Cr spectroscopy made to characterize the toroidal hohlraum

plasmas[15] yielded temperatures of 3 ± 0.5 keV for the time at which the interaction beam would probe the plasma.

For all three of the targets shown in Fig. 3, we found temperatures of about 3 keV for plasmas of order 2 mm in size at $0.1n_c$. Since this approximates the region of the NIF plasma producing the highest calculated gain for SBS and SRS on the inner beam, we then turned to using these targets to perform interaction experiments. Note that the problem of producing a target with a gain similar to that seen on the outer beam in the Au [Fig. 2(b)] is not solved with these targets. None of them has sufficient radiation temperature to drive off a significant plateau of low-density Au plasma to mimic that region for the NIF outer beam. In fact, the scale-1 Nova hohlraums, when gas-filled, actually produce SBS gain exponents in the Au similar to that in the NIF outer beam. This occurs because inverse bremsstrahlung absorption in the Au, and not the hohlraum size, determines the scalelength in the Au. For gas-filled Nova scale-1 and NIF hohlraums, this absorption length is a few hundred micrometers. This issue is discussed towards the end of this article.

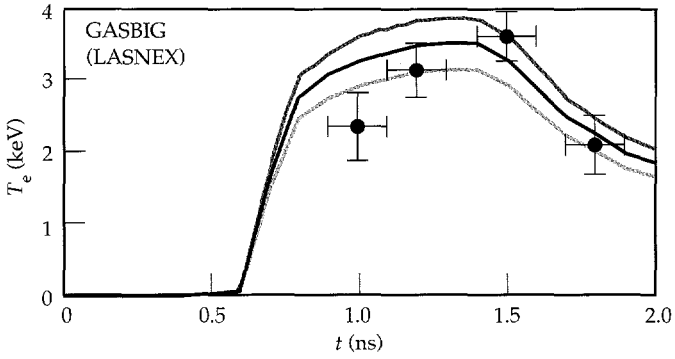

FIGURE 5. GASBIG hohlraum electron temperature history calculated by LASNEX, and corresponding measured temperatures. Top and bottom curves represent ±10% temperature variation.
(20-07-1095-2438pb01)

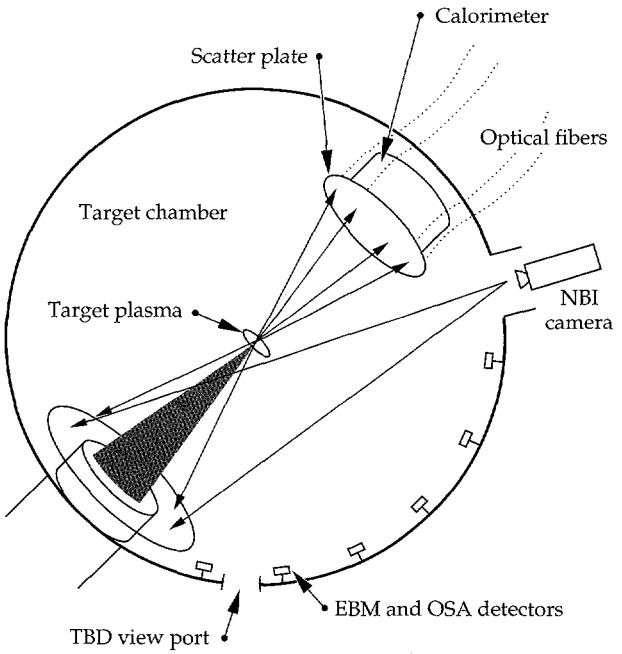

FIGURE 6. Nova target chamber, showing placement of scattered-light diagnostics. Beam shown is the interaction beam (beamline 7), on which the NIF beam smoothing and f/number were replicated. The other nine beams (used to heat the plasma) are not shown.
(20-07-1095-2439pb01)

Diagnostic Development

The development of diagnostics for the long-scale-length plasma experiments was motivated by the desire to better account for the scattered light and at the same time to quantify the light transmitted by the plasma. Figure 6 shows the placement of the various diagnostics in the Nova target chamber. The beam shown is the interaction beam (beamline 7), on which the NIF beam smoothing and f/number were replicated. The other nine beams (used to heat the plasma) are not shown.

Before 1993, measurements of SBS were made by taking a subaperture sample using a Fresnel reflector (uncoated beam splitter) within one of the ten Nova beams, and it was assumed that the backscatter was uniform within the beam aperture. The gain for both SBS and SRS peaks in the direct backscatter direction, so the scattered light should be collinear with the incident beam. In setting up for the long-scalelength plasma experiments, it was decided to move this diagnostic capability to the beam that we would use to mimic the NIF smoothing and focusing geometry, while making the system integrate backscatter over the full beam aperture. Figure 7 shows the new system, called the FABS (full-aperture backscatter diagnostic). The FABS views the scattered light that propagates back down the beamline and is transmitted by the 1ω (1054 nm) turning mirror closest to the chamber [which of course has high reflectivity (~95%) for the incident 1ω light but transmits ~30% of backscattered 3ω light]. A large hole was cut in the back of the mirror mounting box, allowing access to the scattered light transmitted by the mirror. Since light scattered from the target passes back through the Nova focusing lens, it is recollimated and is 70 cm in diameter when it emerges from the back of the mirror box. A second f/4.3 Nova lens was then used to focus the beam into the various diagnostic packages to allow analysis of the scattered light. A time-resolved SBS spectrometer, normalized with a time-integrating calorimeter, allowed the power history for SBS to be recorded; the time-resolved SBS spectrometer provided additional information on the spectral features of the SBS. A CCD camera also recorded a time-integrated image of the SBS backscatter angularly resolved within the diagnostic acceptance angle (i.e., SBS imaged in the plane of the Nova lens).

Viewing light scattered from the target through the Nova focus lens and refocusing it with a similar Nova lens introduces a large amount of chromatic aberration. The Nova lenses were intentionally designed with large chromatic aberration to separate the foci of 1ω, 2ω, and 3ω light (wavelengths 1054, 527, and 351 nm, respectively) in the target plane. This property causes problems when trying to focus the scattered light spectrum, which extends from 350 to 700 nm, into the diagnostic packages. A later version of the FABS will use a collecting mirror in place of the second lens and will correct the chromatic aberration through a series of small-aperture optics. This system[16] was not ready for the experiments described here; when it is implemented, it will have the capabilities of the current FABS but also will have the ability to image the target plane using the scattered light. The primary mission of the FABS in its original inception was to measure the SBS scattered light from the target. Because the SBS spectrum is quite narrow (~1 to 2 nm), the issue of chromatic aberration was not as severe as it is for broader-band SRS measurements.

SRS diagnosis was initially made through monitoring diodes placed 27° from the incident laser beam together with a streaked optical spectrometer. This setup was complemented by measurements of the fast-electron yield using the FFLEX filter–fluorescer, viewing x rays produced by electrons slowing down in the target material. As discussed below, the suspicion that SRS yields from targets were higher than implied by FFLEX led to the development of improved monitoring of the light scattered by SRS. The FABS diagnostic was modified (as indicated in Fig. 7) by having a diffuser placed soon after the focusing lens that scattered the light, which was then recorded by a filtered diode. This reduced the problem with chromatic aberration discussed above by making the measurement as close to the second focusing lens as possible, before the disparities in focal length could significantly change the beam size as a function of wavelength.

A further complication was introduced by severe modulations in the transmission of the turning mirror (inset in Fig. 7). The modulation is due to the multilayer coating on the mirror, which is optimized to reflect narrow-band 1ω laser light efficiently, not to transmit a broad-band signal. This modulation makes quantitative measurements of SRS difficult. The difficulty was addressed by using a streaked optical spectrometer to spectrally resolve the SRS signal seen by the diode. The spectrum could then be corrected using the calibrated mirror transmission function, and the diode signal (which represents an integral of the spectrum) could be corrected accordingly. This spectrometer also allowed us to record the spectrally resolved SRS reflectivity for comparison with our expectations [e.g., Figs. 2(c) and (d)] and also to study changes in the spectrum as a function of beam smoothing and laser f/number. All of the SRS spectra shown below were corrected to remove the modulation of the mirror transmission.

The FABS diagnostic was calibrated by using an uncoated spherical mirror placed on the far side of the chamber from the instrumented beamline (beamline 7). Beam 7 was then focused through a large hole (~6 mm diam) in a plate positioned at chamber center. The plate absorbed the unwanted harmonics of the laser beam (e.g., 1ω and 2ω in the case of a 3ω calibration shot), because the chromatic aberration in the Nova lens meant that only one color was focused at the hole. The light then diverged before it was reflected by the uncoated mirror and sent back down the beamline, where is was recorded as a known amount (~6%) of backscattered light.

The SBS detectors were calibrated using the 3ω calibration shots that are run routinely to maintain confidence in the precision Nova incident-beam diagnostics. To calibrate the SRS detectors, 2ω light was used, since its wavelength is in the middle of the spectral range of SRS light from most of our experiments. The sensitivity of the other components in the diagnostic relative to their sensitivity at 2ω were calibrated off-line. This process resulted in a typical uncertainty of 10% in the SBS and 20% in the FABS SRS measurements.

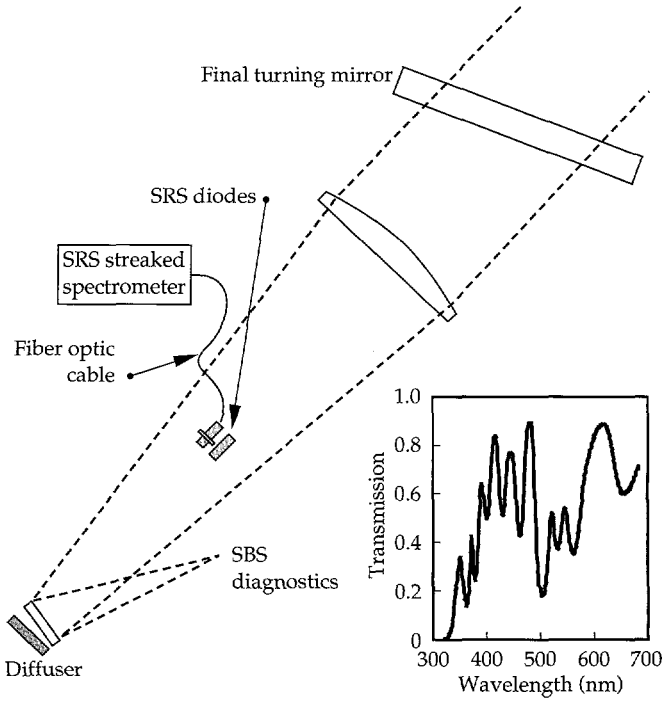

FIGURE 7. Full-aperture backscattering station (FABS) diagnostic, and (inset) transmission of final 1ω turning mirror through which FABS views scattered light. SBS light is reflected from a beam-splitter before it is injected into the SBS diagnostic package. A diffuser behind the beam-splitter reflects broader-band light into the SRS diagnostics. (20-07-1095-2440pb01)

To complement the FABS, the diagnostic set included time-integrated diodes (Fig. 6) spaced at ~10° intervals around the chamber to look at sidescattered light. As discussed below, there were indications in the first experiments with these diagnostics that the scattered SBS was coming back outside the collection angle of the FABS (defined by the incident beam f/number). Initial estimates were therefore made of the energy outside the lens using similar time-integrated diodes. An estimate of the spreading of the backscattered SBS was also obtained by restricting the aperture of the incident beam and using the FABS to image the light that scattered outside the angle of the incident sub-aperture beam. These estimates led us to conclude that up to three times as much scattered SBS energy may have been outside the lens as inside it for gasbag targets. At the time, the precision of this measurement was sufficient, because the amount of SBS in the lens was negligible. However, in the second phase of the experiments we planned to push the amount of SBS upward, so we expected that the energy outside the lens would play a large part in determining the energy budget of the interaction beam. Therefore a new diagnostic for near backscattered light was developed for the second series of experiments.

The near-backscattering imager (NBI) extended the continuous coverage of SBS and SRS backscattering outside the lens to 20° from the lens axis. This was achieved by placing a large annular plate of bead-blasted aluminum around the outside of the lens assembly within the target chamber (Fig. 6). The near-backscattered light from the target scatters from the plate as if from a diffuse screen and is then imaged by two TV cameras on the far side of the target chamber. Filters on the TV cameras allowed us to separately measure SBS (near 351 nm) and SRS (400 to 700 nm). Off-line calibration of the plate reflectivity and the known filter and TV camera throughput allowed us to spatially integrate an image frame at shot time to determine the total amount of scattered light. The images could also be combined with the images recorded by the FABS SBS and SRS cameras to provide an image of the angular distribution of scattering inside and outside the interaction beam solid angle. The diagnostic was supplemented by time-integrated diodes and fiber optics viewing the target through holes in the plate. The fiber optics allowed samples of the scattered light to be transported to an optical streak camera, where differences in time history as a function of scattering angle could be quantified.

The calibration of the plate reflectivity plus camera sensitivity could be checked *in situ* by comparing the scattered intensity with that recorded on the diodes. We could also compare the sensitivity of the FABS and the NBI by using a Au foil target at the chamber center to reflect energy from one of the other beam lines towards beam 7. This technique uses the "glint" reflected from the Au foil to fill both diagnostics with light. Comparison of the glint imaged in both diagnostics then revealed any inconsistencies as sharp jumps in image intensity where the coverage of the two diagnostics abutted one another. Contamination of the plate by target debris is a potential source of inconsistency. Initially a large effort was made to compare NBI and FABS to keep confidence in the calibration of NBI. As the use of the NBI diagnostic has become more routine, we have instituted a schedule of installation, removal, and recalibration of sections of the plate, and we use the diodes inset in the plate to maintain confidence in the evolution of the calibration. Problems with the time-integrating diodes (described below) have been eliminated by using more linear diodes with better dynamic range. The uncertainty in the NBI SRS and SBS numbers is about 30% for the data discussed below.

Sidescattered SBS light in these experiments was studied with a diode array. The diodes were time-integrating, so they could not distinguish the contributions due to sidescattering from the heater beams. The solution to this problem was to put fiber optics inside the chamber beside each diode to relay the SBS light from there to an optical streak camera, which then provided a time-resolved history of the sidescattering that could be normalized with the time-integrated diode signal. The contributions due to sidescattering from the heater beams could then be seen occurring early in time; those due to the interaction beam would come later. This system of combined diodes and fiber optics was called the oblique scattering array (OSA).[16] The system was not operational during the first $f/8$ campaign (April 1994) and was only partially operational during the second $f/8$ campaign (February 1995). In all applications involving diode measurements, it was necessary to absolutely calibrate the detectors, filters, and blast shields off-line and then monitor how their calibration changed in the target chamber due to debris buildup by frequent recalibration and replacement of debris shields and filters. During the first $f/8$ campaign, when the diodes were being used to quantify SBS near backscatter outside the lens cone, the diodes became nonlinear in their sensitivity to 3ω light at distressingly low fluences. This effect required characterization of the diode sensitivity over a wide range of incident fluences and also reduced the effective dynamic range of the diodes.[17] Individual diode readings fluctuated from shot to shot, and diodes next to one another often gave conflicting measurements. This may have been due to diode nonlinearity or damage or to small-scale structure in the scattered light intensity, which is difficult to resolve with single-point diode measurements. This latter consideration was one motivation for making the imaging NBI system for near backscatter. We may build a similar imaging system for sidescatter that will avoid the poor statistics of the single-point diode

measurements. New diodes were identified that had better dynamic range and that were linear up to higher fluences. These diodes were installed in the NBI plate as described above and were retrofitted into the OSA array.

The last diagnostic shown in Fig. 6 is the Transmitted Beam Diagnostic (TBD), whose purpose is to measure the amount of light transmitted by our open-geometry plasmas and to study the effect of processes such as diffraction from filaments on the divergence of the transmitted beam. This diagnostic was first set up during the 1994 $f/8$ campaign. The device was a frosted glass plate mounted on the opposite side of the chamber from Beam 7 (see Fig. 6). In its original form, the plate intercepted, transmitted, and forward-scattered light over an angle equivalent to $f/7.2$. However, it was quickly realized that the beam expanded beyond the $f/8$ original beam divergence as a consequence of refraction, diffraction in filaments, or forward SBS. For the second $f/8$ campaign, the TBD was enlarged to detect light over a $f/3.6$ cone. The plate was viewed by an optical framing camera that recorded the beam angular spread at four distinct times, together with a streak camera that resolved the divergence in one dimension continuously in time. Absolute measurement of the transmitted light was made using a fast diode that gave the history of the beam integrated in both spatial dimensions. The system was calibrated by firing a shot with known 3ω laser energy through an aperture placed at chamber center to remove the 1ω and 2ω light. A secondary measurement made with the TBD system was quantification of forward Raman scattering by injecting some of the transmitted light through a fiber optic into a low-resolution streaked optical spectrometer. Fiber-optic coupling was also used to inject the forward-scattered light into a high-resolution spectrometer to investigate the effects of filamentation on laser wavelength.

The main purpose of the TBD was to reveal changes in transmission due to the onset of scattering processes. Quantifying all the loss mechanisms due to parametric processes is very difficult. However, since the main objective of our experiments is to show that we can propagate a NIF-like beam through a NIF-like plasma without adverse effects, it was decided that by looking at the beam after it has traversed such a plasma we can directly discern if some as-yet unquantified process is serving as a loss mechanism. By looking at the characteristics of the beam after it has passed through one of our open-geometry gasbag plasmas, as a function of beam smoothing and laser intensity, we can ensure that the laser will propagate according to design in the NIF hohlraum.

1994 NIF Experiments

In April 1994 the NIF beam geometry was reproduced on Nova by modifying one beam to have the $f/$number and smoothing characteristics of a cluster of four NIF beamlets. Nine of the Nova beams were used to produce the long-scalelength plasma; the tenth was configured as an interaction beam that was sent through the preformed plasma after a 500-ps delay. The SRS and SBS scattered from the plasma, together with the effects of the plasma on the transmitted beam, were studied as a function of the interaction beam intensity, beam smoothing, and plasma constituents. The interaction beam was smoothed by using RPPs,[18] and four different colors within the $f/8$ beam to mimic the NIF laser architecture.[19] The four-color setup divided the $f/8$ beam into four separate quadrants, each of which had its wavelength shifted relative to the others. The wavelength separation of the colors was approximately 1.4 Å at 3ω. Since each beam quadrant could have its frequency conversion crystals individually tuned for its wavelength, the four-color scheme approximated "bandwidth" on the interaction beam without losing 3ω conversion efficiency. We also studied the use of additional laser bandwidth of approximately 1.6 Å at 1ω on each color, coupled with SSD,[20] to further reduce reflected SBS. These studies were performed with both $f/4.3$ and $f/8$ interaction beam focusing.

The main results of the 1994 $f/8$ campaign were the observation of low amounts of SBS, with indications of more SBS scattered around the lens (a factor 2 or 3 in gasbags), but not enough to be a significant loss mechanism. Figure 8 shows the total SBS backscatter as a function of laser beam intensity and beam smoothing for the gasbag targets. The data are separated into the three smoothing conditions that were studied: four-color as described above, "one color," in which the four quadrants were set to be the same color, and "one-color SSD," which had an additional bandwidth of 1.6 Å at 1ω put on the one-color setup. The data plotted is the peak SBS reflectivity in time (reflected power/incident power), not corrected to account for SBS light reflected outside the lens acceptance angle. Our estimates based on the use of diodes to measure the energy outside the lens indicate that these numbers should be increased by a factor of 2 to 3, making the maximum SBS seen in these experiments only ~6%.

Low levels of SBS were observed for irradiances up to 6×10^{15} W cm^{-2} (well above that planned for the NIF). There was little difference in the levels observed with one-color or four-color irradiation; however, the addition of SSD beam smoothing to the one-color case reduced the SBS to below 0.5%. The observation of these low

scattering levels did raise the interesting possibility that the highest intensity planned for the NIF was too conservative, and that a design with higher laser beam intensity and hence higher hohlraum radiation temperature might be viable. The benefit in higher capsule gain and relaxed surface roughness specifications for instability growth made experiments at higher intensity very attractive.

The low level of SBS backscatter and the scaling of the SBS with intensity are perplexing. The apparent observation that four-color beam smoothing produces more SBS backscatter than one-color smoothing at high intensity was contrary to our expectation that four-color smoothing should suppress filamentation at least as well as one-color smoothing, if not better. The observation that SBS is reduced with the addition of a small amount of bandwidth and SSD beam smoothing is more sensible.

During this 1994 campaign we made the first transmitted-beam measurements, but these were limited to collecting light over an $f/7.2$ aperture; the transmitted $f/8$ probe beam broadened to overfill the detector, making quantification of the transmitted fraction uncertain.

Quantification of SRS backscattering from the long-scalelength plasmas was limited to large-angle diode measurements and measurements of the hard x-ray

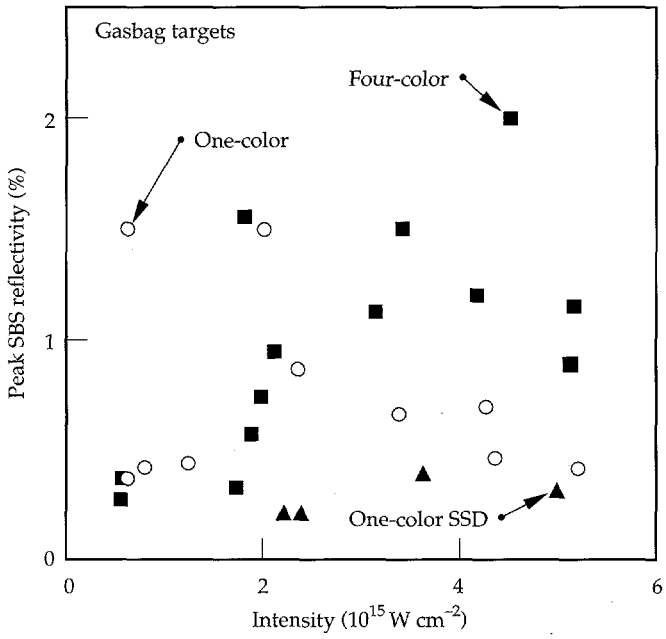

FIGURE 8. Measured SBS reflectivity from gasbag targets from April 1994 $f/8$ campaign. Quantity plotted is peak reflectivity (scattered power/incident power) into an $f/8$ collection angle; contributions due to scattering outside this solid angle are estimated to increase these numbers by a factor of 2 to 3. (20-07-1095-2441pb01)

spectrum produced by fast electrons striking the Au hohlraum wall. These measurements showed that at most 1% of the incident energy was converted to fast electrons, with the limitation that the time-integrated technique did not distinguish between electrons produced by the heater beams and those produced by the probe beam. Experiments with the probe beam energy set to zero showed fast-electron yields similar to those with high power on the probe. In all of the interaction experiments carried out at $f/4.3$ and $f/8$ during this period, the inferred levels of SRS were low (<1%). This was perplexing, because a few experiments with gasbag targets in the Two Beam chamber area of Nova produced larger levels of SRS (of the order of 4%). However, those experiments were done with plasmas that were cooler (1.5 keV) than the plasmas heated by nine Nova beams (3.2 keV). This observation is consistent with the higher temperature, in the plasmas heated with nine beams, resulting in strong electron Landau damping of the electron plasma waves at $0.1n_c$ for 3ω and so reducing SRS. In either case, however, the plasma should have had a peak gain exponent of at least 20 for SRS [e.g., Fig. 10(d), below]. The Two Beam experiments did not have a filter–fluorescer measurement for fast electrons produced by SRS. The SRS was measured by observing the scattered optical light that went back into the interaction beam lens. This difference motivated the installation of a similar optical SRS detection system in the Ten Beam chamber for the second $f/8$ campaign to better quantify SRS.

Several issues were left unresolved by the first $f/8$ campaign:

1. The effectiveness of SSD beam smoothing in suppressing filamentation and how it compared with four-color smoothing.
2. The effectiveness of four-color versus one-color beam smoothing in suppressing filamentation.
3. The low level of SBS.
4. The low level of SRS inferred from FFLEX.
5. No real quantification of the characteristics of the transmitted beam.
6. Sidescattering was not quantified.

Furthermore, the possibility of beams with different colors (e.g., four-color) transferring energy when crossing within the plasma had been raised by experiments that showed such an effect in long-wavelength (10.6 μm), low-density experiments.[21] This possibility merited investigation in more NIF-relevant plasmas using 3ω light.

For the initial $f/8$ experiments, the peak SBS observed from the C_5H_{12} plasmas was less than 6% for all irradiation conditions tested. It was therefore decided to perform a second series of $f/8$ experiments

with improved diagnostic capability to explore higher intensities than those expected in the NIF baseline design. These experiments would also attempt to resolve the issue of what beam smoothing is most effective for the NIF; however, these initial results were encouraging.

Ion-Landau Damping Experiments

To address the issue of low levels of SBS in our NIF-like plasmas, we looked at data obtained from plasmas that had a reduced level of ion-Landau damping. Some experiments carried out at $f/4.3$ showed that changing the material in the target to one with a lower expected ion Landau damping of sound waves led to a strong increase in SBS. Figure 9 shows the results of an experiment performed at $f/4.3$ that investigated the effect of removing the light ions (protons) from the plasma. Since the hydrogen ions in C_5H_{12} are lighter than the carbon ions, their average velocity is significantly higher than that of carbon ions at the same ion temperature. The presence of these faster protons near the phase velocity of the ion-acoustic wave, which is pumped by the SBS process, allows them to extract energy from the wave and so damp it.

The data in Fig. 9(a) are from gasbag targets with a variety of gas fills. Backscattering levels as high as 35% were observed for CO_2 plasmas, while subtly changing

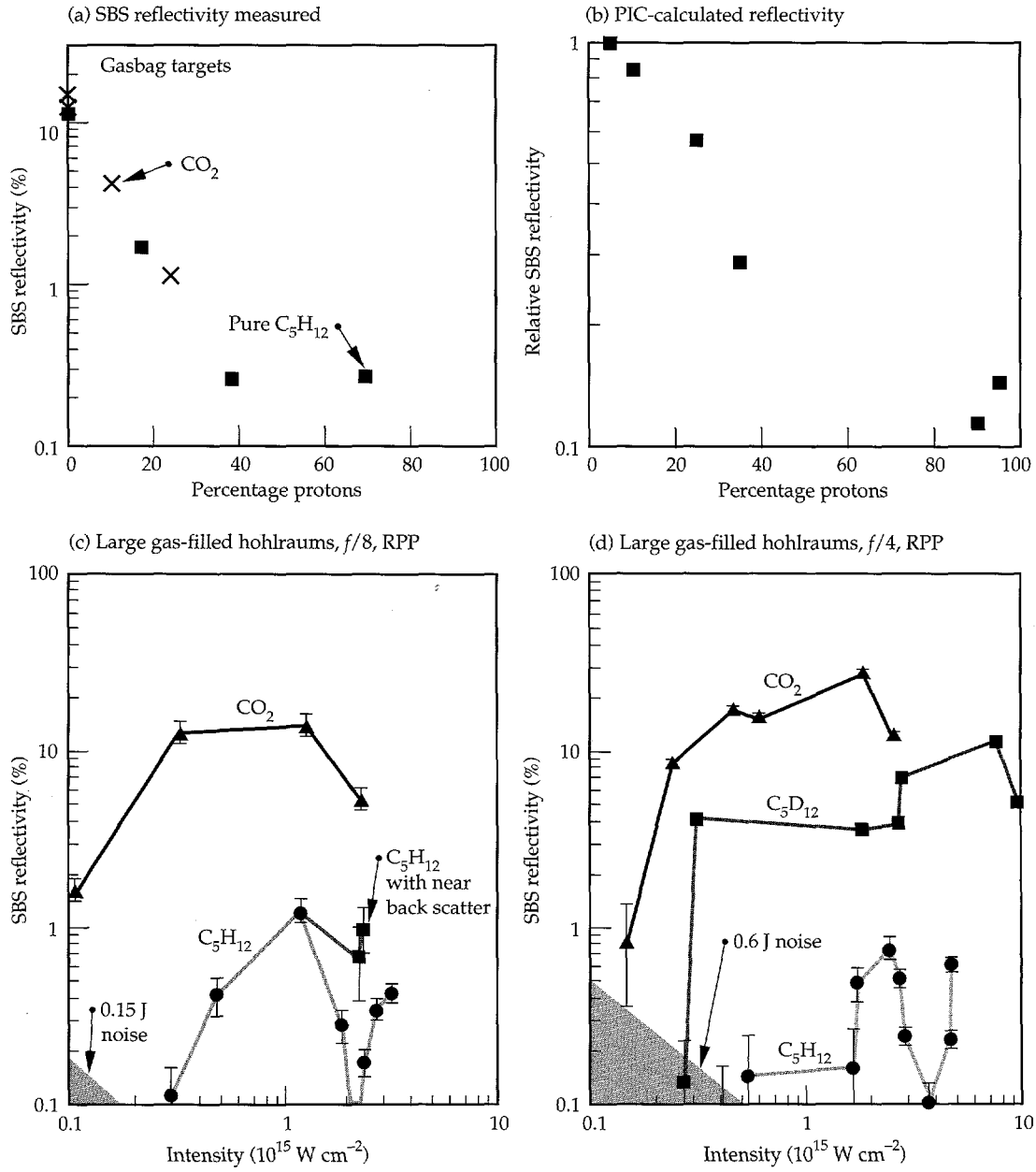

FIGURE 9. (a) Time-integrated SBS reflectivity from gasbag targets containing mixtures of CO_2 and C_3H_8 (crosses) or C_5D_{12} and C_5H_{12} (solid squares). The amount of the second material is varied and is expressed as percentage of ions that are protons vs proton concentration. (b) PIC calculation of SBS reflectivity from a CH plasma (normalized to unity for pure carbon) vs proton concentration. (c) Time integrated SBS backscatter from toroidal hohlraums, $f/8$ experiments; (d) SBS back-scatter from toroidal hohlraums, $f/4$ experiments.
(20-07-1095-2442pb01)

the plasma from C_5H_{12} to C_5D_{12} (i.e., changing protons to deuterons) increased the peak SBS from ~3% to ~25%. Both CO_2 and C_5D_{12} are expected to have lower ion Landau damping than C_5H_{12} at the range of ion temperatures expected in the experiments.[22] The higher damping of the C_5H_{12} plasma arises because of the mixing of a light ion (H) that does the damping with a heavier ion (C) that determines the sound speed. The high thermal speed of the hydrogen relative to the ion-acoustic wave speed allows the many protons moving at the wave speed to efficiently extract energy from the wave, damping the wave and reducing the SBS gain. This phenomenon was first reported by Clayton[23] in low-T_e, low-density discharge plasmas irradiated with 10.6-μm CO_2 laser light. The experiment reported here was the first observation of this effect in a high-T_e, high-density plasma relevant to ICF. To demonstrate that the protons within the plasma provided the damping, Clayton altered the concentration of hydrogen in the plasma and observed the effect on the SBS threshold. We performed similar measurements with our C_5D_{12} and CO_2 plasmas by adding small concentrations of C_5H_{12} or C_3H_8 to provide more protons. The gasbag experiments did not attempt to measure an intensity threshold for SBS, but instead kept the average intensity in the target fixed and varied the proton concentration.

Figure 9(a) shows the results, which illustrate the reduction in total SBS with increasing proton density. The SBS that we see has essentially saturated. This result has been modeled and essentially reproduced with PIC simulations [see Fig. 9(b)],[24] which is interesting because the ion-Landau damping argument is an argument for a reduction in the linear gain for SBS. The PIC calculations obviously include this linear mechanism plus important nonlinear kinetics effects such as particle trapping and nonlinear frequency shifts. These latter effects reduce the gain beyond what would be calculated with the linear damping only. Figure 9(b) shows the calculated SBS reflectivity for a CH plasma, as a function of proton concentration, normalized to unity for pure carbon. The calculation gave a reflectivity of about 70% for this case. Note that a 1-D PIC simulation always overestimates the SBS reflectivity, because 2-D and 3-D effects that can also limit ion wave growth are obviously omitted.

Figures 9(c) and (d) show SBS reflectivity data (reflected energy/incident energy of the interaction beam) for the toroidal hohlraum experiments. These data are from the 1994 $f/8$ series and from subsequent experiments carried out at $f/4$. The figures also show the effect of the ion species on SBS reflectivity. The reflectivity appears to correlate inversely with the Landau damping rates of the SBS ion wave. For these hohlraum conditions ($T_i/T_e \approx 0.2$), the estimated Landau damping rates normalized to the ion-acoustic frequency (ν_i/ω_i) for He/H, C_5H_{12}, C_5D_{12}, He, and CO_2 are 0.35, 0.25, 0.15, 0.01, and 0.01, respectively.

The plasmas we have produced seem homogeneous enough that the SBS is sensitive to the damping from different materials. This effect was not observed in exploding-foil experiments,[25] in which the SBS reflectivities of CH and Ti plasmas were similar, presumably because of the large flow gradients ($L_v \approx 300$ μm), which reduce the effective interaction length because of dephasing proportional to the acoustic wave damping rate. The total gain is equal to the product of the gain rate ($\sim 1/\nu_a$) and the interaction length ($\sim \nu_a L_v/\omega_a$) and is then independent of the damping rate. Since our results show an SBS reflectivity that is sensitive to damping, they may indicate that the interaction length is being determined by something other than the velocity gradient scalelength L_v. We are continuing to study the relation between velocity gradients in our long-scalelength targets and those expected in NIF plasmas. Because our results show an SBS reflectivity that is sensitive to damping, they suggest that the interaction length is not dominated by inhomogeneities such as the global velocity-gradient scalelength L_v. Fluctuations in the velocity cannot be ruled out, but they should be similar in NIF plasmas to those in our long-scalelength targets, because the initial gases are uniform and nonuniformities are produced by similar laser heating processes.

The phenomenon of enhanced damping by adding protons to the plasma will be used in NIF hohlraums by filling them with mixtures of H_2 and He. Calculations indicate that this mixture will provide even higher ion-Landau damping than in our C_5H_{12} experiments.[22] The LIP calculations for the NIF plasma use the damping appropriate for this He/H mixture. The gain exponent of 20 for the inner beam SBS taking place in the low-Z plasma already takes into account the large ion-Landau damping in such a plasma.

1995 NIF Experiments

As discussed above, the first round of $f/8$ laser–plasma interaction experiments left many issues unresolved. After the diagnostic development described above, we embarked on a second $f/8$ campaign with the intent of finding the optimum smoothing required for the NIF and of determining the beam intensity above which laser–plasma instabilities prevented efficient beam propagation.

In this section we describe these most recent experiments and present some of the details of the experimental observations that were omitted in previous sections. Gasbag, GASBIG hohlraums, and toroidal hohlraum targets were all used in these experiments. The main results were that the levels of SRS backscattering were higher than inferred previously with the FFLEX

technique. The SRS was collimated so that it came back straight into the lens. The levels of SBS were even lower than those observed previously; in fact, there is the distinct possibility that those measurements were contaminated by SRS getting into the SBS calorimeter. The levels of backscattering were sensitive to beam smoothing in the form of SSD and insensitive to differences between four-color or one-color beam smoothing. Scattering at 2×10^{15} W cm^{-2} was at a level acceptable in NIF designs, but higher intensities produced far more SRS. The NBI diagnostic showed that the SBS scattered outside the lens multiplied the FABS-only number by a factor of 2 to 3 for gasbags, but GASBIG hohlraums produced much less symmetric SBS backscattering that had as much as a factor of 10 more SBS outside $f/8$ than inside it.

Figures 10(a) and (b) show gasbag SBS and SRS spectra recorded in the direct backscatter direction with the FABS diagnostic. The data are for a C_5H_{12}-filled gasbag irradiated with 2.2×10^{15} W cm^{-2} with a four-color $f/8$ beam with 1.6 Å of SSD beam smoothing. Figure 10(a) shows SBS spectra recorded from the gasbag plasma. Early in time (0 to 500 ps) the spectrum shows sidescattering from the nine heater beams scattering from the cold gasbag. The sidescattering contribution is small (~20 J/sr) and fades at later time (~500 ps) as the plasma heats up and the density peaks at the edge subside. Data taken with only heater beams (i.e., no interaction beam) show the same signals up to 500 ps. At 500 ps, the interaction beam turns on and produces a narrow SBS spectrum with a red shift of about 10 Å. This shift is consistent with that expected

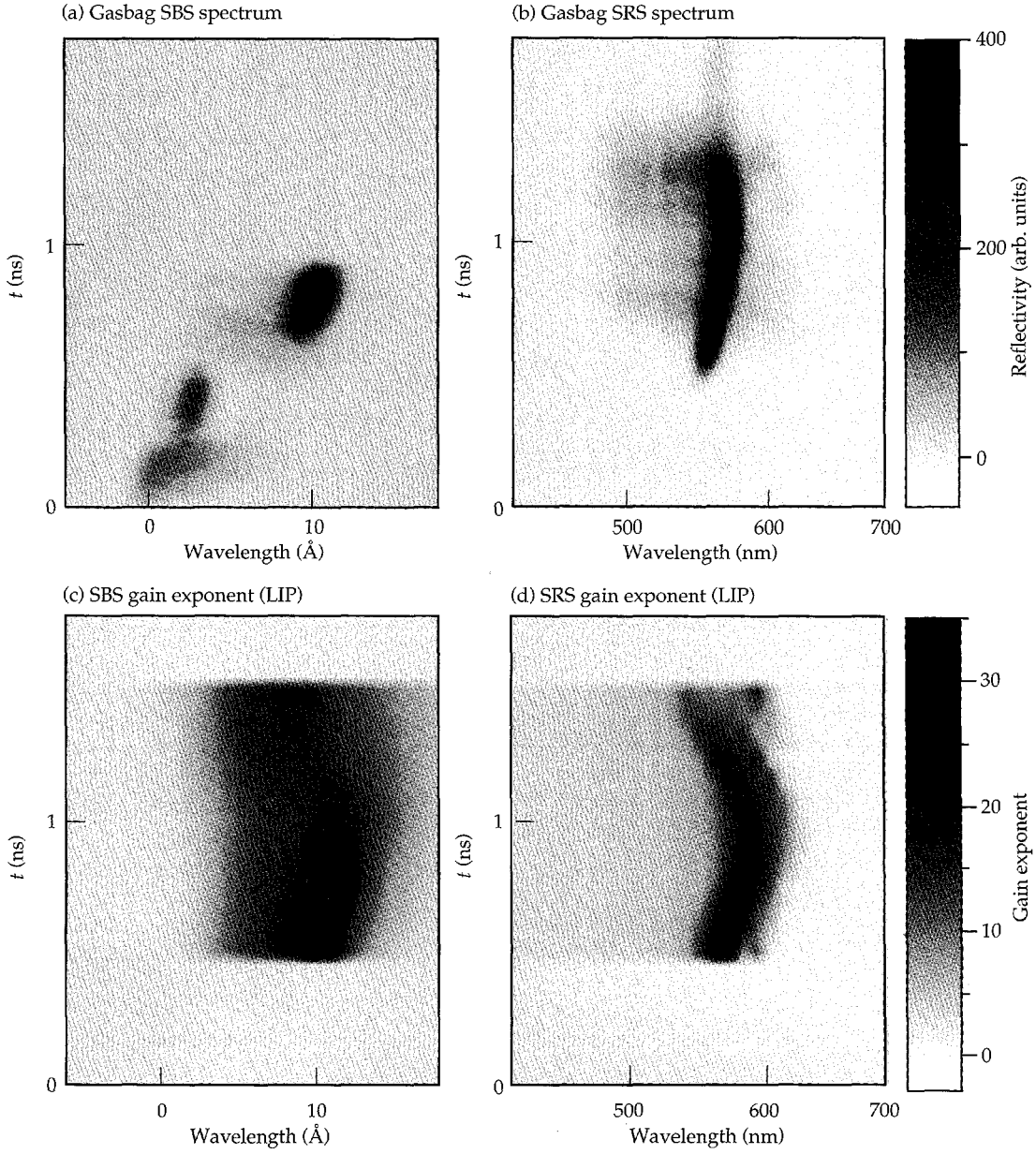

FIGURE 10. Gasbag SBS and SRS spectra. (a) Time-resolved SBS spectrum; features appearing up to 500 ps are sidescattering contributions from the nine heater beams interacting with a bag that is initially cold with high density at the edge. (b) Time-resolved SRS spectrum; (c) LIP-calculated gain exponent for SBS; (d) LIP-calculated gain exponent for SRS. (20-07-1095-2443pb01)

for SBS from a stationary C_5H_{12} plasma at 3 keV. This result can be compared with spectra from exploding-foil plasmas, for which the SBS spectrum is usually broad and blue-shifted, indicating that it may be coming from a plasma that is flowing, giving various amounts of Doppler shift to the backscattered light wave. The fact that there is no shift other than that expected from conservation of energy is a good indication that the plasma is stagnant and that velocity gradients are low. After 1 ns, the data show a strong reduction in the SBS signal.

The spectrum in Fig. 10(a) should be compared with the LIP gain exponent calculation using plasma parameters from a gasbag simulation, shown in Fig. 10(c). The calculation shows no gain before 500 ps, because the interaction beam is off LIP does not calculate sidescattering from the heater beams. After 500 ps, the calculation shows a narrow peak in the gain, which is 30 to 50 until 1 ns and then decreases. At late time, the gain exponent is reduced because the plasma is shrinking, making less interaction length available for amplification. The gain exponent is also decreasing because the ratio of ion to electron temperature is changing. The damping of SBS by ion-Landau damping is a strong function of this ratio (since the ion temperature determines the magnitude and slope of the ion distribution function at the ion wave speed, while the electron temperature determines the speed of the ion wave). At 1 ns, when the heater beams turn off, the electron temperature starts to fall and, since the ion temperature responds much more slowly, T_i/T_e rises rapidly, increasing the damping of SBS.

The correspondence between the gasbag SBS data and the LIP calculation is encouraging. The narrowness, red shift, and time history of the SBS spectrum are consistent, implying that we can predict the fundamental plasma parameters in the experiments. Since the gain exponent calculated at early time is 30 to 50, well in excess of that calculated in the NIF inner beam (20), the measured SBS reflectivity of ~0.2% for this experiment is promising for the NIF.

The LIP calculations [Fig. 10(d)] reproduce a number of features in the gasbag SRS spectrum shown in Fig. 10(b). The time history is interesting: there is a bright peak at 570 nm, which is consistent with SRS scattering from electron plasma waves in plasma at 9×10^{20} cm^{-3} (the average density of the plasma) and a temperature of 3.2 keV. The narrowness of the peak is consistent with a small range of densities that have sufficiently shallow density gradients to permit the growth of SRS. This narrow peak is reproduced in the LIP calculation shown in Fig. 10(d), but that calculation shows the peak at slightly longer wavelength (585 nm). Because the peak position depends on both temperature and density, it is possible that the disagreement arises because the plasma density or temperature is lower in the experiment than in the calculation. The peak moves towards long wavelengths from 500 ps to 1 ns, consistent with an increasing temperature, as the heater beams continue to deposit energy in the plasma. After 1 ns, when the heater beams turn off, the peak moves back to shorter wavelengths as the plasma cools. The peak movement associated with the rise and fall of the temperature is visible in the data, but the movement is not as great as in the simulation. The narrow SRS spectrum shown in Fig. 10(b) is reminiscent of those seen from exploding-foil plasmas, in which only the flat top of the density profile results in SRS because of the shallow density gradient there.[26]

Another remarkable feature in Fig. 10(b) is the scattered light that appears between 470 and 550 nm; this represents scattering from lower densities (0 to $0.1n_c$), which may be present as a result of filamentation. The short-wavelength SRS appears and disappears as a function of beam smoothing and intensity (as shown in Fig. 16, below). Both these parameters affect filamentation of hot spots in the beam. The short wavelengths also appear in Fig. 10(b) to increase as the plasma cools; again, this is consistent with a reduction of filamentation thresholds as the temperature is reduced. These observations are therefore consistent with the short-wavelength light coming from filaments where the high intensities produced by filamentation are needed to overcome the heavy electron-Landau damping of the electron plasma wave at such low densities.

For comparison, Figs. 11(a) and (b) show SBS and SRS spectra from C_5H_{12}-filled GASBIG hohlraum targets irradiated with 2.3×10^{15} W cm^{-2} with a four-color $f/8$ beam with 1.6 Å of SSD beam smoothing. The small amount of scattering seen at early time in Fig. 11(a) is light from the heater beams scattering from the thin membrane that constitutes the window of the hohlraum. The interaction beam is 1 ns long and turns on 1 ns after the heater beams; the heater beams have a long, shaped pulse that is on for the entire duration of the experiment. Once the SBS turns on, it is red-shifted as was the gasbag SBS, but it is not red-shifted as much and is broader than for the gasbag. Both these observations are consistent with a more ramped profile [such as that shown in Fig. 3(d)], which has plasma flowing towards the observer (back towards the laser entrance hole), giving a range of Doppler shifts to the SBS light. The SRS spectrum shown in Fig. 11(b) is also consistent with scattering from such a ramped profile. The lower wavelength SRS (500 to 550 nm) corresponds to densities below $0.1n_c$ (0.04 to $0.1n_c$). These lower densities may be on the profile or they may be present in filaments, as discussed above for the gasbag data. The time-integrated SBS and SRS reflectivities for this shot were 1.3 and 4.8%, respectively.

Figure 12 illustrates some of the combined FABS and NBI data showing the collimation of the SRS backscattering and the large blob of SBS from the hohlraum that

lies outside the FABS acceptance. The images are made by superposing the near-field image of the backscatter as seen by the FABS (0 to 3.6°) on the image recorded on the NBI camera (5.3 to 20°) to produce an image that covers 0 to 20° from the beam axis (a small annulus is missing between 3.6 and 5.3°). The SRS measurement is complicated by parallax in the view of the SRS camera inside the FABS, which results in distortion in the central part of the image. The examples shown in Fig. 12 are (a) gasbag SBS, (b) gasbag SRS, (c) GASBIG hohlraum SBS, and (d) GASBIG hohlraum SRS. The SRS images show that the SRS is well collimated. While the gasbag SBS image shows that the SBS is centered on the lens, that from the GASBIG [Fig. 12(c)] is mostly in a blob that is to one side of the lens. This energy was missed in our earlier (1994) experiments. Figures 12(e) and (f) are more informative, in that they show lineouts through the images and express the result in joules per steradian per incident joule. The lineouts are taken diagonally, such that they pass through the blob in Fig. 12(c). This direction is the radial direction where the center of symmetry is the long axis of the hohlraum. The lineouts show the collimated nature of the SBS and SRS for the gasbag target [Fig. 12(e)]. The GASBIG lineouts in Fig. 12(f) show that although SRS is collimated, the SBS appears about 8° from the beam axis. The appearance of the SBS at such an angle may be due to deflection of the incoming beam as it filaments in the low-density plasma near the laser entrance hole. Filamentation in a plasma that is flowing at near the sound speed can introduce deflection of the beam.[27,28] If after deflection the beam continues to higher density, where direct SBS backscatter is produced, that SBS will not necessarily deflect again on the way out of the hohlraum and so will not retrace its path back out of the hohlraum. Hence there can be a net deflection of SBS that occurs after beam deflection. The direction of the deflection is consistent with the direction of deflection of the forward-propagating beam in x-ray spot motion experiments performed with gas-filled hohlraums.[29]

Figure 13 summarizes the SBS backscattering data for gasbags and GASBIG hohlraums as a function of laser intensity and beam smoothing. Figure 13(a) shows the new SBS data for gasbags; it is noticeable that the backscattering levels are still low and in fact are lower than those observed in 1994 (Fig. 8). One explanation for this is that the time-integrated SBS signal in the earlier experiments was contaminated by stray light or by contributions from short-wavelength SRS. In these newer experiments, we used a diode that (1) was filtered to reject everything but SBS light (near 3ω), (2) had enough time resolution to discriminate against stray light reflected from objects such as the KDP crystal array, within the beam line, and (3) that could be calibrated in a similar manner to the SRS diode. The original motivation for using the diode in place of the calorimeter was that there was a finite reflection from the KDP array that had increased in severity since the first experiments and seemed to vary strongly with crystal tuning. In the 1994 experiments this stray reflection (quantified by observing the calorimeter signal when the beamline was fired with no target present) was small enough to ignore, but with the new experiment it produced random offsets in the signals recorded by the calorimeter. The new diode eliminated this problem and had the side benefit that it was insensitive to any SRS light that would be seen by the SBS calorimeter.

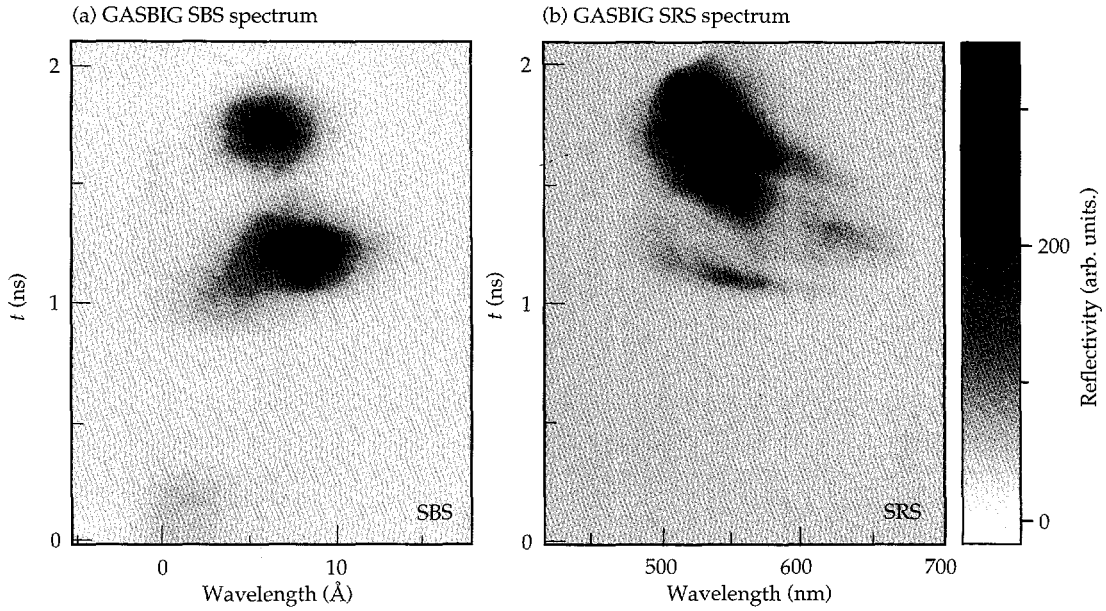

FIGURE 11. GASBIG hohlraum SBS and SRS spectra. (a) Time-resolved SBS spectrum. (b) Time-resolved SRS spectrum; data from FABS direct backscattering diagnostic. (20-07-1095-2444pb01)

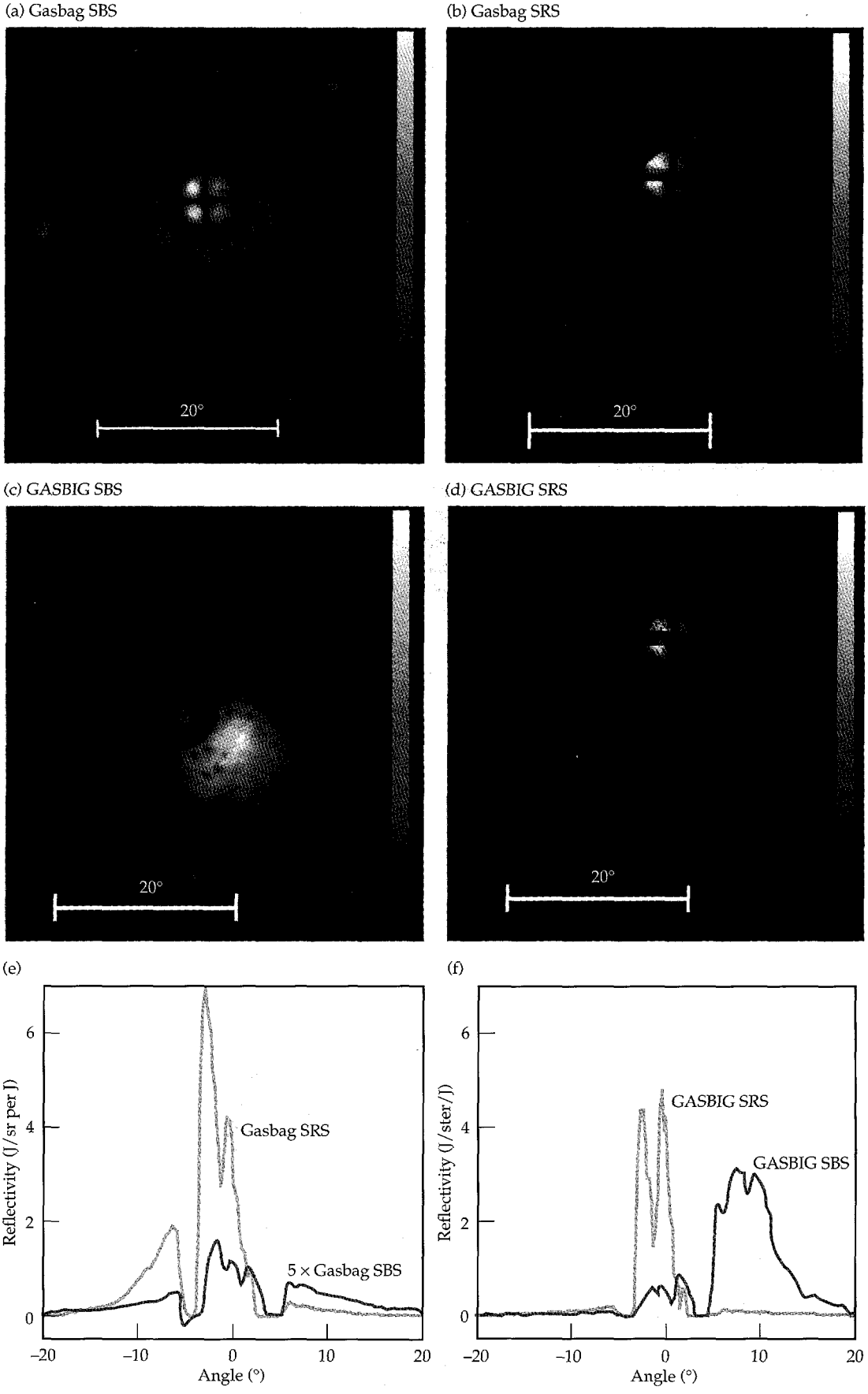

FIGURE 12. Angular distribution of scattered light gasbags and hohlraums. (a) Gasbag SBS; (b) gasbag SRS; (c) GASBIG hohlraum SBS; (d) GASBIG hohlraum SRS; (e), (f) lineouts showing angular dependence of SRS and SBS: (e) gasbag target; (f) GASBIG target. (20-07-1095-2445pb01)

Figure 13(a) shows the peak SBS reflectivity into $f/8$, for the gasbag targets. There has been no attempt to include the contribution due to near-backscattered light. Again, that contribution increases these numbers by a factor of 2 to 3, but the scattered light levels are so low that stray light transmitted by the target striking the NBI plate reduces the precision of the NBI measurement, which then is only good on high-SBS shots. Therefore it is not possible to show the intensity scaling of the data. Figure 13(b) shows similar SBS data for GASBIGS hohlraums; again the NBI contribution has been omitted (the detector malfunctioned on some of the shots), but here the correction factor for the NBI is 6 to 10. In both sets of data it is evident that the addition of SSD reduces the SBS backscattering but that there is no obvious benefit to using four-color smoothing.

Figure 14 summarizes the SRS backscatter data for gasbags and GASBIG hohlraums as a function of laser intensity and beam smoothing. Figure 14(a) shows the data for gasbags. The quantity plotted is the time-resolved SRS reflectivity at the point of maximum plasma temperature (i.e., when the heater beams turn off at 1 ns). The reflectivities for four-color and one-color beam smoothing approach 10% for the NIF intensity of 2×10^{15} W cm^{-2}; the values for experiments that used additional SSD smoothing are closer to 5%. Figure 14(b) shows similar data for the GASBIG hohlraums; the SRS levels at 2×10^{15} W cm^{-2} are similar to those for the gasbag plasmas. The data in both Figs. 14(a) and (b) have had the contributions due to the NBI added and have been scaled to account for energy that would fall into the annulus between 3.6 and 5.3°. These SRS numbers therefore represent the total reflectivity into a cone up to 20° around the beam axis; however (for SRS), most of that energy is within the original $f/8$ solid angle.

The SRS signals are stronger than previously inferred using the FFLEX x-ray technique. An explanation of this discrepancy is that the low phase velocity of electron

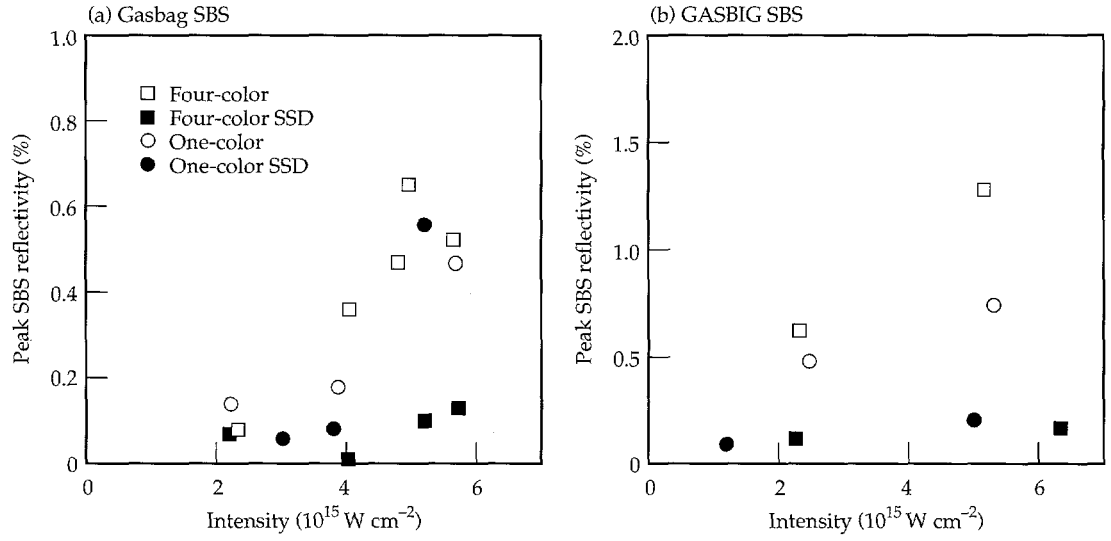

FIGURE 13. SBS vs intensity for various kinds of smoothing. (a) Gasbags. (b) GASBIGS; numbers do not include scattering outside the $f/8$ lens and are the peak reflectivity in time (reflected power/incident power). (20-07-1095-2446pb01)

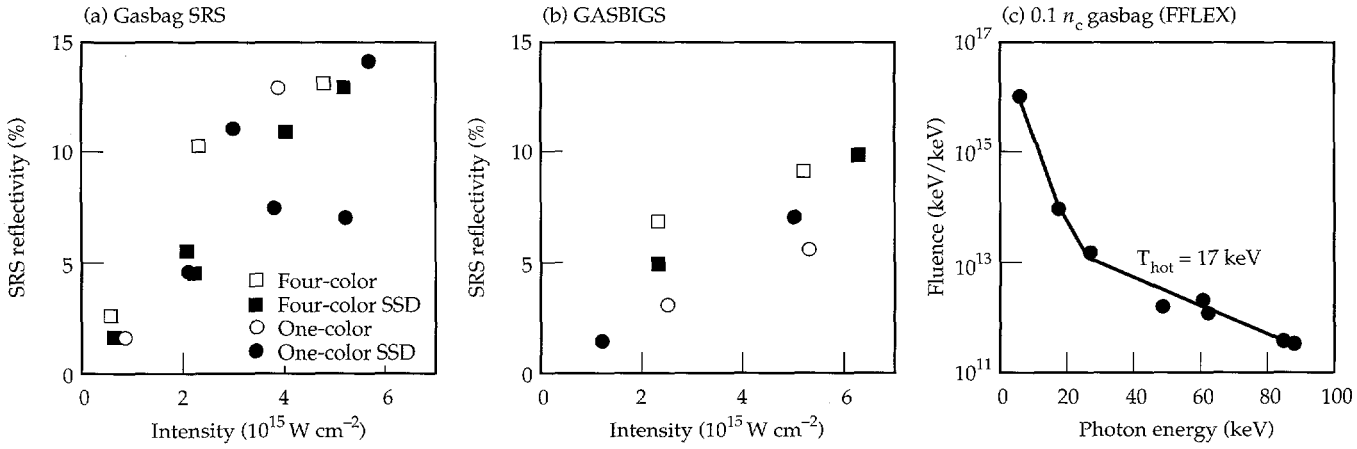

FIGURE 14. SRS vs intensity for various kinds of smoothing. (a) Gasbags; (b) GASBIGS (c) FFLEX data from $0.1n_c$ gasbag. (20-07-1095-2447pb01)

plasma waves in $0.1n_c$ plasma produces low-velocity electrons as the electrons damp the wave. Hence we expect electron energies of 10 to 20 keV to be produced by the SRS that we are detecting. The FFLEX technique is flawed in a gas-filled hohlraum because a significant fraction of any 10-keV electrons will be stopped in the gas (range 400 μm) before they reach the wall. Thus if they produce x rays as they are slowed, it will be through bremsstrahlung resulting from interactions with the lower-Z gas ions rather than with Au. The radiation production scales as Z, so carbon is much less efficient than Au. (The FFLEX analysis requires a knowledge of the Z of the plasma ion.) Even worse, the x rays that are produced cannot then get out of the hohlraum, because the opacity of the Au wall is high for x rays below 40 keV. Hence the FFLEX diagnostic was useful when the fast electrons that were being detected were 100 keV, such as are produced at $0.25n_c$; FFLEX is not useful at the low n_e/n_c encountered in 3ω experiments unless the target has a well-defined Z and has a low opacity to the x rays that are produced. The up side of all this is that 10- to 20-keV electrons are not a preheat threat. The FFLEX is sensitive to electrons that are a preheat threat, because significant quantities of 100-keV electrons could preheat a capsule while 10- to 20-keV electrons would not penetrate the capsule ablator.

Figure 14(c) shows x-ray filter–fluorescer (FFLEX) data from a gasbag shot fired with 10 heater beams (i.e., Beam 7 was also configured as a heater beam, with no RPP or bandwidth and with the same $f/4.3$ focus as the other heater beams) with a total energy of 25 kJ. This setup allowed us to measure the optically scattered SRS on Beam 7 (150 J, 6%) and then (by assuming that all beams were the same) to estimate a total scattered SRS level of 1500 J for the target. The FFLEX data in Fig. 14(c) were fitted to a suprathermal-electron temperature of 17 keV, which is consistent with electrons accelerated by damping of electron plasma waves due to SRS at $0.1n_c$, which is the plasma density expected. The SRS optical spectrum (not shown) peaked at 560 nm, also consistent with $0.1n_c$.

The amount of fast electrons inferred from the spectrum, in Fig. 14(c), is 680 J assuming that the x rays are produced by electrons colliding with the C and H in the C_5H_{12}. Hence the ratio of electron energy to SRS optical light is 1:2.2. The expected division of energy between the electron plasma wave and the scattered light wave at $0.1n_c$ is 1:1.7, implying that there should be 880 J of fast electrons. Although we detected 680 J, our estimate of the energy transferred to the electrons does not take into account ways, other than electron Landau damping, by which energy can be removed from the electron plasma waves. We conclude that the FFLEX provides a useful time-integrated diagnostic of SRS losses if the converting material is known and the target is optically thin to the radiation produced by the electrons. Even in hohlraums, however, the FFLEX is a useful monitor of the electrons (50 to 100 keV) that are capable of preheating the capsule.

As mentioned above, the final test for beam propagation through a NIF plasma is to show that there are no adverse effects to the light that has propagated through such a plasma. Figure 15 shows a summary of the transmitted light from the $f/8$ experiments with gasbag plasmas. The quantity plotted is the time-integrated transmission of the interaction beam through the gasbag. Since the laser light is being absorbed by inverse bremsstrahlung, the transmission at any instant is a function of the temperature and density of the plasma. Using LASNEX-generated density profiles, the expected transmission of the gasbag is 41% for a peak temperature of T_e =3.2 keV and 37% for T_e = 2.8 keV. The transmission values in Fig. 15 are consistent with these numbers for NIF-relevant intensities (up to 2×10^{15} W cm^{-2}) but drop below this value as the intensity is increased above 2×10^{15} W cm^{-2}. Possible explanations for the decrease in transmission at higher intensity are increased losses due to SRS backscattering and spreading of the transmitted beam outside the detector solid angle. The time-integrated SRS for many of the shots above 4×10^{15} W cm^{-2} approached 15%. Adding in losses due to fast electron generation (1/1.7 times the scattered optical energy) results in a total time-integrated "loss" to SRS of order 25% for the higher-intensity shots. This 25% "loss" will reduce the expected transmission to 31% and 28% for peak temperatures of 3.2 and 2.8 keV.

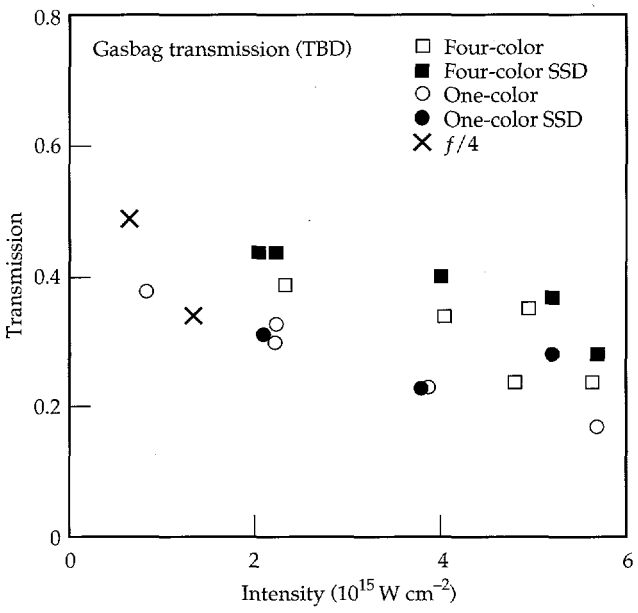

FIGURE 15. Time-integrated transmission of gasbag targets from TBD diagnostic for various kinds of beam smoothing. Expected gasbag transmission is 41% for T_e =3.2 keV and 37% for T_e = 2.8 keV.
(20-07-1095-2448pb01)

(The energy put into fast electrons is not really a loss, because the energy will stay in the plasma as the electrons are rapidly thermalized). The time-resolved aspects of these data are still being studied to correlate the SRS and transmitted beam as a function of time.

One interesting aspect of the data shown in Fig. 15 is that the highest transmission is seen in experiments with four-color beam smoothing. This is consistent with four-color smoothing providing better suppression of filamentation and therefore less losses due to parametric processes or beam breakup due to filamentation. However, none of the backscattering data shows any reduction in reflectivity with four-color smoothing. This inconsistency is under study.

A secondary goal of the TBD was to quantify forward Raman scattering. Spectral measurements of forward SRS (400 nm < λ < 900 nm) within 0.2 sr of the probe beam center show spectra that do not appear to depend on the presence of the probe beam. We observe no detectable change in the spectra for similar experiments with the probe beam on or off. The measured spectrum appears to come almost entirely from the sidescattered SRS produced by the heater beams. The level of this sidescattering is about 10 J/sr (wavelength-integrated). We estimate an upper bound on the forward SRS level only from the probe beam to be less than about 5% of the heater beam sidescattering, or about <0.5 J/sr (wavelength-integrated).

Figure 16(a) shows time-integrated backscattered SRS spectra from targets shot with different intensity or beam smoothing. The short-wavelength SRS appears and disappears with changes in the beam smoothing and laser intensity. The lowest intensity case shows very little short-wavelength SRS, while the case with four-color smoothing and 2×10^{15} W cm^{-2} shows significant reflected light at short wavelength. The addition of 1.6 Å of bandwidth reduces the peak reflectivity but also greatly reduces the short-wavelength SRS. Since the short-wavelength SRS is probably associated with low densities in filaments, the above observations are consistent with suppression of filamentation in the lower two curves by low intensity or by SSD. Figure 16(b) shows the results of an F3D calculation of the filamentation of an $f/8$ beam in a $0.1n_c$ plasma at 3 keV. The plot shows the lowest density present within filaments as a function of average laser intensity for four-color smoothing and four-color with additional SSD smoothing. On the axis at right the density is converted to an SRS wavelength assuming 3 keV. The onset of filamentation in F3D occurs at 2×10^{15} W cm^{-2} and correlates with the appearance of the short-wavelength SRS in the data. Hence we may be able to use the short-wavelength SRS as a measure of beam filamentation.

A similar effect is seen in the late-time behavior of the SRS spectra, where the short-wavelength SRS appears as the plasma cools and filamentation thresholds go down. This increase in filamentation sometimes coincides with an increase in the SRS reflectivity, because intensities are higher in filaments, but also the damping of SRS by electron Landau damping is a strong function of temperature near 3 keV (where $k\lambda_D \approx 0.3$). Hence the higher intensities from increased filamentation can conspire with the reduced damping to increase SRS reflectivity as the plasma cools, making time resolved data analysis important.

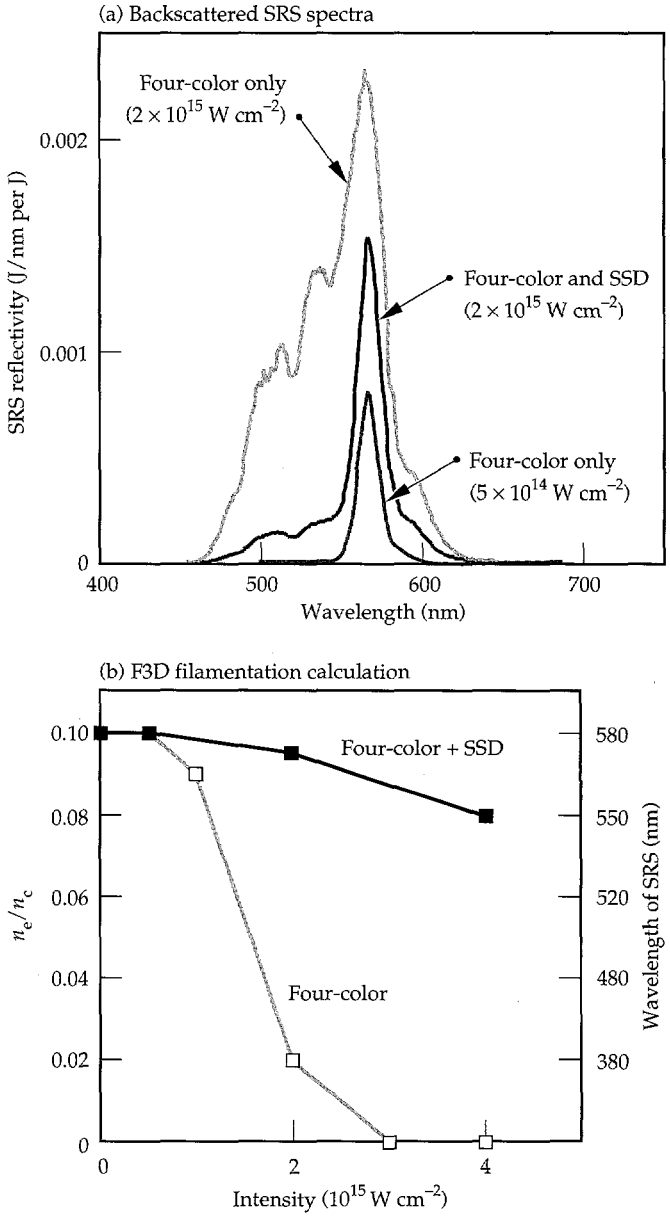

FIGURE 16. (a) Time-integrated backscattered SRS from targets with various intensity or beam smoothing. (b) F3D calculation of filamentation of an $f/8$ beam in a $0.1n_c$ plasma at 3 keV. Plot shows lowest density present within filaments vs average laser intensity for four-color smoothing with and without additional SSD smoothing. (20-07-1095-2449pb01)

Crossed-Beam Experiments

The presence of multiple laser beams with substantial bandwidth in the next generation of ICF experiments will allow a new class of laser–plasma instabilities to take place in which energy from a high-frequency beam is scattered into a low-frequency beam. The mechanisms for these interactions are the same as for the stimulated backscattering instabilities that have been studied for many years in single-color, single-beam experiments. These instabilities grow from plasma wave noise that scatters the incident beam. The interference of the incident and scattered light creates a ponderomotive force on the plasma that reinforces the amplitude of the scattering plasma waves and causes both scattered and plasma waves to grow. The new instability arises when two laser beams cross with different frequency spectra. When the frequencies and crossing angles match, the lower-frequency beam can act as a seed for the sidescattering from the higher-frequency beam. The lower-frequency beam is then amplified by the transfer of energy from the higher-frequency beam. This type of interaction is important both because it can potentially occur near the laser entrance hole of an indirect-drive target and affect the drive symmetry and because it provides an opportunity to study fundamental backscattering processes in experiments in which both the incident and scattered frequencies can be controlled.

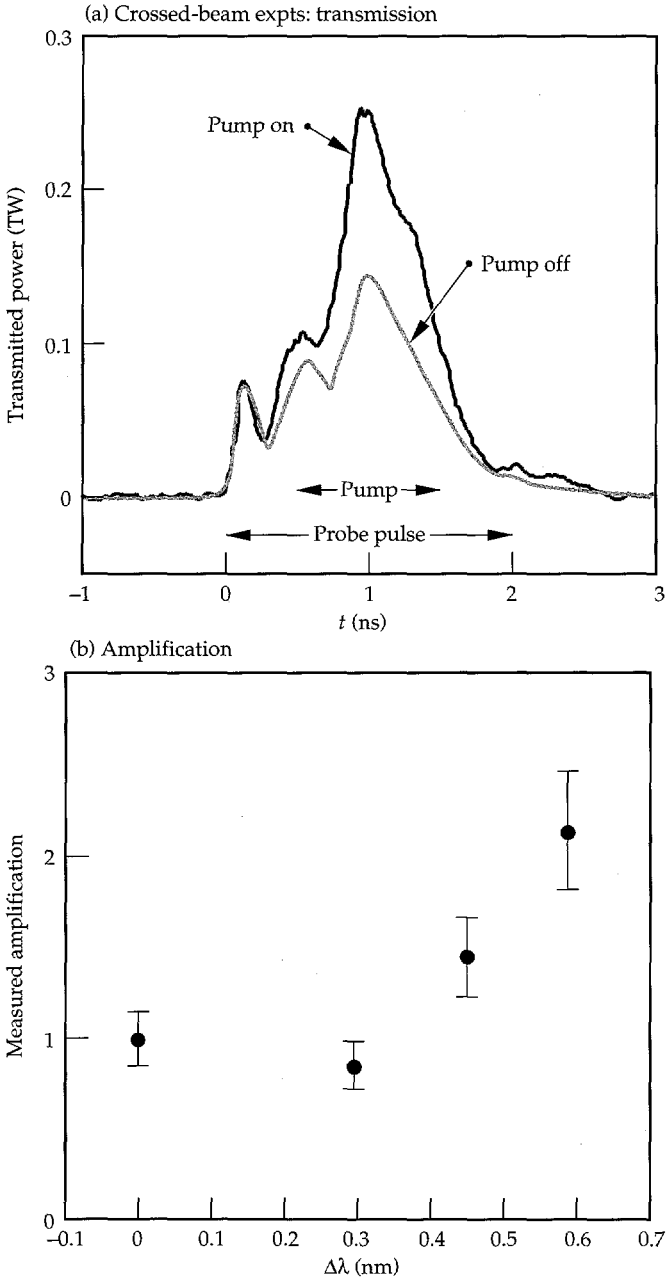

FIGURE 17. Crossed-beam experiments. (a) Typical transmitted light signal; (b) amplification vs tuning of pump with respect to probe beam. (20-07-1095-2450pb01)

Experiments have been carried out at Nova in the past year to study the energy of two beams crossing in a plasma with parameters similar to those expected in NIF hohlraums. The beams cross at a 53° angle and have slightly mismatched frequencies, so that the frequency difference is close to the frequency of the resonant ion-acoustic wave, and Brillouin sidescattering is seeded. The power transmitted through the plasma by the low-frequency probe beam is measured as a function of time by the TBD. The amplification is determined by comparing an experiment in which the high-frequency pump beam is present with one in which it is absent. As shown in Fig. 17(a), the transmitted power rises rapidly after the pump beam is turned on to a value well above what is measured when the pump is off. It has been demonstrated that as much as several hundred joules of energy can be transferred during a 1-ns interaction time, resulting in an amplification of the probe beam by a factor of as much as 2.5. Further, it has been shown that energy transfer occurs only when the difference in the beam frequencies is as large as the frequency of the resonant ion wave, corresponding to $\Delta\lambda = 0.5$ nm in Fig. 17(b). Further experiments are planned to measure the gain vs frequency curve and to directly study the spatial gain rate of Brillouin scattering in laser plasmas for the first time.[30]

Nova Scale-1 Hohlraum Experiments

Most of the diagnostics described above were specifically developed for the long-scalelength plasma experiments, but their larger field of detection made them very useful in other experiments. There is a significant, ongoing effort to understand radiation conversion in gas-filled hohlraums. These experiments use standard "scale-1" Nova hohlraums and a shaped drive pulse that has rapid rise to a "foot" power of ~1 TW/beam, followed by a gradual ramp up to a peak of

about 2 TW/beam at ~1.5 ns. This is the standard PS22 pulse used in the symmetry experiments described in the article "Nova Symmetry: Experiments, Modeling, and Interpretation (HLP3 and HLP4)" on p. 293 of this *Quarterly*. The total pulse duration is ~ 2.2 ns; Fig. 20 shows examples. Measurement of the backscattering from such hohlraums showed that energy loss due to reflection by SBS and SRS played a significant role in determining the hohlraum energetics.

Table 1 summarizes the (time-integrated) backscattering levels observed from the gas-filled hohlraums for various gases and the standard, empty Nova hohlraum. The scale-1 results are all for unsmoothed Nova beams. The quoted reflectivities include contributions from the NBI. For the scale-1 gas-filled hohlraums, the NBI detects a large fraction of the SBS, which appears in a blob similar to that seen with the GASBIG hohlraums [Fig. 12(c)]. The total backscattering losses for gas-filled hohlraums often exceed 15%. Time-resolved measurements show that the peak loss to SBS and SRS combined can be as high as 40% in some targets. LIP calculations of the expected SBS and SRS gain, using plasma conditions from 2-D LASNEX hydrodynamic calculations and average beam intensities, show that although peak gains for SBS are quite high (~30 for both propane- and methane-filled hohlraums), the SRS gain exponents are lower (~20).

TABLE 1. Summary of scattered light levels from NIF-scale and Nova scale-1 hohlraums.

	NIF scale[a]				Nova scale[b]			
	Gasbag		Large hohlraum		Scale-1 hohlraum			
	$0.5–1.0\times10^{15}$	2×10^{15}	1×10^{15}	2×10^{15}	Au	CH_4	C_3H_8	C_5H_{12}
SBS	<1%	<1%	~0.1%	1.3%	6.5%	9%	11%	4%
SRS	1–2%	4–8%	1.5%	5%	2.5%	5%	12%	14%

[a]All with smoothed "NIF" beam.
[b]All with unsmoothed beams.

The SBS gain exponents calculated for the scale-1 gas-filled hohlraums are similar to or higher than that calculated for the NIF outer beams [Fig. 2(c)] within the Au part of the plasma. Hence in some ways the scale-1 hohlraums let us study that particular problem. The gasbag plasmas mimic the low-Z part of the NIF SBS problem, but of course have no plateau of Au to grow SBS at shorter wavelength. The LIP calculations of the SBS gain exponent are shown in Figs. 18(a) and (b) for methane and propane, respectively; both show a peak gain late in time that is red-shifted by 2 to 3 Å from 3ω and corresponds to SBS occurring in the Au shelf that has been ablated from the Au wall by radiative and laser ablation. A time-resolved SBS spectrum from each hohlraum is shown in Figs. 19(a) and (b). The data do not bear much resemblance to the spectral features of the LIP calculations. In particular, the SBS peak sweeps across the spectrum from 8 Å red shifted to 3 Å blue shifted. This feature could be due to SBS growing in the slow-moving Au near the wall at early time. As the pulse intensity ramps up, the point at which SBS grows moves out towards the laser entrance hole, where the faster-moving plasma imposes a blue shift on the scattered light. Such a motion would be consistent with the beam filamenting further out (at lower density) as the intensity ramps up.

The LIP calculations assume a beam intensity spatially averaged in the transverse direction, while the

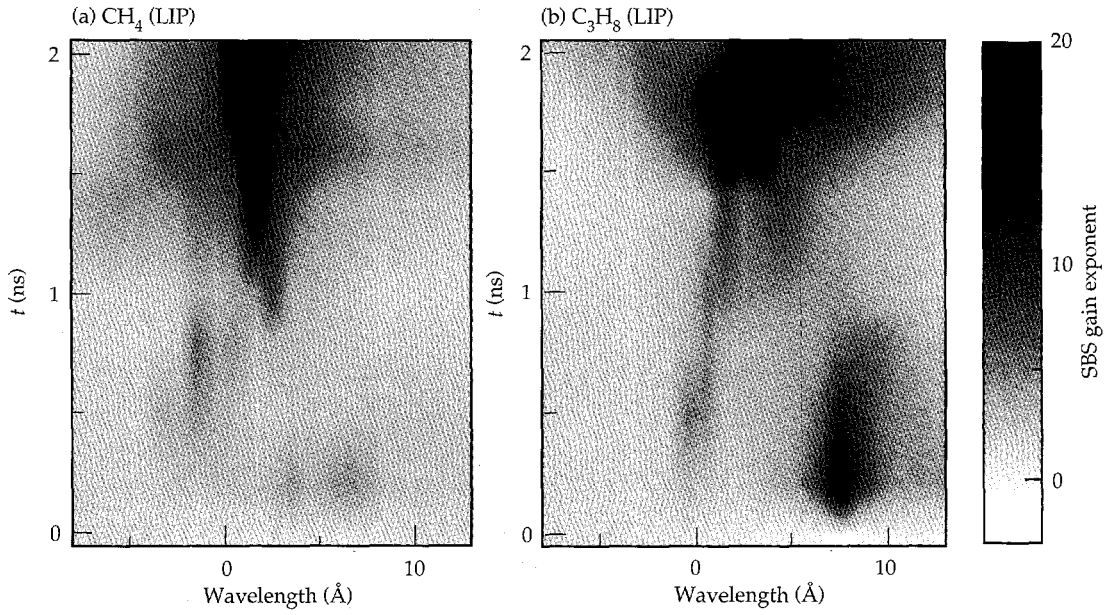

FIGURE 18. Scale-1 hohlraum experiments. (a) LIP gain calculation for a methane-filled scale-1 hohlraum; peak gain exponent is ~30 late in the pulse; (b) LIP calculation for propane; peak gain exponent is ~20 late in the pulse. (20-07-1095-2451pb01)

experiments not only have the short-wavelength speckle structure described earlier but also have longer-wavelength intensity modulations due to the aberration of the Nova beam when it is used without a random phase plate. If we clean up the Nova beam to make it look more like the LIP assumptions, i.e., put on a random phase plate to get rid of the long-wavelength structure and use SSD beam smoothing to reduce the short-wavelength structure, we get the results shown in Figs. 19(c) and 19(d). These figures show the time-resolved SBS spectra from gas-filled hohlraums irradiated with such a smoothed beam. As can be seen by comparing Figs. 18 and 19 for methane and propane, the smoothed-beam data approaches the LIP calculation both in terms of time history and spectral location. The unsmoothed data showed reflected SBS that swept from red shifted to blue shifted as a function of time. The SRS data from these shots (not shown) also showed a significant amount of the SRS coming from low density (~$0.02n_c$), where the LIP calculations showed very low gain exponents. The application of beam smoothing moved the density at which SRS peaked closer to $0.1n_c$, more consistent with the LIP calculations.

The SBS and SRS reflectivity from the scale-1 hohlraums also dropped when beam smoothing was applied. Figure 20 summarizes the time history of the scattered light from the data shown in Fig. 19. For methane, with standard Nova beams [Fig. 20(a)], the SRS and SBS are 6% and 11% respectively; with beam smoothing [Fig. 20(c)], the time-integrated SRS and SBS

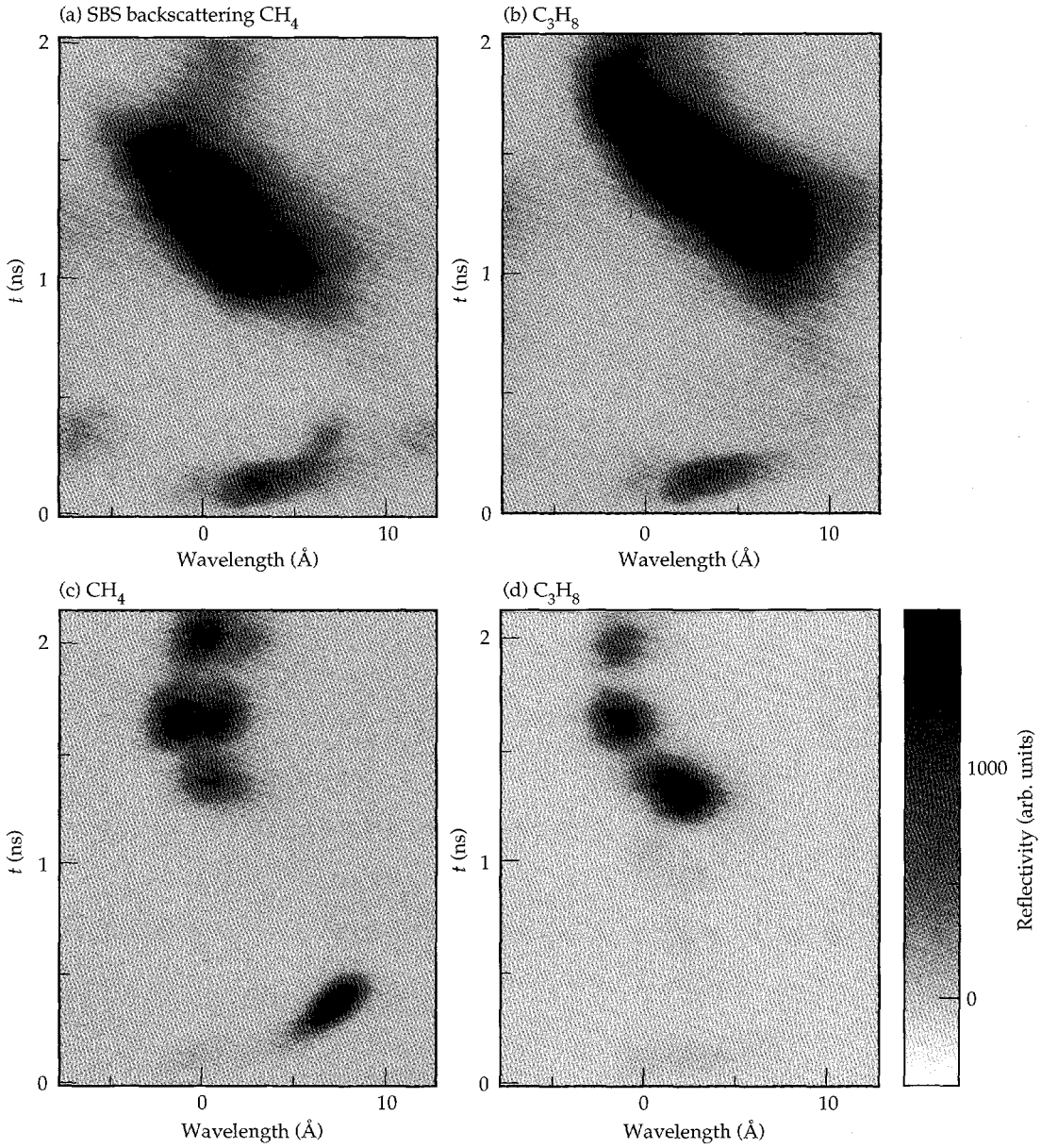

FIGURE 19. Observed SBS backscattering from scale-1 hohlraums. (a) methane-filled; (b) propane-filled; (c) methane-filled, with SSD beam smoothing; (d) propane-filled, with SSD beam smoothing. (20-07-1095-2452pb01)

are 0.1% and 1.4%. For propane the numbers are 11% and 13% before smoothing [Fig. 20(b)] and 1.7% and 1.5% after smoothing Fig. 20(d)] for SRS and SBS, respectively.

These results are encouraging for two reasons:

1. They indicate that if beam smoothing were applied to all ten arms of Nova, we would be able to couple significantly more energy into the gas-filled hohlraums. The implication (which we will explore in future experiments) is that backscattering losses from higher-temperature hohlraums that have higher densities and higher laser intensities may be reduced by smoothing.
2. The fact that the gain in the Au plasma predicted by LIP calculations for scale-1 hohlraums is comparable with that for the NIF outer-beam SBS implies that the smoothed-beam results also apply to the NIF SBS. Note that on the NIF, the beam intensity at the Au wall will be 10^{15} W cm^{-2} [Fig. 1(c)], while in our smoothed-beam hohlraum experiments we have an intensity of 2.5×10^{15} W cm^{-2}. Hence with a smaller target we are mimicking the expected gain exponent on the NIF outer beam in the Au and find that with beam smoothing we can produce low SBS reflectivity.

Conclusion

We have demonstrated that, with appropriate plasma composition and levels of beam smoothing, stimulated scattering in NIF-scale hohlraums can be limited to a few percent for the NIF range of intensities, $I \approx 5 \times 10^{14}$ to 2×10^{15} W cm^{-2}. At this level, stimulated scattering is not expected to have a significant effect on either the energetics or the symmetry of NIF hohlraums. Also, in the NIF intensity range, the light transmitted through the NIF-scale plasmas is consistent with calculations.

Using specially constructed gas-filled plastic balloons and large-scale hohlraums, we have been able to produce plasmas, using 8-9 of Nova's beams, whose density, electron temperature, velocity gradient, and integral interaction path length reproduce the conditions in the low-Z interior of NIF hohlraums. A single Nova beamline was modified to simulate an $f/8$ cluster of four NIF beams in which the wavelength of each beam could differ from that of the others by a few angstroms. Diagnostics were implemented to measure the transmitted laser light and light scattered by SBS and SRS. We measured scattering levels for a variety of smoothing techniques that could be implemented on

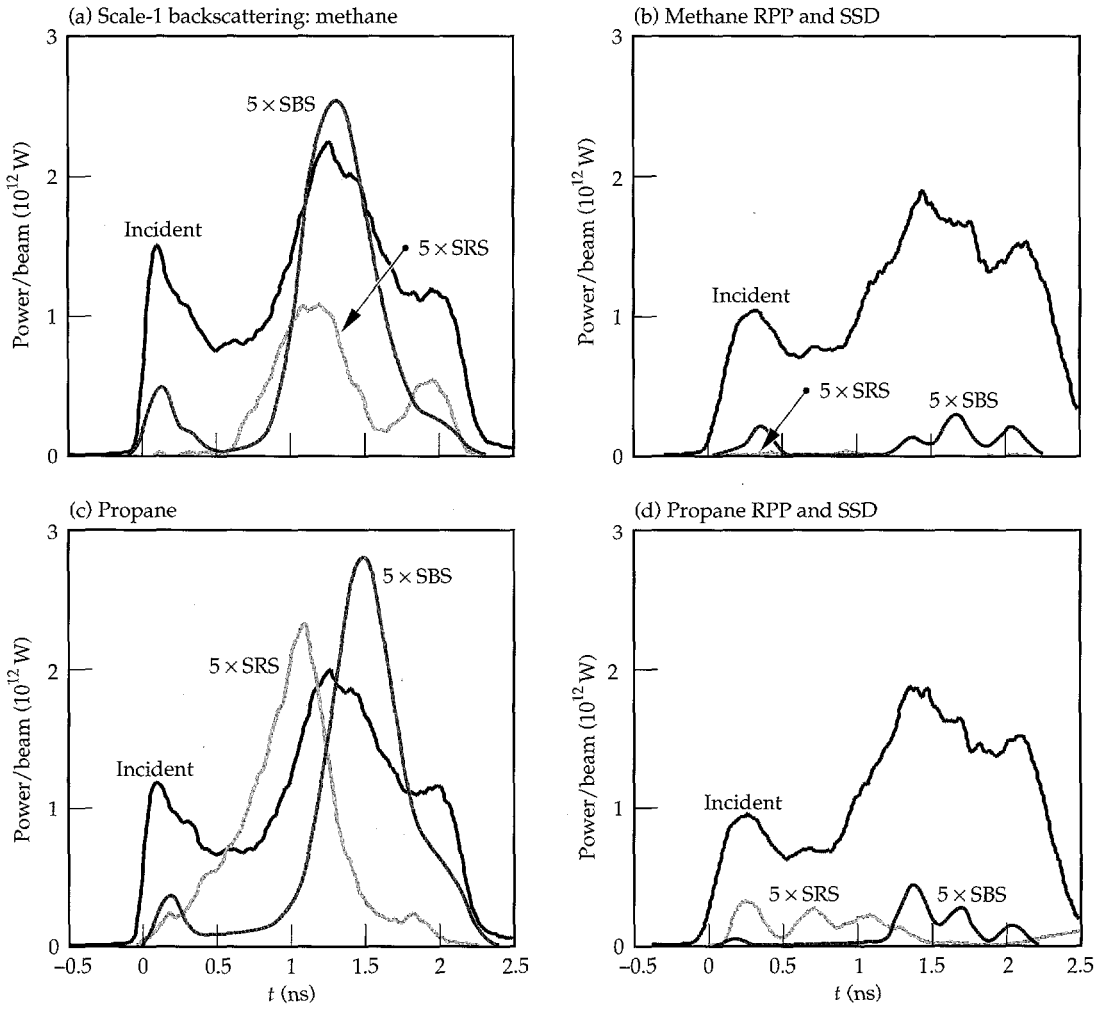

FIGURE 20. Scale-1 hohlraum backscattering pulse shapes. (a) Standard beam conditioning, methane-filled; (b) standard conditioning, propane-filled; (c) SSD, methane-filled; (d) SSD, propane-filled. (20-07-1095-2453pb01)

the NIF, including one- and four-color beams with RPPs only or with 1.6 Å of SSD for temporal smoothing.

For all beam-smoothing schemes and for all intensities of interest to NIF, we find that SBS levels can be limited to ~1% if the ion-acoustic wave is sufficiently damped. This can be achieved by adding hydrogen as a minority species in the low-Z gas fill.

At an intensity of 5×10^{14} W cm^{-2} (the low end of the NIF range), SRS is also limited to a few percent for all smoothing schemes. However, at an intensity of 2×10^{15} W cm^{-2}, near the upper end of the NIF range, SRS is about 10% with RPPs only. With 1.6 Å of SSD, the SRS is limited to about 4 to 5%. With SSD, the frequency spread of SRS is reduced, consistent with theoretical expectations of reduced plasma filamentation with SSD. There appears to be no benefit to having separate frequencies for each of the four beams, with or without SSD. In fact, experiments to explore coupling between beams crossing in the laser entrance hole show that it is possible to transfer energy from one beam to another, potentially affecting hohlraum symmetry, when the frequency difference between beams matches the ion-acoustic frequency.

Although the gasbags and large hohlraums provide a plasma that is a good match to the low-Z interior of a NIF hohlraum, neither reproduces the conditions of a NIF hohlraum near the high-Z wall. The gas balloon has no high-Z wall, and (because of their size) little laser energy reaches the wall in the large hohlraums. However, we find that standard Nova scale-1 hohlraums have conditions in the high-Z wall that are very similar to those of NIF hohlraums. This is because the high-Z conditions are set by inverse bremsstrahlung and x-ray emission and not by the hohlraum scale. Since standard Nova gas-filled hohlraums have a laser intensity comparable to that of the NIF, the inverse bremsstrahlung absorption lengths (of a few hundred micrometers) are also comparable. Although the high-Z shelf is short, it is relatively high density (~$0.2n_c$), has only weak velocity gradients, and has weak Landau damping, so that the gain for SBS can be quite high. Without smoothed beams, SBS levels in Nova gas-filled hohlraums are about 10%, mostly from the Au shelf. As in the case of the low-Z interior, a low-mass minority plasma can provide increased Landau damping to suppress SBS in the high-Z plasma near the wall. We are presently studying this idea, which has application to the NIF. We also find that SBS in the scale-1 hohlraums can be suppressed with sufficient beam smoothing, even without adding a low-Z minority species.

More work remains to be done to fully characterize the range of operating conditions for NIF ignition hohlraums. There would be a substantial benefit if we could extend the range of hohlraum temperatures above that specified for the nominal ignition targets. This would require that hohlraums be operated above the nominal intensity and plasma density range. We have not yet determined the optimum combination of beam smoothing and plasma composition for controlling stimulated scattering, but the techniques examined so far result in low levels of stimulated scattering, and can all be implemented on the NIF.

Notes and References

1. L. J. Suter, A. A. Hauer, L. V. Powers, D. B. Ress, et al., *Phys. Rev. Lett.* **73** (17), 2328–2331; A. Hauer, L. Suter, N. Delameter, D. Ress, et al., *Phys. Plasmas* **2** (6), 2488–2494 (1995).
2. W. L. Kruer, *Phys. Fluids B* **3**, 2356 (1991); also "Interaction Physics for Megajoule Laser Targets," in *Laser Interaction and Related Plasma Phenomena*, Vol. 10 (Plenum, New York, 1993), p. 503.
3. See, e.g., M. N. Rosenbluth and R. Z. Sagdeev. *Handbook of Plasma Physics, Volume 3: Physics of Laser Plasma*. A. M. Rubenchik and S. Witkowski, Eds. (Elsevier, Amsterdam, 1991), ch. 9, and references therein.
4. R. L. Berger, B. F. Lasinski, T. B. Kaiser, E. A. Williams, A. B. Langdon, and B. I. Cohen, *Phys. Fluids B* **5**, 2243 (1993); R. L. Berger, T. B. Kaiser, B. F. Lasinski, C. W. Still, et al., "Modeling the Effects of Laser-Beam Smoothing on Filamentation and Stimulated Brillouin Scattering," *ICF Quarterly Report* **5** (3), 130, Lawrence Livermore National Laboratory, Livermore, CA, UCRL-LR-105821-95-3 (1995).
5. J. D. Lindl, *Phys. Plasmas* **2** (11), 3933–4024 (Nov. 1995); S. W. Haan, S. M. Pollaine, J. D. Lindl, L. J. Suter, et al., *Phys. Plasmas* **2** (6), 2480–2487 (June 1995).
6. R. L. Berger et al., *Phys. Fluids* **1**, 414 (1989).
7. L. V. Powers, R. L. Berger, R. L. Kauffman, B. J. MacGowan, et al., *Phys. Plasmas* **2** (6), 2473 (1985); L. V. Powers, R. L. Berger, D. H. Munro, B. F. Lasinski, et al., *Phys. Rev. Lett.* **74**, 2957 (1995).
8. J. Denavit and D. W. Phillion, *Phys. Plasmas* **1**, 1971 (1994).
9. M. D. Rosen and J. H. Nuckolls, *Phys. Fluids* **22**, 1393 (1979).
10. D. H. Kalantar, B. J. MacGowan, T. P. Bernat, D. E. Klem, et al., *Rev. Sci. Instrum.* **66**, 782 (1995); D. H. Kalantar et al., *Phys. Plasmas* **2**, 1361 (1995).
11. D. E. Klem, Lawrence Livermore National Laboratory, Livermore, CA, personal communication (1995).
12. R. W. Lee, B. L. Whitten, and R. E. Strout, II, *J. Quant. Spectros. Radiat. Transfer* **32**, 91 (1984).
13. J. D. Lindl, "Cairn Hohlraum Scaling Study," in *Laser Program Annual Report—1979*, Lawrence Livermore National Laboratory, Livermore, CA, UCRL-50055-79 (1979), p. 5-80.
14. J. M. Auerbach, K. R. Manes, and D. W. Phillion, "Cairn Scaling Study—The Experiments," in *Laser Program Annual Report—1979*, Lawrence Livermore National Laboratory, Livermore, CA, UCRL-50055-79 (1979), p. 5-62.
15. B. H. Wilde, J. C. Fernandez, W. W. Hsing, J. A. Cobble, et al., "The Design and Characterization of Toroidal-Shaped Nova Hohlraums that Simulate National Ignition Facility Plasma Conditions for Plasma Instability Experiments," presented at the *12th International Conference on Laser Interaction and Related Plasma Phenomena*, Los Alamos National Laboratory, Los Alamos, NM, LA-UR-95-1439 (April 1995), to be published.
16. J. C. Fernandez et al., *Rev. Sci. Instrum.* **66**, 626 (1995).
17. R. Kirkwood, J. Moody, and B. MacGowan, "Analysis of Schottky Barrier Diodes for Detection of Pulsed UV Light," Lawrence Livermore National Laboratory, Livermore, CA, internal memorandum (June 1994).

18. Y. Kato, K. Mima, N. Miyanaga, S. Aringa, et al., *Phys. Rev. Lett.* **53**, 1057 (1984); H. T. Powell, S. N. Dixit, and M. A. Henesian, *Laser Program Annual Report—1991*, Lawrence Livermore National Laboratory, Livermore, CA, UCRL-LR-105820-91 (1991), pp. 28–38.
19. See National Technical Information Service Document Nos. DE95017671 through DE95017673 and DE95017676 through DE95017700 (J. A. Paisner, E. M. Campbell, and W. J. Hogan, The National Ignition Facility Project, UCRL-JC-117397 and UCRL-PROP-117093, May 1994). Copies may be obtained from the National Technical Information Service, Springfield, VA 22161; D. M. Pennington, *ICF Quarterly Report* **5** (2), 130, Lawrence Livermore National Laboratory, Livermore, CA, UCRL-LR-105821-95-2 (1995).
20. S. Skupsky, R. W. Short, T. Kessler, R. S. Craxton, et al., *J. Appl. Phys.* **66**, 3456 (1989).
21. K. Marsh, C. Joshi, and C. McKinstrie, *Bull. Am. Phys. Soc.* **39** (1994).
22. E. A. Williams et al., *Physics of Plasmas*. 2, **1** (1995); H. X. Vu, J. M. Wallace, and B. Bezzerides, *Phys. Plasmas* **1** (11), 3542–3556 (1994).
23. C. E. Clayton, C. Joshi, A. Yasuda, and F. F. Chen, *Phys. Fluids* **24**, 2312 (1981).
24. S. C. Wilks, W. L. Kruer, J. Denavit, K. Estabrook, et al., *Phys. Rev. Lett.* **74**, 5048 (1995).
25. J. D. Moody, H. A. Baldis, D. S. Montgomery, R. L. Berger, et al., *Phys. Plasmas* **2**, 4285 (1995).
26. D. S. Montgomery, J. D. Moody, H. A. Baldis, B. B. Afeyan, et al., "Effects of Laser Beam Smoothing on Stimulated Raman Scattering in Exploding Foil Plasmas," Lawrence Livermore National Laboratory, Livermore, CA, UCRL-JC-123014; submitted to *Phys. Plasmas* (1995).
27. R. W. Short, R. Bingham, and E. A. Williams, *Phys. Fluids* **25** (12), 2302–2303 (1982); D. E. Hinkel, E. A. Williams, R. L. Berger, and L. V. Powers, *Bull. Am. Phys. Soc.* **40** (11) (Oct. 1995), p. 1778 (Annual Meeting of the Division of Plasma Physics).
28. D. F. Dubois and H. A. Rose, *Bull. Am. Phys. Soc.* **40** (11), 1824 (1995); H. A. Rose, *Bull. Am. Phys. Soc.* **40** (11), 1778 (1995).
29. S. G. Glendinning, L. V. Powers, R. L. Kauffman, O. L. Landen, et al., "Measurements of Wall X-Ray Emission Patterns in Gas-Filled Hohlraums," Lawrence Livermore National Laboratory, Livermore, CA, UCRL-JC-123021; to be submitted to *Phys. Rev. Lett.* (1996).
30. R. K. Kirkwood, B. B. Afeyan, W. L. Kruer, B. J. MacGowan, et al., "Observation of Energy Transfer Between Frequency Mismatched Laser Beams in a Large-Scale Plasma," Lawrence Livermore National Laboratory, Livermore, CA, UCRL-JC-122102; submitted to *Phys. Rev. Lett.* (1995).

Appendix: Nova Technical Contract as presented to the 1990 NAS Review of ICF

Physics Program

The primary focus of the Lawrence Livermore National Laboratory (LLNL) Program has been, and will continue to be, x-ray driven "indirect-drive" inertial confinement fusion (ICF). The physics of this approach is naturally divided into capsule physics and driver/hohlraum development. As a result, the LLNL target physics program has two principal elements:

1. The Hydrodynamically Equivalent Physics (HEP) program to address the capsule physics associated with ignition and gain. Elements of this program include:
   - hydrodynamic stability,
   - the effects of drive nonuniformity on capsule performance, and
   - the physics associated with ignition (energy gain/loss to the fuel) in the absence of alpha deposition.
2. Hohlraum Laser–Plasma Physics (HLP) to address driver–plasma coupling, generation and transport of x-rays, and the development of energy-efficient (i.e., coupling of the driver energy to the capsule) hohlraums that provide the appropriate x-ray drive (spectral, temporal, and spatial) to a high-performance capsule.

While meeting specific milestones is important, the emphasis of the target physics program is to demonstrate and refine our ability to model/predict target performance, particularly those aspects that scale to, and influence, ignition and gain. The LLNL Program is thus directed toward instilling confidence in the successful outcome of ICF and of specifying the performance and characteristics of both the driver and target required to achieve these objectives.

We expect to undertake and complete the HEP and HLP elements described here in 2 to 3 years, depending upon the funding level available.

Capsule Physics (HEP)

An extensive program addressing the implosion physics of ignition and gain is presently underway on Nova. The goal of this effort is to further develop and demonstrate a quantitative and predictive understanding of the performance of capsules (properly scaled from ignition/gain designs) including the effects of hydrodynamic instability and x-ray drive nonuniformities (with known initial fabrication tolerances of the target and a detailed knowledge of the hohlraum environment). The extensive diagnostics used in the HEP program also allows confirmation of our ability to model ignition physics in imploding capsules, i.e., the balance between PdV work and electron conduction and radiative losses in the fuel in the absence of alpha heating.

The HEP experiments use both planar targets and capsules with/without prescribed perturbations (in capsule fabrication or x-ray flux uniformity). The targets do not include cryogenic fuel configurations. The experiments are extensively diagnosed with x-ray and neutron diagnostics including x-ray backlighting. The experiments also emphasize pulse-shaped drive to enable minimum entropy implosion trajectories to be examined. The pulse shapes are properly scaled from ignition/gain target requirements.

Although not principal objectives of the HEP program, the pulse shaping and the reduced levels of preheat from high-energy photons and superthermal electrons lead to noncryogenic implosions with final fuel and pusher (CH_2 or S_iO_2) densities in the range of 40 g/cm^3 and 100–200 g/cm^3, respectively.

The HEP program is divided into five specific goals (HEP1–HEP5) described below.

HEP1 Summary of Tasks

To demonstrate increased fuel/pusher compressions with high contrast pulse shaping using noncryogenic targets. These experiments have been successfully conducted, but due to the high compressions achieved, limited diagnostics were employed. For example, the pusher and fuel density increase were inferred from a measurement of the pusher areal density $\rho\Delta R$.

HEP1 Goals

To diagnose fuel densities in the range of 20–40 g/cm^3 inferred from measurements of fuel areal density ρR using advanced neutron-based diagnostics. This quantity and other features of target performance (neutron yield, ion temperature, fusion burnwidth) will be modeled considering both hydrodynamic stability and x-ray flux nonuniformities.

HEP2 Summary of Tasks

To measure reduced growth and early nonlinear behavior of the Rayleigh–Taylor (RT) instability at the ablation surface for x-ray driven targets. The goals of HEP2 are to experimentally demonstrate and model reductions in the growth rate of the RT instability due to finite density gradients and mass advection at the ablation surface. Planar targets with single fourier component areal density variations will be examined over a range of peak T_R and with pulse shaping. Initial perturbations will be small and the acceleration history designed so that linear analysis is ($ka_0 << 1$) valid for large growth factors (3 to 5 *e*-folds). Successful experiments to date, on which the HEP2 project is based, have observed ~1 *e*-fold of growth rather than the 2 to 3 *e*-folds predicted if finite density gradients and mass advection are not included. Perturbation wavelength and material opacity will be varied to establish an extensive database for comparison with detailed numerical simulation. The tasks in HEP2 will also include planar targets to simulate the ablation physics of HEP4 and HEP5 capsules. These targets use CH ablators doped with intermediate atomic number elements to control hydrodynamic stability. Experiments will include shock wave propagation and other appropriate measurements to confirm our overall understanding of the hydrodynamic behavior of such targets.

The experiments will also address early nonlinear behavior such as harmonics (due to bubble and spike growth) and examine mode coupling. In these latter experiments, the foils will nominally have two initial perturbation wavelengths.

HEP2 Goals

To observe single-mode growth factors at the ablation surface >30 from which reductions in the classical RT growth rate of 2 to 3 are inferred. The experiments will use planar targets driven by x-ray ablation at several peak T_R ranging from 150 eV < T_R < 220 eV. Experiments will be compared with detailed simulations to confirm our ability to model RT growth at the ablation surface. Targets of various composition (including doped CH ablators) will be used to confirm our ability to properly account for plasma opacity in modeling the x-ray driven hydrodynamics.

To observe early nonlinear behavior (harmonics) and mode coupling. Planar targets with single or multiple fourier components will be used. Detailed comparison with numerical simulations to demonstrate our ability to model this nonlinear behavior will be made.

HEP3 Summary of Tasks

To analyze implosion experiments using capsules with deliberately perturbed surface finishes to validate mix models with a multimode initial noise spectrum. These "bumpy ball" experiments are designed to validate our multimode hydrodynamic mix models. Detailed time-resolved x-ray spectroscopy of dopant materials in both the fuel and pusher are used to infer mix and to compare with our modeling of both mix and its effect on the imploded state of the fuel. While the growth factors for these experiments are approximately 10 to 30 for $10 \lesssim l \lesssim 30$ (compared with growth factors of ~500 for ignition/gain targets), the initial surface perturbation amplitudes are sufficiently large ($0.1 < a_0 \lesssim 0.2$ μm for $10 \le l \le 30$) to result in diagnosable mixing between the pusher and fuel. The target convergence is limited to $\lesssim 10$ so that the effects of drive asymmetry on target performance are limited. Targets with no deliberately fabricated surface perturbations are used for control and a well defined "null."

HEP3 Goals

To observe pusher/fuel mix that is dependent on initial target surface quality using x-ray spectroscopy. Targets use an initial multimode spectrum of surface perturbations. The implosion is designed for overall hydrodynamic mix growth factors of 10 to 30. Peak hohlraum temperatures of >200 eV will be used. Detailed comparison of experimental results with numerical simulations employing multimode mix modeling will be performed. Experiments will include targets with no deliberately perturbed surface finish as "null" comparisons.

In addition to the HEP1 through HEP3 objectives, to conduct a series of sophisticated experiments, which directly address the hydrodynamic stability of the Nova Upgrade ignition targets. For example, these experiments will diagnose the performance of capsules when the instability growth factors (including both linear and, where appropriate, nonlinear behavior) as a function of *l*-mode

number are similar to that of ignition gain target designs. Other features of the experiments, such as achievable implosion velocity and convergence, will be either limited or influenced by the existing capabilities of Nova. For example, the limited number of Nova beams (10) will limit the drive uniformity and thus capsule convergence before degradation from one-dimensional (1-D) performance will be expected. The Nova Upgrade addresses this limitation by the use of a large number ($N > 200$) of independent beamlets. Specific laser technology issues addressable on Nova that impact drive uniformity and that are required for the Nova Upgrade will be demonstrated as part of the Precision Nova program. Issues include beam-to-beam power balance and beam pointing.

These experiments, HLP4, and the associated modeling will specifically identify the performance and flexibility required of the Nova Upgrade and will further validate our predictive capability of capsule performance including both hydrodynamic stability and drive nonuniformity.

The HEP4 and HEP5 experimental programs address these issues. The two projects differ primarily in the associated capsule convergences, which impact the choice and applicability of the target diagnostics.

HEP4 Summary of Tasks

To analyze implosion experiments to convergences of ~10 with overall hydrodynamic mix growth factors of 100 to 500 for an l-mode spectrum similar to ignition target designs. These experiments, which will make use of techniques developed in HEP3, will use plastic D_2-filled capsules whose hydrodynamic stability (number of growth factors) is varied by target design and by selective doping of the ablator and/or fuel. The targets will use pulse-shaped drive with peak $T_R \lesssim 230$ eV. Capsule convergences will be limited to ~10 so that the effects of drive nonuniformity on capsule performance will be minimized. The growth factors will be systematically varied from ~10 to levels exceeding that of ignition targets (peak growth factor ~500). This systematic variation in hydrodynamic stability will also ensure that the effects of drive asymmetry are isolated.

HEP4 Goals

To compare detailed diagnosis and modeling of D_2-filled plastic capsules with doped ablators to control hydrodynamic stability. Diagnostics will be primarily (but not exclusively) x-ray based. Hydrodynamic instability growth factors will range from 10 to 500 in an *l*-mode spectrum, similar to ignition designs (i.e., maximum growth at $l \approx 30$).

Targets will be imploded with pulse-shaped drive at a peak $T_R < 230$–250 eV and will be limited to convergences of $\lesssim 10$ to minimize the effects of x-ray flux nonuniformity.

HEP5 Summary of Tasks

To analyze implosion experiments to convergences of ~20 to 40 with overall hydrodynamic mix growth factors of 100 to 500 for an l-mode spectrum similar to ignition target designs. These experiments, which will make use of techniques developed in HEP3 and HEP4, will use plastic D_2- and DT-filled capsules whose hydrodynamic stability (number of growth factors) is varied by target design and by selective doping of the ablator and fuel. The targets will use pulse-shaped drive with peak $T_R \lesssim 230$ eV.

HEP5 is similar to HEP4 with the exceptions of higher target convergence (20 to 40) and a reliance on both x-ray and advanced neutron-based diagnostics to measure imploded core conditions. As stated above, the convergence will be limited by Nova's finite number of beams and will be as large as possible commensurate with diagnosability (the majority of measurements will rely on target emission). Convergences in the range of 20 to 40 are expected. As in HEP4, the growth factors will be systematically varied from ~10 to levels exceeding that of ignition targets (peak growth factor ~500). This systematic variation in hydrodynamic stability will enable the effects of drive asymmetry to be isolated from that due to mix from higher *l*-mode target fabrication "noise" sources.

HEP5 Goals

To compare detailed diagnosis and modeling of D_2- and DT-filled plastic capsules with doped ablators to control hydrodynamic stability. Diagnostics will be neutron and x-ray based. Hydrodynamic instability growth factors will range from 10 to 500 in an *l*-mode spectrum, similar to ignition designs (i.e., maximum growth at $l \approx 30$).

Targets will be imploded with pulse-shaped drive at a peak $T_R < 230$–250 eV. Convergences will be in the range of 20 to 40, but at yields degraded from 1-D performance due to the uniformity limitations of Nova. The achievable convergence will be commensurate with experimental diagnosability.

Hohlraum Laser–Plasma (HLP) Physics

An extensive experimental and modeling hohlraum physics effort has been underway at LLNL for over a decade. In particular, substantial progress has been made on Nova. As a result, the Nova Upgrade hohlraums are in many aspects an extension of the ongoing experiments. For example, the ignition/moderate gain hohlraums are typically scale 2.9 to 4.5 that of the

nominal Nova targets. Nova scale 1 targets are right circular cylinders 1600 μm diam, 2550 μm long, with typical laser entrance holes (LEHs) 800 μm diam. The Nova Upgrade has LEHs 1.5–4 mm diam.

Present calculations give the following performance specifications for the Nova Upgrade hohlraums:

1. Peak $T_R \approx$ 300–350 eV in a picket fence pulse or continuous pulse of overall duration 10 to 20 ns.
2. Time average drive uniformity with P_2, P_4 components of <2% (peak to peak) with instantaneous values several times larger. While meeting this uniformity requirement, the hohlraum must deliver 8 to 15% of the laser energy to the capsule.
3. Hot electron energy fraction $f_{hot} \lesssim 5\%$ at a temperature $T_{hot} \gtrsim 50$ keV. The exact levels are dependent on capsule design details, the time and location of the hot electron generation, and their transport to the capsule.
4. Scattered light from stimulated Brillouin and Raman scattering <5–10%. The exact values depend primarily on the influence of this scattering on drive symmetry control. For symmetry/coupling efficiency, the hohlraums are lined with low to moderate Z ($Z \lesssim 28$) material.

The objectives of the Nova experiments are to experimentally demonstrate and predictively model hohlraum performance in properly scaled targets consistent with Nova's performance limitations and to further develop our understanding (experimental and theoretical) of laser–plasma interaction physics in the millimeter-size plasmas associated with ignition hohlraums. Where appropriate, the hohlraums will also contain capsules to better simulate the Nova Upgrade targets.

The hohlraum/plasma physics program will also continue to explore, within the limits of Nova, the limits of achievable peak T_R in laser-driven hohlraums. While specific objectives will not presently be assigned to this task, these experiments will help define the "operating experimental parameters" of the Nova Upgrade. The availability of peak T_R's > 300 to 350 eV is of general interest to the weapons community.

The HLP program is divided into seven specific goals (HLP1–HLP7) described below.

HLP1 Summary of Tasks

To demonstrate acceptable hohlraum–plasma coupling and gross hohlraum energetics with targets (properly scaled from Nova Upgrade designs) having temporally shaped pulses. Equivalent T_R during the pulse will range from ~100 to 210 eV and both continuous and picket fence pulses of overall duration $\lesssim 4$ ns will be used. The high-Z hohlraums will be lined with low-Z material, whose peak n_e within the hohlraum at the peak of the pulse is 0.03 to 0.25 n_c.

HLP1 Goals

To achieve acceptable hohlraum coupling for a pulse-shaped drive with an equivalent T_R ranging from ~100 to 210 eV, as follows:

- Absorption fraction $f_{abs} > 90\%$
- Stimulated Brillouin scattering fraction $f_{SBS} <$ 5–10%
- Hot electron fraction $f_{hot} < 5\%$ at $T_{hot} \gtrsim 50\%$ keV
- Stimulated Raman scattering fraction $f_{SRS} < 5\%$

HLP2 Summary of Tasks

To demonstrate acceptable hohlraum–plasma coupling with peak equivalent $T_R \gtrsim 270$ eV using lined hohlraums. It is important to experimentally demonstrate $T_R \approx 300$ eV to establish credibility for Nova Upgrade target designs. Nova's power capability of ~40 TW limits the target scale and pulse duration for these high temperatures. Laser pulse formats will be limited to square 1 ns and appropriately scaled pulses i.e., shorter overall pulses or more limited shaped pulses (both continuous and picket fence) compared with those used in HLP1. Experiments will include hohlraums with capsules. "First bounce" laser intensities will be equivalent to that planned for the Nova Upgrade ($1–3 \times 10^{15}$ W/cm^2).

HLP2 Goals

To achieve acceptable hohlraum–plasma coupling, the following values must be attained in hohlraums that have a peak $T_R > 270$ eV.

- $f_{abs} > 90\%$
- $f_{SBS} <$ 5–10%
- $f_{hot} < 5\%$ at $T_{hot} \gtrsim 50$ keV
- $f_{SRS} < 5\%$

HLP3 Summary of Tasks

To obtain hohlraum experiments with peak T_R ranging from 100 to $\lesssim 230$ eV with a variety of pulse formats and targets (lined and unlined hohlraums). Examine hohlraums up to ignition scale albeit at lower temperature and shorter pulse duration. When appropriate, capsules will be contained in the hohlraum. Measurements will focus on the x-ray environment (including photons with $h\upsilon > 2$ keV) within the hohlraum. The deliverable will be confirmation of our ability to calculate energy balance in a hohlraum with emphasis on wall loss/albedo and to diagnose and predict the position of the time-dependent laser produced x-ray source within the hohlraum. Both of these topics are important to understand drive symmetry in hohlraums. These experiments (and the tasks in HLP4) will demonstrate our knowledge of the hohlraum physics required to implement beam phasing on the Nova Upgrade to control time-dependent drive symmetry.

This task will also include characterization of x-ray and laser-driven ablation plasmas. The experiments will verify detailed models of plasma formation at the laser aperture, the tamping of the high-Z hohlraum plasma by the low to moderate Z liner plasma, and plasma stagnation within the hohlraum (including the effects of capsules). Measurements of $n_e(\bar{x},t)T_e(\bar{x},t)Z(\bar{x},t)$ will be included.

HLP3 Goals

To confirm our ability to calculate energy balance in a hohlraum (with emphasis on wall loss/albedo) and to model the details of the plasma and x-ray emission within the hohlraum.

HLP4 Summary of Tasks

To demonstrate symmetry control with low and intermediate Z-lined hohlraums. Experiments will use a variety of x-ray imaging techniques to measure time-integrated x-ray drive asymmetry in low-order l modes, particularly P_2 and P_4. Supporting experiments, measuring/inferring x-ray source-spot motion, and time-dependent x-ray albedo will also be conducted.

HLP4 Goals

To achieve low-order l-mode asymmetry (time integrated) $\lesssim$ 2–4% (P_2, P_4) in a lined hohlraum with pulse shaping properly scaled to ignition targets. In these experiments, the hohlraum case area will nominally be ~16× that of the capsule, and LEH losses will be comparable to the capsule absorbed energy. Peak $T_R < 230$ eV, consistent with Nova's power and focusing capabilities, will be used. A limited number of experiments with peak $T_R \approx 250$ eV (and corresponding shaped pulses consistent with Nova's capabilities) will also be conducted. The achievable flux uniformity is limited by the number of Nova's beams (10) and potentially by the individual beam quality. Experiments to measure time-dependent laser produced x-ray source motion and hohlraum wall albedo will further establish our understanding of time-dependent drive asymmetry. The experiments will reach the stated level of flux uniformity with Nova and demonstrate our quantitative understanding of the limitations (physics and technology) so that flux uniformities (both instantaneous and time integrated) required for ignition/moderate gain will be achieved on the Nova Upgrade.

To experimentally demonstrate time-integrated flux asymmetry control by varying P_2 nonuniformity from 10 to 20% (waist high) to 10 to 20% (pole high). These experiments, supported by quantitative modeling, will further demonstrate our ability to control and achieve the flux uniformity required for ignition/gain targets. The majority of the experiments will use lined hohlraums and shaped pulses with peak $T_R < 230$ eV. A limited number of experiments with $T_R \approx 230$ eV will also be included. The capsule convergences that we employ will be limited by our diagnostic resolution and sensitivity, but we expect it will range from 15 to 20.

HLP5 Summary of Tasks

To demonstrate acceptable levels of stimulated Brillouin (back and side scatter) and Raman scattering (back, side, and forward) in plasmas where the overall gain and I/I_{th} ratio are equal to that of Nova Upgrade targets. (Here, I is the laser intensity and I_{th} is the threshold intensity for the particular process.) The present Nova hohlraum experiments, in which good laser–plasma coupling is observed, have many relevant features that are nearly equivalent to an ignition hohlraum but differ in scale lengths and plasma dimensions (1 mm compared with 3–4 mm). As such, the experimental goals described in HLP1, HLP2, and HLP4 will continue to be relevant.

Experiments will also involve exploiting open-geometry targets such as exploding foils/disks of varying atomic number and will focus on long scale length plasmas where $n_e \lesssim 0.15\, n_c$, at which collisional damping of the various instabilities will not be effective. Experimental techniques will exploit the use of 8 to 9 Nova beams (operating at 0.53 or 0.35 μm) to independently create large ($L > 2$ mm), hot ($T_e > 1.5$ keV) plasmas $n_e/n_c < 0.15$, which will then be irradiated by an independently controlled interaction beam (operating at 0.53, 0.35, or 1.05 μm). Plasma conditions will be characterized and experimentally controlled (e.g., allowing sufficient delay between the plasma forming beams and interaction beam to allow hydrodynamic smoothing of density ripples and bumps and to reduce fluctuation and other noise sources to thermal levels). Freely expanding and interpenetrating plasma sources will be examined. A variety of pulse shapes including continuous and picket fence pulses will be studied.

HLP5 Goals

To quantify:

- *fSBS (back, side) < 5–10%*
- *fSRS (back, side) < 5–10%*
- *fSRS (forward) < 5%,*

In long scale length plasmas with the following characteristics of L (density and velocity scale length 2 mm), $T_e \approx 1.5$ keV, $n_e/n_c < 0.15$, and <3 <Z> <28.

These experiments will initially be conducted with the narrow frequency ($\Delta\nu/\nu < 10^{-5}$), spatially modulated

Nova beams and thus represent a "worst case" scenario. Experiments using spatially smooth beams (with smoothing times $\lesssim 20$ ps) are planned as part of the Nova program. Initial experiments will be conducted on the 2-beam facility in parallel with HLP6 and will eventually be performed on the 10-beam chamber where larger interaction plasmas are possible. Only the interaction beam, however, would have a smooth intensity profile. These latter experiments would be completed after the approval for the Nova Upgrade (provided the successful completion of HLP1, HLP2, HLP4, and HLP6) and would be complete in time to impact the Nova Upgrade configuration. Since laser wavelength effects are generally well understood and the purpose of this program is to examine laser coherence effects, the experiments will use 0.53-μm light where, at minimal facility cost, we can study relevant phenomena at laser energy/power >10 to 100 times that presently available on other facilities. Experiments will be conducted at both the 2-beam (spatial and temporal coherence variations) and 10-beam (temporal coherence) target areas. Continuous and comb spectra will be used with total fractional bandwidth of 0.2 to 0.3% ($\tau_{coh} \approx 0.6$–0.8 ps). The experiments will use both open geometry (disks, foils) and hohlraums. Extensive plasma characterization (e.g., an optical interferometer to measure plasma n_e profiles is nearing completion on the 2-beam facility) will be part of this program so that quantitative plasma physics experiments will be performed (i.e., well-defined laser intensities interacting with known plasmas).

HLP6 Summary of Tasks

To study the influence/coupling of filamentation with large scale length plasmas.

HLP6 Goals

To experimentally characterize the nonlinear state and the influence/coupling of filamentation with other instabilities (SBS, SRS) in the low-density ($n_e/n_c < 0.15$) plasma within the hohlraum channel. Experiments will also examine the predicted stabilizing effects of multiple beams, angular divergence, and beam smoothing. This effort will proceed in parallel but extend beyond the completion dates of HLP1, HLP2, HLP4, and HLP5. If objectives in these other tasks are not met, then the priority of the HLP6 activity would be increased with a resulting completion date before the Nova Upgrade construction starts. The results would then be of importance in establishing the baseline beam smoothing requirements for the new facility.

HLP7 Summary of Tasks

To achieve the hohlraum temperatures required for ignition/moderate gain within the output performance of the Nova Upgrade, x-ray conversion efficiencies >35 to 50% are required for $I \gtrsim 10^{15}$ W/cm^2. Disk experiments on Nova have already demonstrated these efficiencies with measured values exceeding 70% (and instantaneous values exceeding 80%) at relevant intensities and pulse lengths equal to that of the main pulse of the ignition target. Temperatures achieved in recent hohlraum experiments have implied conversion efficiencies $\gtrsim 50\%$ at laser $I > 3$ to 5×10^{15}W/cm^2.

In addition, experiments with disks have demonstrated or inferred that x-ray conversion efficiency (at a given wavelength, plasma composition, and intensity) increases with pulse length, spot size, and potentially beam quality. Furthermore, Nova experiments have also implied that the effective conversion efficiency in a hohlraum environment is also larger than that obtained in open-geometry targets. While our present modeling can match much of the data, some of the trends seen in the data (e.g., spot-size dependence) are not quantitatively understood.

X-ray conversion experiments planned over the next several years will further build upon our extensive database and attempt to develop an improved modeling capability. Experiments will focus on areas of applicability to the Nova Upgrade, i.e., long pulse, $I > 5 \times 10^{14}$W/cm^2, hohlraum environment, and beam uniformity. The power and energy capabilities of Nova will limit the overall parameter range that can be experimentally addressed. Irradiations will include both continuous and picket fence pulse shapes.

HLP7 Goals

Since the required conversion efficiency η (more importantly ηI) has already been achieved and the favorable trends in conversion efficiency as a function of the parameters associated with the Nova Upgrade (compared with Nova) have also been observed, we feel no additional milestones are required. The experiments will be used primarily to improve our understanding of the appropriate physics to enable better predictions in the range of hohlraum performance available on the Nova Upgrade.

FACILITY REPORT
OCTOBER–DECEMBER 1994

G. Hermes
Nova Operations Group
Nova Experiments Group
Laser Science Group

During this quarter, Nova Operations fired a total of 252 system shots resulting in 308 experiments. These experiments were distributed among ICF experiments, Defense Sciences experiments, X-Ray Laser experiments, Laser Sciences, and facility maintenance shots. Only four of these experiments were classified.

The fail-safe chirp system was successfully demonstrated. The system produces a small frequency "chirp" on the laser pulse that spoils stimulated Brillouin scattering (SBS) induced in the large-aperture chamber optics when operating with long pulses of high energy at 3ω. High levels of SBS can damage the final focus lenses and therefore limit the amount of energy we can direct into the chamber for use in target experiments. The fail-safe chirp system will allow us to increase the current energy limit by about 33% at a 3-ns pulse length.

Effort continued in support of the Petawatt Laser Project, which involves the modification of a Nova beamline and development of the necessary technology to produce a short-pulse beam on-target in the 10-beam chamber of ~1000 J at 1 ps. Beam transport experiments to the 2-beam target area were performed using the Petawatt laser front end as the pulse source with amplification through the Nova laser chain. The purpose of these experiments was to measure the spectral, temporal, and spatial modification of a broadband, linearly chirped pulse as a function of laser energy. Beamline 6 (BL-6) of Nova was configured according to the Petawatt design to produce a high-spatial-quality 40-cm-diam beam at the output of the laser chain. This included removal of the 46-cm amplifiers and spatial filter #6 on this beamline.

The Petawatt configuration of BL-6 significantly improved the beam quality relative to conventional Nova operation. Preliminary analysis indicates a far-field spatial distribution at the 2-beam chamber of approximately three times diffraction limited for the first shot of the day. Convection currents induced by temperature gradients in the disk amplifiers severely degraded the beam quality on subsequent laser shots.

Significant spectral and temporal reduction of the pulse was observed on propagation through Nova. This bandwidth limitation arises due to passive components in the Nova chain. Gain narrowing of the spectrum was also observed with increasing pulse energy at the predicted level. The impact of convective currents on the Petawatt beam quality should be minimized in an alternative configuration of Nova with spatial filter #6 left in place. This concept will be tested on an upcoming Nova/Petawatt shot series.

Engineering effort continued on the Petawatt project. A component design review was held on the vacuum compressor vessel, an aluminum chamber ~2.7 m across × ~12.8 m long. This vessel will house large-diam (94-cm) gratings for use in pulse compression. We plan to have the chamber installed in the 10-beam bay and demonstrate Petawatt capability by the end of FY 1995. Modifications to the 10-beam chamber to use the Petawatt beam in target experiments will be done in FY 1996.

A final design review was held on the 100-TW system for use on the 2-beam target chamber. This system will use a pulse from the Petawatt master oscillator with some non-Nova amplification to produce a beam on-target

of ~36 J at 400 fs (or ~30 J at 300 fs using mixed glass in the amplifiers). The system will be used for investigation of ignitor concepts and compressed-pulse issues prior to installation of the Petawatt system on the 10-beam chamber. Fabrication of the large vacuum vessel began, all the major optics were ordered or bid, and many other off-the-shelf items were ordered. Completion is scheduled for the 3rd quarter of FY 1996.

Effort continued on converting x-ray pinhole cameras from film to charge-coupled-device data recording. One system has been installed on the Nova target chamber and has recorded many images on a variety of target shots. Software has also been developed to process the raw data and more quickly determine beam offsets for use in precision pointing. The system lacks only a communication link to the open lab net to become a routine instrument on Nova. A second camera is planned to be installed on the chamber in the 3rd quarter of FY 1996 and will have the ability to change filtering as well as magnification without venting the target chamber. The first camera will then be retrofitted to incorporate this same capability.

We are working on improving the resolution of our gated microchannel plate detectors used in many of our x-ray diagnostics. The armed forces have shown an interest in this technology, as it is also applicable to night vision goggle detectors.

Most of the Nova operations personnel attended Total Quality Leadership classes sponsored by Allied Signal Corporation (the Nova facility contractor). These classes are intended to aid in team interactions, help understand performance measures, and improve overall Nova productivity.

FACILITY REPORT JANUARY–MARCH 1995

G. Hermes
Nova Operations Group
Nova Experiments Group
Laser Science Group

During this quarter, Nova Operations fired a total of 242 system shots resulting in 299 experiments. These experiments were distributed among ICF experiments, Defense Sciences experiments, X-Ray Laser experiments, Laser Sciences, and facility maintenance shots.

To support continued experiments in FY 1995, the Nova target chamber, Master Oscillator Room (MOR), and beamline 7 (BL7) were reconfigured to conduct $f/8$ and four-color operations. Several scattered light diagnostics were also installed and activated in the target chamber. At the completion of these experiments, the system was again reconfigured for normal $f/4$ single-color operations.

Work began to convert the old Nova safety interlock system to a new Programmable Logic Controller (PLC) system with expanded capability to support the 100 TW project: Phase I supports the 100 TW project and is scheduled for completion in early May; Phase II completes the system conversion in FY 1995.

A digital oscilloscope (SCD 5000) and a fast diode replaced the MOR Fidu Diagnostic (MFD) streak camera. After the system is validated by the MOR personnel, it will be integrated into the Laser Diagnostics controls software.

All major optics procurements have been awarded for the 100 TW project, with delivery expected by mid-April. We completed the installation of the 100 TW capacitor bank, and high-voltage cabling between the bank and the 9.4-cm amplifier will be installed early in the third quarter FY 1995. We received the 100 TW compressor chamber from EG&G, Inc. on March 21, 1995 and installed it in the two-beam area the following week.

In support of precision alignment operations, we performed two 2ω alignment shots to determine the consistency between the 2ω and 3ω transverse offsets. The data show that it is probably reasonable to use the 3ω offsets for the 2ω precision pointing series. However, the z (focus) offsets were quite different, as expected. Therefore, it might be necessary to perform 2ω alignment shots periodically to update the z offsets.

A series of shots verified beam timing—nine of the ten beams were within the Precision Nova specification of ± 10 ps (BL7 was approximately 30 ps early). As a result, five timing adjustments were made and confirmed using the 1ω streak camera data.

The BL7 potassium dihydrogen phosphate array was replaced with a refurbished unit, increasing the conversion efficiency by ~20%.

FACILITY REPORT APRIL–JUNE 1995

G. Hermes
Nova Operations Group
Nova Experiments Group
Laser Science Group

During this quarter, Nova Operations fired a total of 313 system shots resulting in 337 experiments. These experiments were distributed among ICF experiments, Defense Sciences experiments, X-Ray Laser (XRL) experiments, Laser Sciences, and facility maintenance shots.

Work has begun in support of a series of XRL experiments planned for mid-August on Nova's 10-beam chamber. This effort includes planning and preparation to install cylinder lenses on beamline 3, the XRL assembly, the imaging diagnostics, and the alignment system.

The gated x-ray imager 4 was also completed, installed, and activated on Nova's 10-beam chamber.

We implemented a new "precision pulse shape" capability on Nova. This enables us to produce a power balance report immediately after each shot. Data from the 3ω streak camera and Incident Beam Diagnostic energy diodes are used to show plots of power vs time for the 10 beams and the power balance error vs time.

We began installation and activation of the 100-TW system with full-system activation planned for early fourth quarter. The compressor chamber was delivered and installed, and the 10-cm amplifier, spatial filters, other beamline components, and optical components for the compressor and diagnostics systems were installed and aligned. The vacuum system for the compressor chamber was completed. The control systems and interlock systems were installed and tested, including firing the 10-cm amplifier.

Two Total Quality Management working groups were formed—one to focus on shot quality and the other on shot quantity. We have also made significant progress in cross training personnel among the operations groups.

Facility Report
July–September 1995

G. Hermes
Nova Operations Group
Nova Experiments Group
Laser Science Group

During this quarter, Nova Operations fired a total of 279 system shots resulting in 301 experiments. These experiments were distributed among ICF experiments, Defense Sciences experiments, X-Ray Laser experiments, Laser Sciences, and facility maintenance shots.

This is the final report for FY 1995. During the past year, Nova fired a total of 1101 system shots resulting in a total of 1228 experiments. There were 856 target experiments done in the 10-beam chamber and 128 experiments done in the 2-beam chamber. As a result of the declassification of ICF, there were only six target shots that were classified. There were 92 experiments conducted in support of laser science work, including precision pointing, failsafe chirp activation, and miscellaneous beam propagation experiments. We fired 150 calibration shots in support of routine and precision operations.

The first 8× CCD camera was installed and activated on the 10-beam chamber. This camera, plus one more, will eventually replace the film-based pinhole cameras currently being used to acquire x-ray images from precision pointing shots. Using the CCD cameras will greatly reduce the time required to analyze data from the pointing shots.

A set of cylinder lenses was removed from the 2-beam chamber and installed on beamline 3 of the 10-beam chamber in support of a series of x-ray laser experiments. This lens set was removed after several days of experiments and reinstalled on the 2-beam chamber. These lenses will be reinstalled next quarter with an additional spacer to allow for a longer line focus on the x-ray laser targets.

The 100-TW system was activated this quarter. We fired a shot at ~129 TW with a pulse width of 395 fs and an energy of 51 J. Work will continue to complete the target system activation to support target shots with the 100-TW system next quarter.

Work continues in support of the Petawatt system. The support frames for the compressor vacuum chamber and turning mirrors have been installed in the 10-beam target bay. The fabrication of the three major sections of the compressor tank is well under way. We are planning to install the compressor chamber in mid-November.

PUBLICATIONS

A

Afeyan, B. B., and Williams, E. A., *Unified Theory of Stimulated Raman Scattering and Two Plasmon Decay in Inhomogeneous Plasmas: the High Frequency Hybrid Instability,* Lawrence Livermore National Laboratory, Livermore, CA, UCRL-JC-121846 (1995). Submitted to *Phys. Rev. Lett.*

Afeyan, B. B., Berger, R. L., Bonnaud, G., Decker, C. D., Kruer, W. L., Langdon, A. B., Still, C. W., and Yang, T. B., *Numerical Simulations of Stimulated Raman Scattering in Laser Hot Spots and Speckles,* Lawrence Livermore National Laboratory, Livermore, CA, UCRL-JC-120886 ABS (1995). Prepared for *25th Annual Anomalous Absorption Conf,* Aspen, CO, May 27–Jun 1, 1995.

Afeyan, B. B., Berger, R. L., Cohen, B. I., Kaiser, T. B., and Williams, E. A., *Generalization of the Multi-Dimensional Theory of Stimulated Brillouin Scattering to Include Ponderomotive Filamentation,* Lawrence Livermore National Laboratory, Livermore, CA, UCRL-JC-120768 ABS (1995). Prepared for *25th Annual Anomalous Absorption Conf,* Aspen, CO, May 27–Jun 1, 1995.

Afeyan, B., Berger, R. L., Kaiser, T. B., and Kruer, W. L., *Theory and Simulations of the Effects of Long Wavelength Fluctuations on Parametric Instabilities,* Lawrence Livermore National Laboratory, Livermore, CA, UCRL-JC-121299 ABS (1995). Prepared for the *37th Annual Mtg of the American Physical Society Div of Plasma Physics,* Louisville, KY, Nov 6–10, 1995.

Aikens, D. M., *New Directions in Large Optics Fabrication,* Lawrence Livermore National Laboratory, Livermore, CA, UCRL-JC-120180 ABS (1995). Prepared for the *Society of Photo-Optical Instrumentation Engineers 1995 Int'l Conf on Optical Fabrication and Testing,* Tokyo, Japan, Jun 5–7, 1995.

Aikens, D., Roussel, A., and Bray, M., *Derivation of Preliminary Specifications for Transmitted Wavefront and Surface Roughness for Large Optics Used in Inertial Confinement Fusion,* Lawrence Livermore National Laboratory, Livermore, CA, UCRL-ID-121339 (1995).

Aikens, D., *The Origin and Evolution of the Optics Specifications for the National Ignition Facility,* Lawrence Livermore National Laboratory, Livermore, CA, UCRL-ID-121333 (1995).

Akunets, A., Dorogotovtsev, V. M., Merkuliev, Y. A., Startsev, S. A., and Cook, R., *Production of Hollow Microspheres from Plastic Solid Granules,* Lawrence Livermore National Laboratory, Livermore, CA, UCRL-JC-120206 (1995). Submitted to *Fusion Technology.*

Amendt, P., and Cuddeford, P., *Pseudomoment Stellar Dynamics I: Spheroidal Galactic Equilibria,* Lawrence Livermore National Laboratory, Livermore, CA, UCRL-JC-116166 Rev. 1 (1995). Submitted to the *Astrophys. J.*

Amendt, P., and Murphy, T. J., *Symmetry Tuning and Increased X-Ray Drive in Modified Nova Hohlraums,* Lawrence Livermore National Laboratory, Livermore, CA, UCRL-JC-121632 (1995). Submitted to *Phys. Rev. Lett.*

Amendt, P., Glendinning, S. G., Hammel, B. A., Landen, O., Suter, L. J., Laffite, S., and Jadaud, J. P., *Nova Hohlraum Time-Dependent Drive Asymmetry Diagnostic with Surrogate Foam Targets,* Lawrence Livermore National Laboratory, Livermore, CA, UCRL-JC-121602 ABS (1995). Prepared for the *37th Annual Mtg of American Physical Society Div of Plasma Physics,* Louisville, KY, Nov 6–10, 1995.

Amendt, P., Glendinning, S. G., Hammel, B. A., Landen, O., Suter, L. J., Laffite, S., and Jadaud, J. P., *Shocked Witness Foam-Ball Diagnostic for Nova Hohlraum Time-Dependent Drive Asymmetry,* Lawrence Livermore National Laboratory, Livermore, CA, UCRL-JC-117033 ABS Rev. 1 (1995). Prepared for *25th Annual Anomalous Absorption Conf,* Aspen, CO, May 27–Jun 1, 1995.

Amendt, P., Strauss, M., London, R. A., *Plasma Fluctuations and X-Ray Laser Transverse Coherence,* Lawrence Livermore National Laboratory, Livermore, CA, UCRL-JC-119012 (1995). Submitted to *Phys. Rev. Lett.*

Amendt, P., *Witness Foam-Ball Diagnostic for Nova Hohlraum Time-Dependent Drive Asymmetry,* Lawrence Livermore National Laboratory, Livermore, CA, UCRL-JC-116322 (1995); *Rev. Sci. Inst.* **66**(1), 785–787 (1995).

Antoun, T., Seaman, L., and Glinsky, M. E., *Modeling of Ablation by Photospallation Using the Computer Program PUFF/DFRACT,* Lawrence Livermore National Laboratory, Livermore, CA, UCRL-JC-120177 (1995). Prepared for the *Society of Photo-Optical Instrumentation Engineers' 1995 Int'l Symp on Lasers and Applications/ Biomedical Optics,* San Jose, CA, Feb 4–10, 1995.

Auerbach, J. M., Eimerl, D., Hunt, J. T., Milam, D., Trenholme, J. B., and Milonni, P. W., *Perturbation Theory for Frequency Doubling and Tripling of Electric Field Amplitude and Phase Ripples,* Lawrence Livermore National Laboratory, Livermore, CA, UCRL-JC-121452 (1995). Prepared for the *1st Annual Int'l Conf on Solid-State Lasers for Application to Inertial Confinement Fusion,* Monterey, CA, May 30–Jun 2, 1995.

Auerbach, J. M., Lawson, J. K., Rotter, M. D., Sacks, R. A., Van Wonterghem, B. M., and Williams, W. H., *Performance Modeling of Beamlet,* Lawrence Livermore National Laboratory, Livermore, CA, UCRL-JC-121453 (1995). Prepared for the *1st Annual Int'l Conf on Solid-State Lasers for Application to Inertial Confinement Fusion,* Monterey, CA, May 30–Jun 2, 1995.

Azevedo, S. G., Brase, J. M., Mast, J. E., McEwan, T. E., and Twogood, R. E., *Project Guardian,* Lawrence Livermore National Laboratory, Livermore, CA, UCRL-ID-120802 (1995).

Azevedo, S. G., Gavel, D. T., Mast, J. E., and Warhus, J. P., *Statement of Capabilities: Micropower Impulse Radar (MIR) Technology Applied to Mine Detection and Imaging,* Lawrence Livermore National Laboratory, Livermore, CA, UCRL-ID-120801 (1995).

Azevedo, S., Gavel, D., Mast, J., Trebes, J., Brase, J., Wan, T., Johansson, E., Wieting, M., *Symposium on Autonomous Systems in Mine Counter Measures,* Lawrence Livermore National Laboratory, Livermore, CA, UCRL-JC-119284 ABS (1995). Prepared for the *Symp on Autonomous Systems in Mine Counter Measures,* Monterey, CA, Apr 4–7, 1995.

B

Back, C. A., Berger, R. L., Estabrook, K., Failor, B. H., Hsing, W. W., Hsieh, E. J., Hockaday, R., Kalantar, D. H., Kauffman, R. L., Keane, C. J., Klem, D. E., MacGowan, B. J., Montgomery, D. S., Moody, J. D., Powers, L. V., Shepard, T. D., Stone, G. F., Suter, L. J., and Turner, R. E., *Measurements of Large Scale-Length Plasmas Produced from Gas-Filled Targets,* Lawrence Livermore National Laboratory, Livermore, CA, UCRL-JC-118834 (1995). Prepared for the *6th Int'l Workshop on Radiative Properties of Hot Dense Matter,* Sarasota, FL, Oct 31–Nov 4, 1994.

Back, C. A., Glenzer, S. H., Estabrook, K., Kauffman, R. L., Landen, O. L., MacGowan, B. J., Powers, L. V., Shepard, T. D., and Stone, G. F., *Localized Measurements of Electron Temperature in Hohlraum Targets by X-Ray Spectroscopy,* Lawrence Livermore National Laboratory, Livermore, CA, UCRL-JC-121290 ABS (1995). Prepared for the *37th Annual Mtg of the American Physical Society Div of Plasma Physics,* Louisville, KY, Nov 6–10, 1995.

Back, C. A., Glenzer, S. H., Estabrook, K., MacGowan, B. J., Montgomery, D. S., Munro, D. H., Shepard, T. D., and Stone, G. F., *Electron Temperature Scalings of Gasbag Targets,* Lawrence Livermore National Laboratory, Livermore, CA, UCRL-JC-120783 ABS (1995). Prepared for *25th Annual Anomalous Absorption Conf,* Aspen, CO, May 27–Jun 1, 1995.

Back, C., *Characterization of Nova Plasmas Using an X-Ray Spectrometer with Temporal and Spatial Resolution,* Lawrence Livermore National Laboratory, Livermore, CA, UCRL-JC-116211 (1995); *Rev. Sci. Inst.* **66**(1), 764–766 (1995).

Back, C., Failor, B. H., Hsieh, E. J., Kalantar, D. H., Keane, C. J., Lasinski, B. F., Montgomery, D. S., Powers, L. V., Stone, G., Turner, R. E., Hsing, W. W., Hockaday, R., Kauffman, R. L., Klem, D. E., MacGowan, B. J., Moody, J. D., Shepard, T. D., Sutter, L. J., *Measurements of Large Scale-Length Plasmas Produced from Gas-Filled Targets,* Lawrence Livermore National Laboratory, Livermore, CA, UCRL-JC-118834 ABS (1995). Prepared for the *6th Int'l Workshop on Radiative Properties of Hot Dense Matter,* Sarasota, FL, Oct 31–Nov 4, 1994.

Baldis, H. A., Labaune, C., Schifano, E., Michard, A., Bahr, R., Baker, K., Baton, S. D., Renard, N., Seka, W., Bauer, B. S., Estabrook, K., *Strongly Driven Ion Acoustic Waves in Laser Produced Plasmas,* Lawrence Livermore National Laboratory, Livermore, CA, UCRL-JC-118835 (1995). Prepared for the *23rd Eclim,* Oxford, UK, Sept 19–23, 1994.

Barnard, J. J., Cable, M. D., Callahan, D. A., Fessenden, T. J., Friedman, A., Grote, D. P., Judd, D. L., Lund, S. M., Newton, M. A., Sharp, W. M., and Yu, S. S., *Physics Design and Scaling of Recirculating Induction Accelerators: From Benchtop Prototypes to Drivers,* Lawrence Livermore National Laboratory, Livermore, CA, UCRL-JC-121457 ABS (1995). Prepared for the *Int'l Symp on Heavy Ion Fusion,* Princeton, NJ, Sept 6–9, 1995.

Barnard, J. J., *Emittance Growth from Rotated Quadrupoles in Heavy Ion Accelerators,* Lawrence Livermore National Laboratory, Livermore, CA, UCRL-JC-119385 (1995). Prepared for *Institute for Electrical and Electronics Engineers (IEEE) 1995 Particle Accelerator Conf,* Dallas, TX, May 1–5, 1995.

Barnard, J. J., *Emittance Growth from Rotated Quadrupoles in Heavy Ion Accelerators,* Lawrence Livermore National Laboratory, Livermore, CA, UCRL-JC-119385 ABS (1995). Prepared for the *IEEE 1994 PAC,* Dallas, TX, May 1–5, 1995.

Barrett, K. A., Chiu, Y. H., Painter, J. F., Motteler, Z. C., Dubois, P. F., *Basis System, Part I: Running a Basis Program—A Tutorial for Beginners,* Lawrence Livermore National Laboratory, Livermore, CA, UCRL-MA-118543, Vol. 1 (1995).

Beach, R. J., *A Classical Geometric Theory of Matter and Electromagnetism,* Lawrence Livermore National Laboratory, Livermore, CA, UCRL-JC-121633 (1995). Submitted to *Phys. Rev. B.*

Beach, R. J., *CW Theory of Quasi-Three Level End-Pumped Laser Oscillators,* Lawrence Livermore National Laboratory, Livermore, CA, UCRL-JC-121121 (1995). Submitted to *IEEE J. Quantum Electron.*

Beach, R. J., *Optimization of Quasi-Three Level End Pumped Q-Switched Lasers,* Lawrence Livermore National Laboratory, Livermore, CA, UCRL-JC-119952 (1995). Submitted to *IEEE J. Quantum Electron.*

Beach, R. J., Sutton, S. B., Skidmore, J. A., and Emanuel, M. A., *High Power 2 μm Diode-Pumped Tm:YAG Laser,* Lawrence Livermore National Laboratory, Livermore, CA, UCRL-JC-121647 ABS (1995). Prepared for the *Society of Photo-Optical Instrumentation Engineers 1996 Symp on Lasers and Integrated Optoelectronics,* San Jose, CA, Jan 27–Feb 2, 1996.

Beach, R., Emanuel, M., Skidmore, J., Benett, W., Carlson, N., Freitas, B., and Solarz, R., *Applications of Microlens-Conditioned Laser Diode Arrays,* Lawrence Livermore National Laboratory, Livermore, CA, UCRL-JC-119257 (1995). Prepared for *Laser Diode Optics II, SPIE Photonics West '95,* San Jose, CA, Feb 4–10, 1995.

Beach, R., Marshall, C., Emanuel, M., Payne, S., Benett, W., Freitas, B., Mill, S., Mitchell, S., Petty, C., and Smith, L., *All-Solid-State Laser With Diode Irradiance Conditioning,* Lawrence Livermore National Laboratory, Livermore, CA, UCRL-JC-119690 (1995). Submitted to the *R&D Magazine.*

Berger, R. L., Afeyan, B. B., Bonnaud, G., Langdon, A. B., Lasinski, B. F., Still, C. W., and Williams, E. A., *Simulations of the Interaction of Filamentation with SRS and SBS,* Lawrence Livermore National Laboratory, Livermore, CA, UCRL-JC-120773 ABS (1995). Prepared for *25th Annual Anomalous Absorption Conf,* Aspen, CO, May 27–Jun 1, 1995.

Berger, R. L., Afeyan, B. B., Cohen, B. I., Hinkel, D., Kaiser, T. B., Kirkwood, R., Langdon, A. B., Lasinski, B. F., MacGowan, B. J., Montgomery, D. S., Moody, J. D., Powers, L. V., Still, C. W., Williams, E. A., and Bonnaud, G., *Influence of Filamentation on the Growth and Angular Width of SBS and SRS,* Lawrence Livermore National Laboratory, Livermore, CA, UCRL-JC-121477 ABS (1995). Prepared for the *37th Annual Mtg of the American Physical Society Div of Plasma Physics,* Louisville, KY, Nov 6–10, 1995.

Berger, R. L., Lasinski, B. F., Kaiser, T. B., Cohen, B. I., Williams, E. A., Afeyan, B. B., Langdon, A. B., and Still, C. H., *Influence of Spatial and Temporal Laser Beam Smoothing on Stimulated Brillouin Scattering in Filamentated Laser Light by Three-Dimensional Simulations,* Lawrence Livermore National Laboratory, Livermore, CA, UCRL-JC-119259 (1995). Submitted to *Phys. Rev. Lett.*

Berger, R., *The Influence of Spatial and Temporal Laser Beam Smoothing on Stimulated Brillouin Scattering in Filamentary Laser Light,* Lawrence Livermore National Laboratory, Livermore, CA, UCRL-JC-119259 (1995); *Phys. Rev. Lett.* **75**(8), 1078–1081 (1995).

Berzins, L. V., Anklam, T. M., Chambers, F., Galanti, S., Haynam, C. A., and Worden, E. F., *Diode Laser Absorption Spectroscopy for Process Control—Sensor System Design Methodology,* Lawrence Livermore National Laboratory, Livermore, CA, UCRL-JC-118757 (1995). Prepared for the *Intl Conf on Metallurgical Coatings and Thin Films,* San Diego, CA, Apr 24–28, 1995.

Bibeau, C., *Evaluation of the $^4I_{11/2}$ Terminal Level Lifetime for Several Neodymium-Doped Laser Crystals and Glasses,* Lawrence Livermore National Laboratory, Livermore, CA, UCRL-LR-120895 (1995).

Bibeau, C., Payne, S. A., Trenholme, J., *Three Independent Measurements of the Terminal-Level Lifetime of Nd-Doped Phosphate Glass,* Lawrence Livermore National Laboratory, Livermore, CA, UCRL-JC-119006 ABS & SUM (1995). Prepared for *CLEO '95,* Baltimore, MD, May 22–26, 1995.

Bibeau, C., Trenholme, J. B., and Payne, S. A., *Pulse Length and Terminal Level Lifetime Dependence of Energy Extraction for Neodymium-Doped Phosphate Amplifier Glass,* Lawrence Livermore National Laboratory, Livermore, CA, UCRL-JC-120909 (1995). Submitted to *IEEE J. Quantum Electronics.*

Bittner, D., Bernat, T., Giedt, W., Monsler, M., Sater, J., Mapoles, E., Bieri, B., Sanchez, J., *Recent Results of Thermal Gradient Layering Experiments,* Lawrence Livermore National Laboratory, Livermore, CA, UCRL-JC-119395 ABS (1995). Prepared for the *10th Target Fabrication Specialists Mtg,* Taos, NM, Feb 6–10, 1995.

Bittner, D., Collins, G., Mapoles, E., and Bernat, T., *Formation of Uniform Solid D2 Layers by IR Irradiation,* Lawrence Livermore National Laboratory, Livermore, CA, UCRL-JC-121117 ABS (1995). Prepared for *42nd Nat'l Symp of the American Vacuum Society,* Minneapolis, MN, Oct 16–20, 1995.

Bliss, E. S., Feldman, M., Murray, J. E., and Vann, C. S., *Laser Chain Alignment with Low Power Local Light Sources,* Lawrence Livermore National Laboratory, Livermore, CA, UCRL-JC-120520 (1995). Prepared for the *1st Annual Int'l Conf on Solid-State Lasers for Application to Inertial Confinement Fusion,* Monterey, CA, May 30–Jun 2, 1995.

Boley, C. D., Early, J. T., *Computational Model of Drilling with High Radiance Pulsed Lasers,* Lawrence Livermore National Laboratory, Livermore, CA, UCRL-JC-117078 Rev. 1 (1995). Prepared for the *Int'l Conf on Applications of Lasers and Electro-Optics,* Orlando, FL, Oct 17–20, 1994.

Boley, C. D., Rhodes, M. A., and Bauer, B. S., *Modeling of Plasma–Electrode Pockels Cells,* Lawrence Livermore National Laboratory, Livermore, CA, UCRL-JC-116684 ABS Rev 1 (1995). Prepared for the *37th Annual Mtg of the American Physical Society Div of Plasma Physics,* Louisville, KY, Nov 6–10, 1995.

Bonnaud, G., Afeyan, B. B., Berger, R. L., Bouchut, F., Bouvet, C., Chiron, A., and Bers, A., *Numerical Simulations of High-Frequency Parametric Instabilities, Brillouin Scattering and Beam Crossing in the Gas-Bag Experiment Context,* Lawrence Livermore National Laboratory, Livermore, CA, UCRL-JC-120883 ABS (1995). Prepared for *25th Annual Anomalous Absorption Conf,* Aspen, CO, May 27–Jun 1, 1995.

Boone, T., Cheung, L., Nelson, D., Soane, D., Wilemski, G., and Cook, R., *Modeling of Microencapsulated Polymer Shell Solidification,* Lawrence Livermore National Laboratory, Livermore, CA, UCRL-JC-120184 (1994). Prepared for *Materials Research Society Symp on Hollow and Solid Spheres and Microspheres,* Boston, MA, Nov 28–Dec 2, 1994.

Boyd, R. D., Britten, J. A., Decker, D. E., Shore, B. W., Stuart, B. C., Perry, M. D., and Li, L., *High-Efficiency Metallic Diffraction Gratings for Laser Applications,* Lawrence Livermore National Laboratory, Livermore, CA, UCRL-JC-115589 (1994); *Appl. Opt.* **34**(10), 1697–1706 (1995).

Boyd, R., *High-Efficiency Metallic Diffraction Gratings for Laser Applications,* Lawrence Livermore National Laboratory, Livermore, CA, UCRL-JC-115589 (1995); *Applied Optics* **34**(4), 1697–1706 (1995).

Branham, K. E., Mays, J. W., Sanner, R. D., Cook, R. C., Overturf, G. E., Gray, G. M., *Reactions of Titanocene Derivatives with Molecular Carboxylic Acids and Copolymers Bearing Carboxylic Acid Groups,* Lawrence Livermore National Laboratory, Livermore, CA, UCRL-JC-119545 (1995). Submitted to *J of Organometallic Chemistry.*

Britten, J. A., Boyd, R. D., Perry, M. D., Shore, B. W., and Thomas, I. M., *Low Efficiency Gratings for 3rd Harmonic Diagnostics Applications,* Lawrence Livermore National Laboratory, Livermore, CA, UCRL-JC-120707 (1995). Prepared for the *1st Annual Int'l Conf on Solid-State Lasers for Application to Inertial Confinement Fusion,* Monterey, CA, May 30–Jun 2, 1995.

Britten, J. A., Boyd, R. D., Perry, M. D., Shore, B. W., and Thomas, I. M., *Low Efficiency Gratings for 3rd Harmonic Diagnostics Applications,* Lawrence Livermore National Laboratory, Livermore, CA, UCRL-JC-120707 ABS (1995). Prepared for *1st Annual Int'l Conf on Solid-State Lasers for Application to Inertial Confinement Fusion,* Monterey, CA, May 30–Jun 2, 1995.

Brown, D. L., and Mannell, G. T., *Thermal Analysis of the Large Close Packed Amplifiers in the National Ignition Facility (NIF)*, Lawrence Livermore National Laboratory, Livermore, CA, UCRL-JC-120211 (1995). Prepared for *1st Annual Int'l Conf on Solid-State Lasers for Application to Inertial Confinement Fusion*, Monterey, CA, May 30–Jun 2, 1995.

Brown, S. A., Dubois, P. F., and Munro, D. H., *Creating and Using PDB Files*, Lawrence Livermore National Laboratory, Livermore, CA, UCRL-JC-119607 (1995). Submitted to *Comput. Phys.*

Brusasco, R. M., Cook, R. C., *Preparation of Germanium-Doped Plasma Polymerized Coatings as ICF Target Ablators*, Lawrence Livermore National Laboratory, Livermore, CA, UCRL-JC-117325 (1995). Prepared for the *41st National Symp of the AVS*, Denver, CO, Oct 24–28, 1994.

Brusasco, R. M., Dittrich, T., and Cook, R. C., *Feasibility of Organo-Beryllium Target Mandrels Using Organo-Germanium PECVD as a Surrogate*, Lawrence Livermore National Laboratory, Livermore, CA, UCRL-JC-119533 (1995). Prepared for the *10th Target Fabrication Specialists' Mtg*, Taos, NM, Feb 6–9, 1995.

Brusasco, R. M., Dittrich, T., and Cook, R. C., *Feasibility of Organo-Beryllium Target Mandrels Using Organo-Germanium PECVD as a Surrogate*, Lawrence Livermore National Laboratory, Livermore, CA, UCRL-JC-119533 Rev 1 (1995). Submitted to *Fusion Technology.*

Brusasco, R. M., Dittrich, T., Cook, R. C., *Feasibility of Organo-Beryllium Target Mandrels Using Organo-Germanium Plasma-Enhanced Chemical Vapor Deposition (PECVD) as a Surrogate*, Lawrence Livermore National Laboratory, Livermore, CA, UCRL-JC-119533 ABS (1995). Prepared for the *10th Target Fabrication Specialists Mtg*, Taos, NM, Feb 6–10, 1995.

Brusasco, R. M., Letts, S. A., Saculla, M. D., and Cook, R. C., *High Beryllium Content Plasma Polymer Ablator Coatings for ICF Targets*, Lawrence Livermore National Laboratory, Livermore, CA, UCRL-JC-120897 ABS (1995). Prepared for *42nd Nat'l Symp of the American Vacuum Society*, Minneapolis, MN, Oct 16–20, 1995.

Brusasco, R. M., Wilemski, G., Cook, R. C., Letts, S. A., *Mass Spectrometric Determination of the Coating Environment in Plasma Polymerization under Rough and Smooth Coating Conditions*, Lawrence Livermore National Laboratory, Livermore, CA, UCRL-JC-119531 ABS (1995). Prepared for the *10th Target Fabrication Specialists Mtg*, Taos, NM, Feb 6–10, 1995.

Burkhart, C., Behrendt, W., Smith, I., *Laser Diagnostic for High-Energy, Laser Fusion Drivers*, Lawrence Livermore National Laboratory, Livermore, CA, UCRL-JC-119065 (1995). Prepared for the *CLEO '95*, Baltimore, MD, May 22–26, 1995.

Burkhart, S. C., and Penko, F. A., *High-Speed Temporal Laser Beam Modulation*, Lawrence Livermore National Laboratory, Livermore, CA, UCRL-JC-120510 ABS (1995). Prepared for the *Solid-State Lasers for Application to Inertial Confinement Fusion (ICF) 1st Annual Int'l Conf*, Monterey, CA, May 30–Jun 2, 1995.

Burkhart, S. C., Beach, R. J., Crane, J. H., Davin, J. M., Perry, M. D., and Wilcox, R. B., *The National Ignition Facility Front-End Laser System*, Lawrence Livermore National Laboratory, Livermore, CA, UCRL-JC-119019 (1995). Prepared for the *1st Annual Int'l Conf on Solid-State Lasers for Application to Inertial Confinement Fusion*, Monterey, CA, May 30–Jun 2, 1995.

Burkhart, S. C., Beach, R. J., Crane, J. K., Davin, J. M., Perry, M. D., and Wilcox, R. B., *The National Ignition Facility Front-End Laser System Overview*, Lawrence Livermore National Laboratory, Livermore, CA, UCRL-JC-120511 ABS (1995). Prepared for the *Solid-State Lasers for Application to Inertial Confinement Fusion (ICF) 1st Annual Int'l Conf*, Monterey, CA, May 30–Jun 2, 1995.

Burkhart, S. C., *National Ignition Facility Front-End Laser Systems*, Lawrence Livermore National Laboratory, Livermore, CA, UCRL-JC-119019 ABS (1995). Prepared for the *Western Washington University*, Nov 22, 1994, Bellingham, WA.

Burkhart, S. C., *Voltage Controlled Metal Semiconductor Field Effect Transistor (MESFET) Pulse Shape Generator*, Lawrence Livermore National Laboratory, Livermore, CA, UCRL-ID-116054 (1995).

Burkhart, S. C., Wilcox, R. B., Perry, M. D., Beach, R. J., Crane J. K., *Front-End Oscillator System for the National Ignition Facility*, Lawrence Livermore National Laboratory, Livermore, CA, UCRL-JC-119018 ABS & SUM (1995). Prepared for *CLEO '95*, Baltimore, MD, May 22–26, 1995.

Burmann, J., Letts, S., Schroen-Carey, D., Sanchez, J., *Fabrication Techniques for Cryogenic Targets*, Lawrence Livermore National Laboratory, Livermore, CA, UCRL-JC-119534 ABS (1995). Prepared for the *10th Target Fabrication Specialists Mtg*, Taos, NM, Feb 6–10, 1995.

C

Cable, M. D., Barnard, J. J., Callahan, D. A., Deadrick, F. J., Eylon, S., Fessenden, T. J., Friedman, A., Grote, D. P., Hopkins, H. A., Judd, D. L., Hawkins, S. A., Karpenko, V. P., Kirbie, H. C., Logan, B. G., Longinotti, D. B., Lund, S. M., Nattrass, L. A., Nelson, M. B., Newton, M. A., and Ollis, C. W., *Recirculating Heavy Ion Accelerator Experiment,* Lawrence Livermore National Laboratory, Livermore, CA, UCRL-JC-121479 ABS (1995). Prepared for the *37th Annual Mtg of the American Physical Society Div of Plasma Physics,* Louisville, KY, Nov 6–10, 1995.

Cable, M. D., *Target Diagnostics for the National Ignition Facility,* Lawrence Livermore National Laboratory, Livermore, CA, UCRL-JC-119887 ABS (1995). Prepared for the *IEEE ICOP's '95 Conf,* Madison, WI, Jun 5–8, 1995.

Callahan, D. A., and Langdon, A. B., *Chamber Transport Physics for Heavy Ion Fusion,* Lawrence Livermore National Laboratory, Livermore, CA, UCRL-JC-121480 ABS (1995). Prepared for the *37th Annual Mtg of the American Physical Society Div of Plasma Physics,* Louisville, KY, Nov 6–10, 1995.

Callahan, D. A., and Langdon, A. B., *Partially-Neutralized Chamber Transport for Heavy Ion Fusion,* Lawrence Livermore National Laboratory, Livermore, CA, UCRL-JC-119919 ABS (1995). Prepared for the *HCM High Energy Density Advanced Research Workshop,* Les Houches, France, Mar 13–17, 1995.

Callahan, D. A., and Langdon, A. B., *Transport of a Partially-Neutralized Ion Beam in a Heavy-Ion Fusion Reactor Chamber,* Lawrence Livermore National Laboratory, Livermore, CA, UCRL-JC-119359 (1995). Prepared for *IEEE 1995 Particle Accelerator Conf,* Dallas, TX, May 1–5, 1995.

Callahan, D. A., *Chamber Propagation Physics for Heavy Ion Fusion,* Lawrence Livermore National Laboratory, Livermore, CA, UCRL-JC-121279 (1995). Prepared for the *Int'l Symp on Heavy Ion Fusion,* Princeton, NJ, Sept 6–9, 1995.

Callahan, D. A., *Chamber Propagation Physics for Heavy Ion Fusion,* Lawrence Livermore National Laboratory, Livermore, CA, UCRL-JC-121279 ABS (1995). Prepared for *Int'l Symp on Heavy Ion Inertial Fusion,* Princeton, NJ, Sept 6–9, 1995.

Callahan, D. A., *Interactions between Neighboring Beams in a Heavy Ion Fusion Reactor Chamber,* Lawrence Livermore National Laboratory, Livermore, CA, UCRL-JC-121132 (1995). Submitted to *Appl. Phys. Lett.*

Callahan, D. A., Langdon, A. B., *Transport of a Partially-Neutralized Ion Beam in a Heavy-Ion Fusion Reactor Chamber,* Lawrence Livermore National Laboratory, Livermore, CA, UCRL-JC-119359 ABS (1995). Prepared for the *IEEE 1995 PAC,* Dallas, TX, May 1–5, 1995.

Campbell, J. H., Atherton, L. J., De Yoreo, J. J., Kozlowski, M. R., Maney, R. T., Montesanti, R. C., Sheehan, L. M., and Barker, C. E., *Large-Aperture, High-Damage-Threshold Optics for Beamlet,* Lawrence Livermore National Laboratory, Livermore, CA, UCRL-ID-119932 (1995).

Campbell, J. H., Barker, C. E., Van Wonterghem, B. M., Speck, D. R., Behrendt, W. C., Murray, J. R., Caird, J. A., Decker, D. E., and Smith, I. C., *Performance Results for Beamlet: a Large Aperture, Multipass Nd:Glass Laser,* Lawrence Livermore National Laboratory, Livermore, CA, UCRL-JC-120779 (1995). Prepared for *Conf on Lasers and Electro Optics/Pacific Rim '95,* Chiba, Japan, Jul 11–14, 1995.

Campbell, J. H., Edwards, G. J., and Marion, J. E., *Damage and Fracture in Large Aperture, Fused Silica, Vacuum Spatial Filter Lenses,* Lawrence Livermore National Laboratory, Livermore, CA, UCRL-JC-120780 (1995). Prepared for the *1st Annual Int'l Conf on Solid-State Lasers for Application to Inertial Confinement Fusion,* Monterey, CA, May 30–Jun 2, 1995.

Campbell, J. H., Edwards, G., and Marion, J., *Damage and Fracture in Large Aperture, Fused Silica, Vacuum Spatial Filter Lenses,* Lawrence Livermore National Laboratory, Livermore, CA, UCRL-JC-120780 ABS (1995). Prepared for *1st Annual Int'l Conf on Solid-State Lasers for Application to Inertial Confinement Fusion,* Monterey, CA, May 30–Jun 2, 1995.

Campbell, J., and Correll, D., *ICF Quarterly Report, 5(1),* Lawrence Livermore National Laboratory, Livermore, CA, UCRL-LR-105821-95-1 (1995).

Campbell, M., *National Ignition Facility for America's National Security, Energy, Science, and Economic Future,* Lawrence Livermore National Laboratory, Livermore, CA, UCRL-TB-118550 (1995).

Celliers, P., Da Silva, L. B., Dane, C. B., Mrowka, S., Norton, M., Harder, J., Hackel, L., Matthews, D., Fiedorowicz, H., Barnick, A., and Maldonado, J., *Optimization of X-Ray Sources for Proximity Lithography Produced by a High Average Power Nd:Glass Laser,* Lawrence Livermore National Laboratory, Livermore, CA, UCRL-CR-121294 (1995).

Celliers, P., Da Silva, L., Mrowka, S., Dane, B., Norton, M., Matthews, D., Fiedorowicz, H., Bartnik, A., Abate, J., and Maldonado, J., *Characterization and Optimization of Solid and Gas Target X-Ray Sources for Proximity Lithography,* Lawrence Livermore National Laboratory, Livermore, CA, UCRL-JC-120781 ABS (1995). Prepared for *ARPA Advanced Lithography Program Review,* Scottsdale, AZ, Jan 23–27, 1995.

Celliers, P., *Fringe Formation and Coherence of a Soft X-Ray Laser Beam Illuminating a Mach–Zehnder Interferometer,* Lawrence Livermore National Laboratory, Livermore, CA, UCRL-JC-120921 (1995). Submitted to *Optics Lett.* (1995).

Celliers, P., Weber, F., Da Silva, L. B., Barbee, T. W., Cauble, R., Wan, A. S., and Moreno, J. C., *Fringe Formation and Coherence of a Soft X-Ray Laser Beam Illuminating a Mach-Zehnder Interferometer,* Lawrence Livermore National Laboratory, Livermore, CA, UCRL-JC-120921 (1995). Submitted to *Opt. Lett.*

Center for Beam Phys Laser Programs, *Relativistic Klystron Two-Beam Accelerator Research Proposal Part C,* Lawrence Livermore National Laboratory, Livermore, CA, UCRL-PROP-119356 (1995).

Chang, J. J., and Warner, B. E., *Properties of High Radiance Laser-Material Interaction for Manufacturing,* Lawrence Livermore National Laboratory, Livermore, CA, UCRL-ID-119698 (1995).

Chang, J. J., *High-Power Copper Vapor Lasers and Applications,* Lawrence Livermore National Laboratory, Livermore, CA, UCRL-JC-120599 ABS (1995). Prepared for *NATO Advanced Research Workshop on Pulsed Metal Vapour Lasers,* St Andrews, Scotland, Aug 7–10, 1995.

Chang, J. J., Martinez, M. W., Dragon, E. P., Solarski, M. E., Huete, G., Warner, B. E., *New Applications of Copper Vapor Lasers in Micro Machining,* Lawrence Livermore National Laboratory, Livermore, CA, UCRL-JC-117091 (1995). Prepared for *Photonics Technology Transfer Conference,* Washington, DC, Nov 9, 1994.

Chang, J. J., Warner, B. E., Boley, C. D., and Dragon, E. P., *High-Power Copper Vapour Lasers and Applications,* Lawrence Livermore National Laboratory, Livermore, CA, UCRL-JC-121626 (1995). Prepared for the *NATO Advanced Research Workshop on Pulsed Metal Vapour Lasers,* St Andrews, Scotland, Aug 7–10, 1995.

Chang, T., and Havstad, M., *Design of a Substrate Heater for Calcium Hydroxyapatite Coating by Pulsed Laser Ablation,* Lawrence Livermore National Laboratory, Livermore, CA, UCRL-ID-121808 (1995).

Chenais-Popovics, C., Rancu, O., Renaudin, P., Gauthier, J. C., Gilleron, F., Lindenmeyer, O., Kawagoshi, H., Dirksmoller, M., Uschmann, I., Missalla, T., Sondhauss, P., Forster, E., Renner, O., Krousky, E., Pepin, H., Larroche, O., Peyrusse, O., and Shepard, T. D., *X-Ray Spectroscopy and Imaging of a Plasma Collision,* Lawrence Livermore National Laboratory, Livermore, CA, UCRL-JC-121582 (1995). Prepared for the *Society of Photo-Optical Instrumentation Engineers Conf,* San Diego, CA, Jul 12–14, 1995.

Chiu, Y. H., Dubois, P. F., *Basis System, Part IV: EZD User Manual,* Lawrence Livermore National Laboratory, Livermore, CA, UCRL-MA-118543, Vol. 4 (1995).

Chiu, Y. H., Dubois, P. F., *Basis System, Part III: EZN User Manual,* Lawrence Livermore National Laboratory, Livermore, CA, UCRL-MA-118543, Vol. 3 (1995).

Cohen, B. I., Afeyan, B. B., Langdon, A. B., Lasinski, B. F., and Williams, E. A., *Ion Wave Nonlinearities in Stimulated Brillouin Scattering,* Lawrence Livermore National Laboratory, Livermore, CA, UCRL-JC-120774 ABS (1995). Prepared for *25th Annual Anomalous Absorption Conf,* Aspen, CO, May 27–Jun 1, 1995.

Cohen, B. I., Lasinski, B. F., Langdon, A. B., and Williams, E. A., *2D Hybrid Simulations of Ponderomotively Driven Nonlinear Ion Waves,* Lawrence Livermore National Laboratory, Livermore, CA, UCRL-JC-121297 ABS (1995). Prepared for the *37th Annual Mtg of the American Physical Society Div of Plasma Physics,* Louisville, KY, Nov 6–10, 1995.

Collins, G. W., Mapoles, E. R., Bernat, T. P., Unites, W. G., *Structure of Vapor Deposited Hydrogen Crystals,* Lawrence Livermore National Laboratory, Livermore, CA, UCRL-JC-119376 ABS (1995). Prepared for *1995 March Mtg of the APS,* San Jose, CA, Mar 20–24, 1995.

Collins, G. W., Mapoles, E. R., Unites, W. G., and Bernat, T. P., *Vapor Deposited Solid Hydrogen Crystals: Size, Structure, and Roughening,* Lawrence Livermore National Laboratory, Livermore, CA, UCRL-JC-117324 ABS Rev. 1 (1995). Prepared for *Institute for Surface and Interface Science,* Newport Beach, CA, Feb 15–18, 1995.

Collins, G. W., Unites, W. G., Mapoles, E. R., and Bernat, T. P., *Structure of Thick Solid Hydrogen Films,* Lawrence Livermore National Laboratory, Livermore, CA, UCRL-JC-119619 (1995). Submitted to *Phys. Rev. Lett.*

Collins, G. W., Unites, W., *Structure of Vapor Deposited Solid Hydrogen Crystals,* Lawrence Livermore National Laboratory, Livermore, CA, UCRL-JC-119530 ABS (1995). Prepared for the *10th Target Fabrication Specialists Mtg,* Taos, NM, Feb 6–10, 1995.

Collins, G., Unites, W., Mapoles, E., and Bernat, T., *Raman Study of Solid D-T,* Lawrence Livermore National Laboratory, Livermore, CA, UCRL-JC-121118 ABS (1995). Prepared for *42nd Nat'l Symp of the American Vacuum Society,* Minneapolis, MN, Oct 16–20, 1995.

Cook, R. C., *Production of Hollow Microspheres for Inertial Confinement Fusion Experiments,* Lawrence Livermore National Laboratory, Livermore, CA, UCRL-JC-117389 (1995). Prepared for the *Materials Rsch Soc Mtg,* Boston, MA, Nov 28–Dec 2, 1994.

Cook, R. C., *Production of Hollow Microspheres for Inertial Confinement Fusion Experiments,* Lawrence Livermore National Laboratory, Livermore, CA, UCRL-JC-117389 ABS (1995). Prepared for the *1994 Fall Mtg Materials Rsch Soc,* Boston, MA, Nov 28–Dec 2, 1994.

Correll, D. L., Vergino, E. S., and Bibeau, C., *Laser Fusion Education at LLNL,* Lawrence Livermore National Laboratory, Livermore, CA, UCRL-JC-121496 ABS (1995). Prepared for the *37th Annual Mtg of the American Physical Society Div of Plasma Physics,* Louisville, KY, Nov 6–10, 1995.

Coverdale, C. A., *The Interaction of Intense Subpicosecond Laser Pulses with Underdense Plasmas,* Lawrence Livermore National Laboratory, Livermore, CA, UCRL-LR-120922 (1995).

Coverdale, C. A., Darrow, C. B., Decker, C. D., Mori, W. B., Tzeng, K.-C., Clayton, C. E., Marsh, K. A., and Joshi, C., *Electron Acceleration in Relativistic Plasma Waves Generated by a Single-Frequency Short-Pulse Laser,* Lawrence Livermore National Laboratory, Livermore, CA, UCRL-JC-120891 (1995). Prepared for *IEEE 1995 Particle Accelerator Conf,* Dallas, TX, May 1–5, 1995.

Coverdale, C. A., Darrow, C. B., Decker, C. D., Mori, W. B., Tzeng, K.-C., Marsh, K. A., Clayton, C. E., and Joshi, C., *Propagation of Intense Subpicosecond Laser Pulses Through Underdense Plasmas,* Lawrence Livermore National Laboratory, Livermore, CA, UCRL-JC-119542 (1994); *Phys. Rev. Lett.* **74**(23), 4659–4662 (1995).

Coverdale, C. A., Darrow, C. B., Decker, C. D., Naumova, N., Bulanov, S., Mori, W. B., and Tzeng, K. C., *Spectral Anomalies and Reflectivity Saturation of Stimulated Raman Backscatter from a Sub-Picosecond Laser in an Underdense Plasma,* Lawrence Livermore National Laboratory, Livermore, CA, UCRL-JC-121142 (1995). Submitted to *Phys. Rev. Lett.*

Coverdale, C. A., Darrow, C. B., Decker, C. D., Naumova, N., Bulanov, S., Mori, W. B., and Tzeng, K. C., *Temporal Bursting of Stimulated Raman Backscatter in Underdense Plasmas,* Lawrence Livermore National Laboratory, Livermore, CA, UCRL-JC-121490 ABS (1995). Prepared for the *37th Annual Mtg of the American Physical Society Div of Plasma Physics,* Louisville, KY, Nov 6–10, 1995.

Coverdale, C. A., Darrow, C. B., Mori, W. B., Marsh, K. A., Joshi, C., Tzeng, K. C., Decker, C. D., Clayton, C. E., *Propagation of Intense Subpicosecond Laser Pulses Through Underdense Plasmas,* Lawrence Livermore National Laboratory, Livermore, CA, UCRL-JC-119542 (1995). Submitted to *Phys Rev Lett.*

Crane, J. K., Nguyen, H., Wilks, S. C., Ditmire, T., Coverdale, C. A., Glover, T. E., Perry, M. D., and Zakharenkov, Y., *Strong Anomalous Emission from He and H-Like Neon in Short-Pulse Laser Driven Plasmas,* Lawrence Livermore National Laboratory, Livermore, CA, UCRL-JC-120223 (1995). Submitted to the *J. Opt. Soc. Am. B.*

D

Da Silva, L. B., Barbee Jr., T. W., Cauble, R., Celliers, P., Ciarlo, D., Libby, S., London, R. A., Matthews, D., Mrowka, S., Moreno, J. C., Ress, D., Trebes, J. E., Wan, A. S., and Weber, F., *Electron Density Measurements of High Density Plasmas Using Soft X-Ray Laser Interferometry,* Lawrence Livermore National Laboratory, Livermore, CA, UCRL-JC-120243 (1995); *Phys. Rev. Lett.* **74**(20), 3991–3994 (1995).

Da Silva, L. B., Barbee, T. W., Cauble, R. C., Celliers, P. M., Ciarlo, D. R., London, R. A., Moreno, J. C., Mrowka, S., Trebes, J. E., Wan, A. S., and Weber, F. A., *High Resolution Soft X-Ray Interferometer,* Lawrence Livermore National Laboratory, Livermore, CA, UCRL-JC-119941 (1995). Submitted to *R&D Magazine.*

Da Silva, L. B., Barbee, T. W., Cauble, R., Celliers, P., Ciarlo, D., Libby, S., London, R. A., Matthews, D. L., Mrowka, S., Moreno, J. C., Trebes, J. E., Wan, A. S., and Weber, F., *Development of XUV-Interferometry (155 A) Using a Soft X-Ray Laser,* Lawrence Livermore National Laboratory, Livermore, CA, UCRL-JC-121629 (1995). Prepared for the *Society of Photo-Optical Instrumentation Engineers 40th Annual Mtg,* San Diego, CA, Jul 9–14, 1995.

Da Silva, L. B., Barbee, T. W., Cauble, R., Celliers, P., Ciarlo, D., Libby, S., London, R. A., Matthews, D., Mrowka, S., Moreno, J. C., Ress, D., Trebes, J. E., Wan, A. S., and Weber, F., *Electron Density Measurements of High Density Plasmas Using Soft X-Ray Laser Interferometry,* Lawrence Livermore National Laboratory, Livermore, CA, UCRL-JC-120243 (1995). Submitted to *Phys. Rev. Lett.*

Da Silva, L. B., Barbee, T. W., Cauble, R., Celliers, P., Kalantar, D. H., Key, M. H., Moreno, J. C., Trebes, J. E., Wan, A. S., and Weber, F., *Application of X-Ray Lasers to Probe High Density Plasmas,* Lawrence Livermore National Laboratory, Livermore, CA, UCRL-JC-121623 ABS (1995). Prepared for the *37th Annual Mtg of the American Physical Society Div of Plasma Physics,* Louisville, KY, Nov 6–10, 1995.

Da Silva, L., Barbee, T., Celliers, P., Moreno, J., Trebes, J., Weber, F., Ciarlo, D., Cauble, R., Mrowka, S., and Wan, A., *XUV Interferometry at 15.5 nm Using Multilayer Optics,* Lawrence Livermore National Laboratory, Livermore, CA, UCRL-JC-119577 (1995); *Appl. Opt.*, **1** (1995).

Da Silva, L., *Electron Density Measurements of High Density Plasmas Using Soft X-Ray Laser Interferometry,* Lawrence Livermore National Laboratory, Livermore, CA, UCRL-JC-120243 (1995); *Phys. Rev. Lett.* **74**(5), 3991–3994 (1995).

Da Silva, L., *X-Ray Lasers for High Density Plasma Diagnostics,* Lawrence Livermore National Laboratory, Livermore, CA, UCRL-JC-116411 (1995); *Rev. Sci. Inst.* **66**(1), 574–578 (1995).

Dahlburg, J. P., Fyfe, D. E., Bodner, S. E., Dollen, G. D., Haan, S. W., Gardner, J. H., *Three-Dimensional Multimode Simulations of the Ablative Rayleigh–Taylor Instability,* Lawrence Livermore National Laboratory, Livermore, CA, UCRL-JC-118845 (1995). Submitted to *Phys Plasmas.*

Dahlburg, J., Fyfe, D. E., Gardner, J. H., Haan, S. W., Bodner, S. E., and Doolen, G. D., *Three Dimensional Multimode Simulations of the Ablative Rayleigh-Taylor Instability,* Lawrence Livermore National Laboratory, Livermore, CA, UCRL-JC-118845 (1994); *Phys. Plasmas* **2**(6), 2453–2459 (1995).

Dahlburg, J., *Three Dimensional Multimode Simulations of the Ablative Rayleigh–Taylor Instability,* Lawrence Livermore National Laboratory, Livermore, CA, UCRL-JC-118845 (1995); *Phys. Plasmas* **2**(6), 2453–2459 (1995).

Darrow, C., Clayton, C., Marsh, K., Mori, W., Joshi, C., Dangor, A. E., Modena, A., Najmudin, Z., Melka, V., Neeley, D., and Danson, C., *Observation of 44 MeV Electrons Generated by High-Intensity, Subpicosecond Laser Irradiation of an Underdense Plasma,* Lawrence Livermore National Laboratory, Livermore, CA, UCRL-JC-119632 ABS (1995).

Darrow, C., Hay, G., Zakharenkov, Y., Nguyen, H., Hammel, B., and Perry, M. D., *Experimental Investigation of the Interaction of 1 μm, 0.7 ps, 10^{19} W/cm^2 Laser Pulses with Solid Targets,* Lawrence Livermore National Laboratory, Livermore, CA, UCRL-JC-120245 ABS (1995). Prepared for *25th Annual Anomalous Absorption Conf,* Aspen, CO, May 27–Jun 1, 1995.

Darrow, C., Hay, G., Zakharenkow, Y., Nguyen, H., Hammel, B., and Perry, M. D., *Experimental Investigation of the Interaction of 1 μm, 0.7 ps, 10^{19} W/cm^2 Laser Pulses with Solid Targets,* Lawrence Livermore National Laboratory, Livermore, CA, UCRL-JC-120245 ABS Rev 1 (1995). Prepared for the *37th Annual Mtg of the American Physical Society Div of Plasma Physics,* Louisville, KY, Nov 6–10, 1995.

De Yoreo, J. J., Malkin, A. J., Land, T. A., Kuznetsov, Y. G., Lee, J. D., and McPherson, A., *An AFM Study of the Growth Mechanisms and Morphologies of Solution-Based Crystals,* Lawrence Livermore National Laboratory, Livermore, CA, UCRL-JC-121610 ABS (1995). Prepared for the *Metallurgical Society Annual Mtg,* Anaheim, CA, Feb 4–8, 1996.

De Yoreo, J. J., Rek, Z. U., Zaitseva, N. P., and Woods, B. W., *Sources of Strain in Rapidly Grown Crystals of KH_2PO_4,* Lawrence Livermore National Laboratory, Livermore, CA, UCRL-ID-119645 (1995).

De Yoreo, J. J., Rek, Z. U., Zaitseva, N. P., Woods, B. W., and Land, T. A., *Sources of Strain in Rapidly Grown Crystals of KH_2PO_4,* Lawrence Livermore National Laboratory, Livermore, CA, UCRL-JC-119645 (1995). Prepared for *Int'l Conf on Crystal Growth XI,* The Hague, Netherlands, Jun 18–23, 1995.

De Yoreo, J. J., Rek, Z., Zaitseva, N. P., Torres, R., Lee, J. D., and Woods, B. W., *The Dependence of Optical Homogeneity on Growth Rate in KH_2PO_4,* Lawrence Livermore National Laboratory, Livermore, CA, UCRL-JC-120235 ABS (1995). Prepared for *14th Conf on Crystal Growth and Epitaxy,* Fallen Leaf Lake, CA, Jun 4–7, 1995.

De Yoreo, J. J., Zaitseva, N. P., Rek, Z. U., Land, T. A., and Woods, B. W., *The Connection between Optical Distortion and Elemental Growth Processes in Rapidly-Grown, Single Crystals of KH_2PO_4*, Lawrence Livermore National Laboratory, Livermore, CA, UCRL-JC-120701 (1995). Submitted to *Appl. Phys. Lett.*

De Yoreo, J., Land, T. A., Lee, J. D., *Atomic Force Microscopy Study of KDP Growth*, Lawrence Livermore National Laboratory, Livermore, CA, UCRL-JC-119343 ABS (1995). Prepared for the *Amer Ceramic Soc 1995 Annual Mtg*, Cincinnati, OH, Apr 20–May 4, 1995.

Deadrick, F. J., Barnard, J. J., Fessenden, T. J., Meridith, J. W., and Rintamaki, J., *Development of Beam Position Monitors for Heavy Ion Recirculators*, Lawrence Livermore National Laboratory, Livermore, CA, UCRL-JC-119539 (1995). Prepared for *IEEE 1995 Particle Accelerator Conf*, Dallas, TX, May 1–5, 1995.

Deadrick, F., Barnard, J., Meredith, J., Rintamaki, J., Fessenden, T., *Development of Beam Position Monitors for Heavy Ion Recirculators*, Lawrence Livermore National Laboratory, Livermore, CA, UCRL-JC-119539 ABS (1995). Prepared for the *IEEE 1994 PAC*, Dallas, TX, May 1–5, 1995.

Decker, C. D., Eder, D. C., and London, R. A., *Ionization Induced Refraction in Recombination X-Ray Lasers*, Lawrence Livermore National Laboratory, Livermore, CA, UCRL-JC-119324 (1995). Submitted to *Physics of Plasmas.*

Decker, C. D., Mori, W. B., and Tzeng, K. C., *Short-Pulse Propagation at Ultra-High Laser Intensities*, Lawrence Livermore National Laboratory, Livermore, CA, UCRL-JC-119610 ABS (1995). Prepared for *2nd Canadian Int'l Workshop on High-Field Laser Plasma Interactions Physics*, Banff, Canada, Feb 22–25, 1995.

Decker, C., Eder, D., and London, R., *Ionization Induced Refraction in Recombination X-Ray Lasers*, Lawrence Livermore National Laboratory, Livermore, CA, UCRL-JC-119324 ABS (1995). Prepared for *Soft X-Ray Lasers and Applications*, San Diego, CA, Jul 9–14, 1995.

DeGroot, J. S., Estabrook, K. G., Williams, E. A., Wilks, S. C., Wallace, R. J., and Stone, G. F., *High Z Hydrides to Simultaneously Suppress Raman and Brillouin in Laser–Plasmas*, Lawrence Livermore National Laboratory, Livermore, CA, UCRL-JC-121459 ABS (1995). Prepared for the *37th Annual Mtg of the American Physical Society Div of Plasma Physics*, Louisville, KY, Nov 6–10, 1995.

DeLoach, L. D., Page, R. H., Wilke, G. D., Payne, S. A., and Krupke, W. F., *Properties of Transition Metal-Doped Zinc Chalcogenide Crystals Evaluated for Tunable IR Laser Radiation*, Lawrence Livermore National Laboratory, Livermore, CA, UCRL-JC-118192 (1995). Prepared for *Advanced Solid State Lasers 10th Topical Mtg*, Memphis, TN, Jan 30–Feb 2, 1995.

DeLoach, L. D., Page, R. H., Wilke, G. D., Payne, S. A., and Krupke, W. F., *Transition Metal-Doped Zinc Chalcogenides: Spectroscopy and Laser Demonstration of a New Class of Gain Media*, Lawrence Livermore National Laboratory, Livermore, CA, UCRL-JC-120816 (1995). Submitted to *IEEE J. Quantum Electron.*

DeLoach, L., *Laser Demonstration of Neodymium–Doped Strontium Chlorovanadate*, Lawrence Livermore National Laboratory, Livermore, CA, UCRL-JC-115592 (1994); *Appl Phys Lett* **65**, 1208–1210 (1994).

Dendooven, P., *A Freon-Filled, Holographic Bubble Chamber as a High-Energy Photon Burst Spectrometer*, Lawrence Livermore National Laboratory, Livermore, CA, UCRL-JC-116184 (1995); *Rev. Sci. Inst.* **66**(1), 571–573 (1995).

Ditmire, T., *Amplification of Femtosecond Pulses to 1 J in $Cr:LiSrAlF_6$*, Lawrence Livermore National Laboratory, Livermore, CA, UCRL-JC-118531 (1995). Prepared for *CLEO '95*, Baltimore, MD, May 15–19, 1995.

Ditmire, T., *Amplification of XUV Harmonic Radiation in a Gallium Amplifier*, Lawrence Livermore National Laboratory, Livermore, CA, UCRL-JC-119550 (1995); *Phys. Rev.* **A51**(6), R4337–R4340 (1995).

Ditmire, T., and Perry, M. D., *Amplification of Femtosecond Pulses to Above 1 J With Large Aperture $Cr:LiSrAlF_6$ Amplifiers*, Lawrence Livermore National Laboratory, Livermore, CA, UCRL-JC-119611 (1995). Prepared for *SPIE's 1995 Int'l Symp on Lasers and Applications*, San Jose, CA, Feb 4–10, 1995.

Ditmire, T., *Calculation and Measurement of High Order Harmonic Energy Yields in Helium*, Lawrence Livermore National Laboratory, Livermore, CA, UCRL-JC-121469 (1995). Submitted to *J. Opt. Soc. Am. B* (1995).

Ditmire, T., Crane, J. K., Nguyen, H., Da Silva, L. B., and Perry, M. D., *Energy-Yield and Conversion-Efficiency Measurements of High Order Harmonic Radiation*, Lawrence Livermore National Laboratory, Livermore, CA, UCRL-JC-118146 (1994); *Phys. Rev. A* **51**(2), R902-R905 (1995).

Ditmire, T., *Energy Yield and Conversion Efficiency Measurements of High Order Harmonic Radiation,* Lawrence Livermore National Laboratory, Livermore, CA, UCRL-JC-118146 (1995); *Phys. Rev.* **A51**(2), R902–R905 (1995).

Ditmire, T., Hutchinson, M. H. R., Key, M. H., Lewis, C. L. S., MacPhee, A., Mercer, I., Neely, D., Perry, M. D., Smith, R. A., Wark, J. S., and Zepf, M., *Amplification of XUV Harmonic Radiation in a Gallium Amplifier,* Lawrence Livermore National Laboratory, Livermore, CA, UCRL-JC-119550 (1995). Submitted to *Phys. Rev. A.*

Ditmire, T., Hutchinson, M. H. R., Key, M. H., Lewis, C. L. S., Mac Phee, A., Mercer, I., Neely, D., Perry, M. D., Smith, R. A., Wark, J. S., and Zepf, M., *Amplification of XUV Harmonic Radiation in a Gallium Amplifier,* Lawrence Livermore National Laboratory, Livermore, CA, UCRL-JC-119550 (1994); *Phys. Rev. A* **51**(6), R4337–R4340 (1995).

Ditmire, T., Kulander, K., Crane, J. K., Nguyen, H., and Perry, M. D., *Calculation and Measurement of High Order Harmonic Energy Yields in Helium,* Lawrence Livermore National Laboratory, Livermore, CA, UCRL-JC-121468 (1995). Submitted to *J. Opt. Soc. Am. B.*

Ditmire, T., Nguyen, H., and Perry, M. D., *Amplification of Femtosecond Pulses to 1 J in Cr:LiSrAlF$_6$,* Lawrence Livermore National Laboratory, Livermore, CA, UCRL-JC-118531 (1995); *Opt. Lett.* **20**(10), 1142–1144 (1995).

Ditmire, T., Nguyen, H., and Perry, M., *Amplification of Femtosecond Pulses to 1 J in Cr:LiSrAlF$_6$,* Lawrence Livermore National Laboratory, Livermore, CA, UCRL-JC-118531 Rev. 1 (1995). Submitted to *Opt. Lett.*

Ditmire, T., Nguyen, H., Perry, M. D., Britten, J., *Amplification of Femtosecond Pulses to 1 J in Cr:LiSrAlF$_6$,* Lawrence Livermore National Laboratory, Livermore, CA, UCRL-JC-118531 ABS (1995). Prepared for *OSA Annual Mtg/ILS-X,* Dallas, TX, Oct 2–7, 1994.

Ditmire, T., Perry, M. D., *Amplification of Femtosecond Pulses to 1 J in Cr:LiSrAlF$_6$,* Lawrence Livermore National Laboratory, Livermore, CA, UCRL-JC-118531 SUM (1995). Prepared for *OSA Annual Mtg/ILS-X,* Dallas, TX, Oct 2–7, 1994.

Dittrich, T. R., and Haan, S. W., *Some Criteria for Designing Robust NIF Capsules,* Lawrence Livermore National Laboratory, Livermore, CA, UCRL-JC-121300 ABS (1995). Prepared for the *37th Annual Mtg of the American Physical Society Div of Plasma Physics,* Louisville, KY, Nov 6–10, 1995.

Dittrich, T. R., Keane, C. J., Hammel, B. A., Haan, S. W., Langer, S. H., Colvin, J., Turner, R. E., Suter, L. J., McEachern, R., Landen, O. L., Levedahl, W. K., Munro, D. H., Cook, R., Wallace, R. J., *Pusher-Fuel Mix in Indirectly Driven Nova ICF Capsule Implosions: Observations and Simulations,* Lawrence Livermore National Laboratory, Livermore, CA, UCRL-JC-119370 ABS (1995). Prepared for *12th Int'l Conf on Laser Interaction and Related Plasma Phenomena '95,* Osaka, Japan, Apr 24–28, 1995.

Dixit, S. M., Rushford, M. C., Thomas, I. M., and Perry, M. D., *Continuous Contour Phase Plates for Tailoring the Focal Plane Irradiance Profile,* Lawrence Livermore National Laboratory, Livermore, CA, UCRL-JC-121127 (1995). Prepared for the *1st Annual Int'l Conf on Solid-State Lasers for Application to Inertial Confinement Fusion,* Monterey, CA, May 30–Jun 2, 1995.

Dixit, S., *Documentation Concerning KPP Development Work,* Lawrence Livermore National Laboratory, Livermore, CA, UCRL-ID-119912 (1995).

Dubois, P. F., *Basis System, Part V: Writing Basis Programs: A Manual For Program Authors,* Lawrence Livermore National Laboratory, Livermore, CA, UCRL-MA-118543, Vol 5 (1995).

Dubois, P. F., *Basis System, Part VI: The Basis Package Library, a Manual for Program Authors,* Lawrence Livermore National Laboratory, Livermore, CA, UCRL-MA-118543, Vol 6 (1995).

Dubois, P. F., Motteler, Z., *Basis System, Part II: Basis Language Reference Manual,* Lawrence Livermore National Laboratory, Livermore, CA, UCRL-MA-118543, Vol 2 (1995).

Duenas, A., Brusasco, R. M., *Accurate, Low Cost Partial Pressure Calibration Apparatus for Use on Mass Spectrometers,* Lawrence Livermore National Laboratory, Livermore, CA, UCRL-JC-119532 ABS (1995). Prepared for the *10th Target Fabrication Specialists Mtg,* Taos, NM, Feb 6–10, 1995.

E

Eddleman, J. L., DeGroot, J. S., Speilman, R. B., Hartman, C. W., Gee, M., Hammer, J. H., Estabrook, K. G., Harte, J. A., Bateson, W. B., and Hewett, D. W., *Effect of Lower Hybrid Instabilities on Radiating Z-Pinches,* Lawrence Livermore National Laboratory, Livermore, CA, UCRL-JC-121461 ABS (1995). Prepared for the *37th Annual Mtg of the American Physical Society Div of Plasma Physics,* Louisville, KY, Nov 6–10, 1995.

Eder, D. C., Amendt, P., Donnelly, T. D., London, R. A., Wilks, S. C., Falcone, R. W., Da Silva, L. B., Rosen, M. D., *Theory of Recombination X-Ray Lasers Based on Optical-Field Ionization,* Lawrence Livermore National Laboratory, Livermore, CA, UCRL-JC-117006 (1994). Prepared for the *4th Int'l Colloquium on X-Ray Lasers,* Williamsburg, VA, May 16–20, 1994.

Ehrlich, R. B., Miller, J. L., Saunders, R. L., Thompson, C. E., Weiland, T. L., and Laumann, C. W., *Precision Nova Operations,* Lawrence Livermore National Laboratory, Livermore, CA, UCRL-JC-120175 (1995). Prepared for *1st Annual Int'l Conf on Solid-State Lasers for Application to Inertial Confinement Fusion,* Monterey, CA, May 30–Jun 2, 1995.

Ehrlich, R. B., Weiland, T. L., Saunders, R. L., Laumann, C. W., Thompson, C. E., and Miller, J. L., *Precision Nova Operations,* Lawrence Livermore National Laboratory, Livermore, CA, UCRL-JC-120175 ABS (1995). Prepared for *Solid-State Lasers for Application to Inertial Confinement Fusion (ICF) 1st Annual Int'l Conf,* Monterey, CA, May 30–Jun 2, 1995.

Eimerl, D., *Configuring the National Ignition Facility for Direct-Drive Experiments,* Lawrence Livermore National Laboratory, Livermore, CA, UCRL-ID-120758 (1995).

Eimerl, D., Rothenberg, J., Key, M., Weber, S., Verdon, C., Skupsky, S., Soures, J., and Craxton, S., *Configuring NIF for Direct Drive Experiments,* Lawrence Livermore National Laboratory, Livermore, CA, UCRL-JC-121271 (1995). Prepared for the *1st Annual Int'l Conf on Solid-State Lasers for Application to Inertial Confinement Fusion,* Monterey, CA, May 30–Jun 2, 1995.

English, R. E., Aikens, D. M., Whistler, W. T., Walmer, C. D., and Maney, R. T., *Implementation of ISO 10110 Optics Drawing Standards for the National Ignition Facility,* Lawrence Livermore National Laboratory, Livermore, CA, UCRL-JC-121608 (1995). Prepared for the *Society of Photo-Optical Instrumentation Engineers 40th Annual Mtg,* San Diego, CA, Jul 9–14, 1995.

English, R. E., *Trip Report—Assessment of CILAS Interferometer,* Lawrence Livermore National Laboratory, Livermore, CA, UCRL-ID-120250 (1995).

Erlandson, A. C., Rotter, M. D., Frank, D. N., and McCracken, R. W., *Design and Performance of the Beamlet Amplifiers,* Lawrence Livermore National Laboratory, Livermore, CA, UCRL-ID-119931 (1995).

Estabrook, K. G., Glenzer, S., Back, C., Montgomery, D., Kornblum, H., Kirkwood, B., MacGowan, B., and Moody, J., *Quarter Critical Resonance in Gasbags,* Lawrence Livermore National Laboratory, Livermore, CA, UCRL-JC-121460 ABS (1995). Prepared for the *37th Annual Mtg of the American Physical Society Div of Plasma Physics,* Louisville, KY, Nov 6–10, 1995.

F

Feit, M. D., Garrison, J. C., and Rubenchik, A. M., *Intense Beam Channeling in Underdense Plasmas,* Lawrence Livermore National Laboratory, Livermore, CA, UCRL-JC-120188 ABS (1995). Prepared for *Solid-State Lasers for Application to Inertial Confinement Fusion (ICF) 1st Annual Int'l Conf,* Monterey, CA, May 30–Jun 2, 1995.

Feit, M. D., Musher, S., Rubenchik, A. M., and Shapiro, E., *Increased Glass Damage Thresholds Due to the Modulation of the Laser Pulse,* Lawrence Livermore National Laboratory, Livermore, CA, UCRL-JC-120186 ABS (1995). Prepared for *Solid-State Lasers for Application to Inertial Confinement Fusion (ICF) 1st Annual Int'l Conf,* Monterey, CA, May 30–Jun 2, 1995.

Feit, M. D., Rubenchik, A. M., Stuart, B. C., Perry, M. D., Shore, B. W., *Laser Induced Damage in Dielectrics with Nanosecond to Subpicosecond Pulses: II Theory,* Lawrence Livermore National Laboratory, Livermore, CA, UCRL-JC-118156 (1995). Prepared for *Laser-Induced Damage in Optical Materials Conf,* Boulder, CO, Oct 24–26, 1994.

Fessenden, T. J., Grote, D. P., and Sharp, W. M., *Accelerator Waveform Synthesis and Longitudinal Beam Dynamics in a Small Induction Recirculator,* Lawrence Livermore National Laboratory, Livermore, CA, UCRL-JC-119580 (1995). Prepared for *IEEE 1995 Particle Accelerator Conf,* Dallas, TX, May 1–5, 1995.

Fessenden, T., Grote, D., and Sharp, W., *Accelerator Waveform Synthesis and Longitudinal Beam Dynamics in a Small Induction Recirculator,* Lawrence Livermore National Laboratory, Livermore, CA, UCRL-JC-119580 ABS (1995). Prepared for *IEEE 1994 PAC,* Dallas, TX, May 1–5, 1995.

Foster, J. M., Rosen, P. A., Dunne, A. M., Stevenson, R. M., Shepard, T. D., and Orzechowski, T. J., *Interface Motion in Gas-Tamped Laser-Heated Hohlraums,* Lawrence Livermore National Laboratory, Livermore, CA, UCRL-JC-121601 ABS (1995). Prepared for the *37th Annual Mtg of the American Physical Society Div of Plasma Physics,* Louisville, KY, Nov 6–10, 1995.

Foster, J. M., Rosen, P. A., Levedahl, W. K., Shepard, T. D., Orzechowski, T. J., *Interface Motion in CH-Lined and Gas-Filled Laser-Heated Hohlraums,* Lawrence Livermore National Laboratory, Livermore, CA, UCRL-JC-118545 ABS (1995). Prepared for the *36th Mtg of the APS Div of Plasma Physics,* Minneapolis, MN, Nov 7–11, 1994.

G

Galakhov, I. V., Gruzin, I. A., Gudov, S. N., Kirillov, G. A., Logutenko, S. L., Murugov, V. M., Osin, V. A., and Zolotovskii, V. I., *Final Report Task Order No. B239641 between Regents of the University of California and Institute of Experimental Physics Task 2: Switch Development,* Lawrence Livermore National Laboratory, Livermore, CA, UCRL-CR-120302 (1995), p 2.

Galakhov, I. V., Kirillov, G. A., and Murugov, V. M., *Final Report Task Order No. B239641 between Regents of the University of California and Institute of Experimental Physics Task 1: Conceptual Design,* Lawrence Livermore National Laboratory, Livermore, CA, UCRL-CR-120302 (1995), p 1.

Gavel, D. T., Mast, J. E., Warhus, J., and Azevedo, S. G., *An Impulse Radar Array for Detecting Land Mines,* Lawrence Livermore National Laboratory, Livermore, CA, UCRL-JC-120550 (1995). Prepared for *Autonomous Vehicles in Mine Countermeasures, Naval Postgraduate School,* Monterey, CA, Apr 4–7, 1995.

Glendinning, S. G., Amendt, P., Budil, K. S., Hammel, B. A., Kalantar, D. H., Key, M. H., Landen, O. L., Remington, B. A., and Desenne, D. E., *Laser–Plasma Diagnostics of Dense Plasmas,* Lawrence Livermore National Laboratory, Livermore, CA, UCRL-JC-121494 (1995). Prepared for the *Society of Photo-Optical Instrumentation Engineers Conf on Applications of Laser Plasma Radiation II,* San Diego, CA, Jul 9–14, 1995.

Glendinning, S. G., Powers, L. V., Landen, O. L., Hammel, B. A., Kauffman, R. A., Suter, L. J., Richard, A. L., and Stone, G., *Drive Symmetry Measurements in Gas-Filled Hohlraum,* Lawrence Livermore National Laboratory, Livermore, CA, UCRL-JC-121609 ABS (1995). Prepared for the *37th Annual Mtg of the American Physical Society Div of Plasma Physics,* Louisville, KY, Nov 6–10, 1995.

Glenzer, S. H., Back, C. A., Estabrook, K., MacGowan, B. J., Montgomery, D. S., Moody, J. D., and Stone, G. F., *Electron Temperature and Density Measurements in Gasbag Plasmas by X-Ray Spectroscopy,* Lawrence Livermore National Laboratory, Livermore, CA, UCRL-JC-121498 ABS (1995). Prepared for the *37th Annual Mtg of the American Physical Society Div of Plasma Physics,* Louisville, KY, Nov 6–10, 1995.

Glinsky, M. E., Bailey, D., Belak, J., Eder, D., London, R. A., Zimmerman, G. B., Antoun, T., Curran, D. R., Seaman, L., and Jacques, S. L., *Medical Applications of Stress Wave Propagation and Material Failure Physics,* Lawrence Livermore National Laboratory, Livermore, CA, UCRL-JC-121278 ABS (1995). Prepared for *American Physical Society Topical Conf,* Seattle, WA, Aug 13–16, 1995.

Glinsky, M. E., London, R. A., Zimmerman, G. B., and Jacques, S. L., *Computer Modeling of Endovascular Patch Welding Using Temperature Feedback,* Lawrence Livermore National Laboratory, Livermore, CA, UCRL-JC-120751 ABS (1995). Prepared for *BiOS Europe '95,* Barcelona, Spain, Sept 12–16, 1995.

Glinsky, M. E., London, R. A., Zimmerman, G. B., and Jacques, S. L., *Modeling of Endovascular Patch Welding Using the Computer Program LATIS,* Lawrence Livermore National Laboratory, Livermore, CA, UCRL-JC-120178 (1995). Prepared for the *Society of Photo-Optical Instrumentation Engineers' 1995 Int'l Symp on Lasers and Applications/Biomedical Optics,* San Jose, CA, Feb 4–10, 1995.

Glinsky, M., *Diversification and Strategic Management of LLNL's R&D Portfolio,* Lawrence Livermore National Laboratory, Livermore, CA, UCRL-ID-119576 (1995).

Glinsky, M., Matthews, D. L., *Your Solutions for Highest Brightness and Power Laser X-Ray Sources,* Lawrence Livermore National Laboratory, Livermore, CA, UCRL-TB-118541 (1995).

Glinsky, M., *Regimes of Suprathermal Electron Transport,* Lawrence Livermore National Laboratory, Livermore, CA, UCRL-JC-118514 (1995); *Phys. Plasmas* **2**(7), 2796–2806 (1995).

Green, M., Peterson, N., Sato, T., Teramoto, A., Cook, R., and Lifson, S., *A Helical Polymer with a Cooperative Response to Chiral Information,* Lawrence Livermore National Laboratory, Livermore, CA, UCRL-JC-121098 (1995); *Science* **268**, 1860-1866 (1995).

Grote, D. P., Friedman, A., and Haber, I., *Three Dimensional Simulations of a Small Induction Recirculator Accelerator,* Lawrence Livermore National Laboratory, Livermore, CA, UCRL-JC-119579 (1995). Prepared for *IEEE 1995 Particle Accelerator Conf,* Dallas, TX, May 1–5, 1995.

Grote, D. P., Friedman, A., Haber, I., and Yu, S., *Three-Dimensional Simulations of High-Current Beams in Induction Accelerators with WARP3D,* Lawrence Livermore National Laboratory, Livermore, CA, UCRL-JC-121280 (1995). Prepared for the *Int'l Symp on Heavy Ion Fusion,* Princeton, NJ, Sept 6–9, 1995.

Grote, D. P., Friedman, A., Haber, I., and Yu, S., *Three-Dimensional Simulations of High-Current Beams in Induction Accelerators with WARP3D,* Lawrence Livermore National Laboratory, Livermore, CA, UCRL-JC-121280 ABS (1995). Prepared for *Int'l Symp on Heavy Ion Inertial Fusion,* Princeton, NJ, Sept 6–9, 1995.

Grote, D. P., Sharp, W., Fessenden, T., *End Dynamics of Intense Ion Beams During Acceleration and Compression,* Lawrence Livermore National Laboratory, Livermore, CA, UCRL-JC-119369 ABS (1995). Prepared for the *IEEE 1994 PAC,* Dallas, TX, May 1–5, 1995.

Grote, D. P., *Three Dimensional Simulations of Space Charge Dominated Heavy Ion Beams with Applications to Inertial Fusion Energy,* Lawrence Livermore National Laboratory, Livermore, CA, UCRL-LR-119363 (1995).

Grote, D. P., *Three-Dimensional Simulations of the Small Recirculator Experiment: Injection and Dipole Plate Design,* Lawrence Livermore National Laboratory, Livermore, CA, UCRL-JC-119367 ABS (1995). Prepared for the *IEEE 1994 PAC,* Dallas, TX, May 1–5, 1995.

Grote, D., Friedman, A., and Haber, I., *Three-Dimensional Simulations of a Small Induction Recirculator Accelerator,* Lawrence Livermore National Laboratory, Livermore, CA, UCRL-JC-119579 ABS (1995). Prepared for *IEEE 1994 PAC,* Dallas, TX, May 1–5, 1995.

H

Haan, S. W., *Modeling of NIF Ignition Targets with Irradiation Asymmetry and Short-Wavelength Hydrodynamic Instabilities,* Lawrence Livermore National Laboratory, Livermore, CA, UCRL-JC-121810 ABS (1995). Prepared for the *Nuclear Explosives Design Physics Conf (NEDPC),* Los Alamos, NM, Oct 30–Nov 3, 1995.

Haan, S. W., Pollaine, S. M., Chandler, E. A., and Strobel, G. L., *Implosion Modeling of Indirect Drive Ignition Targets for the National Ignition Facility,* Lawrence Livermore National Laboratory, Livermore, CA, UCRL-JC-121464 ABS (1995). Prepared for the *37th Annual Mtg of the American Physical Society Div of Plasma Physics,* Louisville, KY, Nov 6–10, 1995.

Haan, S. W., Pollaine, S. M., Lindl, J. D., Suter, L. J., Berger, R. L., Powers, L. V., Alley, W. E., Amendt, P. A., Futterman, J. J., Levedahl, W. K., Rosen, M. D., Rowley, D. P., Sacks, R. A., Shestakov, A. I., Strobel, G. L., Tabak, M., Weber, S. V., Zimmerman, G. B., Krauser, W. J., Wilson, D. C., Coggeshell, S. V., Harris, D. B., Hoffman, N. M., and Wilde, B. H., *Design and Modeling of Ignition Targets for the National Ignition Facility,* Lawrence Livermore National Laboratory, Livermore, CA, UCRL-JC-117034 (1994); *Phys. Plasmas* **2**(6), 2480–2487 (1995).

Haan, S. W., Strobel, G. L., Pollaine, S. M., and Marinak, M. M., *Hydrodynamic Instability Modeling on Ignition ICF Capsules,* Lawrence Livermore National Laboratory, Livermore, CA, UCRL-JC-120888 ABS (1995). Prepared for *5th Int'l Workshop on the Physics of Compressible Turbulent Mixing,* Stonybrook, NY, Jul 18–21, 1995.

Haan, S., *Design and Modeling of Ignition Targets for the National Ignition Facility,* Lawrence Livermore National Laboratory, Livermore, CA, UCRL-JC-117034 (1995); *Phys. Plasmas* **2**(6), 2480–2487 (1995).

Haddad, W. S., Trebes, J. E., Goodman, D. M., Lee, H.-R., McNulty, I., Anderson, E. H., and Zalensky, A. O., *Ultra High Resolution Soft X-Ray Tomography,* Lawrence Livermore National Laboratory, Livermore, CA, UCRL-JC-121622 (1995). Prepared for the *Society of Photo-Optical Instrumentation Engineers 1995 Int'l Society for Optical Engineering and Instrumentation,* San Diego, CA, Jul 9–14, 1995.

Hammer, J. H., and Mattor, N., *Magnetic Fast Ignition,* Lawrence Livermore National Laboratory, Livermore, CA, UCRL-JC-121809 ABS (1995). Prepared for the *Advanced Approaches to Economical Fusion Power Conf,* Monterey, CA, Sept 11–15, 1995.

Hammer, J., Eddleman, J., Estabrook, K., Osterheld, A., Springer, P., Tabak, M., Toor, A., Wilson, B., Zimmerman, G., DeGroot, J., Allshouse, G., Humphries, R., Matsen, K., Sanford, T., and Speilman, R., *2D MHD Simulations of Radiating Z-Pinch Dynamics with LASNEX,* Lawrence Livermore National Laboratory, Livermore, CA, UCRL-JC-121482 ABS (1995). Prepared for the *37th Annual Mtg of the American Physical Society Div of Plasma Physics,* Louisville, KY, Nov 6–10, 1995.

Hermes, G. L., *Nova Experimenters Users Guide,* Lawrence Livermore National Laboratory, Livermore, CA, UCRL-MA-121291 Rev 1 (1995).

Hinkel, D. E., Williams, E. A., and Berger, R. L., *Stimulated Brillouin Backscatter of Short-Pulse Lasers,* Lawrence Livermore National Laboratory, Livermore, CA, UCRL-JC-117056 ABS Rev. 1 (1995). Prepared for the *2nd Canadian Int'l Workshop on High-Field Laser Plasma Interactions Physics,* Canada, Feb 22–25, 1995.

Hinkel, D. E., Williams, E. A., Berger, R. L., and Powers, L .V., *Laser Beam Deflection Induced by Transverse Plasma Flow,* Lawrence Livermore National Laboratory, Livermore, CA, UCRL-JC-121493 ABS (1995). Prepared for the *37th Annual Mtg of the American Physical Society Div of Plasma Physics,* Louisville, KY, Nov 6–10, 1995.

Hinkel, D. E., Williams, E. A., Berger, R. L., and Powers, L. V., *Beam Steering Induced by Transverse Plasma Flow,* Lawrence Livermore National Laboratory, Livermore, CA, UCRL-JC-120771 ABS (1995). Prepared for *25th Annual Anomalous Absorption Conf,* Aspen, CO, May 27–Jun 1, 1995.

Hinkel, D. E., Williams, E. A., Berger, R. L., *Stimulated Brillouin Backscatter of a Short-Pulse Laser,* Lawrence Livermore National Laboratory, Livermore, CA, UCRL-JC-117056 (1995). Prepared for the *36th Annual Mtg APS Div of Plasma Physics,* Minneapolis, MN, Nov 7–11, 1994.

Ho, D. D. M., Harte, J. A., Tabak, M., *Configurations of Radiation-Driven Targets for Heavy-Ion Fusion,* Lawrence Livermore National Laboratory, Livermore, CA, UCRL-JC-119546 (1995). Submitted to *Nuclear Fusion.*

Ho, D., *Autoneutralization of Space-Charge-Dominated Beams for Heavy-Ion Fusion,* Lawrence Livermore National Laboratory, Livermore, CA, UCRL-JC-120830 (1995). Submitted to *Nuclear Fusion.*

Honea, E. C., Collins, G. W., McEachern, R. L., and Wallace, R. J., *Surface Roughness Scaling in Sputter-Deposited Beryllium and Beryllium-Boron Films,* Lawrence Livermore National Laboratory, Livermore, CA, UCRL-JC-121145 ABS (1995). Prepared for *Material Research Society 1995 Fall Mtg,* Boston, MA, Nov 27–Dec 1, 1995.

Honea, E., Correll, D., *ICF Quarterly Report* 4(4), Lawrence Livermore National Laboratory, Livermore, CA, UCRL-LR-105821-94-4 (1994).

Hsieh, E. J., Behymer, R. D., Greenfield, B. J., and Lindsey, E. F., *Properties of Be Films Sputter Coated onto Hemispherical Substrates under Various Conditions Including Gas Pulsing,* Lawrence Livermore National Laboratory, Livermore, CA, UCRL-JC-120892 ABS (1995). Prepared for *42nd Nat'l Symp of the American Vacuum Society,* Minneapolis, MN, Oct 16–20, 1995.

Hsieh, E. J., Behymer, R. D., Spragge, M. R., Wallace, R. J., Sanchez, J. J., *Strength and Other Information on Hitachi L-100 Polyimide Films,* Lawrence Livermore National Laboratory, Livermore, CA, UCRL-JC-119400 ABS (1995). Prepared for the *10th Target Fabrication Specialists Mtg,* Taos, NM, Feb 6–10, 1995.

J

Johnson, R. R., *Laser Fusion Efforts in the United States,* Lawrence Livermore National Laboratory, Livermore, CA, UCRL-JC-117893 (1994); *Optics and Photonics News* **6**(3), 16–23 (1995).

Judd, D. L., Rintamaki, J., Lund, S. M., Barnard, J. J., Fessenden, T., Grote, D. P., and Deadrick, F. J., *Heavy Ion Fusion Notes 94-1 through 94-9,* Lawrence Livermore National Laboratory, Livermore, CA, UCRL-ID-120197 (1995).

K

Kaiser, T. B., Afeyan, B. B., Berger, R. L., and Kruer, W. L., *Near-Forward Stimulated Brillouin Scattering and Filamentation Simulations with F3D,* Lawrence Livermore National Laboratory, Livermore, CA, UCRL-JC-121298 ABS (1995). Prepared for the *37th Annual Mtg of the American Physical Society Div of Plasma Physics,* Louisville, KY, Nov 6–10, 1995.

Kalantar, D. H., Barbee, T. W., Da Silva, L. B., Glendinning, S. G., Key, M. H., Knauer, J. P., Weber, F., and Weber, S. V., *XUV Laser Radiography of Perturbations due to Imprint of Laser Speckle in 0.35 μm Laser Irradiation of a Thin Si Foil,* Lawrence Livermore National Laboratory, Livermore, CA, UCRL-JC-121625 (1995). Submitted to *Rev. Sci. Instrum.*

Kalantar, D. H., Budil, K. S., Hammel, B. A., Landen, O. L., and Keane, C. J., *X-Ray Backlit Imaging of an Implosion Core to Measure the In-Flight Pusher Density of an Indirect Drive Capsule,* Lawrence Livermore National Laboratory, Livermore, CA, UCRL-JC-121491 ABS (1995). Prepared for the *37th Annual Mtg of the American Physical Society Div of Plasma Physics,* Louisville, KY, Nov 6–10, 1995.

Kalantar, D. H., Da Silva, L. B., Glendinning, S. G., Key, M. H., Weber, F., Weber, S. V., and Knauer, J. P., *X-Ray Laser Backlighting Applied to Measure Laser Imprint,* Lawrence Livermore National Laboratory, Livermore, CA, UCRL-JC-120244 ABS (1995). Prepared for *25th Annual Anomalous Absorption Conf,* Aspen, CO, May 27–Jun 1, 1995.

Kalantar, D. H., Da Silva, L. B., Glendinning, S. G., Key, M. H., Weber, F., Weber, S. V., and Knauer, J. P., *XUV Probing of Laser Imprint Using an Yttrium X-Ray Laser,* Lawrence Livermore National Laboratory, Livermore, CA, UCRL-JC-121492 ABS (1995). Prepared for the *37th Annual Mtg of the American Physical Society Div of Plasma Physics,* Louisville, KY, Nov 6–10, 1995.

Kalantar, D., *Production and Characterization of Large Plasmas from Gas Bag Targets on Nova,* Lawrence Livermore National Laboratory, Livermore, CA, UCRL-JC-119910 (1995); *Phys. Plasmas* **2**(8), 3161–3168 (1995).

Kalantar, D., *X-Ray Imaging of Uniform Large Scale-Length Plasmas Created from Gas-Filled Targets on Nova,* Lawrence Livermore National Laboratory, Livermore, CA, UCRL-JC-116195 (1995); *Rev. Sci. Inst.* **66**(1), 782–784 (1995).

Kane, J., Arnett, D., Remington, B. A., Dearborn, D., Rubenchik, A., Castor, J., Woosley, S., Wood-Vasey, M., Liang, E. P., and London, R., *Simulations of a Supernova-Relevant Hydrodynamic Instability Experiment on the Nova Laser,* Lawrence Livermore National Laboratory, Livermore, CA, UCRL-JC-121487 ABS (1995). Prepared for the *37th Annual Mtg of the American Physical Society Div of Plasma Physics,* Louisville, KY, Nov 6–10, 1995.

Karpenko, V., Barnard, J., Friedman, A., Lund, S., Nattrass, L., Newton, M., Sangster, C., Fessenden, T., Ward, C., Grote, D., Deadrick, F., Meredith, J., Nelson, M., Repose, G., Sharp, W., and Longinotti, D., *Mechanical Design of Recirculating Induction Accelerator Experiments for Heavy-Ion Fusion,* Lawrence Livermore National Laboratory, Livermore, CA, UCRL-JC-119583 ABS (1995). Prepared for the *IEEE 1995 PAC,* Dallas, TX, May 1–5, 1995.

Kauffman, R. L., *Review of Hohlraum Coupling,* Lawrence Livermore National Laboratory, Livermore, CA, UCRL-JC-118517 (1994). Prepared for the *23rd European Conf on Laser Interaction with Matter,* Oxford, UK, Sept 19–23, 1994.

Kauffman, R., *Drive Characterization of Indirect Drive Targets on the Nova Laser,* Lawrence Livermore National Laboratory, Livermore, CA, UCRL-JC-116765 (1995); *Rev. Sci. Inst.* **66**(1), 678–682 (1995).

Keane, C. J., Landen, O. L., Hammel, B. A., Cable, M., Cook, R., Dittrich, T., Haan, S., Hatchett, S. P., McEachern, R., Murphy, T., Nelson, M., Suter, L., Wallace, R., Chrien, R., Colvin, J., Hoffman, N., Hsing, W., and Pollak, G., *Nova High Growth Factor Implosion Experiments and Analysis,* Lawrence Livermore National Laboratory, Livermore, CA, UCRL-JC-120800 ABS (1995). Prepared for *25th Annual Anomalous Absorption Conf, Aspen,* CO, May 27–Jun 1, 1995.

Keane, C. J., Pollak, G. W., Cook, R. C., Dittrich, T. R., *X-Ray Spectroscopic Diagnostics of Mix in High Growth Factor Spherical Implosions,* Lawrence Livermore National Laboratory, Livermore, CA, UCRL-JC-119917 (1995); *J. Quant. Spectros. & Radiat. Transfer* **54**(7/8), 207–220 (1995).

Keane, C., *Diagnosis of Pusher–Fuel Mix in Spherical Implosions Using X-Ray Spectroscopy,* Lawrence Livermore National Laboratory, Livermore, CA, UCRL-JC-116787 (1995); *Rev. Sci. Inst.* **66**(1), 689–696 (1995).

Kershaw, D. S., Prasad, M. K., Shaw, M. J., *3D Unstructured Mesh ALE Hydrodynamics with the Upwind Discontinuous Finite Element Method,* Lawrence Livermore National Laboratory, Livermore, CA, UCRL-JC-122104 (1995). Submitted to *J. Comput. Phys.*

Key, M. H., Barbee, T. W., Da Silva, L. B., and Glendinning, S. G., *New Plasma Diagnostic Possibilities from Radiography with XUV Lasers,* Lawrence Livermore National Laboratory, Livermore, CA, UCRL-JC-118848 (1995); *J. Quant. Spectros. & Radiat. Transfer* **54**(1/2), 221–226 (1995).

Key, M. H., Kalantar, D. H., Barbee, T. W., Da Silva, L. B., Glendinning, S. G., Knauer, J. P., Remington, B. A., Rose, S. J., Weber, F. A., and Weber, S. V., *Measurement by XUV Laser Radiography of Hydrodynamic Perturbations in Laser Accelerated Thin Foil Targets,* Lawrence Livermore National Laboratory, Livermore, CA, UCRL-JC-121586 (1995). Prepared for the *Society of Photo-Optical Instrumentation Engineers, Soft X-Ray Lasers and Applications,* San Diego, CA, Jul 9–14, 1995.

Kilkenny, J. D., LANL ICF Team, LLNL ICF Team, *X-Ray Driven Implosions on the Nova Laser,* Lawrence Livermore National Laboratory, Livermore, CA, UCRL-JC-116192 ABS, Rev 1 (1995). Prepared for *Evaluation of Current Trends in Fusion Rsch,* Washington, DC, Nov 14–18, 1994.

Kirkwood, R. K., Afeyan, B. B., Kruer, W. L., MacGowan, B. J., Montgomery, D. S., Moody, J. D., and Wilks, S. C., *Observation of Energy Transfer between Frequency Mismatched Laser Beams in a Large Scale Plasma,* Lawrence Livermore National Laboratory, Livermore, CA, UCRL-JC-120249 ABS (1995). Prepared for *25th Annual Anomalous Absorption Conf,* Aspen, CO, May 27–Jun 1, 1995.

Kirkwood, R. K., Afeyan, B. B., Kruer, W. L., MacGowan, B. J., Montgomery, D. S., Moody, J. D., Pennington, D. M., and Wilks, S. C., *Observation of Energy Transfer between Frequency Mismatched Laser Beams in a Large Scale Plasma,* Lawrence Livermore National Laboratory, Livermore, CA, UCRL-JC-120249 ABS Rev 1 (1995). Prepared for the *37th Annual Mtg of the American Physical Society Div of Plasma Physics,* Louisville, KY, Nov 6–10, 1995.

Kirkwood, R. K., Afeyan, B. B., Kruer, W. L., MacGowan, B. J., Moody, J. D., Montgomery, D. S., Pennington, D. M., Weiland, T. L., and Wilks, S. C., *Observation of Energy Transfer between Frequency Mismatch Laser Beams in a Large Scale Plasma,* Lawrence Livermore National Laboratory, Livermore, CA, UCRL-JC-122102 (1995). Submitted to *Phys. Rev. Lett.*

Kirkwood, R. K., Back, C. A., Estabrook, K. G., Kalantar, D. H., MacGowan, B. J., Montgomery, D. S., and Moody, J. D., *Imaging of Near to Back Scattered Light in Gas Target Plasmas,* Lawrence Livermore National Laboratory, Livermore, CA, UCRL-JC-120248 ABS (1995). Prepared for *25th Annual Anomalous Absorption Conf,* Aspen, CO, May 27–Jun 1, 1995.

Kruer, W. L., and Wilks, S. C., *Higher Temperature Hohlraums Using Laser Beam Smoothing,* Lawrence Livermore National Laboratory, Livermore, CA, UCRL-JC-121287 ABS (1995). Prepared for *37th Annual Meeting of the American Physical Society Division of Plasma Physics,* Louisville, KY, Nov 6–10, 1995.

Kruer, W. L., and Wilks, S. C., *Novel Techniques to Control Stimulated Raman and Brillouin Scattering in Laser Plasmas,* Lawrence Livermore National Laboratory, Livermore, CA, UCRL-JC-120876 ABS (1995). Prepared for *25th Annual Anomalous Absorption Conf,* Aspen, CO, May 27–Jun 1, 1995.

Kruer, W. L., *Control of Laser–Plasma Instabilities in Hohlraums,* Lawrence Livermore National Laboratory, Livermore, CA, UCRL-JC-121584 ABS (1995). Prepared for *La Jolla Summer School '95, La Jolla Int'l School of Physics,* La Jolla, CA, Aug 8–18, 1995.

Kruer, W. L., *Interaction of Intense Laser Light with Matter,* Lawrence Livermore National Laboratory, Livermore, CA, UCRL-JC-119375 ABS (1995). Prepared for *UCLA Physics Dept Seminar,* Los Angeles, CA, Dec 9–10, 1994.

Kruer, W. L., *Laser Beam Deflection in Self-Consistent Flow Profiles,* Lawrence Livermore National Laboratory, Livermore, CA, UCRL-JC-121481 ABS (1995). Prepared for the *37th Annual Mtg of the American Physical Society Div of Plasma Physics,* Louisville, KY, Nov 6–10, 1995.

Kruer, W. L., *Laser Physics Issues for the Ignition Target Design,* Lawrence Livermore National Laboratory, Livermore, CA, UCRL-JC-118529 (1995). Submitted to *Comments on Plasma Physics.*

Kruer, W. L., *Laser Plasma Interactions in Hohlraums,* Lawrence Livermore National Laboratory, Livermore, CA, UCRL-JC-118752 (1994). Prepared for the *45th Scottish Universities Summer School in Physics Laser Plasma Interactions,* St. Andrews, Scotland, Aug 7–13, 1994.

Kruer, W. L., *Laser-Induced Circulating Currents,* Lawrence Livermore National Laboratory, Livermore, CA, UCRL-JC-117870 ABS (1995). Prepared for the *36th Annual Mtg APS Div of Plasma Physics,* Minneapolis, MN, Nov 7–11, 1994.

Kruer, W. L., Wilks, S. C., Afeyan, B. B., and Kirkwood, R. K., *Energy Transfer between Crossing Laser Beams,* Lawrence Livermore National Laboratory, Livermore, CA, UCRL-JC-120776 (1995). Submitted to *Physics of Plasmas.*

Kruer, W. L., Wilks, S. C., Afeyan, B. B., and Kirkwood, R. K., *Energy Transfer between Crossing Laser Beams,* Lawrence Livermore National Laboratory, Livermore, CA, UCRL-JC-120776 Rev 1 (1995). Submitted to *Phys. of Plasmas.*

Kruer, W. L., Wilks, S. C., Kirkwood, R., and Afeyan, B., *Energy Transfer between Crossing Laser Beams,* Lawrence Livermore National Laboratory, Livermore, CA, UCRL-JC-120776 ABS (1995). Prepared for *25th Annual Anomalous Absorption Conf,* Aspen, CO, May 27–Jun 1, 1995.

L

Labaune, C., Baldis, H. A., Schifano, E., Renard, N., Baton, S. D., Michard, A., Seka, W., Bahr, R., Bauer, B. S., Baker, K., and Estabrook, K., *Strongly Driven Ion Acoustic Waves in Laser Produced Plasmas,* Lawrence Livermore National Laboratory, Livermore, CA, UCRL-JC-118835 Rev. 1 (1995). Submitted to *Phys. Rev. Lett.*

Lambert, S., Overturf, G., Cook, B., and Schroen-Carey, D., *EGDM Foam Shell Status Report (TAT 95-049),* Lawrence Livermore National Laboratory, Livermore, CA, UCRL-ID-121332 (1995).

Land, T. A., De Yoreo, J. J., and Lee, J. D., *Growth Morphology of Vicinal Hillocks on the (101) Face of KH_2PO_4: Evidence of Surface Diffusion,* Lawrence Livermore National Laboratory, Livermore, CA, UCRL-JC-119608 ABS (1995). Prepared for *Materials Research Society Conf,* Boston, MA, Nov 27–Dec 1, 1995.

Land, T. A., De Yoreo, J. J., Lee, J. D., and Ferguson, J. R., *Growth Morphology of Vicinal Hillocks on the (101) Face of KH_2PO_4: Evidence of Surface Diffusion,* Lawrence Livermore National Laboratory, Livermore, CA, UCRL-JC-119608 (1994). Prepared for *Materials Research Society,* Boston, MA, Dec 5–9, 1994.

Land, T. A., De Yoreo, J. J., Malkin, A. J., Lee, J. D., Kuznetsov, Y. G., and McPherson, A., *Growth Mechanisms and Morphologies of Solution-Based Crystals: An AFM Perspective,* Lawrence Livermore National Laboratory, Livermore, CA, UCRL-JC-119905 EXT ABS (1995). Prepared for *Scanning '95,* Monterey, CA, Mar 28–31, 1995.

Land, T. A., De Yoreo, J. J., Malkin, A. J., Lee, J. D., Kuznetsov, Yu. G., and McPherson, A., *Growth Mechanisms and Morphologies of Solution-Based Crystals: an AFM Perspective – II,* Lawrence Livermore National Laboratory, Livermore, CA, UCRL-JC-120239 ABS (1995). Prepared for *14th Conf on Crystal Growth and Epitaxy,* Fallen Leaf Lake, CA, Jun 4–7, 1995.

Land, T. A., Malkin, A. J., Kuznetsov, Yu. G., McPherson, A., and De Yoreo, J. J., *Mechanisms of Protein and Virus Crystal Growth: An Atomic Force Microscopy Study of Canavalin,* Lawrence Livermore National Laboratory, Livermore, CA, UCRL-JC-120183 (1995). Prepared for *ICCG XI,* The Hague, Netherlands, June 18–21, 1995.

Land, T. A., Malkin, A., Kuznetsov, Y. G., De Yoreo, J. J., and McPherson, A., *Investigation of Canavalin Crystallization Using In-Situ Atomic Force Microscopy,* Lawrence Livermore National Laboratory, Livermore, CA, UCRL-JC-121141 ABS (1995). Prepared for *6th Int'l Conf on Crystallization of Biological Macromolecules (ICCBM-6),* Hiroshima, Japan, Nov 12–17, 1995.

Landen, O. L., Abare, A., Bell, P. M., Bradley, D. K., Hammel, B. A., *Detailed Measurements and Shaping of Gate Profiles for Microchannel-Plate-Based X-Ray Framing,* Lawrence Livermore National Laboratory, Livermore, CA, UCRL-JC-115937 (1994). Prepared for *SPIE Int'l Symp on Optical Instrumentation & Applied Science,* San Diego, CA, Jul 24–29, 1994.

Landen, O. L., Bell, P. M., Kalantar, D. H., and Bradley, D. K., *X-Ray Framing Cameras for >5 keV Imaging,* Lawrence Livermore National Laboratory, Livermore, CA, UCRL-JC-119326 (1995). Prepared for the *Society of Photo-Optical Instrumentation Engineers' 1995 Int'l Symp on Optical Science, Engineering, and Instrumentation,* San Diego, CA, Jul 9–14, 1995.

Landen, O. L., Keane, C. J., Cable, M. D., Dittrich, T. R., Hatchett, S. P., Lerche, R. A., McEachern, R., Nelson, M. B., Wallace, R. J., Cook, R., Hammel, B. A., Haan, S. W., Hay, R. G., Levedahl, W. K., Murphy, T. J., Suter, L., *High Growth Factor Indirectly Driven ICF Implosions on Nova,* Lawrence Livermore National Laboratory, Livermore, CA, UCRL-JC-118832 ABS (1995). Prepared for *Radiative Properties of Hot Dense Matters,* Sarasota, FL, Oct 31–Nov 4, 1994.

Landen, O. L., Keane, C. J., Hammel, B. A., Cable, M. D., Colvin, J., Cook, R., Dittrich, T. R., Haan, S. W., Hatchett, S. P., Hay, R. G., Kilkenny, J. D., Lerche, R. A., Levedahl, W. K., McEachern, R., Murphy, T. J., Nelson, M. B., Suter, L., and Wallace, R. J., *Indirectly Driven, High Growth Rayleigh–Taylor Implosions on Nova,* Lawrence Livermore National Laboratory, Livermore, CA, UCRL-JC-120196 (1995). Submitted to the *J. Quant. Spectros. Radiat. Transfer.*

Landen, O. L., *Large Rayleigh–Taylor Growth, Indirectly-Driven Implosions at Nova,* Lawrence Livermore National Laboratory, Livermore, CA, UCRL-JC-121497 ABS (1995). Prepared for the *37th Annual Mtg of the American Physical Society Div of Plasma Physics,* Louisville, KY, Nov 6–10, 1995.

Landen, O., *An X-Ray Technique for Precision Laser Beam Synchronization,* Lawrence Livermore National Laboratory, Livermore, CA, UCRL-JC-115599 (1995); *Rev. Sci. Inst.* **66**(1), 788–790 (1995).

Landen, O., Bell, P., and Bradley, D., *X-Ray Framing Cameras for >5 keV Imaging,* Lawrence Livermore National Laboratory, Livermore, CA, UCRL-JC-119326 ABS (1995). Prepared for *SPIE 1995 Int'l Symp on Optical Science, Engineering and Instrumentation,* San Diego, CA, Jul 9–14, 1995.

Langer, S. H., Keane, C. J., and Scott, H. A., *Emission Line Ratios from ICF Target Implosions with Rayleigh–Taylor Perturbations,* Lawrence Livermore National Laboratory, Livermore, CA, UCRL-JC-121462 ABS (1995). Prepared for the *37th Annual Mtg of the American Physical Society Div of Plasma Physics,* Louisville, KY, Nov 6–10, 1995.

Langer, S. H., Keane, C. J., and Scott, H. A., *Two-Dimensional Models of Emission Line Ratios in ICF Target Implosions,* Lawrence Livermore National Laboratory, Livermore, CA, UCRL-JC-120788 ABS (1995). Prepared for *25th Annual Anomalous Absorption Conf,* Aspen, CO, May 27–Jun 1, 1995.

Larson, D. W., Anderson, R., and Boyce, J. D., *Fault Tolerance of the Pulsed Power Circuit Architecture for the NIF,* Lawrence Livermore National Laboratory, Livermore, CA, UCRL-JC-120516 ABS (1995). Prepared for the *Solid-State Lasers for Application to Inertial Confinement Fusion (ICF) 1st Annual Int'l Conf,* Monterey, CA, May 30–Jun 2, 1995.

Larson, D. W., *Final Report for 1.7 Megajoule Prototype Bank Testing,* Lawrence Livermore National Laboratory, Livermore, CA, UCRL-CR-120303 (1995).

Larson, D., Anderson, R., and Boyes, J., *Fault Tolerance of the NIF Power Conditioning System,* Lawrence Livermore National Laboratory, Livermore, CA, UCRL-JC-121817 (1995). Prepared for the *1st Annual Int'l Conf on Solid-State Lasers for Application to Inertial Confinement Fusion,* Monterey, CA, May 30–Jun 2, 1995.

Lasinski, B. F., Afeyan, B. B., Cohen, B. I., Langdon, A. B., and Williams, E. A., *Ion Wave Modeling in PIC-Fluid Simulations,* Lawrence Livermore National Laboratory, Livermore, CA, UCRL-JC-120775 ABS (1995). Prepared for *25th Annual Anomalous Absorption Conf,* Aspen, CO, May 27–Jun 1, 1995.

Lasinski, B. F., Langdon, A. B., Cohen, B. I., and Williams, E. A., *Ion Wave Modeling in PIC-Fluid Simulations,* Lawrence Livermore National Laboratory, Livermore, CA, UCRL-JC-120775 ABS Rev 1 (1995). Prepared for the *37th Annual Mtg of the American Physical Society Div of Plasma Physics,* Louisville, KY, Nov 6–10, 1995.

Latkowski, J. F., Sanz, J., Vujic, J. L., and Tobin, M. T., *Charged Particle and Neutron Activation of Flibe in HYLIFE-II Inertial Fusion Energy Power Plant,* Lawrence Livermore National Laboratory, Livermore, CA, UCRL-JC-121292 SUM (1995). Prepared for the *American Nuclear Society 1995 Winter Mtg,* San Francisco, CA, Oct 29–Nov 2, 1995.

Lawson, J. K., Wolfe, C. R., Manes, K. R., Trenholme, J. B., Aikens, D. M., and English, R. E., *Specification of Optical Components Using the Power Spectral Density Function,* Lawrence Livermore National Laboratory, Livermore, CA, UCRL-JC-120920 (1995). Prepared for *Society of Photo-Optical Instrumentation Engineers' 40th Annual Mtg,* San Diego, CA, Jul 9–14, 1995.

Lawson, J., *Simulation of Phase Structure,* Lawrence Livermore National Laboratory, Livermore, CA, UCRL-ID-120900 (1995).

Lerche, R. A., Cable, M. D., and Dendooven, P. G., *Fusion Gamma Rays Observed in ICF Experiments,* Lawrence Livermore National Laboratory, Livermore, CA, UCRL-JC-121485 ABS (1995). Prepared for the *37th Annual Mtg of the American Physical Society Div of Plasma Physics,* Louisville, KY, Nov 6–10, 1995.

Lerche, R. A., Cable, M. D., and Dendooven, P. G., *ICF Burn-History Measurements Using 17-MeV Fusion Gamma Rays,* Lawrence Livermore National Laboratory, Livermore, CA, UCRL-JC-119537 (1995). Prepared for *12th Int'l Conf on Laser Interaction and Related Plasma Phenomena,* Osaka, Japan, Apr 24–28, 1995.

Lerche, R. A., Cable, M. D., Caird, J. A., Kornblum, H. N., Laumann, C., Murray, J., Phillion, D. W., Ress, D. B., Kilkenny, J. D., Hatchet, S. P., Lane, S. M., Murphy, T. J., Nelson, M. B., Powell, H., *High Convergence, Indirect Drive Inertial Confinement Fusion Experiments at Nova,* Lawrence Livermore National Laboratory, Livermore, CA, UCRL-JC-119536 ABS (1995). Prepared for the *12th Int'l Conf on Laser Interaction and Related Plasma Phenomena,* Osaka, Japan, Apr 24–28, 1995.

Lerche, R. A., Cable, M. D., Hatchett, S. P., Caird, J. A., Kilkenny, J. D., Kornblum, H. N., Lane, S. M., Laumann, C., Murphy, T. J., Murray, J., Nelson, M. B., Phillion, D. W., Powell, H., and Ress, D., *High Convergence, Indirect Drive Inertial Confinement Fusion Experiments at Nova,* Lawrence Livermore National Laboratory, Livermore, CA, UCRL-JC-119536 (1995). Prepared for *12th Int'l Conf on Laser Interaction and Related Plasma Phenomena,* Osaka, Japan, Apr 24–28, 1995.

Lerche, R. A., Dendooven, P. G., *ICF Burn-History Measurements Using 17-MeV Fusion Gamma Rays,* Lawrence Livermore National Laboratory, Livermore, CA, UCRL-JC-119537 ABS (1995). Prepared for the *12th Int'l Conf on Laser Interaction and Related Plasma Phenomena,* Osaka, Japan, Apr 24–28, 1995.

Lerche, R. A., *Future ICF Burn-History Measurements Using Fusion Gamma Rays,* Lawrence Livermore National Laboratory, Livermore, CA, UCRL-JC-119902 ABS (1995). Prepared for the *22nd IEEE Int'l Conf on Plasma Science,* Madison, WI, Jun 5–8, 1995.

Lerche, R., *25 ps Neutron Detector for Measuring ICF-Target Burn History,* Lawrence Livermore National Laboratory, Livermore, CA, UCRL-JC-116183 (1995); *Rev. Sci. Inst.* **66**(1), 933–935 (1995).

Letts, S. A., Collins, G. W., *Effects of Process Conditions on Surface Roughness of Plasma Polymer Coatings,* Lawrence Livermore National Laboratory, Livermore, CA, UCRL-JC-119391 ABS (1995). Prepared for the *10th Target Fabrication Specialists Mtg,* Taos, NM, Feb 6–10, 1995.

Letts, S. A., Fearon, E. M., Buckley, S. R., Saculla, M. D., Allison, L. M., and Cook, R. C., *Fabrication of Hollow Shell ICF Targets Using a Depolymerizable Mandrel,* Lawrence Livermore National Laboratory, Livermore, CA, UCRL-JC-117393 ABS Rev. 1 (1995). Prepared for the *10th Target Fabrication Specialists Mtg,* Taos, NM, Feb 6–10, 1995.

Letts, S. A., Fearon, E. M., Buckley, S. R., Saculla, M. D., Allison, L. M., and Cook, R. C., *Fabrication of Polymer Shells Using a Depolymerizable Mandrel,* Lawrence Livermore National Laboratory, Livermore, CA, UCRL-JC-120194 (1995). Submitted to *Fusion Technology.*

Letts, S. A., Fearon, E. M., Buckley, S. R., Saculla, M. D., Allison, L. M., and Cook, R., *Fabrication of Special ICF Targets Using a Depolymerizable Mandrel Technique,* Lawrence Livermore National Laboratory, Livermore, CA, UCRL-JC-121115 ABS (1995). Prepared for *42nd Nat'l Symp of the American Vacuum Society,* Minneapolis, MN, Oct 16–20, 1995.

Letts, S. A., Fearon, E. M., Saculla, M. D., Cook, R. C., Allison, L. M., Buckley, S. R., *Preparation of Hollow Shell ICF Targets Using a Depolymerizing Mandrel,* Lawrence Livermore National Laboratory, Livermore, CA, UCRL-JC-119346 (1995). Prepared for *Materials Rsch Soc Mtg,* Boston, MA, Nov 28–Dec 2, 1994.

Letts, S., Fearon, E., Allison, L., Buckley, S., Saculla, M., and Cook, R., *Decomposable Mandrel Project— Progress Report,* Lawrence Livermore National Laboratory, Livermore, CA, UCRL-ID-120913 (1995).

Li, L., *User's Guide to LAMBDA—A Computer Program for Gratings in Classical Mountings,* Lawrence Livermore National Laboratory, Livermore, CA, UCRL-CR-118522 (1995).

Lindl, J. D., *Target Physics Basis for Indirect Drive Targets for Inertial Fusion Energy,* Lawrence Livermore National Laboratory, Livermore, CA, UCRL-JC-121143 ABS (1995). Prepared for *Int'l Symp on Heavy Ion Inertial Fusion,* Princeton, NJ, Sept 6–9, 1995.

Lindl, J., and Correll, D., *1994 ICF Annual Report,* Lawrence Livermore National Laboratory, Livermore, CA, UCRL-LR-105820-94 (1995).

Lindl, J., *Development of the Indirect Drive Approach to ICF and the Target Physics Basis for Ignition and Gain on the National Ignition Facility,* Lawrence Livermore National Laboratory, Livermore, CA, UCRL-JC-119015 (1995). Submitted to *Plasma Physics.*

Lindl, J., *Progress and Future Application of Indirect Drive Inertial Confinement Fusion (ICF),* Lawrence Livermore National Laboratory, Livermore, CA, UCRL-JC-119620 ABS (1995). Prepared for the *American Association for the Advancement of Science,* Atlanta, GA, Feb 16–21, 1995.

Lindl, J., *Review of Indirect Drive ICF,* Lawrence Livermore National Laboratory, Livermore, CA, UCRL-JC-119351 ABS (1995). Prepared for the *36th Annual Mtg APS Div of Plasma Physics,* Minneapolis, MN, Nov 7–11, 1994.

Logan, B. G., *Inertial Fusion Commercial Power Plants,* Lawrence Livermore National Laboratory, Livermore, CA, UCRL-JC-118199 (1995). Submitted to the *J. of Fusion Energy.*

Logan, B. G., Moir, R. W., Hoffman, M. A., *Requirements for Low Cost Electricity and Hydrogen Fuel Production From Multi-Unit Inertial Fusion Energy Plants with a Shared Driver and Target Factory,* Lawrence Livermore National Laboratory, Livermore, CA, UCRL-JC-115787, Rev 1 (1995). Submitted to *Fusion Technology.*

Logan, B. G., *Relevance of the U.S. National Ignition Facility for Driver and Target Options to Next-Step Inertial Fusion Test Facilities,* Lawrence Livermore National Laboratory, Livermore, CA, UCRL-JC-120766 (1995). Prepared for *12th Int'l Conf on Laser Interaction and Related Plasma Phenomena,* Osaka, Japan, Apr 24–28, 1995.

Logan, B. G., *Relevance of the U.S. National Ignition Facility for Heavy-Ion and Diode-Pumped Laser Driver and Target Options for Inertial Fusion Energy*, Lawrence Livermore National Laboratory, Livermore, CA, UCRL-JC-119379 ABS (1995). Prepared for the *12th Int'l Conf on Laser Interaction and Related Plasma Phenomena*, Osaka, Japan, Apr 24–28, 1995.

Logan, B. G., *Role of the U.S. National Ignition Facility within an Overall Plan for Inertial Fusion Energy*, Lawrence Livermore National Laboratory, Livermore, CA, UCRL-JC-121579 ABS (1995). Prepared for the *16th Institute for Electrical and Electronics Engineers/Nuclear and Plasma Sciences Society Symp on Fusion Engineering*, Champaign, IL, Sept 30–Oct 5, 1995.

Logan, B. G., *The NIF and Its Role in Inertial Fusion Energy*, Lawrence Livermore National Laboratory, Livermore, CA, UCRL-ID-120777 (1995).

Logan, G., and Tobin, M., *White Paper: Laser System and Target Chamber Design Needs for Inertial Fusion Energy Experiments in the National Ignition Facility*, Lawrence Livermore National Laboratory, Livemore, CA, UCRL-AR-120757 (1995).

London, R. A., Decker, C., Powers, L. V., Harte, J. A., Trebes, J. E., Cauble, R., Wan, A. S., and Da Silva, L. B., *Simulations of X-Ray Laser Probing of Hohlraums*, Lawrence Livermore National Laboratory, Livermore, CA, UCRL-JC-121484 ABS (1995). Prepared for the *37th Annual Mtg of the American Physical Society Div of Plasma Physics*, Louisville, KY, Nov 6–10, 1995.

London, R. A., Glinsky, M. E., Eder, D. C., Jacques, S. L., Zimmerman, G. B., *Coupled Light Transport/Heat Diffusion Model for Laser Dosimetry with Dynamic Optical Properties*, Lawrence Livermore National Laboratory, Livermore, CA, UCRL-JC-119377 ABS (1995). Prepared for *SPIE Conf Laser–Tissue Interaction VI*, San Jose, CA, Feb 4–10, 1995.

London, R. A., Powers, L., Trebes, J. E., Da Silva, L. B., Wan, A., Ress, D., Harte, J. A., Prasad, M. K., and Cauble, R., *Design and Analysis of X-Ray Laser Probing Experiments of Laser-Fusion Plasmas*, Lawrence Livermore National Laboratory, Livermore, CA, UCRL-JC-119493 ABS (1995). Prepared for *Soft X-Ray Lasers and Applications (SPIE)*, San Diego, CA, Jul 9–14, 1995.

M

MacGowan, B. J., Back, C. A., Bradley, K. S., Dixit, S. N., Estabrook, K. G., Henesian, M. A., Kalantar, D. H., Klem, D. E., Miller, J. L., Moody, J. D., Colvin, J. D., Berger, R. L., Eimerl, D. I., Failor, B. H., Hsing, W. W., Kauffman, R. L., Kruer, W. L., Montgomery, D. S., Munro, J. D., *Study of Parametric Instabilities in NIF-Scale Plasmas on Nova*, Lawrence Livermore National Laboratory, Livermore, CA, UCRL-JC-118524 (1995). Prepared for the *15th Int'l Conf on Plasma Physics and Controlled Nuclear Fusion Rsch*, Seville, Spain, Sept 26–Oct 1, 1994.

MacGowan, B. J., *Laser–Plasma Interactions in Ignition-Scale Hohlraum Plasmas*, Lawrence Livermore National Laboratory, Livermore, CA, UCRL-JC-121499 ABS (1995). Prepared for the *37th Annual Mtg of the American Physical Society Div of Plasma Physics*, Louisville, KY, Nov 6–10, 1995.

MacGowan, B. J., *The Study of Parametric Instabilities in Large-Scale-Length Plasmas on Nova*, Lawrence Livermore National Laboratory, Livermore, CA, UCRL-JC-120911 ABS (1995). Prepared for *25th Annual Anomalous Absorption Conf*, Aspen, CO, May 27–Jun 1, 1995.

Mapoles, E. R., Pipes, J. W., Ellefson, R. E., and Sowders, M. H., *A Self-Contained Deuterium-Tritium Source for Inertial Fusion Target Development*, Lawrence Livermore National Laboratory, Livermore, CA, UCRL-JC-121116 ABS (1995). Prepared for *42nd Nat'l Symp of the American Vacuum Society*, Minneapolis, MN, Oct 16–20, 1995.

Mapoles, E. R., Pipes. J. W., Sowders, M. W., Ellefson, R. E., *Self-Contained Deuterium–Tritium Source for Cryogenic ICF Target Development*, Lawrence Livermore National Laboratory, Livermore, CA, UCRL-JC-119399 ABS (1995). Prepared for the *10th Target Fabrication Specialists Mtg*, Taos, NM, Feb 6–10, 1995.

Marinak, M. M., Remington, B. A., Weber, S. V., Tipton, R. E., Haan, S. W., Budil, K., Landen, O. L., Kilkenny, J. D., and Wallace, R. J., *Three-Dimensional Single Mode Rayleigh–Taylor Experiments on Nova*, Lawrence Livermore National Laboratory, Livermore, CA, UCRL-JC-120191 (1995). Submitted to *Phys. Rev. Lett.*

Marinak, M. M., *Three-Dimensional Simulations of Nova Capsule Implosions and Planar Hydrodynamic Experiments*, Lawrence Livermore National Laboratory, Livermore, CA, UCRL-JC-121475 ABS (1995). Prepared for the *37th Annual Mtg of the American Physical Society Div of Plasma Physics*, Louisville, KY, Nov 6–10, 1995.

Marshall, C. D., Krupke, W. F., Orth, C. D., *Diode-Pumped Sol-State Laser Drivers for Inertial Fusion Energy,* Lawrence Livermore National Laboratory, Livermore, CA, UCRL-JC-119366 ABS (1995). Prepared for the *IAEA Laser Interaction and Related Plasma Phenomena,* Osaka, Japan, Apr 24–28, 1995.

Marshall, C. D., Payne, S. A., Emanuel, M. A., Smith, L. K., Powell, H. T., and Krupke, W. F., *Diode-Pumped Solid-State Laser Driver Experiments for Inertial Fusion Energy,* Lawrence Livermore National Laboratory, Livermore, CA, UCRL-JC-121614 (1995). Prepared for the *1st Annual Int'l Conf on Solid-State Lasers for Application to Inertial Confinement Fusion,* Monterey, CA, May 30–Jun 2, 1995.

Marshall, C. D., Payne, S. A., Powell, H. T., Chai, B. H. T., Krupke, W. F., and Smith, L. K., *1.047 μm Yb:$Sr_5(PO_4)_3F$ Energy Storage Optical Amplifier,* Lawrence Livermore National Laboratory, Livermore, CA, UCRL-JC-118512 (1995). Submitted to the *IEEE J. of Quantum Electron.*

Marshall, C. D., Payne, S. A., Schaffers, K. I., Emanuel, M., Krupke, W. F., Beach, R., Smith, L. K., Powell, H. T., Chai, B. H. T., *Laser Emission Properties of Diode Pumped Yb:$Sr_5(PO_4)_3F$,* Lawrence Livermore National Laboratory, Livermore, CA, UCRL-JC-119007 ABS & SUM (1995). Prepared for *CLEO '95,* Baltimore, MD, May 22–26, 1995.

Marshall, C. D., Payne, S. A., Smith, L. K., Beach, R. J., Emanuel, M. A., Powell, H. T., and Krupke, W. F., *Diode-Pumped Yb:$Sr_5(PO_4)_3F$ Laser Performance,* Lawrence Livermore National Laboratory, Livermore, CA, UCRL-JC-118194 (1995). Prepared for the *Advanced Solid State Lasers 10th Topical Mtg,* Memphis, TN, Jan 30–Feb 2, 1995.

Marshall, C. D., Payne, S. A., Speth, J. A., Krupke, W. F., Quarles, G. J., Castillo, V., and Chai, B. H. T., *Ultraviolet Laser Emission Properties of Ce:$LiSrAlF_6$ and Ce:$LiCaAlF_6$,* Lawrence Livermore National Laboratory, Livermore, CA, UCRL-JC-120814 ABS (1995). Prepared for *Optical Society of America Annual Mtg,* Portland, OR, Sept 10–15,1995.

Marshall, C. D., Smith, L. K., Beach, R. J., Emanuel, M. A., Schaffers, K. I., Payne, S. A., and Chai, B. H. T., *Diode-Pumped Ytterbium-Doped $Sr_5(PO_4)_3F$ Laser Performance,* Lawrence Livermore National Laboratory, Livermore, CA, UCRL-JC-122010 (1995). Submitted to the *J. Appl. Phys.*

Marshall, C. D., Speth, J. A., DeLoach, L. D., and Payne, S. A., *Neutron and Gamma Irradiated Optical Property Changes for the Final Optics of the National Ignition Facility,* Lawrence Livermore National Laboratory, Livermore, CA, UCRL-JC-120213 (1995). Prepared for the *1st Annual Int'l Conf on Solid-State Lasers for Application to Inertial Confinement Fusion,* Monterey, CA, May 30–Jun 2, 1995.

Marshall, C., Smith, L., and Payne, S., *Update on Diode-Pumped Solid-State Laser Experiments for Inertial Fusion Energy,* Lawrence Livermore National Laboratory, Livermore, CA, UCRL-ID-118509 (1995).

Matthews, D. L., *White Paper to the U.S. Department of Energy for a Center for the Development and Application of Laser Produced Light Sources,* Lawrence Livermore National Laboratory, Livermore, CA, UCRL-AR-118540 (1995).

Maxon, S., and Suter, L., *Prediction of Energy Radiated and Spectra of Laser-Irradiated Xe Gas Bags,* Lawrence Livermore National Laboratory, Livermore, CA, UCRL-JC-121466 ABS (1995). Prepared for the *37th Annual Mtg of the American Physical Society Div of Plasma Physics,* Louisville, KY, Nov 6–10, 1995.

McEachern, R. L., Moore, C. E., Wallace, R. J., *The Design, Performance, and Application of an Atomic-Force Microscope-Based Profilometer,* Lawrence Livermore National Laboratory, Livermore, CA, UCRL-JC-117322 (1995). Prepared for the *41st National Symp of the AVS,* Denver, CO, Oct 24–28, 1994.

McEachern, R. L., Wallace, R. J., *Measuring and Analyzing the Performance of an Atomic Force Microscope-Based Profilometer,* Lawrence Livermore National Laboratory, Livermore, CA, UCRL-JC-119398 ABS (1995). Prepared for the *10th Target Fabrication Specialists Mtg,* Taos, NM, Feb 6–10, 1995.

McEwan, T. E., *Micropower Impulse Radar Technical Information,* Lawrence Livermore National Laboratory, Livermore, CA, UCRL-ID-120903 (1995).

Moir, R. W., *Feasibility and Advantages of Liquid Walls for MFE Power Plants,* Lawrence Livermore National Laboratory, Livermore, CA, UCRL-JC-122007 ABS (1995). Prepared for *Advanced Approaches to Economical Fusion Power,* Monterey, CA, Sept 11–15, 1995.

Moir, R. W., *IFE Power Plant Requirements on the Focused Beam, the Target, and the Chamber: the HYLIFE-II Example,* Lawrence Livermore National Laboratory, Livermore, CA, UCRL-JC-119612 ABS (1995). Prepared for *HCM-High Energy Density Advanced Research Workshop,* Les Houches, France, Mar 13–17, 1995.

Moir, R. W., *Liquid First Wall and Blanket Development on the NIF and Other Facilities,* Lawrence Livermore National Laboratory, Livermore, CA, UCRL-JC-121580 ABS (1995). Prepared for the *16th Institute for Electrical and Electronic Engineers/Nuclear and Plasma Sciences Society Symp on Fusion Engineering,* Champaign, IL, Sept 30–Oct 5, 1995.

Moir, R. W., *Liquid Wall IFE Power Plants,* Lawrence Livermore National Laboratory, Livermore, CA, UCRL-JC-121588 ABS (1995). Submitted to the *J. Fusion Engineering Design.*

Moir, R. W., *The High-Yield Lithium-Injection Fusion-Energy (HYLIFE-II) Inertial Fusion (IFE) Power Plant Concept and Implications for IFE,* Lawrence Livermore National Laboratory, Livermore, CA, UCRL-JC-119070 Rev. 1 (1995). Submitted to *Phys. of Plasmas.*

Moir, R. W., *The Hylife-II Inertial Fusion Energy Power Plant Concept and Implications for IFE,* Lawrence Livermore National Laboratory, Livermore, CA, UCRL-JC-119070 (1995). Prepared for the *36th Annual Mtg the APS Div of Plasma Physics,* Minneapolis, MN, Nov 7–11, 1994.

Moir, R. W., *The Inertial Fusion Energy Approach to Economical Fusion Power: HYLIFE-II,* Lawrence Livermore National Laboratory, Livermore, CA, UCRL-JC-122008 ABS (1995). Prepared for *Advanced Approaches to Economical Fusion Power,* Monterey, CA, Sept 11–15, 1995.

Molau, N. E., Genin, F. Y., Shang, C. C., and Kozlowski, M. R., *Electro-Mechanical Modeling of Nodular Defects in Multilayer Optical Coatings,* Lawrence Livermore National Laboratory, Livermore, CA, UCRL-JC-121308 ABS (1995). Prepared for *1st Biennial Tri-Laboratory Engineering Conf on Computational Modeling,* Pleasanton, CA, Oct 31–Nov 2, 1995.

Montesanti, R. C., and Thompson, S. L., *A Procedure for Diamond Turning KDP Crystals,* Lawrence Livermore National Laboratory, Livermore, CA, UCRL-ID-121651 (1995).

Montesanti, R. C., Thompson, S. L., Latanich, L. L., and Marion, J. E., *Fabrication of Large Potassium Di-Hydrogen Phosphate (KDP) Crystals for the National Ignition Facility,* Lawrence Livermore National Laboratory, Livermore, CA, UCRL-JC-120713 ABS (1995). Prepared for *1st Annual Int'l Conf on Solid-State Lasers for Application to Inertial Confinement Fusion,* Monterey, CA, May 30–Jun 2, 1995.

Montgomery, D. S., Kirkwood, R. K., MacGowan, B. J., Moody, J. C., Back, C. A., Glenzer, S. H., Kalantar, D. H., Afeyan, B. B., Berger, R. L., Munro, D. H., Desenne, D., Richard, A., and Rousseaux, C., *Angular Distribution of SRS from Nova Gasbag Plasmas,* Lawrence Livermore National Laboratory, Livermore, CA, UCRL-JC-120246 ABS (1995). Prepared for *25th Annual Anomalous Absorption Conf,* Aspen, CO, May 27–Jun 1, 1995.

Montgomery, D. S., Kirkwood, R. K., MacGowan, B. J., Moody, J. D., Afeyan, B. B., Berger, R. L., and Munro, D. H., *Effects of Laser Smoothing on Strongly Damped SRS from Gasbag Plasmas,* Lawrence Livermore National Laboratory, Livermore, CA, UCRL-JC-121289 ABS (1995). Prepared for the *37th Annual Mtg of the American Physical Society Div of Plasma Physics,* Louisville, KY, Nov 6–10, 1995.

Montgomery, D. S., Landen, O. L., Drake, R. P., Estabrook, K. G., Baldis, H. A., Batha, S. H., Bradley, K. S., Procassini, R. J., *Measurements of Radial Heat Wave Propagation in Laser-Produced Exploding-Foil Plasmas,* Lawrence Livermore National Laboratory, Livermore, CA, UCRL-JC-111514 (1992); *Phys Rev Lett* **73**(15), 2055–2058 (1994).

Moody, J. D., Baldis, H. A., Montgomery, D. S., Berger, R. L., Estabrook, K., Kruer, W. L., Lasinski, B. F., Williams, E. A., Dixit, S., and LaBaune, C., *Beam Smoothing Effects on the SBS Instability in Nova Exploding Foil Plasmas,* Lawrence Livermore National Laboratory, Livermore, CA, UCRL-JC-119892 Rev. 1 (1995). Submitted to *Phys. of Plasmas.*

Moody, J. D., MacGowan, B. J., Kirkwood, R. K., Montgomery, D. S., Berger, R. L., Hinkel, D. E., Shepard, T. D., and Williams, E. A., *Experimental Studies of Beam Deflection through an Exploding Foil Plasma,* Lawrence Livermore National Laboratory, Livermore, CA, UCRL-JC-121486 ABS (1995). Prepared for the *37th Annual Mtg of the American Physical Society Div of Plasma Physics,* Louisville, KY, Nov 6–10, 1995.

Moody, J. D., MacGowan, B. J., Kirkwood, R. K., Montgomery, D. S., Berger, R. L., Hinkel, D. E., Shepard, T. D., and Williams, E. A., *Whole Beam Deflection through a Hohlraum Window Plasma,* Lawrence Livermore National Laboratory, Livermore, CA, UCRL-JC-120915 ABS (1995). Prepared for *25th Annual Anomalous Absorption Conf,* Aspen, CO, May 27–Jun 1, 1995.

Moody, J. D., MacGowan, B. J., Kirkwood, R. K., Montgomery, D. S., Desenne, D., Rousseaux, C., Berger, R. L., Kalantar, D. H., and Munro, D., *Propagation of High Intensity Lasers through Large Scalelength Plasmas,* Lawrence Livermore National Laboratory, Livermore, CA, UCRL-JC-120247 ABS (1995). Prepared for *25th Annual Anomalous Absorption Conf,* Aspen, CO, May 27-Jun 1, 1995.

Moon, S. J., and Eder, D. C., *Generation of X-Ray Pulses with Rapid Rise Times to Pump Inner-Shell Photo-Ionized X-Ray Lasing in Carbon at 45 Å,* Lawrence Livermore National Laboratory, Livermore, CA, UCRL-JC-118103 (1995). Prepared for the *Society of Photo-Optical Instrumentation Engineers '95 Int'l Society for Optical Engineering,* San Diego, CA, Jul 10–11, 1995.

Moon, S. J., Eder, D. C., Strobel, G. L., *Inner-Shell Photo-Ionized X-Ray Laser Schemes for Low-Z Elements,* Lawrence Livermore National Laboratory, Livermore, CA, UCRL-JC-117020 (1994). Prepared for the *4th Int'l Colloquium on X-Ray Lasers,* Williamsburg, VA, May 16–20, 1994.

Moore, C. E., McEachern, R. L., *Design and Operation of the LLNL Sphere Mapping System,* Lawrence Livermore National Laboratory, Livermore, CA, UCRL-JC-119397 ABS (1995). Prepared for the *10th Target Fabrication Specialists Mtg,* Taos, NM, Feb 6–10, 1995.

Morales, R., *High Precision Wolter Optic Calibration Facility,* Lawrence Livermore National Laboratory, Livermore, CA, UCRL-JC-116181 (1995); *Rev. Sci. Inst.* **66**(1), 700–702 (1995).

Munro, D. H., *Using the Yorick Interpreted Language,* Lawrence Livermore National Laboratory, Livermore, CA, UCRL-JC-121811 (1995). Submitted to *Computers and Physics.*

Murphy, T. J., Delamater, N. D., Richard, A. L., Cable, M. D., Chrien, R., Gifford, K., Hauer, A. A., Lindman, E. L., Magelssen, G. R., Moore, J. B., Nelson, M. B., Pollaine, S. M., Powers, L. V., Suter, L. J., Wallace, R. J., and Wilde, B. H., *Results from Implosion Experiments with Gas-Filled Nova Hohlraums,* Lawrence Livermore National Laboratory, Livermore, CA, UCRL-JC-120761 ABS (1995). Prepared for *25th Annual Anomalous Absorption Conf,* Aspen, CO, May 27-Jun 1, 1995.

Murphy, T. J., Landen, O. L., Keane, C. J., Hammel, B. A., Brusasco, R. M., Cable, M. D., Cook, R. C., Dittrich, T., Haan, S., Hatchett, S. P., Marinak, M. M., McEachern, R. L., Nelson, M. B., Suter, L., Wallace, R. J., Chrien, R., Colvin, J., Hoffman, N., and Hsing, W., *High Growth Factor Implosion Experiments on Nova,* Lawrence Livermore National Laboratory, Livermore, CA, UCRL-JC-116982 ABS Rev 1 (1995). Prepared for the *37th Annual Mtg of the American Physical Society Div of Plasma Physics,* Louisville, KY, Nov 6–10, 1995.

Murphy, T. J., *Recent Implosion Experiments on Nova,* Lawrence Livermore National Laboratory, Livermore, CA, UCRL-JC-120918 ABS (1995). Prepared for *16th IEEE /NPSS,* Champaign, IL, Sept 30–Oct 5, 1995.

Murphy, T., *Ion-Temperature Measurement of Indirectly Driven Implosions Using a Geometry-Compensated Neutron Time-of-Flight Detector,* Lawrence Livermore National Laboratory, Livermore, CA, UCRL-JC-116199 (1995); *Rev. Sci. Inst.* **66**(1), 930–932 (1995).

Murray, J. E., Van Wonterghem, B., Seppala, L., Speck, D. R., and Murray, J. R., *Parasitic Pencil Beams Caused by Lens Reflections in Laser Amplifier Chains,* Lawrence Livermore National Laboratory, Livermore, CA, UCRL-JC-121125 (1995). Prepared for the *1st Annual Int'l Conf on Solid-State Lasers for Application to Inertial Confinement Fusion,* Monterey, CA, May 30–Jun 2, 1995.

Murray, J., and Correll, D., *ICF Quarterly Report, 5(2),* Lawrence Livermore National Laboratory, Livermore, CA, UCRL-LR-105821-95-2 (1995).

N

Nelson, M. B., *Fuel Areal Density (<Pr>) Measurements Using Secondary and Tertiary Reaction for ICF Targets,* Lawrence Livermore National Laboratory, Livermore, CA, UCRL-JC-119909 ABS (1995). Prepared for the *IEEE ICOPS '95 Conf,* Madison, WI, Jun 5–8, 1995.

Newton, M. A., Deadrick, F. J., Hanks, R. L., Hawkins, S. A., Holm, K. A., Kirbie, H. C., Karpenko, V. P., Longinotti, D. B., and Nattrass, L. A., *Engineering Development for a Small-Scale Recirculator Experiment,* Lawrence Livermore National Laboratory, Livermore, CA, UCRL-JC-121456 (1995). Prepared for the *Int'l Symp on Heavy Ion Fusion,* Princeton, NJ, Sept 6–9, 1995.

O

Oraevsky, A. A., Da Silva, L. B., Feit, M. D., Glinsky, M. E., Mannini, B. M., Paquette, K. L., Perry, M. D., Rubenchik, A. M., Small, W., and Stuart, B. C., *Plasma Mediated Ablation of Biological Tissues with Ultrashort Laser Pulses,* Lawrence Livermore National Laboratory, Livermore, CA, UCRL-JC-120215 (1995). Prepared for the *Society of Photo-Optical Instrumentation Engineers' 1995 Int'l Symp on Lasers and Applications/Biomedical Optics,* San Jose, CA, Feb 4–10, 1995.

Orth, C. D., and Payne, S. A., *A System Study of a DPSSL Driver for IFE,* Lawrence Livermore National Laboratory, Livermore, CA, UCRL-JC-120221 ABS (1995). Prepared for the *Solid-State Lasers for Application to Inertial Confinement Fusion (ICF) 1st Annual Int'l Conf,* Monterey, CA, May 30–Jun 2, 1995.

Orth, C. D., and Payne, S. A., *System Study of a Diode-Pumped Solid-State-Laser Driver for Inertial Fusion Energy,* Lawrence Livermore National Laboratory, Livermore, CA, UCRL-JC-120221 (1995). Prepared for *1st Annual Int'l Conf on Solid-State Lasers for Application to Inertial Confinement Fusion,* Monterey, CA, May 30–Jun 2, 1995.

Orzechowski, T. J., Kauffman, R. L., Kirkwood, R. K., Kornblum, H. N., Levedahl, W. K., Montgomery, D. S., Powers, L. V., Shepard, T. D., Stone, G. F., Suter, L. J., Wallace, R. J., Foster, J. M., and Rosen, P., *Dynamics of Gas-Filled Hohlraums,* Lawrence Livermore National Laboratory, Livermore, CA, UCRL-JC-119372 (1995). Prepared for *12 Int'l Conf on Laser Interaction and Related Plasma Phenomena,* Osaka, Japan, Apr 24–28, 1995.

Orzechowski, T. J., Kauffman, R. L., Kirkwood, R. K., Kornblum, H. N., MacGowan, B. J., Montgomery, D. S., Powers, L. V., Stone, G. F., Suter, L. J., Wallace, R. J., Desenne, D., Dulieu, A. G., Juraszek, D., and Richard, A. L., *Energetics of Gas-Filled Hohlraums,* Lawrence Livermore National Laboratory, Livermore, CA, UCRL-JC-120760 ABS Rev 1 (1995). Prepared for the *37th Annual Mtg of the American Physical Society Div of Plasma Physics,* Louisville, KY, Nov 6–10, 1995.

Orzechowski, T. J., Kauffman, R. L., Kirkwood, R. K., Kornblum, H. N., Montgomery, D. S., Powers, L. V., Stone, G. F., Suter, L. J., and Wallace, R. J., *Energetics of Gas-Filled Hohlraums,* Lawrence Livermore National Laboratory, Livermore, CA, UCRL-JC-120760 ABS (1995). Prepared for *25th Annual Anomalous Absorption Conf,* Aspen, CO, May 27–Jun 1, 1995.

Orzechowski, T. J., Kauffman, R. L., Levedahl, W. K., Shepard, T. D., Suter, L. J., Foster, J. M., Powers, L. V., Kornblum, H. N., Stone, G. F., Wallace, R. J., Rosen, P., *Dynamics of Gas-Filled Hohlraums,* Lawrence Livermore National Laboratory, Livermore, CA, UCRL-JC-119372 ABS (1995). Prepared for *12th Int'l Conf on Laser Interaction and Related Plasma Phenomena'95,* Osaka, Japan, Apr 24–28, 1995.

Overturf, G. E., Buckley, S. R., Cook, R. C., Schroen-Carey, D., McClellan, M. R., Letts, S. A., *Progress in the Development of Foam Targets,* Lawrence Livermore National Laboratory, Livermore, CA, UCRL-JC-119392 ABS (1995). Prepared for the *10th Target Fabrication Specialists Mtg,* Taos, NM, Feb 6–10, 1995.

Overturf, G. E., Buckley, S. R., Letts, S. A., Wilemski, G., Cook, R., McClellan, M. R., and Schroen-Carey, D., *Low Density Resorcinol-Formaldehyde Aerogel Foam Shells for Use as Cryogenic ICF Experiments,* Lawrence Livermore National Laboratory, Livermore, CA, UCRL-JC-120898 ABS (1995). Prepared for *42nd Nat'l Symp of the American Vacuum Society,* Minneapolis, MN, Oct 16–20, 1995.

Overturf, G. E., Cook, R. C., Letts, S. A., Buckley, S. R., McClellan, M. R., and Schroen-Carey, D., *Resorcinol-Formaldehyde Foam Shell Targets for ICF,* Lawrence Livermore National Laboratory, Livermore, CA, UCRL-JC-120195 (1995). Submitted to *Fusion Technology.*

Overturf, G. E., Cook, R. C., *Process Issues Associated with Making Foam Microshells,* Lawrence Livermore National Laboratory, Livermore, CA, UCRL-JC-119396 ABS (1995). Prepared for the *10th Target Fabrication Specialists Mtg,* Taos, NM, Feb 6–10, 1995.

P

Page, R. H., DeLoach, L. D., Payne, S. A. , Krupke, W. F., and Wilke, G. D., *New Class of Tunable Mid-IR Lasers Based on Cr^{2+}-Doped II-VI Compounds,* Lawrence Livermore National Laboratory, Livermore, CA, UCRL-JC-119005 ABS & SUM (1995). Prepared for *CLEO '95,* Baltimore, MD, May 22–26, 1995.

Page, R. H., DeLoach, L. D., Wilke, G. D., Payne, S. A., and Krupke, W. F., *New Tunable Infrared Laser Materials,* Lawrence Livermore National Laboratory, Livermore, CA, UCRL-JC-119935 ABS (1995). Prepared for the *Chemical Analysis by Laser Interrogation of Proliferation Effluents Second Annual Interim Technical Review,* Los Alamos, NM, Mar 28–30, 1995.

Page, R. H., DeLoach, L. D., Wilke, G. D., Payne, S. A., Beach, R. J., and Krupke, W. F., *Cr^{2+}-Doped II-VI Crystals: New Widely-Tunable, Room-Temperature Mid-IR Lasers,* Lawrence Livermore National Laboratory, Livermore, CA, UCRL-JC-120815 SUM (1995). Prepared for the *Lasers and Electro Optics Society '95,* San Francisco, CA, Oct 30–Nov 2, 1995.

Page, R. H., DeLoach, L. D., Wilke, G. D., Payne, S. A., Beach, R. J., and Krupke, W. F., *Cr^{2+}–Doped II-VI Crystals: New Widely-Tunable, Room-Temperature Mid-IR Lasers,* Lawrence Livermore National Laboratory, Livermore, CA, UCRL-JC-120815 ABS (1995). Prepared for *Lasers and Electro Optics Society '95 8th Annual Mtg,* San Francisco, CA, Oct 30–Nov 2, 1995.

Page, R. H., Schaffers, K. I., Wilks, G. D., Tassano, J. B., Payne, S. A., Krupke, W. F., and Chai, B. H. T., *Spectroscopy and Decay Kinetics of Pr^{3+}-Doped Chloride Crystals for 1300-nm Optical Amplifiers,* Lawrence Livermore National Laboratory, Livermore, CA, UCRL-JC-118195 (1995). Prepared for *Advanced Solid State Lasers 10th Topical Mtg,* Memphis, TN, Jan 30–Feb 2, 1995.

Paisner, J. A., Campbell, E. M., Hogan, W. J., *National Ignition Facility Project,* Lawrence Livermore National Laboratory, Livermore, CA, UCRL-JC-117397 Rev 1 (1994). Prepared for *ANS Annual Mtg,* New Orleans, LA, Jun 19–23, 1994.

Paisner, J. A., *Letter to the Editor on the National Ignition Facility,* Lawrence Livermore National Laboratory, Livermore, CA, UCRL-JC-119373 COM (1995). Submitted to *Physics Today.*

Patton, H. G., *National Ignition Facility—The Next Step in Inertial Confinement Fusion,* Lawrence Livermore National Laboratory, Livermore, CA, UCRL-JC-119357 (1995). Submitted to *Amer Vaccum Soc Nat'l Newsletter.*

Payne, S. A., Krupke, W. F., Beach, R. J., DeLoach, L. D., Emanuel, M. A., Marshall, C. D., Page, R. H., Schaffers, K. I., and Skidmore, J. A., *New Solid State Lasers from the Ultraviolet to the Mid-infrared,* Lawrence Livermore National Laboratory, Livermore, CA, UCRL-JC-121646 (1995). Prepared for the *American Ceramic Society Annual Mtg,* Cincinnati, OH, Apr 30–May 4, 1995.

Payne, S. A., Krupke, W. F., Marshall, C. D., Emanuel, M. A., Orth, C. D., *Diode-Pumped Solid State Laser for Inertial Fusion Energy,* Lawrence Livermore National Laboratory, Livermore, CA, UCRL-JC-117302 (1995). Prepared for *IAEA Technical Committee Mtg on Drivers for Inertial Confinement Fusion,* Paris, France, Nov 14–18, 1994.

Payne, S. A., Marshall, C. D., Bayramian, A. J., Wilke, G. D., and Hayden, J. S., *Properties of a New Average Power Nd-Doped Phosphate Laser Glass,* Lawrence Livermore National Laboratory, Livermore, CA, UCRL-JC-118191 (1995). Prepared for *Advanced Solid State Lasers 10th Topical Mtg,* Memphis, TN, Jan 30–Feb 2, 1995.

Payne, S. A., Marshall, C. D., Emanuel, M. A., Beach, R. J., Orth, C. D., Powell, H. T., and Krupke, W. F., *Scalable Diode-Pumped Solid State Laser Architecture for Inertial Fusion Energy,* Lawrence Livermore National Laboratory, Livermore, CA, UCRL-JC-120011 (1995). Prepared for the *Conf on Lasers and Electro Optics/Pacific Rim '95,* Chiba, Japan, Jul 11–14, 1995.

Payne, S. A., Marshall, C. D., Wilke, G. D., Hackel, L. A., Hayden, J. S., Marker, A. J., and Sapak, D. L., *High Average Power Laser Glass,* Lawrence Livermore National Laboratory, Livermore, CA, UCRL-JC-119693 (1995). Submitted to *R&D Magazine.*

Payne, S. A., Marshall, C. D., Wilke, G. D., Hayden, J. S., and Bayramian, A. J., *Laser Properties of an Improved Average-Power Nd-Doped Phosphate Glass,* Lawrence Livermore National Laboratory, Livermore, CA, UCRL-JC-118120 (1994). Prepared for *SPIE Properties and Characteristics of Optical Glass III,* San Diego, CA, Jul 24–29, 1994.

Payne, S. A., *New Solid State Laser Materials for the Infrared and the Ultraviolet,* Lawrence Livermore National Laboratory, Livermore, CA, UCRL-JC-119381 ABS (1995). Prepared for the *Amer Ceramic Soc Annual Mtg,* Cincinnati, OH, Apr 30–May 4, 1995.

Payne, S. A., Powell, H. T., and Krupke, W. F., *Can Solid-State Laser Technology Serve Usefully beyond Fusion Ignition Facilities?* Lawrence Livermore National Laboratory, Livermore, CA, UCRL-JC-120887 ABS (1995). Prepared for *1st Annual Int'l Conf on Solid-State Lasers for Application to Inertial Confinement Fusion,* Monterey, CA, May 30–Jun 2, 1995.

Payne, S. A., Powell, H. T., and Krupke, W. F., *Can Solid-State Laser Technology Serve Usefully beyond Fusion Ignition Facilities?*, Lawrence Livermore National Laboratory, Livermore, CA, UCRL-JC-120887 (1995). Prepared for the *1st Annual Int'l Conf on Solid-State Lasers for Application to Inertial Confinement Fusion*, Monterey, CA, May 30–Jun 2, 1995.

Payne, S., Smith, L. K., and Krupke, W. F., *Cross Sections and Quantum Yields of the 3 μm Emission for Er^{3+} and Ho^{3+} Dopants in Crystals*, Lawrence Livermore National Laboratory, Livermore, CA, UCRL-JC-117882 (1994); *J. Appl. Phys.* **77**(5), 4274–4279 (1995).

Pennington, D. M., Henesian, M. A., Brown, C. G., Eimerl, D., Danforth, P. M., Rothenberg, J. E., *Temporal Dynamics of the Multi-Frequency Spectrum Generated by the Nonlinear Mixing of Two Frequencies in a Single-Mode Fiber*, Lawrence Livermore National Laboratory, Livermore, CA, UCRL-JC-119016 ABS & SUM (1995). Prepared for *CLEO '95*, Baltimore, MD, May 22–26, 1995.

Pennington, D. M., Henesian, M. A., Milam, D., and Eimerl, D., *Efficient Broadband Third Harmonic Frequency Conversion via Angular Dispersion*, Lawrence Livermore National Laboratory, Livermore, CA, UCRL-JC-121197 (1995). Prepared for the *1st Annual Int'l Conf on Solid-State Lasers for Application to Inertial Confinement Fusion*, Monterey, CA, May 30–Jun 2, 1995.

Pennington, D. M., Henesian, M. A., Wilcox, R. B., Weiland, R. B., Eimerl, D., Ehrlich, R. B., Laumann, C. W., and Miller, J. L., *A Four-Color Beam Smoothing Irradiation System for Laser–Plasma Interaction Experiments at LLNL*, Lawrence Livermore National Laboratory, Livermore, CA, UCRL-JC-121270 (1995). Prepared for *1st Annual Int'l Conf on Solid-State Lasers for Application to Inertial Confinement Fusion*, Monterey, CA, May 30–Jun 2, 1995.

Perry, M. D., Boyd, R. D., Decker, D., Shannon, C., Li, L., Shore, B. W., Britten, J. A., Shults, E., *High-Efficiency Multilayer Dielectric Diffraction Gratings*, Lawrence Livermore National Laboratory, Livermore, CA, UCRL-JC-117687 (1995). Submitted to *Optics Letters*.

Perry, M. D., Boyd, R., Decker, D., Shore, B., Shults, E. M., Withrington, R. J., Powell, H. T., Britten, J. A., Garvin, H. L., Shannon, C., *Efficient Multilayer Dielectric Gratings*, Lawrence Livermore National Laboratory, Livermore, CA, UCRL-JC-116727 (1995). Submitted to *R&D Magazine*.

Perry, M. D., Dixit, S. N., Shore, B. W., Boyd, R. D., Britten, J. A., and Powell, H. T., *High Efficiency Gratings for Beam Steering on the National Ignition Facility (NIF) Laser*, Lawrence Livermore National Laboratory, Livermore, CA, UCRL-JC-120185 (1995). Prepared for *1st Annual Int'l Conf on Solid-State Lasers for Application to Inertial Confinement Fusion*, Monterey, CA, May 30–Jun 2, 1995.

Perry, M. D., *High Power Ultrashort Pulse Lasers*, Lawrence Livermore National Laboratory, Livermore, CA, UCRL-JC-118539 (1994). Prepared for the *6th Workshop on Advanced Accelerator Concepts*, Fontana, WI, Jun 12–18, 1994.

Perry, M. D., *Self-Phase Modulation in Chirped Pulse Amplification*, Lawrence Livermore National Laboratory, Livermore, CA, UCRL-JC-118114 (1994); *Optics Letters* **19**, 2149–2151 (1994).

Petzoldt, R. W., and Moir, R. W., *Target Injection, Tracking, and Beam Pointing Requirements and Feasibility Considerations for Inertial Fusion Energy*, Lawrence Livermore National Laboratory, Livermore, CA, UCRL-JC-120880 (1995). Submitted to *Fusion Engineering and Design*.

Petzoldt, R. W., *Inertial Fusion Energy Target Injection, Tracking, and Beam Pointing*, Lawrence Livermore National Laboratory, Livermore, CA, UCRL-LR-120192 (1995).

Petzoldt, R., *Ron Petzoldt's Doctoral Dissertation Project*, Lawrence Livermore National Laboratory, Livermore, CA, UCRL-ID-118735 (1995).

Pollaine, S. M., Haan, S. W., Amendt, P. A., Moreno, J. C., and Wan, A. S., *National Ignition Facility Point Design*, Lawrence Livermore National Laboratory, Livermore, CA, UCRL-JC-121473 ABS (1995). Prepared for the *37th Annual Mtg of the American Physical Society Div of Plasma Physics*, Louisville, KY, Nov 6–10, 1995.

Pollaine, S. M., Haan, S. W., Amendt, P. A., Moreno, J. C., and Wan, A. S., *Robustness Studies and Beam Angles for the National Ignition Facility*, Lawrence Livermore National Laboratory, Livermore, CA, UCRL-JC-120785 ABS (1995). Prepared for *25th Annual Anomalous Absorption Conf*, Aspen, CO, May 27–Jun 1, 1995.

Pollaine, S. M., Suter, L. J., Powers, L. V., Kauffman, R. L., Murphy, T. J., and Shepard, T. D., *Gas Hohlraum Simulations*, Lawrence Livermore National Laboratory, Livermore, CA, UCRL-JC-120786 ABS (1995). Prepared for *25th Annual Anomalous Absorption Conf*, Aspen, CO, May 27–Jun 1, 1995.

Powers, L. V., Berger, R. L., Kauffman, R. L., MacGowan, B. J., Amendt, P. A., Back, C. A., Bernat, T. P., Dixit, S. N., Eimerl, D., Estabrook, K. G., Harte, J. A., Kalantar, D. H., Klem, D. E., Lasinski, B. F., Montgomery, D. S., Moody, J. D., Munro, D. H., Shepard, T. D., Suter, L. J., Turner, R. E., Williams, E. A., Fernandez, J. C., Hsing, W. W., Wilde, B. H., and Failor B. H., *Gas-Filled Targets for Large Scale-Length Plasma Interaction Experiments on Nova,* Lawrence Livermore National Laboratory, Livermore, CA, UCRL-JC-117735; *Phys. Plasmas* **2**(6), 2473–2479 (1995).

Powers, L. V., Berger, R. L., Lasinski, B. F., MacGowan, B. J., Back, C. A., Dixit, S. N., Estabrook, K. G., Kalantar, D. H., Montgomery, D. S., Turner, R. E., Kauffman, R. L., Munro, D. H., Amendt, P., Bernat, T. P., Eimerl, D. I., Harte, J. A., Klem, D. E., Shepard, T. D., Suter, L. J., *Gas-Filled Targets for Large Scalelength Plasma Interaction Experiments on Nova,* Lawrence Livermore National Laboratory, Livermore, CA, UCRL-JC-118104 (1995). Prepared for *36th Annual Mtg APS Div of Plasma Physics,* Minneapolis, MN, Nov 7–11, 1994.

Powers, L. V., Suter, L. J., Glendinning, S. G., Kauffman, R. L., Kirkwood, R., Montgomery, D. S., Murphy, T. J., Orzechowski, T. J., Pollaine, S. M., Ress, D. B., Shepard, T. D., Delamater, N. D., Hauer, A. A., Lindman, E. L., and Magelssen, G. R., *Analysis of Effect of Gas Fills on Nova-Scale Hohlraum Dynamics and Energetics,* Lawrence Livermore National Laboratory, Livermore, CA, UCRL-JC-120789 ABS (1995). Prepared for *25th Annual Anomalous Absorption Conf,* Aspen, CO, May 27–Jun 1, 1995.

Powers, L. V., Turner, R. E., Kauffman, R. L., Berger, R. L., Amendt, P., Back, C. A., Bernat, T. P., Dixit, S. N., Eimerl, D., Harte, J. A., Henesian, M. A., Kalantar, D. H., Lasinski, B. F., MacGowan, B. J., Montgomery, D. S., Munro, D. H., Pennington, D. M., Shepard, T. P., Stone, G. F., Suter, L. J., and Williams, E. A., *Low Stimulated Brillouin Backscatter Observed from Large, Hot Plasmas in Gas-Filled Hohlraums,* Lawrence Livermore National Laboratory, Livermore, CA, UCRL-JC-118394 (1994); *Phys. Rev. Lett.* **74**(4), 2957–2960 (1995).

R

Rainer, F., Atherton, L. J., Kozlowski, M. R., Sheehan, L. M., Marion, J. E., De Yoreo, J. J., Stolz, C, J., *Addressing Laser-Induced Damage Issues for the National Ignition Facility,* Lawrence Livermore National Laboratory, Livermore, CA, UCRL-JC-119020 ABS & SUM (1995). Prepared for *CLEO '95,* Baltimore, MD, May 22–26, 1995.

Rambo, P., *A Comparison of Kinetic and Multifluid Simulations of Laser-Produced Colliding Plasmas,* Lawrence Livermore National Laboratory, Livermore, CA, UCRL-JC-117498 Rev 1 (1995); *Phys. Plasmas* **2**(8), 3130-3145 (1995).

Ratowsky, R., *Propagation of Mutual Coherence in Refractive X-Ray Lasers Using a WKB Method,* Lawrence Livermore National Laboratory, Livermore, CA, UCRL-JC-116772 (1994); *Phys. Rev. A* **51**(3), 2361–2370 (1995).

Reibold, R., Letts, S., and Cook, R., *Development of Acoustic Levitation for PVA Coating of Microshells,* Lawrence Livermore National Laboratory, Livermore, CA, UCRL-JC-119601 ABS (1995). Prepared for the *10th Target Fabrication Specialists' Mtg,* Taos, NM, Feb 6–10, 1995.

Remington, B. A., Marinak, M. M., Budil, K. S., Glendinning, S. G., Kilkenny, J. D., Wallace, R. J., Weber, S. V., Haan, S. W., *2-D and 3-D Ablation Front Hydrodynamic Instability Experiments on Nova,* Lawrence Livermore National Laboratory, Livermore, CA, UCRL-JC-119388 ABS (1995). Prepared for the *12th Int'l Conf on Laser Interaction and Related Plasma Phenomena,* Osaka, Japan, Apr 24–28, 1995.

Remington, B. A., Marinak, M. M., Weber, S. V., Budil, K. S., Landen, O. L., Haan, S. W., and Wallace, R. J., *Ablation Front Hydrodynamic Instability Experiments on Nova,* Lawrence Livermore National Laboratory, Livermore, CA, UCRL-JC-119888 ABS (1995). Prepared for the *IEEE ICOP's '95 Conf,* Madison, WI, Jun 5–8, 1995.

Remington, B. A., Marinak, M. M., Weber, S. V., Budil, K. S., Landen, O. L., Glendinning, S. G., Haan, S. W., Kilkenny, J. D., Wallace, R. J., and Dimonte, G., *2D and 3D Ablation Front Hydrodynamic Instability Experiments on Nova,* Lawrence Livermore National Laboratory, Livermore, CA, UCRL-JC-119388 (1995). Prepared for *12th Int'l Conf on Laser Interaction and Related Plasma Phenomena,* Osaka, Japan, Apr 24–28, 1995.

Remington, B. A., Marinak, M. M., Weber, S. V., Budil, K. S., Landen, O. L., Haan, S. W., Kilkenny, J. D., and Wallace, R. J., *Single-Mode Rayleigh–Taylor Experiments in 2D and 3D,* Lawrence Livermore National Laboratory, Livermore, CA, UCRL-JC-120906 ABS (1995). Prepared for *5th Int'l Workshop on the Physics of Compressible Turbulent Mixing,* Stonybrook, NY, Jul 18–21, 1995.

Remington, B. A., Marinak, M. M., Weber, S. V., Budil, K. S., Landen, O. L., Shepard, T., Peyser, T., Kalantar, D., Wallace, R. J., and Rothman, S., *Planar Hydrodynamics Experiments in Indirect-Drive,* Lawrence Livermore National Laboratory, Livermore, CA, UCRL-JC-121489 ABS (1995). Prepared for the *37th Annual Mtg of the American Physical Society Div of Plasma Physics,* Louisville, KY, Nov 6–10, 1995.

Remington, B., Dimonte, G., *Laser-Induced Fluorescence Diagnostic for the LEM Turbulent Hydrodynamics Experiment,* Lawrence Livermore National Laboratory, Livermore, CA, UCRL-JC-115959 (1995). Prepared for *the Mtg of the APS Div of Fluid Dynamics,* Atlanta, GA, Nov 20–22, 1994.

Remington, B., *Single-Mode and Multimode Rayleigh–Taylor Experiments,* Lawrence Livermore National Laboratory, Livermore, CA, UCRL-JC-116897 (1994); *Phys. Plasmas* **2**(1), 241–255 (1995).

Rhodes, M. A., Boley, C. D., Tarditi, A. G., and Bauer, B. S., *Plasma–Electrode Pockels Cell for ICF Lasers,* Lawrence Livermore National Laboratory, Livermore, CA, UCRL-JC-121180 (1995). Prepared for the *1st Annual Int'l Conf on Solid-State Lasers for Application to Inertial Confinement Fusion,* Monterey, CA, May 30–Jun 2, 1995.

Rhodes, M. A., Woods, B., Roberts, D., Atherton, L. J., De Yoreo, J. J., *Performance of Large-Aperture Optical Switches for High-Energy ICF Laser,* Lawrence Livermore National Laboratory, Livermore, CA, UCRL-JC-118537 (1995). Submitted to *Applied Optics: Lasers, Photonics & Environmental Optics Div.*

Rosen, M. D., *Recent Results in Inertial Confinement Fusion with Lasers,* Lawrence Livermore National Laboratory, Livermore, CA, UCRL-JC-121472 (1995). Submitted to *1997 McGraw–Hill Yearbook of Science & Technology.*

Rosen, M. D., *The Physics of Radiation Driven ICF Hohlraums,* Lawrence Livermore National Laboratory, Livermore, CA, UCRL-JC-121585 (1995). Prepared for the *Plasma Physics and Technology,* La Jolla, CA, Aug 8–18, 1995.

Rosen, M. D., *The Science Applications of the High Energy Density Plasmas Created on the Nova Laser,* Lawrence Livermore National Laboratory, Livermore, CA, UCRL-JC-121476 ABS (1995). Prepared for the *37th Annual Mtg of the American Physical Society Div of Plasma Physics,* Louisville, KY, Nov 6–10, 1995.

Rothenberg, J. E., Dixit, S. N., *Two Dimensional Beam Smoothing for Direct Drive Inertial Confinement Fusion Using Spectral Dispersion,* Lawrence Livermore National Laboratory, Livermore, CA, UCRL-JC-119017 ABS & SUM (1995). Prepared for *CLEO '95,* Baltimore, MD, May 22–26, 1995.

Rothenberg, J. E., Eimerl, D., Key, M. H., and Weber, S. V., *Illumination Uniformity Requirements for Direct Drive Inertial Confinement Fusion,* Lawrence Livermore National Laboratory, Livermore, CA, UCRL-JC-121195 (1995). Prepared for the *1st Annual Int'l Conf on Solid-State Lasers for Application to Inertial Confinement Fusion,* Monterey, CA, May 30–Jun 2, 1995.

Rothenberg, J. E., *Two Dimensional Beam Smoothing by Spectral Dispersion for Direct Drive Inertial Confinement Fusion,* Lawrence Livermore National Laboratory, Livermore, CA, UCRL-JC-121198 (1995). Prepared for the *1st Annual Int'l Conf on Solid-State Lasers for Application to Inertial Confinement Fusion,* Monterey, CA, May 30–Jun 2, 1995.

Rotter, M. D., and McCracken, R. W., *Development of the NIF Regenerative Amplifier,* Lawrence Livermore National Laboratory, Livermore, CA, UCRL-JC-120514 ABS (1995). Prepared for the *Solid-State Lasers for Application to Inertial Confinement Fusion (ICF) 1st Annual Int'l Conf,* Monterey, CA, May 30–Jun 2, 1995.

Rotter, M. D., and McCracken, R. W., *Thermal Recovery Measurements on Multi-Segment Amplifiers,* Lawrence Livermore National Laboratory, Livermore, CA, UCRL-JC-120513 ABS (1995). Prepared for the *Solid-State Lasers for Application to Inertial Confinement Fusion (ICF) 1st Annual Int'l Conf,* Monterey, CA, May 30–Jun 2, 1995.

Rotter, M. D., and Zapata, L. E., *Optical Performance Modeling of Large-Aperture Amplifiers for ICF,* Lawrence Livermore National Laboratory, Livermore, CA, UCRL-JC-120515 ABS (1995). Prepared for the *8th Laser Optics Conf,* St. Petersburg, Russia, Jun 27–Jul 1, 1995.

S

Salmon, J. T., Bliss, E. S., Byrd, J. L., Feldman, M., Kartz, M. A., Toeppen, J. S., VanWonterghem, B., and Winters, S. E., *An Adaptive Optics System for Solid-State Laser Systems Used in Inertial Confinement Fusion,* Lawrence Livermore National Laboratory, Livermore, CA, UCRL-JC-120525 ABS (1995). Prepared for the *Solid-State Lasers for Application to Inertial Confinement Fusion (ICF) 1st Annual Int'l Conf,* Monterey, CA, May 30–Jun 2, 1995.

Salmon, J. T., Bliss, E. S., Van Wonterghem, B. M., Kartz, M. W., *Absolute Wavefront Measurements of High-Energy Laser Beams in the Beamlet Demonstration Project for the National Ignition Facility,* Lawrence Livermore National Laboratory, Livermore, CA, UCRL-JC-119004 (1995). Prepared for *CLEO '95,* Baltimore, MD, May 22–26, 1995.

Sanchez, J., Bittner, D., Giedt, W., Pipes, J., Mapoles, E., Burmann, J., Sater, J., *Measurement and Control of Liquid Hydrogen Mixtures on Capsules with Attached Fill Tubes,* Lawrence Livermore National Laboratory, Livermore, CA, UCRL-JC-119394 ABSS (1995). Prepared for the *10th Target Fabrication Specialists Mtg,* Taos, NM, Feb 6–10, 1995.

Sawicki, R. H., Shang, C. C., Swatlowski, T. L., *Failure Characterization of Nodular Defects in Multi-Layer Dielectric Coatings,* Lawrence Livermore National Laboratory, Livermore, CA, UCRL-JC-118164 (1995). Prepared for the *Annual Symp on Optical Materials for High Power Lasers,* Boulder, CO, Oct 26–29, 1994.

Schaffers, K. I., DeLoach, L. D., and Payne, S. A., *Crystal Growth, Frequency Doubling, and Infrared Laser Performance of Yb^{3+}:$BaCaBO_3F$,* Lawrence Livermore National Laboratory, Livermore, CA, UCRL-JC-119643 (1995). Submitted to the *IEEE J. Quantum Electron.*

Schaffers, K. I., DeLoach, L. D., Ebbers, C. A., and Payne, S. A., *Yb^{3+}:$BaCaBO_3F$: A Potential New Self-Frequency-Doubling Laser Material,* Lawrence Livermore National Laboratory, Livermore, CA, UCRL-JC-118193 (1995). Prepared for the *Advanced Solid State Lasers 10th Topical Mtg,* Memphis, TN, Jan 30–Feb 2, 1995.

Schmitt, A. J., and Afeyan, B. B., *Filamentation Dynamics with Full Nonlinear Transverse and Axial Hydrodynamics,* Lawrence Livermore National Laboratory, Livermore, CA, UCRL-JC-121621 ABS (1995). Prepared for the *37th, Annual Mtg of the American Physical Society Div of Plasma Physics,* Louisville, KY, Nov 6–10, 1995.

Schroen-Carey, D., Overturf, G. E., Letts, S. A., Cook, R. C., and Lambert, S. M., *Polymer Overcoated Resorcinol-Formaldehyde Foam Microshells for Inertial Confinement Fusion Targets,* Lawrence Livermore National Laboratory, Livermore, CA, UCRL-JC-122015 ABS (1995). Prepared for the *10th Int'l Symp on Microencapsulation,* Austin, TX, Sept 26–28, 1995.

Schroen–Carey, D., Overturf, G., Reibold, R., Buckley, S., Letts, S., and Cook, R., *Hollow Foam Microshells for Liquid-Layering Cryogenic ICF Targets,* Lawrence Livermore National Laboratory, Livermore, CA, UCRL-JC-117327 (1995). Submitted to the *J. Vac. Sci. Technol.*

Seppala, L. G., English, R. E., and Bliss, E. S., *The Use of an Intermediate Wavelength Laser for Alignment to Inertial Confinement Fusion Targets,* Lawrence Livermore National Laboratory, Livermore, CA, UCRL-JC-120509 ABS (1995). Prepared for the *Solid-State Lasers for Application to Inertial Confinement Fusion (ICF) 1st Annual Int'l Conf,* Monterey, CA, May 30–Jun 2, 1995.

Shaw, M., Correll, D., *ICF Quarterly Report* **4**(3), Lawrence Livermore National Laboratory, Livermore, CA, UCRL-LR-105821-94-3 (1994).

Sheehan, L., and Kozlowski, M., *Detection of Inherent and Laser-Induced Scatter in Optical Materials,* Lawrence Livermore National Laboratory, Livermore, CA, UCRL-JC-119613 (1995). Prepared for the *Society of Photo-Optical Instrumentation 1995 Int'l Symp on Optical, Science, Engineering and Instrumentation,* Tucson, AZ, Jul 9–14, 1995.

Sheehan, L., Kozlowski, M., and Rainer, F., *Diagnostics for the Detection and Evaluation of Laser Induced Damage,* Lawrence Livermore National Laboratory, Livermore, CA, UCRL-JC-118837 (1994). Prepared for the *Boulder Damage Symp,* Boulder, CO, Oct 27–29, 1994.

Sheehan, L., Kozlowski, M., and Stolz, C., *Application of Laser Conditioning to Increase the Damage Threshold of HfO_2/SiO_2 Multilayer Coatings Over Large Areas,* Lawrence Livermore National Laboratory, Livermore, CA, UCRL-JC-119647 ABS & SUM (1995). Prepared for the *Optical Interference Coatings Topical Mtg '95,* Tucson, AZ, Jun 5–9, 1995.

Sheehan, L., Kozlowski, M., and Trench, B., *Full Aperture Laser Conditioning of Multilayer and Polarizers,* Lawrence Livermore National Laboratory, Livermore, CA, UCRL-JC-120203 (1995). Prepared for *1st Annual Int'l Conf on Solid-State Lasers for Application to Inertial Confinement Fusion,* Monterey, CA, May 30–Jun 2, 1995.

Sheehan, L., Kozlowski, M., Rainer, F., and Runkel, M., *Detection of Inherent and Laser-Induced Scatter in Optical Materials,* Lawrence Livermore National Laboratory, Livermore, CA, UCRL-JC-119604 ABS (1995). Prepared for *Optical Science, Engineering and Instrumentation,* San Diego, CA, Jul 9–14, 1995.

Sheehan, L., Kozlowski, M., Rainer, F., and Runkel, M., *Detection of Inherent and Laser-Induced Scatter in Optical Materials,* Lawrence Livermore National Laboratory, Livermore, CA, UCRL-JC-119613 ABS (1995). Prepared for the *Optical Science, Engineering and Instrumentation,* San Diego, CA, Jul 9–14, 1995.

Sheehan, L., Kozlowski, M., Rainer, F., Runkel, M., Stolz, C., and Schwartz, S., *Large Area Damage Testing of Optics,* Lawrence Livermore National Laboratory, Livermore, CA, UCRL-JC-122006 ABS (1995). Prepared for *Optical Systems Design and Projection II,* Glasgow, Scotland, May 12–16, 1996.

Sheehan, L., Kozlowski, M., Stolz, C., and Tench, B., *Full Aperture Laser Conditioning of Multilayer Mirrors and Polarizers,* Lawrence Livermore National Laboratory, Livermore, CA, UCRL-JC-120203 ABS (1995). Prepared for the *Solid-State Lasers for Application to Inertial Confinement Fusion (ICF) 1st Annual Int'l Conf,* Monterey, CA, May 30–Jun 2, 1995.

Shepard, T. D., Back, C. A., Kalantar, D. H., Kauffman, R. L., Keane, C. J., Klem, D. E., Lasinski, B. F., MacGowan, B. J., Powers, L. V., Suter, L. J., Turner, R. E., Failor, B. H., and Hsing, W. W., *Isoelectronic X-Ray Spectroscopy to Determine Electron Temperatures in Long-Scale-Length ICF Plasmas,* Lawrence Livermore National Laboratory, Livermore, CA, UCRL-JC-121575 (1995). Submitted to *Phys. Rev. E.*

Shepard, T. D., Orzechowski, T. J., Murphy, T. J., Suter, L. J., Delamater, N. D., Richard, A. L., Foster, J. M., and Rosen, P. A., *Interface-Motion Modeling for Nova Gas Hohlraums,* Lawrence Livermore National Laboratory, Livermore, CA, UCRL-JC-120787 ABS (1995). Prepared for *25th Annual Anomalous Absorption Conf,* Aspen, CO, May 27–Jun 1, 1995.

Shepard, T. D., Orzechowski, T. J., Murphy, T. J., Suter, L. J., Delamater, N. D., Richard, A. L., Foster, J. M., and Rosen, P. A., *Gas-Hohlraum Interface-Motion Modeling,* Lawrence Livermore National Laboratory, Livermore, CA, UCRL-JC-121465 ABS (1995). Prepared for the *37th Annual Mtg of the American Physical Society Div of Plasma Physics,* Louisville, KY, Nov 6–10, 1995.

Shepard, T., *Te Measurements in Open- and Closed-Geometry Long-Scale-Length Laser Plasmas via Isoelectronic X-Ray Spectralline Ratios,* Lawrence Livermore National Laboratory, Livermore, CA, UCRL-JC-116180 (1995); *Rev. Sci. Inst.* **66**(1), 749–751 (1995).

Shore, B. W., Feit, M. D., Perry, M. D., Boyd, B., Britten, J., and Li, L., *Diffractive Coherence in Multilayer Dielectric Gratings,* Lawrence Livermore National Laboratory, Livermore, CA, UCRL-JC-120189 ABS (1995). Prepared for the *Seventh Rochester Conf on Coherence and Quantum Optics,* Rochester, NY, Jun 7–10, 1995.

Shore, B. W., Feit, M. D., Perry, M. D., Boyd, R. D., Britten, J. A., and Li, L., *Diffractive Coherence in Multilayer Dielectric Gratings,* Lawrence Livermore National Laboratory, Livermore, CA, UCRL-JC-120189 (1995). Prepared for *7th Rochester Conf on Coherence & Quantum Optics,* Rochester, NY, Jun 7–10, 1995.

Shore, B. W., Feit, M. D., Perry, M. D., Boyd, R. D., Britten, J. A., and Li, L., *Electric Field Enhancement in Metallic and Multilayer Dielectric Gratings,* Lawrence Livermore National Laboratory, Livermore, CA, UCRL-JC-121128 (1995). Prepared for *1st Annual Int'l Conf on Solid-State Lasers for Application to Inertial Confinement Fusion,* Monterey, CA, May 30–Jun 2, 1995.

Shore, B. W., Stuart, B. C., Britten, J. A., Feit, M. D., Rubenchik, A. M., and Perry, M. D., *Laser Induced Damage in Multilayer Dielectric Gratings due to Ultrashort Laser Pulses,* Lawrence Livermore National Laboratory, Livermore, CA, UCRL-JC-120187 ABS (1995). Prepared for the *Solid-State Lasers for Application to Inertial Confinement Fusion (ICF) 1st Annual Int'l Conf,* Monterey, CA, May 30–Jun 2, 1995.

Shore, B. W., Stuart, B. C., Feit, M. D., Rubenchik, A. M., and Perry, M. D., *Laser Induced Damage in Multilayer Dielectric Gratings due to Ultrashort Laser Pulses,* Lawrence Livermore National Laboratory, Livermore, CA, UCRL-JC-120187 (1995). Prepared for *1st Annual Int'l Conf on Solid-State Lasers for Application to Inertial Confinement Fusion,* Monterey, CA, May 30–Jun 2, 1995.

Shore, B. W., Stuart, B. C., Feit, M. D., Rubenchik, A. M., and Perry, M. D., *Laser Induced Damage in Multilayer Dielectric Gratings due to Ultrashort Laser Pulses,* Lawrence Livermore National Laboratory, Livermore, CA, UCRL-JC-120187 Rev 1 (1995). Prepared for the *1st Annual Int'l Conf on Solid-State Lasers for Application to Inertial Confinement Fusion,* Monterey, CA, May 30–Jun 2, 1995.

Skidmore, J., *High-Power CW 690 nm Al Gain P Laser-Diode Arrays,* Lawrence Livermore National Laboratory, Livermore, CA, UCRL-JC-117679 (1995); *Appl. Phys. Lett.* **66**(3), 1163–1165 (1995).

Skidmore, J., *High-Power CW Operation of Al Gain P Laser-Diode Arrays,* Lawrence Livermore National Laboratory, Livermore, CA, UCRL-JC-115945 (1995); *IEEE J. Quantum Electron.* **66**(2), 133–135 (1995).

Smolski, I., De Yoreo, J. J., Zaitseva, N. P., Lee, J. D., and Land, T. A., *Oriented Liquid Inclusions in KDP Crystals,* Lawrence Livermore National Laboratory, Livermore, CA, UCRL-JC-122011 (1995). Submitted to *Crystal Growth.*

Still, C. H., Berger, R. L., Langdon, A. B., Miller, D. S., and Williams, E. A., *Nonlinear Eulerian Hydrodynamics in 3D,* Lawrence Livermore National Laboratory, Livermore, CA, UCRL-JC-121122 ABS (1995). Prepared for the *37th Annual Mtg of the American Physical Society Div of Plasma Physics,* Louisville, KY, Nov 6–10, 1995.

Stolz, C., Genin, F., Kozlowski, M., Lalazari, R., and Wu, Z., *Influence of Microstructure on Laser Damage Threshold of IBS Coatings,* Lawrence Livermore National Laboratory, Livermore, CA, UCRL-JC-121627 ABS (1995). Prepared for the *Annual Symp on Optical Materials for High Power Lasers,* Boulder, CO, Oct 30–Nov 1, 1995.

Stolz, C., Tench, R., Kozlowski, M., and Fornier, A., *A Comparison of Nodular Defect Seed Geometries from Different Deposition Techniques,* Lawrence Livermore National Laboratory, Livermore, CA, UCRL-JC-121628 ABS (1995). Prepared for the *Annual Symp on Optical Materials for High Power Lasers,* Boulder, CO, Oct 30–Nov 1, 1995 .

Stone, G. F., *Nova Gas Target Series—Target Fabrication Reference Manual,* Lawrence Livermore National Laboratory, Livermore, CA, UCRL-MA-119389 (1995).

Stone, G. F., Rivers, C. J., Wallace, R. J., Spragge, M., *Fabrication and Testing of Gas Filled Targets for Large Scale Plasma Experiments on Nova,* Lawrence Livermore National Laboratory, Livermore, CA, UCRL-JC-119390 ABS (1995). Prepared for the *10th Target Fabrication Specialists Mtg,* Taos, NM, Feb 6–10, 1995.

Stone, G., *Fabrication and Testing of Gas Filled Targets for Large Scale Plasma Experiments on Nova,* Lawrence Livermore National Laboratory, Livermore, CA, UCRL-JC-119390 (1995). Submitted to *Fus. Tech.*

Strobel, G. L., and Haan, S. W., *Source for Indirect Drive NIF Preheat Studies,* Lawrence Livermore National Laboratory, Livermore, CA, UCRL-JC-120919 ABS (1995). Prepared for *Symp on Fusion Engineering,* Champaign, IL, Sept 30–Oct 5, 1995.

Stuart, B. C., Perry, M. D., *Laser-Induced Damage in Dielectrics with Nanosecond to Subpicosecond I. Experimental,* Lawrence Livermore National Laboratory, Livermore, CA, UCRL-JC-118156 (1995). Prepared for *Laser-Induced Damage in Optical Materials Conf,* Boulder, CO, Oct 24–26, 1994.

Stuart, B. C., Perry, M. D., Rubenchik, A. M., *Laser-Induced Damage in Dielectrics with Nanosecond to Subpicosecond Pulses,* Lawrence Livermore National Laboratory, Livermore, CA, UCRL-JC-118175 ABS & SUM (1995). Prepared for *CLEO '95,* Baltimore, MD, May 15–19, 1995.

Stuart, B., *Broadband Amplification in Ti:Sapphire Beyond 1 μm,* Lawrence Livermore National Laboratory, Livermore, CA, UCRL-JC-115176 (1995); *IEEE J. Quant. Elect.* **31**(3), 528–538 (1995).

Stuart, B., Herman, S., and Perry, M. D., *Chirped-Pulse Amplification in Ti-Sapphire Beyond 1 μm,* Lawrence Livermore National Laboratory, Livermore, CA, UCRL-JC-115176 (1995); *IEEE J. Quantum Electron.* **31**(3), 528–538 (1995).

Stuart, B., *Laser Induced Damage in Dielectrics with Nanosecomd to Subpicosecond Pulses,* Lawrence Livermore National Laboratory, Livermore, CA, UCRL-JC-118175 (1995); *Phys. Rev. Lett.* **74**(3), 2248–2251 (1995).

Suter, L. J., Hauer, A. A., Ress, D. B., Hsing, W. W., Thiessen, A. R., Delameter, N., Powers, L. V., Landon, O. L., Turner, R. E., *Modeling of Nova's Symmetry Scaling Data Base,* Lawrence Livermore National Laboratory, Livermore, CA, UCRL-JC-117361 Rev 1 (1994); *Phys Rev Lett* **73**, 2328–2331 (1994).

Suter, L. J., Kauffman, R. L., Darrow, C. B., Hauer, A. A., Kornblum, H., Landen, O. L., Orzechowski, T. J., Phillion D. W., Porter, J. L., Powers, L. V., Rosen, M. D., and Thiessen, A. R., *Radiation Drive in Laser Heated Hohlraums,* Lawrence Livermore National Laboratory, Livermore, CA, UCRL-JC-121483 ABS (1995). Prepared for the *37th Annual Mtg of the American Physical Society Div of Plasma Physics,* Louisville, KY, Nov 6–10, 1995.

Suter, L. J., Pollaine, S. M., and Powers, L. V., *Power Balance and Radiation Production in Laser Heated Hohlraums,* Lawrence Livermore National Laboratory, Livermore, CA, UCRL-JC-120790 ABS (1995). Prepared for *25th Annual Anomalous Absorption Conf,* Aspen, CO, May 27–Jun 1, 1995.

Sutton, S. B., and Albrecht, G. F., *Thermal Management in IFE Slab Amplifiers,* Lawrence Livermore National Laboratory, Livermore, CA, UCRL-JC-120220 ABS (1995). Prepared for the *Solid-State Lasers for Application to Inertial Confinement Fusion (ICF) 1st Annual Int'l Conf,* Monterey, CA, May 30–Jun 2, 1995.

Sutton, S. B., and Albrecht, G. F., *Thermal Management in Inertial Fusion Energy Slab Amplifiers,* Lawrence Livermore National Laboratory, Livermore, CA, UCRL-JC-120220 (1995). Prepared for the *1st Annual Int'l Conf on Solid-State Lasers for Application to Inertial Confinement Fusion,* Monterey, CA, May 30–Jun 2, 1995.

T

Tabak, M., *Old and New Trick to Symmetrize Hohlraum Radiation,* Lawrence Livermore National Laboratory, Livermore, CA, UCRL-JC-121474 ABS (1995). Prepared for the *37th Annual Mtg of the American Physical Society Div of Plasma Physics,* Louisville, KY, Nov 6–10, 1995.

Tabak, M., *What Is the Role of Tritium Poor Fuels in ICF?* Lawrence Livermore National Laboratory, Livermore, CA, UCRL-JC-118168 Rev. 1 (1995). Submitted to *Nuclear Fusion.*

Tench, R. J., Kozlowski, M. R., Chow, R., and Stolz, C., *Structural Characterization of Nodular Defects in Multi-Layer Optical Coatings,* Lawrence Livermore National Laboratory, Livermore, CA, UCRL-JC-120202 ABS (1995). Prepared for the *Int'l Conf on Metallurgical Coatings and Thin Films,* San Diego, CA, April 24–28, 1995.

Tench, R., Kozlowski, M. R., Cohen, J., and Chow, R., *Laser Damage and Conditioning of Defects in Optical Coatings,* Lawrence Livermore National Laboratory, Livermore, CA, UCRL-JC-119903 EXT ABS (1995). Prepared for the *Optical Interference Coatings '95 Optical Society of America,* Tucson, AZ, Jun 5–9, 1995.

Thomas, I. M., Dixit, S. N., Rushford, M. C., *Preparation of Random Phase Plates for Laser Beam Smoothing,* Lawrence Livermore National Laboratory, Livermore, CA, UCRL-JC-118504 (1995). Prepared for *Annual Symp on Optical Materials for High Power Lasers,* Boulder, CO, Oct 26–29, 1994.

Thomas, I. M., *Preparation of Dielectric HR Mirrors from Colloidal Oxide Suspensions Containing Organic Polymer Binders,* Lawrence Livermore National Laboratory, Livermore, CA, UCRL-JC-115940 (1994). Prepared for *SPIE Int'l Symposia on Optical Instruments,* San Diego, CA, Jul 25–29, 1994.

Tietbohl, G., Dorsey, G., Frank, N., Marion, J., Murray, J., Murray, J., Riddle, B., Roberts, D., Sutton, S., and Taylor, J., *Incident Analysis Report; Failure of a Spatial Filter Lens on the Beamlet Laser at LLNL on 4/3/95,* Lawrence Livermore National Laboratory, Livermore, CA, UCRL-ID-120912 (1995).

Tobin, M., Anderson, A., Diaz de la Rubia, T., Peterson, P., Peterson, B., and Perlado, M., *Phenomenology of Chamber Responses to Target Emissions: NIF Experiments,* Lawrence Livermore National Laboratory, Livermore, CA, UCRL-JC-121293 ABS (1995). Prepared for the *16th Institute for Electrical and Electronic Engineers/Nuclear and Plasma Sciences Society Symp on Fusion Engineering,* Champaign, IL, Sept 30–Oct 5, 1995.

Tobin, M., Anderson, A., Latkowski, J., Singh, M., Marshall, C., and Bernat, T., *Physics Issues Related to the Confinement of ICF Experiments in the U.S. National Ignition Facility,* Lawrence Livermore National Laboratory, Livermore, CA, UCRL-JC-119378 (1995). Prepared for *12th Int'l Conf on Laser Interaction and Related Plasma Phenomena,* Osaka, Japan, Apr 24–28, 1995.

Tobin, M., Karpenko, V., Anderson, A., Warren, R., Garcia, R., Latkowski, J., Hagans, K., Wavrik, R., Boyes, J., *Target Area Design Basis and System Performance for the National Ignition Facility,* Lawrence Livermore National Laboratory, Livermore, CA, UCRL-JC-115583 Rev 1 (1995). Prepared for the *41st Nat'l Symp of the Amer Vacuum Soc,* Denver, CO, Oct 24–28, 1994.

Tobin, M., Logan, G., Schrock, V., Tokheim, R., Bangerter, R., Schultz, K., De La Rubia, T., Abdous, M., *Contributions of the National Ignition Facility to the Development of Inertial Fusion Energy,* Lawrence Livermore National Laboratory, Livermore, CA, UCRL-JC-117698 Rev 1 (1994). Prepared for the *3rd Int'l Symp on Fusion Nuclear Tech,* Los Angeles, CA, Jun 27–Jul 1, 1994.

Tobin, M., Marshall, C., Latkowski, J., Bernat, T., Anderson, A., *Physics Issues Related to the Confinement of ICF Experiments in the U.S. National Ignition Facility,* Lawrence Livermore National Laboratory, Livermore, CA, UCRL-JC-119378 ABS (1995). Prepared for the *12th Int'l Conf on Laser Interaction and Related Plasma Phenomena,* Osaka, Japan, Apr 24–28, 1995.

Trebes, J. E., Barbee, T. W., Cauble, R., Celliers, P., Da Silva, L., Decker, C., London, R., Moreno, J. C., Ress, D., Wan, A. S., and Weber, F., *Soft X-Ray Interferometry,* Lawrence Livermore National Laboratory, Livermore, CA, UCRL-JC-121631 ABS (1995). Prepared for the *Synchrotron Research and Instrumentation '95 Mtg of American Physical Society X-Ray Centennial Symp,* Argonne, IL, Oct 18–20, 1995.

V

Van Wonterghem, B. M., Barker, C. E., Campbell, J. H., Caird, J. A., Murray, J. R., and Speck, D. R., *Recent Results of the National Ignition Facility Beamlet Demonstration Project,* Lawrence Livermore National Laboratory, Livermore, CA, UCRL-JC-120917 (1995). Prepared for the *1st Annual Int'l Conf on Solid-State Lasers for Application to Inertial Confinement Fusion,* Monterey, CA, May 30–Jun 2, 1995.

Van Wonterghem, B. M., Barker, C. S., Campbell, J. H., Smith, I., Murray, J. R., Burkhart, S. C., Speck, D. R., *Laser Performance of the National Ignition Facility Beamlet Demonstration Project,* Lawrence Livermore National Laboratory, Livermore, CA, UCRL-JC-118844 ABS & SUM (1995). Prepared for *CLEO '95,* Baltimore, MD, May 22–26, 1995.

Van Wonterghem, B. M., Caird, J. A., Barker, C. E., Campbell, J. H., Murray, J. R., and Speck, D. R., *Performance of the Beamlet Laser, a Testbed for the National Ignition Facility,* Lawrence Livermore National Laboratory, Livermore, CA, UCRL-JC-121272 (1995). Prepared for *Laser Optics '95,* St Petersburg, Russia, Jun 27–Jul 1 , 1995.

Van Wonterghem, B. M., Caird, J. A., Barker, C. S., Campbell, J. H., Murray, J. R., and Speck, D. R., *Recent Results of the National Ignition Facility Beamlet Demonstration Project,* Lawrence Livermore National Laboratory, Livermore, CA, UCRL-JC-120917 ABS (1995). Prepared for *1st Annual Int'l Conf on Solid-State Lasers for Application to Inertial Confinement Fusion,* Monterey, CA, May 30–Jun 2, 1995.

Van Wonterghem, B. M., Campbell, J. R., Campbell, J. H., Speck, D. R., Barker, C. E., Smith, I. C., Browning, D. F., and Behrendt, W. C., *System Description and Initial Performance Results for Beamlet,* Lawrence Livermore National Laboratory, Livermore, CA, UCRL-ID-119933 (1995).

Vogel, D., *High-Pressure Positron-Sensitive Proportional Counter,* Lawrence Livermore National Laboratory, Livermore, CA, UCRL-JC-117449 (1995); *Rev. Sci. Inst.* **66**(1), 776–778 (1995).

Vu, B.-T. V., Landen, O. L., and Szoke, A., *Time-Resolved Probing of Femtosecond-Laser-Produced Plasmas in Transparent Solids by Electron Thermal Transport,* Lawrence Livermore National Laboratory, Livermore, CA, UCRL-JC-117456 (1995); *Phys. Plasmas* **2**(2), 476-485 (1995).

Vu, B.-T. V., Lee, R. W., Landen, O. L., and Price, D. F., *Temporally and Radially-Resolved Femtosecond Optical Measurement of Solid Density Plasma Reflectivities and Transmissivities,* Lawrence Livermore National Laboratory, Livermore, CA, UCRL-JC-118332 (1995); *J. Quant. Spectros. & Radiat. Transfer* **54**(1/2), 413–418 (1995).

W

Wallace, R. J., McEachern, R. L., Behymer, R., Mance, S., Wilcox, W. W., *Imposed Perturbations of ICF Capsules and 3D R-T Target Foils Using Excimer Laser Ablation,* Lawrence Livermore National Laboratory, Livermore, CA, UCRL-JC-119393 ABS (1995). Prepared for the *10th Target Fabrication Specialists Mtg,* Taos, NM, Feb 6–10, 1995.

Walton, C. C., Genin, F. Y., Chow, R., Kozlowski, M. R., Piece, E., and Loomis, G., *Laser Damage Threshold Dependence on Overlayer Film Thickness for Non-normal Incidence Hafnia-Silica High Reflectors,* Lawrence Livermore National Laboratory, Livermore, CA, UCRL-JC-121638 ABS (1995). Prepared for the *Annual Symp on Optical Materials for High Power Lasers,* Boulder, CO, Oct 30–Nov 1, 1995.

Wang, P., Orzechowski, T. J., MacFarlane, J. J., and Moses, G. A., *An Investigation of the Opacity of High-Z Mixtures and Implications for ICF Hohlraums Design,* Lawrence Livermore National Laboratory, Livermore, CA, UCRL-JC-121500 ABS (1995). Prepared for the *37th Annual Mtg of the American Physical Society Div of Plasma Physics,* Louisville, KY, Nov 6–10, 1995.

Warhus, J., Mast, J., and Nelson, S., *Imaging Radar for Bridge Deck Inspection,* Lawrence Livermore National Laboratory, Livermore, CA, UCRL-JC-120901 (1995). Prepared for *Nondestructive Evaluation of Aging Bridges and Highways,* Oakland, CA, Jun 6–8, 1995.

Warner, B. E., Boley, C. D., Chang, J. J., Dragon, E. P., Havstad, M. A., and McLean II, W., *Industrial Applications of High Power Copper Vapor Lasers,* Lawrence Livermore National Laboratory, Livermore, CA, UCRL-JC-120702 ABS (1995). Prepared for *NATO Advanced Research Workshop on Pulsed Metal Vapour Lasers,* St Andrews, Scotland, Aug 7–10, 1995.

Warner, B. E., Boley, C. D., Chang, J. J., Dragon, E. P., Havstad, M. A., Martinez, M., and McLean, W., *Ablative Material Removal Utilizing the Copper Vapor Laser,* Lawrence Livermore National Laboratory, Livermore, CA, UCRL-JC-121130 (1995). Prepared for *LEOS '95 8th Annual Mtg Institute of Electrical and Electronic Engineers,* San Francisco, CA, Oct 30–Nov 2, 1995.

Warner, B., Boley, C., Chang, J., Dragon, E., Havstad, M., Martinez, M., and McLean II, W., *Ablative Material Removal Utilizing the Copper Vapor Laser,* Lawrence Livermore National Laboratory, Livermore, CA, UCRL-JC-121130 ABS (1995). Prepared for *Lasers and Electro Optics Society '95 8th Annual Mtg,* San Francisco, CA, Oct 30–Nov 2, 1995.

Warren, R., *NIF Target Fill, Transport and Insertion Cryostat,* Lawrence Livermore National Laboratory, Livermore, CA, UCRL-ID-118528 (1995).

Weber, S. V., Dalhed, S., Eimerl, D., Key, M. H., and Verdon, C. P., *Hydrodynamic Stability of NIF Direct Drive Capsules,* Lawrence Livermore National Laboratory, Livermore, CA, UCRL-JC-121451 ABS (1995). Prepared for the *37th Annual Mtg of the American Physical Society Div of Plasma Physics,* Louisville, KY, Nov 6–10, 1995.

Weber, S. V., Dalhed, S., Eimerl, D., Key, M. H., and Verdon, C. P., *NIF Direct Drive Capsule Design Studies,* Lawrence Livermore National Laboratory, Livermore, CA, UCRL-JC-120759 ABS (1995). Prepared for *25th Annual Anomalous Absorption Conf,* Aspen, CO, May 27–Jun 1, 1995.

Weber, S. V., Munro, D., *Electron Thermal Conduction in LASNEX,* Lawrence Livermore National Laboratory, Livermore, CA, UCRL-ID-119541 (1995).

Weber, S. V., Remington, B. A., Nash, J. K., Wilson, B. G., Haan, S. W., *Modeling of Nova Indirect Drive Rayleigh–Taylor Experiments,* Lawrence Livermore National Laboratory, Livermore, CA, UCRL-JC-116225 Rev. 1 (1994); *Phys Plasmas* **1**, 3652–3661 (1994).

Wegner, P. J., and Feit, M. D., *Characterization and Suppression of Self-Phase Modulation in a Commercial Modelocked and Q-Switched Nd:YLF Oscillator,* Lawrence Livermore National Laboratory, Livermore, CA, UCRL-JC-119930 (1995). Submitted to *Opt. Commun.*

Wegner, P. J., Feit, M. D., Fleck, A. J., and Eimerl, D., *Measurement of the Bespalov–Talanov Gain Spectrum in a Dispersive Medium with Large* N_2, Lawrence Livermore National Laboratory, Livermore, CA, UCRL-JC-121196 (1995). Prepared for *1st Annual Int'l Conf on Solid-State Lasers for Application to Inertial Confinement Fusion,* Monterey, CA, May 30-Jun 2, 1995.

Wegner, P., and Feit, M. D., *High-Power Narrow-Band Pulses with Wavelength Tunable about 1.053 μm from a Synchronously-Pumped Optical Parametric Oscillator,* Lawrence Livermore National Laboratory, Livermore, CA, UCRL-JC-120908 (1995). Submitted to *Appl. Opt.*

Wegner, P., Feit, M., *Observation of Spectral Broadening in a Commercial Mode Locked and Q-Switched Nd:YLF Oscillator,* Lawrence Livermore National Laboratory, Livermore, CA, UCRL-ID-119155 (1995).

Westenskow, G. A., Caporaso, G. J., Chen, Y.-J., Houck, T. L., Newton, M., Yu, S. S., Chattopadhyay, S., Sessler, A. M., Reginato, L., Peters, C., and Wurtele, J. S., *Relativistic Klystron Two-Beam Accelerator Research Proposal Part A,* Lawrence Livermore National Laboratory, Livermore, CA, UCRL- PROP-119356 Part A (1995).

Wilcox, R. B., and Browning, D. F., *Fiber Lasers for Fusion Laser Oscillator Systems,* Lawrence Livermore National Laboratory, Livermore, CA, UCRL-JC-120512 ABS (1995). Prepared for the *Solid-State Lasers for Application to Inertial Confinement Fusion (ICF) 1st Annual Int'l Conf,* Monterey, CA, May 30–Jun 2, 1995.

Wilcox, R. B., Browning, D. F., Burkhart, S. C., and VanWonterghem, B. W., *Optical Pulse Generation Using Fiber Lasers and Integrated Optics,* Lawrence Livermore National Laboratory, Livermore, CA, UCRL-JC-120517 (1995). Prepared for the *Int'l Conf on Integrated Optics and Optical Fibre Communication,* Tokyo, Japan, Jun 26–30, 1995.

Wilcox, R. B., Van Wonterghem, B. W., Davin, J. M., Burkhart, S. C., *Multiple-Beam Pulse Shaping and Preamplification,* Lawrence Livermore National Laboratory, Livermore, CA, UCRL-JC-117491 (1995). Prepared for *IAEA Conf,* Paris, France, Nov 14–18, 1994.

Wilemski, G., and Wyslouzil, B. E., *Binary Nuclear Kinetics 1. Self-Consistent Size Distribution,* Lawrence Livermore National Laboratory, Livermore, CA, UCRL-JC-118536 Pt 1 (1995); *J. Chem. Phys.* **103**(3), 1127–1136 (1995).

Wilemski, G., Boone, T., Cheung, L., Nelson, D., and Cook, R., *Prediction of Phase Separation During the Drying of Polymer Shells,* Lawrence Livermore National Laboratory, Livermore, CA, UCRL-JC-117329 (1995). Submitted to *Fusion Tech.*

Wilemski, G., Cook, R., Cheung, L., Nelson, D., Boone, T., *Prediction of Phase Separation During the Drying of Polymer Shells,* Lawrence Livermore National Laboratory, Livermore, CA, UCRL-JC-117329 ABS Rev 1 (1995). Prepared for the *10th Target Fabrication Specialists Mtg,* Taos, NM, Feb 6–10, 1995.

Wilemski, G., *Kelvin Equation and Self-Consistent Nucleation Theory,* Lawrence Livermore National Laboratory, Livermore, CA, UCRL-JC-118535 (1995). Submitted to *J of Chemical Physics.*

Wilks, S. C., and Kruer, W. L., *Nonlinear Aspects of SBS in Multi-Species Plasmas,* Lawrence Livermore National Laboratory, Livermore, CA, UCRL-JC-120882 ABS (1995). Prepared for *25th Annual Anomalous Absorption Conf,* Aspen, CO, May 27–Jun 1, 1995.

Wilks, S. C., *Critical Issues Regarding Ultra-Intense, Short-Pulse Laser-Plasma Interactions in the Fast Ignitor,* Lawrence Livermore National Laboratory, Livermore, CA, UCRL-JC-120885 ABS (1995). Prepared for *1995 Canadian Association of Physicists' 50th Anniversary Congress CAM-95,* Quebec City, Quebec, Canada, Jun 11–16, 1995.

Wilks, S. C., *Introduction to Ultra-Intense, Short Pulse Laser–Plasma Interactions,* Lawrence Livermore National Laboratory, Livermore, CA, UCRL-JC-121611 ABS (1995). Prepared for *Plasma Physics and Technology,* La Jolla, CA, Aug 8–18, 1995.

Wilks, S. C., Kruer, W. L., Denavit, J., Estabrook, K., Hinkel, D. E., Kalantar, D., Langdon, A. B., MacGowan, B. J., Montgomery, D. S., and Williams, E. A., *Nonlinear Theory and Simulations of Stimulated Brillouin Backscatter in Multispecies Plasmas,* Lawrence Livermore National Laboratory, Livermore, CA, UCRL-JC-117313; *Phys. Rev. Lett.* **74**(25), 5048–5051 (1995).

Wilks, S. C., Kruer, W. L., Hammel, B., Hammer, J., Tabak, M., and Young, P. E., *Fast Ignitor Plasma Physics Issues,* Lawrence Livermore National Laboratory, Livermore, CA, UCRL-JC-120884 ABS (1995). Prepared for *25th Annual Anomalous Absorption Conf,* Aspen, CO, May 27–Jun 1, 1995.

Wilks, S. C., Kruer, W. L., Williams, E. A., Amendt, P., and Eder, D. C., *Stimulated Raman Backscatter in Ultra-Intense, Short Pulse Laser–Plasma Interactions,* Lawrence Livermore National Laboratory, Livermore, CA, UCRL-JC-118111 (1994); *Phys. Plasmas* **2**(1), January 1995.

Wilks, S. C., Kruer, W. L., Young, P. E., Hammer, J., and Tabak, M., *Ultra-Intense, Short Pulse Laser–Plasma Interactions with Applications to the Fast Ignitor,* Lawrence Livermore National Laboratory, Livermore, CA, UCRL-JC-121326 (1995). Prepared for *12th Int'l Conf on Laser Interaction and Related Plasma Phenomena,* Osaka, Japan, Apr 24–28, 1995.

Wilks, S. C., Kruer, W. L., Young, P. E., Tabak, M., Hammer, J., and Feit, M. D., *Laser–Plasma Interactions Relevant to the Fast Ignitor,* Lawrence Livermore National Laboratory, Livermore, CA, UCRL-JC-121478 ABS (1995). Prepared for the *37th Annual Mtg of the American Physical Society Div of Plasma Physics,* Louisville, KY, Nov 6–10, 1995.

Wilks, S. C., Kruer, W., Hammer, J., Tabak, M., and Young, P., *Fast Ignitor Plasma Physics Issues,* Lawrence Livermore National Laboratory, Livermore, CA, UCRL-JC-120884 ABS Rev 1 (1995). Prepared for *Plasma Physics and Technology,* La Jolla, CA, Aug 8–18, 1995.

Wilks, S., Kruer, W., Perry, M., Young, P., Tabak, M., and Hammel, B., *Ultra-Intense, Short Pulse Laser-Plasma Interactions With Applications to Advanced Fusion Concepts,* Lawrence Livermore National Laboratory, Livermore, CA, UCRL-JC-119578 ABS (1994). Prepared for the *12th Int'l Conf LIRPP,* Osaka, Japan, Apr 24–28, 1994

Wilks, S., *Stimulated Raman Backscatter in Ultraintense, Short Pulse Laser–Plasma Interactions,* Lawrence Livermore National Laboratory, Livermore, CA, UCRL-JC-118111 (1995); *Phys. Plasmas* **2**(1), 274–279 (1995).

Williams, E. A., and Hinkel, D. E., *Beam Steering by Filamentation in Flowing Plasmas,* Lawrence Livermore National Laboratory, Livermore, CA, UCRL-JC-120770 ABS (1995). Prepared for *25th Annual Anomalous Absorption Conf,* Aspen, CO, May 27–Jun 1, 1995.

Williams, E. A., and Hinkel, D. E., *Laser Filamentation and Deflection in a Transverse Plasma Flow,* Lawrence Livermore National Laboratory, Livermore, CA, UCRL-JC-121495 ABS (1995). Prepared for the *37th Annual Mtg of the American Physical Society Div of Plasma Physics,* Louisville, KY, Nov 6–10, 1995.

Williams, E. A., *Nonlinear Frequency Shifts and Harmonic Generation in Finite Amplitude Ion Acoustic Waves,* Lawrence Livermore National Laboratory, Livermore, CA, UCRL-JC-119609 ABS (1995). Prepared for the *Second Canadian Int'l Workshop zon High-Field Laser Plasma Interactions Physics,* Banff, Canada, Feb 22–25, 1995.

Williams, E. A., *Nonlinear Frequency Shifts and Harmonic Generation in Finite Amplitude Ion Acoustic Waves,* Lawrence Livermore National Laboratory, Livermore, CA, UCRL-JC-120769 ABS (1995). Prepared for *25th Annual Anomalous Absorption Conf,* Aspen, CO, May 27-Jun 1, 1995.

Williams, E. A., *Parametric Instabilities in Inertial Confinement Fusion: Basic Theory,* Lawrence Livermore National Laboratory, Livermore, CA, UCRL-JC-121612 ABS (1995). Prepared for *Plasma Physics and Technology,* La Jolla, CA, Aug 8–18, 1995.

Williams, E., *The Frequency and Damping of Ion Acoustic Waves in Hydrocarbon (CH) and Two-Ion-Species Plasmas,* Lawrence Livermore National Laboratory, Livermore, CA, UCRL-JC-118343 (1995); *Phys. Plasmas* **2**(1), 129–138 (1995).

Wolfe, C. R., and Lawson, J. K., *The Measurement and Analysis of Wavefront Structure from Large Aperture ICF Optics,* Lawrence Livermore National Laboratory, Livermore, CA, UCRL-JC-121148 (1995). Prepared for *1st Annual Int'l Conf on Solid-State Lasers for Application to Inertial Confinement Fusion,* Monterey, CA, May 30–Jun 2, 1995.

Wolfe, C. R., Lawson, J. K., Aikens, D. M., and English, R. E., *A Database of Wavefront Measurements for: Laser System Modeling, Optical Component Development and Fabrication Process Qualification,* Lawrence Livermore National Laboratory, Livermore, CA, UCRL-JC-120767 (1995). Prepared for *Interferometry VII Applications,* Tucson, AZ, Jul 14, 1995.

Wolfe, C. R., Lawson, J. K., Kellam, M., Maney, R. T., and Demiris, A., *Measurement of Wavefront Structure from Large Aperture Optical Components by Phase Shifting Interferometry,* Lawrence Livermore National Laboratory, Livermore, CA, UCRL-JC-121471 (1995). Prepared for the *Society of Photo-Optical Instrumentation Engineers' 1995 Int'l Symp on Optical Science, Engineering, and Instrumentation,* San Diego, CA, Jul 9–14, 1995.

Wolfe, C. R., Lawson, J. K., Manes, K. R., Aikens, D. M., and English, R. E., *Specification of Optical Components Using the Power Spectral Density Function,* Lawrence Livermore National Laboratory, Livermore, CA, UCRL-JC-120920 ABS (1995). Prepared for *Society of Photo-Optical Instrumentation Engineers' 40th Annual Mtg,* San Diego, CA, Jul 9–14, 1995.

Wood-Vasey, M., Remington, B. A., Kane, J., Arnett, D., Dearborn, D., Rubenchik, A., Glendinning, S. G., Budil, K. S., Castor, J., Woosley, S., Liang, E. P., and London, R., *A Supernova-Relevant Hydrodynamic Instability Experiment on the Nova Laser,* Lawrence Livermore National Laboratory, Livermore, CA, UCRL-JC-121488 ABS (1995). Prepared for the *37th Annual Mtg of the American Physical Society Div of Plasma Physics,* Louisville, KY, Nov 6–10, 1995.

Woods, B., Runkel, M., De Yoreo, J., and Kozlowski, M., *High Resolution Imagery of Defects and the Morphology of Laser-Induced Damage in KDP Crystals,* Lawrence Livermore National Laboratory, Livermore, CA, UCRL-JC-120204 ABS (1995). Prepared for the *Solid-State Lasers for Application to Inertial Confinement Fusion (ICF) 1st Annual Int'l Conf,* Monterey, CA, May 30–Jun 2, 1995.

Woods, B., Runkel, M., Yan, M., De Yoreo, J., and Kozlowski, M., *Optical Scatter as a Diagnostic Tool for Studying Bulk Defects Which Cause Laser Damage in Conventional and Rapid Growth KDP and DKDP,* Lawrence Livermore National Laboratory, Livermore, CA, UCRL-JC-121652 (1995). Prepared for the *Society of Photo-Optical Instrumentation Engineers San Diego 1995,* San Diego, CA, Jul 10–14, 1995.

Woodworth, J. G., Kreisler, M. N., and Kerman, A. K., *A Free Wave Accelerator,* Lawrence Livermore National Laboratory, Livermore, CA, UCRL-JC-120712 (1995). Prepared for *Tamura Symp,* Austin, TX, Nov 14–16, 1995.

Wu, C. H., Zory, P. S., and Emanuel, M. A., *Characterization of Thin p-Clad InGaAs Single Quantum Wall Lasers,* Lawrence Livermore National Laboratory, Livermore, CA, UCRL-JC-120237 (1995). Submitted to *Photonics Technology Letters.*

Wyslouzil, B. E., and Wilemski, G., *Binary Nucleation Kinetic 2. Numerical Solution of the Birth-Death Equations,* Lawrence Livermore National Laboratory, Livermore, CA, UCRL-JC-118536 (1995); *J. Chem. Phys.* **103**(3), 1137–1151 (1995).

Y

Yan, M., De Yoreo, J., Zaitseva, N., and Torres, R., *Impurity Contamination in Fast Grown KDP,* Lawrence Livermore National Laboratory, Livermore, CA, UCRL-JC-122004 ABS (1995). Prepared for the *1995 Boulder Damage Symp,* Boulder, CO, Oct 30–Nov 1, 1995.

Yan, M., Rothberg, L., Galvin, M. E., Miller, T. M., and Padimitrakopoulos, F., *Defects and Morphological Concerns in Electroluminescent Polymers,* Lawrence Livermore National Laboratory, Livermore, CA, UCRL-JC-121620 (1995). Prepared for the *27th Int'l Society for the Advancement of Materials and Process Engineering,* Albuquerque, NM, Oct 9–12, 1995.

Yang, T. Y. B., Kruer, W. L., More, R. M., *Absorption of Laser Light in Overdense Plasmas by Sheath Inverse Bremsstrahlung,* Lawrence Livermore National Laboratory, Livermore, CA, UCRL-JC-119068 (1995). Prepared for *American Physical Soc 36 Annual Mtg,* Minneapolis, MN, Nov 7–11, 1994.

Yang, T.-Y. B., Kruer, W. L., and Langdon, A. B., *Collisionless Absorption of Light Waves Incident on Overdense Plasmas with Steep Density Gradients,* Lawrence Livermore National Laboratory, Livermore, CA, UCRL-JC-121624 (1995). Prepared for *Plasma Physics and Technology,* La Jolla, CA, Aug 8–18, 1995.

Yang, T.-Y. B., Kruer, W. L., and Langdon, A. B., *Collisionless Absorption of Light Waves Obliquely Incident on Overdense Plasmas with Steep Density Gradients,* Lawrence Livermore National Laboratory, Livermore, CA, UCRL-JC-121296 ABS (1995). Prepared for the *37th Annual Mtg of the American Physical Society Div of Plasma Physics,* Louisville, KY, Nov 6–10, 1995.

Yang, T.-Y. B., Kruer, W. L., Langdon, A. B., and More, R. M., *Collisionless Absorption of Light Waves Obliquely Incident on Overdense Plasmas with Sharp Density Gradients,* Lawrence Livermore National Laboratory, Livermore, CA, UCRL-JC-120772 ABS (1995). Prepared for *25th Annual Anomalous Absorption Conf,* Aspen, CO, May 27–Jun 1, 1995.

Yang, T.-Y. B., Kruer, W. L., More, R. M., and Langdon, A. B., *Absorption of Laser Light in Overdense Plasmas by Sheath Inverse Bremsstrahlung,* Lawrence Livermore National Laboratory, Livermore, CA, UCRL-JC-119068 (1995); *Phys. Plasmas* **2**(8), 3146–3154 (1995).

Young, P., *Experimental Observation of Filamentation Growth in Laser-Produced Plasmas,* Lawrence Livermore National Laboratory, Livermore, CA, UCRL-JC-119827 (1995); *Phys. Plasmas* **2**(7), 2815–2824 (1995).

Young, P., Foord, M. E., Hammer, J. H., Kruer, W. L., Tabak, M., and Wilks, S. C., *Time-Dependent Channel Formation in a Laser-Produced Plasma,* Lawrence Livermore National Laboratory, Livermore, CA, UCRL-JC-120577 (1995); *Phys. Rev. Lett.* **75**(8), 1082–1085 (1995).

Young, P., Hammer, J. H., Wilks, S. C., and Kruer, W. L., *Laser Beam Propagation and Channel Formation in Underdense Plasmas,* Lawrence Livermore National Laboratory, Livermore, CA, UCRL-JC-119828 (1995); *Phys. Plasmas* **2**(7), 2825–2834 (1995).

Yu, S. S., Deadrick, F., Goffeney, N., Henestroza, E., Houck, T. L., Li, H., Peters, C., Reginato, L., Sessler, A. M., Vanecek, D., and Westenskow, G. A., *Relativistic Klystron Two-Beam Accelerator Research Proposal Part B,* Lawrence Livermore National Laboratory, Livermore, CA, UCRL-PROP-119356 Part B (1995).

Z

Zaitseva, N. P., De Yoreo, J. J., Montgomery, K. E., Vital, R. L., De Haven, M. R., and Richardson, M. J., *The Effect of Impurities at Rapid Growth of KDP Crystals,* Lawrence Livermore National Laboratory, Livermore, CA, UCRL-JC-120242 ABS (1995). Prepared for *14th Conf on Crystal Growth and Epitaxy,* Fallen Leaf Lake, CA, Jun 4–7, 1995.

Zakharenkov, Y. A., Hay, R. G., Darrow, C. B., Fews, A. P., Hammel, B. A., Nguyen, H., and Perry, M. D., *Energetic Ions, Produced in Short-Pulse-Laser Interaction with Solid Targets,* Lawrence Livermore National Laboratory, Livermore, CA, UCRL-JC-120762 ABS (1995). Prepared for *25th Annual Anomalous Absorption Conf,* Aspen, CO, May 27–Jun 1, 1995.

ARTICLES BY AUTHOR